



PHYSICAL CHEMISTRY 2010

**10th International Conference on
Fundamental and Applied Aspects of
Physical Chemistry**

Proceedings

**The Conference is dedicated to the
100th Anniversary of the academician Pavle Savić birthday
and
20th Anniversary of the Society of Physical Chemists of Serbia**

**21-24 September 2010
B E L G R A D E**

ISBN 978-86-82475-17-0

Title: Physical Chemistry 2010. (Proceedings)

Editors: S. Anić and Ž. Čupić

Published by: Society of Physical Chemists of Serbia, Studentski trg 12-16
P.O.Box 47, 11158 Beograd, 218, Srbija

Publisher: Society of Physical Chemists of Serbia

For Publisher: S. Anić, President of Society of Physical Chemists of Serbia

Printed by: “Jovan” Printing and Publishing Company; 200 Copies;

Number of pages 16 + 388, **Format:** B5; Printing finished in September
2010.

Text and Layout: “Jovan”

200 - Copy printing

CONTENTS

VOLUME I

Organizers	IV
Committees	V
Sponsors	VII
Twenty years of Society of physical chemists of Serbia	VIII
Plenary lectures	1
Chemical Thermodynamics	35
Spectroscopy, Molecular Structure and Physical Chemistry of Plasma	55
Kinetics and Catalysis	91
Nonlinear Dynamics	191
Electrochemistry	263
Biophysical Chemistry, Photochemistry and Radiation Chemistry	299

VOLUME II

Radiochemistry and Nuclear Chemistry	389
Material Science	397
Solid State Physical Chemistry	451
Macromolecular Physical Chemistry	471
Environmental Protection, Forensic Sciences and Pharmaceutical Physical Chemistry	525
Phase Boundaries	621
Complex Compounds	633
General Physical Chemistry	647
Education	683
Author index	695
Participating Institutions	703

The Society of Physical Chemists of Serbia

in co-operation with

Institute of Catalysis, Bulgarian Academy of Sciences

*Boreskov Institute of Catalysis, Siberian Branch of
the Russian Academy of Sciences*

Faculty of Physical Chemistry, University of Belgrade, Serbia

*Institute of Chemistry Technology and Metallurgy, University of
Belgrade, Serbia*

Vinča Institute, University of Belgrade, Serbia

Institute of General and Physical Chemistry, Serbia

International Organizing Committee

Chairman: S. Anić (Serbia)
Vice-chairman: N. Stepanov (Russia)
B. Adnađević (Serbia)

Members:

M. Gabrovska (Bulgaria), N. Cvijetićanin (Serbia), T. Grozdić (Serbia),
D. Jovanović (Serbia), M. Lalić (BiH), D. Marković (Serbia), B. Milosavljević
(USA), N. Miljević (Serbia), M. Mojović (Serbia), N. Ostrovski (Serbia), C. Pona
(Italy), B. Simonović (Serbia), D. Stanisavljev (Serbia), A. G. Stepanov (Russia),
V. Vasić (Serbia), N. Vukelić (Serbia), V. Vukojević (Sweden)

International Scientific Committee

Chairman: Ž. Čupić (Serbia)
Vice-chairmans: V. N. Parmon (Russia)
M. Franko (Slovenia)
V. Vasić (Serbia)

Members:

A. Antić-Jovanović (Serbia), G. Bačić (Serbia), R. Cervellati (Italy), R. Compton
(United Kingdom), V. Gaspar (Hungary), M. Jeremić (Serbia), A. L. Kawczyński
(Poland), Lj. Kolar-Anić (Serbia), S. Kuchanov (Russia), R. Leblanc (USA),
S. Mentus (Serbia), S. Milonjić (Serbia), Lj. Morozova-Roche (Sweden),
D. Moscone (Italy), J. Nedeljković (Serbia), Z. Noszticzus (Hungary), M. Perić
(Serbia), V. Petruševski (Macedonia), M. Plavšić (Serbia), G. Smulevich (Italy),
G. Schmitz (Belgium), I. Schreiber (Czech), P. Ševčík (Slovakia), N. Stepanov
(Russia), M. Trtica (Serbia), D. Veselinović (Serbia)

Local Executive Committee

Chairman: B. Adnađević
Vice-chairmans: S. Blagojević
A. Ivanović

Members:

A. Abu Rabi-Stanković, P. Banković, N. Begović, S. N. Blagojević,
N. Cvjetičanin, M. Daković, A. Đerić, A. Ignjatović, Lj. Ignjatović, A. Jović,
J. Krstić, S. Kuprešak, D. Lončarević, J. Maksimović, V. Marković, M.
Milenković, M. Milojević, Z. Mojović, B. Nedić, I. Pašti, N. Pejić, A. Popović-
Bjelić, M. Petković, N. Potkonjak, D. Ranković, R. Ranković, M. Stević,
I. Stojković, B. Šljukić, M. Vujković

Honorary Committee

Nikola Hajdin,	President of Serbian Academy of Sciences and Arts
Branko Kovačević,	Rector of University of Belgrade
Paula Putanov,	Member of Serbian Academy of Sciences and Arts
Momčilo Ristić,	Member of Serbian Academy of Sciences and Arts
Ankica Antić Jovanović,	Honorary President of Society of Physical Chemists of Serbia
Ivan Draganić,	Honorary Member of Society of Physical Chemists of Serbia
Roger M. Leblanc	(Canada) Honorary Member of Society of Physical Chemists of Serbia
Preben Graae Sørensen	(Denmark) Honorary Member of Society of Physical Chemists of Serbia
Guy Schmitz (Belgium)	Honorary Member of Society of Physical Chemists of Serbia
Miroslav Kopečni,	Honorary Member of Society of Physical Chemists of Serbia
Vladimir Petruševski	(Macedonia), Honorary Member of Society of Physical Chemists of Serbia
Biljana Minčev Šukarova	(Macedonia), Honorary Member of Society of Physical Chemists of Serbia
Ljiljana Kolar-Anić,	Honorary Member of Society of Physical Chemists of Serbia
Milorad Jeremić,	Honorary Member of Society of Physical Chemists of Serbia
Čedomir Radenović,	Honorary Member of Society of Physical Chemists of Serbia

SPONSORS

Ministry of Science and Technological Development

University of Belgrade, Belgrade

The Faculty of Physical Chemistry, University of Belgrade

Institute of Chemistry Technology and Metallurgy, University of Belgrade

Vinča Institute, University of Belgrade

Institute of General and Physical Chemistry, Belgrade

NovoLab, Belgrade

MOL, Belgrade

Gradski zavod za zaštitu zdravlja, Belgrade

*On the occasion of the hundredth anniversary of the birth of Academician Pavle Savić and twentieth anniversary of founding Society of Physical Chemists of Serbia, instead of the usual introduction, here is given translation of the text **20 years of Society of Physical Chemists of Serbia 1989 – 2009**, published in a special Issue of Chemical Industry Vol. 63 (5a).*

Editors

TWENTY YEARS OF SOCIETY OF PHYSICAL CHEMISTS OF SERBIA



1989–2009

Society of physical chemists of Serbia (SPCS: 1989) derived at the achievements of our pioneers and doyens of Physical Chemistry, above all, Professor Miloja Stoiljković and academician Pavle Savić (President of Serbian Academy of Sciences and Arts, SASA, from 1971 to 1981, the first Honorary President of SPCS, 1990), which founded the physical chemistry in this area and made to become powerful, modern and indispensable natural science.



Professor Miloje Stoiljković
(1873–1962)



Academician Pavle Savić
(1909–1994)

Viewed chronologically on a global scale, from the 1740s, when the Russian scientist MV Lomonosov (Михаил Васильевич Ломоносов) defined term, the content and attributes of the first interdisciplinary natural science, and ten years later (1752) wrote the first textbook of physical chemistry *Introduction to the law of physical chemistry*, it had to go 150 years to launch the first journal of physical chemistry *Zeitschrift für physikalische chemie* (Leipzig, 1887), and ten years later,

physical chemistry has arrived in our region. Then, 1903. year, in difficult social and economic conditions, in conditions of crisis that preceded the Balkan wars, a professor Stoilković introduced the first courses in physical chemistry. On the other hand, after forty years, in 1947, just two years after the Second World War, Academician Savić designs and fits the head of the Study Group of Physical Chemistry, one of ten in the Faculty of Sciences in Belgrade (the forerunner of today the Faculty of Physical Chemistry, established 1990). A year later, 1948. he also founded the Institute of nuclear sciences „Vinča“; which created the conditions for new, important and significant period of development of physical chemistry and natural sciences in our Country.



Михаил Васильевич Ломоносов
(1711–1765)

In the Institute of Nuclear Sciences Vinča, corps of outstanding scholars arises: academics Milenko Šušić (first President of SPCS, 1989, Honorary President of SPCS, 1995), Slobodan Ribnikar (Honorary Member of SPCS, 1997, Editor of Proceedings of Conferences *Physical Chemistry* in 1992, 1994, 1996 and 1998) and Momčilo Ristić (Honorary Member of SPCS, 1999), professors Slobodanka Veljković and Ivan Draganić (Honorary Member of SPCS, 1998) and many others who full of strength and inspiration, individually and collectively, as well as tsunami wave, unstoppably permeate space of the physical chemistry.

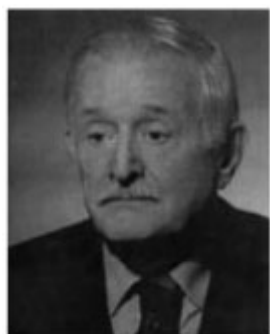


Academician Milenko Šušić
(1925–2006)



Academician Slobodan Ribnikar
(1929–2008)

In parallel, at the Department of Physical Chemistry of the Faculty of Sciences are working, rising and developing teachers and researchers: Slobodan Ristić, Vladimir Vukanović, Dragan Veselinović, Vukica Radak (1926–2001), Nadežda Petranović, Ankica Jovanović (Vice-president SPCS, 1989-1995, President SPCS, 1995-2005, Honorary President SPCS, 2007), Milorad Jeremić (Honorary Member SPCS, 2007), academician Paula Putanov (Honorary Member SPCS, 2007), and many others, creating generations and generations of *thinking people*, as they were called by the academician Aleksandar Despić (President of the Academy, 1994-1998; Honorary Member SPCS, 1996) at the meeting of Physical Chemists organized in Njegoševa 12 regarding the reform of higher education, appealing that such achievements, being Physical Chemists characteristics, must not be lost due to future reforms of the Faculty of Physical Chemistry.



Professor Slobodan Ristić
(1912–1993)



Professor Slobodanka Veljković
(1924–1989)

On this occasion, it must be noted that physical chemistry is by no means related only to faculty of Physical Chemistry and Institute Vinča. It is strongly present in other faculties (Faculties of Technology, Pharmacy, Chemistry, Physics, Agriculture and other one of the University of Belgrade, University of Novi Sad, Niš, Kragujevac, Priština, Novi Pazar) and research institutions (Institute of Chemistry, Technology and Metallurgy, Institute of General and Physical Chemistry, Institute for Technology of Nuclear and Other Mineral Raw Materials, Institute for the Application of Nuclear Energy Zemun, Maize Research Institute Zemun Polje, and many others), SASA, institutions and laboratories of the Ministry of Internal Affairs, Police Academy, and enterprises (NIS, Belgrade water supply and sewerage, Hydrometeorological Institute of Serbia, HIPOL, POLYESTER and others).



Academician Aleksandar Despić
(1927–2005)



Academician Momčilo Ristić
(1929)

The idea of the institutional organization in the frame of the scientific and professional society was present among Physical Chemists since their gathering around the Mendeleev club at the Institute of Physical Chemistry, ancient 70^s of last century. It was supposed to proceed more nearly two and half decades to the realization of this idea. In fact, although scattered throughout the country and the world, but deeply interconnected, 27 December 1988th (about 250 years since the introduction of the term physical chemistry) at the Academy, on the occasion of the celebration of 85 years since the introduction of teaching physical chemistry at the University of Belgrade and 80 years Physical Chemistry Department of Philosophy Faculty (founded 1908), later Study Group of Physical Chemistry (1947) and after that the Institute of Physical Chemistry (1971) in Faculty of Sciences and finally the Faculty of Physical Chemistry (1990), it was agreed to establish a Society. The idea of founding the Society was strongly supported by the academicians Savić and Šušić. Also, many letters of support were sent to Chairman of the Committee for Jubilee celebration, Ljiljana Kolar-Anic, a professor of the Faculty of Physical Chemistry (Honorary member SPCS, 2007). Not for long, 27 April 1989th a Steering Committee was formed for the establishment of the Society, headed by academician Milenko Šušić and members: dr Ankica Jovanović, associate professor at Institute for physical Chemistry of Faculty of Sciences (Belgrade);

Milija Jovanović, teacher at VIII Belgrade gymnasium; Milan Stanković, RO Naftagas (Pančevo); dr Branislav Radak, principal research fellow at Institute „Boris Kidrič“ (Vinča); professor Pavle Premović, Philosophy Faculty (Niš); Stefan Pongrec, Institute „Boris Kidrič“ (Vinča); Dragan Milošević, RHMZ SR (Serbia); dr Ana Terlecki-Baričević, Institute of catalysis and chemical engineering IHTM (Belgrade); dr Slobodan Anić, senior research fellow, Institute of security (Belgrade); Danica Stanković, teacher in secondary school (Grocka); dr Aleksandar Aleksić, assistant professor, Faculty of Pharmacy (Belgrade); dr Čedomir Radenović, professor, Maize Institute, Zemun Polje; dr Miroslav Kopečni, director of Institute „Boris Kidrič“ (Vinča); dr Dragan Vučković, vice-director of Institute „Boris Kidrič“ (Vinča); Božidar Perović, RO „Đuro Salaj“ (Niš); mr Dragan Vujasinović, Military-technical Institute (Belgrade); Zoran Laušević, research fellow at Institute „Boris Kidrič“ (Vinča); Milan Kunjadić, GSUP (Belgrade). Finally, 9 June 1989. in the Conference Hall of SANU, there was a Constituent Assembly Society of Physical Chemists of Serbia, which is signed in the Register of community organizations 16th August of that year. Afterward, the Branch in Vršac was established in 2005th and Branch of Velika Plana in 2006th.

Today, we can conclude that the Society of Physical Chemists of Serbia emerged in a very painful time of radical change in a large community of Balkan nations, and then continued to act in anything better times. Nevertheless, its members have found strength and ways to make a Society of Physical Chemists of Serbia of reference, both within the borders of our country, and globally, primarily due to conferences in fundamental and applied physical chemistry, which are from 1992nd continuously held in September every two years. The first two conferences were national, third with international participation, and then all the next international. The value of conferences is best illustrated by their citation in periodicals *Chemical Abstracts (CAS)* from the fourth conference (1998), as well as publishing original research papers inspired by the conference presentations from 2006th and 2008th, in regular issues of the *Russian Journal of Physical Chemistry*, Issue 9, Vol. 81, 2007, and Issue 9, Vol. 83, 2009. In addition, many other papers resulting from the presentations at our conferences were published in other international journals. The availability of conference papers is realized through the Society web site (www.socphyschemserb.org). SPCS organized other scientific meetings: Selforganization of nonequilibrium processes 95, 8-9. April, 1995, Ečka; Selforganization in nonequilibrium Systems, International Conference of Nonlinear Sciences, September 24-25, 2004, Belgrade, (indexed in *CAS*); Specific Methods for Food Safety and Quality, September 26-29, 2008, Belgrade.

Without a broader view of activities and results achieved by SPCS because it exceeded the scope of this editorial, we are kept on a short view, those relating to scientific meetings, and without referring to such significant results that are related to, for example, the popularization of physical chemistry in secondary schools of Serbia, which has lasted since the founding of the Society.

On the occasion of 20th anniversary since the establishment of Society of Physical Chemists of Serbia, *Journal Chemical Industry*¹ in this issue published works by invited members of the Society. Fourteen review and original research papers in the field of electrochemistry, chemical kinetics, catalysis, nonlinear dynamics and physical chemistry of materials provide at least partial, insight into current research in physical chemistry.



The front pages of some of the publications of SPCS: First National (1992) and the International Conference of Physical Chemistry (1998), First National (1995) and the International Conference on Nonlinear Sciences (2004), Monography dedicated to Professor Dragan Veselinović (2001) and the International meeting on food (2006).

And what's next? Still together

¹ In the same way *Chemical Industry* marked the 90th anniversary of the Faculty of Physical Chemistry (*Chemical Industry* 52 (9) (1998) 337-370).



Participants of the fourth International Conference „Physical Chemistry 98“; in the lobby of I. M. Kolarac Foundation before the Opening of the Conference

Shoulder to shoulder



Nenadović, father and son, at the closure of Fourth International Conference „Physical Chemistry 98“; in I. M. Kolarac Foundation

There are those for whom...



Mojović Jr. has something to say to perofessor Bačić during Poster Section of Fourth International Conference „Physical Chemistry 98“; in I. M. Kolarac Foundation.

In Belgrade, November 2009.

*Dr Slobodan Anić,
President of Society of Physical Chemists of Serbia
Dr Željko Čupić,
Member of Presidency of Society of Physical Chemists of Serbia*

PL
Plenary Lectures

STRUCTURAL PROPERTIES OF TRUNCATED HEMOGLOBINS FROM UNICELLULAR ORGANISMS AS REVEALED BY RESONANCE RAMAN SPECTROSCOPY

Enrica Droghetti, Alessandro Feis, Barry D. Howes, Francesco P. Nicoletti, and Giulietta Smulevich

Dipartimento di Chimica “Ugo Schiff”, Università di Firenze, Via della Lastruccia 3, I-50019 Sesto Fiorentino (FI), Italy (giulietta.smulevich@unifi.it)

Introduction

In bacteria, three classes of “Hb-like proteins” have been identified: flavo-Hbs, monomeric Hbs and 2/2 globins (also named truncated Hbs or trHbs). TrHbs are characterized by the absence of the A-helix and the presence of an extended loop substituting for most of the F-helix [1]. On the basis of the amino-acid sequence, trHbs have been further classified into groups I (HbN), II (HbO) and III (HbP). Group II is the most populated. The crystal structures of members of group II trHbs revealed that their active site is characterized by the invariant Fe-histidine covalent link on the proximal side and by multiple combinations of different amino acid side chains within the heme distal pocket, which provides a highly polar distal environment (Figure 1).

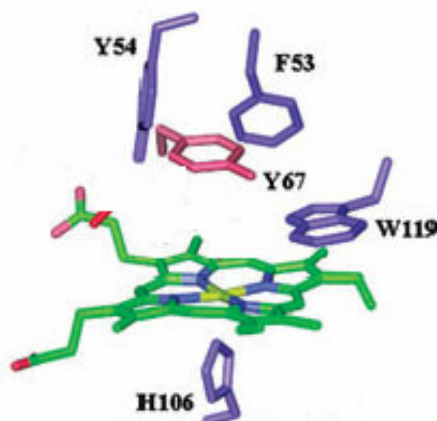


Fig.1. Heme pocket of *Thermobifida fusca*. [2]

These proteins can bind oxygen with high affinity; however, their function is not yet fully understood. Possible roles include NO scavenging [3], redox reactions [4], and sulfide metabolism [5]. The distal amino acid residues play an important role in regulating ligand binding. In particular, usually three potential H-bond donor in

the distal cavity, are present. The binding of exogenous ligands could be stabilized by TrpG8, TyrB10, and TyrCD1 (or GlnE11). Therefore, identifying the residues which actually interact with the Fe-bound ligand is not a simple task. In addition the spectroscopic characterization in solution of various wild-type Group II TrHbs has highlighted that their heme group may exist in the high spin (HS) and low-spin (LS) state.

Results and Discussion

To obtain incisive information on ligand binding, it is important to apply complementary crystallographic and steady-state spectroscopic approaches, such as resonance Raman (RR), FTIR, electronic paramagnetic resonance (EPR), and nuclear paramagnetic resonance (NMR). The steady-state techniques are helpful in revealing the nature of trHbs under various solution conditions. Among these spectroscopic tools, RR spectroscopy is especially versatile and informative. In order to highlight the structural properties of these proteins, Hb from thermophilic actinobacterium *T. fusca* [6] and from the Antarctic marine eubacterium *P. haloplanktis* TAC125 [7] have been characterized by RR, electronic absorption and EPR spectroscopies. Both proteins contain the polar distal triad TrpG8/TyrB10/TyrCD1. In order to single out the contribution of each of the three key distal amino acids (TyrB10, TyrCD1, TrpG8), single, double, and triple Phe mutants have been obtained at each position for *T. fusca* HbO. The spectroscopic characterization indicates that the bound ligand can either interact with the Trp residue alone or be caged by Trp and the distal Tyr couple, where TyrCD1 has a prevalent role. Moreover, the results indicate an increased mobility of the distal Tyr residues as compared to other trHbO members.

P. haloplanktis TAC125 HbO is the first cold-adapted bacterial haemoglobin which has been studied in detail by spectroscopic methods. Although many cold-adapted marine species have been investigated, we still have limited knowledge about molecular adaptations at low temperatures. The ability of cold-adapted organisms to survive at permanently low temperatures implies that, to perform their physiological functions at adequate rates in freezing habitats, they have overcome constraints imposed by the cold environment through biochemical and physiological adaptations.

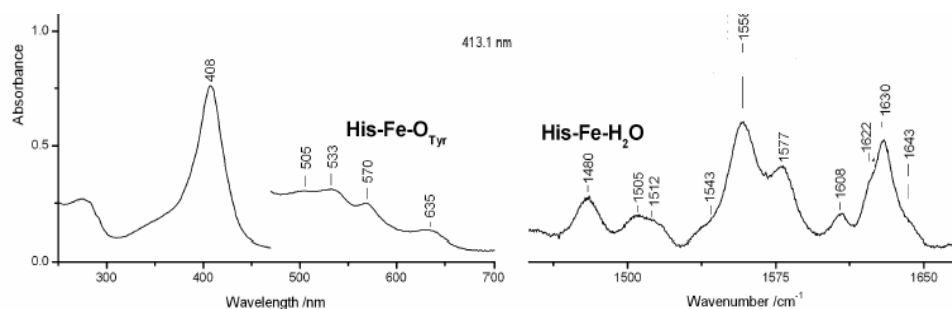


Fig.2. UV-Vis (left) and RR (right) spectra of ferric *P. haloplanktis* TAC125 HbO at pH 7.6. Experimental conditions: 413.1 nm excitation wavelength, 15 mW laser power at the sample, 1 cm^{-1} spectral resolution; average of seven spectra with 600 s integration time.

The present study strongly indicates that the protein has unique features in the ferric state among Group II trHbs. In fact, unlike other bacterial Hbs, at neutral pH the ferric state, in addition to the aquo hexacoordinated high-spin form, shows two (by RR) (Figure 2), or three (by EPR) hexa-coordinated LS forms.

While one LS form should correspond to a deprotonated Tyr, the other two 6cLS forms are suggested to correspond to either TyrCD1-O⁻ or TyrB10-O⁻, coordinated to the heme Fe(III) atom and distinguished by different H-bonding properties for each heme bound Tyr. This is the first example in which both TyrCD1 and TyrB10 are proposed to be the residues alternatively involved in heme hexacoordination by endogenous ligands.

Conclusion

The results indicate that the spectroscopic features and ligand binding properties of the two proteins are quite different. TrpG8 is the key residue in ligand stabilization. However, while TyrCD1 plays an ancillary role in *T. fusca*, in *P. haloplanktis* TAC125 both TyrCD1 and TyrB10 are capable of coordinating the heme iron in the ferric form giving rise to different 6-coordinate low spin His-Fe^{III}-Tyr species.

In addition, the ensemble of results obtained for *P. haloplanktis* TAC125 HbO indicates high structural flexibility, probably linked to the peculiarity of the cold environment. This is an important aspect, since the ability of cold-adapted organisms to survive at permanently low temperatures implies that they have overcome constraints imposed by a permanently cold environment through biochemical and physiological adaptations, which maintain the flexibility of DNA, RNA and proteins.

References

- [1] D. A. Vuletich and J.T.J. Lecomte, *J. Mol. Evol.*, 2006, **62**, 196–210.
- [2] A. Bonamore, A. Ilari, L. Giangiacomo, A. Bellelli, V. Morea, A., and Boffi, *Febs J.*, 2005, 272, 4189-4201.
- [3] M. Milani, A. Pesce, M. Nardini, H. Ouellet, Y. Ouellet, S. Dewilde, A. Bocedi, P. Ascenzi, M. Guertin, L. Moens, J. M. Friedman, J. B. Wittenberg, M. Bolognesi, *J. Inorg. Biochem.*, 2005, 99, 97-109.
- [4] R. Torge, A. Comandini, B. Catacchio, A. Bonamore, B. Botta, A. Boffi, *J. Mol. Catalysis B: Enzymatic*, 2009, 61, 303–308.
- [5] F. P. Nicoletti, A. Comandini, A. Bonamore, L. Boechi, F. Boubeta, A. Feis, G. Smulevich, A. Boffi, *Biochemistry*, 2010, 49, 2269–2278.
- [6] E. Droghetti, F. P. Nicoletti, A. Bonamore, L. Boechi, P. A. Mañez, D. A. Estrin, A. Boffi, G. Smulevich and A. Feis, 2010, in preparation.
- [7] B. D. Howes, D. Giordano, L. Boechi, R. Russo, S. Mucciacciaro, C. Ciaccio, F. Sinibaldi, M. Fittipaldi, M. A. Martí, D. A. Estrin, G. di Prisco, M. Coletta, C. Verde and G. Smulevich, 2010, submitted.

ROOM TEMPERATURE IONIC LIQUIDS FOR ELECTROCHEMISTRY

R. G. Compton,¹ L. Aldous,¹ A. M. O'Mahony,¹
E. I. Rogers¹ and F. Javier del Campo²

¹*Department of Chemistry, Physical & Theoretical Chemistry Laboratory,
University of Oxford, South Parks Road, Oxford, OX1 3QZ, UK
(Richard.compton@chem.ox.ac.uk)*

²*Centro Nacional de Microelectrónica (CNM-IMB), CSIC, Campus Universidad
Autónoma de Barcelona, 08193, Bellaterra, Barcelona, Spain.*

Abstract

The use of microelectrodes for the sensing of gases in Room Temperature Ionic Liquids (RTILs) is described, focussing on O₂, CO₂, H₂S, NH₃ and H₂. In addition, the effect of these dissolved gases on the voltammetry of other solutes will be discussed. Finally, the combination of RTILs and microarrays to form membrane-free gas sensors will be described.

Content

Room temperature ionic liquids have generated a large amount of interest in the electrochemistry community, hence a number of reviews have already been dedicated to this topic, e.g. [1-3].

This plenary lecture will focus on the application of microelectrodes, the amperometric detection of gases, and the influence that dissolved gases can have on voltammetric experiments. Firstly a cell designed for working on tiny volumes (~10 µL) of RTILs under controlled conditions (e.g. prior degassing and drying under vacuum followed by equilibration with gas mixtures) will be described (Figure 1).

The effect of carbon dioxide content on the microdisc voltammetry of other solutes in RTILs will be discussed.[4] In

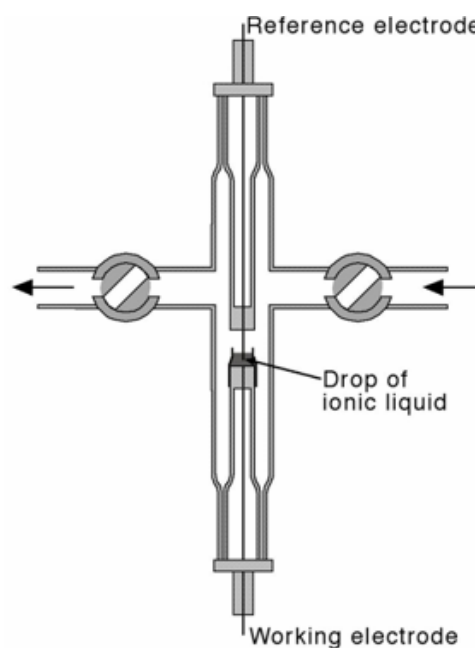


Fig.1. Cell for µL-scale voltammetry under controlled conditions.

addition the electrochemistry of a number of other gases, namely hydrogen,[5] ammonia,[6] hydrogen sulfide [7] and sulfur dioxide [8] will also be discussed, and the unusual voltammetry of dioxygen will be explained as a function of RTIL structure.[9,10]

Double potential step chronoamperometry is a useful technique for electrochemical investigations as it allows for the simultaneous determination of both diffusion coefficients and concentrations (Figure 2). The determination of the diffusion coefficients of both analyte and product is especially pertinent in RTILs, as associated changes in charge can result in diffusion coefficients that differ by orders of magnitude.[3] This technique and its mathematical simulation will be described, and various examples of its use highlighted.

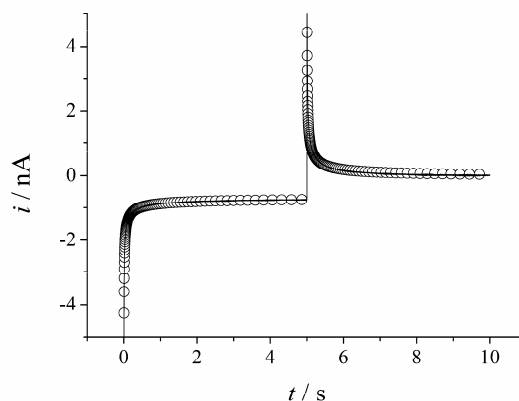


Fig.2. Double potential step chronoamperometry then simulation, for the rapid determination of both analyte concentration and the diffusion coefficients of the redox species.

Finally, the recent application of microelectrode arrays in conjunction with thin layers of RTIL to form membrane-free gas sensors will be discussed (Figure 3).[11]

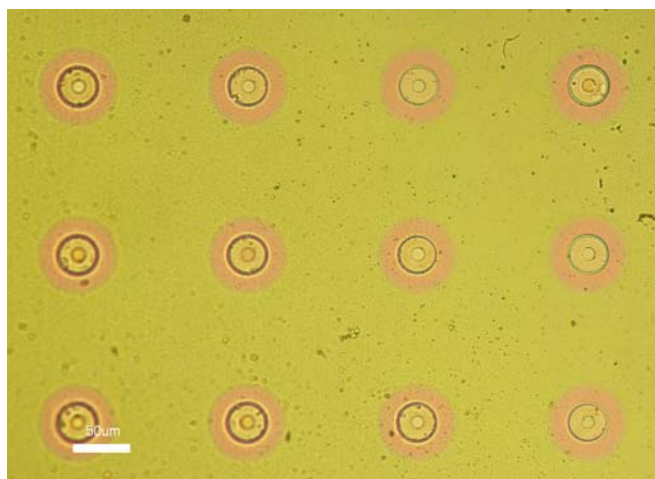


Fig.3. Microelectrode arrays coated in RTILs; commercially relevant current and sensitivity values, utilising tailored electrolytes that remove evaporation and membrane issues (scale bar 50 μm).

References

- [1] L. E. Barrosse-Antle, A. M. Bond, R. G. Compton, A. M. O'Mahony, E. I. Rogers, D. S. Silvester, *Chemistry-An Asian Journal*, 2010, **5**, 202-230.
- [2] D. S. Silvester, R. G. Compton, *Zeitschrift Fur Physikalische Chemie-International Journal Of Research In Physical Chemistry and Chemical Physics*, 2006, **220**, 1247-1274.
- [3] M. C. Buzzeo, R. G. Evans, R. G. Compton, *ChemPhysChem*, 2004, **5**, 1106-1120.
- [4] L. E. Barrosse-Antle, C. Hardacre, R. G. Compton, *Journal of Physical Chemistry B*, 2009, **113**, 2805-2809.
- [5] D. S. Silvester, L. Aldous, C. Hardacre, R. G. Compton, *Journal of Physical Chemistry B*, 2007, **111**, 5000-5007.
- [6] X. B. Ji, D. S. Silvester, L. Aldous, C. Hardacre, R. G. Compton, *Journal of Physical Chemistry C*, 2007, **111**, 9562-9572.
- [7] A. M. O'Mahony, D. S. Silvester, L. Aldous, C. Hardacre, R. G. Compton, *Journal of Physical Chemistry C*, 2008, **112**, 7725-7730.
- [8] L. E. Barrosse-Antle, D. S. Silvester, L. Aldous, C. Hardacre, R. G. Compton, *Journal of Physical Chemistry C*, 2008, **112**, 3398-3404.
- [9] R. G. Evans, O. V. Klymenko, S. A. Saddoughi, C. Hardacre, R. G. Compton, *Journal of Physical Chemistry B*, 2004, **108**, 7878-7886.
- [10] A. S. Barnes, E. I. Rogers, I. Streeter, L. Aldous, C. Hardacre, G. G. Wildgoose, R.G. Compton, *Journal of Physical Chemistry C*, 2008, **112**, 13709-13715.
- [11] X.-J. Huang, L. Aldous, A. M. O'Mahony, F. J. del Campo, R. G. Compton, *Analytical Chemistry*, 2010, **82**, 5238-5245.

BIOSENSORS AND BIOASSAYS BASED ON CHOLINESTERASE INHIBITION FOR PESTICIDES, NERVE AGENTS AND AFLATOXINS DETECTION

D. Moscone¹ and F. Arduini¹

¹ *Dipartimento di Scienze e Tecnologie Chimiche, Università di Roma Tor Vergata,
Via della Ricerca Scientifica, 00133 Rome, Italy (moscone@uniroma2.it)*

Abstract

In the present work, ChEs based biosensors for pesticides, nerve agents and aflatoxin B detection developed by our research group are reported together with applications in food areas.

Introduction

Electrochemical biosensors using acetylcholinesterase (AChE) as a biological recognition element are based on the inhibition of the enzyme natural catalytic activity by substances that are to be detected because of their high toxicity.

Between them, organophosphorus compounds (OP) are the most toxic substances. They are used as insecticides and nerve agents [1]. These compounds inhibit the hydrolysis of acetylcholine (ACh), the principal step that concludes intercellular communication pathways, and this inhibition poses serious physiological threats due to its extreme toxicity [2].

The electrochemical detection of AChE inhibition can be performed through the measurement of its enzymatic products using a single or a bienzyme system. In the first case, the native substrate acetylcholine is replaced by the synthetic one acetylthiocholine, while, in the latter case, the enzyme choline oxidase (ChOx) is coupled with the AChE. The amperometric measurement of AChE activity is frequently carried out in both cases, monitoring the electrochemical oxidation of thiocholine or the oxidation or reduction of hydrogen peroxide [3].

The inhibition of AChE by OP compounds is irreversible, so cheap disposable biosensors are particularly attractive [4]. Screen-printed electrodes (SPEs), in particular, can combine ease of use and portability with simple, inexpensive fabrication techniques.

Such as organophosphates, mycotoxins (e.g., aflatoxin B₁ (AFB₁)) are also classified as extremely hazardous compounds, because of their potent toxicity to the human nervous system [5, 6]. In particular, AFB₁ is a carcinogenic contaminant of food and animal feeds.

This mycotoxin has been demonstrated to also inhibit the AChE, but reversibly in this case [7].

Chromatographic techniques and different types of spectroscopy are the most commonly used methods to analyze these toxic compounds. Although these systems possess high selectivity and adequate sensitivity, however they are time consuming, expensive, demand a qualified and experienced personnel, are not amenable to rapid screening in emergencies or in remote settings, and cannot be used for continuous monitoring.

Biological techniques such as immunoassays are also used for the determination of organophosphorus compounds and mycotoxins, but they require the use of antibodies that have to be produced sacrificing animals.

Therefore, it is crucial to develop robust, sensitive, portable and user-friendly methods to test for the presence of toxic compounds.

Experimental

Acetylcholinesterase (AChE) from *electric eel* (EC 3.1.1.7), butyrylcholinesterase (BChE) from *equine serum* (EC 3.1.1.8), S-butrylthiocholine chloride, acetylthiocholine chloride (ACTh), DTNB (5,5'-dithiobis-(2-nitrobenzoic acid)), Nafion (perfluorinated ion-exchange resin, 5 % v/v solution in lower alcohols/water), cysteamine, potassium chloride, cupric sulfate, mercury chloride, zinc sulphate, aluminium potassium sulfate, manganese chloride, arsenic acid (sodium salt) iron(III) chloride, iso-hexane PESTANAL[®] Riedel de Haen, paraoxon (O,O-diethyl-O-(4-nitro-phenylphosphate), chlorpyrifos-methyl(O,O-diemethyl-O-(3,5,6-trichloro-pyridyl)phosphoro-thioate), aldicarb (2-methyl-2-(methylthio)propionaldehyde-O-methylcarbamoyloxime), carbaryl (1-naphthyl methylcarbamate) were purchased from Sigma, St. Louis, MO, USA. Silver, cadmium, lead and nickel nitrates and ferric (II) sulfate, potassium ferricyanide, were obtained from Carlo Erba (Milano, Italy). The AChE from *Drosophila melanogaster* wild type and mutants were obtained from Marty's group (University of Perpignan, France). Aflatoxin B₁, were purchased from Vinci-Biochem, Italy. Sarin gas was provided by TNO, the Netherlands.

Screen-printed electrodes (SPEs) were produced in our laboratory with a 245 DEK (Weymouth, UK) screen printing machine. Graphite-based ink (Elettrodag SS 423) from Acheson (Milan, Italy) was used to print the working and counter electrode. The substrate was a flexible polyester film (Autostat HT5) obtained from Autotype Italia (Milan, Italy). The diameter of the working electrode was 0.3 cm. Silver ink was used to print the reference electrode. Gold SPE was purchased from Ecobioservice.

For spectrophotometric measurements an Unicam 8625 UV/VIS spectrophotometer was used. Amperometric measurements were carried out using a portable PalmSens, (Palm Instruments, the Netherlands) or using a VA 641 amperometric detector (Metrohm, Herisau, Switzerland), connected to an X-t recorder (L250E, Linseis, Selb, Germany).

The SPE were modified with Prussian Blue according the procedure developed by Ricci et al. [8]. The immobilisation of the enzyme was carried out as described by Arduini et al. [9].

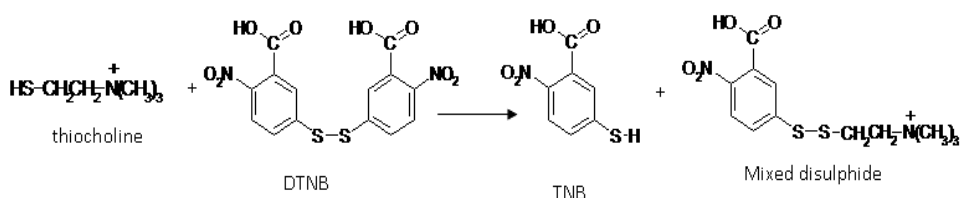
The inhibitory effect of AChE inhibitors (pesticides, nerve agents or AFB₁) was evaluated by determining the decrease of enzymatic activity. To do this, the cholinesterase activity was measured before (A_0) and after (A_i) the exposure of the enzyme to inhibitors and the degree of inhibition was calculated using the Equation 1.

$$I\% = [(A_0 - A_i) / A_0] \times 100 \quad (1)$$

Results and Discussion

Measurements in real samples can be often revealed as more difficult than expected because the real samples are usually complex mixtures, and some components could interfere with the selected method of analysis.

In this respect, the interference of heavy metals occurring in the detection of pesticides based on free Acetylcholinesterase (AChE) inhibition and spectrophotometric Ellman's method [10] (Scheme 1) has been investigated.



Scheme 1

The heavy metal cations could, in fact, represent a major interference in the measurement of thiocholine produced by free AChE when enzyme inhibition is used as a means for pesticide detection. **Figure 1** shows the concentration of different heavy metals that gave a 15% signal decrease when present with thiocholine.

This study demonstrates that most of the metal cations such as copper, usually present in aqueous samples, react with thiocholine greatly affecting the spectrophotometric measurement. The approach proposed in order to eliminate the heavy metals interferences, is based on the pesticides extraction using organic solvent (hexane) and after the extract, insoluble in aqueous phase, is put in contact with an aqueous phase in which the enzyme is solubilised: the pesticide interacts with the enzyme at the interface between an organic and an aqueous phase. Given that virtually all the pesticides inhibit AChE by binding irreversibly to a hydroxyl group at the catalytic center, this reaction could have the effect of extracting the pesticide into the aqueous phase.

After a defined period of time (10 min), the residual enzyme activity in the aqueous phase is measured by Ellman's method. The calibration curve for paraoxon dissolved in hexane allows reaching a limit of detection (LOD) of 40 ppb [11].

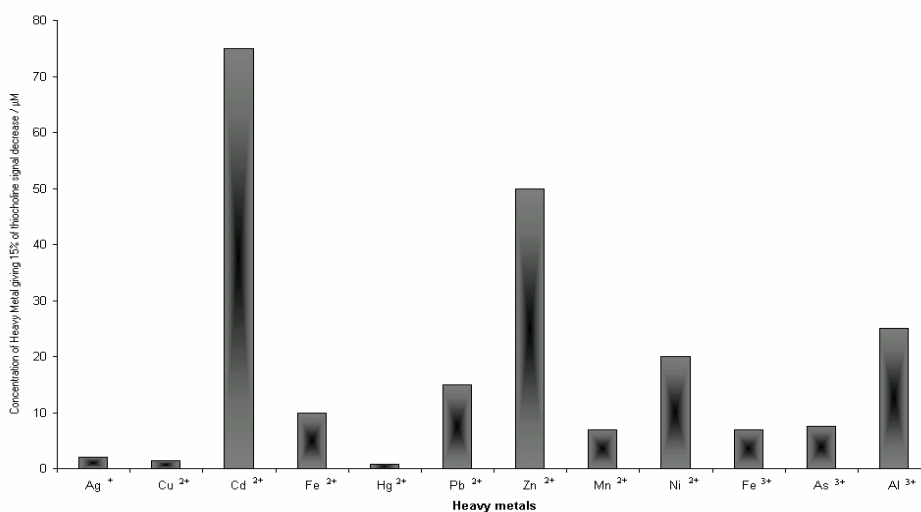


Fig.1 Concentrations of different heavy metals cations giving a decrease of 15% of thiocholine signal. Thiocholine concentration $1 \cdot 10^{-5}$ M. Phosphate buffer 0.1 M, pH = 8.

An alternative method to measure pesticides avoiding interferences is the use of the electrochemical biosensors and the “medium exchange method”. Screen-printed electrodes (SPEs) modified with Prussian Blue were used as platform for the successive immobilisation of two different ChE enzymes (AChE or Butyrylcholinesterase, BChE) by cross-linking method to obtain the biosensor. The advantage of using the biosensor is the possibility to miniaturise the system, allowing the “in situ” pesticides detection (Figure 2).



Fig.2. Portable instrument for electrochemical biosensor

The BChE and AChE biosensors were tested using standard solutions of organophosphate and carbamate pesticides. Analytical parameters such as linear range, limit of detection (LOD) and reproducibility (RDS) of the AChE and BChE biosensors were then selectively investigated. The AChE biosensor was tested with aldicarb and carbaryl due to its higher affinity toward these compounds. For the same reason, paraoxon and chlorpyrifos-methyl oxon were tested with the BChE biosensor, which shows a higher sensitivity to these latter than the AChE biosensor. The detection limit (LOD), defined as the concentration giving an inhibition of 20%, was found to be 24 and 25 ppb respectively for aldicarb and carbaryl using the AChE biosensor. With BChE biosensor, 2 and 0.5 ppb were the LOD values obtained for paraoxon and chlorpyrifos-methyl oxon, respectively. Reproducibility and linear range (corresponding to concentrations giving 20-60% of inhibition) were satisfactory with both biosensors [9].

The need for adopting a medium exchange method in the protocol for pesticide measurement has been demonstrated by testing the biosensors with various interfering species such as heavy metals and fluoride (well known reversible cholinesterase inhibitors) [12,13] as well as detergents [14]. The test was performed by measuring the residual enzymatic activity in the same buffer solution (without washing steps after the incubation time) and by using the medium exchange method.

With this procedure, the enzyme acts as a high affinity capture agent for the pesticide, and, because of the irreversibility of the inhibition, the successive enzymatic reaction can be carried out in a fresh buffer solution, thereby circumventing the effect of reversible inhibitors that could present in real food and environmental samples. In order to test the developed biosensor in food area, the drinking water was analysed. Commercially available mineral drinking water samples were analysed before and after the fortification with Aldicarb and Paraoxon, obtaining recovery values of (98±3)% and (90±5)%, then showing the good accuracy of the proposed method. In addition, biosensors were also challenged with wastewater in Acea Laboratory (Municipal company for drinking and wastewater) showing again good recovery values [9].

For Paraoxon detection, another electrochemical biosensor was also developed, based on self assembled monolayer of AChE by means of cysteamine and glutaraldehyde onto gold SPEs. The AChE activity was measured using ferricyanide as electrochemical mediator. The biosensor is characterised by a linear range up to 40 ppb. The biosensor was challenged with drinking water and river water obtaining a good accuracy.

The storage stability of developed biosensors was also investigated. The biosensor that showed the best storage stability was adopted for nerve agent detection at TNO, chemical warfare specialised centre in Holland. The biosensor was challenged against the Sarin gas (0.1 and 0.5 mg/m³) at different incubation times. A 30 sec incubation time was sufficient to detect 0.1 mg/m³ of Sarin gas, showing an inhibition of 30% with 10 min of total analysis time (Figure 3) [15].

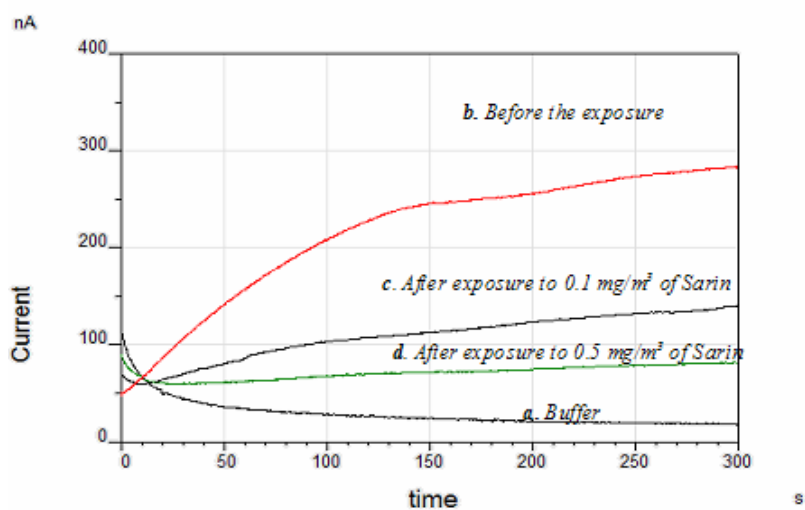


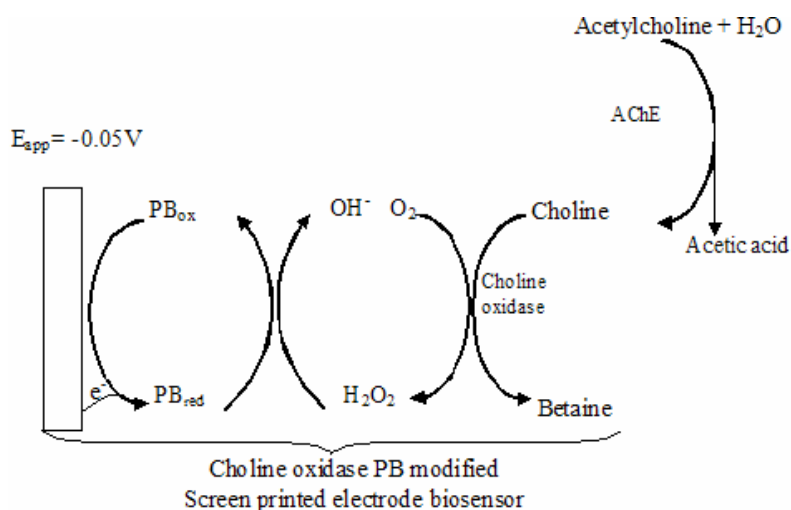
Fig.3 Original recording obtained using biosensor in phosphate buffer solution 0,05 M + KCl 0,1 M, pH 7.4. Applied potential: + 200 mV vs Ag/AgCl. Signal recorded in phosphate buffer (a), signal recorded using a solution of butyrylthiocholine 5 mM in phosphate buffer before the exposure of biosensor (b) or after the exposure of biosensor for 1 min at 0.1 mg/m³ (c) or 0.5 mg/m³ (d) of Sarin gas.

Recently it was demonstrated the ability of aflatoxin B₁ (AFB₁) to inhibit the mouse brain AChE at ppm level [7]. We developed a novel method for AFB₁ determination based on AChE inhibition with the AChE residual activity determined using the colorimetric method (Ellman's method). ChEs from various sources were tested using AFB₁ as reference aflatoxin. AChE from *electric eel* showed the highest sensitivity to AFB₁ and it was chosen for the rest of the work. To select and optimize the analytical procedures, the investigation on type of AChE inhibition by AFB₁ was carried out. The AChE degree of inhibition by AFB₁ was independent of the incubation time and the enzyme concentrations, showing the reversibility of the inhibition. This reversibility of the inhibition permits a rapid analysis of AFB₁ in a linear range of 10-60 ppb; in fact, only 3 minutes of analysis time are required. The suitability of the assay for AFB₁ quantification at 100, 120 and 150 ppb in barley was also favorably evaluated [16].

Successively, in order to reduce the detection limit in real sample analysis, an electrochemical bioassay was developed, in which the AChE was used in solution and its residual activity was monitored using an amperometric ChOx biosensor. The ChOx was immobilized by cross-linking onto screen printed electrodes modified with Prussian Blue, an electrochemical mediator able to detect the reduction of the H₂O₂ produced by ChOx at low potential (-0.05 V versus screen printed internal silver pseudoreference electrode) Scheme 2.

For the development of the AFB₁ assay, various parameters such as AChE and substrate concentration, methanol effect and pH study were evaluated and optimized. The linear working range was assessed to be 10-60 ppb. Finally, the

matrix effect and recovery studies were carried out using commercially available olive oils. The suitability of the developed method for the directly analysis of AFB₁ in olive oil samples was demonstrated, reaching a detection limit of 10 ppb of AFB₁ in real samples [17].



Scheme 2

Conclusion

AChE based biosensors have demonstrated their suitability for being applied to testing for maximum pesticide residue verification, and for measuring the mycotoxin B₁ content in cereals and olive oils.

Electrochemical biosensors can be then used for extremely sensitive and specific measurement of contamination by toxic compounds, and applicable to the routine analysis, especially when performed with disposable biosensors. Their inherent specificity, selectivity and adaptability make them ideal candidates for use in environmental and food industry.

References

- [1] Y Sun, K. Y. Ong, Detection technologies for chemical warfare agents and toxic vapors, CRC Press, Boca Raton, 2005.
- [2] H. Soreq, H. Zakut, Human Cholinesterases and Anticholinesterases, Academic Press, San Diego, 1993.
- [3] F. Arduini, A. Amine, D. Moscone, G. Palleschi, Microchim. Acta, 2010, DOI 10.1007/s00604-010-0317-1, *in press*.
- [4] S. Sole, A. Merkoci, S. Alegret, Crit. Rev. Anal. Chem., 2003, **33**, 89-126.
- [5] T. C. Marrs, Pharmacol. Ther., 1993, **58**, 51-66.
- [6] C. A. Rosenfeld, L. G. Sultatos, Toxicol. Sci., 2006, **90**, 460-469.

- [7] M. F. Cometa, P. Lorenzini, S. Fortuna, M. T. Volpe, A. Meneguz, M. Palmery, *Toxicol.*, 2005, 206, 125-135.
- [8] F. Ricci, A. Amine, G. Palleschi, D. Moscone, *Biosens. Bioelectron.*, 2003, 18, 165-174.
- [9] F. Arduini, F. Ricci, C. S. Tuta, D. Moscone, A. Amine, G. Palleschi. *Anal. Chim. Acta.*, 2006, 580, 155-162.
- [10] G. L. Ellman, *Arch. Biochem. Biophys.*, 1959, 82, 70-77.
- [11] F. Arduini, F. Ricci, I. Bourais, A. Amine, D. Moscone, G. Palleschi. *Anal. Lett.*, 2005, 38, 1703-1719.
- [12] T. Danzer, G. Schwedt, *Anal. Chim. Acta*, 1996, 318, 275-286.
- [13] G. A. Evtugyn, A. N. Ivanov, E. V. Gogol, J. L. Marty, H. C. Budnikov, *Anal. Chim. Acta*, 1999, 385, 13-21.
- [14] L. Jaganathan, R. Boopathy, *Bioorg. Chem.*, 2000, 28, 242-251.
- [15] F. Arduini, F. Ricci, A. Amine, D. Moscone, G. Palleschi, *Anal. Bioanal. Chem.*, 2007, 388, 1049-1057.
- [16] F. Arduini, I. Errico, A. Amine, L. Micheli, G. Palleschi, D. Moscone, *Anal. Chem.*, 2007, 79, 3409-3415.
- [17] I. Ben Rejeb, F. Arduini, A. Arvinte, A. Amine, M. Gargouri, L. Micheli, B. Bala, G. Palleschi, *Biosens. Bioelectron.*, 2009, 24, 1962-1968.

SYNTHESIS, CHARACTERIZATION AND POSSIBLE APPLICATIONS OF TiO₂ NANOPARTICLES

Jovan M. Nedeljković

*Vinča Institute of Nuclear Sciences, University of Belgrade, P.O. Box 522, 11001
Belgrade, Serbia (jovned@vinca.rs)*

Abstract

Different synthetic procedure for preparation of TiO₂ nanoparticles with desired shape and size were developed. Structural characterization of TiO₂ nanoparticulates was performed using XRD and different microscopy techniques. Influence of surface modification on the charge separation process was studied and possible application in photocatalysis, solar cells and fabrics with antibacterial effects were discussed. Optical characterization with special emphasis on photoluminescence, up-conversion effect and formation of surface charge transfer complexes was performed. Also, synthesis of polymer based nanocomposites with usage of TiO₂ nanoparticles as filler was described, as well as their influence on thermal properties of polymer matrix.

Introduction

Recently, significant progress in the synthesis of numerous metal-oxide particles has been achieved, providing possibility to control their shape, size on the nano level and surface properties. The interest in nanomaterials has been primarily motivated by their fundamental properties, but the technological aspects of these materials are being given full consideration. Titanium dioxide (TiO₂) nanoparticles are of particular significance due to their potential applications in different fields such as environmental cleanup and remediation (oxidation of hazardous industrial organic byproducts and reduction of heavy metal ions), nanocrystalline solar cells, catalysis, sensors, optics, fillers, etc.

We have recently shown by using X-ray absorption spectroscopic techniques that nanocrystalline TiO₂ material (particle size smaller than 20 nm) differ from the bulk material, and have unique surface chemistry due to distortions in surface Ti sites from octahedral geometry to a penta-coordinate square pyramid with one double Ti-O bond [1, 2]. Consequently, decrease of TiO₂ particle size below some critical point does not only lead to the increase of specific surface area, but also lead to the formation of surface active sites. The existence of such unique surface structure of TiO₂ nanoparticles opens up possibility to take advantage in different directions of fundamental research as well as applications.

In this review, different methods for controlled synthesis of TiO₂ nanoparticles with desired shape and size will be presented, as well as their structural characterization. Special attention will be paid to: (a) the improvement of charge separation process which is prerequisite for all photocatalytic reactions, (b) optical properties with special emphasis on charge transfer complex formation upon surface modification, as well as photoluminescence and “up-conversion” effects, and (c) usage of TiO₂ nanoparticles as fillers and their influence on the thermo-mechanical properties of polymer matrix. Also, possible applications in photocatalysis, solar cells and preparation of fabrics with antibactericidal and self cleaning effects will be discussed.

Experimental

The colloids consisting of spherical 45 Å TiO₂ particles were prepared by the controlled hydrolysis of titanium tetrachloride, as described elsewhere [3].

The detailed information concerning surface modification of TiO₂ nano-spheres for photocatalytic reduction of heavy metal ions can be found in literature [4, 5]. Photovoltaic characterization of hybrid solar cells using surface modified TiO₂ nanoparticles and poly(3-hexyl)thiophene is also described in literature [6]. Antibactericidal and self cleaning effects of polyester fabrics loaded with TiO₂ nanoparticles are described elsewhere [7, 8].

Synthesis and photoluminescent properties of TiO₂ nano-rods, as well as “up-conversion effect are described elsewhere [9, 10]. Surface modification of the 45 Å TiO₂ nano-spheres that led to the formation of charge transfer complexes and appearance of optical absorption in visible spectral range can be found in literature [2, 11, 12].

Synthesis of polymer based nanocomposites using either PMMA or PS and TiO₂ nanoparticles, as well as influence of TiO₂ nanoparticles on thermal properties of polymer matrix are described in details in literature [13-15].

Used instruments for structural (XRD, TEM), optical (UV-Vis, FTIR, PL), thermal (DSC, TGA), etc., characterization are described in above mentioned literature.

Results and Discussion

Excitation of TiO₂ with light energy greater than its band gap (3.2 eV) generates electron-hole (e⁻/h⁺) pairs that can participate in reduction and oxidation processes at the particle interface. Because the life time of charged pairs is very short, only efficient charge separation that involves species adsorbed on the surface of nanoparticles can lead to the desired redox processes. Our approach for the improvement of the efficiency of the photocatalytic reduction of various metal ions relies on usage of nanometer in size TiO₂ particles whose surface is modified with multifunctional ligands. Nanosized surface-modified TiO₂ offers several advantages over the commercially available TiO₂: (a) high surface area: (b)

increased adsorption of metal ions; and (c) enlarged initial charge separation distances.

The IR measurements were performed in order to understand the surface structure of 45 Å TiO₂ after modification with various amino acids. As an example, surface structure of alanine- and histidine-modified TiO₂ nanoparticles in the presence of cadmium ions, derived from detailed IR measurements [5], is presented in Figure 1.

It is important to point out that in this case proper surface modification opened-up possibility to perform photocatalytic reduction of cadmium ions which is thermodynamically not possible with unmodified TiO₂ nanoparticles [5]. Also, photocatalytic reduction of silver [4], copper [4] and gold [16] ions was achieved on dry supported nanocrystalline TiO₂ films allowing deposition of metallic patterns in one step process.

In addition to recombination processes that must be suppressed in order to achieve efficient photocatalytic performance of TiO₂, another obstacle is low absorption (less than 5%) of the available solar light photons due to its large band gap. One way to overcome this problem is again surface modification and charge transfer complex formation between coordinatively unsaturated surface Ti atoms and various ligands such as ascorbic acid [2], and bidentate benzene derivatives (salicylic acid, catechol, pyrogallol, gallic acid, etc.) [11, 12]. In such hybrid structures, localized orbitals of surface-attached ligands are electronically coupled with the delocalized electron levels from the conduction band of a TiO₂ semiconductor.

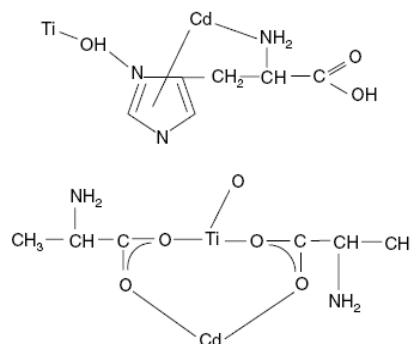


Fig.1. Surface structure of His-modified and Ala-modified TiO₂ nanoparticles in the presence of cadmium ions.

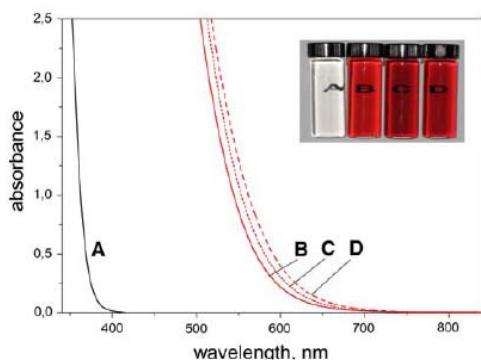


Fig.2. Absorption spectra of surface modified 45 Å TiO₂ nanoparticles with different ligands: (A) bare TiO₂; (B) catechol; (C) gallic acid, and (D) pyrogallol.

As a consequence, absorption of light by the charge transfer complex yields to the excitation of electrons from the chelating ligand directly into the conduction band of TiO₂ nanocrystallites. This results in a red shift of the semiconductor absorption compared to that of unmodified nanocrystallites and enables harvesting of solar photons in visible spectral range.

Absorption spectra of colloids consisting of bare 45 Å TiO₂ nanoparticles as well as surface

modified 45 Å TiO₂ nanoparticles with catechol, pyrogallol and gallic acid are shown as an example in Figure 2. The effective band gaps upon surface modifications were found to be around 1.9 eV. Possibility to take advantage of improved solar response upon charge transfer complex formation was tested by preparing hybrid solar cells based on surface modified TiO₂ nanoparticles with 6-palmitate ascorbic acid and poly(3-hexyl)thiophene [6]. It was found that incident photon to current efficiency has a maximum photocurrent contribution of about 5% at 520 nm. Also, it was clearly seen that optical absorption and incident photon to current efficiency spectra well match.

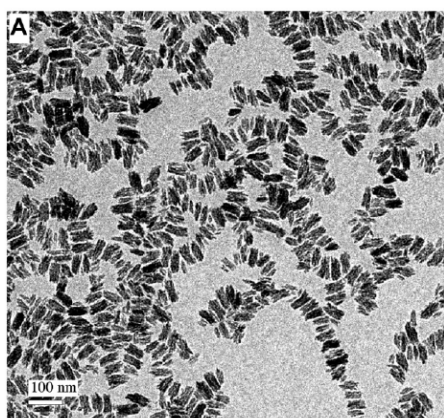


Fig.3. Typical TEM image of TiO₂ nano-rods.

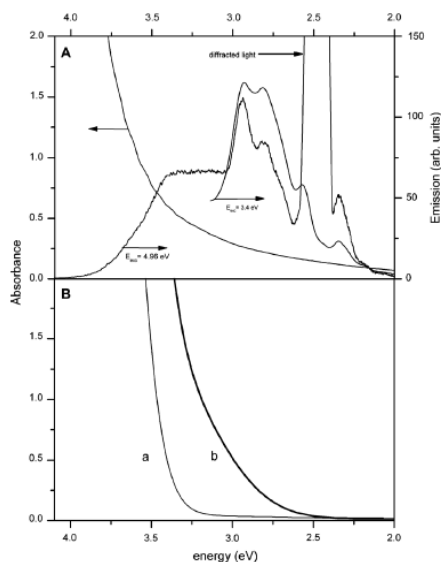


Fig.4. The UC photoluminescence spectra of TiO₂ nano-rods in THF.

The TiO₂ nanoparticles prepared in water are usually non-emissive due to the presence of large number of surface traps. The lack of photoluminescence restricts their possible applications either in optics or where optical detection is necessary. In order to prepare emissive TiO₂ nanoparticles synthesis in non-aqueous media was performed [9, 10]. Typical TEM image of synthesized TiO₂ nano-rods (45±10 nm x 20±5 nm, length by diameter) is presented in Figure 3.

Well-resolved photoluminescence spectra of TiO₂ nano-rods indicated the presence of band to band transitions in high energy range, as well as the presence of four shallow trap levels, most likely originating from oxygen vacancies at various energies. As unexpected result, photoluminescence was observed with excitation energies smaller than band gap energy (see Figure 4). It is important to point out that up-conversion photoluminescence spectra have the same position of peaks/shoulders and similar intensities compared to the normal photoluminescence spectra, and that the spectral features of the up-conversion photoluminescence spectra are independent on the solvent polarity. Also, it was found that the lowest excitation energy for which the up-conversion photoluminescence can still be detected is 1.89 eV. Several mechanisms leading to photon energy up-conversion have been

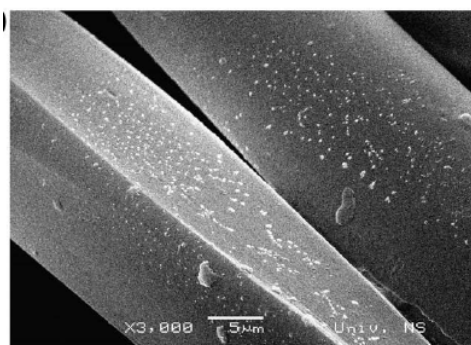


Fig.5. SEM image of TiO₂ nanoparticles on the PES+ALG fibres.

proposed in the literature, and additional experiments must be performed in order to exclude any ambiguity about up-conversion mechanism in this case.

So far, influence of shape, size and surface structure on different properties of TiO₂ nanoparticles (charge separation, optical) was covered. On the other hand, TiO₂ is suitable component for synthesis of different kinds of composite materials. Surface modification of polyester fibres with the 45 Å TiO₂ nano-spheres will be described, as well as in situ radical polymerization of methyl methacrylate in the presence of surface modified, hydrophobic TiO₂ nanocrystallites.

The SEM image of TiO₂ nanoparticles on the polyester fibres is shown in Figure 5. The TiO₂ nanoparticles, loaded on polyester fabrics, at the same time, have antibactericidal activity confirmed on Gram-negative bacterium *E. coli*, self cleaning effect tested using blueberry juice and methylene blue, as well as UV protection effect [7, 8]. As an example, degradation kinetic of methylene blue on the polyester fabrics surface modified with TiO₂ nanoparticles is shown in Figure 6. Roughly speaking, the efficiency/level of observed effects is dependant on the TiO₂ loading, which can be increased by different treatments that make fibre's surface more hydrophilic.

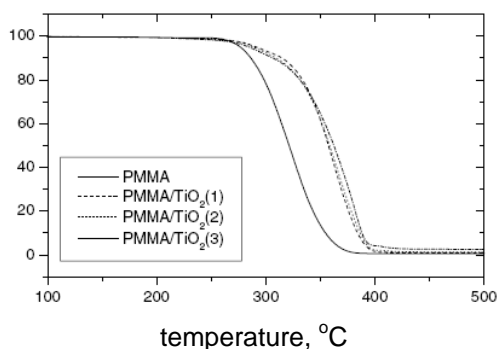


Fig.7. TG curves of pure PMMA and PMMA/TiO₂ nanocomposites obtained in air.

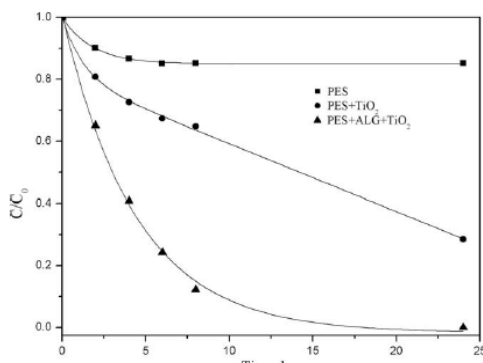


Fig.6. The dependence of C/C_0 versus time of UV illumination for the PES, PES+TiO₂ and PES+ALG+TiO₂ fabrics.

The main problem in polymer nanocomposite technology is the prevention of particle aggregation. This problem can be overcome by modification of the surface of the particles. The modification improves the interfacial interactions between the inorganic particles and polymer matrix. We synthesized poly(methyl methacrylate) and polystyrene by in situ radical polymerization of corresponding monomers in the presence of surface modified 45 Å

TiO₂ nanoparticles with 6-palmitate ascorbic acid [13-15]. The embedded nanoparticles have great influence on the thermal properties of polymer matrix (glass transition temperature and thermal degradation) even at concentration smaller than 1 wt.-%. As an example, comparison between thermogravimetric curves of neat poly(methyl methacrylate) and nanocomposites with different contents of inorganic phase is shown in Figure 7. It can be noticed that thermal stability of nanocomposites is improved for about 50 °C. Compared to fillers in micron or submicron size range, main advantage of nanoparticles is that improvement of desired properties of polymer matrix can be achieved at very low concentrations allowing preservation of intrinsic properties of polymers.

Conclusion

In this brief review, our effort to synthesize TiO₂ nanoparticles with desired shape, size and surface properties is presented, as well as our approach to improve charge separation processes on interface and to adjust optical properties of titanium dioxide. Also, special attention was paid to some possible applications involving usage of TiO₂ nanoparticulates (photocatalytic reduction of heavy metal ions, nanocrystalline solar cells, fabrics with antibactericidal and self cleaning effect, improvement of thermal properties of polymers). At the end, I would like to express gratitude to my colleagues from Vinča and other institutions, whose permanent interest, skill and hard work during last decade made all of this possible, bringing, at the same time, a lot of fun.

References

- [1] L. X. Chen, T. Rajh, W. Jäger, J. Nedeljković, M. C. Thurnauer, J. Synchrotron Radiat., 1999, **6**, 445-447.
- [2] T. Rajh, J. M. Nedeljković, L. X. Chen, O. Poluektov, M. C. Thurnauer, J. Phys. Chem. B, 1999, **103**, 3515-3519.
- [3] T. Rajh, Z. V. Šaponjić, O. I. Mičić, Langmuir, 1992, **8**, 1265-1270.
- [4] T. Rajh, J. Nedeljković, L. X. Chen, D. M. Tiede, M. C. Thurnauer, J. Adv. Oxid. Technol., 1998, **3**, 292-298.
- [5] I. A. Ruvarac-Bugarčić, Z. V. Šaponjić, S. Zec, T. Rajh, J. M. Nedeljković, Chem. Phys. Lett., 2005, **407**, 110-113.
- [6] S. Günes, N. Marjanović, J. M. Nedeljković, N. S. Sariciftci, Nanotechnology, 2008, **19**, 424009. J. M. Nedeljković,
- [7] D. Mihailović, Z. Šaponjić, M. Radoičić, T. Radetić, P. Jovančić, J. Nedeljković, M. Radetić, Carbohyd. Polym., 2010, **79**, 526-532.
- [8] D. Mihailović, Z. Šaponjić, R. Molina, N. Pauč, P. Jovančić, J. Nedeljković, M. Radetić, ACS Appl. Mater. Inter., 2010, **2**, 1700-1706.
- [9] N. D. Abazović, M. I. Čomor, M. D. Dramićanin, D. J. Jovanović, S. P. Ahrenkiel, J. M. Nedeljković, J. Phys. Chem. B, 2006, **110**, 25366-25370.

- [10] N. D. Abazović, I. A. Ruvarac-Bugarčić, M. I. Čomor, N. Bibić, S. P. Ahrenkiel, J. M. Nedeljković, *Opt. Mater.*, 2008, **30**, 1139-1144.
- [11] I. A. Janković, Z. V. Šaponjić, M. I. Čomor, J. M. Nedeljković, *J. Phys. Chem. C*, 2009, **113**, 12645-12652.
- [12] I. A. Janković, Z. V. Šaponjić, E. S. Džunuzović, J. M. Nedeljković, *Nanoscale Res. Lett.*, 2010, **5**, 81-88.
- [13] E. Džunuzović, K. Jeremić, J. M. Nedeljković, *Eur. Polymer J.*, 2007, **43**, 3719-3726.
- [14] E. Džunuzović, V. Vodnik, K. Jeremić, J. M. Nedeljković, *Mater. Lett.*, 2009, **63**, 908-910.
- [15] E. Džunuzović, M. Marinović-Cincović, J. Vuković, K. Jeremić, J. M. Nedeljković, *Polym. Compos.*, 2009, **30**, 737-742.
- [16] I. Ruvarac-Bugarčić, I. Janković, Z. Konstantinović, Z. Šaponjić, J. Nedeljković, *Acta Chim. Slovenica*, 2008, **55**, 268-172.

**FROM NONLINEAR DYNAMICS OF COMPLEX
CHEMICAL REACTIONS TO FUNCTIONAL DYNAMICS
OF BIOLOGICAL SYSTEMS**

Igor Schreiber

*Institute of Chemical Technology Prague, Department of Chemical Engineering
and Center for Nonlinear Dynamics of Chemical and Biological Systems,
Technická 5, 166 28 Prague 6, Czech Republic; tel. +420-220443033*

THERMAL LENS SPECTROMETRY AS A TOOL FOR PHYSICO-CHEMICAL CHARACTERISATION OF LIQUIDS AND SOLUTIONS

Mladen Franko

*University of Nova Gorica, Laboratory of Environmental Research,
Vipavska 13, SI-5000 Nova Gorica, Slovenia; mladen.franko@ung.si*

Abstract

Thermal lens spectrometry (TLS) is based on measurement of the refractive index gradient produced in an illuminated sample as a result of non-radiative relaxation of the absorbed energy of light. Because the technique is based on the measurement of the absorbed optical energy, its sensitivity is higher than conventional absorption techniques. However, advantages of TLS are not limited to its ultrasensitivity, but also include other unique characteristics such as dependency of the signal on thermo-optical properties of solvents. The main focus of this review is on the applications of TLS based on unique characteristics of the technique. Discussion will focus on examples of applications based on the ultrasensitivity of the technique exploited for chemical analysis, and applications based on exploitation of its dependency on thermal physical properties of solvents to determine physical properties of solvent or to further enhance the sensitivity of the technique.

Introduction

The availability of lasers makes it possible to observe and measure a variety of phenomena which would not be feasible using other light sources. One such phenomenon is the thermal lens effect [1-3] which is observable when a sample is irradiated by a laser beam having a symmetrical intensity distribution (TEM_{00}). The nonradiative relaxation subsequently releases the absorbed energy in the form of heat. The heat generated is strongest at the center of the beam because that is where the beam intensity is strongest. As a result, a lens-like optical element is formed in the sample owing to the temperature gradient between the centre of the beam and the bulk material. The thermal lens effect can be generated by laser beams in the power range of only milliwatts in samples normally thought to be transparent, and is thus suitable for the low absorption measurement of non-fluorescent samples. The sensitivity of TLS is relatively higher than that of the conventional transmission or reflection measurements because in this technique, the signal is proportional to absorbed energy.

The first measurement of the thermal lens effect was performed by Gordon *et al.* in 1965 using a simple single beam apparatus [1]. Theories have since been derived to explain the effect and to facilitate its applications to chemical analysis and characterization. Recent advances in optics, electronics, quantum electronics,

and material science have been synergistically exploited to develop novel instruments which have lower background noise, higher sensitivity and selectivity, and wider spectral range [4]. The unique characteristics of lasers, namely low beam divergence, pure polarization, high spectral and spatial resolution, and the ability to focus laser beams to a diffraction-limited spot, have been fully exploited to use thermal lens as a detection technique for microfluidic devices [5]. As a consequence of these developments, the TLS technique has been established as a highly sensitive technique for trace chemical characterization, including single molecule detection.

In addition to its ultrasensitive and small volume capabilities, the TLS technique offers other features which cannot be rivalled by other techniques. Namely, the thermal lens signal is dependent not only on sample concentration and excitation laser power, but also on the position and thermo-physical properties of the sample. These unique features have been exploited either to further increase its sensitivity or to use it for sensitive and accurate determination of thermal physical properties of a variety of substances including solids, liquids, and gases.

Due to its advantages and unique features, the TLS technique has been extensively reviewed [2-8]. This review however focuses on features of TLS which could be important from physical chemist's point of view. This includes a brief theoretical background of TLS technique to provide a fundamental understanding of this approach as well as to enable readers to follow discussion in the following chapters. Subsequent sections are devoted to selected applications based on unique features and capabilities of the TLS technique, primarily its ultrasensitivity (applications in chemical analysis and reaction kinetics), its use for determination of thermal physical properties of liquids, and their use to enhance the sensitivity of TLS.

Theoretical background

Thermal lens signal, when recorded as the time dependent change in the far field beam center intensity ($I_{bc}(t)$) after the onset of illumination by excitation laser when $I_{bc}(t) = I_{bc}(0)$, is given by [9]:

$$I_{bc}(t) = I_{bc}(0) \left\{ \begin{aligned} & \left[1 - \theta \tan^{-1} \left(\frac{1}{(1 + t_c/t)\sqrt{3}} \right) + \left[\frac{\theta}{2} \tan^{-1} \left(\frac{1}{(1 + t_c/t)\sqrt{3}} \right) \right]^2 \right]^2 + \\ & \left[\frac{\theta}{4} \ln \left(\frac{(1 + t/t_c)^2 + 1/3}{(2 + t_c/t)^2} \right) \right]^2 \end{aligned} \right\} \quad (1)$$

The thermal time constant t_c which depends on the spot size (ω), of the excitation beam in the sample, the density (ρ), specific heat capacity (C_p) and thermal conductivity (k) of the solvent, is given by:

$$t_c = \frac{\omega^2 \rho C_p}{4k} \quad (2)$$

while θ is defined as:

$$\theta = \frac{2.303P(-dn/dT)A}{k\lambda} \quad (3)$$

where P is power of the excitation beam, A absorbance of the sample, (dn/dT) the temperature coefficient of sample's refractive index, and λ the wavelength of the probe beam.

For low absorbances, the steady state thermal lens signal ($t \gg t_c$) which is measured as the relative change in the beam center intensity in the far field, $\Delta I_{bc}/I_{bc}$, is given by:

$$\frac{\Delta I_{bc}}{I_{bc}} = \frac{2.303P(-dn/dT)A}{\lambda k} \tan^{-1}\left(\frac{1}{\sqrt{3}}\right) \quad (4)$$

The relative change in the beam intensity, when determined by conventional absorption techniques for a weakly absorbing species, is:

$$\frac{I_0 - I}{I_0} = 1 - 10^{-A} = 2.303A \quad (5)$$

It is therefore clear from Eqs. 4 and 5 that the sensitivity of the TLS technique is relatively higher than that of conventional absorption methods. The sensitivity enhancement factor E , as derived from Eqs. 4 and 5 is:

$$E = \frac{P(-dn/dT)}{1.91\lambda k} \quad (6)$$

It is evidently clear from Eqs. 4 and 6 that the sensitivity of the TLS technique is not only directly proportional to the excitation laser power but also depends on the thermal physical properties of the sample. The dependency of the thermal lens signal on the thermal physical properties of sample or solvent can, in principle, be exploited to enhance the sensitivity and selectivity of the technique. Organized assemblies such as micelles, reversed micelles and crown ethers can be effectively used to modify the thermal physical properties, (i.e., dn/dT and k values) of the medium which, in turn will enhance sensitivity of the TLS measurements. Sensitivity enhancement through manipulation of thermal physical properties of the medium can also be achieved by use of room temperature ionic liquids, or by changing measurement temperature of aqueous solutions, as will be explained later.

As can be calculated from Eq. 2 typical time constants in TLS experiments are in the range of milliseconds in liquids and even shorter in gasses, depending also on the focusing of the pump beam. Thermal lens signal is therefore independent of changes in absorbances of the sample, unless such changes occur at times much shorter than the experimental time constant t_c .

When the absorbing species transforms rapidly during the excitation due to some chemical reaction, the changes in absorbance must be considered in theoretical treatment of the thermal lens. On the other hand, this gives the possibility to deduce the reaction rate constants and information on the order of fast chemical reactions. For this purpose, novel theories have been derived to describe the thermal lens signal for reactions of zero, first and second order [10].

For example, for the case of zero order reaction the following expression indicating the decrease of the thermal lens signal due to disappearance of the analyte (second term on the right hand side of Eq. 7) was derived [10]:

$$\frac{\Delta I_{bc}}{I_{bc}} = \theta \tan^{-1} \left(\frac{1}{(1 + t_c/t)\sqrt{3}} \right) - \theta \frac{k_r}{C_0} \left[\left(t + \frac{3t_c}{4} \right) \tan^{-1} \left(\frac{1}{(1 + t_c/t)} \right) + \frac{t_c \sqrt{3}}{8} \ln \left(\left(1 + \frac{t}{t_c} \right)^2 + \left(\frac{t}{t_c \sqrt{3}} \right)^2 \right) \right] \quad (7)$$

When the reaction rate constant k_r equals zero, the expression becomes identical to the case with constant concentration of analyte with initial concentration C_0 .

Trace chemical analysis by TLS

Many applications of TLS in trace chemical analysis including food and environmental samples have been reported and reviewed in papers and book chapters recently [3, 8]. However, few detailed validations of proposed new analytical methods were carried out. The first reported validation of TLS was performed for batch mode determination of Cr^{VI} using a standard reference material and was followed by comparative determination of chromium species (Cr^{III} and Cr^{VI}) in drinking water samples by ion chromatography (IC) with spectrometric and TLS detection. Limits of detection (LOD) lowered by almost two orders of magnitude compared to transmission mode UV-Vis measurements and good agreement of measured values with reference values, and those provided by an independent technique, have definitely established TLS as accurate and reliable analytical tool [11].

Improvements in LODs, compared to IC with UV-Vis detection were reported also for the IC-TLS determination of Cr^{VI} and Cr^{III} where both species are separated as anions after pre-column derivatization of Cr^{III} with pyridine dicarboxylic acid. For detection of Cr^{VI} a post-column derivatization with diphenylcarbazide (DPC) is needed, which however results in dilution of the initial sample by a factor of two, and therefore in proportionally higher LOD [12]. Comparative analysis of drinking water samples has revealed another advantage of TLS detection, which was found much less

affected by light scattering, resulting from CO₂ released in acidified samples containing higher levels of carbonate. As a result of light scattering the UV-Vis detection was subject to up to 20% positive errors.

By exploiting addition of organic solvents such as methanol, acetone or acetonitrile, it was possible to significantly improve sensitivity of the IC-TLS. Addition of acetonitrile to the eluent and post-column reagent (30% v/v) enables simultaneous determination of Cr^{VI} at 0.1 µg L⁻¹ and of Cr^{III} at 10 µg L⁻¹ level [13]. The improvement stems from the fact that due to lower k and higher dn/dT of acetonitrile compared to water, the enhancement factor was increased by a factor of 5.4 compared to measurements in an aqueous eluent. Such low LOD value for Cr^{VI} is comparable to the LOD for ET-AAS, which is however not capable of performing on-line detection during separation of both Cr species.

The sensitivity of TLS determination of Cr^{VI} was further improved by performing measurements in a flow injection (FIA) mode. As it will be explained later, the Cr-DPC complexes are photolabile and were shown to degrade rapidly under the influence of intensive (100 – 500 mW) and tightly focused laser light. The application of FIA is therefore advantageous since it reduces the exposure of analyte to laser light and thereby reduces photodegradation of Cr-DPC, which is known to hinder the sensitivity. Furthermore, the uncertainty of the measurement arising from uncontrolled photodegradation in batch mode measurement is also reduced. As a result of measurements in FIA mode, the LOD for TLS determination of Cr^{VI} was reduced down to 67 ng L⁻¹ [14] without adding organic solvents to improve thermo-optical properties. This represents an improvement by almost a factor of two compared to the batch mode measurement [11].

Studies of reaction kinetics

Based on theories developed for TLS under conditions of changing absorbance, computer calculations were performed to simulate conditions for various chemical reactions. The agreement of measured experimental results with the values predicted by the developed theories confirmed that the TLS technique provides kinetic results which are not only accurate and precise but also can be obtained with reagents whose concentrations are about 100 times lower compared to conventional methods [15].

The possibility to study fast chemical reactions in solution by TLS method was further confirmed by investigating the photo labile Cr-DPC complexes in water [16]. Lower thermal lens signal and abnormal behavior of the thermal lens transient induced by a photochemical reaction were observed during optical excitation. The existing theoretical model of thermal lens effect was further generalized in order to take into account the time dependence of the absorbance of the sample due to changes in concentration resulting from photochemical reaction as well as from diffusion of absorbing species. The comparison of experimental measurements under different reaction conditions demonstrated the usefulness of time-resolved TLS method for the study of photochemical reactions under the presence of absorbing species diffusion and confirmed its capability of monitoring the

processes in a quantitative way and with a temporal resolution of a few milliseconds. The applicability of the technique is however limited by the time constant t_c , which can not be decreased infinitely by reducing the radius of the probe beam. Photothermal techniques such as the temperature grating must be used to investigate faster chemical reactions occurring on the ns time scale [17].

Thermal physical properties of solvents studied by TLS

In addition to sensitive detection of trace chemical species, it is also possible to use the TLS technique as an accurate and sensitive method for the determination of the thermal physical properties of solvents, namely their dn/dT and k values. These two thermal physical properties can be individually determined by measuring the transient of the thermal lens. Thus, θ and t_c values can be obtained by curve fitting of the thermal lens transient to Eq. 1. Using the obtained t_c value in Eq. 2 will yield either the thermal conductivity or the heat capacity of the sample, when one of them is known. The dn/dT value can then be calculated from Eq. 3 using the θ and k values.

Using the method described above, the k and dn/dT values of water at different temperatures were obtained [18]. It was also reported that, within experimental error, the k value remains constant at different temperatures. The dn/dT value, however, undergoes significant change as the temperature varies. For instance, an increase of temperature by 16 degrees C (from 1.26°C to 17.98°C) leads to a 14-fold increase in the dn/dT value. This observation can be explained in terms of the structure of water. Specifically, it is known that the structure of water is greatly affected by the temperature of the solution. Increasing the temperature of the aqueous solution will have the "hydrogen bond breaking effect". As a consequence, the water has less hydrogen bonds, becomes less structured (or less ordered) and hence can have large changes in the density and in the refractive index with temperature (i.e., higher dp/dT and dn/dT values).

It was found from the study of temperature effect on TLS measurements in water, that depending on whether the measurements are performed at temperatures lower or higher than -0.01°C, the thermal lens can have either a positive (converging) or negative (diverging) focal length. At $-0.01 \pm 0.04^\circ\text{C}$, no thermal lens signal could be observed. This is because the dn/dT values of water are positive at $T < -0.01^\circ\text{C}$, negative at $T > -0.01^\circ\text{C}$, and equal to zero at $T = -0.01^\circ\text{C}$ (i.e., maximum refractive index) [19]. These results are of particular interest considering the fact that water exhibits maximum density at +4.0 °C which is different from the temperature at which its refractive index is maximum. This behavior is distinctly different from other liquids which are known to undergo maximum density and refractive index at the same temperature. As predicted based on Lorentz-Lorenz equation relating refractive index and density for liquids, dn/dT of water is expected to go through zero at the temperature where dp/dT is positive, i.e., at the temperature lower than 4°C, which is in agreement with the results obtained with TLS measurements.

This unique behavior of water has been exploited in other types of photothermal techniques for measurements which otherwise are not possible. For instance, it has been demonstrated that by measuring aqueous solutions of biopolymers at -0.01°C

where dn/dT of water is zero, it was possible to remove signal due to dn/dT from the total thermal lens signal, thereby enabling determination of change in volume or the conformation of polymers induced by temperature change [20]. Conversely, by measuring thermal lens signal at +4.0 °C where density of water is maximum, it was possible to eliminate contribution due to change in volume (of aqueous solution) with temperature, which as a consequence, makes it possible to measure change in concentration of solution as a function of temperature [17].

The dn/dT and k values of organic solvents such as methanol, CCl_4 , chloroform, DMF, DMSO and heptane, as well as various aqueous solutions were also accurately determined by use of described TLS method [21]. Recently, room temperature ionic liquids (RTILs) were studied by TLS [22], since they are of particular technological importance. For example, the k and dn/dT values for $BMIIm^+Tf_2N^-$ were found to be $1.785 \text{ mW cm}^{-1} \text{ K}^{-1}$ and $-7.5 \times 10^{-4} \text{ K}^{-1}$, respectively. The lower k and higher $-dn/dT$ values of RTILs compared to water ($k_w = 6.04 \text{ mW cm}^{-1} \text{ K}^{-1}$, $(dn/dT)_w = -8.8 \times 10^{-5} \text{ K}^{-1}$) are similar to those expected for nonpolar, volatile organic solvents (e.g., benzene, hexane and CCl_4), which should provide good media for TLS measurements owing to their high dn/dT and low k values. Water, which is the universal solvent for biochemical and biological samples is unfortunately the worst medium for TLS technique because of a very low $-dn/dT$ and high k values. In fact, it has been calculated and experimentally confirmed that at the same laser power, TLS measurements in CCl_4 and n-pentane are 38 and 40 times more sensitive than those in water [23]. As a consequence, considerable efforts have been made to use novel solvents that have better thermo-optical properties than water but do not cause pollution and environmental concern like traditional volatile organic solvents. It is expected that RTILs with their unique properties (nonvolatile, no vapor pressure, high solubility power, adjustable polarity) should serve as a greener solvent providing higher sensitivity for TLS measurements [22].

It was in fact demonstrated that RTILs can be used as an attractive and superior solvent for TLS measurements [22]. RTILs are superior to water as they have relatively high solubility power, and by judiciously selecting either the cation and/or anion, they can dissolve many different types of compounds including polar as well as non polar compounds. More importantly, RTILs provide a relatively better medium for TLS measurements than water. Not only that the RTILs offer at least 20 times higher sensitivity but the enhancement can be appropriately adjusted by changing either the cation and/or the anion of the RTILs. For example, the sensitivity in $[BMIIm]^+[Tf_2N]^-$ is about 26 times higher than in water. It can be increased up to 31 times by changing the anion to $[PF_6]^-$ (i.e., $[BMIIm]^+[PF_6]^-$) or to 35 times by changing the cation to $[OMIm]^+$ (i.e., $[OMIm]^+[Tf_2N]^-$). In fact, the sensitivity of TLS measurements in RTILs is comparable to those in volatile organic solvents such as benzene, CCl_4 , hexane, but RTILs are more desirable as they have virtually no vapor pressure.

Conclusion

This review exposed some advantages of the TLS techniques, which are not just limited to its ultrasensitivity but also include other unique features that no other techniques have, such as for example the dependency on thermo-optical properties of solvents. Because of its unique features, TLS technique can be used for measurements and studies which are otherwise not possible using other existing techniques. These include determination of thermal physical properties (thermal conductivity, temperature coefficient of refractive index) of solvents, studies of reaction kinetics of weakly absorbing species, and sensitive determination of various chemical species, which actually represents the majority of applications of TLS.

References

- [1] J. P. Gordon, R. C. C. Leite, R. S. Moore, S. P. S. Porto, J. R. Whinnery, *J. Appl. Phys.*, 1965, **36**, 3-8.
- [2] S. E. Bialkowski, *Photothermal Spectroscopy Methods for Chemical Analysis*, John Wiley & Sons, Inc., New York, 1996.
- [3] C. D. Tran, M. Franko, *Thermal Lens Spectroscopy*, in *Encyclopedia of Analytical Chemistry*, R. A. Meyers (ed.), John Wiley, Chichester., 2010. DOI: 9780470027318.
- [4] M. Franko, C. D. Tran, *Rev. Sci. Instrum.*, 1996, **67**, 1-18.
- [5] T. Kitamori, M. Tokeshi, A. Hibara, K. Sato, *Anal. Chem.*, 2004, **76**, 52A-60A.
- [6] A. Mandelis, *Principles & Perspectives of Photothermal & Photoacoustic Phenomena*, Elsevier, New York, 1992.
- [7] C. D. Tran, *Photothermal Detectors for High-Performance Liquid Chromatography*, in: *HPLC Detection, Newer Methods*, G. Patonay (ed.), VCH, New York, 1992.
- [8] M. Franko, *Appl. Spectrosc. Rev.*, 2008, **43**, 358-388.
- [9] S. J. Sheldon, L. V. Knight, J. M. Thorne, *Appl. Opt.*, 1982, **21**, 1663-1669.
- [10] M. Franko, C. D. Tran, *Rev. Sci. Instrum.*, 1991, **62**, 2430-2437.
- [11] M. Šikovec, M. Franko, F. G. Cruz, S. A. Katz, *Anal. Chim. Acta*, 1996, **330**, 245-250.
- [12] A. Madžgalj, M. L. Baesso, M. Franko, *Eur. Phys. J. Special Topics*, 2008, **153**, 503-506.
- [13] M. Šikovec, Mi. Novič, V. Hudnik, M. Franko, *J. Chromatogr. A*, 1995, **706**, 121-126.
- [14] M. Šikovec, M. Franko, Mi. Novič, M. Veber, *J. Chromatogr. A*, 2001, **920**, 119-125.
- [15] M. Franko, C. D. Tran, *Rev. Sci. Instrum.*, 1991, **62**, 2438-2442.
- [16] P. R. B. Pedreira, L. R. Hirsch, J. R. D. Pereira, A. N. Medina, A. C. Bento, M. L. Baesso, M. C. E. Rollemberg, M. Franko, *J. Shen, J. Appl. Phys.*, 2006, **100**, 044906.
- [17] M. Terazima, *J. Chem. Phys.*, 1996, **104**, 4988-4998.

- [18] M. Franko, C. D. Tran, *Anal. Chem.*, 1989, **61**, 1660-1666.
- [19] M. Franko, C. D. Tran, *Chem. Phys. Lett.*, 1989, **158**, 31-36.
- [20] S. E. Braslavski, G. E. Heibel, *Chem. Rev.*, 1992, **96**, 1381-1410.
- [21] M. Franko, C. D. Tran, *J. Phys. Chem.*, 1991, **95**, 6688-6696.
- [22] C. D. Tran, S. Challa, M. Franko, *Anal. Chem.*, 2005, **77**, 7442-7447.
- [23] C. D. Tran, T. A. Van Fleet, *Anal. Chem.*, 1988, **60**, 2478-2482.

Chemical Thermodynamics ^A

PREDICTION OF CALCIUM SULFATE DIHYDRATE SOLUBILITY IN THE SYSTEM $\text{CaSO}_4 + \text{Na}_2\text{SO}_4 + \text{H}_2\text{O}$ AT $T = 298.15 \text{ K}$

G. Stupar, D. Popović, J. Miladinović and M. Todorović

*Faculty of Technology and Metallurgy, University of Belgrade
Karnegijeva 4, 11 000 Belgrade, Serbia*

Abstract

Prediction of Calcium Sulfate Dihydrate solubility, as well as other present phases in the system $\text{CaSO}_4 + \text{Na}_2\text{SO}_4 + \text{H}_2\text{O}$ at $T = 298.15 \text{ K}$ was performed using the Pitzer's ion–interaction model for pure and mixed electrolyte solutions and criteria of phase equilibria. Predicted solubility behaviour of five different salts was compared with experimental results from literature. The agreement between calculated and experimental solubility of Calcium Sulfate Dihydrate, Mirabilite, Glauberite, Thenardite and Labile Salt, was excellent in the ionic strength range up to $10.881 \text{ mol}\cdot\text{kg}^{-1}$.

Introduction

The purpose of this investigation was to obtain solubility and phase data on the system $\text{CaSO}_4 + \text{Na}_2\text{SO}_4 + \text{H}_2\text{O}$ at $T = 298.15 \text{ K}$. The study has some practical importance since the informations can be applied to sodium sulfate recovery from brines as well as scale formation in sea water distillation plants. At this temperature four phases can be present in the investigated system: Calcium Sulfate Dihydrate (Gypsum) – $\text{CaSO}_4 \cdot 2\text{H}_2\text{O}(\text{cr})$; Mirabilite – $\text{Na}_2\text{SO}_4 \cdot 10\text{H}_2\text{O}(\text{cr})$; Thenardite – $\text{Na}_2\text{SO}_4(\text{cr})$ and two double salts, Glauberite – $\text{Na}_2\text{Ca}(\text{SO}_4)_2(\text{cr})$ and Labile Salt – $\text{Na}_4\text{Ca}(\text{SO}_4)_3 \cdot 2\text{H}_2\text{O}(\text{cr})$. To predict the solubility behaviour of these salts, Pitzer's ion interaction model for pure and mixed electrolyte solution was used [1-3]. Following relations of the model, for the osmotic coefficients of the system (1) and relations for activity coefficients of ions Na^+ , Ca^{2+} and SO_4^{2-} (2), (3) and (4), respectively, appear in the criteria of the phase equilibria [4].

$$\phi - 1 = \left\{ \frac{2}{2m_1 + 3m_2} \right\} \left[-A_\phi I^{3/2} / (1 + bI^{1/2}) + (m_1 + m_2)m_1 \left\{ B^\phi(\text{Ca}, \text{SO}_4) \right\} + 2m_2(m_1 + m_2) \left\{ B^\phi(\text{Na}, \text{SO}_4) + ZC^T(\text{Na}, \text{SO}_4) \right\} + 2m_1m_2 \left\{ \theta(\text{Na}, \text{Ca}) + (m_1 + m_2)\psi(\text{Na}, \text{Ca}, \text{SO}_4) \right\} \right] \quad (1)$$

$$\ln \gamma(\text{Na}^+) = F + (m_1 + m_2) \left\{ 2B(\text{Na}, \text{SO}_4) + ZC^T(\text{Na}, \text{SO}_4) \right\} + m_1 \left\{ 2\theta(\text{Na}, \text{Ca}) + (m_1 + m_2)\psi(\text{Ca}, \text{Na}, \text{SO}_4) \right\} + 2m_2(m_1 + m_2) C^T(\text{Na}, \text{SO}_4) \quad (2)$$

$$\ln \gamma(\text{Ca}^{2+}) = 4F + (m_1 + m_2) \left\{ 2B(\text{Ca}, \text{SO}_4) + ZC^T(\text{Ca}, \text{SO}_4) \right\} + 2m_2 \left\{ 2\theta(\text{Na}, \text{Ca}) + (m_1 + m_2)\psi(\text{Ca}, \text{Na}, \text{SO}_4) \right\} + 4m_2(m_1 + m_2) C^T(\text{Na}, \text{SO}_4) \quad (3)$$

$$\ln \gamma(\text{SO}_4^{2-}) = 4F + m_1 \left\{ 2B(\text{Ca}, \text{SO}_4) + 2m_2 \{ 2B(\text{Na}, \text{SO}_4) \} + ZC^T(\text{Na}, \text{SO}_4) \right\} + 2m_2 m_1 \psi(\text{Ca}, \text{Na}, \text{SO}_4) + 2m_2 (m_1 + m_2) C^T(\text{Na}, \text{SO}_4) \quad (4)$$

Results and Discussion

Parameters of the Pitzer's ion-interaction model of pure electrolytes $\text{CaSO}_4(\text{aq})$ and $\text{Na}_2\text{SO}_4(\text{aq})$ β^ϕ , B , $C^{T\phi}$, C^T and of mixed electrolyte solution $\text{CaSO}_4 + \text{Na}_2\text{SO}_4 + \text{H}_2\text{O}$, $\theta(\text{Na}, \text{Ca})$ and $\psi(\text{Na}, \text{Ca}, \text{SO}_4)$ at $T = 298.15$ K, from equations (1)–(4), are given in Table 1.

Table 1. Parameters of the Pitzer's ion–interaction model valid at $T = 298.15$ K and $p = 101.325$ kPa

Pure electrolyte solution		
	$\text{Na}_2\text{SO}_4(\text{aq})$	$\text{CaSO}_4(\text{aq})$
$\beta^{(0)}(\text{M}, \text{X})$	0.011976	–1.9762
$\beta^{(1)}(\text{M}, \text{X})$	0.951276	2.8696
$\alpha_1(\text{M}, \text{X})$	2.0	1.4
$\beta^{(2)}(\text{M}, \text{X})$	–	–57.7
$\alpha_2(\text{M}, \text{X})$	–	12
$C^{(0)}(\text{M}, \text{X})$	0.0024359	–
$C^{(1)}(\text{M}, \text{X})$	0.236044	–
$\omega(\text{M}, \text{X})$	2.5	–
Mixed electrolyte solution $\text{CaSO}_4 + \text{Na}_2\text{SO}_4 + \text{H}_2\text{O}$		
$\theta(\text{Ca}, \text{Na})$	1.1104	
$\psi(\text{Ca}, \text{Na}, \text{SO}_4)$	– 0.0165	
max. I ($\text{mol} \cdot \text{kg}^{-1}$)	10.881	

Comparing the experimental [5-8] and calculated salt solubilities by Pitzer's ion–interaction model and parameters given in Table 1, excellent agreement was obtained. Standard deviation of the fit for calculated calcium sulfate dihydrate solubility in the investigated system was $3.1 \cdot 10^{-4}$ in the ionic strength range up to $I = 10.881$ $\text{mol} \cdot \text{kg}^{-1}$.

The solubility curve for calcium sulfate dihydrate passes through a minimum at 0.08 $\text{mol} \cdot \text{kg}^{-1}$ molality of Na_2SO_4 in the system and through a maximum at about 2.0 $\text{mol} \cdot \text{kg}^{-1}$. For other salts, present in the system at $T = 298.15$ K, the agreement is acceptable, especially for Mirabilite – $\text{Na}_2\text{SO}_4 \cdot 10\text{H}_2\text{O}(\text{cr})$ and Glauberite – $\text{Na}_2\text{Ca}(\text{SO}_4)_2(\text{cr})$. In Figure 1. are presented results of salts solubility predictions together with experimental results from literature data [5-8]. From Figure 1. it can be concluded that the isothermally invariant point for calcium sulfate dihydrate and

mirabilite, shows a very little change in the solubility of mirabilite caused by the small amount of calcium sulfate present. Of the two double salts formed at $T = 298.15$ K, the labile salt has a greater region of stability at the lower concentrations of Na_2SO_4 in the system and glauberite predominates at higher concentration of Na_2SO_4 in the $\text{CaSO}_4 + \text{Na}_2\text{SO}_4 + \text{H}_2\text{O}$.

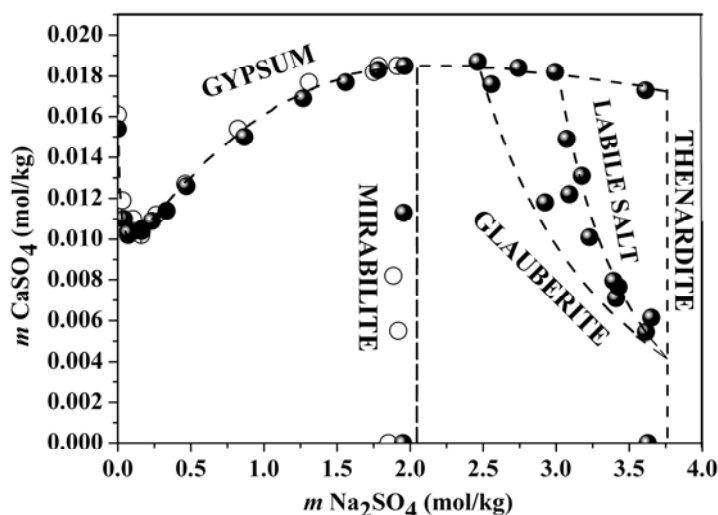


Fig.1. Solubilities of salts in the system $\text{CaSO}_4 + \text{Na}_2\text{SO}_4 + \text{H}_2\text{O}$ at $T = 298.15$ K: curves – calculated values by Pitzer ion-interaction model; O– data of Block and Waters [5]; □ – data of Hill and Wills [8] ; / – data of Yeatts and Marshall [6,7]

Conclusion

Pitzer's ion–interaction model for pure and mixed electrolyte solutions gave excellent agreement between predicted and experimental solubilities for calcium sulfate dihydrate in the system $\text{CaSO}_4 + \text{Na}_2\text{SO}_4 + \text{H}_2\text{O}$ at $T = 298.15$ K for the concentration range up to $10.881 \text{ mol}\cdot\text{kg}^{-1}$. Predicted behaviour of other salts, present in the system, is acceptable.

Acknowledgments

This work was supported by the Ministry for Science and Environmental Protection of the Republic of Serbia under Project No. 142064.

References

- [1] K. S. Pitzer, J. J. Kim, J. Am. Chem. Soc., 1974, **96**, 5701-5710.
- [2] J. A. Rard, S. L. Clegg, and D. A. Palmer, J. Solution Chem., 2000, **29**, 1-48
- [3] K. S. Pitzer, G. Mayorga, J. Solution Chem., 1974, **3**, 539-562.
- [4] C. E. Harvie, J. H. Weare, Geochim. Cosmochim. Acta, 1980, **44**, 981-997.
- [5] J. Block, O. B. Jr., Waters J. Chem. Eng. Data, 1968, **13**, 336-344.
- [6] L. B. Yeatts, W. L. Marshall, J. Phys. Chem., 1969, **73**, 81-90.
- [7] L. B. Yeatts, W. L. Marshall, J. Phys. Chem., 1972, **17**, 163-168.
- [8] A. E. Hill, J. H. Wills., J. Am. Chem. Soc., 1938, **60**, 1674-1655.

DEVELOPMENT OF COMPUTER MODELING SYSTEM FOR ALKANES C₉-C₁₄ DEHYDROGENATION PROCESS ON THE BASE OF THERMODYNAMIC AND KINETIC ANALYSIS

E.V. Frantsina, J. I. Afanasjeva and E. D. Ivanchina

*Chemistry department, National Research Tomsk Polytechnic University,
Lenina avenue 30, Tomsk, Russia (evf86@sibmail.com)*

Abstract

Based on mathematical approach method, computer modeling system was applied to higher alkanes dehydrogenation process optimization. Use of the system allows determination of the optimal technological characteristics; calculation of process characteristics taking into account feed composition, technological conditions and type of catalyst.

Introduction

Optimization of the processes, search for new ways of effective stuff use are possible on models, having high reliability and forecasting ability in a wide range of technological conditions changes [1]. Such models are formed on the basis of reactants transformation chemical system that takes into account formalized mechanism of most probable reactions and their thermodynamic probability.

The best of all mathematical modeling methods are developed for mixtures consisting of some components [2, 3]. In this case there are no fundamental problems with development of mathematical model reactions and determination of their characteristics. This task is complicated for oil treatment reactor processes of broad hydrocarbons stuff fractions. On the one hand adequacy of model increases taking into account detailed mechanism; on the other hand it results in complexity of mathematical description and embarrasses practical application over inaccuracy of characteristics determination. At the same time hydrocarbons transformation mechanism formalization must be conducted taking into account reactivity of mixture components that depends on entropy and enthalpy characteristics determining character of molecular bonds and their energies.

Thus the main difficulty in industrial processes and manufactures modeling lies in choice of necessary level of mechanism refinement and description of complicated hydrocarbon mixtures transformation kinetics taking into account peculiarity of used catalysts.

The purpose of present work is creation of alkanes C₉-C₁₄ dehydrogenation process mathematical model sensitive to stuff composition and technological characteristics with refinement of substances transformation scheme on basis of quantum-chemical calculations and conceptions of reactions mechanism, kinetic characteristics estimation for all reactions occurring during the process.

Results and Discussion

On basis of dehydrogenation mechanism conceptions presumable transformation scheme of present process was formed. With usage of Gaussian program package containing PM3 procedure of NDDO method, based on quantum-chemistry modeling, electron molecule structures were calculated and reaction thermodynamic characteristics estimation (ΔG_r , ΔH_r , ΔS) was conducted under 753 K and 0,2 MPa. Method under consideration takes into account oscillatory and rotator movements of atoms, electron orbit pattern, effects of double bonds conjugation and reproduces the structure and energy hyper valence compounds with high accuracy, providing adequate accuracy for high-quality reproduction of molecule physiochemical characteristics.

On the basis of these results formalized scheme of higher alkanes C₉-C₁₄ dehydrogenation process was formed (fig. 1) and substances were combined into groups of pseudo components according to their reactionary ability that is evaluated according to isobaric-isothermal potential ΔG_r . Thus 11 groups of pseudo components take part in 22 types of chemical reactions.

This level of mechanism formalization permits to cut down mathematical description of passing reactions and time solution of material and thermal balance equations, as well as keep the sensitivity concerning stuff components and the self-descriptiveness concerning products of passing reactions.

Higher hydrocarbons C₉-C₁₄ dehydrogenation process modeling represents a difficult task. Fair quantities of passing reactions bring to high dimensionality of mathematical model and demands determination of a great number of kinetic parameters (preexponential factors k_0 and activation energies E_a) for all chemical reaction types. Kinetic experiment realization on industrial installation is not possible. Therefore a more effective variant of k_0 and E_a determination is decision of reverse kinetic task.

When deciding the differential equations system that describes real chemical process numerical method of calculation is to be used, in this case we used net method. Hereby differential equations system decision was provided kinetic parameters were calculated.

Ideal spilling model of reactor was used. Present assumption was controlled by force of diffusion criterion Pickle Pe_D estimation. General mathematical model of process taking heat balance into account is presented in the following way:

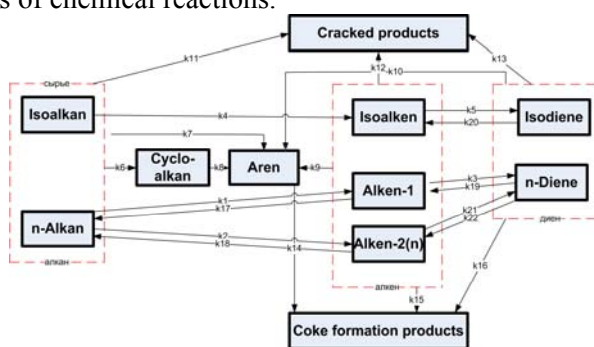


Fig.1. Formalized scheme of dehydrogenation process mechanism.

$$\begin{cases} G \frac{\partial C_i}{\partial z} + G \frac{\partial C_i}{\partial V} = (1-\varepsilon) \sum_{j=1}^N w_j, i=1...M, j=1...N \\ G \frac{\partial T}{\partial z} + G \frac{\partial T}{\partial V} = -(1-\varepsilon) \frac{\sum_{j=1}^N (\Delta H_j w_j)}{c_p \cdot \rho}, \end{cases}$$

where G – hour consumption of stuff, meter³/hour; C_i – i hydrocarbon concentration, mole/meter³; V – catalyst volume, meter³; ε – fractional void volume of catalyst layer, $\varepsilon = 0...1$; w_j – j reaction rate, mole/(meter³·hour); z – «reduced time» or summary volume of processed stuff after catalyst regeneration, meter³, $z = Gt$; t – time, hour; M – number of components; N – number of reactions; T – process temperature, K; ΔH_j – reaction thermal effect, Joule/mole; C_p – mixture heat, Joule/(kilogram·K); ρ – mixture density, kilogram/meter³.

Initial and boundary conditions:

$$\begin{aligned} z=0: C_i=0, T=T_{first}; \\ V=0: C_i=C_{i,enter}, T=T_{enter}. \end{aligned}$$

Mathematical model is formed taking stationary factors of industrial process into account that relate to coke structures sediment on surface of catalyst. Exponential dependence of catalyst activity from coke accumulation:

$$a_j = A e^{-\alpha_j C_k},$$

where a_j – relative catalyst activity which is equal to ratio of reaction rates passing on coked and fresh catalyst; A – entropy factor of process; α_j – poisoning coefficient that depends on ratio of acid and basis factors in the given type of reaction; C_k – coke concentration on catalyst.

Conclusion

Offered mechanism formalization layer lies in hydrocarbons association in reactionary series by ΔG_r index. Reactionary ability of compounds is estimated with quantum-chemical method NDDO usage that contains PM3 procedure. Mechanism layer formalization does not overload mathematical description on the one hand, at the same time it permits to take olefins and dienes with double bonds in different position formation into account, as well as isoparaffines formation as stuff components.

Kinetic parameters for all reactions estimation is carried out. Calculation mistake does not exceed 4 % that is compared to chromatographic analysis method mistake usually used for product components concentration determination. Program realized model of process permits to calculate material and thermal reactor balances with enough accuracy, as well as investigates the influence of different technological conditions change on effectiveness of process realization.

References

- [1] A. V. Kravtsov, E. D. Ivanchina, *Petrol. treat. and Petrochem.*, 2005, **9**, 40–43.
- [2] G. Padmavathi, *Chemical Engineering Science*, 2005, **60**, 4119–4129
- [3] P. M. Bidgani, S. Sahebdehfar, *Kinetics and catalysis*, 2008, **4**, 625–632

KINETICS OF STRUCTURAL TRANSFORMATIONS OF $\text{Fe}_{75}\text{Ni}_2\text{Si}_8\text{B}_{13}\text{C}_2$ AMORPHOUS ALLOY INDUCED BY THERMAL TREATMENT

D. M. Minić^{a1}, Lj. Mihajlović^a, A. Gavrilović^b, L. Rafailović^b and D. M. Minić^c

^aFaculty of Physical Chemistry, University of Belgrade, Belgrade, Serbia;

^bECHEM Kompetenzzentrum für Angewandte Elektrochemie GmbH, Wiener

Neustadt, Austria; ^cMilitary Technical Institute, Belgrade, Serbia

Abstract

The kinetics of structural transformations of the $\text{Fe}_{75}\text{Ni}_2\text{Si}_8\text{B}_{13}\text{C}_2$ amorphous alloy under non-isothermal conditions was studied. It showed that the amorphous alloy was stable up to the temperature of 723 K when the multi-step structural transformations started involving the processes of formations new phases, Fe_3Si and Fe_2B and the growth of formed crystallites. The kinetic parameters corresponding to each step were evaluated and kinetic triplet for every single step was established.

Introduction

Metallic glasses are kinetically metastable and thermodynamically unstable materials and undergo transformation to more stable crystal forms at higher temperatures [1]. The change of structure can lead to change in their technologically important properties, such as the heat capacity, electrical resistivity, volume and magnetic properties [2]. This imposes the importance of studying thermal properties and kinetics of phase transformations induced by thermal treatment of amorphous alloys.

The present paper is concerned with the non-isothermal kinetics of multi-step process of structural transformations of $\text{Fe}_{75}\text{Ni}_2\text{Si}_8\text{B}_{13}\text{C}_2$ amorphous alloy in temperature range 293-1273 K by resolution multi-step process to single steps.

Experimental procedures

The ribbon-shaped samples of $\text{Fe}_{75}\text{Ni}_2\text{Si}_8\text{B}_{13}\text{C}_2$ amorphous alloy were obtained using the standard procedure of rapid quenching of the melt on a rotating disc (melt-spinning method).

The thermal stability of the alloy as well as the structural transformations has been investigated by the differential scanning calorimetry (DSC) in a nitrogen atmosphere using a DSC-50 analyzer (Shimadzu, Japan). In this case, samples weighing several milligrams were heated in the DSC cell from room temperature to 973 K in a stream of nitrogen with a flowing rate of 20 ml min^{-1} at the different

¹Corresponding author: Tel +381-11-3336-689; E-mail address: dminic@ffh.bg.ac.rs

heating rates. The overlapping exo-peak was resolved by using the peak fit software version 4.11.

Results and discussion

DSC showed that $\text{Fe}_{75}\text{Ni}_2\text{Si}_8\text{B}_{13}\text{C}_2$ amorphous alloy is stable up to 723K when the multi-step of crystallization began giving the overlapping crystallization peaks in the temperature range of 790-860 K [3]. The appearance of such overlapping crystallization peaks in the process of crystallization of amorphous alloys could be provoked by several stages of crystallization affecting more compounds produced during a reaction or by a single compound of different stoichiometries. The overlapping peaks also can appear if the nucleation and growth of crystals take place simultaneously. In the case of overlapping peaks there is a temperature interval where there are not experimental data concerning a single step but there are the summed values of a number of simultaneous steps. If the overlap is negligible (the second step begins as first one is almost finishing) it can be ignored, but when the degree of overlapping is significant (mainly simultaneous steps) it is necessary to perform the resolution of complex peak.

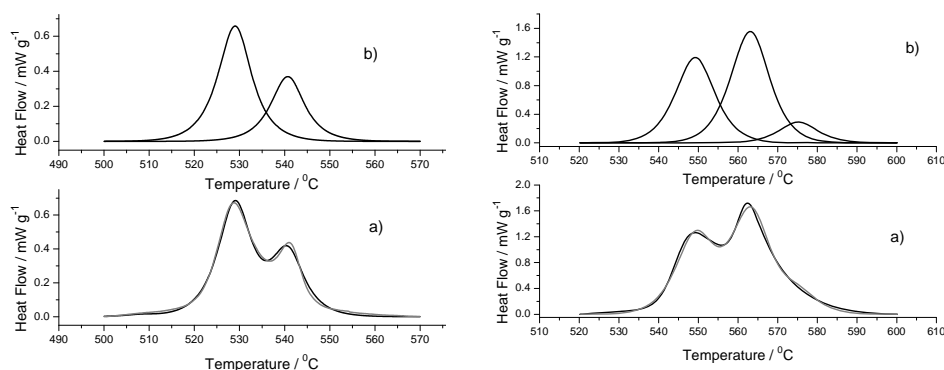


Fig.1. DSC curves: a) as-recorded; b) resolved curves; left at heating rate 5 K min^{-1} ; right at 20 K min^{-1} .

The resolution of complex peaks obtained for different heating rates gave two single peaks corresponding to the formation two crystal phases, Fe_3Si and Fe_2B , at low heating rate (5 K min^{-1}) and three single peaks for higher heating rates (10 , 20 and 40 K min^{-1}) corresponding to the formation crystal phases Fe_3Si and Fe_2B (peaks 1 and 2) followed by recrystallization of formed phases and further growth of crystallites (peak 3). The change of intensities and characteristic temperatures with the heating rate indicate that the heating rate has an important influence on the crystallization process. By increasing the heating rate, the intensities of all peaks rise and relocate in direction to higher temperatures indicating the thermal activation of the observed steps of the crystallization process. The ratio of intensities and interval between the peaks change with the increasing heating rate as the activation energies of different crystallization steps are different.

By applying the isoconversional methods, it was found that for all three steps, the determined apparent activation energies as well as intercepts of obtained dependences are practically constant in the range 0.3-0.7 of degree transformation, α . This suggests that the apparent activation energy-as well as the pre-exponential factor depends in the same way on the crystallization degree of considered process.

In order to find the invariant kinetic parameters by the IKP method, the Coats-Redfern method was applied. The criterion for choosing the conversion functions was good linearity of dependence conversion function on reciprocal temperature at different heating rates for all three obtained peaks. The detail inspection of our results it was shown the best linearity ($R > 0.995$) for the set of conversion functions denoted as "An" based on the Avrami-Erofeev equation in general form $g(\alpha) = [-\ln(1-\alpha)]^{1/n}$ where $n=3/2, 2, 3, 4$, concerning the process involving the nucleation and nuclei growth.

To confirm the obtained kinetic model IKP method was associated with the Perez-Maqueda criterion [4-5].

Conclusions

By annealing in the temperature range of 790-860K, the amorphous $\text{Fe}_{75}\text{Ni}_2\text{Si}_8\text{B}_{13}\text{C}_2$ alloy undergoes multi-step structural transformations, giving two asymmetric overlapping exo-maximums. The primary crystallization starts by forming Fe_3Si phase in an amorphous matrix. At higher temperatures (780 K) beside the Fe_3Si phase, weak peaks of the metastable boron-iron-silicon phase ($\text{B}_2\text{Fe}_{15}\text{Si}_3$) and the iron-boron (Fe_2B) phase became visible. At 923 K the intensity of the iron-boron peaks increased, while the peaks of the boron-iron-silicon phase completely disappeared. The asymmetric peaks were resolved giving three well-formed peaks corresponding to different steps of the phase transformation. The kinetic triplets for every step were established involving the conversion function $f(\alpha) = 3(1-\alpha)[- \ln(1-\alpha)]^{2/3}$ for all steps and invariant kinetic parameters $E_a = 323 \pm 9 \text{ kJ mol}^{-1}$, $\ln A = 47 \pm 1.3 \text{ min}^{-1}$, for first step; $E_a = 304 \pm 13 \text{ kJ mol}^{-1}$, $\ln A = 43.1 \pm 1.8 \text{ min}^{-1}$, for the second step and $E_a = 276 \pm 20 \text{ kJ mol}^{-1}$, $\ln A = 38.4 \pm 5.0 \text{ min}^{-1}$, for the third step of crystallization.

Acknowledgements

The investigation was partially supported by the Ministry of Science and Environmental Protection of Serbia, Project 142025.

References

- [1] T. Kulik, Journal of Non-Crystalline Solids. 2001, **287**, 145.
- [2] A.A. Soliman, S. Al-Heniti, A. Al-Hajry, M. Al-Assiri, G. Al-Barakati, Thermochim. Acta 2004, **413**, 57.
- [3] D. M. Minić, A. Gavrilović, P. Angerer, D.G. Minić, A. Maričić, Journal of Alloys and Compounds 2009, **476**, 705.
- [4] P. Budrugaec and E. Segal, Rev. Roum. Chim., 2004, **49**, 193.
- [5] L.A. Perez-Maqueda, J.M. Criado, f. J. Gotor and J. Malék, J. Phy.Chem., 2002, **106**, 2862.

TEMPERATURE DEPENDENCE OF THE PITZER'S ION-INTERACTION MODEL PARAMETERS OF NaCl(AQ) AND KCl(AQ)

D. Popović, J. Miladinović and M. Todorović

*Faculty of Technology and Metallurgy, University of Belgrade
Karnegijeva 4, 11 000 Belgrade, Serbia*

Abstract

The subject of this study was to investigate temperature dependence of the Pitzer's ion-interaction model parameters of NaCl(aq) and KCl(aq). A large database of thermodynamic properties such as osmotic coefficients for both solutions were treated in order to provide improved parameter values for series of temperatures ranging from 273.15 K to approximately 500 K and $p = 101.325$ kPa. At all temperatures, a differences of the measured values of osmotic coefficients from those calculated using determined values of model parameters fall within 0.1 %. The suitable analytical forms for describing the temperature dependence of model parameters were found. Pitzer's ion-interaction model can successfully represent the activity coefficients data for both solutions in the investigated temperature range and in solution molality range of NaCl(aq) up to app. $10.0 \text{ mol}\cdot\text{kg}^{-1}$ and KCl(aq) up to app. $8.4 \text{ mol}\cdot\text{kg}^{-1}$.

Introduction

Solutions of NaCl(aq) and KCl(aq) are two common reference standards used in isopiestic measurements and for testing and calibration of solution calorimeters. Therefore, a need to determine parameters of the frequently used Pitzer's ion-interaction model [1] in wide temperature and concentration range is evident. Osmotic coefficients of the Pitzer's ion-interaction model for electrolytes can be presented as follows:

$$\begin{aligned} \phi = 1 - |z_M z_X| A^\phi \left(\frac{I^{1/2}}{1 + bI^{1/2}} \right) + \left(\frac{2\nu_M \nu_X}{\nu} \right) m \left\{ \beta_{MX}^{(0)} + \beta_{MX}^{(1)} \exp(-\alpha_{MX} I^{1/2}) \right\} \\ + \left(\frac{4\nu_M^2 \nu_X z_M}{\nu} \right) m^2 \left\{ C_{MX}^{(0)} + C_{MX}^{(1)} \exp(-\omega_{MX} I^{1/2}) \right\} \end{aligned} \quad (1)$$

where $\beta_{MX}^{(0)}$, $\beta_{MX}^{(1)}$, $C_{MX}^{(0)}$ and $C_{MX}^{(1)}$ are adjustable parameters (ion-interaction parameters) that are dependent on temperature and pressure; α_{MX} , ω_{MX} and b were chosen to be constants with the values 2.0, 2.5 and $1.2 \text{ kg}^{1/2}\cdot\text{mol}^{-1/2}$, respectively; ν_M and ν_X are the stoichiometric numbers of cations and anions formed upon dissociation and $\nu = \nu_M + \nu_X$; I is the ionic strength and A^ϕ is the Debye-Hückel coefficients that were calculated from the equation of state for water [1] and the dielectric-constant equation [2]. These adjustable parameters, reflecting appropriate interactions, were determined in wide temperature range through treatment of experimental osmotic

coefficients data for both solutions [2-9]. Obtained results of parameters were assumed to be linear combinations of functions of temperature.

Results and Discussion

Through treatment of osmotic coefficients of KCl(aq) and NaCl(aq) obtained values of model parameters fitted experimental results up to $\pm 0.1\%$ in wide temperature range. The values of model parameters were assumed to fit the following analytical forms for describing its temperature dependence: for the solution of KCl(aq), function (2) or (3) and for the solution of NaCl(aq) functions (2) and (4). Least square estimated coefficients for the temperature dependence relations of Pitzer's ion interaction model parameters of KCl(aq) and NaCl(aq), valid for temperature range from 273.15 K to app. 500 K and $p = 101.325$ kPa are given in Table 1.

$$f(T) = q_1 + q_2[(1/T) - (1/T_r)] + q_3 \ln(T/T_r) + q_4(T - T_r) + q_5(T^2 - T_r^2) \quad (2)$$

$$f(T) = q_6 + q_7(T - T_r) + q_8(T - T_r)^2 + q_9[1/(T - 225)] + q_{10}(1/T) + q_{11}[1/(T - 225)]^3 \quad (3)$$

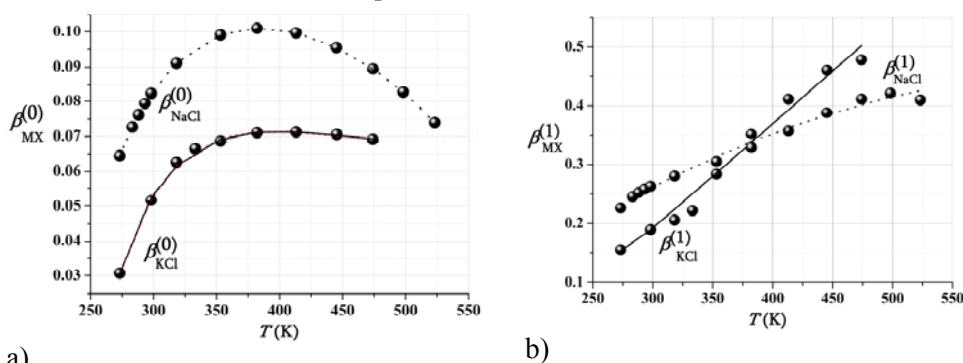
$$f(T) = q_{12} + q_{13}T + q_{14}T^2 + q_{15}T^3. \quad (4)$$

where $T_r = 298.15$ K

Table 1. Least square estimated coefficients for the temperature dependence relations of Pitzer's ion interaction model parameters of KCl(aq) and NaCl(aq), valid for temperature range from 273.15 K to app. 500 K and $p = 101.325$ kPa

Coefficient	$\beta_{\text{KCl}}^{(0)}$	$\beta_{\text{KCl}}^{(1)}$	$C_{\text{KCl}}^{(0)}$	$C_{\text{KCl}}^{(1)}$
q_1	0.05178	0.19001	$-6.5225 \cdot 10^{-4}$	-
q_2	-777	-	33.3	-
q_3	-4.163	-	0.15333	-
q_4	$6.7304 \cdot 10^{-3}$	$2.6639 \cdot 10^{-3}$	$-1.7459 \cdot 10^{-4}$	-
q_5	$-1.4929 \cdot 10^{-6}$	$-1.2182 \cdot 10^{-6}$	-	-
q_6	0.43416	0.18627	$-1.9962 \cdot 10^{-4}$	-
q_7	$-9.9531 \cdot 10^{-5}$	$1.7944 \cdot 10^{-4}$	-	-
q_8	$1.3058 \cdot 10^{-7}$	-	-	-
q_9	$-2.1527 \cdot 10^{-1}$	-	$2.4912 \cdot 10^{-4}$	-
q_{10}	-10.504	-	$-1.1912 \cdot 10^{-4}$	-
q_{11}	-	$1.3041 \cdot 10^2$	-	-
Coefficient	$\beta_{\text{NaCl}}^{(0)}$	$\beta_{\text{NaCl}}^{(1)}$	$C_{\text{NaCl}}^{(0)}$	$C_{\text{NaCl}}^{(1)}$
q_1	$8.2275 \cdot 10^{-2}$	0.25908	$2.5345 \cdot 10^{-5}$	-
q_2	-776.99	-	33.299	-
q_3	-5.1591	-	0.14235	-
q_4	$1.2383 \cdot 10^{-2}$	$1.9049 \cdot 10^{-3}$	$-1.5137 \cdot 10^{-4}$	-
q_5	-5.489810^{-6}	-1.430810^{-6}	-	-
q_{12}	-	-	-	-2.0478
q_{13}	-	-	-	$1.5358 \cdot 10^{-2}$
q_{14}	-	-	-	$-3.843 \cdot 10^{-5}$
q_{15}	-	-	-	$3.2374 \cdot 10^{-8}$

The values of $\beta_{MX}^{(0)}$ and $\beta_{MX}^{(1)}$ as computed from Equations (2) and (3) are plotted against temperature in Figure 1. Shown as points for comparison, are the values of $\beta_{MX}^{(0)}$ and $\beta_{MX}^{(1)}$ obtained at each temperature from the separate analysis of the osmotic coefficients at that temperature.



a) **Fig.1.** Temperature dependence of Pitzer's ion-interaction model parameters of KCl(aq) and NaCl(aq): •-estimated parameter values, curve-calculated parameter values from Eqs. (2) or (3) a) $\beta_{MX}^{(0)}$ b) $\beta_{MX}^{(1)}$

Conclusion

Pitzer's ion-interaction model can successfully represent the osmotic coefficients of KCl(aq) and NaCl(aq) in temperature range from 273.15 to app. 500 K and $p = 101.325$ kPa.

Acknowledgments

This work was supported by the Ministry for Science and Environmental Protection of the Republic of Serbia under Project No. 142064.

References

- [1] D. G. Archer, J. Chem. Ref. Data, 1992, **21**, 793-829.
- [2] D. G. Archer, J. Chem. Ref. Data, 1999, **28**, 1-17.
- [3] R. F. Platford, J. Chem. Eng. Data, 1973, **18**, 215-217.
- [4] E. Amado G., L. H. Blanco, Fluid Phase Equilib., 2004, **226**, 261-265.
- [5] G. Scatchard, W. J. Hamer, S. E. Wood, J. Am. Chem. Soc., 1938, **60**, 3061-3070.
- [6] T. M. Davis, L. M. Duckett, J. F. Owen, C. S. Patterson and R. Saleby, J. Chem. Eng. Data, 1985, **30**, 432-434.
- [7] W. T. Humpries, C. F. Kohrt and C. S. Patterson, J. Chem. Eng. Data, 1968, **13**, 327-330.
- [8] J. T. Moore, W. T. Humpries, C. S. Patterson, J. Chem. Eng. Data, 1972, **17**, 180-182.
- [9] H. F. Holmes, C. F. Baes JR, R. E. Mesmer, J. Chem. Thermodyn., 1978, **10**, 983-996.

THE GENERAL APPROACH TO THE DERIVATION OF THE PARTITION FUNCTION ON THE BASIS OF GIBBS ENSEMBLE THEORY

I. M. Stanković and Ljiljana Z. Kolar-Anić

*Faculty of Physical Chemistry, University of Belgrade, Studentski trg 12 – 16,
11158 Belgrade, P.O Box 47, Serbia*

Abstract

Partition function and thermodynamic quantities of the system open with respect to all three: energy, volume and number of particles whereas T , μ and P are kept constant, is considered by the procedure proposed by Gibbs. The obtained thermodynamic quantities are compared with the corresponding ones evaluated when the system is open with respect to energy, energy and volume, or, energy and number of particles.

Introduction

The aim of this paper is to derive the partition function and thermodynamic quantities for a system that exchanges energy E , the number of particles N and volume V with the environment (reservoir), the system which we shall call totally open system. The analysed system is in thermal, chemical and mechanical equilibrium with the environment. It means that temperature T , chemical potential μ and pressure P must be constant.

In the literature available to the authors, the consideration of such system from statistical thermodynamic point of view is not found, whereas the analogue analysis of a system open with respect to energy, energy and volume, or, energy and number of particles is widespread. [1-5].

Results and Discussion

Partition function. To determine the expression for the partition function of the system, it is necessary to start from the expression for the probability that the system has the energy E_i , number of particles N_k and volume V_j . The system is in equilibrium with the reservoir with the energy E_i^0 , number of particles N_k^0 , and volume V_j^0 . The total energy of the reservoir and the system E^0 , the total number of particles N^0 and the total volume V^0 are constants. The probability that the system is in the state (E_i, N_k, V_j) is proportional to the number of microstates that the reservoir could have $G(E_i^0, N_k^0, V_j^0)$, and in the same time to the number of microstates that the system could have $G(E_i, N_k, V_j)$. After usual approximation

that $E_i^0 = E^0$, $N_k^0 = N^0$ and $V_j^0 = V^0$ which permits to keep only linear terms in expanded Taylor series of the function $\ln G(E_i, N_k, V_j)$ and normalization the expression for the probability that a system will be in the selected state, we get:

$$W(E_i, N_k, V_j) = \frac{G(E_i, N_k, V_j) e^{\frac{\mu N_k - E_i - PV_j}{kT}}}{\sum_i \sum_j \sum_k G(E_i, N_k, V_j) e^{\frac{\mu N_k - E_i - PV_j}{kT}}} \quad (1)$$

The expression in denominator is the partition function or the total number of possible different states of a system that exchanges energy E , the number of particles N and volume V with the environment.

$$\Pi = \sum_i \sum_j \sum_k G(E_i, N_k, V_j) e^{\frac{\mu N_k - E_i - PV_j}{kT}} \quad (2)$$

Thermodynamic functions. Deriving the thermodynamic functions for totally open systems has been performed in analogy with deriving the same expressions of other well known systems which exchange lower number of quantities with environment. If we start from the general statistical definition for the entropy

$$S = -k \sum_l \sum_j \sum_k W(E_l, N_j, V_k) \ln W(E_l, N_j, V_k) \quad (3)$$

and, further, for the Helmholtz free energy, by differentiating, then comparing with the classical expression $dA = -PdV + \mu dN - SdT$, the thermodynamic potential $dX = -kdT \ln \Pi$ is obtained:

$$dX = -SdT - \bar{N}d\mu + \bar{V}dP \quad (4)$$

The expressions for the entropy, mean number of particles and volume are obtained directly from (3):

$$S = k \ln \Pi + kT \left(\frac{\partial \ln \Pi}{\partial T} \right)_{\mu, P}; \quad \bar{N} = kT \left(\frac{\partial \ln \Pi}{\partial \mu} \right)_{T, P};$$

$$\bar{V} = -kT \left(\frac{\partial \ln \Pi}{\partial P} \right)_{T, \mu} \quad (5)$$

The other thermodynamic functions are obtained by putting these ones into the classical expressions.

The mean energy:

$$\bar{E} = \mu kT \left(\frac{\partial \ln \Pi}{\partial \mu} \right)_{T,P} + PkT \left(\frac{\partial \ln \Pi}{\partial P} \right)_{T,\mu} + kT^2 \left(\frac{\partial \ln \Pi}{\partial T} \right)_{\mu,P} \quad (6)$$

The Gibbs energy:

$$G = \mu kT \left(\frac{\partial \ln \Pi}{\partial \mu} \right)_{T,P} - kT \ln \Pi \quad (7)$$

The Helmholtz free energy:

$$A = \mu kT \left(\frac{\partial \ln \Pi}{\partial \mu} \right)_{T,P} + PkT \left(\frac{\partial \ln \Pi}{\partial P} \right)_{T,\mu} - kT \ln \Pi \quad (8)$$

Conclusion

There is analogy with the other types of systems in the obtained expressions for thermodynamic quantities. The derived thermodynamic quantities, entropy, mean number of particles and mean volume, are the same functions of the partition function, the only difference is that the partition function has different value for different systems.

Acknowledgement

Present investigations are partially supported by the Ministry of Sciences of Serbia under the projects no. 142025 and 172015.

References

- [1] T. L. Hill, An Introduction to Statistical Thermodynamics, Addison-Wesley Publishing Company, New York, 1962.
- [2] D. A. McQuarrie, Statistical Mechanics, University Science Books, Sausalito, 2000.
- [3] M. H. Everdell, Statistical Mechanics and its Chemical Applications, Academic Press, London, 1975.
- [4] http://en.wikipedia.org/wiki/Statistical_mechanics
- [5] <http://farside.ph.utexas.edu/teaching/sm1/lectures/lectures.html>

THERMODYNAMIC STUDY OF THE COMPLEXATION OF CRYPTAND 222 WITH TCNE IN DI AND TRICHLORO-METHANE SOLUTIONS

A.Semnani, A. R. Firooz² and L.Kashefi²

¹*Department of chemistry, University of Shahrekord, P.O.Box 115, Shahrekord, IRAN. (a.semnani1341@gmail.com)*

²*Department of chemistry, university of Isfahan, Isfahan, IRAN*

Abstract

A spectrophotometric study concerning the interaction between 4, 7,13, 16, 21, 24-hexaoxa-1, 10-diazabicyclo[8.8.8]hexacosane (cryptand 222) as n-donor and tetracyanoethylene (TCNE) as π -acceptor has been performed in di- and trichloromethane solutions at temperatures 5,10,15,20,25°C. The results of continuous variation and mole ratio methods indicate the formation of 1:1 complexes in both solvents and at all temperatures. The stability constants and the molar absorption coefficients at different temperatures have been calculated from the computer fitting of absorbance-mole ratio data in MATLAB soft ware. The values of absorptivity coefficient are higher in CH₂Cl₂ solution than CHCl₃ solution. The ΔH° and ΔS° values were obtained by Van't Hoff method. The obtained data show that the enthalpy of complex formation in two solvents is favorable. The entropy is favorable in the case of CHCl₃ and unfavorable in the case of CH₂Cl₂. The kinetic results confirm a second order reaction that is first order with regard to each reactant. The conductometric study rejects the formation of free ions. The obtained results due to each solvent were discussed. Comparison of IR spectra of complex with those of free donor and acceptor proves the rigidity of methylene groups through complexation.

Introduction

Since the first synthesis of crown ethers [1] and cryptands [2], there has been an intensive amount of research work on the thermodynamic and kinetics of complexation of these ligands with various cations in a wide variety of solvent systems [3]. Moreover, the molecular complexes of crowns and cryptands have been followed [4]. Interest in molecular complexes is strongly stimulated by their possible applications in different areas such as separation processes, biomimetic receptors, catalytic reactions and conversion of chemical energy to optical or electronic signals. In this paper we report the results of complexation of cryptand 222 with TCNE in di- and trichloromethane solutions.

Experimental

C222 from Merck company was recrystallized from reagent grade n-hexane and dried under vacuum over P₂O₅. Reagent grade TCNE (Merck) was used after recrystallization in CH₂Cl₂ and dried under vacuum over P₂O₅. Solvents from Merck were of highest purity available and used without any further purification. All UV-Vis spectra were recorded on a Cary 500 spectrophotometer and the absorbance

measurements were made with the same instrument at temperatures 5,10,15 and 20°C. The conductance measurements were carried out with a Metrohm 660 conductivity meter. IR spectra were recorded on a Shimadzu 435 using KBr pellets. The formation constants of different donor-acceptor reactions were obtained by fitting the absorbance-mole ratio data using MATLAB software. A function is used to find the equilibrium constant that fit the absorbance mole ratio profiles using the multiparameter minimum search in MATLAB based on the Nelder Mead algorithm [5]. This function uses the modeled equilibrium constant, simulates the absorbance-mole ratio profiles and calculates the difference between the simulated and measured absorbance profiles.

Results and Discussion

Absorption spectra of C222 in the presence of different amounts of TCNE, in both solvents show new band in visible region ($\lambda_{\text{max}} = 437\text{nm}$), which proves the formation of charge transfer complex between C222 and TCNE [5]. The plots of absorbance at 437nm vs. TCNE/C222 mole ratio at different temperatures and in both solvents confirms 1:1 stoichiometry (sample plot is shown in Fig.1). The values of $\log K_f$ have been calculated by fitting the absorbance- mole ratio data. The obtained data show that the stabilities in trichloromethane are higher than those of dichloromethane. Formation of more stable complex in trichloromethane can be assigned to stronger dipole-dipole interaction between solvent and complex. Thermodynamic parameters were obtained from the plots of $\log K_f$ vs. $1/T$ (sample plot is shown in Fig.2). The obtained ΔH° are -26.60 and -25.4 kJ/mol in di- and trichloromethane solutions, respectively. The corresponding ΔS° are -16.3 and +25.1 J/mol K. The positive ΔS° in the latter solvent can be attributed to breaking the initial hydrogen bonds between solvent and reactants and realization of some solvent molecules through complexation. The kinetic of complexation reactions were followed by monitoring the absorbance at 437 nm in conditions of i)the concentration of C222 is much higher than TCNE and ii) the concentration of TCNE is much higher than C222. The results proves first order for both reactants. Monitoring the conductance does not show any considerable change through complexation, so the formation of free ions is rejected.

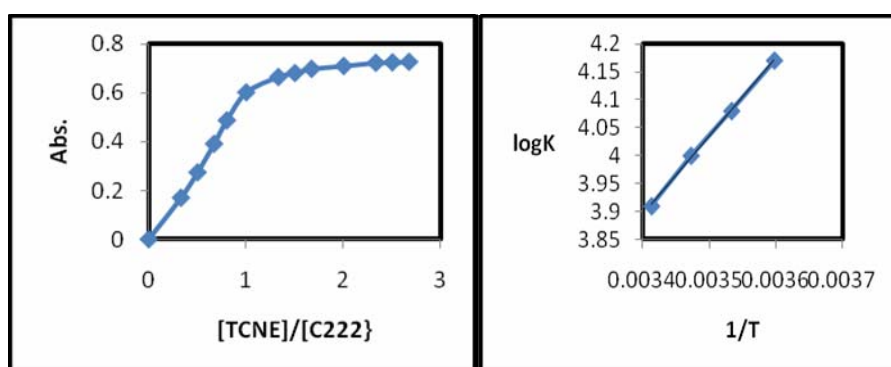


Fig. 1 Plot of Absorbance vs. TCNE/C222 mole ratios at 5°C and in dichloromethane solution.

Fig. 2 Plot of $\log K_f$ vs. $1/T$ in CH_2Cl_2 .

Conclusion

- 1) In both solvents and in all temperatures 1:1 complexes are formed.
- 2) The stability of complexes is higher in trichloromethane.
- 3) The ϵ of complexes is higher in dichloromethane.
- 4) The complexes are nonionic.
- 5) Hydrogen bonding in trichloromethane causes positive ΔS° of complex formation
- 6) Complexes in both solutions have favorable ΔH° .
- 7) The reaction is first order relative to both reactants.

References

- [1] C. J. Pederson, J. Am. Chem. Soc., 1967, **89**, 7017.
- [2] B. Dietrich, J. M. Lehn and J. P. Sauvage, Tetrahedron Lett., 1969, 2885.
- [3] R. M. Izatt, K. Pawlak, J. S. Bradshaw and R. L. Bruening, Chem. Rev., 1991, **91**, 1721.
- [4] R. M. Izatt, K. Pawlak, J. S. Bradshaw, R. L. Bruening and B. J. Tarbet, Chem. Rev., 1992, **91**, 1261.
- [5] A. Semnani, A. R. Firooz, H. R. Pouretedal, M. H. Keshavarz and M. Oftadeh, Chemistry. 2010, **19**, 80.

B

Spectroscopy, Molecular Structure,
Physical Chemistry of Plasma

RESONANCES OF ENDOHEDRAL ATOMS

A. R. Tančić

VINČA Institute of Nuclear Sciences, 11001 Beograd, POB 522, Serbia

Abstract

We investigated the complicated resonance structure of the endohedral atom (EA) photoionization (PI) cross section (c.s.). The effect of the fullerene shell upon PI of the caged atom in an EA can result in formation of giant endohedral resonances (GER). In the case of the $Xe@C_{60}$ we see that the PI c.s. exhibits at $\cong 17eV$ a giant resonance (as a pointed in recently published paper [1]). The two factors have influence in obtaining the c.s.: the strong fullerene polarization (under the action of the incoming electromagnetic (e.m.) wave) and oscillation of this c.s. (due to the reflection of the photoelectron from Xe by the C_{60}). Atomic system of units is used.

Introduction

During last fifteen years new objects consisting many carbon atom forming a closed almost empty and two-dimensional surface (so-called fullerenes), were discovered. (In the investigation of their structure a lot attention was given using photoabsorption data). As a result PI spectrum is characterized by a maximum called giant resonance [2,3]. The total number of electrons of the system is close to the integrated power of the resonance (its total oscillator strength, OS).

It exists a deep similarity between multi-electron atom and an EA from the point of view of the multi-electron effects. Using the simplified description of the fullerene shell [1], an EA can be treated as an atom with additional multi-electronic shell. In the same way one can consider multi-layer fullerenes (so called fullerene onions) in which, in the central empty volume the caged atom is located.

In the PI of the endohedral Xe atom, the role of the C_{60} is twofold. C_{60} acts as a potential resonator that reflects the photoelectronic wave coming from the Xe atom (leads to oscillations in the frequency dependence of the PI c.s. [2]). At same frequencies the C_{60} shell acts as a dynamical screen (screening effect, SE) that is capable to suppress (or enhance) the incident e.m. radiation action upon the doped atom [3,4]. This effect is due to the dynamical polarization of the collectivized electrons in the fullerene shell [5]. The dipole momentum which is generated by plasma electron-excitations causes the ionization of the electronic shell of the EA. The SE of the C_{60} shell are very strong for the frequency radiation (ω) about C_{60} giant resonance. These two effects act together by transform a $5p^6$ c.s. in Xe into a dominant maximum (GER) in $Xe@C_{60}$.

Results and Discussion

In the dipole approximation (DA) the differential c.s. (d.c.s.) by non-polarized light is given by the expression [1,3]:

$$d\sigma_{nl}(\omega)/d\Omega = \sigma_{nl}(\omega)[1 - \beta_{nl}(\omega)P_2(\cos\theta)/2]/(4\pi), \quad (1)$$

where $\kappa = \omega/c$, $P_\ell(x)$ are the Legendre polynomials, θ is the angle between photon \vec{k} and photoelectron velocity \vec{v} , β_{nl} is the dipole anisotropy parameter. From subshell $5p^6$ there are two dipole transition ($p \rightarrow d, s$); the corresponding amplitude in HFA are denoted by d_d, d_s and the c.s. is:

$$\sigma_{np}(\omega) \sim \text{const.}(d_d^2 + d_s^2), \quad (2)$$

and $\beta_{np} = f(d_d, d_s; \delta_d, \delta_s)$ [1,5]. To taking into account the random phase approximation RPA one has to perform the following substitutions: $d_d, d_s; \delta_d, \delta_s \rightarrow D_d, D_s; \tilde{\delta}_d, \tilde{\delta}_s$; ($\tilde{\delta}_i \equiv \delta_i + \Delta_i$; $D_{d,s} \equiv \tilde{D}_{d,s} \exp[i\Delta_{d,s}(\varepsilon)]$). The RPA equation for dipole amplitude has to be solved numerically [6]. We include some third order contributions in resolution of this equation (i.e. improved RPA- imRPA [5]. The confinement effects can be described within the framework of the recently published article [1]. The corresponding c.s. for the EA (AC) is [1,8]:

$$\sigma_{5p \rightarrow kd,s}^{AC}(\omega) \equiv F_{d,s}^2(k)S(\omega)\sigma_{5d \rightarrow kd,s}^A(\omega), \quad (3)$$

where the fullerene polarization factor $S(\omega) = \left|1 - \alpha_{C_{60}}^d(\omega)/R_{C_{60}}^3\right|^2$. $R_{C_{60}}$ is the radius of the C_{60} , and $\alpha_{C_{60}}^d$ is their dipole polarizability. The quantity $F_{d,s}$ is defined in [7].

In Fig.1 we present the photoionization c.s. of the $5p$ electrons of $Xe@C_{60}$. The PI c.s. of $5p$ electrons in $Xe@C_{60}$ very much exceeds the PI c.s. of isolated Xe atom. The total OS increased remarkable, also – that comes from the influence of the fullerene shell.

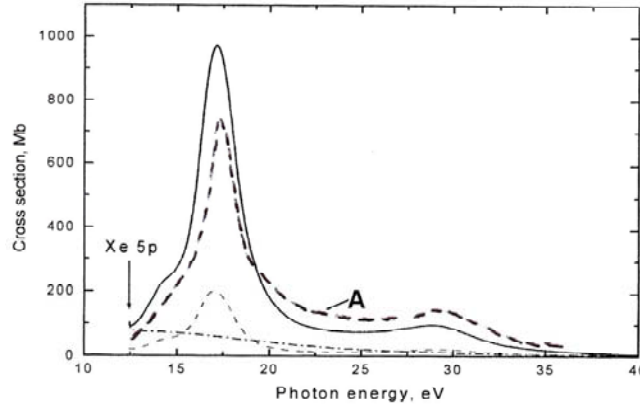


Fig.1. Photo ionization cross-section of $5p$ electrons of $Xe@C_{60}$ (ref.[1], RPA: dashed-dotted line - free Xe , dashed line - $Xe@C_{60}$, solid line - $Xe@C_{60}$ + screening; the dashed curve **A** - our results in imRPA).

Conclusion

The photoionization cross-section for presented case exceeds the photoionization cross section of isolated Xe atom. The decreasing curve of PI c.s. in the isolated atom is transformed into a curve with big maximum. Our results (imRPA) are closed to the previous RPA calculation. The corresponding oscillator strength have a big maximum, also. Their is much bigger compare to $4d$ atomic resonance in isolated Xe .

Acknowledgement

I am very grateful to Professors M. Ya. Amusia, A. Baltenkov and L. Chernisheva for many help and fruitful discussion about this work.

References

- [1] M. Ya. Amusia, A. Baltenkov and L. Chernisheva, JETP Lett., 2008, **87**, 230.
- [2] J. P. Connerade, V. Dolmatov and S. Manson, J. Phys. B, 2000, **33**, 2279.
- [3] M. Ya. Amusia and A. Baltenkov, Phys. Rev. A, 2006, **73**, 062723.
- [4] J.-P. Connerade and A. Solov'yov, J. Phys. B, 2005, **38**, 807.
- [5] A. R. Tancic, Jpn. J. of App. Phys., 1998, **81**, 4737.
- [6] M. Ya. Amusia and L. Chernisheva, *Computation of Atomic Processes*, "A. Higler", IOP, Bristol, 1997.
- [7] M. Ya. Amusia, A. Baltenkov and B. Krakov, Phys. Lett. A 1998, **243**, 99.

MASS SPECTROMETRIC INVESTIGATION OF SILVER CLUSTERS

J. Cvetičanin^{1,xx}, A. Krklješ¹, Z. Kačarević-Popović¹, Đ. Trpkov¹, M. Cindrić² and O. Nešković^{1,x}

¹ Vinca Institute of Nuclear Sciences, Belgrade, Serbia; ² „Pliva“, Zagreb, Croatia.
^x oliveran@vinca.rs; ^{xx} cvetic@vinca.rs

Abstract

Silver clusters were produced by two different synthesis procedures, related with different reduction species. PVA (polyvinyl alcohol) was successfully utilized as a source to reduce silver (Ag) metal ions without using any additional reducing agents to obtain Ag clusters. Silver clusters with atoms numbering 5-29 are registered through mass spectrometry using MALDI TOF and MALDI TOF/TOF techniques. Analysis showed that clusters with magic numbers are the largest, while those with an odd number of atoms are larger than clusters with an even number of atoms. Stability of these molecules, magic number actually, is in relation with their electronic configuration.

Introduction

For the first time some ten years ago, absorption spectra of silver clusters produced by different techniques in the 2.5–6.2 eV energy range were measured on clusters embedded in gas matrices or by gamma irradiation [1–3]. The spectra of small clusters ($n < 12$) are made of several narrow or broad peaks in the 3.0–4.5 eV range, while those of larger clusters are characterized by the emergence of a dominant and relatively broad peak between 3.2 and 3.8 eV. The position of this later was interpreted by the authors using a model based on the Mie theory in which the peak was described as the excitation of s-type electrons without direct contributions from d-type electrons. Nevertheless, the nature of the excitations needed to be confirmed by calculations in which the effect of d electrons would be taken explicitly into account. Hence, several theoretical *ab initio* studies have been investigated in order to reproduce the experimental spectra and to elucidate the real role played by the interband transitions associated to d-electrons. There are few experimental results, as we lack information about the stability and amplitude of different clusters as well as on ionisation energy.

The experimental mass spectrometry spectra of neutral, small and intermediate-size Ag_n ($n=5-29$) silver clusters produced by gamma irradiation, have been measured.

Materials and Methods

Silver clusters are created using radiolysis of the aqueous solution of $AgNO_3$ system, carbon nanotubes and PVA. Silver clusters and silver cluster decorated carbon nanotubes were created and have been further examined using mass

spectrometry methods. Reduction of silver ions was performed in the current of Ar or N₂O. The experiment showed that larger clusters were created and are more stable when radiolysis takes place in the current of N₂O. The irradiation was performed at a dose rate of 10 kGy/h up to the absorbed dose of 55 kGy. MALDI TOF and MALDI TOF/TOF techniques were used to analyze produced silver clusters.

An aliquot of each sample solutions containing an internal standard was combined 1:1, with the CHCA matrix and mixed thoroughly. Aliquots (0.50 μL) of the mixtures were spotted onto a 100-spot sample plate (Applied Biosystems) and air-dried. Mass analysis was performed in the positive ion reflector mode using a 200 Hz frequency pulsed N₂ laser operating at 337 nm. Five spectra at each of 10 randomly selected positions were accumulated per spot between 170 and 500 g/mol using the MS positive ion reflector mode acquisition method. Calibration of the instrument was realized using Calibration mixture 2 as the external standard. To generate spectra with high mass accuracy, an internal calibration was performed. For the analysis of silver clusters, 1.0 mg/mL solutions in 0.10 % trifluoroacetic acid were prepared. Positive-ion MALDI-TOF and MALDI-TOF/TOF mass spectra were performed using the 4700 Proteomics Analyzer (Applied Biosystems).

Results and Discussion

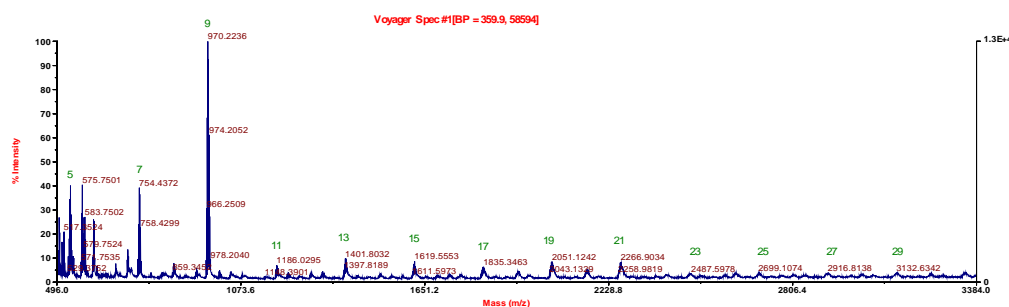


Fig.1. MALDI TOF spectrum of silver clusters. Numbers above the mass values (5 to 29) show the number of silver atoms in the clusters.

Silver clusters with the number of atoms from 5 to 21 showed satisfactory stability. Only clusters with 11 atoms of silver appeared to be unstable, and decomposed in the time of flight reflectronic way. Fragments which were produced during this process, were cationized with Na positive single ions. The ancestry of these ions is unknown, and it may be speculated that these have appeared out of a cluster forming system. MALDI TOF spectrum of the obtained positive cluster ions is shown on Figure 1.

Conclusion

Our novel method of silver cluster formation from silver salts is reproductive and very simple. Clusters with the number of atoms from 5 to 29 were registered by

mass spectrometry, where silver clusters with the number of atoms from 5 to 21 showed satisfactory stability. The literature predicted the matching magic numbers which are in relation with the electronic configuration of the cluster. Evidently, the most stable clusters are those with closed electron shells.

The results obtained from MS/MS analysis of the different clusters clearly demonstrate that MALDI-TOF/TOF can be used to discriminate unstable silver clusters with good reproducibility.

Acknowledgement

This work was financially supported by the Ministry of Science and Technological Development, Republic of Serbia, under Project No. 142001.

References

- [1] S. Fedrigo, W. Harbish, J. Buttet, *Phys. Rev. B*, 1993, **47**, 10706.
- [2] A. Krklješ, M. Marinović-Cincović, Z. Kačarević-Popović, J. Nedeljković, *Thermochim. Acta*, 2007, **460**, 28-34.
- [3] J. Cvetičanin, A. Krklješ, Z. Kačarević-Popović, M. Mitrić, Z. Rakočević, Đ. Trpkov, O. Nešković, *Appl. Surf. Sci.*, in press, DOI 10.1016-j.apsusc.2010.05.023.

HYPERBERYLLIUM MOLECULE BEOBE - *AB INITIO* CALCULATIONS OF THE POTENTIAL ENERGY SURFACES FOR THE $X^1\Sigma_g^+$ AND $A^3\Sigma_u^+$ ELECTRONIC STATES

B. Ostojić

*Institute of Chemistry, Technology and Metallurgy, University of Belgrade,
Studentski trg 14-16, 11 000 Belgrade, Serbia*

Abstract

Ab initio calculations of the three dimensional potential energy surfaces and dipole moment surfaces of each of two electronic states of BeOBe molecule, $X^1\Sigma_g^+$ and $a^3\Sigma_u^+$, are performed using a multi-reference singles-and-doubles configuration-interaction (MRSDCI) method based on full-valence complete active space self-consistent field (FV-CASSCF) wavefunctions. The dipole polarizabilities for both states at their equilibrium geometry are also calculated.

Introduction

Hypermetallation is a concept that applies to molecules having metal stoichiometries that exceed normal valence. BeOBe is one example of such a molecule. Earlier experimental and theoretical works on BeOBe [1–4] have established it as a strongly bound linear molecule with an $X^1\Sigma_g^+$ ground electronic state and a very low lying triplet excited electronic, $a^3\Sigma_u^+$. The matrix-isolation spectrum of BeOBe was first observed by Thompson and Andrews [1,2], and electronic transitions were investigated by Merritt, Bondybey and Heaven [3] using laser-induced fluorescence and resonance enhanced multi-photon ionization techniques. The Be-O bond is far from being a weak bond, as the dissociation energy of $^1\Sigma_g^+$ and $^3\Sigma_u^+$ electronic states of BeOBe into the corresponding $^1\Sigma^+$ and $^3\Pi$ states of BeO (and 1S Be) is estimated to be around 4.3 eV [4].

Results and discussion

The potential energy surfaces for the electronic $X^1\Sigma_g^+$ ground state and the close-by lying $a^3\Sigma_u^+$ state were computed by employing the complete active space (CASSCF) technique followed by a multi-reference configuration interaction (MRCI) treatment [5,6]. The Be and O atoms were both described using the correlation-consistent core-valence quadruple-zeta basis sets of Dunning et al., cc-pCVQZ [7]. The CASSCF active space used consists of all configurations obtained by distributing the 10 valence electrons in 12 molecular orbitals denoted as CAS(10,12). In MRCISD calculations all ten valence electrons were correlated and the effect of higher excitations were taken into account by using the Davidson correction (FV-CAS(10,12)-MRCISD+Q/cc-pCVQZ). All electronic structure

calculations were carried out using the MOLPRO 2008.1 program package [8]. The grid of points for both electronic states consisted of 55 selected geometries with bond lengths between 1.28 Å and 1.58 Å and bond angles between 180° and 90°. The geometries were chosen such that energies up to 3000 cm⁻¹ above the minimum of the X¹Σ_g⁺ state were covered. Both X and a states are of linear equilibrium geometry and the obtained equilibrium BeO bond lengths are 1.4086 Å and 1.4085 Å, respectively. The energy difference between the a³Σ_u⁺ state and the ground electronic state is computed to be 293cm⁻¹. The static dipole polarizabilities of the X¹Σ_g⁺ and a³Σ_u⁺ states of BeOBe were calculated at their equilibrium geometries using the FV-CAS(10,12)-MRCISD+Q method and various basis sets. Scalar relativistic effects were taken into account.

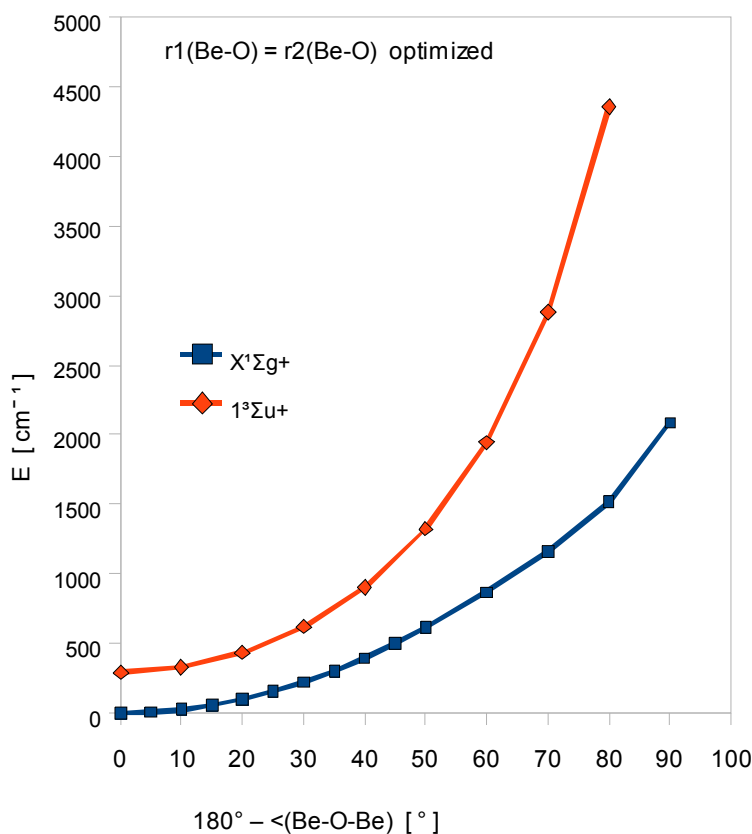


Fig.1. The potential energy curves for the X¹Σ_g⁺ and a³Σ_u⁺ electronic states of BeOBe along the minimum energy bending path as a function of $\theta = 180^\circ - \langle(\text{Be-O-Be})$ calculated employing the full valence AS (10,12)-MRCI+Q/cc-pCVQZ level of theory.

The parallel and perpendicular polarizability tensor components, α_{\parallel} and α_{\perp} , relative to the molecular axis, were obtained using a numerical finite-field method and a parabolic fit of tightly converged energies with respect to the external electric field. The obtained ν_1 , ν_2 , and ν_3 values for the singlet state compare very favorably with the experimental gas phase values. The calculated potential energy and dipole moment surfaces were used to determine rovibrational term values and to simulate the infrared absorption spectrum of both the singlet and triplet states [9].

Conclusion

Little is known about the properties of Group 2 M_2O compounds, and the present work is the first to report full-dimensional (3D) potential energy and dipole moment surfaces for the two low-lying electronic states of BeOBe, and to use the results of such *ab initio* calculations to simulate the infrared absorption spectrum of each state. We also calculated the static dipole polarizabilities of both states at their equilibrium geometries in order to assist the interpretation of future beam deflection studies in inhomogeneous electric fields.

Acknowledgement

The financial support of the Ministry of Science and Technological Development of Serbia (Contract No. 142019) is gratefully acknowledged.

References

- [1] C. A. Thompson and L. Andrews, *J. Chem. Phys.*, 1994, **100**, 8689-8699.
- [2] L. Andrews, G. V. Chertihin, C. A. Thompson, J. Dillon, S. Byrne and C. W. Bauschlicher Jr., *J. Phys. Chem.*, 1996, **100**, 10088-10099.
- [3] J. M. Merritt, V. E. Bondybey and M. C. Heaven, *J. Phys. Chem. A*, 2009, **113**, 13300-13309.
- [4] A. I. Boldyrev and J. Simons, *J. Phys. Chem.*, 1995, **99**, 15041-15045.
- [5] H.-J. Werner and P. J. Knowles, *J. Chem. Phys.*, 1988, **89**, 5803-5814.
- [6] P. J. Knowles and H. -J. Werner, *Chem. Phys. Lett.*, 1988, **145**, 514-522.
- [7] D. E. Woon and T. H. Dunning Jr., *J. Chem. Phys.*, 1995, **103**, 4572-4585.
- [8] MOLPRO, version 2008.1, a package of *ab initio* programs, H. -J. Werner, P. J. Knowles, R. Lindh, F. R. Manby, M. Schuütz, and others, see <http://www.molpro.net>.
- [9] B. Ostojić, P. Jensen, P. Schwerdtfeger, B. Assadollahzadeh, and P. R. Bunker, in press in *J.Mol.Spectrosc.* (2010) doi:10.1016/j.jms.2010.06.008.

VIBRONIC BAND STRENGTH DISTRIBUTION IN THE $C^1\Pi_u - X^1\Sigma_g^+$ TRANSITION OF Ag_2

A. Antić-Jovanović¹, M. Kuzmanović¹, V. Bojović¹, M. A. Khakoo² and
R. R. Laher³

¹*Faculty of Physical Chemistry, University of Belgrade, P. O. Box 47, 11158
Belgrade 118, Serbia;* ²*Department of Physics, California State University,
Fullerton CA 92834, U. S. A;* ³*Spitzer Science Center, California Institute of
Technology, M/S 314-6, Pasadena, CA 91125, U. S. A.*

Abstract

Band strength measurements for eight C-X vibronic bands recorded in absorption were performed for the first time. Observed band strength ratios for the bands having a common lower vibronic state were correlated to theory through the computed Franck-Condon factors assuming Condon approximation. The agreement between two sets of values was found to be within 20-25%.

Introduction

The C-X bands of silver dimer, Ag_2 , were firstly identified by Ruamps [1] who analyzed a number of bands recorded in absorption between 264 and 271 nm. After that, the bands were the subject of several studies results of which up to 1979 are collected in compilation of Huber and Herzberg [2], and later in the papers [3] and [4]. In all of these studies the attention was focused on the analysis of the bands in order to evaluate accurate spectroscopic constants. However, data concerning the analysis of band intensity and the evaluation of transition probability parameters, which are needed in the study of vibronic intensity distribution, are scarce. The only existing set of Franck-Condon factors (FCFs) based on Morse approximate potential wavefunctions are that reported by Vujisic and Pesic [5] who gave also the visual estimation of intensity of the recorded bands. Consequently, further work in refining these Morse FCF calculations and accurate measuring (versus visual estimation) of the band strengths are needed.

In this work we report the first intensity measurements of the C-X bands of Ag_2 and their analysis using our calculated vibronic transition wavenumbers and FCFs based on realistic potentials. More details are expected to be obtained from our further study that is in progress

Experiment and method of calculation

Band strength measurements were carried out on absorption C-X bands recorded at about 2000 K using, as in our previous works [6, 7], conventional spectroscopic technique with a carbon furnace for producing vapor of natural silver and 400 W high pressure xenon lamp to provide background continuum. From a densitometer tracing of recorded spectrum, the peak heights at the position of R heads above the corresponding background were measured for eight bands belonging to $\Delta v = 0$ and

+1 sequences and took as the observed band strengths. Uncertainty of measurement was estimated to be not more than 30%.

To analyze the measured absorption band strengths, we used theoretical relation

$$I_{\nu',\nu''} = D N_{\nu''} \nu_{\nu',\nu''} R_e(r)^2 \left[\int \Psi_{\nu'} \Psi_{\nu''} dr \right]^2 \quad (1)$$

where $I_{\nu',\nu''}$ is measured signal (relative absorption band strength), D is a constant, $N_{\nu''}$ is the density number in lower vibronic state, $\nu_{\nu',\nu''}$ is the frequency of the $\nu' \leftarrow \nu''$ transition, $R_e(r)$ is the electronic transition moment function (ETMF) and $\left[\int \Psi_{\nu'} \Psi_{\nu''} dr \right]^2$ is square of the overlap integrals or FCF, $q_{\nu',\nu''}$, associated with $\nu' \leftarrow \nu''$ transition. Wavefunctions $\Psi_{\nu'}$ and $\Psi_{\nu''}$ are those for the rotationless ($J=0$) vibrational states.

Under assumption of constancy of the ETM (i. e. Condon approximation), the band strength in each ν' -progression, depend mainly from FCFs.

The values of these parameters for the *C-X* bands involving ν' and ν'' levels up to 20 we calculated using Rydberg-Klein-Rees (RKR) potentials and the latest available molecular constants from Ref. [4] as input data in Espy's computer program. Obtained FCFs and transition wavenumbers were then used in calculation of theoretical band strengths.

Results and discussion

Due to economy of space, only transition wavenumbers (band origin positions) and FCFs for measured bands are listed in Table 1 (second and third columns). The forth and fifth columns contain the observed and calculated band strengths.

ν',ν''	$\nu_0(\text{cm}^{-1})$	$q_{\nu',\nu''}$	I_{obs}	I_{cal}
4,3	37714.69	6.5280E-2	0.86	0.73
5,4	37690.02	9.9240E-2	1.57	1.11
6,5	37664.94	1.4065E-1	2.14	1.58
7,6	37639.46	1.8843E-1	2.00	2.11
3,3	37550.41	8.9466E-1	10.00	10.00
4,4	37527.42	8.3776E-1	9.71	9.36
5,5	37504.03	7.6889E-1	9.14	8.58
6,6	37480.22	6.8931E-1	6.00	7.69

Table 1. Band origin wavenumbers, ν_0 , Franck-Condon factors, $q_{\nu',\nu''}$, observed (I_{obs}) and calculated ($I_{\text{cal}} = \nu_0 q_{\nu',\nu''}$) band strengths for selected bands. The I_{obs} and I_{cal} for the 3,3 band are assigned the value 10 and the intensities of other bands normalized accordingly.

Since a natural silver is a mixture of ^{107}Ag (51.4%) and ^{109}Ag (48.6%) isotopes, each measured peak ($I_{\nu',\nu''}$ in above relation) represents the respective sum of the contributions from the heads of three disilver isotopomers: $^{107}\text{Ag}^{107}\text{Ag}$ (26.85 %),

$^{107}\text{Ag}^{109}\text{Ag}$ (49.93%) and $^{109}\text{Ag}^{109}\text{Ag}$ (23.22%), which are not resolved under dispersion used (1.2 Å/mm). Because of this, wavenumber for each transition, $\nu_{v'v''}$, should be an average with respect to three band origins, and $q_{v'v''}$ should be a weighted average of FCFs with respect to respective abundance. However, since three band origins are very close together and because the isotope effect on FCFs of measured bands is very small, we used the band origins and FCFs of the most abundant isotopomer, $^{107}\text{Ag}^{109}\text{Ag}$ (listed in second and third columns of Table 1) in our calculation of theoretical band strength, I_{cal} (forth column in Table 1).

In order to examine how match the experimental and theoretical results, we compared ratios of measured relative band strengths of the bands having the identical lower vibrational levels and different upper levels and those theoretically predicted for the same bands using FCFs from Table 1 and quoted wavenumbers. Resulting ratios are given in Table 2.

Ratio	Obs.	Cal.	Dev. ^a (%)
$I_{4,3}/I_{3,3}$	0.09	0.07	- 22
$I_{5,4}/I_{4,4}$	0.16	0.12	- 25
$I_{6,5}/I_{5,5}$	0.23	0.18	- 22
$I_{7,6}/I_{6,6}$	0.33	0.27	- 18

Table 2. Observed and calculated absorption band strength ratios for the $\text{Ag}_2 C^1\Pi_u - X^1\Sigma_g^+$ band system.
^a Deviation: $100 \times (\text{Calculated} - \text{Observed})/\text{Observed}$.

Conclusion

The band strength distribution in vibrational structure of the C-X bands of Ag_2 was investigated experimentally and theoretically. Despite the considerable uncertainty of performed measurements (going up to about 30%), good agreement between observed and predicted band strength patterns is obtained, offering a good test of the reliability of computed FCFs. Both the measured data and computed FCFs will be useful for further quantitative study of C-X band system.

Acknowledgments

This work was supported by the Ministry of Sciences of the Republic of Serbia, Project No. 142065.

References

- [1] J. Ruamps, Ann. Phys. Paris, 1959, **4**, 1111-1132.
- [2] K. P. Huber and G. Herzberg, Constants of Diatomic Molecules, New York: Van Nostrand – Reinhold, 1979
- [3] V. I. Srdanov and D. S. Pešić, J. Mol. Spectroscopy, 1981, **90**, 27-32.
- [4] V. Beutel et al. J. Chem Phys., 1993, **98**, 2699-2708.
- [5] B. R. Vujisić and D. S. Pešić, Spectrosc. Lett., 1990, **23**, 1081-1089.
- [6] R. R. Laher, M. A. Khakoo and A. Antić-Jovanović, J. Mol. Spectroscopy, 2008, **248** 111-121.
- [7] A. Antić-Jovanović, M. Kuzmanović, V. Bojović, M. A. Khakoo and R. R. Laher, J. Quantitative Spectroscopy and Radiative Transfer, 2010, **111**, 1357-1362.

COMPERATIVE SPECTROSCOPIC AND MECHANISTIC STUDY OF CHELATION PROPERTIES OF BAICALEIN AND QUERCETIN WITH IRON

J. M. Dimitrić Marković ^{1*}, Z. S. Marković ²,
T. P. Brdarić ³, V. M. Pavelkić ³

¹ Faculty of Physical Chemistry University of Belgrade

Studentski trg 12-16, 11000 Belgrade, Republic of Serbia,

² Department of Bio-chemical and Medical Sciences, State University of Novi Pazar, Vuka Karadžića bb, Novi Pazar 36300, Republic of Serbia

³ Kirilo Savić Institute, Vojvode Stepe 51, 11000 Belgrade, Republic of Serbia

Abstract

Combined spectroscopic (UV/visible, Raman, MS) and theoretical approaches were used to assess relevant interaction of iron (III) with quercetin and baicalein in a wide range of pH values of acetate buffered solutions. The chelation sites, stoichiometry, stability and the dependence of the complexes structures on pH were defined. The equilibrium geometries were optimized in at the B3LYP/6-31G (d, p) level of theory, which predicted structural modifications between the ligand molecule in free state and in the complex structure. The correlation between experimental and theoretical results was very good.

Introduction

Flavonoids are reported to exert a wide range of positive attributes like: detoxification of hydrogen peroxide through non-enzymatic defense mechanisms, reduction of lipid peroxidation, elimination of singlet oxygen, termination of the propagation phase in which hydro-peroxy lipids are formed, diminishing the oxidative stress and many others. The significance of iron is enormous because it is essential element for most life on Earth including human beings, most bacterial species, plants and animals. The control of its toxicity in “free” state, when it binds non-specifically to many cellular components, is an important part of many aspects of human health and disease. Besides the possibility of direct free radical scavenging, through rapid donation of the hydrogen atom to a radical form ($\text{ArOH} + \text{HO}^\bullet \rightarrow \text{ArO}^\bullet + \text{HOH}$) and the chain-breaking mechanism leading to indirect H-abstraction ($\text{ArOH} + \text{HO}^\bullet \rightarrow \text{ArOH}^\dagger + \text{OH}^- \rightarrow \text{ArO}^\bullet + \text{HOH}$), flavonoids can also chelate potentially toxic transition metal ions (Fe(II); Fe(III), Cu(II)...) preventing the metal-catalyzed free radical generation reactions.

This paper addresses experimental and theoretical research regarding the complexation of iron (III) ion with quercetin and baicalein in aqueous buffered solutions at ambient temperature. Because of its specific structural features quercetin is considered as a highly potent ligand, capable of chelation iron especially in neutral and alkaline media. Baicalein is one of the major flavonoids

contained in the dried roots, possessing a multitude of pharmacological activities. It is considered as less potent ligand, since it possesses only three hydroxyl groups in the A ring.

Results and Discussion

Spectroscopic studies indicate quercetin (Fig. 1a) as a potent ligand capable of chelating iron (III) in a wide range of pH values (pH 3-10). On addition of iron (III) to acidic (Fig. 2a) or alkaline acetate buffered quercetin solutions quercetin long-wavelength band shifts bathochromically ($\Delta\lambda \approx 30-50 \text{ nm}$) giving simultaneous rise to the new absorption band which corresponds to the complex formed. Unlike quercetin baicalein (Fig. 1b) enters complexation reaction only at pH 6. In more acidic and alkaline solutions complexation does not occur implying the importance of the general structural features like the number and position of hydroxyl groups in the basic skeletal flavonoid structure.

Without knowing exact values of iron hydrolysis and ligand dissociation constants, obtained stability constant values are relative ones, valid for the certain experimental conditions. Calculated constants for 1:2 and 1:1 iron-quercetin complexes are $\beta = 3.6 \times 10^9 \text{ dm}^6 \text{ mol}^{-2}$ and $\beta = 3.2 \times 10^5 \text{ dm}^3 \text{ mol}^{-1}$ respectively and $\beta = 2.7 \times 10^4 \text{ dm}^3 \text{ mol}^{-1}$ for 1:1 iron-baicalein complex. Quercetin binds iron much stronger than baicalein (in 1:1 complexes) which is another proof of the importance of so called "iron-binding motifs" present in quercetin.

To confirm the obtained stoichiometry of the complexes formed and the iron oxidation states electrospray ionization mass spectroscopy (ESI-mass) experiments are carried out. Besides the peak of free quercetin detected at $m/z = 303.05$, $[\text{Q} + \text{H}]^+$, there is also a peak detected at $m/z = 658.00$, which can be assigned to a 1: 2 iron (III)-quercetin complex, $[\text{Fe}^{3+}(\text{Q}-\text{H})_2]^+$, confirmed by molar ratio method as well. The isotopic pattern, however implies a mixture of iron (III) (the peak at $m/z = 658$) and iron (II) (the peak at $m/z = 659$). This finding suggests a reduction of iron (III) to iron (II), also confirmed by bipyridyl test.

Much information on complexes structures has been provided by analyzing Raman spectra of the molecules, especially the bands in the $1700-1400 \text{ cm}^{-1}$ region which can be associated with aromatic in-plane skeletal vibrations, the aromatic character of the pyrone ring and the double bond character of the carbonyl group. Most of the bands between 1500 and 1300 cm^{-1} involve in-plane C-H bending vibrations, C-H wag, and O-H bending vibrations of the rings A and B. Below the 1300 cm^{-1} , the bands involve C-OH stretch (B ring), in-plane C-H wag, C-C deformation (rings A and B) and O-H bend vibrations. The plurality of the spectral bands observed, assigned to different modes of O-H vibrations, is due to the fact that there are five hydroxyl groups in quercetin molecule which are expected to have noticeable effect on the spectra.

The results of mechanistic study show that the molecule of quercetin in its isolated state adopts planar conformation with the θ (O1-C2-C1'-C2') angle value of 0.0° . The molecular structure of isolated quercetin is stabilized with three intramolecular hydrogen bonds: O3-H-O4 = 2.005 \AA , O5-H-O4 = 1.733 \AA , and O3'-

H–O4' = 2.125 Å with the first and the second one stronger allowing the formation of a five-member ring coplanar to the chromone part of the molecule, $\theta(\text{C2–C3–O3–H})=179.9^\circ$. The structure of quercetin is affected by iron coordination. Calculations show that the molecule of baicalein in its isolated state retains planar structure as quercetin with the $\theta(\text{O1–C2–C1'–C2'})$ angle value of 0.0° . The molecule of baicalein has also three hydrogen bonds that additionally stabilize the molecule: O5–H–O4 = 1.696 Å, O6–H–O5 = 2.281 Å and O7–H–O6 = 2.166 Å. The smallest BDE value for O6H bond indicates this hydroxyl group as possible reactive site. The structure of baicalein is also affected by iron coordination.



Fig. 1. Structural formulas of quercetin (a) and baicalein (b)

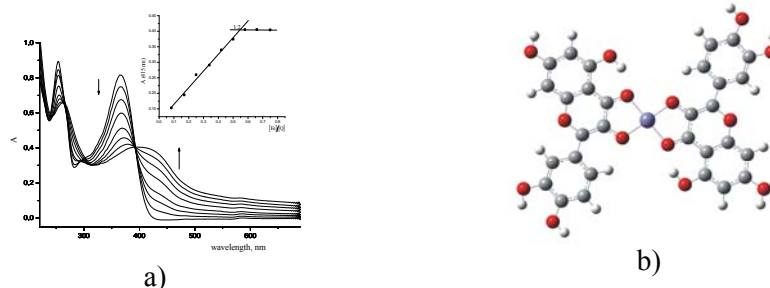


Fig.2. Titration curves of quercetin with iron at pH 4. Inset: complex absorbance at 415 nm versus concentrations (a); Geometry optimized structure of the 1:2 iron (II)-quercetin complex (b)

Conclusion

This study shows that chelation properties depend upon the structure of the molecules, medium and its pH. With respect to the structure of the molecules, stoichiometric composition of the complexes formed, experimental spectra and theoretical calculations, it is possible to implicate 3-hydroxyl-4-carbonyl and catechol structural units as those with chelating power for quercetin and 5-hydroxyl-6-hydroxyl group for baicalein. The theoretical treatment performed using the B3LYP/6-31G (d, p) level of theory reproduces the experimental results very good.

References

- [1] V. Cody, E. Middleton and J. B. Harborne in Plant flavonoids in biology and medicine: biochemical, pharmacological, and structure-activity relationships, Alan R. Liss, Incorporated New York, 1986.
- [2] M. Grazula, E. Budzisz, Coordination Chemistry Reviews 2009, **253**, 2588.
- [3] L. Danglerterre and J. P. Cornard, Polyhedron, 2005, **24**, 1593.

STUDY ON FISETIN-IRON (III) INTERACTION IN AQUEOUS BUFFERED SOLUTIONS BY COMBINED SPECTROSCOPIC AND THEORETICAL METHODS

J. M. Dimitrić Marković¹, Z. S. Marković²,
T. P. Brdarić³, M. B. Jadranin⁴

¹*Faculty of Physical Chemistry University of Belgrade
Studentski trg 12-16, 11000 Belgrade, Republic of Serbia,*

²*Department of Bio-chemical and Medical Sciences, State University of Novi
Pazar, Vuka Karadžića bb, Novi Pazar 36300, Republic of Serbia*

³*Kirilo Savić Institute, Vojvode Stepe 51, 11000 Belgrade, Republic of Serbia*

⁴*Institute of Chemistry, Technology and Metallurgy, Njegoševa 12, 11000
Belgrade, Republic of Serbia*

Abstract

Fisetin (3, 3', 4', 7-tetrahydroxyflavone) has been investigated for its ability to bind iron in a wide range of pH values of acetate and phosphate buffered solutions. To assess relevant interaction of iron with fisetin combined spectroscopic (UV/visible, Raman, MS) and theoretical approaches were used. The chelation sites, stoichiometry, stability and the dependence of the complexes structures on pH were defined.

Introduction

By virtue of its unique chemical properties, good redox chemistry enabling participation in basic metabolic and electron transport processes and its ability to coordinate and activate oxygen, iron is considered the essential element for most life on Earth including human beings, most bacterial species, plants and animals. As long as the body is healthy any excess of iron, stored in the liver, predominantly within the proteins ferritin and hemosiderin, is no threat. However, under disease conditions, it produces multiple possibilities for harmful superoxide production and the production of its dismutation product, hydrogen peroxide, which *in vivo* usually undergoes iron-catalyzed breakdown leading to the formation (by the Haber-Weiss reaction) of highly reactive hydroxyl radical. This radical specie can attack every class of biological macromolecule. Therefore, iron may be a key factor in the establishment of a prooxidant status in the cell. Organisms have developed a variety of defense mechanisms, like action of some enzymatic compounds, to protect themselves against reactive oxygen species. There are also some external factors including dietary substances, such as flavonoids, vitamins C and E, hydroquinones and various sulfhydryl compounds. Flavonoid family is the vast and the most prevalent and important group of low molecular weight plant phenolics with more than several thousands known compounds. Their role in plant physiology is essential, as they are involved in the light phase of the photosynthesis, the attraction of pollinating insects, regulating of iron channels

associated with phosphorylation, growth, reproduction, resistance to pathogens and predators and UV-protection of plants. Recently, a variety of beneficial actions is believed to be closely related to their pronounced antioxidant activity which operates at different levels in the oxidative process including scavenging free radicals, chelation of metal ions, scavenging lipid peroxy radicals or removing oxidatively changed and damaged biomolecules.

Results and Discussion

In acetate buffered solutions iron coordinates only on preferential sites of fisetin independently on its concentration proving that complexation is strongly dependent on the experimental conditions *i.e.* oxidizing agent, pH value and solvent system. The molar ratio plots at 413 nm (pH 4) and 420 nm (pH 9) (Inset on Fig. 1) clearly indicate the formation of 1:2 (iron-fisetin) and 1:1 complexes respectively. The 1:2 stoichiometry persists up to pH 5. From pH 6 and higher the complex stoichiometry is 1:1. Unlike complexation in acetate buffers fisetin enters complexation in phosphate buffers only at neutral and alkaline pH values. Addition of iron (III) to fisetin solution produces almost the same bathochromic shifts of about $\Delta\lambda \approx 53 \text{ nm}$ (pH 7) and $\Delta\lambda \approx 62 \text{ nm}$ (pH 9) as in acetate buffers. The molar ratio plot at 356 nm indicates the formation of 1:1 iron-fisetin complex both at pH 7 and pH 9. In acidic phosphate solutions complexation does not occur even at very high iron concentrations most probably because iron must displace tightly bounded phosphate for the binding to proceed or because of the instability of the complex formed. This fact also affects the complexation kinetics.

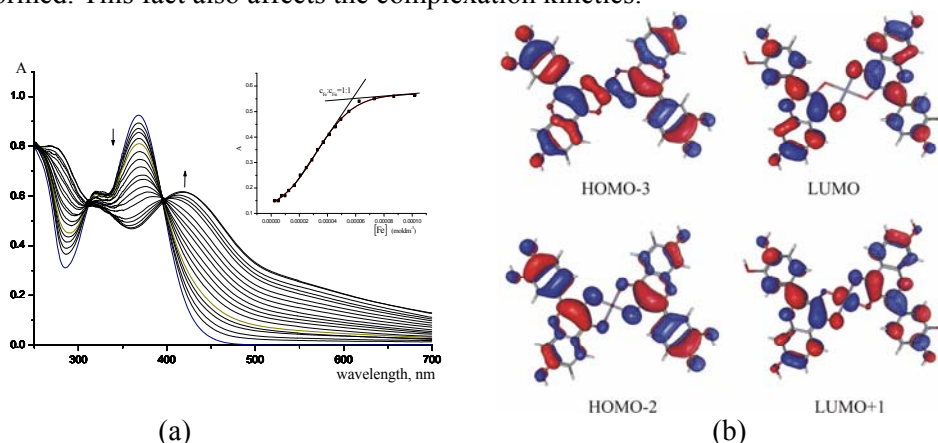


Fig.1 Titration curves of fisetin with iron at pH 9 acetate buffer. Inset: complex absorbance at 420 nm *versus* $[\text{Fe}]$ concentrations (a) The corresponding HOMO and LUMO orbitals responsible for UV-spectrum of complex Fis-Fe-Fis₃₄ (b)

In the absence of iron fisetin undergoes a slow autoxidation in neutral and alkaline solutions. Autoxidation is accelerated by addition of iron to neutral and alkaline solutions and even to acidic ones. The partial reduction of iron (III) to iron (II) by fisetin was confirmed by ESI mass measurements and also indicated by the

kinetic measurements performed in neutral and alkaline acetate buffers. Monitoring complex stability it is evident that upon complex degradation, which happens after some time, a brownish precipitate formation begins. This can implicate two things regarding iron entering complex formation: i) the initial presence of iron (II) which enters the reaction and later, upon complex degradation, oxidizes and undergoes hydroxyl complexes formation or ii) participation of iron (III) hydroxyl complexes in the fisetin complex structure. Most probably the complex formed in neutral and alkaline buffers is a mixture of iron (II) and iron (III) complex. The same situation stands also for neutral and alkaline phosphate buffers. To confirm the obtained stoichiometry of the complexes formed and the iron oxidation states electrospray ionization mass spectroscopy (ESI-mass) experiments are carried out. Besides the peak of free fisetin detected at $m/z = 287.06$, $[\text{Fis} + \text{H}]^+$, there is also a peak detected at $m/z = 626.015$, which can be assigned to a 1: 2 iron (III)-fisetin complex, $[\text{Fe}^{3+}(\text{Fis} - \text{H})_2]^+$, confirmed by molar ratio method as well. However the isotopic pattern implies a mixture of iron (III) (the peak at $m/z = 626$) and iron (II) (the peak at $m/z = 627$) which is also confirmed by bipyridyl test. Because it is formed in alkaline media, not acidic ones, the 1:1 iron-fisetin complex, which is expected to be at $m/z = 341.0$ is not identified under these experimental conditions. The peak at $m/z = 667$ could not imply any meaningful complex stoichiometry while peak at $m/z = 912.06$ could point to the complex of 1:3 (iron:fisetin) stoichiometry which was not experimentally confirmed. Bearing in mind the values of bond dissociation enthalpy (BDE) for fisetin, it is clear that position O3', O4', and some occasional O3 can be reactive sites. Calculations show that both iron (II) and iron (III) can form two types of complexes with stoichiometries 1:2 and 1:1. It was found that the 1:2 complexes in *trans* form is more stable than *cis* form by 10.25 kcal/mol. The agreement between the observed and predicted wavelengths and intensities of the 1:2 (and 1:1) complex absorption band is good. For 1:2 complex relevant transitions are HOMO-3→LUMO transition (65%), accompanied with HOMO-2→LUMO+1 transition (22%), with involving excitation from π to π^* . For 1:1 complex relevant transitions are: HOMO α →LUMO α (29%), HOMO β →LUMO+2 β (22%); and HOMO α →LUMO α (12%), HOMO-7 β →LUMO β (43%), HOMO β →LUMO+2 β (10%), HOMO-5 β →LUMO β (25%).

Conclusion

Two of three so called “iron binding motif” present in fisetin have been confirmed in this study. All of them are capable of binding iron strongly under acidic, neutral and alkaline conditions which could be of relevance in some pathological conditions and in interactions with biological targets, e.g. membranes, at the molecular level.

References

- [1] Celestino Santos-Buelga, Maria Teresa Escribano-Bailon, Vincenzo Lattanzio Recent Advances in Polyphenol Research, Volume 2, Chapter 11, Edited by Santos-Buelga, Escribano-Bailon and Lattanzio, Wiley-Blackwell, 2010

FTIR STUDY OF BIOLOGICAL HYDROXYAPATITE

S. Marković, Lj. Veselinović and D. Uskoković

Institute of Technical Sciences of the Serbian Academy of Sciences and Arts, Knez Mihailova 35/IV, Belgrade 11001, Serbia (smilja.markovic@itn.sanu.ac.rs)

Abstract

In this study Fourier transform infrared (FTIR) spectroscopy was used to resolve setting of carbonate ions in biological hydroxyapatite (BHAp). Even though preliminary XRPD results indicate that BHAp is B-type carbonated hydroxyapatite, the detailed FTIR spectroscopy analysis show that carbonate ions substitute both phosphate and hydroxyl ions in the crystal structure of BHAp, representing a mixed AB-type.

Introduction

Comprehensive studies of natural minerals from bones show that they are not a pure hydroxyapatite ($\text{Ca}_{10}(\text{PO}_4)_6(\text{OH})_2$, HAp); they are associated with elements such as CO_3^{2-} , HPO_4^{2-} , Na^+ , Mg^{2+} , Sr^{2+} , K^+ , Cl^- and F^- [1]. On the basis of the substitution sites carbonated apatites are classified to: A-type where CO_3^{2-} ions occupy the OH^- sites; B-type where CO_3^{2-} ions occupy the PO_4^{3-} sites, and AB-type where they occupy both OH^- and PO_4^{3-} sites [2].

In the 1960's the crystal structure of HAp based materials is determined in details [3]. Until now, crystal structure of carbonated hydroxyapatites (biological, natural minerals, as well as synthetic ones), has been examined in a lot but still remained insufficiently clarified due to the inability to precisely determine the position of the carbonate ions directly based on diffraction data. The main difficulty to unambiguous determination of the carbonated hydroxyapatites structure from XRPD data is very small crystallite size and low crystallinity. However, vibrational spectroscopy techniques, both Raman and FTIR, are irreplaceable for study the nature of carbonate occupancy in the crystal structure of the carbonated apatite. According to the position of the vibrational bands in FTIR and Raman spectra, the occupancies of carbonate ions can be precisely determined; is they A-, B-, mixed AB-type, or an unstable (i.e. surface) carbonate locations [4].

It is found that hydroxyapatite from bone contains from 2.3 to 8 wt% of carbonate ions [4]. The carbonate ions have a large effect on the nature of BHAp; they increase solubility in acids and retard a crystal growth. Since a composition and crystal structure of bone are influenced by age and health status of individual, of the most interest is to determine the type of carbonated apatite in concrete natural bone, at first for the fundamental knowledge of bone regeneration, and further for the design a biocompatible synthetic carbonate-substituted hydroxyapatite appropriate for reparation of a bone defects.

Here, we chose a biological carbonated apatite extracted from human alveolar bone as a model system to resolve the problem of carbonate ions positioning using FTIR spectroscopy technique.

Experimental

The biological apatite (BHAp) was derived from human alveolar bone. To remove organic part, the bone was deproteinated, after that, the sample was dried at room temperature and grinded in an agate mortar.

The crystal phase of BHAp was identified by XRPD analysis obtained on Philips PW-1050 automatic diffractometer. The diffraction measurement was done over scattering angle from 8 to 120 °2 θ with a step of 0.02° and a counting time of 12s. The FTIR measurement was performed on MIDAC M 2000 Series Research Laboratory FTIR Spectrometer using the KBr pellet technique, in the spectral range of 400–4000 cm⁻¹, with spectral resolution of 4 cm⁻¹. The deconvolution of recorded FTIR spectrum was done using PeakFite™ (version 4.05, demo) software.

Results and Discussion

Preliminary results of XRPD analysis show that the BHAp has a poorly crystalline hydroxyapatite phase of B-type.

The FTIR spectrum of BHAp (Fig. 1a) has four typical apatite phosphate (PO₄³⁻) modes: triple degenerative ν_3 asymmetric stretching mode characterized by a strong, complex band in the 1000-1150 cm⁻¹ region; a medium intensity band at 961 cm⁻¹ due to ν_1 symmetric stretching vibration; double degenerative ν_4 bending vibration with bands at 564 and 603 cm⁻¹, and weak band near 470 cm⁻¹ corresponds to double degenerative ν_2 bending vibration. The vibrational band of the water appears at 1635 and 3430 cm⁻¹; and that of OH⁻ libration modes at 635 cm⁻¹. In addition to the phosphate and hydroxide bands of pure HAp, the spectrum of BHAp also shows additional bands. The carbonate bands appear at 755 cm⁻¹ for the ν_4 stretching mode, band at 872 and shoulder at 880 cm⁻¹ are due to ν_2 stretching mode, while bands at 1418, 1456, 1506 and 1558 cm⁻¹ are attributed to ν_3 stretching mode. The bands at 872, 1418 and 1456 cm⁻¹ suggest the B-type of carbonated apatite, while the bands at 880 and 1558 cm⁻¹ are characteristics of the A-type [4]. These results confirmed that the hydroxyapatite from the human alveolar bone is mixed AB-type carbonated apatite.

It is known that the ratio of the intensities of the peaks at 880 and 873 cm⁻¹ corresponds to the ratio of A-type:B-type carbonated apatite. Therefore, the spectral region 860-890 cm⁻¹ was re-examined; after a deconvolution it is found that $I_{880}/I_{872} = 0.32$, indicating that much more carbonate ions are placed on the phosphate (B) site than on the hydroxyl (A) site in the crystal structure of BHAp. The 860-890 cm⁻¹ band (recorded, deconvoluted and fitted) is presented in Fig. 1b.

Besides, absorption band at 1658 cm⁻¹ is assigned to the amide I band, while bands appear at 2850 and 2950 cm⁻¹ belonging to the aliphatic C–H stretching vibrations. These bands point to some organic impurities mixed with the BHAp, must probably of collagen – which is the main organic component of bone.

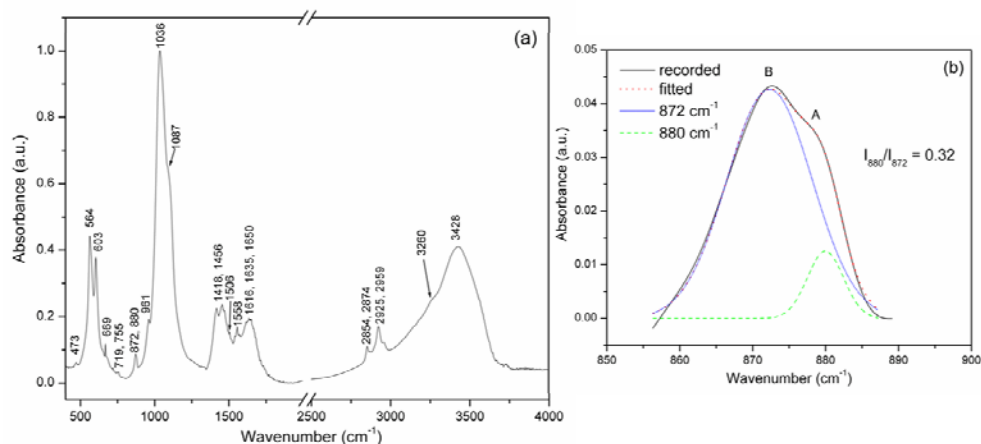


Fig.1 (a) FTIR spectrum of BHAp, and **(b)** recorded, deconvoluted and fitted 860-890 cm^{-1} spectral region.

Conclusion

A biological carbonated hydroxyapatite (BHAp) extracted from human alveolar bone is chosen as a model system to resolve the problem of crystal structure and carbonate ions placing. Rietveld refinement of XRPD data confirmed that BHAp has a crystal structure of hydroxyapatite with the B-type of carbonated hydroxyapatite.

The FTIR results show that BHAp contains small amount of organic part of bone tissue, must probably of collagen. Furthermore, FTIR analysis resolved the nature of carbonated apatite. According to the results carbonate ions are placed in both A and B positions, which indicates mixed AB-type of carbonate apatite. After the deconvolution of FTIR band at 860-880 cm^{-1} it is calculated that $I_{880}/I_{872} = 0.32$, meaning that only a small amount of carbonate ions occupy the OH^- sites while a large amount is at PO_4^{3-} positions. Hence, the BHAp from human alveolar bone is mixed AB-type of carbonated hydroxyapatite but with dominant B-type.

Acknowledgments

This study was supported by the Ministry of Science and Technological Development of the Republic of Serbia under Grant No. 142006. The authors are grateful to Dr. Sci. Z. Ajduković from Faculty of Medicine, Clinic of Stomatology, University of Niš, Serbia, for human alveolar bone sample.

References

- [1] F. Yao, J. LeGeros, R.Z. LeGeros, *Acta Biomaterialia* 2009, 5, 2169-77.
- [2] T. Tonegawa, T. Ikoma, T. Yoshioka, N. Hanagata, J. Tanaka, *J Mater Sci.* 2010, 45, 2419-26.
- [3] M.I. Kay, R.A. Young, A.S. Posner, *Nature* 1964, 204, 1050-1052.
- [4] I.R. Gibson, W. Bonfield, *J Biomed Mater Res.* 2002, 59, 697-708.

method along with geometry optimization. The diradical index y , related to the HOMO and LUMO for singlet states, is defined by the weight of the doubly-excited configuration in the multi-configurational MC-SCF theory, and is formally expressed in the case of the spin-projected UHF (PUHF) theory as [4, 5]

$$y_{PUHF} = 1 - \frac{2T}{1+T^2} \quad (1)$$

where T is the orbital overlap between the corresponding orbital pairs, and can be calculated using the occupation numbers of UHF natural orbitals as

$$T = \frac{n_{HOMO} - n_{LUMO}}{2} \quad (2)$$

The results of our investigation are summarized in Table 1.

Table 1. Difference in free energy (kJ/mol) between open-shell symmetry-broken singlet and closed-shell RB3LYP solution (ΔG_{OS-CS}), singlet – triplet gap (ΔG_{T-OS}), orbital overlap T , and diradical index y (%).

h	ΔG_{OS-CS}^a	ΔG_{T-OS}^b	$\langle S^2 \rangle$	T	y
6	0.0	67.5	0.00	0.335	40
7	-2.4	37.0	0.08	0.249	53
8	-8.5	23.0	0.65	0.171	67
9	-15.8	17.1	0.89	0.131	74
10	-22.9	14.8	1.06	0.108	79
11	-29.7	14.7	1.24	0.091	82
12	-35.5	14.4	1.44	0.080	84

^aOpen-shell singlet free energy minus RB3LYP singlet free energy; ^btriplet free energy minus open-shell singlet free energy

Positive singlet – triplet gaps (ΔG_{T-OS} values) in Table 1 show that all investigated molecules are singlet hydrocarbons. For $h > 9$ the singlet – triplet gap slowly decreases with the increasing size of zethrenes. Negative ΔG_{OS-CS} values (except for $h=6$) indicate that the singlet states are best described by the unrestricted symmetry-broken method. In other words, zethrenes are singlet diradicals, and exhibit diradical character. The ΔG_{OS-CS} values decrease, indicating that the diradical character increases with the increasing size of the investigated molecules. In agreement with this finding, the orbital overlap decreases, whereas the diradical index increases with the increasing size of zethrenes.

The spatial diradical distribution in the singlet diradical structures was examined by inspecting the HOMOs and LUMOs for α and β spin electrons. α -HOMO and β -LUMO, as well as β -HOMO and α -LUMO, of each singlet diradical occupy practically the same part of space. In this way there are no unpaired electrons in a singlet diradical, yet two of them occupy different parts of space, thus allowing the π -electrons to delocalize.

Conclusion

The unrestricted symmetry-broken method was applied to a series of zethrenes. The positive singlet – triplet gap values show that the ground states of these compounds are singlet. On the other hand, they show a pronounced diradical character, and their structures are best presented by those of singlet diradicals. Such structures provide a possibility for an electron pair to occupy different parts of space, and allows for achieving aromatic stabilization.

Acknowledgments

This work is supported by the Ministry of science of Serbia, projects No 144015G and 142025.

References

- [1] A. Knežević,; Z. B. Maksić, *New. J. Chem.*, 2006, **30**, 21.
- [2] M.Nakano, R. Kishi, A.Takebe, M. Nate, H. Takahashi, T. Kubo; K. Kamada, K. Ohta,; B. Champagne, E. Botek, *Co. Le.*, 2007, **3**, 333.
- [3] Gaussian 09, Revision A.01, Gaussian Inc., Wallingford, CT, 2009.
- [4] K. Yamaguchi, in: Carbo, R.; Klobukowski, M. (Eds.), *Self-Consistent Field: Theory and Applications*, Elsevier, Amsterdam, 1990, 727.
- [5] S. Yamanaka, M. Okumura, M.Nakano, K.Yamaguchi, *J. Mol. Struct. (Theochem.)*, 1994, **310**, 205.

ELECTROSPRAY MASS SPECTROMETRY OF ALUMINIUM FLEROXACIN COMPLEXES

M. Cvijović¹, P. Đurđević¹, T. Anđelković², Lj. Svilar², J. C. Tabet³,
M. Jelikić-Stankov⁴, A. Bojić² and V. Stankov²

¹Faculty of Science Kragujevac, ²Faculty of Science Nis, ³University Pier and Marie Curie (UPMC) Paris, ⁴Faculty of Pharmacy Belgrade

Abstract

In this paper the complexation equilibria between Al(III)-ion and fluorinated quinolone–floxacin were investigated by ESI MS spectrometry. In addition, the hydrolytic species of Al(III)-ion were also studied. The examination of the MS spectra with the aid of Xcalibur (Termo, Finnigan) software indicates the formation of the complexes: $[2M-H-CO_2+Al]^{2+}$, $[M+H]^+$, $[2M-H+Al]^{2+}$, $[2M-2H-CO_2+Al]^+$, $[2M-2H+Al]^+$ where M denotes molecular ion of floxacin. The complexes have low ionization potentials.

Introduction

The quinolones work by inhibiting the actions of bacterial DNA gyrase, an enzyme responsible for the “supercoiling” and “uncoiling” of bacterial chromosome. As a class, the quinolone antibacterials are active against gram-negative aerobes [1]. Fleroxacin is quinolone antibacterial that exhibits a wider activity against many gram-positive aerobes (Staphylococcus aureus) The quinolones are with a low resistance.

ESI MS spectrometry is very powerful technique in qualitative and also quantitative study of metal - ligand interactions in solution [2]. Thus, this technique was used to study the complexation equilibria between floxacin and aluminium ion in water solutions with the aim to determine identification number and stoichiometries of the species in solutions. In further examination of this system it will be calculated concentration of the various complexes formed in solutions and stability constants.

Results and Discussion

ESI MS spectra have been taken on LC/MSD instrument Finnigan LCQ Termo Quest operating under Xcalibur software. The spectra were acquired in positive and negative mode. The conditions in ESI source have been: spray voltage: 4,72 V, capillary temperature 220°C, capillary voltage 6V The most of spectra have been processed in MS mode, but some have been processed also as MS /MS experiments. The pH of all solutions was adjusted by the addition of standard HCl or NaOH solutions. The ligand to metal concentration ratios ranged from 1:2 to 2:1 with the total metal concentration $2.0-5.0 \times 10^{-5}$ mol/l. pH was adjusted from 4.0 to 6.0 .

The spectra of the ligand (floxacin) and aluminium ion + floxacin solutions are shown in Figs. 1 and 2 respectively. The ligand reveals little fragmentation but complexes are more fragmented.

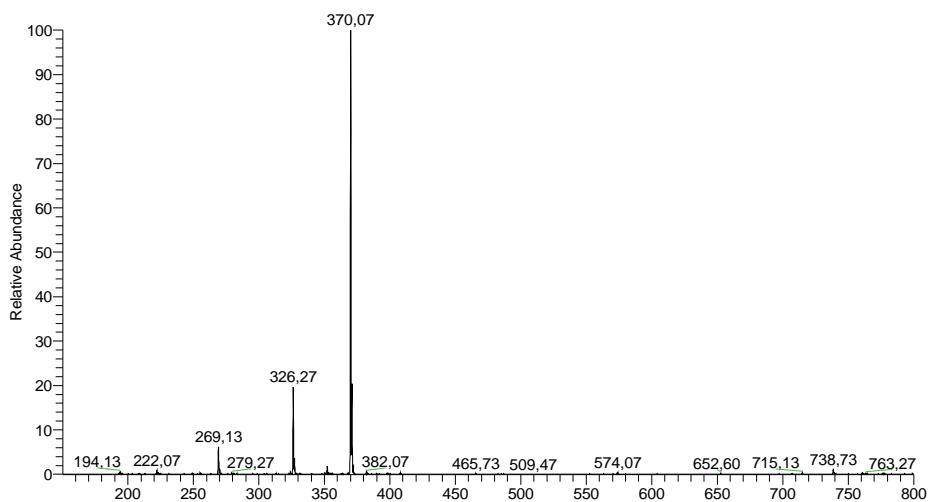


Fig.1. ESI MS spectra of fleroxacin. Molecular ion of fleroxacin at $m/z = 370$. $pH = 4.26$

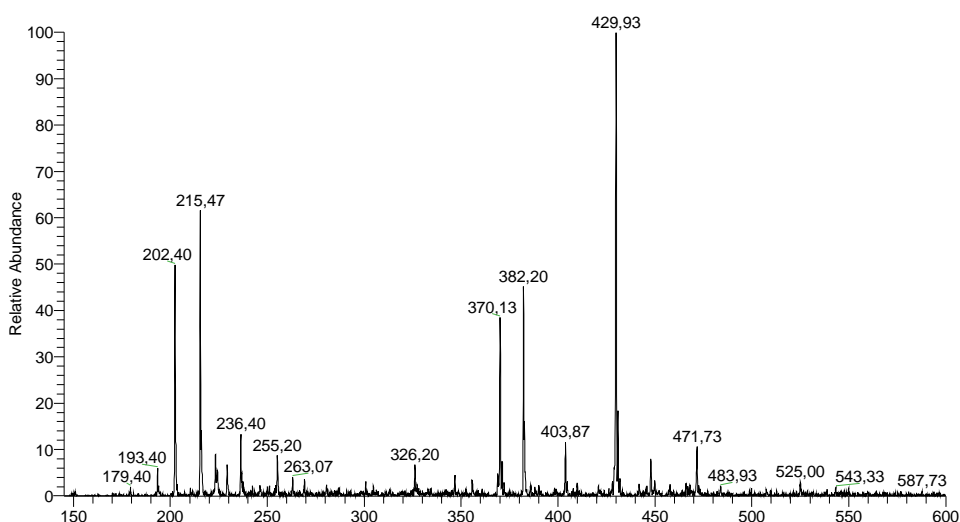


Fig.2. ESI MS spectra of aluminium ion and fleroxacin solution. $pH = 4.20$

The spectra were evaluated with the aid of Xcalibur software. The species whose abundance was higher than 10% were included in evaluation. Adducts with NaCl, H₂O, methanol, chloride and hydroxide were not searched for. However, it is very probable that number of signals reflect adduct formation between afore stated substances and the complex.

Pure hydrolytic species of aluminium were also investigated for aluminium solution with concentration 2.7×10^{-5} mol/l. It has been received well agreement with literature data.[3] Some of them are mononuclear but the most of them are polynuclear.

Table 1. The most abundant species in solution of Al (III) and fleroxacin

m/z	identification
360	$[2M-H-CO_2+Al]^{2+}$
370	$[M+H]^+$
382	$[2M-H+Al]^{2+}$
719	$[2M-2H-CO_2+Al]^+$
763	$[2M-2H+Al]^+$

Conclusion

The most abundant complex in the fleroxacin + aluminium ion solution at ligand to metal concentration ratio 2:1 is AlL_2 . It undergoes fragmentation. In contrast, the ligand itself under the chosen experimental conditions is very little fragmented.

Fragmentation of the complex proceeds *via* protonation/deprotonation of decarboxylation path.

In accordance with signal intensity it can be concluded that the amount of complexes is considerable. The aluminium–quinolone complexes may affect the bio distribution of aluminium ion upon concomitant ingestion of aluminium based antacids or phosphate binders and fluoroquinolones.

References

- [1] V. T. Andriole, The Quinolones, Academic press, London, 1988.
- [2] R. M. Silverstain et al, Spectrom . identif. of organic compounds, John Wiley & Sons Inc, New York, 1999.
- [3] A. Sarapola et al. J. Mass Spectrom., 2004; **39**, 423-430.

OPTICAL EMISSION MEASUREMENT OF PLASMA GENERATED BY INFRARED LASER BEAM WITH Cu TARGET

M. Momčilović^a, D. Ranković^b, B. Kuzmanović^b, M. Kuzmanović^b,
and M. Trtica^a,

^a*VINCA Institute of Nuclear Sciences, University of Belgrade, P.O. BOX 522,
11001 Belgrade, Serbia*

^b*University of Belgrade - Faculty of Physical Chemistry, P.O. BOX 276, 11001
Belgrade, Serbia*

Abstract

A study of visible (VIS) optical emission of Cu-plasma, induced by infrared (IR) Transversely Excited Atmospheric (TEA) CO₂ laser, was carried out. Irradiation of the Cu-target with laser fluence of 8.2 J/cm² at low air pressure resulted in the appearance of intensive plasma over the target. The type, number and intensity of the emission Cu-spectral lines strongly depend on the observing plasma location with respect to the target surface. "Primary" plasma gives the largest number of spectral lines. Also, in contrary to other plasma locations, some ionic lines were detected from this region. "Secondary" plasma, as a rule, gives the atomic lines. This region of plasma is very favourable for possible analytical applications (e.g. quantitative analysis).

Introduction

Studies of the plasma production in front of a solid target, especially copper (Cu), by lasers, are of great fundamental and technological interest. There are not many papers dealing with the interaction of pulsed lasers [1,2] with Cu. Plasma emission method based on TEA CO₂ laser is scarce in literature, too. Investigations of Cu plasma can, among other things, be of interest for analytical applications, i.e. for qualitative and quantitative analysis.

The present paper deals with the plasma emission initiated by pulsed IR TEA CO₂ laser emitting at ~10 μm on a copper target.

Experimental

Copper-target used in the experiment, (diameter and thickness of 4 and 0.5 cm, respectively) possessed high purity of 99.9%. Cu-target, also, has high reflectivity at CO₂ laser emission line(s), thus the preparation of its surface before laser irradiation was an essential process. Absorption of Cu-target surface was enhanced by a deposition of CuO (black colour) layer. All experiments were carried out with this type of layer.

Irradiations of the target were performed using laser beams focused by ZnSe lens with 13.0 cm focal length. The angle of incidence of the laser beams with respect

to the Cu-surface plane was 90°. The irradiation was carried out in a reduced air ambient, at a pressure of 0.1 mbar. Typical laser fluence during irradiation was 8.2 J/cm². The TEA CO₂ laser, employed for the experiment, was operated in the multimode regime. Conventional CO₂/N₂/He gas mixtures were used for the laser [3] yielding pulses with a gain switched peak followed by a slowly decaying tail. Cu-plasma emission analysis was performed by Hilger & Watts model E-498 (medium) quartz spectrograph using monochrome EFKE KB 100 film. Entrance slit during experiments was 50 µm. Plasma is imaged along a horizontal axis onto the entrance slit of a spectrograph. The quartz lens with focal length of 25 cm was used as an imaging lens. Typical time exposition of the film was equivalent to accumulation of 3000 pulses. The Cu-/Fe-arc was used for spectrograph calibration.

Results and discussion

Cu-emission, induced by TEA CO₂ laser, generally depends on the laser parameters (e.g. laser output pulse energy), the conditions of the irradiation (e.g. the type and pressure of atmosphere), the characteristics of the target (e.g. surface absorptivity), etc. Irradiation of the Cu-target under conditions given in the *Experimental* resulted in VIS plasma emission. The plasma consists of two visually distinctly separated regions. The first one (primary plasma), close to the target, is characterized with whitish colour. This region is confined in relatively low volume and it generates an intense continuous emission spectra (as well as atomic/ionic lines) in a short time. This region is regarded as high-temperature [4]. The other region (secondary plasma), larger in volume, has green colour. This region, as a rule, emits atomic line spectra with low background. Emission, from this region can be attributed to existence of shock wave excitation of the ablated atoms [4]. The region has semi-spherical shape. VIS Cu-plasma emission also strongly depends from the location within the plasma from which the emission was observed (i.e. spatially resolved measurement). Plasma emission, for 450 to 650 nm spectral region, at different distances from the target is presented in Table 1. Identification of the emission lines (Table 1.) was based on the reference [5].

Table 1. VIS spectral lines of Cu-plasma induced by TEA CO₂ laser. (Observed spectral region 450 - 650 nm).

Spectral lines λ, [nm]; *(l) = 2mm	<i>Cu I</i>	450,74; 453,97; 458,70; 465,11; 467,48; 469,75; 501,66; 510,55; 515,32; 521,82
	<i>Cu II</i>	450,60; 455,60; 464,93; 490,97; 493,17; 495,37; 621,69; 627,33; 630,10
Spectral lines λ, [nm]; *(l) = 10mm	<i>Cu I</i>	453,97; 458,70; 465,11; 510,55; 515,32; 521,82; 570,02; 578,21

*(l)- the location/distance above the target from which the spectral emission was observed.

Conclusion

A study of VIS optical emission of Cu-plasma, induced by TEA CO₂ laser, was carried out. Irradiation of the Cu-target with laser fluence of 8.2 J/cm² at low air pressure resulted in the appearance of intensive, green, plasma over the target. The investigations showed that the type, number and intensity of the emission Cu-lines strongly depend from the observing plasma location with respect to the target surface. The largest number of spectral lines was detected from “primary” plasma. It can be assumed that this plasma region possesses the highest electron temperature [4]. Also, in contrary to other plasma locations, some ionic lines were detected. “Secondary” plasma, as a rule, gives the atomic lines, whereas the ratio signal-to-background (S/B) is very high. Preliminary measurements showed that S/B ratio is approximately better than 300:1. In this context, the usage of this plasma region is very favourable for possible analytical applications.

Acknowledgements

This research was sponsored by the Ministry of Science and Technological Development of the Republic Serbia.

References

- [1] J. D. Wu, Q. Pan, S. C. Chen, *Appl. Spectroscopy*, 1997, **51**, 883-888.
- [2] Y-I. Lee, K. Song, H-K. Cha, J-M. Lee, M-C. Park, G-H. Lee, J. Sneddon, *Appl. Spectroscopy*, 1997, **51**, 959-964.
- [3] M. S. Trtica, B. M. Gakovic, B. B. Radak, S. S. Miljanic, *Proc. SPIE*, 2002, **4747**, 44-49.
- [4] K. H. Kurniawan, K. Kagawa, *Appl. Spectroscopy Rev.*, 2006, **41**, 99-130.
- [5] <http://physics.nist.gov/PhysRefData/Handbook/periodictable.htm>

MALDI-TOF MS CHARACTERIZATION OF TRANSITION METAL COMPLEXES

B. Damnjanović,¹ B. Petrović,² J. Dimitrić-Marković³ and M. Petković¹

¹Laboratory of Physical Chemistry, Institute of Nuclear Sciences "Vinča",
University of Belgrade, Belgrade, Republic of Serbia ²Department of Chemistry,
Faculty of Science, University of Kragujevac, Kragujevac, Republic of Serbia;³
Faculty of Physical Chemistry, University of Belgrade, Belgrade, Republic of Serbia
Correspondence to Bojana Damnjanović FAX:+381112447207, E-mail:
bojanad@vinca.rs

Abstract

In this work, we have analyzed the positive ion MALDI-TOF mass spectra of cationic complexes [PdCl(*dien*)]Cl and [Ru(*en*)₂Cl₂]Cl acquired with different matrices: 2,5-dihydroxybenzoic acid (DHB), α -cyano hydroxycinnamic acid (CHCA) and quercetin. The necessity to test several matrix/analyte combinations for reliable identification and characterization of metallo-drugs is emphasized in this work.

Introduction

Several methods can be used for the analysis and characterization of new metallo-drugs and for monitoring of their interaction with biomolecules. Among them, matrix-assisted laser desorption and ionization time-of-flight mass spectrometry (MALDI-TOF MS) seems to be promising due to its capability of analysis of both, transition metal complexes and biomolecules. [1]

Choice of the matrix for the MALDI-TOF MS is an important issue since the matrices used for MALDI-TOF mass spectrometric analysis of transition metals complexes exhibit certain drawbacks, as we have recently described, [2-4] and flavonoids appear as good candidates for this purpose.

Main aim of this work was to analyse the spectra of two cationic complexes ([PdCl(*dien*)]Cl and [Ru(*en*)₂Cl₂]Cl) obtained with the assistance of traditional matrices (DHB and CHCA) and with selected flavonoid, quercetin. Moreover, the positive ion MALDI-TOF mass spectra in more acidic environment — addition of trifluoroacetic acid (TFA) to the matrix solution usually applied for biomolecules — were analyzed. [1]

Experimental

Paladium(II) and ruthenium(III) complexes: [Pd(*dien*)Cl]Cl (diethylenetriamine paladium(II) chloride) (*Mr*=280.5) and [Ru(*en*)₂Cl₂]Cl (dichlorido (ethylenediimine)ruthenium(III) chloride) (*Mr*=327.6) were synthesised as described in the literature. [5,6] Other chemicals were purchased from Sigma Aldrich Chemie GmbH (München, Germany). Metal complexes were dissolved in a combination of methanol/physiological solution (10⁻³M). Matrices (2,5-DHB and α -CHCA) were prepared prior to use. MALDI-TOF mass spectra were acquired on a Voyager Biospectrometry DE Pro Workstation (Perseptive Biosystems, Framingham, MA,

USA). The spectra were acquired without a low mass gate and under delayed extraction conditions in the reflector mode. [2-4]

Results and discussion

All peaks detected in the MALDI-TOF mass spectra of selected transition metal complexes with their identity are listed in Table 1.

The positive ion MALDI-TOF mass spectra of $[\text{Pd}(\text{dien})\text{Cl}]\text{Cl}$ acquired with various matrices with or without TFA are given in Fig 1. Two peaks are emphasized in the inset in Fig. 1a to demonstrate the complex structure of the peak group. Neither significant changes nor additional peaks have been detected in the spectra of this complex acquired with DHB matrix after addition of TFA (Figs. 1a and 1b). When CHCA was used as matrix, only one peak (at $m/z=209.4$) arising from the Pd complex with high intensity was detectable (Fig. 1c). After the TFA addition, both peaks arising from the complex could be detected, but with much lower intensity compared to the peak obtained without TFA. Ions generated from the transition metal complex and used matrices were detected with both traditional matrices (Table 1 and Fig. 1). This was also observed in our previous work. [3]

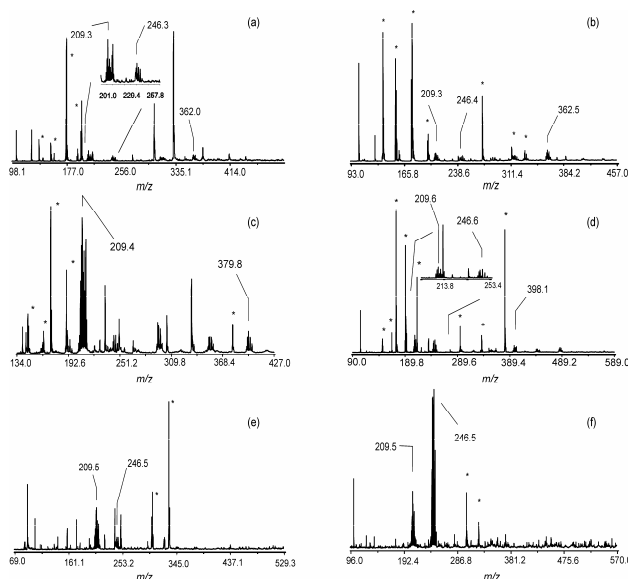


Fig. 1. Positive ion MALDI-TOF mass spectra of Pd complex acquired with DHB (a and b), CHCA (c and d) and quercetin (e and f). Spectra in a, c, and e are acquired without TFA, whereas TFA was added to the matrix solutions for the spectra given in b, d and f. Inset in traces a and d presents expanded mass region from $m/z \sim 200$ to 260.

Quercetin with the addition of TFA appeared to be the most suitable matrix for the analysis of $[\text{Pd}(\text{dien})\text{Cl}]\text{Cl}$. The two peaks arising from the complex have also been detected in the spectra acquired with quercetin (Fig. 1e). After addition of TFA the intensity of these peaks arising from the Pd(II) complex strongly increases in comparison to the matrix peaks.

MALDI-TOF mass spectra of $[\text{Ru}(\text{en})_2\text{Cl}_2]\text{Cl}$ yield only one peak arising from this complex (at $m/z=292.6$). Although quercetin generates simple pattern, addition of TFA to this matrix results in the almost complete suppression of the analyte peaks (data not shown).

[PdCl(dien)]Cl		
Matrix	m/z	Peak assignment
2,5 – DHB ; α – CHCA; Q	104.3	$[N_3C_4H_{14}]^+$
	209.4	$[M - HCl - Cl]^+$
	246.6	$[M - Cl]^+$
2,5 – DHB (TFA)	362.5	$[M - Cl - HCl + 2,5-DHB]^+$
α – CHCA	398.1	$[M + Cl^- - HCl + \alpha-CHCA]^+$
	485.1	n.a.*
[Ru(en) ₂ Cl ₂]Cl		
2,5 – DHB	193.5	n.a.*
2,5 – DHB	292.6	$[M - Cl]^+$
α – CHCA		
Q		
2,5 – DHB	373.4	$[M - H^+ + 2Na^+]^+$
2,5 – DHB	412.6	n.a.*

Table 1. Peaks detected in the positive ion MALDI-TOF mass spectra of the Pd and Ru complexes. The corresponding spectra are given in Figs. 3 and 4. „M“ corresponds to the molecule. Q: quercetin. *, „n.a.“: not assigned

In all spectra recorded, peak at $m/z=104.3$ (ethylenediamine, $[N_3C_4H_{14}]^+$) arises. Although not quantitatively determined, it seems that its intensity increases after addition of TFA to the matrix solution (Figs. 1b, 1d and 1f),

indicating that the TFA might enhance the process of the complex degradation.

Conclusion

Matrices used for MALDI-TOF MS analysis of transition metal complexes exhibited the differences in their behavior with respect to the quality of the positive ion mode MALDI-TOF mass spectra of Pd(II) and Ru(III) complexes used in this study. In general, quercetin gives much simpler spectra, resulting in the easy detection and analysis of the complexes. The generation of clusters with DHB and CHCA matrices complicates the spectra of transition metal complexes, whereas it seems that quercetin stabilizes both Pd(II) and Ru(III) complexes for their detection by MALDI-TOF MS. Taken together, results presented in this study once more point out the necessity to establish reliable conditions for the analysis of the novel metallo-drugs by MALDI-TOF MS and for potential investigation of their interaction with various classes of biomolecules by this method.

Acknowledgments

This work was supported by the Ministry of Sciences and Technological Development of the Republic of Serbia, grant No. 142051b.

References

- [1] F. Hillenkamp, J. Peter-Katalinic, eds., *Maldi Ms*, WILEY-VCH Verlag GmbH & Co. KGaA, Weinheim, 2007.
- [2] M. Petković, A. Vujačić, J. Schiller, Z. Bugarčić, J. Savić, V. Vasić, *Rapid Commun. Mass Spectrom.*, 2009, **23**, 1467-1475.
- [3] A. Vujačić, Ž.D. Bugarčić, J. Schiller, V. Vasić, M. Petković, *Polyhedron* 2009, **28**, 2905-2912.
- [4] M. Petković, B. Petrović, J. Savić, Ž.D. Bugarčić, J. Dimitrić-Marković, T. Momić, V. Vasić, *Int. J. Mass Spectrom.*, 2010, **29**, 39-46.
- [5] L.P. Battaglia, A.B. Corradi, C.G. Palmieri, M. Nardelli, M.E.V. Tani, *Acta Cryst.*, 1973, **B 29**, 762-767.
- [6] G. Mahal, R. Van Eldik, *Inorg. Chim. Acta* 1987, **127**, 203-208.

C Kinetics, Catalysis

CATALYST DEACTIVATION KINETICS. PROBLEMS OF DATA INTERPRETATION

Nikolaj M. Ostrovskii

HIPOL a.d., Odžaci, Serbia

Fax: +381-25-464-702, E-mail: n.ostrovski@hipol.com

Abstract

Problems of catalyst deactivation kinetics and catalyst stability testing are considered. Some causes and effects of erroneous interpretation of experimental data are discussed. Influences of reaction kinetics and of laboratory reactors are also considered. Several helpful and practical equations are presented.

Introduction

Catalyst deactivation (activity decay) is a fundamental phenomenon in catalysis, since it is caused by catalytic process itself. That is why the mechanism and kinetics of catalyst deactivation should be considered as a part of total catalytic process. The rigorous approach, based on quasi-steady state principle [1-3], indicates that the equation of deactivation rate depends on the reaction rate-determining step; on deactivation stages; and on the type of reactor.

Unfortunately, in practice (and in many publications) the formal dependencies are often used for mathematical treatment of experimental data. Besides, catalyst deactivation results usually from several phenomena occurring simultaneously, such as coking, sintering, poisoning, etc. These reasons often lead to erroneous interpretation of catalyst stability testing.

Meanwhile, as reported by Delmon [4], "In industry, a large part of development in catalysis is devoted to deactivation, and 90 % of the total expenditure concerns this problem". Therefore, it is very important to clarify the dominant cause and features of catalyst deactivation, in order to predict the optimal policy of catalyst exploitation during its time on stream.

Deactivation testing

Since the "lifetime" of many commercial catalysts is several months or even years, it is impossible to carry out stability tests in real time. The only way of comparing catalysts is by testing them under special, severe conditions causing accelerated deactivation. Certainly, some requirements should be fulfilled:

1. Accelerated deactivation should not change its nature.
2. The state of active sites should be identical to that in real process.
3. The way of acceleration should be founded on deactivation kinetics.

If the reaction and deactivation mechanisms are known, it is not difficult to derive equations of reaction and deactivation kinetics. Such a model gives the

possibility to substantiate an optimal procedure of catalyst testing, and provides a relatively correct interpretation of experiments. Corresponding examples one can find in literature, including [1, 2].

Dealing with unknown mechanisms, or when author doesn't want to deal with kinetics (that is typical for catalyst stability testing), an erroneous interpretation and faulty estimate are quite possible. First of all, it concerns a correct expression of relative activity $a(t) = r(t) / r^0$ by measurable quantities – concentration (C_i) or conversion (X). A common error is that the activity $a = r/r^0$ is often represented as the conversion ratio $a = X/X^0$.

Effect of reaction kinetics and type of reactor

The activity–conversion relationship $a = f(X)$ depends on the reactor in which a catalyst testing is carried out, and on the reaction kinetics, but it does not depend on deactivation kinetics [1, 2]. The corresponding formulas were derived in [1] and some of them are listed in table 1.

As is demonstrated in the table, the ratio $a = X/X^0$ is correct only for zero-order reaction in both CSTR and PFR reactors. If the first-order reaction $A \rightarrow B$ is analyzed, the difference in estimated activity can amount to three times, which is clearly seen from Figs. 1 and 2.

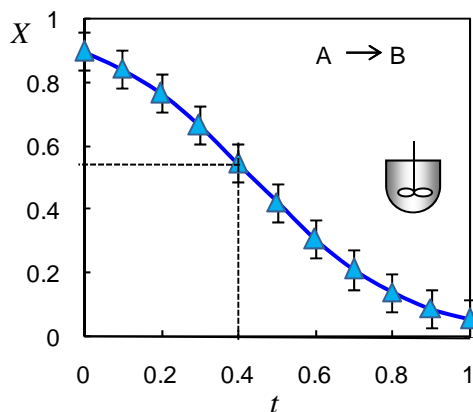


Fig.1. Catalyst deactivation in CSTR.
Conversion vs. time, $X^0 = 0.9$.

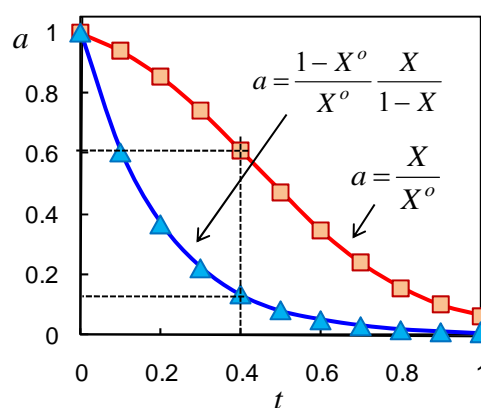


Fig.2. Activity vs. time. Treating of data
from Fig. 1.

When the conversion decreases from 0.9 to 0.55 (Fig. 1), the catalyst activity declines to 0.15 (Fig. 2), if the correct formula is used. Using wrong expression gives 0.6 as the activity level (Fig. 2).

Table 1. Activity – conversion relationships [1].

Characteristic	CSTR	PFR
Reaction rate r	$A \rightarrow B, r = k C_A^n a$	$A \rightarrow B, r = k C_A^n a$
Equation for x	$x = k \tau C_{A_0}^{n-1} (1-x)^n a$	$dx/d\xi = k \tau C_{A_0}^{n-1} (1-x)^n a$
Total conversion X	$X = x$	$X = x (\xi=1)$
Average activity $\langle a \rangle$	$\langle a \rangle = a$	$\langle a \rangle = \int_0^1 a(\xi) d\xi$
$a = f(X)$ – general case	$a = \frac{(1-X^o)^n}{X^o} \frac{X}{(1-X)^n}$	$\langle a \rangle = \frac{(1-X)^{1-n} - 1}{(1-X^o)^{1-n} - 1}, n \neq 1$
$n = 0$: zero-order	$x = k \tau a / C_{A_0}$ $a = X / X^o$	$dx/d\xi = k \tau a / C_{A_0}$ $\langle a \rangle = X / X^o$
$n = 1$: first-order (irreversible)	$x = k \tau (1-x) a$ $a = \frac{1-X^o}{X^o} \frac{X}{1-X}$	$dx/d\xi = k \tau (1-x) a$ $\langle a \rangle = \frac{\ln(1-X)}{\ln(1-X^o)}$
$n = 1$: first-order (reversible)	$x = k \tau a (x_E - x) / x_E$ $a = \frac{X_E - X^o}{X^o} \frac{X}{X_E - X}$	$dx/d\xi = k \tau a (x_E - x) / x_E$ $\langle a \rangle = \frac{\ln(1-X / X_E)}{\ln(1-X^o / X_E)}$
$n = 2$: second-order	$x = k \tau C_{A_0} (1-x)^2 a$ $a = \frac{(1-X^o)^2}{X^o} \frac{X}{(1-X)^2}$	$dx/d\xi = k \tau C_{A_0} (1-x)^2 a$ $\langle a \rangle = \frac{1-X^o}{X^o} \frac{X}{1-X}$

CSTR – continuous stirred-tank reactor. PFR – plug flow reactor. x, X – conversion; x_E, X_E – equilibrium conversion; X^o – initial conversion; τ – contact time; C_{A_0} – inlet concentration; ξ – length of bed, dimensionless.

Table 2. Effect of deactivation kinetics on conversion dynamics [1].

Characteristic	CSTR	PFR
Reaction rate, r In terms of x	$A \rightarrow B, r = k C_A a$ $r = k C_{A_0} (1-x) a$	$A \rightarrow B, r = k C_A a$ $r = k C_{A_0} (1-x) a$
Rate of deactivation, r_D		
Regardless of x By substance A By product B	$r_D = k_D C_{A_0} a$ $r_D = k_D C_{A_0} (1-x) a$ $r_D = k_D C_{A_0} x a$	$r_D = k_D C_{A_0} a$ $r_D = k_D C_{A_0} (1-x) a$ $r_D = k_D C_{A_0} x a$
Activity – conversion relationship		
	$x = k \tau (1-x) a$	$dx/d\xi = k \tau (1-x) a$
Equation of activity ($\gamma = k_D C_{A_0}$)		
Regardless of x By substance A By product B	$da/dt = -\gamma a$ $da/dt = -\gamma (1-x) a$ $da/dt = -\gamma x a$	$da/dt = -\gamma a$ $da/dt = -\gamma (1-x) a$ $da/dt = -\gamma x a$
Equation of outlet conversion		
Regardless of x By substance A By product B	$dX/dt = -\gamma (1-X) X$ $dX/dt = -\gamma (1-X)^2 X$ $dX/dt = -\gamma (1-X) X^2$	$dX/dt = \gamma (1-X) \ln(1-X)$ $dX/dt = -\gamma (1-X) X$ $dX/dt = \gamma (1-X) [X + \ln(1-X)]$

CSTR – continuous stirred-tank reactor. PFR – plug flow reactor. x, X – conversion; $C_A = C_{A_0} (1-x)$; $C_B = C_{A_0} x$.

Effect of deactivation kinetics

As distinct from $a = f(X)$, the activity dynamics $a = f(t)$, or $X = f(t)$ depend directly on deactivation kinetics. The corresponding equations for the first-order reaction, with catalyst deactivation by initial substance, by product, and with rate regardless of X , are presented in table 2.

If, for example, the catalyst is deactivated by the reaction product (B), the only minor difference is observed between outlet conversion dynamics in two types of reactor (Fig. 3). If the initial substance (A) causes the catalyst deactivation (Fig. 4), the plug flow reactor (PFR) is more suitable for testing since requires less time. This, certainly, is valid if the same initial conversion (X^o) is used in testing procedure.

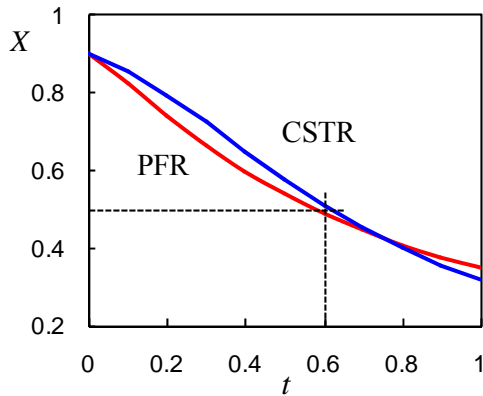


Fig.3. Catalyst deactivation by reaction product (B) in the reaction $A \rightarrow B$.

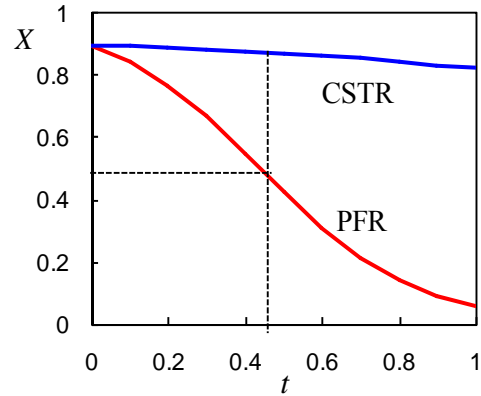


Fig.4. Catalyst deactivation by initial substance (A) in the reaction $A \rightarrow B$.

Cost of formal description

Let's consider the possible consequences of incorrect interpretation of experimental data using an example of figure 1. It shows a calculated curve $X(t)$ corresponding to catalyst deactivation in CSTR under conditions of the reaction rate ($r = k C_A a$) and deactivation rate ($da/dt = -k_D a$).

Using the familiar relationship $a = X/X^o$ (which is wrong because of first-order reaction), it is possible to fit the conversion data to a straight line (Fig. 5a). The slope gives a deactivation rate constant of $k_D = 0.9 \text{ h}^{-1}$. The correct description, based on equation from table 2, gives $k_D = 5.0 \text{ h}^{-1}$.

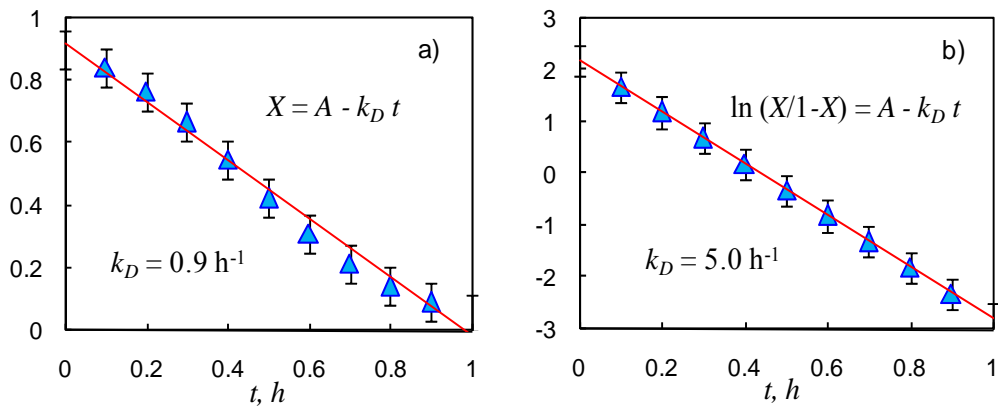


Fig.5. Catalyst deactivation by reaction product (B) in the reaction $A \rightarrow B$.
Data from figure 1: a) – incorrect, and b) – correct description.

Another example represents the deactivation of Pt/Al₂O₃ catalyst in dehydrogenation of cyclohexane. Relevant experimental data have been reported in many publications [1, 6]. The $a(t)$ experimental data (Fig. 6) are characteristic of deactivation accompanied by self-regeneration of the catalyst due to the action of excess hydrogen. According to the approach presented in [1, 3], the deactivation rate in this case follows the equation:

$$-\frac{da}{dt} = k_D C_{MCP} \frac{a - a_S}{1 - a_S} \quad (1)$$

Even at roughly constant methylcyclopentane concentration C_{MCP} , the equation provides good description and adequate interpretation (Fig. 6a). The residual activity (a_S) corresponds to active centers state when the rate of deactivation by MCP becomes equal to rate of self-regeneration by H₂:

$$k_D C_{MCP} a_S \approx k_R C_{H_2} (1 - a_S) \quad (2)$$

Just for this reason, the excess hydrogen is used in the process.

Let's examine now, how using of formal model, like equation (3), can lead to interpretation, which is wrong in principle.

$$-da/dt = k_D a^n \quad (3)$$

In order to describe the experimental data in terms of equation (3), the exponent (n) must be increased above unity (Fig. 6b), reaching $n = 4$.

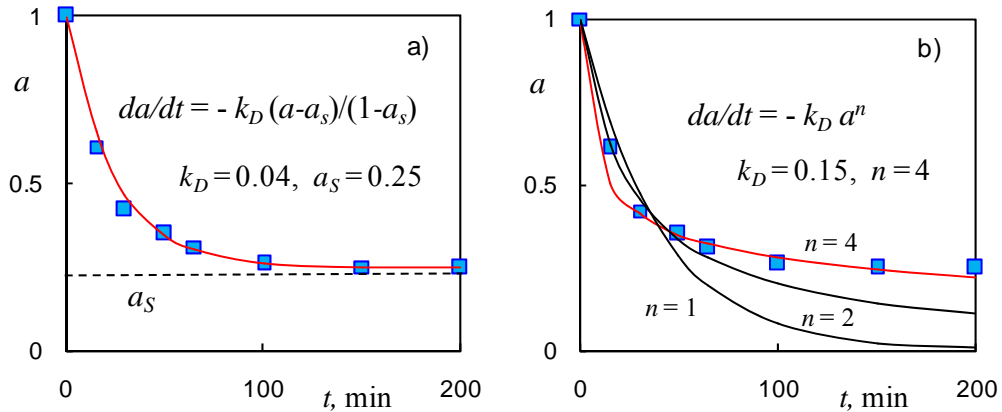


Fig.6. Deactivation of Pt/Al₂O₃ in cyclohexane dehydrogenation.
a) – correct, and b) – incorrect description.

Attempts to interpret this fact lead to the conclusion that four coke precursors interact simultaneously on the active center. The probability of such a mechanism is nearly zero. Furthermore, since the rate of self-regeneration (the

hydrogenation of coke precursors) depends on temperature, n must also be temperature-dependent. This formal inference is in conflict with the very essence of the equation (3).

This example clearly demonstrates that the formal description not only leads to incorrect estimates of kinetic parameters (k_D) but also “incites” the researcher to a misinterpretation of the observed kinetics. This may give rise to errors in process control.

Interpretation of „flex point“

Another mistake comes from interpretation of deactivation curves $a(t)$ and $X(t)$, since their shapes usually differ. Namely, it was shown in [1] that $X(t)$ - curves have the flex points X_f , even in the simplest case, when the rate of deactivation does not depend on conversion $da/dt = -k_D a$ (Fig. 1). The equations of conversion and coordinates of the flex point are listed in table 3.

It is important, that a flex point is a fundamental property of system (reaction + reactor), but not the result of deactivation delay. Thus, the apparent delay in decreasing of conversion at catalyst deactivation not serving as a proof of a special mechanism, but must be analyzed carefully.

Table 3. Flex point coordinates X_m of $X(t)$ - curves [1].

Characteristic	CSTR	PFR
Reaction rate, r	$A \rightarrow B, r = k C_A a$	$A \rightarrow B, r = k C_A a$
Deactivation:	Conversion: equation and flex point	
Regardless of x $da/dt = -k_D a$	$\ln(y/y^0) = -\gamma t$ $X_f = 0.50$	$\ln(\ln z/\ln z^0) = -\gamma t$ $X_f = 0.63$
By substance A $da/dt = -k_D C_A a$	$\ln(y/y^0) + y - y^0 = -\gamma t$ $X_f = 0.33$	$\ln(y/y^0) = -\gamma t$ $X_f = 0.50$
By product B $da/dt = -k_D C_B a$	$\ln(y/y^0) + 1/y^0 - 1/y = -\gamma t$ $X_f = 0.67$	No simple solution $X_f = 0.80$

$$\gamma = k_D C_{A0}; \quad y = X/(1-X); \quad y^0 = X^0/(1-X^0); \quad z = 1-X; \quad z^0 = 1-X^0$$

Nomenclature

$a = r/r^0$ – relative activity of the catalyst; r, r^0 – current and initial reaction rate;
 a_S – residual activity; $\langle a \rangle$ – mean integral activity of catalyst bed;
 r_D, r_R – rates of deactivation and self-regeneration; k, k_D – constants of reaction rate and deactivation; τ – contact time; X, X^0, X_S – current, initial and residual conversion at the reactor exit.

References

- [1] N.M. Ostrovskii, Catalyst Deactivation Kinetics (Russian)., Nauka, Moscow, 2001.
- [2] N..M. Ostrovskii, Kinetics and Catalysis, 2005, **46**, 693-704.
- [3] N. M. Ostrovskii, Chem. Eng. Journ., 2006, **120**, 73-82.
- [4] B. Delmon – Applied Catalysis, 1985, **15**, 1-16.
- [5] A. Monzón, T. F. Garetto, A. Borgna, Applied Catalysis A: General, 2003, **248**, 279-289.
- [6] A. K. Pal, M. Bhowmick, R.D. Srivastava, Ind. Eng. Chem. Proc. Des. Develop., 1986, **25**, 236-241.

PHOTOCATALYTIC PROCEDURES AT WATER AND AIR CLEANING

Slavcho Rakovsky

Institute of Catalysis, Bulgarian Academy of Sciences, Sofia 1113, Bulgaria
(rakovsky@ic.bas.bg; rakovsky@yahoo.com)

Abstract

Different nano-sized powder photocatalytic materials were prepared based on TiO₂ modified with SiO₂, noble metals or semiconductors. Coatings were obtained supporting the powder photocatalytic materials on quartz tubes, glass beads, mullite fibers, SS plates, SS mesh, microscopic glass, TLC silica gel covered Al sheets and cordierite honey comb monolith plates. Samples were tested in the slurry batch reactor with several model pollutants. The rate of photocatalytic degradation of organic pollutants in water is described by the Langmuir-Hinshelwood kinetic model, modified to describe reactions occurring on the solid-liquid interphase surface.

Introduction

Recently photocatalysis is gaining a growing importance among these methods for purification of contaminated water and air. It is a heterogeneous catalytic advanced oxidation process (AOP) involving the generation of highly reactive hydroxyl radicals from water molecules upon UV or visible light illumination of a semiconductor. These radicals are the active particles that destroy all kinds of organic pollutant molecules, converting them into harmless CO₂ and H₂O. The effect of hydroxyl radicals is much more powerful than that of O₃ or H₂O₂. Semiconductor photocatalysis are solving environmental problems in the most economic way as it makes use of cheap and endless solar energy and the oxidant is atmospheric oxygen. In case of using artificial illumination the needed light intensity is small – 1-5 watts/m² of the photocatalyst surface area to achieve activation.

Results and Discussion

Different nano-sized powder photocatalytic materials were prepared based on TiO₂ modified with SiO₂, noble metals (Au, Ag, Pt, Pd) or other semiconductors like WO₃. Modifying TiO₂ with SiO₂ (4%) enables high temperature treatment of the material without the undesired anatase-rutile transition, which deteriorates the photonic efficiency. At modification of TiO₂ surface with noble metals particles the role of the metals is to separate the charge carriers – the photo-excited electrons and the positively charged holes. The appearance in that case of Schottky barriers at

the metal/semiconductor inter-phase surface preventing the return of the electrons and hindering the recombination process.

The powder photocatalytic materials, as prepared, can be tested directly for their activity only in a suspension (the so called slurry reactors), which are effective but these are batch reactors for water purification only. If you want to test your material in a continuous flow water purification process or in gas phase air purification you have to support the powder on different carriers. We obtained coatings on quartz tubes, glass beads, mullite fibers, SS plates, SS mesh, microscopic glass, TLC silica gel covered Al sheets and cordierite honey comb monolith plates.

The Pt/TiO₂ and Ag/TiO₂ samples were tested in the slurry batch reactor with oxalic acid as the model pollutant, the Pd/TiO₂ samples – in the same reactor with xylenol orange as model pollutant and the TiO₂-SiO₂ samples were tested with Acid Black 194 azo dye and chlorophenol.

The TiO₂-SiO₂ powders were coated on glass beads, mullite fibers, SS plates, SS mesh, glass plates, TLC Al sheets achieving a loading of 1 mg of TiO₂ coating per 1 cm² of all carriers surface, using different binding substances. The photocatalytic powder materials and coatings were characterized by BET method and XPS analysis - from the positions of the XPS peaks it was established that the superficially attached Pt or Au are reduced completely to metallic Pt⁰ and Au⁰. In the case of attached Ag it is not possible to draw any definite conclusions with respect to the valence state of silver, owing to the quite close values of the binding energies of metallic Ag⁰ and the two oxides Ag₂O and AgO - after carrying out the photocatalytic oxidation reaction of model pollutants the metallic state is preserved.

The kinetics of the photocatalytic process in aqueous phase is described by the Langmuir-Hinshelwood model. In all cases the adsorption of the pollutant on the photocatalyst is decreasing upon increasing the content of the attached metal on the TiO₂ surface but the charge separation counteracts and as a result the reaction rate passes through a maximum at optimal noble metal loading.

TEM micrographs reveal the surface morphology, roughness and fractality of the noble metal/titania films.

The irradiation sources were UV-A and UV-C lamps. A light intensity of 7 mW/cm² was measured with a microprocessor controlled radiometer. The photooxidation was carried out at room temperature (20°C) and pH 3. The mineralization degree of the pollutant was analysed by means of a TOC analyser model VCSH (Shimadzu, Japan), spectrophotometrically when working with azo-dye pollutant or with gas-analyzer in their-purification experiments using C₂H₄ as model pollutant and continuous flow reactor.

The rate of photocatalytic degradation of organic pollutants in water is described by the Langmuir-Hinshelwood kinetic model, modified to describe reactions occurring on the solid-liquid interphase surface:

$$R^0 = -dC/dt = k_r K C_{eq} / (1 + K C_{eq}) \quad (1)$$

where R^0 is the initial rate of consumption of the organic pollutant, k_r is the rate constant of the rate-limiting step of the reaction at maximum coverage under the given experimental conditions, K is the pollutant adsorption-desorption equilibrium constant and C_{eq} is the equilibrium concentration of the pollutant in the bulk phase.

At high model pollutant concentrations $KC_{eq} \gg 1$ the reaction rate is described by a zero kinetic order with respect to the pollutant: $C_0 - C = k_r t$, where C_0 is the initial concentration of oxalic acid and C is the concentration at a given moment of time t .

The photonic efficiencies $\xi = R_0 I_{hv}^{-1} \times 100$, where I_{hv} is the photon flux, depend on the type of the metal, amount of the metal and on the size of the metal particle. The pure TiO_2 has $\xi = 0.76$, which increases as follows: $\xi = 1.26$ (0.5%Ag, 6nm), $\xi = 1.44$ (0.5%Pt, 4nm), $\xi = 1.55$ (1%Ag, 7nm), $\xi = 1.71$ (1%Pt, 5nm) and finally the highest photonic efficiency evaluated $\xi = 1.76$ (0.16%Au, 5 nm).

Acknowledgements

NATO Project SFP 982835 and Project of the Bulgarian Fund of Scientific Investigations (FNI) - DO 02-252/18.12.08.

FORMATION OF THE METALLIC NICKEL PHASE IN Ni/SILICA GEL PRECURSORS OF VEGETABLE OIL HYDROGENATION CATALYSTS

M. Gabrovska^{1*}, P. Tzvetkov², K. Tenchev¹, L. Spasov¹,
J. Krstić³, N. Vukelić⁴ and D. Jovanović³

¹*Institute of Catalysis, Bulgarian Academy of Sciences, Sofia 1113, Bulgaria*
**(margo@ic.bas.bg; margarita.gabrovska@abv.bg,* ²*Institute of General and Inorganic Chemistry, Bulgarian Academy of Sciences, Sofia 1113, Bulgaria*
³*Institute of Chemistry, Technology and Metallurgy, Department of Catalysis and Chemical Engineering, Belgrade 11000, Serbia,* ⁴*Faculty of Physical Chemistry, University of Belgrade 11000, Serbia*

Abstract

Ni/SiO₂ materials with identical composition were synthesized on silica gel obtained at different pH values. The chemical interaction between Ni²⁺-entities and silica results in formation of Ni-phyllsilicate layers on the surface of the carriers. The effect of the silica gel type on the formation of Ni⁰ phase in Ni/SiO₂ systems was studied by powder X-ray diffraction and temperature programmed reduction. The formation of Ni⁰ phase strongly depends on the strength of interactions between Ni²⁺-species and SiO₂ through the Ni-phyllsilicate layers. Ni²⁺-entities are weakly bonded to the surface of silica gels obtained at acidic and alkaline pH values and strongly to the surface of this prepared at neutral pH. The weakly bonded Ni²⁺-species during reduction form larger Ni⁰ crystallites, while the strongly bonded generates the smallest Ni⁰ crystallites. The silica gel obtained at alkaline pH allows both significant reduction of Ni²⁺ ions at 430°C and the highest metal nickel dispersion on the surface of reduced precursor.

Introduction

Metallic nickel supported on different natural or synthetic sources of silica is commonly used as commercial catalyst for vegetable oil hydrogenation. Considering that the active phase in the process is metallic nickel, the determination of the conditions of its formation is fundamental for the achievement of good catalyst performance [1]. In this study, we employed three types of silica gel having different texture parameters, in order to prepare Ni/SiO₂ catalysts for vegetable oil hydrogenation. Powder X-ray diffraction (PXRD) and temperature programmed reduction (TPR) are applied to study the effect of the support and the reduction temperature on the formation of Ni⁰ phase in reduced Ni/SiO₂ systems.

Experimental

Three types of silica gel (SIG) were prepared at different pH values that demonstrated different texture parameters, namely: acidic (SIG-A, S_{BET}=777 m²/g), neutral (SIG-B, S_{BET}=581 m²/g) and alkaline (SIG-C, S_{BET}=387 m²/g). The precursors were synthesized with identical composition (SiO₂/Ni=1.0) by

precipitation using aqueous solutions of $\text{Ni}(\text{NO}_3)_2 \cdot 6\text{H}_2\text{O}$ and Na_2CO_3 on every type of SIG. As a reference sample unsupported basic nickel carbonate (BNC) was also synthesized. PXRD patterns were recorded on a Bruker D8 Advance powder diffractometer employing CuK_α radiation. BET surface area measurements were performed on a Sorptomatic 1990 (Thermo Finnigan) apparatus. TPR experiments were realized with H_2/Ar stream (10/90 v/v; flow rate: $25 \text{ cm}^3/\text{min}$; heating rate: $10^\circ\text{C}/\text{min}$) in the temperature range $25\text{--}750^\circ\text{C}$ on a differential scanning calorimeter DSC-111 (SETARAM). The precursors were reduced at two temperatures (430 and 530°C) for 5 h with a gas mixture of H_2/N_2 (1/1 v/v; flow rate: $10 \text{ dm}^3/\text{h}$; heating rate: $2^\circ\text{C}/\text{min}$) and passivated with a gas mixture of O_2/N_2 .

Results and Discussion

PXRD patterns of SIGs show broad peak at $2\theta \approx 22^\circ$, that may be attributed to amorphous silica (JCPDS 00-046-1045) (Fig. 1A, inset). The reflections of the unreduced precursors (Fig. 1A) may be assigned to the formation of layered Ni-phyllsilicate phase (JCPDS file 00-049-1859). The diffraction peaks are not clearly defined due to the turbostratic structure of the registered phase [2]. The activation of Ni-based catalysts is commonly accomplished by reduction of the precursors in the temperature interval $430\text{--}550^\circ\text{C}$. TPR experiments revealed quite different properties of the formed Ni^{2+} -species on the surface of the supports (Fig. 1B). TPR profile of BNC shows single peak in the region $220\text{--}310^\circ\text{C}$ that is assumed to represent the full reduction of Ni^{2+} ions to Ni^0 , while TPR profiles of the precursors are characterized by multiply reduction peaks with poorly resolved maxima indicating a complex interaction between the components.

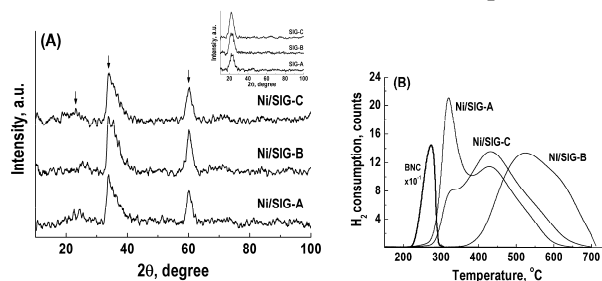


Fig.1. (A) PXRD patterns of the unreduced precursors, where Ni-phyllsilicate phase is marked with arrows; (B) TPR profiles of the precursors

Further PXRD study on samples reduced at both selected temperatures revealed details in the reduction process and the transformation of the formed Ni^{2+} -entities. The patterns of the solids reduced at 430°C (Fig. 2A) display diffraction lines typical of Ni^0 phase (JCPDS file 00-004-0850). The peaks are badly organized for Ni/SIG-B_R430 due to the obtaining of fine Ni^0 crystallites. Contrariwise, the larger Ni^0 crystallites are responsible for the sharper and narrower reflections in Ni/SIG-A_R430. The peaks of lower intensity at $2\theta \approx 32\text{--}40$ and 60° indicate the presence of Ni-phyllsilicate phase in all reduced precursors, however it is better represented in Ni/SIG-B_R430. The reduction of Ni^{2+} ions is increased upon treatment at 530°C as it is evidenced from the sharpness of the Ni^0 reflections (Fig.

2B). The most remarkable changes in the reducibility of Ni-phyllsilicate and the crystallization of Ni⁰ phase is demonstrated by Ni/SIG-B_R530. The treatment of all samples at 530°C provokes not only significant reduction of the Ni-phyllsilicate phase, but causes also growth of the Ni⁰ crystallites. These results are supported by H₂-chemisorption data showing the highest dispersion of Ni⁰ on the surface of Ni/SIG-C_R430 (13 %) and Ni/SIG-B_R530 (8 %) as well as the lowest one on the surface of Ni/SIG-A: 1.4 % and 0.7 % after reduction at 430°C and 530°C, respectively.

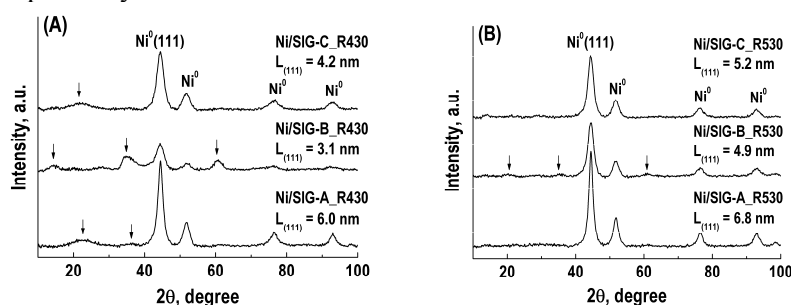


Fig.2. PXRD patterns of the precursors reduced at 430°C (A) and 530°C (B)

The following explanations could be proposed: (i) the reduction process in both Ni/SIG-A and Ni/SIG-C samples starts at ~270°C that may be associated with the reduction of BNC-like species located on the surface of Ni-phyllsilicate (the peak and shoulder at ~320°C), follows by the reduction of Ni-phyllsilicate phase weakly bonded to the silica surface (T_{\max} ~430°C); (ii) the reduction in Ni/SIG-B starts after 350°C due to Ni-phyllsilicate strongly bonded to the silica. The peak at ~520 and shoulder ~630°C documented the low reducibility of the latter sample.

Conclusion

The formation of Ni⁰ phase strongly depends on the strength of interaction between Ni²⁺-species and SiO₂ through the Ni-phyllsilicate layers that could be related to the differences in the pore systems of the used supports. Ni²⁺-entities are weakly bonded to the surface of silica gels obtained at acidic and alkaline pH values and strongly - to the surface of this prepared at neutral pH. The weakly bonded Ni²⁺-species during reduction form larger Ni⁰ crystallites, while the strongly bonded generates the smallest ones. The silica gel obtained at alkaline pH allows both significant reduction of the Ni²⁺ ions at 430°C and the highest metal nickel dispersion on the surface of the corresponding precursor.

Acknowledgments

The authors are grateful to Dr. M. Shopska for the H₂-chemisorption measurements and to Prof. R. Kardjieva and Prof. G. Kadinov (all from Institute of Catalysis, BAS) for the useful discussion. J. K. and D. J. are grateful to the Serbian Ministry of Science (Pr-166001B).

References

- [1] M. Balakos, E. Hernandez, *Catal. Today*, 1997, **35**, 415–425.
- [2] K. Ghuge, A. Bhat, G. Babu, *Appl. Catal. A: Gen.*, 1993, **103**, 183–204.

THE INFLUENCE OF Fe CONTENT IN Al, Fe-PILLARED CLAYS ON ITS PERFORMANCE IN CATALYTIC WET OXIDATION

P. Banković, A. Milutinović-Nikolić, N. Jović-Jovičić, M. Žunić,
Z. Vuković and A. Abu RabiStanković

¹*ICH_{TM}, University of Belgrade, Department of Catalysis and Chemical Engineering, Njegoševa 12, Belgrade, Republic of Serbia*

Abstract

In this work a series of Al,Fe-pillared clays (PILCs) with different Fe³⁺ content was synthesized and characterized. Their catalytic performance was studied in the in catalytic wet peroxide oxidation (CWPO) of food dye tartrazine used as a model compound. Degree of decolorization of tartrazine containing aqueous solution was monitored in relation to Fe³⁺ content. The results of the catalytic tests showed that higher Fe content leads to higher catalyst efficiency in the investigated reaction. The reaction can be described by 0 order kinetics inherent to heterogeneous catalytic processes.

Introduction

Al,Fe-pillared clays (PILCs) have shown good performance in catalytic wet peroxide oxidation (CWPO) of organic pollutants in water. They have predominantly been tested in the degradation of phenol [1]. There are seldom reports on their use in the degradation of other organic pollutants such as toluene [2] and dyes [3]. In this paper local bentonite clay (Bogovina) rich in smectite was used to obtain Al,Fe-PILC with different Fe³⁺ content. Their catalytic performance was studied in the in CWPO of tartrazine dye at moderate temperature.

Experimental

Bentonite was obtained from Bogovina, Serbia. It was crushed, ground and sieved through a 74 μm sieve and by hydroseparation a fine particle fraction < 2 μm was obtained. The PILCs were obtained using a common procedure [4] consisting of the following steps: grinding, sieving, Na exchange, intercalation, drying and calcination. Fe³⁺ to (Al³⁺+Fe³⁺) molar ratios in the pillaring solutions were 0%, 1%, 5%, 10% and 15% and the corresponding materials were denominated Al-PILC, Al,Fe1-PILC, Al,Fe5-PILC, Al,Fe10-PILC and Al,Fe15-PILC, respectively. The chemicals used for the Na⁺ exchange and pillaring were NaCl, NaOH and Al(III) and Fe(III) nitrate.

X-Ray diffraction (Philips PW 1710 X-ray powder diffractometer with a Cu anode) confirmed that the pillaring was successful [5]. Chemical composition of the PILCs was determined using Spectro Spectroflame M - inductively coupled plasma optical emission spectrometer. Catalytic tests were carried out in a

semibatch reactor under stirring and constant temperature maintained by circulation of thermostatic fluid using Julabo MC 4 heating circulator. Initial dye concentration was 50 ppm in the presence of excess of H₂O₂. Catalytic performance of the catalysts was examined using UV-Vis spectrophotometry.

Results and Discussion

The results of chemical analysis for the most abundant cations are given in Table 1.

Table 1. Chemical composition of samples

Sample	Si	Al	Fe
	mmol/100g of sample		
Na -B	910.3	474.3	107.3
Al PILC	916.5	859.3	110.9
Al,Fe-1 PILC	912.4	740.7	132.4
Al,Fe-5 PILC	921.3	715.7	178.9
Al,Fe-10 PILC	911.6	656.4	214.7
Al,Fe-15 PILC	925.5	637.0	304.1

Chemical analysis showed that Al pillaring lead to abrupt increase of the Al³⁺ content, while the inclusion of Fe³⁺ in the pillaring solution lead to gradual increase of the Fe content followed by decrease in the Al content of the obtained materials. These results are in good correlation with the Fe³⁺/Al³⁺ ratios applied in the syntheses.

Fig. 1 represents dependence of tartrazine concentration (C_{tart}) on the reaction time during CWPO at 35 °C and shows the influence of Fe³⁺ content on the kinetics of dye degradation. The dependence acquires linear trend soon after the initiation of the reaction. Therefore, here presented data do not include 0 min point corresponding to the initial dye concentration.

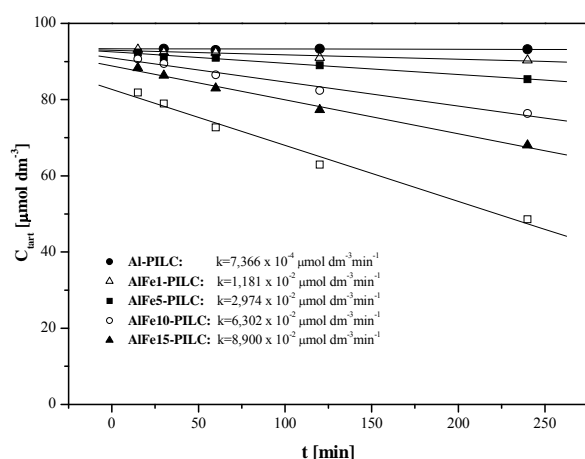


Fig. 1. CWPO of tartrazine on the series of Al,Fe-PILCs at 35°C

Linear dependence of $C_{\text{tart}}=f(t)$ indicates 0 order reaction kinetics established when adsorption/desorption equilibrium at active sites of the catalyst is reached. At that moment the reaction rate becomes independent on the C_{tart} in the solution. Higher Fe content of the catalysts means greater active site concentration resulting in greater reaction rate constant.

Although the investigated method did not involve pH adjustments, the catalytic tests showed good results even at mild temperature. Performance of the obtained Al,Fe-PILCs in the degradation of tartrazine was good. It was found to be dependant on the Fe³⁺ content which was a proof of the activity of incorporated Fe species in the investigated CWPO process.

Conclusion

A series of Al,Fe-pillared clay (PILC) materials with different Fe content was synthesized. The obtained materials were tested in the catalytic wet peroxide oxidation (CWPO) of azo dye tartrazine at mild conditions. It was found that the Al,Fe-PILCs show activity in the dye degradation. The results of the catalytic tests showed that higher Fe content leads to higher catalyst efficiency in the investigated reaction. The reaction can be described by 0 order kinetics inherent to heterogeneous catalytic processes. Here investigated method was proven to be efficient in the decolorization of tartrazine containing water, thus reducing sunlight cut-off effects, and is prospective as a first step in a two stage water purification method, where the second one could be biodegradation.

Acknowledgments

This work was supported by the Ministry of Science and Technological Development of the Republic of Serbia (Projects 166001B and 142019B).

References

- [1] J. G. Carriazo, E. Guelou, J. Barrault, J. M. Tatibouët, S. Moreno, *Appl. Clay Sci.*, 2003, **22**, 303-308.
- [2] P. Banković, A. Milutinović-Nikolić, Z. Mojović, A. Rosić, Ž. Čupić, D. Lončarević, D. Jovanović, *Chin. J. Cat.*, 2009, **30**, 14-18.
- [3] M. N. Timofeeva, S. Ts. Khankhasaeva, Yu. A. Chesalov, S. V. Tsybulya, V. N. Panchenko, E. Ts. Dashinamzhilova, *Appl. Catal. B*, 2009, **88**, 127-134.
- [4] V. Kaloidas, C. A. Koufopoulos, N. H. Gangas, N. G. Papayannakos, *Microporous Mater.*, 1995, **5**, 97-106.
- [5] P. Banković, A. Milutinović-Nikolić, A. Rosić, N. Jović-Jovičić, D. Jovanović, *Russ. J. Phys. Chem. A*, 2009, **83**, 1485-1489.

SWELLING BEHAVIOR OF Ag/PVA HYDROGEL NANOCOMPOSITE SYNTHESIZED BY γ -IRRADIATION

J. Krstić, A. Krklješ and Z. Kačarević-Popović

*Vinča Institute of Nuclear Sciences, University of Belgrade, 11001 Belgrade,
P.O. Box 522, Serbia (krkljes@vinca.rs)*

Abstract

In this study, the Ag/PVA hydrogel nanocomposite was synthesized using γ -irradiation. Incorporated Ag NPs were less than 10 nm in diameter with face centered cubic (*fcc*) crystal structure. Incorporation of Ag NPs into PVA hydrogel significantly affects the characteristic parameters of swelling process.

Introduction

Hydrogels are polymeric three-dimensional networks having the ability to swell, but not to dissolve. They are rendered insoluble by chemical or physical crosslinks, which provide the network structure and physical integrity. Due to characteristic properties such as swellability in water, hydrophilicity, biocompatibility and lack of toxicity, hydrogels have been utilized in a wide range of biological, medical, pharmaceutical and environmental applications.

The materials having metal nanoparticles (NPs) incorporated into polymer network have been widely investigated due to their unique properties induced by the synergy of two different materials. Silver nanoparticles (Ag NPs) have been proved to be effective antimicrobial agent and enhanced antibacterial properties have been demonstrated both *in vitro* and *in vivo*. Recent research efforts are directed towards exploiting the *in situ* synthesis of Ag NPs within polymeric network architectures and products of these approaches are new hybrid nanocomposite systems. Hydrogels in the swollen state provide free spaces within the network, which can serve for nucleation and growth of NPs. In this way, the carrier-hydrogel system acts as a nanoreactor that immobilizes NPs and provides easy handling. Among different synthesis route, γ -irradiation induced synthesis has been recognized as highly suitable tool for production of hydrogel nanocomposites due to formation and sterilization of material in one technological step [1, 2].

In this work the Ag NPs were radiolytically synthesized within poly(vinyl alcohol) (PVA) hydrogel, previously obtained by γ -irradiation induced crosslinking. Optical and structural analyses of synthesized hydrogels were performed as well as of their swelling kinetics behavior.

Experimental

PVA aqueous solution (5 wt%) was aerated for 30 min with argon (Ar), in order to remove oxygen and then γ -irradiated at a dose rate of 0.33 kGy/h, up to absorbed dose of 25 kGy. The obtained hydrogel was immersed in deionized water, for one week, to remove uncrosslinked PVA and dried at room temperature. PVA hydrogel was equilibrated in the solution containing $16 \cdot 10^{-3}$ M AgNO_3 and 0.2 M 2-propanol. Swelling of Ar-saturated gel was carried out for 48 h at room temperature, in the dark. Reduction reaction was performed by γ -irradiation to the absorbed dose of 30 kGy, at a dose rate of 10 kGy/h. γ -irradiation was performed at ^{60}Co radiation source, under ambient condition.

The optical properties of synthesized Ag/ PVA hydrogel nanocomposite were investigated by UV-Vis absorption spectroscopy using Thermo Scientific Evolution 600 spectrophotometer, while the microstructural analysis was performed by XRD measurement on Bruker D8 Advance Diffractometer ($\text{Cu K}_{\alpha 1}$ radiation, $\lambda = 0.1541$ nm).

Dynamic swelling studies were performed in deionized water at temperature of 25 ± 1 °C, using dry gels (xerogels). Hydrogel discs (diameter $d = 10$ mm, thickness $\delta = 5$ mm) were cored out, dried to the constant weight and then used in swelling investigations. The swelling process was observed gravimetrically.

Results and Discussion

After the γ -irradiation, the yellow colored Ag/PVA hydrogel nanocomposite was obtained. Yellow color is characteristic of silver nanoparticles (Ag NPs). Formation of NPs was confirmed by UV-Vis spectroscopy and X-ray diffraction. Absorption spectrum of Ag/PVA hydrogel shows plasmon absorption band at 392 nm (characteristic of Ag NPs), while XRD pattern confirmed that Ag NPs were less than 10 nm in diameter, with face centered cubic (*fcc*) crystal structure [2, 3].

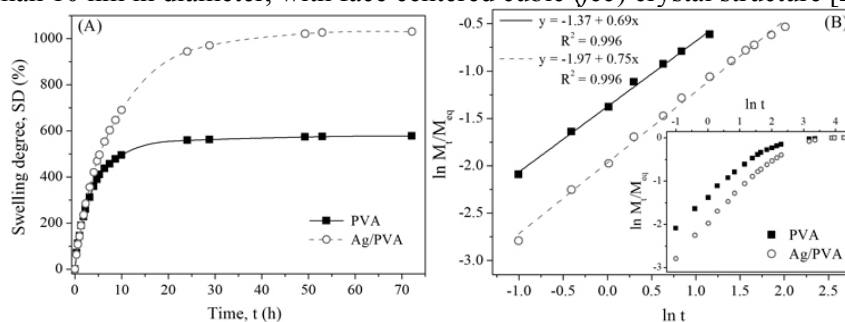


Fig.1. (A) Swelling curves of hydrogels, in deionized water at 25 °C. (B) Best linear fits of linear parts of swelling curves. Inset: Dependence $\ln M_t/M_{eq}$ vs. $\ln t$ in the whole investigated range.

The capacity of swelling is one of the most important parameters for evaluation the properties of hydrogels. Fig. 1(A) depicts the swelling curves of the investigated hydrogels in deionized water at 25 °C. As can be seen, the swelling isotherms are similar in shape, but incorporation of Ag NPs particles in the PVA

hydrogel has significant influence on the swelling properties. The equilibrium swelling degree (SD_{eq}) of Ag/PVA hydrogel nanocomposite was found to be 1.78 times higher in comparison with PVA hydrogel, and swells with the lower initial swelling rate (v_{in}) (Table 1). This can be ascribed to the existence of remnant Ag^+ ions in the *in situ* synthesized nanoparticles in hydrogel, which can be well dissolved in water thus altering the composition of swelling medium [3].

To analyze the model of water diffusion into the polymer network, the water sorption data was used. The logarithmic form of kinetic equation of swelling, $M_t/M_{eq} = k t^n$ (k is the kinetic constant, related to the structure of the network, t is time and n is the diffusion exponent), was presented as an inset on Fig. 1(B). The characteristic constant n and k was calculated from the slope and intercept, respectively, of the linear parts of initial stages of swelling (Fig. 1(B)), and they can be related to the specific transport mechanism. In this case, both hydrogel systems shows non-Fickian or anomalous diffusion ($0.5 < n < 1$) when the rates of diffusion and polymer chain relaxation are comparable [3]. The diffusion coefficient (D) can be calculated as $D = k^{1/n} \pi \delta^2/16$ (δ is thickness of the xerogel). The values for n , k and D were presented at Table 1. For extensive swelling of hydrogels the equation $t/SD = A+Bt$ was used (Fig. 2), and the linear dependence indicated the Schott second order kinetics ($dSD/dt = k_s(SD_{eq}-SD)^2$) [3, 4].

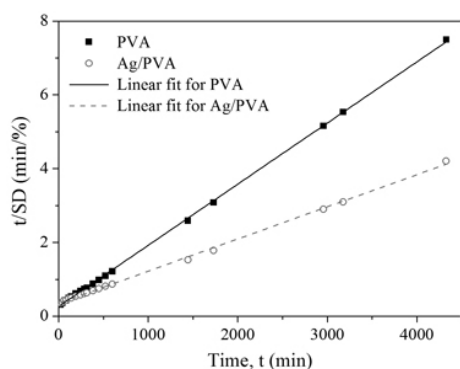


Fig.2. Relation t/SD vs. t for hydrogels, in deionized water at 25 °C.

Table 1. Characteristic parameters of swelling process for hydrogels, in deionized water at 25 °C.

	PVA	Ag/PVA
SD_{eq} (%)	575	1025
v_{in} (%/min)	2.49	2.29
k (1/s)	$7.1 \cdot 10^{-5}$	$3.9 \cdot 10^{-5}$
n	0.69	0.75
D (cm^2/s)	$5.58 \cdot 10^{-6}$	$2.15 \cdot 10^{-6}$

Conclusion

The Ag/PVA hydrogel nanocomposite was successfully synthesized by γ -irradiation. The obtained hydrogel nanocomposite had greater swelling capacity and diffusion coefficient, but it swells slowly, compared to PVA hydrogel, in deionized water at 25 °C. Both hydrogels show non-Fickian diffusion and Schott second order kinetics, at early and extensive stage of swelling, respectively

References

- [1] Y.M. Mohan et al., Polymer, 2007, **48**, 158-164.
- [2] A. Krklješ et al., Polym. Bull., 2007, **58**, 271-279.
- [3] Y.L. Luo et al., Mater. Chem. Phys., 2009, **118**, 329-336.
- [4] H.K. Can et al., Rad. Phys. Chem., 2005, **72**, 483-488.

THE INFLUENCE OF THE MOLAR RATIO [H₂O]/[Ti(OR)₄] ON THE KINETICS OF THE TITANIUM- OXO-ALKOXY CLUSTERS NUCLEATION

Z. Baroš

*Higher Education School of Professional Studies - Belgrade Polytechnic, Brankova
17, 11000 Belgrade, Serbia, zbaros@politehnika.edu.rs*

Abstract

The influence of the molar ratio $h = [\text{H}_2\text{O}]/[\text{Ti}(\text{OR})_4]$ ($\text{R} = {}^i\text{Pr}$) on the kinetics of the titanium-oxo-alkoxy clusters nucleation was studied. Clusters were formed by the titanium tetraisopropoxide $\text{Ti}(\text{O}^i\text{Pr})_4$ chemical reaction with H_2O in n-propanol solution, with the fixed concentration of $\text{Ti}(\text{O}^i\text{Pr})_4$ ($c = 0.04$ M), molar ratio $h \in \{11, 14, 17, 20\}$ and temperature $T \in \{298, 308, 318\}$ K. The isothermal rate of nucleation of titanium(IV) polyoxoalkoxides is a power law function of the molar ratio. The value of kinetic parameter β changes complexly as h and T change. The value of apparent activation energy (E_a) decreases with the increase of value h . It was also found that nucleation is a reaction with complex kinetics whose elementary stages are hydrolysis $\text{Ti}(\text{OR})_4$ to $\text{Ti}(\text{OR})_3\text{OH}$ and the forming of titanium(IV) polyoxoalkoxides $[\text{Ti}_{x+y}\text{O}_y](\text{OR})_{4x+2y}$ through the alcoxolation reaction.

Introduction

The kinetics of the sol-gel hydrolysis-polycondensation reaction based on titanium metal alkoxides has been studied in a number of works [1-5].

In this work, we present the effects of the molar ratio $h \in \{11, 14, 17, 20\}$ and temperature $T \in \{298, 308, 318\}$ K, with the fixed concentration of $\text{Ti}(\text{O}^i\text{Pr})_4$ $c = 0.04$ M, on the kinetics of the titanium-oxo-alkoxy clusters nucleation.

Experimental

The kinetics of the nucleation was observed with the absorption method [6], using the GBC Cintra 10e UV-Visible Spectrometer at predetermined wavelength $\lambda = 550$ nm.

Results and Discussion

The typical kinetics curves of the hydrolysis-polycondensation reaction of $\text{Ti}(\text{OR})_4$ with H_2O in n-propanol solution, at investigated temperatures, are presented in Fig. 1.

On these kinetic curves, at all investigated temperatures, three distinctive regions of absorbance changes over reaction time are clearly observed, each of them corresponding to one of three different reaction stages: nucleation, growth and polycondensation. Assuming that the rate of nucleation and growth of particles to a critical size (v_n), is the inverse value of the induction time, the effects of h and experimental temperature T on v_n were examined. The effects of h and T on v_n are shown in Table 1.

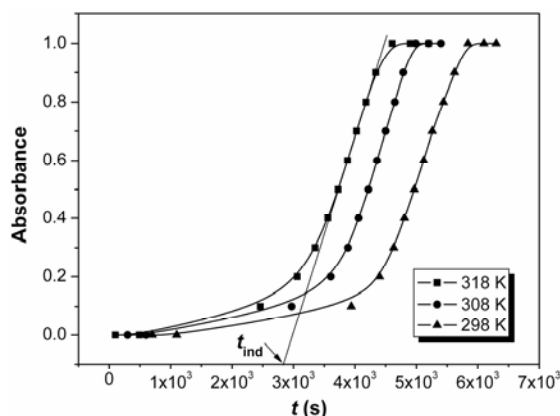


Fig. 1. The isothermal kinetic curves of the hydrolysis-polycondensation reaction of $\text{Ti}(\text{OR})_4$ with H_2O in n-propanol solution, at $c = 0.04 \text{ M}$ and $h = 20$.

Table 1. The effects of h and T on the rate of nucleation of titanium(IV) polyoxoalkoxide particles

$c \text{ (M)}$	0.04		
$T \text{ (K)}$	298	308	318
h	$v_n \text{ (s}^{-1}\text{)}$		
11	$5.0 \cdot 10^{-5}$	$1.3 \cdot 10^{-4}$	$4.8 \cdot 10^{-4}$
14	$9.4 \cdot 10^{-5}$	$3.1 \cdot 10^{-4}$	$5.6 \cdot 10^{-4}$
17	$3.0 \cdot 10^{-4}$	$6.8 \cdot 10^{-4}$	$8.8 \cdot 10^{-4}$
20	$9.1 \cdot 10^{-4}$	$1.7 \cdot 10^{-3}$	$2.0 \cdot 10^{-3}$

Table 2. The effects of temperature T and h on the values of kinetic parameter β

$c \text{ (M)}$	0.04	
$T \text{ (K)}$	β	R^2
298	4.41	0.955
308	3.83	0.990
318	2.12	0.854

Analysis of the obtained results, in all of these investigated cases, leads to a conclusion that the rate of nucleation increases as: a) h values (at $T = \text{const.}$) increase, b) T values (at $h = \text{const.}$) increase.

Assuming that the rate v_n could be described with the equation [7]:

$$v_n = k \cdot (h - 1.45)^\beta$$

where $k = k_1 \cdot c^a$ is a constant, it is possible to determine the value of the kinetic parameter β . Namely, the dependence $\ln v_n$ vs. $\ln (h - 1.45)$ is linear and its plot is a straight line whose slope can be used for the kinetic parameter β calculation. The effects of temperature T and h on the values of kinetic parameters β are shown in Table 2.

Based on the obtain results, it may be conclude that the value of the kinetic parameter β decreases as the temperature T increases.

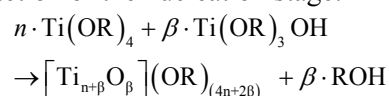
Since the increase in value v_n as T increases is exponential, by applying the Arrhenius equation, the value of apparent activation energy (E_a) in the nucleation reaction was determined. It is known that the dependence $\ln v_n$ vs. $1/T$ is linear and its plot is a straight line whose slope and intercept can be used for the apparent

activation energy (E_a) and pre-exponential factor ($\ln A$) calculation. Table 3 shows the dependence of apparent activation energy (E_a) and pre-exponential factor ($\ln A$) in the nucleation process on h .

Table 3. The dependence of apparent activation energy (E_a) and pre-exponential factor ($\ln A$) on h

c (M)	0.04		
h	E_a (kJ/mol)	$\ln A$ (s^{-1})	R^2
11	(87.7±0.1)	24.70	0.978
14	(70.78±0.08)	19.37	0.968
17	(43.17±0.07)	9.38	0.931
20	(31.07±0.06)	5.86	0.920

Having in mind that the integer values of kinetic parameter β and $n = \text{const.}$ match the number of molecules that take part in the elementary polycondensation reaction, we can formulate the equation for the chemical reaction of the nucleation stage:



The observed changes in structure of titanium(IV) polyoxoalkoxides from $[\text{Ti}_3\text{O}_2](\text{OR})_8$ to $[\text{Ti}_5\text{O}_4](\text{OR})_{12}$, at a change of h from 11 to 20, are in agreement with the results of the X-ray diffraction and NMR spectroscopy analysis of trititanates which were isolated from the reaction of $\text{Ti}(\text{OPr}^i)_4$ with water and methanol in the isopropanol solution [8].

Conclusion

Nucleation is a reaction with complex kinetics whose elementary stages are hydrolysis $\text{Ti}(\text{OR})_4$ to $\text{Ti}(\text{OR})_3\text{OH}$ and the forming of titanium(IV) polyoxoalkoxides $[\text{Ti}_{x+y}\text{O}_y](\text{OR})_{4x+2y}$ through the alcoxolation reaction.

Acknowledgments

This investigation was supported by the Ministry of Science and Technological Development of Serbia, through project 142025G.

References

- [1] E. A. Barringer, H. K. Bowen, *Langmuir*, 1985, **1**, 414-420.
- [2] J. H. Jean, T. A. Ring, *Langmuir*, 1986, **2**, 251-255.
- [3] R. W. Hartel, K. A. Berglund, *Mater. Res. Soc. Symp. Proc.*, 1986, **73**, 633-640.
- [4] M. T. Harris, C. H. Byers, *J. Non-Cryst. Solids*, 1988, **103**, 49-64.
- [5] N. V. Golubko, M. I. Yanovskaya, I. P. Romm, A. N. Ozerin, *J. Sol-Gel Sci. Technol.*, 2001, **20**, 245-262.
- [6] A. Soloviev, H. Jensen, G. Sogaard, A. V. Kanaev, *J. Mater. Sci.*, 2003, **38**, 3315-3318.
- [7] T. Hirai, H. Sato, I. Komasaawa, *Ind. Eng. Chem. Res.*, 1993, **32**, 3014-3019.
- [8] V. W. Day, T. A. Eberspacher, C. Yuewu, H. Jinling, W. G. Klemperer, *Inorg. Chim. Acta*, 1995, **229**, 391-405.

DETERMINATION OF KINETIC PARAMETERS OF ZEOLITE A CRYSTALLIZATION USING *IN SITU* ^{27}Al NMR SPECTROSCOPY

Z. Miladinović and J. Zakrzewska

Institute of General and Physical Chemistry, Studentski trg 12-16, 11000 Belgrade, Serbia

Abstract

Intensity curves obtained by *in situ* ^{27}Al NMR spectroscopy during zeolite A synthesis has been used for comparative kinetic investigation in solution and solid phase. Kinetic analysis was performed using Sharp-Hancock method. Obtained values for rate constant k increase for both phases with increasing of Na_2O batch concentration. Values for Avrami's coefficient n suggest that changes of alumina contents in solid or gel phase are connected with Na_2O batch concentration, while the changes of $\text{Al}(\text{OH})_4^-$ ions in liquid phase were not significantly influenced by Na_2O concentration during of the reaction.

Introduction

Kinetic investigation represents an important stage in understanding the mechanism of zeolite formation. In order to obtain kinetic parameters, different experimental techniques, mostly X-ray and neutron diffraction are used [1]. Particularly their *in situ* applications could provide a satisfying number of experimental data points necessary to perform kinetic analysis [1, 2]. Data obtained from such experiments are then used for evaluation of rate constant k and Avrami coefficient n , typically using Avrami-Erofe'ev equation [1, 2].

In this paper, we put our attention on comparative kinetic investigation of zeolite A crystallization for different chemical batch composition, using *in situ* ^{27}Al NMR spectroscopy and Sharp-Hancock method for determination of kinetic parameters [3].

Experimental

All *in situ* ^{27}Al NMR spectra during zeolite A synthesis were recorded on Bruker MSL 400 NMR spectrometer, using experimental procedure described earlier [3]. The batch composition was $\text{Al}_2\text{O}_3: 2\text{SiO}_2: y\text{Na}_2\text{O}: z\text{H}_2\text{O}$, where y was ranged between 3.1 and 5.0 and z from 62 to 161. Reaction temperature was 82°C for all synthesis.

Results and Discussion

All *in situ* ^{27}Al NMR spectra show two characteristic lines: the narrow one at 79 ppm associated with $\text{Al}(\text{OH})_4^-$ ions in solution phase, and broad line at 59 ppm corresponding to the changes of alumina in solid-gel phase. In Fig. 1 experimental intensity curves for both lines, obtained for different batch Na_2O concentrations during the synthesis are presented.

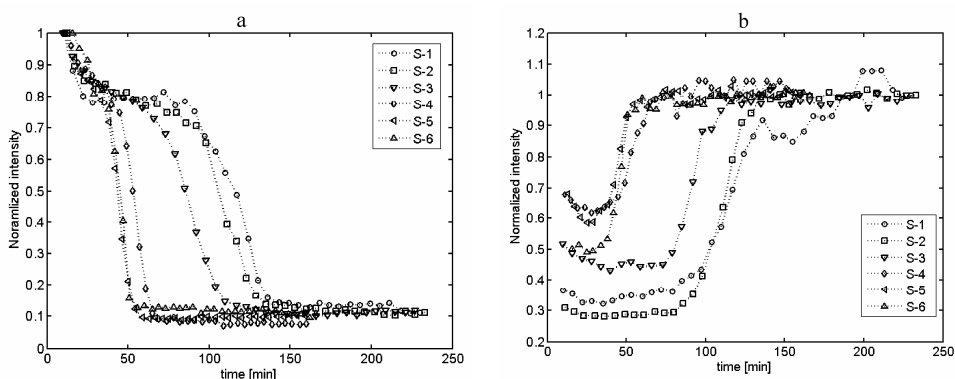


Fig.1. Changes of normalized intensity of ^{27}Al NMR line at 79 ppm (a), and at 59 ppm (b) in the course of different zeolite synthesis (assigned as S-1 – S-6) for molar ratio $\text{SiO}_2/\text{Al}_2\text{O}_3 = 2.0$, and different Na_2O concentration presented in Table 1.

All curves presented in Fig. 1a show decreasing trend, while intensities presented in the Fig. 1b increase during the reaction time, and was explained in detail in our earlier study [3]. As it was shown, presented intensity curves could be exploited to estimate kinetic parameters of crystallization process using Sharp-Hancock's equation [3], and obtained results are presented in Table 1.

From Table 1, general increasing trend of values for rate constant k with increasing Na_2O batch concentration could be observed on the basis of analysis of both lines. These results are consistent with previous kinetic investigations of zeolite A crystallization [1–3]. Obtained results for Avrami's coefficients n for line at 79 ppm are rounded about 1.8 for all synthesis, indicating that diffusion and phase boundary process dominated in liquid phase [3]. On the other hand, analysis of the line at 59 ppm gives values for Avrami's coefficients between 2 and 3 for smaller Na_2O batch concentrations ($\sim 1.7 \text{ mol/dm}^{-3}$), while in the case of higher Na_2O concentrations ($\sim 2.7 \text{ mol/dm}^{-3}$) n was varied from 1.5 – 1.8. These results could be explained assuming that the distribution of nuclei in the gel matrix is related to the distribution of various silicate anions in silicate solutions and to the dependence of this distribution on the alkalinity of the system [4]. The reaction of $\text{Al}(\text{OH})_4^-$ ions with silicate monomers and dimers that exist at higher alkalinities and further polymerization of the formed aluminosilicate anions may result in the formation of a gel with homogeneous distribution of aluminum and silicon and thus a homogeneous distribution of the particles of the quasi-crystalline phase through the formed gel which explain obtained values for n rounded about 1.5 and consequently, dominated diffusion and phase boundary mechanism. On the other hand, the preferential reaction of $\text{Al}(\text{OH})_4^-$ ions with higher silicate polymers [5] in the systems with lower alkalinities may result in the formation of a gel with a higher Si/Al molar ratio (i.e., $\text{Si}/\text{Al} > 1$) with an inhomogeneous distribution of Al in the gel matrix and therefore, dominating Avrami-Erife'ev nucleation growth model in these syntheses ($n = 2 - 3$). Overall above trends indicate obvious connection between Na_2O batch composition and mechanism of crystal growth.

Table 1. Kinetic parameters of zeolite A crystallization for different Na₂O batch concentration, for line at 79 ppm and 59 ppm; t₀ represent induction time estimated for any particular synthesis.

No. of	Line at	79 ppm	Line at	59 ppm	Na ₂ O	
Samp.	t ₀ [s]	n	k [s ⁻¹] 10 ⁻⁴	n	k [s ⁻¹] 10 ⁻⁴	[mol/dm ³]
S 1	3960	1.80	3.06	2.09	3.64	1.681
S 2	4080	1.80	3.69	3.34	3.88	1.703
S 3	2880	1.83	3.67	2.37	4.24	1.711
S 4	2100	1.75	8.55	1.48	13.34	2.646
S 5	1740	1.73	9.76	1.58	14.45	2.683
S 6	1740	1.97	9.27	1.80	12.26	2.686

Conclusion

The use of intensity curves obtained from ²⁷Al NMR spectra during synthesis provides valuable information about processes, which took part in both solid and solution phase. Comparative kinetic analysis was achieved using Sharp-Hancock method. Based on this analysis, increasing of the rate of crystallization with the increase of Na₂O content is observed. Values for Avrami's coefficient *n* suggest a connection between Na₂O concentration and Al/Si distribution in solid/gel phase, which is more homogeneous at higher Na₂O concentration resulting in values of *n* ~ 1.5, then for lower Na₂O concentration (*n* = 2 – 3). On the other hand, such dependency was not observed in solution phase where the coefficient *n* stays nearly constant (*n* ~ 1.8).

References

- [1] R. J. Francis, D. O'Hare, J. Chem. Soc., Dalton Trans., 1998, 3133-3148.
- [2] R. I. Walton, F. Millange, D. O'Hare, A. T. Davies, G. Sankar, C.R.A. Catlow, J. Phys. Chem. B, 2001, **105**, 83-90.
- [3] Z. Miladinović, J. Zakrzewska, in: Proceedings of the 8th International Conference on Fundamental and Applied Aspects of Physical Chemistry, Belgrade, Serbia, 2006, 561-563.
- [4] T. Antonic, B. Subotic, N. Stubicar, Zeolites, 1997, **18**, 291-300.
- [5] G. Harvey, L. S. Dent Glasser, ACS Symp. Ser. 398, Am. Chem. Soc., Washington, DC, 1989, 49-65.

KINETICS OF SWOLLEN HYDROGEL WATER EXCHANGE WITH ETHANOL

A. Pavicevic, V. Radonjic, J. Jovanovic and B. Adnadjevic

Faculty of Physical Chemistry, Studentski trg 12-16, 11001 Belgrade, R. Serbia

Abstract

Kinetic of isothermal process of exchange of water of swollen hydrogel with ethanol was investigated. The kinetics curves of water exchange process were recorded at temperature range from 295 K to 313 K. The kinetics model of exchange solvent from hydrogel was suggested. The values of kinetic parameters, activation energy and pre-exponential factor, were determined. The model of mechanism of solvent exchange was proposed.

Introduction

Hydrogels are a type of slightly cross-linked, hydrophilic polymers, with a three-dimensional structure that can swell, absorb and retain a large volume of water or other fluids [1]. Structural properties, equilibrium swelling degree and rate of hydrogel swelling are caused with the dewatering method [2]. Water exchange from hydrogel structure with an aliphatic alcohol is an effective method to preserve structural properties of hydrogel and to achieve higher equilibrium swelling degree and initial swelling rate of hydrogel. In order to develop new technology of hydrogel drying, kinetic of exchange water in hydrogel with absolutely ethanol was investigated.

Experimental

Hydrogel of poly(acrylic acid) synthesized according to the previously described procedure was used [3]. Structural properties and equilibrium swelling degree were determined using the methods described [3, 4]. Basic properties of the used hydrogel was: equilibrium swelling degree in distilled water at 298K: $S_{Deq}=118\text{g}$ of $\text{H}_2\text{O}/\text{g}$ of xerogel ; cross-link density: $\rho_c = 1.39 \times 10^{-4} \text{ mol}/\text{cm}^3$; Molar mass between the crosslinks: $M_c=8200\text{g}/\text{mol}$; distance between the macromolecular chains: $d=1.47\text{nm}$. Kinetics of exchange was carried out as following. In 50 mL of absolutely ethanol, preheated at predetermined temperature a $1.0 \pm 0.1 \text{ g}$ of equilibrium swollen, grounded hydrogel was added. The reaction mixture was stirred with a mechanic stirrer with 400 rpm. At predetermined time intervals, samples of reaction mixture (ethanol-water) were withdrawn from the reaction mixtures in order to determine water content. Water concentration was used determined by measuring the refractive index of reaction mixture.

Degree of water exchange was determined as:
$$DE = \frac{C_{H_2O} \cdot m_{RS}}{M_{HG}} \quad (1)$$

Where: C_{H_2O} is mass concentration of water in reaction system at reaction time (t) and m_{RS} is mass of reaction system, M_{HG} is mass of water in hydrogel. The degree of conversion of water exchange with ethanol was calculated as:

$$\alpha = \frac{DE}{DE_{max}} \quad (2)$$

Where: DE_{max} is maximal degree of conversion.

Results and Discussion

Conversion curves of water exchange with ethanol for investigated hydrogel are present in Figure 1, whereas Figure 2 presents the dependence of rate of solvent exchange

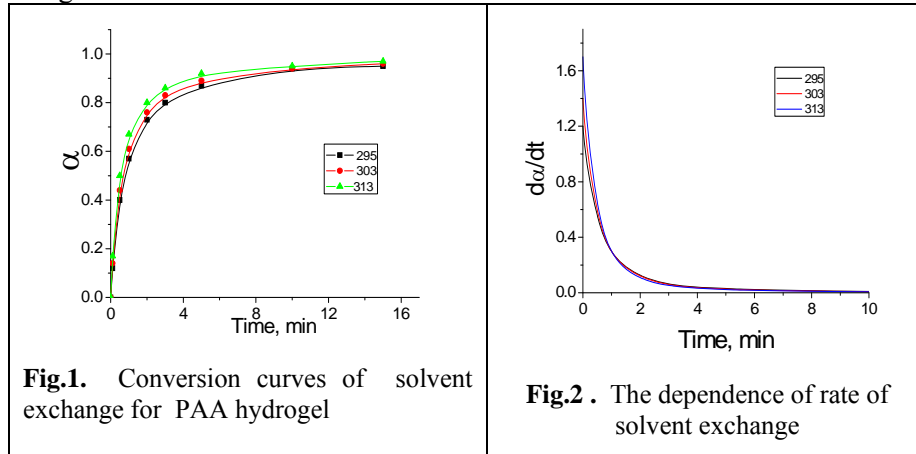


Fig.1. Conversion curves of solvent exchange for PAA hydrogel

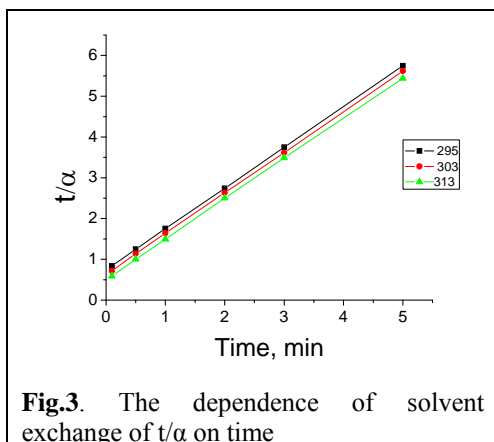
Fig.2. The dependence of rate of solvent exchange

Three characteristic regions of the changes of the exchange degree with reaction time can be distinguished in all of the isothermal conversion curves, a linear, non-linear and the saturation part or plateau. Increasing the temperature resulted in a decrease of the duration the linear part of the dependence of the exchange degree vs. time while the values of maximal exchange degree increase.

Based on the shape of the dependence $d\alpha/dt$ vs. time it can be shown that isothermal conversion curves can be described by Eq:

$$\alpha = \frac{kt}{1 + kt} \quad (3)$$

where k is rate constant of solvent exchange. If Eq (3) describes conversion curve of solvent exchange, the dependence t/α on time should give straight line. The intercept of these straight lines give values of rate constants of solvent exchange. Figure 3. shows the dependence of t/α on time.



The dependence t/α on time at all of the investigated temperatures gives straight line, which confirms validity of the proposed kinetic model and enable to calculate the values of rate constant of solvent exchange. The changes of rate constants of solvent exchange with temperature are given in Table 1.

As the values of k increase exponentially with temperature, it was possible to determine the kinetics parameters: E_a and $\ln A$ using the Arrhenius Equation.

Table 1. Rate constants and the kinetics parameters of solvent exchange

T, K	k, min^{-1}	$E_a, \text{kJ/mol}$	$\ln A$
295	1.326	18.4 kJ/mol	7.8
303	1.590		
313	2.020		

The established value of activation energy $E_a=18.4$ kJ/mol is in well accordance with the model of Flory [5] and Dusek [6] of shrinking polymer gels. Also, this value is connected with energetically barrier which hydrogels had to overcome during the shrinking which is caused by solvent exchange.

Conclusions

Kinetics of water exchange within the hydrogel with the ethanol can be described by Eq: $\alpha = \frac{kt}{1+kt}$. Activation energy of the solvent exchange within the hydrogel process is predetermined with the energetically barrier which hydrogel should overcome due to the shrinking.

Acknowledgement

The investigation was supported by the Ministry of Science and Environmental Protection of Serbia, through project G 142025.

References:

1. N. A Peppas,; A. G Mikos,. In Hydrogels in Medicine and Pharmacy; Peppas, N. A., Ed.; CRC Press: Boca Raton, 1986,. **1**, 2-20.
2. J. Zhang,, Li Wang, A.Wang. Macromol. Mater. Eng. 2006, **291**, 612-620.
3. B. Adnadević, J. Jovanović, J. Appl. Pol. Sci., 2008, **107**, 3579-3587.
4. L. F Gudeman,. N. A. Peppas, J Appl Polym Sci., 1995, **55**, 919-925.
5. P.J Flory., J.A.Chem.Soc., 1956 , **78**, 5222-5228.
6. K.Dusek, W.Prins, Adv.Polym.Sci., 1969, **6**, 1-20.

SYNTHESIS AND CHARACTERIZATION OF CATALYSTS OF Rh SUPPORTED IN CLAYS MATERIALES. APLICATION IN THE ACETONE TRANSFORMATION

C. Blanco^a, M. J. Montero^a, B. Ortiz^a, V. Krstic^b, C. Pesquera^a,
F. González^a and A. Perdigón^a

^a*Group of Inorganic Chemistry. University of Cantabria E-39005 Santander, Spain.*
^b*Mining and Metalurgy Institute Bor, 19320 Bor, Serbia*

Abstract

Layered clays materials as natural, synthetic and modified smectites (dioctahedral (Wy) and trioctahedral (S) silicates) as supports for catalysts based on Rh have been prepared by using the organometallic Rh complex as metal precursor and, in some cases, previous to this process, the support has been subjected to an ultrasonic process for 30 minutes. Supports and catalysts have been characterized by different techniques. Catalytic behaviour in the vapour phase for the hydrogenation of acetone has been analyzed. The catalysts with the previous ultrasonic process get lower time of contact with the organometallic complex (active phase of Rh) to reach a percentage of incorporated Rh near 100%. All the catalysts have resulted very actives in the acetone transformation in mild conditions. Moreover, the catalyst containing the trioctahedral silicate pillared with Al (S-Al) is much more selective towards MIBK (methyl isobutyl ketone) than the other synthesized catalysts.

Introduction

Layered silicates can be used as catalytic supports in metal support catalysts or as a precursor in which a metallic phase is incorporated within the interlaminar space.

In this work, we present a family of catalysts of Rh supported in two different clays: dioctahedral montmorillonite (mainly aluminium in the octahedral layer), supplied by Missouri University, and denominated here as Wy and the exchange capacity is 106 mequiv/100g of clay and the trioctahedral (S) clay (mainly magnesium in the octahedral layer), which is a fluorohectorite-like synthetic silicate, SOMASIF ME100 (denoted S) supplied by Co-Op Ltd Japan with a cation exchange capacity (CEC) given by the supplier of 120 meq/100g. The two clays have been modified in the laboratory by pillaring with aluminium (S-Al and Wy-Al). Moreover, the support have been subjected to an ultrasonic process fro 30 minutes, the samples will be denoted: S-US and Wy-US, in order to study the possible effect of this treatment.

It is well known the great dependence that there are between the surface properties of the support and the method and conditions in the preparation of a catalyst, in the incorporation of the catalytic active phase and the metallic dispersion and also the catalytic behaviour of some heterogeneous catalysts [1-5].

Therefore, the objective of this work is to synthesize (by using the organometallic complex as metal precursor), characterize and study the catalytic behaviour, in the hydrogenation or transformation of acetone, in gas phase and (mild conditions) atmospheric pressure, of catalysts of Rh (1%), supported in different clays synthesized in the laboratory. Moreover, it will be analysed the effect when the supports have been subjected to an ultrasonic process for 30 minutes previous the incorporation of the active phase and also, to study the effect of the acid properties of support as well as of different work variables (temperature of Rh reduction and temperature reaction) in the activity/selectivity in the hydrogenation or transformation of acetone.

Experimental

In order to carry the objective of this work the supports and catalysts were characterized by various physical-chemical techniques: XRF, XRD, SEM, IRTF, adsorption-desorption nitrogen, adsorption-desorption of ammonia, thermal analysis, UV-Visible spectroscopy and chemisorption of O₂-H₂.

All the Rh/supports systems were reduced in situ with hydrogen at different temperatures (200-500°C) in order to study the influence of the reduction temperature in the metallic dispersion

The incorporation of the metallic phase (1% Rh) on the supports was made in kenotic medium by adsorption in organometallic solution of Rh at room temperature. The catalytic behaviour was studied in the hydrogenation or transformation of acetone in gas phase and atmospheric pressure (mild conditions) at temperatures between 60 and 100°C and 80-200°C. The products were analyzed through Gas Chromatography.

Results and Discussion

Supports. The textural parameters of the S, Wy, S-Al and Wy-Al supports have been analyzed through the nitrogen adsorption isotherm technique. The data show that the S-Al sample presents a much greater specific surface area (424 m²/g) and the presence of micropores (0.160cc/g) than S sample (4 m²/g and without micropores). With respect to Wy sample, the specific surface area is 33 m²/g and without micropores, while the Wy-Al sample, the specific surface area is higher, 255 m²/g, and has presence of micropores (0.080 cc/g). However, when the two supports were subjected to an ultrasonic process, the textural properties of them have not changed.

Catalysts. When the supports were treated under an ultrasonic process before the incorporation of the metallic phase (S-US and Wy-US samples), the time of contact of these supports with the organometallic complex was much lower (from five days to one hour) [1, 3-5] and also, the obtained precursor reached a percentage of Rh incorporated (determined by UV-Visible spectroscopy) near 100%. For the S-Al

sample the percentage of Rh incorporated was smaller (83%) than for the raw supports or the ones modified by the ultrasonic process. Even that, this sample has the highest specific surface area. This can be due to the fact that the cation exchange capacity of this sample has to be smaller because of the pillaring process. The dispersion (determined by chemisorption of O₂-H₂) of the Rh/support catalysts decreases when the temperature of reduction increases (from 300 to 500°C). The catalyst with the highest dispersion is the Rh/Wy catalyst with a dispersion of 35.4(%) and a particle size of 3.1 Ø (nm).

Catalytic behaviour. All the prepared catalysts have resulted actives in the hydrogenation or transformation of acetone in gas phase and atmospheric pressure (mild conditions) and they mainly yield a greater quantity of 2-propanol [1-3]. The catalysts supported on the pillared clays have resulted as bifunctional catalysts, because of this; there is a parallel production of 2-propanol and MIBK products in the reaction.

The S-Al catalyst, due to the surface acid properties generated by the pillaring process, was the most selective catalyst in the transformation of acetone towards MIBK, in a mild conditions, for temperatures between 80 and 110°C (when the active phase was reduced at 300°C).

Conclusion

Layered clays materials as natural, synthetic and modified smectites have resulted adequate supports for the Rh catalysts. The catalysts with the previous ultrasonic process get lower time of contact with the organometallic complex (active phase of Rh) to reach a percentage of incorporated Rh near 100%. All the prepared catalysts have resulted actives in the hydrogenation or transformation of acetone in gas phase and atmospheric pressure (mild conditions). Only the catalysts supported on pillared clays have resulted selective towards MIBK.

Acknowledgments

MICINN (Ministerio de Ciencia e Innovación of Spain) for financial projects: MAT2006-03683 & MAT2009-10727.

References

- [1] C. Blanco, R. Ruiz, C. Pesquera, F. González, *Current Topics Catal.*, 2005, **4**, 113.
- [2] A. B. Melo, G. F. Santori, J. Sambert, G. J. Siri, M. L. Casella, O.A.Ferreti, *Catalysis Communications*, 2006, **7**, 204.
- [3] C. Blanco, R. Ruiz, C. Pesquera, F. González, *Appl. Organometal. Chem.*, 2002, **16**, 84.
- [4] C. Blanco, V. Krstic, C. Pesquera, A. Perdigón, F. González, *Studies in Surface Science and Catalysis.*, 2008, **174 B**, 1343.
- [5] C. Blanco, V.Krstic, C. Pesquera F. González. *En Catálisis del siglo XXI. Hacia una Química Sostenible I*, Málaga, Spain, 2008, 239.

RhSn CATALYSTS FOR CROTONALDEHIDE HYDROGENATION USING CLAY'S MODIFIED LIKE SUPPORTS

C. Blanco^a, V. Krstic^b, B. Ortiz^a, C. Pesquera^a and F. González^a

^aGroup of Inorganic Chemistry, University of Cantabria E-39005 Santander, Spain.

^bMining and Metallurgy Institute Bor, 19320 Bor, Serbia

Abstract

In this work, the capability of materials, PILC's, previously synthesized in the laboratory from a Spanish Bentonite with two sources of Al, as supports for catalysts based on Rh or on Sn promoted Rh has been studied. Rh catalysts were reduction by hydrogen at atmospheric pressure of a cationic organometallic Rh complex. The catalysts have been tested in the hydrogenation of crotonaldehyde in the vapour phase at atmospheric pressure, analysing the effect of some working parameters in the formation and distribution of the reaction products, the reaction temperature, and the addition of Sn. Both the natural clays and the PILC's materials have resulted adequate supports for the Rh and RhSn catalysts.

Introduction

The interlamellar swelling property and the adsorption capacity of clay minerals and PILC's, nanoparticles of catalytically active noble metals may be generated in the interlamellar space [1-3]. Thus the noble metal containing clay minerals or PILC's plays a significant role in the studies of the heterogeneous catalytic reactions.

Monometallic Rh and Pt catalysts usually produce the saturated aldehyde [4,5] in the hydrogenation of crotonaldehyde and it is necessary to modify them either by support effects or by addition of a second metal (bimetallic or promoter), for instance Sn, Fe, Mo or Ni, in order to improve the selectivity towards crotyl alcohol (but-2-en-1-ol) [6-11].

In this work, the capability of materials, PILC's, previously synthesized in the laboratory from a Spanish Bentonite with two sources of Al, as supports for catalysts based on Rh or on Sn promoted Rh has been studied.

Experimental

In the present study, we used natural Spanish Bentonite by GADOR. This material was used [1] to intercalated pillars of Al from different sources and than we intercalated the noble metal precursors, and reduced *in situ* [1-3] for the hydrogenation of crotonaldehyde [3-4]. Noble metal like Rh has been impregnated

with promoter of Sn in amounts of 1.7% over these materials and these supports and catalysts were characterized by various physical-chemical techniques.

Results and Discussion

In Table 1 are gathered the textural parameters obtained from the data of the adsorption isotherm of nitrogen for the supports used. S_{BET} is the specific surface area in m^2/g and R_p is the medium radius of the pores in \AA . Both samples BENAI (from $\text{Al}_2(\text{OH})_5\text{Cl}\cdot 2\text{-}3\text{H}_2\text{O}$) and BENPIL (from AlCl_3) show higher specific surface area than natural Spanish clay, denominated BEN, and the sample exchanged with NaCl, denominated BENA. The results the textural characterization of pillared supports are similar (Table 1).

Table 1. Textural parameters of samples.

Sample	$S_{\text{BET}} (\text{m}^2/\text{g})$	$R_p (\text{\AA})$
BEN	64	14.3
BENAI	240	
BENPIL	247	18.0

Table 2. Characterization data of samples: Rh = rhodium incorporated; D(%) = metallic dispersion; d(nm) = average size of particle; C(%) = conversion of crotonaldehyde, S(%) = selectivity of crotyl alcohol at 200 and 220°C; reduction temperature: 500°C.

Catalysts	Rh	D (%)		C (%)		S (%)	
		500	500	200	200	220	220
T (°C) →							
Rh / BEN	0.90	40	2.7	11.6	0.3	17.1	0
Rh 1.7 Sn / BEN	0.68	25	4.4	21.0	10.4	22.7	8.3
Rh / BENAI	0.94	59	1.8	-	-	50.0	0.4
Rh 1.7Sn/BENAI	0.79	96	1.1	16.9	39.0	12.2	17.8
Rh / BENPIL	0.97	65	1.7	64.7	0	80.5	0
Rh1.7Sn/BENPIL	0.88	54	2.0	0.82	0.01	5.1	11.9

All the prepared catalysts have resulted with a high dispersion and a particle size of the Rh particle is nanometric between 1.1 and 4.4 nm [11]. The catalysts with only Rh have resulted actives in the conversion of crotonaldehyde but not selective. The presence of Sn has an inductive effect on them to get a notable selectivity towards crotyl alcohol [4-11].

The catalyst Rh1.7Sn/BENAI (catalyst with the highest dispersion) mainly yield a greater quantity of crotyl alcohol than the catalyst Rh1.7Sn/BENPIL in all of temperatures of reactions, table 3. Probably, the preparation of the sample from $\text{Al}_2(\text{OH})_5\text{Cl}\cdot 2\text{-}3\text{H}_2\text{O}$ has high density of pillars.

Table 3. Conversion of crotonaldehyde (C%) and selectivity of crotyl alcohol (S%) in different temperatures of reaction; reduction temperature 500°C.

T°C	Rh1.7Sn/ BENPIL		Rh1.7Sn /BENAI	
	C%	S%	C%	S%
180	0.52	0.24	10.69	33.84
200	0.82	0.01	16.9	39.00
220	5.10	11.94	12.21	17.84
240	3.29	12.11	22.06	12.86
260	6.51	7.53	24.12	8.48
280	10.23	2.85	26.58	3.96
Rh%	88		79	
D%	54		96	

Conclusion

Both the natural clays and the PILC's materials have resulted adequate supports for the Rh catalysts. All the prepared catalysts have resulted with a high dispersion and a particle size of the Rh particle is nanometre between 1.1 and 4.4 nm. The reaction of crotonaldehyde hydrogenation under mild conditions over heterogeneous 1Rh1.7Sn system prepared by supports pillared with $\text{Al}_2(\text{OH})_5\text{Cl}\cdot 2\text{-}3\text{H}_2\text{O}$ indicate that the catalyst Rh1.7Sn/BENAI is better for the selectivity of crotyl alcohol from crotonaldehyde hydrogenation in gas phase than the catalyst Rh1.7Sn/BENPIL. The former catalyst present higher dispersion and a particle size of Rh of 1.1 nm.

Acknowledgments

MICINN (Ministerio de Ciencia e Innovación of Spain) for financial projects: MAT2006-03683 & MAT2009-10727

References

- [1] C. Blanco, R. Ruiz, C. Pesquera, F. González, *Appl. Organometal. Chem.*, 2002, **16**, 84.
- [2] J. Herrero, C. Blanco, C. Prieto, H. Dexpert, F.J. Lahoz, J. García, *Jpn. J. Appl. Phys.*, 1993, **32**, Suppl. 32-2, 484.
- [3] C. Blanco, V. Krstic, C. Pesquera, F. González; *Materiales Arcillosos: de la Geología a las Nuevas Aplicaciones*, Ed. M. Suárez, M. A. Vicente, V. Rives, M. J. Sánchez, Salamanca, Spain, 2006, 99.
- [4] P. Claus, *Top. Catal.*, 1998, **5**, 51.
- [5] F. Coloma, J. Llorca, N. Homs, P. Ramírez de la Piscina, F. Rodríguez-Reinoso, A. Sepúlveda-Escribano, *Phys. Chem. Chem. Phys.*, 2000, **2**, 3063.
- [6] P. Gallezot, D. Richard, *Catal. Rev. Sci. Eng.*, 1998, **40**, 81.
- [7] A. Guerrero Ruiz, A. Sepúlveda-Escribano, I. Rodríguez-Ramos, *Appl. Catal. A: Gen.*, 1994, **40**, 71.
- [8] M.A. Vannice, B. Sen, *J. Catal.*, 1989, **115**, 65.
- [9] D. Wang, F. Ammari, R. Touroude, D. S. Su, R. Schlögl, *Catal. Today*, 2009, **147**, 224.
- [10] J. Alvarez-Rodríguez, M. Cerro-Alarcon, A. Guerrero-Ruiz, I. Rodríguez-Ramos, A. Arcoya, *App. Cat. A: General*, 2008, **348**, 241.
- [11] C. Blanco, V. Krstic, C. Pesquera, A. Perdígón, F. González, *Stud. in Surf Sci. Catal.*, 2008, **174-B**, 1343.

EFFECT OF THE SUPPORT ON THE COMPONENTS INTERACTION IN THE Ni/SILICA GEL PRECURSORS OF VEGETABLE OIL HYDROGENATION CATALYSTS

M. Gabrovska^{1*}, M. Shopska¹, D. Nikolova¹, D. Simeonov²,
J. Krstić³, M. Stanković³ and D. Jovanović³

¹*Institute of Catalysis, Bulgarian Academy of Sciences, Sofia 1113, Bulgaria*
**(margo@ic.bas.bg; margarita.gabrovska@abv.bg)*

²*Institute of General and Inorganic Chemistry, Bulgarian Academy of Sciences, Sofia 1113, Bulgaria*

³*Institute of Chemistry, Technology and Metallurgy, Department of Catalysis and Chemical Engineering, Belgrade 11000, Serbia*

Abstract

Ni/SiO₂ materials with identical composition were synthesized on silica gel obtained at three different pH values. The effect of the silica gel type on the interaction of the Ni²⁺-species with the support in the unreduced and reduced Ni/SiO₂ systems was estimated by infrared spectroscopy. The silica gels undergo changes due to the chemical interaction between Ni²⁺-entities and silica, resulting in formation of Ni-phyllsilicate layers on the surface of the carriers. Ni²⁺-species are strongly bonded to the surface of silica gel obtained at neutral pH value and weakly to the surface of those prepared in acidic and alkaline conditions. The differences in the localization of the Ni²⁺-moieties in the pores of the supports is supposed to result in various strength of Ni-O-Si interaction, thus determining the overall reducibility of the studied precursors.

Introduction

Fine dispersed metallic nickel on the surface of natural or synthetic silicate carriers is the most commonly used catalyst in the industrial partial hydrogenation of vegetable oils. Silica gel represents widely utilized synthetic source of silica support because of its purity, definite pore system and suitable surface properties. In this study we employed three silica gels being different in texture parameters, in order to prepare Ni/SiO₂ catalysts for vegetable oil hydrogenation. The effect of the silica gel type on the interaction between the Ni²⁺-species and the support in the unreduced and reduced Ni/SiO₂ systems is checked by infrared spectroscopy (IR).

Experimental

Three types of silica gel (SIG) were prepared at different pH values that demonstrated different texture parameters, namely: acidic (SIG-A, S_{BET}=777 m²/g), neutral (SIG-B, S_{BET}=581 m²/g) and alkaline (SIG-C, S_{BET}=387 m²/g). The precursors were synthesized with identical composition (SiO₂/Ni=1.0) by precipitation of an aqueous solution of Ni(NO₃)₂·6H₂O with an aqueous solution of Na₂CO₃ on every type of SIG. IR spectra were recorded on Nicolet 6700 FTIR

spectrophotometer (Thermo Electron Corporation, USA) in the 4000–400 cm^{-1} region at 0.4 cm^{-1} resolution and 50 scans, using KBr pressed disk technique with sample concentration ~ 0.5 wt. %. BET surface area measurements were performed on a Sorptomatic 1990 (Thermo Finnigan) apparatus. The precursors were reduced at two temperatures (430 and 530 $^{\circ}\text{C}$) for 5 h with a gas mixture of H_2/N_2 (1/1 v/v; flow rate: 10 dm^3/h ; heating rate: 2 $^{\circ}\text{C}/\text{min}$) and made passive with O_2/N_2 gas mixture.

Results and Discussion

Although the IR spectra of the supports, unreduced and reduced precursors were obtained in 4000–400 cm^{-1} region, the comparison was conducted in the frequency range of 1800–400 cm^{-1} because the variations in the absorption profiles characterizing Ni-O-Si interaction are observed in this region (Figs. 1 and 2). The spectra of SIGs (Fig. 1A) display vibrations associated with the silica network, namely: asymmetric Si-O-Si (~ 1100 cm^{-1}) and symmetric Si-O-Si stretching vibrations (~ 800 cm^{-1}), stretching vibration of free Si-OH groups on the surface of the solids (~ 970 cm^{-1}) and Si-O-Si bending vibration (~ 470 cm^{-1}). The bands assigned to the carbonate anions at ~ 1380 cm^{-1} and to the water molecule deformation vibrations at ~ 1630 cm^{-1} are also registered [1, 2].

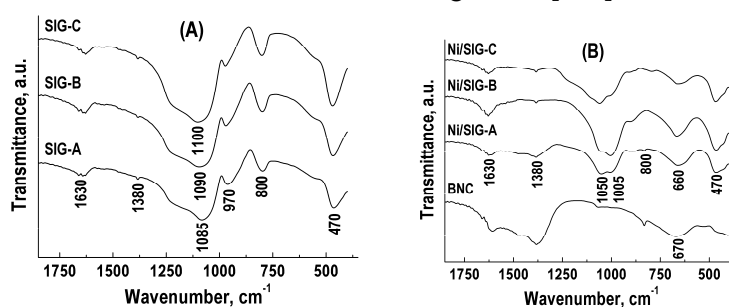


Fig.1. IR spectra of supports (A) and unreduced precursors (B).

IR spectra of the unreduced precursors demonstrate absence of the silica vibration bands at ~ 1100 and ~ 800 cm^{-1} , instead, a doublet appears at 1050 and 1005 cm^{-1} (Fig. 1B). The splitting and the shift towards lower frequencies, as well as the appearance of a new band at ~ 660 cm^{-1} are assigned to the formation of Ni-phyllsilicate linkages ($-\text{Si}-\text{O}-\text{Ni}-$), which cover the surface of the support particles [2, 3]. Their generation seems to be most significant in Ni/SIG-B. An inspection of the bands evidence apparent differences in the band shape and relative intensity that justify the creation of different Ni^{2+} -species on the sample surfaces. The better expressed band at ~ 1380 cm^{-1} in the IR spectrum of Ni/SIG-A may be attributed to the presence of an additional phase of basic nickel carbonate (BNC) located on the surface of Ni-phyllsilicate. IR spectrum of BNC is also shown in Fig. 1B.

The activation of the catalysts is commonly accomplished by reduction of the precursors in the temperature interval 430–550 $^{\circ}\text{C}$. IR spectra of the samples after this procedure provide indirect information on the strength of Ni-O-Si interactions. Most remarkable changes in the spectra demonstrate both Ni/SIG-A and Ni/SIG-C

after reduction at 430°C (Fig. 2A). It is seen a backward shift of the doublet to $\sim 1080\text{ cm}^{-1}$ and reappearance of the band at $\sim 800\text{ cm}^{-1}$, characteristic of silicate vibrations (barring of supports). The presence of the band at 660 cm^{-1} in negligible intensity indicates that significant reduction of the Ni-phyllsilicate occurred, especially for Ni/SiG-A_R430. In contrast, the IR spectrum of Ni/SiG-B_R430 displays well distinguished bands at ~ 1030 and $\sim 660\text{ cm}^{-1}$ thus demonstrates insufficient extent of the Ni-phyllsilicate reduction. It is seen that the tendency of slow reduction of Ni/SiG-B is preserved even at temperature of 530°C (Fig. 2B).

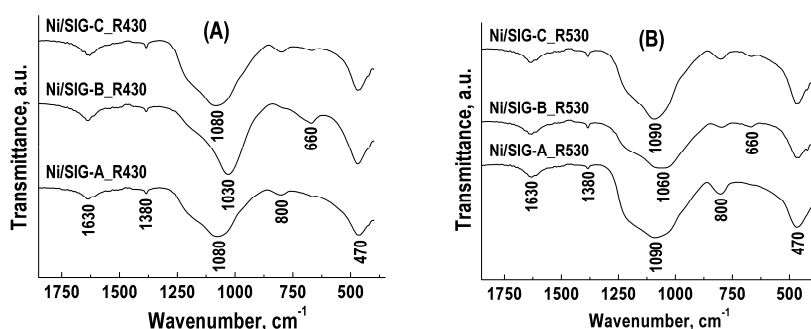


Fig.2. IR spectra of reduced precursors at of 430°C (A) and 530°C (B).

Contrariwise, an additional shift of the band at $\sim 1080\text{ cm}^{-1}$ up to $\sim 1090\text{ cm}^{-1}$ and an increase in the intensity of the band at $\sim 800\text{ cm}^{-1}$ document considerable reduction of the Ni-phyllsilicate in both Ni/SiG-A_R530 and Ni/SiG-C_R530. This phenomenon is better represented in Ni/SiG-A_R530 showing complete disappearance of the band at $\sim 660\text{ cm}^{-1}$. The overall reducibility of the studied precursors may be associated with the reduction of both BNC-like species and Ni-phyllsilicate weakly or strongly bonded to the surface of the corresponding SIGs. The data are supported by our TPR and PXRD study of the same samples.

Conclusion

The silica gels undergo changes due to the chemical interaction between Ni^{2+} -entities and silica, resulting in formation of Ni-phyllsilicate layers on the surface of the supports. Ni^{2+} -species are strongly bonded to the surface of silica gel obtained at neutral pH value and weakly to the surface of those prepared in acidic and alkaline conditions. The differences in the localization of the Ni^{2+} -moieties in the pores of the supports is supposed to result in various strength of Ni-O-Si interaction, thus determining the overall reducibility of the precursors.

Acknowledgments

The authors are grateful to Prof. R. Kardjieva and Prof. G. Kadinov (Institute of Catalysis, Bulgarian Academy of Sciences) for the useful discussion. J. K., M. S. and D. J. are grateful to the Serbian Ministry of Science (Project 166001B).

References

- [1] R. Lenza, W. Vasconcelos, *Materials Research*, 2001, **4**, 189–194.
- [2] K. Ghuge, A. Bhat, G. Babu, *Appl. Catal. A: Gen.*, 1993, **103**, 183–204.
- [3] J. Sohn, *Catalysis Today*, 2002, **73**, 197-209.

Ni-SILICA GEL VEGETABLE OIL HYDROGENATION CATALYSTS: SURFACE STATE OF THE PRECURSORS

D. Nikolova^{1*}, D. Simeonov², L. Spasov¹, D. Lončarević³,
Pl. Stefanov² and D. Jovanović³

¹*Institute of Catalysis, Bulgarian Academy of Sciences, Acad. G. Bonchev str.,
bl. 11, Sofia 1113, Bulgaria,*

**E-mail: dimi@ic.bas.bg; dimi_nik@abv.bg*

²*Institute of General and Inorganic Chemistry, Bulgarian Academy of Sciences,
Acad. G. Bonchev str., bl. 11, 1113 Sofia, Bulgaria*

³*ICHM, Department of Catalysis and Chemical Engineering, Njegoseva 12,
11 000 Belgrade, Serbia*

Abstract

The effect of the type of the silica gel on the surface state of the nickel vegetable oil hydrogenation catalyst precursors was examined by N₂ sorption and XPS. It was established that the usage of the silica gel supports with different texture as source of SiO₂ causes different localization of Ni-species into the support pores and on the external surface area. The XPS data confirm the formation of surface species with different strength of interaction between Ni and silica.

Introduction

The supported nickel-siliceous system is still the most commonly used vegetable oil hydrogenation catalysts. The disadvantages of the natural silica sources (composition variation and remarkable content of different metals as aluminum, iron and heavy metals) defy the search of alternative synthetic SiO₂ supports. The nature of the supports represents a precondition for synthesis of catalyst precursors with well-developed surface and optimal porosity, which are the decisive parameters for mass-transfer of the bulky triglyceride molecules. Silica gels are suitable for application as catalyst supports because of their purity, controlled pore system and surface properties.

The aim of this work is to examine the effect of the type of the silica gel on the surface state of the nickel vegetable oil hydrogenation catalyst precursors by N₂ sorption and XPS.

Experimental

Three types of silica gel (SIG), with different well-defined pore structure have been prepared at different pH values, namely: acidic (SIG-A), neutral (SIG-B) and alkaline (SIG-C). The nickel catalyst precursors with identical composition (SiO₂/Ni=1.0) are synthesized by precipitation of Ni(NO₃)₂·6H₂O with Na₂CO₃ on every type of SIG. The basic nickel carbonate (BNC) is prepared as a referent sample. The samples were dried at 110°C/20h.

Supports and samples were characterized by: (i) N₂ sorption at 77K temperature after out gassing pre-treatment at 110°C/18h. The type of isotherms and hysteresis

loops were characterized according to the IUPAC classification. The texture parameters are calculated by BJH method; (ii) X-ray photoelectron spectroscopy (XPS) (VG ESCALAB II electron spectrometer, using $AlK_{\alpha}=1486.6$ eV) as binding energies (BE) were measured with an accuracy of ± 0.1 eV, utilizing the C1s line at 285.0 eV as a reference. The surface composition of the precursors was determined by measuring the Ni2p_{3/2}, Si2p and O1s peak areas (after linear subtraction of the background) and using Scofield's photoionization cross-sections.

Results and Discussion

The adsorption-desorption isotherm of SIG-A is of Type Ib (Fig. 1), characteristic of microporous solids with some mesopores. It is evident that Ni/SIG-A precursor gave isotherm with complex hysteresis loops at higher relative pressure (Fig. 1). There is no plateau at high p/p_0 , therefore the isotherm should not be regarded as Type IV. Its shape is associated with non-reversible Type II isotherm, classified as Type IIb (pseudo-Type II), characterizing with the Type H3 hysteresis. Such isotherms are given by the aggregates of plate-like particles, which possess non-rigid slit-shaped pores. The isotherms of the SIG-B and SIG-C are of Type IV, with hysteresis loop of type H2 for SIG-B, corresponding to the interconnected network of pores, different in size and shape and a hysteresis loop from Type H1 for SIG-C, given by adsorbents with assemblage of non-intersecting tubular pores. The isotherms of Ni/SIG-B Ni/SIG-C precursors continued to be of Type IV-like, however with different shape. The hysteresis is H2 type for Ni/SIG-B and a combination of H1 and H3 types for Ni/SIG-C [1]. S_{BET} of the parent silica

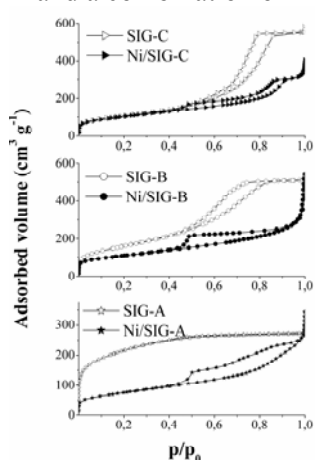


Fig.1. Adsorption-desorption isotherms.

gels decreases in the nickel precursors (Table 1), but this diminution is insignificant at Ni/SIG-C. It is evident, that the lowest S_{BET} has Ni/SIG-A. In order to evaluate the actual change of the surface area due to nickel guest phase insertion, surface area and pore volume of SIG-supported precursors are normalized, relative to the parent silica gels weight in the composite material. The normalized surface area (NS_{BET}) analysis also helps to identify the mode of the transition metal guest phase, assembling the inside of the support pores [2, 3]. NS_{BET} is calculated according to the equation: $NS_{BET} = (S_{BET\text{ of the sample}}) / [(1-x) S_{BET\text{ of the support}}]$, where x —weight fraction of Ni in the samples ($x=0.434$). As it seen from Table 1, a NS_{BET} value of Ni/SIG-A is 0.8. When the NS_{BET} is lower than 1, guest phases is in form of large particles, whose size is comparable or higher than mesostructured support pore diameter, and at least partially located inside of the support pores as blocking them significantly [3]. The increase of average pore diameter (d_{average}) from 2.8 to 5.1 nm for Ni/SIG-A is due to of the formation of pores between the aggregates of plate-like particles, in accordance with the isotherm. The BE values of the main Ni2p_{3/2} peak of Ni/SIG-A precursor and BNC

reference (Table 1) show that these aggregates may contain basic nickel carbonate and/or nickel hydrosilicates [4, 5] situated on the SIG-A surface. NS_{BET} values of Ni/SIG-B and Ni/SIG-C precursors are higher than 1. These values and $d_{average}$ data (Table 1) indicate that the Ni^{2+} -O species does not only block the parent SIG-B and SIG-C pores, but also contribute significantly on the total surface of the precursors. The shift of the peak towards higher BE values for Ni/SIG-B may be assigned to the stronger interaction between Ni^{2+} and the silica gel surface. On contrary, the observed shift towards lower BE for Ni/SIG-C suggested weakening of the interaction.

Table 1. Characteristics of the silica gel supports and dried nickel precursors

Sample	S_{BET} (m^2/g)	NS_{BET}	V_p (cm^3/g)	$d_{average}$ (nm)	Ni2p _{3/2} BE (eV)	Surface Ni/Si atomic ratio
SIG-A	777		0.44	2.8		
SIG-B	581		0.83	4.9		
SIG-C	387		0.96	7.3		
Ni/SIG-A	269	0.6	0.53	5.1	855.7	1.5
Ni/SIG-B	392	1.2	0.84	3.8	856.2	0.8
Ni/SIG-C	367	1.7	0.63	7.0	854.8	1.1
BNC	280		0.30	3.6	855.7	

The estimation of the active component dispersion on the precursor surface by determination of Ni/Si atomic ratio testified that the highest amount of nickel is presented on the surface of SIG-A support. This fact is in agreement with N_2 sorption measurements.

Conclusion

In conclusion, the usage of the silica gel supports with different texture as source of SiO_2 causes different localization of Ni-species into the support pores and on the external surface area. The XPS data confirm the formation of surface species with different strength of interaction between Ni and silica. These surface characteristics of the precursors will pre-determine the formation and dispersion of the active nickel metallic phase as well as the mass transfer of the reactants and products to and from the catalytic sites.

Acknowledgments

The authors are grateful to Prof. R. Kardjieva (Institute of Catalysis, Bulgarian Academy of Sciences) for the useful discussion. D. L. and D. J. are grateful to the Serbian Ministry of Science (Project 166001B).

References

- [1] F. Rouquerol, J. Rouquerol, K. Sing, in Adsorption by Powders and Porous Solids, Principle, Methodology and Applications, Academic Press, 1999.
- [2] M. V. Landau, L. Vradman, M. Herskowitz, Y. Koltypin, A. Gedanken, Journal of Catalysis, 2001, **201**, 22-36.
- [3] L. Vradman, M.V. Landau, D. Kantorovich, Y. Koltypin, A. Gedanken, Micropor. Mesopor. Mater., 2005, **79**, 307-318.
- [4] S. Echeverria and V. Andres, Appl. Catal., 1990, **66**, 73-90.
- [5] M. Rodrigo, L. Daza and S. Mendioroz, Appl. Catal. A: Chemical, 1992, **88**, 101-114.

FORMATION OF $\text{Cr}_x\text{Al}_{2-x}(\text{MoO}_4)_3$ SOLID SOLUTIONS IN $\text{Cr}_2\text{O}_3/\text{Al}_2(\text{MoO}_4)_3$ CATALYSTS AND THEIR ACTIVITIES IN ISOPENTENES DEHYDROGENATION

I. Y. Petrov¹ and B. G. Tryasunov²

¹*Institute of Solid State Chemistry & Mechanochemistry, Kemerovo Division, SB RAS, 18 Sovetsky Ave., Kemerovo 650000, Russia; ipetrov@kemcity.ru*

²*Kuzbass State Technical University, 28 Vessennyaya St., Kemerovo 650026, Russia*

Abstract

During the calcination of aluminum molybdate samples impregnated with aqueous solutions of $(\text{NH}_4)_2\text{Cr}_2\text{O}_7$, chromium (III) oxide produced from ammonium dichromate at $T > 350^\circ\text{C}$ interacts with $\text{Al}_2(\text{MoO}_4)_3$ to form $\text{Cr}_x\text{Al}_{2-x}(\text{MoO}_4)_3$ solid solutions. This results in some increase in catalytic activity of Cr_2O_3 -doped $\text{Al}_2(\text{MoO}_4)_3$ samples in the reaction of isopentenes dehydrogenation. However, at $\text{Cr}_2\text{O}_3 > 18.75$ wt.% dehydrogenation activity of $\text{Cr}_2\text{O}_3/\text{Al}_2(\text{MoO}_4)_3$ catalysts tends to decrease, and such a fact might be interpreted by the covering of the most active sites on $\text{Cr}_2\text{O}_3/\text{Al}_2(\text{MoO}_3)_4$ catalysts with a low-activity bulk $\alpha\text{-Cr}_2\text{O}_3$ phase.

Introduction

$\text{MoO}_3/\gamma\text{-Al}_2\text{O}_3$ catalysts modified with Cr_2O_3 additives exhibit markedly higher activities for dehydrogenation of hydrocarbons, compared to unmodified ones [1,2]. Earlier [2] we have established that some interactions between molybdenum and chromium species could occur during the deposition of chromium precursors onto $\text{MoO}_3/\gamma\text{-Al}_2\text{O}_3$ samples. These interactions may affect the catalytic activities of $\text{Cr}_2\text{O}_3\text{-MoO}_3/\gamma\text{-Al}_2\text{O}_3$ catalysts. One of such interactions is a reaction between $\text{Al}_2(\text{MoO}_4)_3$ particles and chromium compounds. To study this interaction in detail, we prepared several $\text{Cr}_2\text{O}_3/\text{Al}_2(\text{MoO}_4)_3$ samples, characterized them by a number of physical-chemical techniques and measured their dehydrogenation activities.

Experimental

$\text{Al}_2(\text{MoO}_4)_3$ was synthesized by co-precipitation from aqueous solutions of $(\text{NH}_4)_6\text{Mo}_7\text{O}_{24}\cdot 4\text{H}_2\text{O}$ and $\text{Al}(\text{NO}_3)_3\cdot 9\text{H}_2\text{O}$, followed by drying (120°C , 4 h) and calcining (600°C , 4 h) of the precipitate in air. Its crystal structure was confirmed by XRD and IR techniques. $4.0\div 26.3$ wt.% $\text{Cr}_2\text{O}_3/\text{Al}_2(\text{MoO}_4)_3$ samples were prepared by impregnation of aluminum molybdate with aqueous solutions of $(\text{NH}_4)_2\text{Cr}_2\text{O}_7$, followed by drying (120°C , 4 h) and calcining (600°C , 4 h) of the impregnates in air. For comparison, $\text{Cr}_2(\text{MoO}_4)_3$, MoO_3 and Cr_2O_3 samples were

synthesized from the above mentioned Mo- and Cr-containing precursors by thermal decomposition of corresponding salts and mixed Cr-Mo-containing coprecipitates at 600°C for 4 h in air. IR, DRS and ESR spectroscopies, specific surface area measurements, as well as XRD and thermal analyses, were used for characterization of the samples prepared. Catalytic activities of these samples were measured in the reaction of isopentenes (an industrial fraction of *i*-C₅H₁₀ isomers) dehydrogenation to isoprene using a conventional pulse microcatalytic setup under the following conditions: T = 630°C; P = 0.1 MPa; τ_c = 1 s.

Results and discussion

Catalytic properties of Cr₂O₃/Al₂(MoO₃)₄ catalysts studied and some reference samples are presented in Table. Dehydrogenation activities of Cr₂O₃/Al₂(MoO₃)₄ catalysts are generally intermediate between corresponding activities of Al₂(MoO₄)₃ and Cr₂(MoO₄)₃. However, isoprene yields and selectivities to *i*-C₅H₈ for the Cr-rich Cr₂O₃/Al₂(MoO₃)₄ samples tend to decrease.

Table 1. Characteristics and catalytic activities of Cr₂O₃/Al₂(MoO₃)₄ samples

Catalyst	S (m ² /g)	Phase composition	Catalytic activity	
			Yield of <i>i</i> -C ₅ H ₈ (mol.%)	Selectivity to <i>i</i> -C ₅ H ₈ (%)
Al ₂ (MoO ₃) ₄	0.83	Al ₂ (MoO ₃) ₄	22.1	56
4% Cr ₂ O ₃ /Al ₂ (MoO ₃) ₄	1.77	Cr _x Al _{2-x} (MoO ₄) ₃	24.5	79
12,05% Cr ₂ O ₃ /Al ₂ (MoO ₃) ₄	5.20	Cr _x Al _{2-x} (MoO ₄) ₃	22.5	62
18,75% Cr ₂ O ₃ /Al ₂ (MoO ₃) ₄	5.41	Cr _x Al _{2-x} (MoO ₄) ₃	21.5	52
26,3% Cr ₂ O ₃ /Al ₂ (MoO ₃) ₄	11.30	Cr _x Al _{2-x} (MoO ₄) ₃ α- Cr ₂ O ₃	16.5	50
Cr ₂ (MoO ₃) ₄	1.77	Cr ₂ (MoO ₃) ₄	27.2	71
MoO ₃	0.28	γ-MoO ₃	1.1	61
Cr ₂ O ₃	25.64	α-Cr ₂ O ₃	7.5	70

Thermal analysis data for dried Cr₂O₃/Al₂(MoO₃)₄ samples have shown that besides endotherms at 170-190°C (related to adsorbed and/or crystallized water removal), several exo peaks at 240-290 and 400-425°C [attributed to ammonium dichromate decomposition because the same peaks were observed during thermal decomposition of (NH₄)₂Cr₂O₇, and no exo peaks were discovered in thermograms of Al₂(MoO₄)₃] and an endothermic effect at 930-960°C (due to aluminum molybdate melting accompanied by its decomposition), a novel exoeffect with a small mass loss (which is absent in thermograms of aluminum molybdate and ammonium dichromate) arised at ~ 370-380°C. The same effect at 370-390°C was also observed in DTA and DTG curves of dried Cr₂O₃-MoO₃/γ-Al₂O₃ catalysts prepared by impregnation of molybdena-alumina with ammonium dichromate. But if bulk aluminum molybdate was absent on the surface of Cr₂O₃-MoO₃/γ-Al₂O₃ catalysts,

the exotherm at 370-390°C did not appear. Therefore, it is reasonable to relate this exopeak to thermal decomposition of $(\text{NH}_4)_2\text{Cr}_2\text{O}_7$ adsorbed on the surface of $\text{Al}_2(\text{MoO}_3)_4$. X-ray diffraction patterns of calcined $\text{Cr}_2\text{O}_3/\text{Al}_2(\text{MoO}_3)_4$ samples did not differ essentially from those of $\text{Al}_2(\text{MoO}_3)_4$ and $\text{Cr}_2(\text{MoO}_3)_4$ up to chromium concentration of 26.3% Cr_2O_3 (in the last case, some additional diffraction lines attributed to $\alpha\text{-Cr}_2\text{O}_3$ were registered). IR spectra of calcined $\text{Cr}_2\text{O}_3/\text{Al}_2(\text{MoO}_3)_4$ catalysts also did not differ significantly from those of $\text{Al}_2(\text{MoO}_3)_4$ and $\text{Cr}_2(\text{MoO}_3)_4$ up to 18.75 wt.% Cr_2O_3 . They indicated the presence of MoO_4 tetrahedra (absorption bands at 800-1000 cm^{-1} and 440-460 cm^{-1}) in the $\text{Cr}_2\text{O}_3/\text{Al}_2(\text{MoO}_3)_4$ samples. Only at $\text{Cr}_2\text{O}_3 \geq 18.75$ wt.% two absorption peaks (570-575 and 625-630 cm^{-1}) characteristic for chromium (III) oxide become clearly pronounced. A single, very intensive and almost symmetrical signal belonging to clustered Cr^{3+} ions with $g \sim 1.98$ and $\Delta H \sim 42.5\text{-}50.0$ mT was fixed in the ESR spectra of $\text{Cr}_2\text{O}_3/\text{Al}_2(\text{MoO}_3)_4$ catalysts under investigation. Drastic changes in width and in intensity of this signal (an ESR line narrowing and a rise in its intensity) were observed at chromium concentrations > 18.75 wt. Cr_2O_3 . Such a behavior points to a formation of a novel paramagnetic phase (e.g., amorphous Cr_2O_3 possessing paramagnetic properties at room temperature). DRS spectra of calcined $\text{Cr}_2\text{O}_3/\text{Al}_2(\text{MoO}_3)_4$ samples are very similar to the DRS spectrum of $\text{Cr}_2(\text{MoO}_3)_4$. They suggest the presence of octahedrally coordinated Cr^{3+} ions (absorption bands at ~ 690 and ~ 490 nm) in the crystal structure of $\text{Cr}_2\text{O}_3/\text{Al}_2(\text{MoO}_3)_4$ samples. All the above described physical-chemical characterization methods point to two forms of chromium species formed in the process of calcining $\text{Cr}_2\text{O}_3/\text{Al}_2(\text{MoO}_3)_4$ catalysts: molybdate-like Cr^{3+} species and chromium (III) oxide-like Cr^{3+} species. It can be supposed that during the interaction of chromium species with aluminum molybdate, Cr^{3+} ions formed in the course of thermal decomposition of $(\text{NH}_4)_2\text{Cr}_2\text{O}_7$ would occupy vacant octahedral positions in the $\text{Al}_2(\text{MoO}_4)_3$ crystal lattice or would substitute Al^{3+} ions in these positions to produce $\text{Cr}_x\text{Al}_{2-x}(\text{MoO}_4)_3$ solid solutions. Earlier Machiels et al. [3] showed that a continuous series of $\text{Cr}_x\text{Al}_{2-x}(\text{MoO}_4)_3$ solid solutions was formed in a binary $\text{Cr}_2(\text{MoO}_4)_3\text{-Al}_2(\text{MoO}_4)_3$ system. At $\text{Cr}_2\text{O}_3 > 18.75$ wt.% all the octahedral positions in $\text{Al}_2(\text{MoO}_4)_3$ structure would be occupied by Cr^{3+} ions, and the excess chromium ions would be segregated into a separate $\alpha\text{-Cr}_2\text{O}_3$ phase (as it was fixed by XRD, IR and ESR measurements). A low-activity bulk $\alpha\text{-Cr}_2\text{O}_3$ phase may cover the most active sites of $\text{Cr}_2\text{O}_3/\text{Al}_2(\text{MoO}_3)_4$ catalysts, resulting in the decrease of their dehydrogenating properties.

References

- [1] USSR Pat. N 411837, 1974.
- [2] I. Y. Petrov, B. G. Tryasunov, Pol. J. Environ. Stud., 2005, **14**, 25-29, Suppl. IV.
- [3] C. J. Machiels, U. Chowdhry, W. T. A. Harrison, A. W. Sleight, ACS Symposium series (186th Meet. Amer. Chem. Soc.), in R.K. Grasselli (ed.), Washington D.C., 1985, 103-119.

THE FRACTAL ANALYSIS OF 12-TUNGSTOPHOSPHORIC ACID / ACID ACTIVATED BENTONITE CATALYST BY USING NITROGEN SORPTION AND MERCURY INTRUSION POROSIMETRY

S. Petrović^a, Z. Vuković^a, T. Novaković^a, Z. Nedić^b and Lj. Rožić^a

^a *ICH_{TM}-Department of Catalysis and Chemical Engineering, University of Belgrade, Belgrade, 11000, Republic of Serbia*

^b *Faculty of Physical Chemistry, University of Belgrade, Belgrade, 11000, Republic of Serbia*

Abstract

The experimental adsorption isotherms are used to evaluate the specific surface area and the surface fractal dimensions of acid activated bentonite samples modified with heteropoly acid. The aim of the investigations has been to search for correlations between specific surface area and geometrical heterogeneity, as characterized by the surface fractal dimension and the content of added acid. Also, mercury intrusion is employed to evaluate poros microstructures of these materials.

Results from Frankel-Halsey-Hill method show that, in p/p_0 region from 0.75 to 0.96, surface fractal dimension increase with increasing of content of heteropoly acid. Results from mercury intrusion porosimetry (MIP) data show the generation of mesoporous structures with important topographical modifications indicating an increase in the roughness (fractal geometry) of the surface of the solids as a consequence of the modifying with heteropoly acid. By comparison, MIP is preferable to the characterization for its wide effective probing ranges.

Introduction

The supported heteropolyacids on clay are complex mesoporous systems with an enormous potential of application in adsorption and catalysis processes. It is widely known that the optimum performance of solids in several applications requires an exhaustive control of both structural and textural characteristics. Hence, the control of porosity and the surface area are crucial aspects that largely determine the use of these materials [1]. Fractal dimension is a parameter used to quantitatively assess fractal geometry and it represents a measure of the irregularities on the surface of a solid. The value for this parameter may vary from 2 to 3, where the lowest value (2) corresponds to a perfectly smooth surface, while the upper limit (3) corresponds to a totally irregular or rough surface [2]. Within this range of values, subtle variations may be considered significant. One of the simplest relationships used to determine the fractal dimension of a solid, based on the adsorption data, was proposed by Avnir and Jaroniec [3] from the Frankel-Halsey-Hill equation. Also

mercury intrusion is a popular method employed to evaluate porous materials microstructures. Conventional interpretations of original mercury intrusion porosimetry data include porosity, density and pore size distribution. Besides these, other structural factors have also been determined based on calculation model deduced from fractal theories and Washburn equation [4]. A better description of pore size distribution across a wide range of pore size is not possible using one method. Therefore, the aim of this study was to quantify fractal geometry by employing two methods.

Materials and Methods

The results of our previously investigations deal with modeling and optimization process parameters of acid activation of bentonite by response surface methodology [5], were applied to modified bentonite, which is used as a template. The polycrystalline material of $H_3PW_{12}O_{40} \times 6H_2O$ was prepared from a commercial Phosphotungstic Acid for Microscopy $H_3 [P(W_3O_{10})_4]_{aq}$ (Fluka AG, CH-9470 Buchs, #79690) by temperature treatment at 353 K for 1 h.

Examination of the geometrical surface structure was performed by employing an already well-established technique, based on the Frenkel-Hill-Halsey (FHH) scaling law:

$$\ln N = -\frac{1}{m} \ln(-\ln x) + C \quad (1)$$

where N is the experimentally measured amount of adsorbed gas, $x=p/p_0$ is the relative pressure (p_0 is the saturated vapor pressure and p is the pressure), C is a constant and the coefficient m is related to the surface fractal dimension, D .

To calculate D from mercury intrusion porosimetry, an expression is deduced from fractal theories and Washburn equation as follows [4]:

$$\log\left(\frac{dV}{dR}\right) = \log(k_1) + (2 - D)\log R \quad (2)$$

where V is volume of mercury intruded at a given pressure, R is pore radius, k_1 is proportionality constant and D is the fractal dimension. Hence, D values can be derived from the slop of $\log(dV/dR)$ versus $\log R$ plots.

Results and Discussion

The adsorption-desorption isotherms of support and supported sample are type IV, typical for mesoporous materials. The general shape of the isotherms did not change after impregnation with HPW, showing only slight decrease in the amount of nitrogen adsorbed. All isotherms exhibit a hysteresis loop of the H3 type characteristic of slit-shaped pores. Table 1 presents the dependence, both, the fractal dimension obtained from Eq. (1) and the specific surface areas on the amount of HPW used to modify the acid activated bentonite. The fit for data in calculation range $0.75 < p/p_0 < 0.96$ is very good with high correlation coefficient R^2 from 0.998 to 0.999.

Table 1. Fractal dimensions of support and supported sample calculated from the FHH equation

Sample	Fractal dimension	S _{BET} (m ² /g)
AAB	2.907	272
AAB+5%HPW	2.911	246
AAB+10%HPW	2.859	188
AAB+20%HPW	2.858	130

Addition of small amount of HPW to bentonite reduces the geometric heterogeneity of the sample, probably by closing the existing pores. This is also reflected by the decrease of the specific surface area, Table 1. On the other hand, Fig.1 shows the results of the fractal dimension for supported samples, calculated from mercury intrusion porosimetry. In all cases there was a good linear adjustment for the equation 2. The analysis confirmed that fractal dimension calculated from FHH method presents the topological complexity of total pores configuration. Similarly, for mercury intrusion porosimetry, the fractal dimension values are different in each pore size range.

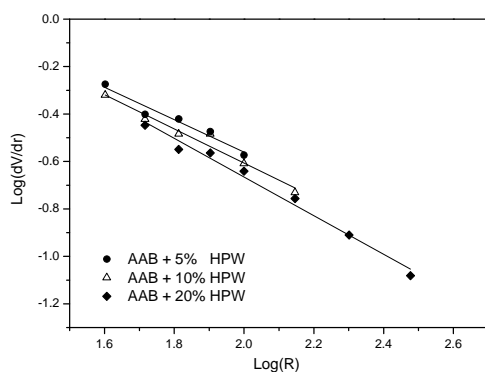


Fig.1. The dependence of the surface fractal dimension of modified acid activated bentonite on the content of HPW.

to various pores within different size ranges and reflect rough surface morphology and/or complex topology of pores.

Conclusions

The porous structures of acid activated bentonite modified with different loading of HPW have been characterized quantitatively by both isothermal N₂ sorption and mercury intrusion porosimetry. The results of the two approaches indicate significant differences in porosity, pore size, surface area and pore size distribution.

Analyzing the adsorption-desorption and intrusion-extrusion data always produces several different D values, which correlate

Acknowledgments

This work was supported by the Ministry of Science and Technological Development of the Republic of Serbia (Projects number ON 142019B)

References

- [1] I. V. Kozhevnikov, J. of Molecular Catalysis A: Chemical, 2007, **262**, 86-92.
- [2] A. B. Jarzebski, J. Lorenc, L. Pajak, Langmuir, 1997, **13**, 1280-1285.
- [3] D. Avnir, M. Jaroniec, Langmuir, 1989, **5**, 1431-1433.
- [4] G. Jozefaciuk, C. Slawinski, E. Vrzhashch, Appl. Clay Sci., 2009, **43**, 63-68.
- [5] Lj Rožić., T. Novaković, S. Petrović, Appl. Clay Sci., 2010, **48**, 154-158.

NEW ASPECTS OF THE HECK CATALYST FORMATION

V. P. Petrović, S. Marković and Z. D. Petrović

Faculty of Science, University of Kragujevac, 34000 Kragujevac, Serbia

Abstract

In our recent papers we reported the use of well-defined trans-dichlorobis(diethanolamine-*N*)palladium(II) complex (*trans*-[PdCl₂(DEA)₂]) as a Heck precatalyst. In this work we present new details on the mechanism of the key, initial steps of the reaction, i.e., the formation of the Pd(0) complex.

Introduction

The palladium-catalyzed arylation of olefins, known as the Heck reaction, deserves considerable attention due to its synthetic versatility [1]. Oxidative addition and reductive elimination, important steps in the Heck reaction mechanism, have been subjects of numerous experimental and computational studies [2, 3]. On the other hand, the mechanism of the preactivation process, where the Pd cation is reduced to Pd(0), has not been completely elucidated. Trans-dichlorobis(diethanolamine-*N*)palladium(II) complex (*trans*-[PdCl₂(DEA)₂, **1**] [4] contains both the necessary amine (diethanolamine, DEA) and Pd(II). For this reason, we used it as precatalyst in phosphine-free Heck reactions in the presence of strong and weaker bases [5-8]. The mechanism of the preactivation reaction, i.e. the formation of the catalytically active Pd(0) complex, was investigated. In this work we report the new mechanistic aspects of the preactivation step of **1**. More precisely, we investigate the possible intramolecular reduction of Pd(II) to Pd(0) using computational methods.

Results and Discussion

When the reaction is performed in the presence of a strong base, it can be expected that a proton of the OH group will be abstracted from **1** (Fig. 1). Following these considerations, H1 was removed from **1** as a proton, and the structure thus obtained was optimized (**2** in Fig. 1). The natural bonds orbital (NBO) charges of **2** show that positive charge is distributed among palladium (0.334), carbons, and hydrogens, whereas negative charge is distributed among oxygen, nitrogen and chlorine atoms. O1 is particularly negatively charged (-0.878). In addition, the greatest contribution to the HOMO of **2** comes from O1. Following this reasons, one can expect that O1 will perform a nucleophilic attack on palladium. This attack leads to the formation of complex **3**, where Pd is coordinated with nitrogen, two chlorines, and oxygen (Fig. 1). Subsequently in the reaction, H2 coordinates with palladium as a hydride ion via transition state **4**, with an energy barrier of 184.9 kJ/mol. In **4** the C1-H2 bond is being broken, whereas the Pd-H2 bond is being formed. In addition, the Pd-O1 bond is completely broken, implying that dehydrogenated DEA is eliminated. In this way complex **5** is yielded. In the basic

environment, **5** undergoes reductive elimination, thus forming **6**. Complex **6** contains Pd(0), and thus is a catalytically active species in the Heck reaction.

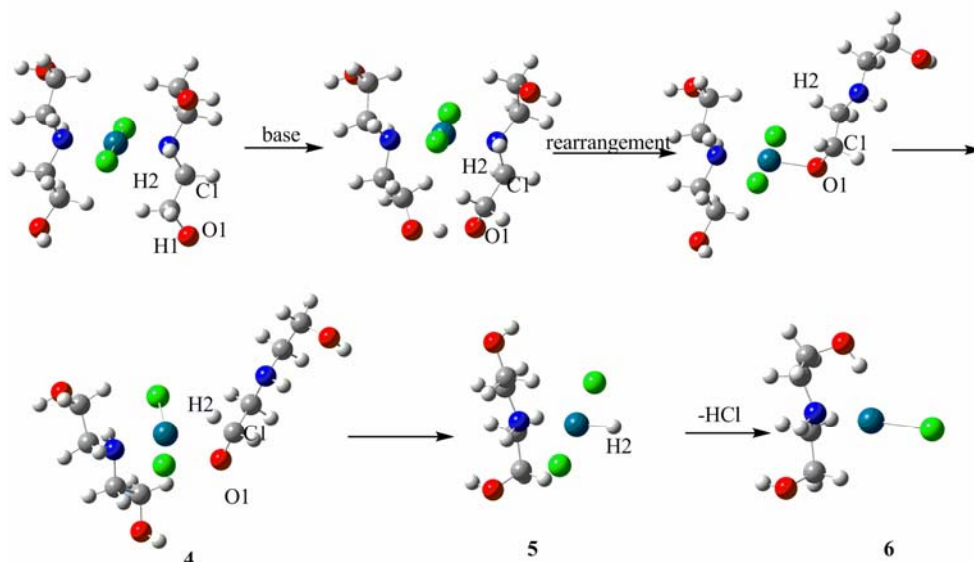


Fig.1. Mechanism for the preactivation reaction of $trans$ -[PdCl₂(DEA)₂] in the presence of a strong base.

Computational method

All calculations were conducted using Gaussian03 [9] with the B3LYP hybrid functional. The 6-311G(d,p) basis set was used for C, H, O, N, and Cl, and LANL2DZ+ECP was employed for the Pd center. Geometrical parameters of all investigated species were optimized in vacuum. All calculated structures were verified to be local minima (all positive eigenvalues) for ground-state structures or first-order saddle points (one negative eigenvalue) for transition-state structures by frequency calculations.

Conclusion

A pathway for the formation of Pd(0) complex from $trans$ -[PdCl₂(DEA)₂] (**1**) was revealed. In a basic environment **1** undergoes abstraction of hydrogen from a hydroxyl group. In this way an anion is formed, whose rearrangement yields a complex where Pd is coordinated with nitrogen, two chlorines, and oxygen. Then, the hydrogen bonded to carbinol C coordinates with palladium as a hydride ion. In the further course of the reaction HCl is eliminated (reductive elimination), and catalytically active species, i.e. the complex containing Pd(0), is formed.

Acknowledgments

This work is supported by the Ministry of Science and Environment of Serbia, project N^o 142025 and 142013 B.

References

- [1] R. Heck, *Acc Chem Res*, 1979, **12**, 146-151.
- [2] X. Wu X, X. Li, M. McConville, O. Saidi, J. Xiao, *J. Mol. Catal. A*, 2006, **247**, 153-158.
- [3] R.J. Deeth, A Smith, K.K. Hii, J.M. Brown, *Tetrahedron Lett.*, 1998, **39**, 3229-3232.
- [4] Z.D. Petrovic, M.I. Djuran, F.W. Heinemann, S. Rajkovic, S. Trifunovic, *Bioorg. Chem.*, 2006, **34**, 225-234.
- [5] S. Marković, Z. D. Petrović, V. Petrović, *Monatsh. Chem.*, 2009, **140**, 171-175.
- [6] Z. D. Petrović, S. Marković, D. Simijonovic, V. Petrović, *Monatsh. Chem.*, 2009, **140**, 371-374.
- [7] Z. D. Petrovic, V. P. Petrovic, D. Simijonovic, S. Markovic, *J. Organomet. Chem.*, 2009, **694**, 3852–3858.
- [8] Z. D. Petrovic, V. P. Petrovic, D. Simijonovic, S. Markovic, *J. Mol. Cat. A*, accepted for publication
- [9] Gaussian Inc. Gaussian 03, Revision E.01-SMP. Gaussian Inc., Pittsburgh, PA, 2003.

PHOTOCATALYTIC ACTIVITY OF TiO₂ NANOPARTICLES MODIFIED WITH DOPAMINE

M. Radoičić¹, I. Janković¹, V. Despotović², D. Šojić², Z. Šaponjić¹,
B. Abramović² and M. I. Čomor*¹

¹*Vinča Institute of Nuclear Sciences, P. O. Box 522, 11001 Belgrade, Serbia*

²*Department of Chemistry, Faculty of Sciences, University of Novi Sad, Trg D.
Obradovića 3, 21000 Novi Sad, Serbia*

Abstract

Photocatalytic activity of bare colloidal TiO₂ nanoparticles (NPs, d~45Å) and surface modified with dopamine was obtained following degradation reaction of herbicide RS-2-(4-chloro-o-tolyloxy)propionic acid (mecoprop, MCP, C₁₀H₁₁ClO₃) under UV light irradiation. Results indicated that inner sphere charge transfer (CT) complex is formed on the surface of TiO₂ NPs due to modification with dopamine which induced decreasing of the photocatalytic efficacy of TiO₂ NPs.

Introduction

Titanium dioxide is the photocatalytic material which has been studied extensively over the past decade because it is inexpensive, nontoxic, and photostable. The absorption of photons with energy greater than band gap energy of TiO₂ (3.2 eV, λ < 390 nm) promotes electron from the valence band to conduction band, leaving a positively charged hole in the valence band. Most of the charges recombine either radiatively or nonradiatively, while only a small fraction of the charges moves to the surface and react with adsorbed species or be trapped in the midgap surface states [1]. One of the possible ways to minimize charge recombination is to enlarge separation distances before desired redox reaction occurs. This can be done by surface modification of TiO₂ NPs with electron-accepting/donating species [2]. In the nanosize regime, because of the large curvature of TiO₂ particles, the surface reconstruct in such a way that distorts the crystalline environment of surface Ti atoms forming coordinatively unsaturated Ti atoms, coordination change from octahedral (bulk, inside the NP) to square-pyramidal for NP surface. Formation of charge-transfer complex at the surface of NPs can adjust their coordination to octahedral geometry and change the electronic properties of TiO₂ [3]. This type of electronic coupling yields to instantaneous separation of photogenerated charges, the holes localize on organic modifier and electrons delocalize in the conduction band of TiO₂ NPs. In the scope of this work, we wanted to study the effect of fast and enlarged separation distance of photogenerated charges induced by surface modification of TiO₂ NPs and formation of CT complex, on photocatalytic activity of TiO₂ NPs. Photocatalytic degradation of herbicide RS-2-(4-chloro-o-tolyloxy)propionic acid (mecoprop, MCP, C₁₀H₁₁ClO₃) was used as model reaction because of its wide use all over the world and usual occurrence in drinking water [4].

Experimental

All chemicals used were of the highest purity available. All solutions were prepared with triply distilled water. The TiO₂ NPs were prepared by controlled hydrolysis of titanium (IV) chloride (Fluka), as described elsewhere [3]. Particle size was determined using a transmission electron microscope, JOEL CXII. The surface modification of TiO₂ NPs was accomplished by dissolution of Dopamine (3-hydroxytyramine, puriss, Fluka) in TiO₂ colloidal solution. Spectrophotometric measurements were carried out on a Evolution 600 UV-VIS spectrophotometer. Photocatalytic degradation was carried out in a way described previously [4]. The kinetics of MCPP degradation were studied by liquid chromatography- diode array detection, Agilent Technologies 1100 Series, details as in ref. [4].

Results and Discussion

The absorption spectra of bare and surface modified TiO₂ NPs are presented in Figure 1.

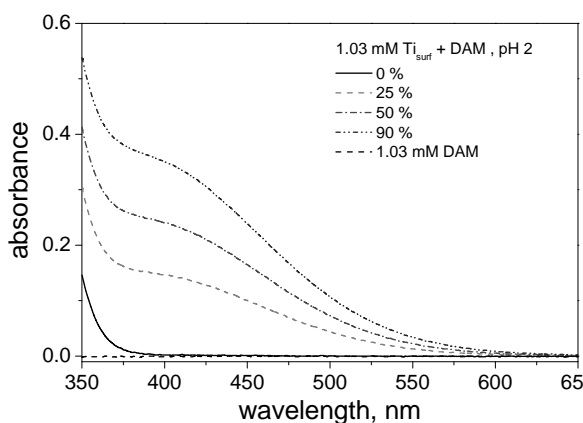


Fig.1. Absorption spectra of bare, surface modified TiO₂ NPs and pure Dopamine (DAM), concentrations and surface coverage are presented in inset.

It can be seen that the optical properties of bare TiO₂ NPs are changed due to CT formation with Dopamine. We used three concentrations of Dopamine which produced 25 %, 50% and 90% coverage of surface, undercoordinated Ti atoms (for NPs with $d \sim 45 \text{ \AA}$, about 30% of Ti atoms are on the surface).

As can be seen in Fig. 2, MCPP can be decomposed with all applied photocatalysts under UV irradiation. The best results were obtained with bare TiO₂ NPs. Modified TiO₂ NPs showed lower photocatalytic activity, without linear dependence with surface coverage of TiO₂ NPs with CT complex with Dopamine. As the matter of fact, all applied coverages had almost the same photocatalytic activity. One of the possible reasons for such results can be decreased adsorption of MCPP on the surface of modified TiO₂. This fact must be considered for 50% and 100% of coverage, but even 25 % of coverage reduced photocatalytic activity. The other reason can be based on the nature of the formed CT complex. Namely, all concentration of CT complex on the surface of TiO₂ NPs was capable to extract photogenerated positive holes from TiO₂ NPs. Obviously, extracted holes are not

able to produce OH radicals which can oxidize MCPP and it seems that only electrons from TiO₂ conduction band participate in the degradation of MCPP. As can be seen in Fig. 1, surface modification induced red shift of the absorption onset and charge transfer interaction between the modifier and surface Ti atoms also induced fine tuning of the electrochemical potential of semiconductor NPs indicating changes in oxidizing/reducing abilities. As already stressed in literature [3], TiO₂ conduction band potential is kept constant while valence band potential is moved due to modification, to lower potential and holes extracted through CT complex are not capable to react with MCPP.

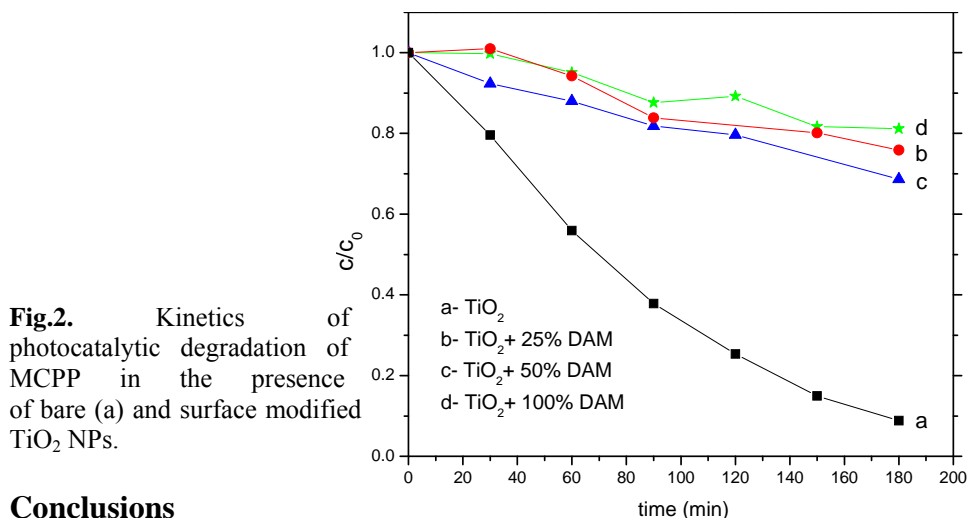


Fig.2. Kinetics of photocatalytic degradation of MCPP in the presence of bare (a) and surface modified TiO₂ NPs.

Conclusions

Binding of the Dopamine molecules to undercoordinated surface Ti atoms (defect sites) results in formation of inner-sphere charge-transfer complex, observed by changes in the onset of absorption and effective band gap. Photocatalytic degradation of herbicide MCPP was followed as model reaction for evaluation of photocatalytic activity of applied catalysts. Modified TiO₂ NPs showed reduced photocatalytic activity compared to bare TiO₂ NPs. Observed results can be explained by reduced TiO₂ surface after modification, at which MCPP can be adsorbed and inappropriate potential of holes extracted from TiO₂ NPs in Dopamine molecule, for direct oxidation of MCPP molecule.

References

- [1] A. J. Nozik, *Annu.Rev. Phys.Chem.*, 1978, **29**, 189-193.
- [2] Z. V. Šaponjić, N. M. Dimitrijević, D. M. Tiede, J. A. Goshe, X. Zuo, L. X. Chen, A. S. Barnard, P. Zapol, L. Curtiss, T. Rajh, *Adv. Mater.*, 2005, **17**, 965-971.
- [3] I. A. Janković, Z. V. Šaponjić, M. I. Čomor, J. M. Nedeljković, *J. Phys. Chem. C*, 2009, **113**, 12645-12652.
- [4] D.V. Šojić, V.N. Despotović, N.D. Abazović, M.I. Čomor, B.F. Abramović, *J. Hazard. Mater.*, 2010, **179**, 49-56.

PHOTOCATALYTIC PROPERTIES OF POLYANILINE/TiO₂ NANOCOMPOSITE

M. Radoičić¹, Z. Šaponjić¹, G. Ćirić-Marjanović²,
J. M. Nedeljković¹ and M. Čomor¹

¹*Vinča Institute of Nuclear Sciences, P.O. Box 522, 11001 Belgrade, Serbia*

²*Faculty of Physical Chemistry, University of Belgrade, Studentski Trg 12-16,
11158, Belgrade, Serbia*

Abstract

Polyaniline/TiO₂ (PANI/TiO₂) nanocomposite was synthesized by the oxidative polymerization of aniline with ammonium peroxydisulfate (APS) in water, in the presence of colloidal TiO₂ nanoparticles of an average diameter ~5 nm. The resulting PANI/TiO₂ composite powder was used for photocatalytic degradation of methylene blue (MB). Its photocatalytic activity has been compared with activity of neat colloidal TiO₂ nanoparticles.

Introduction

TiO₂ is one of the most investigated semiconductors in the field of photocatalytic degradation of pollutants. Its high chemical stability, adsorption capability, photocatalytic efficacy for decomposition of organic compounds in air and water, relative low-price and nontoxicity are the reasons for such keen researcher's interest. However, the wide band gap of TiO₂ (3.2 eV) only allows it to absorb the photons of ultraviolet light (< 400 nm) that occupies only small fraction (< 5 %) of solar spectrum, which limits its wider use. One of the possible ways to utilize the broader part of the solar spectrum is sensitization of TiO₂ with a suitable sensitizer [1]. High absorption coefficients in the visible part of the spectrum, high mobility of charge carriers (consequence of the presence of extended π -conjugated electron systems) and good environmental stability of conductive polymers make them a good choice for TiO₂ sensitization. Moreover, many conductive polymers in their doped or undoped states are efficient electron donors and good hole transporters upon visible light excitation [2]. The subject of this work was in situ synthesis and characterization of PANI/TiO₂ nanocomposite. Its potential applicability as a photocatalyst was checked using a typical photodegradation reaction of methylene blue (MB) in a suspension. MB is a stable organic dye occasionally used as a model compound for estimation of activity of TiO₂ based photocatalysts, in reactions of photodegradation.

Experimental

Colloidal TiO₂ solution, containing nanoparticles of an average diameter ~5 nm, was prepared according to the procedure described elsewhere [3]. In a typical procedure for preparing PANI in the presence of TiO₂ nanoparticles, the aqueous

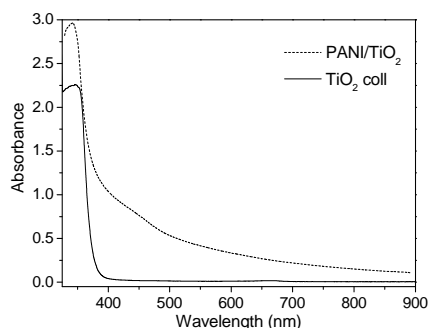


Fig.1. UV/vis absorption spectra of pure TiO_2 and PANI/ TiO_2 nanocomposite.

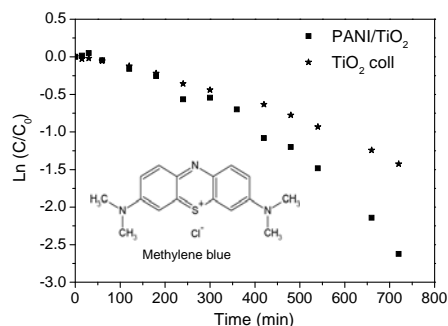


Fig.2. Kinetic plots of degradation of MB using neat TiO_2 and PANI/ TiO_2 nanocomposite as photocatalyst.

solutions of aniline, oxidant (APS), and colloidal TiO_2 were mixed at room temperature [4]. Initial mole ratio of aniline/ TiO_2 was 1:100. The reaction mixture was stirred for 20 days. In order to remove residual monomer, oxidant and low-molecular weight fractions, PANI/ TiO_2 composite was dialyzed in Milli-Q deionized water. Finally, the nanocomposite was dried in vacuum oven at 60°C until a constant mass was reached (~ 3 h). As a reference sample dry colloidal TiO_2 powder was used.

UV/Vis spectra of the samples were obtained using Evolution 600 spectrophotometer (Thermo Scientific).

The photocatalytic activities of the prepared samples were evaluated by the degradation of MB in aqueous solution. MB aqueous solution (50 ml) with concentration of $10 \text{ mg}\cdot\text{L}^{-1}$ was mixed with $1 \text{ g}\cdot\text{L}^{-1}$ catalyst (PANI/ TiO_2 or neat colloidal TiO_2). Suspensions were placed into quartz vessel which was exposed to light of Xenon lamp (300 W). Samples were saturated with air and stirred during the irradiation. Aliquots of 1 ml were taken out from the suspensions every 15 min during the irradiation. The photocatalyst was separated from the solution by centrifugation and absorbance intensity of the MB in the supernatant was measured at $\lambda=664 \text{ nm}$.

Results and Discussion

UV/Vis absorption spectra of the colloidal TiO_2 nanoparticles and PANI/ TiO_2 nanocomposite are shown in Figure 1. It can be seen that both TiO_2 nanoparticles and PANI/ TiO_2 nanocomposite absorb light below 400 nm. Above this wavelength only the nanocomposite absorbs light giving rise to a peak at 440 nm, which corresponds to PANI chains in emeraldine salt form [5]. In addition to the band at about 440 nm, ordinary conducting PANI emeraldine salt usually shows the band at $\sim 780 \text{ nm}$, both bands at ~ 440 and $\sim 780 \text{ nm}$ being connected with creation of polarons (radical cations) [5]. The absence of distinct band at $\sim 780 \text{ nm}$ in the UV-Vis spectrum of PANI/ TiO_2 could be result of partial deprotonation of PANI with water during the dialysis procedure, and reduced extent of delocalization of electrons in PANI.

Kinetic plots of photodegradation of MB, obtained using neat TiO₂ and PANI/TiO₂ nanocomposite as a photocatalyst, are presented in Figure 2. Direct photolysis of MB was also followed and it was less than 10% of the initial MB concentration. At the beginning of the photodegradation process, until about 300 min, both photocatalysts had almost the same efficacy. It can be observed that PANI/TiO₂ nanoparticles significantly enhance photocatalytic activity compared to bare colloidal TiO₂ nanoparticles for longer times of irradiation. This effect could be explained by enhanced absorption and synergistic effect between PANI and TiO₂ nanoparticles [2, 6].

Conclusion

PANI/TiO₂ nanocomposite has been in situ synthesized by the chemical oxidative polymerization of aniline with APS in colloidal TiO₂ solution without added acid. Obtained nanocomposite has enhanced absorption in visible part of spectrum, compared to neat colloidal TiO₂. PANI/TiO₂ nanocomposite was successfully applied for discoloration of methylene blue using whole spectral range of Xenon lamp (simulation of solar spectrum). Nanocomposite catalyst showed higher efficacy toward discoloration of MB compared to bare TiO₂, for longer irradiation times (> 300 min).

References

- [1] X. Chen, S. Mao, Chem. Rev. 2007, **107**, 2891-2959.
- [2] X. Li, D. Wang, G. Cheng, Q. Luo, J. An, Y. Wang, App. Catal. B: Environ., 2008, **81**, 267–273.
- [3] T. Rajh, D. Tiede, M. Thurnauer, J. Non-Cryst. Solids, 1996, **207**, 815.
- [4] M. Radoičić, Z. Šaponjić, J. Nedeljković, G. Ćirić-Marjanović, J. Stejskal, Synth. Met., 2010, **160**, 1325–1334.
- [5] J. Laska, J. Mol. Struct. 2004, **701**, 13–18.
- [6] H. Zhang, R. Zong, J. Zhao, Y. Zhu, Environ. Sci. Technol. 2008, **42**, 3803–3807.

EFFECT OF MECHANICAL TREATMENT ON THE CATALYTIC ACTIVITY OF ZEOLITE IN THE COURSE OF HYDROCARBON CONVERSION

E. V. Urzhumova, L. M. Velichkina and A. V. Vosmerikov

Institute of Petroleum Chemistry, Siberian Branch of the Russian Academy of Sciences, 634021, 4, Akademichesky Avenue, Tomsk, Russia

E-mail: dmps@ipc.tsc.ru

Abstract

Effect of mechanical treatment on the catalytic activity of zeolite in hydrocarbon feedstock refining is studied. It was found, that the preliminary mechanical zeolite treatment results in increased yield of hydrocarbons with an iso-structure and in decreased formation of aromatic hydrocarbons during the straight-run gasoline and n-hexane conversion.

Introduction

Nowadays, the zeolites of pentasil family find expanding applications as catalysts for different processes in oil refining and petrochemistry. Their catalytic activity is due to the presence of hydroxyl bound to aluminum atoms of zeolite lattice. The zeolite acidity may be varied both at the stage of hydrothermal synthesis and during different further treatments.

The purpose of the work was to investigate the influence of preliminary mechanical treatment (MT) of zeolite on its catalytic activity during isomerization of n-hexane and straight-run gasoline oil fraction.

Results and Discussion.

The high-silica zeolite with $\text{SiO}_2/\text{Al}_2\text{O}_3$ molar ratio of 100 was synthesized from alkaline aluminosilicagels. The catalyst obtained was mechanically treated in ball vibratory mill for 24 and 48 hours.

The acidic properties of zeolite samples were studied by thermoprogrammed desorption of ammonia. The decreases in the strength and concentration of acidic sites of both types are due to the mechanical treatment of zeolite (Table 1).

Since the straight-run gasoline oil fraction is a complex multicomponent system, the conversion of n-hexane in the presence of zeolite was firstly studied to reveal the optimal conditions and direction of process behavior.

The process was carried out in a flow installation at the reaction temperatures of 300-420 °C, volumetric flow rate of 2 h⁻¹ and atmospheric pressure. The results of catalytic tests are given in Table 2.

The maximum zeolite isomerization activity in the course of n-hexane conversion is observed in the temperature interval 340-380 °C, while during conversion of straight-run gasoline it falls within the temperature interval

300-340 °C. When the temperature is higher than 340 °C, the yield in aromatic hydrocarbons significantly increases.

Table 1. Acidic properties of zeolite catalysts.

MT duration, h	T _{peak max.} , °C		Acidic sites concentration, mmole/g		
	1	2	1	2	Σ
–	190	405	441	270	711
24	175	400	363	200	563
48	180	395	296	226	522

Table 2. Influence of the process temperature on the composition of products, obtained by straight-run gasoline and n-hexane conversion over the initial zeolite.

Feedstock	Products, wt. %	Process temperature, °C			
		300	340	380	420
n-hexane	Isoalkanes C ₅₊	15.6	28.8	26.8	23.5
	Arenes	6.0	23.5	46.6	57.3
	n-hexane conversion, %	43	74	86	93
straight-run gasoline	Isoalkanes C ₅₊	37.1	34.2	34.0	32.4
	Arenes	37.4	40.3	46.7	47.4
	Octane number	89	90	91	92

The significant increase in isoalkanes in quantity of resulting reaction products suggests that the MT of zeolite increases its isomerization activity. The prolongation of the time of MT from 24 to 48 hours rather decreases the isomerization activity of zeolite but increases its aromatization activity, which allows to obtain the gasoline with 80 octane number at the temperature of 340 °C (Fig. 1).

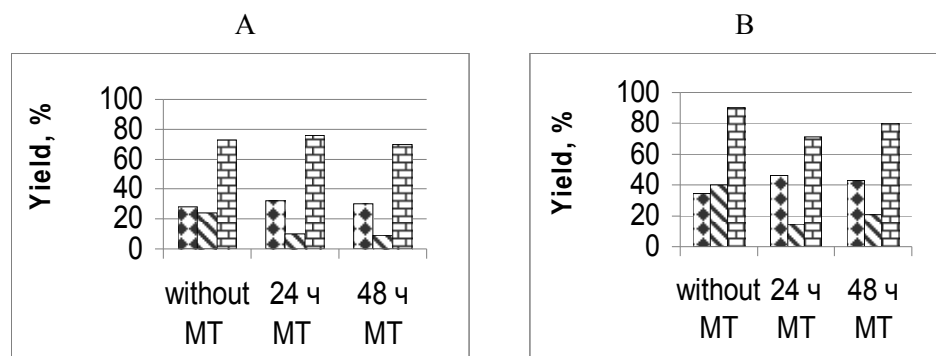


Fig.1. Influence of duration of MT of zeolite on the composition of products, obtained by n-hexane (A) and straight-run gasoline (B) conversion (T= 340 °C).

◆◆ - yield of isoalkanes C₅₊; ▨ - yield of aromatic hydrocarbons; ▤ - conversion of n-hexane (A) and octane number of gasoline (B).

Conclusions

Thus, it was found, that the preliminary mechanical zeolite treatment results in increased yield of hydrocarbons with an iso-structure and in decreased formation of aromatic hydrocarbons during the straight-run gasoline and n-hexane conversion.

Acknowledgements

The work was supported by grant of the Program Presidium of RAS (grant № 73).

INFLUENCE OF HYDROXYBENZYL ALCOHOL ISOMERS ON KINETIC PARAMETERS FOR TRANSGLYCOSYLATION REACTION CATALYSED BY ALPHA GLUCOSIDASE

D. V. Veličković¹, A. S. Dimitrijević², F. J. Bihelović²,
R. M. Jankov² and N. Milosavić³

¹Innovation center of the Faculty of Chemistry, University of Belgrade, Studentski trg 12, Belgrade, Serbia

²Faculty of Chemistry, University of Belgrade, Studentski trg 12, Belgrade, Serbia

³CMT-Department of Chemistry, University of Belgrade, Njegoševa 12, Belgrade, Serbia

Abstract

In the synthesis of physiologically active glycosides selectivity is vital. Therefore biocatalysts that could perform this reaction are very desirable. Additionally, one of the key elements for understanding enzymatic synthesis of physiological active compounds is determination of kinetic parameters of reaction.

Introduction

Enzyme kinetics lies at the heart of drug design and metabolic regulation. Yet despite its fundamental importance, enzyme kinetics is one of the most misunderstood (and often misused) tools in biochemistry.

A number of biologically active compounds are glycosides. Transglycosylation reactions are well known and widely used methods for glucoside synthesis [1], and mechanism is illustrated on Figure 1.

Glycosidase, responsible for catalytic hydrolysis of glycosidic linkage, are increasingly being used in carbohydrate synthesis. With disaccharide as substrate, glycosides can be formed in a kinetically controlled reaction (secondary hydrolysis on Fig.1) that shows optimum in time. Maltase (EC 3.2.1.20; α glucosidase) is one of the most abundant glucosyl hydrolase present in Bakers yeast, and has been used for synthesis of various physiological active compounds [2]. It is known that glucosides of hydroxybenzyl alcohol exhibit pronounced anticoagulant activity [3] as well as tyrosinase inhibitor activity [4].

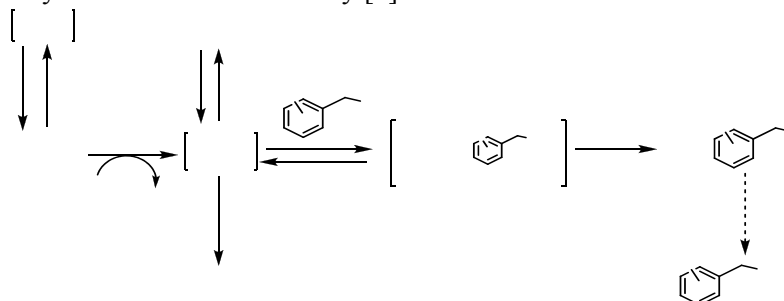


Fig.1. Schematic model for different kind of reaction catalyzed by α glucosidase.

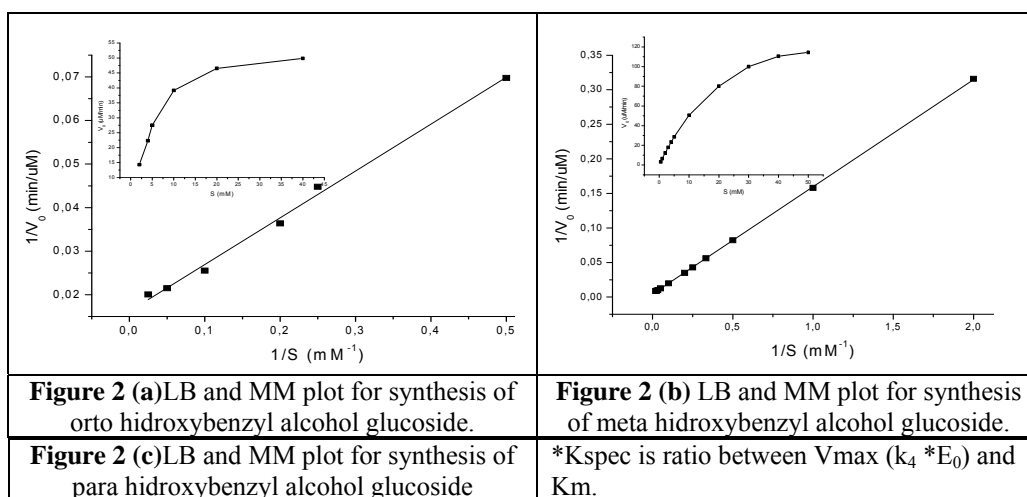
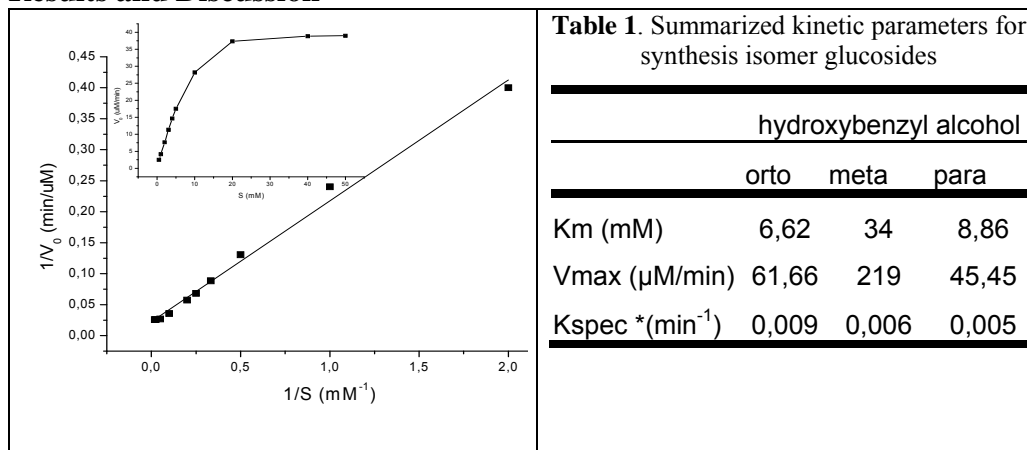
Kinetic of transglucosylation reaction could be described with Michaelis–Menten equation, where K_m (according to Fig.1) is approximately $(k_4 + k_{-3})/k_3$.

The aim of present study was determination and quantification of kinetic parameters (K_m , V_{max} and k_{spec}) for different isomers of hydroxybenzil alcohol.

Experimental

The glucose donor for this reaction was maltose (40% w/v), and concentrations of glucose acceptors, o-, m- and p-hydroxybenzyl alcohols, were varied. The kinetics of transglucosylation reaction were monitored by HPLC (C18 column, solvent A: 10 % AN, solvent B: 20 % AN, spectrophotometric detector at 268nm).

Results and Discussion



Rates for synthetic reactions are presented by Michaelis-Menten (MM) and Lineweaver-Burk (LB) plot on **Figure 2 (a,b,c)** together with summarized kinetic parameters, **Table 1**.

Conclusion

Our data indicate that the transglucosilation specificity of maltase is very different toward isomers of hydroxybenzyl alcohol. When two hydroxyl groups (phenolic and bezoic) move away from each other (o-,m-,p-) specificity (kspec) of maltase for transglucosilation reaction shows significant decrease.

References

- [1] N. B. Milosavic, R. M. Prodanovic , R. M. Jankov, Tetrahedron Lett., 2007, **48**, 7222-7224.
- [2] R. M. Prodanovic, N. B. Milosavic, D. Sladic, T. C. Velickovic , Z. Vujcic, Biotechnol Lett., 2005, **27**, 551-554.
- [3] E. S. Seo, J. H. Lee, J. Y. Park, D. Kim, H. J. Han , J. F. Robyt, J. Biotechnol., 2005, **117**, 31-38.
- [4] H. K. Shin, J. Y. Kong, J. D. Lee , T. H. Lee, Biotechnol Lett., 2000, **22**, 321-325.

NONOXIDATIVE CONVERSION OF METHANE INTO AROMATIC HYDROCARBONS ON Ag–Mo/ZSM-5 CATALYSTS

A. V. Vosmerikov¹, V. I. Zaikovskii², L. L. Korobitsyna¹, N. V. Arbuzova¹,
V. V. Kozlov¹, Ya. E. Barbashin¹ and S. P. Zhuravkov³

¹*Institute of Petroleum Chemistry SB RAS, Tomsk, Russia;* ²*Boreskov Institute of Catalysis
SB RAS, Novosibirsk, Russia;* ³*Research Institute of High-Voltage Equipment,
Tomsk Polytechnic University, Tomsk, Russia*

Abstract

Nonoxidative methane conversion into aromatic hydrocarbons on high-silica zeolites ZSM-5 modified with nanosized molybdenum (4.0 wt %) and silver (0.1–2.0 wt %) powders has been studied. The microstructure, composition and acid properties of Ag–Mo/ZSM-5 catalysts were studied by high-resolution transmission electron microscopy, energy-dispersive x-ray analysis and programmed thermal desorption of ammonia.

Introduction

Methane dehydroaromatization under nonoxidative conditions on zeolite catalysts modified with transition metal ions is a promising process for the efficient utilization of natural gas and casing-head gas. A disadvantage of this process, which occurs at high temperatures (700–800° C), is a rapid catalyst deactivation as a result of intense coke formation. To increase the time of stable catalyst operation in methane dehydroaromatization, the catalysts are modified with various metals (Y, Cu, Zr, La, Pt, and Ni) [1–3]. In this work, we studied the modifying effect of silver on the catalytic properties of molybdenum-containing zeolite ZSM-5 in a methane dehydroaromatization reaction. The formation of coke on the surface of Ag–Mo/ZSM-5 catalysts in the course of the reaction was studied and its structure and concentration were determined using thermal analysis and high-resolution transmission electron microscopy (HP TEM).

Experimental

Catalysts were prepared by mechanically mixing zeolite ZSM-5 of the molar ratio $\text{SiO}_2/\text{Al}_2\text{O}_3 = 50$ and the nanosized powders of Mo and Ag in a KM-1 vibratory ball mill (Germany) for 4 h. Thereafter, the resulting mixtures were calcined at 540° C for 4 h. The nanopowders of Mo and Ag were prepared by the method of electrical explosion of wires in an argon atmosphere. The concentration of Mo in the zeolite was 4.0 wt %, and the concentration of Ag in the 4.0% Mo/ZSM-5 catalytic system was varied from 0.1 to 2.0 wt %.

The non-oxidative conversion of methane (99.99% purity) was performed in a flow setup at 750° C and atmospheric pressure. A catalyst sample (1.0 cm³) was placed in a quartz tube reactor 12 mm in diameter. Before the onset of reaction, the catalyst was heated to 750° C in a flow of helium and kept for 20 min at this temperature; thereafter, methane was supplied at a space velocity of 1000

h^{-1} . The reaction products were determined by gas chromatography. The acid characteristics of the samples were studied by the temperature-programmed desorption (TPD) of ammonia, which allowed us to determine the strength distribution and concentration of acid sites. The formation and nature of coke deposits were studied by thermal analysis on a Derivatograph C (MOM, Hungary) over the temperature range of 20-800° C. A sample (400-500 mg), in a platinum crucible, was heated in air at a rate of 10 K/min (the sensitivity was 100 mg). HR TEM images were obtained on a JEM-2010 electron microscope (JEOL, Japan) with a lattice resolution of 0.14 nm at an accelerating voltage of 200 kV. The high-resolution images of uniform structure were analyzed using the Fourier analysis. Local elemental composition of the samples was determined by the energy-dispersive X-ray analysis (EDX) in an EDAX spectrometer (EDAX Co.) equipped with a Si(Li) detector with an energy resolution of no worse than 130 eV. The samples for HR TEM were prepared on perforated carbon substrates fixed on copper gauzes.

Results and Discussion

Figure 1 illustrates the effects of the concentration of the nanosized Ag powder and the reaction time of methane dehydroaromatization on the methane conversion and catalyst stability. Introduction of silver nanopowder into Mo/ZSM-5 catalyst leads to increase in its activity and stability in reaction of non-oxidative conversion of methane. After the induction period the conversion is maximal and reaches the value of more than 22% using the catalyst sample, containing 0.1% Ag-4.0% Mo/ZSM-5, that is 6% higher when using Mo-ZSM-5. Furthermore, the methane conversion ratio over the 0.1% Ag-4.0% Mo/ZSM-5 catalyst for 380 min of operation decreased by 1.7%, whereas that over the initial sample – by 12.1%. The selectivity of aromatic hydrocarbon formation over the Ag-Mo-containing zeolite was found to be as high as 80%. When the amount of Ag in Mo/ZSM-5 was increased to 0.5% and higher, less active and stable catalysts were obtained

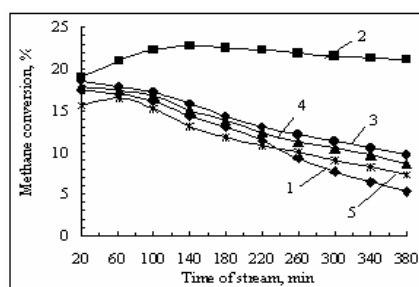


Fig.1. Dependence of the conversion of methane on the time of methane dehydroaromatization on Mo/ZSM-5 with various silver nanopowder contents: (1) initial 4.0% Mo/ZSM-5

Mo₂C particles closely contacting the surface of zeolite crystals (Fig. 2).

The examination revealed no individual Ag particles in the sample after the reaction. According to the EDX-spectroscopy, Ag is present in the structure of Mo₂C particles, with the nuclear parity being Ag:Mo = 6:94. The presence of an Ag impurity in the structure of Mo₂C is indicative of the formation of silver-modified molybdenum carbide (presumably (Ag_{0.06}Mo_{0.94})₂C).

It is obvious that, under conditions of methane activation in the course of the reaction, the active catalytic sites may be subjected to coking to an extent depending on the conversion of methane into intermediate products.

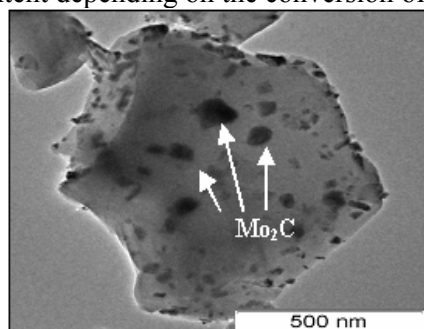


Fig.2. HRTEM images of the 0.1% Ag-4.0% Mo/ZSM-5 after treatment with methane (380 min) at T = 750° C.

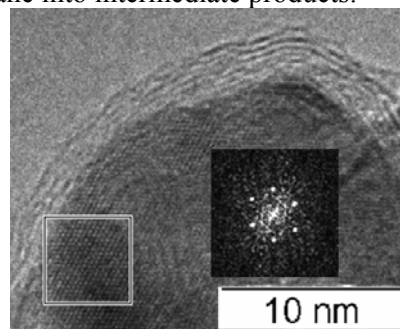


Fig.3. HRTEM images of the Mo₂C particle coked on the zeolite surface after treatment with methane (380 min) at T = 750° C.

After the reaction, as shown in Fig. 3, a 2-4 nm thick graphite-like carbon layer is formed on the surface of Mo₂C particles. A much thinner (no more than 1 nm) graphite-like layer of “island” morphology is also formed on the zeolite surface. Thus, the zeolite surface (and, hence, its channels) in the course of the reaction is less coked than that of Mo₂C modified by silver. The Mo carbide particles in the samples that have worked during different time periods in dehydroaromatization of methane at 700 and 750° C are morphologically identical, the difference being a somewhat larger primary-particle size.

Conclusion

Thus, we can conclude that the Mo-containing zeolite ZSM-5 modified by 0.1% Ag nanopowder is superior over other samples not only in its catalytic activity but also in its stability. Its regenerative advantage is due to a smaller amount of coke formed on this zeolite and characterized by a lower degree of polycondensation and less severe conditions of oxidative thermal treatment required to remove this coke.

Acknowledgments

The study has been performed with financial support from the Presidium of RAS (grant No. 27-50).

References

- [1] L. Chen, L. Lin, Z. Xu, Catal. Lett., 1996, 39, 169-173.
- [2] L. Wang, Y. Xu, S. Wong, W. Cui, X. Guo, Appl. Catal., 1997, 152, 173-182.
- [3] A.V. Vosmerikov, V.I. Zaikovskii, L.L. Korobitsyna, G.V. Echevskii, V.V. Kozlov, Ya.E. Barbashin, S.P. Zhuravkov, Kinetics and Catalysis, 2009, 50, 725-733.

KINETIC MECHANISMS OF CONVERSION OF NATURAL GAS COMPONENTS INTO AROMATIC HYDROCARBONS

A. V. Vosmerikov and, L. N. Vosmerikova

Institute of Petroleum Chemistry Siberian Branch of the Russian Academy of Sciences, 4, Akademichesky Ave., Tomsk, 634021, Russia (pika@ipc.tsc.ru)

Abstract

Kinetics of the natural gas components conversion into aromatic hydrocarbons on zeolite catalysts has been studied. An analysis of the experimentally found kinetic dependences allowed us to suggest that a combination of chemical reactions runs within the process under study. A kinetic model of natural gas aromatization was developed, which allows calculating the most probable reaction routes for conversion of the reaction mixture components.

Introduction

By the volume of its reserves, production efficiency and ecological compatibility natural gas is the most promising resource that can satisfy the demand of humankind for energy and raw hydrocarbon material for as long as the current century [1]. Today, the industrial level of chemical conversion of natural gas into valuable products remains low because it is generally used in power engineering to produce thermal and electrical energy via its combustion [2]. Such a wasteful use of natural gas is inadmissible and requires that advanced technologies for its comprehensive processing be developed without any further delay.

A relatively small number of large-tonnage chemical processes involving the use of natural gas are applied commercially; all are based on its preliminary conversion into synthetic gas or its thermal decomposition into unsaturated hydrocarbons. Of particular interest is a one-stage catalytic synthesis of aromatic hydrocarbons (ArH) from gaseous paraffins and olefins.

Aromatization of natural gas components is characterized by complex kinetic mechanisms, since during this process the hydrocarbons of different homologue series participate in several types of chemical reactions on the active catalytic centres simultaneously [3]. Therefore, it is reasonable to study the kinetics of this process with the methods for mathematical simulation using experimentally found dependences.

Experimental

To study the kinetics of conversion of low alkanes into aromatic hydrocarbons, the experiments were carried out in a laboratory flow type quartz reactor at the reaction temperature 600-750° C, the feedstock space velocity 500-5000 h⁻¹ and atmospheric pressure. The high-silica ZSM-5 zeolite (molar ratio SiO₂/Al₂O₃ = 40),

which contained 0.5 wt % gallium oxide and 4.0 wt % molybdenum oxide was used as a catalyst. The catalyst volume in the reactor was varied from 0.5 to 4.0 cm³. The products were determined by gas chromatography. The duration of the experiment was set depending on the process conditions, taking into account the catalyst operation stability. To evaluate the catalytic activity of the samples in the process, the degree of conversion of the feed gas component and the yield of gaseous and liquid products were determined, and the selectivity for aromatic hydrocarbons was calculated.

Results and Discussion

It seems more reasonable to determine catalytic activity and selectivity in the absence of distorting effects of heat and mass transfer processes [4]. Thus, primarily the reaction zone was experimentally identified. The natural gas conversion was performed at 700° C for 20 min in presence of the catalyst with a grain size of 1.0 mm.

The results of detecting the reaction zone are presented in Fig. 1. The yield of aromatic hydrocarbons increases from 8.33 to 24.99 ml/min with increase in the feedstock consumption, which testifies to the process running in the external diffusion region. For the feedstock consumption higher than 24.99 ml/min the process proceeds to the kinetic region. In the course of further investigations, the initial gas velocity was selected so that to remove external diffusion inhibition and to maintain the process in the kinetic region.

To plot the kinetic curves, the catalyst was investigated at the process temperature 600-750° C and different contact times. During the natural gas conversion gaseous and liquid products were formed. The main liquid products are

presented by benzene, toluene and xylenes (BTX-fraction), naphthalenes and naphthalene hydrocarbons (methyl- and dimethylnaphthalene). The gaseous products contain hydrogen, methane, alkanes, and alkenes C₂-C₄.

Table 1 gives the kinetic results obtained during aromatization of natural gas components at the 700° C. It is evident that the increase in the degree of conversion of the initial feedstock components and in the selectivity of aromatic hydrocarbons formation occurs with increasing the contact time.

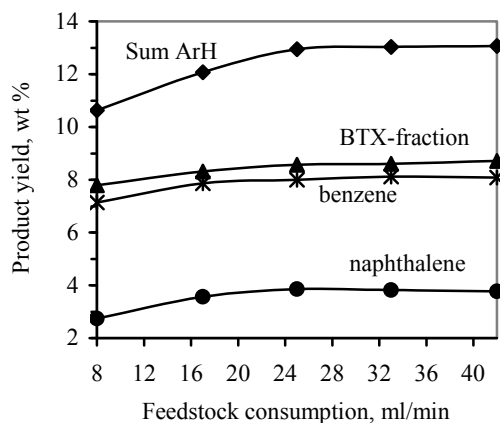


Fig.1. Dependence of the yield of natural gas conversion products on the feedstock consumption at the constant temperature and contact time ($T = 700\text{ }^{\circ}\text{C}$, $\tau = 3.6\text{ s}$).

Note that the yield of benzene and naphthalene in the liquid reaction products increases and the content of toluene and alkylnaphtalenes reaches a maximum, suggesting that they are intermediates. When the contact time is longer than 1.44 s, the rate of toluene and alkylnaphtalene consumption in the secondary conversion reactions exceeds their formation rate.

The amount of low alkanes and alkenes decreases with increasing the contact time, while the concentration of hydrogen in the reaction products increases, which indicates a high intensity of the reactions of dehydration of the initial alkanes and dehydrocyclization of the olefins formed over modified pentacyl. A lower yield of olefin hydrocarbons with increasing the contact time testifies to the fact that these intermediate products are the first to be formed in the course of the process and are then subjected to further transformations resulting in the formation of ArH.

Table 1. Products of natural gas conversion at different contact times (T = 750° C)

Product yield (wt %)	Contact time (s)					
	0.72	0.90	1.44	1.80	2.88	3.60
Hydrogen	1.42	1.50	1.73	2.55	3.08	3.68
Methane	86.41	85.93	85.58	81.62	79.29	76.37
Ethane	1.71	1.63	0.93	0.72	0.55	0.49
Alkenes	2.95	2.94	2.22	1.58	1.07	0.92
Benzene	4.84	5.05	5.91	9.72	10.44	10.88
Toluene	0.38	0.48	0.59	0.48	0.40	0.27
Naphthalene	1.78	1.90	2.34	2.76	4.66	6.82
Naphthalene hydrocarbons	0.21	0.27	0.43	0.37	0.33	0.31
Conversion of gas, %	11.9	12.3	13.5	17.7	20.2	23.1
Selectivity for ArH, %	60.6	62.6	68.7	75.3	78.4	79.1

Conclusion

An analysis the experimentally found kinetic dependences allowed us to suggest that a combination of chemical reactions runs within the process under study, such as: oligomerization, dehydrocyclization, dehydroaromatization, disproportionation, alkylation and dealkylation of aromatic hydrocarbons. Based on the proposed combination of chemical reactions, a kinetic model of natural gas aromatization was developed, which allows calculating the most probable reaction routes for conversion of the reaction mixture components.

References

- [1] A. L. Lapidus, I. A. Golubeva, I. F. Krylov, F.G. Zhagfarov, *Chemistry and Technology of Fuels and Oils*, 2009, **5**, 3-7.
- [2] A. G. Anshits, E. N. Voskresenskaya, *Sorovsky educational Journal*, 1999, **9**, 38-43.
- [3] J. Guo, H. Lou, X. Zheng, *Jour. of Natural Gas Chemistry*, 2009, **18**, 260-272.
- [4] I. I. Ioffe, L. M. Pismen, *Engineering chemistry of heterogeneous catalysis*, Leningrad, 1972, 464 .

THE COMPARATIVE ANALYSIS OF COMMONLY USED SPIN-TRAPS FOR DETECTION OF SUPEROXIDE RADICAL

I. Vučinić¹, I. Spasojević², A. Ignjatović¹ and M. Mojović¹

¹*Faculty of Physical Chemistry, University of Belgrade, Studentski Trg 12–16, 11158 Belgrade, Serbia;* ²*Institute for Multidisciplinary Research, Kneza Višeslava 1, 11000 Belgrade, Serbia*

Abstract

Development of EPR spectroscopy led to the discovery of a number of spin-trapping compounds which could more or less successfully be used for detection of different short-lived free radical species. The goal of this study was to compare the efficiency of four the most frequently used spin-traps: DMPO (5,5-dimethylpyrroline-N-oxide), DEPMPO (5-Diethoxyphosphoryl-5-methyl-1-pyrroline N-oxide), EMPO (5-Ethoxycarbonyl-5-methyl-1-pyrroline N-oxide) and BMPO (5-tert-butoxycarbonyl 5-methyl-1-pyrroline N-oxide) for the detection of superoxide radicals. The results showed the influence of the side group of atoms shielding the unpaired electron on the stability of superoxide adduct; that spin-trap EMPO is overrated for simultaneously analysis of superoxide and hydroxyl radicals and the advantage of Riboflavin-light superoxide radicals generating system over commonly used Hypoxantine-Xantine Oxidase system. The obtained kinetics indicated that EPR signal intensity of analyzed superoxide adducts of all samples depend on at least two concurrent processes.

Introduction

Free radicals play very important role in many biochemical systems. Since they possess an unpaired electron they are extremely reactive species and their detection and analysis is quite difficult. EPR spin-trap spectroscopy can overcome this problem since this method is based on introducing the observed system a compound (spin-trap) that chemically bonds with the free radical, and forms a more stable compound (spin-adduct) which could be successfully detected by commonly used EPR spectroscopy techniques. These stabilizing substances (spin-traps) are specific nitrene or nitroso compounds which have the ability to shield the newly formed unpaired electron long enough to make EPR detection possible. Nevertheless, spin-adducts have a tendency to transform and decompose in several different ways which is usually overlooked or passed over. The customary problem for superoxide trapping is spontaneous transformation of superoxide spin-adducts to hydroxyl-adducts [1] but also, the gradual generation of carbon-centered spin-adducts which is frequently related to the spin-trap's impurity.

For the purpose of this experiment, superoxide radicals were obtained by Riboflavin-light generating system. This method is based on an illumination of a riboflavin solution in the presence of DTPA (Diethylene triamine pentaacetic acid) which causes a reduction of the flavin which then re-oxidizes and simultaneously reduces oxygen to $O_2^{\bullet-}$. Proper EPR method for the recording of superoxide radical was applied [1].

Biochemical systems are usually very complex, containing a number of different radical types and EPR spin-trapping method needs to hold enough information about spin-traps which can be used for specific purposes. This paper is a brief overview of spin-trap comparison, based on the kinetics of their superoxide adducts decomposition.

Results and Discussion

EPR spectra were recorded for DMPO, DEPMPO, EMPO and BMPO spin-traps in duration of one hour after the preparation of superoxide radical generating solutions. DMPO and DEPMPO spin-traps were purified before the experiment [2].

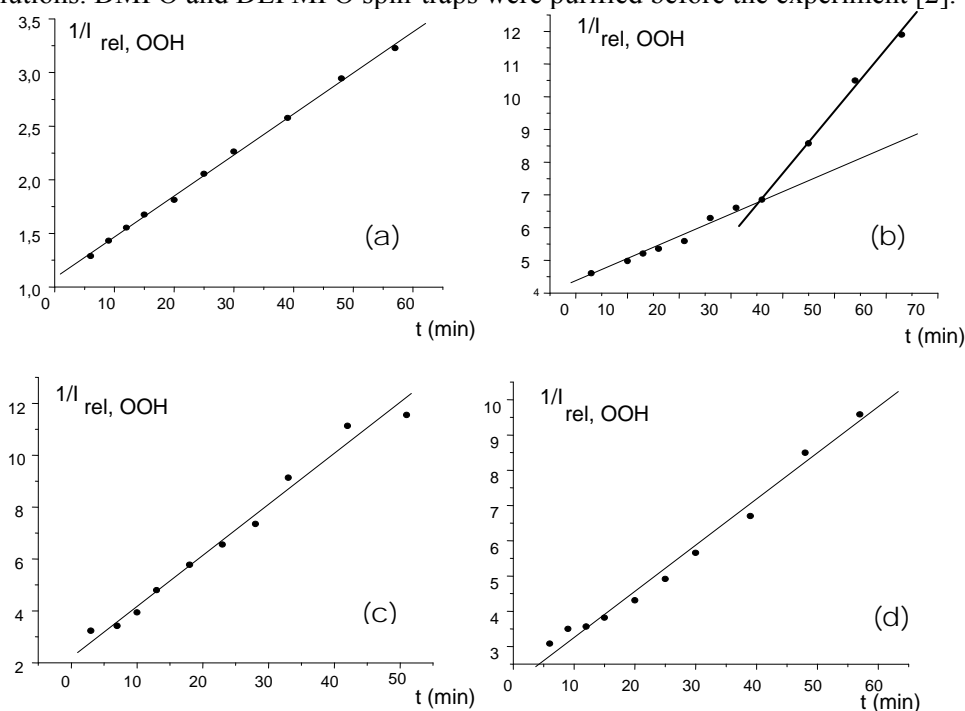


Fig.1. The change of the inverse value of relative intensity for superoxide adduct in the case of DMPO (a), DEPMPO (b), EMPO (c) and BMPO (d) spin-traps.

Unlike Hypoxantine-Xantine Oxidase system, Riboflavin-light generating system produces superoxide radicals only while the solution is exposed to UV radiation.

This means that the superoxide adducts concentration in investigated system was not influenced by the superoxide radical production during spectra recording. The intensity of the selected EPR spectral line of the superoxide adducts related to time was measured in all spectra and presented in Fig. 1. In the case of spin-trap DMPO, DEPMPO, EMPO and BMPO linear dependence presenting second order chemical reaction was obtained showing the presence of at least two concurring processes: spin-adduct decomposition and conversion - which could be observed from the EPR spectra (results not shown). However, in the case of spin-trap DEPMPO a significant change in the second order kinetics could be observed about 40 minutes after the start of the experiment.

Conclusion

None of the spin-traps used in this experiment showed to have a simple superoxide spin-adducts degradation kinetics. Superoxide spin-adducts of DMPO, EMPO and BMPO showed to have relatively similar stability and degradation kinetics all liable to conversion to hydroxyl radical adduct. Although DEPMPO is considered to be the best for trapping superoxide (and other) short-lived radical species, [3] it was shown that in this case the most complex kinetics has been involved. Sudden change of the inverse EPR signal intensity line slope after 40 minutes implies that with DEPMPO/OOH adducts, significant change in the second-order kinetics occurred. The explanation could include predominating one of the concurrent conversion or degradation processes, or else, the promotion of the generation of some additional adduct species this trap is readily capable to form (for example carbon-centered adduct) which overlaps with examined EPR signal.

Since the concentration of spin-traps and superoxide radicals in the initial solution were unknown, further kinetic analysis was impossible, but since these results show courses of second order reactions in all examined cases, they present good grounds for further research.

Acknowledgments

The authors acknowledge their gratitude to the Ministry of Science of Republic of Serbia for the financial support (Project #143016).

References

- [1] G.Bačić, M. Mojović, *Ann. NY Acad. Sci.*, 2005, **1048**, 230-243.
- [2] S. K. Jackson, K. J. Liu, G. S. Timmins, *Free Radical Biology & Medicine*, 2002, **32**, 228-232.
- [3] C. Frejaville, H. Karoui, B. Tuccio, F. Le Moigne, M. Culcasi, S. Pietru, R. Lauricella, P. Tordo, *J. Med. Chem.*, 1995, **38**, 258-265.

OZONATION PRODUCTS DURING PURIFICATION OF WASTEWATERS POLLUTED BY ORGANICS

S. Rakovsky^{1*}, M. Anachkov¹, V. Iliev¹, A. Elias¹ and G. Li Puma²

¹*Institute of Catalysis, Bulgarian Academy of Sciences, Sofia 1113, Bulgaria*
**(rakovsky@ic.bas.bg; srakovsky@yahoo.com)*

²*The University of Nottingham, University Park Nottingham NG7 2RD, United Kingdom*

Abstract

Representatives of all main classes organic compounds like alkanes, alkenes, aromatics, polyaromatics, their derivatives, misceleniuos, natural products, pesticides etc. were subjected to ozonation and the processes were investigated. It has been established that the ozonation is an advance method for decontamination of waste waters. The obtained products possess lower toxicity than the original compounds. The mechanisms of ozonation of organics in water at low pH are the same as in nonparticipared solvents.

Introduction

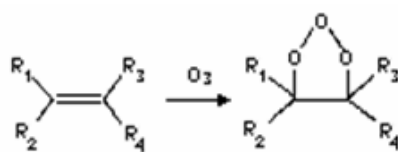
In contrast to the ozone disinfection of natural waters, where it is a conventional approach, the purification of waste waters applying ozone is still an area of intensive research. Ozonation in separate or in combination with UV-irradiation, pH, H₂O₂ or Fenton reagents is among the most appropriate decontamination methods. The present paper is dealing with ozonation of different classes of organic compounds, present in industrial waste waters.

Experimental

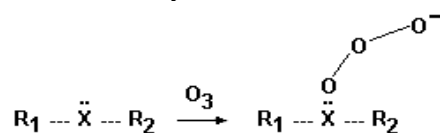
Representatives of all main classes organic compounds like alkanes, alkenes, aromatics, polyaromatics, their derivatives, misceleniuos, natural products, pesticides etc. were subjected to ozonation and the processes were investigated. All together more than 53 different individual compounds have been ozonized. The organic compounds, after dissolution in water were ozonized and analysed by GC, HPLC and MS techniques.

Results and Discussion

The mechanisms of ozonation with different type of organics depend on their structure and electronic properties. In general ozone interacted with them by following mechanisms:



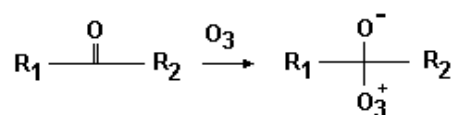
1,3 – cycloaddition



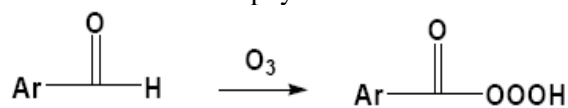
where: X = :NR₃, O:, S::

R₁, R₂, R₃ = alkyl

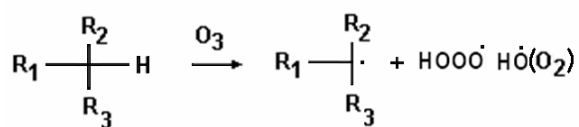
Electrophilic attack



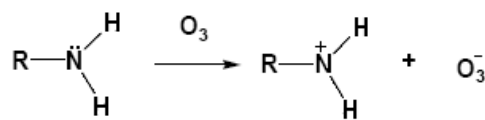
Nucleophilic attack



1, 3 – insertion

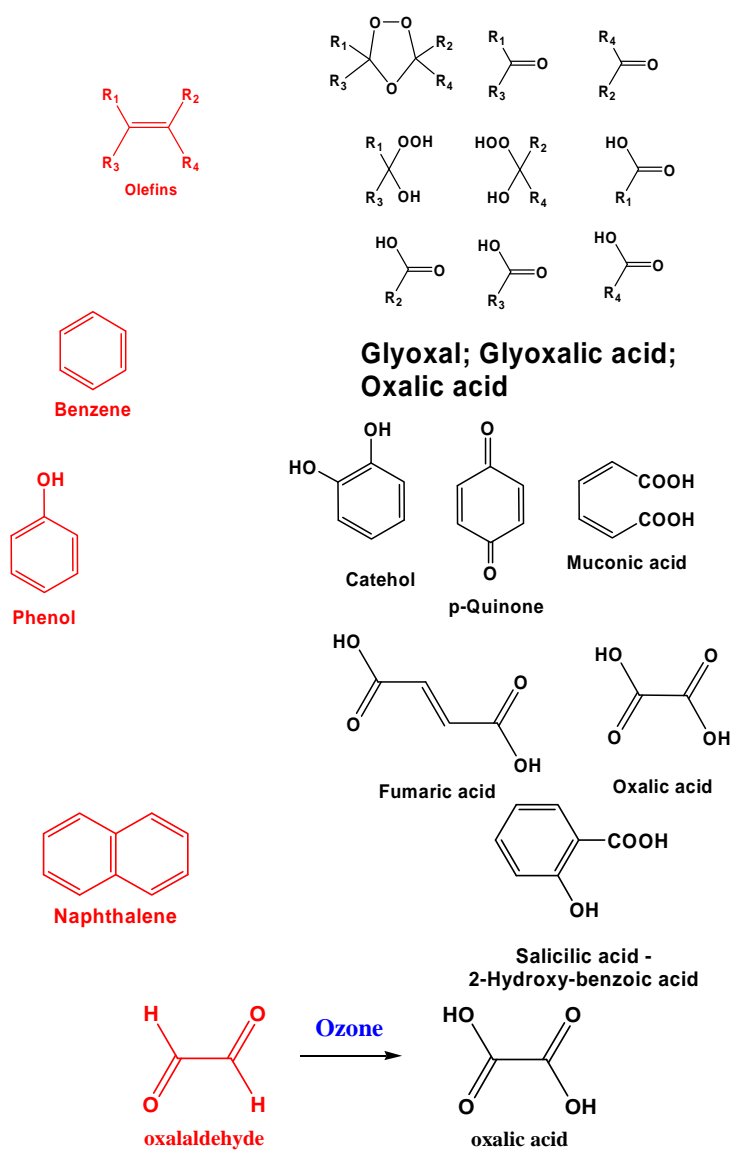


Hydrogen abstraction



Electron transfer

Some of the obtained products after ozonation are presented below:



Conclusion

Ozonation is an advance method for decontamination of waste waters. The obtained products possess lower toxicity than the original compounds. The mechanisms of ozonation of organics in water at low pH are the same as in nonparticipated solvents.

Acknowledgments

NATO Project SfP 982835 and Project of the Bulgarian Fund of Scientific Investigations (FNI) - DO 02-252/18.12.08.

ACID HYDROLYSES OF LIGNOCELLULOSES MATERIAL

B. Adnadjević and J. Jovanović

*Faculty of Physical Chemistry, Studentski trg 12-16, 11001 Belgrade,
R.Serbia*

Abstract

Kinetic of isothermal acid hydrolysis of lignocelluloses material was investigated. The kinetics curves at temperatures $T=303\text{K}$, 323K and 333K were determined. The kinetics model of acid hydrolyses was specified. It was established that kinetics model change with the alteration of the temperature. The value of activation energy was calculated. It was shown that limiting step in hydrolyses was the cleavage of the C-O bond and breakdown of forming conjugate acid.

Introduction

Limited resources of oil in the world, significant variation in oil prices on world market as well as the consequences of global warming, enforce as an imperative, development of novel alternatively fuels and sources for their application. Nowadays, waste lignocelluloses materials (wood, corn stover, straw, municipal sludge, etc.) thanks to huge amounts and low prices are the most perspective materials for the production of bio-ethanol as an alternative fuel. With aim to develop novel technology for bio-ethanol production, in this work the isothermal kinetics of acid hydrolyses of lignocelluloses material (corn stover) was investigated.

Experimental

Grounded sample of corn stover (with the following content: cellulose 35%, hemicelluloses 18.0% pentosan 10%, hexan 23.5%, lignin 11%, ash 1%) was used for hydrolyses. Hydrolyses was performed with different concentration of H_2SO_4 solutions, ranging from 50-75%. The hydrolyze goes as following. In reaction round bottom vessel, 100g of H_2SO_4 solution of defined concentration was heated at predetermined temperature. Then, in this solution a predefined quantity of corn stover was poured and the reaction mixture was homogenized with stirring using a magnetic stirrer, with 400 rpm. At predetermined time intervals, samples for analyses were withdrawn from the reaction mixtures. Each sample for analyses was filtered and neutralized. The total amount of sugars in the neutralized filtrate was determined by using a sugar analyzer (YSI 2700 Select). Degree of hydrolyses (DH) was determined as:

$$DH = \frac{C_s \cdot m_{RS}}{m_s} \quad (1)$$

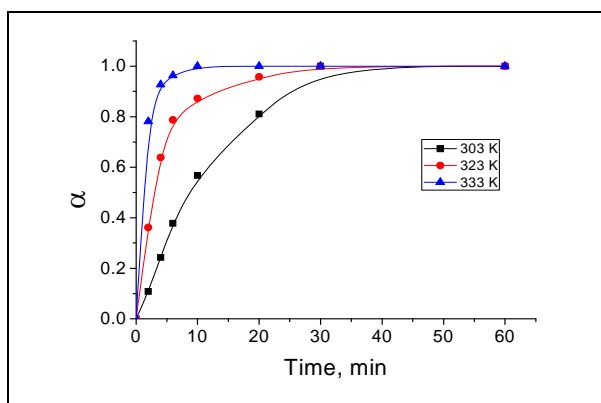
where C_s is mass concentration of sugar in reaction system at reaction time (t) and m_{RS} is the mass of the reaction system; m_s is maximal sugar content at certain temperature. The degree of conversion was calculated as:

$$\alpha = \frac{DH}{DH_{\max}} \quad (2)$$

where DH_{\max} is maximal degree of conversion.

Results and Discussion

Kinetics curves of isothermal hydrolyse of corn stover at different temperatures are presented in Figure 1.



The increase of temperature of the reaction system, leads to change in the shape of the kinetics curves and to the increasing maximal degree of hydrolyses

Fig.1. Kinetics curves of isothermal hydrolyses at different temperatures.

By applying the so-called "Model Fitting Method" [1] it was found that conversion kinetics curves of isothermal acid hydrolyses of corn stover at 303K, may be described by the equation, Eq (3):

$$\alpha = 1 - (1 - kt)^3 \quad (3)$$

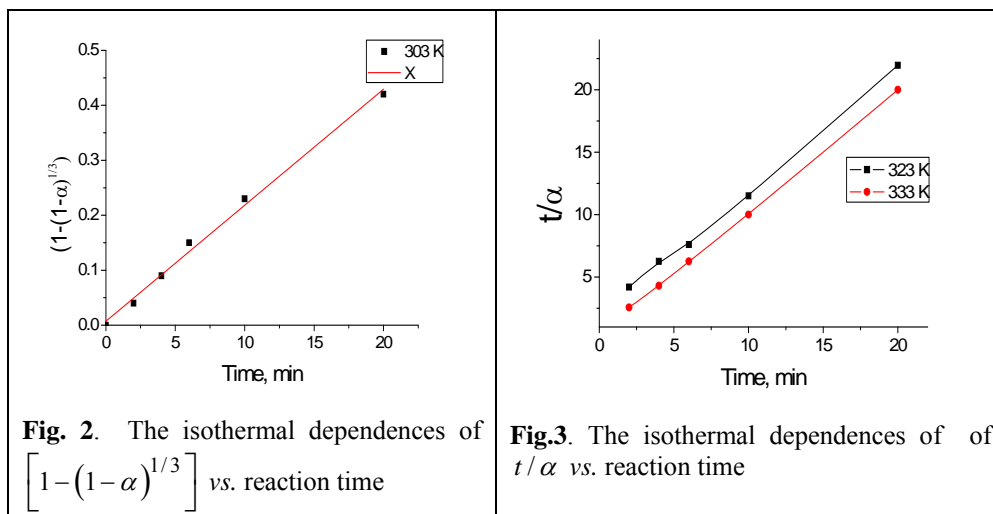
while at 313K and at 323K the following equation is valid:

$$\alpha = \frac{kt}{1 + kt} \quad (4)$$

where k is the rate constant of the hydrolyses. If the Eqs (3) and (4) describe the kinetics of acid hydrolyses, then the dependence of $[1 - (1 - \alpha)^{1/3}]$ as well as the t/α on time, should give the straight lines.

The isothermal dependences of $[1 - (1 - \alpha)^{1/3}]$ vs. reaction time for hydrolyses are shown in Figure 2 and the dependences of t/α on time on Figure 3.

Both the dependences $[1 - (1 - \alpha)^{1/3}]$ and t/α on time give straight lines over a very wide range of the process of hydrolyses. The values of the rate constant k_M were determined from the slopes and intercepts at these lines, respectively.



The rate constant k_M for the predicted theoretical models of corn stover hydrolyze at different temperatures and activation energy (E_a) are given in Table 1.

Table 1. The rate constants and the kinetics parameters of corn stover hydrolyses

T, K	k, min^{-1}	$E_a, \text{kJ/mol}$
303	0.021	116.9 kJ/mol
323	0.380	
333	1.470	

As the values of k_M increase exponentially with temperature, it was possible to determine the kinetics parameters: E_a and $\ln A$ for the applied model using the Arrhenius Equation. The established models of the kinetics of acid hydrolyses, their changes with temperature and calculated values of $E_a = 117$ kJ/mol, revealed that the limiting stage of hydrolyses is the cleavage of the C-O bond and breakdown of forming conjugate acid.

Conclusions

Acid hydrolyses of lignocelluloses material is a kinetically complex process. The increasing temperature leads to the change in kinetics model of acid hydrolyses. The limiting stage of acid hydrolyses is the cleavage of the C-O bond and breakdown of forming conjugate acid.

Acknowledgement

The investigation was supported by the Ministry of Science and Environmental Protection of Serbia, through project G 142025.

References

[1] M. Brown, D. Dollimore, A. Galwey, Reactions in the Solid State, Comprehensive Chemical kinetics, Elsevier, 1980, **22**, 87-91.

CONTINUAL TRANSESTERIFICATION OF ALGAE OIL IN A HYDRODYNAMIC CAVITATION REACTOR

B. Adnadjević and J. Jovanović

Faculty of Physical Chemistry, Studentski trg 12-16, 11001 Belgrade, R.Serbia

Abstract

The effects of operating parameters of a hydrodynamic cavitation reactor (cavitator): cavitation number (0.5-0.05) and orifice opening to pipe diameter ratio (β) (0.05-0.1), on the transesterification degree of algae oil into biodiesel under the defined reaction conditions was investigated. It was established that the decreases in the cavitation number of the cavitator leads to the increasing the degree of the transesterification in power law and that the increasing value of parameter β results in linear decrease of the degree of transesterification of algae oil into biodiesel. The change in the degree of transesterification with the change in operation parameters of cavitator are explained with the increase in the number of the cavities generated and with the increase in the intensity of cavity collapse with the alteration in the operating parameters.

Introduction

Biodiesel is usually obtained from various raw materials by different conventional method such as alkali catalysts, acid catalysis, lipase catalysis etc [1]. Algae oil presents almost an ideal raw material for biodiesel production due to significant productivity, giving yield until 130 t/h of produced biodiesel [2]. P. R. Gogate [3] presented possibilities for significant acceleration of numerous chemical reactions in liquids phase by applying cavitations reactor. With that in mind, in this paper the effects of operating parameters on the achieved cavitation number (CN) of the reactor and orifice opening to pipe diameter ratio (β) on the degree of transesterification of algae oil was investigated. For that purpose algae oil produced from algae *chlorella vulgaris* was used.

Experimental

Transesterification was carried out on sample of algae oil with following fatty acid composition given in Table 1.

Table 1. Fatty acid composition

Fatty acid	wt, %
C17: O	0.2
C18 : O	3.4
C18 : 1	16.3
C18 : 2	79.4
C18 : 3	0.1

Transesterification was carried out under the following reaction conditions: molar ratio CH₃OH/Oil=4.5, T= 25°C, catalyst (CH₃ONa) concentrations 1%, reaction duration of 1 minute.

Cavitation number (CN) was calculated using the equation (1):

$$CN = \frac{2(p_2 - p_v)}{\rho_L \cdot v^2} \quad (1)$$

where p_2 is the fully recovered downstream pressure, p_v is vapor pressure of feed and v is linear velocity of feed.

Transesterification was carried out in hydrodynamic cavitations reactor supplied with multi-holes plates whose construction and mode of action are described in details [4]. Degree of transesterification (DT) was determined by gas chromatography [5] and calculated as:

$$DT = \frac{\frac{\text{weightbiodisel}}{MWb} \text{ biodiselconcentration}(\%)}{\frac{\text{weightoil} \times 3}{MWO}} \quad (2)$$

where $MW = \sum MW_i \times x_i$ is the mean molecular weigh of the biodisel/oil. The MWb is the mean molecular weigh of the biodisel which was calculated averaging the individual molecular weights (MWi) of each methylester, according to biodisel fatty acid alkyl ester analysis (x_i) and the MWO is the mean molecular weigh of the oil. which was calculated averaging the individual molecular weights (MWi) of each constituents triglyceride according to the fatty acid oil analysis (x_i).

Results and Discussion

Table 2 presents the effect of plate's type and inlet pressure on the value of cavitation number of cavitator.

Table 2. Effect of plate's type and inlet pressure on the cavitation number.

Plate	P, at	CN
4	0.35	5.7
4	0.7	1.9
4	2.1	0.87
1	1.4	0.5
1	2.8	0.1
1	5.6	0.05

Effect of cavitation number of the cavitator on the degree of transesterification of algae oil is presented in Table 3.

Degree of transesterification of algae oil increases with the decreasing the cavitation number of the cavitator, which can be described with equation (3):

$$DT = 0.28 + CN^{-0.5} \quad (3)$$

Table 3. Effect of cavitation number of the cavitator on the degree of transesterification of algae oil

CN	DT, %
5.7	9
1.9	15
0.87	23
0.5	31
0.1	69
0.05	99

Effect of orifice opening to pipe diameter ratio of the cavitator on the transesterification degree for CN=0.5 is given in Table 4.

The decreasing values of the orifice opening to pipe diameter ratio under the constant value of cavitation number, leads to the decreasing the degree of the transesterification, according to the equation (4)

$$DT(\%) = 41 - 336\beta \quad (4).$$

Table 4. Effect of parameter β of the cavitator on the degree of transesterification

β	DT, %
0.01	40.2
0.02	31.0
0.05	24.7
0.1	7.5

The established increase in the degree of transesterification with the decrease in the cavitation number and orifice opening to pipe diameter ratio of the cavitator are consequences of the increase in the number of cavitations generated and the intensity of cavity collapse with the alteration in the operating parameters (6).

Conclusions

Degree of transesterification of algae oil complexly changes with change in the operating parameters of the cavitator. The degree of transesterification of algae oil increases in power law with the decreasing the cavitation number of the cavitator while linearly increases with the decreasing the ratio of orifice to pipe diameter ratio.

Acknowledgements

The investigation was supported by the Ministry of Science and Environmental Protection of Serbia, through project G 142025

References

- [1] F. Ma. H. A. Hanna, Biores. Techn., 1990, **70**, 1-15.
- [2] T. M. Meta, A. A. Martins, N.A.Caetano, Energy Reviews, 2010, **14**, 217-232.
- [3] P. R. Gogate, Chem.Eng.Proc., 2008, **47**, 515-527.
- [4] B. Adnadjevic, Zbornik radova sa Medjunarodnog simpozijuma Novi i obnovljivi izvori energije i energetske efikasnosti kao preduslov održivog razvoja AP Vojvodine, Novi Sad, 2009, 51-75.
- [5] C. Plank, E. Lorbeer, J. Chromatography A, 1995, **697**, 461-470.
- [6] P.Senthil Kumar, A.B.Pandit, Chem.Eng.Tecnol; 1999, **22 N12**, 1017-1025

KINETICS OF ADSORPTION OF MIXED POLLUTANTS BY ORGANO-BENTONITE

N. Jović-Jovičić¹, M. Žunić¹, P. Banković¹, Z. Mojović¹,
A. Milutinović-Nikolić¹, B. Dojčinović² and I. Gržetić³

¹*ICH_{TM}, University of Belgrade, Department of Catalysis and Chemical
Engineering, Njegoševa 12, Belgrade, Republic of Serbia*

²*ICH_{TM}, University of Belgrade, Department of Chemistry, Njegoševa 12,
Belgrade, Republic of Serbia*

³*University of Belgrade, Faculty of Chemistry, Studentski trg 12-16, Belgrade,
Republic of Serbia*

Abstract

Quantitative substitution of the interlayer cations of smectite by hexadecyl trimethylammonium ions (HDTMA) was performed in order to prepare adsorbent able to simultaneously adsorb toxic metal cations and organic pollutants. The adsorption of Acid Yellow 99 textile dye and Pb²⁺ ion from their single solutions and mixture was performed. Kinetics data of adsorption were well represented by pseudo-second-order kinetics model for all investigated adsorption systems.

Introduction

Simultaneous adsorption of various organic and inorganic pollutants from textile wastewaters by low cost adsorbent is promising technique for their purification [1]. The modification of clay minerals by surfactants is a method to hydrophobize the mineral and therefore to increase the adsorption capacity for organic pollutants. Numerous studies have been focused on the adsorption of nonionic organic compounds onto organo-clay minerals [2-4] and only few on adsorption of metal ions [5]. The latter revealed that organo-clay minerals have ability to adsorb metal ions. Recently, simultaneous adsorption of various organic and inorganic pollutants has increasingly attracted attention [1]. In this paper local bentonite clay (Bogovina) rich in smectite was modified with HDTMA ion. The obtained organoclay was used for adsorption of Pb²⁺ ion and textile dye Acid Yellow 99 (AY 99) from their single solution and mixture.

Experimental

Bentonite was obtained from Bogovina, Serbia. It was crushed, ground and sieved through a 74 μm sieve. Hexadecyl trimethylammonium (HDTMA) bromide, Acid Yellow 99 (AY 99) dye and lead (II) nitrate was supplied from Alfa-Aesar Chemical Company, with a chemical purity of 98%, 40% and 99.99% respectively. Na-rich bentonite was prepared by procedure according to [6]. The cation exchange capacity (CEC) of Na-rich bentonite (0.633 mmol/g of clay) was determined by standard ammonium acetate method [7]. The surfactant/bentonite ratio was 0.633

mmol HDTMA-bromide per 1 g of bentonite dried at 110 °C in order to replace all exchangeable cations in interlaminar layer (1CEC value). The solution of HDTMA-bromide was dropwisely added into stirred Na-rich bentonite dispersion. After stirring during 24 h, the dispersion was filtered, washed with distilled water until the filtrate was Br⁻ free (tested with 0.1M AgNO₃). The sample was dried at 80 °C [8-9].

All experiments were carried out under conditions: $t=25^{\circ}\text{C}$, solution volume ($v=0.050\text{ dm}^3$); concentration of AY 99 or Pb^{2+} in single and mixed solution ($C_0=50\text{ mg dm}^{-3}$); mass of adsorbent ($m_{\text{adsorb}} = 0.01\text{ g}$). A period of 24 h was taken as equilibrium although in some experiments equilibrium was reached much earlier.

The AY 99 concentration was estimated by Thermo Electron Nicolet Evolution 500 UV-VIS spectro-photometer at $\lambda_{\text{max}}=449\text{ nm}$ while the Pb^{2+} concentration was estimated by iCAP 6500 Duo ICP, Thermo Scientific Spectrometer at $\lambda_{\text{pb}}=220.4\text{ nm}$. It was previously confirmed that the presence of Pb^{2+} in AY 99 solutions did not affect either the position or the intensity of the dye absorption band.

Results and Discussion

The effect of contact time on the adsorption of AY 99 or Pb^{2+} from their single and mixed solution onto HDTMA-bentonite is presented in Fig. 1.

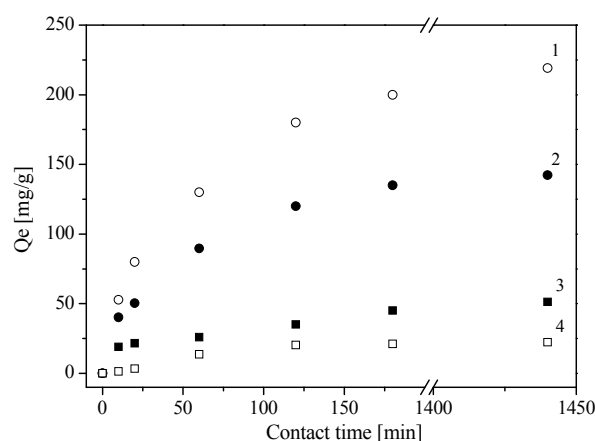


Fig.1. Adsorption of: 1) AY 99 from mixed solution; 2) AY 99 from single solution; 3) Pb^{2+} from single solution and 4) Pb^{2+} from mixed solution

AY99 is better adsorbed from mixture than from single solution, while Pb^{2+} is better adsorbed from single component solution. The kinetic data were fitted with the pseudo-first-order and pseudo-second-order kinetics models [10]. Since the correlation coefficients for the pseudo-second-order kinetic (r_2) model were closer to unity, the second-order kinetics model was considered more adequate.

The pseudo-second-order kinetics model is given in linear form:

$$\frac{t}{q_t} = \frac{1}{k_2 q_e^2} + \frac{1}{q_e} t \quad (1)$$

where: q_t is the amount of adsorbed either AY 99 or Pb^{2+} (mg g^{-1}) at time t , q_e -the amount at equilibrium (mg g^{-1}), k_2 is the pseudo-second-order rate constant ($\text{g mg}^{-1} \text{min}^{-1}$).

The values of q_e , k_2 as well as corresponding correlation coefficients (r) are presented in Table 1. together with the experimentally estimated equilibrium amounts q_e^{exp} .

Table 1. Kinetic parameters for adsorption

Adsorbate	q_e^{exp}	q_e	k_2	r
	[mg g ⁻¹]	[mg g ⁻¹]	[g mg ⁻¹ min ⁻¹]	
AY 99	142.25	166.67	9.9×10^{-5}	0.9985
Pb ²⁺	51.31	52.63	4.8×10^{-4}	0.9995
AY99 from mixture	219.25	250.00	4.7×10^{-5}	0.9985
Pb ²⁺ from mixture	22.26	23.81	5.6×10^{-4}	0.9950

The validity of pseudo-second-order kinetic model was confirmed by r coefficient close to unity and good agreement between $q_{e\ exp}$ and q_e values.

Conclusion

Organobentonite was obtained by modification of local clay (Bogovina) with hexadecyl trimethylammonium ions. The adsorption of Acid Yellow 99 textile dye and Pb²⁺ ion from their single solutions and mixture was performed. AY99 is better adsorbed from mixture than from single solution, while Pb²⁺ is better adsorbed from single component solution. Kinetics data of adsorption were well represented by pseudo-second-order kinetics model for all investigated adsorption systems.

Acknowledgments

This work was supported by the Ministry of Science and Technological Development of the Republic of Serbia (Projects 166001B and 142019B).

References

- [1] V. A. Oyanedel-Craver, M. Fullera, J. A. Smith, J. Colloid Interface Sci., 2007, **309**, 485-492.
- [2] F. Cadena, J. Environ. Eng., 1989, **115**, 756–767.
- [3] J. A. Smith, P. R. Jaffé, Water Air Soil Pollut., 1994, **72**, 205–211.
- [4] G. Lagaly, M. Ogawa, Dékány, *Handbook of Clay Science*, Elsevier, Amsterdam, 2006.
- [5] V. A. Oyanedel-Craver, J. A. Smith, J. Hazard. Mater., 2006, **B137**, 1102-1114.
- [6] H. He, Q. Zhou, W. N. Martens, T. J. Kloprogge, P. Yuan, Y. Xi, J. Zhu, R. L. Frost, Clays Clay Miner., 2006, **54**, 689–696.
- [7] Test Methods for Evaluating Solid Waste, Physical/Chemical Methods - Method 9080, Environmental Protection Agency, 1986.
<http://www.epa.gov/osw/hazard/testmethods/sw846/pdfs/9080.pdf>
- [8] P. Baskaralingam, M. Pulikesi, D. Elango, V. Ramamurthi, S. Sivanesan, J. Hazard. Mater., 2006, **128**, 138–144.
- [9] N. Jović-Jovičić, A. Milutinović-Nikolić, I. Gržetić, D. Jovanović, Chem. Eng. Technol., 2008, **31**, 567-574.
- [10] S. Azizian, J. Colloid Interface Sci., 2004, **276**, 47-2.

HEXAVALENT CHROMIUM SORPTION BY GLYCIDYL METHACRYLATE BASED COPOLYMER

D. Maksin¹, A. Nastasović², Z. Sandić³ and Lj. Suručić⁴

¹*Vinča Institute of Nuclear Sciences, P.O. Box 522, Belgrade, Serbia*

²*ICTM- Center for Chemistry, Polymer Department, Studentski trg 12-16, Belgrade, Serbia*

³*Faculty of Science, Mladena Stojanovića 2, Banja Luka, Republic of Srpska (BIH)*

⁴*Faculty of Forestry, Kneza Višeslava 1, Belgrade, Serbia*

Abstract

Macroporous crosslinked poly(glycidyl methacrylate-*co*-ethylene glycol dimethacrylate), PGME, was synthesized by suspension copolymerization and functionalized with diethylene triamine [PGME-deta]. Competitive sorption kinetics was studied from multicomponent Cr(VI), Cu(II), Co(II) and Cd(II) solution. Two kinetic models (the pseudo-first and the pseudo-second order) were used to determine the best-fit equation for the metals sorption by PGME-deta.

Introduction

Extreme toxicity of Cr(VI), which cannot be destroyed in the natural environment, evokes constant interest of researchers towards its effective removal from industrial waste waters. Employment of macroporous amino-functionalized sorbents based on glycidyl methacrylate may offer an alternative to conventional methods for Cr(VI) sorption from acid solutions. Namely, these copolymers have already shown high capacity and good selectivity for precious and heavy metal ions [1,2]. In this study, poly(glycidyl methacrylate-*co*-ethylene glycol dimethacrylate) [PGME], synthesized by suspension copolymerization in the presence of inert component was additionally functionalized via ring-opening reaction of the pendant epoxy groups with diethylene triamine [PGME-deta]. The sorption kinetics of Cr(VI) was studied under competitive conditions, from mixed metal salt solutions with Cu(II), Co(II) and Cd(II). Kinetic data were analyzed using two sorption kinetic models (the pseudo-first and the pseudo-second order) to determine the best fit equation for heavy metal sorption onto amino-functionalized PGME.

Experimental

Macroporous PGME (surface area 33 m²g⁻¹, pore diameter 87 nm, particle size 150-500 μm) was prepared by suspension copolymerization [3]. PGME-deta was obtained by heating the mixture of 3.6 g of PGME, 15.7 g of diethylene triamine and 100 ml of toluene at 80 °C for 6 h. The modified sample (surface area 50 m²g⁻¹, pore diameter 60 nm) was filtered, washed with ethanol and dried. The Cu(II), Cr(VI), Co(II) and Cd(II) sorption rates were determined at pH 1.80, by contacting 0.2 g of copolymer with 20 cm³ of mixed metal salt solution (5 cm³ of each metal solution). In all experiments, at appropriate times, 0.5 cm³ aliquots were

removed and the concentrations of the metal ions in the aqueous phases were measured by atomic absorption spectrometry (AAS, SpektrAA Varian Instruments). The experimental data were fitted with the pseudo-first and the pseudo-second-order equations [4].

Results and Discussion

The important physicochemical aspects for the evaluation of applicability of chelating copolymers are specific and fast complexation of the metal ions, as well as their regeneration and reusability. Macroporous PGME-deta showed very fast sorption rates for all investigated metals (Table 1, Figure 1), with $t_{1/2} \leq 2$ min for Cr(VI), Co(II) and Co(II) and 2.5 min for Cu(II). It is interesting to note that $t_{1/2}$ values and maximum capacities were quite different compared to our previous results obtained with Cu(II), Cd(II), Ni(II) and Co(II) mixed solution [1]. In that case, the $t_{1/2}$ values for the uptake of Cu(II) and Cd(II) on PGME-deta were approximately 8 and 3.5 min, while $t_{1/2}$ values for Ni(II) and Co(II) were similar, i.e. around 5 min. The presence of Cr(VI) seems to promote sorption of cobalt and cadmium which do not sorb so quickly from the mixed Cu(II), Co(II), Cd(II) and Ni(II) solution. Although the metals sorption rates were slower from the mixed Cu(II), Co(II), Cd(II) and Ni(II) solution, the total amount of bound metals was twice higher (2.22 mmol g^{-1}) than from Cr(VI), Cu(II), Cd(II) and Co(II) solution (1.07 mmol g^{-1}). It appears that, in the case of competitive sorption, the most important influences on sorption rates and capacities are the pH value of the solution and the presence of other metals.

Table 1. Kinetic data for metals sorption on PGME-deta [5].

Sample	$Q_{e, \text{exp}}$, mmol g^{-1}	Pseudo-first order kinetics			Pseudo-second order kinetics		
		k_1 , min^{-1}	Q_{eq} , mmol g^{-1}	R^2	k_2 , $\text{gmmol}^{-1}\text{min}^{-1}$	Q_{eq} , mmol g^{-1}	R^2
Cr(VI)	0.43	0.048	0.23	0.963	0.761	0.44	0.999
Cu(II)	0.35	0.020	0.18	0.813	0.409	0.35	0.993
Co(II)	0.14	0.085	0.07	0.853	5.25	0.14	0.999
Cd(II)	0.15	0.047	0.05	0.779	4.90	0.15	0.999

The rate constants k_1 and k_2 , the experimental equilibrium sorption capacity, $Q_{e, \text{exp}}$, the theoretical equilibrium sorption capacity, Q_e , and the correlation coefficients, R^2 , are presented in Table 1, and the equilibrium sorption capacities vs. time are presented in Figure 1. Theoretical Q_e values for metal ions show excellent agreement with the experimental data for the pseudo-second order kinetics, with correlation coefficients higher than 0.99 (with one exception). This suggests that heavy metals sorption under competitive conditions on PGME-deta obeys pseudo-second order kinetics, meaning that sorption depends both on the properties of the metal and the chelating copolymer.

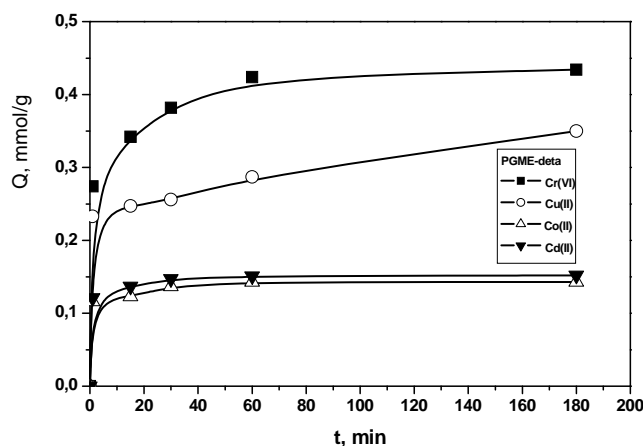


Fig.1. Competitive metal sorption vs. time on PGME-deta [5].

Conclusion

Macroporous PGME-deta showed very fast sorption for all investigated metals, with $t_{1/2} \leq 2$ min for Cr(VI), Co(II) and Co(II) and 2.5 min for Cu(II). From the analysis of two kinetic models, it was concluded that sorption of Cr(VI), Cu(II), Co(II) and Cd(II) by PGME-deta obeys pseudo-second order kinetics, meaning that sorption depends both on the properties of the metal and the chelating copolymer.

Acknowledgement

This work was supported by the Serbian Ministry of Science, Project ON 142039.

References

- [1] A. Nastasović, D. Jakovljević, Z. Sandić, D. Đorđević, Lj. Malović, S. Kljajević, J. Marković, A. Onjia, in: M. I. Barroso (Ed.) *Reactive and Functional Polymers Research Advances*, Nova Science Publishers, New York, 2008, 79-112.
- [2] A. Nastasović, D. Jakovljević, Z. Sandić, D. Đorđević, Lj. Suručić, L. Slavković-Beškoski, *Physical Chemistry 2008, 9th International Conference on Fundamental and Applied Aspects of Physical Chemistry*, Proceedings, Belgrade 2008, 582-584.
- [3] S. Jovanović, A. Nastasović, N. Jovanović, K. Jeremić, *Mater. Sci. Forum*, 1996, **214**, 155-162.
- [4] P. K. Malik, *J. Hazard. Mater. B*, 2004, **113**, 81-88.
- [5] A. Nastasović, Z. Sandić, Lj. Suručić, D. Maksin, D. Jakovljević, Onjia, J. *Haz. Mat.*, 2009, **171**, 153-159.

HIGH SELECTIVITY'S IN CATALYSED ASYMMETRIC HYDROGEN TRANSFER ON KETONES

N. Pannetier¹, J.-B. Sortais¹, L. Barloy¹, H. de Vries²,
M. Pfeffer¹ and C. Sirlin¹

¹Institut de chimie UMR7177CNRS/Université de Strasbourg (France)

²DSM research, Life sciences Geleen (The Netherlands)

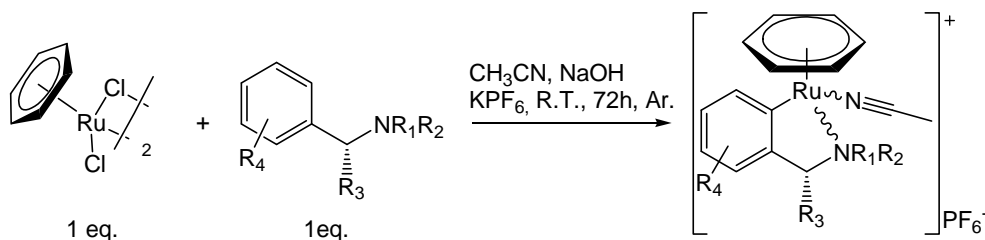
(sirlin@unistra.fr)

Abstract

High selectivity's are displayed in the asymmetric hydrogen transfer reaction on secondary aryl-alkyl carbonyl compounds catalysed by piano-stool bis-(phenyl-ethyl) amine complexes of ruthenium (II).

Introduction

An improved method for realising the bonding of ruthenium to N-molecules has been established for some years. [1] It has been extended to rhodium and iridium complexes of various benzyl amine frameworks.



On the other site, among many catalytic applications of ruthenium (II) in organic synthesis, asymmetric hydrogen transfer [2,3] has become very popular. It is indeed a very powerful tool in asymmetric synthesis as it allows formation of new stereo-centres in a great variety of organic substrates useful in fine chemistry. The method has many advantages compared to alternative ways that are: i) use of safety and low-cost reducer ii) operational simplicity.

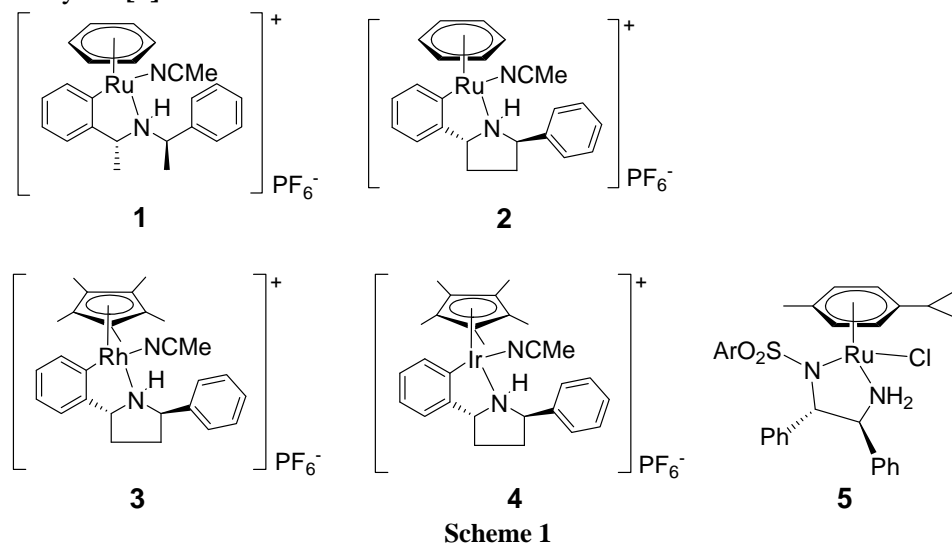
In this paper we would like to present selectivity's displayed by ruthenium catalysts on secondary aryl-alkyl carbonyl compounds.

Experimental

10 μmol catalyst was dissolved in 10 mL *i*-PrOH under Ar. 1 mmol substrate was added, followed by 50 μmol *t*-BuOK. The reaction was monitored by GC. After 3 hours the crude product was filtered over SiO₂ using Et₂O as eluent. Conversions and ee were determined by GC on chiral capillary column (Chiraldex β -PM, 50 m X 0.25 mm).

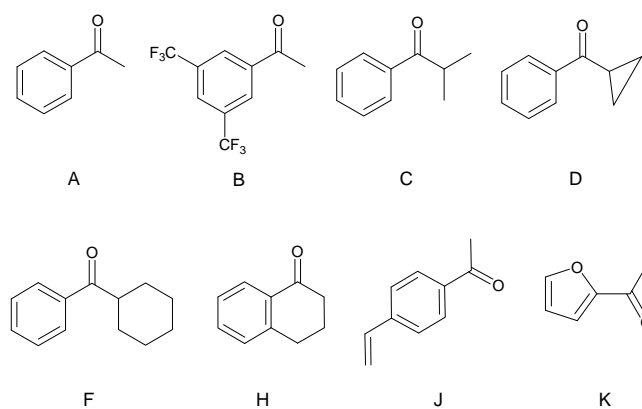
Results and Discussion

A library of metal-organic compounds derived from complexes of ruthenium (II), rhodium (III) and iridium (III) with asymmetric secondary amines of C_2 symmetry [4] has been set up as catalysts for AHT on a library of primary and secondary aryl-alkyl carbonyl compounds. The most relevant members of the libraries are schematised here (scheme 1&2). Comparison is made with Noyori's catalyst **5** [5].



Scheme 1

Ruthenium complex **1** is built on bis-(phenyl-ethyl) amine ligand; ruthenium **2**, rhodium **3** and iridium **4** complexes are built on bis-(phenyl pyrrolidine) ligand.



Scheme 2

Substrates **A**, **H**, **J**, **K** are primary aryl-alkyl ketones, substrates **C**, **D**, **F** are secondary aryl-alkyl carbonyl compounds.

The results obtained in the experiences of hydrogen transfer from methyl-ethanol to aryl-alkyl carbonyl compounds are gathered in Table 1.

Catalysts **2-4** present for primary aryl-alkyl carbonyl substrates **A, H** conversions and enantiomeric excesses comparable to Noyori's catalyst **5**. On the other hand catalyst **1** is more efficient for secondary aryl-alkyl carbonyl substrates **C, D, F**.

Table 1: Asymmetric hydrogen transfers on aryl-alkyl carbonyl compounds. (% of conversion, % ee). Conditions: at RT [substrate 10^{-1} M]:[catalyst]:[tBuOK] = 100 : 1 : 5 in iPrOH.

	1 (%)	ee (%)	2 (%)	ee (%)	3 (%)	ee (%)	4 (%)	ee (%)	5 (%)	ee (%)
A	96	77	92	89	96	89	24	89	95	97
C	97	98	95	48	75	75	38	74	22	84
D	32	89	18	45	32	36	5	31	3	-
F	97	98	74	48	88	85	58	81	1	-
H			57	96	56	91	39	96	65	97
J	75	82	91	86	81	93	91	85		
K	95	68	86	92	94	89	37	89		

Conclusion

The selectivity's obtained in the reaction between bis-(phenyl) pyrrolidine complexes and primary aryl-alkyl carbonyl compounds fit the results obtained by Noyori's team. In contrast high selectivity is observed for the hydrogen transfer on secondary aryl-alkyl carbonyl compounds catalysed by bis-(phenyl ethyl) amine complexes.

References

- [1] S. Fernandez, M. Pfeffer, V. Ritleng, C. Sirlin *Organometallics* **1999**, **18**, 2390-4.
- [2] [http:// www.kanto.com.tw/chinese/catalysis/catalysis_1.htm](http://www.kanto.com.tw/chinese/catalysis/catalysis_1.htm)
- [3] K. Nakamura and T. Matsuda *J. Org. Chem.*, **1998**, 8957-64.
- [4] a) J. B. Sortais, N. Pannetier, A. Holuigue, L. Barloy, C. Sirlin, M. Pfeffer, N. Kyritsakas *Organometallics* **2007**, **26**, 1856-67; b) J. B. Sortais, N. Pannetier, N. Clement, L. Barloy, C. Sirlin, M. Pfeffer, N. Kyritsakas *Organometallics*, **2007**, **26**, 1868-74.
- [5] a) S. Hashiguchi, A. Fujii, T. Ikariya, R. Noyori *J. Am. Chem. Soc.*, **1995**, **117**, 7562-3; b) R. Noyori, S. Hashiguchi, *Acc. Chem. Res.* **1997**, **30**, 97-102.

MOLECULAR ORBITAL INVESTIGATION OF POSSIBLE MECHANISTIC PATHS IN REACTION OF CYCLOHEXANONE WITH BROMOFORM

V. D. Vitnik¹, Ž. J. Vitnik² and I. O. Juranić²

¹ ICTM Center for Chemistry, Njegoševa 12, Belgrade, Serbia

² Faculty of Chemistry, University of Belgrade, Studentski trg 12-16, Belgrade, Serbia

Abstract

The extensive calculations were done to elucidate the mechanism of formation dibromoepoxide from cyclohexanone and bromoform. In this reaction, the formation of dihaloepoxide **2** is postulated as a key step that determines the distribution and stereochemistry of products. Every reaction scheme involves epoxide as a key intermediate. Two reaction mechanisms were investigated: the addition of tribromomethyl carbanion to carbonyl group of ketone and the addition of dibromocarbene to the same (C=O) group. The mechanisms for these two reactions have been theoretically studied using a semi-empirical MNDO-PM3 method. The calculations showed that both mechanisms are possible and exothermic.

Introduction

Ring opening nucleophilic reactions of dihaloepoxides are important because of the large number of biologically active compounds affordable through these reactions [1, 2]. One-pot reactions of aldehydes and ketones with chloroform, bromoform, or iodoform are particularly attractive [3, 4]. In these reactions, the intermediate dihaloepoxides could not be isolated but, nevertheless, they are considered a key factor in the shaping of products. The formation of intermediate dihaloepoxides was proposed in 1940 by Jacobs [5] and was widely accepted by other investigators [3, 4]. Whether the reaction is a free-radical one involving carbene intermediate, or is ionic one involving trihalocarbinol, the formation of dihaloepoxide is postulated as a key step in determining the distribution and stereochemistry of products. Many investigators have studied the reactions of haloform compounds with aldehydes and ketones, both experimentally and computationally [6, 7, 8]. We have carried out extensive calculations on a model system, cyclohexanone– bromoform. We chose this model because of the many experimental data available for it. Most of them are obtained in the course of the optimization of the reaction in order to improve the yield [6]. An additional asset is a relative simplicity of the system, which is lacking the stereodiversity, and has a very low number of conformers.

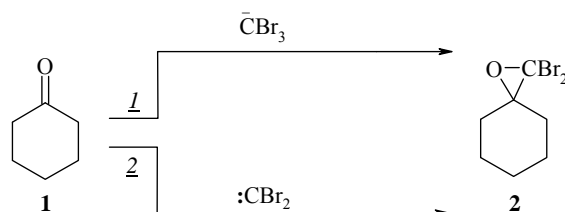
Computational Details

In this work, the MNDO–PM3 method, which is known to be highly reliable for investigating the molecular properties of molecules, ions, and zwitterions, was used. The MOPAC program package, version 7.01, was used. The initial structures

of the compounds were generated by PC MODEL, version 4.0 (Serrene Software Box, Bloomington, IN, USA), which involves an MMX force field and were saved as MOPAC input files for MNDO-PM3 semi-empirical calculations [9]. The geometries of all molecular species, corresponding to the energy minima in vacuum, were optimized by the PM3 method. The transition states for all reactions were explored using corresponding MOPAC facilities (TS, SADDLE).

Results and Discussion

Mechanistic consideration of the reactions of addition of tribromomethyl carbanion and dibromocarbene on carbonyl are exemplified in Scheme 1, using cyclohexanone as the substrate.



Scheme 1. Mechanistic pathways for the studied reaction.

The epoxide **2** could be obtained, in principle, by two different reaction mechanisms. The results provide unambiguous evidence of the asymmetric approach of carbanion or carbene to the carbonyl group.

Potential energy surface (PES) for ionic reaction 1 was obtained by systematic variation of distance between carbonyl bond and tribromomethyl carbanion. Corresponding energy changes referring to critical points on PES are given in Table 1. Two reaction paths are possible: approach of carbanion to carbonyl group targeting carbon (1a) and targeting oxygen (1b). Our calculations showed that the ionic mechanism has activation enthalpies 21.068 and 27.497 kcal/mol, for pathway 1a and pathway 1b, respectively.

Computational analysis of the mechanism 2 was carried out by systematic variation of distance between centre of carbonyl bond and the dibromocarbene. In carbene mechanism the favored attack of dibromocarbene is to oxygen side of carbonyl group. The activation enthalpy for this reaction is 0.338 kcal/mol.

Table 1. Reaction and activation enthalpies, (ΔH_r and ΔH^\ddagger), for various reaction pathways calculated by semi-empirical MNDO-PM3 method.

	ΔH_r (kcal/mol)			ΔH^\ddagger (kcal/mol)		
	Step 1*	Step 2*		Step 1*	Step 2*	
<i>Ia</i>	-14.980	26.098	11.119	16.766	6.088	21.068
<i>Ib</i>	-15.910	27.029	11.119	23.451	11.587	27.497
2	26.136	31.701	57.837	0.338	17.376	0.338

* Step 1 denotes transformation of reactants to intermediate; Step 2 denotes transformation of intermediate to products. Third and sixth column contain overall reaction/activation enthalpies

From Table 1 can be seen that the activation enthalpy for pathway 1 is much higher than that for the pathway 2.

Conclusions

The computational study of the formation of spiro-epoxy intermediate **2** in the reaction of cyclohexanone **1** with bromoform, in alkaline medium, confirmed the reliability of ionic mechanism. It renders these dihaloepoxides as well established intermediates in reaction of ketones with bromoform. Two possible mechanisms for the formation of the spiro-dibromoepoxy intermediate are studied. The calculations showed that both mechanisms are exothermic and possible, and reaction conditions may affect them in a large extent. Ionic mechanism is preferred in polar solvents and alkaline medium.

Acknowledgments

This work has been financially supported by Ministry of Science and Environmental Protection, Republic of Serbia, under Grant No. 142010.

References

- [1] W. Reeve, L. W. Fine, J. Org. Chem., 1964, **29**, 1148-1150.
- [2] J. Palaty, F. S. Abbott, J. Med. Chem., 1995, **38**, 3398-3406.
- [3] A. Merz, Synthesis, 1974, **10**, 724-725.
- [4] E. J. Corey, J. O. Link, J. Am. Chem. Soc., 1992, **114**, 1906-1908.
- [5] R. Jacob, Bull. Soc. Chim., 1940, **7**, 581-587.
- [6] V. D. Vitnik, M. D. Ivanović, Ž. J. Vitnik, J. B. Đorđević, Ž. S. Žižak, Z. D. Juranić, I. O. Juranić, Synt. Comm., 2009, **39** (8), 1457-1471.
- [7] J. R. Jr. Pliego, W. B. De Almeida, J. Chem. Phys., 1997, **106**, 3582-3587.
- [8] Ž. J. Vitnik, V. D. Kiricojević, M. D. Ivanović, I. O. Juranić, Int. J. Quant. Chem., 2006, **106** (6), 1323-1329.

DECOLOURISATION OF TEXTILE AZO DYE REACTIVE ORANGE 16 WITH UV/H₂O₂ SYSTEM: EFFECT OF pH

J. Mitrović*, M. Radović, T. Anđelković, M. Purenović and A. Bojić

Faculty of Science and Mathematics, Višegradska 33, 18000 Niš, Serbia
**jelenam81@gmail.com*

Abstract

Photochemical degradation of the textile azo dye C.I. Reactive Orange 16 (RO16) has been carried out using UVC light, $\lambda = 254$ nm, in the presence of H₂O₂. The UV treatment has been done in batch mode UV photoreactor, with two low pressure UV mercury lamps. Initial concentration of RO16 was 50 mg dm⁻³. The change in concentration of the azo dye RO16 was followed by UV/VIS spectrophotometric measurement of absorbance at 490 nm. Complete decolourisation was achieved after only 20 min of irradiation. The highest decolourisation rates were observed at pH range between 3 and 7 under the given experimental conditions.

Introduction

Azo dyes are the largest group of colorants, with respect to both number and production volume. This compound contains one or more azo groups (-N=N-) mostly linked to benzene or naphthalene rings [1].

Azo dyes have a very broad application field. They are used for dyeing of synthetic and natural textile fibres, plastics, leather, paper, cosmetics and food, for printing purposes and in drugs. It is estimated that 15% of total production of colorants may be released to wastewater during synthesis and processing operation [1]. Dyes in wastewaters cause aesthetic problems, absorb and scatter sunlight and thus affect aquatic ecosystem. Another reason for the open concern about the azo colorants release in environmental is a risk of exposure to potentially carcinogenic aromatic amines, which are result of metabolic cleavage of azo linkage.

Recently, Advance Oxidation Processes (AOPs) has been a technique which is used successfully for complete mineralization of organic pollutants in water. AOPs involve different systems, such as H₂O₂/UV, O₃/UV, H₂O₂/O₃/UV, TiO₂/UV. This system imply the generation of •OH radicals, which have oxidation potential 2.8 V, powerful oxidizing species able to oxidize a variety of wastewater organic contaminants [2].

Some of advantages of use UV/H₂O₂ in comparison to other systems are no sludge formation, no salt formation, considerably safe and easy operation, reduction of chemical oxygen demand (COD), short reaction time [3]. Reaction of

hydroxyl radicals with organic contaminant includes three different mechanisms: hydrogen abstraction, electrophilic addition and electron transfer [4].

The aim of the present work is to investigate degree of decolourisation of textile azo dye C. I. Reactive Orange 16 (RO16) with UV radiation in the presence of H₂O₂. Decolourisation rate of this process depend of many parameters, such as pH, concentration of azo dye, concentration of H₂O₂, UV light intensity. pH is one of the most important parameters, since the coloured effluent from textile industry can be at different pHs. The purpose of this study is to determinate optimal pH value for complete decolourisation of RO16.

Results and discussion

The influence of pH on the rate of decolourisation of the azo dye by UV/H₂O₂ process was investigated at six different pH values 2.0, 3.0, 5.0, 7.0, 9.0 and 10.0. The decolourisation rate constants of RO16 as a function of initial solution pH are shown in Fig 1. As we can see decolourisation rate increases from pH 2 to 3, and than remains almost constant up to pH 7. After this value, we have observed a decrease of k_0 as the pH increases to 10.

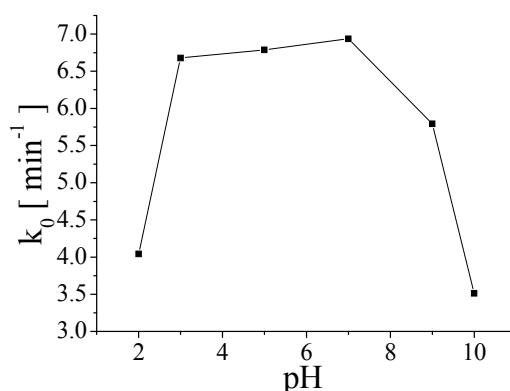


Fig.1. Effect of pH on the rate of decolourisation of the RO16 solutions by UV/H₂O₂ process. [RO16]₀ = 50.0 mg dm⁻³, [H₂O₂]₀ = 25.0 mmol dm⁻³, UV light intensity was 730 μW cm⁻².

One of the reasons of this behavior is that the pH was made more acidic by addition of hydrochloric acid. In this way increased amounts of conjugated base were added to the solution. The anion Cl⁻ is able to react with hydroxyl radicals leading to inorganic radical ions. These inorganic radical anions show a much lower reactivity than •OH, so that they do not take part in the dye decolourisation. There is also a drastic competition between the dye and the anions with respect to •OH.



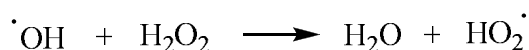
Decrease of reaction rate at pH higher than 7 is due to the oxidative species. At alkaline pH, the conjugate base of H₂O₂ increases.



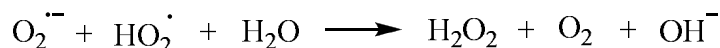
This anion reacts with a nondissociated molecule of H₂O₂ which leads to dioxygen and water, instead of producing hydroxyl radicals under UV radiation. Therefore, the instantaneous concentration of [•]OH is lower than expected.



Furthermore, the deactivation of [•]OH is more important when the pH of the solution is high. The reaction of [•]OH with HO₂⁻ is approximately 100 times faster than its reaction with H₂O₂ [5].



The reactivity of O₂^{•-} and HO₂[•] with organic pollutants is very low. They preferentially disproportionate producing some hydrogen peroxide and dioxygen.



Conclusion

It can be concluded that the UV/H₂O₂ system can be efficiently used for the decolourisation of RO16. Complete destruction of the dye was succeeded in the first 20 min of irradiation. In the pH range between 3 and 7, the rate of decolourisation is improved.

References

- [1] H. Zollinger, Color Chemistry: Syntheses, Properties and Applications of Organic Dyes and Pigments, Wiley, Germany, 2003.
- [2] Y. M. Slokar, Dyes and Pigments, 1998, **37**, 335-356.
- [3] M. Marechal, Dyes and Pigments, 1997, **33**, 281-298.
- [4] O. Lergini, Chemical Reviews, 1993, **93**, 671-698.
- [5] A. Aleboye, Dyes and pigments, 2005, **66**, 129-134.

SPECTROPHOTOMETRIC STUDY OF GALLIC ACID AUTOXIDATION IN ALKALINE AQUEOUS SOLUTIONS

G. M. Nikolić¹, A. M. Veselinović¹, R. S. Nikolić², Ž. J. Mitić¹ and J. V. Živković¹

¹*Faculty of Medicine, Bulevar dr Zorana Djindjića 81, 18000 Niš, Serbia
e-mail: goranhem@yahoo.com*

²*Faculty of Sciences and Mathematics, Višegradska 33, 18000 Niš, Serbia*

Abstract

Autoxidation of gallic acid (GA) in alkaline aqueous solution was studied by UV/Vis spectrophotometry. After initial changes in the UV/Vis spectra due to the deprotonation of GA the equilibrium between two absorbing species was established as confirmed with the graphical analysis of the spectra by the matrix method. Prolonged autoxidation process gave UV/Vis spectra corresponding to a more complex system. The results of this study may help further understanding of the GA behavior in various systems, which is important because of its presence in various foods, and its possible physiological role in living cells.

Introduction

Oxidation of plant phenolic compounds has been studied for many years due to its presence in various foods and their possible physiological role in living cells (mainly as antioxidants). Special attention was given to the autoxidation of GA in alkaline aqueous solutions because its possible transformations during the food processing [1] and because it can serve as a model for similar reactions in various foods and beverages [2]. Recent studies even indicated that vascular pro-oxidant effects in rat aorta are connected with the autoxidation of GA [3].

In this paper we present the results of spectrophotometric study of GA autoxidation in alkaline aqueous solutions with the graphical analysis of the spectra by matrix method which may help to further clarify the mechanism of this process.

Experimental

All chemicals used in this study were of analytical (p.a.) grade. GA (3,4,5-trihydroxybenzoic acid) (Fluka, Germany) was used without additional purification because its purity was proved to be satisfactory by HPLC. Doubly distilled, air saturated, water was used and GA solutions with concentration of 0.3 mmol dm^{-3} were prepared just prior the use by dissolving exactly weighted amount of GA. NaOH solution with concentration of 0.01 mol dm^{-3} was used for pH adjustment. Evolution 60 UV/Vis spectrophotometer (Thermo Scientific, USA) with 1.0 cm quartz cells was employed for recording spectra.

Results and Discussion

Autoxidation of GA in neutral or weakly alkaline aqueous solutions is very slow [1], so we studied this process at pH 10. The UV/Vis spectra of GA in aqueous solution at pH 10 after various time intervals are shown in Figure 1.

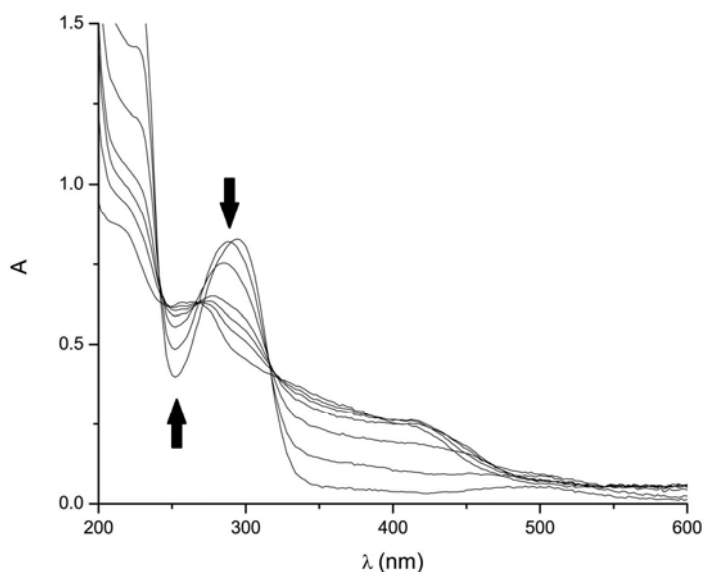


Fig.1. UV/Vis spectra of GA in aqueous solution at pH 10 after various time intervals; immediately after NaOH addition, after 30 s, 1 min, 2 min, 5 min, 15 min, 25 min, and 60 min, respectively.

During the period of 1 hour there was continuous increase of absorbance around 250 nm and continuous absorbance decrease around 300 nm, as indicated by the arrows in the Figure 1. At the same time new absorption bands/shoulders at around 420 nm and 500 nm appeared. While initial changes of UV/Vis spectra may be attributed to the deprotonation of GA, the spectra recorded in the time interval after 1 min up to 45 min after the addition of NaOH displayed three well defined isobestic points at 242 nm, 266 nm, and 316 nm, respectively. The presence of isobestic points suggests that there was equilibrium between two absorbing species in solution during that time interval and this was confirmed with graphical analysis by the matrix method of Coleman, Varga, and Mastin [4] which is capable of identifying such an equilibrium even in the cases where no isobestic points appear in the spectra [5]. The results of the graphical analysis of UV/Vis spectra for the time interval in which isobestic points appeared are shown in Figure 2.

Although the graphical analysis is not unambiguous, it revealed that for three absorbing species there was no fit at all, but for two absorbing species it showed good agreement. Therefore, it was concluded that after initial 1 min interval there was equilibrium of two absorbing species. This equilibrium existed in the solution of GA at pH 10 up to at least 45 min. It is possible that this equilibrium is concerned with the dimer formed by the oxidative coupling of two GA units as indicated by the ESR study of the oxidation of GA at pH 10-11 [6]. This would be in agreement with the observed appearance of new absorption bands/shoulders in UV/Vis spectra at higher wavelengths.

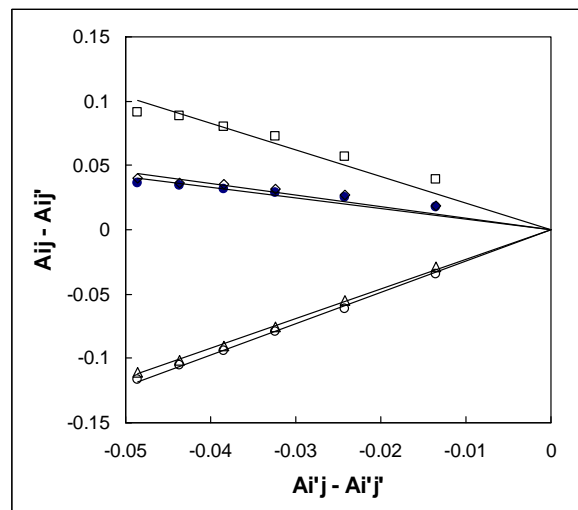


Fig.2. Graphical analysis by the matrix method of UV/Vis spectra of alkaline GA solution. The test for two absorbing species with restrictions was applied, being $i' = 240 \text{ nm}$ and $j' = \text{first scan at } 90 \text{ s}$.

The spectra recorded at 60 min and after indicated some additional changes in the GA solution corresponding to the formation of more complex system.

Conclusion

We performed a spectrophotometric study of autoxidation of gallic acid (GA) in alkaline aqueous solution. Graphical analysis by matrix method of UV/Vis spectra recorded at various time intervals after initial deprotonation of GA showed a good fit for two absorbing species in solution. Prolonged autoxidation of GA gave UV/Vis spectra corresponding to a more complex system. It is suggested that these results could be used to further clarify the mechanisms of GA autoxidation.

References

- [1] M. Friedman, H. S. Jürgens, *J. Agric. Food. Chem.*, 2000, **48**, 2101-2110.
- [2] V. Tulyathan, R. B. Boulton, V. L. Singleton, *J. Agric. Food. Chem.*, 1989, **37**, 844-849.
- [3] J. Gil-Longo, C. Gozález-Vázquez, *J. Nutr. Biochem.*, 2010, **21**, 304-309.
- [4] J. S. Coleman, L. P. Varga, S. H. Mastin, *Inorg. Chem.*, 1970, **9**, 1015-1020.
- [5] G. M. Nikolić, P. I. Premović, R. S. Nikolić, *Spectrosc. Lett.*, 1998, **31**, 327-333.
- [6] T. Oniki, U. Takahama, *J. Wood Sci.*, 2004, **50**, 545-547.

D

Nonlinear Dynamics

CLOCK REACTIONS

Guy Schmitz

Faculty of Applied Sciences, Université Libre de Bruxelles, CP165/63, Av. F.

Roosevelt 50, 1050 Brussels, Belgium. E-mail: gschmitz@ulb.ac.be

Abstract

Clock behaviours, resulting from transitions between different dynamical states, are observed in many different chemical systems. Some examples are discussed and compared: the Landolt reaction, the oxidation of Ce(III) by bromate, the reduction of iodate by hydrogen peroxide and the oxidation of iodine by hydrogen peroxide in the absence of iodate. In the last case, the bell rings when a stable steady state suddenly disappears.

Classical iodine clock reactions

The hydrogen peroxide-iodide reaction is a simple example of classical clock reaction. When a solution containing potassium iodide, sodium thiosulfate and starch is added to an acidic solution of hydrogen peroxide the reactions are:

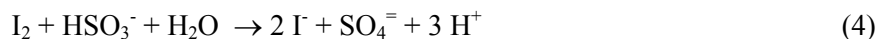


At the beginning, the very fast reaction (2) consumes the triiodide ions as fast as they are produced by reaction (1) and the solution remains colorless. If the initial thiosulfate concentration $[\text{S}_2\text{O}_3^{2-}]_0$ is less than two times the hydrogen peroxide concentration $[\text{H}_2\text{O}_2]_0$, the thiosulfate ends up being totally consumed. The triiodide ions are no longer consumed by reaction (2) and the blue color of their complex with starch appears. The induction time depends on the ratio $[\text{S}_2\text{O}_3^{2-}]_0/[\text{H}_2\text{O}_2]_0$ and on the rate of reaction (1). Increasing the initial concentrations of H_2O_2 , I^- or H^+ decreases the induction time.

This example illustrates a first kind of clock reactions. The induction period ends up when a reactant has been totally consumed. This is also the case of the most famous clock reaction, the Landolt reaction [1-4]. In a mixture of a potassium iodate solution and a slightly acidic solution of sodium bisulfite the first reaction is (3).



The produced iodine reacts very quickly with bisulfite ions.



After a while, so produced iodide reacts with iodate following the classical Dushman reaction (5).



As long as bisulfite remains in the solution, the iodine is reduced by reaction (4) and the net reaction is (6).



Thus, the concentration of the iodide ions increases and, consequently, the rate of reaction (5) increases. Reaction (6) is autocatalytic. Moreover, in non-buffered solution, the acidity increases so that the reaction is doubly catalytic or super catalytic. The rate of iodine formation is the largest at the end of the induction period making the Landolt reaction particularly spectacular. When all the bisulfite has reacted, the iodine appearance, or its blue complex with starch, is not progressive as in the other iodine clock reactions but very abrupt. Beautiful demonstrations can be found on the internet but the detailed mechanisms of these reactions are still not completely understood.

The bromate-cerous reaction

Instead of being controlled by the disappearance of some reactant, the induction time of a clock reaction can be controlled by the appearance of some intermediate compound. This is the case of the bromate-cerous reaction. The global reaction is (7) that is the inorganic part of the oscillating Belousov-Zhabotinskii reaction [5, 6]. Figure 1 shows an example of Ce(IV) production versus time.

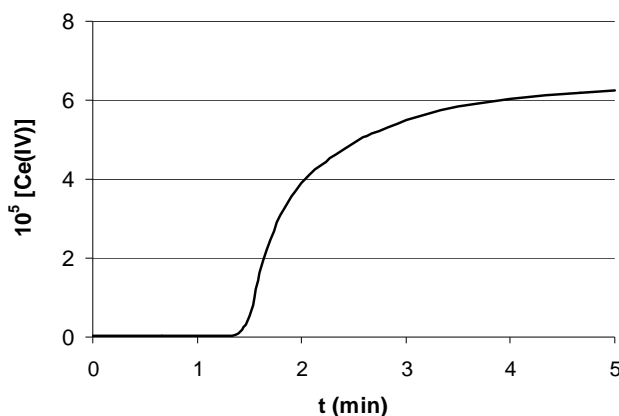
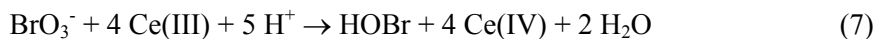


Fig.1. Time evolution of the Ce(IV) concentration. Initial concentrations: $[\text{BrO}_3^-]_0 = 5 \times 10^{-2}$, $[\text{Ce(III)}]_0 = 1.68 \times 10^{-4}$, $[\text{H}_2\text{SO}_4] = 0.5 \text{ M}$.

Different mechanisms were proposed to explain this behavior. The Field, Körös and Noyes (FKN) mechanism [7] includes the following steps.



The sum $2 \times (11) + 4 \times (12) + (13)$ gives the global reaction (7). Bromate does not react directly with Ce(III) but with HBrO₂ giving BrO₂[·] radicals in reaction (11) and these radicals oxidize Ce(III) in reaction (12). Thus, the rate of reaction (7) remains very small until some HBrO₂ has accumulated in the solution. The initial production of HBrO₂ is explained by the traces of bromide ions always present in bromate solutions giving reaction (8). One HBrO₂ giving two BrO₂[·] radicals in reaction (11) and these two radicals giving two HBrO₂ in reaction (12), the reaction is autocatalytic. At the end of the induction period, the rate of Ce(III) oxidation increases exponentially.

The KKN mechanism is widely accepted because it allows reproducing by numerical simulations a wide variety of experimental results especially the Belousov-Zhabotinskii oscillations and the oscillations of the bromate-cerous reaction in a CSTR [8-11]. However, the set of rate constants used for these simulations has changed with time and it is far from evident that all the successful simulations supporting this model could be obtained using a single set of rate constants. Very recently, the group of Belgrade has presented a new experimental study of the Belousov-Zhabotinskii oscillations and has shown that the FNK mechanism should be modified [12-13]. The inorganic part of the proposed model does not include reaction (14) and splits reaction (9) introducing Br₂O as an important intermediate compound in the organic part of the model.



Reaction (8) is neither elementary [14] and must be split into



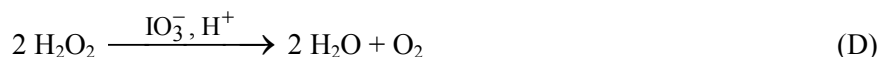
These reactions suggest an analogy with the well-known chlorine system. We have proposed [15] that BrO₂[·] is produced in a reaction similar to the reaction producing ClO₂[·] [16, 17] and that reaction (11) should be replaced with reaction (15).



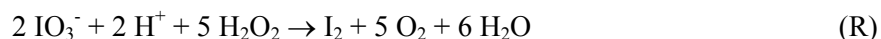
Reaction (15) leads also to an autocatalytic increase of the HBrO_2 and here too further kinetic studies are necessary.

Induction period of the Bray/Liebhafsky reaction

The oscillating Bray-Liebhafsky (BL) reaction [18] is the decomposition (D) of hydrogen peroxide catalyzed by iodate in acidic solutions.



Reaction (D) is the result of two reactions where hydrogen peroxide acts as a reducing (R) and as an oxidizing (O) agent. The sum of reactions (R) and (O) gives reaction (D).



When the rates of these two reactions are equal, the decomposition of hydrogen peroxide is monotonous. However, under some conditions, the reactions (R) and (O) dominate alternately resulting in a cascading consumption of hydrogen peroxide and an oscillatory evolution of the intermediates [5, 19-22]. The concentration of one of them, the iodide ions, can be followed easily using a selective ions electrode, whereas another one, the iodine, can be followed spectrophotometrically. Figure 2 gives an example of measured time evolution of iodide and iodine species [23].

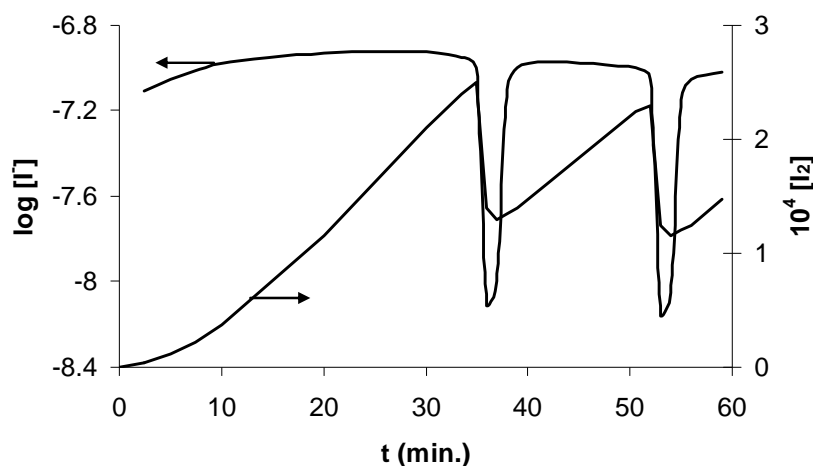


Fig.2. Time evolution of the iodide ions (left hand scale) and of the iodine (right hand scale) concentrations. $T = 60^\circ\text{C}$, $[\text{HClO}_4]_0 = 0.0625 \text{ M}$, $[\text{NaIO}_3]_0 = 0.10 \text{ M}$, $[\text{H}_2\text{O}_2]_0 = 0.050 \text{ M}$.

If we look only at the time evolution of the iodide ions concentration, we could conclude that the reaction begins with an induction period. However, if we look also at the time evolution of the iodine concentration we see that it should rather be called a pre-oscillatory period. It is similar to the following periods of increasing concentration of iodine and is longer only because the initial iodine concentration is zero. Comprehensive studies of this period were presented by S. Anić and Lj. Kolar-Anić [20(c, g, j, l, m)].

Introduction period of the iodine oxidation by hydrogen peroxide

In acidic solutions of iodine and hydrogen peroxide containing no iodate, the iodine concentration can remain nearly unchanged for long. Figure 3 shows an example of characteristic time evolution.

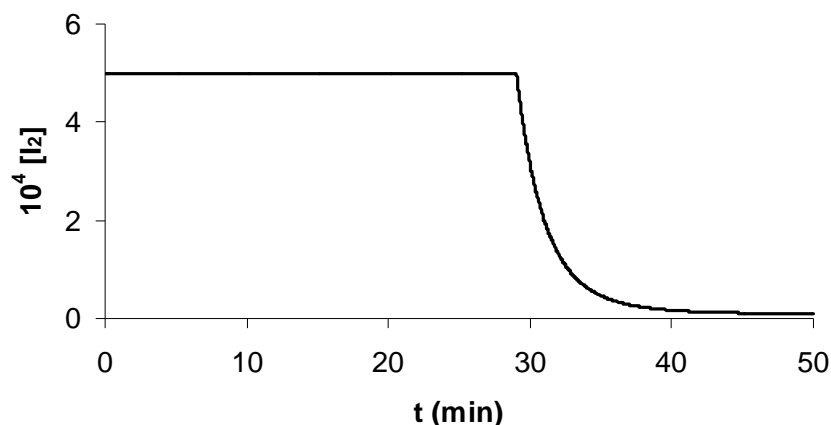


Fig.3. Time evolution of the iodine concentration in a solution containing no iodate initially. $[\text{HClO}_4]_0 = 0.07 \text{ mol/l}$, $[\text{H}_2\text{O}_2]_0 = 0.05 \text{ mol/l}$, $[\text{I}_2]_0 = 5 \times 10^{-4} \text{ mol/l}$. Curve calculated with the model discussed in reference 24.

An induction period is observed because there is no direct reaction between iodine and hydrogen peroxide. The writing of reaction (O) is misleading and the compound actually oxidized by hydrogen peroxide is IOH produced by the iodine hydrolysis (16).



Reaction (O) can start only if the IOH concentration is above a critical level [24] and, taking the equilibrium (16) into account, this means that it can start only if there are reactions removing the iodide ions sufficiently quickly. During the BL reaction, the removal of the iodide ions is provided by reactions of iodate. On the other hand, the model we have proposed to explain the BL oscillations foresees that a mixture of iodine and hydrogen peroxide without iodate reaches a different stable

steady state were the only global reaction is slow hydrogen peroxide decomposition. The iodine oxidation by hydrogen peroxide should never start. To explain that it finally starts, we must consider another reaction. Oxygen produced by the hydrogen peroxide decomposition can oxidize the iodide ions.



The direct reaction between iodide and oxygen is too slow and reaction (17) is the result of complex processes involving probably radicals. Its mechanism remains unclear but adding it to the model with an empirical rate law $r_{17} = k_{17} [\text{I}^-][\text{H}^+][\text{O}_2]$ explains the experimental results [24]. When the oxygen concentration reaches a critical level the mentioned stable steady state disappears and reaction (O) starts. This is a new kind of clock reaction: the bell rings when a steady state disappears.

Conclusion

In the classical clock reactions, the clock time is controlled by the disappearance of some reactant, like sulfite in the Landolt reaction, but there are other kinds of clock behaviors. Some examples are summarized in this paper. In the bromate-cerous reaction, the clock time is controlled by the autocatalytic increase of the concentration of an intermediate compound, HBrO_2 . In the BL reaction, the induction period observed if we measure only the iodide ions concentration appears differently if we measure also the iodine concentration and should rather be named pre-oscillatory period. In the iodine oxidation by hydrogen peroxide a new kind of clock behavior is observed: the clock bell rings when another reaction destroys the stable steady state of the hydrogen peroxide decomposition. Beyond these differences, all clock reactions involve transitions between different dynamical states. The experimental curves can be analyzed identifying time intervals with identical combination of first and second derivative signs of the time concentrations profiles and this trend analysis can give useful information about the involved dynamical state transitions [25].

References

- [1] H. Landolt, Ber. Dtsch. Chem. Ges., 1886, **19**, 1317.
- [2] V. Gaspar and K. Showalter, J. Amer. Chem. Soc., 1987, **109**, 4869.
- [3] E. Edblom, L. Gyorgyi, M. Orban and I. Epstein, J. Amer. Chem. Soc., 1987, **109**, 4876.
- [4] A. Horvath, J. Phys. Chem. A, 2008, **112**, 3935.
- [5] Oscillations and Traveling Waves in Chemical Systems, R.J. Field and M. Burger, ed., Wiley, New York, 1985.
- [6] S.K. Scott, Oscillations, Waves and Chaos in Chemical Kinetics, Oxford University Press, 1994.
- [7] R.J. Field, E. Körös and R.M. Noyes, J. Amer. Chem. Soc., 1972, **94**, 8649.
- [8] W. Geiseler, Ber. Bunsenges. Phys. Chem., 98, **286**, 721.

- [9] K. Bar-Eli and W. Geiseler, *J. Phys. Chem.*, 1983, **87**, 3769.
- [10] L. Gyorgy and R.J. Field, *J. Phys. Chem.*, 1992, **96**, 1220.
- [11] A.K. Dutt and M. Menzinger, *J. Chem. Phys.* 1999, **110**, 7591.
- [12] S. Blagojević, S. Anić, Ž. Čupić, N. Pejić and Lj. Kolar-Anić, *Phys. Chem. Chem. Phys.*, **10**, 2008, 6658.
- [13] S. Blagojević, S. Anić, Ž. Čupić, N. Pejić and Lj. Kolar-Anić, *Russian J. Phys. Chem. A*, 2009, **83**, 1496.
- [14] G. Schmitz, *Int. J. Chem. Kinet.*, 2007, **39**, 17.
- [15] G. Schmitz, *Can. J. Chem.*, 1976, **54**, 2628.
- [16] G. Gordon, R. Kieffer and D. Rosenblatt, *Prog. Inorg. Chem.*, 1972, **15**, 201.
- [17] R. Kieffer and G. Gordon, *Inorg. Chem.*, 1968, **7**, 235 and 239.
- [18] (a) W. C. Bray, *J. Am. Chem. Soc.*, 1921, **43**, 1262; W. C. Bray and H. A. Liebafsky, *J. Am. Chem. Soc.*, 1931, **53**, 38.
- [19] G. Schmitz, *J. Chim. Phys.*, 1987, **84**, 957.
- [20] (a) S. Anić, D. Mitić and Lj. Kolar-Anić, *J. Serb. Chem. Soc.*, 1985, **50**, 53; (b) S. Anić, D. Mitić, D. Veselinović and Lj. Kolar-Anić, *J. Serb. Chem. Soc.*, 1985, **50**, 529; (c) S. Anić and Lj. Kolar-Anić, *Ber. Bunsenges. Phys. Chem.*, 1986, **90**, 539; (d) S. Anić and Lj. Kolar-Anić, *Ber. Bunsenges. Phys. Chem.*, 1986, **90**, 1084; (e) S. Anić and Lj. Kolar-Anić, *Ber. Bunsenges. Phys. Chem.*, 1987, **91**, 1010; (f) S. Anić, D. Mitić and M. Čurčija, *J. Serb. Chem. Soc.*, 1987, **52**, 575; (g) S. Anić and Lj. Kolar-Anić, *J. Chem. Soc., Faraday Trans. 1*, 1988, **84**, 3413; (h) S. Anić, D. Stanisavljev, G. K. Belovljjev and Lj. Kolar-Anić, *Ber. Bunsenges. Phys. Chem.*, 1989, **93**, 488; (i) Lj. Kolar-Anić, D. Misljenović, D. Stanisavljev and S. Anić, *J. Phys. Chem.*, 1990, **94**, 8144; (j) Lj. Kolar-Anić, D. Stanisavljev, G. Krnajski Belovljjev, Ph. Peeters and S. Anić, *Computers Chem.*, 1990, **14**, 345; (k) S. Anić and Lj. Kolar-Anić, *J. Serb. Chem. Soc.*, 1996, **61**, 885; (l) S. Anić, Lj. Kolar-Anić and E. Körös, *React. Kinet. Catal. Lett.*, 1997, **61**, 111; (m) S. Anić, D. Stanisavljev, Ž. Čupić, M. Radenković, V. Vukojević and Lj. Kolar-Anić, *Science of Sintering*, 1998, **30**, 49.
- [21] G. Schmitz, Lj. Kolar-Anić, S. Anić and Ž. Čupić, *J. Phys. Chem. A*, 2008, **112**, 13452.
- [22] Lj. Kolar-Anić, Ž. Čupić, G. Schmitz and S. Anić, *Chem. Engineering Sci.*, 2010, **65**, 3718.
- [23] G. Schmitz, Thesis, Université Libre de Bruxelles, 1983.
- [24] G. Schmitz, *Phys. Chem. Chem. Phys.*, 2010, **12**, 6605.
- [25] Ž. Čupić, D. Lončarević, A. Ivanovic, P. Banković and S. Petrović, *Computers Chem. Eng.*, 2008, **32**, 1293 and references therein.

STOICHIOMETRIC NETWORKS: FROM REACTION ROUTES TO METABOLIC FLUXES AND BACKWARD

Ž. Čupić¹, V. Marković² and Lj. Kolar-Anić²

¹ *Institute of Chemistry, Technology and Metallurgy, University of Belgrade,
Department of Catalysis and Chemical Engineering,*

Njegoševa 12, 1100 Belgrade, Serbia (zcupic@nanosys.ihtm.bg.ac.rs)

² *Faculty of Physical Chemistry, University of Belgrade, Studentski trg 12-16,
11000 Belgrade, Serbia*

Abstract

Stoichiometric Network Analysis is a known method for analyzing complex reaction systems including biochemical ones. Historical background of the theory is briefly given, followed with fundamental statements of the method. Special attention is given to modern approaches in Stoichiometric Network Analysis and its most advantageous applications. Alternative approaches to the analysis of stoichiometric networks and most progressively developing research areas are also briefly discussed.

Historical Background

The idea to represent complex reactions or processes as stoichiometric networks, comes from chemical kinetics investigations published during sixties of the twentieth century. [1-4] Stoichiometric networks are used to denote interconnected reaction routes resulting in some stoichiometric expression characteristic for considered process. Critical concept of single reaction route was developed by Horiuti and Nakamura [4] in their analysis of heterogeneous catalysis at steady state. They defined the route as such combination of elementary reaction steps in one complex chemical reaction, obeying that as a result of their summation, no intermediary species occur either as a reactant or a product. Following the spirit of minimization, and simplification, they focused on identification of minimal set of independent reaction routes. Horiuti and Nakamura method of reaction routes was widely applied [5] in chemical kinetics and catalysis for many years before Stoichiometric Network Analysis (SNA) was invented by Bruce Clarke, [6, 7] and moreover, until today. [8]

Fundamentals of Stoichiometric Network Analysis

Matrix representation of stoichiometric relations between single steps in complex reaction networks is essential for the SNA theory. For this purpose the kinetic equations of any stoichiometric model, consisting of species X_i where $i = 1, \dots, n$, presented by the set of differential equations, would be written in the compact form $d[\mathbf{X}]/dt = \mathbf{S} \mathbf{r}$, where $d[\mathbf{X}]/dt$ is the time derivative of the concentration vector $[\mathbf{X}]$, \mathbf{r} the reaction rate vector and \mathbf{S} the matrix of the stoichiometric coefficients that can

be read directly from the model (stoichiometric matrix). The rates at a steady state r_{ss} are solutions of the relation $S r_{ss} = 0$. According to the SNA, [6, 7] whole process in a steady state can be presented as linear combination of several elementary reaction pathways with non-negative coefficients. These elementary reaction pathways are known in SNA as extreme currents E_i , although they have the same meaning as the previously invented [4] reaction routes. The extreme currents E_i are the components of the extreme current matrix E , whereas the current rates j_i are contributions of the extreme currents to reaction rates, and they are the components of the corresponding vector j . Having the matrix E , we can write the reaction rates at the steady state as linear combinations of the extreme current rates using the relation $r_{ss} = E j$. These equations imply the relations between the reaction rates at the steady state.

Clarke's research was from the very beginning, directed toward stability analysis of complex reaction networks, [9–12] leading him towards discovery of invariant topological properties of reaction networks, caused by the stoichiometric relations among single reaction steps. At first, Clarke was focused on these invariant topological properties and therefore he developed procedure to analyze network stability based on semi-directed graph construction (Figure 1).

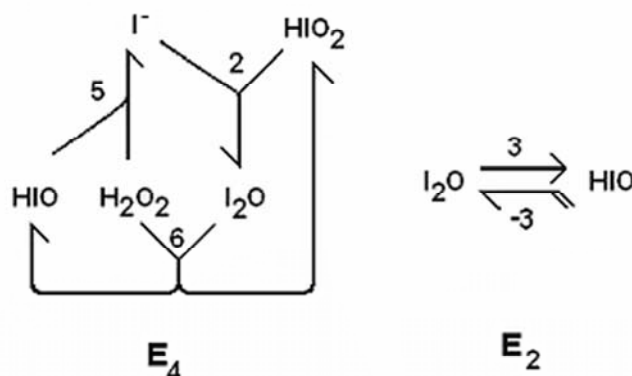
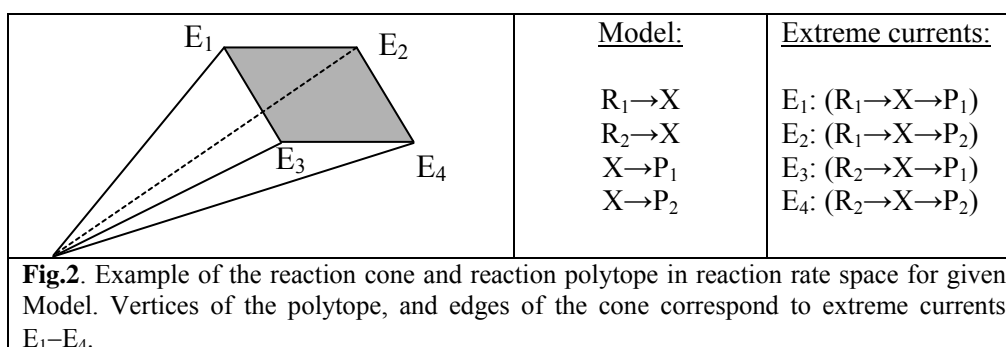


Fig.1. Example of semi-directed graphs for the most important extreme currents in the model of Bray-Liebhafsky oscillatory reaction in CSTR. Published in [13].

Clarke has underlined [7] that E plays a fundamental role in the theory of reaction networks, since stoichiometry is the most essential element of a reaction network, and since the matrix E is determined solely by stoichiometry. The SNA method, was evaluated in the stability analysis of many models of some classic chemical oscillators. [6, 14, 15]

The main difference between SNA and previous concept of Horiuti and Nakamura [4] lays in fact that in SNA, only positive contributions are used for all reactions in describing each steady state. On the other side, using only independent set of reaction routes, it is often necessary to assign negative contributions for some irreversible reactions. Thus, their reversibility is therefore forced, in despite of model assumptions. Hence, the complete set of steady states could be obtained with

linear combinations of Clarke's extreme currents, using only non-negative contributions. [16] The SNA made it possible by accounting for all irreducible sets of reaction steps, which could be combined, to result in an overall reaction without intermediary species on either side. These sets, named extreme currents can be interpreted geometrically as the edges (extreme points; see Figure 2) of the corresponding cone in the reaction rates space. (This is where extreme currents get their name from - Clarke was inspired by Kirchhoff's laws from electric current theory that also describes network properties of the object.) Due to conservation constraints, for any fixed initial conditions, reaction cone is being reduced to lower-dimensional polytope. This is the part of the reaction rate space in which, all the steady states can be found and extreme currents are represented with its vertices (Figure 2).



Most important advantage of SNA was recognized by the Clarke as possibility to determine if some reaction network could be unstable or not. Generally, the stability can be recognized by analyzing the dynamics of small concentration perturbations $\Delta[\mathbf{X}] = [\mathbf{X}] - [\mathbf{X}]_{ss}$ near a steady state $[\mathbf{X}]_{ss}$, given by the equation $d[\mathbf{X}]/dt = \mathbf{M}[\mathbf{X}]$ obtained by linearization of the general equation of motion about this steady state. Its stability depends on the sign of the real part of the eigenvalues of the Jacobian matrix \mathbf{M} given in the form

$$\mathbf{M} = \mathbf{S} (\text{diag } \mathbf{E} \mathbf{j}) \mathbf{K}^T (\text{diag } \mathbf{h}),$$

where \mathbf{K} is the matrix of the orders of reaction and \mathbf{K}^T is its transpose, $\text{diag } \mathbf{h}$ is a diagonal matrix whose elements are the reciprocals of steady state concentrations and $\text{diag } \mathbf{E} \mathbf{j}$ is a diagonal matrix whose elements are nothing else, but the reaction rates at the steady state, as already given above. The matrix \mathbf{M} , written as function of the SNA parameters has particular advantages for the stability analysis since the parameters j_i and h_i are non-negative. The steady state stability is determined by the eigenvalues of \mathbf{M} , which are the roots λ of the characteristic polynomial

$$|\lambda \mathbf{I} - \mathbf{M}| = \lambda^n + \alpha_1 \lambda^{n-1} + \alpha_2 \lambda^{n-2} + \dots + \alpha_n = 0$$

where n is the number of independent intermediate compounds and the α_i the sums of all diagonal minors of dimensions i of matrix \mathbf{M} multiplied by the product of the corresponding h_i values. Each diagonal minor of the matrix \mathbf{M} , as the determinant of square matrix having dimension i , can be formed of any combinations of i independent intermediate species. In one α_i the number of minors is equal to number of different combinations of i intermediates. It has been shown that the SNA allows to approximate the Routh-Hurwitz criteria with a much simpler condition: the steady state is unstable if any α_i is negative (α approximation) [6, 17-19]. Besides, since $\text{diag } \mathbf{h}$ introduces only scaling factors, it is useful to define

$$\mathbf{V}(\mathbf{j}) = -\mathbf{S}(\text{diag } \mathbf{Ej})\mathbf{K}^t$$

giving $\mathbf{M} = -\mathbf{V}(\mathbf{j}) (\text{diag } \mathbf{h})$. As any α_i is the sum of minors of $\mathbf{V}(\mathbf{j})$ with dimension i multiplied by the product of the corresponding h_i values, we look for a negative diagonal minors of $\mathbf{V}(\mathbf{j})$, only. If we find negative minors in one α_i we ask if the sum of negative terms can be larger than the sum of positive terms in same α_i . Clarke developed so called exponential approximation to identify dominant terms in polynomial expressions. However, due to several applied approximations, his approach often gives bifurcation diagrams with rather low accuracy.

Besides, Clarke also successfully applied SNA to the analysis of reaction networks with finite attractor regions, [20], reaction network sensitivity analysis, [21], and also analysis of bistability, [22], mixed-mode oscillations, [23], and chaos [24] in chemical reaction networks.

Modern approaches

Since 1991 studies of oscillatory reactions [25-29] that produced a mechanistic classification of such systems on the basis of SNA have been published. All reaction species involved in oscillatory reactions are divided in essential and nonessential ones. If the concentration of one nonessential species is held constant, the oscillations of the other species would not stop. However, there upon holding concentration of one essential species constant, all oscillations stop. In terms of these essential species all known oscillatory reactions can be classified into two categories, one with three subcategories, and the other with two subcategories. For each subcategory there is a skeleton of elementary reaction steps. The experiments were designed which allow the determination of the skeleton reaction mechanism of a given oscillatory reaction.

Hynne *et al* combined quenching data with extreme current representation of stationary states, for systematic analysis and optimization of models of oscillatory chemical reactions at a Hopf bifurcation. [30, 31] The method compares Hopf bifurcations with experimental (quenching) data at one or more operating points. Also, the graphical method of testing the compatibility of a reaction network with a set of experimental quenching data was developed to select possible networks for systematic optimization. The method exploits the eigenvector

property of quenching amplitudes, and it is kind of generalization of the Wei and Prater method, for the case of non-linear dynamics in chemical reactions [3].

An biological application of SNA [32-34] permits an understanding of tumor induction, carcinogenesis, and chemotherapy. The essential role of autocatalysis in biology and the drawbacks of either controlled or spontaneous cell division were used to understand crucial aspects of carcinogenesis and chemotherapy because SNA describes and predicts effects of autocatalysis, including phase effects that may be due to some kind of intervention. [32-34]

In Belgrade school of nonlinear dynamics, the SNA was used in several branches of investigation. High influence on this research was done buy G. Schmitz with his own contribution, [35] but also as a coworker and in private communication. The role of several additional reactions was studied [36-38] by SNA method applied on the variants of model of Bray-Liebhfasky reaction proposed initially by G. Schmitz. Following Clarke's results on topologically invariant reaction networks, contraction of complex models was done in few occasions with expected success, while preserving the oscillating dynamics of original model. [39, 40] Various dynamical states were characterized by SNA method in the model of Bray-Liebhfasky oscillatory reaction, including relaxation oscillations over the nullclines. [13, 41, 42]

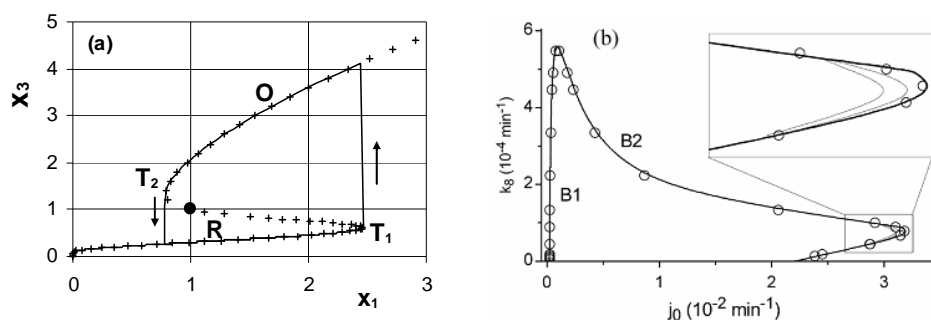


Fig.3. (a) Projections of the s-form trajectory and the slow manifold (+ + +) onto the x_3 - x_1 plane, where x_3 and x_1 are dimensionless iodine and iodide concentrations of the BL reaction model for batch reactor. [42] (b) The instability region for the BL reaction model in CSTR reactor obtained by numerical simulations (–) and by applying the instability condition (solid line) as a function of the value of the flow rate j_0 and rate constant k_8 . [13] The transition from the stable steady state to the limit cycle is given at the left side (B1), whereas the opposite transition is presented at the right side (B2). The mixed-mode oscillations and chaotic states are found only in a very narrow region in the vicinity of the B2 (the region between two thin lines in the insert).

We found [13] that instability condition from SNA parametrization could always be transformed into the reaction rate values at steady state – the form that can be directly compared with experimental measurements or numerical simulation, unlike the current rates. Thereafter, careful choice of the instability condition can lead to highly precise agreement between predicted and numerically obtained bifurcation diagrams (Figure 3-b) and, thus exact testing the proposed model. Moreover, we found [42] that SNA form of kinetic equations quite naturally expresses the slow-fast dynamics of the reaction model, leading to slow manifold and nullclines structure

(Figure 3-a). Our area of interest is spreading now toward modeling of some biochemical systems, also. [43, 44]

Gatermann *et al* [45] made significant extension to the SNA when applied concepts from toric geometry and convex geometry to examples from chemistry. As usual in SNA, they considered the solution set as a convex polyhedral cone, but then, they intersected it with the deformed toric variety of the monomials, corresponding to algebraic constraints from rate laws. Using Gröbner bases the polynomial entries of the Jacobian were expressed in different coordinate systems. Then the Hurwitz criterion was applied in order to determine parameter regions where a Hopf bifurcation occurs. The procedure is applied to the galvanostatic electro-oxidation of methanol by Sauerbrei *et al* [46].

Another extension of SNA could be found also in the paper of Domijan *et al.* [47] This paper, using the theory of SNA and notions from algebraic geometry, presents sufficient conditions for a reaction network to display bifurcations associated with oscillations. The advantage of sufficient conditions is that they impose fewer algebraic conditions on model parameters than conditions associated with standard bifurcation theorems. To derive the new conditions, a coordinate transformation was made that guarantee the existence of branches of positive equilibria in the system. The theory can also be used in a second step for a systematic bifurcation analysis of larger reaction networks.

Perspectives

The analysis of complex systems is promising area for the application of SNA. Metabolic networks and catalysis are the two most prominent examples.

The analysis of metabolic networks has become a major topic in biotechnology in recent years. Applications range from the enhanced production of selected outputs to the prediction of genotype-phenotype relationships. [48-51] The concepts used are based on the assumption of a pseudo steady-state of the network, so that for each metabolite inputs and outputs are balanced. Genome scale analysis of the metabolic network of a microorganism is a major challenge in bioinformatics. The combinatorial explosion, which occurs during the construction of elementary fluxes (non-redundant pathways) requires sophisticated and efficient algorithms to tackle the problem. SNA is high performance toolbox for analysing the possible steady state behaviour of metabolic networks by computing the generating and elementary vectors of their flux and conversions cones. It also supports analyzing the steady states by linear programming. However, it is already conceptually replaced with equivalent Elementary Mode Analysis or Extreme Pathways Analysis [52, 53] and commonly passed over in reference list of numerous applications in the area.

Besides simple oscillation detection, the SNA is increasingly used for the search of various complex dynamic states, including deterministic chaos in heterogeneous catalytic systems. [54] However, applications of SNA in catalysis remains uncommon. The main stream of reaction network investigations in catalysis could rather become Reaction Route Graph Analysis.

Recently, a theory and algorithm for reaction route network analysis is developed in analogy with electrical networks and is based on the combined use of reaction route theory, graph theory, and Kirchoff's laws. The result is claimed to be a powerful new approach of Reaction Route Graph Analysis that is useful in revealing insights into the mechanism as well as the kinetics of the overall reactions involving multiple elementary reaction steps including the effect of topological constraints. [55]

The reaction route graph approach recently developed for complex, nonlinear kinetic mechanisms is applied also to the hydrogen oxidation reactions. Using a set of rate constants for the hydrogen evolution reaction in alkaline solutions from the literature, the dominant reaction routes are identified and simplified mechanisms and kinetics derived. [56] A new graph-theoretic reaction route network approach, is presented to analyze MeOH decomposition on Pt(111) and shows dominant reaction pathways, thus resolving the issue of the initial C-H vs O-H bond activation of MeOH over Pt(111). [57] The method is also applied to enzymatic reactions, [58] and to water gas shift reaction. [59]

The idea of reaction route graph analysis lays in the same topological properties of reaction networks as the SNA. Terminology is different, but the reaction routes are the same as extreme currents. The authors returned also to the concept of graph theory, but they use electric current laws either, that was also the basis for naming reaction pathways extreme currents in SNA. However, they made the significant advances in calculating useful catalytic properties of complex reaction networks. Therefore, their approach could underline the directions of future development in the area, even if it would leave most of the SNA possibilities unused.

Acknowledgement

This work was partially supported by the Ministry for Science of the Republic of Serbia (Grants no. 142025 and 142019).

References

- [1] W. F. Grütter and B. H. Messikommer, *Chem. Eng. Sci.*, 1961, **14**, 231-239.
- [2] W. F. Ames, *Ind. Eng. Chem, Fundamentals*, 1962, **1**, 214.
- [3] J. Wei, C. D. Prater, *Adv. Catal.*, 1962, **13**, 203-392.
- [4] J. Horiuti and T. Nakamura, *Adv. Catal.*, 1967, **17** (1967), 1-74.
- [5] M. I. Temkin, *Adv. Catal.*, 1979, **28**, 173-281.
- [6] B. Clarke, in: *Advances in chemical physics. I. Prigogine, S. Rice, (Eds).* Wiley, New York, 1-216, 1980.
- [7] B. L. Clarke, *Cell Biophysics*, 1988, **12**, 237-253.
- [8] D. Y. Murzin, A. K. Avetisov, *Chem. Eng. Sci.*, 2007, **62**, 6492 – 6494.
- [9] B. L. Clarke, *J. Chem. Phys.*, 1973, **58**, 5605-5614.
- [10] B. L. Clarke, *J. Chem. Phys.*, 1974, **60**, 1481-1492.
- [11] B. L. Clarke, *J. Chem. Phys.*, 1974, **60**, 1493-1501.
- [12] B. L. Clarke, *J. Chem. Phys.*, 1975, **62**, 773-775.

- [13] Lj. Kolar-Anić, Ž. Čupić, G. Schmitz and S. Anić, *Chem. Eng. Sci.*, 2010, **65** 3718–3728.
- [14] B. L. Clarke, *J. Chem. Phys.*, 1976, **64**, 4165-4178.
- [15] B. L. Clarke, *J. Chem. Phys.*, 1976, **64**, 4179-4191.
- [16] B. L. Clarke, *J. Chem. Phys.*, 1981, **75**, 4970-4979.
- [17] B. L. Clarke, *J. Chem. Phys.*, 1992, **97**, 2459-2472.
- [18] B. L. Clarke, *J. Chem. Phys.*, 1992, **97**, 4066-4071.
- [19] B. L. Clarke, W. Jiang, *J. Chem. Phys.*, 1993, **99**, 4464-4478.
- [20] B. L. Clarke, J. Clark, *J. Chem. Phys.*, 1985, **82**, 3107-3117.
- [21] R. Larter, B. L. Clarke, *J. Chem. Phys.*, 1985, **83**, 108-116.
- [22] B. D. Aguda, B. L. Clarke, *J. Chem. Phys.*, 1987, **87**, 3461-3470.
- [23] B. D. Aguda, R. Larter, B. L. Clarke, *J. Chem. Phys.*, 1989, **90**, 4168-4175.
- [24] B. D. Aguda, B. L. Clarke, *J. Chem. Phys.*, 1988, **89**, 7428-7434.
- [25] M. Eiswirth, A. Freund, J. Ross, *Adv. Chem. Phys.*, 1991, **90**, 127-199.
- [26] J. D. Stemwedel, I. Schreiber, J. Ross, *Adv. Chem. Phys.*, 1995, **89**, 327-388.
- [27] I. Schreiber, J. Ross, *J. Phys. Chem.*, 2003, **107**, 9846-9859.
- [28] J. Ross, I. Schreiber, M. O. Vlad, *Determination of Complex Reaction Mechanisms – Analysis of Chemical, Biological, and Genetic Networks*, Oxford University Press, Oxford, 2006.
- [29] P. Strasser, J. D. Stemwedel, J. Ross, *J. Phys. Chem.*, 1993, **97**, 2851-62.
- [30] F. Hynne, P. Graae Sørensen, and T. Møller, *J. Chem. Phys.*, 1993, **98**, 211-219.
- [31] F. Hynne, P. Graae Sørensen, T. Møller, *J. Chem. Phys.*, 1993, **98**, 219–230.
- [32] S. Franzle, B. Markert, *The Scientific World*, 2003, **3**, 319-341.
- [33] S. Franzle, B. Markert, *Science of the Total Environment*, 2000, **249**, 223-241.
- [34] S. Franzle, B. Markert, *Environmental pollution*, 2002, **120**, 27-45.
- [35] G. Schmitz, *Stationarite et Reactions Periodiques*, Thesis, Universite Libre de Bruxelles, 1983.
- [36] Lj. Kolar-Anić and G. Schmitz, *J. Chem. Soc. Faraday Trans.*, 1992, **88**, 2343-2349.
- [37] Lj. Kolar-Anić, Dj. Mišljenović and S. Anić, *React. Kinet. Catal. Lett.*, 1996, **57**, 37-42.
- [38] Lj. Kolar-Anić, Dj. Mišljenović, S. Anić and G. Nicolis, *ECAL '93, Self Organization and life, From simple rules to global complexity*, Brussels, 1993.
- [39] Ž. Čupić and Lj. Kolar-Anić, in *Advanced Science and Technology of Syntering*, B. D. Stojanović, V. V. Skorokhod and M. V. Nikolić, (Eds) Kluwer Academic / Plenum Publishers, New York, 1999, 75-80.
- [40] Ž. Čupić, Lj. Kolar-Anić, *J. Chem. Phys.*, 1999, **110**, 3951-3954.
- [41] Lj. Kolar-Anić, Ž. Čupić, S. Anić and G. Schmitz, *J. Chem. Soc. Faraday Trans.*, 1997, **93**, 2147-2152.
- [42] G. Schmitz, Lj. Z. Kolar-Anić, S. R. Anić, and Ž. D. Čupić, *J. Phys. Chem. A*, 2008, **112**, 13452–13457.

- [43] S. Jelić, Ž. Čupić, Lj. Kolar-Anić, in: *New Research on Neurosecretory Systems*, Chapter XIII, Elissa Romano and Sara de Luca (Eds), Nova Science Publishers, Inc, Hauppauge NY, 2008, 225-245.
- [44] S. Jelić, Ž. Čupić, Lj. Kolar-Anić, V. Vukojević, *Int. J. Nonlin. Sci. & Num. Simul.*, 2009, **10**, 1451-1472.
- [45] K. Gatermann, M. Eiswirth, A. Sensse, *J. of Symbolic Comput.*, 2005, **40** 1361–1382.
- [46] S. Sauerbrei, M. A. Nascimento, M. Eiswirth, H. Varela, *The Journal of Chemical Physics*, 2010, **132**, 154901.
- [47] M. Domijan, M. Kirkilionis, *J. Mat. Biol.*, 2009, **59**, 467-501.
- [48] R. Urbanczik; C. Wagner, *BMC Bioinformatics*, 2005, **21**, 1203-1210.
- [49] J. Maertens, P. A. Vanrolleghem, *Biotechnology Progress*, 2010, **26**, 313-331.
- [50] R. Urbanczik, *BMC Bioinformatics*, 2006, **7**, 129.
- [51] C. Wagner, R. Urbanczik, *Biophysical Journal*, 2005, **89**, 3837-3845.
- [52] J. A. Papin, J. Stelling, N. D. Price, S. Klamt, S. Schuster and B. O. Palsson, *Trends in Biotechnology*, 2004, **22**, 400-405.
- [53] C. T. Trinh, A. Wlaschin and F. Srienc, *Appl. Microbiol. Biotechnol.*, 2009, **81**, 813–826.
- [54] M. Marek, M. Schejbal, P. Koci, V. Nevoral, M. Kubicek, O. Hadac, I. Schreiber, *Chaos*, 2006, **16**, 037107.
- [55] I. Fishtik, C. A. Callaghan, R. Datta, *Journal of Physical Chemistry B*, 2004, **108**, 5671-5682.
- [56] I. Fishtik, C. A. Callaghan, J. D. Fehribach, R. Datta, *Journal of Electroanalytical Chemistry*, 2005, **576**, 57-63.
- [57] S. A. Vilekar, I. Fishtik, R. Datta, *Journal of Catalysis*, 2007, **252**, 258-270.
- [58] R. Datta, S. A. Vilekar, I. Fishtik, J. P. Dittami, *Physica A: Statistical Mechanics and Its Applications*, 2008, **387**, 3348-3372.
- [59] C. A. Callaghan, S. A. Vilekar, I. Fishtik, R. Datta, *Applied Catalysis, A: General*, 2008, **345**, 213-232.

STOICHIOMETRIC NETWORK APPROACH TO THE REACTION MECHANISM OF A THREE-WAY CATALYTIC CONVERTER

^{a,c}O. Hadač, ^{a,c}M. Kohout, ^{a,c}I. Schreiber, ^{a,c}V. Nevoral, ^{a,c}M. Marek ^{b,c} and M. Kubíček

Institute of Chemical Technology, Prague, ^aDepartment of Chemical Engineering, ^bDepartment of Mathematics and ^cCenter for Nonlinear Dynamics of Chemical and Biological Systems, Technická 5, 166 28 Prague 6, Czech Republic, tel.: +420 220443107, e-mail: Otto.Hadac@vscht.cz, Igor.Schreiber@vscht.cz

Abstract

Results of a stoichiometric network analysis (SNA) for a detailed reaction mechanism of a three-way catalytic converter (TWC) are reported. The SNA decomposes the entire chemical network into irreducible elementary subnetworks. The positive and negative feedback loops causing exotic dynamics can be easily found by inspection of elementary subnetworks. We use these results to identify possible sources of oscillatory instabilities in bifurcation diagrams.

Introduction

Nowadays, the TWC is the most common reactor for detoxification of automobile exhaust gases. This reactor is typically operated with periodic variation of inlet oxygen concentration. In the TWC CO and hydrocarbons are oxidized and nitrogen oxides are reduced [1].

Kinetic models of heterogeneous catalytic reactions may display various types of dynamical behaviour (multiple steady states, oscillations and deterministic chaos) [2]. Those are caused by a complex interaction of multiple reaction and adsorption steps. An isothermal model of TWC is based on mass balances for the bulk gas and for the porous catalytic layer. We assume ideally mixed gas phase and pseudo-homogenous catalyst with mutual mass exchange. This lumped parameter model [3] is used for bifurcation analysis. The continuation methods [4] implemented in the software CONT enable us to locate the positions of the saddle-node bifurcation points and the Hopf bifurcation points in dependence of the solution on chosen parameters.

A stoichiometric (chemical) network is a set of chemical species, chemical reactions and its kinetics. A detailed reaction mechanism [5-7] of the TWC forms the network which is decomposed into elementary subnetworks (ESs) [8], i.e. the simplest subnetworks of the system. Then the SNA identifies unstable ESs. Those bring in an instability of stationary state. At the conditions for the Hopf bifurcation, a classification and determination of the role of species in oscillations [9] can be done, for example, by calculating mutual phase shifts of oscillating species [10] or other methods [11-12]. The oscillatory instabilities predicted by SNA are used to elucidate bifurcation diagrams calculated from the model with using numerical continuation techniques.

Results and discussion

The analysis of possible sources of oscillatory behaviour in the TWC reaction mechanism was initiated in [2]. Model situation indicates that two different unstable subnetworks generating oscillations are associated with the sub- and super-stoichiometric regions. According to the classification system of chemical oscillators [9], each of the two oscillatory regions is tied up with a particular topologically distinct oscillatory subnetwork. The subnetwork in Fig. 1a corresponds to the surplus of oxygen. It involves the *Langmuir-Hinshelwood mechanism* whereby both O_2 and CO adsorb first, and the adsorbed forms react to produce CO_2 and regenerate active catalytic sites. The autocatalytic cycle involves reactions 1 and 3 and passes through the species CO^* and $*$ (*autocatalytic species*). An instability is achieved by combining this cycle with an exit reaction 2, see [8], involving O_2 (*exit species*). Finally, the oscillatory instability is made possible by the presence of CO and its flow-controlled availability. There is a negative cycle feedback exerted by CO (*negative feedback species*) upon itself via the path through CO^* and $*$ implying that the autocatalysis depletes the supply of CO, which must be replenished by the feed at a later time leading thus to oscillations. The subnetwork in Fig. 1b corresponds to a sub-stoichiometric oscillator. The autocatalytic cycle passes through $*$, O^* and OCO^* . The exit and the negative feedback species are CO and O_2 , respectively. The topology of the subnetwork corresponds to the *Eley-Riedel mechanism*: oxygen is adsorbed on an active site and subsequently reacts with gaseous CO to provide an adsorbed carbon dioxide species OCO^* .

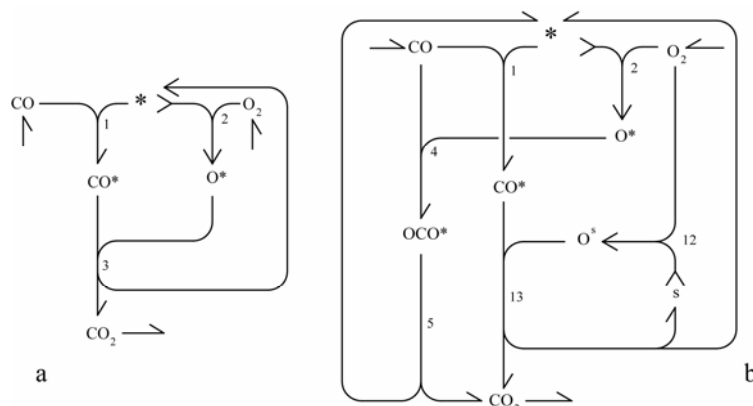


Fig.1. Dominant oscillatory subnetworks; a) super-stoichiometric, b) sub-stoichiometric. Each reaction is represented as a multi-tail/multi-head arrow, where the number of feathers/barbs determines the stoichiometric coefficients of reactants/products and the number of left feathers determines the reaction order.

Conclusions

A systematic approach to the analysis of complex reaction networks was applied to a realistic detailed kinetic scheme of a TWC. The SNA was used to find positive and negative feedbacks that may cause an oscillatory instability. The phase shift

analysis helps us to identify the unstable subnetworks actually causing the oscillations observed in the model. These results were used to explain the structure of the bifurcation diagrams [2].

Acknowledgements

This work was supported by the Grants No. 203/09/2091 and No. 104/08/H055 from the Czech Science Foundation and by the project MSM 6046137306 from the Ministry of Education of Czech Republic.

References

- [1] R. M. Heck, R. J. Farrauto, Mathematical-modeling of monolithic catalysts, *Appl. Cat. A: Gen.*, 2001, **221**, 443.
- [2] M. Marek et al., Oscillations, period doublings, and chaos in CO oxidation and catalytic mufflers, *Chaos*, 2006, **16**, 037107.
- [3] P. Kočí, Nonlinear dynamics of automobile exhaust gas converters: the role of nonstationary kinetics, *Chem. Eng. Sci.*, 2004, **59**, 5597.
- [4] M. Marek and I. Schreiber, *Chaotic Behaviour of Deterministic Dissipative Systems*, Cambridge Univ. Press, Cambridge, 1991; 1995.
- [5] R. H. Niebelke et al., *Applied Catalysis B: Env.*, 1998, **229**, 508.
- [6] J. M. Harmsen et al., *Ind. Eng. Chem. Res.*, 2000, **39**, 599.
- [7] J. M. Harmsen et al., *Chem. Eng. Sci.*, 2001, **56**, 2019.
- [8] B. L. Clarke, Stability of complex reaction networks, *Adv. Chem. Phys.*, 1980, **43**, 1.
- [9] M. Eiswirth, A. Freund and J. Ross, Mechanistic classification of chemical oscillators and the role of species, *Adv. Chem. Phys.*, 1991, **80**, 127.
- [10] T. Chevalier et al., Toward a systematic determination of complex-reaction mechanism, *J. Phys. Chem.*, 1993, **97**, 6776.
- [11] J. D. Stemwedel et al., Formulation of oscillatory reaction-mechanisms by deduction from experiments, *Adv. Chem. Phys.*, 1995, **89**, 327.
- [12] J. Ross, I. Schreiber and M. O. Vlad, *Determination of Complex Reaction Mechanisms*, Oxford University Press, New York, 2006.

MODELLING THE HYPOTHALAMIC-PITUITARY-ADRENAL (HPA) AXIS RESPONSE TO EXTERNAL PERTURBATIONS WITH CORTISOL

V. Marković¹, S. Jelić², V. Vukojević³ and Lj. Kolar-Anić¹

¹*Faculty of Physical Chemistry, University of Belgrade, Studentski trg 12-16, 11000 Belgrade, Serbia (wladimirmarkovic@gmail.com)*

²*Department of Theoretical Physics and Physics of Condensed Matter 020/2, Vinča Institute of Nuclear Sciences, University of Belgrade, P. O. Box 522, 11001 Belgrade, Serbia*

³*Department of Clinical Neuroscience, Karolinska Institutet, CMM L8:01, 17176 Stockholm, Sweden*

Abstract

Glucocorticoids, the end products of the Hypothalamic-Pituitary-Adrenal (HPA) axis, are widely used as anti-inflammatory and immunosuppressive drugs. However, the feed-back effects of externally induced glucocorticoids on the HPA axis activity remain widely unknown. In this study, we use numerical simulations to investigate changes in the HPA axis activity caused by externally introduced cortisol. We emulate the basal HPA activity using a stoichiometric model of the HPA axis, and perturb its dynamics by abruptly changing cortisol levels during the course of numerical integration, thereby mimicking cortisol increase under treatment. Our study shows that the HPA axis activity is susceptible to perturbations by cortisol and that external cortisol pulses elicit different responses, depending on the dose and the time of cortisol introduction.

Introduction

The HPA axis is a complex regulatory system that maintains homeostasis under basal physiological conditions and stress. It comprises interactions between key elements of the neuroendocrine system, the hypothalamus, pituitary and adrenal glands [1]. The HPA axis regulates the levels of glucocorticoids, a group of steroid hormones of which cortisol is the most significant representative in humans. Glucocorticoids exert a dual role on the immune system. They are essential for normal immune response functioning, but may also act as potent immunosuppressors [2]. The effect of glucocorticoid therapy on the HPA axis activity is not well understood.

Mathematical modeling and numerical simulations provide a convenient way to investigate how individual components and processes in the HPA axis are integrated to yield a coherent, systemic response. We proposed recently a stoichiometric model to describe the HPA axis activity [3] and validated its predictions under basal conditions and stress [3, 4]. We use here this model to investigate changes in the HPA axis dynamics caused by sudden cortisol increase, thereby mimicking the effect of treatment with glucocorticoids [2].

Results

The HPA model used is described in detail in references [3] and [4]. Numerical simulations were performed using the Matlab program. Single-pulse cortisol perturbations were modeled by abruptly changing the cortisol concentration during the course of the numerical integration.

Cortisol dynamics is governed by complex processes that are characterized by two distinct periods, the ultradian cortisol release occurring every 20-60 minutes (small-amplitude oscillations, Fig. 1) that are superimposed on the 24 h circadian oscillations (large-amplitude oscillations with a 24 h period, Fig. 1) [1, 3, 4]. Single-pulse cortisol perturbations (indicated by arrows in Fig. 1) alter the ultradian cortisol dynamics. Sudden increase in cortisol levels during the night (represented in humans by the ascending phase of the daily cortisol levels, Fig. 1 A) may increase the amplitude of the following ultradian cortisol oscillations, whereas the same perturbation applied during the daytime (represented by the descending phase of the daily cortisol levels, Fig. 1 B) may elicit an opposite response, and decreases the amplitude of the following ultradian oscillation (Fig. 1).

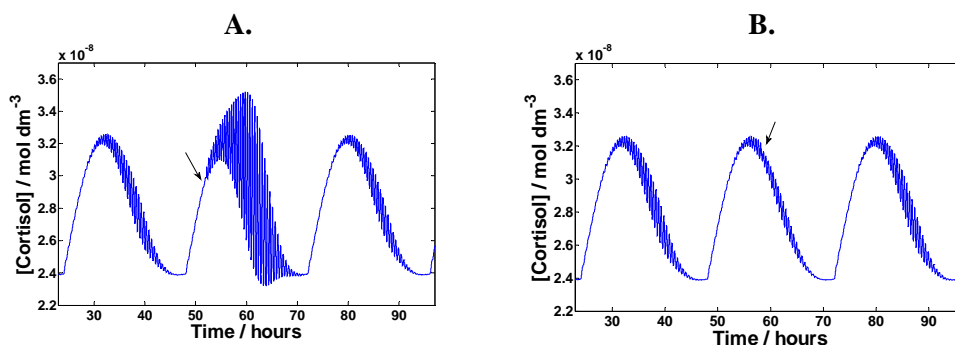


Fig.1. Temporal evolution of cortisol and change in its dynamics after a sudden increase in cortisol levels occurring during the night (A) and the daytime (B). In both instances, the amount of “added” cortisol is the same, $4 \cdot 10^{-10}$ mol dm⁻³. The perturbations were applied during the descending phase in arbitrarily chosen ultradian oscillations.

For different cortisol “doses”, ranging from $1 \cdot 10^{-11}$ – $1 \cdot 10^{-9}$ mol dm⁻³, a complex response of the HPA axis was observed (Fig. 2). Sudden increase in cortisol levels may either decrease or increase the amplitude of the following ultradian oscillations. For example, a decrease in the amplitude of ultradian oscillations was observed during the night phase for cortisol perturbations that were $\leq 1 \cdot 10^{-10}$ mol dm⁻³, reaching a minimum for perturbations with [cortisol] = $5 \cdot 10^{-11}$ mol dm⁻³. For perturbations that were $> 1 \cdot 10^{-10}$ mol dm⁻³, an increase in ultradian cortisol amplitude was observed (Fig. 2, solid rectangles). A similar effect, somewhat less pronounced, was observed for perturbations applied during the daytime (Fig. 2, open rectangles).

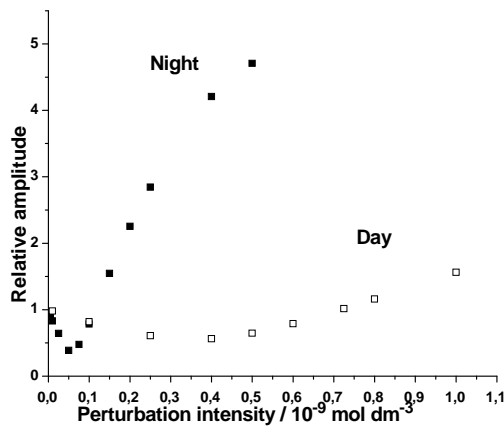


Fig.2. Changes in the amplitude of ultradian cortisol oscillations following a sudden increase in cortisol levels. The intensity of the applied cortisol pulse is given on the abscissa. The relative amplitude is the ratio of the amplitude of a referent ultradian oscillation following cortisol “addition” with respect to the amplitude of the same oscillation prior cortisol “addition”.

Discussion and Conclusion

Our results show that even very low doses of externally introduced cortisol, which are 1000 times smaller than the basal cortisol concentration, elicit a response and alter the dynamics of the HPA axis. Mathematical modelling emphasized the significance of ultradian and circadian regulation for the HPA axis plasticity, in agreement with increasing number of experimental findings [5,6].

Modeling revealed the intrinsic rhythmicity of the HPA axis and the existence of “sensitive decision points”, *i.e.* bifurcation points where the dynamics of the HPA axis changes qualitatively. These phenomena give rise to self-organization and complex dynamic behavior that is not easy to understand intuitively. Realistic models, with good predictive potential enable us to expose the underlying dynamic regulatory mechanisms, predict and explain different responses of the HPA axis to glucocorticoids administration in humans [2].

Acknowledgments

Present investigations were partially supported by the Ministry of Sciences and Technology Development of Serbia under the project no. 142025. The work was realized in collaboration with Dr. Željko Čupić.

References

- [1] C. Tsigos, G. Chrousos, J. Psychosom. Res., 2002, **53**, 865-871.
- [2] G. Chrousos, in Endocrinology & Metabolism, P. Felig, L. Frohman (Eds.), McGraw-Hill, New York, 2001, 461-474, 609-632.
- [3] S. Jelić, Ž. Čupić and Lj. Kolar-Anić, Math Biosci, 2005, **197**, 173-187.
- [4] S. Jelić, Ž. Čupić, Lj. Kolar-Anić and V. Vukojević, International Journal of Nonlinear Science & Numerical Simulation, 2009, **10**, 1451-14.
- [5] R. Windle, S. Wood, N.Shanks, S. Lightman and C. Ingram, Endocrinology, 1998, **139**, 443-450.
- [6] J. Walker, J. Terry and S. Lightman, Proc. R. Soc. B, 2010, **277**, 1627-1633.

NUMERICAL CALCULATION OF THE KINETICS OF HOCl \rightleftharpoons H(2 S)+OCl($X^2\Pi_i$) THERMAL REACTION IN GAS PHASE

N. Begović¹ and S. Anić²

¹*Institute of General and Physical Chemistry, Belgrade, Serbia*

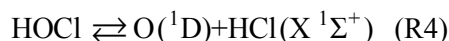
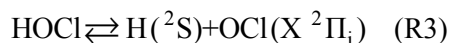
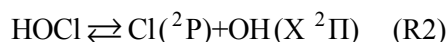
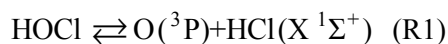
²*Institute of Chemistry, Technology and Metallurgy, University of Belgrade,
Belgrade, Serbia*

Abstract

Using the MP4 method in the temperature range of 100 – 373 K we were analyzing the kinetics of HOCl \rightleftharpoons H(2 S)+OCl($X^2\Pi_i$) gas reaction. The temperature dependence of rate constants ($k_f = 4.26 \times 10^{-173} \text{ s}^{-1}$ at T = 100 K to $k_f = 5.50 \times 10^{-48} \text{ s}^{-1}$ at T=373 K; and $k_r = 6.85 \times 10^{-39} \text{ s}^{-1}$ at T = 100 K to $k_r = 4.59 \times 10^{-27} \text{ s}^{-1}$ at T = 373 K) and equilibrium constants (K = 6.22×10^{-135} at T = 100 K to K = 1.20×10^{-21} at 373 K) were determined. In the above temperature range, the activation energies of the forward (E_f) and reverse (E_r) reactions of 78.22 and 7.39 kcal/mol were found.

Introduction

It is well known that the reaction of HOCl decomposition is very important for atmospheric chemistry and can proceed via four possible channels.



This type of reactions can be generally useful for understanding the mechanism of oxy-chloride oscillating reactions.

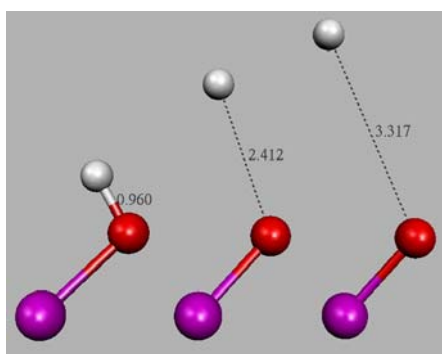
Methodology

Gaussian 09 [3] quantum-mechanical program package was used to elucidate all necessary data for kinetic calculation. All calculation was done at the MP4 [4], a Møller-Plesset correlation energy correction truncated at fourth-order level of theory. The 6-311++G(df,pd) basis set was used. The rate constants were calculated using canonical variational theory (CVT) with multidimensional approximation for tunneling, specially small-curvature (SCT) and large-curvature (LCT) tunneling methods. For interfacing the Polyrate 2008 [5] (program for the calculation of polyatomic specie's chemical reaction rates) and Gaussian 09

program and for the purpose of carrying out direct dynamical calculations of chemical reaction rates of interest we used Gaussrate 2008 [5] scripts.

Results and Discussion

The mechanism of the reaction R3 can be presented by the following schema. The left picture correspond to HOCl in his equilibrium ground state conformation. On the right picture is the system of H and OCl, which is near his local minimum (distance 4.55 angstroms), which correspond to products. The all distances on schema are in angstroms.



Reactant (HOCl) Transition state (TS) Product (H + OCl)

Potential energy curve along MEP (minimum energy path) in hartrees (atomic units) as a function of the reaction coordinate s (atomic units) for decomposition of HOCl is shown in Fig. 1. There has been found rate constant for forward and reverse reaction in temperature range from 100-373 K. At this condition k_f is from $4.26 \times 10^{-173} \text{ s}^{-1}$ to $5.50 \times 10^{-48} \text{ s}^{-1}$ and k_r from $6.85 \times 10^{-39} \text{ s}^{-1}$ to $4.59 \times 10^{-27} \text{ s}^{-1}$ while in the same time the equilibrium constant has value from 6.22×10^{-135} to 1.20×10^{-21} . The determined activation energies for forward and reverse reactions are 78.22 and 7.39 kcal/mol, and are calculated for temperature interval 100 – 373 K, while

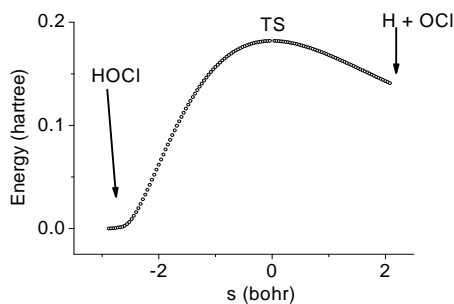


Fig.1. Energetic profile of R3 reaction at 0 K
enthalpy ΔH_r is 70.83 kcal/mol.

From calculation we get the transmission coefficient for forward and reverse reaction which is $2.2532 \times 10^{+42}$ and 2.112 at 100 K and 373 K, respectively.

The tunneling probabilities for reverse reaction are significant at low energies but for forward reaction, they take values only at higher energies. This is one of the reasons why diagram for forward reaction rate on Fig. 2 shows deviation from linearity at high temperature. On the opposite, tunneling is active mechanism for reverse reaction even at low temperature when the system is in low energetic condition. For reverse reaction, Figure 2, two different temperature ranges exists. In one, on low temperature, we can say that reaction rate is weakly dependent of temperature. In that range reaction rate curve is almost parallel with $1/T$ axis. In second temperature range, at higher temperature, reaction is faster and show lower influence of tunneling.

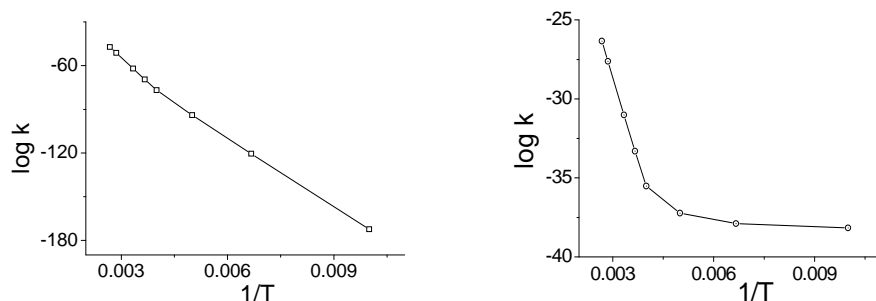


Fig.2. Influence of temperature on rate constant. On the left side is diagram for forward and on the right for reverse R3 reaction.

Conclusion

Kinetic values for $\text{HOCl} \rightleftharpoons \text{H}(^2\text{S}) + \text{OCl}(X^2\Pi_i)$ thermal decomposition were calculated for the first time. The high value for reverse rate constant suggest us that the reverse reaction can be understand as concurrent to photolysis reactions which produce ClO, Cl and other reactive species responsible for ozone layer depletion.

Acknowledgments

This work is supported by Ministry of Science and Environmental of Serbia, project no. 142025.

References

- [1] R. Vogt and R. N. Schindler, Ber. Bunsenges. Phys. Chem., 1993, **97**, 819-829.
- [2] A. Bell, P. Pardon, C. Hickman and J. Frey, J. Chem. Soc. Faraday Trans., 1990, **86**, 3831-3836.
- [3] Gaussian 09, Revision A.1, Gaussian, Inc., Wallingford CT, 2009.
- [4] K. Raghavachari and J. A. Pople, Int. J. Quantum Chem., 1978, **14**, 91-100.
- [5] POLYRATE 2008, GAUSSRATE 2008, Donald G. Truhlar, Department of Chemistry and Supercomputing Institute University of Minnesota, Minneapolis

NEW REACTION SCHEME FOR THE NUMERICAL SIMULATIONS OF THE BELOUSOV-ZHABOTINSKY REACTION WITH Br_2O AND RADICAL SPECIES

S. Blagojević¹ and S. Anić²

¹*Faculty of Pharmacy, University of Belgrade, Vojvode Stepe 450, Belgrade*

²*ICH_{TM} – Department of Catalysis and Chemical Engineering, Belgrade, Njegoševa 12*

Abstract

The numerical simulation of the Belousov-Zhabotinsky (BZ) reaction under batch condition was performed and compared with experimental data.

Introduction

The classical Belousov-Zhabotinsky (BZ) reaction, [1–4] is the decomposition of malonic acid (MA), by bromated ions in acid solution containing Ce^{3+} or Ce^{4+} as a catalyst. Although the mechanism of the BZ reaction which was introduced by György, Turányi and Field (GTF) model, [1] is so far the most complete chemical mechanism, numerous modification of this model were proposed [2–4]. Promising results were obtained with one optimized version of these models [3,4], noted in these papers as model BG [3,4] (Table 1, reactions (R1), (R3)-(R9), (R-1)-(R15)). The BG model with the Br_2O species was derived from the GTF model referred to as model B (Table 1, reactions (R1)-(R11)) [2] of the BZ reaction in a CSTR. With the aim of reaction dynamics evaluation, the BG model is expanded in present Paper by the four reactions with malonyl (MA^\bullet), bromomalonyl (BrMA^\bullet) and tatronyl (TTA^\bullet) radicals, which are taken from GTF model.

Results and Discussion

The potentiometric traces of the BZ systems and time evolutions obtained by the numerical simulation according to new kinetic scheme, BGM (Table 1, reactions (R1), (R3)-(R9), (R11)-(R18)), are presented in Figure 1.

Although global phenomena were simulated numerically by proposed B and BG models [2,3], improvement by the model BGM proposed in this work would be done in order to attain better quantitative agreement with the experiment.

For that purpose, BG model was modified by including (R11), (R16), (R17) and (R18) reactions with different organic free radical species. The characteristic oscillatory parameters (preoscillatory period (τ_1) and the time elapsed from the beginning of the reaction to the end of the last incomplete oscillation (τ_{end})) are presented in Figure 2(a) i 2(b) as a function of malonic acid initial concentration, obtained experimentally and calculated by numerical simulations using different models.

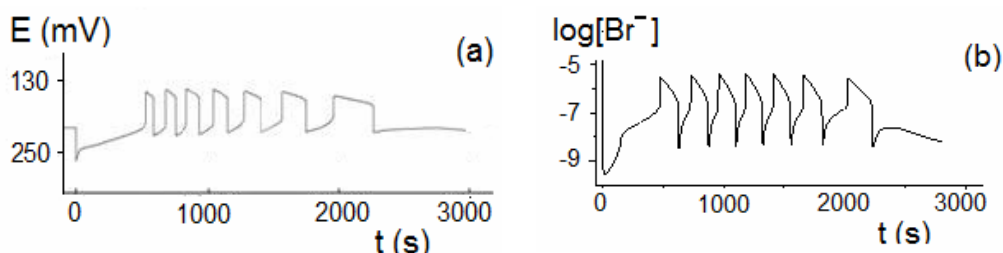


Fig.1. Oscillatory evolution of the bromide ion in the BZ reaction realised under batch conditions ($[MA]_0 = 1.60$, $[H_2SO_4]_0 = 1.00$, $[KBrO_3]_0 = 6.20 \times 10^{-2}$, $[KBr]_0 = 1.50 \times 10^{-5}$, $[Ce_2(SO_4)_3]_0 = 2.50 \times 10^{-3}$ at the temperature $30\text{ }^\circ\text{C}$). Experimental (a) and numerical simulation obtained using the BGM model (b).

Tabela 1. Reactions and their rate constants used in the numerical simulations.

Reaction		Rate constant [3,4]	
(R1)	$Br^- + HOBr + H^+ \rightarrow Br_2 + H_2O$	2.55×10^9	$dm^6 mol^{-2} s^{-1}$
(R2)	$HBrO_2 + Br^- + H^+ \rightarrow 2HOBr$	5.93×10^6	$dm^6 mol^{-2} s^{-1}$
(R3)	$Br^- + BrO_3^- + 2H^+ \rightarrow HOBr + HBrO_2$	2.86	$dm^9 mol^{-3} s^{-1}$
(R4)	$2HBrO_2 \rightarrow BrO_3^- + HOBr + H^+$	3.49×10^9	$dm^3 mol^{-1} s^{-1}$
(R5)	$BrO_3^- + HBrO_2 + H^+ \rightarrow 2BrO_2^\bullet + H_2O$	40.70	$dm^6 mol^{-2} s^{-1}$
(R-5)	$2BrO_2^\bullet + H_2O \rightarrow BrO_3^- + HBrO_2 + H^+$	6.72×10^7	$dm^3 mol^{-1} s^{-1}$
(R6)	$Ce^{3+} + BrO_2^\bullet + H^+ \rightarrow Ce^{4+} + HBrO_2$	3.20×10^4	$dm^6 mol^{-2} s^{-1}$
(R-6)	$Ce^{4+} + HBrO_2 \rightarrow Ce^{3+} + BrO_2^\bullet + H^+$	1.12×10^4	$dm^3 mol^{-1} s^{-1}$
(R7)	$MA + Br_2 \rightarrow BrMA + Br^- + H^+$	4.24	$dm^3 mol^{-1} s^{-1}$
(R8)	$MA + Ce^{4+} \rightarrow Ce^{3+} + H^+ + P$	0.36	$dm^3 mol^{-1} s^{-1}$
(R9)	$BrMA + Ce^{4+} \rightarrow Ce^{3+} + Br^- + P$	47.17	$dm^3 mol^{-1} s^{-1}$
(R10)	$MA^\bullet + BrMA \rightarrow MA + Br^- + P$	2.40×10^4	$dm^3 mol^{-1} s^{-1}$
(R11)	$2MA^\bullet + H_2O \rightarrow MA + TTA$	3.20×10^9	$dm^3 mol^{-1} s^{-1}$
(R-1)	$Br_2 + H_2O \rightarrow Br^- + HOBr + H^+$	3.18	s^{-1}
(R12)	$HBrO_2 + Br^- + H^+ \rightarrow Br_2O + H_2O$	5.93×10^6	$dm^6 mol^{-2} s^{-1}$
(R13)	$Br_2O + H_2O \rightarrow 2HOBr$	3.21×10^3	s^{-1}
(R-13)	$2HOBr \rightarrow Br_2O + H_2O$	3.22×10^8	$dm^3 mol^{-1} s^{-1}$
(R14)	$MA + Br_2O \rightarrow BrMA + HOBr$	4.23×10^{-2}	$dm^3 mol^{-1} s^{-1}$
(R15)	$Br_2(sol) \rightarrow Br_2(g)$	1.10×10^{-2}	s^{-1}
(R16)	$MA^\bullet + TTA \rightarrow MA + TTA^\bullet$	1.00×10^5	$dm^3 mol^{-1} s^{-1}$
(R17)	$BrMA + TTA^\bullet \rightarrow BrMA^\bullet + TTA$	2.00×10^5	$dm^3 mol^{-1} s^{-1}$
(R18)	$BrMA^\bullet + TTA^\bullet + H_2O \rightarrow BrTTA + TTA$	1.00×10^9	$dm^3 mol^{-1} s^{-1}$

Abbreviations: In the B and BGM models, in the reaction (R8) product P was replaced with MA^\bullet radicals.

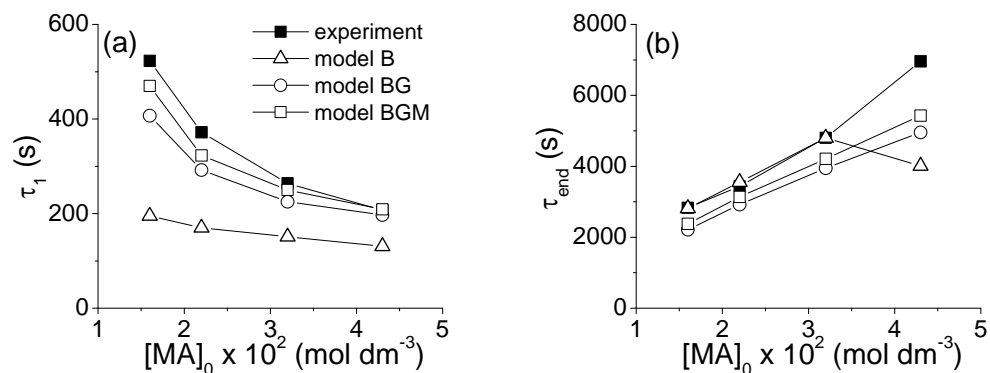


Fig.2. Values for τ_1 (a) and τ_{end} , (b), versus initial concentrations of malonic acid $[MA]_0$ at the temperature value equal to 30 °C.

Conclusion

Based on the presented results it can be concluded that the theoretical predictions, obtained by numerical simulation used BGM model, are in satisfactory agreement with the ones evaluated from experimental investigations.

Acknowledgments

We gratefully acknowledge the partial financial support in grant no.142025 of the Ministry for Science and Technological development of the Republic of Serbia.

References

- [1] T. Turanyi, L. Györgyi, R. Field, J. Phys. Chem., 1990, **94**, 7162–7170.
- [2] L. Györgyi, R. Field, J. Phys. Chem., 1991, **95**, 6594–6602.
- [3] S. Blagojević, S. Anić, Ž. Čupić, N. Pejić, Lj. Kolar–Anić, Phys. Chem. Chem. Phys. 2008, **10**, 6658–6664.
- [4] S. Blagojević, S. Anić, Ž. Čupić, N. Pejić, Lj. Kolar–Anić, Russ. J. Phys. Chem., 2009, **83**, 1496–1501.

EXPERIMENTAL STUDY OF DYNAMICS OF THE ENZYMATIC REACTION GLUCOSE – CATALASE – GLUCOSE OXIDASE – HYDROGEN PEROXIDE IN A BATCH REACTOR

M. Číp and L. Schreiberová

The Institute of Chemical Technology Prague, Department of Chemical Engineering and Center for Nonlinear Dynamics of Chemical and Biological Systems, Technická 5, 166 28 Prague 6, Czech Republic; tel. +420-220443033, fax: +420-220444320, e-mail: martin.cip@vscht.cz

Abstract

The article is focused on experiments with the glucose – catalase – glucose oxidase – hydrogen peroxide reaction carried out in a batch reactor. This reaction belongs to the large family of enzymatic oscillatory reactions often found in biological systems. The aim of this work is to verify oscillatory course of dissolved oxygen concentration in this enzymatic system reported in literature and a parametric study of dependence on mixing rate, temperature and initial concentrations of components (hydrogen peroxide, glucose, catalase and glucose oxidase). The knowledge of nonlinear batch dynamics will be subsequently used in designing and carrying out experiments in a novel continuous-flow stirred reactor.

Introduction

Chemical oscillations, distinguished by periodic variations of the concentrations of species, are a prototypical phenomenon of nonlinear chemical dynamics [1] and can be divided into inorganic oscillations and biochemical oscillations which represent complex enzyme-catalyzed reactions. Biochemical oscillations include oscillations in living cells (e.g. glycolytic oscillations [2, 3]) or enzyme-catalyzed reactions *in vitro* such as the well-known peroxidase-oxidase reactions or the glucose – catalase – glucose oxidase – hydrogen peroxide reaction.

The enzymatic reaction glucose – catalase – glucose oxidase – hydrogen peroxide was proposed by Sasaki [4]. Experiments were carried out in an open batch unstirred reactor separated by a PVC plate with a hole to the two cells. A dialysis membrane was placed over this hole. The principle of the reaction system is that H_2O_2 in the first cell permeates through the dialysis membrane to the second cell containing buffer solution (KH_2PO_4) with glucose (Glc), glucose oxidase (GOD) and catalase (CAT) (all together called in short the reaction solution). In the second cell take place the enzyme-catalyzed reaction: CAT-catalyzed decomposition of H_2O_2 to H_2O and O_2 and GOD-catalyzed reaction of O_2 and Glc to H_2O_2 and D-glucono-1,5-lactone. D-glucono-1,5-lactone can be spontaneously hydrolyzed to gluconic acid. Dissolved oxygen (DO) probe immersed into the reaction solution measured the oscillatory course of the DO concentration with a period 450 seconds

and an amplitude 11 mg/l. The waveform depends on the concentration of reacting species and additional chemicals (ascorbic acid, urea etc.)

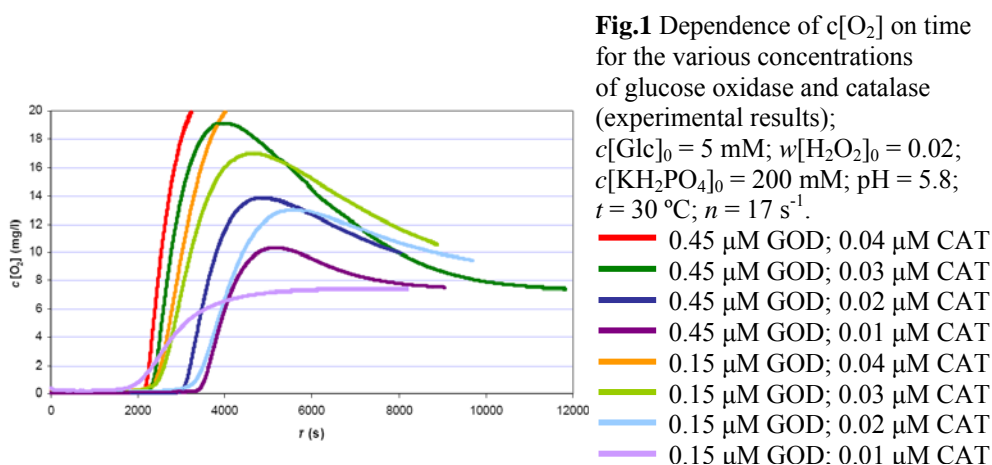
Experimental

The enzymatic system was carried out in a batch reactor open to atmosphere. The reactor with a volume of 26.1 ml (a double glass wall in which thermostated water was circulating) was filled with 10 ml of the reaction solution. A bent glass tube filled with H₂O₂ (1.5 ml) was immersed into the reaction solution with its bottom outlet (inner diameter 6 mm) overlaid by the dialysis membrane and DO probe. All solutions were prepared freshly on the day of use except for the buffer solution.

Results and Discussion

The first experiments in the batch reactor were designed to verify the oscillatory behavior mentioned in the article [4]. However, it was not possible to reproduce the same course of the DO concentration in this enzymatic system for the initial conditions specified in the article: $c[\text{CAT}]_0 = 14.84 \mu\text{M}$; $c[\text{GOD}]_0 = 5.81 \mu\text{M}$; $c[\text{Glc}]_0 = 5 \text{ mM}$; $w[\text{H}_2\text{O}_2]_0 = 0.02$; $c[\text{KH}_2\text{PO}_4]_0 = 200 \text{ mM}$; $\text{pH} = 5.8$; $t = 30 \text{ }^\circ\text{C}$; $n = 0 \text{ s}^{-1}$. The course of DO was not periodic, instead the concentration irregularly increased to the limit value of 20 mg/l.

Therefore, a parametric study of dependence on mixing, temperature and initial concentrations of components was carried out. All subsequent experiments were performed in the batch stirred reactor ($n = 17 \text{ s}^{-1}$) to ensure the mixing of all components of the system and the results were not affected by interfering oxygen bubbles with the DO probe. Results of the parametric study showed that the course of the DO concentration was not significantly modified in the interval 23 – 37 °C. Due to the high concentration of GOD the rapid decline of the oxygen concentration in the reaction solution to 0 mg/l was measured. The decrease of $c[\text{Glc}]_0$ and increase of $w[\text{H}_2\text{O}_2]_0$ resulted in extending time for which there was an increase of oxygen concentration from 0 mg/l to its stabilization (13 mg/l). The concentrations of enzymes were further decreased at intervals 5.810 – 0.005 μM GOD and 14.84 – 0.01 μM CAT.



The dynamics of the enzymatic reaction is much more sensitive to the decrease of $w[\text{H}_2\text{O}_2]_0$ rather than the decrease of CAT at the interval $14.84 - 0.40 \mu\text{M}$. When the concentration of enzymes satisfied the condition $c[\text{GOD}]_0 \leq 0.45 \mu\text{M}$ and $c[\text{CAT}]_0 \leq 0.03 \mu\text{M}$, the DO concentration tended to reach the equilibrium concentration (7.5 mg/l at $30 \text{ }^\circ\text{C}$), see Fig. 1. The stabilization of $c[\text{O}_2]_0$ at the equilibrium concentration can be explained by utilization of all the glucose in the reaction solution and inactivation of one or both enzymes by hydrogen peroxide.

Fig. 2 indicates that further decrease of the concentrations of enzymes contributed to the finding of the initial condition ($c[\text{GOD}]_0 = 0.005 - 0.015 \mu\text{M}$; $c[\text{CAT}]_0 = 0.03 \mu\text{M}$; $c[\text{Glc}]_0 = 5 \text{ mM}$; $w[\text{H}_2\text{O}_2]_0 = 0.02$; $t = 30 \text{ }^\circ\text{C}$; $n = 17 \text{ s}^{-1}$) where the course of DO shows nonlinear behavior. The concentrations of enzymes respond to the activity $0.09 - 0.26 \text{ U/ml}$ GOD and 53 U/ml CAT (approximately 500 times smaller than previously reported [4]).

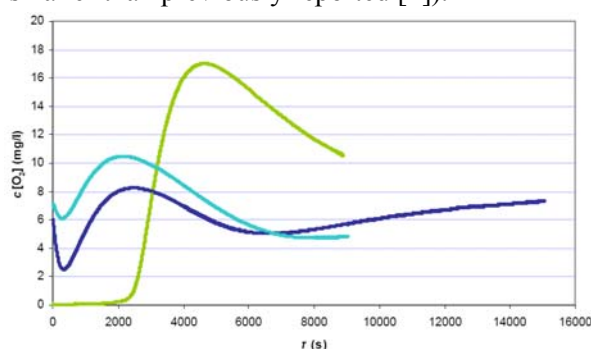


Fig. 2 Dependence of $c[\text{O}_2]$ on time for the various concentration of glucose oxidase (experimental results); $c[\text{CAT}]_0 = 0.03 \mu\text{M}$; $c[\text{Glc}]_0 = 5 \text{ mM}$; $w[\text{H}_2\text{O}_2]_0 = 0.02$; $c[\text{KH}_2\text{PO}_4]_0 = 200 \text{ mM}$; $\text{pH} = 5.8$; $t = 30 \text{ }^\circ\text{C}$; $n = 17 \text{ s}^{-1}$.

— 0.150 μM GOD
— 0.015 μM GOD
— 0.005 μM GOD

Conclusion

The enzymatic reaction glucose – catalase – glucose oxidase – hydrogen peroxide was studied in the batch reactor for the same initial condition as in Ref. [4]. We were not successful in finding sustained oscillations of DO reported in [4]. The article [4] does not provide exact information about experimental procedure; hence dependence on mixing rate, temperature and initial concentrations of components was carried out. We found certain initial conditions where the course of DO shows nonlinear behavior. This initial condition will be used for experiments carried out in a continuous stirred-tank reactor (CSTR) designed for this enzymatic reaction. Experiments in the CSTR have not been reported in literature so far.

Acknowledgment

This work was supported by grant GACR 203/09/2091.

References

- [1] F. Sagués, I. R. Epstein, J. Chem. Soc., Dalton Trans., 2003, **7**, 1201–1217.
- [2] L. N. M. Duysens, J. Amesz, Biophys. Acta, 1957, **24**, 19–26.
- [3] G. Nicolis, J. Portnow, Chemical Reviews, 1973, **73**, 365–384.
- [4] S. Sasaki, T. Uchida, D. Nakano, T. Hideshima, Electroanalysis, 2004, **16**, 1598–1602.

EVOLUTION OF THE BRAY-LIEBHAFSKY OSCILLATORY REACTION IN THE PRESENCE OF POLYMER SUPPORTED COBALT CATALYST

J. P. Maksimović¹, Ž. D. Čupić², D. Lončarević², N. Pejić³ and S. Anić²

¹ Faculty of Physical Chemistry, University of Belgrade, Serbia

² IChTM, University of Belgrade - Center of Catalysis and Chemical Engineering, Serbia; ³ Faculty of Pharmacy, University of Belgrade

Abstract

The Bray-Liebhafsky (BL) reaction generated in the batch reactor was exposed to the influence of the cobalt(II)-nitrate, supported on the macroreticular copolymer of poly-4-vinylpyridine with divinylbenzene. It was found that linear relations exist, between quantity of the catalyst and characteristic periods τ_1 (preoscillatory period), and τ_{end} (duration of the oscillogram). The parameters of linearity are connected with the apparent activation energies of the reaction responsible for emergence of the preoscillatory period and the overall BL reaction.

Introduction

The Bray-Liebhafsky reaction has been successfully applied as sensitive matrix system for the characterization of catalysts [1].

The BL reaction is the decomposition of hydrogen peroxide into water and oxygen [2,3]:



in the presence of iodate and hydrogen ions. The reaction (D) is result of two complex consecutive reactions:



In closed reactor, transient periods alternate with domination of either reaction R or reaction O, and therefore, intermediate concentrations oscillate in time. It was found that the overall reaction, independent of its complexity, is the pseudo-first order with respect to hydrogen peroxide:

$$-\frac{d[\text{H}_2\text{O}_2]}{dt} = k_{\text{D}}[\text{H}_2\text{O}_2]. \quad (1)$$

It was also found that there is a correspondence between the rate constants of the reactions (R) and (O), and characteristic kinetic parameters such as τ_1 (preoscillatory period) and τ_{end} (the period between beginning of reaction and the end of oscillatory evolution):

$$k_R = C_1 \frac{1}{\tau_1} \quad k_O \cong k_D = C_2 \frac{1}{\tau_{\text{end}}} \quad (2)$$

where C_1 and C_2 are constants characteristic for the considered system. It is known too, that the kinetics of the overall reaction (D) is controlled by reaction (O). [4]

Experimental

Catalyst is prepared by wetness impregnation of cobalt(II)-nitrate on the macroreticular copolymer of poly-4-vinylpyridine with divinylbenzene. The content of octahedral Co^{2+} coordination on polymer was 5.72 mas.% [5].

The experiments were carried out in the thermostated ($\pm 0.1^\circ\text{C}$), closed well-stirred (900 rpm) reactor at different temperatures (62, 64, 66 and 68°C) in dark. The reaction volume was 52 ml. Initial concentrations were for $[\text{KIO}_3]_0 = 7.2 \cdot 10^{-2} \text{ mol/dm}^3$, $[\text{H}_2\text{SO}_4]_0 = 4.8 \cdot 10^{-2} \text{ mol/dm}^3$, and $[\text{H}_2\text{O}_2]_0 = 4.6 \cdot 10^{-2} \text{ mol/dm}^3$. The catalyst was placed in the reactor prior to other components. The time evolution of the BL reaction was followed potentiometrically, by means of iodide ion sensitive electrode connected to the Ag/AgCl reference electrode.

Results and Discussion

In all cases, iodide oscillograms with one preoscillatory period and one sequence of the regular relaxation oscillations are obtained. The kinetic parameters τ_1 and τ_{end} are linear functions of the amount of polymer supported cobalt catalyst (Fig.1). These dependences are preserved at different temperatures (62-68 $^\circ\text{C}$). It is obvious that k_R decreases and k_O (k_D) increases when the amount of catalysts increases. Hence, the catalyst act as inhibitor for the reaction R, but at the same time, for the global or overall reaction D, it stimulates the decomposition of the hydrogen peroxide.

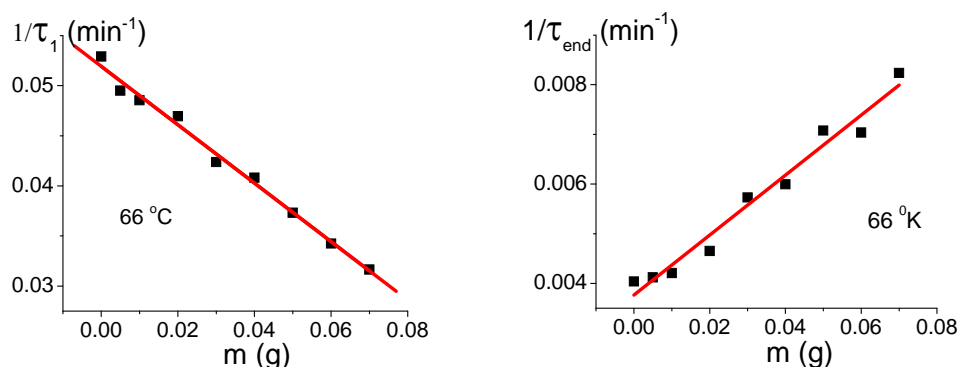


Figure 1. Dependences of τ_1 and τ_{end} from amount of catalyst m .

The intercepts (a) and slopes (b) of the lines in Fig.1. are dependent on temperature. Using the Arrhenius equation for this relation, the apparent activation energies are determined, for the reaction in the preoscillatory period, and for the overall BL reaction, from temperature dependences of both intercepts and slopes (Table 1).

Table 1. The apparent activation energies of the reactions R and O or D.

Source	E_R in kJ/mol		E_O <i>i.e.</i> E_D in kJ/mol	
	$a(\tau_1)$	$b(\tau_1)$	$a(\tau_{end})$	$b(\tau_{end})$
Apparent activation energy values	56	49	108	86

Conclusion

It is clear that the influence of examined catalyst on the BL matrix is evident and it could be quantified. However, the results of this investigation provoke new ones. One of them is the search for the model which can describes the interaction between the BL matrix and the catalyst, and some research related to application of BL reaction as analytical matrix for quantitative analysis of polymer supported cobalt catalyst. Also, it is necessary to define the role of the polymer on the BL reaction.

Acknowledgment

This work was partially supported by the Ministry for Science of the Republic of Serbia (Grants no. 142025 and no. 142019).

References

- [1] Lj. Kolar-Anić, S. Anić, Ž. Čupić, Characterization of the catalysts by means of an oscillatory reaction In “Finely Dispersed Particles: Micro-, Nano-, and Atto-Engineering”, Eds. A. Spasić and Jyh-Ping Hsu, CRC (earlier: Marcel Dekker), Inc., New York 2005, 191-216 and references therein.
- [2] W. C. Bray, J. Am. Chem. Soc., 1921, **43**, 1262.
- [3] W. C. Bray, H.A. Liebhafsky, J. Am. Chem. Soc., 1931, **53**, 38.
- [4] S. Anić, Lj. Kolar-Anić, E. Körös, React. Kinet. Catal. Lett., 1997, **61**, 111.
- [5] D. Lončarević, Ž. Čupić, Mater. Sci. Forum, 2005, **494**, 363.

DYNAMICS OF AN ENZYMATIC REACTION IN THE BATCH REACTOR

A. Nováková, L. Schreiberová and I. Schreiber

The Institute of Chemical Technology Prague, Department of Chemical Engineering and Center for Nonlinear Dynamics of Chemical and Biological Systems, Technická 5, 166 28 Prague 6, Czech Republic; tel. +420-220443033, fax: +420-220444320, e-mail: alena.novakova@vscht.cz

Abstract

The article is focused on the study of dynamics of the enzymatic reaction glucose – glucose oxidase – ferricyanide – sodium hydroxide in a batch reactor. This simple reaction provides an interesting nonlinear dynamic behaviour (bistability, excitability). The reaction serves as a model of certain function of living systems due to presence of the enzyme glucose oxidase which is ubiquitous in organisms. pH in the reactor depends on input parameters. We observed well-pronounced autocatalytic effect in the batch reactor in agreement with earlier observations.

Introduction

The principles of complexity in living systems can be to certain extent investigated on the basis of simple chemical reaction systems with nonlinear dynamical behaviour [1]. Characteristics of this system are observed by well-measured quantities *e.g.* pH, changes of concentration of hydrogen ions [2]. In the recent years inorganic pH-oscillators were investigated in detail [3]. One method to create a new pH-oscillatory system closer to living systems is a possibility to use enzymatic reactions. This approach was used by Vanag *et al.* [4] in the system peroxide oxidase – sulfite – ferrocyanide – HRP (horseradish peroxidase) or Hauser *et al.* [5] in the system peroxide oxidase – sulfite – hemin. Newly, the connection between the pH-oscillating reaction and the pH-response polymer leads to a design of equipment which could be used for drug delivery systems [6].

Our investigated system is the reaction glucose – glucose oxidase – ferricyanide – sodium hydroxide carried out in a batch reactor. Glucose which is key-substrate for many processes in organisms is the important species in this reaction system. A significant role in this reaction is played by the enzyme glucose oxidase (EC 1.1.3.4). Glucose oxidase catalyzes the oxidation of β -D-glucose to δ -D-glukonolactone and hydrogen peroxide (H_2O_2). Both products of this reaction can further spontaneously react. δ -D-glukonolactone hydrolyzes to gluconid acid ($C_6H_{12}O_7$) which decreases pH of the solution.

The reaction system glucose – glucose oxidase – ferricyanide – sodium hydroxide was proposed by Vanag *et al.* [7]. They studied the system for the most part experimentally but a significant part of their work was focused on the reaction mechanism and mathematical model. The experimentally observed behaviour was in good agreement with data from simulations. They described in detail the strategy

to design this system and introduction of a computer-assisted negative feedback providing the oscillations. This negative feedback represents reaction step of consumption hydrogen ions. If a negative feedback is introduced in a system which provides bistability in a continuous-flow stirred tank reactor (CSTR) then oscillations can be obtained.

Vanag *et al.* found bistability over a broad range of flow rate (reciprocal residence time) k_0 and the rate of concentration of sodium hydroxide NaOH and ferricyanide, $[\text{NaOH}]_0/[\text{Fe}(\text{CN})_6^{3-}]_0$. The oscillations were reached by a so-called physical approach, *i.e.* changing input flow NaOH which was from 2 to 20 minutes depending on parameters especially k_0 . The amplitude of oscillations depends also on parameters but the wave form of oscillations is unchanged, with shorter fraction of the oscillation staying at low pH and at larger fraction at higher pH. The enzyme glucose oxidase was physically immobilized in the gel. In this paper we present experiments showing autocatalytic behaviour in batch reactor.

Experimental

All solutions were prepared freshly on the day of use except for the glucose. Glucose need to mutarotate therefore solution was prepared one day before measurement. The batch reactor was a 25 mL beaker with an immersed pH-electrode (Cole-Parmer). The volume of the reactor was mixed by a magnetic stirrer. We carried out a set of experiments under batch conditions and recorded kinetic traces of the reaction of glucose with ferricyanide catalyzed by glucose oxidase. The values of input concentrations were taken from [7]. The main control parameters were the concentration of glucose oxidase and the ratio of the input concentration of sodium hydroxide and ferricyanide $P = [\text{OH}^-]_0/[\text{Fi}]_0$. P was varied from 0.1 to 0.5 with step 0.05 according to selected concentration of sodium hydroxide and ferricyanide.

Results and Discussion

Typical runs of the reaction are shown in Fig. 1 and Fig. 2. In Fig. 1 the pH time series for various ratios P is shown and in Fig. 2 traces for various concentration of glucose oxidase are displayed.

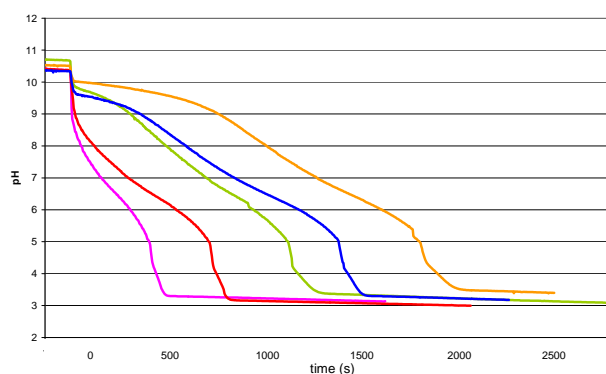


Fig. 1 The pH time series for various ratios P . $[G]_0 = 21$ mM, $[\text{GO}]_0 = 0.33$ mg/mL. *

* $P = 0.1$ ($[\text{OH}^-]_0/[\text{Fi}]_0 = 0.3/3$),
 $P = 0.2$ ($[\text{OH}^-]_0/[\text{Fi}]_0 = 0.6/3$),
 $P = 0.3$ ($[\text{OH}^-]_0/[\text{Fi}]_0 = 0.9/3$),
 $P = 0.4$ ($[\text{OH}^-]_0/[\text{Fi}]_0 = 0.8/2$),
 $P = 0.5$ ($[\text{OH}^-]_0/[\text{Fi}]_0 = 1/2$).

* $[\text{OH}^-]_0$ and $[\text{Fi}]_0$ are in mM

The kinetic curves have two distinct regions: a slower region for pH above 5, and a fast region for pH below 5. The final pH is slightly above 3. For the $P = 0.1$ (420s) reaction is faster than for $P = 0.5$ (1980s) (Fig.1). But there is some irregularity for the ratios $P = 0.3$ and $P = 0.4$ which could be caused by the fact that for these ratios the reaction occurs in the region of bistability [7]. In Fig. 2 the decrease of the concentration of glucose oxidase lead to longer reaction times. For $[GO]_0 = 0.33$ mg/ml the reaction reached pH = 3 at 500s which corresponds to the residence time $k_0 = 0.00219$ s⁻¹. This feature could be used for experiments in the CSTR.

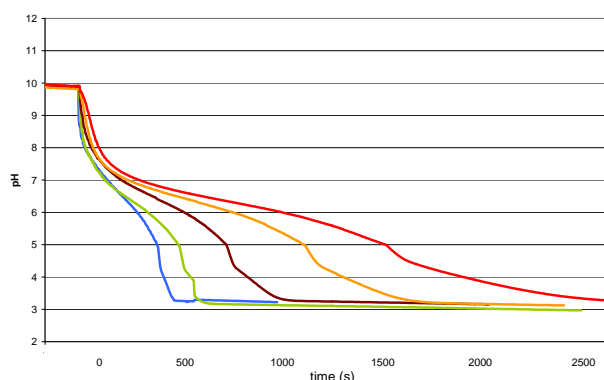


Fig. 2 The pH time series for concentration of glucose oxidase. $[G]_0 = 21$ mM, $P = 0.1$ ($[OH^-]_0/[Fi]_0 = 0.3$ mM/3 mM),
 [GO]₀ = 0.33 mg/mL,
 [GO]₀ = 0.20 mg/mL,
 [GO]₀ = 0.10 mg/mL,
 [GO]₀ = 0.05 mg/mL,
 [GO]₀ = 0.025 mg/mL.

Conclusion

We studied the reaction in the batch reactor for various input parameters (concentration of enzyme glucose oxidase and ratio of input concentration of sodium hydroxide and ferricyanide). There is a well-pronounced autocatalytic effect of the glucose oxidase. We observed the time-dependence the rate of reaction on the concentration of enzyme. Further experiments in the batch will be aimed at the role of concentration of glucose and sodium hydroxide in the reaction. Our next aim is to verify the bistability of the system glucose – glucose oxidase – ferricyanide – sodium hydroxide in the CSTR and subsequently replace a computer assisted negative feedback leading to oscillations by a more natural one, *e.g.* by a limited availability of glucose.

Acknowledgment

This work was supported by grant GACR 203/09/2091, GACR 104/08/H055 and by financial support from specific university research (MSMT no. 21/2010).

References

- [1] R. Larter, J. Phys. Chem. B, 2003, **107**, 415-429.
- [2] F. Sagués, I. R. Epstein I. R., Dalton Trans., 2003, 1201-1217.
- [3] G. Rábai, M. Orbán, I. R. Epstein, Acc. Chem. Res., 1990, **23**, 258-263.
- [4] V. K. Vanag, J. Phys. Chem. A, 1998, **102**, 601-605.
- [5] M. J. B. Hauser, A. Strich, R. Bakos, Z. Nagy-Ungvarai, S.C. Müller, Faraday Discuss., 2001, **120**, 229-236.
- [6] G. P. Misra, R. A. Siegel, J. Controlled Release, 2002, **79**, 293-297.
- [7] V. K. Vanag, D. G. Míguez, I. R. Epstein, J. Chem. Phys., 2006, **125**, 194515-1 – 194515-9.

TEMPERATURE INFLUENCE ON POSITION OF THE HOPF BIFURCATION POINT IN THE BRAY-LIEBHAFSKY OSCILLATORY REACTION

M. Vujković^{1*}, J. Maksimović¹, M. Milenković¹,
D. Stanisavljev¹ and N. Pejić²

¹Faculty of Physical Chemistry, University of Belgrade, Studentski trg 12-16, P.O. Box 137, Belgrade, Serbia, e-mail: milicavuj5@yahoo.com

²Faculty of Pharmacy, University of Belgrade, Vojvode Stepe 450, Belgrade, Serbia

Abstract

The non-periodic, periodic and chaotic regimes in the Bray-Liebhafsky (BL) reaction observed in a continuously fed well stirred tank reactor (CSTR) under isothermal conditions at various inflow concentrations of the H₂SO₄ were experimentally studied. In every series that is at any fixed temperature, termination of oscillatory behavior *via* some kind of the Andronov–Hopf bifurcation is presented. In addition, it was found that an increase of temperature, in different series of experiments resulted in the shift of bifurcation point towards high values of sulfuric acid concentration. Moreover, these values depend linearly on the temperature.

Introduction

The investigation of the chemical system which possesses non-linear properties, such as self-organized temporal dynamic structures, has become one of the most active areas in chemical dynamics. The Bray–Liebhafsky (BL) reaction is a good example of mentioned system. There are only few studies of the BL reaction [1] realized in continuously fed well stirred tank reactor (CSTR) when the control parameter is sulfuric acid [2, 3]. The experimental evidences for the termination of oscillatory behavior *via* the Hopf bifurcation were noticed.

The aim of this study was to investigate the influence of temperature on the position of the Hopf bifurcation point in the Bray–Liebhafsky oscillatory reaction.

Experimental

We investigated dynamic behavior of the BL reaction (the reaction where H₂O₂ decomposes into the H₂O and O₂ in the presence of both IO₃⁻ and H⁺ ions) in the CSTR. These examinations were carried out in independent series of experiments performed at different temperatures (from 55.0 °C to 67.0 °C). In every series (at any fixed T), the dynamic behavior of the BL reaction is examined when inflow concentration of H₂SO₄ (control parameter) varied from 0.0610 M to 0.0978 M. In all experiments, [KIO₃]₀ = 0.059 M, [H₂O₂]₀ = 0.15 M and the specific flow rate, j₀ = 0.0295 min⁻¹. Temporal evolution of the system was recorded by means of a Pt

electrode and double junction Ag/AgCl electrode interfaced to a PC-AT 12 MHz compatible computer *via* a PC-Multilab EH4 16-bit ADC. The temperature was controlled within ± 0.1 °C by a circulating water thermostat.

Results and Discussion

Characteristic examples of BL oscillograms obtained at different temperatures are illustrated in Fig. 1. In one series, concentration of H₂SO₄ varied (Fig. 1. (a₁)–(a₆)), while the other parameters (T, j₀ and concentration of both KIO₃ and H₂O₂) remain unchanged.

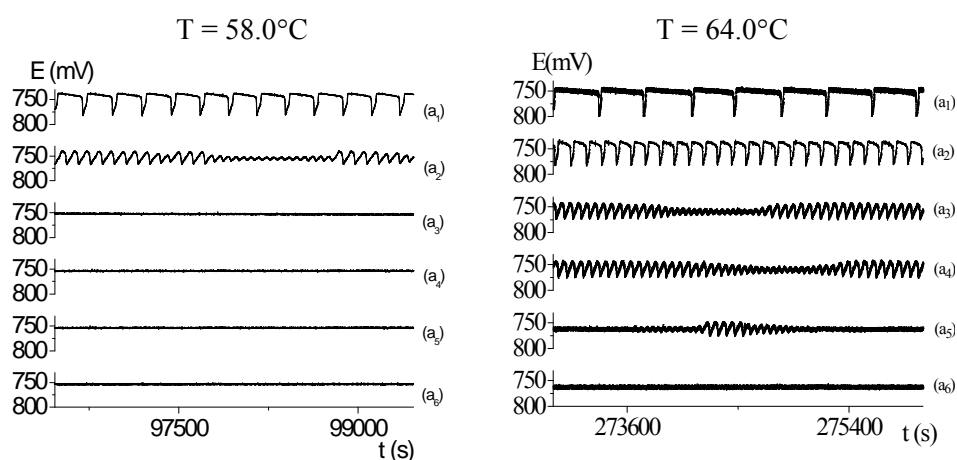


Fig.1. Time series obtained under the given experimental conditions and temperatures 58.0°C and 64 °C. Inflow concentration of H₂SO₄ are (a₁) 0.0610 M (a₂) 0.0744 M (a₃) 0.0830 M (a₄) 0.0835 M (a₅) 0.0845 M and (a₆) 0.0848.

For H₂SO₄ concentration in the range from 0.0610 M to different values such as 0.0690 M (T = 55.0°C), 0.0732 M (T = 58.0°C), 0.0769 M (T = 61.0°C), 0.0819 M (T = 64.0°C) and 0.0892 M (T = 67.0°C), simple periodic oscillations are found. Transition from the oscillatory state to the stable nonequilibrium stationary state goes through an aperiodic dynamic (Fig 1). Particularly, when [H₂SO₄] increases above these values, chaotic dynamic with different complexity is revealed (Fig. 1 (a₂) at 58.0°C, and (a₃) – (a₅) at 64.0°C). Last dynamic states with regular sustained oscillations before bifurcation point are analyzed by linear extrapolation of a plot of square of the amplitude of the oscillations. The critical values are [H₂SO₄] = 0.0720 M, 0.0757 M, 0.0820 M, 0.0880 M and 0.0970 M at temperatures 55.0°C, 58.0°C, 61.0°C, 64.0°C and 67.0 °C, respectively. In additions, the bifurcations occur at the same value of the control parameter, when approached from either side, i.e. hysteresis was not observed. Also, when these bifurcation points are approached, the period of the large-amplitude oscillations remains constant. Thus, we assumed that the underlying dynamic structure consist a stationary state loosing stability through probably Andronov-Hoph bifurcation,

but this intersection cannot be the simple Hopf bifurcation point since two kinds of oscillations emerge from it [3]. In different series of experiment that is at different temperatures type of bifurcation is not change, but the temperature variation change the position of bifurcation point (Fig. 2).

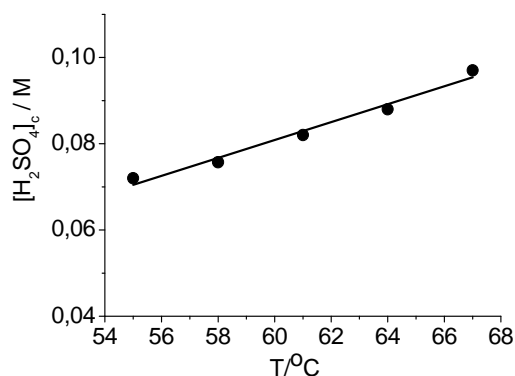


Fig.2. Plot of the value of bifurcation point as a function of the temperature

Conclusion

The dynamic behavior of the BL reaction realized in the CSTR is performed. The experimental evidence for the termination of oscillatory behavior *via* some kind of the Andronov–Hopf bifurcation were noticed. Moreover, the complex dynamic behavior including transition from simple periodic oscillation to mixed-mode oscillations was also discovered. The temperature variation in different series of experiments does not change the type of bifurcation point, but rather its value.

Acknowledgement

The present investigations were partially supported by the Ministry of Sciences and Environmental Protection of Serbia, under Project 142025.

References

- [1] W. C. Bray, J. Am. Chem. Soc., 1921, **43**, 1262.
- [2] V. Vukojević, S. Anić, Lj. Kolar-Anić, J. Phys. Chem. A, 2000, **104**, 10731.
- [3] N. Pejić, J. Maksimović, D. Ribić, Lj. Kolar-Anić, Russ. J. Phys. Chem. A, 2009, **83**, 1490.

ANALYSIS OF THE CHAOTIC STATES IN THE BRAY-LIEBHAFSKY REACTION WHEN SULFURIC ACID IS THE CONTROL PARAMETER

M. J. Vujković¹, A. Z. Ivanović², J. P. Maksimović¹ and M. C. Milenković¹

¹*Faculty of Physical Chemistry, University of Belgrade, Studentski trg 12-16, Belgrade, Serbia (milicavuj5@yahoo.com)*

²*IChTM, University of Belgrade, Department of Catalysis and Chemical Engineering, Njegoševa 12, Belgrade, Serbia*

Abstract

The influence of the inflow sulfuric acid concentration, $[\text{H}_2\text{SO}_4]_{\text{in}}$, as the control parameter, on the dynamics of the Bray-Liebhafsky oscillatory reaction was explored in CSTR reactor, at 61°C. In these experiments, various simple, complex and chaotic oscillations are observed. Using the attractor reconstruction, Lyapunov exponent's evaluation and multifractal analysis, different forms of chaos were identified in the same concentration range, depending on increasing or decreasing changes of the control parameter value.

Introduction

It has been found that Bray-Liebhafsky (BL) reaction [1,2], as the other oscillatory ones, can be realized through the regular and irregular dynamics (chaos), depending on the value of the chosen control parameters. [3] In the present paper the influence of the $[\text{H}_2\text{SO}_4]_{\text{in}}$ as the control parameter, on the dynamics of the BL oscillatory reaction in the CSTR, is explored at 61°C and flow rate $j_0=0.0295 \text{ min}^{-1}$. Using attractor reconstruction, it is possible to remove experimental noise from time series, enabling a better understanding of inherent dynamics. [4] Lyapunov exponents are the scalar measure of the irregularity in deterministic chaos time series. [4] Multifractal analysis gives more details on complexity of the chaotic dynamics. [5]

Materials and Methods

The temporal evolution of the BL system was monitored potentiometrically in a continuously fed well stirred tank reactor (CSTR). Experiment was performed at $T = 61^\circ\text{C}$ and specific flow rate $j_0 = 0.0295 \text{ min}^{-1}$. The initial concentrations were $[\text{KIO}_3]_0 = 0.059 \text{ M}$ and $[\text{H}_2\text{O}_2]_0 = 0.15\text{M}$. The inflow concentration of H_2SO_4 (control parameter) was varied between 0.0610 M and 0.0978 M, in both directions.

Results and Discussion

Various simple, complex and chaotic oscillations are observed in the range of $[\text{H}_2\text{SO}_4]_{\text{in}}$ values between 0.0610M and 0.0978M. Chaos emerges in these experiments from periodic oscillatory state when value of the control parameter increases above 0.0782M. However, when control parameter is decreased from

high values, the BL reaction remains in stable steady state down to 0,0806M. Change of the $[H_2SO_4]_{in}$ could not be continual and the next lower value of the control parameter 0.0799M leads the system right into deterministic chaos, due to very narrow interval corresponding to periodic oscillations.

Forms of chaos that were observed in the same concentration range between 0.0782M and 0.0799M, in both directions, are different depending on the direction of $[H_2SO_4]_{in}$ change (Figure 1). However, it is not possible to approve this difference without quantification of the chaotic dynamics.

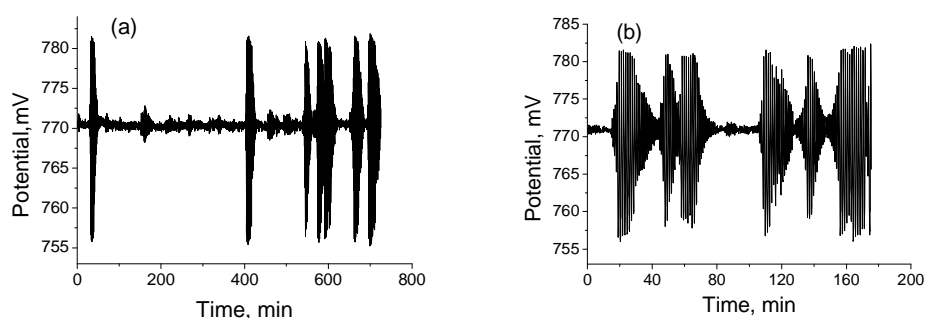


Fig.1. Selected time series from the experiment that correspond to same $[H_2SO_4]_{in}$ value (7.94×10^{-2} M) in: (a) increasing and (b) decreasing direction of changes of the $[H_2SO_4]_{in}$ as the control parameter.

Singular Value Decomposition method was applied on experimental time series present in figure1, and used to obtain the best possible attractor reconstruction invariant on particular choice of time delay parameter.

Accumulation point in central part of the reconstructed attractor corresponds to small amplitude oscillations for both cases. Difference between reconstructed attractors is present at the peripheral part, corresponding to large amplitude oscillations.

Lyapunov exponents are calculated using Wolf method that allows the estimation of the largest non-negative Lyapunov exponents from an experimental time series. It is shown that the largest Lyapunov exponent is positive, which is a strong indicator for the chaotic behavior of the system. In the direction of the increasing $[H_2SO_4]_{in}$ Lyapunov exponent is 3.75×10^{-3} and in the direction of the decreasing $[H_2SO_4]_{in}$ it is 1.069×10^{-2} . Higher Lyapunov exponent value indicates more irregular dynamics.

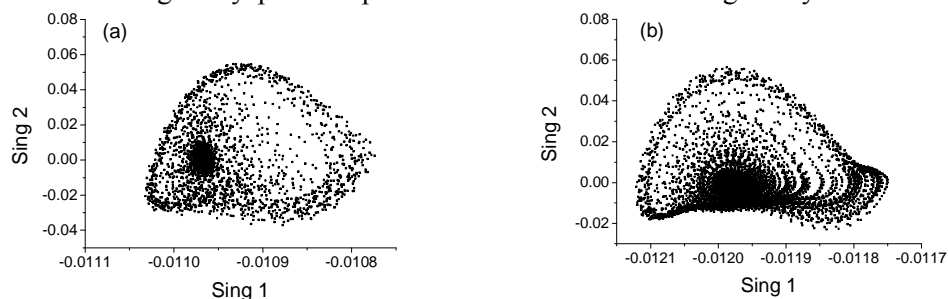


Fig.2. Reconstructed attractors which correspond to the time series from Fig. 1.

By application of Large Deviation Spectrum on chaotic time series obtained at different $[\text{H}_2\text{SO}_4]_{\text{in}}$ values, wide distribution with only one maximum is found. The shape and the width of the graph indicate different contributions of dynamics with differing fluctuation amplitudes. Hence, chaotic state obtained in decreasing of control parameter exhibits more pronounced multifractal properties. This difference between two chaotic dynamic states could be correlated with time series from Fig 1, where it could be seen that decreasing control parameter leads to chaotic dynamics, more abundant with various amplitudes of oscillations.

Conclusion

Different forms of chaos were obtained experimentally in BL reaction. The appearance of deterministic chaos is confirmed and proven in experiment, determining Lyapunov exponents, for different dynamical states obtained by increasing or decreasing $[\text{H}_2\text{SO}_4]_{\text{in}}$ values. Difference between these forms of chaos was characterized using Large Deviation Spectrum.

Acknowledgment

The authors thank the partial support of the Ministry of Science and Technological Development of Serbia. Proj. 142019 and 142025.

References

- [1] W. C. Bray, J. Am. Chem. Soc., 1921, **43**, 1262.
- [2] W. C. Bray, H. A. Liebafsky, J. Am. Chem. Soc., 1931, **53**, 38.
- [3] G. Schmitz, Lj. Kolar-Anić, S. Anić, T. Grozdić and V. Vukojević, J. Phys. Chem. A, 2006, **110**, 10361.
- [4] A. Z. Ivanović, Ž. D. Čupić, M. M. Janković, Lj. Z. Kolar-Anić and S. R. Anić, Phys. Chem. Chem. Phys., 2008, **10**, 5848, and references therein.
- [5] A. Z. Ivanović, Ž. D. Čupić, Lj. Z. Kolar-Anić, M. M. Janković, and S. R. Anić, Russ. J. Phys. Chem. A, 2009, **83**, 1526.

CRITICAL MANIFOLD OF THE MODEL FOR BRAY-LIEBHAFSKY OSCILLATORY REACTION

A. Z. Ivanović¹, Ž. D. Čupić¹, S. R. Marinović¹,
G. Schmitz³ and Lj. Z. Kolar-Anić²

¹ *Institute of Chemistry, Technology and Metallurgy, University of Belgrade,
Department of Catalysis and Chemical Engineering, Njegoševa 12,
(ana.ivanovic@nanosys.ihtm.bg.ac.rs)*

² *Faculty of Physical Chemistry, University of Belgrade, Studentski trg 12-16,*

³ *Faculté des Sciences Appliquées, Université Libre de Bruxelles, CP165/63, Av.
Roosevelt 50, 1050 Bruxelles, Belgium*

Abstract

Mixed mode oscillations are obtained in numerical simulations of the Bray-Liebhafsky oscillatory reaction in CSTR, for appropriate choice of the parameter set. In this paper, we analyze critical manifold of the slow-fast system in three dimensional phase subspace. We found that small amplitude oscillations obtained as a part of mixed mode dynamics are governed by canard solutions.

Introduction

The Bray-Liebhafsky (BL) reaction [1, 2] is the decomposition of hydrogen peroxide into the water and oxygen in the presence of iodate and hydrogen ions:



With increasing flow rate j_0 in a CSTR, various simple, complex and chaotic oscillations were observed in experiment and numerical simulations. [3] Shape of the oscillations depends on the value of control parameter j_0 , but in a wide region of parameter space it is typical for oscillations of the relaxation type. It was shown [4] that reaction dynamics of the relaxation oscillations in the BL reaction in closed reactor consists of long periods of slow iodine accumulation (reduction branch R) and sharp spikes with fast concentration changes of all intermediary species. This type of dynamics is described by nullclines of the model taking iodine as the only one slow intermediary. [4] Oscillatory dynamics of the BL reaction in CSTR can be simulated with a model consisting of seven reactions where three of them are reversible and the reactions due to flow of hydrogen peroxide through the system and outflow of all species from the reaction vessel. [5] Mixed mode oscillations in simulations using the BL reaction model in a CSTR appear as sequences of X large ones, and Y small ones, denoted as X^Y . Large oscillations in those sequences are also relaxation ones, while the small ones are nearly harmonic.

A mechanism of mixed mode oscillations was proposed recently, based on slow-fast dynamics and canard solutions of three dimensional dynamical systems.

[6] Since the BL reaction in CSTR also belongs to slow-fast systems with two slow variables (iodine and hydrogen peroxide) and four fast ones, here we explore its critical manifold and slow nullclines on it.

Methods

All calculations were done with the MATLAB program package. Deterministic simulations were performed using the ode15s solver with rate constants from ref. [5]. Critical manifold were calculated in self-made MATLAB application, from quasi-steady state equations. Fold line and nullclines were identified using a numerical search algorithm on the critical manifold surface.

Results and Discussion

Critical manifold was calculated from quasi-steady state equations for four fast variables. Since the solution of these equations depends on concentrations of two slow variables, it is represented with two dimensional surfaces in six dimensional phase space. For any fixed value of $[H_2O_2]$, we obtained one dimensional curves resembling the shape of the slow nullclines for the batch reactor. One sample curve is presented in figure 1, for the model of the BL reaction in a CSTR with $j_0=0.002874 \text{ min}^{-1}$ and $[H_2O_2] = 0.16 \text{ M}$. Shape of these curves weakly depends on $[H_2O_2]$. Putting together sequences of such curves (generatrices), we obtained the critical manifold for the BL system in a CSTR, figure 2.

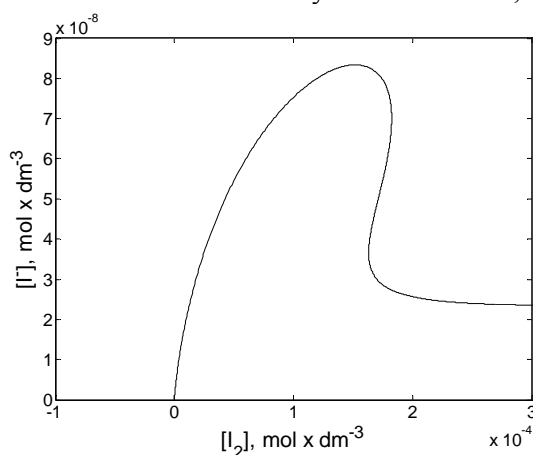


Fig.1. Sample generatrix of the critical manifold for the flow rate $0.002874 \text{ min}^{-1}$ and $[H_2O_2]=0.16 \text{ M}$.

Two nullclines of the BL model in a CSTR are found as the points on the critical manifold surface in which quasi-steady state condition is satisfied for each of two slow species (bold solid line for hydrogen peroxide and dash line for iodine in Figure 2). Fold line of the critical manifold and BL system trajectory are also presented in figure 2 as solid line.

Observing trajectories of the BL system in a wide interval of control parameter j_0 , we noticed that small amplitude oscillations in mixed-modes appear around the fold curve and iodine nullcline. Therefore, there is time interval during the oscillations when the system remains near the unstable part of the critical manifold surface. This situation is typical for canard solutions in dynamical systems with three or more dimensions. [6]

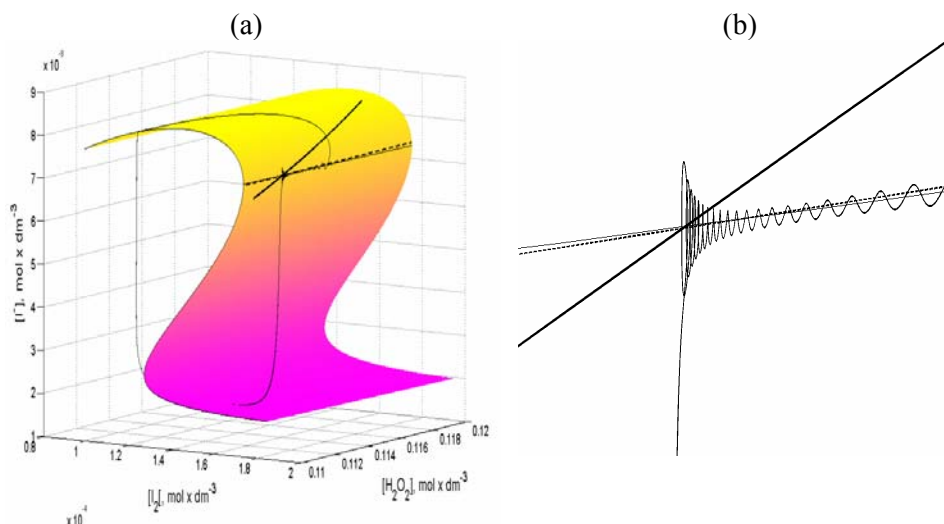


Fig.2. (a) Critical manifold of the slow-fast BL reaction model for the flow rate $0.002874 \text{ min}^{-1}$; (b) the enlarged intersection between BL system trajectory and fold line.

Conclusion

The critical manifold of the slow-fast system in three dimensional phase subspace was analyzed. Small amplitude oscillations obtained as a part of mixed mode dynamics appeared around the fold curve and iodine nullcline and they are governed by canard solutions.

Acknowledgments

The authors thank the partial support of the Ministry of Science and Technological Development of Serbia. Proj. 142019 and 142025.

References

- [1] W. C. Bray, J. Am. Chem. Soc., 1921, **43**, 1262.
- [2] W. C. Bray, H.A. Liebhafsky, J. Am. Chem. Soc., 1931, **53**, 38.
- [3] A. Z. Ivanović, Ž. D. Čupić, M. M. Janković, Lj. Z. Kolar-Anić and S. R. Anić: Phys. Chem. Chem. Phys., 2008, **10**, 5848, and references therein.
- [4] G. Schmitz, Lj. Z. Kolar-Anić, S. R. Anić, and Ž. D. Čupić, J. Phys. Chem. A, 2008, **112**, 13452.
- [5] Lj. Kolar-Anić, Ž. Čupić, G. Schmitz and S. Anić, Chemical Engineering Science, 2010, **65**, 3718.
- [6] M. Wechselberger, SIAM J. Appl. Dyn. Syst., 2005, **4**, 101.

IMPROVED STOICHIOMETRIC NETWORK ANALYSIS (SNA) OF THE MODEL OF HYPOTHALAMIC-PITUITARY-ADRENAL (HPA) AXIS

V. Marković¹ and Ž. Čupić²

¹ Faculty of Physical Chemistry, University of Belgrade, Studentski trg 12-16, 11000 Belgrade, Serbia (wladimirmarkowic@gmail.com)

² Institute of Chemistry Technology and Metallurgy, University of Belgrade, Department of Catalysis and Chemical Engineering, Njegoševa 12, 11000 Belgrade, Serbia

Abstract

Stoichiometric Network Analysis (SNA) is a mathematical procedure for stability analysis of complex reaction networks. Recently, substantial improvement of the method has been made having shown that stability relations, thus far expressed in terms of SNA parameters, (reciprocal concentrations of the species and current rates) can be transformed to a form comprising purely classic kinetic parameters (species concentrations and reaction rates). Thus, values of the stability relations can be calculated without making any approximation. In this paper, the improved SNA was performed on the model of the Hypothalamic-Pituitary-Adrenal (HPA) axis, a complex physiological system for maintaining homeostasis in basal as well as stress conditions.

Introduction

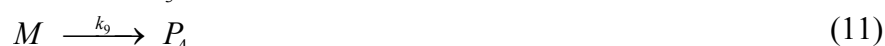
SNA is a powerful mathematical method for stability analysis of complex reaction networks [1], such as those occurring in a variety of oscillatory systems, when these processes can be properly represented by adequate stoichiometric models. SNA enables determination of the instability region of an observed system, and thus contributes to determining values of a control parameter for which main steady state is unstable and where different dynamic states, such as oscillations, can be simulated numerically or attained experimentally.

Temporal evolution of concentrations of species of a stoichiometric model is described by the set of corresponding differential equations. In SNA, they are typically written in the form $d[\mathbf{X}]/dt = \mathbf{S} \cdot \mathbf{r}$, where $d[\mathbf{X}]/dt$ is the time derivative of the concentration vector $[\mathbf{X}]$, \mathbf{r} the reaction rate vector and \mathbf{S} the matrix of the stoichiometric coefficients that can be read directly from an analyzed model. Reaction rates at a steady state \mathbf{r}_{ss} can be determined from the expression $\mathbf{S} \cdot \mathbf{r}_{ss} = 0$. As a result, rates at a steady state are expressed via linear combinations of elementary reaction pathways, commonly referred to as extreme currents E_i [1]. The extreme currents E_i are components of the extreme current matrix \mathbf{E} , whereas

their contributions, so called current rates j_i , form the corresponding vector \mathbf{j} . Thus, the basic equation of the SNA can be written: $\mathbf{r}_{ss} = \mathbf{E} \cdot \mathbf{j}$.

To derive instability conditions of an investigated model, the dynamics of small concentration perturbations $\Delta[\mathbf{X}] = [\mathbf{X}] - [\mathbf{X}]_{ss}$ near a steady state $[\mathbf{X}]_{ss}$, given by the equation $d\Delta[\mathbf{X}]/dt = \mathbf{M} \cdot \Delta[\mathbf{X}]$, obtained by linearization of the general equation of motion about this steady state, is analyzed. The essential feature of the SNA is the fact that the matrix \mathbf{M} is the function of the SNA parameters (j_i and h_i - the reciprocals of steady state concentrations), which are all non-negative. The steady state stability is determined by the eigenvalues of \mathbf{M} , which are the roots λ of the characteristic polynomial $|\lambda \mathbf{I} - \mathbf{M}| = \lambda^n + \alpha_1 \lambda^{n-1} + \alpha_2 \lambda^{n-2} + \dots + \alpha_n = 0$, where n is the number of independent intermediate compounds and α_i represents the sums of all diagonal minors of dimension i of matrix \mathbf{M} multiplied by product of the corresponding set of h_i values.

For the majority of models, number of SNA parameters exceeds the number of experimental ones, thus the complete set of rate currents remains undefined. Large improvement in the SNA has been made recently [2,3] when it was shown that instability terms, which in classical SNA are functions of rate currents, can be completely substituted by reaction rates at a steady state. In this paper, the improved SNA was used for stability analysis of the slightly modified model of Hypothalamic-Pituitary-Adrenal (HPA) axis [4]:



Results and Discussion

All conditions for the model [4] to exhibit simple Hopf or saddle-node bifurcation were derived in form of reaction rates. Complete expression for saddle-node bifurcation criterion is given as an example:

$$\begin{aligned} \alpha_4 = & (r_2 + 2r_5 + r_8 + r_9 + r_{10} - r_{11}) \cdot \{2r_{11}^3 + (-4r_2 - 8r_5 - 2r_8 - 2r_9)r_{11}^2 \\ & + [4r_2r_8 + (12r_2 - 2r_4 + 4r_8 + 3r_9)r_5 + r_2r_9 + 2r_2^2 + 10r_5^2]r_{11} - 4r_5^3 \\ & + (-8r_2 + 4r_4 - 2r_8 - 2r_9)r_5^2 + (-4r_2^2 + 4r_2r_4 - 4r_2r_8 - r_2r_9 + 2r_4r_8 - r_8r_9 + r_9^2)r_5 \\ & - 2r_2^2r_8 + r_2^2r_9 + 2r_2r_4r_8 - r_2r_8r_9 + r_2r_9^2\} < 0 \end{aligned}$$

where r_i ($i = 1 - 11$) are reaction rates, defined for the model given above.

Additionally, for the proposed set of rate constant values, stationary concentrations of the model's species were calculated. Since reaction rates could be calculated based on given set of rate constants and previously calculated stationary concentrations of the species, it was determined whether the proposed set had met complete criteria for the model to display simple Hopf or saddle-node bifurcation.

This procedure could be used for plotting precise bifurcation diagrams, by varying value of a rate constant playing the role of a bifurcation parameter. This could be particularly helpful in determining the set of rate constants such that the model exhibits the values of the hormones' concentrations according to experimental data, concomitantly maintaining its oscillatory dynamics.

Conclusion

The improved SNA was utilized for stability analysis of the model of the HPA axis, a physiological system with complex oscillatory dynamics. Exact relations for existence of single Hopf or saddle-node bifurcation in the model were derived. In that way, the set of rate constants could be determined for which the model's behaviour is adjusted to experimental data.

Acknowledgments

Present investigations were partially supported by Ministry of Sciences and Technology Development of Serbia under projects no. 142025 and 142019. The work was realized in collaboration with Prof. Lj. Kolar-Anić.

References

- [1] B. Clarke, in: *Advances in Chemical Physics*, I. Prigogine, S. Rice (Eds.), Wiley, New York, 1980, 1-216.
- [2] G. Schmitz, Lj. Kolar-Anić, S. Anić and Ž. Čupić, *Journal of Physical Chemistry*, 2008, **112**, 13452-13457.
- [3] Lj. Kolar-Anić, Ž. Čupić, G. Schmitz and S. Anić, *Chemical Engineering Science*, 2010, **65**, 3718-3728.
- [4] S. Jelić, Ž. Čupić and Lj. Kolar-Anić, *Math Biosci*, 2005, **197**, 173-187.

THE KINETICS OF REACTION BETWEEN IODIDE AND HYDROGEN PEROXIDE IN ACID SOLUTION

M. C. Milenković, D. R. Stanisavljev, T. M. Mudrinić and M. J. Vujković

*Faculty of Physical Chemistry, University of Belgrade, Studentski trg 12-16, 11000
Belgrade, Serbia*

Abstract

The kinetics of the complex reaction between Γ^- and H_2O_2 in acid media is investigated. The particular attention is focused on the determination of the rate constant of the reaction between HIO and H_2O_2 involved in investigated complex process. The examination of the whole kinetics was performed by monitoring evolution of O_2 pressure, I_3^- and Γ^- concentrations. We modeled behavior of experimentally followed components based on Liebhafsky research. Our preliminary results suggest a significantly higher rate constant of the reaction between HIO and H_2O_2 from those proposed in the literature.

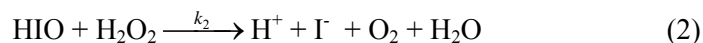
Introduction

Generally, the reactions of iodine are of environmental interest in the evaluation of the consequences of a nuclear reactor accident, in marine chemistry, and they are also part of several chemical oscillators. As an important part of iodine chemistry, the reaction between iodide and hydrogen peroxide was first investigated by Liebhafsky. He observed complex kinetics of this reaction and found that the rate constant in the neutral solution for the rate-determining step is $k_1 = 0.0115 \text{ M}^{-1}\text{s}^{-1}$. This rate constant [1] depends of the concentration of H^+ ($k_1 = 0.0115 + 0.175[\text{H}^+]$) and refers to the reaction (1):



More recently, Hansen has reexamined reaction between iodide and hydrogen peroxide in neutral solution [2]. Using initial rate method, he has measured $k_1 = 0.0173 \text{ M}^{-1}\text{s}^{-1}$ in good agreement with Liebhafsky's value.

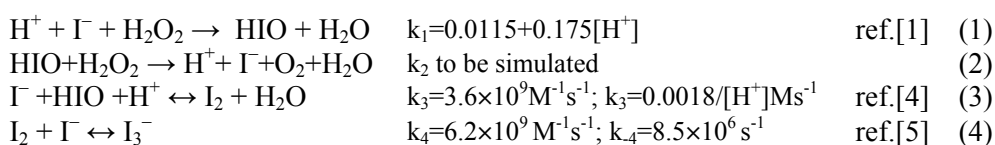
The rate-determining step (1) is followed by the reaction (2), the rate constant of which was, also, calculated by Liebhafsky $k_2 = 37 \text{ M}^{-1} \text{ s}^{-1}$ [3].



For the determination of the rate constant of reaction (2), its rate and concentrations of HIO and H_2O_2 should be known. The rate of (2) was calculated from the rate of oxygen evolution. Liebhafsky assumed that the reacted peroxide can be obtained from the amount of evolved oxygen and that the concentration HIO can be calculated from the equilibrium constant of iodine hydrolysis $[\text{HIO}] = K_h[\text{I}_2] / ([\Gamma^-$

][H⁺]). In order to further simplify calculations of [HIO], it is assumed that: a) the concentration of iodide ions is solely determined by the solubility product constant of the precipitated TII, b) iodine is mostly determined by its solubility in water due to its high excess relatively to added TI⁺, c) because of the low I⁻ concentration, the triiodide complex formation is neglected.

To simulate our experimental results and reexamine k₂, we considered all reactions proposed by Liebhafsky without his simplifications. The reactions are summarized in the model consisting of four major processes:



Experimental

The experiments were carried out in the closed, well sealed reaction glass vessel at room temperature. The volume of the whole system was 162.9±0.8 ml. Ports for ion sensitive electrode, reference electrode Ag/AgCl, pressure sensor and quartz fiber optic probe were found in the reactor cap. Temporal evolution of oxygen is followed by recording the potential of pressure sensor. The iodide concentration is monitored by recording the potential of iodide ion-sensitive electrode versus double junction Ag/AgCl reference electrode. The formation of triiodide complex was followed at 351 nm by quartz fiber optic probe interfaced to the UV/VIS spectrophotometer.

The initial composition of the reaction mixture was: [H₂O₂]₀ = 10⁻² mol/dm³, [KI]₀ = 8.8×10⁻⁴ mol/dm³ and [H₂SO₄]₀ = 4.9×10⁻² mol/dm³. All solutions are prepared in deionized water and all chemicals were of P.A. grade. The experiment was monitored for 500 seconds.

Results and Discussion

The evolution of oxygen, iodide and triiodide, obtained in experiments and in numerical simulations using proposed model, are shown in Fig. 4. Simulations were performed with the E-Z Solve program. If k₂ is Liebhafsky's value 37 M⁻¹s⁻¹ [3], investigated model relatively well simulates iodide and triiodide concentrations (Fig.1a and 1b), but oxygen is not considerably evolved even after 500 s (Fig.1c). From Fig.1c it is clearly evident that the rate constant for the formation of oxygen (2), should be considerably higher form the proposed value of 37 M⁻¹s⁻¹.

From six rate constants related with the examined model (1)-(4), five values are resumed from the literature and only k₂ is changed to get simulations of experiments. The value of k₂=2.8×10⁷ M⁻¹s⁻¹, simulates all experimental results, including oxygen, with accuracy up to 50 % (Fig.2 a, b and c). Although the better evolution of oxygen is obtained, further development of model is needed.

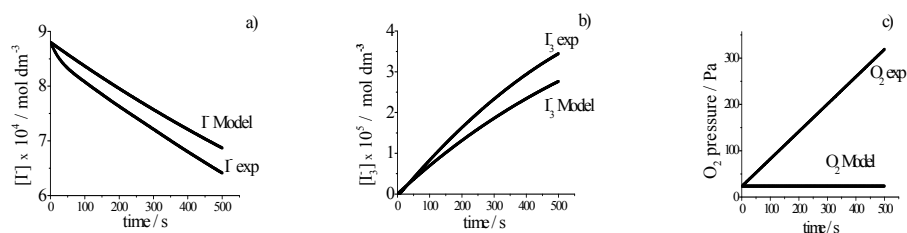


Fig.1 Experimental and simulating results for a) iodide concentration b) triiodide concentration and c) oxygen pressure; for k_2 used Liebhafsky's value $37 \text{ M}^{-1}\text{s}^{-1}$.

Our results, also, show that usual kinetics assumptions, related with the establishment of preequilibrium or stationary states, may lead to incorrect conclusions. It is stressed that the fitting of parameters in theoretical models should be performed using more experimentally followed reaction components.

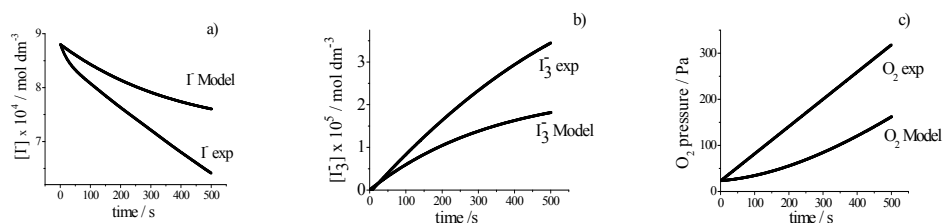


Fig.2 Experimental and simulating results for a) iodide concentration, b) triiodide concentration and c) oxygen pressure; for k_2 used value $2.8 \times 10^7 \text{ M}^{-1}\text{s}^{-1}$.

Conclusion

Our results suggest that the investigated model for reaction between Γ and H_2O_2 should be extended for better agreement between experimental and simulated results. Even the preliminary results show that the rate constant k_2 for the participating reaction of HIO with H_2O_2 is much higher ($2.8 \times 10^7 \text{ M}^{-1}\text{s}^{-1}$) than the value previously proposed by Liebhafsky ($37 \text{ M}^{-1}\text{s}^{-1}$).

Acknowledgments

This work is supported by the Ministry of Science of the Republic of Serbia. (Proj. No. 142025)

References

- [1] H. Liebhafsky and A. Mohammad, J. Am. Soc., 1933, **54**, 3977-3983.
- [2] J. C. Hansen, J. Chem. Edu., 1996, **73**, 728-732.
- [3] H. Liebhafsky, J. Am. Soc., 1932, **54**, 3504-3508.
- [4] S. Furrow, J. Phys. Chem., 1987, **91**, 2129-2135.
- [5] D. Turner, G. Flynn, J. Beitz, J. Am. Chem. Soc., 1972, **94**, 1554-1559.

RESPONSE DYNAMICS OF PH-OSCILLATORY REACTION

T. Veber, L. Schreiberová and I. Schreiber

Institute of Chemical Technology Prague, Department of Chemical Engineering and Center for Nonlinear Dynamics of Chemical and Biological Systems, Technická 5, 166 28 Prague 6, Czech Republic; tel. +420-220443033, e-mail: tomas.veber@vscht.cz;

Abstract

This work deals with the experimental study of the effect of single pulse forcing on pH-oscillation in hydrogen peroxide-thiosulphate-sulfite reaction operated in a continuous-flow stirred tank reactor. We studied the influence of external-pulsed perturbation by hydrogen ions solutions. Responses to pulsed forcing were used to construct the phase transition curves.

Introduction

The hydrogen peroxide-thiosulphate-sulfite reaction in acidic solution carried out in continuous-flow stirred tank reactor is a pH-oscillatory reaction which provides various steady states, periodic and aperiodic oscillations. Hydrogen ion is the key governing species responsible for the dynamical behaviour in this system. Dynamical regimes occurring in this system depend on external constrains such as temperature, flow rate or inlet concentrations of reactants. The mechanism is understood only partially [1]. The most important feature of the reaction mechanism is the positive feedback in hydrogen ions mainly provided by autocatalytic oxidation of hydrogen sulfite ions by hydrogen peroxide. The main inhibiting process is a rapid consumption of hydrogen ions by hydroxide ions created the reaction between hydrogen peroxide and thiosulphate ions. Negative feedback leading to the oscillations is provided by reactions that focus hydrogen sulfite. Phase transition curve (PTC) [2] characterizes the dynamics of the system and may help define its chemical mechanism. Our main interest is to obtain phase transition curves from stimulation of the pH-oscillations with brief single pulse additions of hydrogen ions solutions.

Phase transition curves (PTC)

The definition of the PTC is indicated in Fig. 1. Let us assume that the system oscillates periodically with a period T . Time t_{ri} marks the beginning and t_{r0} marks the end of the period for one oscillation. Certain amount of chosen species at time t_{pi} is injected to the system causing the perturbation. Because of assumed periodicity, **old phase** φ is introduced, defined as $(t_{pi} - t_{ri})/T$ restricted to the interval $[0,1]$. Phase $\varphi = 0$ corresponds to the beginning and $\varphi = 1$ corresponds to the end of oscillatory cycle and marks the state of the system. The perturbation affects the successive oscillations causing a temporal shortening or elongation of the measured period. After a sufficiently long time the system stabilizes and continues to oscillate with its normal period. However, new oscillations are phase shifted in comparison with the oscillations before the perturbation. Consequently time t_{ri+1} is

marked. The **phase shift** $\Delta\phi$ is obtained from t_{ri+1} and t_{r0} and depends on the phase of perturbation, thus $\Delta\phi = \Delta\phi(\phi)$. It can attain both positive and negative values. The **new phase** Θ is obtained as $\Theta = \phi - \Delta\phi(\phi)$. The time interval between t_{ri+1} and t_{pi} provides a dimensionless quantity $co\Theta$ called **cophase** (complementary phase) to the new phase Θ , which is defined by $\Theta = 1 - co\Theta$. According to Fig. 1, the relation for the above mentioned quantities is $1 + \Delta\phi = \phi + co\Theta$, where $co\Theta$ can be substituted by $co\Theta = 1 - \Theta$ and thus $\Theta = \phi - \Delta\phi$. Here all quantities are taken modulo 1, that is, restricted to the interval $[0,1]$. The PTC can have two topologically different forms, see Fig.2. Type 1 for relatively weak perturbations and type 0 for relatively large amplitudes of perturbations.

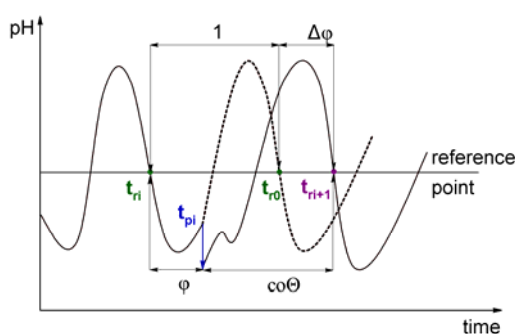


Fig.1. Demonstration of phase transition curve.

Experimets

Fresh demineralized water was prepared daily and used for preparing two stock solutions. First solution contained diluted hydrogen peroxide ($[H_2O_2]_0=0.0135$ mol/L) and the other contained the mixture of thiosulphate ($[Na_2S_2O_3]_0=0.005$ mol/L) with sulfite ($[Na_2SO_3]_0=0.0025$ mol/L) and sulfuric acid ($[H_2SO_4]_0=5.10^{-4}$ mol/L). Both stock solutions were

bubbled with N_2 for at least 12 hours before the experiment for elimination of CO_2 impurities. The experiments were carried out in a cylindrical-shaped plexiglass cell of 18.5 mL volume liquid under stirring by a teflon-covered magnetic stirrer (1.0 cm long), see Fig. 3. RM6 Lauda E103 thermostat was used for keeping constant temperature of $26 \pm 0.2^\circ C$. The external hydrodynamic perturbations were applied at the entry of the reactor using a syringe pump. pH-time series were measured by a pH-electrode (Theta '90, HC 139) with a pH-meter (Orion research, model 525A) connected through an A/D converter to the computer (Octek, Intel Pentium 200 MHz). Stock solutions were pumped into the reactor by a peristaltic pump (Ismatec IPC). pH=6 was experimentally established as the most suitable value of pH for the reference point. All experiments were carried out in the range of the flow rate $k_0 = 2.0 \times 10^{-3} - 2.8 \times 10^{-3} s^{-1}$. The concentration increment due to the pulse constitutes the

modulo 1, that is, restricted to the interval $[0,1]$. The PTC can have two topologically different forms, see Fig.2. Type 1 for relatively weak perturbations and type 0 for relatively large amplitudes of perturbations.

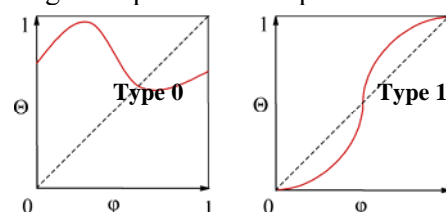


Fig.2. Two topological types of PTC.

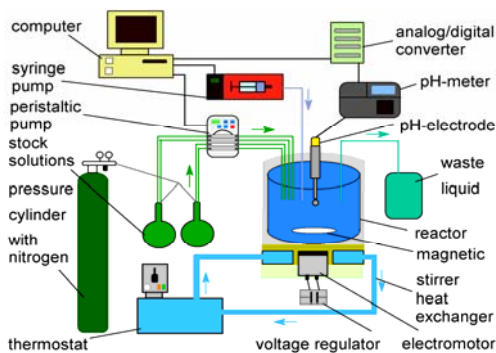


Fig.3. Experimental setup.

variable parameter. Its value was systematically changed from the lowest value to the gently affecting by the highest concentration increment of added hydrogen ions solutions. Throughout the experiments stock solutions were bubbled with N_2 .

Results and discussion

The method of external pulse perturbation of sustained pH-oscillations was used for the experimental determination of PTC. A regression was used to construct the dependence of new phase on old phase of the oscillation. By using this method we expected to find both topological types of PTC.

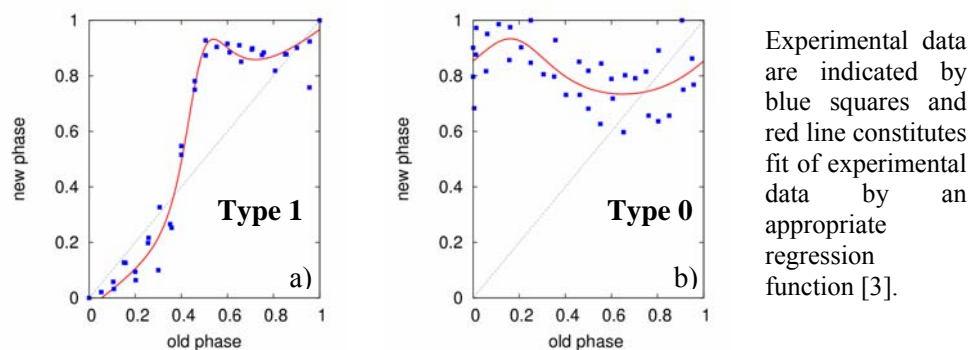


Fig.4. Construction of phase transition curves. The case a) 0.0491 mL of $c [H^+] = 0.0007$ mol/L, case b) 0.0491 mL of $c [H^+] = 0.002$ mol/L.

We carried out stimulations by hydrogen ions with known concentrations and given volume ratios. In the lowest additions was observed distribution of experimental data extending along the diagonal line, which represents no phase shift. In the following experiments with small perturbations (Fig. 4a) a curve of topological type 1 was obtained. In other experiments concentration of injected hydrogen ions was increased. Under these conditions the curve becomes much more flat corresponding to type 0 (Fig. 4b).

Conclusion

We have carried out experiments with hydrogen peroxide-thiosulphate-sulfite reaction and have found both topological types of phase transition curves for hydrogen ions additions. The type 1 is characteristic for low amplitude of perturbations. In our case type 1 was obtained for the 0.0491 and 0.0982 mL pulse volume with the concentration 0.0007 mol/L. PTC of type 0 was observed for a higher concentration corresponding to 0.0491, 0.0982, 0.1473 and 0.1964 mL pulse volume with the concentration 0.002 mol/L.

Acknowledgements

This work was supported by GACR 104/08/H055, GACR 203/09/2091 and by financial support from specific university research (MSMT no. 21/2010).

References

- [1] G. Rabai, I. Hanazaki, J. Phys. Chem. A, 1999, **103**, 7268-7273.
- [2] A.T. Winfree: *The Geometry of Biological time*, Springer-Verlag, New York, 1980.
- [3] J. Zagora, M. Voslař, L. Schreiberová, I. Schreiber, Faraday Discussions, 2001, **120**, 313-324.

THE EFFECT OF POSITIVE FEEDBACK IR COMPENSATION ON CURRENT OSCILLATIONS OF Cu | TFA ELECTROCHEMICAL SYSTEM

N. I. Potkonjak¹, T. N. Potkonjak² and S. N. Blagojević¹

¹*Institute of General and Physical Chemistry, Studentski trg 12-16, 11000
Belgrade, Serbia*

²*Town Planning Institute of Belgrade, Palmotićeveva 30, 11000 Belgrade, Serbia*

Abstract

The effect of positive feedback IR compensation on polarization curves and on oscillatory behavior of current during the electrodisolution of copper in 1 M trifluoroacetic acid was studied. Results are presented to show that the appearance of current oscillations, during electrodisolution process, is under the strong influence of Ohmic potential drop.

Introduction

The occurrence of nonlinear phenomena i.e. electrochemical oscillations in electrochemical systems is linked to the interplay between electrode kinetics, transport processes, and the electrical circuit. Thus, any attempt to understand the physico-chemical origin of the electrochemical instabilities has to take into account all elements of an electrochemical system [1].

The existence of the resistance (R_{Ω}) of electrolyte solution between the working and the reference electrode leads to the phenomenon of Ohmic potential drop (IR_{Ω} -drop, where I is the total current), caused by the flow of current through electrolyte. This means that the applied potential is split into IR_{Ω} -drop and the actual potential of working electrode. Ohmic potential drop is an inescapable consequence of polarization measurements. It has been argued by several authors that IR_{Ω} -drop plays an important role in arising of the current oscillation phenomenon during the electrodisolution of metals [2].

Experimental

The electrochemical cell consists of copper disc as working electrode, Pt-foil as auxiliary electrode and saturated calomel electrode (SCE) as reference electrode. The electrolyte solution was 1M trifluoroacetic acid (TFA), prepared from TFA (Merck) and deionized water ($18 \text{ M}\Omega \text{ cm}^{-1}$). Before each electrochemical measurement the electrolyte solution in the cell was deoxygenated with purified nitrogen by continuous bubbling for 10 min. In order to avoid dissolution of oxygen into the electrolyte, purified nitrogen was continuously passed above electrolyte surface during measurements. Electrochemical experiments were performed using Solartron SI 1286 electrochemical interface, supported with

corrosion measurement software (CorrWare[®]). The scan rate was 5 mV s^{-1} . The working electrode was polarized anodically starting from 0 mV vs. SCE. The positive feedback IR compensation technique was applied with compensation resistance (R_{comp}) of 0, 1, 5, 10, 15 Ω . The temperature of cell was 293 K.

Results and discussion

The effect of positive feedback IR compensation on current oscillation was studied by applying various R_{comp} during potentiodynamic measurements of copper electrodislution in 1M TFA, Fig. 1. As shown, current oscillations are affected by R_{comp} mostly throughout decrease of the amplitude. It appears that with increase of R_{comp} the amplitude of current oscillations decreases, changing from relaxation type to small amplitude oscillations. Furthermore, the shifted of the potential region of current oscillations more cathodically with the increase of R_{comp} can be noticed, Fig.1.

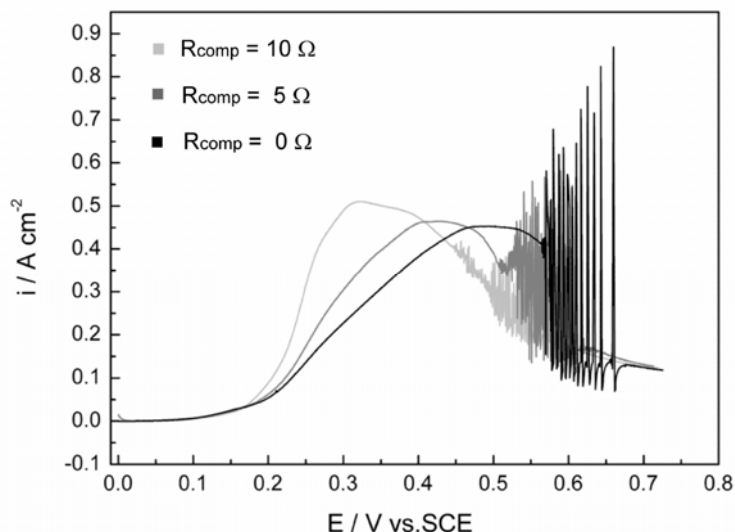


Fig.1. Anodic polarization curves of the electrodislution of Cu in 1M TFA under various IR compensation values. Scan rate was 5 mV s^{-1} .

The shift of the potential of first bifurcation point, which appears during forward anodic scan, was found to be linear with increase of R_{comp} . Results are presented in the Fig. 2. The shift is equal to the compensative potential which was calculated by multiplication of R_{comp} and current just before bifurcation point, Fig. 2. Applied positive feedback IR compensation technique have showed that appearance of instabilities such as current oscillations are closely related with the existence of Ohmic potential drop and that global feedback mechanisms need to take into account the effect of IR drop.

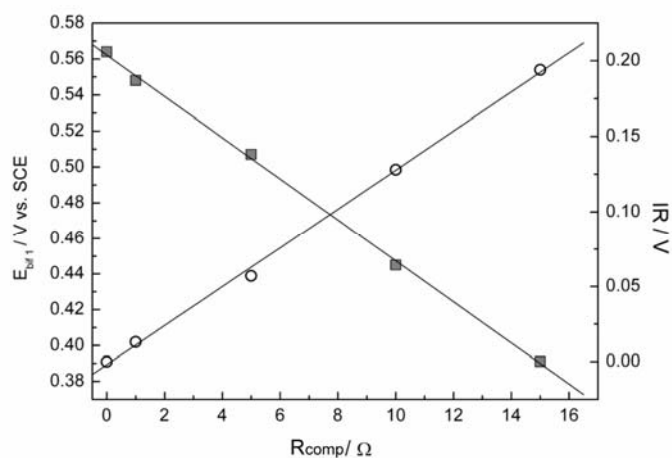


Fig.2. The potential of bifurcation point, E_{bif} , (gray squares) and the calculated compensation potential, IR , (white circles) as a function of the compensation resistance (R_{comp}).

Conclusion

The positive feedback IR compensation (PFIRC) was applied in potentiodynamic measurements of anodic electrodissoolution of copper electrode in 1 M trifluoroacetic acid. The strong effect of (PFIRC) on current oscillations of investigated electrochemical system was observed. The experiments have proved that IR potential drop play an important roll in interpretation of current oscillatory behavior observed during metal electrodissoolution in corrosive media.

Acknowledgement

The support of this research by the Ministry of Science and Technological Development of Republic of Serbia through projects No. 142025 is gratefully acknowledged.

References

- [1] S. Jain, I. Z. Kiss, J. Breidenich, J. L. Hudson, *Electrochim. Acta*, 2009, **55**, 363-373.
- [2] M. T. M. Koper, J. H. Sluyters, *J. Electroanal. Chem.*, 1993, **347**, 31-48.

ANALYSIS OF SINUSOIDAL CODED MODEL: ANALYSIS OF CODE

D. Golobočanin¹ and N. Miljević²

¹*Vinča Institute of Nuclear Sciences, POB 522, 11001 Belgrade, Serbia*
²*Jaroslav Černi Institute for Development of Water Resources, Jaroslava Černog
80, 11226 Belgrade, Serbia*

Abstract

This article presents a procedure for transformation of measured data and application of the proposed sinusoidal coded model to fit better seasonal stable isotope variations in precipitation and stream water. The utility of proposed model was validated by the comparison between measured data and numerical evaluations for oxygen isotopic content in precipitation over the period 2004-2008. The proposed sinusoidal coded model offers an accurate fit with low standard deviation per month only with one fitting parameter.

Introduction

Oxygen isotope composition (^{18}O) is an ideal tracer for characterizing hydrological processes because it can be reliably measured. Surface waters (precipitation and stream water) exhibit $\delta^{18}\text{O}$ seasonal variations which are usually generalized by an expression of the sine function equation (1):

$$\delta^{18}\text{O} = \text{mean}(\delta^{18}\text{O}) + A \sin[(2\pi t / b) + c] \quad (1)$$

where $\text{mean}(\delta^{18}\text{O})$ is the annual mean $\delta^{18}\text{O}$ expressed in ‰, A is the seasonal amplitude of $\delta^{18}\text{O}$, b is the period of the seasonal cycle (i.e. 365 days), t (days) is time, and c (radians) is the phase lag [1]. A typical sinusoidal model neither provides a satisfactory fit to the data of isotope content of precipitation nor meets Fisher's condition for the existence of periodical processes. Although, this model treats one year in the same way as the following, statistical noise is too large that the variations caused by non-periodic natural processes would be analyzed. As long as the obtained correlation coefficients for the assumed $p = 95\%$ are low ($r^2 < 0.76$), which is common in hydrologic investigations, this model is inadequate. It is important to note that most authors do not generally use statistical test to confirm the existence of periodicity (equation 2).

$$q_{\text{var}} = \frac{A_1^2}{\sum_{i=2}^n A_i^2} \geq 0.638 \quad \text{for } 95\% \text{ significance level} \quad (2)$$

where A_1 is the amplitude of basic frequency with the period of 12 months, and A_i stands for i -th harmonic in Fast Fourier Technique (FFT) series [2] for the total

number of measurements, n . The q_{var} is a variance ratio, which in our cases exhibit rather low values of around 0.219. Therefore, the coded sinusoid method has been proposed [3]. This method represents a new technique for a better fitting of periodic data. It is based on two assumptions. The first one is in advance known a period of time (t), which is usually one year in the case of hydrological data. It is implicit in all cyclical hydrologic models, and until recently it was the default, and neither examined nor criticized. Basically, it is assumption that all hydrologic processes on Earth are coordinated with its revolution. The second assumption concerns the shape of the observed periodic function. The basic idea is that parts of the original sinusoids (12 parts) are shifted along the time axis, of unequal value. These shifted values we call codes, by which the sine-coded model was named. The objective of this paper is to present a procedure for transformation of measured data and application of the proposed sinusoidal coded model.

Results and discussion

Our observed data are measured monthly values for period of N years (2004-2008). The application of sinusoidal coded method requires performing mathematical transformations to the measured data set (n). The first step is a subtraction of the trend line (list square line, LSQ) from all original data along the time axis. Then, monthly mean values (or weighed averages) are calculated by summing all transformed data for N years. The result is a set of 12 data. Next, the most important step is coding procedure shown in Table 1. In order to achieve the sine waveshape, calculated maximum and minimum monthly mean values are set at the position of maximum and minimum of a sinus function, respectively. A shift lag code should be noted for each month. Lagged data (CodD, Table 1) should be subjected to Fisher's condition for sinusoidal periodicity (2). If they pass, the procedure should be continued.

Table 1. The arrangement for coding procedure

	Jan	Feb	Mar	Apr	May	Jun	Jul	Aug	Sep	Oct	Nov	Dec
Data	-1	-0.8	-0.81	-0.5	-0.5	0	0.1	0.5	0.51	0.8	0.9	1
x_i	$0\pi/6$	$1\pi/6$	$2\pi/6$	$3\pi/6$	$4\pi/6$	$5\pi/6$	$6\pi/6$	$7\pi/6$	$8\pi/6$	$9\pi/6$	$10\pi/6$	$11\pi/6$
$\sin x_i$	0	1/2	0.87	1	0.87	1/2	0	-0.5	-0.87	-1	-0.87	-0.5
CodD	0	0.5	0.8	1	0.9	0.51	0.1	-0.5	-0.8	-1	-0.81	-0.5
Cod	-5	-6	-7	-8	-6	-3	0	+4	+7	+9	+8	+7

Data - transformed monthly mean values, x_i - x-axis, CodD – coded data (Y^{cod}), Cod - noted shift code

The amplitude of coded sinusoids is computed by the formula (3) which is obtained with minimization of simple non linear sine function with one parameter, A.

$$A^{cod} = \frac{1}{6} \sum_{i=0}^{11} Y_i^{cod} \cdot \sin x_i \quad (3)$$

where A^{cod} is coded amplitude and x_i is the time expressed in $2\pi/12$. Coded sinusoid is calculated using equation 4 in which Y_i^{cf} stands for fitted coded data.

$$Y_i^{cf} = A^{cod} \cdot \sin x_i \quad (4)$$

The following step is a decoding of generated sinus function. Fitted values are displaced to their coded positions according to their noticed order. Then, twelve obtained data should be repeated N-1 times. One set of data is produced for each year giving a coded fit. The final step is the addition of the trend line to the data obtained by decoding algorithm. The obtained periodical curve fits well measured data with the low standard deviation per month (σ_k) as the measure for a good fit (Fig. 1). Calculated efficiency index [4] for a simple sinusoidal and coded model is about 46% and 87%, respectively.

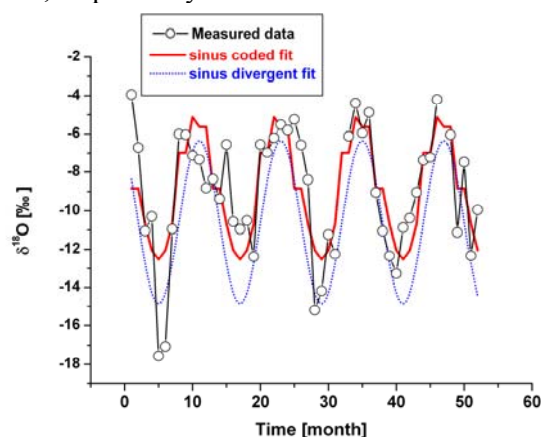


Fig.1. Measured and calculated oxygen-18 content of precipitation over the Velika Morava catchment using sinusoidal coded model for the period 2004-2008

Conclusion

In conclusion, the proposed sinusoidal coded model is established on basic hydrological assumption that neither the annual average nor the magnitude of isotopic variations in meteoric precipitation remains constant year to year. The amplitude of the isotopic variations of the system of interest is the only one fitting parameter, which can provide an accurate fit with low standard deviation per month.

References

- [1] M. M. Reddy, P. Schuster, C. Kendall, M. B. Reddy, *Hydrol. Process.*, 2006, **20**, 1753–1772.
- [2] R. Fisher, *Tests of significance in harmonic analysis, Contribution to mathematical statistics*, J. Wiley and Sons, New York, 1950.
- [3] D. Golobočanin, N. Miljević, *Sinusoidal coded model*, in A. Antić-Jovanović (ed.), *Physical Chemistry 2008*, SPCS, Belgrade, 2008, 647-649
- [4] R. H. McCuen, Z. Knight, G. Cutter, *J. Hydrol. Eng.*, 2006, **11**, 597-602.

THEORY OF ELECTROVISCOELASTICITY AND ITS IMPLICATIONS

A. M. Spasic

*Institute for Technology of Nuclear and Other Mineral Raw Materials
86 F. d'Esperey St. 11000 Belgrade, Serbia*

Abstract

This brief presentation consists of five parts that were experimentally and theoretically driven over the last twenty five years. The first part presents a historical review and motivation, giving short description of a developed pilot plant for solvent extraction of uranium, and the solution of the inevitable, undesirable, entrainment problems that occur during the extraction operations/processes. Further on, a new classification of finely dispersed systems based on entities is briefly introduced. The central part presents a new theory of electroviscoelasticity using a developed constitutive model of liquids. Three possible mathematical formalisms have been derived and discussed related to this physical formalism. Also, a new idea related to the probably possible discussion of the problems in the theoretical and experimental status of decoherence is mentioned. Finally, the implications and/or applications of the presented, both, theoretical and experimental issues are discussed considering two philosophical breakpoints.

History and motivation

Twenty five years ago the idea, at first very foggy, came out from the pilot plant experiments related to the extraction of uranium from wet phosphoric acid. In particular the solution of the entrainment problems, breaking of emulsions/double emulsions, as the succession of the extraction and stripping operations/processes, was performed. In this pilot plant, secondary liquid-liquid phase separation loop was designed and carried out. The loop consisted of a lamellar coalescer and four flotation cells in series. Central equipment in the loop, relevant to this investigation, was the lamellar coalescer. The phase separation in this equipment is based on the action of external forces of mechanical and/or electrical origin, while adhesive processes at the inclined filling plates occur. Since many of related processes, e.g. adhesive processes, rupture processes and coalescence, were not very well understood deeper research of these events and phenomena was a real scientific challenge [1-7].

A new classification of finely dispersed systems

The presented classification is based on *entities*, and may be considered as *the first philosophical breakpoint!* Therefore, an entity can be defined as the smallest indivisible element of matter that is related to the particular transfer phenomenon. Hence, the entity can be either differential element of mass/demon, or an ion, or a phonon as quantum of acoustic energy, or an infon as quantum of information, or a photon, or an electron [1-3, 7].

Also, it seems sensible to think about the further structure of entities, *the second philosophical breakpoint* e.g., the basic entity can be understood as an energetic ellipsoid (based on the model of electron following Maxwell-Dirac Isomorphism, i.e.: electron is an entity at the same time quantum-mechanical/microscopic $N = -2$ and electrostatics/macrosopic $N=3$) [1-3, 7].

Theory and modeling

The electroviscoelastic behavior of, e.g. liquid/liquid interfaces (emulsions and double emulsions) is based on three forms of “instabilities”; these are rigid, elastic, and plastic. The events are understood as interactions between the internal (immanent) and external (incident) periodical physical fields. Since the events at the interfaces of finely dispersed systems have to be considered at the molecular, atomic, and/or entities level it is inevitable to introduce the electron transfer phenomenon beside the classical heat, mass, and momentum transfer phenomena commonly used in chemical engineering [1-3, 7].

Three possible mathematical formalisms have been derived and discussed related to this physical formalism, i.e. to the developed constitutive model of liquids and theory of electroviscoelasticity. The first is stretching tensor model, where the normal and tangential forces are considered, only in mathematical formalism, regardless to their origin (mechanical and/or electrical). The second is classical integer order van der Pol derivative model. Finally, the third model comprise an effort to generalize the previous van der Pol differential equations, both, linear and nonlinear; where the ordinary time derivatives and integrals are replaced by corresponding fractional-order time derivatives and integrals of order $p < 2$ ($p = n - \delta$, $n = 1, 2$, $\delta \ll 1$).

In order to justify and corroborate more general approach the obtained calculated results were compared to those experimentally measured using the representative liquid-liquid system [1- 3, 6].

Recent development

Classical limit of quantum mechanics: One important question of the classical limit of quantum mechanics is: is a quantum mechanics applicable at macroscopic level? This question resulted during the research of complex systems by the end of the last century. According to the developed strategy the proposition appeared is: if the macroscopic physical systems are only the special case of a quantum-mechanical systems (e.g. like in von Neumann’s theory of the measurement problem) than it is possible to observe, under the specified conditions, their quantum mechanical behavior [4, 7].

The behavior of a droplet-film structure submerged into the droplet homophase or double emulsion, including its formation-existence-destruction states will be considered as a close to the representative open macroscopic quantum system (OMQS) under the specified conditions. Hence, OMQS are quantum subsystems, i.e. open quantum systems that are in inevitable permanent interaction with other physical systems, which may be named environment [4, 7]. Does the theory of electroviscoelasticity, here presented, may be useful in discussion and/or

further elucidation related to the problems of the experimental and theoretical status of decoherence?

Suggested experimental confirmation: Since the equivalent electrical circuit, cluster, defined in a developed theory of electroviscoelasticity, may be considered as a kind of Superconducting Quantum Interference Device (SQUID), probably, it may be possible to couple, (at resonant frequency, where all events occur) one adjusted, sensitive tunnel diode oscillator as one detector of Macroscopic Quantum Tunneling Effect (MQTE) [4, 7].

Implication

The first philosophical breakpoint: A theory of electroviscoelasticity using fractional approach constitutes a new interdisciplinary approach to colloid and interface science. Hence, 1-more degrees of freedom are in the model, 2-memory storage considerations and hereditary properties are included in the model, and 3-history impact to the present and future is in the game!

This theory and models discussed may facilitate the understanding of e.g. entrainment problems in solvent extraction, very developed interfaces in colloid and interface science, chemical and biological sensors, electro-analytical methods, biology/biomedicine (hematology, genetics, and electroneurophysiology).

Furthermore, both, the model and theory may be implemented in studies of structure; interface barriers/symmetries – surface (blipped membrane cells, free bubbles of surfactants, Langmuir Blodgett films), - line (genes, liquid crystals, microtubules), - point (fullerenes, micro-emulsions) and – overall (dry foams, polymer elastic and rigid foams).

the second philosophical breakpoint: The further evaluation of the idea, here introduced, related to the entity understood as an energetic ellipsoid. Such approach and consequent knowledge may be implemented in the studies of, e.g. ionics, spintronics, fractional-quantum Hall effect-fluids, decoherence sensitivity, quantum computation, entities/quantum particles entanglement [2, 7].

Acknowledgments

Financial support Min. of Sci. RS, Grant: 142034.

References

- [1] A. M. Spasic, M. P. Lazarevic, M. V. Mitrovic and D. N. Krstic In A. M. Spasic and J. P. Hsu (Eds.) *Finely Dispersed Particles: Micro-, Nano-, and Atto-Engineering*, CRC Press/Taylor and Francis, Boca Raton London New York, 2006, 3-23 & 371-394.
- [2] Jyh-Ping Hsu & A. M. Spasic *Interfacial Electroviscoelasticity and Electrophoresis*, CRC Press/Taylor & Francis, B. Raton London New York 2010.
- [3] A. M. Spasic, M. P. Lazarevic, *J. Coll.Interf.Sci.*, 2007, **316**, 984-995.
- [4] A. M. Spasic *Russian J. Phys. Chem.*, 2009, **83**, 1563-1570.
- [5] A. M. Spasic In A. V. Delgado (Ed.) *Interfacial Electrokinetics & Electrophoresis*, Marcel Dekker, New York, 2002, 837-868.
- [6] M. P. Lazarevic, A. M. Spasic, *Math. Comp. Mod.*, 2009, **49**, 475-481.
- [7] A. M. Spasic, *Finely Dispersed Systems: Colloid Electrohydrodynamics*, 19th CHISA & 7th ECCE, Prague, Aug 28-Sep 01, 2010.

NOVEL CLASS OF OSCILLATING REACTIONS: ALKYNES CARBONYLATION CATALYZED WITH Pd COMPLEXES

S. N. Gorodsky and O. N. Temkin

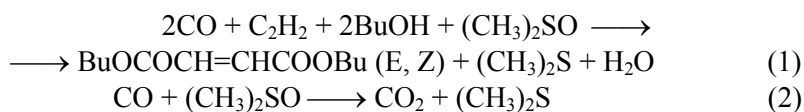
*M.V. Lomonosov State Academy of Fine Chemical Technology,
Vernadsky av. 86, 119571 Moscow, Russia
E-mail: Gorodsky@yandex.ru*

Introduction

The oscillating reactions were discovered in many chemical and biological systems. The most part of oscillatory homogeneous reactions investigated in chemistry are processes of organic substrate oxidation by strong oxidants.

Results and discussion

Our team has discovered the critical phenomena in typical reactions of the organometallic catalysis in which synthesis of complex molecules occurs. So, the reactions (1, 2) proceed in the system PdBr₂ – KBr – HBr – BuOH–dimethylsulphoxide:



with periodic change of carbon monoxide and acetylene consumption rate, values of platinum electrode potential (E_{Pt}), pH and color of the reaction solution [1]. Oscillations of E_{Pt} and pH were found out [2] during the study of various alkynes oxidative carbonylation reactions in the system PdI₂ - KI - MeOH (reaction 3)



where R: Ph, Me, C(CH₃)₂OH. Oxidation CO to CO₂ in this system occurs also. It was the first example of oscillating process including the complex molecules synthesis occurs on the base of relatively simple reagents using (Fig. 1)

We have showed that the phenomenon of oscillations can be observed for reactions with participation of different alkynes, and also in different catalytic systems, for example, in system PdBr₂ - LiBr, in which the occurrence of chaotic oscillations was demonstrated. One more reaction - oxidative carbonylation of phenylacetylene in system PdBr₂-LiBr-H₂O-acetone can proceed in an oscillatory mode also. The preliminary mechanism of this process is proposed.

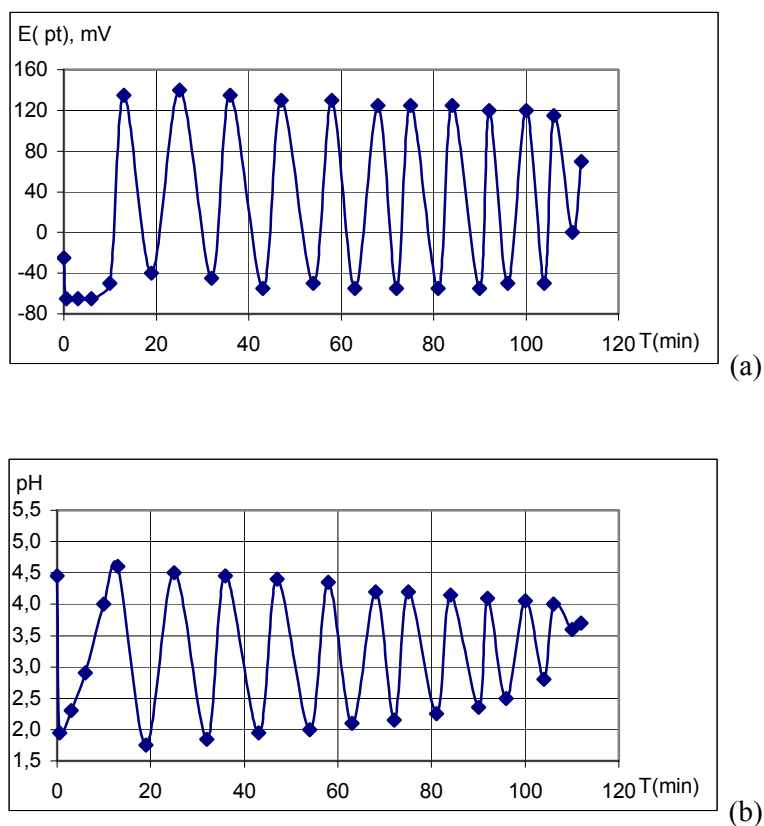


Fig.1. The change of E_{Pt} (a) and pH (b) in the contact solution during of phenylacetylene oxidative carbonylation reaction;
 $KI(0,4\text{ M}) - PdI_2(0,01\text{ M}) - PhC\equiv CH(0,1\text{ M}) - CO(60\% \text{ v.}) - O_2(40\% \text{ v.})$

Conclusion

The study of mechanisms of some other processes in organometallic catalysis allows us to expect occurrence of self-oscillations and other critical phenomena. The searching for such phenomena is important for development of the theory of catalytic reaction mechanisms.

Acknowledgements

This work was supported by the Russian Foundation for Basic Research (project № 09-03-01072).

References

- [1] G. M. Shul'akovsky, O. N. Temkin, N. V. Bykanova, A. N. Nyrkova, in *Chemical kinetics in catalysis: Kinetic models of liquid-phase reactions*, Chernogolovka: IPC, 1985, 112.

- [2] S. N. Gorodsky, E. S. Kalenova, L. G. Bruk, O. N. Temkin, Russ. Chem. Bull., 2003, **52**, 1534 - 1543.

REACTION OF PROPARGYL ALCOHOL CARBONYLATION TO DIMETHYL ESTER OF ITACONIC ACID PROCEEDING IN OSCILLATORY MODE

S. N. Gorodsky, A. V. Kurdiukov, O. N. Temkin

*M.V. Lomonosov State Academy of Fine Chemical Technology,
Vernadsky av. 86, 119571 Moscow, Russia*

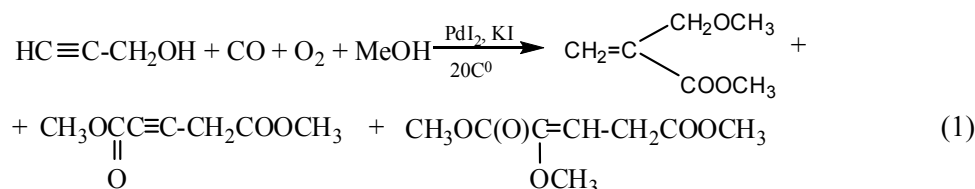
E-mail: Gorodsky@yandex.ru

Abstract

It was shown that the carbonylation of propargyl alcohol can proceed in system KI - PdI₂ - CO - O₂ - CH₃OH in an oscillatory regime.

Experimental

The carbonylation of propargyl alcohol (reaction 1):



was carried out in the closed system at T=20⁰C with intensive mixing of liquid and gas phases. The values of electric potential of a platinum electrode (E_{Pt}) and glass electrode (pH) were continuously measured during the reaction. Products of reaction were identified using gas chromatography and mass spectrometry. The triethyl amine (TEA) in concentration 0.7-4.0 M was added into the system before the propargyl alcohol addition.

Results and Discussion

Dimethyl ester of pentyne-2-dioic acid, dimethyl ester of 2-methoxypentene-2-dioic acid, dimethyl ester of itaconic acid have been found out in a reaction solution as main products. It was shown that the carbonylation of propargyl alcohol can proceed in an oscillatory regime, in the system KI - PdI₂ - CO - O₂ - CH₃OH (Fig. 1). TEA addition created necessary acidity in reaction system (pH = 5-6) for

the beginning of oscillations of intermediates concentrations. These oscillations occur in accordance with E_{Pt} and pH values oscillations.

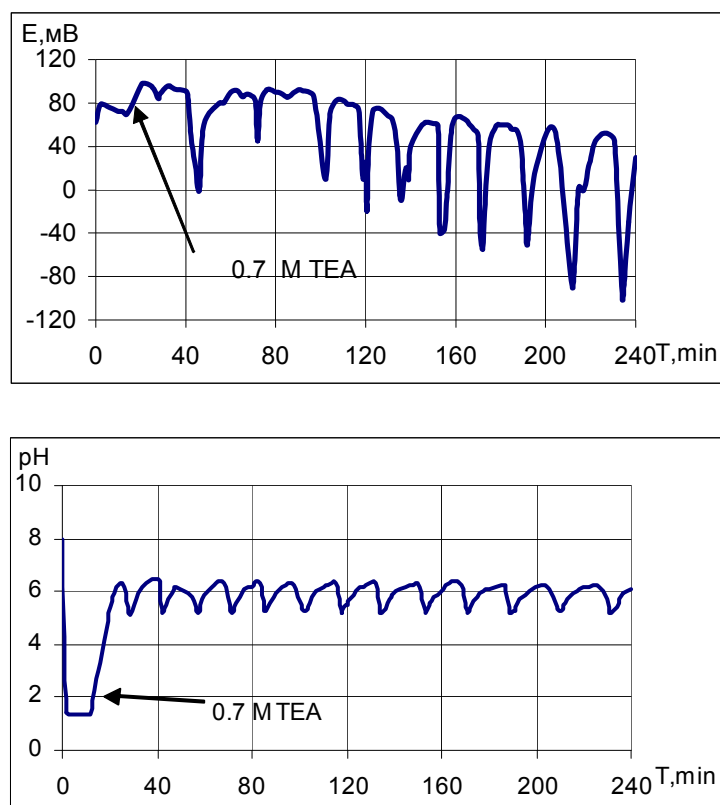


Fig.1 Change of E_{Pt} and pH during reaction
[KI (0,4M), PdI_2 (0,01M), propargyl alcohol (0,068M), TEA (0,7M)]

Conclusions

The preliminary mechanism of propargyl alcohol carbonylation reaction including formation of all identified products has been offered. The ranges of an oscillatory area for substances concentrations and a gas mixture composition are determined. The dependence between amounts of TEA that are necessary to add for the beginning of oscillations and $[PdI_2]_0$ was established.

Acknowledgements

This work was supported by the Russian Foundation for Basic Research (projects № 09-03-01072).

References

- [1] L. G. Bruk, I. V. Oshanina, S. N. Gorodsky, O. N. Temkin, *Russ. Khim. Zhurn.*, 2006, **50**, 103-114
- [2] S. N. Gorodsky, O. V. Kasatkina., L. G. Bruk, O. N. Temkin, 5th International Conference on Unsteady-State Processes in Catalysis, 2006, 59

E

Electrochemistry

THE ELECTROCHEMISTRY OF BIOLOGICALLY RELEVANT MOLECULES; ANALYSING COMPLEX MECHANISTIC PATHWAYS

C. Batchelor-McAuley and R. G. Compton

Department of Chemistry, Physical and Theoretical Chemistry Laboratory, Oxford University, South Parks Road, Oxford OX1 3QZ.

Abstract

Understanding the oxidation of the purines adenine and guanine is primary to improving electrochemical methods of DNA detection and analysis. This work presents the quantitative analysis of the oxidation of both adenine and guanine at graphitic electrodes, providing insight into how variation in scan rate alters the observed voltammetry.

Introduction

Both adenine and guanine have long been studied within a number of fields, this is primarily due to them being two of the main nucleobases, used for the coding of genetic information within DNA. DNA's fundamental role within biological systems has led to the desire for quick and effective methods of its analysis.[1] One of the first electrochemical approaches to the detection of DNA involves its direct oxidation, which is commonly done at a mercury electrode, allowing the measurement of nanogram quantities of DNA through the use of adsorptive transfer stripping voltammetry.

The electrochemical oxidation mechanism associated with both adenine and guanine is complex and involves the transfer of multiple electrons and protons and involving coupled homogenous reactions. Further complications arise due to the possibility of adsorption of the species to various electrode substrates including carbon. Work by Banks *et al.* demonstrated that in many case for graphitic surfaces the edge-plane defects are the electroactive sites.[2] Further to this with guanine, the observed voltammetry may be explained in terms of the varying densities of basal and edge plane sites present for the adsorption and electro-oxidation of the species respectively. Through varying the methods utilized for the preparation of these carbon electrodes the surface may be tailored so as to minimize or enhance the level of adsorption occurring, such that adsorption may be practically blocked through the pre-adsorption of acetone leading to the measurement of a purely diffusional response of guanine.[3]

The work presented here outlines how the voltammetry of both adenine and guanine maybe quantified so as to provide greater insight into the oxidative process. Such that a generic method for the analysis of systems involving weakly adsorbed surface species in which both the adsorbed and solution phase species contribute to the total peak current is provided.

Results and Discussion

The oxidation of guanine is known to undergo to involve the transfer of $4e^-$, $4H^+$, with the presence of a fast and irreversible chemical step after the transfer of the second electron. The voltammetry of guanine on graphitic electrodes is in general dominated by the adsorption of the species, with the majority of previous work employing the use of an accumulation time, so as to 'optimize' the peak signal. Through the pre-adsorption of acetone to the electrode surface, the adsorption of guanine to the electrode may be effectively blocked. As such the voltammetry of guanine at this acetone modified electrode is found to be diffusional in nature, this is shown through the lack of linearity between the measured peak current and scan rate and an apparent dependence of the peak current with the square root of the scan rate. Further to this the gradient of the associated Tafel analysis of the voltammetric feature was shown to have a distinct dependence with scan rate. It should be noted that the Tafel analysis in this case is not providing a measurement of the transfer coefficient due to all electron transfers being reversible in nature. As such this change in gradient is labeled as n_{app} , where the value of n_{app} is found to vary from a value of 1.2 to 0.8 at low and high scan rates respectively.

The presence of the chemically irreversible chemical step has a significant influence in as much as it imparts a scan rate dependence upon the equilibrium potential for the second electron transfer. In order to provide greater insight into the electrochemical processes involved a simple model of the system was produced through the use of the commercially available software DIGISIM[®] (version 3.0, BASi Technicol, USA), details of this simulation are provided in work by Li *et al.*[4] Figure 1 shows the comparison between the experimental and computational results, noting that the divergence at higher potentials is as a result of the oxidation of the oligomerised species which is not considered by the simulation. The simulation successfully demonstrates that over the range of experimental scan rates used the equilibrium potential for the second electron changes from being less than to greater than that for the first electron transfer. It is this change in potential that is responsible for the variation in the measured value of n_{app} .

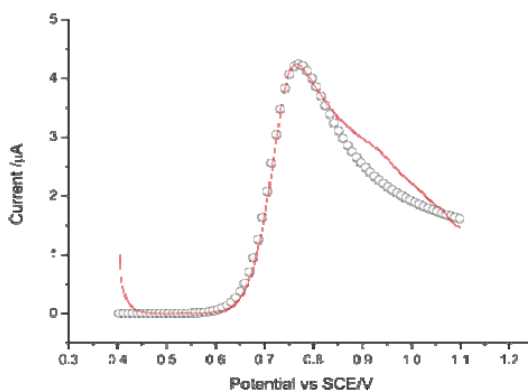


Fig.1. Comparison of the simulated and experimental voltammetry of the oxidation of guanine on an acetone modified graphite electrode.

The binding of adenine to both carbon and gold surfaces is stronger than guanine. This is most clearly exemplified by the ability of adsorbed adenine to hinder the oxidation of the gold substrate. As a result of this increase in binding strength it is not possible to block its adsorption to the electrode through the pre-adsorption of acetone. One voltammetric feature is observed for the oxidation of adenine on an edge plane pyrolytic graphite electrode, this peak current is clearly a result of the oxidation of both surface and solution phase species. The variation of peak current for a surface bound and solution phase species exhibit a scan rate and square root of scan rate dependence respectively, as such on this basis the two contributions to the peak current may be resolved. In order to quantitatively analyse this data it is necessary to make a number of assumptions including, the electron transfers are fully reversible, the chemical step is fast and irreversible and that the peak current for the voltammetric feature is the sum of the diffusional and adsorptional responses (i.e. they occur at the same potential). An adapted form of the Randles-Ševčík equation is provided in which the peak current is described in terms of the number of electrons occurring before and after the chemically irreversible step.[4] This expression is able to fully describe the variation of peak height with scan rate for the experimentally obtained data for the oxidation of adenine on a EPPG electrode with bulk concentrations of adenine between 12 and 50 μM , where the adsorption is shown to vary linearly with bulk concentration. As a result of this analysis a diffusion coefficient for adenine in aqueous solution is found to be $1.25 \pm 0.2 \times 10^5 \text{ cm}^2 \text{ s}^{-1}$, which is close to that found by other independent studies within the literature.

Conclusion

To the best of the authors knowledge this is the first time purely diffusional voltammetry for the oxidation of guanine at a carbon substrate has been observed. This diffusional response has been modeled, providing insight into how the presence of the irreversible chemical step influences the observed voltammetry.

The adsorption of adenine to the electrode surface is stronger as such it is not possible to completely block adsorption through the modification of the surface with acetone. Hence the peak signal must be analyzed on the basis of a number of assumptions as provided above. This analysis successfully enables the contributions to the current from adsorption and diffusion to be resolved.

References

- [1] C. Batchelor-McAuley, G. G. Wildgoose, R. G. Compton, *Biosens. Bioelec.*, 2009, **34**, 3138-3190.
- [2] C. E. Banks, R. G. Compton, *The Analyst*, 2006, **131**, 15-21.
- [3] Q. Li, C. Batchelor-McAuley, R. G. Compton, *J. Phys. Chem. B*, 2010, **114**, 7423-7428.
- [4] L. M. Gonçalves, C. Batchelor-McAuley, A. A. Barros, R. G. Compton, Submitted.

MICROWAVE-ASSISTED SYNTHESIS OF Pt AND Pt₃Sn ELECTROCATALYSTS FOR ETHANOL OXIDATION

S. Stevanović¹, D. Tripković², J. Rogan³, D. Minić⁴, A. Gavrilović⁵,
A. Tripković¹ and V. M. Jovanović¹

¹*ICTM, Department of Electrochemistry, University of Belgrade,
Njegoševa 12, Belgrade, Serbia*

²*Materials Science Division, Argonne National Laboratory, Argonne, IL 60439, USA*

³*Faculty of Technology and Metallurgy, University of Belgrade,
Karnegijeva 4, Belgrade, Serbia*

⁴*Faculty of Physical Chemistry, University of Belgrade, Studentski trg 12, Belgrade, Serbia*

⁵*CEST Centre of Electrochemical Surface Technology, Viktor-Kaplan-Strasse 2,
A-2700 Wiener Neustadt, Austria*

Abstract

High surface area carbon supported Pt and Pt₃Sn catalysts were synthesized by microwave heating and investigated for oxidation of ethanol in perchloric acid. The catalysts were characterized in terms of structure, morphology and composition. The diffraction peaks of Pt₃Sn/C catalyst in X-ray diffraction (XRD) patterns are shifted to lower 2θ values with respect to the corresponding peaks at Pt/C catalyst as a consequence of alloy formation. Scanning transmission microscopy (STM) analysis of unsupported catalysts show that the particles are of a small diameter (~2 nm) with a narrow size distribution. Pt₃Sn/C catalyst is highly active in ethanol oxidation with the onset potential shifted for ~ 150 mV to more negative values in comparison to Pt/C.

Introduction

Platinum-based nanomaterials with high surface areas have been receiving increased attention due to their unique properties and application as catalysts in fuel cells [1]. The use of ethanol as a fuel represents an important alternative as it can be obtained from biomass. However, to oxidize ethanol efficiently it is necessary to develop a catalyst capable for converting it completely to CO₂. Pt is an excellent catalyst for dehydrogenation of small organic molecules but, on the other hand, it is extremely susceptible to poisoning by CO and expensive. Efforts to minimize this poisoning and quantity of Pt in the catalyst have been centered around the addition of metals such as Ru, Sn, Mo, Rh, etc. creating bifunctional catalysts to promote CO oxidation [2,3]. Electrocatalytic performance of the Pt-based catalysts is highly dependent not only on the nature of the added metal, but also on a variety of conditions of the synthesis methods which determine surface composition and morphology of synthesized materials. Microwave assisted synthesis has advantage since it enables homogeneous nucleation and shorter crystallization time leading to formation of uniform metal colloids [4].

In this work, nanoparticle Pt and Pt₃Sn catalysts, synthesized by microwave assisted polyol method, were characterized for ethanol electro-oxidation reaction.

Experimental

Preparation of Pt/C and Pt₃Sn/C electrocatalysts. Pt and Pt₃Sn nanocatalysts were prepared by polyol method. H₂PtCl₆ and SnCl₂ solutions were mixed with ethylene glycol and NaOH was added to adjust pH>12. The solution was heated in a microwave oven for 90 s at 700 W. After microwave heating, colloidal solution was uniformly mixed with high-area carbon (Vulcan XC-72), water and H₂SO₄ solution and stirred for 3h. The resulting suspension was filtered and the residue was washed with deionized water. The solid product was dried at 160^oC for 3h in N₂ atmosphere. The metal loading for all the catalysts was 20 wt%.

Characterization of Pt/C and Pt₃Sn/C electrocatalyst. The particle size and surface morphology of unsupported Pt and Pt₃Sn catalysts were characterized by STM (Nanoscope IIIa). The XRD measurement was performed for determining of bulk composition with D5005 diffractometer (Bruker-AXS Germany).

Electrochemical measurement. All of the electrochemical experiments were performed at room temperature in three-electrode compartment electrochemical cell. The working electrode was a thin layer of Nafion-impregnated Pt/C and Pt₃Sn/C composites cast on a glassy carbon disk electrode with the loading of 20 μg/cm² of the catalyst. The electrocatalytic activity of as prepared Pt/C and Pt₃Sn/C was studied in 0.1M HClO₄ + 0.5M C₂H₅OH solution. A commercially available Pt/C catalyst (Tanaka) with a nominal Pt loading of 20 wt% was used as a benchmark.

Results and Discussion

Two phases were identified in XRD patterns of the carbon supported Pt and Pt₃Sn catalysts, one with the main characteristic peaks of Pt crystalline structure and another with diffraction peak at around 25^o related to hexagonal structure of Vulcan support. The shift of the diffraction peaks of Pt₃Sn/C catalyst to lower 2θ values and increased lattice parameter with respect to the corresponding values for Pt/C indicate the alloy formation between Pt and Sn but in lower degree. STM analysis of unsupported Pt₃Sn and Pt particles show that they are rather uniform in size of ~2 nm.

Ethanol oxidation on as prepared Pt/C, Pt₃Sn/C and commercial Pt/C-Tanaka catalysts in acid solution is presented in Fig1. Pt₃Sn/C catalyst is highly active for this reaction with the onset potential shifted for ~ 150 mV to more negative values relative to Pt/C and more rapid kinetics than Pt/C and Pt/C-Tanaka. This enhanced activity could be explained by the electronic effect due to incorporation of Sn atoms in Pt lattice. Since adsorption of OH species proceeds at considerably lower potentials on Sn compared to Pt, bifunctional mechanism as well can play a role in promotion of ethanol oxidation at Pt₃Sn/C catalyst. It should be mentioned also that Pt/C catalyst synthesized by microwave assisted polyol method is more active than commercial Pt/C-Tanaka catalyst probably due to its

better dispersion. However, the activity of Pt₃Sn/C catalyst synthesized by polyol method is lower in comparison with activity of commercial Pt₃Sn/C-Tanaka catalyst [5]. The higher activity of Pt₃Sn/C-Tanaka catalyst most likely is the consequence of higher alloying degree of this catalyst.

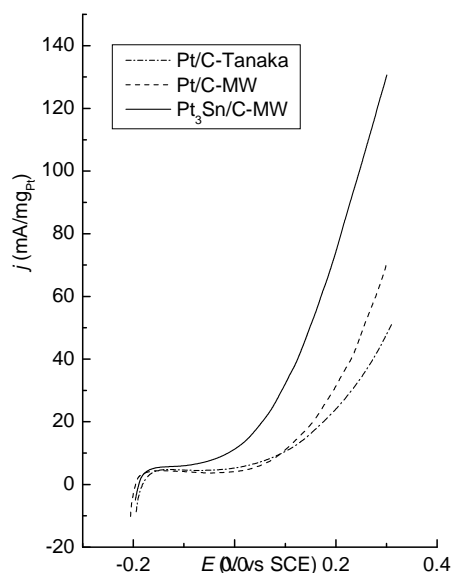


Fig.1. Potentiodynamic curves for the electrooxidation of 0.5 M C₂H₅OH in 0.1 M HClO₄.

Conclusion

The presented results point out the enhanced activity of bimetallic catalyst for the electrooxidation of ethanol which may be mainly ascribed to changes in electronic structure due to the alloy formation.

References

- [1] J. Luo, N. Kariuki, L. Han, L. Wang, C. J. Zhong, T. He *Electrochim. Acta*, 2006, **51**, 4821.
- [2] L. Colmenares, H. Wang, Z. Jusys, L. Jiang, S. Yan, G. Q. Sun, R. J. Behm, *Electrochim. Acta*, 2006, **52**, 221.
- [3] F. Colmati, E. Antolini, E. R. Gonzalez, *J. Alloy and Compounds*, 2008, **456**, 264.
- [4] Z. Liu, B. Guo, L. Hong, T. H. Lim, *Electrochem. Communications*, 2006, **8**, 83.
- [5] A. V. Tripković, K. Dj. Popović, J. D. Lović, V. M. Jovanović, S. I. Stevanović, D. V. Tripković, A. Kowal, *Electrochem. Comm.*, 2009, **11**, 1030.

MANGANESE DIOXIDE MODIFIED CARBONIZED POLYANILINE NANOSTRUCTURES: SYNTHESIS AND APPLICATION IN ELECTROANALYSIS

B. Šljukić, I. Stojković, N. Cvjetićanin and G. Ćirić-Marjanović

University of Belgrade, Faculty of Physical Chemistry, Studentski trg 12-16, 11158 Belgrade, Serbia

Abstract

Manganese dioxide modified carbonized polyaniline (MnO₂/Carb-nanoPANI) was prepared *via* a novel hydrothermal procedure. The synthesized material was characterised and examined for potential application in the field of electroanalysis showing a high electrocatalytic activity for the sensing of hydrogen peroxide in aqueous media.

Introduction

In recent times, special attention has been given to the use of transition metal oxide-based catalysts as an alternative to noble metal catalysts. Manganese dioxide (MnO₂) in particular is interesting as a low-cost material possessing a unique combination of beneficial physicochemical and electrochemical properties. Although having excellent activity, the unloaded manganese oxides suffer from very low surface areas. Loading manganese oxides onto a suitable support, either by direct synthesis or post grafting, provides highly dispersed surface oxides. The direct synthesis of the oxide onto a support provides a good linkage between the active phase and the support. Carbonized polyaniline nanostructures (Carb-nanoPANI) were used as a high surface support for MnO₂ in the present communication.

Experimental

Carb-nanoPANI was prepared by the procedure reported in the literature [1]. The modification of Carb-nanoPANI, with MnO₂ was carried out by a hydrothermal procedure. First, a reaction mixture was made by adding Carb-nanoPANI (60 mg) in 25 ml of aqueous solution of ammonium peroxydisulphate (0.06 M) and manganese sulphate (0.06 M). The reaction mixture was then heated in a Teflon-lined reactor for 15 h at 135°C. The resulting MnO₂/Carb-nanoPANI powder was separated from the solution by decanting and subsequently dried at 50°C for 2 hours.

Catalytic ink was prepared by adding MnO₂/Carb-nanoPANI (4 mg) in 1 ml of mixture of ethanol and water (2:3) followed by sonication for 30 min. A polished glassy carbon (GC) electrode was modified with catalytic ink by pipetting 10 µL of the ink onto a GC electrode and allowing the solvent to

evaporate off at room-temperature. Then, 10 μL of nafion (0.05%) was pipetted onto the electrode surface and again left to dry at room temperature.

Results and discussion

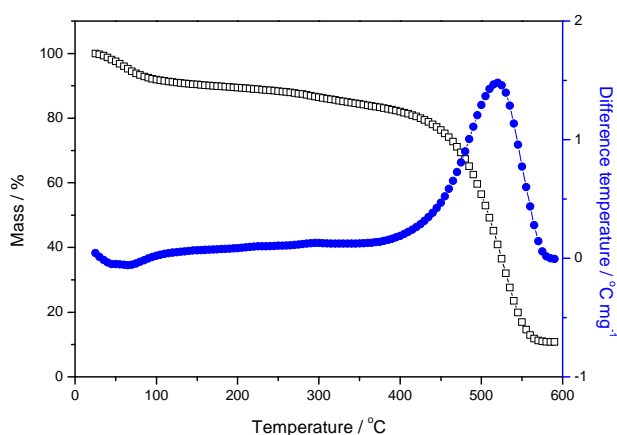


Fig.1. TG-DTA curves of the $\text{MnO}_2/\text{Carb-nanoPANI}$.

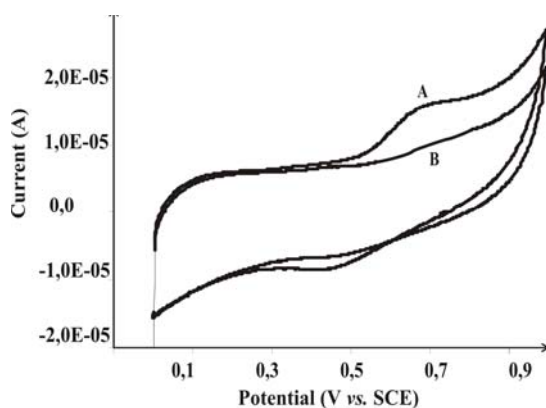


Fig.2. CVs of $\text{MnO}_2/\text{Carb-nanoPANI-GC}$ electrode in 1 mM H_2O_2 solution (A) and a blank solution (B).

investigated. Direct electrochemical oxidation of H_2O_2 on many conventional electrodes usually requires undesirably large overpotentials. Figure 2 compares the voltammetric response of the $\text{MnO}_2/\text{Carb-nanoPANI-GC}$ electrode in blank and 1 mM hydrogen peroxide solution in the potential range 0 to +1.0 V (vs. SCE) at a scan rate of 50 mVs^{-1} . The modified electrode responded favorably to H_2O_2 with a distinct peak corresponding to H_2O_2 oxidation appearing at *ca.* +0.75 V (vs. SCE). The limit of detection, LOD, for H_2O_2 using the $\text{MnO}_2/\text{Carb-nanoPANI-GC}$ electrode was determined using chronoamperometry holding the potential at +0.75 V (vs. SCE) with 100 μM H_2O_2 additions in 90 s intervals. LOD for H_2O_2 was

The formation of MnO_2 by hydrothermal procedure was previously confirmed by XRD analysis. TG-DTA curves of the $\text{MnO}_2/\text{Carb-nanoPANI}$ dried for 2 h at 50°C in air were also recorded, *Figure 1*. The sample gradually lost water: physically absorbed water at 100°C and chemically bound water at 298°C . DTA curve displayed the exothermic peak at 520°C that could be ascribed to the transformation of MnO_2 into Mn_2O_3 (470°C) [2] and degradation of Carb-nanoPANI (starting at 380°C and finishing at 600°C) [3]. The mass ratio of Carb-nanoPANI/ MnO_2 calculated on the basis of loss mass was 6.

Next, the synthesized material was used for electrode modification and its application for sensing of hydrogen peroxide, H_2O_2 ,

evaluated from standard additions plot data using the 3 sigma method and it was calculated to be 8.4 μM . Note that LODs for H_2O_2 attainable with existing methods range from 0.2 to 10.3 μM . Obviously further improvement of $\text{MnO}_2/\text{Carb-nanoPANI-GC}$ electrode performances is possible with optimisation of parameters such as amount of starting materials used for hydrothermal procedure, amount of prepared material used for preparation of the catalytic ink etc.

Conclusions

Manganese dioxide was synthesized onto carbonized polyaniline nanostructures using a simple hydrothermal procedure. The synthesized material was characterised and investigated for electrochemical detection of hydrogen peroxide, proving to be useful as electrode material for sensing of this analyte.

References

- [1] S. Mentus, G. Ćirić-Marjanović, M. Trchová, J. Stejskal, *Nanotechnology*, 2009, **20**, 245601 (10pp).
- [2] S. J. Bao, B. L. He, Y. Y. Liang, W. J. Zhou, H. L. Li, *Mater. Sci. Eng. A*, 2005, **397**, 305-309.
- [3] M. Trchová, E.N. Konyushenko, J. Stejskal, J. Kovářová, G. Ćirić-Marjanović, *Polym. Degrad. Stab.*, 2009, **94**, 929-938.
- [4] C. E. Langley, B. Šljukić, C. E. Banks, R. G. Compton, *Anal. Sci.*, 2007, **23**, 165-170.
- [5] B. Šljukić, R. G. Compton, *Electroanalysis*, 2007, **19**, 1275-1280.

ELECTROCHEMICAL BEHAVIOR OF METAL TUNGSTEN ELECTRODE IN STRONG ALKALINE SOLUTIONS: ELECTROANALYTICAL ASPECT

T. Tuvic¹, I. Pašti^{1,*} and S. Mentus^{1,2}

¹University of Belgrade, Faculty of Physical Chemistry, Studentski trg 12, 11158 Belgrade, Serbia; ²Serbian Academy of Science and Arts, Knez Mihajlova 35, 11158 Belgrade, Serbia; e-mail: igor@ffh.bg.ac.rs

Abstract

Electrochemical behavior of tungsten in strong alkaline solutions ($11 < \text{pH} < 13$) was studied in order to investigate its applicability in the measurement of OH⁻ ion concentration at high pH values. Using RDE technique it was demonstrated that the rate of anodic dissolution of metallic tungsten is controlled by OH⁻ ion diffusion. The reaction obeys the first order kinetics with respect to OH⁻ ion. The linear relationship between the values of limiting anodic current plateau and the concentration of OH⁻ ions was evidenced. The effect of supporting electrolyte was also investigated. The results indicate that metallic tungsten electrode can be used without any surface treatment, as a fast, robust, calibration-free amperometric sensor for analytical determination of OH⁻ ions at high pH range, where the potentiometric measurements based on glass electrode lose their high reliability.

Introduction

Tungsten (W) is a technologically important metal with a numerous practical applications. Electrochemical behavior of tungsten was investigated in many details [1-4]. According to available data, W electrode displays particularly interesting behavior in alkaline media, characteristic of a potential region of anodic dissolution that extends to extremely high anodic potentials [5]. This property is very attractive as it indicates that W might be applied for the amperometric determination of pH in highly concentrated alkaline solutions, where glass pH sensing electrodes [6,7] lose their reliability, and the noble-metal electrodes give non-reproducible amperometric response.

In this contribution, electrochemical behavior of W electrode in highly alkaline KOH solutions and the effects of supporting electrolyte (K₂SO₄) were investigated using rotating disk electrode (RDE) technique. It was demonstrated that W electrode may be used as an efficient amperometric sensor of OH⁻ ions both in presence and absence of supporting electrolyte.

Materials and methods

A rod shaped W electrode mounted in a cylindrical Teflon holder to expose its base surface (0.084 cm²), was used without any preparation treatment. All the chemicals used (KOH and K₂SO₄) were p.a. purity grade. Standard three-electrode cell with

Pt foil as a counter electrode and SCE electrode as reference electrode was used throughout all the experiments. Solutions were purged with N₂ (5N) before and during each experiment. Cyclic voltammograms (CV) were collected at a scan rate 20 mVs⁻¹ on a Gamry PC4 system.

Results and discussion

The RDE-CV curves show a large anodic current plateau due to the dissolution of anodically formed WO₄²⁻. Supporting electrolyte, K₂SO₄, if used, causes faster dissolution at lower anodic potentials (Fig. 1, left). This can be ascribed to corrosive nature of K₂SO₄. Performed Levich analysis revealed that anodic dissolution of W is under diffusion control by OH⁻-ions. Hence, the occurrence of higher current densities at high anodic potentials in unsupported KOH solutions (Fig. 1, right) is attributed to the higher mobility of OH⁻-ions in the absence of strong ion-ion interactions.

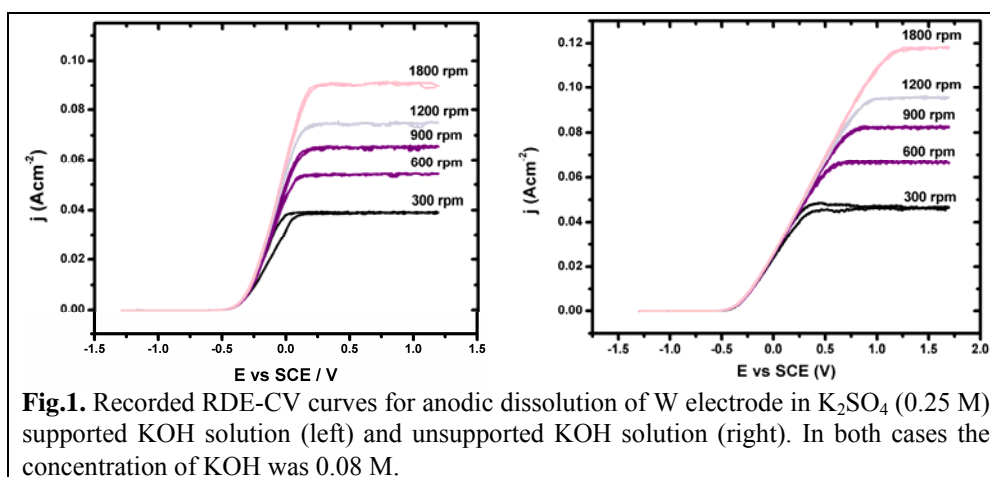
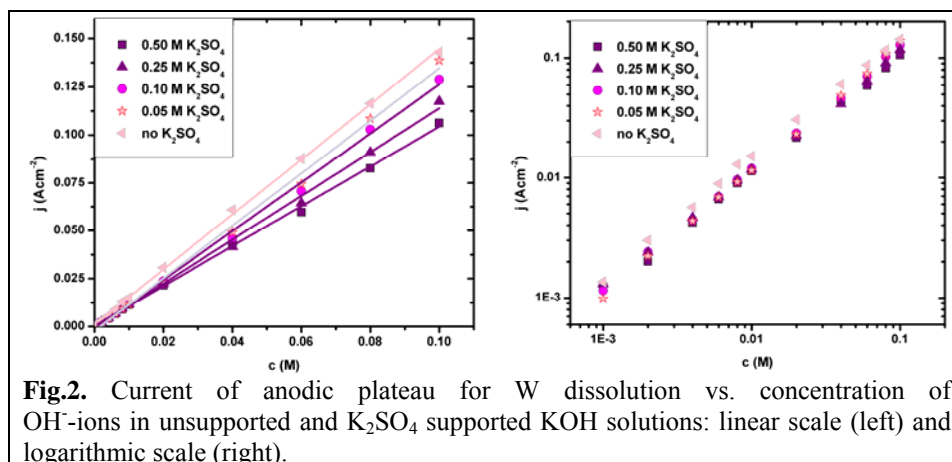


Fig.1. Recorded RDE-CV curves for anodic dissolution of W electrode in K₂SO₄ (0.25 M) supported KOH solution (left) and unsupported KOH solution (right). In both cases the concentration of KOH was 0.08 M.

Linear relationship between measured current densities (for rotation rate 1800 rpm) and concentration of OH⁻-ions was found ($R^2 > 0.99$) regardless on the ionic strength of the solution (Fig 2, left). In order to obtain a rough insight in the mechanism of anodic dissolution of W, the reaction order with respect to OH⁻-ions was determined from the slope of the $\log j = f(\log c(\text{OH}^-))$ curve (for rotating rate 1800 rpm) and it was found to be $\frac{d \log j}{d \log(c(\text{OH}^-))} = 1$. This indicates first order kinetics

of W dissolution with respect to OH⁻-ions. This value was found to be quite independent on the ionic strength of the solution.

Here presented results clearly suggest the applicability of metallic W electrode for the determination of OH⁻-ions in highly concentrated alkaline solutions.



Conclusion

Electrochemical behavior of W electrode in alkaline KOH solution (pH 11-13) was investigated using RDE-CV technique. Anodic reaction of W proceeds through WO₄²⁻ dissolution, at a rate controlled by the diffusion of OH⁻ions, in both supported and unsupported aqueous solutions. Dissolution proceeds as a first order reaction with respect to OH⁻ion. Direct linear relationship found between anodic current density plateau and the concentration of OH⁻ions in the solution indicates that metallic tungsten electrode can be used as a fast, robust, calibration-free amperometric sensor for OH⁻ions in the solutions with high pH values.

References

- [1] M. Anik, K. Osseo-Asare, J. Electrochem. Soc., 2002, **149**, B224.
- [2] A. Di Paola, F. Di Quarto and G. Serravalle, J. Less-Common. Met., 1975, **42**, 315.
- [3] D. D. Macdonald, E. Sikora and J. Sikora, Electrochim. Acta, 1998, **43**, 2851.
- [4] T. Heumann and N. Stolica, Electrochim. Acta, 1971, **16**, 1635.
- [5] P.I. Ortiz, M. Lopez Tejjelo, M. Giordano, J. Electroanal. Chem., 1988, **243**, 379.
- [6] T. Grubb, L. H. King, Anal. Chem., 1980, **52**, 270.
- [7] R. E. F. Einerhanda, W. H. M. Visschera, E. Barendrecht, Electrochim. Acta, 1989, **34**, 345.

INFLUENCE OF OXIDATION TREATMENT OF CARBONIZED PANI NANOTUBES/NANOSHEETS SUPPORT ON THE EFFECTIVENES OF PLATINUM NANOPARTICLE ELECTROCATALYST

N. Gavrilov and I. Pašti

*University of Belgrade, Faculty of Physical Chemistry, Studentski trg 12, 11158
Belgrade, Serbia; e-mail: gavrilov@ffh.bg.ac.rs*

Abstract

Nitrogen-containing carbonized polyaniline nanotubes/nanosheets (carb-PANI) were treated with mild oxidizers to modify and functionalize the surface and promote fine dispersion of platinum nanoparticles. The Pt nanoparticles, ranging between 5 and 9 nm in diameter, were deposited by modified polyol method on the treated samples. The rotating disc electrode technique was employed to study the kinetics of O₂ reduction in 0.1 M HClO₄. High electrocatalytic activity of treated PtNP/carb-PANI electrocatalyst toward O₂ reduction reaction (ORR) in acidic and alkaline media was evidenced.

Introduction

Platinum nanoparticles (PtNP) supported by nanodispersed carbon are used to catalyse electrode reactions (oxygen reduction, ethanol oxidation) in fuel cells. Due to high cost of platinum, much effort is invested to enhance its catalytic effectiveness. In this sense the attempts are directed either to maximize real Pt area [1] or to reduce platinum used by making the alloys with more abundant metals [2]. Nitrogen-containing carbonized polyaniline nanotubes/nanosheets have only recently been proposed as a support material for ORR [3]. Acid treatment is one of the most commonly employed methods for oxidation of carbon supports, given its versatility, efficiency and potential to scale-up. The most common reagents used for liquid-phase oxidation treatment are HNO₃, H₂SO₄, and H₂O₂ [4,5]. Modifying and functionalizing the surface of carb-PANI, by means of oxidative treatment with (NaOH, H₂O₂ and HNO₃), to enhance the electrocatalytic activity is proposed here.

Results and discussion

Chemical oxidation of carb-PANI was carried out with tree different oxidation agents using p.a. chemicals. Modification was done in a way that carbonized material was dispersed within a desired aqueous solution in an ultrasonic bath for 6h, followed by washing with distilled water. Table 1. lists the reagents used and their concentrations, and labels each treatment.

Pt nanoparticles were deposited by modified polyol method. The existence and distribution of platinum particles in treated PtNP/carb-PANI composites was confirmed by transmission electron microscopy (TEM), Fig.1 (left).

Table 1. Oxidative treatments conducted on the carb-PANI.

Label	Treatment	d / nm
PtNP/carb-PANI - HNO ₃	3M HNO ₃ for 6h	5.11
PtNP/carb-PANI-H ₂ O ₂	30% H ₂ O ₂ for 6h	5.55
PtNP/carb-PANI-NaOH	1M NaOH for 6h	8.29

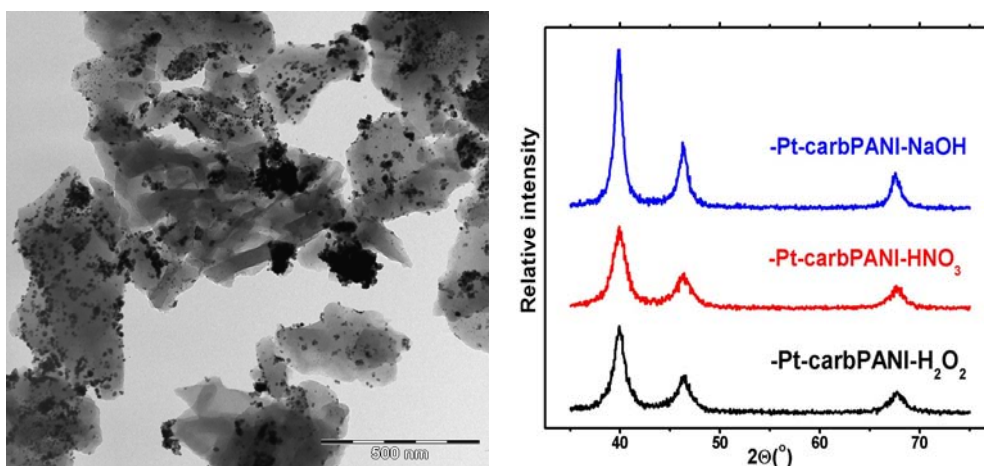


Fig.1. TEM image of PtNP/carb-PANI electrocatalyst (left) and XRPD of modified samples (right).

The thermogravimetric analysis confirmed the Pt loading in all modified samples is close to 20 %. The XRPD analysis, by means of the line broadening and the Debye-Scherer equation, revealed the PtNP size, between 5 and 9 nm in diameter, for differently treated samples. The same particle size we determined by means of cyclic voltammetry in N₂-purged

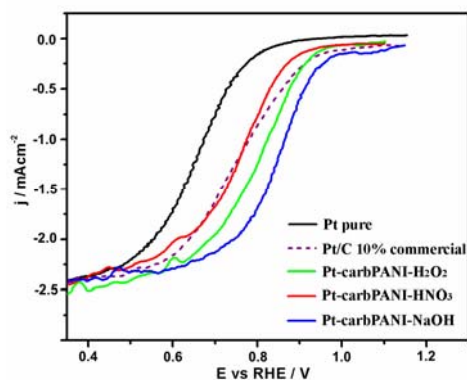


Fig.2. Comparative plot of ORR current densities on smooth Pt disk, Pt10%/C electrocatalyst (Degussa) and modified PtNP/carb-PANI, collected at 300 rpm in 0.1M HClO₄.

solutions, using both the peaks of underpotentially adsorbed hydrogen (HUPD) and the Pt loading. In order to investigate electrocatalytic activity of treated PtNP/carb-PANI toward ORR in acidic (0.1M HClO₄ and 0.05M H₂SO₄)

and alkaline (0.1M NaOH) media, a series of RDE experiment have been performed with oxygen saturated solutions. The comparison of current densities of ORR observed on here-synthesized electrocatalyst and on the commercial Pt/C electrocatalyst (10% Pt (w/w), Degussa) is presented in Fig. 2. Since the Pt loading was adjusted to be identical in all experiments, the improved electrocatalytic activity of modified PtNP/carb-PANI is evident.

Conclusion

In this contribution, we demonstrated that the mild oxidation treatment of carbonized PANI, by modifying the material surface, could successfully influence size of platinum nanoparticles applied by polyol method. Also, modification of carb-PANI surface coupled with limited nanoparticles growth improved remarkably the activity of this material toward O₂ reduction in both acidic and alkaline media.

Acknowledgement

This work was supported by the Serbian Ministry of Science and Technological Development under the contract number 142047.

References

- [1] K.-Y. Chan, J. Ding, J. Ren, S. Cheng, K. Y. Tsang, *J. Mater. Chem.*, 2004, **14**, 505.
- [2] V. R. Stamenkovic, B. Fowler, B. S. Mun, G. Wang, P. N. Ross, C. A. Lucas, N. M. Markovic, *Science*, 2007, **315**, 493.
- [3] S. Mentus, G. Ćirić-Marjanović, M. Trchová, J. Stejskal, *Nanotechnology*, 2009, **20**, 245601.
- [4] M. Carmo, M. Linardi, J. G.e Rocha Poco, *Int. J. Hydrogen Energy*, 2008, **33**, 6289.
- [5] Zdenko Špitalsky, Christoforos A. Krontiras, Stavroula N. Georga, Costas Galiotis, *Composites: Part A*, 2009, **40**, 778.

(5-ETHOXYCARBONYLMETHYLIDENE-4-OXOTHIAZOLIDINE-2-ILYDENE)-1-PHENYLETANONE IN APROTIC MEDIA: ELECTROCHEMICAL AND SPECTRAL STUDY

I. Cekić-Lasković^{1,2*}, D. Minić^{1,2}, R. Marković^{2,3} and E. Volanschi⁴

¹*Faculty of Physical Chemistry, Studentski trg 12, Beograd, University of Belgrade, Serbia,*

²*Center for Chemistry ICTM, P.O. Box 473, 11001 Belgrade,*

³*Faculty of Chemistry, University of Belgrade, Studentski trg 16, 11001 Belgrade,*

⁴*Faculty of Chemistry, University of Bucharest, Romania*

Abstract

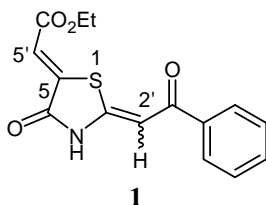
Cyclic voltammetry study coupled with spectral methods (UV-VIS, EPR) has been used to (i) elucidate the mechanism and (ii) determine the reaction intermediates of the electrochemical reduction of (5-ethoxycarbonylmethylidene-4-oxothiazolidine-2-ilydene)-1-phenylethanone. The comparison between experimental data and theoretical curves, calculated by means of the DigiSim software, indicates an ECE reaction sequence as a major reaction pathway. The chemical step, following the first electron transfer (ET), is the deprotonation of the starting compound, under the action of the electrogenerated base (EGB) anion radical. The dianion radical obtained at the second reduction step is observed by both, optical and electron paramagnetic resonance (EPR) spectra.

Introduction

Since the concept of *push-pull* alkenes, was reviewed by Sandström in 1983 [1], these compounds, consisting of one or two electron-donating groups (EDG) at the terminus of the C=C bond and one or two electron-withdrawing groups (EWG) at the other terminus, have been widely studied on the account of their low rotational barrier around the C-C double bond. This is attributed to the high degree of polarization, or in valence-bond language, to the importance of zwitterionic limiting forms of the *push-pull* alkenes as convenient description of their ground states. The further interest for these compounds lies in their possible biological activity [2] and utility as organic intermediates for the synthesis of different heterocyclic compounds [3]. Previous electrochemical studies of selected 5-substituted 2-alkylidene-4-oxothiazolidines in aprotic polar solvents gave valuable insight on electrochemical behavior of these compounds [4,5]. The aim of the present work is to study (5-etoxy carbonylmethylidene-4-oxotiazolidine-2-ylidene)-1-phenylethanone (**1**) in order to assess the role of the C-C double bond at C(5) position, as well as electron withdrawing substituent (EWG) on the electro-

* isidora@ffh.bg.ac.rs

chemical behaviour of selected 4-oxothiazolidines in terms of the reduction mechanism and the reactivity of the intermediate species.



Results

The cyclic voltammogram of investigated compound, presented in Fig. 1, exhibits two reduction waves, which correspond to successive ET. The first reduction peak, appearing at -0.92 V, has no anodic counterpart and corresponds to an ET followed by a second order chemical reaction (EC process) according to the electrochemical criteria. The second reduction couple is located at $E_{1/2} = -1.29$ V. The analysis of the second reduction step shows that it corresponds to rapid (reversible) electron transfer [6]. Further information supporting all the assumptions discussed above was obtained by following the shape of cyclo-voltammograms with the gradual addition of a strong base, tetrabutylammonium hydroxide (TBOH). The results obtained with RDE confirm the monoelectronicity of both ET. The values of the electron transfer rate k_s , and diffusion coefficient D_o for both cathodic waves were determined.

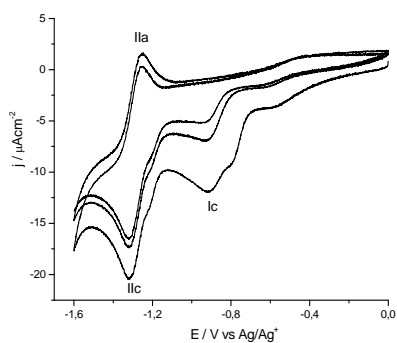


Fig.1. Cyclic voltammogram of compound **1** in 0,1 M TBAHPF/DMSO, potential range -1.6 to 0.1 V, $c = 4 \cdot 10^{-3}$ M, $v = 0.1$ Vs^{-1}

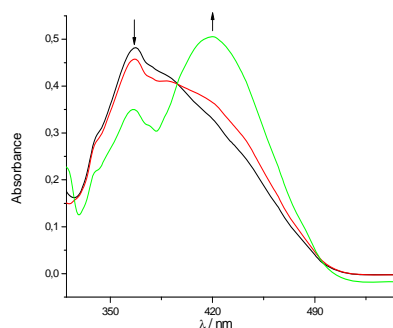


Fig.2. Absorption spectra registered on electrochemical reduction of compound **1** in 0.1 M TBAHPF/DMSO at the potential in between the first and second reduction wave

In order to obtain further support for the proposed reduction mechanism and evidence regarding the supposed intermediate species, UV-VIS spectro-electrochemical measurements were performed during the electrochemical (Fig. 2) and chemical (tetrabutylammonium hydroxide, TBOH) reduction of the starting compound, at a potential value in a range between the first and second reduction

wave. Similitude of the results indicates an analogous action of the electrogenerated base and chemical base, allowing the identification of the following intermediate species: anion at 422 nm and dianion radical at 440 nm, sufficiently stable to be well characterised by EPR spectroscopy. By acidifying the solution with trichloroacetic acid, it was observed that the process is reversible for molar ratio $c_{(\text{TBOH})}/c_{(\text{compound})}$ smaller than 2.

The experimental EPR spectrum, recorded in de-aerated 0.1 M TBAHFP/DMSO, is well resolved, confirming the presence of a relatively stable paramagnetic species, formed at the potential corresponding to the second redox couple on the cyclovoltammogram and it was ascribed to the electrogenerated dianion radical of the starting compound **1**. The hyperfine pattern is due to the interaction of the odd electron with seven protons and one nitrogen atom. The highest hyperfine splitting was assigned to the proton of the double bond in the C(5') position, close to the lactam carbonyl group, followed by the vinylic proton of the C=C bond at the C(2') position, i.e. to the conjugated system consisting of the thiazolidinone ring and double bonds. The EPR pattern, evidenced experimentally, is compatible with an absence of the lactam proton, and the assignment of other proton splittings to the phenyl group.

Conclusion

The proposed mechanism is supported by the ECE pattern outlined by the cyclic voltammetry results and by the similitude of the behaviour at the electrochemical reduction with the exogeneous base, added TBOH, revealed by both optical and EPR spectra and verified by the DigiSim simulation. It consists of monoelectronic reduction of the investigated compound to the anion radical (E), followed by deprotonation of the substrate by the anion radical to form the anion (C) and reduction of the anion to dianion radical (E).

Acknowledgement

We wish to acknowledge financial support by the Ministry of Science of the Republic of Serbia, Grant No. 142007 (to R.M.).

References

- [1] J. Sandström, *J. Top. Stereochem.*, 1983, **14**, 83-181.
- [2] K. Yoneda, A. Ota, Y. Kawashima, *Chem. Pharm. Bull.*, 1993, **41**, 876-881.
- [3] F. Meyers, S. R. Marder, B. M. Pierce, J. L. Brédas, *J. Am. Chem. Soc.*, 1994, **116**, 10703 -10714.
- [4] D. M. Minić, I. Cekić, F. T. Pastor, V. Jovanović, R. Marković, *Russian Journal of Physical Chemistry A*, 2007, **81**, 1458-1463.
- [5] I. Cekić-Lasković, D. Minić, M. Baranac-Stojanović, R. Marković, E. Volanschi, *Russian Journal of Physical Chemistry A*, 2009, **83**, 1571-1576.
- [6] A. Bard, L. R. Faulkner, *Electrochemical Methods, Fundamentals and Applications*, 2nd ed., Wiley, New York, 2001, 239-271.

HYDROXIDE ION OXIDATION ON NAFION COVERED PLATINUM ELECTRODE

A. Abu Rabi-Stanković, Z.Mojović, A. Ivanović and D. Jovanović

¹*Institute of Chemistry, Technology and Metallurgy, University of Belgrade,
Department of Catalysis and Chemical Engineering, Njegoševa 12, 11000
Belgrade, Republic of Serbia.*

Abstract

Voltammetric study of hydroxide ion oxidation in aqueous solution of sodium sulphate made basic with sodium hydroxide was performed on nafion covered platinum rotating disc electrode. Dependence of voltammetric response on hydroxide ion concentration and rotation speed are presented. The wave height was found to be proportional to the hydroxide ion concentration and to the square root of the rotation speed. Nafion covered electrode gave stable, reproducible and well defined wave attributed to the hydroxide ions oxidation, but the wave height was lower than on bare platinum, under the same experimental conditions. Tafel plots and Koutecky-Levich plots are obtained to establish influence of nafion on mechanism and kinetics of hydroxide oxidation.

Introduction

Voltammetric determination of hydroxide ions in aqueous solutions was investigation topic for Daniele et al. in series of papers [1-5]. The concentration of the hydroxide ion in both strong [1-3] and weak [4, 5] alkaline solutions has been measured by means of both gold microelectrode [1-4] and gold rotating disc electrode [3]. The influence of the nature of the microelectrode material, on the shape of voltammograms was studied too [2, 5] and it was concluded that gold appears to be the most promising for the voltammetric detection of basicity of aqueous solutions. One could notice that the voltammograms attained by using the gold microelectrode coated with Nafion film were characterized with broader and better defined current waves [6]. So, it was assumed that possible stabilization of the signal could be achieved by applying thin Nafion film on the surface of Pt electrode.

Experimental

757 VA Computrace (Metrohm) was used to perform the voltammetric investigations. Commercial Metrohm polycrystalline 2 mm Pt disc electrode, was used as a working electrode. Pt foil served as an auxiliary electrode, while the Ag/AgCl electrode was used as the reference. Before each set of measurements, the working electrode was polished with dry α -alumina powder ($\sim 1 \mu\text{m}$) applied to a polishing cloth. The solutions, prepared from analytical grade reagents and twice distilled water, were deoxygenated by bubbling with oxygen-free nitrogen (99.9995%) during the experiments. Commercial Nafion alcoholic solution (5 wt%, Aldrich) was used to prepare Nafion modified platinum electrode. In order to obtain uniform film, a known

volume of Nafion solution was deposited on electrode and let to dry on room temperature for 1h. Film thickness was evaluated using $\delta = BV/100dA$, where B is percentage concentration of the Nafion solution employed, V is the volume of the Nafion solution deposited (cm^3), d is the density of the Nafion membrane, assumed equal to 1.58 g/cm^3 and A is the polymer coated surface (cm^2) [6].

Results and Discussion

For a reasonable small concentrations of hydroxide ions, in the presence of supporting electrolyte, the voltammograms of hydroxide ion oxidation indicate clear diffusion limitation [1-5]. Figure 1 presents voltammograms of 50 mM NaOH in 0,5 M Na_2SO_4 on bare Pt RDE (a) and Pt RDE covered with 3,2 μm (b), 6.4 μm (c) and 16 μm nafion film (d).

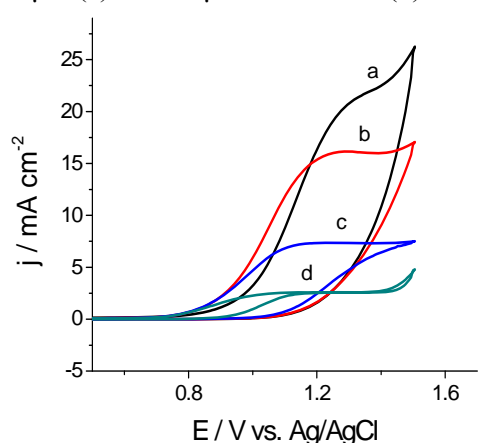


Fig.1 Voltammograms of 50 mM NaOH in 0,5 M Na_2SO_4 on bare Pt RDE (a) and Pt RDE covered with 3,2 μm (b), 6.4 μm (c) and 16 μm Nafion film (d).

The current waves presented in Figure 1 are broader, more stable and clearly defined than those obtained on bare Pt electrode, but the limiting current of hydroxide ion oxidation on nafion covered platinum electrode is significantly lower. Since the same supporting solution was used for the both bare and nafion covered electrode, it is obvious that the presence of nafion on the surface of the platinum electrode caused this current drop. This was to be expected because polymer film represents another barrier for mass transport of hydroxide ions to the electrode surface. However, sigmoidal wave is

clearly defined for the potential range of 400 mV at the nafion covered electrode for all used solutions, while at the bare platinum electrode plateau is no longer well defined with increase of OH^- ions concentration. Nafion is permselective, being more permeable to cations than anions [7]. Therefore, the presence of nafion reduced hydroxide ions concentration on electrode surface resulting in decrease oxidation currents.

By applying the Koutecky-Levich law one obtains parallel straight lines, as shown in Figure 2 a. The parallelism of Koutecky-Levich plots and the fact that number of electrons exchanged remains the same indicate that the reaction pathway is not altered by the presence of Nafion film. One more criteria to confirm that is the slope of the Tafel plots, presented in Figure 2 b. The Tafel slope is practically the same at the bare and filmed electrodes, which leads to a conclusion that the reaction mechanism is most likely the same in both cases.

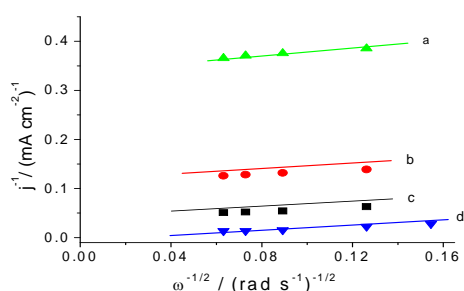


Fig.2. a Koutecky-Levich plots of the voltammograms given in Fig.1 at 1.2 V: bare Pt RDE (a) and Pt RDE covered with 3,2 μm (b), 6.4 μm (c) and 16 μm nafion film (d).

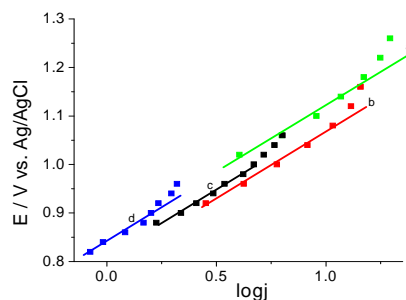


Fig.2. b Tafel plots (corrected for diffusional effects) for hydroxide ion oxidation on : bare Pt RDE (a) and Pt RDE covered with 3,2 μm (b), 6.4 μm (c) and 16 μm nafion film (d).

Conclusion

Hydrodynamic voltammetry was employed to determine kinetic parameters for OH^- oxidation on nafion covered Pt electrode. Results obtained in this study showed clearly defined oxidation waves in wide concentration range on Nafion covered Pt electrode, but significantly lower than the current obtained for the bare electrode. The limiting current of these waves was found to be proportional on both concentration and rotation speed, indicating that OH^- oxidation is diffusion controlled.. Koutecky-Levich plots for OH^- oxidation on bare and Nafion coated Pt electrode showed no change in number of electrons, indicating that reaction mechanism remained the same in both cases. Tafel slopes for bare electrode and the one with Nafion films of various thickness were the same, which confirms that nafion coating didn't affect reaction mechanism.

Acknowledgments

This work was supported by the Ministry of Science Technological Development of the Republic of Serbia, (Projects ON 166001).

References

- [1] M. E. Abdelsalam, G. Denuault, M. A. Baldo, S. Daniele, J. Electroanal. Chem., 1998, **449**, 5-7.
- [2] S. Daniele, M.A. Baldo, C. Bragato, Anal. Chem., 1999, **71**, 811-818.
- [3] M. E. Abdelsalam, G. Denuault, M.A. Baldo, C. Bragato, S. Daniele, Electroanalysis, 2001, **13**, 289-294.
- [4] S. Daniele, M. A. Baldo, C. Bragato, Anal. Chem., 2002, **74**, 3290-3296.
- [5] I. Ciani, S. Daniele, J. Electroanal. Chem., 2004, **564**, 133-140.
- [6] S. Daniele, P. Ugo, C. Bragato, G. A. Mazzocchin, J. Electroanal. Chem., 1996, **418**, 29-34.
- [7] S. J. Xia, V. I. Birss, Electrochim.Acta, 1998, **44**, 467-482.

METHANOL ELECTROOXIDATION FROM ALKALINE SOLUTION ON Pt AND PtRu MODIFIED ZEOLITE X

Z. Mojović, P. Banković, N. Jovičić, M. Žunić, A. Abu Rabi-Stanković and S. Marinović

ICHTM-Center of Catalysis and Chemical Engineering, Njegoševa 12, Belgrade

Abstract

Zeolite NaX was modified by Pt and Pt/Ru nanodispersed metallic clusters. This modification was achieved by zeolite impregnation with acetylacetonate salt/acetone solution, followed by acetone evaporation and thermal decomposition of organometallic complex. The mixture of modified zeolite and 10 wt.% of carbon black, in a form of thin layer, was pasted to a glassy carbon surface by nafion. Electrocatalytic properties of metal-modified zeolites were tested in methanol electrooxidation reaction.

Introduction

Pt-Ru alloy is considered as the most active electrocatalyst for both CO and methanol oxidation. However, even PtRu still suffers from a significant overpotential for the oxidation of organic fuels and from poisoning by sulfur-containing compounds, each of which results in loss of catalytic efficiency. Therefore, properties of PtRu alloys, possible improvements of their catalytic activity and application for methanol electrooxidation are still subject of investigation. One approach to the problem was to investigate different support materials such as conventional Vulcan XC carbon black [1], graphite or carbon nanotubes [2]. The zeolite material, as pointed out by Samant and Fernandes [3], is more hydrophilic than carbon due to acidic protonic entities on its surface. Therefore, zeolite support provides lower resistance and less ohmic drop than carbon support.

In this work, zeolite NaX (faujasite type) was used as a support of platinum and platinum-ruthenium catalyst. A procedure of thermal decomposition of noble metal acetylacetonates to deposit noble metal clusters on the surface of solid support [4], was adapted by some of the present authors to introduce noble metal clusters in zeolite cavities. Metal acetylacetonates were used as zeolite impregnation agents very rarely, but were not decomposed to metals. Zeolites are expected to both enable to obtain effective catalyst in a form of nano-dispersion and prevent the occurrence of agglomeration. There is the evidence that solid aluminosilicate framework hinders the metal nanocluster agglomeration [5].

Experimental

Pt-acetylacetonate and Ru-acetylacetonate were dissolved in acetone. Zeolite 13X was soaked by the solution, dried to evaporate acetone and heated to 350⁰C in air in order to decompose the complex compounds and desorb the decomposition products. In this way nanodispersed PtRu clusters were incorporated into the zeolite cages. Procedure was repeated until Pt/zeolite PtRu/zeolite weight ratios of 0.1 and 0.2, respectively, were reached.

Powdered mixture of the sample and 10 % carbon black, was homogenously dispersed in a solution of Nafion (5 wt.%), at Nafion solution/powder wt. ratio 2.5, and a droplet of the suspension was applied on glassy carbon disc of rotating electrode. Solvent evaporation resulted in a thin film of modified zeolite bonded, by a Nafion film, to glassy carbon support. The electrochemical performance of this material was investigated in 0.1M NaOH solution using rotating disc technique.

Results and Discussion

Methanol electrooxidation on 13XPt and 13XPtRu was examined in 0.5M CH₃OH + 0.5M NaOH. Steady state voltammograms recorded at scan rate of 10 mV/s for modified zeolites are presented at the Fig 1 in comparison with bare Pt recorded under the same conditions.

Methanol electrooxidation peak is visible at forward scan at all three electrodes at

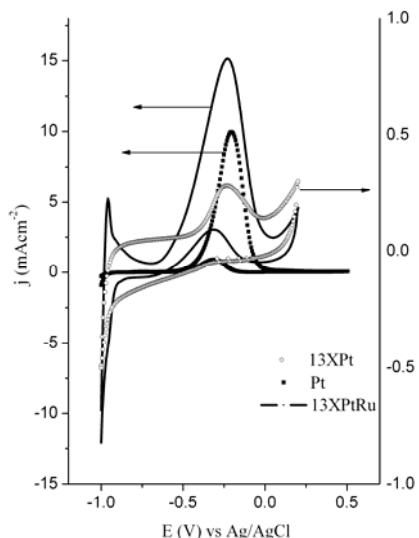
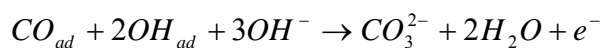


Fig.1. Cyclic voltammograms of 13XPt (—), 13XPtRu (---) and bare Pt (!) in 0.5M CH₃OH + 0.5M NaOH at scan rate of 10mV/s

potential around -0.2V. At the reverse scan another oxidation peak appear at -0.3 corresponding probably to oxydation of residual species adsorbed on the surface of the electrode after methanol electrooxidation. The onset for methanol electrooxidation is shifted to somewhat lower potential on 13XPtRu in comparison to Pt electrodes, bare and zeolite modified. The peak is symethric indicating that activation and deactivation of electrode run with similar rate with potential increase. Current maximum is formed at the potentials where the kinetics are optimized by a delicate balance between the rate of dehydrogenation of methanol [6]:

$$CH_3OH_{sol} \rightarrow CH_3OH_{ad} \rightarrow CO_{ad} + 4H^+ + 4e^-$$
 and the rate of oxidation of dehydrogenation products (CO_{ad}) with oxygen-containing species in Langmuir – Hinshelwood type reaction :



Pt-modified electrode shows the lowest activity toward methanol electrooxidation. Since three adjacent Pt sites are initially needed for dissociative methanol adsorption to COH_{ads} [7] it is reasonable to assume that Pt is dispersed over the inner surface of zeolite. Methanol adsorption on the pure platinum surface commences after complete hydrogen desorption and is neglectable at potentials below 0.1V vs RHE. Methanol does not adsorb on pure ruthenium at low potentials and small degree of adsorption is noticed for PtRu alloy with Pt/Ru atomic ration of 1. Much better results are achieved

with Pt/Ru alloys where surface composition is 10 atomic % Ru [8]. However, the bulk alloy composition is not necessarily identical to its surface composition. McNicol et al [9] investigated electrocatalytic activity of PtRu catalyst dispersed on carbon toward methanol electrooxidation and came to the conclusion that heating of catalyst at the hydrogen atmosphere lead to platinum enriched surface, while by heating in the air ruthenium enriched surface was obtained. Miura et al [10] established that surface of PtRu alloy dispersed on alumina is platinum rich if at the end of synthetic procedure reduction in hydrogen atmosphere at elevated temperatures is performed. Since modification of zeolite by Pt/Ru at this work was performed under the hydrogen atmosphere we expect that surface of metal clusters formed on zeolite is platinum rich. Methanol dehydrogenation on bare Pt electrode shows no dependence on rotation speed of the electrode [11]. Contrary to this zeolite-modified electrodes show linear dependence of the peak current with rotation speed of the electrode. These results indicate that the methanol electro-oxidation process on zeolite-modified electrodes is controlled by the diffusion of methanol to the electrode surface and/or through zeolite cavities.

Conclusion

Impregnation/thermal decomposition technique was used in order to obtain Pt and Pt/Ru metal nanodispersion on zeolite. The mutual influence between Pt and Ru atoms enhanced electroactivity of Pt/Ru-modified zeolite toward methanol electrooxidation in comparison to Pt-modified zeolite.

Acknowledgments

This work was supported by the Ministry of Science and Technological Development of the Republic of Serbia (Projects 166001B and 142019).

References

- [1] C. T.Hsieh, J.Y. Lin, S. Y. Yang, *Physica E*, 2009, **41**, 373-378
- [2] G. Che, B. B. Lakshmi, C. R. Martin, E. R. Fisher, *Langmuir*, 1999, **15**,750-758.
- [3] P. V. Samant, J. B. Fernandes, *J. Power Sources*, 2004, **125**, 172 – 177.
- [4] M. Okumura, K. Tanaka, A. Ueda, M. Haruta, *Solid State Ionics*, 1997, **95**,143-149.
- [5] D. Barthoment, *Catal.Rev.*, 1996, **38**, 521-612.
- [6] E. A. Batista, G. R. P. Majpass, A. J. Motheo, T.Iwasita, *J.Electroanal.Chem.*, 2004, **571**, 273-282.
- [7] S. Wasmus, A. Küver, *J. Electroanal. Chem.*, 1999, **461**, 14-31.
- [8] H. Gasteiger, N.Marković, P. N.Ross, E. J.Cairns, *J. Phys. Chem.*, 1993, **97**, 12020-12029.
- [9] B. D. McNicol, R. T. Short, *J. Electroanal. Chem.*, 1977, **81**, 249-260.
- [10] H. Miura, T. Suzuki, Y. Ushikubo, K. Sugiyama, T. Matsuda, R. D. Gonzalez, *J. Catal.*, 1984, **85**, 331-338.
- [11] S. Lj.Gojković, T. R. Vidaković, *Electrochim. Acta*, 2001, **47**, 633-642.

DEVELOPMENT OF $^{90}\text{Sr}/^{90}\text{Y}$ GENERATOR USING ELECTROCHEMICAL SEPARATION

Dj. Petrović, D. Djokić, R. Dobrijević, D. Stanković and P. Glodić

*Laboratory for Radioisotopes, Vinča Institute of Nuclear Sciences
P.O.Box 522, 11001 Belgrade, Serbia*

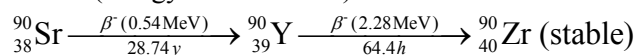
Abstract

Using of radiopharmaceuticals based on ^{90}Y in the treatment of solid cancer is increasing in recent years. Therefore, generators have been developed for obtaining the ^{90}Y using a feature of ^{90}Sr for spontaneous breakthrough and its equilibrium with ^{90}Y . Electrochemical separation of ^{90}Y from ^{90}Sr has become the basic method for obtaining ^{90}Y in high radiochemical yield. For the preliminary study, we used the electrochemical system with two electrochemical cells. Quality control was performed using extraction paper chromatography (EPC). Preliminary results showed that the separation completed successfully in both ways, quantity and quality.

Introduction

Because of its properties yttrium-90 (^{90}Y) is widely used for labelling of targeted molecules which could be useful in the treatment of cancer. These characteristics are reflected in the radiation of high β -energy ($E_{\text{max}\beta^-} = 2.27 \text{ MeV}$) and half-life time ($t_{1/2} = 64.4\text{h}$) [1-3]. ^{90}Y is almost pure beta emitter; the gamma photon emission from yttrium breakthrough was so weak that it could be ignored. Significant advantage in the treatment of solid tumors represents a penetration of β^- particles in tissue with range of 5.9 mm [4].

Y-90 can be obtained as the product of neutron activation of the ^{89}Y in nuclear reactors ($^{89}\text{Y} (n,\gamma)$), but thus obtained yttrium has small specific activity. The second method is the generator system that is based on equilibrium $^{90}\text{Sr}/^{90}\text{Y}$. Generators systems consist of long life parent that spontaneous breakthrough and gives short-life daughter. ^{90}Sr with the half-life of 28.74 years decays by emission of β^- particles (energy of 0.546MeV) to ^{90}Y . A scheme of breakthrough is presented as:



^{90}Sr is extremely toxic due to similar chemical behaviour to calcium, it deposits in bones. Therefore it is very important that strontium could not be found in the final product. The current generators are based on chromatographic separation, extraction, separation by liquid membrane and electrochemical separation [5-8].

In preliminary research we used electrochemical method to provide the most efficient $^{90}\text{Sr}/^{90}\text{Y}$ separation [9]. Also, using this method radioactive waste is minimized.

Experimental

Electrolysis was performed potentiostatically on Potenciostat/Galvanostat/ZRA, Serie G 750, Gamry Instruments. Electrochemical cells consisted of three electrodes. Working and counter electrode were platinum electrodes and the reference electrode was saturated calomel electrode. Electrochemical cells of 100 cm³ capacity was filled up to 75 cm³ with 0.001M HNO₃. pH value was adjusted with 3 % ammonia and 0.003 M HNO₃ to 2.5-3.0. Before electrolysis the argon was bubbled through solution for a period of 15 min. Electrolysis was performed at -2.5 V with respect to SCE; the current of 100 mA was used. The first electrolysis lasted 90 min and then the working electrode was washed in acetone and transferred to second electrochemical cell, where it was used as counter electrode. The second electrolysis was performed at the same potential (-2.5 V) with respect to SCE, and pH of solution 2.5-3. After the second electrolysis, the working electrode with deposited ⁹⁰Y was washed out in acetate buffer. Quality control is performed using EPC with chromatography paper impregnated with 2-ethyl hexyl, 2-ethyl hexyl phosphonic acid (KSM-17). Paper strip (Whatman N^o1) was developed in saline. ⁹⁰Y remains at the beginning of the strip (Rf=0) while strontium was moved with mobile phase (Rf=1). As in the first experiments the mixture of ⁹⁰Sr and ⁹⁰Y with low activity, at the megabecquerel level, was used, the activity at the solvent front was estimated by use of dose calibrator (Capintec CRC 15R, USA) which contains calibration factor and compared with the total spotted activity. In addition, activity of solution was tested during the month and activity was measured.

Results and Discussion

Comparative results of radiochemical purity of ⁹⁰Y before and after electrolysis, obtained by paper chromatography, are given in Figure 1.

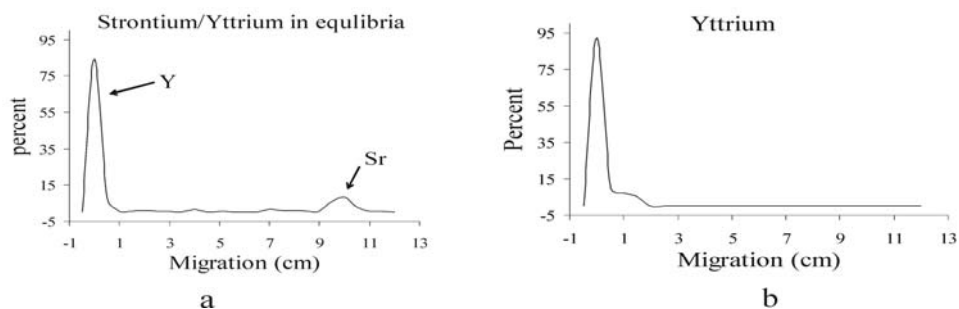


Fig.1. Extraction paper chromatography a) strontium/yttrium in equilibrium; b) yttrium after electrolyses

Solution of strontium and yttrium is in balance, and its layout is shown in Fig. 1a, where two peaks are visible. The absence of peak at 10cm (Fig. 1b) which

represents strontium, indicate that separation of yttrium from strontium by electrochemical separation was successful.

The quality of separation was investigated by measuring radioactivity of obtained ^{90}Y – solution during 35 days. Results are presented in figure 2 in CPM (counts per minute) versus time. The absence of deviation at the lower end of the straight line confirms the absence of ^{90}Sr .

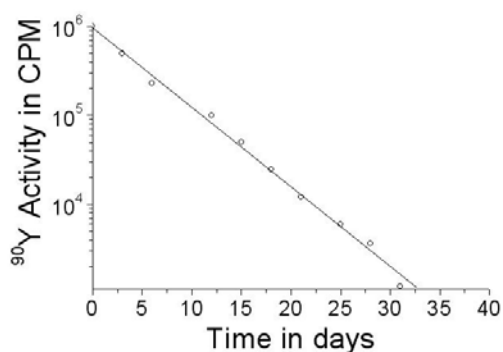


Fig.2. Radioactive decay of ^{90}Y prepared by the separation method studied for 35 days

therapeutic use. Advanced technology has the potential for widespread use that would bring significant benefits to patients. Unlike other generators, the amount of radioactive waste produced by electrochemical generator is reduced to a minimum, which present significant advantage.

Conclusion

Electrochemical separation method has a practical application for obtaining yttrium from $^{90}\text{Sr}/^{90}\text{Y}$ generator in routine nuclear medicine practice. The efficiency of the $^{90}\text{Sr}/^{90}\text{Y}$ generator was above 96% of the theoretical value and represent good basis for further development of this generator. Also, a satisfactory quality of the $^{90}\text{Sr}/^{90}\text{Y}$ separation makes this product suitable for further use. Operating costs of such generators can be very low ensuring a stable supply of ^{90}Y for

References

- [1] W. A Volkert, et al., J. Nucl. Med., 1991, **32**, 174.
- [2] M. Chinol, et al., J. Nucl. Med., 1987, **28**, 1465.
- [3] P. A., Schubiger, et al., Hoffman-LaRoche & Co. Ltd: Basel, Switzerland, 1986.
- [4] H. Kobayashi, et al., J. Nucl. Med., 1998, **39**, 829-836.
- [5] W.J. Skraba, H. Arino, H. H. Kramer, Int. J. Appl. Rad. Isot., 1978; **29**, 91-96.
- [6] P. Vanura, V. J. Krizova., Czech. J. Phys., 2003, **53**, A459-A464.
- [7] S. Happel, R. Streng, P. Vater, W. Ensinger, Radiat. Meas., 2003, **6**, 761-766.
- [8] P. S. Dhami, et al., Sep. Sci. Technol., 2007, **42**, 5.
- [9] R. Chakravarty, et al., Nucl. Med. Biol., 2008, **35**, 2.

ELECTROCHEMICAL CHARACTERISATION OF MIXED LIGAND DINUCLEAR COPPER(II) COMPLEXES

S. Stevanović¹, B. Petković², M. Budimir², S. P. Sovilj³ and V. M. Jovanović¹

¹*ICTM, Department of Electrochemistry, University of Belgrade, Njegoševa 12, P.O. Box 815, 11000 Belgrade, Serbia*

²*Department of Chemistry, Faculty of Natural Sciences and Mathematics, University of Priština, 38220 Kosovska Mitrovica, Serbia*

³*Faculty of Chemistry, University of Belgrade, P.O. Box 158, 11001 Belgrade, Serbia*

Abstract

Electrochemical properties of mixed ligand dinuclear copper(II) complexes were studied in 0.1 M HClO₄ and NaClO₄ solutions by cyclic voltammetry on glassy carbon electrode. Examined were Cu(II) complexes with octaazamacrocyclic ligand *tpmc* (N,N',N'',N'''-tetrakis(2-pyridyl methyl)-1,4,8,11-tetraazacyclotetradecane) and heterocyclic dithiocarbamates (Rdtc⁻) i.e., morpholine-(Morphdtc), piperazine-(Pzdtc), piperidine-(Pipdtc), and 4-methyl-piperidine-(4-Mepipdtc) carbodithionato-S,S ions, of the general formula [Cu₂(*tpmc*)Rdtc](ClO₄)₄ as well as [Cu₂(*tpmc*)](ClO₄)₄ complex. The electrochemical results are compared with spectroscopic data obtained previously. The same effects i.e., structural and electronic, which have influence on shifted values in the IR spectra, results difference on the peak regions in CVs for all the complexes.

Introduction

Tetraamine N₄-2-pyridylmethyl substituted octaamine ligand *tpmc* (N,N',N'',N'''-tetrakis(2-pyridyl methyl)-1,4,8,11-tetraazacyclotetradecane) as a macrocyclic flexible ring through coordination provides interesting structural and chemical properties[1]. In this respect the ligand is especially useful to form and stabilize mixed-ligand complexes with additional exocyclic ligand(s)[2]. A number of dinuclear Cu(II) complexes with the *tpmc* is known, in which the macrocycle exhibits the *chair* or the *boat* coordination mode. While the *chair* coordination is rarely obtained [3], when two simple anions, as additional ligands occupy apical positions, the latter one is favorable especially in presence of some bidentate ligand [4], which forms a bridge between the two copper atoms. Dithiocarbamate ligands have high tendency of MS₄ and MS₆ coordination and act as almost uninegative bidentate ligands coordinating through the both sulphur atoms.

Therefore, dinuclear Cu(II) complexes with heterocyclic dithiocarbamates and a cyclic octadentate ligands can contribute to gain new informations concerning the behaviour of the different ligands. These complexes could be interesting from electrochemical point as well, because structural and electronic factors may simultaneously affect the potential of some possible reaction.

We embarked on the present study to describe electrochemical characterization of these compounds and to compare these results with spectroscopic data obtained previously.

Experimental

Glassy carbon (GC) disc electrode (Sigradur-Sigri Electrographite, GmbH, Germany) was used as working electrode. The electrode was mechanically refreshed with emery paper of decreasing grain size followed by polishing with aluminium oxide (0.5 μm particle size) and then cleaning in 18 M Ω water in an ultrasonic cleaner. For each experiment the electrode prepared was first examined in 0.1 M NaClO₄ and 0.1 M HClO₄ solutions by cyclic voltammetry before addition of the substances that would be studied.

The experiments were carried out at room temperature in 0.1 M HClO₄ and in 0.1 M NaClO₄ solution, with ligand and complex concentration of 10⁻⁵ and 10⁻⁴ M. The counter electrode was a platinum wire. Saturated calomel electrode (SCE) was used as reference. All the substances were examined by cyclic voltammetry, performed with sweep rate of 25, 50 and 100 mV/s, in the potential range between -1.0 V to 1.0 V.

Results and Discussion

We showed earlier[5] that CVs of all of the Rdtc⁻ ligands in 0.1 M NaClO₄ solution exhibit the irreversible anodic peaks, one in the region of 0.25–0.30 V and another in the region of 0.78–0.95V vs SCE. None of the mentioned peaks appears on the CVs of the examined [Cu₂(tpmc)Rdtc](ClO₄)₄ complexes, but there is in all the cases, reversible peak in the range from -0.2 to -0.4 V as presented in Fig. 1. The potentials of these reversible peaks differ from complexes to complexes and are influenced by the presence of different heterocyclic Rdtc⁻ ligand.

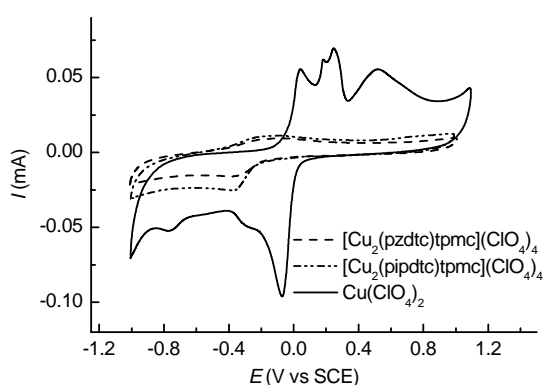
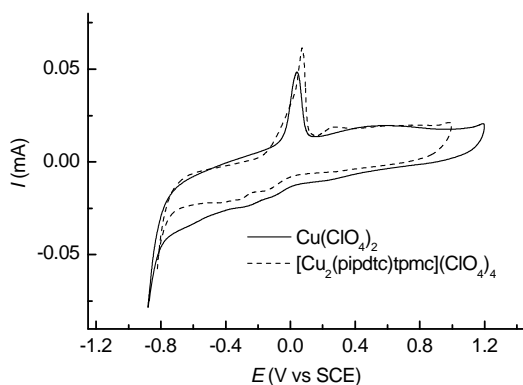


Fig.1. Cyclic voltammograms at GC electrode in 0.1 M NaClO₄ in the presence of 10⁻⁴ M [Cu₂(tpmc)Rdtc](ClO₄)₄ complexes and Cu(ClO₄)₂; sweep rate 50 mV/s.

Considering the CV of GC electrode in 0.1 M NaClO₄ in the presence of Cu(ClO₄)₂, this pair of redox peaks should mark the redox reaction of central metal ion from the complex.

However, in acidic solution the CVs of all the examined copper(II) complexes resemble the CV of GC electrode in 0.1 M HClO₄ in the presence of Cu(ClO₄)₂ exhibiting the sharp anodic peak around 0.1 V vs SCE (Fig.2). The potential of this peak also differs from complex to complex and is strongly influenced by the presence of different heterocyclic Rdtc⁻ ligands.

Fig.2. Cyclic voltammograms at GC electrode in 0.1 M HClO₄ in the presence of 10⁻⁴ M [Cu₂(tpmc)Rdtc](ClO₄)₄ complex and Cu(ClO₄)₂; sweep rate 50 mV/s.



Heteroatom in the cyclic ring and the position of methyl group on the piperidine ring from the Rdtc⁻ ligands in their complexes, have influence on IR spectra[4]. Heteroatom gives higher electron density on >NCS₂ group while the positive inductive effect of methyl group has opposite influence. Thus, if the C-N bond is stronger i.e. $\nu(\text{C—N})$ values are higher, the peak potentials are shifted to more positive values.

Conclusion

Based on the presented results it may be concluded that the same effects *i.e.*, structural and electronic, which have influence on shifted values in the IR spectra, results difference on the peak regions in CVs for all the ligands and the corresponding complexes.

References

- [1] J. Costamagna, G. Ferraudi, B. Matsuhiro, M. Campos-Vallete, J. Canales, M. Villagran, J. Vargas, M. J. Aguirre, *Coord. Chem. Rev.*, 2000, **196**, 125.
- [2] S. P. Sovilj, G. Vučković, K. Babić, N. Matsumoto, M. Avramov-Ivić, V. M. Jovanović, *J. Coord. Chem.*, 1994, **31**, 167.
- [3] E. Asato, H. Toftlund, S. Kida, M. Mikurya, K. Murray, *Inorg. Chim. Acta*, 1989, **165**, 207
- [4] S. P. Sovilj, N. Avramović, N. Katsaros, *Trans. Metal. Chem.*, 2004, **29**, 737.
- [5] V. M. Jovanović, K. Babić-Samardžija, S. P. Sovilj, *Electroanalysis*, 2001, **13**, 1129.

IMPROVEMENT OF ELECTROCHEMICAL BEHAVIOR OF V₂O₅ - XEROGEL IN AQUEOUS SOLUTION

I. Stojković^a, N. Cvjetičanin^a, M. Mitrić^b and S. Mentus^{a,*}

^aUniversity of Belgrade, Faculty of Physical Chemistry, Studentski Trg 12-16, 11158 Belgrade, Serbia

^bThe Vinca Institute of Nuclear Sciences, P.O. Box 522, 11001 Belgrade, Serbia

*The Serbian Academy of Science and Arts, Knez Mihajlova 35, 11158, Belgrade, Serbia

ivana@ffh.bg.ac.rs

Abstract

Composite xerogel V₂O₅/C was synthesized by sol-gel method starting from the solution of crystalline V₂O₅ in hydrogen peroxide. The investigations of Li⁺ intercalation/deintercalation reaction in aqueous solutions of LiNO₃ with addition of additive vinylene carbonate (VC) in concentration of 0 and 1% were performed by galvanostatic cycling. Upon addition of VC, the initial discharge capacity increased for 5.6% and the capacity fade after 50 cycles was reduced for 1.8%. These facts indicate that the addition of VC to the aqueous electrolyte solution improved markedly the electrochemical performance of the composite xerogel V₂O₅/C used as an anodic lithium intercalation material.

Introduction

The rechargeable lithium-ion batteries with organic electrolyte are widely used in mobile phones. However, the organic electrolyte is toxic, inflammable and expensive, and there is the tendency to replace them by aqueous solutions [1]. The main problem in this sense is to find anode and cathode materials able to reversibly intercalate Li⁺ ions within the potential range of electrochemical stability of water. Different forms of vanadium oxide were investigated as anode materials, while other transition metal oxides were investigated as cathode materials in aqueous solutions.

Lithium ions may intercalate/deintercalate reversibly into the crystalline form of V₂O₅ from both organic and aqueous electrolyte solutions [2]. The amorphous- xerogel form of V₂O₅ usually displayed higher capacity than the crystalline form and its electrochemical performance were improved by addition of nanostructured carbon during synthesis [3]. The performances of lithium-ion batteries with organic electrolytes may be improved by addition additives in the electrolyte, such as vinylene carbonate (VC) [4]. It was also shown that the addition of VC to the aqueous solution can improve electrochemical performance of spinel-type cathode materials, but there does not exist analogous literature data on the anode materials [4].

In this work, by a simple sol-gel method, we synthesized composite electrode material composed of nanostructured carbon (carbon black) and xerogel V₂O₅ starting from aqueous solution of crystal V₂O₅ in H₂O₂ with suspended carbon. The intercalation/deintercalation of Li ions was investigated by galvanostatic cycling in a saturated aqueous solution of LiNO₃ to which VC was added.

Experimental

Crystalline V_2O_5 (p.a. Merck) was dissolved in 10% solution of hydrogen peroxide in an amount providing 0.06 M solution. Upon homogenization by magnetic stirring, carbon black (CB) was added in an amount to provide mass ratio V_2O_5 :CB of 10. The solution was stirred for 24 hours and dried in air. The solid power obtained upon water evaporation was dried at 200°C for one hour.

The X-ray power diffraction (XRPD) data were collected using Bruker D8 Advance with $CuK\alpha_{1,2}$ radiations in 10-70° 2θ range with 0.05° step and 2 seconds exposition time. Simultaneous TGA/DTA measurements were carried out under air flow, at a heating rate of 10 ° min^{-1} using the device TA SDT Model 2960.

Galvanostatic charge/discharge measurements were performed in a two-electrode arrangement, with composite xerogel V_2O_5/C as active mass of the working electrode and $LiMn_2O_4$ as active component of the counter electrode, using software-controlled device Arbin BT-2042. The active material for working (or counter) electrodes was made by mixing composite xerogel V_2O_5/C (or $LiMn_2O_4$), carbon black and PVDF binder in a weight ratio 85:10:5 in N-methyl 2-pyrrolidone solvent. A drop of the suspension was deposited on stainless steel (Fe-18%Ni) plates (~6.2 cm^2). These electrodes were dried one hour at 80°C in air and 12 hours at 140°C under vacuum. The filter paper soaked with saturated aqueous solution $LiNO_3$ with 0 and 1wt.% of vinylene carbonate separated the electrodes. The coulombic capacity during charging/ discharging process was measured within the voltage window 0.01 to 1.3V.

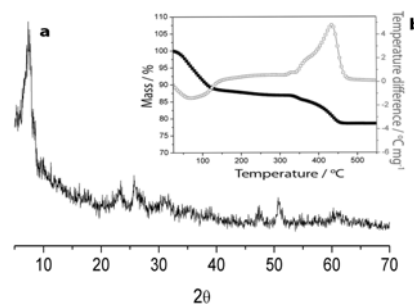


Fig.1. a) The XRD patterns of composite xerogel V_2O_5/C dried at 200°C, and b) TGA-DTA curves of composite xerogel V_2O_5/C dried at ambient temperature.

Results and discussion

XRPD analysis of composite V_2O_5/C after drying at 200°C evidenced amorphous structure, Figure 1a. After heating at 400°C, xerogel V_2O_5 crystallized and all diffraction lines of crystalline V_2O_5 of orthogonally symmetry (JCPDS card No 41-1426) became visible. Figure 1b shows the TG-DTA curves of the precursor powder of composite V_2O_5/C . The TG curve shows gradual loss of water. The total amount of water in the sample is 2.7 mole of water per mol of oxide. This sample lost 2.3 mole of H_2O per mole of oxide after heating to 200°C. However, due to the presence of carbon, which burns at 435°C (a pronounced exothermic peak in the DTA curve), the mass becomes constant just above the temperature of 450°C. The amount of carbon in the synthesized material, calculated from the mass loss caused by combustion, corresponds to the initial amount of carbon in the material.

Figure 2 shows the cycling performance of composite xerogel V_2O_5/C in aqueous solution of $LiNO_3$ with addition of VC in concentration of 0 and 1%. This is the first study of intercalation/deintercalation of Li ions into composite xerogel V_2O_5/C from aqueous solution. The initial capacity of composite xerogel V_2O_5/C was 58.8 mAhg^{-1} and its value after 50 cycles was 43.1 mAhg^{-1} without VC addition. If 1% of VC was added to the electrolyte, the initial discharge capacity increased for 5.6% and the capacity fade after 50 cycles was reduced for 1.8% compared to the case that when VC was absent. The dissolution of V_2O_5/C , being otherwise significant, was reduced in the presence of additive VC. A similar improvement was achieved by coating crystalline V_2O_5 with polypyrrole [5].

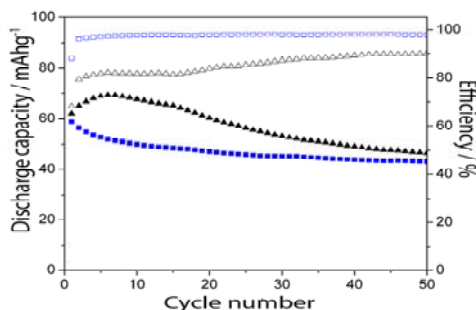


Fig.2. The discharge capacity (full symbols) and coulombic efficiency (empty symbols) of composite xerogel V_2O_5/C in saturated aqueous $LiNO_3$ solution with 0% VC (■) and 1 wt.% VC (▲) added. The rate was 50 mA g^{-1} and the potential difference limit was 1 V.

Conclusion

The composite xerogel V_2O_5/C used as electrode material in an aqueous saturated solution of $LiNO_3$ displayed better electrochemical performance if the additive VC was added in concentration of 1 wt.%. Namely, with the additive, the initial capacity increased for 5.6% while the capacity fade after 50 cycles was reduced for 1.8%.

Acknowledgement

This work was supported by Serbian Ministry of Science, project No. 142047. The Serbian Academy of Science and Arts supported the investigations too, through the project "Electrocatalysis in the contemporary processes of energy conversion".

References

- [1] N. Cvjeticanin, I. Stojkovic, M. Mitric, S. Mentus, J. Power Sources, 2007, **174**, 1117-1120.
- [2] L. Yu, X. Zhang, J. Colloid Interface Sci., 2004, **278**, 160-165.
- [3] D. Imamura, M. Miyayama, M. Hibino, T. Kudo, J. Electrochem. Soc., 2003, **150**, A753-A758.
- [4] I.B. Stojković, N.D. Cvjetićanin, S. V. Mentus, Electrochem. Commun., 2010, **12**, 371-373.
- [5] H. Wang, Y. Zeng, K. Huang, S. Liu, L. Chen, Electrochim. Acta, 2007, **52**, 5102-5107.

F

Biophysical Chemistry,
Photochemistry, Radiation Chemistry

PHYSICO-CHEMICAL MECHANISMS OF AMYLOID FORMATION-DISAGGREGATION: *in vitro* AND *ex vivo* STUDIES

Ludmilla Morozova-Roche

Department of Medical Biochemistry and Biophysics, Umeå University, Umeå, 90781 Sweden.

Abstract

Amyloid formation is a universal behavior of proteins central to many important human pathologies and industrial processes. The extreme stability of amyloid structures towards chemical and proteolytic degradation is an acquired property compared to the conformations of precursor proteins and is a major prerequisite for their accumulation in the body and *in vitro*. Here, we report two examples on (1) how amyloid deposits are stabilized in a protease rich environment of the ageing prostate and (2) how the lability of common biopharmaceutical product insulin is modulated by solution conditions and amyloid ageing.

Introduction

A wide range of human diseases are associated with the deposition of protein aggregates known as amyloids. Amyloid deposits can develop into plaques in Alzheimer's disease brains, α -synuclein-based Lewy bodies in the *substantia nigra* during Parkinson's disease, islet peptide amyloidosis in the pancreas, while lysozyme and transthyretin deposits involved in systemic amyloidosis can spread throughout the whole body. Recently we have discovered that pro-inflammatory S100A8/A9 proteins form age-dependent amyloidosis in the ageing prostate [1]. The amyloid precursor proteins and peptides involved in amyloidoses are characterized by highly diverse secondary and tertiary structures, but all amyloids possess common properties. Their internal structure is based on a cross- β -sheet core, supported by a dense network of inter- and intra-molecular hydrogen bonds. In addition, π - π stacking of aromatic rings can also contribute to the fibrillar assembly and stability.

As a result, once formed the amyloids are characterized by a remarkable mechanical stability, to such an extent that the physical strength of insulin fibrils is comparable to that of steel and their mechanical stiffness is similar to that of silk. The amyloids are also stable against heat and chemical denaturing treatments within a wide range of conditions, and they are generally viewed to be protease resistant. Therefore, the amyloid fibrils have been suggested to represent the global minimum in the free-energy landscape of protein folding and aggregation. In spite of their mechanical and chemical stability, amyloid fibrils are non-covalently bonded assemblies and their constituting building blocks can undergo continuous recycling. Given the aforementioned medical relevance and diverse views on the biophysical properties of amyloid fibrils, the ability of amyloid to either grow or

dissociate under various solution conditions, which we have defined as “lability” [2], represents a significant interest in the field of amyloid formation.

S100A8/A9 amyloid formation and stabilization in the ageing prostate

By using multidisciplinary analysis of *corpora amylacea* inclusions in prostate glands of patients diagnosed with prostate cancer we have revealed that their major components are the amyloid forms of S100A8 and S100A9 proteins associated with numerous inflammatory conditions and types of cancer [1]. In prostate protease rich environment the amyloids are stabilized by dystrophic calcification and lateral thickening. We have demonstrated that material closely resembling *corpora amylacea* can be produced from S100A8/A9 *in vitro* under native and acidic conditions and shows the characters of amyloids. This process is facilitated by calcium or zinc, both of which are abundant in *ex vivo* inclusions. These observations were supported by computational analysis of the S100A8/A9 calcium-dependent aggregation propensity profiles. We found DNA and proteins from *Escherichia coli* in *corpora amylacea* bodies, suggesting that their formation is likely to be associated with bacterial infection. These findings, taken together, suggest a link between bacterial infections, inflammation and amyloid deposition of pro-inflammatory proteins S100A8/A9 in the prostate gland, such that a self-perpetuating cycle can be triggered and may increase the risk of malignancy in the ageing prostate.

The hetero-oligomeric complexes of S100A8/A9 are characterized by remarkable stability and protease resistance comparable to those of prions. In the protease rich environment of prostate gland, and especially at sites of inflammation, proteases are present at even higher levels than in other tissues. Protease resistance of the S100A8/A9 proteins could favour their accumulation and conversion into amyloid structures in prostate tissue. The bundles of amyloid fibrils of S100A8/A9 proteins, that are formed both *in vivo* and *in vitro*, are amongst the largest super-molecular species reported for amyloid assemblies [1]. The lateral association or thickening of the fibrils is likely to be a contributory factor to their stability in the prostate gland. Indeed, it has been suggested that the various functions of the S100A8/A9 hetero and homo-oligomers may be regulated by their differential protease sensitivity. If so, the amyloid structures formed by the S100A8/A9 will be at the extreme end of the scale of resistance to proteolysis.

Prostate amyloid deposits are present in calcified form. A recently reported function of S100A9 is associated with the promoting calcification, suggesting that this protein may also play a role in dystrophic calcification of *corpora amylacea*. The mineral content of *corpora amylacea* was rather uniform in all the patients we studied, suggesting that calcification is a regulated process and therefore could be influenced by the activities of S100A8/A9. In our *in vitro* studies we have shown that the formation of the amyloid structures of the S100A8/A9 proteins is promoted by the presence of calcium and zinc, while proteins themselves influence the process of calcification, which together may produce a synergistic effect, leading to further enlargement of *corpora amylacea* deposits.

Lability landscape and protease resistance of human insulin amyloid

Using a range of methods such as atomic force microscopy, thioflavin T fluorescence, circular dichroism and gas-phase electrophoretic mobility macromolecule analysis, we probed the propensity of human insulin amyloid to propagate or dissociate in a wide span of pH values and ageing periods in a low concentration regime. We generated a three-dimensional amyloid lability landscape in coordinates of pH and amyloid ageing, which displays three distinctive features: (i) a maximum propensity to grow near most amyloid-prone conditions of pH 3.8 and an age corresponding to the inflection point of the growth phase, (ii) an abrupt cutoff between growth and disaggregation at pH 8–10, and (iii) isoclines shifted towards older age during the amyloid growth phase at pH 4–9, reflecting the greater stability of aged amyloid compared to newly formed structures. Thus, lability of amyloid strongly depends on the ionization state of insulin and on the structure and maturity of amyloid fibrils.

The stability of insulin amyloid towards protease K was assessed by using real-time atomic force microscopy and thioflavin T fluorescence. We estimated that amyloid fibrils can be digested both from the free ends and within the length of the fibril with a rate of ca 4 nm/min. Our results highlight that amyloid structures, depending on solution conditions, can be less stable than commonly perceived.

Preformed fibrils of human insulin will effectively dissociate and disappear if the pH in their local environment is shifted to alkaline values. However, once formed, the amyloid replicas significantly lower the concentration of amyloid precursor required for amyloid propagation, and therefore, the introduction of the seed can trigger this malignant process even in the presence of extremely low concentration of initial protein. The balance between the fibrillar amyloid stability and ability to propagate can have profound impact for both localized and widely spread systemic amyloidoses. The low concentration of insulin and the neutral pH in the bloodstream, however, disfavors its propagation from the places of its recurrent injections.

The same approach of calculation of the lability landscape, which we have developed using insulin as a model protein, can be applied to multiple proteinaceous amyloids and to multiple environmental cues, including the effect of metal ions, denaturing agents, surfactants and others. If other proteins were to be subjected to the same analysis, it would be beneficial to follow the standard conditions outlined in [2]. This would enable us to compare the thermodynamic and kinetic properties of different preformed amyloid structures.

References

- [1] K. Yanamandra et al., L. A. Morozova-Roche, PLOS One, 2009, **4**, e5562.
- [2] M. Malisauskas, C. Weise, M. Wolf-Watz, L. A. Morozova-Roche, J. Mol. Biol., 2010, **396**, 60-74.

KINETIC STUDY OF TRANSCRIPTION FACTOR–DNA INTERACTIONS IN LIVE CELLS

Vladana Vukojević¹

Dimitrios K. Papadopoulos², Lars Terenius,¹ Walter J. Gehring², Rudolf Rigler^{3,4}

¹*Department of Clinical Neuroscience, Karolinska Institutet, Stockholm, Sweden*

²*Department of Cell Biology, Biozentrum, University of Basel, Basel, Switzerland*

³*Department of Medical Biochemistry and Biophysics, Karolinska Institutet, Stockholm, Sweden*

⁴*Laboratory of Biomedical Optics, Swiss Federal Institute of Technology, Lausanne, Switzerland*

Abstract

Quantitative methods with single-molecule sensitivity, confocal laser scanning microscopy with avalanche photodiode detectors (APD imaging) and fluorescence correlation spectroscopy (FCS) were used to study the kinetics of protein-DNA interactions in their native environment, the live cell nuclei. Using functional and non-functional synthetic variants of the *Drosophila Hox* gene *Sex combs reduced* (*Scr*), we studied in live salivary glands the molecular mechanisms of the Scr-homeodomain (Scr-HD) interactions with DNA, which is the first step in Hox-mediated transcription. We discerned freely moving Scr-HD molecules, characterized the specific and non-specific Scr-HD interactions with the DNA and estimated their corresponding dissociation constants (K_d) *in vivo*. Our results suggest that the synthetic Scr-HD transcription factors find their specific target sites primarily by multiple association/dissociation events, the rapidity of which is largely owed to electrostatic interactions. Based on these new findings, we formulate a model mechanism and emulate the kinetics of Scr homeodomain-DNA interactions in live cells using numerical simulations.

Introduction

Transcription factor-DNA interactions, the assembly of functional transcriptional complexes and the mechanisms involved in target site recognition are central to understanding gene regulation *in vivo*. In spite of such relevance, kinetic studies of transcription factor-DNA interactions are limited to date and have been performed only for a hand-full of proteins [1-8]. The majority of these studies are carried out with naked DNA or reconstituted chromatin, reflecting the *in vivo* situation only to a limited extent. Chromatin structure in live cells is highly dynamic, involving multiple interactions and transformations [9-11]. Moreover, a number of co-factors and co-activators/co-repressors are involved in transcriptional regulation, suggesting that gene expression is accomplished through a dynamic, spatio-temporally entangled interplay between concomitant processes – protein searching for specific target sites, rearrangements of DNA conformation and recruitment of co-factors and/or co-regulators [5,12,13].

In order to study these interactions nondestructively, in the living cell sophisticated biophysical methods are required. The great complexity of the problem – low number of molecules of interest in comparison to the surrounding molecules (concentrations of the order 0.1 – 100 nM), fast molecular interactions (characterized by on-off rates of the order $10^5 - 10^8 \text{ M}^{-1}\text{s}^{-1}$), short life time of transient molecular complexes ($10^{-6} - 10^{-3} \text{ s}$) and rapid molecular movement (diffusion coefficients of the order $10^{-13} - 10^{-10} \text{ m}^2\text{s}^{-1}$), requires ultra-fast methods with high spatial (sub-micrometer) and temporal (sub-millisecond) resolution and single-molecule sensitivity. We are using in our study two such methods, confocal laser scanning microscopy imaging with avalanche photodiode detectors (APD imaging) [14] and fluorescence correlation spectroscopy (FCS) [15-18]. These complementary methods enable us to visualize the sparse transcription factor molecules in the cell nucleus, measure their local concentrations, quantitatively characterize their mobility and identify the underlying modes of motion – distinguish free Brownian diffusion from directed movement or motion impeded by molecular interactions. Local concentration and mobility are in addition to chemical affinities critical determinants of transcription factor reactivity and, hence the kinetics of transcription factor-DNA interactions.

Results

Controllable Hox peptide expression in live cells. In order to study the interactions of synthetic HD peptides with nuclear DNA in live cells we needed to compose first a controllable live cell expression system with properties as close as possible to native conditions. Therefore we used synthetic *Scr* genes in live salivary gland cells, where *Scr* is normally expressed during development. Taking advantage of the expression ‘leakage’ of the *hsp70* minimal promoter of the UAS constructs, we expressed the fluorescently labelled *mCitrine-Scr*-HD in the salivary glands without the use of any *Gal4* driver and regulate its expression levels by heat-shock (Fig. 1).

We modified the chemical reactivity of *Scr*-HD by substituting the thr-7 and ser-8 of the wild type *Scr*-HD (*Scr*-HD_{wt}) with alanines (*Scr*-HD_{AA}) or aspartates (*Scr*-HD_{DD}), thereby rendering the *Scr*-HD constitutively active or inactive, respectively. Additional mutations of residues 50 and 51 of the third helix of the HD into alanines (*Scr*-HD_{DD}^{Q50AN51A}) completely abolish binding of the HD to the DNA. These active and inactive variants allowed us to analyze and compare the differential behaviour of functional transcription factors, as compared to their non-functional counterparts (Fig. 2). At low concentrations of the *Scr*-HD, $30 \text{ nM} < [\text{Scr-HD}] < 200 \text{ nM}$, we could now clearly visualize marked differences in molecular distribution and dynamics among the transcriptionally active active *Scr*-HD_{wt} and the inactive *Scr*-HD_{DD} (Fig. 2). While the wild type (Fig. 2 A) variant showed patterned distribution, staunchly reflecting the contours of the polytene chromosomes, *Scr*-HD_{DD} was uniformly distributed in the nucleus (Fig. 2 B).

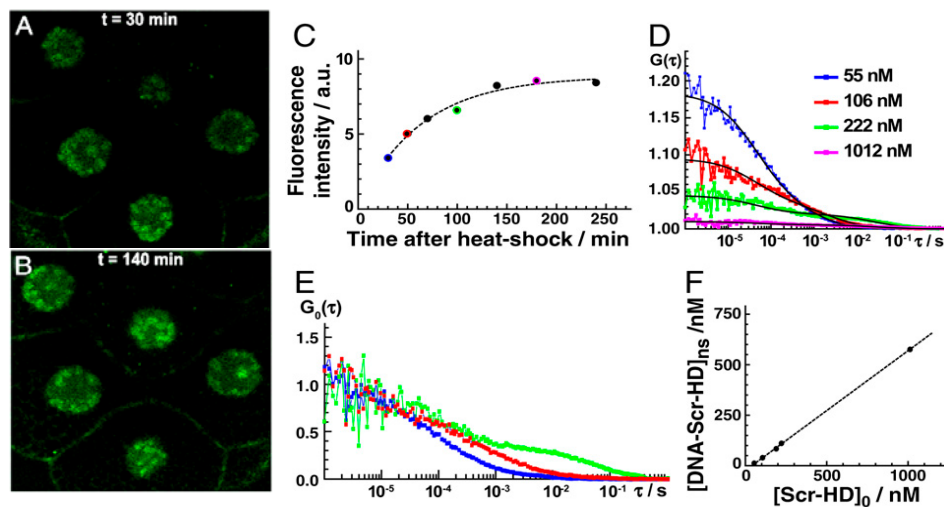


Fig.1. Controllable Scr-HD expression in vivo. (A) APD image of salivary gland nuclei expressing the synthetic Scr-HDwt transcription factor. Heat shock was applied by keeping the *Drosophila* larvae at 37 °C for 30 min. The image was recorded 30 min after heat shock, when the expression was still low and close to physiological levels. Minimal expression was obtained by the UAS construct without the Gal4 driver. (B) APD imaging showing elevated expression of Scr-HDwt 140 min after heat shock. (C) Gradual increase of Scr-HDwt concentration in live salivary gland cells recorded by time-lapse APD imaging. (D) Gradual increase of Scr-HDwt concentration in live salivary gland cells recorded by FCS. The color code indicates FCS measurements performed just after APD imaging, represented in (C) by the corresponding color. (E) Normalized autocorrelation curves showing changes in Scr-HDwt dynamics as a function of its concentration. All FCS measurements were performed at the same location in the same cell. (F) The concentration of the second component increases linearly with the total concentration of Scr-HDwt.

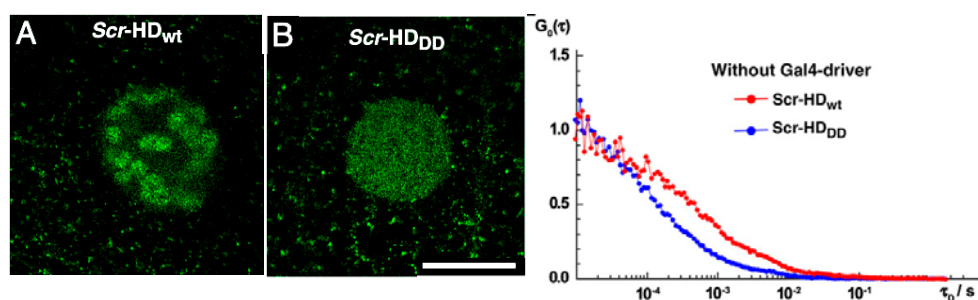


Fig.2. Differences in DNA–Scr-HD interactions between different Scr-HD variants visualized in polytene nuclei of live salivary gland cells by APD imaging and FCS. Polytene nuclei expressing the synthetic Scr-HD_{wt} (A) and Scr-HD_{DD} (B) at low, physiologically relevant concentrations $[\text{Scr-HD}_{wt}] = 105$ nM, and $[\text{Scr-HD}_{DD}] = 66$ nM. (C) Differences in DNA–Scr-HD dynamics/interactions between the transcriptionally active and inactive variants can be readily observed at low Scr-HD concentrations.

In line with this observation, FCS analysis also revealed that the Scr-HD variants differ in their ability to interact with the genomic DNA, which is reflected as difference in mobility and, thus the shifted autocorrelation curves (Fig. 2 C).

Discerning specific from non-specific DNA–Scr-HD interactions in live cells and determination of DNA–Scr-HD binding constants from FCS measurements. In order to construct DNA–Scr-HD binding curves (Fig. 3), we exploited the responsiveness of the *hsp70* minimal promoter of the UAS constructs to heat-shock to generate different Scr-HD expressing levels. Autocorrelation curves recorded in individual nuclei were analyzed using a two-component model with triplet formation [18]. FCS analysis revealed that Scr-HD_{DD} and Scr-HD^{Q50AN51A}_{DD} binding increased linearly with their concentration in a fashion that is characteristic for non-specific binding (Fig. 3, black line). In contrast, Scr-HD_{wt} and Scr-HD_{AA} binding profiles showed a “shifted” line, suggesting that interactions other than the non-specific ones are also involved (Fig. 3, red line). The same, “shifted” binding profile was observed in an individual cell (Fig. 1 F) and in a collection of cells (Fig. 3 B, red line).

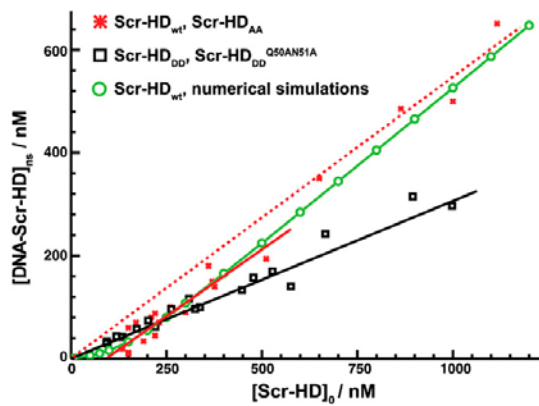
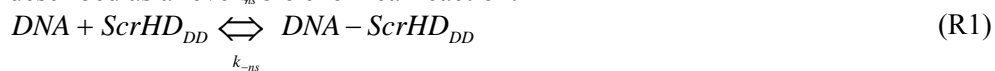


Fig.3. In vivo DNA– Scr-HD binding. FCS measurements show that the concentration of DNA–Scr-HD_{DD} and DNA–Scr-HD^{Q50AN51A}_{DD} complexes increases linearly with the total concentration of the transcription factor (black line), suggesting, in accordance with Eq. 2, that Scr-HD_{DD} and Scr-HD^{Q50AN51A}_{DD} interact only nonspecifically with the genomic DNA. In contrast, Scr-HD_{AA} and Scr-HD_{wt} undergo both specific and nonspecific interactions with the DNA (solid red line), showing

a binding profile that is in accordance with Eq. 7. In the absence of specific DNA–Scr-HD_{wt} interactions, the nonspecific DNA–Scr-HD_{wt} binding would follow the dashed red line. DNA–Scr-HD_{wt} interactions were also numerically simulated (green curve) as described in the text.

In order to understand these results, we proceeded to analyze the kinetics of underlying chemical interactions numerically.

Dissociation constant of the non-specific DNA–Scr-HD_{DD} and DNA–Scr-HD^{Q50AN51A}_{DD} complexes. Previous genetic experiments [19], imaging analysis and FCS measurements suggest that Scr-HD_{DD} and Scr-HD^{Q50AN51A}_{DD} interact non-specifically with the DNA. These interactions, exemplified for Scr-HD_{DD}, can be described as a reversible chemical reaction:



where k_{ns} and k_{-ns} are rate constants for the formation and dissociation of the non-specific DNA–Scr-HD_{DD} complex, respectively. Using mass balance equations [18], we could show that the concentration of non-specific DNA–Scr-HD_{DD} complex increases linearly with the total concentration of the transcription factor:

$$[DNA - ScrHD_{DD}] = \frac{k_{ns} \cdot [DNA]_0}{(k_{-ns} + k_{ns} \cdot [DNA]_0)} \cdot [ScrHD_{DD}]_0 \quad . \quad (R2)$$

Using equation (R2) and the experimentally determined slope (Fig. 3, black line)

$$\frac{k_{ns} \cdot [DNA]_0}{(k_{-ns} + k_{ns} \cdot [DNA]_0)} = (0.35 \pm 0.15) \quad , \quad (R3)$$

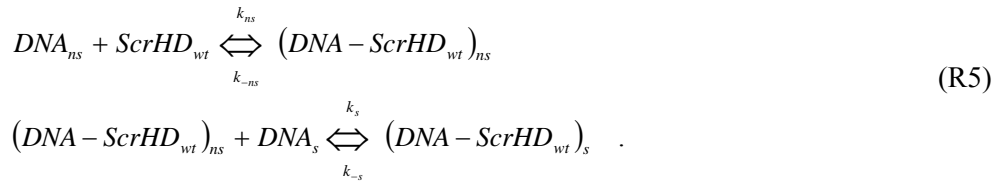
we derived the equilibrium dissociation constant for the non-specific DNA–Scr-HD_{DD} complex:

$$\frac{k_{-ns}}{k_{ns}} = K_d^{ScrHD_{DD},ns} = \frac{[DNA]_0}{0.54} \quad . \quad (R4)$$

where $[DNA]_0$ is the total concentration of potential sites for non-specific binding. The total concentration of potential binding sites for non-specific interactions is not easily estimated. Following the assumptions detailed out in Supplement 2, we estimated that $[DNA]_0 = 46 \mu\text{M}$. Under these assumptions, the dissociation constant for non-specific DNA–Scr-HD binding is estimated to be:

$$K_d^{ScrHD_{DD},ns} = (80 \pm 50) \mu\text{M} \quad .$$

Dissociation constant of the specific DNA–Scr-HD_{wt} and DNA–Scr-HD_{AA} complexes. The transcriptionally active variants Scr-HD_{wt} and Scr-HD_{AA}, undergo both specific and non-specific interactions with the DNA. Supposing that non-specific interactions precede the specific ones, a two-step process of consecutive reactions was assumed:



Applying the quasi-steady state approximation, we could show that the concentration of non-specific DNA–Scr-HD_{wt} complexes increases linearly with the total concentration of the transcription factor, but only after equilibrium for

specific binding is reached (complete derivation of equation (R6) can be found in [18]):

$$\begin{aligned} [(DNA - ScrHD_{wt})_{ns}] = & \frac{k_{ns} \cdot [DNA]_0}{k_{-ns} + k_s \cdot [DNA_s] + k_{ns} \cdot [DNA]_0} \cdot [ScrHD_{wt}]_0 - \\ & - \frac{k_{ns} \cdot [DNA]_0 - k_{-s}}{k_{-ns} + k_s \cdot [DNA_s] + k_{ns} \cdot [DNA]_0} \cdot [(DNA - ScrHD_{wt})_s] \end{aligned} \quad (R6)$$

This is in agreement with our experimental findings by FCS (Fig. 2 F and Fig. 6, solid red line). Accordingly, the slope of the linear dependence gives:

$$\frac{k_{ns} \cdot [DNA]_0}{k_{-ns} + k_s \cdot [DNA_s] + k_{ns} \cdot [DNA]_0} = (0.60 \pm 0.05) \quad (R7)$$

and the intercept:

$$\frac{k_{ns} \cdot [DNA]_0 - k_{-s}}{k_{-ns} + k_s \cdot [DNA_s] + k_{ns} \cdot [DNA]_0} \cdot [(DNA - ScrHD_{wt})_s] = (50 \pm 30) \text{ nM} \quad (R8)$$

If k_{-s} is small compared to $k_{ns} \cdot [DNA]_0$ and can therefore be neglected, then

$$0.6 \cdot [(DNA - ScrHD_{wt})_s] = 50 \text{ nM} \quad (R9)$$

and the total concentration of the specific complex DNA–Scr–HD_{wt} in the polytene nucleus could be determined

$$[(DNA - ScrHD_{wt})_s] = (80 \pm 50) \text{ nM} \quad (R10)$$

Using the experimentally determined concentration of specific DNA–Scr–HD_{wt} complexes (eq. R10) and the estimated total concentration of specific DNA binding sites derived in [18], $[DNA_s] = 92 \text{ nM}$, we could estimate the dissociation constant for the specific DNA–Scr–HD_{wt} complex

$$K_d^{wt,s} = \frac{[DNA_s]_{free} \cdot [ScrHD_{wt}]_{free}}{[(DNA - ScrHD_{wt})_s]} = \frac{12 \text{ nM} \cdot 48 \text{ nM}}{80 \text{ nM}} = (7 \pm 5) \text{ nM} \quad (R11)$$

Dissociation constant of the non-specific DNA–Scr–HD_{wt} and DNA–Scr–HD_{AA} complexes. FCS data enabled us also to estimate the dissociation constant for the non-specific DNA–Scr–HD_{wt} and DNA–Scr–HD_{AA} complexes. Using the analysis presented above and the data from Fig. 6 (dotted red line) we could estimate the dissociation constant for the non-specific DNA–Scr–HD_{wt} and DNA–Scr–HD_{AA} complexes

$$\frac{k_{ns} \cdot [DNA]_0}{(k_{-ns} + k_{ns} \cdot [DNA]_0)} = (0.65 \pm 0.05) \quad (R12)$$

$$\frac{k_{-ns}}{k_{ns}} = K_d^{wt,ns} = \frac{[DNA]_0}{1.9} . \quad (R13)$$

Under the assumptions outlined in Supplement 2, we estimated

$$\frac{k_{-ns}}{k_{ns}} = K_d^{wt,ns} = (25 \pm 15) \mu M . \quad (R14)$$

This three-fold difference in non-specific interactions between DNA–Scr-HD_{DD} and DNA–Scr-HD_{DD}^{Q50AN51A} on one side and DNA–Scr-HD_{wt} and DNA–Scr-HD_{AA} on the other can be naturally explained by differences in the intensity of electrostatic interactions with the negatively charged DNA [18]. Charge analysis revealed that at relevant pH (34) Scr-HD_{wt} and Scr-HD_{AA} are more positively charged than Scr-HD_{DD} and Scr-HD_{DD}^{Q50AN51A}, explaining also the difference in their mobility observed by FCS (Fig. 2 C).

Numerical simulation of DNA–Scr-HD_{wt} interactions. FCS measurements provided important, experimentally derived relationships between rate constants, enabling us to take one step further and attempt to simulate the dynamics of DNA–Scr-HD interactions. Using the experimentally determined relations between rate constants (R3), (R7) and (R8) and the estimated concentration of specific and non-specific binding sites we derived by fitting the macroscopic rate constant for Scr-HD_{wt} interactions with the DNA, $k_{ns} = 1 \times 10^7 \text{ M}^{-1} \text{ s}^{-1}$, $k_{ns} = 3.25 \times 10^2 \text{ s}^{-1}$, $k_s = 1.5 \times 10^7 \text{ M}^{-1} \text{ s}^{-1}$ and $k_s = 1 \times 10^{-1} \text{ s}^{-1}$. Using these values, the experimental data derived by FCS could be readily fitted by the simple two-step model given in (R6) (Fig. 3, green curve).

Discussion

Our results suggest that the synthetic Scr-HD transcription factors find their specific target sites primarily by multiple association/dissociation events, the rapidity of which is largely owed to electrostatic interactions. A model mechanism for DNA–Scr-HD interactions is schematically depicted in Fig. 4.

By advanced APD imaging and FCS, we detected free Scr-HD molecules that move in the nucleoplasm at a rate that is similar to free 3D diffusion of the purified recombinant mCitrine-Scr-HD_{wt} peptide in solution, $D_{\text{Scr-HD, solution}} = (2 \pm 1) \times 10^{-11} \text{ m}^2 \text{ s}^{-1}$ Fig. 4 (red spheres).

On the chromosomes and in regions of pronounced accumulation, the Scr-HD molecules undergo numerous non-specific interactions with the DNA (Fig. 4, yellow spheres). The dissociation constant for the non-specific DNA–Scr-HD complexes was estimated to be $K_d^{\text{ScrHD}_{DD},ns} = (80 \pm 50) \mu M$ for DNA–Scr-HD_{DD} and Scr-HD_{DD}^{Q50AN51A}, and for DNA–Scr-HD_{wt} and DNA–Scr-HD_{AA}. These somewhat high K_d values suggest that Scr-HD affinity for non-specific binding

sites is rather low, a feature that allows the DNA-Scr-HD complex to assemble/disassemble rapidly in the polytene nucleus densely packed with DNA. Scr-HD molecules undergoing nonspecific interactions with the genomic DNA are slowed down by the on/off interactions and seem to move in a diffusion-like fashion with an apparent diffusion constant $D = (4 \pm 2) \times 10^{-13} \text{ m}^2 \text{ s}^{-1}$.

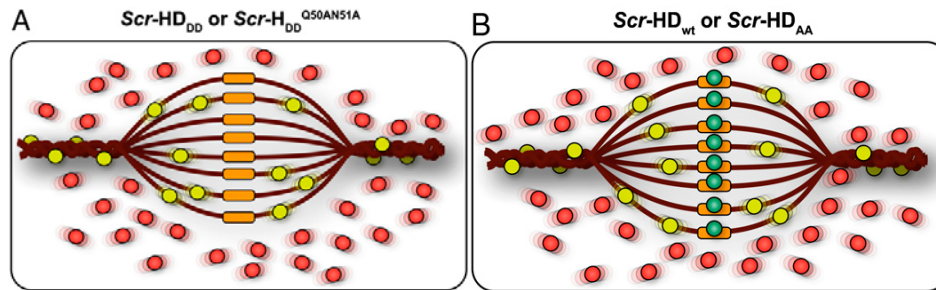


Fig.4. Schematic representation of the differential behavior of Scr-HD variants. (A) In nuclei expressing the transcriptionally inactive variants Scr-HD_{DD} or Scr-HD_{DD}^{Q50AN51A} FCS can distinguish between free Scr-HD molecules diffusing in the nucleoplasm (red spheres) and transcription factor molecules interacting nonspecifically with the DNA (yellow spheres). Binding sites within the region of loose chromatin conformation (orange rectangles) cannot be bound specifically by Scr-HD_{DD} or Scr-HD_{DD}^{Q50AN51A} because binding is abolished by the corresponding amino acid substitutions. (B) DNA– Scr-HD_{wt} or DNA–Scr-HD_{AA} interactions are more complex. In addition to the free Scr-HD molecules in the nucleoplasm (red spheres) and transcription factor molecules interacting nonspecifically with the DNA (yellow spheres), the transcriptionally active variants undergo also specific interactions (green spheres) with putative specific binding sites.

Nonspecific DNA–Scr-HD_{wt} interactions always precede the specific ones. However, if the binding site is a putative specific binding site in a region of loose chromatin conformation (Fig. 4, orange rectangles), the nonspecific complex readily transforms into a specific complex (Fig. 4, green spheres). The number of specific binding sites is lower than the number of nonspecific sites and the mobility of the specific DNA–Scr-HD complexes seems to be rather low, rendering these complexes “invisible” for direct observation by FCS. Nevertheless, we were able to characterize the specific interactions using a rigorous kinetic analysis that was based on FCS measurements performed at very low Scr-HD concentrations. We estimated the dissociation constant of the specific DNA–Scr-HD_{wt} complexes to be in the nanomolar range, $K_d^{\text{ScrHD}_{wt} \rightarrow S} = (7 \pm 5) \text{ nM}$, and the concentration of specific DNA–Scr-HD_{wt} complexes $[(\text{DNA} - \text{ScrHD}_{wt})_S] = (80 \pm 50) \text{ nM}$.

References

- [1] F. Jacob and J. Monod, J. Mol. Biol., 1961, **3**,318-356.
- [2] A.D. Riggs, S. Bourgeois and Cohn M, J. Mol. Biol., 1970, **53**, 401-417.
- [3] J. Elf, G. W. Li and X. S Xie, Science, 2007, **316**, 1191-1194.

- [4] X. Wang, R. Reyes-Lamothe and D. J. Sherratt, *Biochem. Soc. Trans.*, 2008, **36**,749-753.
- [5] R. Metivier, G. Reid and F. Gannon, *EMBO Rep.*, 2006, **7**, 161-167.
- [6] S. Myong, I. Rasnik, C. Joo, T .M. Lohman and T. Ha, *Nature*, 2005, **437**, 1321-1325.
- [7] S.E. Halford and J.F. Marko, *Nucleic Acids . Res.*, 2004, **32**, 3040-3052.
- [8] M. D. Szczelkun, *Biochem.*, 2000, **35**, 131-143.
- [9] T. Cremer, et al, *Crit. Rev. Eukaryot Gene. Expr.*, 2000, **10**, 179-212.
- [10] R. Schneider and R. Grosschedl, *Genes. Dev.*, 2007, **21**, 3027-3043.
- [11] M. Wachsmuth, M. Caudron-Herger and K. Rippe, *Biochim. Biophys. Acta.*, 2008, **1783**, 2061-2079.
- [12] M.D. Biggin and W. McGinnis, *Development*, 1997, **124**, 4425-4433.
- [13] S. Hayashi and M.P. Scott, *Cell*, 1990, **63**, 883-894.
- [14] V. Vukojević, M. Heidkamp, Y. Ming, B. Johansson, L.Terenius, R. Rigler, *Proc. Natl. Acad. Sci. USA*, 2008, **105**,18176-18181.
- [15] E. L. Elson, *J. Biomed. Optics*, 2004, **9**, 857–864.
- [16] V. Vukojević, A. Pramanik, T. Yakovleva, R. Rigler, L. Terenius, G. Bakalkin, *Cell Mol. Life Sci.*, 2005, **62**, 535-550.
- [17] A. J. García-Sáez, P. Schwille, *Appl. Microbiol. Biotechnol.*, 2007, **76**, 257–266.
- [18] V. Vukojević, D. K. Papadopoulos, L. Terenius, W. Gehring, R. Rigler, *Proc. Natl. Acad. Sci. USA*, 2010, **107**, 4087-4092.
- [19] D. K. Papadopoulos, V. Vukojević, J. Adachi, L. Terenius, R. Rigler, W. Gehring, *Proc. Natl. Acad. Sci. USA*. 2010, **107**, 4093-4098.

STATISTICAL MODELS IN ANALYSIS OF STEADY-STATE FLUORESCENCE SPECTRA OF A PROTEIN. A NEW APPROACH IN FOLLOWING CONFORMATION TRANSITIONS

D. Mutavdžić¹, A. Savić¹, M. Nyitrai² and K. Radotić¹

¹*Institute for multidisciplinary research, Kneza Višeslava 1, 11000 Beograd, Serbia*

²*Department of Biophysics, Faculty of Medicine, University of Pécs, Pécs, Hungary*

Abstract

We measured and analysed emission spectra of tryptophan and actin, for different temperatures. Factor scores for pure tryptophan spectra recorded show presence of two fluorophores. Actin spectra recorded on 40⁰C and 60⁰C share two factors with emission maximum on 338 nm and 353 nm, while on 80⁰C both factor scores maxima are shifted to longer wavelengths 348 nm and 356 nm.

Introduction

Emission spectrum of a macromolecule could be a sum of contributions of two or more individual fluorophores. It is of crucial importance to use a valid mathematical model for the emission spectrum of a single fluorophore, and then to apply such model in deconvolution of the complex spectra. Here we used factor analysis for decomposition of excitation-emission matrix (EEM). We followed the effect of microenvironment on the genuine fluorophore Trp during the conformational changes [1] induced by high temperature.

Materials and Methods

For each protein sample, a series of emission spectra were measured by varying excitation wavelengths with 3 nm steps. Fluorescence spectra were collected using a Fluorolog-3 spectrofluorimeter (Jobin Yvon Horiba, Paris, France) equipped with a 450W xenon lamp and a photomultiplier tube. Actin was dissolved in deionised water. The actin concentration in all experiments was 10⁻⁶ M. The spectra were corrected for the dark counts. In each measurement an optimal number of scans were averaged. The emission spectrum of the solvent was subtracted. All measurements were performed at controlled temperature by means of a Peltier element. Fluorescence spectra of tryptofan were obtained under the same conditions. The concentration of tryptophan in all measurements was 10⁻⁶ M.

Decomposition of excitation-emission matrix (EEM), in matrix notation can be written like $\mathbf{D}_{n \times p} = \mathbf{S}_{n \times c} \mathbf{C}_{c \times p}^T + \mathbf{E}_{n \times p}$ n is a number of emission wavelengths used to obtain spectra, p is a number of collected spectra, and

$c = \overline{1, p}$ is a number of presence fluorophores. In decomposition of excitation-emission matrix, first and very important step is determining the exact value of c in analysed system. In this research, for deducing the number of components evolving factor analysis, EFA, is used as the most trustable. For extraction of matrix \mathbf{C} elements, principal component analysis, PCA, is used. For evaluating single fluorophore spectra regression method is used after rotation of matrix \mathbf{C} by promax method [2, 3].

Results and Discussion

Depending on the number of components contained in the whole emission spectrum, as well as on the position of their emission maxima, we can estimate how many different microenvironments (domains) are present in the protein and how they change in the course of conformation changes.

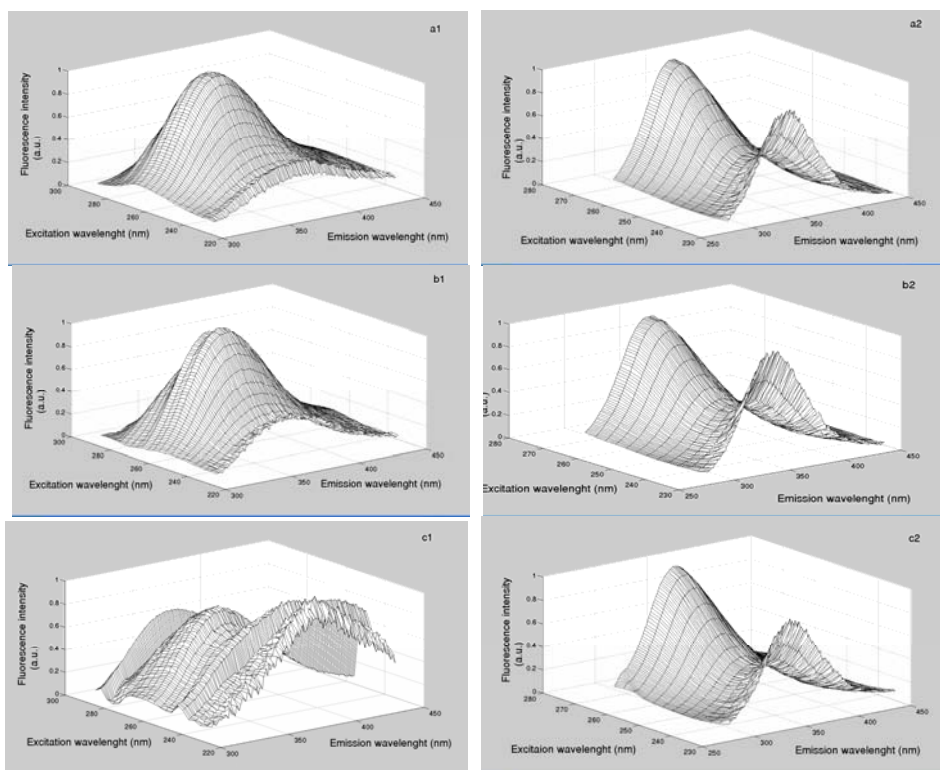


Fig.1. Fluorescence spectra of tryptophan recorded on 40⁰C (a1), 60⁰C (b1), 80⁰C (c1) and fluorescence spectra of actin on 40⁰C (a2), 60⁰C (b2), 80⁰C (c2).

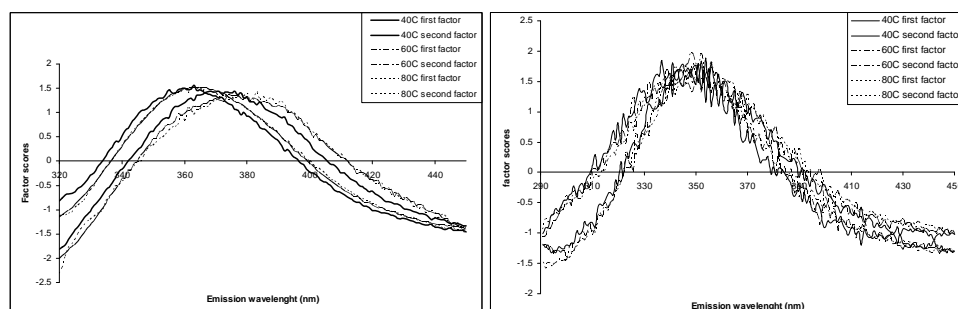


Fig.2. Factor scores for tryptophan fluorescence spectra recorded on 40⁰C, 60⁰C and 80⁰C (left) Factor scores for actin fluorescence spectra recorded on 40⁰C, 60⁰C and 80⁰C (right).

Factor scores for pure tryptophan spectra recorded on different temperatures show presence of two fluorophores. One fluorophore is found in all three spectra, with emission maximum on 363 nm. Second fluorophore is shifted to longer wavelengths as temperature rise (368 nm, 374 nm, 383 nm).

Actin spectra recorded on 40⁰C and 60⁰C share two factors with emission maximum on 338nm and 353nm. It means that there is not significant conformational change observed. On 80⁰C actin become denatured, so both factor scores maxima are shifted to longer wavelengths 348nm and 356nm.

There are four tryptophan molecules in actin. Two of them are positioned closer to surface, and their emission maximum is 353 nm. When temperature is between 60⁰C and 80⁰C, actin molecule becomes unfolded. Because of that all tryptophan residues share almost the same environment, and show presence of two similar factors with maxima on 348 nm and 356 nm.

Conclusions

Actin fluorescence spectra recorded on 40⁰C and 60⁰C share two factors, while on 80⁰C both factor scores maxima are shifted to longer wavelengths. This indicates significant conformation changes in the protein.

References

- [1] A. S. Ladokhin, Encyclopedia on Analytical Chemistry, 2000, 5762-5779.
- [2] C. G. Joaquim, Esteves da Silva, Adelio A.S.C. Machado, Chemometrics and Intelligent Laboratory Systems, 1995, **27**, 115-128.
- [3] S. Sasic, A. Antic-Jovanovic, M. Kuzmanovic, M. Jeremic, Analyst, 1999, **124**, 1481-1487.

FLUOXETINE DECREASES GLUTATHIONE REDUCTASE IN ERYTHROCYTES OF CHRONICALLY ISOLATED WISTAR RATS

M. Adzic ^{a*}, A. Djordjevic ^a, J. Djordjevic ^a, I. Elakovic ^b, I. Simic ^a, M. Mitic ^a, G. Rackov ^a, G. Matic ^b and M. Radojic ^a

^a *Department of Molecular Biology and Endocrinology, VINCA Institute of Nuclear Sciences, Belgrade, Serbia,* ^b *Department of Biochemistry, Institute for Biological Research "Siniša Stanković", University of Belgrade, 142 Despot Stefan Blvd., 11060 Belgrade, Serbia*

Abstract

Alterations in the antioxidative defense parameters upon chronic stress are considered critical for pathophysiology of stress related psychiatric disorders and their status in blood serves as biomarker for effects of pharmacological treatments. We investigated the modulation of erythrocyte antioxidant enzymes (AOEs): superoxide dismutase (SOD), catalase (CAT), glutathione peroxidase (GPx) and glutathione reductase (GLR) protein expression and activity in Wistar male rats subjected to chronic psychosocial isolation and/or treated with fluoxetine. Chronically isolated animals exhibited decreased levels of plasma corticosterone (CORT). AOEs status was not altered either by chronic social isolation or by fluoxetine. The only exception was GLR, whose level and activity were both markedly reduced by fluoxetine. Our study indicates that fluoxetine treatment of chronically isolated male Wistar rats, leads to significant reduction in the level and activity of GLR in the erythrocytes.

Introduction

Oxidative stress is defined as the imbalance between production of reactive oxygen species (ROS) and the activity of antioxidant defense system [1]. During chronic exposure to neuroendocrine stress, alterations in antioxidative defense are considered to be one of critical conditions promoting pathophysiology of stress induced psychiatric disorders. Treatment with fluoxetine (selective serotonin reuptake inhibitor, SSRI) can reverse and prevent oxidative damage induced by stress, due to elevation of antioxidative defense [2]. Thus, alterations of antioxidant parameters, particularly in blood, can serve as valuable biomarker to follow effects of chronic stress and/or pharmacological treatment of stress induced psychiatric disorders [3]. Therefore, the present study was designed to examine the pharmacological modulation of antioxidant enzymes by fluoxetine in the erythrocytes of Wistar male rats stressed by chronic psychosocial isolation.

Experimental

Animals, adult male Wistar rats, were divided into four experimental groups: control group; group II animals were subjected to chronic psychosocial isolation for 21 days; group III was subjected to chronic isolation stress for 21 days and treated with distilled water for another 21 days (vehicle), group IV was subjected to chronic isolation for 21 days and treated with fluoxetine for another 21 days.

For Western blot, erythrocyte lysates were prepared according to Laemmli [4], and 30 µg of proteins were subjected to electrophoresis (SDS-PAGE). Western blot technique was performed using following antibodies: anti-β-actin anti-CuZnSOD, anti-catalase (CAT), anti-GPx, anti-glutathione reductase (GLR), to detect β-actin, CuZnSOD, CAT, GPx and GLR, respectively.

Total SOD activity in the erythrocytes lysates was determined using a commercial kit. Catalase activity was determined according to Claiborne [5]. Activity of glutathione peroxidase was determined according to Maral *et al.* [6] and activity of glutathione reductase was measured according to Glatzle *et al.* [7]. Activities of AOE were expressed as unit per mg of proteins.

Results and Discussion

The corticosterone (CORT) levels were only significantly decreased in animals subjected to chronic social isolation for 3 weeks (Table 1, *p<0.05). In all other treatments, the CORT levels remained unaltered.

Table 1. Serum corticosterone concentration (ng/ml) in the experimental groups. Data are presented as mean ± SD. *p<0.05 vs control.

	Control	Chronic stress	Chronic stress/Vehicle	Chronic stress/Fluoxetine
Corticosterone (ng/ml)	84.6±16.8	45.8±8.8 *	78.1±22.4	66.7±20.1

Antioxidant enzymes activities

The only significant change was observed in decreased activity of glutathione reductase (GLR) in chronically stressed animals treated with fluoxetine, both in respect to the control and chronically stressed animals that received distilled water (Table 1, *p<0.05, vs control, #p<0.05 vs chr+veh).

Table 2. Antioxidant enzyme activities in the control and treated animals.

Enzyme	Control	Chronic stress	Chronic stress/Vehicle	Chronic stress/Fluoxetine
CuZnSOD	15.7±3.1	18.0±3.8	15.4±3.1	16.5±3.0
Catalase	233.8±32.8	239.8±34.5	215.1±20.8	225.2±46.8
Glutathione peroxidase	149.2±16.3	172.4±29.2	176.7±32.5	166.0±30.5
Glutathione reductase	56.5±7.1	46.6±2.9	52.1±6.22	29.3±3.7 * #

Level of antioxidant enzymes in the rat erythrocytes

The only change was observed in the protein level of GLR in chronically stressed animals treated with fluoxetine (Fig. 2, * $p < 0.05$, vs control, # $p < 0.05$ vs chr+veh) where its level was decreased. The consequences of reduced levels of GLR under fluoxetine treatment may be multiple. Namely, GLR is required for the stability and integrity of the red cells, while its decrease was connected induced haemolytic anaemia, eye cataracts, and its reduction may compromise haemoglobin function and consequently affect oxygen transport [8].

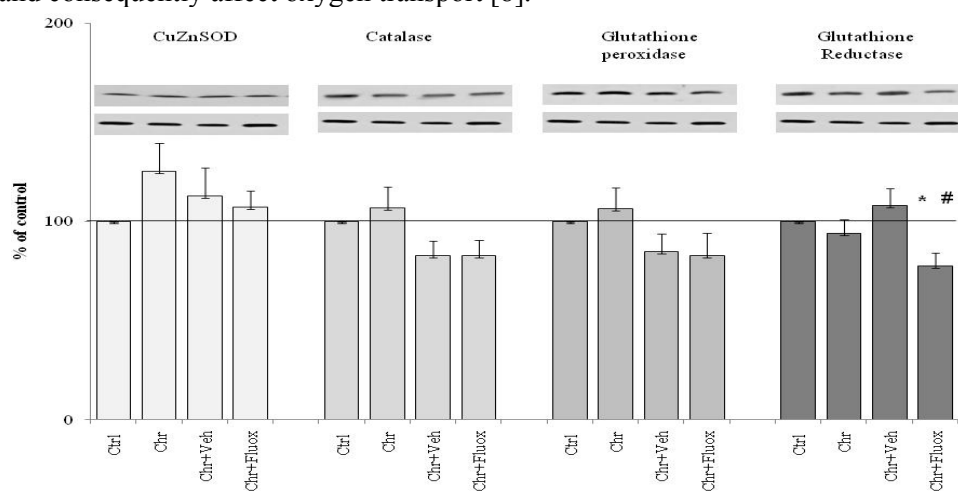


Fig.2. Representative Western blot of CuZnSOD, Catalase, Glutathion peroxidase and Glutathion reductase and their relative levels in the erythrocytes of control (Ctrl), chronically stressed (Chr), chronically stressed and vehicle treated (Chr+Veh) and chronically stressed and fluoxetine treated (Chr+Fluox) Wistar rats Data are presented as mean \pm SD of 10-11 animals per group.

Conclusion

Fluoxetine treatment significantly reduced the level and activity of glutathione reductase in the erythrocyte of chronically isolated male Wistar rats, potentially disturbing overall oxido-reductive balance in those cells and organism as whole.

References

- [1] D. B. Sawyer, D. A. Siwik, L. Xiao, D. R. Pimentel, K. Singh, W. S. Colucci, *J. Mol. Cell Cardiol.*, 2002, **34**, 379-388.
- [2] M. E. Ozcan, M. Gulec, E. Ozerol, R. Polat, O. Akyol, *Int. Clin. Psychopharmacol.*, 2004, **19**, 89-95.
- [3] A. Zafir, A. Ara, N. Banu, *Prog Neuropsychopharmacol Biol Psychiatry.*, 2009, **33**, 220-228
- [4] U. K. Laemmli, *Nature*, 1970, **227**, 680-685.
- [5] A. Claiborne, *Handbook of Methods for Oxygene Radical Research.*, 1985, 283-284.
- [6] J. Maral, K. Puget, A. M. Michelson, *Biochem Biophys Res Commun.*, 1977, **77**, 1525-1535
- [7] D. Glatzle, J. P. Vuilleumier, F. Weber, K. Decker, *Experientia*, 1974, **30**, 665-667.
- [8] H. Loos, D. Roos, R. Weening, J. Houwerzijl, *Blood*, 1976, **48**, 53-62.

INVESTIGATION OF PLANT CELL WALLS WITH QUANTUM DOTS AS A MARKER

D. Djikanović¹, A. Kalauzi¹, M. Jeremić¹, M. Mičić^{3,4},
J. Xu², R. Leblanc² and K. Radotić¹

¹*Institute for Multidisciplinary Research, University of Belgrade, Bul. Despota Stefana 142, 11000 Belgrade, Serbia,* ²*Department of Chemistry, University of Miami, Coral Gables, FL 33124, USA; mmicic@mpbio.com,* ³*MP Biomedicals, LLC, 3 Hutton Center, Santa Ana, CA 92707, USA,* ⁴*BioMEMS Lab, Dept of Mechanical and Aerospace Engineering, University of California – Irvine, 4200 Engineering Gateway, Irvine, CA92697-3975, USA*

Abstract

We used quantum dots to mark cell walls (CWs) isolated from a conifer - *Picea omorika* (Panč) *Purkyně* branch. The aim was to obtain data about structure of the CWs. The differences in interaction of wet and dry CWs with QDs/chloroform were studied. The QDs predominantly bind to the lignin and possibly to some polysaccharide parts of the CW. In the reaction of the dry CW sample with QDs/chloroform, hydrophobic interactions are dominant and in wet sample, hydrophilic interactions enabled a partial reconstruction of the double C=C chains.

Introduction

Cell wall protects plant cell from various types of stress [1]. It can be considered as a nano-composite in which cellulose, lignin and hemicelluloses are interconnected in a specific manner. Assembly of components in a cell wall and its structural organization is not sufficiently understood.

Quantum dots (QDs) are semiconductor nanoparticles with increasing application as fluorescent markers in biology. We used 3.5 nm CdSe QDs to mark cell wall. Our goal was to obtain structural information about complex structure of the cell walls and its components by following interactions of QDs with cell walls.

Results and discussion

First, we investigated influence of solvents, with either hydrophobic (chloroform) or hydrophilic (water) properties on CW fluorescence. Addition of chloroform to dry omorika CW increased fluorescence by about 1.5 times, but it did not change band shape, neither the number of APD components (approximate distribution of the probability density for positions of all the components). Addition of water to dry omorika CW decreased intensity by about 2.5 times, but without change of band shape and the number of APD components. We further investigated influence of QDs/chloroform on dry CW and interaction CW with water and with chloroform as solvent and studied hydrophobic (with chloroform) and hydrophilic (with water) interaction in CW.

It is obvious that the spectra of omorika CWs changed in intensity and shape after addition of the QDs (Fig. 2b, c). A decrease of emission intensity of

both, dry CW and CW treated with chloroform was observed after addition of QDs/chloroform.

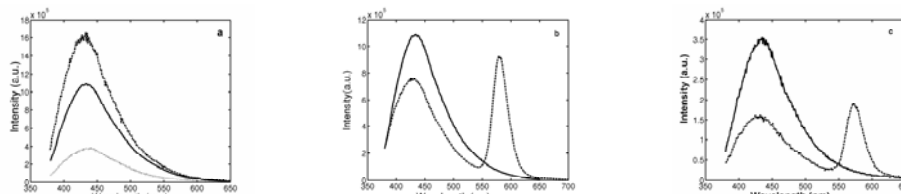


Fig.1. Emission spectra of CWs from *P. omorika* branch excited at 360 nm. (a) Overlaid dry CW (solid), dry CW/chloroform (dashed) and dry CW/water (dotted); (b) dry CW (solid) and dry CW+ (dashed); (c) dry CW+chloroform (solid) and omorika dry CW+QDs/chloroform (dashed).

When water was added to the CW previously treated with QDs in chloroform, the CW emission intensity decreased in comparison with the intensity of CW emission before addition of water. In the reversed procedure, when CW was wet, the addition of QD/chloroform slightly increased the CW emission intensity comparing to the emission of dry CW treated with QDs/chloroform (data not shown).

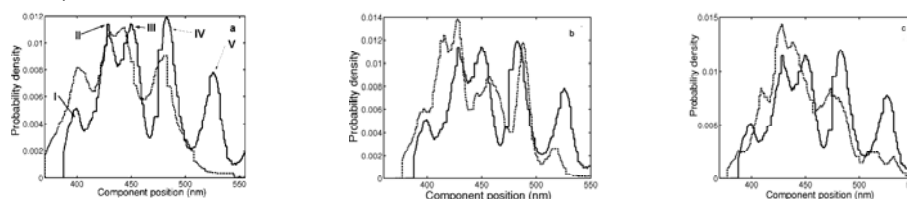


Fig.2. Overlaid APDs of CWs from (a) dry omorika CW (solid) and dry CW+QDs/chloroform (dashed); (b) dry CW (solid) and dry CW + QDs/chloroform + water (dashed); (c) dry CW (solid) and dry CW + water + QDs/chloroform (dashed).

Deconvolution of spectra gives approximate position distribution (APD) of CW spectral components position (Fig2). Spectra of dry CWs had five APD peaks (Fig. 2 solid lines) (five independent fluorophores). When QDs/chloroform were added on dry CW sample, the longest wavelength APD component (V) disappeared, leading to a blue shift of the long-wavelength components in APDs of *P. omorika* (Figs. 2 a-b). In these CW sample there was also a decrease in the number of APD components, from 5 to 4 (Fig. 2a). When water was present in the CW sample, the number of components remained the same after addition of QDs in chloroform. The longest wavelength APD component did not disappear completely. The other long wavelength APD components were red shifted in case of addition of QDs before water, while they were blue shifted when QDs were added after water.

The changes in the FTIR spectra of the cell walls after addition of QDs were observed. The bands at 1060, 1630 and 1750 cm^{-1} disappeared in the samples containing QDs. These bands were assigned to the polysaccharide component of the CW, C=C double bond in the lignin side chain conjugated to the ring and ester bonds, respectively [4, 5].

Conclusion

The CW structure generally contains both hydrophobic (lignin polymer, and polysaccharide [2, 3]) and hydrophilic (polysaccharide blocks) domains. The solvents chloroform or water, interact with CW polymers modifying the intensity of fluorescence spectra and induce redistribution of charge density within conjugated structures. Hydrophobic interaction (chloroform as solvent) leads to a more rigid structure of mainly lignin macromolecule (increases fluorescence intensity). Contrary to this, CW treated with water becomes more flexible (easier energy transfer to its environment). This indicates that CW polymers, especially lignin, have dynamic electronic structure that easily adapts to electrostatic stimuli. By combining CW treatments with chloroform and water as solvents and simultaneous binding of QDs, we were able to study effect of the hydrophilic and hydrophobic interactions in CW structure.

Our results show that CdSe QDs predominantly bind to the lignin and possibly to some polysaccharide parts of the CW. Structural rearrangements in the CW in the reaction with QDs strongly depend on the presence of water in the CW. This is a consequence of the structural arrangement of the CW polymers in the whole CW network, as well as the extremely small size of the QDs. These characteristics enable a feasible penetration of the nanoparticles inside polymer structures in the CW composite. In the cases when the CW autofluorescence disables the other methods of measurements, QDs may reduce the emission from the CW and make it more suitable for analysis.

Acknowledgements

This work was supported by the grant 143043 from the Ministry of Science and Technology of Serbia, and by the University of Miami, College of Arts and Sciences Bridge funding.

References

- [1] N. Lewis, E. Yamamoto, *Annu. Rev. Plant Physiol. Plant Mol. Biol.*, 1990, **41**, 455-496.
- [2] H. Hatakeyama, T. Hatakeyama, *Thermochim. Acta.*, 1998, **308**, 3-22.
- [3] I. Boukari, J. L. Putaux, B. Cathala, A. Barakat, B. Saake, C. Remond, M. O'Donohue, B. Chabbert, *Biomacromolecules*, 2009, **10**, 2489-2498.
- [4] I. Levine, *Physical Chemistry*, McGraw Hill Book Company, New York, 1988.
- [5] O. Faix, In *Methods in Lignin Chemistry*, Edited by S. Y. Lin, and C. W. Dence, Springer-Verlag, Berlin, 1992, 83-109.

RADIO-SENSITIVITY OF HUMAN MELANOMA, OVARIAN AND LUNG CARCINOMA CELLS TO GAMMA RADIATION

O. Keta¹, L. Korićanac¹, J. Žakula¹, N. Popović¹, G. Cuttone²,
I. Petrović¹ and A. Ristić-Fira¹

¹*Vinča Institute of Nuclear Sciences, P.O.Box 522, Belgrade, Serbia.*

²*INFN Laboratori Nazionali del Sud, via S. Sofia 62, Catania, Italy*

Abstract

Radio-sensitivity of human melanoma, ovarian and lung cancer cells after the exposure to gamma-rays was studied using three different methods. The results showed that gamma rays reduce the number of viable cells for all analyzed cell lines. However, these cells display high level of radio-resistance. The highest radio-sensitivity was attained for the CRL5876 lung cells, while the most sensitive assay was the clonogenic assay.

Introduction

Ionizing radiation initiates many diverse biochemical processes that determine cellular response to radiotherapy. The efficiency of DNA repair mechanisms and apoptosis are probably the most important once [1]. It is well known that various tumors respond differently to the same type of treatment. For example, lymphomas and leukemias are generally highly sensitive, squamous cell carcinomas show intermediate sensitivity, while melanomas are considered to be the most resistant to radiation therapy [2, 3]. This is the reason why conventional radiation therapy can be successfully used to control certain types of tumors, while performing less success in others [4]. Many assays have been developed for the prediction of the individual radio-sensitivity of tumor cell, but they have practical limitations. Despite disadvantages of the clonogenic assay such as its long duration and limitations by the ability of cells to form colonies, clonogenic assay is still considered to be the “gold standard” for radio-sensitivity checking. The microtetrazolium (MTT) assay is based on the ability of viable cells to reduce tetrazolium salts to formazan crystals, thus overcoming the need for cells to form colonies, but it is not linear at high cell densities [5]. Moreover, sulforhodamine B (SRB) assay has some advantages over the MTT assay, such as higher sensitivity and linearity even at higher cell densities [6]. Unlike the MTT, the results obtained with SRB assay are independent of metabolic conditions [7].

Using the three assays, in the present study we investigated radiobiological response to gamma irradiation of the three human cancer cell lines - the human HTB140 melanoma, the human 59M ovarian cancer cells and the lung CRL5876 adenocarcinoma derived from metastatic lymph node.

Results and Discussion

The three cell lines were irradiated with ^{60}Co gamma rays with the doses of 2, 4, 8, 12 and 16 Gy, at the dose rate of ~ 1 Gy/min. Irradiations were performed at the Vinča Institute of Nuclear Sciences, Belgrade, Serbia. After irradiation, the cells were incubated for 7 days, when viability assays were performed using Cell proliferation Kit I, MTT (Roche, Germany) and SRB (MP Biomedicals, Inc). The absorbance was measured at 550 nm (Victor, Wallac, Turku, Finland).

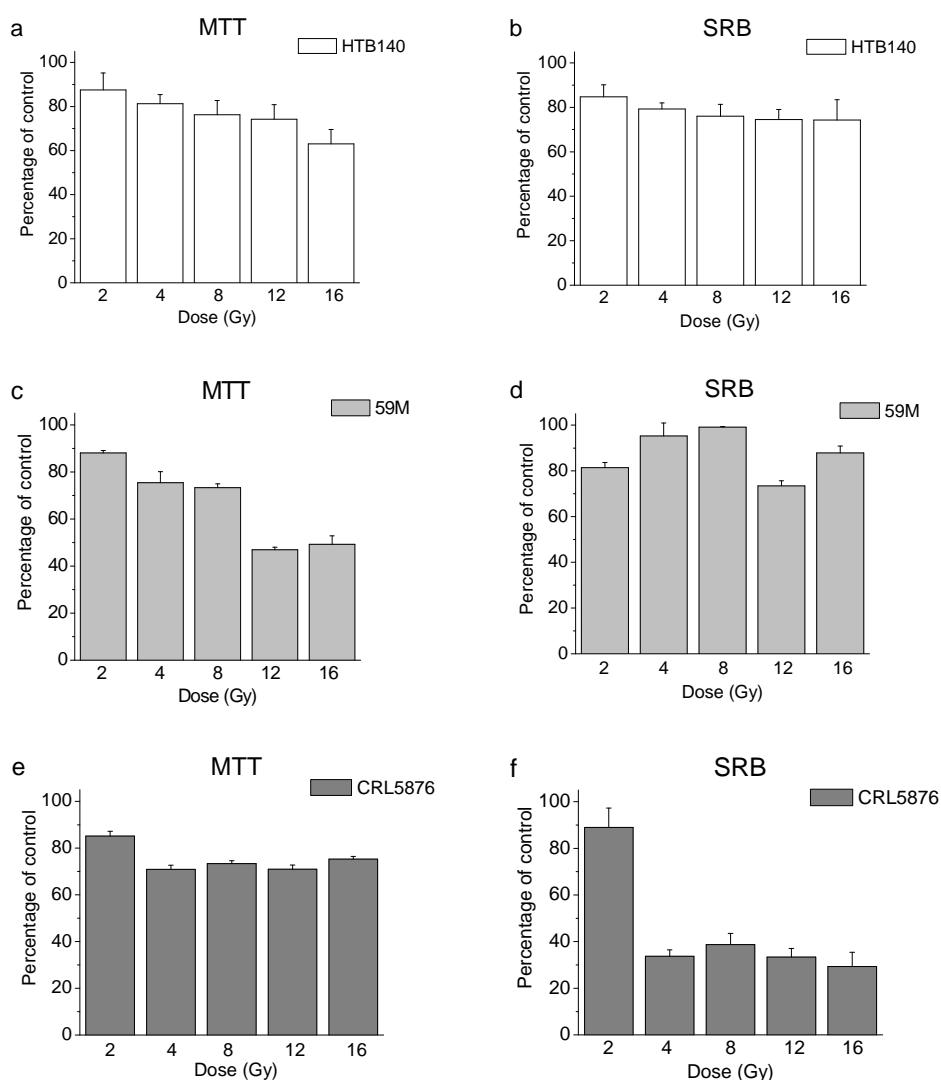


Fig. 1. Effects of gamma rays on HTB140 (a, b), 59M (c, d) and CRL5876 (e, f) cell lines, 7 days after irradiation, estimated by MTT and SRB assays.

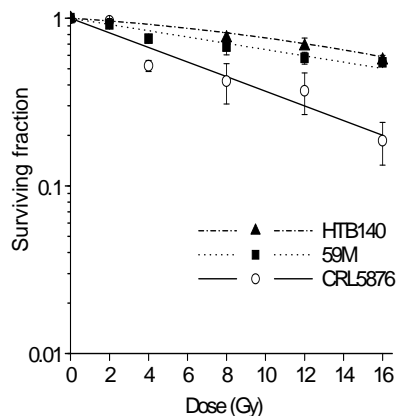


Fig.2. Dose-response curves of HTB140, 59M and CRL5876 cells exposed to gamma rays, obtained by clonogenic assay.

were extremely resistant to gamma irradiation, with the surviving fraction at 2 Gy (SF2) of 0.96. Ovarian 59M cells pointed out similar level of radio-resistance, with SF2 of 0.91. Lung CRL5876 adenocarcinoma cells were more sensitive to gamma rays with SF2 of 0.81. Obtained SF2 values indicated that HTB140, 59M and CRL5876 belong to the radio-resistant group of cell lines.

Results obtained by the three assays implicated that higher radiation doses provoked better elimination of cells. Clonogenic assay showed higher level of cell inactivation. Lower sensitivities of MTT and SRB could be explained by limitations of these assays [8].

Conclusion

Gamma radiation inactivated the analyzed cancer cell lines. They revealed different levels of radio-sensitivity. The HTB140 and 59M cells are more radio-resistant than the CRL5876 cells. The obtained results are the starting point for further investigations with non-conventional, high ionizing radiation.

References

- [1] A. T. Gordon et al., *Clin. Oncol.*, 1997, **9**, 70-78.
- [2] B. Fertil et al., *Int. J. Radiat. Oncol. Biol. Phys.*, 1985, **11**, 1699-1707.
- [3] I. Petrović et al., *Int. J. Radiat. Biol.*, 2006, **82**, 251-265.
- [4] R. R. Weichselbaum et al., *Amer. J. Roentgenol.*, 1976, **127**, 1027-1032.
- [5] M. V. Berridge et al, *Biochemica*, 1996, **4**, 15-20.
- [6] Y. P. Keepers et al, *Eur. J. Cancer*, 1991, **27**, 897-900.
- [7] D. Banasiak et al, *Radiat. Oncol. Investig.*, 1999, **7**, 77-85.
- [8] G. Griffon et al, *Anticancer Drugs*, 1995, **6**, 115-123.

Viability for the HTB140 cells ranged from 63 to 87.5 % by MTT, while slightly lower values (74 - 85 %) were detected with SRB (**Fig. 1a and b**). Viability of 59M cells is given in **Fig. 1c and d**. According to MTT assay, these values were from 49 to 88 %. The SRB assay provided higher values as compared to MTT (73 - 99 %). Finally, the viability of CRL5876 cells detected by the MTT was between 71 and 85%, whilst SRB values were in the range from 29 to 89% (**Fig. 1e and f**). SRB assay showed strong response to radiation starting from 4 Gy. For the three cell lines, the results obtained by clonogenic assay revealed dose-dependent inhibitory effects of gamma rays (**Fig. 2**).

According to these results, HTB140 cells

INFLUENCE OF HETEROPOLY ACIDS ON RAT SYNAPTIC PLASMA MEMBRANE ATP -ASE ACTIVITY

D. Krstić^a, M. Čolović^b, D. Bajuk-Bogdanović^c, N. Bošnjaković-Pavlović^c, I. Holclajtner-Antunović^c, V. Vasić^b

^a*Institute of Medicinal Chemistry, School of Medicine, University of Belgrade, Serbia*

^b*Vinča Institute of Nuclear Sciences, P.O.Box 522, 11001 Belgrade, Serbia*

^c*Faculty of Physical Chemistry, University of Belgrade, Belgrade, Serbia*

e-mail: ivanka@ffh.bg.ac.rs

Abstract

The *in vitro* influence of 12-tungstosilicic acid (WSiA) and 12-tungstophosphoric acid (WPA) on Na⁺/K⁺-ATPase activity, using rat synaptic plasma membrane (SPM) as a model system was investigated. The half-maximum inhibition (IC₅₀) of the enzyme activity was achieved with 5.80 · 10⁻⁵ mol/L of WPA and 1.17 · 10⁻⁴ mol/L of WSiA. The both examined compounds showed a dose-dependent inhibitory effect on the enzyme activity in the concentration higher than 1 μmol/L.

Introduction

Polyoxometalates (POMs) are polyanionic, condensed oligomeric aggregates of transition-metal ions, usually in their d⁰ electronic configurations, and oxide ions, held together only by metal-oxygen bonds. POMs made up of a great number of structures and compositions, constitute a large category of compounds interesting for theoretical investigations and practical applications. Heteropoly oxometalates which possess the Keggin-type anion, such as WPA and WSiA, attract the greatest interest. In medicinal chemistry, polyoxometalates exhibit biological activity, such as highly selective inhibition of enzymes, *in vitro* and *in vivo* antitumor, antiviral, and antiretroviral activities [1,2]. Considering the key role of Na⁺/K⁺-ATPase in normal functioning of most animal cells as well as pivotal roles in cancer cell migration, the aim of this work was to examine the influence of heteropoly acids H₃PW₁₂O₄₀ (WPA) and H₄SiW₁₂O₄₀ (WSiA) on Na⁺/K⁺-ATPase activity.

Material and methods

WPA was prepared by a previously described method [3] and confirmed by infrared spectroscopy, while WSiA was commercially available (Fluka). Both acids were recrystallized prior to use. The enzymatic activity of commercial porcine cerebral Na⁺/K⁺-ATPase was followed in the absence and presence of increasing concentration of WPA and SiWA (within the range of 10⁻⁸ - 10⁻³ mol/L). The SPM were isolated from the whole rat (albino, vistar) brain according to the standard method. The standard assay medium for investigation of SPM Na⁺/K⁺-ATPase activity contained: 50 mM Tris-HCl buffer, pH 7.4; 100 mM NaCl; 20 mM KCl; 5 mM MgCl₂; 2 mM ATP; and 25 μg SPM protein. Assay mixtures were preincubated for 10 min at 37°C in the presence of investigated compounds or distilled water (control). Reaction was

initiated by addition of ATP and stopped after 10 min by addition of 22 μL ice cold HClO_4 (3 M) and immediate cooling on ice. The released Pi (inorganic orthophosphate) released from the enzymatic hydrolysis of ATP was determined by spectrophotometric method. The spectrophotometric measurements were performed on a Perkin Elmer Lambda 35UV VIS spectrophotometer.

Results and discussion

The influence of WPA and WSiA on SPM ATPases activity was investigated by *in vitro* exposure to enzymes in the concentration range from $1 \cdot 10^{-8}$ to $1 \cdot 10^{-3}$ mol/L. The results show that increasing concentrations of WPA and WSiA induced inhibition of enzymatic activity in a concentration-dependent manner in both cases (Fig.1). The half-maximum inhibitory concentrations (IC_{50}) of the investigated compounds for Na^+/K^+ -ATPases were determined by sigmoid fitting of the experimental results as well as by Hill analysis and are summarized in Table 1. The half-maximum inhibition (IC_{50}) of the enzyme activity was achieved at $5.80 \cdot 10^{-5}$ mol/L for WPA acid and $1.17 \cdot 10^{-4}$ mol/L for WSiA. Complete inhibition of the enzyme was achieved at the concentration of $5 \cdot 10^{-4}$ mol/L WPA, while the same effect was achieved at a two times higher concentration of SiWA.

The obtained dose-dependent inhibition of sodium pump by heteropoly acids is in agreement with previously reported findings that decameric vanadate species block the active side of P-type ATPases and consequently prevent formation of the phosphoenzyme intermediary [4,5].

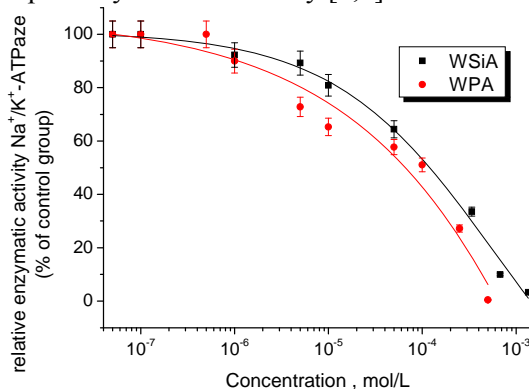


Fig. 1. Na^+/K^+ -ATPase specific activity in dependence of the concentration of the WPA and SiWA.

Table 1. IC_{50} values of WPA and WSiA for ATPase obtained by fit of sigmoidal inhibition curves and by Hill analysis.

Compound	IC_{50} , mol/L	
	Sigmoidal fit	Hill analysis
$\text{H}_4\text{SiW}_{12}\text{O}_{40} \cdot 6\text{H}_2\text{O}$	$(1.15 \pm 0.05) \times 10^{-4}$	$1.17 \cdot 10^{-4}$
$\text{H}_3\text{PW}_{12}\text{O}_{40} \cdot 6\text{H}_2\text{O}$	$(6.57 \pm 0.80) \times 10^{-5}$	$5.80 \cdot 10^{-5}$

Conclusion

It could be concluded that WPA and SiWA induce inhibition of SPM ATPases activity in a concentration-dependent manner, probably directly affecting phosphorylation step in the enzyme cycle of P-type ATPases.

References

- [1] M. T. Pope, A. Muller, *Polyoxometalates: From Platonic Solids to Anti-Retroviral Activity*, Kluwer, Dordrecht, 1994.
- [2] Polyoxometalates, C. Hill (Ed.) in *Chem. Rev.*, 1998, **98**, 1-390.
- [3] N. V. Apolonov, E. M. Feklichev, N. V. Timofeeva, A. Kalashnikov, V. E. Svinticki, *Dokl. ANSSSR*, 1970, **191**, 1048-104.
- [4] S. Varga, P. Csermely, A. Martonosi, *Eur. J. Biochem.*, 1985, **148**, 119- 126.
- [5] D. Krstić, M. Čolović, N. Bošnjaković-Pavlović, A. Spasojević-De Bire, V. Vasić. *Gen Physiol Biophys.*, 2009, **28**, 302-308.

OXIDATION OF SOME ORGANOPHOSPHATE PESTICIDES WITH ENZYME MYELOPEROXIDASE

T. Lazarević-Pašti, T. Momić and V. Vasić

*Vinča Institute of Nuclear Sciences, University of Belgrade,
P.O.Box 522, 11001 Belgrade, Serbia e-mail: tamara@vinca.rs*

Abstract

Some organophosphorous pesticides (OPs) containing phosphorothioate group were oxidized *in vitro* by enzyme myeloperoxidase (MPO) in the presence of hydrogen peroxide. The products were identified as oxon derivatives (phosphates), where the sulfur atom from thioate group is substituted by an oxygen atom. The oxidation efficiency was determined using acetylcholinesterase (AChE) bioassay and discussed in the terms of MPO concentration, OPs concentration and incubation time.

Introduction

The heme enzyme myeloperoxidase (MPO) acts as an oxidant enzyme in the processes of inflammation and atherogenesis [1]. MPO is relatively nonspecific with respect to its reducing substrates and is able to oxidize different substrates.

Organophosphorous insecticides, characterized by one thione moiety (P=S) and three –OR groups are very effective and widely used group of pesticides. OPs and their activated metabolites are potent anti-cholinesterases (anti-ChEs) [2]. They can be activated in the environment to highly reactive oxons (P=O). The oxons are considerably more potent as anti-ChEs than their corresponding phosphorothionates. Therefore, efficient methods for their *in vitro* oxidation are important in their toxicological studies and for the development of methods for their detection [3,4].

In this work the ability of MPO to biocatalyze the transformation of OPs (diazinon and malathion) from thio- to oxo- forms was examined. The aim was to use MPO mediated oxidation of thio OPs to oxo OPs without any preconcentration or extraction step under normal laboratory conditions in order to improve the sensitivity of AChE based bioanalytical assays for their detection.

Material and methods

Myeloperoxidase (MPO) from human neutrophils was obtained from Planta Natural Products, Vienna, Austria. Catalase, from bovine liver, acetylcholinesterase (AChE) from electric eel, acetylthiocholine iodide (ASChI) and 5,5'-dithio-bis-(2-nitrobenzoic acid) (DTNB) were purchased from Sigma-Aldrich (St. Louis, MO, USA). Hydrogen peroxide solutions were prepared daily by diluting a 30% (m/v) stock solution. The pesticides (at least 93% purity) malathion, malaaxon, diazinon and diazoxon were purchased from Pestinal[®], Sigma-Aldrich, Denmark. The pesticide working solutions were prepared by dilution of the $1 \cdot 10^{-3}$ M stock solutions in ethanol.

Results and discussion

The desired concentrations of OPs in the range from $1 \cdot 10^{-5}$ - $1 \cdot 10^{-7}$ M were incubated in 50 mM phosphate buffer, pH 6.0, with various concentrations of MPO in a final reaction volume of 0.5 - 1.0 mL. Reaction was started by addition of $50 \cdot 10^{-6}$ M H_2O_2 , and stopped after incubation at various time intervals by adding catalase ($100 \mu\text{g mL}^{-1}$). The oxidation products were analyzed by UPLC (Ultra Performance Liquid Chromatography) and GC/MS (Gas Chromatography - mass spectrometry) measurements and chromatograms were compared with those of authentic standards. The identification of the oxidation products yielded only one major oxidation product – the oxo-form of pesticides. UPLC chromatograms that were recorded during 60 min, after the oxidation was stopped by catalase, confirmed that there were no other products of oxidation, i.e. the further cleavage of oxo-forms was not observed.

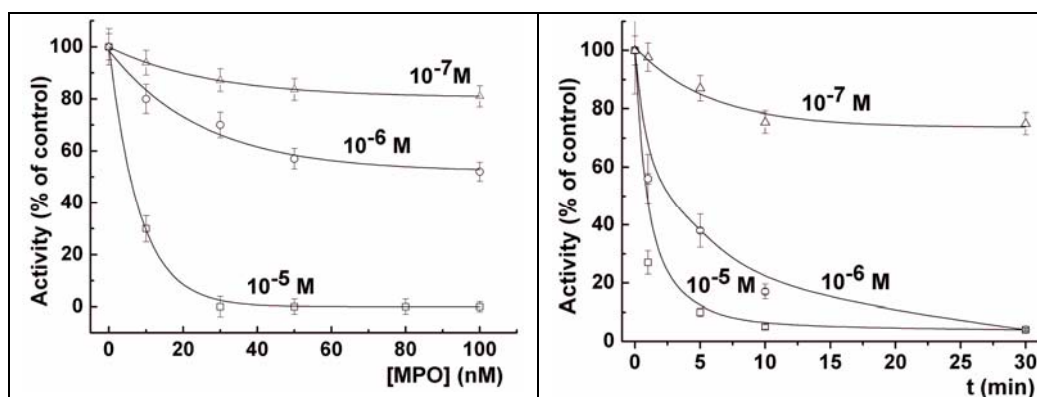


Fig.1. Dependence of AChE inhibition induced by malathion oxidized by MPO during 5 min incubation with OPs as a function of MPO concentration (A) and incubation time of 100 nM MPO with OP (B).

Since the oxidized forms of OPs are more potent inhibitors of AChE than the parent compounds, the efficiency of oxons formation was followed using AChE test [2]. Briefly, the free enzyme was exposed to oxidized samples (10 μl) in a final volume of 0.65 mL. The incubation time with AChE in the presence of inhibitors was 20 min, before the reaction was initiated and followed during 8 min. Fig 1A represents the results of the influence of MPO concentration (after 5 min incubation with malathion) on AChE inhibition with oxidised sample. It is obvious, that the increase of MPO concentration above 30 nM resulted in the saturation concentration of the oxo-form. In order to investigate the influence of incubation time between OPs and MPO to achieve the most efficient oxidation, the incubation time between OPs and 100 nM MPO was varied from 1 – 30 min. AChE test was used for monitoring the oxidation efficiency, as described above using 10 fold diluted OPs samples. The results obtained for malathion are presented in Fig 1B. The AChE activity in the presence of the oxidized OPs compared to non-oxidized

samples decreased with increased oxidation times, indicating the increase in the concentration of oxo forms. The saturation level of oxo-forms was reached after 10 min incubation of parent compounds with MPO.

The results for oxidation efficiency after 10 min incubation with 100 nM MPO for diazinon and malathion, obtained using AChE test and UPLC measurements, are given in Table 1. The calibration graph for AChE induced inhibition by oxo forms was constructed for determination of oxo forms concentration formed upon the oxidation. It is obvious that 10 min exposure of $1 \cdot 10^{-4}$ and $1 \cdot 10^{-5}$ M diazinon to 100 nM MPO yielded the formation of about $(3 - 5) \cdot 10^{-6}$ M diazoxon, since $1 \cdot 10^{-6}$ M diazinon was about 50% oxidized. The conclusion can be made that the conversion efficiency increased by lowering diazinon concentration. Similar results were also obtained for malathion.

Table 1. Efficiency of OPs oxidation after 10 min incubation with 100 nM MPO based on UPLC and GC/MS determination of concentration of thio- and oxo- forms.

OPs	Parent OP (M)		Oxo form (M)		³ Oxidation efficiency (%)	
	Initial concentr. (M)	¹ After incubation (M)	¹ UPLC (M)	² AChE test (M)	UPLC	² AChE test
diazinon	$1 \cdot 10^{-4}$	$0.95 \cdot 10^{-4}$	$0.05 \cdot 10^{-4}$	$0.02 \cdot 10^{-4}$	5	2
	$1 \cdot 10^{-5}$	$0.73 \cdot 10^{-5}$	$0.27 \cdot 10^{-5}$	$0.04 \cdot 10^{-5}$	27	4
	$1 \cdot 10^{-6}$	$0.85 \cdot 10^{-6}$	$0.50 \cdot 10^{-6}$	$0.10 \cdot 10^{-6}$	50	10
malathion	$1 \cdot 10^{-4}$	$0.93 \cdot 10^{-4}$	-	$>1 \cdot 10^{-5}$	-	>10
	$1 \cdot 10^{-5}$	$0.77 \cdot 10^{-5}$	-	$>1 \cdot 10^{-5}$	-	>25
	$1 \cdot 10^{-6}$	-	-	$>1 \cdot 10^{-7}$	-	>50

¹ Determined by UPLC; ² Based on AChE inhibition measurements using 10 fold diluted initial solutions and recalculated to initial concentration; ³ [formed oxo form]/[initial OP].

Conclusion

The oxidation of OPs by the enzyme MPO yield only one major oxidation product – the oxo-form of pesticides. The degree of OPs oxidation depends on the OPs and MPO concentrations, as well as on incubation time between OPs and MPO. The 10 min incubation time of OPs in phosphate buffer, pH 6.0, with 50 - 100 nM MPO was found to be applicable for OPs oxidation, to produce oxo-forms with stronger inhibitory power towards AChE.

References

- [1] S. J. Klebanoff, P. Assoc. Am. Physician, 1999, **111**, 383-389.
- [2] J. Casida, Chem. Res. Toxicol., 2009, **22**, 609-619.
- [3] H. S. Lee, Y. Ah Kim, Y. Ae Cho, Y. Tae Lee, Chemosphere, 2002, **46**, 571-576.
- [4] J. Hernandez, N. R. Robledo, L. Velasco, R. Quintero, M. A. Pickard, R. Vazquez-Duhalt, Pestic. Biochem. Phys., 1998, **61**, 87-94.

INFLUENCE OF MICROWAVE RADIATION ON BACTERIOPHAGE λ PROLIFERATION IN *Escherichia coli*

N. B. Milojević^a, D. R. Stanisavljev^b, B. J. Nikolić^a,
M. V. Beljanski^{c*} and J. B. Knežević-Vukčević^a

^aFaculty of Biology, Belgrade University, Belgrade, Serbia, ^bFaculty of Physical Chemistry, Belgrade University, Belgrade, Serbia, ^cInstitute of General and Physical Chemistry, Belgrade, Serbia

Abstract

The influence of microwaves (MWs) on bacterial metabolism was investigated using the proliferation of bacteriophage λ in *Escherichia coli* cells as a model system. The kinetic curve of phage release was decreased with irradiation at optimal temperature (37°C), presumably due to thermal effects, while it was increased at suboptimal temperature (33°C). Comparison with the curves obtained without MW irradiation at 33°C, 37°C, 41°C and 45°C, indicated that MW irradiation at 33°C provoked more significant increase of phage proliferation than it could be expected from pure thermal effects. Results obtained suggest the existence of non-thermal effects of MWs.

Introduction

It is generally recognised that microwaves (MW) effects include thermal effects, specific thermal effects and non-thermal effects [1, 2].

Due to increased use of MW appliances in everyday life, understanding of possible MW effects on biological systems is of particular interest. The earlier research of MW effects on bacteria and viruses pointed at their inactivation by MW entirely by heat, through the same mechanisms as conventional heating. However, in recent years, there is growing evidence that the MWs may have the non-thermal effects on structure and function of biological systems [3].

Materials and methods

For biological materials we used *E. coli* C600 and SY252, as well as bacteriophage λ . MW irradiation (0.83W/g) was performed in a commercial single mode focused CEM reactor working at 2.45 GHz with the ability to control output power. Temperature in the system was measured by fiber optic temperature sensor and was constant (± 1 °C). In order to keep uniform temperature the sample was mixed in the magnetic stirrer at 400 rpm. All experiments were done under the same conditions by keeping constant irradiation power, temperature, and initial mixture volume.

Proliferation of λ phage in *E. coli* SY252 was monitored by scoring PFU/ml in C600 indicator strain. To analyze the existence of MWs non-thermal effects we compared the effects of different incubation temperatures (without MW) with obtained effects of MW irradiation on PFU/ml numbers.

Results and Discussion

The obtained results had shown that MW irradiation had no significant effect on bacterial and viral viability (data not shown).

The influence of MW irradiation on phage proliferation was monitored in experiments performed at two temperatures: optimal for host cells (37°C), and suboptimal (33°C).

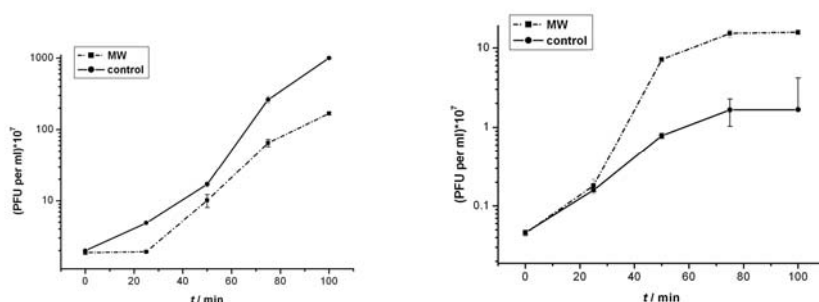


Fig.1. The MW effects on λ phage proliferation in *E. coli* at 37°C (A) and 33°C (B).

While the kinetic curve of phage release was decreased with irradiation at optimal temperature (37°C), it was increased at suboptimal temperature (33°C) for the approximately same absorbed MW energy (Fig. 1 A and B). The effects could be ascribed to the local rise of temperature in *E. coli* cells which could influence cell metabolism and phage proliferation. It is possible that local temperature inside MW irradiated cells could be 5-6°C higher than the temperature of surrounding medium. When the medium is kept at 37°C, this increase may lead to local non-optimal temperature of 42-43°C inside the cells, thus lagging the phage life cycle and its proliferation. On the other hand, when medium is kept at 33°C, the same temperature increase in MW heated sample gives rise to almost optimal thermal conditions.

The changes of temperature in the range 33°C - 41°C did not affect significantly the number of PFU in time. However, the incubation of infected cells at 45°C stopped viral proliferation and consequently there were no changes of PFU during entire experiment (Fig.2). Obtained results have two important implications: (1) they show that the maximum possible local MW overheating in the cells at the bulk temperature of the mixture of 37°C must be higher than 4°C and lower than 8°C; (2) the same overheating at the bulk temperature of 33°C should provoke only negligible effect on phage proliferation.

To emphasize the contribution of non-thermal effects, the relative PFU values were calculated, taking values at 33°C as a reference (Fig. 3).

The observed difference exceeds the uncertainty arising from experimental errors and emphasizes that MW accelerate the viral proliferation in infected host cells at 33°C presumably by some non-thermal effects.

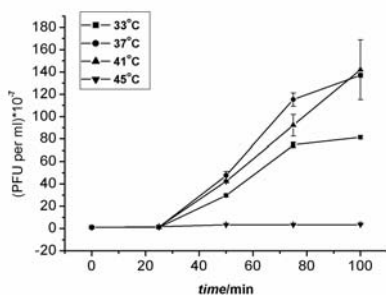


Fig. 2. The effects of different temperatures on λ phage proliferation in *E. coli*.

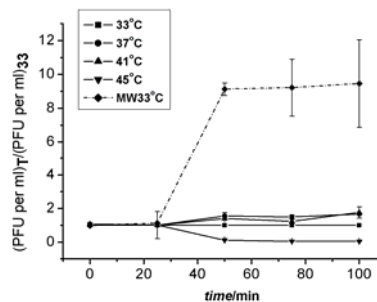


Fig. 3. The relative values of the PFU, taking the numbers of PFU at 33°C as a reference.

Conclusion

We have investigated the influence of microwave irradiation on the proliferation of bacteriophage λ in *E. coli* cells, at constant bulk temperature and MW density, which enabled reliable comparison of experimental results. Obtained results suggest the existence of thermal and non-thermal effects of MWs on the process of phage replication.

Acknowledgment

This study was supported by Ministry of Science of Republic of Serbia, Projects No. 142025 and 143060.

References

- [1] A. Loupy, Wiley-VCH, 2002.
- [2] O. Kappe and A. Stadler, Wiley-VCH, 2005.
- [3] D. I. de Pomerai, B. Smith, A. Dawe, K. North, T. Smith, D. B. Archer, I. R. Duce, D. Jones, E. P. M. Candido, FEBS Lett., 2003, **543**, 93–97.

L-CYSTEINE MODULATES THE ecto-ATPase ACTIVITY INHIBITION IN PRESENCE OF CADMIUM (II) AND MERCURY (II) IONS

M. Milošević, D. Drakulić, S. Petrović, I. Stanojević,
N. Veličković and A. Horvat

*Laboratory of Molecular Biology and Endocrinology,
Institute of Nuclear Sciences "VINČA", University of Belgrade, P.O. Box 522,
11001 Belgrade, Serbia*

Abstract

L-cysteine is used as effective oral chelating agent due to property of its sulfhydryl group to bind heavy metal ions. The aim of this study was to investigate ability of L-cysteine to prevent mercury (II) and cadmium (II) induced ecto-ATPase activity inhibition of rat uterus plasma membranes. Results show that 10 mmol/l L-cysteine have protective effect on enzyme activity in the presence of cadmium and mercury ions.

Introduction

Heavy metals could be accumulated in the body during low, chronic exposure, originate from various sources such as drinking water, cigarette smoke or even from tooth fillings made of silver-mercury amalgam. According to numerous data cadmium and mercury are classified as reproductive toxicants [1] and their effects on uterine plasma membrane ecto-ATPase activity were reported previously [2].

During the years, the importance of purinergic signaling in mammalian reproductive tract has been emphasized [3]. Extracellular nucleotides and/or their degradation products affect via purinoceptors various functions of uterine tissue such as contraction, growth, remodeling and immunity. In uterine tract, ATP is co-released from autonomic nerves with neurotransmitters, but physiological sources of extracellular nucleotides are also platelets and semen. Ecto-ATPase is a member of E-NTPDases family (EC 3.6.1.5), the most abundant enzyme family among ectonucleotidases. Ectonucleotidases are surface plasma membrane bound enzymes that modulate purinergic signaling by hydrolyzing nucleotide di- and tri phosphates.

Experimental procedure

Animals: Experiments were performed on 3-month-old female Wistar albino rats obtained from the local colony. Animals were maintained under standard conditions with *ad libidum* access to food and water. Myometrial plasma membranes (MPM) were isolated as previously described [4].

ATP assay: Incubation medium contained: 50 mmol/l Tris-HCl buffer (pH 7.4), 5 mmol/l MgCl₂, increasing concentration of metal ions in absence or presence of 10 mmol/l L-cysteine and 7 μg MPM protein. The enzyme reaction was started by addition of 2 mmol/l ATP, allowed to proceed for additional 10 min and stopped with 22 μl of the ice cold 3 mol/l perchloric acid. The inorganic phosphate (Pi) liberated from the ATP hydrolysis was determined by the spectrophotometric method. All measurements were performed in triplicate.

Results and discussion

Cadmium chloride (CdCl₂) and mercury chloride (HgCl₂) were added to the reaction mixture in concentration ranges from 1×10⁻⁷ to 1×10⁻¹ mol/l. The effects of increasing metal ion concentrations were measured in the absence and in the presence of 10 mmol/l L-cysteine.

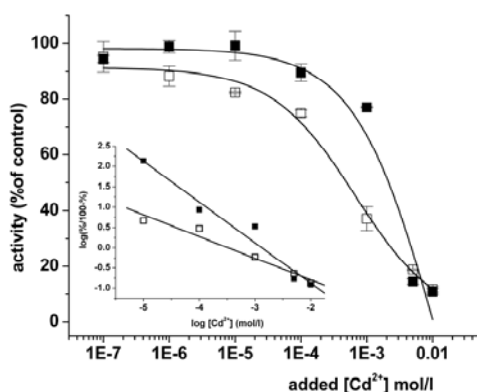


Fig.1. Inhibition of ecto-ATPase activity by CdCl₂ in the absence (open symbol) and in the presence (solid symbols) of 1×10⁻² mol/l L-cysteine.

The values given are the mean ±S.E.M of three independent MPM isolation done in triplicate.

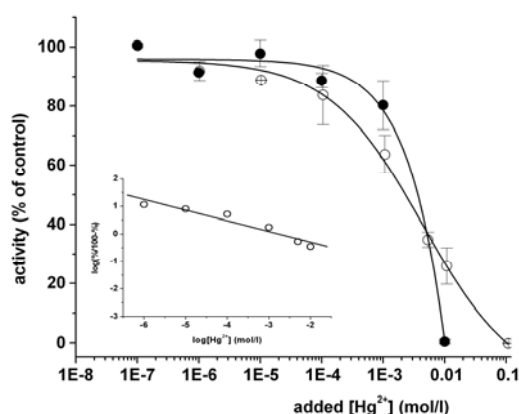


Fig.2. Inhibition of ecto-ATPase activity by HgCl₂ in the absence (open symbol) and in the presence (solid symbols) of 1×10⁻² mol/l L-cysteine.

The values given are the mean ±S.E.M of three independent MPM isolation done in triplicate.

Compared to the control samples, in the absence of L-cysteine and in the presence of 0.01 mol/l of CdCl₂ (Fig. 1.) ecto-ATPase activity showed up to 90% inhibition, while total enzyme inhibition was detected in presence of 0.1 mol/l HgCl₂ (Fig. 2.). The half-maximum inhibitory activities (IC₅₀) determined by Hill

analysis of experimental curves in the absence or presence of L-cysteine were: 3.49×10^{-4} and 1.34×10^{-3} mol/l for cadmium (II) (Fig.1 inset) and 1.74×10^{-3} and 2.06×10^{-3} for mercury (II) (Fig.2 inset), respectively. The IC_{50} value for mercury (II) ions in the presence of 10 mmol/l L-cysteine was determined directly from inhibition curve. When cysteine and mercuric chloride mole ratio approached 2:1, white precipitation was formed and enzyme activity disappeared. Precipitation occurs due to formation of $Hg(Cys)_2$ and $Hg(Cys)_2 \cdot 2HgCl_2$ [5].

L-cysteine is an important constituent of proteins, largely by virtue of its sulfhydryl group to form disulfide bonds and stabilize protein molecular configuration. Cadmium and mercury have high affinity for sulfur and sulfhydryls and therefore potential of binding to proteins throughout the body, disrupting their structure and function. Binding tightly to glutathione (GSH), they might deplete cell's antioxidant capacity. At the same time, cadmium and mercury promote formation of reactive oxygen species that alter plasma membrane structure as a result of lipid peroxides formation.

Ecto-ATPase contains 10 cysteine residues on its extracellular domain but has no free sulphhydryl groups, so this might explain relatively high IC_{50} value for cadmium and mercury in the absence of chelator.

Conclusion

According to the results presented in this study, 10 mmol/l L-cysteine increased by one order of magnitude $CdCl_2$ concentration for half-maximal inhibition (IC_{50}), as a consequence of decreasing metal ions concentrations capable to interact with enzyme amino acid residues. In the presence of mercuric ions, L-cysteine was less efficient in prevention of enzyme activity, probably because of complex compounds formation at higher concentrations of metal ions.

Acknowledgements

This study was supported by the Serbian Ministry of Sciences, Project No. 143044.

References

- [1] P. Kovačić, J. D. Jacintho, *Curr. Med. Chem.*, 2001, **8**, 863-892.
- [2] M. Milošević, M. Demajo, A. Horvat, *Physical Chemistry 2006*, A. Antić-Jovanović (ed.), SPCS, Belgrade, 2006, **1**, 395-397.
- [3] M. Martín-Satué, E.G. Lavoie, M. Fausther, J. Lecka, E. Aliagas, F. Kukulski, J. Sévigny, *Histochem. Cell Biol.*, 2009, **131**, 615-628.
- [4] M. Milošević, S. Petrović, M. Demajo, A. Horvat, *Ann. N.Y. Acad. Sci.*, 2005, **1048**, 445-448.
- [5] W. Stricks and I. M. Kolhoff, *J. Am. Chem. Soc.*, 1953, **75**, 5673-5681.

FLUOXETINE DECREASES THE LEVEL OF NUCLEAR GLUCOCORTICOID RECEPTOR IN WISTAR RAT HIPPOCAMPUS UNDER CHRONIC STRESS

M. Mitić, I. Simić, A. Djordjević, J. Djordjević, M. B. Radojčić and M. Adžić

VINCA Institute of Nuclear Sciences, P.O. Box 522, 11001 Belgrade, Serbia

Abstract

Dysregulation of the hypothalamic-pituitary-adrenal (HPA) axis has been implicated in the pathophysiology of depression and stress disorders. Glucocorticoids, key regulators of stress response, have diverse effects on cellular processes in the hippocampus. Beside non genomic pathways, glucocorticoids effects are mediated through activation of the glucocorticoid receptor (GR), a ligand activated transcriptional factor that belongs to the nuclear hormone receptor superfamily. We analysed the GR protein level both, in the cytoplasmic and nuclear compartments in Wistar rat hippocampus, exposed to 3 week social isolation stress upon chronic fluoxetine treatment. Under chronic stress, corticosterone level was decreased compared to the control and treatment with fluoxetine did not change its level significantly in stressed animals. At the molecular level, fluoxetine significantly decreased the level of nuclear GR protein in the brain hippocampus of the chronically stressed rats. Fluoxetine reversed the nuclear level of GR disrupted by chronic psychosocial isolation (CPSI), but it failed to normalize HPA axis activity.

Introduction

Stress disorders are characterized by a reduced ability of the brain to cope and adapt under challenging conditions [1]. Activation of the hypothalamic-pituitary-adrenocortical (HPA) axis mediates physiological responses that enable an organism to maintain or return to homeostasis. The end product of HPA axis activation is synthesis and secretion of glucocorticoids from the adrenal cortex thus enabling coping with stress that is essential for survival [2]. The magnitude and duration of stress responses are controlled, in large part, by glucocorticoid receptor (GR), which provides feedback signals that inhibit the activity of HPA axis [3]. The GR is a member of nuclear hormone receptor superfamily of the ligand-activated transcription factors. Along this line, the aim of this study has been to investigate the ability of chronic SSRI antidepressant fluoxetine treatment to modulate the responsiveness of GR under challenging conditions. Accordingly, we have examined its changes in response to the chronic 3 week CPSI. We focused our analysis on the effects of fluoxetine treatment on the cytoplasmic and nuclear distribution of GR in the rat hippocampus, a brain structure that is affected in animals exposed to chronic psychosocial isolation [4].

Experimental

The experiments were performed on adult (3-months old) male albino Wistar rats that were divided into four groups: control group consisted of unstressed animals treated with vehicle for 3 weeks (VEH;water); group II consisted of unstressed animals treated with fluoxetine 3 weeks (FLU); Two other groups (groups III and IV) consisted of 3 weeks chronically isolated animals that were further treated with either vehicle or fluoxetine for another 3 weeks. Blood from each animal was collected at the time of sacrifice. Corticosterone (CORT) concentration was determined from blood serum by using the OSTEIA Corticosterone EIA kit according to manufacturers instructions (American Laboratory Products Co.). The cytoplasm and nucleus samples were prepared by differential centrifugation and western blot technique was performed using following antibodies: M20 (Affinity Bioreagents) and rabbit polyclonal anti- β -actin as a loading control.

Results and discussion

Effect of stress and fluoxetine on CORT level: To assess the effectiveness of the stress paradigm adopted, the serum CORT was first measured. Even though, two-way ANOVA showed a significant relevance of chronic psychosocial isolation stress on CORT concentration, post-hoc tukey analysis did not reveal any differences between experimental groups due to high variations in individual values of corticosterone. These results showed that the responsiveness of the HPA axis was not affected either in control or in stressed groups by fluoxetine.

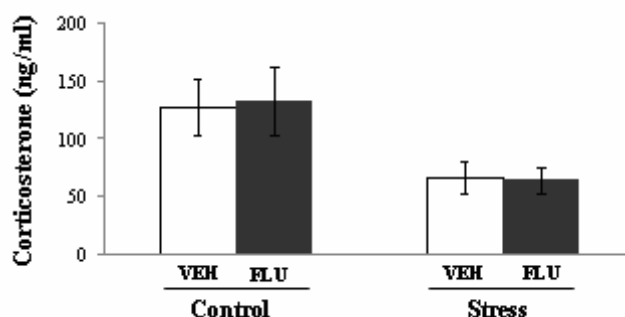


Fig.1. Serum corticosterone concentration (ng/ml) in rats treated for 3 weeks with vehicle (VEH) or fluoxetine (FLU) either in basal condition (control) or exposed to 3 weeks chronic psychosocial isolation (stress). Values are presented as mean \pm SEM and measured individually.

Effect of stress and fluoxetine on GR level: Furthermore, as shown in Figure 2a, GR levels in the cytosolic compartment were not affected either by stress ($F=0.005$, $p>0.05$) or by FLU treatment ($F=0.795$, $p>0.05$). In contrast, the GR level in the nucleus was significantly increased by CPSI in respect to the control ($F=21.691$, $p<0.05$) and its level was reversed by additional fluoxetine treatment ($F=26.031$, $p<0.05$).

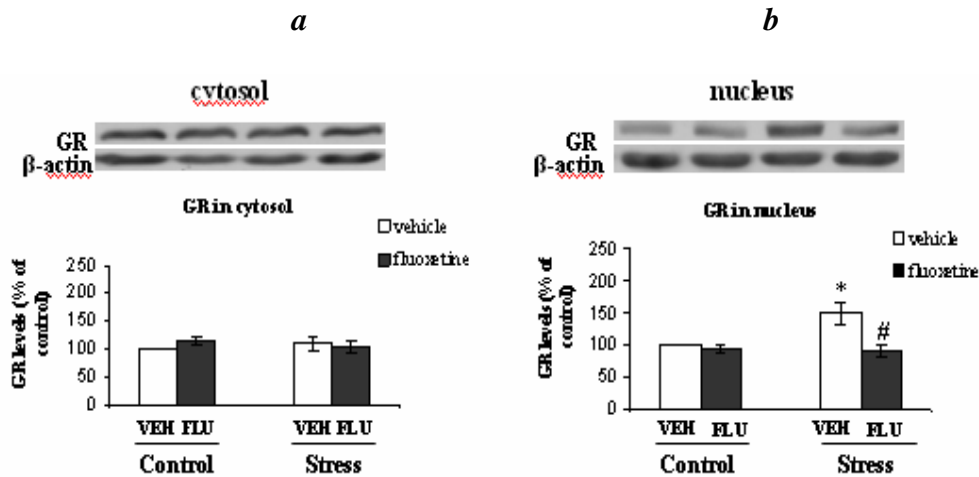


Fig.2. Western blot (WB) experiment demonstrating the effect of chronic social isolation stress on glucocorticoid receptor protein levels in the cytosolic (a) and nuclear (b) compartments obtained from the hippocampus of rats chronically treated with fluoxetine (FLU;5 mg/kg) or vehicle (VEH). Data are analysed with two-way ANOVA followed by post-hoc Tukey test and presented as a percentage of control values (unstressed animal treated with VEH, set as 100%). Results are presented as mean \pm S.E.M, * $p < 0.05$ Stress vs Control, # $p < 0.05$ VEH stress vs FLU stress.

Conclusion

Fluoxetine reversed the nuclear level of GR disrupted by chronic psychosocial isolation, but it failed to normalize HPA axis activity. The changes in nuclear GR trafficking observed in fluoxetine treatment of chronically isolated animals might have impact on the regulation of several hippocampal genes and therefore on the coping responses to a challenging conditions.

Acknowledgements

The work was supported by MN project 143042B.

References

- [1] R. S. Duman, L. M. Monteggia, *Biol. Psychiatry*, 2006, **59**, 1116-1127.
- [2] J. P. Herman, C. M. Prewitt, W. E. Cullinan, *Crit. Rev. Neurobiol.*, 1996, **10**, 371-394
- [3] E. R. De Kloet, E. Vreugdenhil, M. S. Oitzl, M. Joels, *Endocr. Rev.*, 1996, **19**, 269-301.
- [4] M. Adzic, J. Djordjevic, A. Djordjevic, A. Niciforovic, C. Demonacos, M. Radojicic, M. Krstic-Demonacos, *J Endocrinol.*, 2009, **202**, 87-97.

ANALYSIS OF AMINO ACID DISTANCES IN PROTEINS

N. S. Mitić¹, N. Petrović¹, G. M. Pavlović-Lažetić¹, M. D. Pavlović² and M. V. Beljanski²

¹*Faculty of Mathematics, Belgrade University, Belgrade, Serbia
(nenad@matf.bg.ac.rs)*

²*Institute of General and Physical Chemistry, Belgrade, Serbia*

Abstract

Protein primary structure and amino acid (AA) side chains properties determine protein 3D structure and stability. Knowledge about AA interactions is of importance for better prediction of protein 3D structure and *de novo* design. The program for AA pair distance determination in proteins has been developed and tested on 1667 proteins from Protein Data Bank, previously selected by PDB-SELECT. Results obtained can be correlated with those previously published, but the algorithm used highlighted details which had not been previously observed.

Introduction

The packing of protein amino acid (AA) chain into its final 3D structure is governed by the interactions of its AA side chains. Non-covalent interactions (such as hydrophobic interactions in the protein core, hydrogen bonds, salt bridges etc.), along with the covalent (disulfide bridges) are of particular importance for stability and overall architecture of protein. However, there are strong reasons to believe that not all of the forces that govern protein 3D structure have been identified [1]. Therefore, there is a need for an empirical determination of proteins AA packing distances, i.e. distributions of AA pair distances. An early result has been published by Singh and Thornton [2] for 533 protein chains solved by X-ray diffraction analysis. Our attempt was to get larger and more accurate data on AA pair distances by analysis of 1667 different proteins from Protein Data Bank (PDB) [3].

Experimental

The program for AA distance processing takes a file with proteins structure description in PDB format, as an input. From various input sections, the program calculates distances among all AA pairs. Using position of every atom in an AA (represented by its coordinates), and taking Euclidean distance as a distance measure, distance of an AA pair can be calculated in four different ways: as a minimal and a maximal distance between any two atoms in different AAs from the pair, as a distance between (mathematical) centroids of the AAs, as well as a distance between in-advance selected atoms in each AA in the pair. The program also enables user to define his own distance calculation method.

The program has been tested on a dataset consisting of 1667 proteins extracted from PDB by PDB SELECT program [4]. Distance between AA pairs is

calculated using in-advance selected C α atoms in each AA in the pair. Generated results are additionally processed for achieving summary results for tabular representation.

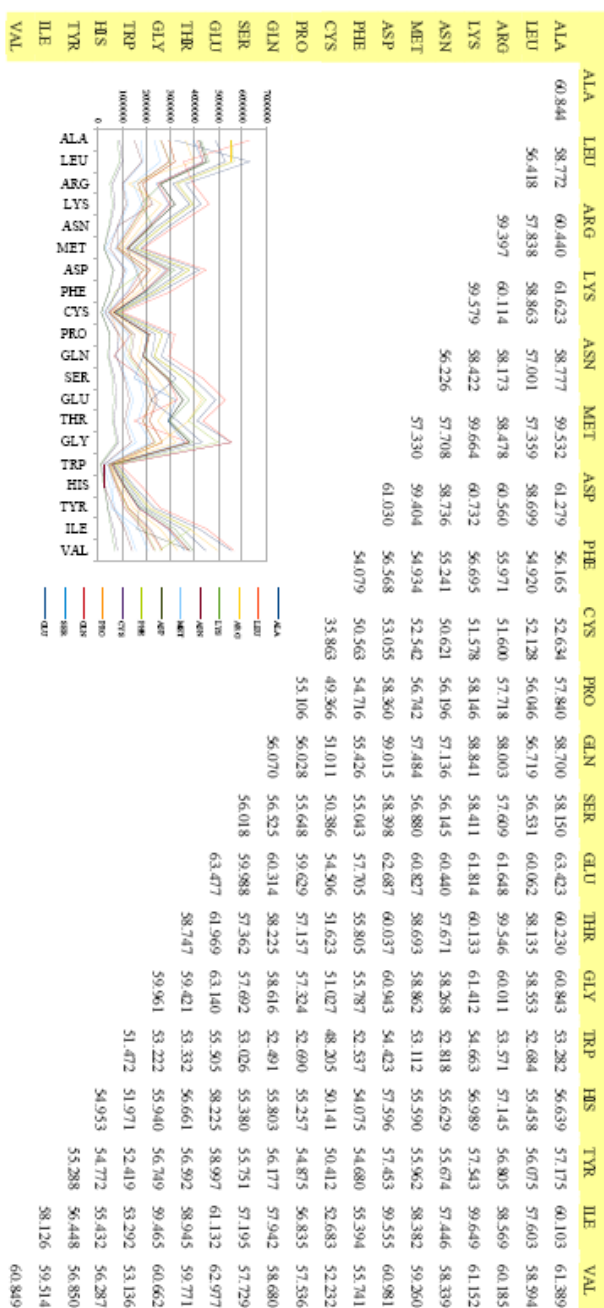
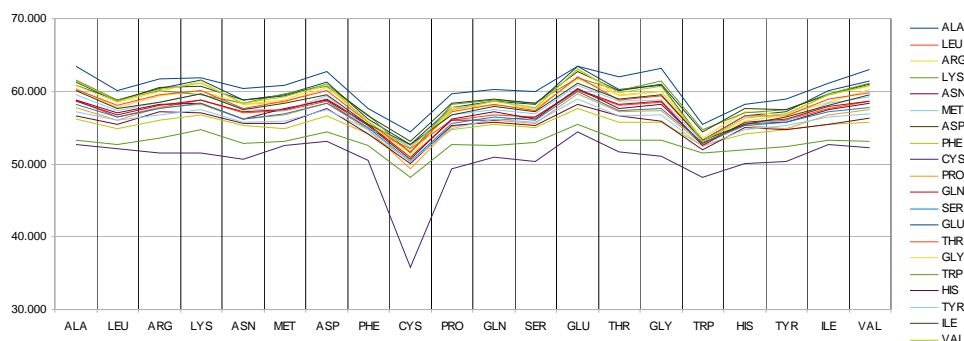


Table 1: Average distances of AA pairs in proteins. Figure inside: number of AA pairs in analyzed material

Results and Discussion

Table I represents average AA pair distances in all 1667 proteins (in Å units), while graphical representation is shown in Figure 1. Only Cys, Trp and Glu are well separated from other AAs. For all other AAs, an average distance position depends

Figure 1: Average amino-acids distance in Å



on the second AA in the pair. Distance of two Cys is the smallest in comparison with other pairs, as expected, since two Cys often form disulphide bridges in proteins. This pair is followed by Cys-Trp and Cys-Pro (and, by symmetry Trp-Cys and Pro-Cys). Cys is the most ‘social’ AA, since it has the smallest average distance with all other AAs. As opposed to these, the least ‘social’ is Glu (in order Glu-Glu, Glu-Ala, Gly-Gly, ..., Gly-Cys) and their symmetric pairs. Concerning AA properties, hydrophobic AAs (Cys, Trp, Phe, His) form a group with closer distances, while polar AAs (Gly, Asp, Lys) form another group with wider distance ranges. In conclusion, results obtained in this study are in correlation with those previously published [2]. Data obtained may be used for protein 3D structure prediction improvement, as well as de novo protein design. Further exploration will concentrate on possible new, not previously observed interactions between AAs.

Acknowledgments

The work presented has been financially supported by the Ministry of Science and Technological Development, Republic of Serbia, Project No. 144030.

References

- [1] K. Gehenn, J. Stege, J. Reed, *Anal. Biochem.*, 2006, **356**, 12-17.
- [2] J. Singh, J. M. Thornton, *Atlas of Protein Side-Chain Interactions*, Vols. I & II, IRL Press, Oxford, 1992. <http://www.biochem.ucl.ac.uk/bsm/sidechains/>
- [3] H. M. Berman, J. Westbrook, Z. Feng, G. Gilliland, T. N. Bhat, H. Weissig, I. N. Shindyalov, P. E. Bourne, *NAR*, 2000, **28**, 235-242. (<http://www.pdb.org/pdb/home/home.do>).
- [4] U. Hobohm, C. Sander, *Prot. Sci.*, 1994, **3**, 522-524.

DETERMINATION OF LIGAND BINDING CONSTANTS FROM DSC DATA

V. Pavelkić¹, M. Beljanski², K. Antić¹, M. Babić¹, T. Brdarić¹ and K. Gopčević³

¹*Institute “Kirilo Savić”, Vojvode Stepe 51, Belgrade, Serbia;*

²*Institute of General and Physical Chemistry, Studentski trg 12-14, Belgrade, Serbia*

³*School of Medicine, University of Belgrade, Višegradska 26, Belgrade, Serbia;*

Abstract

Differential scanning calorimetry (DSC) was used to measure the binding constants from T_m shifts small molecule binding to a protein. The Gibbs free energy, $\Delta(\Delta G)$, of Al(III) binding to pepsin, equilibrium binding affinity K_L , as well as an average number of ligands bound to the native protein were calculated.

Introduction

The stability of proteins and their interactions with other molecules is a topic of special interest in biochemistry because many cellular processes depend on that. In this regard, various approaches to describe macromolecular unfolding coupled to ligand binding have been reported [1]. More recently, DSC has been proved to be a very useful tool to estimate very tight binding constants [2] as well as to characterize the energetic of binding and unfolding [3]. Binding of ligand to protein occurs only if there is release of free energy. Accordingly, the protein–ligand complex is more stable than the free partners are. The extent of stabilization depends upon the magnitude of the binding energy. Comparison of stability of the complex with that of the free partners allows estimation of binding energy.

Experimental

Differential scanning calorimetry (DSC) measurements were carried out on a MicroCall “MC-2” Differential Scanning Calorimeter (MicroCall Inc., Northampton, MA) with cell volumes 1.14 ml, at heating rates 1.5°C/min. DSC scans were obtained in the temperature range from 10 to 100°C. For all the measurements, the protein (pepsin from Sigma-Aldrich) concentrations were 0.03 mM, pH 2. Ligand (aluminium chloride ($\text{AlCl}_3 \cdot 6\text{H}_2\text{O}$)) was purchased from Merck and used without further purification.

Results and discussion

DSC measurements were used to assess the conformational stability of pepsin and pepsin-aluminium interaction in water solutions acidified with HCl and in the presence of Al(III) ions with concentrations of 1, 5 and 10 mM at pH 2.

Since DSC protein stability data contain information on related aspects of protein structure and interactions, these can be used to estimate metal binding affinities in metalloprotein complex. To estimate the magnitude of Al(III) binding affinity to pepsin, we used an expression for equilibrium binding affinity [4] derived from the theory of coupled equilibrium:

$$K_{Al(III)}(T_{Al}) = \frac{\exp\left[\frac{-\Delta H_0^{VH}}{R}\left(\frac{1}{T_{Al}} - \frac{1}{T_0}\right) + \frac{\Delta C_p}{R}\left(\ln\frac{T_{Al}}{T_0} + \frac{T_0}{T_{Al}} - 1\right)\right]}{[Al(III)]_{T_{Al}}}$$

where $K_{Al(III)}(T_{Al})$ is the equilibrium binding affinity for formation of the pepsin–Al(III) complex at the transition temperature for unfolding Al(III)-pepsin, ΔH_0^{VH} is the transition enthalpy for pepsin unfolding, T_0 is the transition temperature for pepsin unfolding, T_{Al} is the transition temperature for pepsin–Al(III) complex, and $[Al(III)]_{T_{Al}}$ is the concentration of free metal ion at T_{Al} . From the shift in T_m , the changes in the apparent stability of the particular units of aluminium treated pepsin relative to the native form $\Delta(\Delta G)$ was evaluated at the transition temperature as a difference between ΔG calculated for native and aluminium treated pepsin [5]. Calorimetric ΔH^{cal} and van't Hoff ΔH^{VH} enthalpies for the complete transition were estimated from the total peak area, and also according to the van't Hoff equation, as well as the enthalpy for the each stage of pepsin unfolding (Table 1). Depending on concentrations of bound Al (III) the shifts in T_m values ranges of about 4 to 11 degrees for the first transition, and for the second transition T_m values for all aluminium concentrations are shifted from 4 to about 7 degrees. From the shift in T_m values the changes in apparent stability of the treated pepsin relative to the native form was evaluated from the equation: $\Delta(\Delta G) = \Delta G_{Al(III)} - \Delta G_{(native)}^0$, where $\Delta G_{(native)}^0$ is zero at T_m , while $\Delta G_{Al(III)}$ was obtained from Gibbs-Helmholtz equation. The obtained values of $\Delta(\Delta G)$, the Gibbs free energy of aluminium binding are listed in Table 1. As the process of pepsin unfolding is complex process, and proceeds in two different stages, the free energy of unfolding was calculated at both temperatures of transition. Compared to the temperatures where native pepsin unfolds, and to calculated free energies for the both transition temperatures, aluminium binding causes stabilization of the pepsin structure for all applied concentrations. The DSC curve profiles suggest two kinds of binding sites for Al (III) on pepsin. At each transition midpoints, T_{m1} and T_{m2} , and from ligand-induced shifts and calorimetric parameters for reversible transitions, an equilibrium binding affinity K_L was calculated (Table 1). Estimation of the average number of ligands bound to the native protein X_N can be accomplished in a term of total Gibbs energy of unfolding that is defined by the difference between the Gibbs energies of the denatured and native state, with the assumption that no ligand - binding occurs in the unfolded state [5]. Starting from the relation

$$\left(\frac{\partial \Delta G_{tot}^0}{\partial \ln[x]}\right)_T = RT \left(\frac{\partial \ln(Q - K_0)}{\partial \ln[x]}\right)_T = RT \overline{X_N},$$

the average numbers of ligands bound to the native protein were graphically determined as a slope of the G_{tot}^0 versus $\ln[x]$ (data not shown). In the above equation ΔG_{tot}^0 is a total Gibbs energy, Q - partition function of all residual native states which include native ligand free and native ligand bounded protein molecules, K_0 the equilibrium constant of unfolding, and X_N - an average number of ligands bound to the native protein.

Table 1. Thermodynamic parameters of pepsin unfolding in a presence of Al (III).

$C_{Al(III)}$ (mM)	peak	T_m (K)	ΔH^{cal} (kJ/mol)	ΔH^{VH} (kJ/mol)	$^*\Delta G^0$ (kJ/mol)	$\Delta(\Delta G^0)$ (kJ/mol)	$K_L(T_m)$ (M^{-1})
0	1	304.5 ± 0.2	535 ± 21	196 ± 8	3.93	0	-
	2	336.9 ± 0.2	556 ± 12	531 ± 17	36.51	0	-
1	1	308.6 ± 0.2	138 ± 12	389 ± 42	11.87	7.94	$1.05 \cdot 10^3$
	2	340.9 ± 0.2	769 ± 21	568 ± 8	35.99	-0.52	$9.26 \cdot 10^8$
5	1	309.2 ± 0.2	171 ± 4	422 ± 8	13.25	9.32	$7.30 \cdot 10^2$
	2	342.5 ± 0.2	518 ± 35	627 ± 42	40.25	3.74	$5.71 \cdot 10^8$
10	1	315.6 ± 0.2	159 ± 21	529 ± 44	12.71	8.78	$6.76 \cdot 10^5$
	2	343.5 ± 0.2	481 ± 17	567 ± 21	36.28	-0.23	$1.43 \cdot 10^6$

*Standard Gibb's energy was calculated at 25°C; K_L is equilibrium-binding affinity. Reported values are the means of minimum three independent replicates.

The obtained average number of ligands bound per molecule of native pepsin from DSC data was 1.35 for the first transition temperature and 3.58 for the second transition temperature. The obtained values for binding affinity for site I are lower than on site II, which is in agreement with obtained values for average number of bound ligand. Also it can be assumed that the site II has a higher affinity for Al(III) than site I.

Conclusion

In summary, the present thermodynamic analyses show that DSC method is useful to measure the binding constants from T_m shifts. The stabilization effect of Al(III) binding on pepsin molecule, as well as an average number of ligands bound to the native protein, equilibrium binding affinity K_L were also calculated.

Acknowledgement

This study was supported by Ministry of Science of Republic of Serbia, Project No. 142025.

References

- [1] D. M. Crothers, Biopolymers, 1971, **10**, 2147–2160.
- [2] T. L. Blundell, et al, J. Mol. Biol., 1990, **211**, 919-941.
- [3] M. S. Celey et al, Anal. Biochem., 2006, **350**, 277-284.
- [4] L. N. Lin, , et al, Biochem. J., 1993, **293**, 517–522.
- [5] R. Jorg, H. Hans-Jurgen, J. Mol. Biol., 2002, **306**, 809-824.

EFFECT OF γ -IRRADIATION ON ANTIOXIDANT ACTIVITY AND FREE RADICAL CONTENT OF SPICES

M. D. Pavlović¹, M. Novaković², D. Sužnjević¹, S. Gorjanović¹, D. Mitić-Ćulafić³, S. Kolarević³ and Z. Miladinović¹

¹*Institute of General and Physical Chemistry, Studentski trg 12/V, Belgrade, Serbia*

²*Institute of Chemistry, Technology and Metalurgy, 12/III, Belgrade, Serbia*

³*Faculty of Biology, Studentski trg 2/III, Belgrade, Serbia*

Abstract

Six spices (clove, sage, basil, ginger, black pepper, anise) and a mushroom (*B. edulis*) were γ -irradiated at a dose of 10 kGy. Antioxidant activities of water-ethanolic extracts remained the same in irradiated (10 kGy) and unirradiated samples, (with exception of basil), as measured by a DPPH (1,1-diphenyl-2-picrylhydrazyl) radical-scavenging assay, inhibition of lipid peroxidation (TBA assay) and a novel antioxidative assay, measuring hydrogen peroxide scavenge (HPS). Total phenolic contents was, also, unchanged after irradiation. Irradiation resulted in increased total EPR signal area in all investigated samples, as revealed by electron paramagnetic resonance spectroscopy (EPR) during storage.

Introduction

γ -irradiation has been recognized as radiologically, microbiologically and toxicologically safe technique to sanitize dry herbs. Nevertheless, questions focusing antioxidant [1] loss, as well as free radicals and radiolytic byproduct formation [2], are still being discussed. Antioxidant (AO) content of ethanolic extracts of aromatic herbs may be changed upon irradiation. AO activities of spices (in particular sage and ginger) in several assays correlated positively with total phenolics. Electrochemical techniques, based on phenolic OH groups' behavior to act as hydrogen- or electron- donating agents, offer direct determination of the total AO activity (the overall reducing power). Direct current polarography has been used to survey hydrogen peroxide scavenge (HPS) upon gradual addition of different samples and correlation with total phenolic content and DPPH scavenge was found [3]. In this study HPS method was applied on ethanolic extracts of γ -irradiated (10 kGy, a maximum absorbed dose for dry aromatic herbs) spices and mushroom and compared to DPPH and TBA assays and total phenolic content. Electron paramagnetic resonance spectroscopy is the technique to detect radiolytically produced radicals trapped within the solid matrix in dry herbs [2] and was used to quantify the free radical production in irradiated dry samples.

Experimental

Samples were prepared as 80 % ethanolic extract of dried spices and mushroom *Boletus edulis*, for 2 h at room temperature. DPPH radical-scavenging assay was monitored at 517 nm and inhibition of DPPH radical and EC₅₀ values, in the

presence of antioxidants, calculated as described previously [3]. Measurement of total phenolic content was determined by the Folin-Ciocalteu assay at 740 nm and expressed in gallic acid equivalents (GAE) [3]. The extent of Fe²⁺/ascorbate-induced lipid peroxidation (LP) was determined by the TBA assay [5] at 532 nm. Polarographic measurement of hydrogen peroxide scavenge (HPS) was expressed as decrease in limiting anodic current value (i_l) in the presence of antioxidant species. EPR spectra of additionally dried samples were recorded at a room temperature using a Varian E104-A EPR spectrometer operating at X-band (9.51 GHz) using following settings: modulation amplitude, 2 G; modulation frequency, 100 kHz; microwave power, 5 mW; scan range, 200 G with field centre at 3410 G. Spectra were recorded and analyzed using EW software (Scientific Software) [5].

Results and discussion

Dried spices (clove, sage, basil, ginger, black pepper and anise) and a mushroom (*Boletus edulis*) were γ -irradiated at a dose of 10 kGy. AO activities of their water-

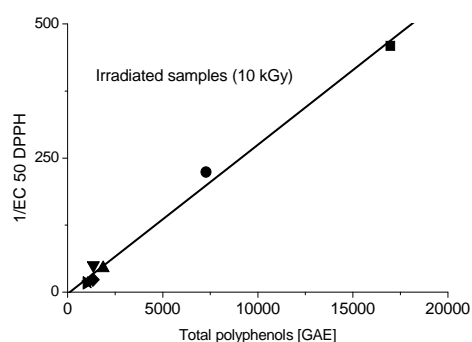
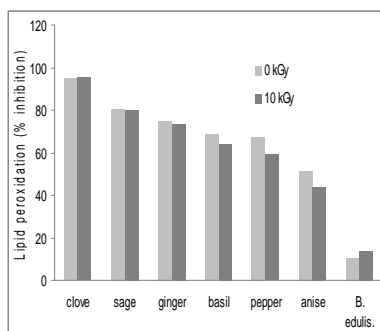


Fig.1 The relationship between antioxidant activity (1/EC₅₀ DPPH scavenge) and total polyphenols (GAE) of the extracts of irradiated (10 kGy) ($r^2=0.9928$) samples of clove (■), sage (●), basil (▲), ginger (▼), *B.edulis* (◆), black pepper (★) and anise (►). The data for unirradiated samples ($r^2=0.9738$) are not shown.

A.



B.

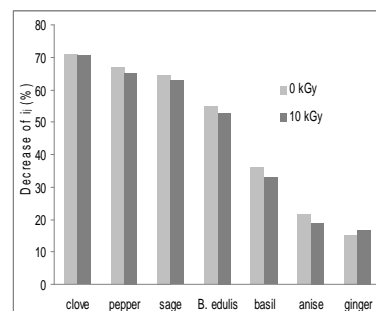


Fig. 2. Antioxidative activity of extracts of unirradiated and irradiated (10 kGy) samples in A. lipid peroxidation (TBA assay) and B. hydrogen peroxide-scavenge (HPS) assay.

ethanolic extracts remained the same (with exception of basil) in irradiated and unirradiated samples, as measured by a DPPH radical-scavenging assay compared with total polyphenol content, Fig. 1, inhibition of lipid peroxidation (TBA assay),

Fig.2.A. and a novel antioxidant assay, based on direct current polarography (hydrogen peroxide scavenging, HPS assay), Fig. 2.B. Contents of total polyphenolic compounds were also unchanged after irradiation, with exception of basil, Fig. 1. The strict correlation of total phenolic content and DPPH radical-scavenging assay of samples was observed. Irradiation resulted in the increase of total EPR signal area in all samples of dried herbs, which decreased after storage of 9 weeks. The cellulose and sugar radical signals were observed. Decrease of intensity of EPR signal in unirradiated samples was, also, observed, Fig. 3, due to the increase of humidity.

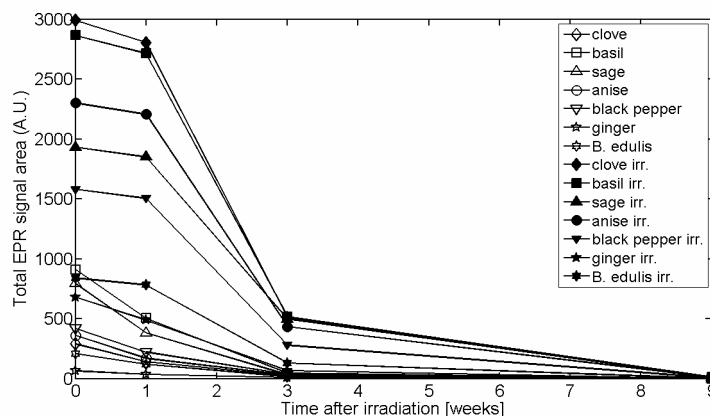


Fig.3. Total EPR signal area (arbitrary units) of unirradiated (white signs) and irradiated (10 kGy) (black signs) samples of clove, basil, sage, anise black pepper, ginger and *B. edulis* kinetics after irradiation.

Conclusion

Two standard AO assays, DPPH and TBA, and a recently developed DC polarographic assay have been applied to determine AO activity changes in ethanolic extracts of dried herbs exposed to γ -irradiation. A direct correlation of AO activity in DPPH and polyphenolic assay was found. The enhancement of the total EPR signal area was observed in irradiated dried herbs and lasted for 9 weeks.

Acknowledgments

The present investigations are supported by Ministry of Science, Technologies and Development of Serbia, project No TR 20120 and project No 143020.

References

- [1] M. Suhaj, J. Racova, M. Polovka, V. Brezova, Food Chem.. 2006, **97**, 696-704.
- [2] L. Calucci, C. Pinzino, M. Zandomenoghi, A. Capocchi, S. Ghiringhelli, F. Saviozzi, S. Tozzy, L., Gallechi, J. Agric. Food Chem., 2003, **51**, 927-934.
- [3] S. Ž. Gorjanović, M. M., Novaković, N. I., Potkonjak, D. Ž., Sužnjević, J. Agric. Food Chem., 2010, **58**, 4625-4631.
- [4] N. Mimica-Dukić, B. Bozin, M. Sokovic, N. Simin, J. Agric. Food Chem., 2004, **52**, 2485-2489.
- [5] J. Ram. Detection methods for irradiated foods, Royal Chemical Society Printing House, Cambridge, 1996, 93-97.

Na⁺-DEPENDENT Ca²⁺ ION FLUX INHIBITION BY 17 beta-ESTRADIOL IN CAUDATE NUCLEUS MITOCHONDRIA

S. Petrović, M. Milošević, I. Stanojević, D. Drakulić, N. Jovanović,

N. Veličković and A. Horvat

*Laboratory of Molecular Biology and Endocrinology
Institute of Nuclear Sciences "VINČA", University of Belgrade, P.O.Box 522,
11001 Belgrade, Serbia*

Abstract

In this study the Ca²⁺ ion flux modulation in the synaptosomal mitochondria isolated from caudate nucleus (CN) of the ovariectomised rats was examined. 17 beta-estradiol (E2), E2-conjugated to bovine serum albumin (E-BSA), estradiol receptor α (ER α) agonist 4,4',4''-(4-propyl-[1H]-pyrazole-1,3,5-triyl) trisphenol (PPT), ER β agonist 2,3-bis(4-hydroxyphenyl)-propionitrile (DNP) and ER α/β antagonist 7 α ,17 β -[9[(4,4,5,5,5-pentafluoropentyl)sulfinyl]nonyl]estra-1,3,5(10)-triene-3,17-diol (ICI 182,780) were used. The Ca²⁺ efflux inhibition of about 27% was detected in the presence of 0.5 nmol/l E2, and of about 20% in the case of E-BSA. DNP (10 nmol/l) was as much potent Ca²⁺ efflux inhibitor as E2, while PPT (10 nmol/l) hardly had any inhibitory effect (9% efflux decrease). When E2 binding to ER α and ER β was prevented by 1 μ mol/l ICI 182,780, the Ca²⁺ efflux inhibition of about 15% was detected. Our results suggest that E2 prevents Ca²⁺ efflux from synaptosomal mitochondria due to ER β activation rather than ER α . The involvement of the external E2 binding site on the mitochondrial membrane probably different from ER α/β should not be excluded because of Ca²⁺ efflux inhibition detected in the presence of E-BSA and ICI 182,780. The Ca²⁺ efflux modulation could be the mechanism through which E2 exerts its neuromodulatory role in specific brain structures.

Introduction

Due to their Ca²⁺ transport mechanisms mitochondria are organelles critical for Ca²⁺ buffering in neuronal cells. The concentration of Ca²⁺ in mitochondrial matrix ([Ca²⁺]_m) regulates the respiration rate, ATP production, reactive oxygen species generation, $\Delta\Psi_m$ collapse occurrence and also, it is a critical trigger for the permeability transient pore opening and therefore for apoptosis [1].

The CN is an important brain structure necessary for learning and memory, particularly regarding feedback processing. Also, it prevents explosive activation of excitatory synapses by measuring the general activity of cerebral cortex and controlling the threshold potential. Permanently high neuronal activity in this brain region could be the reason for intensive movements of ions, especially Ca²⁺ ions.

The steroid hormone E2 could modulate the activity of two main mitochondrial Ca^{2+} transport mechanisms: I) Ca^{2+} influx by the ruthenium red (RR) sensitive uniporter and II) Ca^{2+} efflux by the $\text{Na}^+/\text{Ca}^{2+}$ exchanger. In our previous work using synaptosomal mitochondria isolated from whole rat's brains, the Na^+ -dependent Ca^{2+} efflux inhibition by physiological E2 concentrations was detected [2]. Therefore, the aim of present study was to determine if E2 could influence mitochondrial Ca^{2+} transport in CN and to estimate the contribution of $\text{ER}\alpha$ and/or $\text{ER}\beta$ in Ca^{2+} transport modulated by E2, using ERs antagonist and specific agonists. The observed effects on mitochondrial functions as well as on mitochondrial Ca^{2+} sequestration might be a consequence of membrane binding sites and/or mitochondrial estradiol receptors ($\text{ER}\alpha$ and/or $\text{ER}\beta$) activation.

Experimental

Synaptosomal mitochondria used for Ca^{2+} transport measurements were isolated from the CN of ovariectomised (3 weeks prior to use) female rats. For Ca^{2+} transport monitoring mitochondria were preincubated at 22°C for 10 min in medium containing: 300 mmol/l mannitol, 10 mmol/l KCl, 1 mmol/l maleate, 5 mmol/l glutamate, 10 mmol/l Tris-HCl, pH 7.4. The influx of Ca^{2+} to synaptosomal mitochondria was initiated by adding 0.2 mmol/l CaCl_2 ($0.6 \mu\text{Ci } ^{45}\text{CaCl}_2$). The reaction lasted 5 min and stopped by RR ($17.5 \mu\text{g}/\text{mg}$ protein). For Ca^{2+} efflux monitoring, mitochondria were loaded with Ca^{2+} in the same way and after adding RR, the Ca^{2+} efflux was initiated by adding NaCl (20 mmol/l) and 0.2 mmol/l EDTA and lasted 5 min. The different agents effects on Na-dependent Ca^{2+} efflux were measured by incubating Ca^{2+} -preloaded mitochondria with 0.5 nmol/l E2 (10 min), 10 nmol/l DNP (10 min), 10 nmol/l PPT (10 min) and 1 $\mu\text{mol}/\text{l}$ ICI 182,780 (20 min) before efflux initiation.

Results and discussion

In the present study the Ca^{2+} movements through the CN mitochondrial membrane were monitored in order to determine the direct effect of E2 on mitochondrial Ca^{2+} flux.

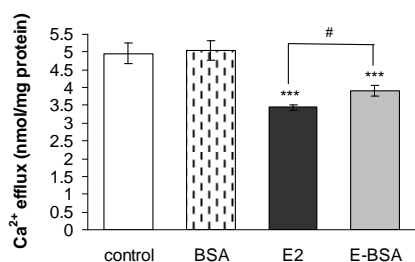


Fig.1. Effects of E2 and E-BSA *in vitro* on mitochondrial Na^+ -dependent Ca^{2+} efflux.

In our model system no effect of E2 on mitochondrial Ca^{2+} influx that occurs through the RR-sensitive uniporter was detected (data not shown). To verify if E2 affects Na^+ -dependent Ca^{2+} efflux by acting directly on the mitochondrial membrane, the Ca^{2+} -preloaded mitochondria with 0.5 nmol/l E2 or membrane-impermeable E-BSA before efflux initiation were incubated. The efflux in control mitochondria and in the presence of E2, BSA or

E-BSA is presented in Figure 1. The Ca^{2+} efflux was decreased by 27% in the presence of E2. BSA did not affect Ca^{2+} efflux, while the same concentration of E-BSA reduced Ca^{2+} efflux by 20%, indicating inhibition due to an external binding site on the mitochondrial membrane, independent of E2 diffusion into mitochondrial matrix.

The involvement of mitochondrial $\text{ER}\alpha/\beta$ during E2 modulation of Ca^{2+} efflux, also, was tested. When E2 binding to mitochondrial $\text{ER}\alpha$ and $\text{ER}\beta$ was prevented by ICI 182,780 pretreatment, the E2 inhibitory effect on Ca^{2+} efflux was lowered, but the Ca^{2+} efflux decrease of 15% comparing to control still persisted (Fig. 2). The mitochondria incubation with $\text{ER}\alpha$ agonist, PPT, led to no change in Ca^{2+} efflux with respect to control. However, the $\text{ER}\beta$ agonist DNP was almost as much potent inhibitor as E2 and inhibited Ca^{2+} efflux by 25% (Fig. 3).

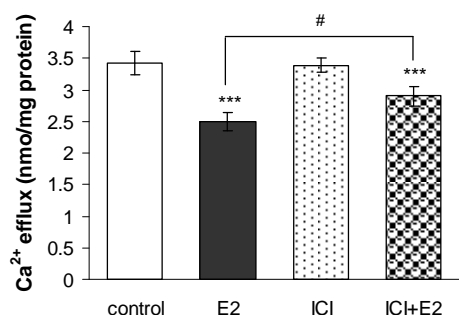


Fig.2. Effects of E2 and ICI *in vitro* on mitochondrial Na^{+} -dependent Ca^{2+} efflux.

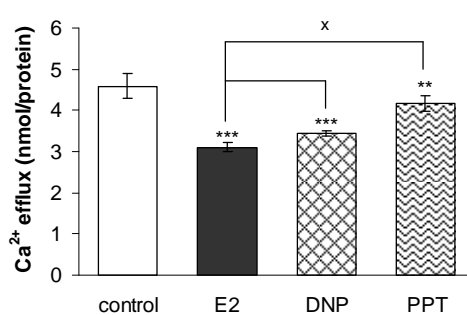


Fig.3. Effects of E2, DNP and PPT *in vitro* on mitochondrial Na^{+} -dependent Ca^{2+} efflux.

Conclusion

In summary, our results confirm that E2 prevents Ca^{2+} efflux from caudate nucleus synaptosomal mitochondria by I) direct acting on still unknown membrane E2 binding sites (about 20% inhibition) and II) $\text{ER}\beta$ activation (about 25% inhibition), rather than $\text{ER}\alpha$. Most likely, these are the mechanisms through which E2 could exert its neuromodulatory role in specific brain structures.

Acknowledgements

This study was supported by Serbian Ministry of Sciences, Project No. 143044.

References

- [1] R. Rizzuto, P. Pinton, D. Ferrari, M. Chami, G. Szabadkai, P.J. Magalhaes, F. Di Virgilio, T. Pozzan, *Oncogene*, 2003, **22**, 8619-8627.
- [2] A. Horvat, S. Petrovic, N. Nedeljkovic, J. V. Martinovic, G. Nikezic, *Gen. Physiol. Biophys.*, 2000, **19**, 59-71.

BROWNING OF BASIL-BASED EMULSIONS - COLOUR EVALUATION -

L. Pezo¹, M. Kićanović¹, S. Zlatanović¹,
O. Kovačević¹, A. Jovanović¹ and J. Gvozdenović²

¹*Institut of General and Physical Chemistry, Beograd, Studentski trg 12/V, Serbia,*

²*Faculty of Technology, Novi Sad, bul. Cara Lazara 1, Serbia*

Abstract

Colour evaluation, by means of multivariate image analysis was applied on colour lightness changes, corresponding to enzymatic and non-enzymatic browning of mild-heat processed basil-based food emulsions. The colourgram of digitalized images, taken during oxidation of samples, was evaluated. Basic colour information was derived from frequency colour distribution for *RGB* (red, green and blue) and *HSV* (hue, saturation and value) colour system, while the Principal Component Analysis was carried out by evaluating covariance matrix, for raw, mean centered and autoscaled matrix of the basic *R*, *G*, *B* colour information, and the evaluation of eigenvalues and eigenvectors for all three numeric models. Influence of metal-chelating protein lactoferrin and organic acids on changes in lightness frequency distribution (*L*), corresponding to browning, was determined.

Introduction

Minimally-processed basil-based food emulsion, similar to “*pesto*”, an Italian pasta sauce, undergoes colour deterioration (attributed to combined enzymatic and non-enzymatic oxidation) [1,2]. We have analysed the effect of combinations of ascorbic, citric and lactic acid, and metal-chelating protein lactoferrin, on browning, which was determined by colour lightness changes, applying colour evaluation, by means of PCA analysis [3].

Materials and methods

Basil-based emulsions were prepared from fresh basil (which was treated with short temperature shocks during washing), virgin olive oil, high-oleic sunflower oil, parmesan and kashkaval, whey, walnuts, salt and garlic, as well as 9 combinations of organic acids (ascorbic, citric and lactic acids) and lactoferrin. Colour images of 9 basil-based emulsions were captured by a Canon PowerShot A550 and A590 CCD camera. All the acquired images were recorded as 24 bit *RGB* (16.8 millions of colours) with a 1024 x 768 spatial resolution. The macro function of the digital camera has been used, to cover a scene area of approximately Ø10 cm. Images of each different formulation were taken periodically by camera 22 times during the period of approximately 320 minutes.

Results

The first step in the elaboration of every single digital *RGB* image with size $\{r, c\}$ (where *r* is the number of pixel rows and *c* is the number of columns) consists of

unfolding it to a two-dimensional matrix of three dimensional array of colour data (R, G, B). Since the imported files are 24 bit colour images, each one of the three R, G and B "slices" of the 3D array are (24/3) 8 bit greyscale images, and therefore the three R, G and B variables can assume all the integer values in the range 0-255. Then, the lightness (L) is derived directly by R, G and B variables by summing them and dividing by 3 ($L=(R+G+B)/3$). The frequency distribution vector with a length of 256 elements is calculated over all the single pixels ($r \times c$), for each one of the considered variables: R, G, B, and L. In this work, only lightness (L) was used to represent data recorded during the experiment, and these data is represented in relative form, i.e., lightness was divided by initial lightness: $L_{rel} = L / L_{init}$. This represents the maximum value reached in frequency distribution vector. It is been found that the pesto sample is getting darker while exposed to atmosphere (browning effect), according to exponential law $y = y_0 + A \cdot \exp(x/t)$. Evaluated correlation coefficient for these curves were $R^2 = 0.90-0.93$, which is not very accurate, and these data show only the first, fast estimation of oxidation process.

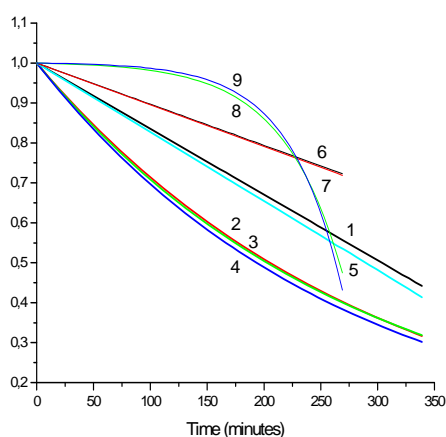


Figure 1. Relative lightness of basil-based (*pesto*) emulsions during oxidation (first day). The effect of 9 treatments with ascorbic, citric, lactic acid, NaCl and lactoferrin. 1. 0,5 g/kg, asc.acd., 0,4 % NaCl, 2 .0,5 g/kg asc.acd., lactoferrin 80 mg/kg, 0,4 % NaCl, 3. 0,5 g/kg asc.acd., lactoferrin 400 mg/kg , 0,4% NaCl, 4. 0,5 g/kg asc.acd., lactoferrin 2000 mg/kg, 0,4 % NaCl, 5. 0,5 g/kg asc.acd., 3% NaCl, 6. 1 g/kg asc.acd., 1,5 g/kg cit.acd., 0,4 % NaCl, 7. 1 g/kg asc.acd., 1,5 g/kg cit.acd., lactoferrin 400 mg/kg , 0,4 % NaCl, 8. 1 g/kg asc.acd., 1,5 g/kg cit.acd., 3,6% lact.ac., 0,4 % NaCl, 9. 1 g/kg asc.acd., 1,5 g/kg cit.acd., 3,6% lact.ac. lactoferrin 400 mg/kg , 0,4 % NaCl

Samples 8 and 9 (with ascorbic, citric and lactic acid) are less sensitive to oxidative browning than other formulas, Fig. 1. The slope of curves 6 and 7 (ascorbic and citric acid) drop more rapidly than curves 8 and 9 but slower than curves 1 (ascorbic acid), and 5. Lactoferrin (curves 2, 3 and 4) has shown negative effect on browning at the lowest concentration of ascorbic acid.

After evaluation the first three colour coordinates, relative red ($RR=R/(L \cdot 3)$), relative green ($RG=G/(L \cdot 3)$) and relative blue ($RB=B/(L \cdot 3)$) were evaluated. The relative values have been considered since a particular colour, e.g. red colour does not correspond to a high absolute value of the corresponding R variable, but to a high value of the ratio between R and L. The hue, saturation and intensity (HSV) values are also calculated, for the conversion from the RGB to the HSV colour space. The V values are computed for every pixel as the maximum value between R, G, and B, while the saturation is evaluated

as $S = (\max(R, G, B) - \min(R, G, B)) / \max(R, G, B)$. All these variables are represented by frequency distribution vectors on the colourgram.

The PCA analysis [3] of frequency distribution vectors of R , G and B , was done using the score matrix of raw data, the score matrix of mean centred score data, and the score matrix of auto scaled unfolded RGB distribution matrix. Mean centred matrix was evaluated by evaluating the subtracting the mean value of each colour vector to each element of the vector, and the autoscaled matrix was evaluated by dividing the mean centred matrix vectors with standard deviations for each vector. The evaluation of covariance matrix for raw, mean centred and autoscaled matrix followed, with the evaluation of eigenvectors and eigenvalues of covariance matrix. The eigenvectors of covariance matrix for all three models were treated as loading vectors in PCA analysis. The eigenvalues (λ) of evaluated covariance matrix were calculated, as usually, using the equation: $\det(COV - \lambda \cdot I) = 0$. The eigenvectors of covariance matrix are then calculated as $P = COV - \lambda \cdot I$, for all three models, raw, mean centred and autoscaled. Finally, the score matrix is evaluated as $T = X \cdot P$, for all three models. The final form of colourgram is completed after normalisation of loading vectors for all three models (each of this matrix is defined by 3 x 3 values), and eigenvalues of three PCA models (each model has three eigenvalues). The resulting colourgram information is one dimensional signal, and it describes the colour properties of the image, Fig. 2.

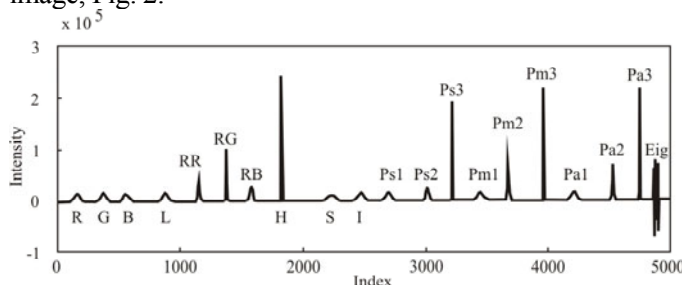


Figure 2. Typical colorogram of basil-based emulsion, from which the lightness peak value (L) was determined

Conclusion

As seen from Figures 1 and 2, colour analysis is the acceptable method for fast and accurate evaluation of oxidative browning in inhomogeneous basil-based emulsions. Ascorbic, citric and lactic acids showed a significant impact on prolonging the oxidation time, i.e. the stability of the product.

Acknowledgements

The present investigations are supported by Ministry of Science, Technologies and Development of Serbia, project No TR 20120.

References

- [1] B. Fabiano, P. Perego, R. Pastorino, M. Del Borghi, *Int. J. Food Sci Technol.*, 2000, **35**, 293-303.
- [2] A. Antonelli, M. Cocchi, G. Fava, G. C. Franchini, D. Manzini, A. Ulrici, *Anal. Chim. Acta*, 2004, **515**, 3-13.
- [3] J. Huang, H. Wium, K. B. Qvist, K. H. Esbensen, *Chemometrics Intell. Lab. Syst.*, 2003, **66**, 141 – 158.

PCA & SWOT ANALYSIS APPLIED TO LIPID OXIDATION OF BASIL-BASED EMULSIONS

L. Pezo¹, M. D. Pavlović,¹ J. Gvozdenović,² S. Zlatanović¹,
O. Kovačević¹ and S. Stanojlović¹

¹*Institut of General and Physical Chemistry, Beograd, Studentski trg 12/V, Serbia,*

²*Faculty of Technology, Novi Sad, bul. Cara Lazara 1, Serbia*

Abstract

The quantified SWOT (Strengths, Weaknesses, Opportunities and Threats) and PCA (principal component analysis) were applied in multi-variant analysis of lipid oxidation criteria of basil-based food emulsions. Ascorbic, citric and lactic acid had shown significant impact on prolonging lipid oxidation, according to both PCA and SWOT analysis, while lactoferrin, metal-chelating protein, had negative effect on lipid oxidation at high pH (5,2).

Introduction

Presence of divalent cations (Ca^{2+} , Mg^{2+} , Fe^{2+}), pH, elevated NaCl or citrate/bicarbonate ratio, could markedly diminish the antimicrobial and antioxidative effect of lactoferrin, metal-chelating protein, isolated from whey, which influence lipid oxidation [1] and is an antimicrobial agent of broad spectrum [2]. The objective of the present study was to assess the effect of combinations of lactoferrin with ascorbic, citric, lactic acid, and NaCl on lipid oxidation in fresh basil-based emulsions, similar to “*pesto*”- pasta sauce.

Materials and methods

Basil-based emulsions, were prepared in 9 combinations of ascorbic, citric, lactic acid, NaCl and lactoferrin. **1.** 0,5 g/kg, asc.acd., 0,4 % NaCl, **2.** 0,5 g/kg asc.acd., lactoferrin 80 mg/kg, 0,4 % NaCl, **3.** 0,5 g/kg asc.acd., lactoferrin 400 mg/kg , 0,4% NaCl, **4.** 0,5 g/kg asc.acd., lactoferrin 2000 mg/kg, 0,4 % NaCl, **5.** 0,5 g/kg asc.acd., 3% NaCl, **6.** 1 g/kg asc.acd., 1,5 g/kg cit.acd., 0,4 % NaCl, **7.** 1 g/kg asc.acd., 1,5 g/kg cit.acd., lactoferrin 400 mg/kg , 0,4 % NaCl, **8.** 1 g/kg asc.acd., 1,5 g/kg, 3,6% lact.ac., 0,4 % NaCl, **9.** 1 g/kg asc.acd., 1,5 g/kg cit.acd., 3,6% lact.ac. lactoferrin 400 mg/kg , 0,4 % NaCl. Lipid oxidation criteria were: primary products of lipid oxidation, analyzed by peroxide value (PV) [1], free fatty acid content, analyzed by acid value (AV) [1] and total oxidative stability, determined by oxidation-induction time (OIT_{DSC}), according to the method of differential scanning calorimetry (DSC) [3] in the separated oil phase of emulsions.

The SWOT [4] was evaluated on lipid oxidation criteria, according to the four factors of decision-making: alternatives, criteria, performance, and weight. Alternatives refer to data (objects) to be compared with (e.g., emulsions on 0th and 30th day). Criteria refer to the key factors of value assessment (e.g. the factors that represent the state of

the objects to be compared, AV, PV and OIT_{DSC}. Performance structure refers to the values of the key factors representing their importance. The Quantified SWOT analytical method consists of few steps, and the first is the decision of what is to be compared, i.e.: basil-based emulsions on 0th and 30th day. After that, the research of the main key factors (parameters of influence) takes place, and also the collection of data represented by key factors. The weights of key factors are evaluated according to previous investigation or by some analytical method (analytic hierarchy method – AHP, principal component analysis – PCA [4], etc.)

Results and discussion

The determined values of lipid oxidation criteria: Peroxide Value (PV), Acid Value (AV) and oxidation induction time – DSC (OIT_{DSC}) (on 0th and 30th day) for 9 types of basil based emulsions were the input values for SWOT calculation. The input values were normalized both for quantified and qualified performance, for objective performance scoring (e.g., 1–5 points, or 0.0 – 1.0 score). The aim of normalization is to unify the scales of the key factors (it could be also done by autoscaling). The used normalization method is made by using fuzzy set, and calculated as benefit-criteria normalization (the higher the better for OIT_{DSC}), or cost-criteria normalization (the lower the better for PV and AV). In this article, A matrix is the correlation matrix, and the calculation of key factor weights is done as suggested by Saaty [4]. If A is a consistency matrix, eigenvector w can be calculated by the formula $(A - \lambda_{\max} \cdot I) \cdot w = 0$, where λ_{\max} is the largest eigenvalue of matrix A ; w is the vector of weights; and I is the identity matrix (n x n).

After calculation of the 0th and 30th day weight scores of the comparing objects, and the normalization of key factors, the score value was calculated for each data object. The mean was accepted as the benchmarking value. The scores of the compared basil-based emulsions were added together and the benchmarking value subtracted. The final value was the coordinate value of the compared samples in the SWOT analysis matrix. In order to show the comparison on the four-quadrant coordinate system, the ordinate is prescribed to stand for the 30th day of basil-based emulsion, while the abscissa is prescribed to stand for the 0th day. Each type of emulsion has its coordinate (x, y), so its position in the competition can be clearly realized. The final benchmark values of lipid oxidation parameters are, also, calculated using weight factors for 0th and 30th day and their score values. The values of weight factors are also calculated using PCA analysis. The score values and SWOT coordinates obtained by evaluation are multiplied by 4 and added to 1 (in order to present the results in range 1 – 5 points, which are far more understandable, then the calculation range 0 – 1).

0th day score vector shows results that fit very well to those acquired by color image analysis of basil-based emulsion, corresponding to oxidative browning, as shown in the accompanying paper [5]. Both analysis showed that the score of basil-based emulsions 2, 3 and 4 (containing lactoferrin and low acid concentration, 0,5 g/kg ascorbic acid, pH 5,2) oxidize much faster than other emulsions, and gain the worst scores, compared to the control (emulsion1). The

best antioxidative effects were obtained with combination of ascorbic, citric and lactic acid, pH 4.4 (emulsion 8 and 9). There are variations in results obtained by image (benchmark value) and SWOT analysis, especially in emulsion type 6, which seems to be more like emulsions 8 and 9, as seen from SWOT analysis, while it is much closer to emulsion 7 according to benchmark value, Figure 1.

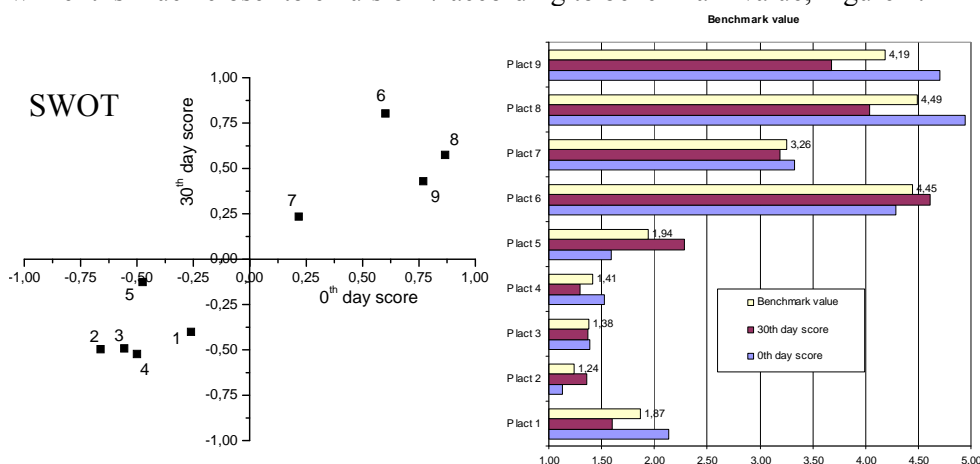


Fig.1. SWOT based scores for 0th and 30th day, represented in SWOT diagram and benchmark value of lipid oxidation parameters (PV, AV and OIT_{DSC}) of basil-based emulsions 1 - 9.

Conclusion

Ascorbic, citric and lactic acid had shown significant impact on prolonging lipid oxidation in basil-based emulsions, according to both PCA and SWOT analysis, while lactoferrin had negative impact, especially at high pH (5.2). 0th day score vector revealed results that fit very well to those acquired by color image analysis, corresponding to oxidative browning, of same products [5].

Acknowledgements

The present investigations are supported by Ministry of Science, Technologies and Development of Serbia, project No TR 20120.

References

- [1] C. Jacobsen, M. B. Let, N. S. Nielsen, A. S. Meyer, *Trends Food Sci. Technol.* 2008, **19**, 76-93.
- [2] A. S. Naidu, *Food Technol.*, 2002, **56**, 40-45.
- [3] J. Velasco, M. L. Andersen, L. H. Skibsted, *Food Chem.*, 2004, **85**, 623-625.
- [4] T.L. Saaty, L. G. Vargas, *Models, Methods, Concepts & Applications of the Analytic Hierarchy Process*, Kluwer Academic Publishers, Boston, 1990.
- [5] L. Pezo, M. Kićanović, S. Zlatanović, O. Kovačević, A. Jovanović, J. Gvozdrenović, *Phys. Chem. 2010, SPCS, Belgrade, 2010, in current Proceedings (F-P-13)*.

BIO-PHYSICO-CHEMICAL CHARACTERISTICS OF PHOTOSYNTHETIC MODEL OF INBREED LINES AND MAIZE HYBRIDS

Č. Radenović,^{1,2} N. Delić,¹ G. Stanković¹ and Ž. Jovanović¹

¹*Maize Research Institute, Zemun Polje, S. Bajića 1, Belgrade-Zemun, Serbia*

²*Faculty of Physical Chemistry, University of Belgrade, Studentski trg 12-16, Belgrade, Serbia (mbel@matf.bg.ac.rs)*

Abstract

This study confirms the hypothesis that there are elite maize inbred lines and hybrids with erect top leaves, which have a dominant property of an efficient photosynthetic model, that is successfully used in efficient breeding, increased production and diverse utilisation of commercial maize. The displayed results on the erect position of the top leaves, increased density, the dynamics of grain dry down during the maturation period, seed quality of commercial maize and photosynthetic and fluorescent parameters: the temperature dependence of the delayed chlorophyll fluorescence intensity, the Arrhenius criterion for the determination of critical temperatures (phase transition temperatures) and the activation energies, show that properties of observed maize inbreds and their hybrids are based on positive effects and the nature of conformational and functional changes that occur in their thylakoid membranes and other chemical structures of grain and leaf tissues.

Introduction

The second half of the 20th and the first decade of the 21st century are characterized by a great success achieved in maize breeding and the production of basic and certified seed. The number of plants per area unit has been growing since 1976. This trend in maize breeding was referred to as a "plant density" programme and it further directly affected the yield increase of high quality certified seed [1]. In addition, a programme on the development of maize inbred lines with erect top leaves was established at the same time as the "plant density" programme. It was considered that these inbreds were the closest to the proposed efficient photosynthetic model [2]. The complementary implementation of these programmes led to new results in both, maize breeding and the hybrid seed production [3]. New and numerous hybrids with high grain and silage yields were developed and grown on large areas due to their high yielding potential and the appropriate quality of the plant and the grain [4]. The objective of the present study was to prove that prestigious inbred lines with erect top leaves and high-yielding maize hybrids, derived from these inbreds, can be an efficient photosynthetic model, meaning that they can contribute to efficient breeding, increased production and diverse utilisation of commercial maize.

Materials and Methods

The studies were performed with three elite maize inbred lines with erect top leaves, ZPPL 16, ZPPL 218 and ZPPL 62, belonging to the collection of the Maize Research

Institute, Zemun Polje. Overall studies of the stated inbred lines and selected maize hybrids with erect top leaves encompassed several series of experiments in which standard and other appropriate methodological procedures were applied. Following experiments have been performed: 1. The measure of an angle and leaf area, 2. Photosynthetic fluorescence measurements, 3. Dynamics of water status changes in grain, 4. Functional dependence of the yield of the selected maize hybrids with erect top leaves on their crop density, 5. Chemical composition, physical properties and grain structure of maize hybrids with erect top leaves.

Results and discussion

This study was an attempt to answer the following questions by using different tests and analyses: 1) are there reliable and dominant traits of maize inbred lines with erect top leaves by which planned and satisfactory progress in maize breeding and the high-quality hybrid seed and commercial maize production can be achieved? and 2) which traits maize inbred lines should have? According to the achieved results it can be established that non-invasive photosynthetic fluorescence method can be applied in breeding and the maize hybrid seed production and that the estimation of prestigious maize inbred lines for their resistance and adaptability to increased and high temperatures, as well as, to drought, can be performed. The application of the stated method provided the determination of many properties and parameters of photosynthetic apparatus of observed prestigious maize inbred lines with erect top leaves: (a) Temperatures at which smaller or greater conformational and functional changes in the thylakoid membrane occur, (b) Values of activation energies (E_a , kJ mol^{-1}) along straight lines before and after the occurrence of critical temperatures in the thermal process (Table I), (c) Different monotony of the increasing part of the thermal curve, which points out to uneven resistance and adaptability to increased and high temperatures, as well as, to drought, and (d) It was shown that observed inbred lines have a trait of the erect position of top leaves and a greater dry down rate in the grain maturation period.

The following relevant properties of maize hybrids, developed from the stated maize inbred lines with erect top leaves, were analysed: dependence of their yields on the crop density and quality of commercial maize of observed maize hybrids. It was presented that observed maize hybrids tolerated crop densities up to 70,000 plants ha^{-1} . It was shown that commercial maize of observed maize hybrids with erect top leaves was of exceptional quality that provided its diversified utilisation (Table II).

Tab.1. Changes in activation energies (E_a) and critical temperatures (t , $^{\circ}\text{C}$) in the course of thermal processes in the thylakoid membrane of the intact above-ear leaf of studied maize inbred lines with erect top leaves

ZPPL 16		ZPPL 218		ZPPL 62	
E_a , kJ mol^{-1}	t , $^{\circ}\text{C}$	E_a , kJ mol^{-1}	t , $^{\circ}\text{C}$	E_a , kJ mol^{-1}	t , $^{\circ}\text{C}$
-	29.5	-	27.0	-	28.0
48.4	45.9	43.1	29.0	45.0	36.0
84.3	48.0	27.3	36.9	91.8	41.0
46.7	53.0	37.0	43.5	119.7	46.9
49.2	54.8	42.5	47.8	132.0	49.0
-	60.0	51.1	49.9	-	-

Tab.2. Yields (t ha⁻¹) of maize hybrids with erect top leaves under irrigation conditions of Zemun Polje obtained in seven plant densities*

Plant density in 1000/ha	ZP 341 FAO 300	ZP 434 FAO 400	ZP 578 FAO 500	ZP 684 FAO 600
40,8	10.02	10.90	11.32	11.16
50,1	12.01	11.95	12.67	12.96
59,5	12.73	12.04	13.10	13.80
69,7	13.48	13.17	14.18	13.49
79,4	13.55	13.89	15.00	13.84
89,3	13.48	13.61	14.90	13.86
98,5	13.34	13.36	14.67	14.00
\bar{X}	12.66	12.70	13.69	13.30

*Results obtained in the 2003-2008 period

References

- [1] Č. Radenović, D. Ristanović, V. Trifunović,: The theoretical and the development programme on the increase of the plant number per area unit for the development of erect leaf maize lines and for their more effective application in breeding. -The internal note (in Serbian), Maize Research Institute, Zemun Polje, Belgrade, 1978, 1-3.
- [2] Č. Radenović, D. Grodyinskij, Erect leaf maize inbred lines - an efficient photosynthetic model. - A written communication Belgrade-Kiev and vice versa, 1998.
- [3] L. Kojič, Yield of ZP maize hybrids of different selection periods, Kukuruz (in Russ.), 1993, **93**: 1-13.
- [4] M. Ivanović, R. Petrović, G. Drinić, V. Trifunović, L. Kojić, M. Vuković, M. Mišović, G. Radović, D. Ristanović, Z. Pajić, B.V. Trifunović, D. Jelovac, Fifty years of ZP hybrids breeding. in: Book on Proceedings of Breeding, Production and Maize Utilisation - 50 Years of Maize Research Institute (in Serbian), Maize Research Institute, Zemun Polje, Belgrade, 1995, 3-16.

THE APPLICATION OF PHYSICOCHEMICAL METHODS FOR THE ANALYSIS OF RADIATION PROCESSED FOOD PRODUCTS

Z. Rogić¹, I. Spasojević², A. Ignjatović¹ and M. Mojović¹

¹*Faculty of Physical Chemistry, University of Belgrade, Studentski Trg 12–16,
11158 Belgrade, Serbia*

²*Institute for Multidisciplinary Research, Kneza Višeslava 1, 11000 Belgrade, Serbia
milos@ffh.bg.ac.rs*

Abstract

The aim of this study was to investigate the occurrence and stability of free radicals in freeze-dried samples of cow milk, pineapple and banana after irradiation (10 kGy dose), using the ESR spectroscopy, as well as to assess possible changes in their protein structure by means of electrophoresis.

Introduction

The application of irradiation in order to preserve food quality has been neglected for a long time in comparison to other methods, mainly due to prejudices. However, the attitude of consumers towards food irradiation is now becoming more positive due to spreading of information and knowledge of this process as well as to the availability of a number of analytical methods to detect aftermath of radiation treatment [1]. ESR spectroscopy due to its ability to reveal the presence of minute amounts of free radicals generated by irradiation plays a leading role in such studies [2]. The procedure for food samples used in these experiments is based on the fact that non-irradiated samples give poor signals, while in irradiated samples the significant increase of amplitude of EPR signal is noticed. Although the nutrient proprieties of irradiated food are no longer in question, there is a need for irradiation control in the international food trade in order to enhance consumer confidence in the regulation [3].

Experimental

Samples of cow milk, pineapple and banana were cryogenically dried, pulverized and then freeze-dried. The ESR spectra of irradiated and non-irradiated samples (control) of the same mass were obtained using X-band EPR spectrometer, and standard SDS-PAGE electrophoreses was used for detection of radiation induced protein degradation products.

Results and Discussion

The difference in the EPR peak heights of free radicals of the control and irradiated samples is obvious (Fig.1). Radiation induced signal decay with time (banana sample week II shows aberration most likely due different orientation of the sample in the EPR cavity), but clearly indicate that radiation treatment can be detected long after its application.

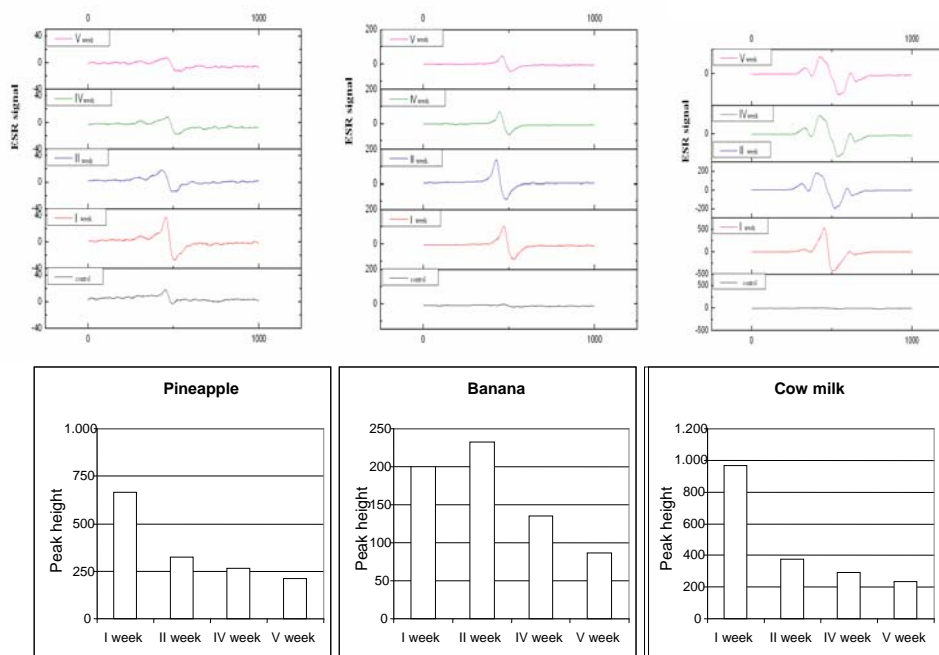


Fig.1. Typical ESR spectra and calculated absolute EPR peak heights of different food samples

In the second part of the experiment samples were subjected to SDS electrophoresis in order to detect any changes in the concentration of proteins.

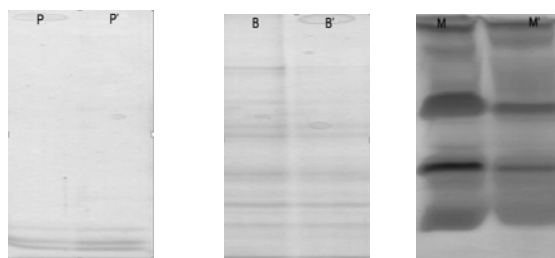


Fig.2. SDS-PAGE gels of: P - pineapple, P' - irradiated pineapple, B - banana, B' - irradiated banana, M - milk, M' - irradiated milk.

Pineapple (Fig.2.P, P') sample shows very small number of low molecular weight proteins, but also no change in the concentration of proteins. Banana (Fig.2.B, B') shows different molecular weight proteins, as well as the loss of some higher molecular mass proteins during radiation. Milk sample (Fig.2.M, M') is extremely sensitive to radiation. Gel presents proteins in a wide range of molecular weight, as well as many proteins of similar molecular weight. Reduction of the intensity and of the number of strips on gel of irradiated milk sample is present. Tested samples of banana and cow milk showed the destruction of proteins, while a change in the sample of pineapple is negligible. Changes in the number and width of protein fragments in gel are a clear proof that during the radiation degradation of existing protein molecules into smaller molecular fragments occurred.

Conclusion

Based on the results obtained by ESR spectroscopy and electrophoresis, we demonstrated that the tested samples suffered a series of changes after the application of 10 kGy ionizing radiation which is commonly used for food preservation.

Electrophoresis shows that radiation treatment undoubtedly breaks peptide links affecting the decomposition of certain proteins, reducing their concentration, and decays polypeptide chains of high molecular weight proteins into smaller fragments.

EPR spectra showed that ionizing radiation enhances cellulose and sugar radical EPR signal in tested samples of cow milk, banana and pineapple. By investigating EPR signal attenuation in time it can be reliably determined whether any of these groceries had been treated by radiation even after longer periods of time after the radiation. Furthermore, we concluded that sample of cow milk powder could potentially be used as radiation dosimeter since free radicals generated under the influence of ionizing radiation showed a weak recombination in time.

Acknowledgments

The authors acknowledge their gratitude to the Ministry of Science of Republic of Serbia for the financial support (Project #143016).

References

- [1] M. P. Esteves, M. E. Andrade, J. Empis, *Radiation Physics and Chemistry*, 1999, **55**, 737-742.
- [2] O. G. Dului, R. Georgescu, S. I. Ali, *Radiation Physics and Chemistry*, 2007, **76**, 1031-1036.
- [3] J. Raffi, N. D. Yordanov, S. Chabane, L. Douifi, V. Gancheva, S. Ivanova, *Spectrochimica Acta Part A*, 2000, **56**, 409-416.

NOTES ON THE CALIBRATION OF ROUTINE DOSIMETERS IN RADIATION PROCESSING

B. Šećerov¹ and G. Bačić²

¹*Institute of Nuclear Sciences "Vinča", Serbia*

²*Faculty of Physical Chemistry, University of Belgrade, Serbia*

Abstract

The essential prerequisite of radiation dosimetry is to provide quality assurance and documentation that the irradiation procedure has been carried out according to specifications requirement of the correct calibration of the chosen dosimetry system. In the Radiation Plant at the Vinča Institute, we compared two recommended protocols in calibration of dosimetry systems in radiation processing: (i) by using standardized routine dosimeters (ethanol-chlorobenzene ECB) from the reference laboratory and (ii) by in-plant calibration with the alanine transfer dosimeters. The analysis of results showed that our in-plant calibration is as good as when standardized dosimeters are used, thus validating our irradiation geometry in the irradiation process.

Introduction

Radiation processing in all areas requires proper use and selection of a dosimetric system for the measurement of the absorbed dose. Quality control is based on the validation of the calibration procedure and the assurance that the process was performed within prescribed dose limits. International guides for calibration of dosimeters recognize two possible procedures [1]: (i) Calibration of the routine dosimetry system can be carried out directly in a national or accredited standard laboratory by standardized irradiation of routine dosimeters. (ii) An alternative method requires routine dosimeters to be irradiated together with reference or transfer-standard dosimeters in the production irradiator (in-plant calibration). The first method is preferred by many, however one NPL report [2] recommends in the first place calibration by irradiation in the plant where the dosimeters are to be used, because this procedure accurately reflects conditions under which actual irradiation occurs. The present article evaluates both of the recommended methods and investigates their advantages and disadvantages in concrete irradiation conditions in gamma radiation processing at the Radiation Plant of the Vinča Institute using ethanol-chlorobenzene (ECB) dosimeters as routine dosimeters.

Experimental

The ECB dosimeters were prepared at the Vinča Institute in accordance with the procedures described in the corresponding standard [3] and placed in 2 ml glass pharmaceutical ampoules and flame-sealed. One batch (I) was sent for calibration to the Riso High Dose Reference Laboratory (HDRL). The second batch (II) was prepared to be used as routine dosimeters. The phantom with dosimeters consisted

of: (i) three ampoules with an ECB solution (batch II), (ii) two ECB ampoules from batch I, and (iii) an alanine dosimeter, supplied by HDRL, for in-plant calibration were placed in the central part of the box with the product for sterilization and irradiated in sterilization cycles between 5 – 35 kGy. The absorbed doses of the ECB dosimeters were measured by the oscillotitrator OK – 302/2, while the alanine dosimeters were sent to HDRL for dose determination.

Results and Discussion

The results of the calibration procedure of routine dosimeters are presented in Table 1 and in Fig. 1. The differences of absorbed doses measured by standard alanine and ECB dosimeters are within 1%, which is an excellent agreement between two methods. This is important since these two dosimeters have different geometry (thin alanine pellets vs. ‘bulky’ ECB ampoules) and the dose gradient within the calibration phantom can induce a difference in the dose delivered to these two dosimeters. The absorbed doses from Table 1 were used for construction of the calibration diagram for the new batch of ECB dosimeters (Fig.1).

Table 1. Absorbed dose as measured by standard alanine and ECB dosimeters.

Alanine dosimeters measured in HDRL	6.2 kGy	12.7 kGy	23.8 kGy	34.5 kGy
ECB dosimeters calibrated by HDRL	6.2 kGy	12.8 kGy	23.9 kGy	34.1 kGy

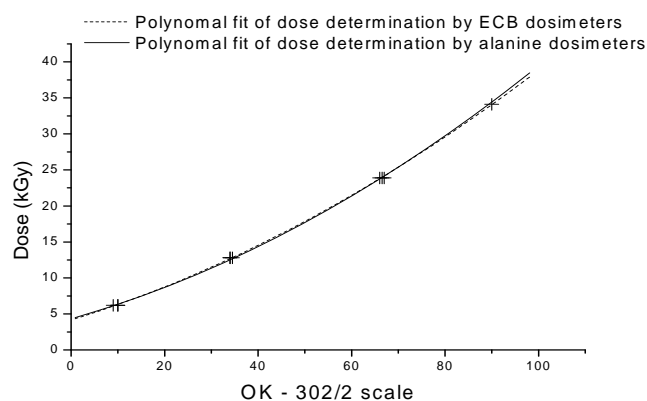


Fig.1. Calibration curves for the new batch of ECB dosimeters (routine dosimeters). The oscillotitrator readings are compared to doses measured by the two standard dosimeters. Curves represent the second order polynomial fit for doses between 5 – 35 kGy.

According to the international standards [2, 4] the test for the goodness of fit for the calibration curve is a residual difference between the measured and predicted values. The lower value for residual means a better fit. Figure 2 presents the residuals of calibration curves presented in Fig.1. As can be seen, residuals of these two calibrations are also very similar. The highest value for residuals is $\pm 2\%$ for doses below 10 kGy. Residual decreases when the absorbed dose increases, which is expected because the relative error is smaller when the measured value increases. This shows that our in-plant calibration using the alanine dosimeters appears to be as good as the one using the ECB standards.

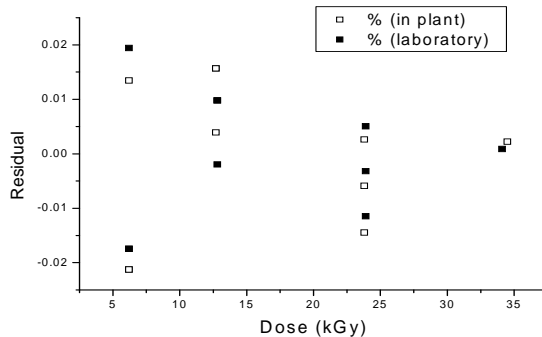


Fig.2. Residuals for curves presented in Fig. 1.

For in-plant calibration the critical point is irradiation geometry. An erroneous positioning of the irradiation phantom during irradiation can be the source of error in dose determination for calibration, so this position shall be validated. For that purpose one should calculate overall uncertainties according to [2, 4, 5]. The uncertainties of the nominal dose for dosimeters irradiated in HDRL are: ECB ampoules 3%; alanine 2.6%. In our conditions, the difference between the two dosimeters is less than 1% (Table 1). The effect of irradiation temperature on the reading of the dosimeter should be considered, since readings of alanine dosimeters are temperature sensitive, while ECB dosimeters are not. Knowing the temperature range during irradiation and according to the standard [6], the estimated uncertainty is 1.3%. Hence, the combined standard uncertainty is 3.1% for in-plant calibration using alanine dosimeters.

In conclusion, both irradiation procedures for dosimeter calibration have the same level of uncertainty; hence in-plant calibration is certainly the method of choice providing the careful placement of the irradiation phantom.

References

- [1] ISO/ASTM 51261, Guide for selection and calibration of dosimetry systems for radiation processing, 2002.
- [2] P. Sharpe, A. Miller, NPL Report CIRM, Guidelines of calibration of dosimeters for use in radiation processing, 1999.
- [3] ISO/ASTM 51538, Standard practice for use of the ethanol-chlorobenzene dosimetry system, 2002.
- [4] ISO/ASTM 51707, Standard guide for estimating uncertainties in dosimetry for radiation processing, 2002.
- [5] Guide to expression of uncertainty in measurements, International Organization for Standardization, Geneva, Switzerland, 1993.
- [6] ISO/ASTM 51607, Practice for use of alanine – EPR dosimetry system, 2002.

CHRONIC PSYCHOSOCIAL ISOLATION ALTERS HSP70/GR AND HSP90/GR RATIOS IN RESPONSE TO NOVEL ACUTE STRESS IN RAT HYPOTHALAMUS

I. Simić, A. Đordjević, J. Đorđević, M. Mitić, M. Radojčić and M. Adžić

Vinča Institute of Nuclear Science, P.O. Box 522, 11001 Belgrade, Serbia

Abstract

It is known that chronic psychosocial isolation (CPSI) exerts maladaptive effect on the hypothalamic-pituitary-adrenal (HPA) axis activity. Since the hypothalamus (HT) is a major driver of the HPA axis activity and since glucocorticoid receptor protein (GR) mediates HPA axis negative feedback particularly in this structure, we studied the effect of CPSI by following the expression of GR and its chaperones hsp70 and hsp90 in HT. Our results showed that the ratios of HSPs/GR set by the CPSI were altered in response to a novel acute stress, which indicated negative CPSI influence on GR functions in HT.

Introduction

Stress response involves the activation of the hypothalamic-pituitary-adrenal (HPA) axis and the key driver of this activity is hypothalamus (HT). The final products of the HPA axis activity are glucocorticoids (GCs) that act through glucocorticoid receptor (GR) and mediate feedback inhibition of the HPA axis particularly *via* the HT [1]. The GR is a ligand-dependent transcription factor that in absence of GCs resides in the cytoplasm as a multiprotein heterocomplex with heat shock proteins (HSPs) hsp70 and hsp90 [2]. While hsp70 protein is essential for maturation of GR, hsp90 helps GR to achieve a hormone-binding conformation [2]. Upon hormone binding, GR dissociates from hsp90 and translocates to the nucleus where both HSPs continue to influence its further functions. Namely, hsp90 is required for nuclear GR to regain hormone-binding competence [2], but it may also reduce GR activity when hsp90/GR ratio is increased [3]. Hsp70 plays a general role in sequestering denatured proteins in nucleus including GR [2]. Considering the essential role of HT in regulating HPA activity under stress conditions, as well as, the role of hsp70 and hsp90 in GR signaling, we investigated a pattern of expression of these proteins and their cellular redistribution in the HT of Wistar rat under different types of stress. We were mostly interested in the effect of CPSI on mentioned parameters and in their reversibility in response to subsequent acute stress [4].

Experimental

The animals (adult Wistar male rats) were divided into four groups: (I) controls (untreated); (II) acute stress (30 min of immobilization); (III) chronic psychosocial isolation (CPSI) (for 21 days) and (IV) combined stress (chronic isolation followed by 30 min immobilization). After sacrifice, blood was collected and corticosterone

(CORT) concentration was determined by OCEIA Corticosterone kit. The cytosolic and nucleosolic samples of HT were prepared by differential centrifugation. The proteins were detected using Western blot technique and antibodies M-20, hsp70 (N27F3-4) and hsp90 (F-8) for GR, hsp70 and hsp90, respectively. β -actin was used as a loading control.

Results and discussion

All results are represented in Figure 1.

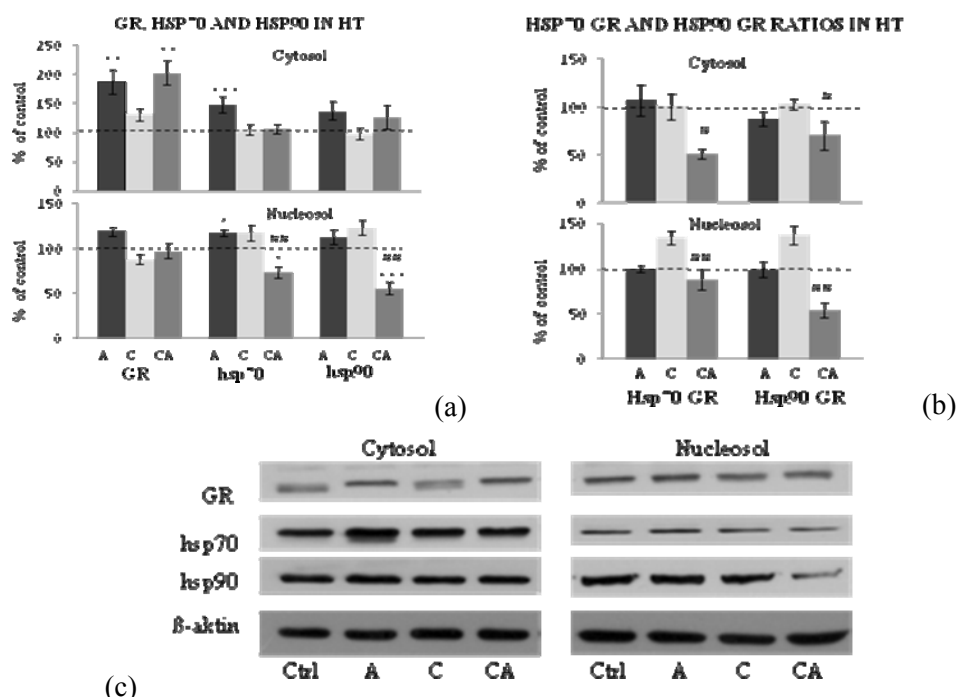


Fig.1. Hypothalamic GR, hsp70 and hsp90 in the cytosol and nucleosol of animals exposed to acute (A), chronic (C) and combined (CA) stresses: expression levels (a); hsp70/GR and hsp90/GR ratios (b) and representative Western blots (c). Data are presented as mean \pm SEM (n=10) and analyzed by one-way ANOVA (*p<0.05, ** p<0.01, *** p<0.001 stress vs control; #p<0.05, ##p<0.01 chronic vs combined stress).

In response to acute stress, when CORT levels were elevated (612.75 \pm 20.12 ng/ml) in respect to control (98.35 \pm 20.76 ng/ml), significantly increased levels of GR in the cytosol and hsp70 in both compartments were detected. This elevation of GR in the cytosol could be result of increased synthesis and/or stability and could represent enhanced sensitivity to GCs of this brain structure. The augmentation of hsp70 could indicate activation of cellular stress response [5].

Chronically stressed animals showed decreased CORT levels (54.26 \pm 9.21 ng/ml) which were consistent with our previous experiments [4]. The levels of either studied proteins were not statistically changed.

When chronically stressed animals were subjected to novel acute stress, CORT levels (604.31 ± 21.05 ng/ml) as well as GR levels in the cytosol were elevated again. In contrast to acute stress, HSPs levels were decreased in the nucleosol. That could represent inadequate cellular stress response [5] and thus maladaptive effect of CPSI regarding this parameter.

Examining the hsp70/GR and hsp90/GR ratios we found that response of chronically stressed animals to novel acute stress was different from response of control animals to acute stress. Particularly, novel acute stress turned both HSPs/GR ratios in favor of GR, in both compartments. Considering the fact that for appropriate GR function optimal levels of its HSPs in both cellular compartments are required, these results indicated maladaptive influence of CPSI on GR function in the HT.

Conclusion

Chronic stress (CPSI) altered hypothalamic HSPs/GR ratios and compromised response of this structure to a subsequent acute stress. This finding suggested potentially maladaptive influence of CPSI with regard to the HPA axis feedback activity in hypothalamus.

References

- [1] E. R. de Kloet et al., *Endocr. Rev.*, 1998, **19**, 269-301.
- [2] D. B. DeFranco, *Kidney International*, 2000, **57**, 1241-1249.
- [3] K. I. Kang et al., *Proc. Natl. Acad. Sci.*, 1999, **96**, 1439-1444.
- [4] A. Djordjevic et al., *Neuropsychobiology*, 2009, **59**, 213–221.
- [5] R. I. Morimoto, M. G. Santoro, *Nature Biotechnology*, 1998, **16**, 833-838.

POLARIZED FT-IR STUDY OF CELL WALL OF A HARDWOOD (MAPLE BRANCH)

J. Simonović¹, J. Stevanic², D. Đikanović¹, J. Bogdanović Pristov¹,
L. Salmén² and K. Radotić¹

¹ Institute for multidisciplinary study, Kneza Višeslava 1, 11000 Belgrade, Serbia

² Innventia, Box 5604, SE-114 86 Stockholm, Sweden

Abstract

Mechanical and physical properties of wood fibres are dependent on the orientation of constituent polymers (cellulose, hemicellulose, lignin). Fourier transform infrared (FTIR) microscopy was used to examine the orientation of the main wood polymers in transversal and longitudinal direction of the isolated cell wall of the maple branch. The polarised FTIR measurements indicated that glucomannan and xylan appear to have parallel orientation with regard to the orientation of cellulose. Lignin has also parallel orientation.

Introduction

Cell wall can be considered as a nano-composite in which cellulose, lignin and hemicelluloses are interconnected in a specific manner. Structural organisation of the cell wall and related polymers is important for both mechanical properties of plants and chemical reactions occurring in the wall space, especially in the response to stress. By using imaging FT-IR microscopy, run in transmission mode and at different polarisation modes (from 0° to 90°), it is possible to follow the chemical variability and the orientation of cell wall polymers [1]. The orientation of cellulose, glucomannan, xylan and lignin, as essential components of the wood, were analysed by iFTIR with regard to the sample axis.

Materials and methods

The purified isolated cell wall material was obtained from maple (*Acer sp.*) branches by methanol extraction and subsequent purification using a series of solvents (phosphate buffer, 1% Triton X-100, 1M sodium chloride, distilled water, methanol, acetone) [2]. FTIR microscopy measurements were carried out using a Spectrum Spotlight 400 FTIR Imaging System (Perkin Elmer Inc, Shelton, CT, USA). Spectral resolution: 8 cm⁻¹; spectral range: from 1800 cm⁻¹ to 720 cm⁻¹. Polarisation: the incident IR radiation was polarised by a gold wire grid polariser from 0° to 90° polarisation in relation to the fibre orientation with intervals of 5°. The sample was mounted on the sample stage as parallel as possible to the orientation of the 0° polarisation. The IR spectra were processed by the software Spotlight 1.5.1, HyperView 3.2 and Spectrum 6.2.0 (Perkin Elmer Inc., Shelton, CT, USA) [1].

Results and discussion

From the in-depth study of polymer orientation, three areas from the sample were selected. The transmission spectra recorded at 0° and 90° polarisation modes were

processed using a ratio function to produce an orientation spectrum ($R = T_{0^\circ} / T_{90^\circ}$), where R is ratio spectra, T_{0° is the transmission spectra recorded at 0° and T_{90° is transmission spectra recorded at 90° . Spectral signals related to absorptions from cellulose, hemicellulose (glucomannan and xylan) and lignin in the wavenumber range between 1800 cm^{-1} and 720 cm^{-1} can be identified. Figure 1 a) shows average absorbance spectra at 0° and 90° polarization angle and Figure 1b) shows the average orientation spectra for the maple branch cell wall. In Figure 1b), the positive signals indicate that their corresponding functional groups are arranged in a more parallel orientation to the fibre axis, and the negative signals indicate that their corresponding functional groups are arranged in a perpendicular orientation to the fibre axis.

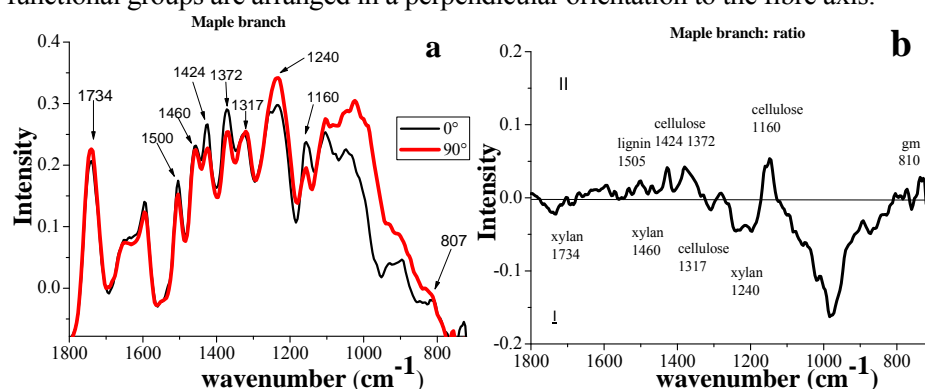


Fig.1. a) Average absorbance spectra of maple branch cell wall at 0° and 90° polarization angle; b) The average orientation spectra of maple branch cell wall.

The relative absorbance spectra are presented (Figure 2) as specific absorption peaks ($RA = (I_p - I_{\min}) / (I_{\max} - I_{\min})$) where RA is relative absorbance, I_p is intensity of the absorbed IR radiation at a given angle of the polarisation, P , I_{\max} is maximal intensity observed for a given vibration and I_{\min} is minimal intensity observed for a given vibration. These relative absorbance values were presented in relation to the angle of the incident IR polarisation (from 0° to 90°).

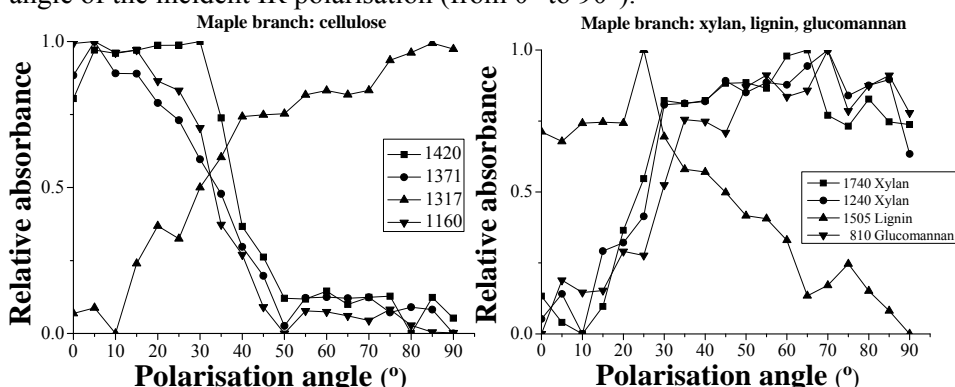


Fig.2. The relative absorbance of IR specific absorption wavenumbers plotted against the polarisation angle for the different wood polymers for maple branch.

Tree vibration peaks of cellulose, the antisymmetric C-O-C bridge stretching vibration at 1160 cm^{-1} , the C-H bending vibration at 1370 cm^{-1} and the C-OH bending vibration of the $\text{CH}_2\text{-OH}$ group at 1424 cm^{-1} was found to be oriented parallel to the fibre axis. The cellulose vibration (CH_2 wagging vibration at 1317 cm^{-1} oriented perpendicular to the cellulose chain was also found. Hemicelluloses (xylan - vibrations at 1734 cm^{-1} , 1240 cm^{-1} , and glucomannan - vibration at 810 cm^{-1}) are parallel with the longitudinal axis of the isolated cell wall of maple. A lignin vibration, i.e. the C=C aromatic ring vibrations at 1505 cm^{-1} showed a positive signal [3-5].

Conclusion

One can be concluded that both hemicelluloses are arranged in parallel with the cellulose microfibrils. These components show anisotropic behaviour. Lignin is also oriented parallel to the fibre axis in the cell wall.

Acknowledgements

This work was supported by Ministry of Science of Republic Serbia (Project #143043) and COST Action FP0802.

Reference

- [1] J. S. Stevanic, L. Salmén, *Holzforschung*, 2009, **63**, 497-503.
- [2] M. Chen et al, *Phytochem. Anal.*, 2000, **11**, 153-159.
- [3] R. H. Marchessault, *Pure Appl. Chem.*, 1962, **5**, 107-129.
- [4] R. H. Marchessault, C. Y. Liang, *J. Polym. Sci.*, 1962, **59**, 357-378.
- [5] M. Åkerholm et al, *Carbohydr. Res.*, 2004, **339**, 569-578.

KINETIC PROPERTIES OF NTPDases IN RAT BRAIN SYNAPTIC PLASMA MEMBRANES

I. Stanojević, M. Milošević, S. Petrović, D. Drakulić, N. Veličković and A. Horvat

Laboratory of Molecular Biology and Endocrinology, Institute of Nuclear Sciences "VINČA", University of Belgrade, P.O. Box 522, 11001 Belgrade, Serbia

Abstract

Kinetic properties of ecto-nucleoside triphosphate diphosphohydrolase (NTPDases) in synaptic terminals from whole rat brain were characterised. Three different NTPDases are present in nervous system and hydrolysing ATP and ADP with different affinities. ATP and ADP hydrolysis exhibited kinetic properties typical for all members of the NTPDase, low substrate specificity for tri- and diphosphonucleosides, divalent cation dependency and insensitivity towards ion-transporting ATPase inhibitors. Kinetic properties of ATPase and ADPase component of NTPDases depend on postnatal developmental stages of rats, and indicated different NTPDase family members present in various ontogeny stages. Lowering in the NTPDases activities could result in a decreased production of adenosine and change in extracellular ATP/adenosine ratio.

Introduction

Extracellular adenine nucleotides, such as ATP and adenosine, are important signalling molecules in central nervous system (CNS). They are involved in the regulation of a variety of physiological and pathological processes in the CNS, including development. Like classical neurotransmitters, ATP is stored in presynaptic vesicles and released into synaptic cleft, where it acts as P2 nucleotide receptors ligand, exerting immediate effects, such as neurotransmission and long lasting trophic effects [1]. Extracellular ATP actions are terminated by ecto-nucleoside triphosphate diphosphohydrolases (NTPDase), a group of membrane-bound ecto-nucleotidases that hydrolyze terminal phosphate residues of nucleotides. Three NTPDases (NTPDase1–3), differing in their preference for a substrate, have been localized in the brain. Thus, NTPDase1 hydrolyzes ATP and ADP equally well, resulting in AMP formation, whereas NTPDase2 have strong preference for ATP producing ADP. NTPDase3 degrades ATP to AMP with a transient ADP accumulation [2]. Ecto-5'-nucleotidase further hydrolyse AMP to adenosine. The aim of this study was to investigate the divalent cation dependency and effects of different inhibitors on NTPDases in SPM from adult rat brain and to determine kinetic parameters for ATP and ADP hydrolysis in brain SPM obtained from rats in different stages of ontogeny.

Experimental procedures

Female Wistar Albino rats at different developmental stages, 15- (juvenile), 30- (pre-pubertal), 60- (young adult) and 90- (adult) days old, were used in this study. Synaptic plasma membranes (SPM) were isolated from whole rat brains. Rate of

ATP and ADP hydrolysis were measured under *in vitro* conditions, by colorimetric determination of released phosphate, in the presence of 40 µg SPM proteins, 1 mM ATP or ADP, 5 mM MgCl₂, and 50 mM Tris-HCl buffer, pH 7.8, incubated at 37 °C for 15 min. Incubation time and protein concentration were chosen in order to ensure the linearity of the reaction. Activation of ATPase and ADPase was estimated by increasing concentrations of ATP or ADP under the same conditions as previously described in the presence of 0.05 - 2.5 mM ATP/ADP. Kinetic analysis of NTPDase activity in each membrane preparation was performed by computer-assisted least square fitting of the data to the Michaelis-Menten equation, while kinetic parameters, V_{max} (apparent maximal velocity) and K_m (apparent Michaelis constant) values, were calculated from Eadie-Hofstee semi-reciprocal plot of V versus V/[S]. Statistical analyses were performed by Student's *t*-test, considering *p* < 0.05 as significant.

Results and discussion

NTPDases are activated by divalent cations, and EDTA inhibits their activity almost completely (Table 1). Both, ATP and ADP hydrolysis were more effective with Mg²⁺ in respect to Ca²⁺ ions with 2 times higher activity for ATPase and 3-12 times for ADPase activity. The contributions of other ATP/ADP hydrolyzing enzymes in our experimental conditions were summarized in Table 2. As shown, inhibitors of non-specific alkaline phosphatase (NaF, teophiline and levamisole) do not significantly affect ATP and ADP hydrolysis, indicating that these enzymes do not participate in the reaction. In this assay conditions there is no ecto-nucleotide pyrophosphatase (E-NPP) activity as shown by implying E-NPP substrate (pNp-TMP) instead of ATP or ADP. Other inhibitors, orthovanadate, 10 mM NaN₃ and ouabain, were found to be a potent but non-specific inhibitors of ATPase and/or ADPase.

Table 1. Effect of divalent cations on ATPase and ADPase activity in SPM preparations.

Hydrolyzing activity (nmol Pi/min/mg)		
Cation	Total ATPase activity	ADPase activity
<i>basal</i>	66.43 ± 4.62	12.63 ± 1.73
<i>basal + 5 mM EDTA</i>	0	0
<i>1 mM MgCl₂</i>	179.48 ± 5.26	33.28 ± 2.71
<i>5 mM MgCl₂</i>	151.20 ± 6.32	29.08 ± 2.36
<i>1 mM CaCl₂</i>	79.57 ± 1.82	9.96 ± 1.22
<i>5 mM CaCl₂</i>	72.65 ± 2.64	2.40 ± 0.39
<i>5 mM MgCl₂ + 5 mM EDTA</i>	15.73 ± 1.82	0
<i>5 mM CaCl₂ + 5 mM EDTA</i>	0	0

The influence of divalent cations on ATPase and ADPase activity was determined in the presence of 1 mM ATP or ADP as substrates and different concentration of cations with or without EDTA.

ATP and ADP were hydrolysed by SPMs NTPDases in accordance with Michaelis-Menten kinetics. The V_{max} and K_m values derived from these plots are shown in Table 3. Similar patterns of the activation by increasing ATP or ADP

concentrations were observed at all ages, but with activities plateau in day 30 and 60. The highest apparent affinity for ATP was observed in SPM from 15 day-old rats, and for ADP in SPM from 30 day-old rats.

Table 2. Effect of different inhibitors on ATPase and ADPase activity in SPM preparations.

Residual activity in the presence of inhibitor (% of control)		
Inhibitor	Total ATPase activity	ADPase activity
<i>NaN₃</i> (10 mM)	71.3 ± 3.3 ***	68.5 ± 1.5 ***
<i>NaF</i> (1 mM)	94.3 ± 1.5	99.5 ± 1.5
<i>teophylline</i> (1 mM)	93.0 ± 1.2	93.5 ± 4.5
<i>ouabain</i> (1 mM)	89.3 ± 3.8	80.5 ± 0.5 ***
<i>orthovanadate</i> (0.1 mM)	50.0 ± 3.2 ***	33.5 ± 3.7 ***
<i>levamisole</i> (1 mM)	97.0 ± 1.0	105.0 ± 6.0
<i>vNv-TMP</i> (1 mM)	0	0

*** p > 0.001

Table 3. Kinetic parameters of ATPase and ADPase activities in total SPM preparations from whole rat brains in different postnatal stages. Kinetic parameters K_m and V_{max} were obtained by Eadie–Hofstee transformation of the data obtained from Michaelis-Menten kinetics.

Age	ATP-		ADP-	
	K_m (mM)	V_{max} (nmol Pi/mg/min)	K_m (mM)	V_{max} (nmol Pi/mg/min)
15 days	0.338 ± 0.031	161.557 ± 7.324	0.722 ± 0.147	66.621 ± 5.745
30 days	0.367 ± 0.019	220.298 ± 5.438	0.290 ± 0.277	53.122 ± 1.809
60 days	0.380 ± 0.024	216.150 ± 6.636	0.304 ± 0.040	51.259 ± 2.192
90 days	0.441 ± 0.031	198.227 ± 5.914	0.702 ± 0.161	46.517 ± 4.439

Conclusion

ATP and ADP hydrolysis exhibited kinetic properties typical for all members of the NTPDase, low substrate specificity for tri- and diphosphonucleosides, divalent cation dependency and insensitivity towards other ATPase inhibitors. Kinetic properties of ATPase and ADPase component of NTPDases are different in various postnatal stages, and indicate the presence of different NTPDase-family members during ontogeny. Lowering in NTPDases activities during rat maturation could result in a decreased production of adenosine and change in extracellular ATP/adenosine ratio.

Acknowledgements

The Serbian Ministry of Sciences, Project No. 143044 supported this study.

Literature

- [1] G. Burnstock, *Physiol Rev.*, 2007, **87**, 659–797
- [2] H. Zimmermann, *Naunyn-Schmied. Arch. Pharmacol.*, 2000, **362**, 299–309.

CARBON ION BEAM AS INDUCER OF MELANOMA CELL APOPTOSIS

J. Žakula¹, L. Korićanac¹, O. Keta¹, G. A. P. Cirrone², G. Cuttone²,
A. Ristić-Fira¹, I. Petrović¹

¹*Vinča Institute of Nuclear Sciences, P.O.Box 522, Belgrade, Serbia.*

²*INFN Laboratori Nazionali del Sud, via S. Sofia 62, Catania, Italy*

Abstract

In vitro effect of carbon ions on apoptosis was studied. The human melanoma HTB140 cells were irradiated with the 62 MeV/u ¹²C ion beam. Percentage of apoptotic cells was evaluated by flow-cytometry and the corresponding apoptotic indexes were calculated. The expression of apoptosis-associated proteins, p53, Bax and Bcl-2 was estimated by Western blot analyses. A dose dependent increase of apoptosis was revealed, with the maximum value of 17 % after irradiation with 16 Gy, and the apoptotic index of 7.7. Pro-apoptotic effects of carbon ion beams were confirmed by the detected changes of key regulators of the mitochondrial apoptotic pathway, the p53 protein expression and the Bax/Bcl-2 ratio.

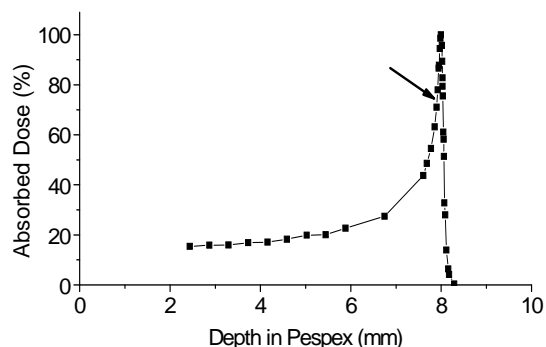
Introduction

It is well known that cancer is a major health problem. Approximately 11 million people worldwide are diagnosed with cancer, while each year almost 7 million people die of the disease. About 40 % of cured patients are treated by radiotherapy. Its main aim is to deliver a maximally effective dose of radiation to the tumor site while sparing the surrounding healthy tissues as much as possible [1]. Melanoma, a highly aggressive form of cancer, is known to be radio-resistant with powerful metastatic potential and dissimilar response to conventional radiotherapy [2]. With respect to conventional radiotherapy, carbon ions have a unique advantage due to their physical properties. Thus, due to high linear energy transfer (LET) quite better dose effect on malignant tissue is achieved [3]. In the response to a variety of stresses, the tumor suppressor protein p53 plays a protective role to the genome provoking either cell cycle arrest or programmed cell death - apoptosis [4]. The mechanism by which p53 protein might trigger apoptotic machinery involves transcriptional activation of the pro-apoptotic members of Bcl-2 family and repression of the anti-apoptotic regulators [5]. After an apoptotic stimulus, the ratio of Bax protein, an inducer of apoptosis, to Bcl-2, an inhibitor of apoptosis, determines cell survival or death [6].

With the intent to better understand mechanisms involved in the induction of apoptosis, the effects of accelerated carbon ions on the apoptotic status and the regulatory molecules involved in apoptosis were investigated.

Results and discussion

Analysis of the apoptotic status of the HTB140 human melanoma cells were performed within the Bragg curve of the 62 MeV/u ^{12}C ion beam produced by the superconducting cyclotron at Istituto Nazionale di Fisica Nucleare, Laboratori Nazionali del Sud (INFN-LNS), in Catania (**Fig.1**). The doses ranged from 2 to 16 Gy, with the average dose rate of 11.45 ± 0.31 Gy/min. At the irradiation position the relative dose was 73.37 ± 3.92 %, while the LET value was ~ 285 keV/ μm .



Dose (Gy)	Apoptosis (%)	Apoptotic index (AI)
0	2.23 ± 0.06	1
2	5.46 ± 0.14	2.45
4	9.08 ± 0.06	4.07
8	14.2 ± 0.09	6.37
12	13.2 ± 0.01	5.92
16	17.2 ± 0.02	7.71

Table 1. The dose dependent apoptosis in the HTB140 cells 48 h after irradiation with ^{12}C ions.

Fig. 1. Depth dose distribution in Perspex of the 62 MeV/u ^{12}C ion beam produced at INFN – LNS. Arrow indicates irradiation position.

The percentage of apoptotic cells was evaluated 48 h after irradiation by flow-cytometry. Corresponding apoptotic indexes of HTB140 cells were calculated and the obtained values are given in Table 1.

Carbon ions induced the dose dependent increase of apoptotic cells 48 h after irradiation. Percentage of apoptosis ranged from 5.46 to 17.2 %. Similar level of apoptosis was already reported for the same cell line exposed to protons and γ -rays [7]. All these results point out high radio-resistance of the HTB140 cells. The dose dependent increase of apoptotic cells in this irradiation position could be attributed to the severe damage induced by high LET of carbon ions, leading to the induction of late apoptosis or necrosis.

Apoptotic index also showed a dose dependent increase with maximum value of 7.71 when the cells were irradiated with 16 Gy of ^{12}C ions. At 48 h after irradiation it clearly indicated the ability of ^{12}C ion beam to provoke programmed cell death of the resistant HTB140 cells.

To examine the molecular level of the observed induction of apoptosis, key regulatory molecules of the mitochondrial apoptotic pathway were analyzed under the described experimental conditions. This included the analysis of p53 protein expression (Fig. 2A), as well as the expression of Bax and Bcl-2 regulatory proteins, presented as the ratio of Bax and Bcl-2 (Fig. 2B).

Transcription factor p53 is known to provoke cell cycle arrest or apoptosis in response to cellular stress, such as DNA damage induced by drugs or radiation [8].

The dose dependent increase in the expression of p53 protein confirmed induction of apoptosis. It ranged from 238 to 554 % (Fig. 2A).

Literature data suggest that in certain cell types, after the DNA damage, Bax appears to be transcriptionally induced by p53 [9]. In this study it was shown that with the rise of the radiation dose the level of Bax increased. Moreover, the level of Bcl-2 protein decreased and the calculated Bax/Bcl-2 ratio clearly demonstrated induction of apoptosis. The dose dependent increase of Bax/Bcl-2 from 1.04 to 3.08 was estimated (Fig. 2B).

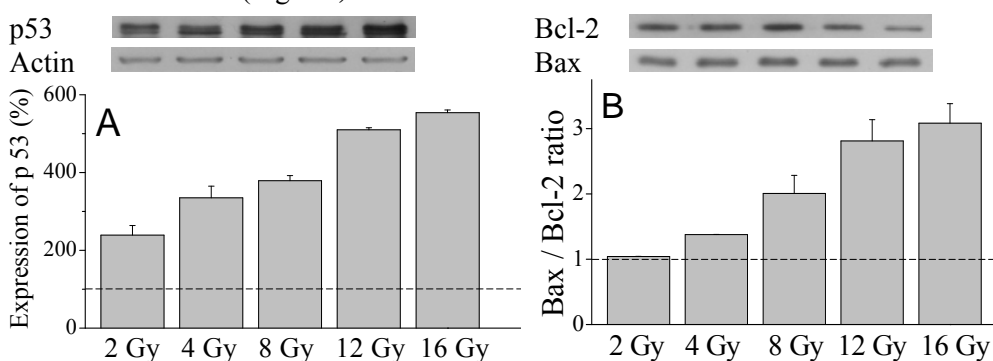


Fig.2. Western blot analysis of p53 protein expression (A) and Bax/Bcl-2 ratio (B) - 48 h after irradiation of HTB140 cells with 62 MeV/u ^{12}C ions.

Conclusions

To better understand biological mechanisms involved in cellular response to irradiation with ^{12}C ions having high-LET, the investigation of apoptotic cell death and corresponding protein expression was undertaken.

The results obtained pointed out a dose dependent increase of apoptosis in HTB140 cells after their irradiation with ^{12}C ions. The induction of apoptotic cell death was associated with the increase of the expression of p53 protein and Bax/Bcl-2 ratio.

References

- [1] M. Dosanjh, Proc. of 10th Symp. Med. Phys., 2008, **CP1032**, 12-16.
- [2] S. C. Barranco, et al, Cancer Research, 1971, **31**, 830-833.
- [3] I. Serizawa, et al, Int J Radiat Oncol Biol Phys., 2009, **75**, 1105-1110.
- [4] D. P.Lane, Nature, 1992, **358**, 15-16.
- [5] E. C. Thornborrow et al, Oncogene, 2002, **21**, 990-999.
- [6] T. Miyashita, et al., Oncogene, 1994, **9**, 1799-1805.
- [7] I. Petrović et al., Int. J. Radiat. Biol., 2006, **82**(4), 251-265.
- [8] D.W. Meek, Nat Rev Cancer, 2009, **9**(10), 714-723.
- [9] T. Miyashita et al., Cell, 1995, **80**(2), 593-601.

EFFECT OF VANADATE ON ^{31}P NMR SPECTRA OF *PHYCOMYCES BLAKESLEEANUS* IN VIVO

M. Žižić ¹, M. Živić ², T. Cvetić-Antić ³, and J. Zakrzewska ⁴

¹*Institute for Multidisciplinary Research, Kneza Višeslava 1, 11030 Belgrade, Serbia.*

²*Department of Biology, University of Novi Pazar, Vuka Karadžića bb, 36300 Novi Pazar, Serbia.*

³*Institute of Botany, Faculty of Biology, University of Belgrade, Takovska 4, 11000 Belgrade, Serbia*

⁴*Institute of General and Physical Chemistry, Studentski trg 12-16, 11000 Belgrade, Serbia.*

Abstract

The effects of vanadate on phosphate metabolism of fungus *Phycomyces blakesleeanus* was investigated by ^{31}P NMR spectroscopy. Addition of vanadate results in increase sugars phosphate and polyphosphate level measured by ^{31}P NMR signal intensities. These findings, together with appearance of new signal after addition of glucose-6-phosphate into vanadate treated mycelium, suggest vanadate influence on sugar phosphate metabolism.

Introduction

Vanadium is an ultra trace element essential for growth and development in plants and animals. Studies on *Neurospora crassa* and erythrocytes show that vanadate enters the cells through the phosphate transport system [1, 2] and can substitute for organic phosphate in key molecules of oxidoreductive and energy metabolism [3]. Vanadate reacts with a number of enzymes and is a potent inhibitor of Na^+K^+ -ATPase of the plasma membrane, glucose-6-phosphatase and fructose-2, 6-bisphosphatase, but can also activate some enzymes, including glucose-6-P-dehydrogenase [4]. The influence of vanadate on phosphate metabolism in yeast *Hansenula polymorpha* manifested by a change in intracellular polyphosphate (PP_n) level has been shown by *in vivo* ^{31}P -NMR [5]. However, so far there is no evidence that vanadate has effect on sugar phosphate level measured by ^{31}P NMR spectroscopy. The sugar phosphates are the important factor in phosphate metabolism because they are a participant of glycolysis and pentose phosphate pathways. Vanadate is known to affect glycolysis [6]. Inhibitory effects of vanadate on the pentose phosphate pathways have been studied in yeast [7] and in *L. mesenteroides* [8]. In present study we show that milimolar concentration of sodium orthovanadate causes a change in level of sugar phosphate and affect phosphate metabolism of *P. blakesleeanus*.

Experiments

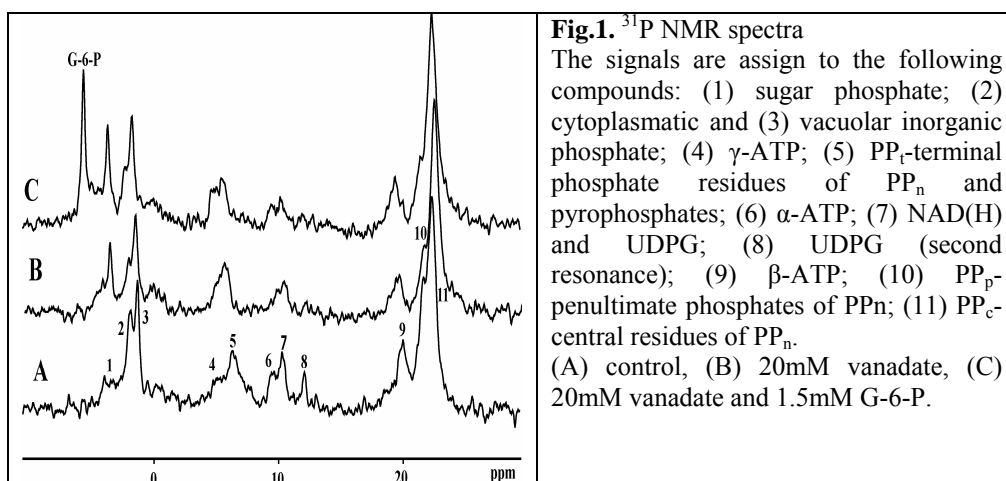
The wild type strain of the fungus *P. blakesleeanus* (Burgeff) (NRRL 1555(-)) was used in this work. The mycelium was grown in minimal medium [9] in Erlenmeyer

flasks which were shaking and aerating in the growth cabinet with continuous overhead white fluorescent light of 10 W/m², at temperature of 20°C, and ca. 95% relative humidity. For NMR measurements, 24h old mycelia were collected by vacuum filtration, washed with modified minimal medium without phosphates. An amount of about 0.5 g of mycelia was suspended in 2 ml of aerated modified minimal medium and packed in a 10-mm NMR tubes.

The ³¹P NMR measurements were performed using Apollo upgrade, Bruker MSL 400 spectrometer operating at 161 978 MHz. Stock solution of 100 mM sodium orthovanadate (Na₃VO₄) was prepared by the method of Gordon [10].

Results

The effect of vanadate on the ³¹P NMR spectra of 24 h old mycelium of *P. blakeleeanus* is shown in Fig. 1. The assignments of resonance are according to our previous paper [11].



As can be seen from Fig.1B addition of 20mM Na₃VO₄ to mycelium induces significant enhancement of resonance at 3.2 ppm, which according to chemical shift may corresponds to glucose-1-phosphate. The influence of vanadate on ³¹P NMR spectra result also in the enhancement of PP_c signal intensity by about 20 percent and in reduction of UDPG signal. The increase of core polyphosphate signal intensity after vanadate treatment has also been observed in *Dictyostelium amoebae* [12] and *H. polymorpha* [5], and was explained by sequestering function of polyphosphate which trapped metal ions in vacuole.

Noteworthy, changes in the ³¹P NMR spectrum of *P. blakeleeanus* were also observed after addition of 1.5 mM glucose 6 phosphate (G-6-P) to vanadate-containing sample (Fig.1C). The changes are manifested by appearance of additional signal at about 4.5 ppm, which may be attributed to one of resonance of fructose-bis-phosphate. It should be mentioned that after addition of G-6-P to untreated mycelium no changes in spectrum are observed. These suggest that

vanadate has an effect on G-6-P and G-1-P metabolism. Observed changes may be attributed to the reactivity of vanadate with a number of enzymes involved in glycolysis and metabolism of glycogen.

The concentration and time dependent influence of vanadate, as well as the identification of sugar phosphates and estimation of enzymes activity will be the subject of our further studies.

Conclusion

In this paper we demonstrated that vanadate induced significant changes in ^{31}P NMR spectra of *P. blakelseeanus*. The increase of signal intensities in sugar phosphate region of the spectrum, and appearance of new signals after addition of G-6-P into vanadate treated mycelium of *P. blakelseeanus*, indicate reactivity of vanadate with enzymes involved in sugar phosphate metabolism. To the best of our knowledge it is the first evidence that vanadate influence the sugar phosphate part of the ^{31}P NMR spectrum.

References

- [1] B. J. Bowman, J. Bacteriol., 1983, **153**, 286-291.
- [2] L. C. Cantley, M. D. Resh, G. Guidiotti, Nature, 1978, **272**, 552-554.
- [3] D. C. Crans, M. Mahroof-Tahir, A. D. Keramidas, Mol. Cell. Biochem., 1995, **153**, 17-24.
- [4] E. Tsiani, I. G. Fantus, Trends Endocrinol Metab., 1997, **8**, 51-58.
- [5] I. Mannazzu, E. Guerra, R. Strabbioli, A. Masia, G.B. Maestrone, M.A. Zoroddu, F. Fatichenti, FEMS Microbiol. Letters, 1997, **147**, 23-28.
- [6] E. J. Benabe, L. A. Echegoyen, B. Pastrana, M. Martinez-Maldonado, J. Biol. Chem., 1987, **262**, 9555-9560.
- [7] M. D. Cohen, A. C. Sen, C-I. Wei, Inorg. Chim. Acta, 1987, **138**, 179-186.
- [8] D. C. Crans, E. M. Willging, S. R. Butler, J. Am. Chem. Soc., 1990, **112**, 427-432.
- [9] R. P. Sutter, Proc. Natl. Acad. Sci. USA, 1975, **72**, 127-130.
- [10] J. Gordon, Methods Enzymol., 1991, **201**, 477-482.
- [11] M. Živić, J. Zakrzewska, M. Žižić, G. Bačić, Antonie Van Leeuwenhoek, 2007, **91**, 169-177.
- [12] G. Klein, G.G. Cotter, J-B. Martin, M. Satre, J. Cell Sci., 1989, **94**, 127-134.

STRESS-INDUCED ALTERNATIONS OF CuZn- and Mn-SUPEROXIDE DISMUTASE ACTIVITY IN RAT LIVER

J. Zlatković, S. B.Pajović and D.Filipović

Laboratory of Molecular Biology and Endocrinology, VINČA Institute of Nuclear Sciences, University of Belgrade, P.O.Box 522, Belgrade. Serbia

Abstract

Superoxide dismutases (SODs) represent the first line of antioxidant defense and any alternation in their function might be potentially damaging. Therefore, changes of the CuZnSOD activity in cytosolic and nuclear fractions and MnSOD activity in mitochondrial fraction in liver of male rats exposed to 2h of either immobilization (IM) or cold (4°) as acute stressors, 21 day of social isolation (IS) as chronic stress, or their combination (acute+chronic stress), were investigated. Serum corticosterone (CORT) level was monitored as a stress marker. Acute stress IM with elevated CORT level led to increased CuZnSOD activity in nuclear fraction. Chronic isolation, where CORT was close to control value did not change the CuZnSOD activity neither in nuclei nor cytosol fraction, while combined stress IS+Cold led to increased cytosolic CuZnSOD activity. MnSOD activity in mitochondrial fraction was decreased in all treated groups. Data indicate that unchanged or increased cytosolic or nuclear CuZnSOD activity after different stressors mediate liver restoration of homeostasis, while decrease of mitochondrial MnSOD activity may results in cellular injury and inefficient ROS defense.

Introduction

Glucocorticoids have been implicated as a regulatory factor for antioxidant enzymes in peripheral tissues, such as liver, where initiate the anabolic processes. Although beneficial, these high- energy-depended processes generate large amounts of reactive oxygen species (ROS) which could be harmful for the cells. In order to neutralize ROS, living cells possess superoxide dismutases (SODs), which catalyze the dismutation of the highly reactive superoxide anion to O₂ and hydrogen peroxide. Accumulation of ROS results in cellular oxidative stress, and if not corrected, can lead to the damage of important biomolecular structures such as membrane lipids, proteins and DNA. Three forms of SODs are detected: predominantly cytosolic CuZnSOD, mitochondrial MnSOD and ECSOD in the extracellular matrix. Because the liver is a prime target tissue for glucocorticoid action, we have investigated the alternations of CuZnSOD activity in cytosolic and nuclear fractions and MnSOD activity in mitochondrial fraction after 2h of acute stress immobilization or cold, 21 day of chronic social isolation or their combinations (chronic stress followed by acute stress).

Experimental

Male Wistar rats (3 months old, 300-400g weight) were housed according to standard conditions. The animals were divided into six groups: control group, groups exposed to 2h of acute stress immobilization (IM) or cold (4°C), group of animals exposed to chronic isolation *i.e.* the rats were individually housed for 21 days, and groups of chronically stressed animals which were subsequently exposed to single 2h either IM or cold (4°C) stress (IS+IM, IS+Cold). After series of tissue centrifugations, in obtain cytosolic, nuclear and mitochondrial fraction, CuZnSOD and MnSOD activities were measured using commercially available RANSOD kit (Randox). Serum corticosterone (CORT) level was monitored by enzyme-linked immunosorbent assay (ELISA). Analysis of variance (Two-way ANOVA) followed by Duncan post hoc test was used for statistical data analysis.

Results and discussion

No change in cytosolic CuZnSOD activity after acute IM or cold stress (Fig.1.left) was found, although increased CORT level was detected in both acutely stressed groups (Fig.3.). In nuclear fraction, increased CuZnSOD activity in IM group (Fig.1.right) indicates protective effect of CuZnSOD on DNA [1]. Concerning MnSOD, decreased activity in mitochondrial fraction (Fig.2.) after acute cold was found. Since main site for ROS generation is respiratory chain, MnSOD represents first line of defense but also a major target for oxidative damage.

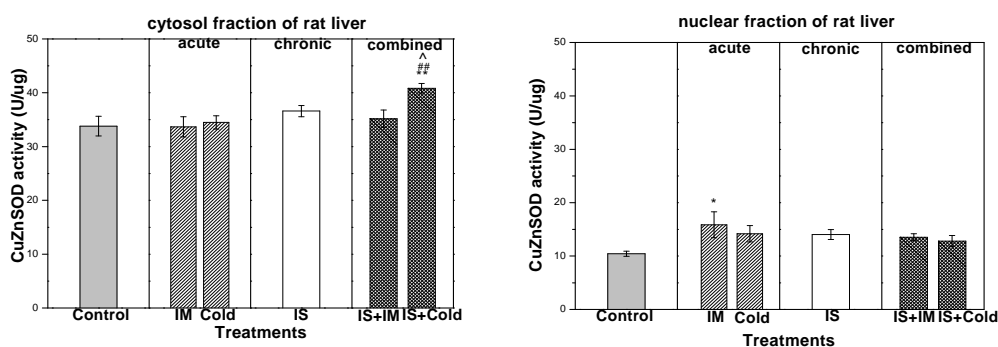


Fig.1. Hepatic CuZnSOD activity in cytosolic (left) and nuclear (right) fractions. In cytosolic fraction symbols indicate significant difference between: IS+Cold and unstressed control ** $p < 0.01$; IS+Cold and acute Cold stress ## $p < 0.01$; IS+Cold and chronic isolation stress ^ $p < 0.05$. In nuclear fraction symbol indicates significant difference between acute IM stress and unstressed control * $p < 0.05$.

In chronically stressed animals, where serum CORT level returned to basal level (Fig.3.), CuZnSOD activities in cytosolic and nuclear fractions were unchanged indicating maintenance of superoxide scavenging capacities. Opposite to that, significant decrease of mitochondrial MnSOD activity was shown suggesting that its detoxifying capacity was compromised by the oxidative stress [2], which may also exist under unchanged CORT level compared to control.

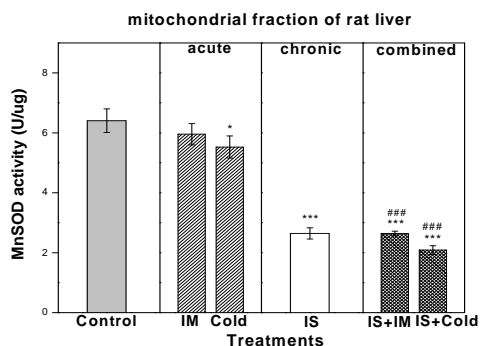


Fig.2. Hepatic MnSOD activity in mitochondrial fraction. The symbols indicate significant differences between: stressed animals and unstressed control * $p<0.05$, *** $p<0.001$; combined stress compared to appropriate acutely stressed animals ### $p<0.001$.

Chronically stressed animals showed a lesser increase in serum CORT level in response to novel acute stressors compared to acutely stressed animals, suggesting deregulation of hypothalamic-pituitary adrenal axis (Fig.3.). Under these conditions cytosolic or nuclear CuZnSOD activity was unchanged, except in cytosolic IS+Cold group where its activity was increased, while decreased mitochondrial MnSOD activity in both combined stress was found (Fig.2.).

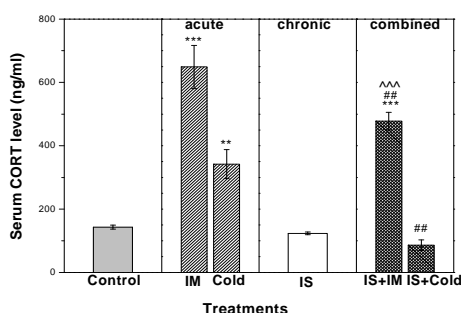


Fig 3. Serum CORT level (ng/mL) in control and stressed groups. Symbols indicate a significant difference between: respective stress treatment and unstressed control ** $p<0.01$, *** $p<0.001$; combined stressors and respective acute stressors ## $p<0.01$; combined stress IS+IM and chronic isolation ### $p<0.001$.

Conclusions

Results indicate that unchanged or increased cytosolic or nuclear CuZnSOD activity after different stressors mediate liver adaptation and restoration of homeostasis (oxidative balance). Decreased mitochondrial MnSOD activity suggests state of oxidative stress. Probably, stress-related ROS increase alters enzyme activity, creates harmful environment and therefore could be associated with pathological conditions.

References

- [1] D. Filipović, Lj. M. Mandić, D. Kanazir, S. B. Pajović, Mol. Cell Biochem., 2010, **338**, 167-174.
- [2] E. Pigeolet, P. Corbisier, A. Houbion, D. Lambert, C. Michiels, M. Raes, M. Zachary, J. Remacle, Mechanisms of Ageing and Development, 1990, **51**, 283-297.

INCREASE OF β -CAROTENE ANTIOXIDANT ACTIVITY AGAINST BENZOPHENONE-PHOTOSENSITIZED LIPID PEROXIDATION IN HEXANE

D. Cvetković and D. Marković

University of Nis, Faculty of Technology, 16000, Leskovac, Serbia

Abstract

The aim of this work is to estimate the antioxidant activity of β -carotene in the presence of a mixture of phospholipids in hexane solution, under continuous UV-irradiation from three different ranges (UV-A, UV-B and UV-C). β -Carotene is employed to control lipid peroxidation process generated by UV-irradiation, in the presence and in the absence of selected photosensitizer, benzophenone, by scavenging the involved, created free radicals. The results show that β -carotene undergoes a substantial, probably structurally dependent destruction (bleaching), highly dependent on UV-photons energy input, more expressed in the presence than in the absence of benzophenone. The excess of bleaching is synchronized with further increase of its antioxidant activity in the presence of benzophenone, implying the same cause: increase of its chain-breaking activities toward UV-induced phospholipids peroxidation.

Introduction

The depletion of the ozone shield leads to the increase of biologically damaging UV-light at ambient levels. UV-light has been especially recognized as one of the major agents to initiate a lot of harmful free radical mediated processes, such as lipid peroxidation (LP). Lipid peroxidation is tightly related to many pathological processes that may result in some form of cancer at the very end [1]. Typical lipid peroxidation initiators are reactive oxygen species (ROS), like hydroxy radicals (OH) or peroxy radicals (ROO). They can be created through a variety of chemical reactions [2]; additionally they can be induced through a variety of stresses, implying very commonly an external radiation, which, in case of UV-irradiation may include a special type of LP initiators, photosensitisers [3] in very different media. We have used benzophenone (BZP), a lipid soluble photosensitizer, which is an UV-absorbing agent, frequently used in research and industry. Benzophenone has been chosen as the sensitizer because of its most known organic photochemistry reaction, H-abstraction by its long lived triplet state [4,5]. To obtain basic data, deprived of the influence of surrounding molecular organization, the experiments were performed in hexane solution. The similar studies have been shown recently [6,7], but without BZP, and with a different lipid material (soy bean lecithin). Lipid peroxidation is mostly controlled by antioxidants action *in vivo*. In recent years, carotenoids have received wide research interest as potential

antioxidants [9] and it is related to the conjugated chemical structures with multiple potential sites approachable for attack by ROS species.

Experimental

β -Carotene was isolated from spinach purchased at the local market. All experiments and experimental procedures were described previously [7,8]. Phospholipids, Pro Lipo Duo[®] (PLD), were a gift from Lucas Meyer Cosmetics S.A., Champlan, France. The PLD mixture were kept in dark to prevent the photooxidation process. The phospholipids, β -carotene and BZP were dissolved separately in hexane and then mixed in final concentration of $3.5 \times 10^{-3} \text{ g/dm}^3$, $6.5 \times 10^{-7} \text{ mol/dm}^3$ and $2 \times 10^{-8} \text{ mol/dm}^3$, respectively. Peroxidation of phospholipids was generated by UV-irradiation at 254 nm (UV-C), 300 nm (UV-B) and 350 nm (UV-A). The hexane solutions of BZP only, and PLD only (with or without BZP), as a kind of blank, were irradiated simultaneously with the PLD/ β -carotene and PLD/ β -carotene/BZP mixtures. The increase in the absorbance at 234 nm, as an indication of a formation of peroxidative dienes structures was determined by VIS spectrophotometric measurements. The maximal β -carotene absorbances (450 nm) were recorded as a function of UV-irradiation time periods to follow the rate of β -carotene destruction, *i.e.* its bleaching (observed as a loss of colour).

Results and Discussion

The slopes calculated from kinetic log-plots representing the rates of UV-induced BZP bleaching – k_1 , the slopes which represent the rates of UV-induced lipid peroxides production (LPP - k_2) - in the presence or in the absence of BZP, and the slopes which represent the rates of simultaneous UV-induced lipid peroxides production (at 234 nm – k_3) and β -carotene bleaching (at 450 nm – k_4) in the investigated PLD/ β -carotene mixtures - in the presence or in the absence of BZP, are given in Table 1. Changes of absorption spectra and kinetic log-plots of PLD/BZP/ β -carotene mixture exposed to UV-B irradiation at 300 nm in hexane are given in Fig.1. The changes of absorption spectra of the same sample but obtained following continuous irradiation with UV-A and UV-C light expressed very similar shapes as the presented one.

Table 1 Kinetics of the BZP bleaching, and of PLD peroxidation (in the presence or in the absence of BZP); kinetics of β -carotene bleaching and lipid peroxides production in PLD/ β -carotene mixture, in the presence or in the absence of BZP; k_1 – first order rate constant for BZP bleaching; k_2 – first order rate constant for PLD and PLD/BZP mixture peroxidation; k_3 – first order rate constant for the PLD/ β -carotene and PLD/ β -carotene/BZP mixture peroxidation; k_4 – first order rate constant for β -carotene bleaching in PLD/ β -carotene and PLD/ β -carotene/BZP mixture.

wavelength nm	k_2/min^{-1}		k_3 and k_4/min^{-1}				
	without BZP	with BZP	without BZP		with BZP		
			at 234nm (k_3)	at 450nm (k_4)	at 234nm (k_3)	at 450nm (k_4)	
350 (UV-A)	-0.0039	0.0060	0.0771	0.0039	-0.0022	0.0602	-0.0084
300 (UV-B)	-0.0077	0.0736	0.2293	0.1152	-0.0342	0.2024	-0.0604
254 (UV-C)	-0.0576	0.2396	0.3250	0.2013	-0.1660	0.2659	-0.2376

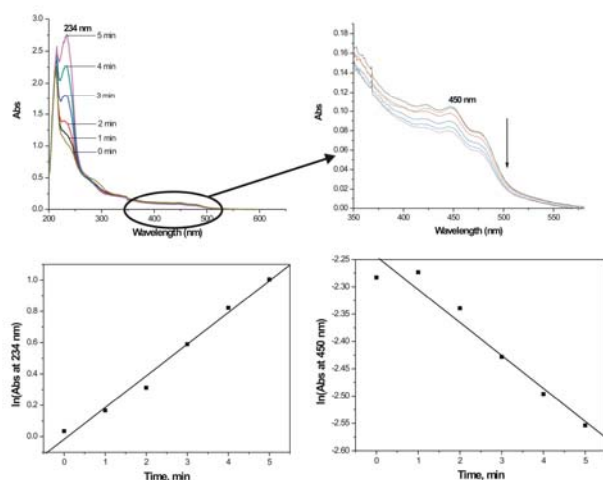


Figure 1. Changes of absorption spectrum of PLD/BZP/ β -carotene mixture exposed to continuous UV-B radiation at 300 nm in hexane (the upper part of the figure). The initial concentrations of BZP, PLD and β -carotene were $2 \times 10^{-8} \text{ mol dm}^{-3}$, $3.5 \times 10^{-3} \text{ g dm}^{-3}$ and $6.5 \times 10^{-7} \text{ mol dm}^{-3}$, respectively; Kinetic logarithmic plots for the peroxides production, obtained by measuring the absorbance of the PLD/BZP/ β -carotene mixture at 234 nm, and for β -carotene bleaching in the mixture (by measuring A_{max} at 450 nm), following increasing periods of UV-B irradiation (the lower part).

Both, BZP bleaching and lipid peroxides production, taken separately, are controlled by UV-energy input, causing the drop in the corresponding rate constants values, going from UV-C from to UV-A (Table 1). Since BZP is the less affected by UV-A, the corresponding LPP rates are the highest in its presence. The introduction of BZP into lipid/ β -carotene UV-irradiated system led to “excess” of the UV-induced β -carotene bleaching; the excess of bleaching was attributed to a substantial increase of scavenging of (BZP-created) lipid radicals by the β -carotene. Suppression of lipid peroxidation by β -carotene in the studied system is detected in significant amount. The introduction of benzophenone made the additional acting impact in both cases (in the presence and in the absence of β -carotene) emphasizing more β -carotene’s antioxidant function.

References

- [1] A. Ouhtit, H. N. Ananthaswamy, *Journal of Biomedicine and Biotechnology*, 2001, **1**, 5-6.
- [2] R. A. Wheatley, *Trends in analytical chemistry*, 2000, **19**, 617 – 628.
- [3] N. Paillous, S. Fery-Forgues, *Biochimie*, 1994, **76**, 355-368.
- [4] D. Z. Markovic, L. K. Patterson, *Photochemistry and Photobiology*, 1989, **49**, 531 – 535.
- [5] D. Z. Markovic, T. Durand, L. K. Patterson, *Photochemistry and Photobiology* 1990, **51**, 389 – 394.
- [6] D. Cvetkovic, D. Z. Markovic, *Journal of Serbian Chemical Society*, 2007, **72**, 235 – 250.
- [7] D. Cvetkovic, D. Z. Markovic, *Journal of Serbian Chemical Society*, 2008, **73**, 15 – 27.
- [8] G. W. Burton, K. U. Ingold, *Science*, 1984, **224**, 569-573.

G
Radiochemistry
and Nuclear Chemistry

DISTRIBUTION OF PRIMORDIAL RADIONUCLIDES IN SURFACE SOILS AROUND A COAL-FIRED POWER PLANT

M. Momčilović¹, Lj. Janković Mandić² and S. Dragović¹

¹*Institute for the Application of Nuclear Energy – INEP, University of Belgrade, Banatska 31b, 11080 Belgrade, Serbia;* ²*Military Medical Academy, Crnotravska 17, 11000 Belgrade, Serbia*

Abstract

The specific activities of ²³⁸U, ²³²Th and ⁴⁰K in soil around coal-fired power plants ranged from 25.5 to 105 Bq kg⁻¹ for ²³⁸U, from 29.9 to 104 Bq kg⁻¹ for ²³²Th and from 323 to 886 Bq kg⁻¹ for ⁴⁰K. The ²³²Th/²³⁸U, ⁴⁰K/²³⁸U and ⁴⁰K/²³²Th activity ratios were also determined. The measured specific activities were found to be higher than those in soils from background areas.

Introduction

One of the major sources of increased exposure of human population due to technologically enhanced radioactivity is energy production from coal. Coal contains natural radionuclides and their decay products, such as ⁴⁰K and the radioactive series of ²³⁸U and ²³²Th. The combustion of coal results in the release of a considerable amount of naturally occurring radionuclides into the atmosphere [1-5]. The coal-fired power plants (CPPs) “Nikola Tesla” A and B, located 42 km from the Serbian capital Belgrade, produce 3,015 MW of electrical energy at full load. These CPPs consume about 30,000,000 tonnes of coal per year and the ash yield is about 5,500,000 tonnes per year. The ash is deposited in open dumps of the total area of about 12 km². In this study the activity levels of natural radionuclides in surface soils in the surroundings of CPPs were determined.

Materials and Methods

A total of 45 soil samples (soil layer 0-10 cm) were collected during 2007. All soil samples were weighed and air-dried until constant mass is achieved. The samples were then pulverized, homogenized and sieved through a 2 mm mesh. They were kept hermetically sealed for one month to ensure equilibrium between ²³⁸U and its daughters before being taken for gamma spectrometric analysis.

Samples were measured in Marinelli beakers of total volume 1,000 cm³. The measurements were performed using HPGe gamma-ray spectrometer ORTEC-AMETEK (25% relative efficiency and 1.65 keV FWHM for ⁶⁰Co at 1.33 MeV, 8192 channels). The activity of ²³⁸U was evaluated from area under gamma line at

609.3 keV of ^{214}Bi peak and 351.9 keV of ^{214}Pb , while 911.2 and 969.1 keV gamma-ray lines emitted by ^{228}Ac and 238.6 keV emitted by ^{212}Pb were used to determine ^{232}Th . The activity of ^{40}K was determined using its 1460.8 keV gamma-ray line.

Results and Discussion

Table 1 gives the descriptive statistics for specific activities of ^{238}U , ^{232}Th and ^{40}K for all soil samples.

Table 1. Descriptive statistics of specific activities of ^{238}U , ^{232}Th and ^{40}K for analyzed soil samples

Parameter	Specific activities (Bq kg^{-1})		
	^{238}U	^{232}Th	^{40}K
Range	79.5	74.1	563
Mean	44.3	51.9	600
St. deviation	21.2	14.6	148
Minimum	25.5	29.9	323
Maximum	105	104	886
Median	34.9	48.2	590
Mode	34.0	43.5	548

The specific activities of ^{238}U , ^{232}Th and ^{40}K in the analyzed samples varied by a factor of up to 4.1, 3.5 and 2.7, respectively.

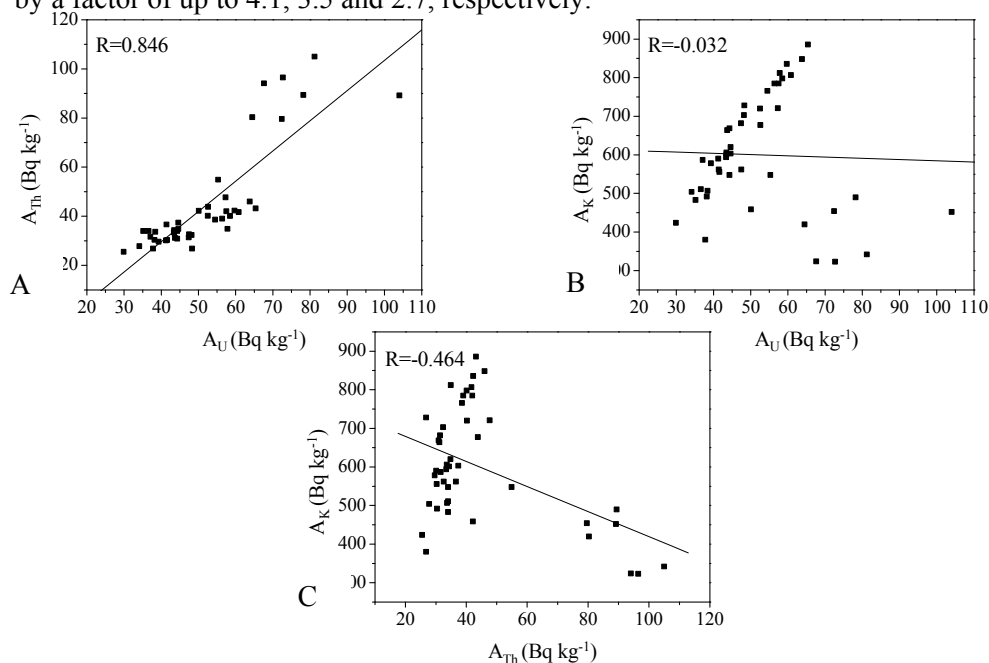


Fig. 1. ^{232}Th vs. ^{238}U (A), ^{40}K vs. ^{238}U (B) and ^{40}K vs. ^{232}Th (C) specific activities

The frequency distributions were found to be normal for ^{238}U and ^{232}Th , and log-normal for ^{40}K .

The mean values of specific activities were found to be 44.3 Bq kg^{-1} for ^{238}U , 51.9 Bq kg^{-1} for ^{232}Th and 600 Bq kg^{-1} for ^{40}K . The uranium and thorium specific activities obtained in this study are higher than those reported earlier for the same area [6]. Also, these values are higher than those reported for Serbia and Montenegro [7]. The specific activities of radionuclides in soils around the CPP in Hungary were found to be 116, 26.9 and 337 Bq kg^{-1} for ^{238}U , ^{232}Th and ^{40}K , respectively [3]. Papastefanou et al. reported specific activities of 200 Bq kg^{-1} for ^{238}U and 48 Bq kg^{-1} for ^{232}Th in soils near three CPPs in Greece [8].

The original uranium, thorium and potassium concentrations in rocks may vary because of alteration or metamorphic processes [9]. Fig. 1 displays the $^{232}\text{Th}/^{238}\text{U}$, $^{40}\text{K}/^{238}\text{U}$ and $^{40}\text{K}/^{232}\text{Th}$ ratios, which may indicate whether relative depletion or enrichment of radionuclides had occurred. The best-fitting relations between ^{232}Th and ^{238}U , ^{40}K and ^{238}U and ^{40}K and ^{232}Th are of the linear type, with correlation coefficients of 0.846, -0.032 and -0.464, respectively. In our study the $^{232}\text{Th}/^{238}\text{U}$ ratio was 1.17 which is close to the value expected for a normal continental crust 1.20-1.30. The $^{40}\text{K}/^{238}\text{U}$ ratio was calculated to be equal to 13.5, and $^{40}\text{K}/^{232}\text{Th}$ ratio was 11.6. It should be mentioned that these values are highly variable and depend on the geological origin of the sample.

The results obtained in this study can be used for preliminary estimations of population exposure to natural radionuclides in the surroundings of the CPPs "Nikola Tesla". Before definite conclusions on this issue are drawn, more systematic data and further analyses are required.

Acknowledgments

This work was funded by the Ministry of Science and Technological Development of the Republic of Serbia (contract 142039).

References

- [1] D. E. Barber, H. R. Giorgio, *Health Phys.*, 1977, **32**, 83-88.
- [2] G. A. Ayçik, A. Ercan, *J. Environ. Radioact.*, 1997, **35**, 23-35.
- [3] Z. Papp, Z. Dezső, S. Daróczy, *J. Environ. Radioact.*, 2002, **59**, 191-205.
- [4] L. I. Tsikritzis, *J. Radioanal. Nucl. Chem.*, 2004, **264**, 651-656.
- [5] C. Papastefanou, *J. Environ. Radioact.*, 2010, **101**, 191-200.
- [6] Ž. Vuković, M. Mandić, *J. Environ. Radioact.*, 1996, **33**, 41-48.
- [7] S. Dragović, Lj. Janković, A. Onjia, G. Bačić, *Radiat. Meas.*, 2006, **41**, 611-616.
- [8] C. Papastefanou, M. Manolopoulou, S. Charalambous, *Radiat. Prot. Dosim.*, 1988, **24**, 439-443.
- [9] M. Verdoya, P. Chiozzi, V. Pasquale, *Eclogae. Geol. Helv.*, 2001, **94**, 1-7.

DETERMINATION OF URANIUM CONCENTRATION IN THE VICINITY OF FORMER URANIUM MINES ON STARA PLANINA MOUNTAIN: A RADIATION RISK ASSESSMENT FROM GAMMA-RADIATION OF TERRESTRIAL RADIONUCLIDES

M. Tanić^a and G. Bačić^b

^a*CBRN Training Centre, Kruševac, Serbia,* ^b*Faculty of Physical Chemistry, University of Belgrade, Serbia*

Abstract

The aim of this work was to assess the potential radioactive contamination of soils and waters of the surrounding area of abandoned uranium mines on the mountain Stara planina. Soil samples were collected from within the flotation facilities, their surroundings and more distant locations. Increased concentrations of U and Th were observed only in samples that were collected from sites where uranium ore was processed, while soils surrounding these compounds showed concentrations of U and Th that are typical for this mountain. Calculations of the annual effective dose from gamma radiation of these nuclides and the external hazard index within the affected sites showed that there is no significant radiation risk from external irradiation for the population in this region. The presence of U and Th was detected in all water samples from creeks nearby facilities, but only in the water from the facility drainage pipe their concentration exceed the limits given for the content of uranium in drinking water.

Introduction

The uranium mines near the villages of Gabrovnica and Mezdreja (near the town of Kalna) were active during the 1960s with a capacity of 60-200 tons of uranium ore per day. Today the mines are closed; the processing facilities are abandoned and almost completely ruined. From the environmental point of view the increased uranium concentration at the sites of the abandoned mines and processing facilities is expected and not of much concern in itself. The more important issue is whether this local contamination has spread to wider areas; especially since the development of a ski resort has been planned on this mountain. We therefore performed an investigation of the uranium content within the facilities, as well as in their vicinity, with the ultimate goal of estimating the radiation risk for the local and seasonal population.

Materials and Methods

Sampling and sample preparation. The soil samples were taken from the topsoil of the surface of 1 m x 1 m to a depth of 5 cm [1]. The sampling sites included flotation facilities, surrounding areas outside the fence of the facilities, and a

location further away (by the ski track). The samples were dried at 105°C, homogenized by mechanical mixing, transferred to Marinelli beakers (total volume 0.5 dm³) and kept hermetically sealed for about 40 days prior to measurement. The water samples were taken from the drainage pipe of the Gabrovnica mine and from two creeks that flow immediately by the processing facilities. After sampling, the water was acidified, pre-concentrated to a tenth part of its initial volume [1], and transferred into Marinelli beakers.

Radioactivity measurements. The specific activities of radionuclides of interest were measured using an HPGe gamma-ray spectrometer (ORTEC-AMETEK). The specific activities of ²³⁸U, ²³⁴Th, and ⁴⁰K were determined according to standard procedures [2, 3].

Data analysis. Measured specific activities of ²³⁸U, ²³²Th and ⁴⁰K were converted into massic elemental concentration of these elements [2]. The external gamma dose rate, *D* (in the air at 1 m above ground level), the annual effective dose, *E*_{year} (using 0.2 as the outdoor occupancy factor), and the external hazard index, *H*_{ex} were calculated from these measurements (see [4] for procedures).

Results and Discussion

Table 1 summarizes results obtained for soil samples and gives the comparison with similar measurements on other locations in Serbia. Massic elemental concentrations of U and Th in soils collected within the processing facilities are several times higher than in soils collected on different locations on the mountain. This is only to be expected since sampling points were in direct contact with the uranium ore at the time the mine was in operation. However, soil samples collected in the immediate vicinity of these facilities do not differ from other locations on the mountain indicating that nowadays no contamination of the surrounding area exists.

Table 1. Massic elemental concentrations of U, Th and K in soil samples.

Location	²³⁸ U [ppm]	²³² Th [ppm]	⁴⁰ K [ppm]
Processing facilities	16.59±4.89	16.70 ± 3.74	2.07 ± 0.60
Vicinity of processing facilities	2.66 ± 0.62	5.64 ± 1.09	1.34 ± 0.21
Ski resort	1.29 ± 0.12	3.92 ± 0.23	1.13 ± 0.05
Stara planina – different locations [2]	2.52	8.89	2.10
Various mountains in Serbia [2]	2.91	10.78	1.98

Table 2 presents results pertinent to the assessment of radiation risk on the selected locations. For comparison, the world average value of the external gamma dose rate in the air at 1 m above ground level from terrestrial radionuclides is 51 nGy h⁻¹, with the individual contributions of isotopes: ⁴⁰K with 17 nGy h⁻¹, radionuclides from the radioactive series ²³⁸U with 16 nGy h⁻¹, and radionuclides from the radioactive series ²³²Th with 18 nGy h⁻¹ [4]. Data in Table 2 show that the calculated dose rates at measured locations around the processing facilities are well within the worldwide average values. The situation within the processing facilities is quite different due to the increased amounts of ²³⁸U, ²³²Th in the soil.

Table 2. Average values of D , E_{year} , and (H_{ex}) for various locations.

Location	D [nGy h ⁻¹]	E_{year} [mSv]	H_{ex}
Processing facilities	188.2±11.4	0.199±0.014	0.57±0.09
Vicinity of processing facilities	47.7±8.5	0.059±0.019	0.11±0.04
Ski resort	32.2±2.8	0.038±0.09	0.04±0.01
Stara planina – different locations [5]	58.4	0.072	0.23
Various mountains in Serbia [5]	68.6	0.084	0.39
Serbia overall	62.8	0.077	0.35

In estimating the E_{year} , we used 0.2 for the value of the outdoor occupancy factor (20% per year) which is certainly an overestimate since the area is almost uninhabited. The world average of the E_{year} due to the terrestrial radionuclide is 0.07 mSv and only locations within the processing facilities exceed that value. Nevertheless, all calculated values are well below the value of 1 mSv, set as a limit for external irradiation of the human body. Likewise, all values H_{ex} are below 1, which implies that concentrations of radionuclides of interest do not present an increased radiation risk.

Results of radioactivity measurements of water samples are given in Table 3. The concentration of U and Th in water coming from the drainage pipe by far exceeds values found in the creeks and are above the maximum allowable concentration for drinking water (domestic regulations 50 $\mu\text{g dm}^{-3}$ [6], 30 $\mu\text{g dm}^{-3}$ the EPA, USA). Soil samples from the creeks' bed also did not show increased concentrations of U and Th. Consequently, waters from creeks do not represent a health hazard.

Table 3. Massic elemental concentrations of U, Th and K in water samples.

Locations	²³⁸ U [$\mu\text{g dm}^{-3}$]	²³² Th [$\mu\text{g dm}^{-3}$]	⁴⁰ K [$\mu\text{g dm}^{-3}$]
Drainage pipe – Gabrovnica	80.26 ± 7.29	116.32 ± 3.12	7.40 ± 0.70
Creek - Gabrovnica	1.86 ± 0.65	5.60 ± 0.74	0.40 ± 0.10
Creek - Mezdreja	0.57 ± 0.49	5.18 ± 0.25	51.30 ± 4.00

References

- [1] C. Zhang, Fundamentals of Environmental Sampling and Analysis, John Wiley & Sons, Inc., Hoboken, 2007.
- [2] S. Dragović, Lj. Janković, A. Onjia, G. Bačić, Radiat. Measur. 2006, **41**, 611.
- [3] C. A. Papachristodoulou, *et al.*, J. Environm. Radioact., 2003, **64**, 195 – 203.
- [4] UNSCEAR, Report on Sources and Effects of Ionization, UN, New York, 2000.
- [5] S. Dragović, Lj. J. Mandić, M. Momčilović, A. Onjia, Arch. Oncology, 2007, **15**, 78.
- [6] Pravilnik o granicama izlaganja jonizujućim zračenjima, Službeni list SRJ, 32/98.

H Material Science

PHOTOLUMINESCENCE PROPERTIES OF Eu^{3+} DOPED TiO_2 NANOPARTICLES

M. Vranješ, J. Kuljanin-Jakovljević, J. Nedeljković and Z. Šaponjić

Vinča Institute of Nuclear Sciences, 11001 Belgrade, Serbia

Abstract

Eu^{3+} doped TiO_2 nanoparticles were synthesized during extended hydrothermal treatment of TiO_2 nanotubes dispersion in the presence of $\text{Eu}(\text{NO}_3)_3$. Eu^{3+} ions occupy two different sites of titania nanoparticles having different binding energies: core octahedral sites and undercoordinated surface sites. Photoluminescence spectra of Eu^{3+} doped TiO_2 nanoparticles independently of dopant concentration consist of three characteristic peaks located at $\lambda=543$, 596, and 617 nm attributed to the intra-4f transitions of Eu^{3+} ion. Removal of excess of Eu^{3+} ions from the surface and from the undercoordinated surface sites applying post synthetic dialysis of the sample affects its photoluminescence spectrum. The peak intensity at $\lambda=617$ nm (${}^5\text{D}_0 \rightarrow {}^7\text{F}_2$ transition) decreases after dialysis. Such “self-purification” process of nanoparticles is a consequence of fact that dopant ions which substitute Ti atoms in the undercoordinated coordination environment of reconstructed surfaces are weakly bound to the anatase lattice.

Introduction

Rare earth ions doped semiconductors have attracted considerable attention in recent years due to their high potential of becoming a new class of luminescent materials with a wide range of applications in many different fields such as photoelectric devices, solid state laser materials, optical data storage, and medical diagnostics [1]. The TiO_2 is considered as promising host material for sensitizing luminescence of Eu^{3+} ions due to its wide band gap, low absorbance in the visible region and thermal properties. On the other hand, Eu^{3+} ions show stable and bright red luminescence due to intra-4f transitions at room temperature. The luminescence signal in doped materials coming from fixed lines of rare earth ions, and their positions are almost independent of the host matrix. However, the line width and its relative intensity are often affected by the nature of the matrix [2]. In this paper we report on the synthetic procedure of Eu^{3+} doped TiO_2 nanoparticles and their photoluminescence properties dependence of dopant position. Using titania nanotubes as a precursor we eliminated driving force problem that arises from the increase in the activation energy for nanocrystal nucleation in the presence of the dopant ions and consequent exclusion of the Eu^{3+} ions during nanoparticle growth.

Experimental

Titania nanotubes were synthesized according to procedure described elsewhere [3]. Eu^{3+} doped TiO_2 nanoparticles were synthesized using hydrothermal treatment

(90 min/250°C) of suspension of 3×10^{-2} M titania nanotubes (pH=3) in the presence of 6.4×10^{-4} M $\text{Eu}(\text{NO}_3)_3$. The excess of Eu^{3+} ions in dispersion of doped nanoparticles was removed by filtration or dialysis. The sample (25mg of $\text{Eu}^{3+}/\text{TiO}_2$ nanoparticles powder in 10ml H_2O) was dialyzed using Spectra/Por Dialysis Membrane, MWCO: 3,500 (Spectrum Laboratories) against 200ml of acidified water (pH=3) at 4°C for 3 days. Transmission electron microscopy (Hitachi H-700 FA TEM) at 125kV was used for determining the shape and size of the titania nanotubes and nanoparticles. The photoluminescence spectra of powdered samples were recorded on Perkin-Elmer LS-45 Fluorescence Spectrometer, in front-face mode ($\lambda_{\text{exc}}=396$ nm).

Results and discussion

We showed in our previous work that titania nanotubes contain large amounts of undercoordinated surface sites [3]. The TEM measurements revealed that the outer diameter of nanotubes is about 10 nm while the inner diameter is about 7 nm, Figure 1A. Hydrothermal treatment of nanotubes dispersion containing Eu^{3+} ions adsorbed on undercoordinated sites result in the formation of Eu^{3+} doped anatase TiO_2 nanoparticles. The majority of the nanoparticles have polygonal shapes with average dimension of ~15 nm, Figure 1B.

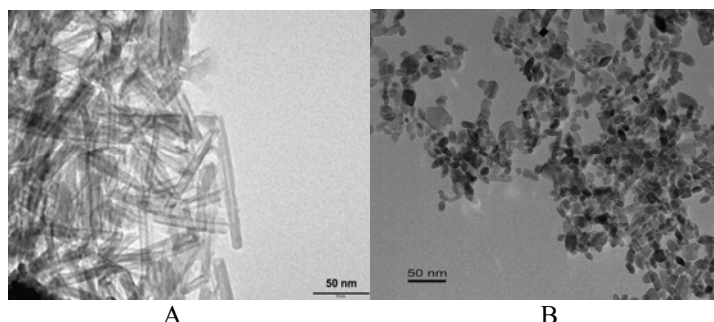


Fig.1. TEM images of scrolled titania nanotubes (A) and Eu^{3+} doped TiO_2 nanoparticles (B).

We used fluorescence spectroscopy to investigate the coordination environment of Eu^{3+} dopant ions within anatase TiO_2 matrix. Photoluminescence spectra of filtrated and dialyzed samples of TiO_2 nanoparticles doped with 6.4×10^{-4} M Eu^{3+} ions are shown in Figure 2. Three peaks in fluorescence spectra, Figure 2, located at $\lambda=543$, 596, and 617 nm are ascribed to the ${}^5\text{D}_1 \rightarrow {}^7\text{F}_0$, ${}^5\text{D}_0 \rightarrow {}^7\text{F}_1$ and ${}^5\text{D}_0 \rightarrow {}^7\text{F}_2$ transitions of Eu^{3+} ion, respectively [2, 4]. As can be seen, there is a noticeable difference in photoluminescence spectra of filtrated and dialyzed samples.

Namely the intensity of the ${}^5\text{D}_0 \rightarrow {}^7\text{F}_2$ transition decreases in dialyzed sample. The ${}^5\text{D}_0 \rightarrow {}^7\text{F}_2$ transition is a hypersensitive forced electric-dipole transition being allowed only at low symmetries with no inversion center, whereas the magnetically allowed ${}^5\text{D}_0 \rightarrow {}^7\text{F}_1$ transition is almost independent of the surroundings of the Eu^{3+} ion [2]. In our samples the Eu^{3+} ion can be located at two

different sites: on the surface of the nanoparticles (low, unordered symmetry), and within crystal lattice replacing the Ti^{4+} ion with octahedral symmetry. After filtration of the sample the large amount of the Eu^{3+} ions located on the surface of the TiO_2 nanoparticles is left behind, and due to low site symmetry the probability of the ${}^5\text{D}_0 \rightarrow {}^7\text{F}_2$ transition is significant, that is manifested with strong intensity of the peak at $\lambda=617$ nm. Post-synthetic dialysis process represents a more efficient method for removing excess of dopant ions, leaving only Eu^{3+} ions that substitute Ti^{4+} ions located in the octahedral lattice sites. Due to the high symmetry of octahedral site the probability of the ${}^5\text{D}_0 \rightarrow {}^7\text{F}_2$ transition is low and the intensity of peak at $\lambda=617$ nm decreases, Figure 2.

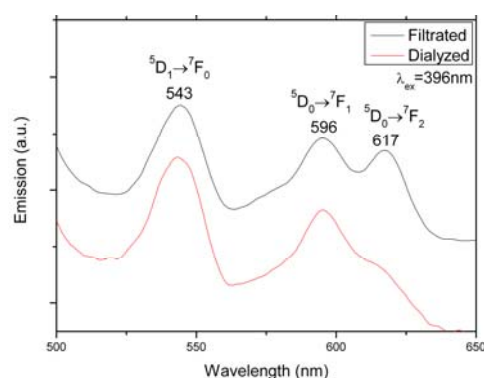


Fig.2. Photoluminescence spectra of filtrated and dialyzed Eu^{3+} doped TiO_2 NP.

Conclusion

TEM analysis revealed that nanoparticles mainly have polygonal shape with average dimension of 15 nm. Post-synthetic dialysis of doped titania nanoparticles affects its photoluminescence spectra. Intensity of the hypersensitive forced electric-dipole ${}^5\text{D}_0 \rightarrow {}^7\text{F}_2$ transition decreases in dialyzed samples, indicating the removal of the excess of Eu^{3+} ions and Eu^{3+} ions from the low symmetry surface sites, leaving only dopant ions that substitute Ti^{4+} ions located in the lattice site with octahedral symmetry. Post-synthetic treatment of Eu^{3+} doped TiO_2 nanoparticles open up possibility to manipulate the dopant position.

References

- [1] Y. H. Li, G. Y. Hong, J. Solid State Chem., 2005, **178**, 645
- [2] Z. Zhao, Q. G. Zeng, Z. M. Zhang, Z. J. Ding, Journal of Luminescence, 2007, **122-123**, 862-865.
- [3] Z. Šaponjić, N. Dimitrijević, D. Tiede, A. Goshe, X. Zuo, L. Chen, A. Barnard, P. Zapol, L. Curtiss, T. Rajh, Advanced Materials, 2005, **17**, 965-971.
- [4] C. Jia, E. Xie, J. Zhao, Z. Sun, A. Peng, Journal of Applied Physics, 2006, **100**, 023529.

DFT STUDY OF HYDROGEN ADSORPTION ON TRANSITION METAL SURFACES: RELATIONSHIP TO ELECTROCATALYSIS

I. Pašti,¹ Z. Ristanović,² N. Gavrilov¹ and S. Mentus^{1,3}

¹University of Belgrade ¹Faculty of Physical Chemistry., Studentski trg 12, Belgrade, Serbia; ²Department of Inorganic Chemistry and Catalysis, Debye Institute, Utrecht University, The Netherlands; ³SANU, Knez Mihajlova 35, Belgrade, Serbia

Abstract

The presented work is aimed to elaborate computational search for new (electro)catalytic materials. For the case of hydrogen evolution reaction, multi-step procedure was developed by combining the knowledge obtained on model systems, both theoretical and experimental, with theoretical models for atomic adsorption to search for materials with high (electro)catalytic activity. In this procedure, the crucial step is the selection of the correct catalytic descriptor that can be obtained theoretically and its correlation with appropriate measure of catalytic activity for variety of model systems.

Introduction

During the last decade, computational approach in material science became complementary to the experiments, giving the data that are usually difficult or even impossible to obtain experimentally. Computational quest for new materials with high (electro)catalytic activity is set as a final goal for theoretical methods in material science [1,2].

Here we propose a unique “training” system, simple for use, which provides a high-level knowledge on the adsorption trends and effects of the electronic structure on the reactivity. Proposed procedure was elaborated for the case of hydrogen evolution reaction (HER). For the first time, the knowledge obtained on the model systems, both theoretical and experimental, was directly combined with theoretical models for atomic adsorption to search for materials with high (electro)catalytic activity. This procedure is considered to be usable in the cases of more complicated systems for development of new materials with high catalytic and electrocatalytic activity.

Materials and methods

All the calculations were performed within generalized gradient approximation, using PWscf code of QUANTUMESPRESSO distribution [3]. Ultrasoft pseudopotentials were employed in order to reduce computational costs. Hydrogen adsorption on FCC transition metal surfaces with (111) crystallographic orientation were modeled using 3-layer slab model, separated by 16Å thick vacuum layer.

Palladium and platinum electrocatalysts were modeled with 7-layer slab model. Brillouin zone was sampled using the appropriate Monkhorst-Pack set of special k-points.

Results and Discussion

Starting point was to calculate hydrogen-metal bond energies (E_{H-M}) on clean transition metal surfaces and check the agreement with available experimental and theoretical data. Next step in our approach was to connect electrocatalytic activity of the investigated systems with available electrocatalytic descriptor. For this purpose we chose E_{H-M} , which is known to be good electrocatalytic descriptor for HER, while experimental exchange current densities (j_0) were used as a measure of electrocatalytic activity. Connecting these two quantities resulted in a well-known volcano-curve with platinum at the apex, in agreement with the literature data [1] (Fig. 1). Although Pt is on the apex of the curve, certain improvement of catalytic activity can be obtained by weakening of Pt-H bond. The same is in the case of Rh-H and Pd-H bond.

Next step was to investigate the effects of the modification of the electronic structure on the strength of M-H bond. For this purpose, simple theoretical models for atomic adsorption were employed [5,6]. These models connect the position of the d-band center (E_{d-band}) of surface atoms with E_{H-M} , demonstrating that fine tuning of E_{d-band} affects the strength of M-H bond. Obtained results are given in Fig. 1. Results indicate that high electrocatalytic activity for HER can be obtained by stabilization of d-bands of surface Pt atoms, and the same holds in the case of Pd. Hence, we chose to investigate further different Pt- and Pd-terminated surfaces.

Possible way to achieve tuning of the E_{d-band} is to deposit Pt or Pd on a suitable substrate with a lattice constant different from the ones of Pt or Pt. Generally, stabilization of d-band is achieved when metal atoms are deposited on the metal substrate with smaller lattice constant, i.e. by introducing compressive surface strain. The results of such analysis are presented in Fig. 2, where hydrogen adsorption energies (E_{ads} , this quantity is connected with E_{H-M} through H_2 dissociation energy and can be used in the same way as E_{H-M}) are correlated with E_{d-band} .

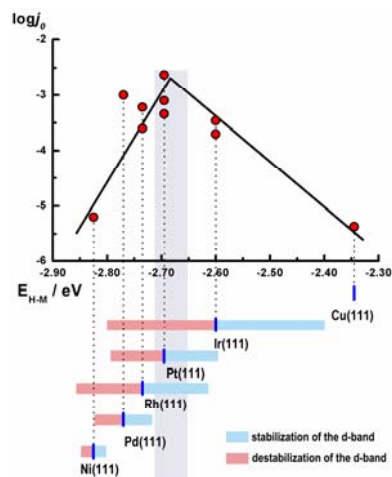


Fig.1. Volcano-curve obtained upon connecting E_{H-M} and j_0 for HER. Effects of tuning of E_{d-band} by 0.25 eV on E_{H-M} are given in the lower part, while the optimal strength of M-H bond for the maximum HER activity are marked with gray rectangle. The detailed list of references is given in Ref. [4].

Observable scattering on Fig. 2 demonstrates that geometry of the adsorption site has important contribution in determination of hydrogen adsorption energies, too. Provided results indicate that high electrocatalytic activity of Pd monolayer on Pt(111) can be expected, while the loss of the activity, compared to Pd(111), can be expected in the case of Pd deposition on Au(111). These results are in perfect agreement with the available experimental studies [7], confirming the correctness of the approach used in this investigation.

Conclusion

In this contribution, multi-step search for new (electro)catalytic materials was described for the case of HER. This reaction was subjected to investigation because there is a large number of available experimental and theoretical data available in the literature related to this reaction. Described procedure did not include new materials, but rather well-know systems, and correct trend of activities was predicted, which confirms the correctness of this procedure. We expect that described procedure can be generalized for the case of more complicated systems. In this procedure, the crucial step is the selection of the correct catalytic descriptor that can be obtained theoretically and its correlation with appropriate measure of catalytic activity for variety of model systems.

References

- [1] J. K. Nørskov, T. Bligaard, A. Logadottir, J. R. Kitchin, J. G. Chen, S. Pandalov, U. Stimming, *J. Electrochem. Soc.*, 2005, **152**, J23.
- [2] J. Greeley, M. Mavrikakis, *J. Phys. Chem. B*, 2005, **109**, 3460.
- [3] www.quantumespresso.org (distributed under general public licence).
- [4] Z. Ristanović, Diploma thesis, Faculty of Physical Chemistry, Belgrade University, 2009.
- [5] A. Ruban, B. Hammer, P. Stoltze, H. L. Skriver, J. K. Nørskov, *J. Mol. Cat. A: Chem.*, 1997, **115**, 421.
- [6] B. Hammer, J. K. Nørskov, *Surf. Sci.*, 1995, **343**, 211.
- [7] a) L.A. Kibler, *Electrochim. Acta* 2008, **53**, 6824.; b) L.A. Kibler, A.M. El-Aziz, R. Hoyer, D.M. Kolb, *Angew. Chem., Int. Ed.* 2005, **44**, 2080.

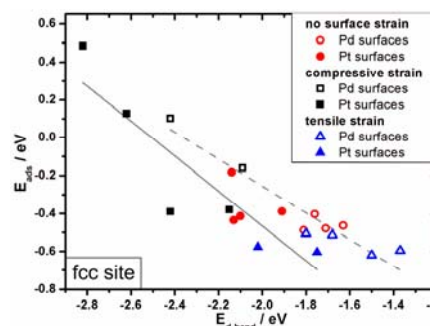


Fig.2. Correlation of hydrogen adsorption energies (E_{ads}) with E_{d-band} on various Pt- and Pd-terminated surfaces.

COMPUTER SIMULATION OF THREE-DIMENSIONAL REARRANGEMENT DURING LIQUID PHASE SINTERING

Z. S. Nikolić¹ and F. Wakai²

¹*Faculty of Electronic Engineering, Department of Microelectronics
University of Nish, Nish, Serbia (zoran.nikolic@elfak.ni.ac.rs)*

²*Materials and Structures Laboratory, Tokyo Institute of Technology, Japan*

Abstract

In this paper three-dimensional method for computer study of capillary force field induced rearrangement of multi-grain system during liquid phase sintering will be discussed.

Introduction

An analytical solution for rearrangement during liquid phase sintering (LPS) has never been attempted and may not be possible. Computer simulation has therefore played a key role in providing insight into rearrangement and its theoretical framework. When no external force is applied to the two spherical grains then the system rigid motion depends upon the driving force only. The driving force available to move two grains is the capillary force in the liquid bridge. However, topological constraints due to surrounding grains can also lead to grains rearrangement and the buildup moments on the grains. Three-dimensional computer simulation method for treating this effect in large scale grain arrays will be discussed in the next.

Modeling of the rearrangement

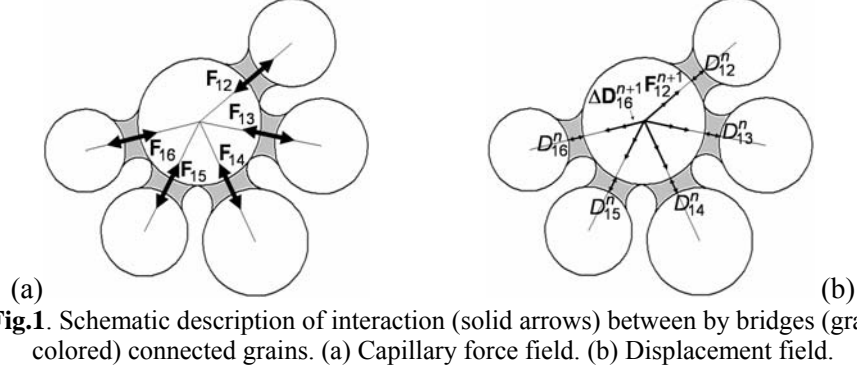
The interparticle force between two spherical grains of radius R_1 and R_2 connected by a liquid bridge is given by equation [1]

$$F = 2\pi\gamma R_1 \sin \varphi_1 \sin(\varphi_1 + \theta) + \pi\gamma (R_1 \sin \varphi_1)^2 \left(\frac{1}{\rho_2} - \frac{1}{\rho_1} \right), \quad (1)$$

where the first term is the force due to the surface tension acting at the wetting perimeter and the second term is the force due to the capillary pressure in the liquid, φ_1 and φ_2 are the angles subtended by the contact at the center of the grains, ρ_1 and ρ_2 are the radii of the meniscus, and γ is the surface free energy of the liquid-vapor interface. The total driving force will be now obtained by distributing all partial capillary forces between interfaces solid-liquid inside each separate liquid bridge (Fig. 1a), i.e.

$$\mathbf{F}_t = \sum_{k=1}^N \sum_{j=1}^{n_k} \mathbf{F}_{kj}. \quad (2)$$

where N is the number of grains, and \mathbf{F}_{kj} is the capillary force (1) between k -th grain with n_k nearest neighbors and j -th grain connected by liquid bridge.



Huppmann and Riegger [2] investigated the rearrangement process to show instantaneous shrinkage dependent on the capillary force per contact. 3-D simulation of rearrangement due to the force (2) can be simulated on similar way.

Let $\Delta\mathbf{D}_{kj}^{n+1}$ is the change of the inter-grain distance per kj -th liquid bridge in direction of capillary force \mathbf{F}_{kj}^{n+1} after time $t + \Delta t$, and D_{kj}^n is the inter-grain distance at previous time step (Fig. 1b). Thus the displacement of k -th grain as vector distance will be obtained by summation of corresponding vector distances

$$\Delta\mathbf{D}_k^{n+1} = \sum_{j=1}^{n_k} \Delta\mathbf{D}_{kj}^{n+1} = \sum_{j=1}^{n_k} D_{kj}^n \chi (\mathbf{F}_{kj}^{n+1} - \mathbf{F}_o), \quad (3)$$

where χ is a constant at a given grain size, and F_o represents an inherent resistance to grain rearrangement defined as $|\mathbf{F}_o| = \min\{|\mathbf{F}_{kj}^o|\}$, where the capillary forces \mathbf{F}_{kj}^o will be computed according to initial inter-grain distances $\{D_{kj}^o\}$.

Results and Discussion

For 3-D simulation of rearrangement of multi-grain system so called grain levels methodology with the central (zero level) grain located at the centre of the experimental space will be applied. Its first neighbors connected by liquid bridges will be denoted as the first level grains, etc. The rearrangement will be simulated around the central grain according to capillary forces across the liquid bridges (two-grain interaction) with its first, second etc. neighbors. Thus the rearrangement procedure (3) will be now applied to all grains starting from the central grain.

Densification by rearrangement during LPS occurs over very short time. As an example the defined algorithm was applied for the simulation of rearrangement of a randomly generated multi-grain system with average radius of $\sim 54 \mu\text{m}$ and average

liquid bridge distance of $\sim 9.5 \mu\text{m}$ (Fig. 2a). We used the normalized liquid volume [1] 0.05, the contact angle of 10° and the same data as in [1]. The result of the computer simulation of rearrangement after 150 sintering time steps is shown in Fig. 2b, where the average liquid bridge distance was now $\sim 3.7 \mu\text{m}$.

As it can be seen, the system responds as a viscous solid to the capillary action during rearrangement, where the rearrangement of grains is a consequence of attractive capillary force action resulting from the liquid wetting the grains. The capillary forces act in direction to change the liquid bridges with no solid contact (solid-liquid-solid contact) to direct contact (solid-solid contact in liquid). They tend to pull the neighboring grains together, up to the zero particle separation. Therefore they decrease the distances between the grains and cause densification. The overall model system rearrangement followed by decreasing of interparticle distances is a result of local relative motion of each grain toward its neighbors, but at the same time the grains are constrained by the neighboring grains during their motion. The total interaction force now depends on each particular force, but also upon the direction in which each of them acts. However, if some grains are constrained by the neighboring ones during their relative motion, it can be expected that some pores will tend to grow (Fig. 2b).

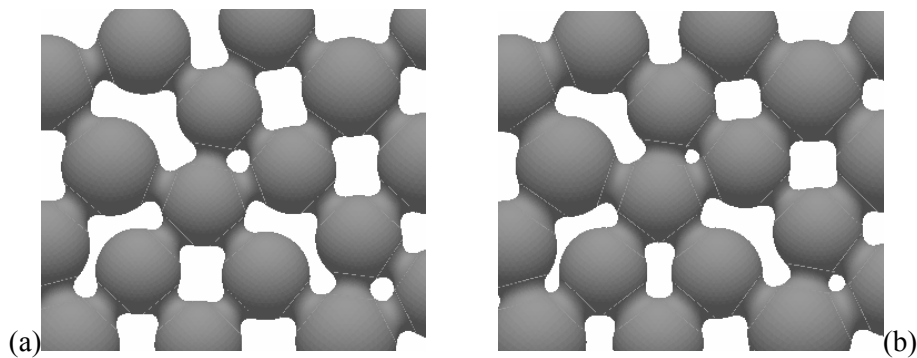


Fig.2. Snapshot of several interacting grains connected by liquid bridges.
(a) Initial structure. (b) After a sequence of sintering (150) time steps.

First attempts to calculate the changes of the positions of grains in a planar (due to better visualization) multi-grain system showed the possibility for solving this problem with moderate amount of mathematical and computer expense.

Acknowledgments

The first author was performed the present work under the project (No. 142011G) supported financially by the Ministry of Science and Technological Development of Republic of Serbia.

References

- [1] Z.S. Nikolic, *Z. Metallkd.*, 2004, **11**, 993-1000.
- [2] W.J. Huppmann and H. Riegger, *Acta Metall.*, 1975, **23**, 965-971.

COMPUTER SIMULATION OF THREE-DIMENSIONAL SKELETAL STRUCTURE EVOLUTION DURING SINTERING

Z. S. Nikolić¹ and M. M. Ristić²

¹*Faculty of Electronic Engineering, Department of Microelectronics
University of Nish, Nish, Serbia (zoran.nikolic@elfak.ni.ac.rs)*

²*Serbian Academy of Sciences and Arts, Belgrade, Serbia*

Abstract

In this paper we will define new computer simulation method to treat topological constraints due to neck growth and their influence on three-dimensional skeletal structure evolution during sintering.

Introduction

Theoretical analysis of densification during sintering must consider skeletal structure evolution influenced by some topological constraints, because they can cause grain rearrangements and the development of the pore distribution during sintering.

Various numerical models have been developed to study sintering, where the most ones were idealized two- and three-grain models. The very early computer study that deals specifically with topological constraint effects in large-scale randomly packed grain arrays was due to Ross *et al.* [1]

The primary task of this paper will be the development of new computer simulation method to treat topological constraints and their influence on three-dimensional (3-D) skeletal structure evolution during sintering. Similar work was reported by Leu *et al.* [2], where physically-based two-dimensional simulation method for treating topological effects during early stage sintering was considered.

Neck Growth and Topological Rearrangement

For simulation of solid skeleton structure evolution during sintering we will use a microstructure consisting of N spherical grains, which are represented by 3-D domains of regular shape, i.e. $G^\ell = G^\ell(\mathbf{C}^\ell, R_\ell)$, $\ell = 1, 2, \dots, N$, where $\mathbf{C}^\ell = (x_c^\ell, y_c^\ell, z_c^\ell)$ is the center of the mass of ℓ -th spherical grain of radius R_ℓ in space. The geometry and topological aspects of multi-grain model can be most easily described by the network in which grain centers are identified by vertices and a link (center-to-center distance) joins a pair of vertices \mathbf{C}^a and \mathbf{C}^b , where the link can be computed as the Euclidean distance function, i.e.

$$D_{ab} = \sqrt{(x_c^b - x_c^a)^2 + (y_c^b - y_c^a)^2 + (z_c^b - z_c^a)^2} . \quad (1)$$

The network corresponding to a model of connected grains is thus made up of a unique, interconnected set of closed polygons.

The basic sintering kinetics can be obtained using idealized two-grain sintering model, $\Delta D/\Delta t = f(D)$, where ΔD is the decrease in center-to-center distance for a given time step Δt and $f(D)$ is the particular neck growth law. Assuming that at time $t + \Delta t$ the decrease of link length is $\Delta D_{ij}^{t+\Delta t} = D_{ij}^t - D_{ij}^{t+\Delta t}$, each network link D_{ij}^t between a pair of vertices C^i and C^j can be updated by sintering transformation

$$D_{ij}^{t+\Delta t} \mapsto D_{ij}^t - f(D_{ij}^t) \cdot \Delta t. \quad (2)$$

The simulation method will be based on the concept that sintering law and the transformation (2) can be applied to each pair of contacting grains within the multi-grain model. The current state will be defined by the topology of the skeletal structure

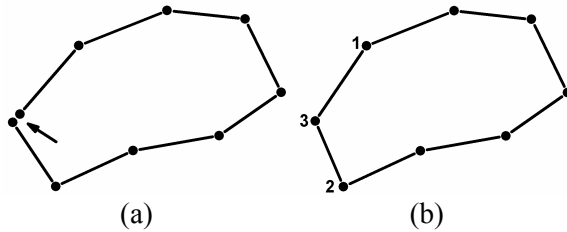


Fig.1. A eight-grain skeleton network illustrating closure errors (black arrow) due to topological constraint (a), and restored network after elastic distortion (b).

which includes the positions and connectivity of all grains.

A central problem in developing the time dependent skeleton structure involves topological constraints. Namely, due to the sintering law initially connected skeleton network at some vertices cannot remain topologically connected under sintering transformation (2) and will possess closure errors

(Fig. 1a). The elastic distortion generated in the grain network due to topological constraint can be evaluated by introduction the fundamental assumption that the multi-grain system remains in quasi-static equilibrium. Disconnected network can be now restored (accommodated, Fig. 1b) by application of the affine transformation

$$C^3 \mapsto \alpha C^1 + \beta C^2 + (1 - \alpha - \beta) C^3,$$

where α and β will be computed for the grains G^1 , G^2 and G^3 taking into account vertices C^1 and C^2 . After reconstruction, previously disconnected network (link-vertex data) must be updated by the function (1) for the next time step ($D_{31}^{t+\Delta t}$ and $D_{32}^{t+\Delta t}$).

Results and Discussion

Skeletal structure evolution will be simulated by algorithm based on levels methodology, on the neck growth between the grain G^n ($n=1,2,\dots,N$) and its first neighbors and on topological adjustment of center-to-center distances (links) between higher levels neighbors.

Figure 2a shows initial skeletal structure (the cluster) consisting of nineteen connected grains. Note that in such system characterized by relatively high packing density, extensive grain rearrangement is not possible. Computation starts with determination and assignment of grain levels. After computation of new center-to-center distances due to applied sintering law (it was assumed that neck growth between grains results in a relative neck size to grain size of about 0.4 after 1 hour) between selected grain and its first neighbors together with corresponding first neighbors relocation, all vertices \mathbf{C}^ℓ of remaining (higher levels) grains must be adjusted. This procedure will be repeated for all grains selected at random. Figure 2b shows a typical 3-D computed microstructure obtained after several time steps. Due to the neck growth, densification manifested by decrease in center-to-center distances as well as by relatively small grain rearrangement occurs.

Note that 3-D computer-generated large-scale random grain arrays should represent unit cell which will be used with periodic boundaries during simulation.

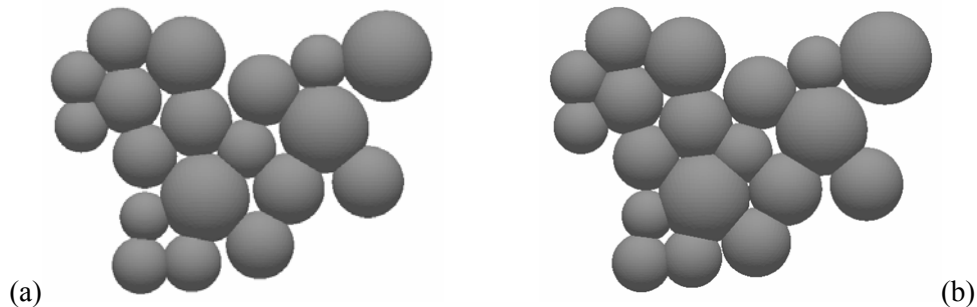


Fig.3. The cluster of nineteen grains before (a) and after neck growth during a sequence of sintering time steps (b). It was assumed that neck growth results in a relative neck size to grain size of about 0.4 after 1 hour.

Conclusion

The new computer simulation method considered here provides an effective methodology for treating topological constraints and their influence on skeleton structure evolution during sintering. Two most important features in this approach are that (i) the method can recognize and resolve topological constraints in large-scale random grain arrays, and (ii) the sintering law can be arbitrarily chosen.

Acknowledgments

The present work was performed under the project (No. 142011G) supported financially by the Ministry of Science and Technological Development of Republic of Serbia.

References

- [1] J. W. Ross, W. A. Miller and G. C. Weatherly, *Acta Metall.*, 1982, **30**, 203-212.
- [2] H. J. Leu, T. Hare and R. O. Scattergood, *Acta Metall.*, 1988, **36**, 1977-1987.

BIOACTIVE GLASS NANOPARTICLES IN BONE HEALING

S. Habibian Dehkordi¹, A. Sadegh Bigham², H. Amini Khoei¹, A. Doostmohammadi³ and M. Saeri⁴

¹*Department of Basic Sciences, School of Veterinary Medicine, University of Shahrekord, Shahrekord, Iran*

²*Department of Clinical Sciences, School of Veterinary Medicine, University of Shahrekord, Shahrekord, Iran*

³*Biomaterials Group, Department of Materials Engineering, Isfahan University of Technology, Isfahan, Iran*

⁴*Department of Materials Engineering, University of Shahrekord, Shahrekord, Iran*

Abstract

Bioactive glass is considered an effective bone graft substitute because of its advantages of forming a strong bond with living tissues, including bone and soft connective tissue. It has been recently showed that different materials in nano size demonstrate unique properties. Therefore, the present study was carried out to improve biological properties of bioactive glass by reducing its particle size and assess the suitability of the nano sized particles of bioactive glass in bone healing.

Introduction

Bone graft materials are used to improve bone healing and bone formation (1-5). These materials stabilize the blood clot, prevent membrane shrinkage and maintain the space available for new bone formation beneath the membrane (5). A variety of graft materials are used as alternatives to autogenous grafts (1). Bioactive glass is considered an effective bone graft substitute because of its advantages of forming a strong bond with living tissues, including bone and soft connective tissue (4). Many studies have demonstrated that bioactive glass has positive effects on bone healing (2). It has been recently showed that different materials in nano size demonstrate unique properties. Therefore, the present study was carried out to improve biological properties of bioactive glass by reducing its particle size and assess the suitability of the nano sized particles of bioactive glass in bone healing.

Introduction

Colloidal solutions (sols) of 63S composition (63 mol% SiO₂, 28 mol% CaO, 9 mol% P₂O₅) were prepared by mixing distilled water, hydrochloric acid, tetraethyl orthosilicate (TEOS), triethyl phosphate (TEP) and calcium nitrate. The result of EDX microanalysis of the glass particles indicated the presence of O, Si, P and Ca in the prepared Bioglass particles. The prepared Bioglass particles compositions were measured by X-ray fluorescence (XRF). The molar percentage of oxides was expressed by computer according to the elemental

analysis and considering the assumption that all the elements are in oxidic form. The BET specific surface area of Bioglass particles was $223.6035 \pm 0.5381 \text{ m}^2/\text{g}$. This value shows that particles have high surface area. 60 rabbits were randomly divided into three groups. General anesthesia was induced and maintained by intramuscular injection of xylazine and ketamine. The animal was positioned, shaved and prepared. A 20-mm linear incision through the skin and periosteum in the ventral portion of the tibia was made. Osteotomies were performed in the medial aspect of the tibia, creating a 2-mm deep hole with a diameter of 2 mm, involving the cortical and medullary bone. In experimental groups 1 and 2 these holes were filled with bioactive glass nanopowder and commercial bioactive glass powder, respectively. In the control or sham group the hole was filled with nothing. Radiological graphs were taken of five rabbits from each group at 7, 14, 28 and 42 days after surgery. They were then killed with an overdose of chloroform. The tibiae were dissected and fixed with 10% neutral buffered formalin for 48 h. The fixed bone specimens were decalcified in 5% nitric acid solution and processed in paraffin wax. 6- μm histological sections were prepared and stained with hematoxylin and eosin. The histological sections were observed and analyzed under a light microscope.

Results and Discussion

TEM images of prepared bioactive glass nanopowder showed that the bioactive glass powder size was less than 100 nanometers (Fig 1), which is necessary to obtain superior bioactivity than coarser crystals, and prepare a homogeneous coating. These results are in agreement with the result of previous studies (3). The DTA graph of the bioactive glass powder at the heating rate of $5^\circ\text{C}/\text{min}$ showed two exothermic peaks on the DTA curve at the range of $160\text{-}180^\circ\text{C}$ and $260\text{-}280^\circ\text{C}$ (Fig 2). These exothermic reactions could be attributed to releasing gaseous compounds from prepared bioactive glass during heating process. These reactions may cause cracks in the coating at these temperatures during drying of coated specimens. Therefore, the selected heating rate of the powder specimens between $160\text{-}180^\circ\text{C}$ and $260\text{-}280^\circ\text{C}$ was $0.1^\circ\text{C}/\text{min}$. The XRD pattern of the prepared bioactive glass nanopowder (Fig 3) confirms the formation of the bioactive glass nanopowder with amorphous structure. In present study, the proposed composition for producing bioactive glass showed a noticeable degree of bioactivity. Radiological and histological analysis revealed that in the experimental group 1 which received bioactive glass nanopowder, bone healing and bone formation was faster and better than experimental group 2 and sham group. These results confirm that bioactive glass in nano size has better performance in bone healing and bone formation.

Conclusion

Bioactive glass nanopowder was prepared by sol-gel technique. The bioactive glass powder size was less than 100 nanometers which is necessary to obtain greater surface area, better bioactivity, and preparing homogeneous coating. The formation

of apatite layer in experimental group 1 faster than in other groups indicate that prepared nanopowdered bioactive glass can be used in bone graft and healing.

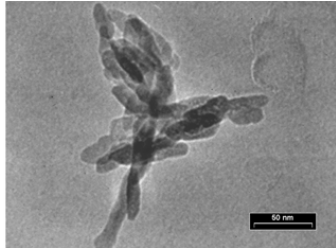


Fig 1. TEM images of the prepared bioactive glass.

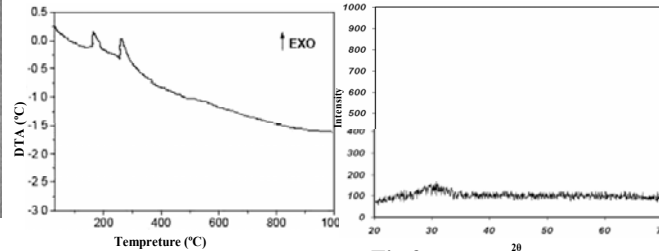


Fig 2. DTA curve for the bioactive glass nanopowder sample.

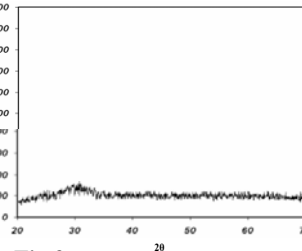


Fig 3. XRD pattern of the prepared bioactive glass nanopowder.

Acknowledgments

The authors are grateful to University of Shahrekord for support of the study

References

- [1] S. Ersanli, V. Olgac, B. Leblebicioglu. *J Periodontol*, 2004, **75**, 750-756.
- [2] S. Froum, S. C. Cho, C. Rosenberg, M. Rohrer, D. Tarnow. *J Periodontol*, 2002, **73**, 94-102.
- [3] C. Garcia, S. Cere, A. Duran. *J. Non-Cryst Solids*, 2004, **348**, 218-24.
- [4] L. L. Hench, *J. Am. Ceram. Soc.*, 1991, **74**, 1487-1510.
- [5] A.K. Lundgren, D. Lundgren, L. Sennerby et al. *Clin. Ora.l Implants. Res.* 1997, **8**, 90-95.

PROPERTIES OF CERIA FILMS GROWN ON STAINLESS STEEL BY ELECTRODEPOSITION METHOD

Lj. S. Živković,^{1,2} V. Lair,¹ O. Lupan^{1,3} and A. Ringuedé¹

¹*LECIME, UMR 7575 CNRS– ENSCP, Paris, France*

²*Vinča Institute of Nuclear Sciences, Belgrade, Serbia*

³*Technical University of Moldova*

Abstract

The study focuses on the elaboration of thin nanostructured ceria films, grown on the stainless steel, in view of high temperature fuel cell applications. Films were prepared electrochemically, via cathodic electrolytic deposition method, at low temperature (30 °C). Structural, morphological and composition analysis of the as-grown and annealed films were performed by means of XRD, Raman, SEM and EDX measurements.

Introduction

Ceria (CeO₂)-based films find many applications in Solid Oxide Fuel Cells (SOFCs), such as promising oxygen conducting electrolyte when doped, interfacial catalytic layer between electrode and electrolyte or protective coating for the interconnect materials [1-3]. Electrodeposition is a cost-effective technique suitable for producing high-quality ceria thin films. It provides an easy way to monitor process parameters (pH, T, reactant concentrations, deposition time) and, therefore, to control or design the deposit characteristics. The method is based on the reduction of oxygen precursor to form hydroxide ions in the vicinity of the working electrode. These OH⁻ ions react with Ce³⁺ cations present in the electrolytic solution, forming, either via Ce(OH)₂²⁺ hydrolysis or Ce(OH)₃ oxidation, thin oxide layer on the surface of working electrode [4,5]. All reported studies were carried out via a galvanostatic method. In this work we suggest depositing ceria by a potentiostatic method and focus on the characterization of composition, structure and morphology of as-deposited and annealed coatings.

Experimental

Experimental details are given previously [3, 6]. Briefly, a classical three cell electrode was used with a stainless steel disk (Goodfellow, 316L, 0.8 cm diameter) as working electrode under rotation (300 rpm), a saturated calomel (SCE) as reference and a Pt wire as counter electrode. Electrolytic bath, made of NaNO₃ (Riedel de Haen, 0.1 M) and Ce(NO₃)₃·6H₂O (Alpha Aesar, 5 mM), kept at 30 °C, was saturated by molecular oxygen, and a slight O₂ bubbling maintained during the deposition. Films were elaborated applying -0.8 V/SCE (EGG 263A) for 20 min. XRD was performed by Siemens D5000 unit. Powder Cell 2.4 program was used to determine the crystallite size and lattice strain. SEM images were made by Ultra 55

Zeiss FEG microscope. Micro-Raman spectra were measured by Horiba Jobin HR system.

Results

X-ray pattern for as-grown ceria, Fig.1, displays distinct diffraction peaks which match well the cubic fluorite CeO_2 crystal structure, referring to JCPDS#34-0394. The line width is large, typical for small crystallite size. With annealing at 600°C for 1h, crystallinity improves and line width becomes narrower, valid for all crystallographic planes. Average crystallite size of 12.1 and 14.8 nm was determined for as-grown and annealed films. Lattice strain was 0.2 % for as-grown, and negligible for annealed ceria. These values suggest that the stress is released with annealing.

Raman spectroscopy was applied to further study the phase and crystal quality of fabricated films. Figure 2 shows that as-grown ceria spectrum is characterized by an intense band at 456 cm^{-1} , attributed to the F_{2g} mode of Ce-O vibrations, in good agreement with reported data for non-calcinated particles [7]. The effect of thermal annealing is presented for comparison. As can be seen, the main peak becomes more symmetric, while its crystallinity enhances. Annealing also produces a shift in the maximum intensity of the Raman band towards bigger wave number, 465 cm^{-1} .

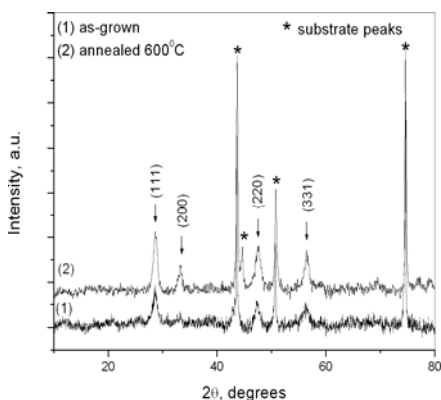


Fig.2. XRD patterns of as-grown and annealed ceria films

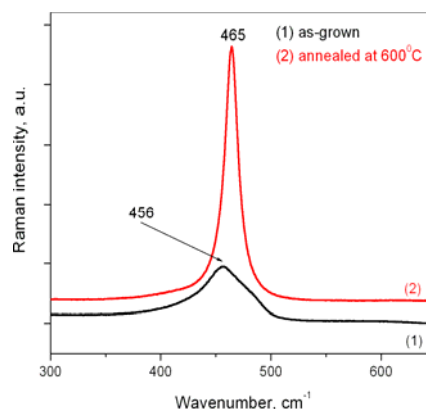


Fig.3. Raman spectra of as-grown and annealed ceria films

Surface morphology of as-grown film is shown in Fig. 5. Film is well-covering, dense and adherent to the substrate, with random cracks. Estimated thickness is around $2\ \mu\text{m}$. The EDX analysis revealed the presence of oxygen peak at 0.5 k eV in the elemental profile, while the Ce signals were registered at 0.9, 4.9 and 6.0 k eV.

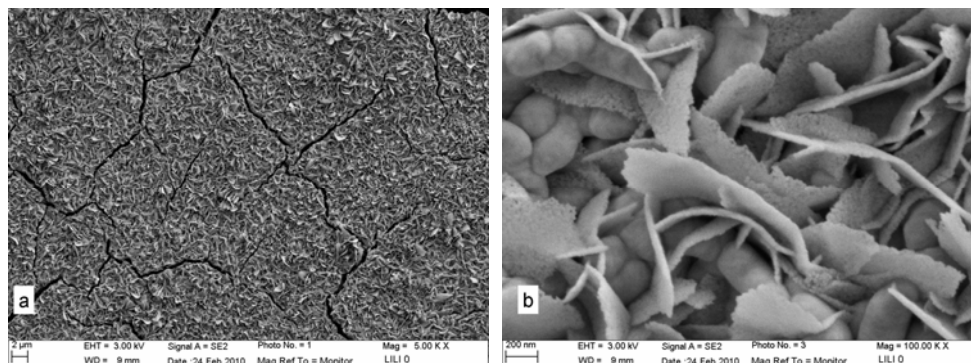


Fig.5. SEM micrographs of ceria film electrodeposited on stainless steel-top view under different magnifications: (a) 5000 x and (b) 100 000 x

Conclusion

Nanostructured ceria thin films have been grown on the stainless steel substrate by the electrodeposition method, applying for 20 min a potential of $-0.8V/(SCE)$ at room temperature. XRD analysis and Raman spectroscopy confirmed the cubic-fluoride structure of deposited ceria. The thermal treatment was found to enhance crystallinity and improve crystal quality. EDX confirmed that Ce and O were electrodeposited. High resolution SEM analysis illustrates that dense and adherent coating of cca $2\ \mu m$ in thickness covers fully the steel substrate.

Acknowledgements

Authors acknowledge funding from the French Research Agency, ANR-JCC06-0131. L. Živković thanks also Ministry of Science of the Republic of Serbia (Pr.No 45012).

References

- [1] B. Daslet, P. Blennow, P. Vang Hendriksen, N. Bonanos, D. Lybye, M. Morensen, *Journal of Solid State Electrochemistry*, 2006, **10**, 547.
- [2] T. Tsai, S. A. Barnet, *Solid State Ionics*, 1997, **98**, 191.
- [3] H. Elbelghiti, V. Lair, A. Ringuedé, M. Cassir, *ECS Transactions*, 2007, **10**, 2261.
- [4] I. Zhitomirsky, A. Petric, *Ceramics International*, 2001, **27**,149.
- [5] J. Schwitzer, *American Ceramic Bulletin*, 1987, 1521.
- [6] V. Lair, A. Ringuedé, P. Vermaut, S. Griveau, *Phys. Stat. Solidi C*, 2008, **205** 3492.
- [7] E. C. C. Souza, E. N. S. Muccilo, *Journal of Alloys and Compounds*, 2009, **473**, 560.

FEMTOSECOND LASER SURFACE TEXTURING OF AISI 1045 STEEL

B. Gaković¹, W. Perrie², J. Stašić¹, M. Trtica¹ and K. G. Watkins²

¹*Institute of Nuclear Sciences “Vinča”, Belgrade, Serbia*

²*University of Liverpool, Department of Engineering, Liverpool, UK*

Abstract

Morphological changes, including texturing and production of highly oriented periodical surface structures (LIPSS), on AISI 1045 steel were carried out by femtosecond laser pulses. The surface changes, induced by laser, are highly localized with minimal hydrodynamic effects and without the presence of a debris. The produced LIPSS have the periodicity of 700 nm, and were more prominent in case of triple scanning. Elemental analysis of the surface showed chemical changes, due to formation of oxides and diffusion of carbon from the bulk. These changes are also more obvious in case of triple scanning.

Introduction

The laser surface modification, including laser beam texturing, is of great fundamental and technological interest. Interaction of pulsed femtosecond laser beam with high quality steels, especially AISI 1045 steel, is not extensively reported in literature. AISI 1045 steel is within the class of medium carbon content steels. Presence of carbon increases steel hardness and strength and improves hardenability. Due to these, as well as other physical and chemical properties, the AISI 1045 steel can be used for component parts in machinery, automotive and allied industries. Carbon steels also have considerable applications in nuclear technology, e.g. piping systems, low and high pressure turbine sections, reactor vessels, etc. Our emphasis in the present paper is on the study of texturing with the production of specific periodic structures, using femtosecond laser emitting at 775 nm on AISI 1045 steel surface.

Experimental

The laser used in this work was Clark-MXR CPA2010 femtosecond laser system. The laser has a central wavelength of 775 nm at a fixed repetition rate of 1 kHz, with a pulse energy of 3 μ J and pulse duration of 160 fs (FWHM), confirmed with an autocorrelator. The output beam was linearly polarized, and directed to scanning galvanometer with 100 mm f-theta focal lenses. Specimen of AISI 1045 steel was mounted on axis precision motion control system, with a repeatability of 0.5 μ m. The laser beam was focused perpendicularly on the top surface of the specimen. Irradiation was conducted in air. The sample was a round plate of 15 mm radius and 2 mm thickness. The surface was mechanically polished down to an average roughness of about 200 nm. Square areas (1 mm side) were modified using scanning rate of 10 mm/second, with one and three overscans.

Results and Discussion

Laser induced periodic surface structures are known since the 1970s. Much work has been carried out on the mechanisms of their origin [1], but it is still an area of extensive research. Investigation of the morphological changes induced by laser on AISI 1045 steel surface has shown their dependence on laser beam characteristics [2], particularly here on the number of pulses (N) and overscans. Generally, interaction of femtosecond laser with AISI 1045 steel, at the fluence of 0.77 J/cm^2 during experiment, resulted in the production of modified area without the presence of debris and hydrodynamic features.

Surface texturing of the steel, at the constant energy, was initially done by a different number of pulses, on the same location of the sample (Fig. 1). Appearance of the primary periodic structures occurred after five successive laser pulses, and the texturing was homogeneous over the modified area. In case of $N > 100$, the LIPSS are distorted and the central part of the area is ablated.

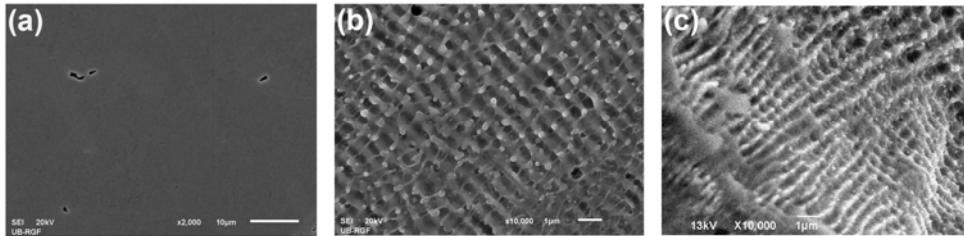


Fig.1. The surface of AISI 1045 steel prior to laser radiation (a), and after $N=10$ (b) and $N=500$ pulses (c).

The LIPSS obtained on the steel surface are, in both cases (deposition of pulses and laser scanning), oriented in the same way, perpendicular to the vector of the incident electric field (Fig. 2).

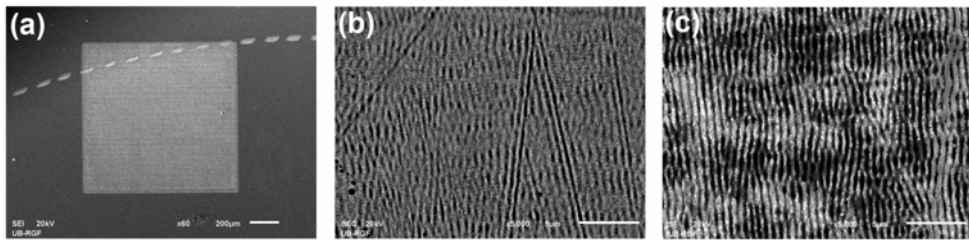


Fig.2. Textured AISI 1045 steel area produced by triple laser scanning (a) and LIPSS occurring after one (b) and three scans (c).

In case of overscan repeated three times, the features self align with features produced by preceding scan lines and are more prominent [3]. The periodicity of the LIPSS is $\sim 700 \text{ nm}$ in all cases, which is approximate to the laser wavelength. The origin of these ripples can be attributed to existing interference of the incident

laser beam with the so-called surface waves scattered off imperfections on the target surface and running along the surface [4].

Elemental EDX analysis showed the changes in the surface chemistry after laser scanning. It can be seen from the Table 1 that the concentration of iron is higher on the irradiated area, and the oxygen content decreases. This can be explained by the formation of iron oxides on the irradiated surface. Concentration of carbon is increased on the textured area, which can be due to diffusion of carbon from the bulk of the sample. These changes are also more prominent in case of triple scanning.

Table 1. EDX analysis of the steel surface prior to irradiation, and after single and triple laser scanning. Other alloying elements (Mn, Cr, Ni, Si) are balanced to a 100 percent and their concentration is not changed significantly with irradiation.

Spectrum	C [wt. %]	O [wt. %]	Fe [wt. %]
Non-irradiated	3.405	0.24	95.815
Single scan	5.44	0.84	93.08
Triple scan	9.31	2.85	87.27

Conclusion

Femtosecond laser pulses were used for the surface texturing and the production of highly oriented periodical surface structures on AISI 1045 steel. It has been shown that the morphological changes induced by femtosecond laser pulses are highly localized, with minimal hydrodynamic effects and without the presence of a debris. Obtained textured surface of the steel, as well as other metallic materials, has numerous potential applications.

References

- [1] I. Ursu, I. N. Mihailescu, A. M. Prokhorov, V. N. Tokarev, V. I. Konov, J. Appl. Phys., 1987, **61**, 2445-2450.
- [2] J. Stasic, M. S. Trtica, B. M. Gaković, B. Radak, D. Batani, T. Desai, Applied Surface Science, 2009, **255**, 4474-4478.
- [3] J. Cheng, W. Perrier, S. P. Edwardson, E. Fearon, G. Dearden, K. G. Watkins, Applied Surface Science, 2009, **256**, 1514-1520.
- [4] B. Tan, K. Venkatakrishnan, J. Micromech. Microeng., 2006, **16**, 1080-1085.

GAMMA-RADIATION AGING OF SILICA FILLED CHLOROSULPHONATED POLYETHYLENE/ BUTADIENE ACRYLONITRILE RUBBER BLENDS

G. Marković¹, M. Marinović-Cincović², S. Samaržija-Jovanović³, V. Jovanović³
and J. Budinski-Simendić⁴

¹Tigar, Nikole Pašića 213, Pirot, (gordana1markovic@gmail.com)

²Vinča Institute of Nuclear Sciences, milena@vinca.rs

³Faculty of science, Kosovska Mitrovica, Lole Ribara 29, (vojani@.sbb.rs)

⁴Faculty of technology, Novi Sad, (jarkamer@gmail.com)

Abstract

In this applicative work curing behavior, mechanical properties and gamma-radiation aging of silica filled elastomeric nanocomposites based on rubber blend: butadiene acrylonitrile rubber (NBR) and chlorosulphonated polyethylene rubber (CSM) were used as network precursors. The vulcanization characteristics were assessed for NBR/CSM rubber blends (50:50, w/w) using oscillating disc rheometer. The gamma radiation resistance of composites was determined from the tensile properties (hardness, tensile strength and elongation at break) after prolonged exposure to γ -irradiation (dose rate of 10 kGyh⁻¹ and total absorbed dose of 100, 200 and 400 kGy.

Introduction

One of the most important phenomena in material science is the reinforcement of rubber by particulate fillers, such as carbon black, silica, clays, silicates and others [1-2]. The mechanism of the changes in irradiated polymers includes both the

degradation and the cross linking processes. In earlier investigation many authors studied high energy radiation resistance of composites for industrial application [3]. The purpose of the present work was to investigate the influence of silica (with an average particle size of 28 μ m) on reinforcement and gamma-radiation resistance of NBR/CSM rubber blends.

Table 1. Formulation of NBR/CSM/silica rubber compounds

Ingredients (phrb)*	Sample					
	1	2	3	4	5	6
NBR	50	50	50	50	50	50
CSM	50	50	50	50	50	50
Silica (28 μ m)	0	20	40	60	80	100
Zink oxide	5	5	5	5	5	5
Stearine	2	2	2	2	2	2
Naphtenic oil	10	10	10	10	10	10
Accelerator	2	2	2	2	2	2
Magnesium oxide	4	4	4	4	4	4
Sulphur	1	1	1	1	1	1
Dyethylene glycol	0	0.2	0.4	0.6	0.8	1

* mass part per hundred mass parts of rubber blend

Experimental

The rubber compounds (Table 1) were prepared by using a laboratory-size two-roll mill maintained at $40\pm 5^\circ\text{C}$ expressed in mass part per hundred mass parts of rubber blend (phrb). All test specimens were compression molded at 160°C during the respective optimum cure time (t_{c90}) determined from the Monsanto Rheometer. The cure characteristics: M_l (minimum torque), M_h (maximum torque), t_{c90} (optimum cure time) and t_{s2} (scorch time) were determined with a Monsanto Rheometer model 100S (Table 2).

Tensile strength was measured at room temperature on an electric tensile testing machine (Zwick 1425) according to ASTM D 412. Hardness was measured using

Table 2. The cure characteristics of silica filled NBR/ CSM rubber compounds

Cure characteristics	Samples					
	1	2	3	4	5	6
MI (dNm)	8	7	7	6	6	5
Mh(dNm)	25	28	30	34	36	38
$\square M$ (dNm)	17	21	23	28	30	33
T_{s2} (min)	5	6	8	10	11	14
T_{c90} (min)	23	24	26	26	27	30

an indentation hardness tester according to ISO7619.

Irradiations have been performed in air in the Co-60 radiation sterilization unit at the Vinča Institute of Nuclear Sciences with the dose rate of 10 kGyh^{-1} and total absorbed dose of 0, 100, 200, and 400 kGy.

Results and Discussion

The shorter M_l and higher $\square M$ (Table 2) for silica filled NBR/CSM rubber blends than unfilled composites indicated stronger interactions between silica and polymer matrix. According silica surface, the scorch time (t_{s2}) and optimum cure time values (t_{c90}) of silica filled NBR/CSM rubber composites is higher than unfilled. The elasticity and tensile strength were sharply improved, also. It is well known that the mechanical properties of filled rubber composites depend strongly on the degree of adhesion between the filler and the rubber. The prepared samples were subjected to different γ -irradiation doses to estimate their aging behavior. Hardness and tensile strength changing values in %, were determined after gamma-radiated ageing in dose up to 400 kGy (Figures 1 and 2). The obtained values of changing hardness and tensile properties show the dependence on the aging dose and silica content.

Conclusion

Curing behavior, mechanical properties and gamma-radiation aging of silica filled elastomeric nanocomposites based on rubber blend: butadiene acrylonitrile rubber (NBR) and chlorosulphonated polyethylene rubber (CSM) was investigated. The scorch time (t_{s2}) and optimum cure time values (t_{c90}) of silica filled NBR/CSM rubber composites is higher than unfilled. The hardness and tensile strength values were sharply improved. Changing hardness and tensile properties show the dependence on the gamma-radiated aging dose and silica content. The degradation process of polymeric chains during irradiation (chain scission $R-R \rightarrow R\bullet + R\bullet$, low

molecular weight fragments may appear with loss of strength and hardness) also notified.

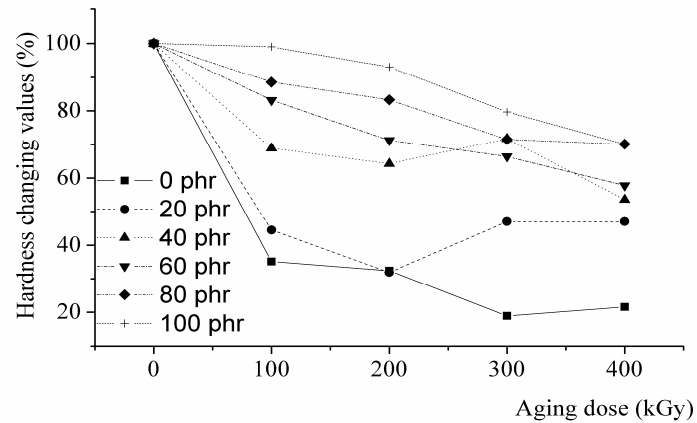


Fig.1 Hardness changing values, %, NBR/CSM rubber blend as a function of the γ -irradiation dose at different concentration of silica.



Fig.2 Tensile strength changing values, %, NBR/CSM rubber blend as a function of the γ -irradiation dose at different concentration of silica.

References

- [1] P. K. Mallick, S. Newman, Composite Materials Technology: Processes and Properties, Hanser, New York, 1990.
- [2] A. Berejka, C. Eberle, Radiation Physical Chemistry, 2002, **63**, 551-558.
- [3] R. L. Clough, Nuclear Instruments and Methods in Physical Research B, 2001, **185**, 8-13.

THE INFLUENCE OF X-RAY RADIATION ONTO THE PHASE TRANSITIONS OF SOME CHOLESTERIC LIQUID CRYSTAL MIXTURES

D. Ž. Obadović¹, M. Stojanović¹, M. Cvetinov¹, A. Vajda²,
N. Éber² and D. Lazar¹

¹*Department of Physics, Faculty of Sciences, Trg D.Obradovića 4,
21000 Novi Sad, Serbia*

²*Research Institute for Solid State Physics and Optics of the Hungarian Academy
of Sciences, H-1525 Budapest, P.O.Box 49, Hungary*

Abstract

We present the study of binary and multicomponent cholesteric mixtures undertaken with the aim of forming a system with the temperature of the phase transition close to the room temperature, which could be suitable for the detection of ionizing radiation. The phase diagrams were established on the basis of data from the optical microscopy and differential scanning calorimetry (DSC). The mixtures were exposed to the continual spectrum of X-Ray radiation in the period of 30/60 min. The mixture reacts by a change of the colour of the mesophase, and the shift of the mesophase transition towards lower temperature. The duration of the effects exceeds about six months.

Introduction

Various factors can have an influence on the pitch of the cholesteric helix [1-3]. In this paper we have examined the influence of X-ray irradiation. Optical and DSC studies have enabled the construction of the phase diagrams. X-ray diffraction data enabled the determination of some molecular parameters of the mixtures: the thickness of smectic layers and the longitudinal spacing distance in the cholesteric phase (d) and the average distance between the long axes of neighbouring molecules (D). The pitch of the cholesteric helix $P = \lambda/n$, was determined on the basis of reflection spectral analysis (λ is the wavelength belonging to maximal reflectance, n is the average refractive index).

Results and Discussion

The optical microscopic (polarizing microscope Carl Zeiss (Jena)) and DSC (Du Pont Instrumental Thermal Analyzer 1090 910) studies have been started with checking the pure substances: cholesteryl oleyl carbonate (**ChOC**), cholesteryl nonanoate (**ChN**) and cholesteryl benzoate (**ChB**) and shown good agreement with existing literature data [4]. We have examined the phase transitions of the binary (50-50%) mixtures: **Mix1** (**ChOC** – **ChN**), **Mix2** (**ChOC** – **ChB**), **Mix3** (**ChN** - **ChB**), as well as of the three component mixture, **Mix4** [**ChN** (55%) - **ChOC** (35%) - **ChB** (10%)]. The binary mixtures form mesophases at room temperature stable for several days, while **Mix4** produces a cholesteric phase stable in period of several months in a broad temperature range (19⁰C-60⁰C). This latter mixture was exposed to the continual X-radiation spectrum with the energy of 0.03 MeV for 30 min (**Mix4A**, dose 1.25 Gy) and for 60 min (**Mix4B**, dose 2.5 Gy) (Table 1).

Table 1. Phase transition temperatures T ($^{\circ}\text{C}$) and transition enthalpies $[\Delta H(\text{J/g})]$ evaluated on heating with DSC; helical pitch P (nm) and wavelength of maximal reflectance λ (nm) at $T = 24^{\circ}\text{C}$.

Code	Cr	$T(^{\circ}\text{C})$ [$\Delta H(\text{J/g})$]	Ch	$T(^{\circ}\text{C})$ [$\Delta H(\text{J/g})$]	I	P (nm)/ λ (nm)
Mix1	•	n.i.	•	37.8 (3.1)	•	413/ 617
Mix2	•	n.i.	•	85.3 (0.5)	•	423/ 633
Mix3	•	94.8 (1.03)	•	125.0 (0.6)	•	418/ 626
Mix4	•	n.i.	•	71.2 (9.3)	•	452/ 685
Mix4A	•	n.i.	•	70.3 (1.4)	•	420/ 633
Mix4B	•	n.i.	•	71.7 (3.0)	•	369/ 556

n.i. – the crystal (Cr) – cholesteric (Ch) phase transition could not be identified, because the mixtures did not crystallize within a few months.

All mixtures have cholesteric phase in a wide temperature region, with a change of color from red to blue. Based on experimental reflection spectra data (SPM-2, Veb Zeiss, Jena), it is obvious that the irradiation induces a shift of the maxima of the reflection peak towards lower wavelengths, compared to the not irradiated mixtures (Figure 1, Table 1). On the base of X-ray diffraction data (Seifert V-14, $\text{CuK}\alpha$), it was concluded that the thickness of smectic layers (d) decrease, and an average distance between the long axes of neighboring molecules (D) increased with temperature (Figure 2).

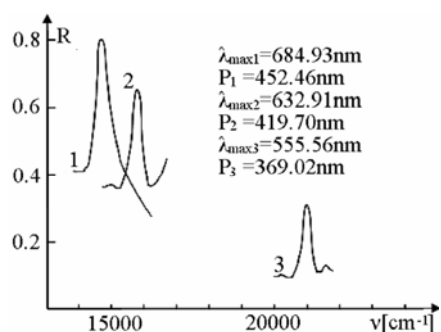


Fig.1. Reflectance spectra at $T = 24^{\circ}\text{C}$ of: Mix4(1), Mix4A(2), Mix4B(3).

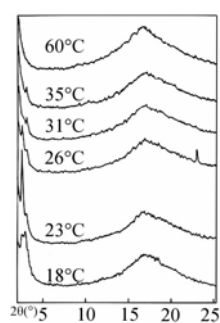


Fig.2. X-ray diffraction spectra of Mix4 at various temperatures.

Conclusion

The above presented results imply that the X-radiation may directly influence the conformation of the molecules. The most probable mechanism is a degradation of the chemical structure. One of possibilities is deformation of the sterane skeleton, which brings the molecule into a metastable state energetically close to the initial conformation of the non-irradiated sample. Another possible explanation is that π -electrons from the C=C or C=O double bonds in the cholesteryl oleyl carbonate or cholesteryl nonanoate become excited or even the bonds are broken, which can also influence the self-assembly of molecules in the cholesteric mesophase. These changes may increase the twist angle of the director from one layer to the other and thus may lead to a shortening of the cholesteric pitch and consequently, in a shift of the wavelength of the maximum of reflected light towards smaller wavelengths. This property enables the use of such samples as indicators of absorbed radiation dose.

Acknowledgements

This work has been supported by Grant No. 141020 from the Ministry of Science and Technological Development of the Republic of Serbia, the Hungarian Research Fund OTKA K81250, the ESF-COST D35 WG-13/05, the SASA-HAS bilateral scientific exchange project #9.

References

- [1] D. Ž. Obadović, A. Vajda, T. Toth-Katona, R. Marinković-Nedučin, *Mol. Cryst. Liq. Cryst.*, 1995, **265**, 135-142.
- [2] D.Ž. Obadović, M. Stojanović, S. Jovanović-Šanta, D. Lazar, A. Vajda and N. Éber, *International Journal of Modern Physics B*, 2006, **20**, 2999-3013.
- [3] A. Chanishvili, G. Chilaya, G. Petriashvili, D. Sikharulidze, *Mol. Cryst. Liq. Cryst.*, 2004, **409**, 209 – 218.
- [4] G.W. Gray and P. A. Winsor, *Liquid Crystals and Plastic Crystals*, J. Wiley and Sons, New York, 1974, **2**, 280.

COMPARATIVE STUDY OF COPPER AND ZINC UPTAKE BY NATURAL AND IRON MODIFIED ZEOLITES

S. Milićević, V. Milošević, M. Kragović and S. Matijašević

*Institute for Technology of Nuclear and Other Mineral Raw Materials, P. O. Box 390,
11 000 Belgrade, Serbia*

Abstract

In this paper the ability of natural zeolite (NZ), and different kind of iron modified zeolites (MZ1 and MZ2) to remove copper and zinc from aqueous solutions in batch reactor has been studied. The mass capacities for the zinc adsorption on NZ, MZ1 and MZ2 were 0.12, 0.23 and 0.46 mmol/l, respectively. Adsorption results for the copper were 0.12 and 0.25 mmol/g on NZ and MZ1, respectively.

Introduction

Because of the enormous amount and toxic impact of this metal contaminated wastewater that is generated during the extraction and processing the raw minerals, purification treatments need to be effective, environmentally acceptable and cost-effective. Natural materials like zeolites that are available in large quantities may have potential as inexpensive sorbents.

Zeolites are hydrated aluminosilicates of alkali and alkaline earth elements with unique crystal structures. This structure causes zeolite to have negatively charged surface which can be used for adsorption of metals such as copper and zinc. Negatively charge surface is balanced by mono and divalent exchangeable cations such as Na^+ , Ca^{2+} , K^+ and Mg^{2+} which give zeolite high cation exchange capacity. In order to enhance the sorption capacity of natural zeolite for heavy metal ions it's possible to modified their surface by metal oxide. In this paper two different modification methods (modified zeolite 1-MZ1 and modified zeolite 2-MZ2) were performed and the effects of various modifications were studied in batch experiments.

Experimental

Mineral with the average clinoptilolite content of 85% from Zlatokop deposit (Vranjska banja, Serbia) was used. After crushing and grinding the clinoptilolite, it was sieved to fractions -0.043mm .

Zeolite modification 1: 100g of zeolite was saturated with 500ml of 0.1M FeCl_3 in the acetate buffer 3.6 during 1h on a magnetic stirrer. Saturated sample was treated with 4% NaOH solution (450ml) stirred for an hour and then treated with 4% NaCl solution (250ml) and stirred for another hour at 50°C. The mixture was rinsed with distilled water, filtered and air dried for 24h [1].

Zeolite modification 2: The clinoptilolite-iron system was synthesized combining the method for pure goethite preparation [2] and method for preparation of iron-coated zeolite [3]. Thus, 50 g of each fraction of clinoptilolite was mixed with 25 ml of freshly prepared 10% $\text{FeCl}_3 \cdot 6\text{H}_2\text{O}$ solution and 700 ml of 0.1 M KOH (pH=10) in 2 l polyethylene container. The container was capped and the suspensions were aged for 20 days at room temperature. After the reaction period the suspensions were filtered, washed (untill Cl^- ions were no longer detected) and dried for 24h at 40°C.

The examination of zinc and copper uptake were carried out by shaking 1g of NZ, MZ1 and MZ2 with 50ml of aqueous solution of $\text{ZnSO}_4 \cdot 6\text{H}_2\text{O}$ and $\text{CuSO}_4 \cdot 5\text{H}_2\text{O}$ containing various initial zinc and copper concentrations (1-14 Cu^{2+} and Zn^{2+} mmol/l). Experiments were performed at room temperature using the batch technique for 24h. After equilibration the suspensions were filtered and in supernatants the concentration of remaining zinc and copper were determined by atomic absorption spectrophotometry using Perkin–Elmer 730 instrument. A JSM-6610LV SEM equipped with EDS was used for the electronic scanning of the samples.

Results and Discussion

The experimental data from the equilibrium studies were analyzed using Langmuir isotherms (in all experiments the correlation parameter r^2 was > 96%).

Similar values of capacities for different NZ particle sizes indicated removal of zinc and copper onto all volumes of zeolite particle and pointed to the ion exchange as the main mechanism for their removal, which was determined in previous paper [4]. The sorption capacity, q_m , which is a measure of the maximum sorption capacity corresponding to complete monolayer coverage, showed that a mass capacity for the Zn^{2+} uptake is twice large on MZ2 (0.23 mmol/g) and four time larger on MZ1 (0.46 mmol/g), compared to the NZ (0.12 mmol/g), Figure 1.

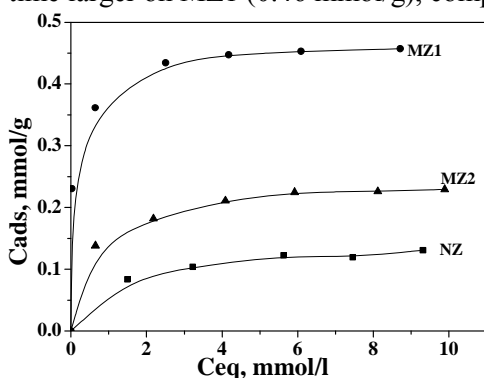


Fig.1 Langmuir isotherms for the ions adsorption by NZ, MZ1 and MZ2.

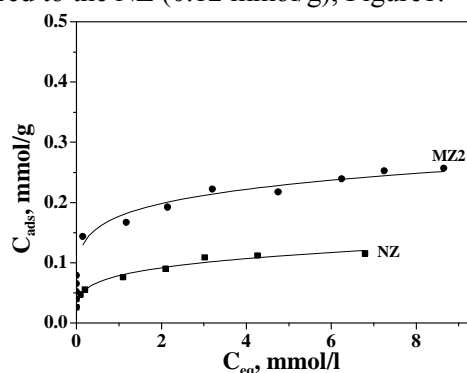


Fig.2 Langmuir isotherms for the Zn(II) Cu(II) ions adsorption by NZ and MZ1.

Because of the zeolite three-dimensional framework ionic radius of the contaminant play important role. The ionic radius for the copper and zinc are very close and the obtained results for copper uptake are similar to those for zinc. Mass

capacity for the copper uptake on the natural zeolite and MZ2 were 0.12mmol/g and 0.25 mmol/g, respectively, Figure 2.

Adsorption results for the copper uptake by the MZ1 weren't possible to obtain. During the contact time (even < 60 min), blue precipitate of $\text{Cu}(\text{OH})_2$ generated and it was unable to determine the mass capacity for the Cu^{2+} adsorption on the MZ1.

Despite the fact that the pH of the solution after reaching the equilibrium was less than 6, $\text{Cu}(\text{OH})_2$ precipitate while $\text{Zn}(\text{OH})_2$ didn't and this is because the solubility product for the $\text{Cu}(\text{OH})_2$ (2.2×10^{-20}) is much smaller than one for the $\text{Zn}(\text{OH})_2$ (1.2×10^{-17}). Both the NZ and MZ1 were analyzed using a scanning electron microscope (SEM). Micrographs presented in Fig. 3, shows that surface of the MZ1 is covered with cubics. The EDS analyses confirm that these are CaO cubics, which hydrolyze during the reaction releasing the OH^- , necessary for the formation of the copper hydroxide precipitate.

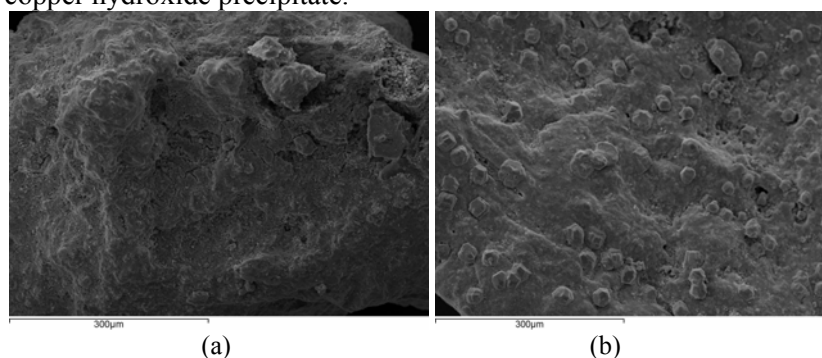


Fig.3. Micrographs of the (a) NZ and (b) MZ1

Conclusions

The uptake of zinc and copper ions by iron modified zeolites is successful and two and four times higher, depending of the modification process, compared to NZ. The experimental results for the zinc and copper removal have been fitted to linearized Langmuir isotherms and the obtained results are in agreement with the experimentally observed capacities. It's still unclear is the ion exchange mechanism responsible for the uptake by the MZ1 and MZ2 and it will be the subject of the further investigations.

References

- [1] M. Habuda-Stanić, B. Kalajdžić, M. Kuleš, N. Velić, *Desalination*, 2008, **229**, 1-9.
- [2] G. Mustafa, B. Singh, R. S. Kookana, *Chemosphere*, 2004, **57**, 1325-1333.
- [3] C. S. Jeon, K. Baek, J. K. Park, Y. K. Oh, S. D. Lee, *Journal of Hazardous Materials*, 2009, **163**, 804-808.
- [4] M. Ugrina, M. Trgo, J. Peric, A. Dakovic, N. Vukojevic-Medvidovic, I. Nuic, S. Milicevic, Z. Sekulic, M. Kragovic, *Zeolite 2010*, Sofia, Bulgaria, 2010, 268-269.

NANOCRYSTALLIZATION OF NIOBIUMGERMANATE GLASSES

M. B. Tošić¹, S. D. Matijašević¹, S. R. Grujić², V. D. Živanović¹, J. N. Stojanović¹
and J. D. Nikolić¹

¹*Institute for Technology of Nuclear and other Mineral Raw Materials, 86
Franchet d' Esperey St, 1100 Belgrade, Serbia*

²*Faculty of Technology and Metallurgy, 4 Karnegijeva St., 11000 Belgrade, Serbia*

Abstract

This paper presents the effect of K₂O content on phase composition of the nanocrystallized germanate glasses. It was shown that the exothermal peak temperature, T_p , shifted toward the higher temperatures with increasing content of K₂O. Such increase of K₂O content causes a decrease of GeO₂ content in the primary phases. The crystals below 100 nm were detected in the samples.

Introduction

Transparent or slightly opalescent crystallizes glasses with second-order optical non-linearity are of great scientific and industrial interest [1,2]. Nanocrystallization of glasses is an effective methods for fabrication of such materials. Developing techniques for creating nanostructures is an area that requires substantial effort. In this study, the attention was focus on K₂O-Nb₂O₅-GeO₂ glasses, because various potassium germanate-based crystals show a second harmonic generation [3]. For this investigation the glass composition 18.86K₂O·53.22Nb₂O₅·27.92GeO₂ (wt%) was selected. The influence of K₂O content on phase composition of the nanocrystallized glasses was studied.

Experimental

The starting materials used are reagent grade GeO₂, K₂CO₃, and Nb₂O₅. The appropriate batch compositions were melted at 1200°C for 1 h in a Pt crucible. The melts were cast on a steel plate and cooled in air. The obtained glass samples were transparent, without visible residual gas bubbles. Powder X-ray diffraction (XRD) analysis confirmed the quenched melts to be vitreous.

The peak temperature of crystallization T_p was determined by DTA run of glass powder with Netzch STA 409 EP instrument and Al₂O₃ powder as the reference material. Powdered glass samples of particle sizes < 0.038 mm were used.

The experiments with bulk glass samples were performed in a two-stage regime. The samples were heated at a heating rate $\beta = 10$ °C/min up to the desired temperature at which they were maintained for different times in an electric furnace, Carbolite CWF 13/13, with automatic regulation and a temperature accuracy of ± 1 °C. The heat treatment temperatures were in the range $T_c = 600 - 800$ °C. Finally, the samples were removed from the furnace and then crushed in an agate mortar. Powdered samples

were used for X-ray analyses. Identification of the phase crystallized was performed with the Powder X-ray diffraction analysis (XRD)(Philips PW-1710). The Powder Cell Program was used for determination of primary phases [4]. A Jeol JSM 6460 microscope was used for the SEM investigations.

Results and Discussion

The results of the chemical analysis show that a glasses with the content of K_2O : 18.25 (G-10), 19.52 (G-15), 20.30 (G-25) and 22.71 (G-28) (% wt) were obtained. In Figure 1 the DTA curves of these samples recorded at heating rate $10\text{ }^\circ\text{C}/\text{min}$ in the temperature range of $20\text{-}800\text{ }^\circ\text{C}$ are shown. At these curves the exothermal temperature peaks which correspond to the crystallization of glass were registered.

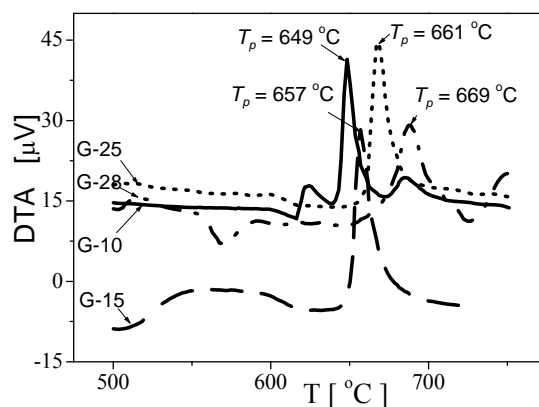


Fig.1. DTA curves recorded for the glasses G-10, G-15, G-25 and G-28.

As can be seen in Figure 1, the exothermal peak temperature, T_p , shifted toward the higher temperatures with increasing content of K_2O . Such behaviour indicates the formation of different crystalline phases during crystallization of these glasses.

To determine the phases appeared the experiments under isothermal conditions were performed with bulk samples. In two-stage regime the samples were first treated isothermally at the nucleation temperature between $T = 600\text{-}610\text{ }^\circ\text{C}$, for different times. The crystallization temperatures were in the range $T_c = 750\text{-}800\text{ }^\circ\text{C}$. The samples were kept at the crystallization temperatures for different times, in the range $t_c = 1\text{-}100\text{ h}$. The XRD patterns of the crystallized glass samples G-10, G-15, G-25 and G-28 are shown in Figure 2. It can be seen that several crystalline phases appeared in the samples which clearly demonstrated a primary crystallization of these glasses. The phase which is present in a largest amount crystallizes as primary one. Other phases appear as secondary ones. The these results shows that the role of some phases changed with increasing K_2O content. In the sample with 18.23 wt % of K_2O , a primary $K_6Nb_6Ge_4O_{26}$ phase appeared. Otherwise, in the samples with 19.52 and 20.30 wt % of K_2O the primary phase is $K_{3.8}Nb_5Ge_3O_{20.4}$ while in the sample with highest K_2O content of 22.71

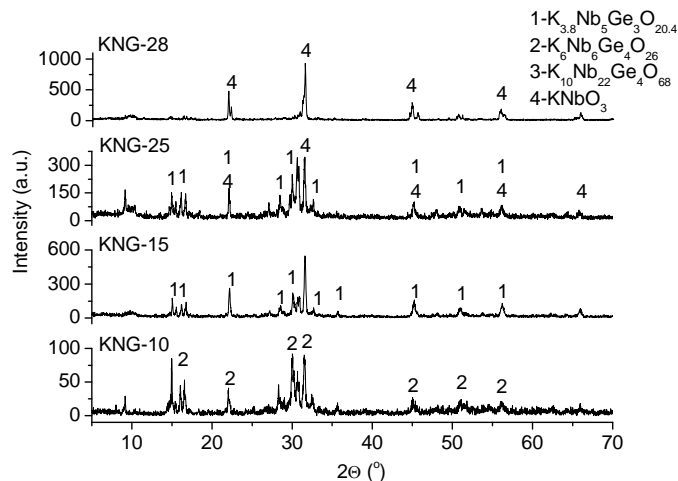


Fig.2. Powder XRD patterns for the crystallized samples of glasses G-10,G-15, G-25 and G-28. The numbers designate the primary phases.

wt% only the KNbO_3 phase appeared. The results show that such compositions of glasses are very sensitive on changes of K_2O content. By increasing of K_2O content as primary germanate phases with low contents of germanium oxide appeared, while in the glasses with K_2O content > 20 wt% the primary phase does not contain germanium oxide. Such behaviour confirms that an increase of K_2O content causes the change of kinetics and mechanism of the phases formation which indicates a very complex crystallization behaviour of these glasses. The samples crystallized are slightly opalescent and the dimensions of crystals were below 100 nm indicating a glass nanocrystallization (SEM micrographs).

Conclusion

The results presented in the study showed that these glasses crystallized with primary crystallization. By increasing K_2O content the germanate phases with low content of germanium oxide were appeared as primary ones. The noncrystallization of these glasses was registered and crystals dimensions below 100 nm were observed.

References

- [1] V. N. Sigaev, S. Y. Stefanovich, B. ChampAGNON, I. Gregora, P. Pernice, A. Aronne, R. Le Parc, P. D. Sarkisov, C. Dewhurst, *J. Non-Cryst.Solids*, 2002, **306**, 238-248.
- [2] Y. Takahashi, Y. Benino, V. Dimitrov, T. Komatsu, *J. Non-Cryst.Solids*, 1999, **260**, 155-159.
- [3] K. Narita, Y. Takahashi, Y. Benino, T. Fujiwara, T. Komatsu, *J. Am. Ceram. Soc.*, 2004, **87**, 113-118.
- [4] W. Kraus, G. Nolze, *Powder Cell for windows 2.4* (2000), www.CCP14.ac.uk.

THE OXIDATION OF ANILINE IN WATER: INFLUENCE OF ANILINE CONCENTRATION ON THE FORMATION OF POLYANILINE NANOSTRUCTURES

A. Rakić, M. Milojević, D. Bajuk-Bogdanović and G. Ćirić-Marjanović

*Faculty of Physical Chemistry, University of Belgrade, Studentski Trg 12–16,
11158, Belgrade, Serbia (gordana@ffh.bg.ac.rs)*

Abstract

The oxidation of aniline with ammonium peroxydisulfate (APS) in water, leading to the precipitation of nanostructured polyaniline (PANI) sulfate/hydrogen sulfate, was studied at various initial aniline concentrations in the range 0.02–0.2 M. The morphology and electrical conductivity of synthesized PANI significantly depended on the initial concentration of aniline (C_{ANI}). The content of nanotubes and conductivity of PANI decreased with the decrease of C_{ANI} . The effect of C_{ANI} on molecular structure of PANI was studied by FTIR, UV-Vis, and EPR spectroscopies.

Introduction

Preparation, characterization and applications of PANI nanostructures have been the subject of intense research during the recent years owing to their significantly improved dispersibility and processability, and enhanced performance in many applications in comparison with ordinary granular PANI [1]. It has been recognized that the oxidation of aniline with APS in aqueous solution in the presence of various acids, starting at $\text{pH} \geq 3.5$ and finishing at $\text{pH} < 2$ (a falling pH method), represents an efficient synthetic route to PANI nanotubes, without the use of an external template [2]. PANI nanotubes, accompanied with nanorods and nanosheets, were also synthesized in water without any added acid by dopant-free template-free method [3]. The purpose of this work is to investigate the influence of C_{ANI} on the molecular structure, morphology and conductivity of PANI nanostructures obtained by dopant-free template-free method.

Materials and Methods

Aniline (p.a., Centrohem), was distilled under reduced pressure and stored under argon at room temperature, prior to use. APS (analytical grade, Centrohem) was used as received. The aqueous solution of APS was poured into the aqueous solution of aniline, with constant stirring, at room temperature. The initial aniline concentrations were $C_{\text{ANI}} = 0.2, 0.1, 0.05$ and 0.02 M and the initial mole ratio of APS to aniline was constant (1.25). The precipitated PANI sulfate/hydrogen sulfate was collected on a filter, rinsed with aqueous solution of sulfuric acid (5×10^{-3} M) and dried in vacuo at 60 °C for 3 h. Corresponding PANI bases were obtained by

deprotonation of PANI sulfate/hydrogen sulfate with 5% ammonium hydroxide. The synthesized PANI samples, as well as corresponding PANI bases, were characterized by FTIR (Nicolet 6700), UV-Vis (GBC Cintra 10e) and EPR (Varian E104-A) spectroscopies, SEM (JEOL JSM 6460 LV) and TEM (Tecnai G2 Spirit) microscopies, and conductivity measurements (Wayne Kerr Universal Bridge B 224).

Results and Discussion

The electrical conductivity of synthesized PANI sulfate/hydrogen sulfate samples decreased in the order 2.8×10^{-3} , 1.1×10^{-3} , 6.6×10^{-5} and 1.4×10^{-7} S cm^{-1} for used C_{ANI} of 0.2, 0.1, 0.05 and 0.02 M, respectively. All PANI samples are nanostructured and their morphology significantly depends on C_{ANI} , as revealed by SEM and TEM (Fig. 1). The nanotubes, coexisting with nanosheets, nanorods and nanogranules, were observed in PANI synthesized at $C_{\text{ANI}}=0.2-0.05$ M. The content of PANI nanotubes, relative to other PANI nanostructures, decreased with the decrease of C_{ANI} . The PANI synthesized at $C_{\text{ANI}}=0.02$ M consists of network of nanorods and nanogranules (Fig. 1b).

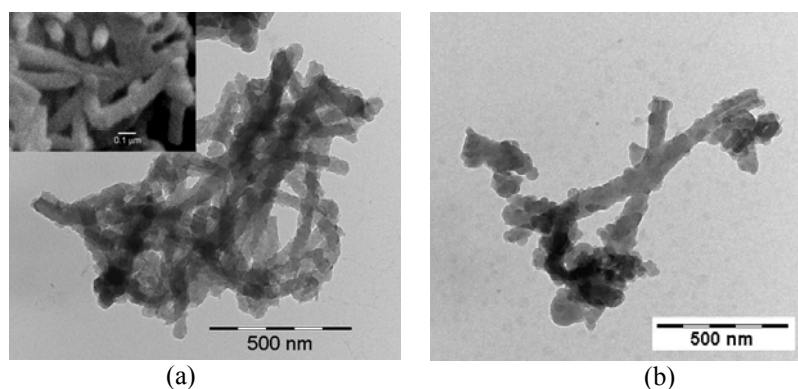


Fig.1. TEM images of PANI nanostructures synthesized at $C_{\text{ANI}} = 0.1$ M (a), and 0.02 M (b). Inset show corresponding SEM image.

The FTIR spectra of deprotonated PANI samples (PANI bases, Fig. 2a) show characteristic bands of PANI emeraldine base at 1586, 1505, 1380, and 830 cm^{-1} [2,3]. The last band reveals the presence of 1,4-disubstituted aromatic rings in PANI chains. The relative intensity of bands at 1415 cm^{-1} (substituted phenazine-like units), ~ 759 , 741, 725 and 695 cm^{-1} (mono- and 1,2-disubstituted aromatic rings), and ~ 906 and 858 cm^{-1} (1,2,4-trisubstituted rings in branched PANI units) increases with decrease of C_{ANI} , indicating that the extent of branching/crosslinking and amount of short chains/branches in PANI nanostructures increase with the decrease of C_{ANI} (these bands are marked with asterisk in Fig. 2.a) [2,3]. The EPR spectra confirm the presence of radical cations in conducting PANI samples prepared at $C_{\text{ANI}}= 0.2-0.05$ M (Fig. 2b). The EPR peak area decreases with decreasing C_{ANI} . The “exciton” band in UV-Vis spectra of PANI bases shows

bathochromic shift from 569 to 618 nm with increasing C_{ANI} from 0.02 to 0.2 M, respectively, due to the change of oxidation state of PANI chains in the samples.

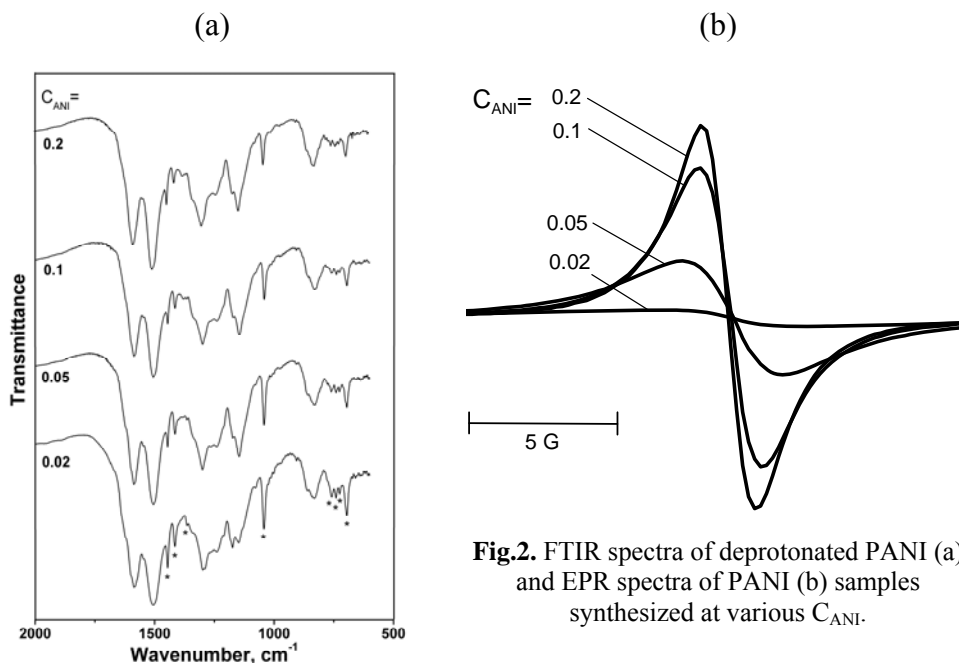


Fig.2. FTIR spectra of deprotonated PANI (a) and EPR spectra of PANI (b) samples synthesized at various C_{ANI} .

Conclusion

The oxidative polymerization of aniline with ammonium peroxydisulfate in water performed at the initial aniline concentration 0.02 M leads to nonconducting nanostructured polyaniline, which has substantially different morphology and molecular structure in comparison with semiconducting polyanilines obtained at the initial aniline concentrations in the range 0.05 – 0.2 M.

References

- [1] G. Ćirić-Marjanović, Polyaniline Nanostructures, Chapter 2, in Nanostructured Conductive Polymers, A. Eftekhari (editor), 1st edn., London: John Wiley & Sons; 2010, 19–98.
- [2] A. Janošević, G. Ćirić-Marjanović, B. Marjanović, P. Holler, M. Trchová and J. Stejskal, Nanotechnology 2008, **19**, 135606 (8 pp).
- [3] M. Trchová, E. N. Konyushenko, J. Stejskal, I. Šeděnková, P. Holler and G. Ćirić-Marjanović, J. Phys. Chem. B., 2006, **110**, 9461–9468.

CONTROLLED SYNTHESIS AND OPTICAL PROPERTIES OF Ag NANOPARTICLES

I. Vukoje, V. Vodnik and J. Nedeljković

*Vinča Institute of Nuclear Sciences, University of Belgrade, P.O. Box 522, 11001
Belgrade, Serbia*

Abstract

Nanosized hydrophobic, oleylamine stabilized silver (Ag) organosols were obtained in the reaction between the related metal salt and oleylamine in various organic solvents. The obtained hydrophobic colloids are stable and retain same particles morphology even after solvent evaporation and redispersion of the dried deposit in chloroform. The sizes of the Ag nanoparticles can be controlled from 8 to 25 nm by reaction temperatures. The position and shape of the surface plasmon resonance band depends upon the size and shape of Ag nanoparticles as well as dielectric constant of the medium.

Introduction

One of the main challenges in the preparation of nanosized colloids is developing the means of directing the particles into specific physicochemical environments, such as organic nonpolar liquids, specific regions within ordered surfactant phases and monolayer assemblies [1,2]. The understanding of the physicochemical properties of metal organosols is important due to their optical and catalytic behaviour [1,3]. From previously described synthetic methods in the literature, it can be assessed that colloidal stability, particle size, and optical properties strongly depend on the specific method and experimental parameters affecting in the efficiency of reaction (temperature, time, solvents, etc.). We present here a simple method for the preparation of dispersions of Ag nanoparticles in different organic solvents (toluene and dichlorobenzene). Special attention was paid to correlation between particle size and optical properties of Ag nanoparticles.

Experimental

Silver nanoparticles in toluene and dichlorobenzene were obtained using modified metod developed by Hiramatsu et al. [4]. 0.3 mM of Ag nitrate and 2.5 ml of oleylamine were dissolved in 50 ml of toluene, was refluxed for 24 h at 110 °C (or 1,2-dichlorobenzene for 8 h at 180 °C). The product was purified with centrifugation-dispersion process to wash off the remaining residues. The solution was first concentrated in a rotary evaporator and purified by precipitation with methanol. The suspension was centrifuged at 12000 rpm for 10 min. The precipitate was dried with argon flow and resuspended in chloroform to give a brown-yellow dispersion. The UV-Vis absorption spectra of the silver organosols were recorded using a Thermo Evolution 600 spectrophotometer. The transmission electron microscopy (TEM) images were acquired with Philips EM-400 at 100 kV.

Results and Discussion

Attempts had been made to make nearly monodisperse Ag nanoparticles with variable size in the mixture of oleylamine and toluene/dichlorobenzene. The mechanism involves the formation of stable complexes of silver ions with amines and then an electron transfer from amines to the silver complex at relatively high temperature [5]. The reduction process leads to formation of dispersions consisting of Ag nanoparticles, which are stable for weeks, although they show a certain tendency to stick to glass walls. The reaction temperature played a key role in nanoparticle size control. The higher reaction temperature (180 °C) results in a faster Ag^+ reduction and growth process, producing large size nanoparticles. At lower reaction temperature (110 °C), the reduction is slowed down and the nucleation process overruns the growth process, yielding small particles.

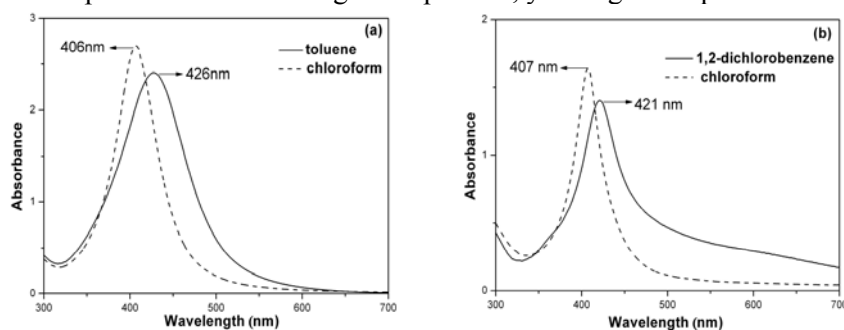


Fig.1 Change in UV-visible spectra of Ag organosols, due to solvent exchange from toluene to chloroform (a), and dichlorobenzene to chloroform (b).

The formation of small particles is kinetically favoured, whereas the formation of large particles is thermodynamically favoured. From a kinetics standpoint, small particles are easier to nucleate but they have a larger surface-area-to-volume ratio and therefore represent a higher energy state compared with larger particles. Hence, small particles are easily formed at lower temperature, but these small particles have a tendency to grow into larger particles to attain a lower energy state when the reaction temperature is higher. The surface modified Ag nanoparticles are characterised by a strong optical surface plasmon resonance band around 400 nm (Fig. 1) [6]. The spectrum of Ag nanoparticles in dichlorobenzene (Fig. 1b) exhibits a considerable tail toward the red, which indicates a size increase of Ag nanoparticles and formations of Ag aggregates. The process of solvent exchange from toluene or dichlorobenzene to chloroform should lead, according to Drude model [3], to a blue shift of the plasmon band, due to the higher refractive index of dichlorobenzene (1.551) and toluene (1.497) with respect to that of chloroform (1.445). Based on TEM measurements (Fig. 2) the diameter of spherical silver nanoparticles was found to be 8.2 ± 3.5 nm when the particles obtained in toluene and 22.1 ± 4.1 nm obtained in dichlorobenzene. The Ag nanoparticles, although closely packed in the case of dichlorobenzene, are well separated due to the presence of the oleylamine layer, adsorbed on the particle surface.

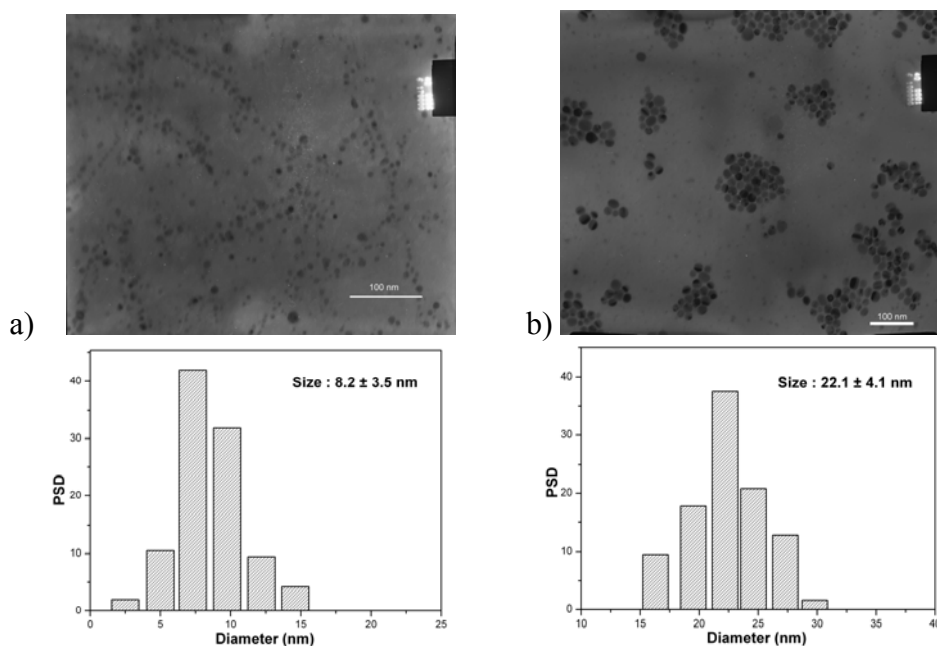


Fig.2 TEM images and the corresponding particle size distributions of the Ag nanoparticles obtained in toluene (a), and dichlorobenzene (b).

Conclusion

From all this work it can be assessed that particle size and its properties depend strongly on the specific method of preparation and the experimental conditions applied. The advantages of such a method can be found in the applications of metal particles as catalysts and has been successfully extended to synthesis of other metallic colloid such as gold and copper.

References

- [1] A. C. Templeton, J. J. Pietron, R. W. Murray, P. Mulvaney, *J. Phys. Chem. B*, 2000, **104**, 564-570.
- [2] F. C. Meldrum, N. A. Kotov, J.H. Fendler, *Langmuir*, 1994, **10**, 2035-2040.
- [3] P. Mulvaney, *Langmuir*, 1996, **12**, 788-800.
- [4] H. Hiramatsu, F. E. Osterloh, *Chem. Mater.*, 2004, **16**, 2509-2511.
- [5] M. Chen, Y-G. Feng, X. Wang, T-C. Li, J-Y. Zhang, D-J. Qian, *Langmuir*, 2007, **23**, 5296-5304.
- [6] V. V. Vodnik, D. K. Božanić, N. Bibić, Z. V. Šaponjić, J. M. Nedeljković, *J. Nanosci. Nanotechnol.*, 2008, **8**, 3511-3515.

INFLUENCE OF LAYER THICKNESS ON THE OPTICAL PROPERTIES OF MICROLENSES

B. Murić, D. Pantelić, D. Vasiljević and B. Panić

Institute of Physics, Pregrevica 118, Belgrade, Serbia

Abstract

Influence of layer thickness on the optical properties of microlenses, formed on the tot'hema and eosin sensitized gelatin (TESG) layer, was investigated. The lens shape was changed with layer thickness. Consequently, the lens focal length was varied.

Introduction

Individual microlenses (or an array of microlenses) are extensively applied in optics and biomedicine: medical devices, confocal microscopy, biosensors, fiber optics, wave-front sensing, imaging sensors, and so on. Photolithography, direct laser writing, thermal melting, and many others microlens fabrication methods were developed. Various materials such as: photoresists, polymers, composites, photosensitive glass were used for microlens manufacture [1-4].

In our previous research, colorless, transparent, aspheric, concave microlenses (individual or array) are produced on the tot'hema and eosin sensitized gelatin layer (short: TESG), by direct laser writing. Optical and imaging properties of microlenses were investigated. The lens parameters, such as focal length, depth and radius were controlled experimentally, by varying the laser beam profile, focus, intensity and exposure time [5-7]. Temperature measurements [8] have shown that, besides melting gelatin, the composition of the TESG layer and the photochemical reactions are important in the complex process of lens formation.

In addition, during our previous research, TESG layer thickness was fixed. As we continued our studies of TESG microlenses, in this paper we decided to examine the influence of TESG layer thickness on the optical properties of microlenses. The main goal of this research was to optimize the process of microlens fabrication and improve optical properties of the lens with establishing the connection between the layer thickness and the lens profile. Also, our intention was to tailor TESG microlenses optical properties to suit different biomedical applications, such as biosensors based on microlenses, and micro fluidic applications.

Experimental

The details of the preparation procedure of TESG layer were described in [5]. The TESG layers, with thicknesses between 50 μm and 200 μm , were prepared by the gravity settling method [6] on well cleaned microscope glass slides. The substrates were dried overnight, in the dark at room temperature. In the dry state, the thickness

of each layer was measured at six different points with a digital micrometer and the average was taken. Microlenses were formed by irradiating TEGS layers with unfocused second harmonic Nd:YAG laser light (532 nm wavelength). The laser power was 80 mW and exposure time was 20 seconds. The spatial distribution and temporal evolution of the layer temperature, during the microlens formation, was measured with an IR camera (FLIR Therma-CAM SC 640 with 640×480 pixel resolution). The radial scans of the profiles of TEGS microlenses were analyzed by a surface profiler (Talystep manufactured by Taylor-Hobson Ltd.).

Results and Discussion

The radial scans of the profiles of TEGS microlenses, formed at different layer thickness, are shown at Fig.1. Below layer thickness of $100 \mu\text{m}$ the lens shape was parabolic, with ring-shaped convex zone on the lens edges (see Fig. 1). The lens shape was changed and became spherical above thickness of $100 \mu\text{m}$. Consequently, the lens focal length is changed too. The lens focal length was enhanced about 10 times (from 1 mm for parabolic lens to 10 mm for spherical lens). 3D microlens profiles (parabola and sphere) with corresponding photograph of the letter 'A' captured through them are presented in Fig. 2.

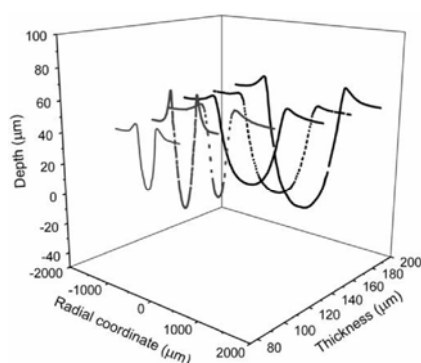


Fig. 1. Microlenses profiles variation with layer thickness.

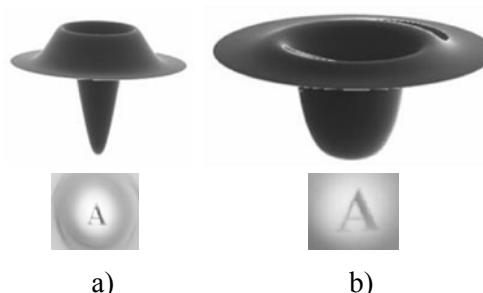


Fig. 2. 3D microlens profiles: a) parabola; b) sphere; and corresponding image of the letter 'A' captured through them.

The temperature radial distribution in the centre of lens is shown in Fig 3. Maximum value temperature- T_m coincides with the centre of the lens and corresponds to moment when the microlens is completely formed. As an illustration (see Fig 4) we can notice that there is an optimal layer thickness ($100 \mu\text{m}$) for which the T_m is maximal. The melting point of gelatin is significantly influenced by the layer thickness. Consequently, the optical properties of microlenses should be influenced by the layer thickness. We notice that for thickness of $50 \mu\text{m}$, TEGS layer is only bleached. Namely, during laser irradiation, eosin bleaches, making transition from pink to colorless state and microlens is not formed. Above $50 \mu\text{m}$ (see Fig 4) the depth of lens was increased with increasing layer thickness.

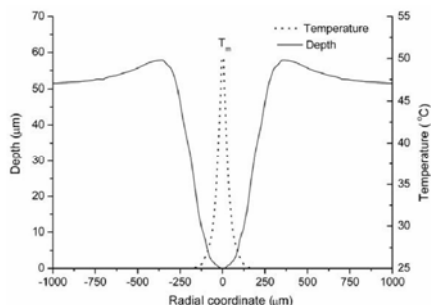


Fig. 3. Microlens profile with temperature radial distribution.

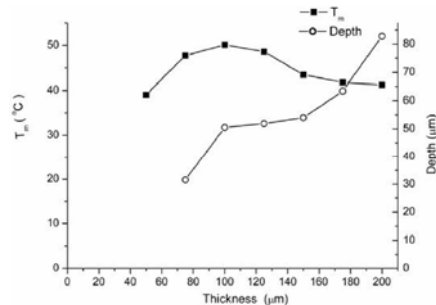


Fig. 4. Variation of T_m and lens depth with layer thickness.

Conclusion

Tot'hema and eosin sensitized gelatin (TESG) microlenses were produced on a cheap, easy available and nontoxic material. From the aspect various microlenses applications, we have shown that layer thickness is significant parameter that influences on optical (and therefore imaging) properties of TESG microlenses. It was shown that there is a limit value of layer thickness for a microlens formation. Also, it was noticed that microlens shape is a function of the layer thickness. There is a layer thickness limit after that the lens shape transforms from parabola to sphere. As a result, the lens focal length was changed.

Acknowledgments

This work is realized with the support of the Serbian Ministry of Science, through contract No. 141003. We thank Radomir S. Petrović for help with scanning of microlenses profiles.

References

- [1]. W. Wang, J. Fang, IEEE Sensors J., 2007, **7**, 11-18.
- [2]. J. Kim, S. Nayak, L. A. Lyon, J. Am. Chem. Soc., 2005, **127**, 9588-9592.
- [3]. K. Li, H-D. Liu, Q. Zhou, D. McIntosh, J. C. Campbell, Opt. Express, 2010, **8**, 11713-11719.
- [4]. G. M-Garnier, J. A. Zimmerlin, C. B. Sikora, P. Wadsworth, A. Crosby, Soft Matter., 2010, **6**, 398-403.
- [5]. B. Murić, D. Pantelić, D. Vasiljević, B. Panić, Opt. Mat., 2008, **30**, 1217-1220.
- [6]. B. Murić, D. Pantelić, D. Vasiljević, B. Panić, Appl. Opt., 2007, **46**, 8527-8532.
- [7]. Vasiljević D, Murić B, Pantelić D, Panić B, Acta Phys. Pol. A, 2007, **112**, 993- 995.
- [8]. B. Murić, D. Pantelić, D. Vasiljević, B. Panić, B. Jelenković, Appl. Opt., 2009, **48**, 3854-3859.

HYDROTHERMAL SYNTHESIS OF LiFePO_4 IN PRESENCE OF DIFFERENT ORGANIC ADDITIVES

M. Jović^{1*}, Z. Stojanović¹, D. Jugović¹, Lj. Veselinović¹, S. D. Škapin² and D. Uskoković¹

¹*Institute of Technical Sciences of the Serbian Academy of Sciences and Arts, Knez Mihailova 35/IV, 11000 Belgrade, Serbia*

²*“Jozef Štefan” Institute, Jamova 39, Ljubljana, Slovenia*

[*maja.jovic@itn.sanu.ac.rs](mailto:maja.jovic@itn.sanu.ac.rs)

Abstract

In this work we have investigated possibility to obtain pure LiFePO_4 powder using different organic additives during hydrothermal synthesis at 180°C . Phase pure phospho olivine was obtained in presence of polyvinylpyrrolidone, while addition of polyvinyl alcohol leads to formation of LiFePO_4 with impurities. Impurity phase was successfully avoided by introducing citric acid into reaction vessel. Phase composition was determined by XRPD. Morphology was revealed by particle size analyzer and FESEM.

Introduction

Lithium iron phosphate has become one of the most promising cathode materials for use in lithium ion batteries, but its application still suffers from tough synthesis procedure resulting from instable nature of Fe(II). One of the advanced techniques for LiFePO_4 powder preparation is hydrothermal synthesis which is quick and simple process and has low energy consumption. Another advantage of hydrothermal synthesis is possibility of introducing different reductive compounds which can suppress Fe(II) oxidation. As reductive compounds ascorbic acid, citric acid, glucose, sucrose, hydrazine [1, 2] etc were used.

The aim of this work was to investigate the possibility of the hydrothermal synthesis of phase pure phospho- olivine in presence of polyvinylpyrrolidone and polyvinyl alcohol and their influence on particle morphologies.

Experimental

LiFePO_4 was prepared by hydrothermal method starting from LiOH , $\text{FeSO}_4 \cdot 7\text{H}_2\text{O}$ and H_3PO_4 in molar ratio 3: 1: 1. First, a desired amount of organic compound i.e. PVP or PVA or PVA/citric acid was dissolved in distilled water. Then H_3PO_4 , FeSO_4 and LiOH water solutions were added under constant stirring and transferred into the stainless steel autoclave. The precursor solution was purged with argon and heated at 180°C for 10-20 hours. The product was dried at 60°C in air overnight.

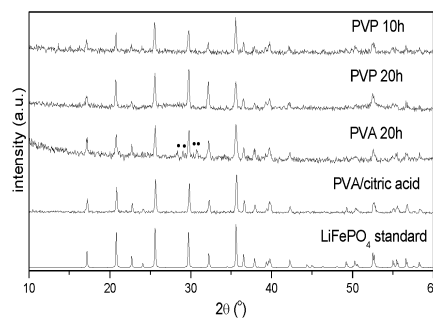


Fig. 1. XRD pattern of LiFePO_4 powders synthesized with PVP after 10 and 20 hours, with PVA and PVA/citric acid

The XRPD patterns were recorded using $\text{CuK}_{\alpha 1,2}$ radiation in 2θ range $10\text{--}60^\circ$ with the 0.05° step and 2 seconds exposition time. The surface morphology was observed using SUPRA 35 VP Carl Zeiss field-emission scanning electron microscope. Particle size distributions of the powders were measured by a particle size analyzer Mastersizer 2000 Malvern instruments.

Results and discussions

XRD patterns of the samples obtained after 10 and 20 hours of the hydrothermal treatment in the presence of PVP show well crystallized single LiFePO_4 phase, Fig 1. On the contrary, in the presence of PVA after 20 hours of the hydrothermal treatment there are some additional diffraction lines which can be mainly attributed to the mixed iron phosphates $\text{Fe}_2\text{Fe}_3(\text{PO}_4)_6$. Apparently PVA wasn't sufficient enough to provide reductive conditions that can prohibit the conversion of Fe^{2+} to Fe^{3+} . When citric acid was added to PVA precursor solution pure LiFePO_4 phase was obtained.

Cubic shape particles (0.5 to 4 μm) with sharp corners were obtained for samples prepared with PVP after 10 h (Fig.2a). By

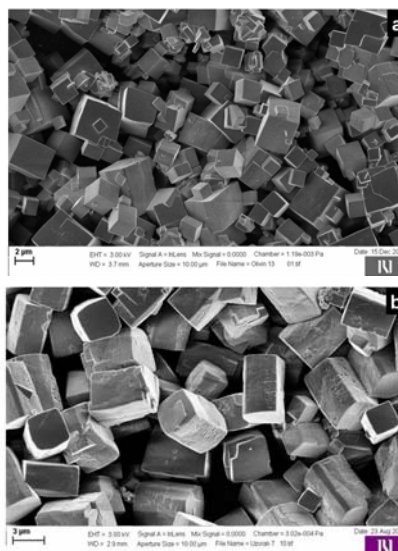


Fig. 2 FESEM images of the LiFePO_4 samples, synthesized with PVP after 10 (a) and 20 (b)

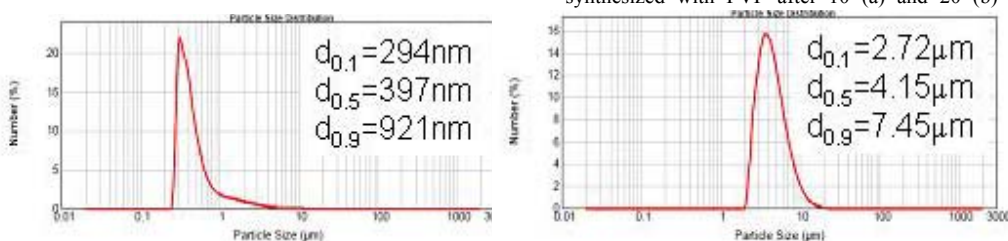


Fig.3. Particle size distributions of the LiFePO_4 samples, synthesized using PVP after 10 and 20 hours

prolonging hydrothermal treatment to 20 h more uniform prismatic particles with much smoother corners were obtained (Fig 2b). Prismatic particles are about $6\mu\text{m}$ long with diameter of about $2\mu\text{m}$. The relative span, defined as $(d_{0.9}-d_{0.1})/d_{0.5}$, is about 1.6 and 1.1 for PVP10h and PVP20h respectively, which suggest that prolonged hydrothermal treatment leads to more uniform particle size distribution inducing particle growth. The growing of bigger particles was most probable enabled by dissolution of smaller particles which resulted in increased and uniform particle size.

Sample prepared with PVA after 20 hours shows two different morphologies (Fig. 4a). This is in compliance with the XRD result where two phase powder was observed. Particle size distribution curve (Fig 5a) shows two peaks that correspond to two different morphologies.

Diamond- like particles (Fig 4b) typical for LiFePO_4 [1] were obtained when both citric acid and PVA were added to the precursor solution. Size of these particles is about 4- 7 μm on a side and about 1-4 μm thick. The average particle size (Fig 5b) is 4.374 μm and the relative span is 0.8. Lower value of the relative span confirms particle size uniformity which is clearly seen from FESEM image. Comparing this with XRD results it can be concluded that needle like particles (Fig 4a) originate from impurity phase which was successfully avoided by introducing citric acid in the reaction vessel.

Conclusions

Well crystallized LiFePO_4 particles were successfully synthesized via hydrothermal reaction operated at 180°C in the presence of PVP and PVA/citric acid. PVA wasn't sufficient enough to provide reductive conditions, so it was necessary to introduce citric acid into reaction vessel to obtain pure LiFePO_4 phase. Organic compounds which were added to precursor solution have significant influence on particles morphologies. Powders prepared with PVP have cubic shape particles, while powders prepared with PVA and citric acid show diamond- like particles.

Acknowledgement

This work was supported by Serbian Ministry of Science and Technological Development, project No. 142006.

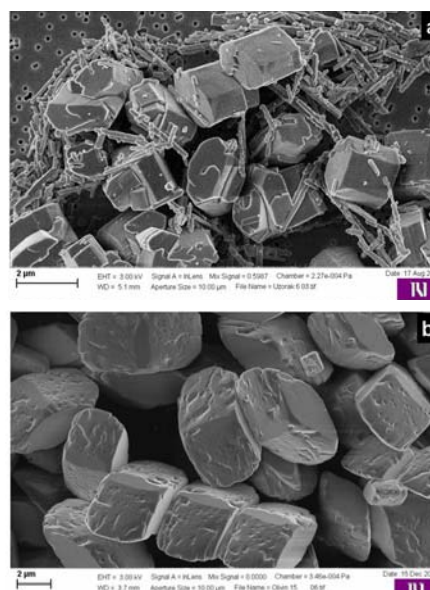


Fig. 4 FESEM images of the LiFePO_4 samples, synthesized with PVA (a) and PVA/citric acid (b)

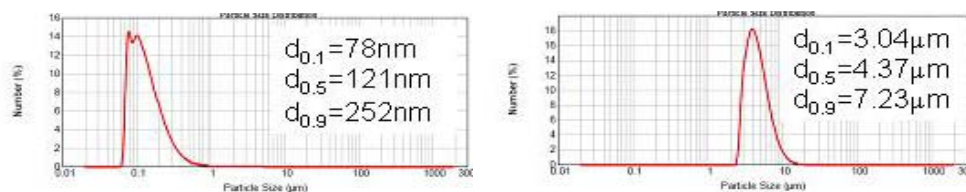


Fig.5 Particle size distributions of the LiFePO_4 samples using PVA and PVA/citric acid after 20 hours.

Literature

- [1] J. Chen, M. J. Vacchio, S. Wang, N. Chernova, P. Y. Zavalij, M. S. Whittingham, *Solid State Ionics*, 2008, **178**, 1676-1693
- [2] J. Ni, M. Morishita, Y. Kawabe, M. Watada, N. Takeichi, T. Sakai, *Journal of Power Sources*, 2010, **195**, 2877-2882

INTRODUCTION OF TRANSITION METAL CATIONS (Co²⁺ and Zn²⁺) INTO DEALUMINATED NaY ZEOLITE OBTAINED BY CITRIC ACID TREATMENT

R. Hercigonja¹, D. Maksin² and V. Dondur¹

¹*Faculty of Physical Chemistry, Belgrade* ²*Vinča Institute of Nuclear Sciences, Belgrade*

Abstract

Aluminum ions were extracted from the framework of the faujasite type zeolite NaY (Si/Al=2.4) by citric acid treatment. Dealuminated CoY and ZnY zeolites of high cobalt and zinc content were prepared by replacing sodium ions with Co²⁺ and Zn²⁺ in dealuminated Y zeolites, with increased framework Si/Al ratio. Chemical and XRD analyses of zeolites were performed and the FTIR-ATR spectra were recorded. The results of physicochemical analyses are discussed in terms of unit cell (u.c.) composition.

Introduction

Framework dealumination is an important method to improve catalytic properties of zeolites. Dealumination treatment process extracts Al atoms from tetrahedral positions in the zeolite framework and converts them to octahedral, amorphous aluminum oxide (extraframework aluminium species), which often remains in the pores of zeolite. Transition-metal-exchanged zeolites are key materials for catalysis and adsorption. Framework Si/Al ratio dictates the amount of transition-metal cations that can be exchanged into zeolite, and therefore the active site density. The aim of presented work was to obtain dealuminated Y zeolites of relatively high cobalt and zinc content through a relatively simple procedure. Chemical, XRD and FTIR-ATR data are presented for these products.

Experimental

The zeolite used in this work was NaY(SK-40) faujasite sample with the u.c. formula Na₅₆[(AlO₂)₅₆(SiO₂)₁₃₆]. Zeolites with different Si/Al framework ratios were prepared by citric acid treatment [1]. Relative crystallinity was estimated from the XRD patterns that were recorded with a XRD Phillips PW 1050 instrument (20 mA, 34 kV, 2.5°/min), by means of comparison of (1 1 1) peak intensities of the dealuminated samples to the reference NaY zeolite. The sodium form of the dealuminated Y zeolite samples was transformed into different cation forms (CoY and ZnY) by ion exchange procedure, using 0.5M solutions of CoCl₂ and ZnCl₂. All samples were microwave digested in aqua regia and analyzed for Na, Co, Zn, Al and Si content by atomic emission spectroscopy (Perkin-Elmer ICP/6500). Infrared attenuated total reflection (ATR) spectra were recorded on a Nicolet 380 FT-IR spectrometer (4000-400cm⁻¹). The lattice cell constants were calculated using FullProf Suite software.

Results and Discussion

According to literature date, in the process of dealumination of faujasite type zeolites (f.e. thermochemical treatment of NH₄Y in steam [2] and treatment of NaY

with SiCl_4), dealuminated zeolites appear as the proton modification, HY. The method presented in this paper provides preparation of dealuminated Co^{2+} and Zn^{2+} exchanged Y zeolites without their conversion to protonated Y form.

Chemical analysis showed that the content of total (framework and extraframework) aluminum decreased from 8.6% (NaY) to 5.4 % (NaY-D) and the content of sodium decreased from 7.3 % (NaY) to 3.6 % (NaY-D). XRD patterns of regular NaY and the obtained dealuminated zeolites are shown in Fig. 1.

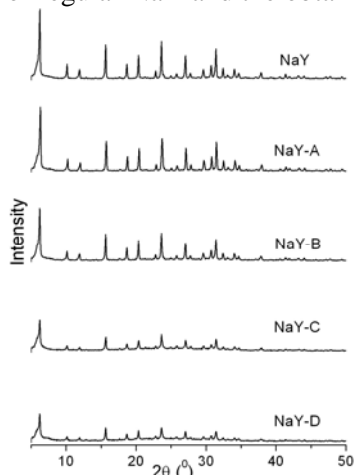


Fig.1. X-Ray diffraction patterns of zeolites: NaY, NaY-A, NaY-B, NaY-C and NaY-D

The peak positions in the observed XRD patterns of the dealuminated samples remained unchanged. The structure of zeolite is not essentially destroyed during the treatment with citric acid solution of low concentration, 0.01 M for NaY-A and 0.02M for NaY-B. The treatment with 0.03 M (NaY-C) and 0.04 M (NaY-D) citric acid solution lead to the collapse of zeolite lattice. The estimated relative crystallinity of NaY-A was 95%, NaY-B - 81%, NaY-C - 61% and NaY-D - 40%. The calculated lattice cell constants for the starting NaY and the dealuminated zeolites with high estimated crystallinity (NaY-A and NaY-B) were 2.4642, 2.4594 and 2.4576 nm, respectively. The decrease of the u.c. size is the consequence of the increasing Si/Al ratio during the dealumination of zeolite [3].

The FTIR-ATR spectra of regular CoY and ZnY and dealuminated CoY-A, CoY-B, ZnY-A and ZnY-B are shown in Fig. 2. Framework sensitive structural bands [4] due to the asymmetric Si-O and Al-O stretching within the tetrahedra at $950\text{-}1050\text{ cm}^{-1}$,

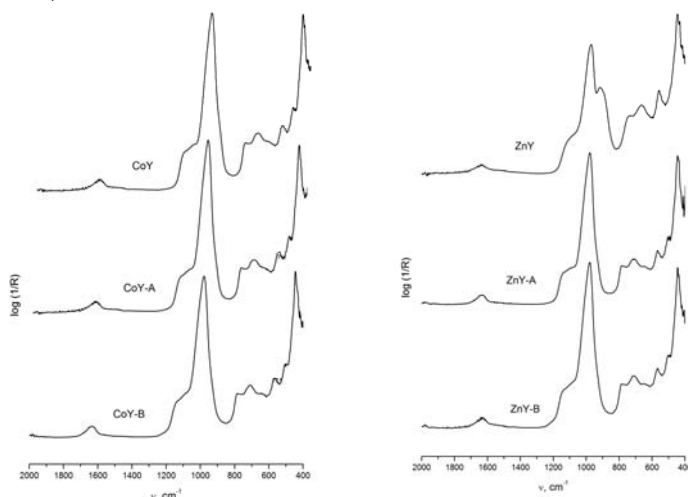


Fig.2. FTIR-ATR spectra of starting and dealuminated CoY and ZnY

symmetric stretching between tetrahedra at 750-820 cm^{-1} , and double six-membered oxygen ring at 500-650 cm^{-1} occur in the spectra of dealuminated CoY and ZnY with the same intensity as in the spectra of regular CoY and ZnY. The frequencies of these bands are very sensitive to the Si/Al framework ratio and with decrease in Al content, i.e. increase in Si content, the bands are shifted to higher frequencies [5]. In our spectra of the dealuminated cation-exchanged zeolites, the frequencies are always higher than in the spectra of regular CoY and ZnY. Using the frequencies of these three bands and the equations given in Refs. [6] the number of framework Al atoms per unit cell in dealuminated CoY and ZnY was calculated. The number of Si atoms per unit cell after dealumination was calculated using the equation $N(\text{Si}) = 192 - N(\text{Al}_{\text{Framework}})$ [6]. Subsequently, the framework Si/Al ratio in dealuminated CoY and ZnY samples was calculated. These data are listed in Table 1, as well as the percent content of Co and Zn determined by chemical analysis.

Table 1. Chemical composition of starting and dealuminated CoY and ZnY

zeolite	% extraframework Al	Framework Al mol/ u.c.	Si mol/ u.c.	Si/Al	% Co	% Zn
CoY	-	56	136	2.4	7.4	
CoY-A	8.2	45	147	3.3	6.5	
CoY-B	7.9	43	149	3.5	5.3	
ZnY	-	56	136	2.4		7.6
ZnY-A	8.2	45	147	3.3		7.1
ZnY-B	7.9	43	149	3.5		5.6

Conclusion

NaY (Si/Al=2.4) was modified by citric acid treatment into highly crystalline NaY-A (95%) and NaY-B (81 %) dealuminated forms with increased framework Si/Al ratio (3.3 and 3.5, respectively). FTIR-ATR spectra of dealuminated CoY and ZnY confirmed that the introduction of Co^{2+} and Zn^{2+} has no adverse effect on the stability of the basic zeolite framework. The number of framework aluminum and silicon, the percent of exchanged Co and Zn and the Si/Al framework ratio in the obtained dealuminated zeolites were calculated.

References

- [1] V. Rakic, Lj. Damjanovic, V. Dondur, R. Dimitrijevic, Proceedings of the Int. Con. on Fundamental and Applied Aspects of Phys.Chem., 2004, **2**, 21-23.
- [2] H. K. Beyer, I. M. Belenykaja, F. Hange, M. Tielen, P. J. Grobet, P. A. Jacobs, J. Chem. Soc., Farad. Trans. I, 1985, **81**, 2889–2901.
- [3] E. Dempsey, G. Kuhl, D. Olson, J. Phys. Chem., 1969, **73**, 387-391.
- [4] E. M. Flanigen, H. Khatami, H. A. Szymynski, Advan. in Chem. Ser., 1971, **101**, 201-208.
- [5] R. Sohn, S. De Canio, J. Lunsford, D. O'Donnelli, Zeolites, 1986, **6**, 225-227.
- [6] O. Carion, K. Thomas, T. Chevreau, Microporous and Mesoporous Materials, 2001, **46**, 327-340.

INFLUENCE OF Na⁺ CONTENT ON SOLID PHASE OF SYSTEMS TPABr-Na₂O-SILICA-H₂O

O. A. Kovačević¹, B. T. Kovačević¹, D. Arandelović¹
V. Dondur² and Ž. Lj. Tešić³

¹ *Institute of General and Physical Chemistry, Belgrade, Serbia,* ² *Faculty of Physical Chemistry, Studenski trg 12, Belgrade, Serbia,* ³ *Faculty of Chemistry, Belgrade, Serbia*

Abstract

Amorphous solid phase from the Na₂O-SiO₂-TPABr-H₂O systems were investigated by the SEM, BET and XRD measurements. Precipitated silica, structured as agglomerates of spheroid nanoparticles, was used as a source of silicon. The content of Na⁺ in the system, determined by Na₂O/SiO₂ ratio, was changed within the range from 0 to 0.25. Micrographs give evidence that in the systems where Na₂O/SiO₂ ≤ 0.1 the morphological basic properties of precipitated silica were not lost, but substantial changes that occur in the solid phases were dependent on Na⁺ content. After the Na₂O/SiO₂ ratio in the system was increased to reach the value 0.25, the nanoparticle in structure of the solid phase was lost.

Introduction

Na⁺ cations present in aluminosilicate and/or silicate systems determine the alkalinity of systems, affect the polymerization-depolymerization processes and strongly determine the crystallization of zeolites [1,2]. We investigated the range of Na₂O/SiO₂ ratios from 0 to 0.25, which is important for the crystallization of some zeolite phases, as is the silicalite-1 (MFI) [2]. In order to investigate the changes in amorphous solid phases of the Na₂O-SiO₂-TPABr-H₂O systems induced by changes of Na⁺ content, we examined the changes of the specific properties of precipitated silica, which was introduced in the systems as a source of silicon.

Experimental

Suspensions were formed from precipitated silica (88.02 % SiO₂, trade mark SIL from 1992, T.G. "Birač", Zvornik, BIH), sodium hydroxide ("Zorka", Šabac, SCG), sulphuric acid ("Zorka", Šabac, SCG), tetrapropylammonium bromide (Merck) and distilled water. The reactants were mixed by vigorously stirring to get a homogeneous gel-mix, with the composition of 0.1 TPABr:SiO₂:27.5H₂O and x Na₂O/SiO₂ (x=0–0.25). After one hour the solid phase was separated in a centrifuge and dried in a static air oven at 333 K. The samples were powdered manually in an agate mortar. A part of the samples have been treated in a furnace during 16 h at 823 K. These samples were signed as "calc".

The specific surface area (BET) was determined on the base of multi-point nitrogen surface areas measurements [ASTM D 4365 – 85, ISO/DIS 4652-2] using Autosorb-6, Quantachrome and Data acquisition software PSORB2PC – enhanced

software for P_o Autosorb 6 Version 2.0. The average particle size was calculated as $D = 6000(\rho S)^{-1}$ [3], where D is average diameter of the particle (nm), $\rho=2.2$ (gcm⁻³) [3] and S is an external surface area (m²g⁻¹). X-Ray diffraction (XRD) patterns were measured on a Philips PW-1710 Automated Powder Diffractometer System, using monochromatic CuK_α radiation. The particle size and habit were examined using a scanning electron microscope JEOL, JSM-6460.

Results and Discussion

Precipitated silica [3] of the trademark SIL was introduced in the Na₂O-SiO₂-TPABr-H₂O systems as a source of silicon. Micrograph of the SIL sample (Fig. 1a) shows material with nanosized particles, globular in the shape, with the size distribution in the region 62±8 nm, interconnected via edges which are not well

Table 1. Specific surface area (BET), average particles size (D_{BET}) and particles size (D_{SEM}) for samples of precipitated silica (SIL) and samples from TPA-Na₂O-SiO₂-H₂O systems A, B or C, where the ratio Na₂O/SiO₂ was 0, 0.1 or 0.25, respectively.

Sample	Surface area (m ² g ⁻¹)	D _{BET} * (nm)	D _{SEM} ** (nm)
SIL	105.00	30.7	62±8
SIL/calc	92.80	32.3	25±5
A			40±5
A/calc	101.00	30.5	40±5
B			38±12
B/calc	43.10	67.0	60±10
C			≤2 μm
C/calc	1.77	1541	≤20 μm

*calculated from BET

**measured from SEM images

defined. The SEM images (magnification up to x300000) of the solid phase of the system where Na₂O/SiO₂=0, give evidence that some reorganization of matter was happened (Fig. 1b). The micrograph given in Fig. 1c represents the solid phase of the system where Na₂O/SiO₂=0.1. The solid phase was built up from agglomerated spheroid nanoparticles which diameters were in the range 40±15 nm. The initial structure of precipitated silica was lost in the solid phase of the system where the content of Na⁺ cations was increased to reach the value Na/SiO₂=0.25 (Fig. 1d). As the size of SIL nanoparticles is highly heat-dependent (Tab. 1) [3,4], a significantly smaller D_{BET} value of the noncalcinated sample in comparison to the D_{SEM} value of the same sample (Tab. 1) is a consequence of the thermal treating of the sample at 443 K during the procedure of the measuring. Samples A, B and C represent systems where the Na₂O/SiO₂ ratio takes values 0, 0.1 and 0.25, respectively. During calcination C sample is melted.

The XRD powder patterns of the solid phases of not calcinated samples give evidence that TPABr is present in all samples. After calcination, in the samples B/calc and C/calc a certain amounts of NaBr are detected. Amorphous SiO₂ is the basic component in the samples.

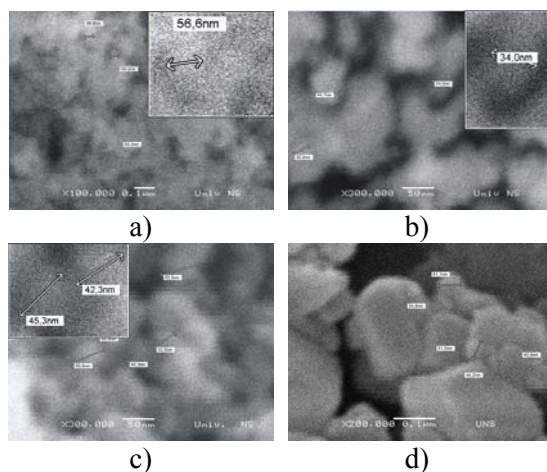


Fig.1. Micrographs of the precipitated silica (a), and amorphous silica phases from the systems A (b), B (c) and C (d), where the ratio $\text{Na}_2\text{O}/\text{SiO}_2$ was 0, 0.1 and 0.25, respectively.

Conclusion

The changes of Na^+ content in the $\text{Na}_2\text{O}-\text{SiO}_2\text{-TPABr}-\text{H}_2\text{O}$ systems, determined by the values of $\text{Na}_2\text{O}/\text{SiO}_2$ ratio within the range from 0 to 0.25, cause changes and strongly determine the morphologies of the solid amorphous phases of the systems. For Na^+ content within the range $\text{Na}_2\text{O}/\text{SiO}_2 \leq 0.1$, any change in Na^+ content causes a change in morphological properties of solid phases, but at the same time the existence of the nanoparticles in structures of the solid phases was preserved. The nano-structure is derived from the structure of precipitated silica, which is entered into the system as a source of silicon. When the $\text{Na}_2\text{O}/\text{SiO}_2$ ratio was increased to reach value 0.25, the polymerization-depolymerization processes were accelerated, and the solid phase of system has no remains of precipitated silica morphology.

Acknowledgment

The authors are grateful to Dr Miloš Bokorov for SEM analysis.

References

- [1] D. W. Breck, Zeolite molecular sieves, A. Wiley, Int. Pub., N. York, 1974.
- [2] E. G. Derouane and Z. Gabelica, Journal of Solid State Chemistry, 1986, **64**, 296–304.
- [3] R. K. Iler, The Chemistry of Silica, A. Wiley, Int. Pub. N. York, 1979.
- [4] O. A. Kovačević, B. T. Kovačević, D. Arandelović, N. L. Lazić, L. Pezo, V. Dondur and Ž. Lj. Tešić, in A. Antić-Jovanović (ed.), Physical Chemistry 2006, SPCS, Belgrade, 2006, II, 522-524.

I

Solid State Physical Chemistry

COMPOSITE NANOMEMBRANES: A MULTIFUNCTIONAL PLATFORM FOR CHEMICAL SENSING

Z. Jakšić¹, J. Matović² and J. Buha¹

¹ *Center of Microelectronic Technologies and Single Crystals,
Institute of Chemistry, Technology and Metallurgy,
University of Belgrade, Belgrade, Serbia*

² *Institute for Sensor and Actuator Systems – ISAS,
Vienna University of Technology, Vienna, Austria*

Abstract

We report on the applicability of freestanding, quasi-2D nanostructures (nanomembranes) in chemical and biological sensing using surface plasmons polaritons (SPP). The electromagnetic response of some nanomembranes can be tailored by structuring and material selection to support propagation of a long-range SPPs. This enables an enhanced sensitivity of sensors which use such structures in comparison to the conventional ones. We describe the main procedures for enriching the nanomembrane functionality by nanocompositing, which provides a tool to improve the selectivity of sensors, increase the sensitivity and enable more freedom in the sensor signal readout. We base our sensing structures on our experimental nanomembranes whose thickness are typically about 10 nm, while their aspect ratios even exceed 1,000,000. An important approach to nanomembrane functionalization is to use nanoparticles, which offers various benefits, including the possibility to tune plasma frequency. An additional advantage is that thus functionalized nanomembranes can be applied to neutralize nanoparticle toxicity. If nanoparticles are bound to nanomembranes, the surface-to-volume ratio of such structures remains high, but the possibility of nanoparticles uncontrollably entering tissues and cells is prevented because of the stability and macroscopic dimensions of the obtained composites.

Introduction

Artificial nanomembranes represent a novel building block for micro- and nano-systems [1,2]. They are defined as freestanding/self-supported quasi-2D nanocomposites with a thickness below 100 nm and reaching down to the monatomic level [3]. The lateral dimensions of a nanomembrane can be a few centimeters, thus furnishing giant aspect ratios in excess of 1,000,000 [4]. Properly designed nanomembranes provide large optical and electrical confinement, resulting in numerous novel and often counter-intuitive properties [5]. Tailoring of their physical and chemical properties ensures their potential use for a vast range of novel applications [6].

Owing to their minute thickness, freestanding nanomembranes support the propagation of long range surface plasmon polaritons (LR SPP) [7], while at the same time the non-existence of a substrate means full electromagnetic symmetry and thus minimization of losses in propagation of evanescent waves [8]. This property makes nanomembranes a choice for ultra-sensitive chemical biological sensors. An additional quality is a vast range of tailorable properties which may be obtained by nanomembrane functionalization [9]. This may be done by using lamination and introduction of nanofillers, but also surface patterning and structuring. This enables engineering of practically all optical parameters of nanomembrane. It is known that nanostructuring and metal-dielectric nano-compositing can furnish practically any desired value of refractive index, including ultralow (near-zero) [10] and negative [11] values (the so-called optical metamaterials [12, 13]). This gives an additional degree of freedom in the design of chemical sensors, one of the reasons why this novel field is expanding rapidly [14-19].

Here we consider theoretically and experimentally the applicability of metallic or metal-composite nanomembranes for a novel generation of adsorption-based chemical sensors utilizing long-range surface plasmons. We analyze their functionalization and its use in sensitivity and selectivity boost. We also consider some issues related to nanoparticles use for nanomembrane functionalization.

Surface Plasmon Polaritons on Freestanding Nanomembranes

Metal or metal-composite nanomembranes support the propagation of surface plasmons polaritons (SPP) if their effective dielectric permittivity is negative in the operating wavelength range. An SPP may be defined as a surface electromagnetic wave at optical frequencies coupled with collective oscillations of free electron gas density within material. SPPs propagate at the interface between material with negative value of effective dielectric permittivity ϵ and material with positive ϵ and are evanescent in both perpendicular directions.

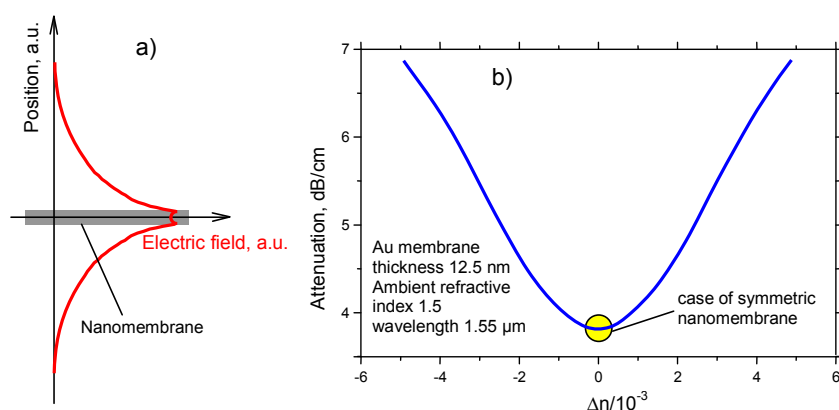


Fig.1. a) Spatial distribution of electric field for an evanescent wave propagating on the freestanding nanomembrane; solid gray: nanomembrane; b) optical signal attenuation in a nanomembrane in dependence on its asymmetry; abscissa shows the deviation of refractive index in the top half-space from that in the bottom half.

If a chemical/biological sensor is exposed to analyte, an ultrathin layer is adsorbed on the nanomembrane surface. The layer can be in the form of a homogenous monolayer or as isolated islands if the amount of the adsorbed species is insufficient to cover the entire sensor surface. The presence of analyte on the surface modifies the propagating conditions for the evanescent electromagnetic waves at the sensor-medium interface (metal-dielectric or, more generally, metamaterial-dielectric) [19]. Since SPPs are confined to the interface plane, even monatomic layers of the adsorbed species will readily modulate the surface refractive index and cause detectable changes in the SPP propagation. The SPP sensors are label-free and ultrasensitive; even in the case of conventional devices the detection limit is a few percents change in a monolayer occupancy [20].

If the thickness of a metal (or metal-composite) structure is in the nanometer range, which is the case with nanomembranes, the SPPs on the top and bottom surfaces couple, forming the long-range surface plasmons (LR SPP), Fig. 1a. The LR SPPs propagate much farther and are less confined to the surface than the conventional SPPs. The most sensitive contemporary plasmon sensors utilize the LR SPP [21]. The LR SPPs are very sensitive to the electromagnetic symmetry of the structure and any minute asymmetry is readily detectable [22]. Fig. 1b shows the calculated attenuation of the LR SPP as function of difference between the refractive indexes at the top and bottom interface. For this reason, nanomembranes represent an almost ideal platform and scaffold for LR SPP sensors, since they ensure a perfect electromagnetic symmetry.

Further improvements of LR SPP sensors are possible through nanostructuring of the nanomembrane. For instance, if a periodic array of nanoapertures is formed through the nanomembrane, its effective refractive index may be tuned in a wide range from positive to negative values by varying the membrane dimensions and material [23]. Even more important is the appearance of the so-called spoof plasmons or designer plasmons [24], whose plasma frequency can be tuned by tailoring the nanostructure parameters. This ensures an additional degree of freedom in LR SPP design.

The dispersion relation for the SPPs on a solid, single-layer nanomembrane is calculated from the Maxwell equations for low-order p-polarized modes, imposing the boundary condition for the continuity of the fields [25].

$$\left[\frac{k_1}{\varepsilon_1} + \frac{k_2}{\varepsilon_2} \left(\frac{k_1}{\varepsilon_1} + 1 \right) \right] \Bigg/ \left[\frac{k_1}{\varepsilon_1} - \frac{k_2}{\varepsilon_2} \left(\frac{k_1}{\varepsilon_1} + 1 \right) \right] = \exp(-2k_1 d) \quad (1)$$

where k is the wavevector, ε is the dielectric permittivity, index 1 denotes the medium material and 2 the nanomembrane material. The modes of Eq. (1) represent the long range SPPs and Eq. (1) becomes

$$\tanh \frac{k_1 d}{2} = - \frac{k_2 \varepsilon_1}{k_1 \varepsilon_2}. \quad (2)$$

The even modes in Eq. (1) represent the short-range SPPs and thus are not taken further into account.

The reflection coefficient for p-polarization can be written as [26]

$$R_p = \left(\frac{k_2 \varepsilon_1}{k_1 \varepsilon_2} - \frac{k_1 \varepsilon_2}{k_2 \varepsilon_1} \right) / \left(\frac{k_2 \varepsilon_1}{k_1 \varepsilon_2} + \frac{k_1 \varepsilon_2}{k_2 \varepsilon_1} \right). \quad (3)$$

Equation (3) is valid generally, regardless of the values of the permittivity and permeability of the nanomembrane and the medium. Modes may be s-polarized only if the effective parameters of the nanomembrane are negative, i.e. it is a double-negative optical metamaterial. In that case

$$R_s = \left(\frac{k_1 \mu_2}{k_2 \mu_1} - \frac{k_2 \mu_1}{k_1 \mu_2} \right) / \left(\frac{k_1 \mu_2}{k_2 \mu_1} + \frac{k_2 \mu_1}{k_1 \mu_2} \right). \quad (4)$$

Nanomembrane Functionalization by Nanocompositing

The path to tailor the nanomembrane response and to obtain targeted physical and chemical properties is through functionalization by nanocompositing [9]. There are four main methods to functionalize nanomembranes, Fig. 2. The first one is the introduction of various nanofillers, e.g. nanoparticles, nanofibers (including carbon nanotubes), nanorings, nanocubes and basically the whole "nano-zoo" of different nanostructures. Next, nanomembranes may be laminated to obtain multilayer structures which may be periodic, aperiodic or non-periodic; this method also includes nanomembrane surface activation. Further, nanomembranes can be patterned by either additive methods (forming "hills" of the same or different material on their surface) or subtractive ones (making various kinds of nanopores within the membrane). The nanomembrane surface may be sculpted and corrugated into various geometrical shapes. It is evident that two or more of these methods may be used simultaneously. In this way multifunctionality is imparted to nanomembranes and a much wider applicability is ensured.

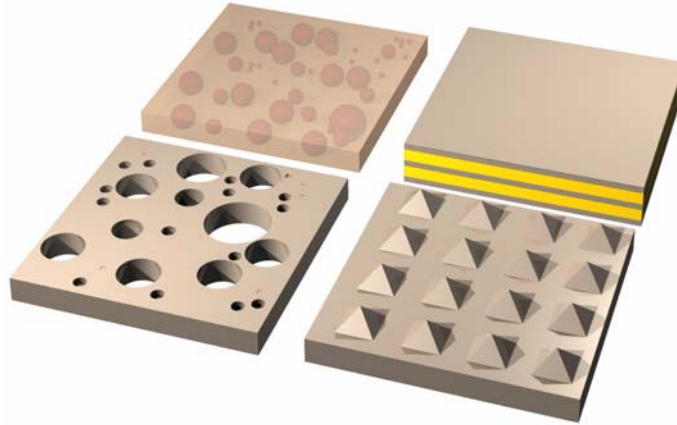


Fig.2. Four basics types of nanomembrane functionalization. Top left: introduction of nanofillers; top right: lamination; bottom left: patterning; bottom right: surface sculpting.

The basic goal of nanomembrane functionalization for plasmon sensing is to tailor the electromagnetic/optical response [19] toward the required SPP

properties. An additional important goal is sensor selectivity boost. This can be done by laminating the structure and by activating its surfaces using various analyte-specific ligands [20]. The sensor selectivity can be further enhanced by using nanomembrane as a separation filter, e.g. by the formation of nanopores as size-selective molecular sieves [19]. Important structures for sensor selectivity improvement through filtering are gated ion channels [27], biomimetic structures analogous to those in living cells. Generally, artificial nanopore-based biomimetic transport gateways [28] ensure highly selective separation of desired analytes.

In [29] we proposed to integrate plasmonic and chemical functionality into a single multipurpose periodic nanoporous structure (the concept of "Catalyst Plus"). Chemical functionality and catalyst-like high effective surface is obtained in conventional way by the use of porous material. However, electromagnetic/plasmonic functionality is further reached by tailoring the pore geometry for the desired kind of plasmonic response. Each pore then serves both as analyte absorber and as dielectric unit in the metal-dielectric nanostructural unit cell. The result is optical metamaterial with catalyst-like large effective surface.

Our previous works on freestanding nanomembrane functionalization include the fabrication of Cr-Si-O metal-composite nanomembranes 8-20 nm thick [4], nanoaperture patterning utilizing focused ion beam method [30] and nanomembrane surface sculpting using double-sided bulk micromachining of sacrificial silicon substrate [31].

Here we present our experimental results on laminar 3-layer freestanding nanomembranes. Fig. 3 shows photos of metal-dielectric-metal nanomembranes being removed from a polished silicon substrate using float-off method in deionized water with sodium phosphate as the parting agent. The total nanomembrane thickness is 35 nm (top and bottom Au layers 10 nm, middle dielectric 15 nm).

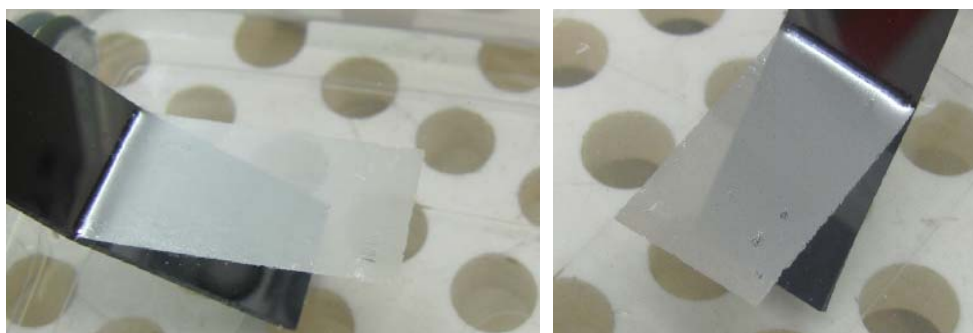


Fig.3. Photos of our experimental nanomembrane being freed from its support (polished Si) and partially floating on the processing solution (deionized water + Na_3PO_4 .) Laminar metal/dielectric/metal structures 10 nm + 15 nm + 10 nm, metal Au, dielectric silica, lateral dimensions 2 cm x 8 mm.

Functionalization by Nanoparticles

Nanoparticle functionalization plays an important role for chemical sensing [32]. Plasmonic nanoparticles are inherently multifunctional, since they can be tuned to various plasma frequencies and simultaneously be sensitive towards different analytes [33]. They may be introduced as nanofillers into the nanomembrane matrix, additively patterned onto the surface or laminated as ultrathin films on both sides of the nanomembrane. Our research interest includes nanoparticles of transparent conductive oxides like indium oxide, tin oxide, indium tin oxide (ITO), zinc oxide and antimony doped zinc oxide (AZO). Their optical absorption losses are lower than in metals their plasmonic parameters are continuously tunable by doping [34]. For application in SPP sensors the nanoparticles may be laminated with supporting nanomembranes as scaffolds, Fig. 4.

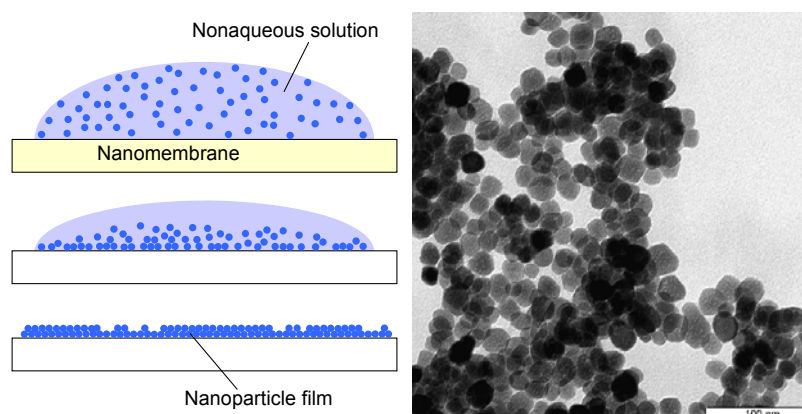


Fig.4. Formation of TCO nanoparticle-based film. Left: nanoparticle drop-coating self-assembly from non-aqueous solution; right: transmission electron microscope image of indium oxide nanoparticles, image size is about 100 nm.

It is very important that the same nanomembrane functionalization utilized for sensor enhancement can be used to neutralize nanoparticle toxicity while retaining their activity. It is known that nanoparticles may cause undesired biological effects and toxicity not observed with larger particles of the same material [35]. This is a combined consequence of the very high active surface to volume ratio of nanoparticles and their ability to readily enter biological tissues and cell interior because of their small overall dimensions.

If nanoparticles are bound to nanomembranes, the surface-to-volume ratio of thus obtained composites and the nanoparticle activity remain high, but the possibility of nanoparticles uncontrollably entering tissues and cells is avoided as they are embedded in macroscopic structures. Thus we neutralize undesirable effects and, since nanomembranes can be readily manipulated with macroscopic tools, even using unaided hand [4], still exert full control on their transport and location.

Conclusion

Nanomembranes represent a platform and scaffold for LR SPP sensors, which is especially useful for biological analytes. In comparison to localized plasmon sensing systems, the nanomembrane-based SPP sensors have the advantages of lower intrinsic noise levels due to larger effective surfaces and thus higher signal-to-noise ratios. The combination of plasmonics and synthetic nanomembranes has potentials both to vastly improve the contemporary chemical and biological sensors and to impart much novel functionality. Especially interesting is the functionalization of nanomembranes using nanoparticles, including transparent metal oxide nanoparticles with tunable plasmonic properties.

Further developments of nanomembrane-based SPP sensors are ensured through the possibility to combine vast array of different metal and dielectric, organic and inorganic materials in novel ways, including the utilization of metamaterials. Another opportunity is to use biomimetic approach, for instance by mimicking gated ion channels using functionalized nanochannels. Thus a novel generation of chemical and biological sensors is made possible.

Besides the application in chemical and biological sensors, nanomembranes functionalized by nanocompositing have a far wider applicability. Some examples include catalysis, separation, microreactors, biointerfaces, etc. It is possible to envision different applications in environmental protection, biomedicine, energy harvesting (especially fuel cells), forensic and homeland defense and many more.

References

- [1] C. Jiang, S. Markutsya, Y. Pikus, V. V. Tsukruk, *Nature Mat.*, 2004, **3**, 721-728.
- [2] C. C. Striemer, T. R. Gaborski, J. L. McGrath, P. M. Fauchet, *Nature*, 2007, **445**, 749-753.
- [3] J. S. Bunch, S. S. Verbridge, J. S. Alden, A. M. Van Der Zande, J. M. Parpia, H. G. Craighead, P. L. McEuen, *Nano Lett.*, 2008, **8**, 2458-2462.
- [4] J. Matović, Z. Jakšić *Microelectron. Eng.*, 2009, **86**, 906-909.
- [5] R. Vendamme, S. Y. Onoue, A. Nakao, T. Kunitake, *Nature Mat.*, 2006, **5**, 494-501.
- [6] J. Matović, Z. Jakšić, In *Micro Electronic and Mechanical Systems*; Takahata, K., Ed.; In-Tech: Vienna, 2010, 61-84.
- [7] P. Berini, R. Charbonneau, N. Lahoud, *IEEE J. Sel. Top. Quant.*, 2008, **14**, 1479-1495.
- [8] P. Berini, N. Lahoud, R. Charbonneau, *J. Vac. Sci. Tech. A*, 2008, **26**, 1383-1391.
- [9] Z. Jakšić, J. Matović, *Materials*, 2010, **3**, 165-200.
- [10] B. T. Schwartz, R. Piestun, *J. Opt. Soc. Am. B*, 2003, **20**, 2448-2453.
- [11] D. R. Smith, W. J. Padilla, D. C. Vier, S. C. Nemat-Nasser, S. Schultz, *Phys. Rev. Lett.*, 2000, **84**, 4184.
- [12] S. Xiao, U. K. Chettiar, A. V. Kildishev, V. P. Drachev, V. M. Shalaev, *Opt. Lett.*, 2009, **34**, 3478-80.

- [13] W. Cai, V. Shalaev, *Optical Metamaterials: Fundamentals and Applications*; Springer: Dordrecht, Germany, 2009.
- [14] Z. Jakšić, D. Vasiljević-Radović, M. Maksimović, M. Sarajlić, A. Vujanić, Z. Djurić, *Microelectron. Eng.*, 2006, **83**, 1786-1791.
- [15] Z. Jakšić, In *Metamaterials: Classes, Properties and Applications*; E. Tremblay, Ed.; Nova Science Publishers: Hauppauge, New York, 2010, 1-45.
- [16] A. V. Kabashin, P. Evans, S. Pastkovsky, W. Hendren, G. A. Wurtz, R. Atkinson, R. Pollard, V. A. Podolskiy, A. V. Zayats, *Nature Mat.*, 2009, **8**, 867-871.
- [17] C. M. Bingham, H. Tao, X. Liu, R. D. Averitt, X. Zhang, W. J. Padilla, *Opt. Express*, 2008, **16**, 18565-18575.
- [18] Z. Jakšić, D. Tanasković, J. Matović, *Acta Phys. Pol. A*, 2009, **116**, 333-335.
- [19] Z. Jakšić, J. Matović, In *Micro Electronic and Mechanical Systems*; K. Takahata, Ed.; In-Tech: Vienna, 2009, 85-107.
- [20] L. S. Jung, C. T. Campbell, T. M. Chinowsky, M. N. Mar, S. S. Yee, *Langmuir*, 1998, **14**, 5636-5648.
- [21] M. Piliarik, J. Homola, *Opt. Express*, 2009, **17**, 16505-16517.
- [22] A. Boltasseva, T. Nikolajsen, K. Leosson, K. Kjaer, M. S. Larsen, S. I. Bozhevolnyi, *J. Lightwave Technol.*, 2005, **23**, 413.
- [23] S. A. Ramakrishna, T. M. Grzegorzczak, *Physics and Applications of Negative Refractive Index Materials*; SPIE Press Bellingham, WA & CRC Press, Taylor & Francis Group, Boca Raton FL, 2009.
- [24] J. B. Pendry, L. Martín-Moreno, F. J. Garcia-Vidal, *Science*, 2004, **305**, 847-848.
- [25] S. A. Maier, *Plasmonics: Fundamentals and Applications*; Springer: New York, NY, 2007.
- [26] A. Ishimaru, S. Jaruwatanadilok, Y. Kuga, *Prog. Electromagn. Res.*, 2005, **51**, 139-152.
- [27] A. Noam, *Chem. Phys. Lett.*, 1995, **244**, 456-462.
- [28] T. Jovanovic-Talisman, J. Tetenbaum-Novatt, A. S. McKenney, A. Zilman, R. Peters, M. P. Rout, B. T. Chait, *Nature*, 2009, **457**, 1023-1027.
- [29] Z. Jakšić, O. Jakšić, Z. Djurić, C. Kment, *J. Opt. A-Pure Appl. Opt.*, 2007, **9**, S377-S384.
- [30] J. Matovic, J. Kettle, E. Brousseau, N. Adamovic, *Proc. 26th Internat. Conf. on Microelectronics MIEL, Niš, 11-14 May, 2008*, **1**, 104-108.
- [31] J. Matović, Z. Jakšić *Microelectron. Eng.*, 2010, **87**, 1487-1490.
- [32] M. Niederberger, G. Garnweitner, J. Buha, J. Polleux, J. Ba, N. Pinna, *J. of Sol-Gel Science and Technology*, 2006, **40**, 259-266.
- [33] S. Franzen, *J. Phys.Chem. C*, 2008, **112**, 6027-6032.
- [34] S. Franzen, C. Rhodes, M. Cerruti, R. W. Gerber, M. Losego, J. P. Maria, D. E. Aspnes, *Opt. Lett.*, 2009, **34**, 2867-2869.
- [35] G. Oberdörster, E. Oberdörster, J. Oberdörster, *Environm. Health Perspectives*, 2005, **113**, 823-839.

TRANSPARENT CONDUCTIVE OXIDE NANOPARTICLES FOR TUNABLE NANOPLASMONICS

J. Buha¹, Z. Jakšić¹ and J. Matović²

¹ *IHTM – Institute of Microelectronic Technologies and Single Crystals
Njegoševa 12, Belgrade University, Belgrade, Serbia*

² *Institute of Sensors and Actuators, Faculty of Electrical Engineering &
Information Technology, TU Vienna, Austria*

Abstract

Transparent conductive oxides (TCO) like tin oxide, indium oxide, indium tin oxide and similar are Drude-type plasmonic materials with tunable plasma frequency and lower losses compared to metals. We investigated the properties of TCO nanoparticles which are of interest for plasmonics and nanoplasmonics, as well as the possibilities to functionalize plasmonic structures and devices using TCO nanoparticle films. We calculated the spectral dispersion of complex dielectric permittivity and refractive index of TCO using fitting of experimental values and lossy Drude model. Experimentally, we investigated TCO nanoparticle synthesis from nonaqueous sol-gels where organic solvents were simultaneously used as reacting substances and stabilizing agents.

Introduction

The nanocomposites which provide the condition for the existence of surface and bulk plasmons are seen today as the key components for merging the electronic and photonic circuitry at nanoscale [1]. They are in the heart of many different applications, including ultrasensitive label-free chemical, biochemical and biological sensors [2] and are the basis for optical metamaterials [3]. Contemporary plasmonic structures are mostly based on good metals with negative real part of relative dielectric permittivity ϵ , typically silver or gold. Their ϵ is described by the Drude model, and their plasma frequency is in the ultraviolet range. They are characterized by strong absorptive losses, detrimental for many applications.

Transparent conductive oxides (TCO) like SnO₂ (TO), In₂O₃ (IO), indium tin oxide (ITO), etc. are seen as a valid alternative to metal-based plasmonics [4]. They are also Drude-type materials, but their plasma frequency is in the visible or near-infrared range. It can be tailored in dependence on the material properties and thus ensures a simple way to tune the operating wavelength range for such devices. An equally important fact is that absorptive losses in such materials in visible are much lower than in metals [5], which can be seen by simple visual observation.

In this work we investigate the applicability of TCO for ultrathin-film laminar nanocomposites for plasmonics. We investigate the properties and applicability of TCO nanoparticles for this purpose. We calculate the doping-tunable optical parameters of TCO. In experimental part, we consider the

nonaqueous fabrication of TCO nanocrystal particles and the approaches to depositing such nanoparticles onto bulk and ultrathin freestanding substrates.

Experimental

In our work we chose to approach the synthesis of TCO crystalline nanoparticles through a nonaqueous route [7]-[8]. The process involves the reaction between metal oxide precursors (which may include organometallics, metal halides) and solvents (acetylacetonates, alcohols, etc.). We investigated TCO formation using benzyl alcohol simultaneously as the basic reacting substance and as the stabilizing agent. TCO precursors are added to the reaction solvent and solvothermal reaction occurs at an elevated temperature, furnishing nanoparticle suspension. The approach to In_2O_3 nanocrystals synthesis is $\text{In}(\text{acac})_3$ with butanone, benzylamine and acetophenone, while tin oxide is obtained from simple solution of SnCl_4 in benzyl alcohol. Our approach further includes drop-coating and dip-coating of already formed nanomembranes. Compositing is thus done by lamination [9].

Results and discussion

We determined the complex relative dielectric permittivity of TCO using the standard Drude model [6]. Fig. 1 shows the calculated real part of ϵ for In_2O_3 where different doping levels with SnO_2 are used and different free electron concentrations are obtained. It can be seen that the plasma resonance can be readily tuned from ultraviolet through visible to near-infrared part of the optical spectrum.

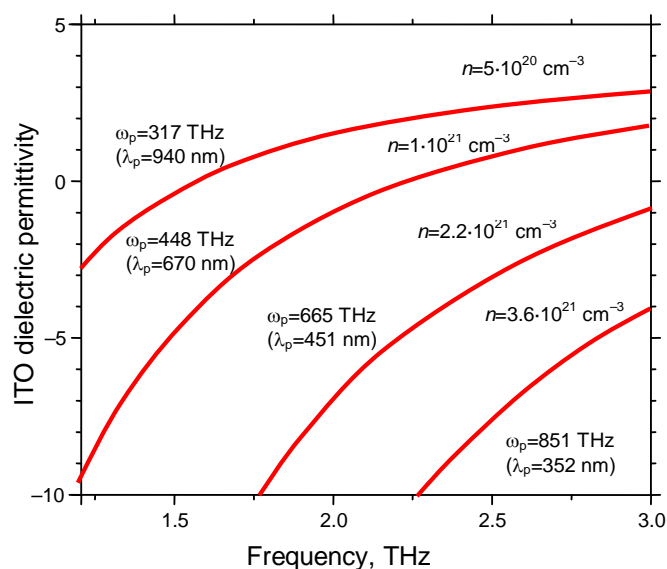


Fig.1. Calculated real part of relative dielectric permittivity of In_2O_3 for different SnO_2 doping levels. Electron concentrations n are shown, as well as plasma frequencies ω_p in THz and corresponding wavelengths λ_p in nanometers.

A transmission electron microscope (TEM) image of fabricated ultra thin indium oxide nanoparticle film is shown in Fig. 2. It can be seen that the uniformity of nanoparticles is very good, the average particle size being about 15 nm.

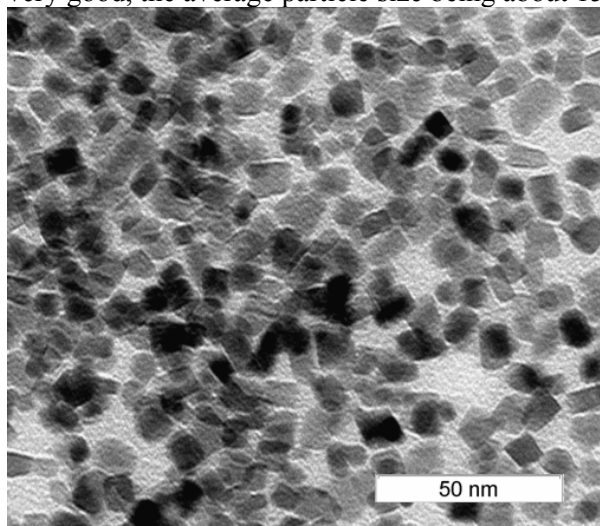


Fig.2. TEM image of nanoparticles of indium oxide.

Conclusion

We investigated the properties of TCO nanoparticles of interest for plasmonic functionalization in the visible and near-infrared range. Material doping and composition can be used to continuously tune the plasma frequency. The experimental samples obtained by nonaqueous approach furnish nanocrystalline material with a good uniformity and overall quality convenient for plasmonics. Currently we are considering different methods for surface functionalization with nanoparticle films, including drop coating and dip coating. We believe our approach could be useful for extending the toolbox of the plasmonic materials.

References

- [1] E. Ozbay, *Science*, 2006, **311**, 189-193.
- [2] J. Homola ed, *Surface Plasmon Resonance Based Sensors*, Springer, Berlin Heidelberg, 2006.
- [3] Z. Jakšić, O. Jakšić, Z. Djurić, C. Kment, *J. Optics A*, 2007, **9**, S377-S384.
- [4] S. Franzen, *J. Phys. Chem. C*, 2008, **112**, 6027-6032.
- [5] S. Franzen, C. Rhodes, M. Cerruti, R. W. Gerber, M. Losego, J. P. Maria, D. E. Aspnes. *Opt. Lett.*, 2009, **34**, 2867.
- [6] M. D. Losego, A. Y. Efremenko, C. L. Rhodes, M. G. Cerruti, S. Franzen, J. P. Maria. *J. Appl. Phys.*, 2009, 106, 024903-1-8.
- [7] M. Niederberger, G. Garnweitner, J. Buha, J. Polleux, J. Ba, N. Pinna, *J. Sol-Gel Sci. Technol.*, 2006, **40**, 259-266.
- [8] J. Buha, I. Djerdj, M. Niederberger, *Cryst. Growth & Design*, 2007, **7** 113-116. [9] Z. Jakšić, J. Matović, *Materials*, 2010, **1**, 165-200.

LASER EXCITED ELECTRONIC ELASTIC VIBRATION OF RECTANGULAR SIMPLY SUPPORTED PLATE

D. M. Todorović¹, B. Cretin² and J. Charnay²

¹*Institute for Multidisciplinary Research, University of Beograd,
P.O.Box33, 11030 Belgrade, Serbia*

²*FEMTO-ST Institut, Université de Franche-Comté, CNRS, ENSMM, UTBM,
32 Avenue de l'Observatoire, F-25044, Besançon Cedex France*

Abstract

The electronic elastic vibrations (the electronic deformation mechanism of elastic wave generation) in a semiconductor rectangular plate (3D geometry), photogenerated by a tightly focused and intensity-modulated laser beam, were studied. The theoretical model for the elastic displacements space and frequency distribution by using the Green function method and Hankel transformation was given. The amplitude and phase of the plasma assisted elastic displacements in the simply supported rectangular plate were calculated and analysed. These investigations are important for many practical experimental situation (atomic force microscopy, thermal microscopy, thermoelastic microscopy, etc) and sensors and actuators.

Introduction

The photoacoustic (PA) and photothermal (PT) science and technology extensively developed new methods in investigation of semiconductors and microelectronic structures during the last ten years. The PA and PT effects can be important as driven mechanisms for micromechanical structures, especially for micro-electro(opto)-mechanical structures (MEMS, OEMS). A new approach for producing compact, lightweight, a highly sensitive detector is provided by MEMS, OEMS technology, which functions based on the elastic bending of a microstructure upon absorption of optical energy.

When a microstructure is exposed to optical radiation, the photogenerated carrier-density (the plasma wave) causes a mechanical strain. The photogenerated plasma waves produce periodic elastic deformation in the sample, the so-called electronic deformation (ED) [1,2]. This mechanism of elastic wave generation is the property of semiconductors and electronic materials.

In previously published papers, the plasma, and elastic fields in one-dimension (1D) micromechanical structures were theoretically and experimentally analyzed by Todorović et al. [1,3,4]. In this work for the first time, the space and frequency distribution of electronic elastic vibrations, as a consequence of the electronic deformation effects, in a rectangular simply supported plate (3D geometry), photogenerated by a tightly focused and intensity-modulated laser beam, are analyzed.

Plasma and Elastic Fields

The theoretical treatment enables quantitative accounts of the carrier density field, $n(\mathbf{r}, t)$ and elastic displacement field, $\mathbf{u}(\mathbf{r}, t)$. In the case of periodical excitation, with angular modulating frequency of the incident beam ω , the excess carrier-density can be assumed as $n(\mathbf{r}, t; \omega) = \text{Re}[N(\mathbf{r}, \omega) \exp(i\omega t)]$ and elastic displacement $\mathbf{u}(\mathbf{r}, t; \omega) = \text{Re}[\mathbf{U}(\mathbf{r}, \omega) \exp(i\omega t)]$, where $N(\mathbf{r}; \omega)$ and $\mathbf{U}(\mathbf{r}; \omega)$ are complex values which define the amplitude and phase of the carrier and displacement fields, respectively.

The plasma (carrier-density) field in an opaque rectangular Si plate with dimensions L_x, L_y, L_z (3D geometry), excited with a tightly focused and intensity-modulated laser beam (Dirac harmonic source) centered at $(x_1, y_1, z_1 = 0)$, is analyzed in our previously published paper [5]. The carrier-density space and frequency distribution $N(x, y, z; \omega)$ in the Si plate were calculated and used as a source term in the elastic bending equation.

The photogenerated plasma can directly produce a local strain, i.e. the various ED effects generate elastic waves in the plate. The electronic strain, $\varepsilon^{ED}(x, y, z, \omega)$, changes linearly with excess carrier density, $N(x, y, z; \omega)$. Then, an elastic displacement $U^{ED}(x, y, z; \omega)$ can be given as a function of the excess carrier density, $N(x, y, z; \omega)$. From the theory of thin elastic plate, the ED component of elastic displacement can be given as the elastic bending, $U^{ED}(x, y, z, \omega) \approx W(x, y, \omega)$:

$$\begin{aligned}
 W(x, y, \omega) &= -(1+\nu)B \int_0^{L_x} dx_o \int_0^{L_y} dy_o M_n(x_o, y_o, \omega) \left(\frac{\partial^2}{\partial x_o^2} + \frac{\partial^2}{\partial y_o^2} \right) W^*(x, y | x_o, y_o) \\
 &= (1+\nu) \frac{4}{L_x L_y} \sum_{m=1}^{\infty} \sum_{n=1}^{\infty} f_{mn}(\omega) I_{mn}(x, y), \\
 f_{mn}(\omega) &= \int_0^{L_x} dx_o \int_0^{L_y} dy_o M_n(x_o, y_o, \omega) \varepsilon_m(x_o) \varepsilon_n(y_o), \\
 M_n(x, y, \omega) &= d_n \frac{12}{L_z^3} \int_0^{L_z} \left(z - \frac{h}{2} \right) N(x, y, \omega) dz, \\
 I_{mn}(x, y) &= \frac{1}{\Delta_{mn}} \varepsilon_m(x) \varepsilon_n(y), \quad \Delta_{mn} = a_m^2 + b_n^2, \\
 \varepsilon_m(x) &= \sin(a_m x), \quad a_m = \frac{m\pi}{L_x}, \quad (m=1, 3, \dots), \\
 \varepsilon_n(y) &= \sin(b_n y), \quad b_n = \frac{n\pi}{L_y}, \quad (n=1, 3, \dots)
 \end{aligned} \tag{1}$$

where $W^*(x, y | x_o, y_o)$ is the elastic Green function and $M_n(x_o, y_o, \omega)$ is the electronic moment (the source term). The function $W^*(x, y | x_o, y_o)$ denotes the deflection at the point (x, y) , due to the action of a unit concentrated force at the point (x_o, y_o) . The set $\{\varepsilon_m(x)\}$ and $\{\varepsilon_n(y)\}$ are the orthogonal eigenfunctions.

Analyze of Dinamic Elastic Vibrations

The theoretical model, derived in this work, enables to calculate and analyzed the 3D elastic displacement field i.e. it enables to study the electronic elastic vibrations in the optically excited plate. These fields were calculated for typical parameters of Si and dimensions: length $L_x = 3000 \mu\text{m}$, width $L_y = 400 \mu\text{m}$ and thickness of the Si plate $L_z = 150 \mu\text{m}$. Fig.1 shows a typical example of the 3D elastic bending of the rectangular Si plate, excited with tightly focused beam centered at point $(x_1 = 100 \mu\text{m}, y_1 = L_y/2 = 200 \mu\text{m})$ on the plate surface.

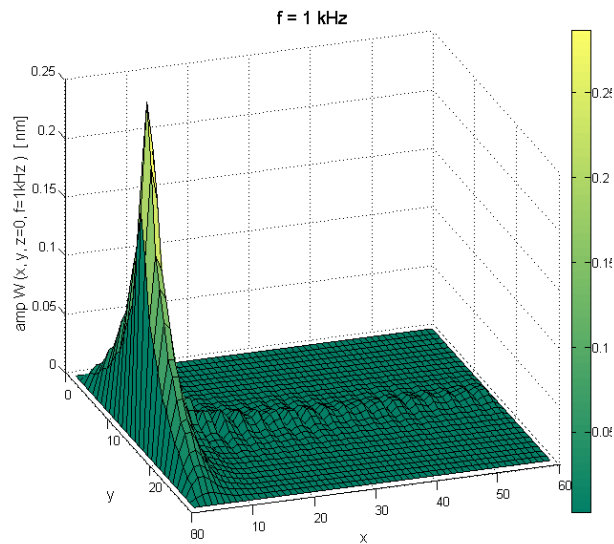


Fig.1 Amplitude of elastic bending of the rectangular plate excited with tightly focused beam, impinges at point $x_1=100 \mu\text{m}, y_1=200 \mu\text{m}$ and modulated at the frequency $f=1 \text{ kHz}$.

Conclusion

The theoretical model for the space and frequency distribution of the electronic elastic displacements in a semiconductor plate (3D geometry), photogenerated by a tightly focused and intensity-modulated laser beam, was given. The amplitude and phase of the plasma assisted elastic vibrations in the simply supported rectangular plate were calculated and analysed. The analysis of the amplitude space distribution shows that the elastic displacements are not only significant around the laser excitation point. The analysis also shows that the transport parameters (the lifetime and surface recombination velocities of the photogenerated carriers) have significant influence to the electronic elastic vibrations.

References

- [1] R. G. Stearns, G. S. Kino, *Appl. Phys. Lett.*, 1985, **47**, 1048-1050.
- [2] D. M. Todorovic, P. M. Nikolic, Ch. 9 in *Semiconductors and Electronic Materials*, SPIE Opt.Eng. Press, Washington, 2000, 273-318.
- [3] D. M. Todorović, *Rev. Sci.Instrum.*, 2003, **74**, 578-581.
- [4] Y.Song, B.Cretin, D.M.Todorović, P.Vairac, *J.Phys.D: Appl Phys.*, 2008, **41**, 155106.
- [5] D. M. Todorović, Y. Song, *J. Phys., Conf. Ser.*, 2010, **214**, 012104.

STUDY ON THE DEPENDENCE OF THE CRITICAL TEMPERATURE T_c ON PRESSURE IN $\text{YBa}_2\text{Cu}_3\text{O}_{6+x}$

M. M. Milić

Laboratory of Theoretical Physics, INN Vinča, P.O.Box 522, 11001 Belgrade, Serbia

Abstract

In the present study experimental data available in the literature have been employed to investigate behavior of the critical temperature T_c as a function of the pressure P , in the $\text{YBa}_2\text{Cu}_3\text{O}_{6+x}$ high temperature superconductor (HTSC). We estimated the maximal critical temperature $T_{c,max}(P)$ which can be achieved in this material under pressure applied at temperatures low enough to prevent oxygen reordering. We found that it approximately equals to 114K corresponding to $x \approx 0.77$.

Introduction

Many studies conducted in the past years on the pressure effect in HTSC materials revealed the complex nature of the pressure dependence of T_c in these materials, since T_c depends on many different parameters such as hole carrier density, interplanar and intra planar spacing, relaxation parameters etc. [1,2]. It is usually

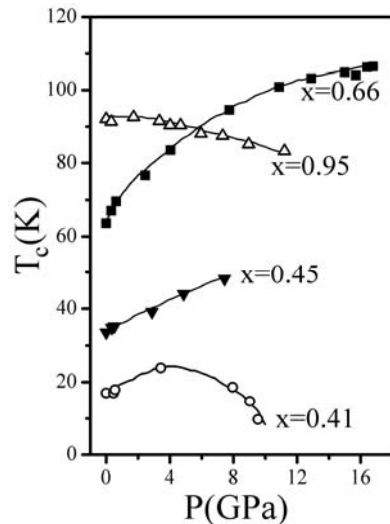


Fig.1. T_c as a function of pressure P for different oxygen concentrations x . The results are reproduced from the Ref. [4].

assumed that two different terms contribute to the pressure coefficient (dT_c/dp), one, which results from the pressure induced charge transfer and the other, intrinsic one, which is not result of the charge transfer [3].

For the HTSC compounds with initially positive pressure coefficient, it is characteristic that the pressure increase leads to the enhancement of the T_c until, for some pressure P_{max} , the maximum T_c is reached, and at yet higher pressures T_c decreases again [4]. In $\text{YBa}_2\text{Cu}_3\text{O}_{6+x}$ material pressure coefficient considerably depends on the oxygen concentration x . For $x \approx 0.97$ the material is optimally doped and the pressure effect is almost negligible. For very under doped samples a giant pressure coefficients up to 30K/GPa was reported when the pressure was applied at room temperatures, while at 100K only moderate T_c increase was achieved (2-4K/GPa) [5]. The T_c enhancement at room

temperature was attributed to the increased doping of CuO_2 planes achieved by the pressure induced oxygen reordering which is suppressed at low temperatures [5].

Results and discussion

Since the pressure application increases number of holes in the CuO_2 planes, there is a certain similarity between doping and pressure experiments. Therefore, the following relation is able to describe the T_c vs P behavior observed in many high- T_c cuprates [6]:

$$T_c(P) = T_{c,\max} \left[1 - A(P - P_{\max})^2 \right]. \quad (1)$$

In the present paper we have employed this relation to fit the experimental results of Sadewasser *et al* [4] who have measured the critical temperature T_c as a function of the hydrostatic pressure P , in $\text{YBa}_2\text{Cu}_3\text{O}_{6+x}$ over the wide range of oxygen concentrations x (figure 1) at temperatures which exclude the oxygen reordering. Then we presented the so obtained T_c values as a function of the concentration x at different $P = \text{const}$ values, and fitted those $T_c(x)$ dependences to the parabolic curve

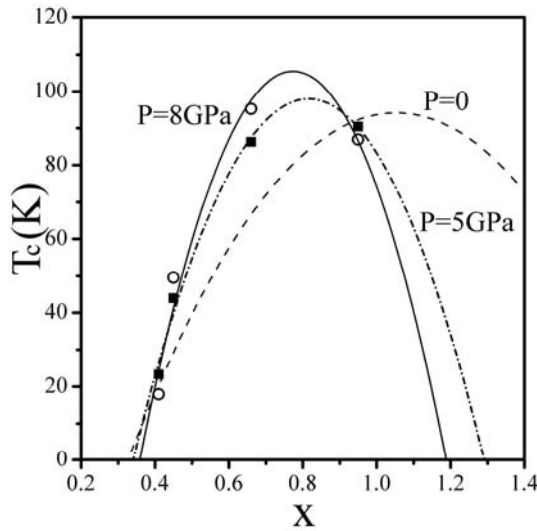


Fig. 2. T_c as a function of the oxygen content x at $P=0$ and under pressure for $P=5\text{GPa}$ and $P=8\text{GPa}$. The lines are parabolic approximation to the experimental results taken from [3].

as shown in the figure 2. Such an approximation was suggested by Stankowski *et al* [6] and it can be seen that the $T_c(x)$ values extracted from (1) for $P = \text{const}$ are fitted by the parabolic approximation very well. However, we must note that it is not strictly valid in the whole range of oxygen concentrations since it does not includes 60K plateau displayed in the T_c vs. x characteristic at $P = 0$ for $0.5 < x < 0.63(3)$. From the fig. 2 (we showed the results only for two values of $P \neq 0$) it can be seen that

with the pressure increase leads to the higher maximal T_c value and that it is achieved for samples with lower oxygen concentration x . This implies that at high pressures the optimal hole doping of CuO_2 planes is achieved for the samples with larger oxygen deficiency, such a behavior being the obvious consequence of the additional pressure induced charge transfer from CuO to the CuO_2 planes.

The parabolic approximation of the existing experimental results for $T_c(x)$ dependence at high constant pressures enabled determination of the $T_c(P)$ dependences for the samples in the wide range of oxygen concentrations where experimental results are available. For those samples, which do not reach their

maximal T_c values for pressures that are too high, the equation (1) is used to determine their maximal T_c under pressure. We presented this way estimated maximal T_c values as well as those determined experimentally a function of the concentration x in the figure 3. We

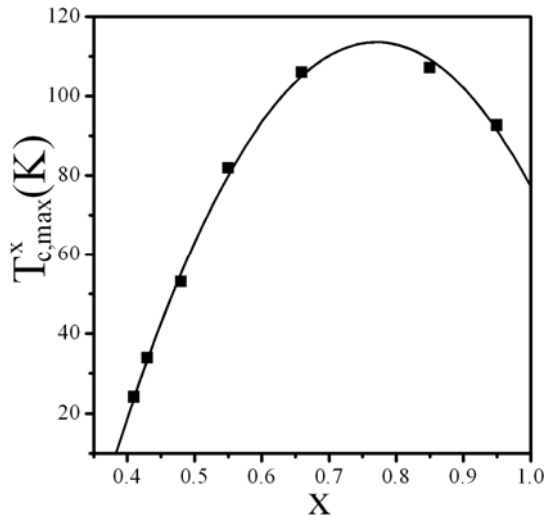


Fig. 3. Maximal T_c which can be achieved in the sample under pressure as a function of the concentration x .

found that this dependence can be also, to a very good approximation fitted to the parabolic curve. This way the maximal T_c under pressure, can be determined for the whole range of concentrations x where the material behaves as a superconductor.

Conclusion

We estimated the maximum T_c , that can be achieved under pressure at low temperatures in $\text{YBa}_2\text{Cu}_3\text{O}_{6+x}$ HTSC, to be approximately 114K, and it is reached for $x \approx 0.77$, which is the concentration close to the one at which the maximal pressure coefficient is measured [5].

However, it was not possible to determine the value of the pressure at which this maximum T_c is reached, though our analyses indicate that it is around 9GPa. For more precise estimation, high pressure experimental results for T_c obtained on the larger set of samples with different oxygen contents are needed.

Acknowledgement

This work was supported by the Ministry of Science of the Republic of Serbia through the project No. 141014.

References

- [1] J. S. Schilling, Treatise on High Temperature Superconductivity, ed. by J. R. Schrieffer, Springer, Verlag, 2006, 427-462.
- [2] B. Lorenz, C. W. Chu, Frontiers in superconducting materials, Springer Berlin Heidelberg, 2005, 459-497.
- [3] J. J. Neumeier, H. A. Zimmerman, Phys. Rev. B, 1993, **47**, 8385.
- [4] S. Sadewasser, J. S. Schilling, A. P. Paulikas, B. W. Veal, Phys. Rev. B, 2000, **61**, 741-749.
- [5] W. H. Fietz, R. Quenzel, H. A. Ludwig, K. Grube, S. I. Schlachter, F. W. Hornung, T. Wolf, A. Erb, M. Klaser, G. Muller-Vogt, Physica C, 1996, **270**, 258-266.
- [6] J. Stankowski, M. Krupski, R. Micnas, Mater. Sci. Poland, 2004, **22**, 175-185.

J

Macromolecular Physical Chemistry

RHEOLOGICAL AND THERMAL PROPERTIES OF BOLTORN[®] HYPERBRANCHED POLYESTERS

J. Džunuzović¹, S. Jovanović², M. D. Lechner³ and V. Vodnik⁴

¹ *IHTM-Center of Chemistry, University of Belgrade, Studentski trg 12-16, 11000 Belgrade, Serbia;* ² *Faculty of Technology and Metallurgy, University of Belgrade, Karnegijeva 4, 11120 Belgrade, Serbia;* ³ *Institute for Chemistry, University of Osnabrück, Barbarasträße 7, 49069 Osnabrück, Germany;* ⁴ *Institute of Nuclear Science "Vinča", P. O. Box 522, 11001 Belgrade, Serbia*

Abstract

Rheological (in solution and in melt) and thermal properties of aliphatic hydroxy-functional Boltorn[®] hyperbranched polyesters of different pseudo generation were investigated in this work. The obtained results show that 40 wt.% solutions of Boltorn[®] samples in N-methyl-2-pyrrolidinon exhibit Newtonian behaviour at 30 °C and that zero shear viscosity increases with increase of the generation number, i.e. molar mass. On the other side, values of the T_g show only slight increase with increase of the molar mass. Thermal stability of investigated samples increases with increase of the number of generation.

Introduction

The scientific importance of hyperbranched polymers (HBPs) has been proved through numerous publications [1-3]. The reasons for such attention are interesting and unique properties of these polymers, similar to those of dendrimers, which enable their use in applications where tedious synthesis of dendrimers can be avoided. Because of the relationship between rheological, thermal and processing properties, characterization of the rheological flow behaviour and thermal stability of HBPs is very important. Therefore, the aim of this work was investigation of three Boltorn[®] aliphatic HBPs of the second (BH-20), third (BH-30) and fourth (BH-40) pseudo generation. The influence of the number of the pseudo generation on the rheological and thermal properties of these polymers was examined.

Experimental

Boltorn[®] samples are aliphatic hydroxy-functional hyperbranched polyesters supplied by Perstorp (Specialty Chemicals AB, Sweden). According to the supplier's data, these polymers were synthesized in a acid-catalyzed polyesterification reaction from the 2,2-bis(hydroxymethyl)propionic acid as AB₂ monomer and a tetrafunctional ethoxylated pentaerythritol core, using pseudo one-step procedure.

Vapour pressure osmometry (VPO) was carried out in N,N-dimethylformamide as a solvent, at 90 °C, using a Knauer vapour pressure osmometer. For the calibration benzil was used. Rheological properties of Boltorn[®] samples in solution (solvent - N-methyl-2-pyrrolidinon (NMP)) and in melt were determined by Carri-Med CSL-100 stress controlled cone and plate rheometer (TA Instruments), fitted with a 2 cm diameter cone of 2° cone angle. The thermal stability of HB polyesters was determined by thermogravimetric (TG) analysis, using a NETZSCH TG 209 instrument in nitrogen atmosphere, at heating rate of 10 °C/min (flow rate of N₂ was 25 cm³/min).

Results and Discussion

Some important properties of investigated Boltorn[®] samples are listed in Table 1. From these results and results presented in Fig. 1a it can be seen that viscosity of 40 wt.% solutions of Boltorn[®] samples in NMP, determined at 30 °C, is independent of the shear rate and approaches a constant value, i.e. zero shear viscosity, η_0 , which increases with increase of the number of pseudo generation. The existence of η_0 indicates that Boltorn[®] samples at these experimental conditions exhibit Newtonian behaviour, because of their globular shape and absence of the physical entanglements. Values of the glass transition temperature, T_g , determined from the maximum of loss modulus temperature dependence (Fig. 1b) and listed in Table 1 do not change significantly with increase of the molar mass.

Table 1. The theoretical molar mass, M_{theor} , theoretical number of –OH groups, n_{OH} , number average molar mass determined by VPO, M_{VPO} , values of degree of branching, DB [1], zero shear viscosity, η_0 , glass transition temperature, T_g , and characteristic temperatures of thermal degradation for the Boltorn[®] samples

Sample	M_{theor} , gmol ⁻¹	n_{OH} theor.	M_{VPO} , gmol ⁻¹	DB	η_0 , mPa · s	T_g , °C	T_{10} , °C	T_{50} , °C	T_{80} , °C
BH-20	1747	16	1340	0.30	63.1	21	274	339	379
BH-30	3604	32	3080	0.31	137.9	31	295	353	409
BH-40	7316	64	-	0.34	209.4	31	301	365	416

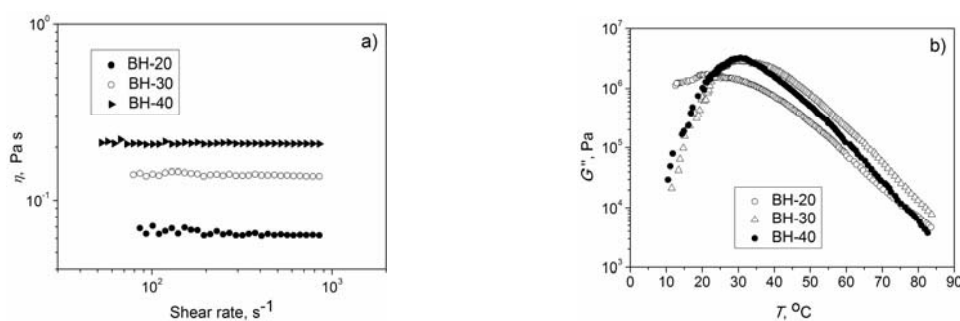


Fig.1. (a) Viscosity versus shear rate of the 40 wt.% solutions in NMP, at 30 °C and (b) temperature dependences of the loss modulus, G'' , of Boltorn[®] samples.

From the TG curves presented in Fig. 2a and temperatures obtained for mass losses of 10, 50 and 80 wt. % (T_{10} , T_{50} and T_{80} , respectively) listed in Table 1 it can be observed that thermal stability of Boltorn[®] samples increases with increase of the generation number. Under the given experimental conditions a measurable mass loss starting between 220 and 275 °C is detected. Using the Ozawa-Flynn-Wall method the activation energy of thermal degradation, E_a , of these samples was determined and presented in Fig. 2b. The various tendencies of E_a for different generations of Boltorn[®] samples imply that the thermal degradation of these polymers is a complex process.

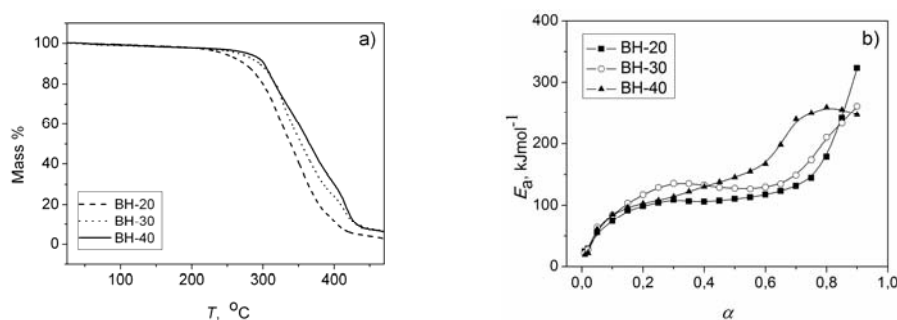


Fig.2. (a) TG curves of Boltorn[®] samples determined at heating rate of 10 °C/min and (b) change of the activation energy of thermal degradation, E_a , with degree of reaction, α .

Conclusions

The results presented in this work show that under the given experimental conditions solutions of Boltorn[®] samples show Newtonian behaviour. Values of the zero shear viscosity increase with increase of the molar mass. Values of the glass transition temperature of investigated samples show only slight increase with increase of the generation number. According to the results obtained by thermogravimetric analysis, it was observed that thermal stability of Boltorn[®] samples increases with increase of the molar mass and that thermal degradation of these polymers is a complex process.

References

- [1] A. Luciani, C. J. G. Plummer, T. Nguyen, L. Garamszegi, J.-A. E. Månson, *J. Polym. Sci. Part B: Polym. Phys.*, 2004, **42**, 1218-1225.
- [2] E. Žagar, M. Huskić, M. Žigon, *Macromol. Chem. Phys.*, 2007, **208**, 1379-1387.
- [3] J. Vuković, *Synthesis and characterization of aliphatic hyperbranched polyesters*, PhD Thesis, University of Osnabrück, Germany, 2006.

OPTIMIZATION OF THE REACTION CONDITIONS FOR THE SYNTHESIS OF POLY(URETHANE-UREA-SILOXANE)S

M. R. Balaban¹⁾, M. V. Pergal²⁾, V. V. Antić³⁾,
M. N. Govedarica²⁾ and J. Đonlagić⁴⁾

¹⁾ Faculty of Science and Mathematics, Mladena Stojanovića 2, 78000 Banja Luka, Bosnia and Herzegovina; ²⁾ ICTM-Center of Chemistry, Studentski trg 12-16, 11000 Belgrade, Serbia; ³⁾ Faculty of Agriculture, Nemanjina 6 11080 Zemun-Belgrade, Serbia; ⁴⁾ Faculty of Technology and Metallurgy, Karnegijeva 4, 11000 Belgrade, Serbia

Abstract

Poly(urethane-urea-siloxane)s (PUUS) based on 4,4'-methylenediphenyl diisocyanate (MDI) and ethylene diamine (ED) as the hard segments and hydroxypropyl-terminated poly(dimethylsiloxane) (PDMS, $M_n=1000$ g/mol) as the soft segments were synthesized in the solution by two-step polyaddition method. The effects of the experimental conditions on the structure, composition and size of the copolymers were studied by NMR spectroscopy, gel permeation chromatography (GPC) and viscometry of the dilute solutions. Thermal properties of synthesized copolymers were studied by differential scanning calorimetry (DSC) and thermogravimetric analysis (TGA).

Introduction

PDMS based urethane-urea copolymers have numerous applications such as antifouling coatings, elastomers, sealants and biomedical implants due to good surface properties, flexibility and biocompatibility. The synthesis of segmented PUUS copolymers using end functionalized PDMS as the single soft segment component is very difficult to carry out, due to the extremely high incompatibility between the urethane and urea hard segments and the siloxane soft segment. The selection of the appropriate solvent is the critical factor for avoiding physical gelation during the chain extension step of polymerization and for obtaining high molecular weight copolymer [1,2]. In this work, the influence of the reaction conditions on the synthesis of PUUS copolymers with constant molar ratio of hard and soft segments (molar ratio ED:MDI:PDMS = 1:2:1; 36 wt.% of the hard segments) was investigated in two different solvent mixtures.

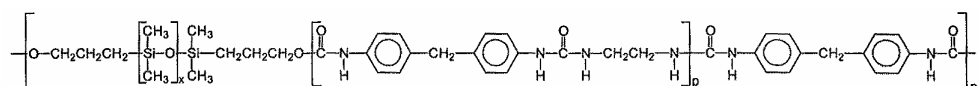
Experimental

The PUUS copolymers were prepared by two-step polyaddition method in the solution. The isocyanate-terminated prepolymer prepared from α,ω -dihydroxypropyl-poly(dimethylsiloxane) ($M_n=1000$ g mol⁻¹) and MDI in the first reaction step, was further chain-extended by addition of stoichiometric amount of

ethylene diamine and the reaction was continued for 1 h. The syntheses were carried out at 40 °C with stannous octanoate as a catalyst (0 to 0.10 mol% based on PDMS). The concentration of the monomers was varied between 7.5 and 25 wt.% in the solvent mixture of tetrahydrofuran/*N,N*-dimethylacetamide, THF/DMAc (1/1) or tetrahydrofuran/*N*-methylpyrrolidone, THF/NMP (1/9). ¹H and ¹³C NMR spectra were recorded on Varian Gemini-200 spectrometer at 25°C using DMSO-*d*₆ as solvent. The intrinsic viscosity, [η], was obtained at 25°C in NMP. The copolymers were characterized by GPC in NMP as the mobile phase. Thermal analyses (DSC and TGA) were performed on Mettler instrument, under nitrogen atmosphere, with a heating rate of 10 °Cmin⁻¹ over a temperature range of -150 to 200 °C (DSC) and 25 to 600 °C (TGA).

Results and discussion

The general structure of the poly(urea-urethane-siloxane)s, represented as:



was confirmed by NMR analysis. The ¹H spectra of copolymers showed characteristic signals at 6.14, 8.44 and 8.52 ppm of the **NH** urea protons and 9.46 ppm of the **NH** urethane protons. In the ¹³C NMR spectra, a resonance signals at 153.8 and 155.7 ppm was observed, which indicates the presence of the carbonyl carbons from urethane and urea bonds, respectively. The effect of different reaction conditions on the intrinsic viscosity of copolymers is shown in Table 1. It was found that the NMP/THF solvent system was a better reaction medium for the synthesis. The results showed that the intrinsic viscosity of copolymers increased with increasing initial concentration of the monomers in NMP/THF (from 7.5 to 25 wt.%), while the viscosities of the samples prepared in DMAc/THF were similar, regardless of the concentration of the reactants.

Table1. The intrinsic viscosities of copolymers, [η], obtained under various conditions

Sample	Catalyst concentration (mol% / PDMS)	Concentration of the monomers in reaction mixture	[η], dLg ⁻¹	
			DMAc/THF (1/1, v/v)	NMP/THF (9/1, v/v)
PUUS7.5	0.10	7.5	0.15	0.16
PUUS10	0.10	10	0.17	0.20
	0.05 without catalyst		-	0.18
PUUS15	0.10	15	0.15	0.22
	0.05 without catalyst		0.18	0.23
PUUS25	0.05	25	-	0.23

It seems that the catalyst concentration does not have significant effect to the intrinsic viscosity of copolymers.

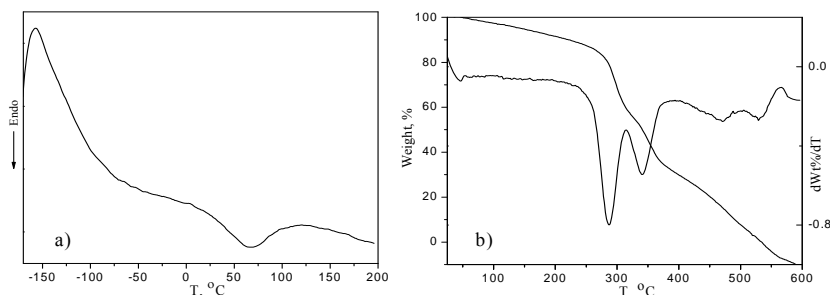


Fig.1. DSC (a) and TG and dTG (b) curves of PUUS/25

In the DSC thermogram of PUUS/25 (Fig. 1, a) T_g of the soft segments was observed at $-108\text{ }^\circ\text{C}$, indicating that the PDMS was microphase separated from the hard segment phase. A broad endothermic peak was observed at about $70\text{ }^\circ\text{C}$. According to some authors, this peak relates to the disruption of short-range order of the hard segments or the hard segments T_g [3]. High temperature transitions were not detected, because the thermal degradation of the urea and urethane bonds occurs around $200\text{ }^\circ\text{C}$, before melting of the copolymer. This corresponds with the results of the TG analysis of copolymers and proposed mechanism of degradation of poly(urethane-urea)s [4]. The TG and dTG curves (Fig. 1.b) indicate that thermal degradation occurs in three steps with the T_d (10%) value at $210\text{ }^\circ\text{C}$.

Conclusion

In this work segmented poly(urethane-urea-siloxane)s were prepared and characterized in two different reaction mediums. It was demonstrated that NMP/THF was a better solvent system than DMAc/THF for the synthesis of PUUS. Copolymers with higher $[\eta]$ were obtained in NMP/THF mixture. The composition of the PUUS was confirmed by NMR spectroscopy. DSC analysis revealed that the copolymers show a high degree of phase separation between hard and soft segments. Thermal gravimetric analysis in nitrogen showed that PUUS copolymers were stable up to $200\text{ }^\circ\text{C}$.

References

- [1] I. Yilgor, J. E. McGrath, *Adv. Polym. Sci.*, 1988, **86**, 1-86.
- [2] J. P. Sheth, A. Aneja, G. L. Wilkes, E. Yilgor, G. E. Atilla, I. Yilgor, F. L. Beyer, *Polymer*, 2004, **45**, 6919-6932.
- [3] J. T. Garrett, R. Xu, J. Cho, J. Runt, *Polymer*, 2003, **44**, 2711-2719.
- [4] L. F. Wang, Q. Ji, T.E. Glass, T. C. Ward, J. E. McGrath, M. Muggli, G. Burns, U. Sorathia, *Polymer*, 2000, **41**, 5083-5093.

SYNTHESIS AND THERMAL PROPERTIES OF POLY(DIMETHYLSILOXANE-URETHANE) COPOLYMERS

M. V. Pergal¹, V. V. Antić², S. Randjelović¹, M. N. Govedarica¹,
S. Ostojić³ and J. Djonlagić⁴

¹*ICTM-Center of Chemistry, Studentski trg 12-16, Belgrade 11000, Serbia*

²*Faculty of Agriculture, Nemanjina 6, Belgrade – Zemun 11080, Serbia*

³*Holding Institute of General and Physical Chemistry, Studentski trg 12-16,
Belgrade 11000, Serbia*

⁴*Faculty of Technology and Metallurgy, Karnegijeva 4, Belgrade 11120, Serbia*

Abstract

A series of thermoplastic elastomers (PUs) based on ethylene oxide-poly(dimethylsiloxane)-ethylene oxide (EO-PDMS-EO), as the soft segments, and 4,4'-methylenediphenyl diisocyanate (MDI)/1,4-butandiole (BD) as the hard segments, was synthesized by two-step polyaddition method. Six copolymers with a content of hard segments between 39 and 67 wt. % were prepared. The influence of the content of soft segments on the structure, molecular weight and thermal properties of TPUs, was investigated. The \overline{M}_n of PUs was in the range from 22630 to 39990 g mol⁻¹ with polydispersity indexes between 1.9 and 2.7. The synthesized PUs were semicrystalline polymers with degree of crystallinity between 11 and 25 %. It was demonstrated that the melting and glass transition temperatures of the PUs increased with increasing MDI/BD segments content.

Introduction

Thermoplastic polyurethane elastomers (PUs) are versatile biomaterials that have found a wide range of biomedical applications due to a combination of good biocompatibility, good processability and excellent mechanical properties.[1] Polydimethylsiloxanes were used as the soft segments in PUs because of their good thermal and oxidative stability, good biostability, good biocompatibility, water repellency and physiological inertness. However, PDMS-based PUs exhibit poor mechanical properties, due to the large differences between the solubility parameters of the PDMS and the comonomers which leads to phase separation during the polyaddition reaction. [2] In this work, the siloxane-containing triblock prepolymer with terminal EO blocks was used to improve the miscibility between the non-polar PDMS and the polar comonomers, i.e. MDI and BD.

Experimental

The PUs were synthesized by two-step polyaddition in solution using α,ω -dihydroxy-EO-PDMS-EO ($\overline{M}_n = 1000$ g mol⁻¹), MDI and BD. A prepolymer was prepared by adding MDI to a reaction vessel containing solution of siloxane

macrodiol in DMAc/THF. For chain extension, solutions of BD in DMAc/THF and the second portion of MDI in DMAc/THF were subsequently added to the prepolymer. The catalyst was stannous-octanoate and mixture DMAc/THF (1/1 v/v) was employed as reaction medium. The PUs were synthesized under the optimal polymerization conditions: concentration of reactants was 15 wt. %, time of the first step of reaction was 30 minutes while time of the second step of reaction was 24 h, reaction temperature of 40 °C and the optimal molar ratio of NCO/OH groups was 1.05.

Gel-permeation chromatography (GPC) was conducted on a Waters 600E instrument equipped with a refractive index detector and three Supelco PL-Gel columns connected in line, at 40 °C in DMAc. Differential scanning calorimetry (DSC) was performed using a DSC Q1000V9.0 Build 275 thermal analyzer. The thermogravimetric (TG) analysis was performed using TGA Q500 V6.3 Build 189 instrument in nitrogen atmosphere, at heating rate of 10 °C min⁻¹.

Results and Discussion

The polyurethane copolymers were synthesized using EO-PDMS-EO as the soft segments and MDI and BD as the hard segments. The hard segment content of PUs was in the range of 39 to 67 wt. %. The GPC results of PUs are presented in Table 1. The number average molecular weight (\bar{M}_n) of the PUs was in the range from 22630 to 39990 g mol⁻¹ with a polydispersity between 1.9 and 2.7 (Table 1).

Table 1. The composition, intrinsic viscosity and results from GPC analysis of the synthesized PUs.

Polymer	Composition of reactants ^a	Hard segments, wt. % ^b	\bar{M}_n , g mol ⁻¹	\bar{M}_w , g mol ⁻¹	PD	$[\eta]_{\text{DMAc}}$, dL g ⁻¹
PU-EO-1	1:2:1	38.7	26084	61384	2.3	0.59
PU-EO-2	1:3:2	46.9	22626	44455	1.9	0.62
PU-EO-3	1:4:3	54.4	32290	83469	2.6	0.63
PU-EO-4	1:5:4	59.6	37510	103512	2.7	0.65
PU-EO-5	1:6:5	63.4	37760	92930	2.4	0.69
PU-EO-6	1:7:6	66.9	39990	87069	2.1	0.76

a) α,ω -Dihydroxy-EO-PDMS-EO: MDI: BD; Molar ratio of NCO/OH = 1.05.

b) Determined by ¹H NMR spectroscopy.

Representative DSC thermogram corresponding to the first heating of the PUs is presented in Fig. 1. A T_g is in the range from 33 to 47 °C and is associated with the mixed phase of the EO sequences of PDMS segments and amorphous hard segments. It was reported that EO-PDMS-EO prepolymer reveal the presence of two T_g s, at -105 and -8 °C. [2] The PUs showed melting temperature in the range from 168 to 192 °C corresponding to the melting of hard segments. As the hard segment content increased, the melting temperature was shifted to higher temperatures, which indicates better ordering of the hard domains. The degree of crystallinity, w_c , was in the range from 11 to 25 % (in the first run).

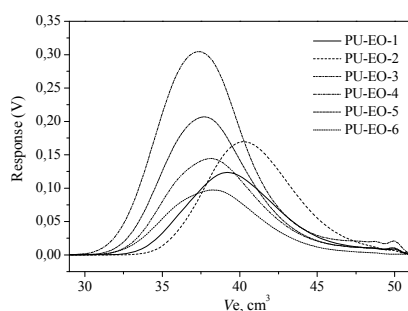


Fig. 1. GPC chromatograms of PUs.

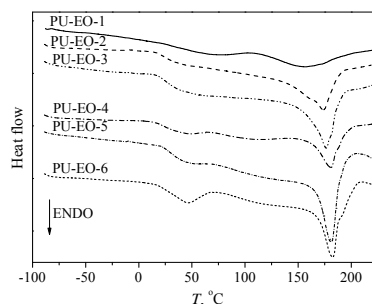


Fig. 2. DSC thermograms of PUs.

Table 2. Thermal properties of the synthesized PUs.

Polymer	T_m , °C	ΔH_m , J g ⁻¹	w_c , %	T_g , °C	$T_{10\%}$, °C	T_{max} , °C
PU-EO-1	168	9.9	10.9	34	293	313/338/530
PU-EO-2	184	19.9	21.8	34	302	322/343/535
PU-EO-3	187	22.4	24.6	35	294	322/345/537
PU-EO-4	191	13.9	15.2	33	295	325/344/539
PU-EO-5	192	23.1	25.3	41	302	325/345/549
PU-EO-6	192	22.0	24.1	47	300	327/347/552

From the TGA results presented in Table 2 it can be observed that the thermal degradation of these PUs is a three-step process in nitrogen. The thermal degradation of copolymers commenced *via* the decomposition of the urethane bonds, followed by degradation of the soft segments. Further decomposition in the region between 500 and 600 °C correlates with the aromatic content in the PUs. [3] The degradation of the PUs commenced between 293 and 302 °C.

Conclusions

A series of PU copolymers with different mass ratio of hard to soft segments was synthesized by two-step solution polyaddition method of 4,4'-methylenediphenyl diisocyanate, 1,4-butanediol and α,ω -dihydroxy-(EO-PDMS-EO). The obtained PUs were semicrystalline polymers. The degree of crystallinity, the melting and glass temperatures of the PUs increased with increasing weight fraction of the hard MDI/BD segments. The inclusion of the siloxane prepolymer with terminal EO units resulted in good thermal stability.

References

- [1] S. Gogolewski, Colloid. Polym. Sci., 1989, **267**, 757-85.
- [2] R. Hernandez, J. Weksler, A. Padsalgikar, J. Runt, Macromolecules, 2007, **40**, 5441-5449.
- [3] F. S. Chuang, W. C. Tsen, Y. C. Shu, Polym. Degrad. Stabil., 2004, **84**, 69-77.

SYNTHESIS OF COPPER CONTAINING EPOXY POLYMER

I. S. Ristić¹, J. Budinski-Simendić¹, S. Cakić², H. Berta³ and K. Mészáros Szécsényi³

¹*Faculty of Technology, Bul. cara Lazara 1, University of Novi Sad, Serbia*

²*Faculty of Technology, Bul. Oslobođenja 124, University of Nis, Serbia*

³*Faculty of Science, Trg D. Obradovića 3, University of Novi Sad, Serbia*

Abstract

Novel copper containing epoxy polymer has been obtained by curing the epoxy resin based on diglycidyl ether of bisphenol A and the organometallic copper(II) complex $[\text{Cu}(\text{ampf})\text{Cl}_2]$ where *ampf* = *N,N'*-bis(4-acetyl-5-methylpyrazole-3-yl)formamidine. The curing reaction was performed at room temperature for 36 h in glass vessel. In order to determine exothermic effect of the polymerization, DSC method was applied. The reaction product was characterized by FT-IR analysis. The Cu(II) complex was prepared by addition of triethylorthoformate into the methanolic solution of copper(II) chloride dihydrate and ligand precursor 4-acetyl-3-amino-5-methylpyrazole.

Introduction

Epoxy resins are one of the most important high-performance polymer systems in use today, ranging from simple two-part adhesives and sports equipment to high-tech applications such as formula one racing cars and the aerospace industry. In order to convert epoxy resins from liquid into thermoset networks it is necessary to use cross-linking agents. These agents promote cross-linking of the monomer or prepolymer (depending on the degree of polymerization). Structurally, epoxy resins contain at least two epoxy (or oxirane) groups within their structure (a planar, three-membered ring comprising two carbon atoms and one oxygen atom). There is substantial ring strain in the epoxy group, due to angular distortion from the tetrahedral carbon angle and the electronegativity of the oxygen atom. Consequently, the group is more reactive than non-cyclic ethers. This enhanced reactivity towards a variety of reagents makes the epoxy very versatile in its cure chemistry. Curing agents based on polyamines are among the most commonly used in epoxy resin systems and make up around 22% of the commercial reagents that are used [1]. Both primary and secondary amines may be used to initiate cure in epoxy systems and are generally employed in stoichiometric amounts. Different classes of metal compounds may be used as cross-linkers of epoxy oligomers: organometallic compounds, salts of metals with inorganic and organic counterions, metal complexes [2], *etc.* As for the latter ones, chelates are predominantly used, namely, P-diketonates and complexes with oxygen and nitrogen ligands, in particular, aliphatic amines [3]. In this work epoxy resin (araldyte) was used for polymer synthesis with metal containing pyrazole-type amine complex as a cross-linker.

Results and discussion

The curing of epoxy resin with the metal complexes was studied using differential scanning calorimetry (DSC). The DSC experiment was performed by heating the mixture of metal complex and epoxy resin to 200 °C with a heating rate of 2 °C/min at the stoichiometric 1:1 Cu(II) to resin mole ratio (1 mg of epoxy resin with 1.12 mg of complex) in a DSC cell using a standard sealed aluminum pans. It was estimated that thermograms have exothermic peak, which indicate curing (Fig. 1). As can be seen, the epoxy monomer was almost completely converted to the corresponding metal-containing polymer at > 190 °C.

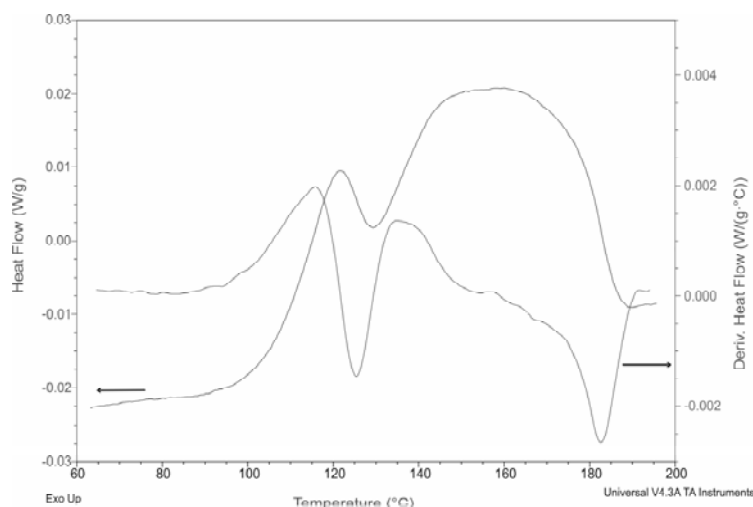


Fig.1. DSC and derivative DSC curves of polymerization reaction between epoxy resin and complex (heating rate 2 °C/min).

The FT-IR spectrum of the complex shows bands at 3240 cm^{-1} and 3444 cm^{-1} from symmetric and asymmetric NH stretching vibration, Fig. 2. Multiple bands are observed since the secondary amine groups can bond and produce dimers and oligomers with *trans* configuration [4]. With reaction progress these bands disappear due to bonding between the NH-group of the complex and the epoxy groups. Band at 1640 cm^{-1} from NH scissoring also disappears in the polymer spectrum, which confirm the polymerization reaction. The intensity of $\text{CH}_2\text{-O-CH}$ epoxy band at 915 cm^{-1} ($\gamma\text{C-O epoxy}$) and 830 cm^{-1} from C-O-C (oxirane) vibrations decrease due to the reaction with the NH-groups of the complex. When epoxy groups react with NH-groups, oxirane rings are opening and form hydroxyl groups. OH-groups from polymer show broad stretching at 3512 cm^{-1} , which confirm opening of oxirane ring.

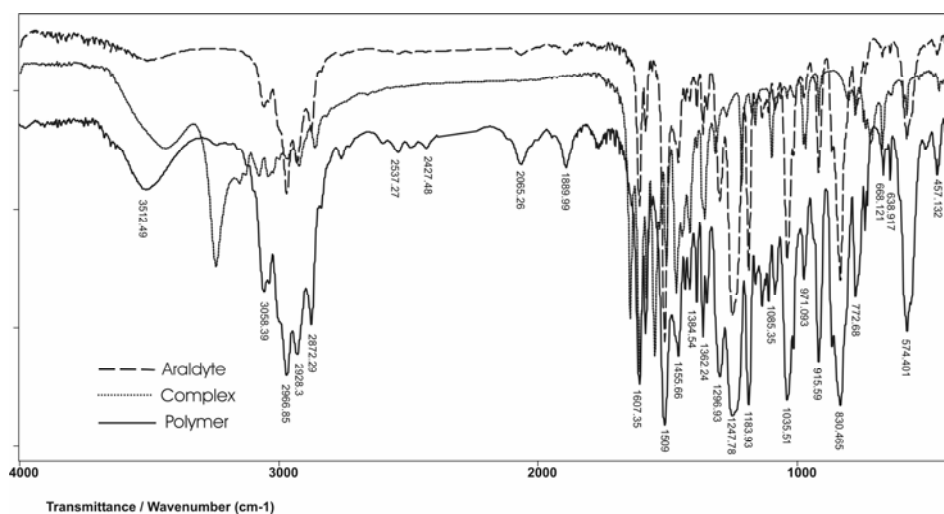


Fig.2. FT-IR spectrum of epoxy monomer, the Cu(II) complex and the polymer.

Conclusion

A novel epoxy polymer has been obtained by curing the epoxy resin based on diglycidyl ether of bisphenol A and $[\text{Cu}(\text{ampf})\text{Cl}_2]$, $\text{ampf} = N,N$ -bis(4-acetyl-5-methylpyrazole-3-yl)formamidine. A new epoxy formation based on the use of metal containing complex as cross-linker was analyzed and characterized by fast FT-IR spectroscopy. Due to polymer formation reaction at about 915 cm^{-1} a decrease of IR band intensity of the epoxy resin is observed.

References

- [1] B. Ellis, Chemistry and Technology of Epoxy Resins, Blackie Academic and Professional, Glasgow, 1993, 37.
- [2] J. Cella, A. Schwabacher, A. Shuls, Cationic Chelate Salts of Main Group Elements as Curing Agents for Epoxy Resins. Znd. Eng.Chem.Prod.Res.Deu., 1983, **22**, 20-25.
- [3] A. V. Kurnoskin, V. A. Lapitsky, Sinteza Struktura Svoistva Medsoderzhashchikh Polimerov, Abstracts of Papers. Vsesoyuznaya Konferentsiya, Zvenigorod, 1988, 55.
- [4] R. Silverstein, C. Bassler, T. Morrill, Spectrometric identification of organic compounds, Wiley International Edition, New York, third edition, 1974, 108.

SYNTHESIS AND ANTIFUNGAL ACTIVITY OF PULLULAN-AMPHOTERICIN B CONJUGATE

J. R. Stefanović¹, D. M. Jakovljević¹, G. Đ. Gojgić-Cvijović¹, M. M. Vrvic²

¹*ChTM - Department of Chemistry, University of Belgrade, Njegoševa 12, P.O. Box 473, 11000 Belgrade, Serbia (jovana_stefanovic@chem.bg.ac.rs)*

²*Faculty of Chemistry, University of Belgrade, Studentski trg 12-16, P.O. Box 51, 11158 Belgrade, Serbia*

Abstract

Polyene antibiotics are antifungal compounds produced by *Streptomyces* strains. In order to decrease toxicity and improve water solubility various pharmaceutical formulations have been prepared. The aim of this work was to prepare conjugate of polysaccharide pullulan and polyene antibiotic amphotericin B. Increasing reactivity of carbohydrate polymer was achieved by introducing of aldehyde groups into polymer chain. Resulting polyaldehyde glucan was coupled with amino groups of amphotericin B to give Schiff base structures. Obtained conjugate is soluble in water and shows significant activity against *Candida albicans*.

Introduction

Polyene antibiotics belong to the class of macrocyclic lactone group of antibiotics. Beside macrocyclic ring, they have series of conjugated double bonds in their molecule, which is essential for their activity.

Although these molecules are very efficient fungicides, their use is limited due to numerous unwanted effects, mostly nephrotoxicity [1]. Toxicity is a consequence of weak water solubility on physiological pH value and affinity toward cholesterol. The main strategies for overcoming these deficiencies are physical and chemical modifications during production of appropriate antibiotic formulations. One of the successful chemical modifications is coupling reaction between antibiotic and polysaccharide molecules, which results in greater water solubility. That makes absorption in gastrointestinal tract better while antimicrobial activity remains similar and toxicity is reduced.

Introduction of aldehyde functions into polysaccharide molecule is possible to obtain by periodate oxidation [2]. That enables coupling reaction with compounds which have available amino functions, like polyene antibiotics. In this paper is described such modification of pullulan, a fungal exopolysaccharide produced by *Aureobasidium pullulans* species. It is a linear molecule which consists of α -(1 \rightarrow 6)-linked maltotriosyl units. It is biodegradable, nontoxic and readily soluble in water [3,4].

Results and Discussion

Periodate oxidation of pullulan. Oxidation of pullulan to polyaldehyde derivative was done with oxidizing agent (sodium periodate) in aqueous solution. Excess periodate and iodate ions were removed from reaction mixture by dialysis and after

that, oxidized glucan was liophilized. Aldehydo groups in polymer were determined by titration with standardized iodine solution [5]. Oxidation was done at room temperature (20 °C). In these conditions, samples of 30% oxidized pullulan were obtained.

Synthesis of pullulan-amphotericin B conjugates. Coupling reaction between oxidized pullulan and amphotericin B was done in borate buffer (pH 11) in the dark, with continual stirring, at 40 °C, during 48 h period.

UV and IR spectroscopy of conjugates. Coupling reaction was monitored by UV and IR spectroscopy, by comparing spectra of pure polysaccharide and conjugate. UV-VIS spectra was obtained on GBC Cintra 40 spectrophotometer. FT-IR spectra was obtained on Nicolet 6700 FT-IR apparatus in ATR technique or in KBr.

UV spectra of pullulan and oxidized pullulan do not have absorption maxima because polysaccharides do not have any chromophore groups in their molecule. After coupling reaction, spectrum of product occurs to be significantly different (Figure 1b). By comparing spectrum of synthesized conjugate with spectrum of pure amphotericin B (Figure 1a), it can be seen that characteristic absorption peaks (on 365 nm, 387 nm and 412 nm) overlaps. Based on this, it can be concluded that aldehydo groups that are introduced in polysaccharide molecule are successfully coupled with antibiotic.

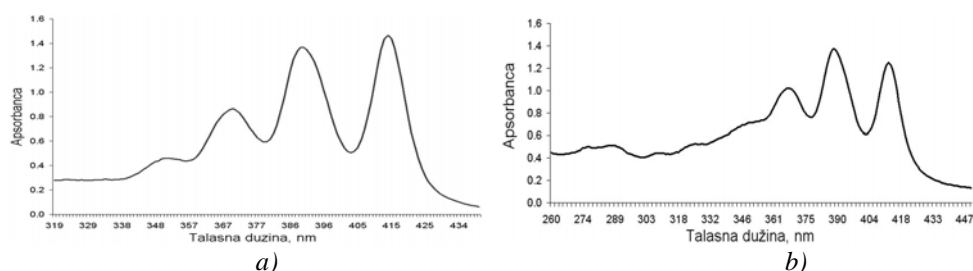


Fig.1: UV spectra of amphotericin B (a) and pullulan-amphotericin B conjugates (b)

FT-IR spectroscopic data suggest on chemical bonding between oxidized pullulan and amphotericin B, too. FT-IR spectrum of native pullulan (Figure 2a) shows wide absorption bands typical for polysaccharides. FT-IR spectrum of pure amphotericin B has bands on 2850 cm^{-1} and 2915 cm^{-1} , which correspond to symmetrical and asymmetrical vibrations of C-H bonds from CH_2 groups, band on 1695 cm^{-1} which is from ester C=O function and absorption band on 1012 cm^{-1} from polyene series [6]. FT-IR spectrum of conjugate (Figure 2b) shows combined absorption bands typical for both pullulan and antibiotic.

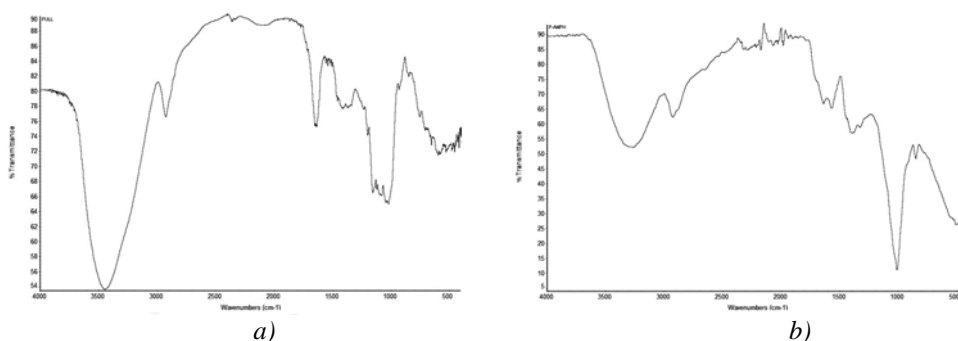


Fig.2: FT-IR spectra of pullulan (a) and pullulan-amphotericin B conjugates (b)

Antifungal activity of conjugates. Antifungal activity was determined by spot-test on *Candida albicans* strain ATCC 24433. Minimal inhibitory concentration (MIC) represents the smallest concentration of solution which leads to growth inhibition after 24 h incubation at 28 °C. For 30% oxidized pullulan-amphotericin B conjugate, calculated MIC was 1.56, and for pure antibiotic in this test 0.78 µg/ml.

Conclusion

The synthesis of pullulan-amphotericin B conjugate was performed by reaction coupling between oxidized polysaccharide and antibiotic. On the basis of its spectral characteristics it was concluded that obtained conjugate have combined spectral properties of both - polysaccharides and polyene antibiotics. Conjugate is soluble in water, which is indication for its potential use in making different nontoxic formulations. It possesses significant antifungal activity against *C. albicans* strain.

Acknowledgement.

This work was supported by the Serbian Ministry of Science and Technology, Project ON 142018B.

References

- [1] A. Lemke, A. F. Kiderlen, O. Kayser, *Appl. Microbiol. Biotechnol.*, 2005, **68**, 151-162.
- [2] K. K. Nishi, A. Jayakrishnan, *Biomacromolecules*, 2004, **5**, 1489-1495.
- [3] M. Rekha, C. Sharma, *Trends Biomater. Artif. Organs*, 2007, **20**, 116-121.
- [4] K. Shingel, *Carbohydr. Res.*, 2004, **339**, 447-460.
- [5] G. Dryhurst, *Periodate Oxidation of Diol and Other Functional Groups*, Pergamon Press, London, 1966, 116
- [6] G. Schwartzman, I. Asher, V. Folen, W. Brannon, J. Taylor, *J. Pharm. Sci.*, 1978, **67**, 398-400.

SYNTHESIS OF POLYROTAXANES FROM POLY(ETHYLENE OXIDE) AND β -CYCLODEXTRIN

I. S. Ristić¹, Lj. Nikolić², V. Nikolić², D. Ilić², V. Jašo¹, Lj. Tanasić¹, N. Vukić¹

¹*Faculty of Technology, Bulevar cara Lazara 1, University of Novi Sad, Serbia*

²*Faculty of Technology, Bulevar Oslobođenja 1, University of Nis, Serbia*

Abstract

Synthesis of network precursors by inclusion of linear polymer chains in β cyclodextrin (β -CD) cavity enables to obtain the topological gels. Polyrotaxanes are intermediary products in the synthesis of topological gels and formed by inserting the linear polymer chains of poly(ethylene oxide) into the β -CD cavities and hindering OH groups at the end of poly(ethylene oxide) chains by stoppers. To avoid reaction of OH groups with stoppers the rings should be protected by reaction with acetic acid anhydride. In this work polyrotaxanes from acetylated- β -CD and poly(ethylene oxide) were synthesized. The acetylation was assessed using the FTIR method according to OH vibration at 3380 cm^{-1} . Inserting of poly(ethylene oxide) in cyclodextrin cavities was monitored via the analysis of asymmetric vibration of $[-\text{CH}_2\text{-O-CH}_2\text{-}]$ at 1117 cm^{-1} .

Introduction

Polymer networks are prepared from precursors, i.e. compounds carrying functional groups capable of bond formation [1]. A typical example of network precursors is provided by polyrotaxanes, in which many cyclic molecules are threaded on a single polymer chain and are trapped by capping the chain with bulky end groups. Today, they are becoming more and more interesting because they enable the production of highly sophisticated functional molecules [2], or become transformed by cross-linking into slide-ring gels [3]. The production of a polyrotaxane is driven by noncovalent attractive forces [4] which are important for the formation of highly organized biological systems. Iodine can provoke the polarization of acetic anhydride, thus it can be used as a catalyst for the acetylation reaction. The goal of this work is to synthesize polyrotaxanes from acetyl- β -CD in which the OH groups are protected.

Results and Discussion

For synthesis the suspension of β -CD and acetic anhydride a small quantity (2% wt.) of iodine is added and stirred vigorously. The end of the reaction was registered by complete dissolution of β -CD, which has become acetylated derivative soluble in acetic anhydride and released acetic acid. The purification of the product was carried out at $5\text{ }^\circ\text{C}$. The inclusion of acetyl- β -CD and PEO is carried out in water at low temperature (up to $5\text{ }^\circ\text{C}$) to avoid the hydrolysis of acetate groups for 9 h. The acetylation of β -CD was monitored by the consumption

of acetic acid anhydride by HPLC (Fig. 1). As can be seen the peak from acetic anhydride decreases due to reaction with CD. The smallest peak in HPLC chromatogram obtained for reaction mixture after 15 min originates from unreacted anhydride used as solvent and reactant.

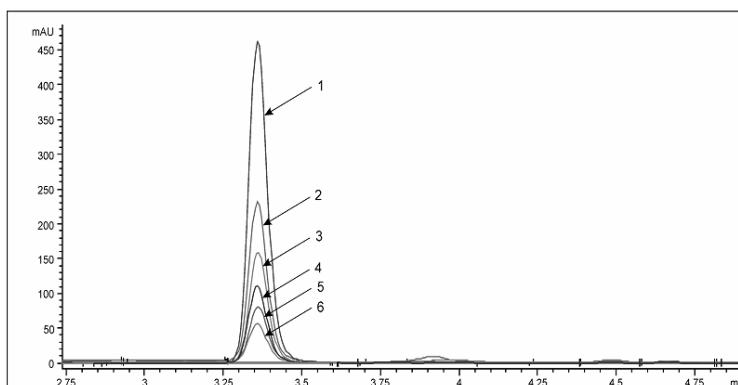


Fig.1. HPLC chromatogram of the acetic acid anhydride during the β -CD acetylation reaction: 1) 0 min; 2) 3 min; 3) 6 min; 4) 9 min; 5) 12 min; 6) 15 min.

In Figure 2 are shown FT-IR spectra of β -CD and acetyl- β -CD. The IR spectrum of β -CD had shown a band at 3384 cm^{-1} from the OH group valence vibrations. Also, there is a band at 1417 cm^{-1} from OH group bending vibrations. These bands disappear altogether in acetyl- β -CD, and a new band appears at 1748 cm^{-1} from the valence vibration of the formed C=O group, which is not present in non-acetylated CD.

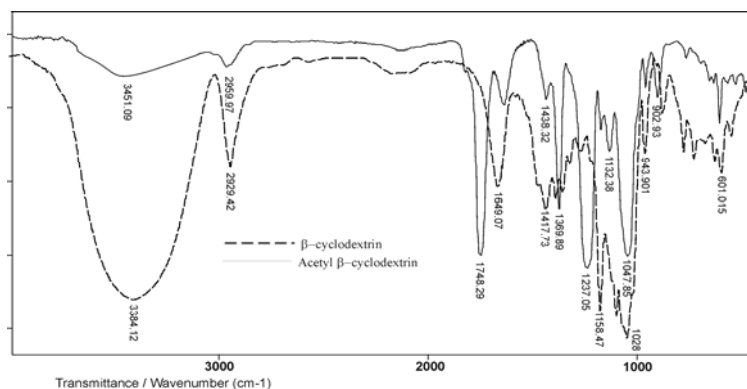


Fig.2. FT-IR spectra of non-acetylated and acetylated β -CD

In pure PEO the band occurs at 1117 cm^{-1} originating from asymmetric valence vibrations of $-\text{CH}_2\text{-O-CH}_2-$ acyclic ether (Figure 3). In the inclusion complex the intensity of this band is reduced because the greater part of these segments is covered (masked) by the cyclodextrin ring. The band at 2887 cm^{-1} originating from OCH_2 valence vibrations occurs in the complex with reduced intensity because the cyclodextrin rings overlay OCH_2 groups of PEO polymer chains.

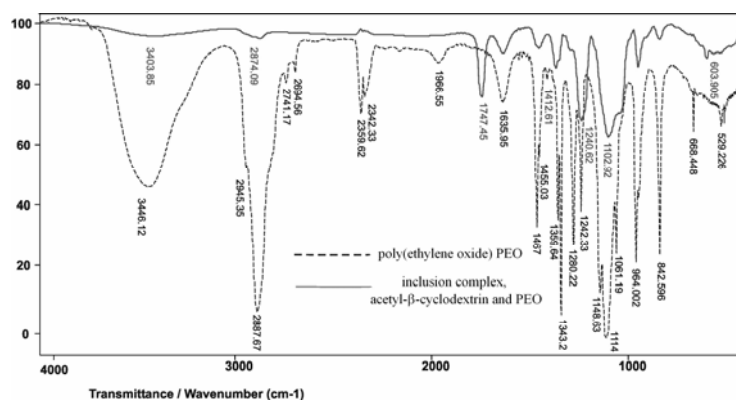


Fig.3. FT-IR spectra of PEO and the included compound of PEO acetyl- β -cyclodextrin

Conclusions

In this work acetylation of β -CD was performed with a high degree of acetylation by acetic acid anhydride with iodine as the catalyst. Modified cyclodextrins show better complexing behavior than unmodified cyclodextrins and hold greater potential in the formulation of rotaxanes. FTIR method was confirmed inclusion reaction of polymer chains and β -CD. The obtained inclusion complexes are polymer network precursors and suitable for topological gels preparation for medical application. To realize the biomedical applications, it is important to apply the concept of the high performance gels to biocompatible polymers. Some progresses have been made recently by combining CD and biopolymers.

Acknowledgment

This paper was supported by Ministry of Science and Technological Development-Republic of Serbia, project number 166007 G.

References

- [1] K. Dusek, M. Duskova-Smrckova, *Progr. Polym. Sci.*, 2000, **25**, 1215.
- [2] A. Harada, J. Li, M. Kamachi, *Nature*, 1992, **356**, 325-327.
- [3] Y. Okumura, K. Ito, *Adv. Mater.*, 2001, **13**, 485.
- [4] T. V. S. Rao, D. S. J. Lawrence, *Am. Chem. Soc.*, 1990, **112**, 3614-3615.

EFFECT OF SYNTHESIS PARAMETERS ON POLY(ACRYLIC ACID)-GELATIN XEROGEL STRUCTURES AND EQUILIBRIUM SWELLING

J. Colić¹, M. Kalagasidis Krušić¹ and J. Jovanović²

¹*Faculty of Technology and Metallurgy, Karnegijeva 4, 11001 Belgrade, R.Serbia*

²*Faculty of Physical Chemistry, Studentski Trg 12-16, 11001 Belgrade, R.Serbia*

Abstract

Composite hydrogels based on crosslinked poly(acrylic acid) and gelatin (AA-G) were synthesized. The influence the neutralization degree (ND) of acrylic acid (AA) and crosslinker concentration on the basic structural properties of the synthesized xerogels and on their equilibrium swelling degree (SD_{eq}) in distilled water at 25°C were investigated and discussed. It was found that the mentioned reaction variables significantly influence the structural properties of xerogels as well as their ability to take in different amounts of water.

Introduction

In recent years, hydrogels based on polyacrylic acid (PAA) and its copolymers have often been used as carriers in drug release systems, because of their multifunctional nature, unique properties and good biocompatibility [1]. Gelatin is a commonly used natural polymer. Biomolecules released from gelatin controlled-release systems are able to retain their biological activity, allowing for their use in tissue engineering, therapeutic angiogenesis, gene therapy, and drug delivery applications [2]. In this work, composite hydrogels based on crosslinked poly(acrylic acid) and gelatin were synthesized and effects of ND of AA and crosslinker concentration on xerogel structures and equilibrium swelling were investigated.

Experimental

Materials: Acrylic acid and Gelatin (G) were used as monomers, N,N'-methylene bisacrylamide (MBA) and 2,2-Azobis-[2-(2-imidazolin-2-il)-propane dihydrochloride were used as a crosslinker and an initiator, respectively whereas KOH was used for neutralization. **Synthesis:** Series of poly(acrylic acid)-gelatin xerogels with different neutralization degrees of AA and crosslinker concentrations, were synthesized via free-radical polymerization and cross-linking in an aqueous solution, by the modified procedure based on the process described in our previous works for poly(acrylic acid) hydrogel synthesis [3]. The resulting products were taken out the moulds and hydrogel disks were punched and immersed in 98% ethanol and "treated" in ultrasonic bath for 10 min in order to remove sol fraction of polymer and unreacted monomer. The washed-out hydrogels

were dried in a thermal oven at 60°C until they reached constant mass. Structural properties of PAA-G xerogels were determined and calculated: average molar mass between the network crosslinks, (M_c), crosslinking density (ρ_c), and distance between macromolecular chains (ζ) by using equations proposed by Flory and Rehner [4,5]. Swelling experiments: xerogel sample was immersed in an excess of water at 25°C and measured until equilibrium was achieved. Equilibrium swelling degree: (SD_{eq}) was calculated using the following equation: $SD_{eq} = (m_{eq} - m_0) / m_0$, where m_{eq} and m_0 are weights of the hydrogel sample in the equilibrium swollen state and in dry state, respectively.

Results and Discussion

The effect of synthetic parameters: neutralization degree of AA, crosslinking concentration on the equilibrium swelling degree of AA-G hydrogels, in distilled water at 25°C, are shown in Figure 1.

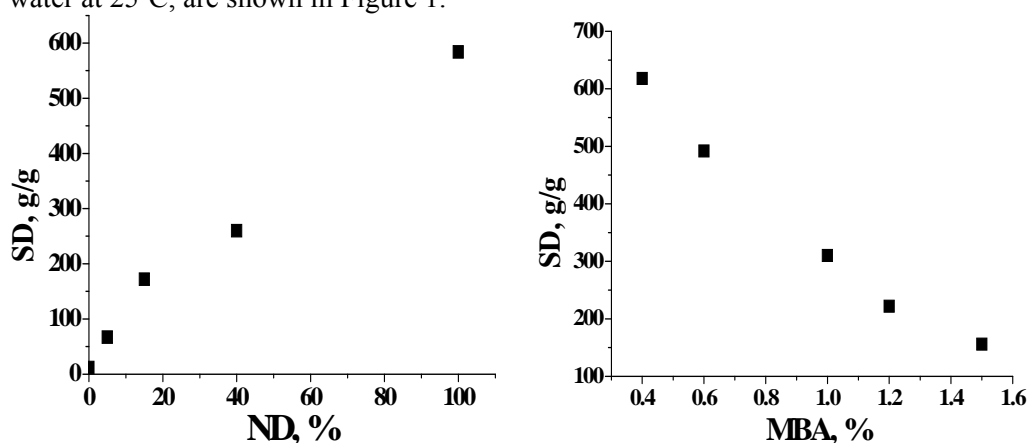


Fig.1. The effects of synthetic parameters on the equilibrium swelling degree of PAA-G hydrogels.

As can be seen from Figure 1, the SD_{eq} increases linearly with the increase in the neutralization degree of AA, while SD_{eq} exponentially decreases with the increasing crosslinker concentration (Cc). The increase in the crosslinker increases generation of more crosslinking points on the polymeric chains and decreases free space between them. Therefore, the space left for water to enter is smaller and SD_{eq} decreases. The effect of the neutralization degree of AA and the MBA concentration on the equilibrium swelling degree can be described by Eqs.:

$$SD_{eq} = 47.5 + 5.44ND \quad (1)$$

$$SD_{eq} = 25.3xCc^{-1.025} \quad (2)$$

Table 1 presents influence of synthesis parameters on the structural properties of PAA-G xerogels.

Table 1. The influence of the synthesis parameters on the structural properties of PAA-G xerogels

	$M_c \times 10^{-4}$, g/mol	$\rho_c \times 10^4$, mol/cm ³	ζ , nm
ND, %			
0	0.1785	6829	44
5	3.324	366.5	341
15	21.45	63.21	1229
40	29.5	47.73	1524
100	204.8	7.176	5865
MBA, mas %			
0.4	229.6	6.449	6344
0.6	161.2	9.278	4943
1.0	69.13	21.03	2748
1.2	40.09	36.45	1875
1.4	17.72	75.71	1078

The increasing neutralization degree of AA leads to the increase in the M_c and the ζ , while the ρ_c decrease. The results show that the M_c and the ζ decrease with the increase in MBA concentration, while the values of ρ_c increase. The changes of structural parameters are in accordance with the changes in the SD_{eq} . The effect of crosslinked-density of AA-G xerogel on the SD_{eq} can be described by Eq.:

$$SD_{eq} = 9.8 \cdot \rho_c^{-0.564} \quad (3)$$

Conclusions

The SD_{eq} increases almost linearly with the increase in the ND of AA while exponentially decreases with the increase in the MBA concentration. The changes of structural parameters are in accordance with the changes in the SD_{eq} .

Acknowledgement

The investigation was supported by the Ministry of Science and technological development of Serbia, through project G 142025.

References

- [1] M. Dittgen, M. Durrani, K. Lehmann, *Pharma. Sci.*, 1997, **7**, 403-410.
- [2] S. Young, M. Wong, Y. Tabata, A. G. Mikos, *Journal of Controlled Release* 2005, **109**, 256– 274.
- [3] B. Adnadjevic, J. Jovanovic, *J Appl. Pol. Sci.*, 2008, **107**, 3579-3587.
- [4] P. J. Flory, J. Rehner, *J. Chem. Phys.*, 1943, **11**, 521-525.
- [5] C. D. Vlad, I. G. Poinescu, I. Costea, *Eur. Polym. J.*, 1996, **32**, 1067-1071.

PREPARATION OF A STAINED POLYSACCHARIDE, A POTENTIAL SUBSTRATE TO EVALUATE CERTAIN SPECIFIC ENZYMES

D. M. Jakovljević¹, J. R. Stefanovic¹, G. Đ. Gojgic¹ and M. M Vrvic^{1,2},

¹*IchTM – Department of Chemistry, University of Belgrade, Njegoševa 12, P.O. Box 473, 11000 Belgrade, Serbia (djakovlj@chem.bg.ac.rs)*

²*Faculty of Chemistry, University of Belgrade, Studentski trg 12-16, P.O. Box 51, 11158 Belgrade, Serbia*

Abstract

A stained biopolymer was prepared by covalently coupling of linear glucan pullulan with anthraquinone dye Remazol Brilliant Blue R (RBBR). In this way was obtained a novel stained polysaccharide material which can be used as potential substrate for evaluation of enzymes that selectively hydrolyzes glycosidic linkages that characterize this polymer.

Introduction

Pullulan is well-known neutral polysaccharide with numerous applications in the food, cosmetic and pharmaceutical industries [1]. It is widely accepted that pullulan is a linear polysaccharide with maltotriosyl repeating units joined by α -(1,6)-linkages. Alternatively, the structural formula of pullulan may be presented as a regular sequence of panoses bonded by α -(1,4)-linkages (Fig. 1). Minor structural abnormalities, like presence of maltotetraose residues or higher maltooligomers which distributed randomly along the pullulan chain not affect the overall physicochemical properties of this polymer.

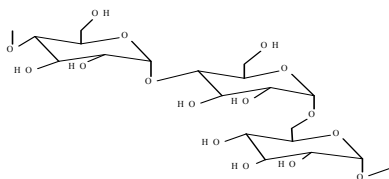


Fig 1.

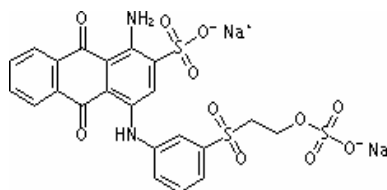


Fig.2.

Anthraquinone dye Remazol Brilliant Blue R (Fig. 2) is dye that is used for staining different substrates, some of which have commercial application [2].

In this work we reported some of our observations on the reaction covalent coupling of pullulan by reagent RBBR to give a novel stained polymer material. The aim of the present work was to prepare sample of this stained polysaccharide and to broaden our knowledge about the some characterisation of the coupling derivative pullulan-RBBR which can be used as potential substrate for evaluation of enzymes that selectively hydrolyzes characteristic linkages of this polymer.

Experimental

Pullulan used in this work is produced by the *A. pullulans*, strain CH-1 (ICHTM, Collection of Microorganisms) [3,4]. Other reagents and solvents were purchased from commercial sources and used as supplied. Pullulan and RBBR were prepared separately, by dissolution in distilled water and then mixed together. The reaction mixture was stirred at 50°C for 1 h and, at different times, equal portions of Na₂SO₄ were added. After that aqueous solution of a Na₃PO₄ was added and reaction maintained at 50°C for another hour with extensive stirring. After cooling the reaction mixture was centrifuged at 4000 rpm for 15 min. The precipitate was resuspended in distilled water and excess of unreacted dye was removed by dialysis. Resulting solution was lyophilized. The FTIR spectra of samples were obtained using Thermo Nicolet 6700 FT-IR Spectrophotometer. The samples were prepared in the form of KBr discs.

UV-VIS spectral characteristics of solutions of dye and stained pullulan (Fig. 3 and Fig. 4) were recorded using a GBC Cintra 40 spectrophotometer.

Results and Discussion

The coupling pullulan with RBBR was confirmed by FTIR (Fig. 3). The FTIR spectrum of pullulan-dye derivative showed a combined characteristic bands for polysaccharide and RBBR. Among polysaccharide bands at 3000-3500 cm⁻¹ (ν OH), 1023 cm⁻¹ ν (CO), 1155 cm⁻¹ ν(C-O-C), this spectrum showed band between 670 and 870 cm⁻¹, which denote aromatic rings, band near 1650 cm⁻¹ characteristic for anthraquinone rings, and bands at 1037 cm⁻¹ and 1120 cm⁻¹ due to of C-NH₂ vibrations.

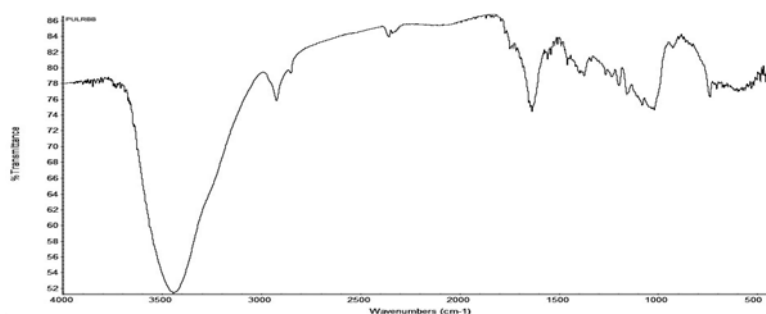


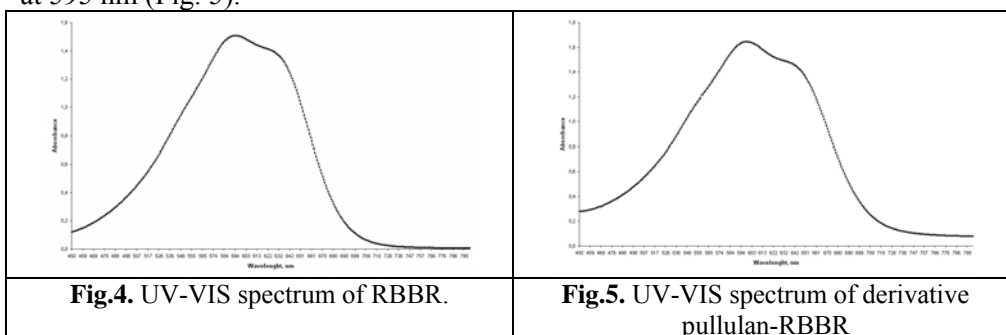
Fig.3. FTIR spectrum of pullulan-RBBR derivative.

Additional evidence that pullulan was coupled with RBBR was found in the results of elemental analysis of pullulan and pullulan-dye derivative (Table 1.). The content of dye in coupled polysaccharide is reflected by the increase of nitrogen content after reaction of this glucan with RBBR.

Table 1. Elemental analysis of starting substances and reaction product

	% N	% C	% H
Pullulan	/	44.4	6.2
RBBR	4.4	42.1	2.5
Pullulan-RBBR	0.6	47.3	6.4

UV-VIS spectral properties of RBBR coupled with pullulan did not differ from those of the free dye. Free RBBR in distilled water (2,13mg/ml) show absorption maximum at 595 nm (Fig. 4). The spectrum of pullulan-coupled RBBR (2,08mg/ml) demonstrated a identical shape of the curve with the broad maximum at 595 nm (Fig. 5).



Conclusion

The results presented in this study show a route to produce stained polymers for potentially useful applications. The pullulan-RBBR derivative was obtained through covalent coupling of pullulan and anthraquinone dye Remazol Brilliant Blue R. This derivative can be used as potential substrate for evaluation of enzymes that selectively hydrolyze characteristic glycosidic linkages of this polymer.

Acknowledgement

This work was supported by the Serbian Ministry of Science, Projects ON 142018B.

References

- [1] K. I. Shingel, *Carbohydr. Res.*, 2004, **339**, 447–460.
- [2] L. Fulop, T. Ponyi, *J. Microbiol. Meth.*, 1997, **29**, 15-21.
- [3] D. M. Jakovljević, M. M. Vrvić, M. Đ. Radulović, M. S. Hranisavljević - Jakovljević, *J. Serb. Chem. Soc.*, 2001, **66**, 377-383.
- [4] M. Đ. Radulović, O. G. Cvetković, S. D. Nikolić, D. S. Đorđević, D. M. Jakovljević, M. M. Vrvić, *Biores. Technol.*, 2008, **99**, 6673-6677.

MODELLING OF FREE RADICAL BULK POLYMERIZATION OF STYRENE

O. Bera, R. Radičević, D. Stoiljković, M. Jovičić and J. Pavličević

University of Novi Sad, Faculty of Technology, Novi Sad, Serbia

Abstract

This work was focused on the modeling of free radical polymerization of styrene. The data were collected from DSC curves of isothermal polymerization at five different temperatures. The obtained typical “S” shape polymerization curves, with a part assigned to auto acceleration were well described by mathematical model proposed in this paper.

Introduction

It is well known that the free radical bulk polymerization of styrene is characterized by auto- acceleration phenomenon after a definite conversion of the monomer [1, 2]. The conversion vs. time curve of polymerization has a typical “S” shape. There are three characteristic points in these curves: the onset of auto-acceleration (point M), the maximum of the polymerization rate (point S) and the end of the polymerization (point K) [3, 4]. The aim of this work was to find a suitable mathematical model of the kinetics of styrene free radical polymerization in bulk using the data obtained from DSC isothermal thermograms.

Experimental

Styrene, from Merck (Darmstadt, Germany), was freed from inhibitor and distilled under nitrogen and reduced pressure. Initiator, 2,2'-azobisisobutyronitrile (AIBN), from Merck, p.a., was recrystallized from methanol. The bulk polymerization of styrene was carried out in differential scanning calorimeter using DuPont Model 910 instrument. Polymerizations were performed under isothermal conditions at five different temperatures (70, 75, 80, 85 and 90 °C). The initiator concentration was 1 wt. %.

Results and discussion

DSC thermograms of styrene free radical bulk polymerizations at different temperatures are presented in Fig. 1, and three characteristic points are clearly observed in them, marked as points M, S and K in Fig. 2. In order to find the degree of monomer conversion, eq. (1) is used:

$$X = \frac{\int_0^{\tau} (dH/d\tau) d\tau}{\int_0^{\tau_k} (dH/d\tau) d\tau} \quad (1)$$

where X is monomer conversion; $dH/d\tau$ reaction enthalpy for an infinitesimal polymerization time τ (min); τ_k is time necessary to achieve the final degree of polymerization (point K). The transformation of DSC data by eq. (1) is presented in Fig. 2.

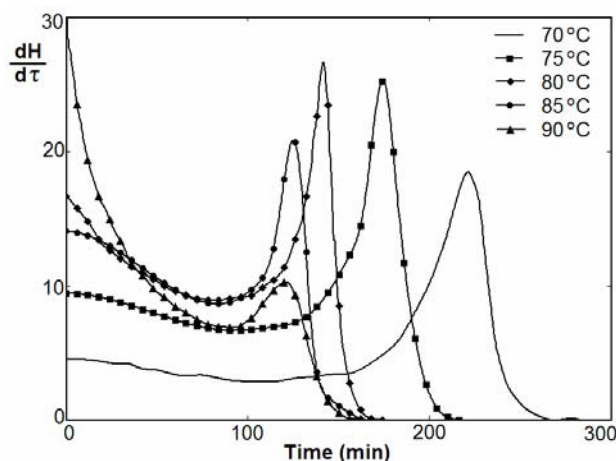


Fig.1. DSC thermograms of styrene polymerization at different temperatures (1 wt. % AIBN).

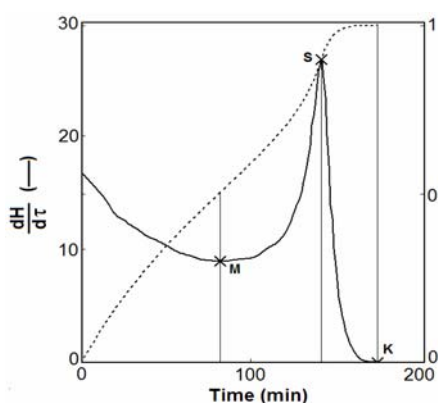


Fig.2. Transformation of DSC thermogram by equation (1) at 80 °C.

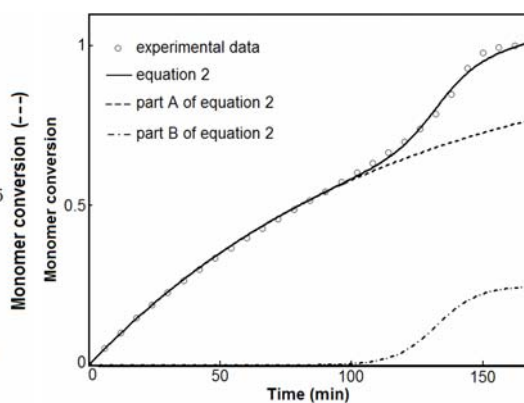


Fig.3. The monomer conversion as function of time at 80 °C.

From Fig. 2 it can be noticed that the whole polymerization course exhibits two stages: first-order reaction stage A (up to point M) and auto-acceleration stage B (from point M to point K). Considering this observation and according to the theory of organized monomer polymerization [5], a mathematical model (2) is proposed

$$X = \underbrace{(1 - e^{-k_1\tau})}_A + \underbrace{\frac{a}{1 + e^{-k_2(\tau - \tau_s)}}}_B \quad (2)$$

where k_1 is the rate constant for the first-order reaction; k_2 is auto-acceleration constant; a is monomer fraction reacted during auto-acceleration; τ_s is time necessary to achieve point S. The dependence of monomer conversion degree on polymerization time according to the mathematical model given in eq. (2) is shown in Fig. 3. The values of all parameters are given in table 1.

Table 1. The values of parameters in eq. (2) determined for styrene polymerization at investigated temperatures (obtained using method of least squares).

t [°C]	k_1 [min ⁻¹]	k_2 [min ⁻¹]	a	τ_s [min]	s^*	R^{2**}
70	$3.276 \cdot 10^{-3}$	0.095	0.441	212.2	0.010	0.999
75	$5.480 \cdot 10^{-3}$	0.104	0.329	166.7	0.011	0.999
80	$8.660 \cdot 10^{-3}$	0.126	0.247	132.2	0.011	0.999
85	$10.06 \cdot 10^{-3}$	0.135	0.219	116.4	0.013	0.998
90	$15.03 \cdot 10^{-3}$	0.210	0.101	117.0	0.012	0.999

*standard deviation of the residuals; **correlation coefficient

Conclusion

Three characteristic points (M, S and K) were observed in DSC thermograms of styrene radical polymerization. The proposed mathematical model confirmed the assumption that up to point M, the monomer conversion degree is mainly influenced by first-order reaction (stage A), and from point M to point K by auto-acceleration (stage B), which is in a good agreement with the theory of organized monomer polymerization. The low values for standard deviation of the residuals and high correlation coefficients at all investigated temperatures verified that the experimental DSC data were well described by estimated kinetic model.

Acknowledgement

The authors wish to express their gratitude to the Ministry of Science and Technological Development of the Republic of Serbia (Project No. 166007G) for financial support of this study.

References

- [1] R. Radičević, S. Kisin, I. Krakovsky, *Chromatographia*, 2004, **59**, 621-624.
- [2] N. Tefera, G. Weickert, K. R. Westerterp, *J. Appl. Polym. Sci*, 1997, **63**, 1649-1661.
- [3] J. Ebdon, B. Hunt, *Anal. Chem.*, 1973, **45**, 804-806.
- [4] R. Radičević, D. Stoiljković, J. Budinski-Simendić, *J. Therm. Anal. Cal.*, 2000, **62**, 237-249.
- [5] R. Radičević, Lj. Korugić, D. Stoiljković, S. Jovanović, *J. Serb. Chem. Soc.*, 1995, **60**, 347-363.

CURE KINETICS OF ALKYD/MELAMINE RESINS STUDIED BY ISOCONVERSIONAL METHODS

M. Jovičić¹, R. Radičević¹, J. Pavličević¹, O. Bera¹ and S. Prendžov²

¹*University of Novi Sad, Faculty of Technology, Novi Sad, Serbia*

²*Faculty of Technology and Metallurgy, Skopje, Macedonia*

Abstract

Curing kinetics of alkyd resin based on dehydrated castor oil with two different melamine-formaldehyde resins was investigated by differential scanning calorimetry under non-isothermal conditions. Isoconversional methods (Ozawa and Kissinger-Akahira-Sunose) were applied with four heating rates (5, 10, 15 and 20 °C/min) in a scanning temperature range from 30 to 250 °C. Obtained results show the dependence of activation energy on the curing degree of resins mixture.

Introduction

Alkyd resins are widely used in surface coating systems usually in combination with other resins, mainly with amino resins [1]. The mixture of melamine-formaldehyde resins and suitable alkyd resin gives the coated film with good hardness and chemical resistance. Alkyd/melamine mixtures are very complex systems and their activation energies change depend on the conversion degree during the curing process. Isoconversional methods reveal changes in the curing kinetics throughout the process and have been applied to the cure of epoxy, epoxy-amine, unsaturated polyester and resol resins using dynamic DSC regime [2]. The aim of this work was to study the curing kinetics of alkyd resin based on dehydrated castor oil with different melamine resins, and to determine the kinetic parameters from DSC measurements. Kinetic analysis of DSC data for the alkyd/melamine systems was performed using Ozawa [3] and Kissinger-Akahira-Sunose [4] methods. These methods were used because it is not necessary to have a prior knowledge of the reaction mechanism to quantify kinetic parameters.

Experimental

Dugal RC-33: a phthalic alkyd resin containing 35 wt. % of dehydrated castor oil ("Duga", Serbia) was used. Two kinds of commercial melamine-formaldehyde resins were used: Maprenal MF 820 (isobutylated melamine-formaldehyde resin, "Ineos Melamines", Germany) and Cymel 303 (hexamethoxymethylmelamine, "Cytec Industries Inc.", USA). The alkyd resin and melamine-formaldehyde resins were mixed at a weight ratio of 50:50 (based on dried mass) and homogenized at room temperature. The designations and the compositions of the samples are:

Sample 1: Dugal RC-33/Maprenal MF 820

Sample 2: Dugal RC-33/Cymel 303

Non-isothermal curing kinetics were studied for four heating rates (5, 10, 15 and 20 °C/min) in the temperature range from 30 to 250 °C using DSC Q20 Ta

Instruments. Ozawa and Kissinger-Akahira-Sunose isoconversional methods were applied to calculate the kinetic parameters of resin mixtures curing from dynamic DSC curves. The Ozawa method is based on the following expression:

$$\log \beta = A' - 0.4567 \cdot \frac{Ea}{R \cdot T} \quad (1)$$

where β is the heating rate, T is the temperature, A' is the constant, Ea is the activation energy (Jmol^{-1}), R is the universal gas constant ($8.314 \text{ Jmol}^{-1}\text{K}^{-1}$).

The isoconversional Ozawa principle is based on the assumption that the reaction rate at a given degree of conversion is only a function of the temperature. Therefore, for different heating rates (β) at a constant degree of conversion ($\alpha(T)$), a linear relationship is observed by plotting $\log \beta$ vs. $1/T$, and the activation energy (Ea) is obtained as the slope of the straight line. Another expression similar to a proposal by Ozawa is the Kissinger-Akahira-Sunose model, which is described by equation (2).

$$\ln\left(\frac{\beta}{T^2}\right) = \ln\left(\frac{R \cdot A}{Ea \cdot g(\alpha)}\right) - \frac{Ea}{RT} \quad (2)$$

Therefore, if Kissinger's assumptions are correct, a plot of $\ln(\beta/T^2)$ vs. $1/T$ (Eq. 2) should be linear and the activation energy might be obtained from the slope.

Results and discussion

DSC thermograms of resin mixtures curing at different heating rates are given in Figs. 1 and 2. From curves it can be seen that a single broad peak is obtained in all experiments, like it was reported in the literature [5]. The heating rate has a great influence on the curing process. The application of the isoconversional methods requires the determination of the absolute temperature at which a fixed extent of reaction from the several DSC curves recorded at different heating rates. The obtained data were applied to isoconversional method of Ozawa and Kissinger-Akahira-Sunose to determine the kinetic parameters in curing process of resins. The conversion range between 0.05 and 0.95 was investigated.

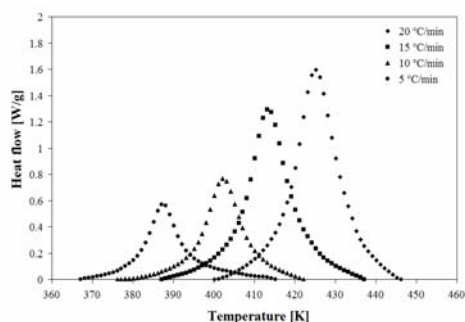


Fig.1. DSC curves of non-isothermal curing of sample 1.

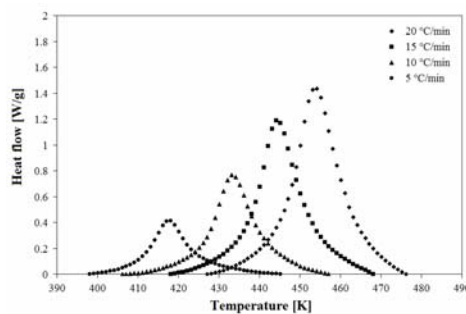


Fig.2. DSC curves of non-isothermal curing of sample 2.

Table 1 shows the results obtained after fitting the data to both, Ozawa (eq. (1)) and Kissinger-Akahira-Sunose (eq. (2)) models. The correlation coefficients for the linear regressions were higher than 0.954 for all cases. Applied models describe similar variation of the activation energy with the curing degree. However, using both methods, activation energy has shown a significant dependence on the apparent degree of curing. That is a typical characteristic of a curing process of thermoset resins [6].

Table 1. Kinetic parameters of samples curing at different conversion degrees determined by isoconversional methods.

α [%]	Ozawa method						Kissinger-Akahira-Sunose method			
	Sample 1			Sample 2			Sample 1		Sample 2	
	A'	Ea [kJ/mol]	R ²	A'	Ea [kJ/mol]	R ²	Ea [kJ/mol]	R ²	Ea [kJ/mol]	R ²
5	7.822	48.66	0.977	7.971	53.39	0.999	44.62	0.969	49.15	0.998
10	7.994	50.29	0.986	8.086	54.77	0.999	46.29	0.981	50.53	0.998
20	7.905	50.10	0.989	8.214	56.30	0.999	46.04	0.985	52.07	0.998
30	7.841	49.89	0.989	8.270	57.04	0.998	45.78	0.985	52.81	0.997
40	7.821	49.93	0.990	8.283	57.36	0.998	45.80	0.986	53.12	0.996
50	7.803	49.96	0.990	8.301	57.69	0.997	45.81	0.986	53.44	0.996
60	7.803	50.13	0.990	8.308	57.95	0.997	45.96	0.986	53.69	0.996
70	7.803	50.33	0.989	8.366	58.66	0.997	46.14	0.985	54.40	0.996
80	7.963	51.82	0.985	8.495	60.03	0.996	47.66	0.981	55.80	0.995
90	8.332	55.10	0.975	8.793	63.00	0.995	51.05	0.968	58.85	0.994
95	8.663	58.09	0.964	9.018	65.35	0.993	54.13	0.954	61.26	0.991

Conclusion

The isoconversional methods can be applied to study the curing process of alkyd/melamine resin. In the Ozawa and Kissinger-Akahira-Sunose methods under investigation, the variation of the activation energy with curing degrees is obtained. Two models under studies show that *R* value is fitted in them and although the results are good.

Acknowledgement

The authors wish to express their gratitude to the Ministry of Science and Technological Development of the Republic of Serbia (Project No. 166007) for financial support of this study.

References

- [1] R. Radičević, J. Budinski-Simendić, J. Serb. Chem. Soc., 2005, **70**, 593-599.
- [2] J.M. Perez, M. Oliet, M. V. Alonso, F. Rodriguez, Thermochim. Acta, 2009, **487**, 39-42.
- [3] T. Ozawa, Thermochim. Acta, 2000, **356**, 173-180.
- [4] H. E. Kissinger, Anal. Chem., 1957, **29**, 1702-1706.
- [5] M. Jovičić, R. Radičević, J. Budinski-Simendić, J. Therm. Anal. Cal., 2008, **94**, 143-150.
- [6] M. V. Alonso, M. Oliet, J. Garcia, F. Rodriguez, J. Echeverria, J. Therm. Anal. Cal., 2006, **86**, 797-802.

CHARACTERIZATION OF NOVEL POLYCARBONATE-BASED POLYURETHANES USING FTIR METHOD

J. Pavličević¹, M. Jovičić¹, O. Bera¹, R. Poreba², M. Špírková², J. Budinski-Simendić¹ and S. Prendžov³

¹*Faculty of Technology, Novi Sad, Serbia*

²*Institute of Macromolecular Chemistry, Academy of Sciences, Czech Republic*

³*Faculty of Technology and Metallurgy, Skopje, Macedonia*

Abstract

Novel aliphatic polycarbonate-based polyurethanes (PC-PUs) were synthesized by one step procedure in a bulk, using hexamethylene-diisocyanate (HMDI), polycarbonate diols and 1,4-butanediol (BD) as chain extender. The structure of elastomeric materials obtained in the form of films was varied either by diol type or chain extender content. In order to investigate the hydrogen bond formation in prepared samples, Fourier transform infrared spectroscopy (FTIR) was performed. The hard segment content of obtained elastomers was determined using Gaussian curves for deconvolution of “-C=O amide I” stretching region peaks.

Introduction

Considerable attentions have been devoted to new PC-PU elastomers due to their improved thermal and dynamic mechanical performances compared to the traditional polyurethanes [1, 2]. The aliphatic polycarbonate-based polyurethanes are used for industrial parts, building materials, sports goods, tissue engineering and medical equipment [2, 3]. This type of material has a distinctly segmented structure, which is the key to its behavior as a strong physical rubbery network. The hard segments (HS) consist of HMDI and chain extender building blocks, while the soft segments (SS) belong to the diol component. Until now, hard domains in neat matrices, formed by hydrogen bonding of hard segments, NCO group conversion and degree of hydrogen bonding between urethane groups have been studied using FTIR method [4, 5]. The main goal of this work was to investigate the hydrogen bond formation in PC-PU samples by Fourier transform infrared spectroscopy.

Experimental

Polycarbonate diols with molecular weight ca. 1000 (PCDL T5651 and T4671), were provided by Asahi Kasei Corporation. For diol T5651 OH value was 111.4 mg KOH/g and for T4671 was 109.9 mg KOH/g. 1,6-hexamethylene diisocyanate, 1,4-butanediol and the catalyst, dibutyltin dilaurate (DBTDL), were produced by Fluka. The films were obtained by one step technique. The ratio $r = [\text{NCO}]/[\text{OH}]$ was 1.05. The ratio $R = [\text{OH}]_{\text{diol}}/[\text{OH}]_{\text{ext}}$ was either 1 or 10. The mixture containing diol, chain extender and catalyst was degassed. Then diisocyanate component was

added, the mixture was again degassed, and finally spread on polypropylene sheets. The constant layer thickness (500 μm) was obtained using a ruler. Samples were kept in nitrogen at 90 $^{\circ}\text{C}$ for 24 h. FTIR was performed with a Thermo Nicolet Nexus 670 FTIR-ATR spectrometer. Single beam spectra were obtained after averaging 40 scans between 4000 cm^{-1} and 500 cm^{-1} with a resolution of 2 cm^{-1} .

Results and discussion

IR spectra of PC-PU prepared with $R=1$ is displayed in Fig. 1a. No isocyanate peak at ca. 2270 cm^{-1} was observed indicating full conversion of NCO groups. The IR spectra also show the absence of the stretch vibration peak of free amidic NH groups, not associated by H-bonds, at 3640 cm^{-1} . The only NH signal is at 3323 cm^{-1} , a vibration peak of hydrogen-bridged amidic NH groups. This indicates that practically all the NH groups participate in the formation of hydrogen bonds. The absorption peaks at 2940 cm^{-1} and 2855 cm^{-1} are assigned to the presence of CH_2 anti-symmetry and symmetry stretch vibration peaks in the soft segment. Those peaks for T4671-based samples are slightly shifted in comparison to the same peaks for samples based on diol T5651, due to different chemical structures. In order to study the correlation of hard segment content on the formation of hydrogen bonding, in the fig. 1b is given in detail the “-C=O amide I” stretching region.

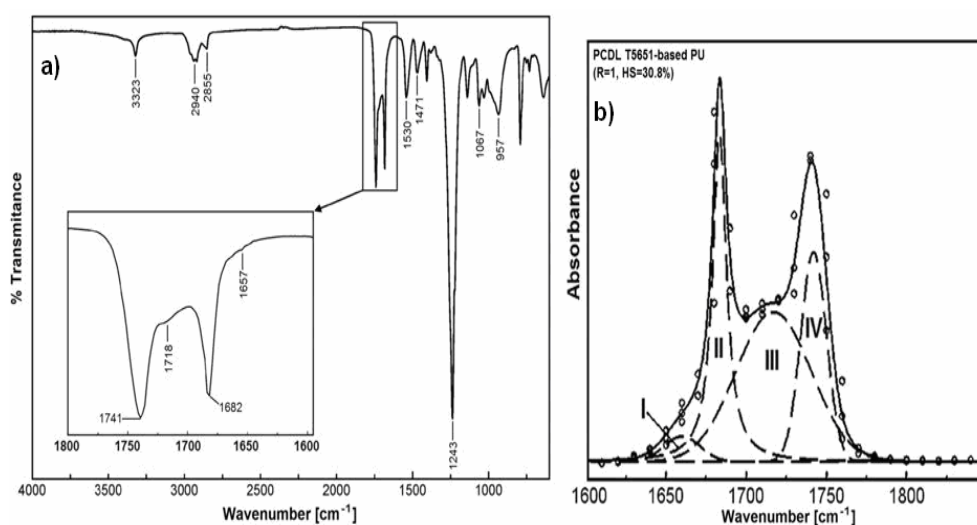


Fig.1. FTIR spectra a) for PU elastomer based on diol T5651 ($R = 1$) and b) for the carbonyl group absorbance region (bands I-IV) of the same sample.

The absorption peak at 1741 cm^{-1} corresponds to non H-bonded (free) carbonyl ($\text{C}=\text{O}$) groups of the aliphatic carbonate (band IV). The peak at 1718 cm^{-1} belongs to $\text{C}=\text{O}$ bonded by a hydrogen bond in disordered (“amorphous”) phases (band III), while H-bonded carbonyl groups in ordered (“crystalline”) hard domains are observed at 1682 cm^{-1} (band II). A shoulder associated with the soft segment

groups in the polycarbonate appears at 1657 cm^{-1} (band I), that is assigned to H-bonded (carbonate) carbonyl diol. The analysis of the group of C=O stretching, signals, using Gaussian curves for deconvolution of the peaks described previously is shown in Table 1. In the case of samples with higher HS content, the band II increases and it produces a decrease of the areas related to bands IV and III, indicating that the strong interactions in the hard segments formed from a larger number of HMDI/1,4-BD units dominate over weaker interactions on hard/soft segment boundaries and so favor phase separation of the domains.

Table 1. Areas of different bands assigned to distinct carbonyl groups in the amide I region for the samples with different hard segment content.

diol	HS content (% wt.) / <i>R</i>	Band I (% area)	Band II (% area)	Band III (% area)	Band IV (% area)
T5651	15.1 / -	2.0	14.9	58.3	24.8
T5651	16.9 / 10	2.5	16.7	59.8	21.0
T5651	30.8 / 1	3.8	30.8	45.9	19.5
T4671	30.6 / 1	2.1	30.3	51.1	16.5

Conclusion

In this work, the synthesis of novel aliphatic polycarbonate-based polyurethanes with very attractive properties was achieved. For prepared elastomeric films no isocyanate peak at 2270 cm^{-1} was observed in the FTIR spectra, indicating full conversion of NCO groups. In order to determine the influence of the hard segment content on the formation of hydrogen bonds, the “-C=O amide I” stretching region was studied in detail. The hard segment content of elastomers (calculated according to mass of the reactive components) was confirmed by quantitative determination the area under Gaussian curves that formed peaks in the deconvoluted part of IR spectra of investigated polyurethanes.

References

- [1] A. Eceiza, K. de la Caba, G. Kortaberria, N. Gabilondo, C. Marieta, M.A. Corcuera, I. Mondragon, *Eur. Polym. J.*, 2005, **41**, 3051-3059.
- [2] P. Król, *Prog. Mater. Sci.*, 2007, **52**, 915–1015.
- [3] K. D. Andrews, P. Feugier, R. A. Black, J. A. Hunt, *J. Surg. Res.*, 2008, **149**, 39-46.
- [4] M. Špírková, A. Strachota, M. Urbanová, J. Baldriand, J. Brus, M. Šlouf, A. Kuta, Z. Hrdlička, *Mater. Manuf. Process.*, 2009, **24**, 1185-1189.
- [5] L. R. Larraz, B. F. d’Arlas, A. Tercjak, A. Ribes, I. Mondragon, A. Eceiza, *Eur. Polym. J.*, 2009, **45**, 2096–2109.

THE INFLUENCE OF EPOXY RESIN ON CURING AND MECHANICAL PROPERTIES OF ALKYD/MELAMINE RESINS

I. S. Ristić¹, S. Cakić², J. Budinski-Simendić¹, R. Radičević¹,
V. Simendić¹ and V. Jašo¹

¹*Faculty of Technology, Bulevar cara Lazara 1, University of Novi Sad, Serbia*

²*Faculty of Technology, Bulevar oslobođenja 124, University of Nis, Serbia*

Abstract

In this paper were studied curing kinetics, hardness, gloss and adhesion properties of alkyd/melamine resin. In order to improve mechanical properties and to achieve lower curing temperature it was added 3 wt% of epoxy resin in alkyd/melamine system. FTIR spectra have confirmed that the epoxy resin reacts and inserts in enamel structure. Activation energy, calculated from DSC thermograms of the curing reaction, becomes lower with the addition of the epoxy resin resulting in higher curing rate (shorter reaction time).

Introduction

Alkyd resins play important roles as coating binders [1]. As alkyd resins have good compatibility with a wide variety of other coating resins [2], the aforementioned properties can be improved via blending with suitable resins. Recent studies assessed that many of properties could be improved by blending with epoxy resin [3]. The medium-oil-length glycerol alkyd based on Mahua oil fatty acid was cured with 20% melamine at 140 °C. The cured resins offered better mechanical properties and adhesion than the commercial alkyds [4]. In an effort to achieve further improvement of resin properties in this work we studied curing of system composed of alkyd, melamine and epoxy resin.

Results and discussion

In this study blends with two different ratio of alkyd/melamine (70 wt% alkyd with 30 wt% melamine (A/M 7/3), and 80 wt% alkyd with 20 wt% melamine (A/M 8/2)) were used. For sample preparation 3 wt% of epoxy resin was added to alkyd/melamine. FTIR spectroscopy was used to follow the curing process. For analysis a standard NaCl crystal was coated with a resin layer. FTIR spectrograms for reaction products after different time (Figure 1 and 2) show decreasing of OH groups band intensity from alkyd, which confirms the progress of reaction. Characteristic band at 910 cm⁻¹ (γ C-O) for epoxy is decreasing with prolonging the reaction time (Figure 3). With progress of the reaction the appearance of an enveloping band between 3000 and 3600 cm⁻¹ was registered. This band was previously reported [5] and was attributed to the tension signal of the hydroxyl group that appears as a result of the epoxy reaction, at 3510 cm⁻¹.

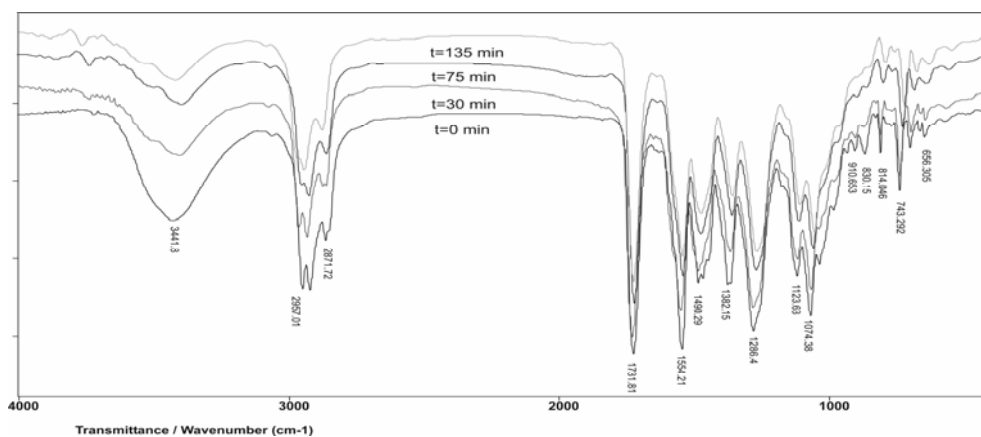


Fig.1. FTIR spectra for A/M 7/3 with epoxy resin system after different reaction time.

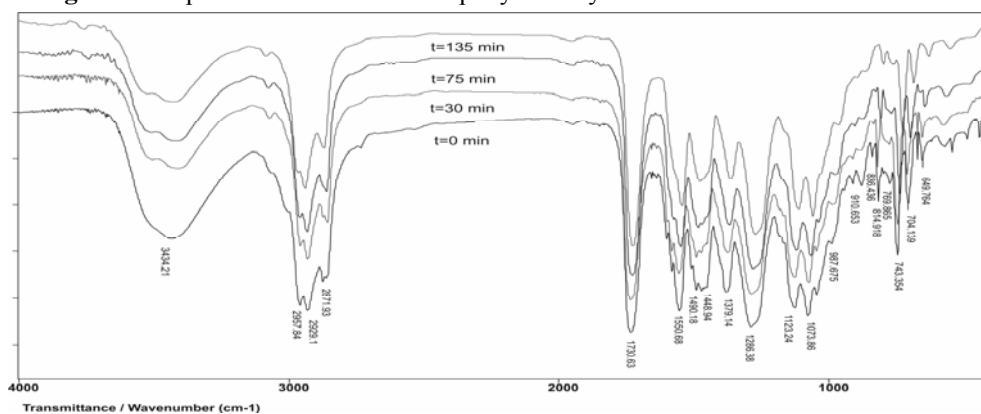


Fig.2. FTIR spectra for A/M 8/2 with epoxy resin system after different reaction time.

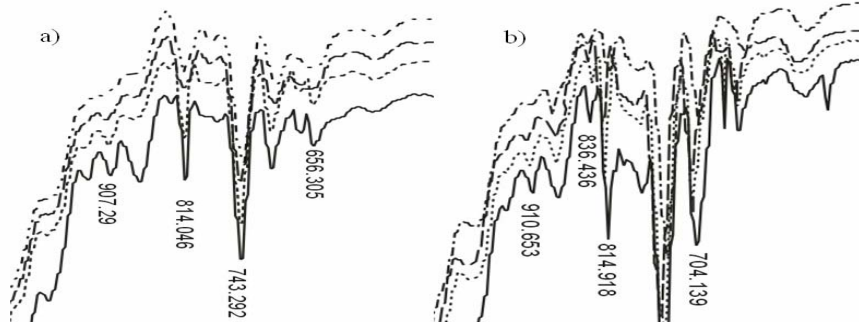


Fig.3. FTIR spectras (wavenumbers from 400 to 1000 cm^{-1}) for a) system A/M 7/3 with epoxy resin, b) system A/M 8/2 with epoxy resin after different reaction time (— $t=0$; $t=30$ min ; ----- $t=75$ min ; -.-.- $t=135$ min).

Activation energy, E_a , for all samples was calculated according to Freeman-Carroll method from thermograms obtained for different heating rate (5, 10 and 20 $^{\circ}\text{C}/\text{min}$), Figure 4. It is obvious that with addition of epoxy resin maximum of DSC curves shifts towards lower temperatures, only for A/M 7/3

system, Figure 5. Addition of epoxy resin results in lower activation energy for curing reaction and increased hardness determined according ASTM - D4366 standard, and gloss of enamel (Table 1).

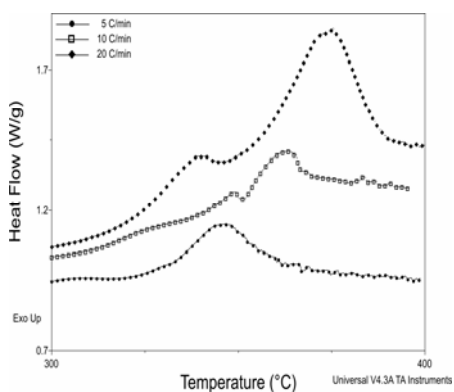


Fig.4. DSC thermogram of A/M 7/3 system with 3 wt% epoxy resins at three different heating rate.

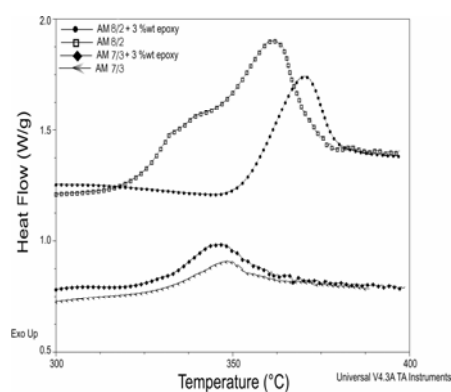


Fig.5. DSC thermograms of curing of different resin mixtures (heating rate 5 °C/min).

Table 1 Activation energy for curing reaction and properties of obtained samples.

	Ea (kJ/mol)	Hardness* (s)	Gloss	Adhesion
A/M 7/3	185.92	114.8	91-92	Gt0
A/M 7/3 + epoxy resin	144.62	131	90-91	Gt0
A/M 8/2	141.89	109.2	97-99	Gt0
A/M 8/2 + epoxy resin	174.92	99.4	92-94	Gt0

Conclusion

In this study, we have found that addition of 3 wt% of epoxy resin to A/M 7/3 makes activation energy of the curing system lower and also improves the properties of a resulting enamel. System A/M 7/3 is suitable for mixing with epoxy resin and provides product with better mechanical properties (improved hardness, gloss and adhesion properties).

Acknowledgment

This paper was supported by Ministry of Science and Technological Development-Republic of Serbia, project number 166007 G.

References

- [1] S. Paul, Surface Coatings Science Technology, 2nd ed., Wiley: New York, 1997.
- [2] M. Abo, M. Akira, K. Mano, K. Sakaguchi, Jpn. Pat. 7528986, 1975.
- [3] N. Dutta, N. Karak, S. K. Dolui, J. Appl. Polym. Sci., 2006, **100**, 516-521.
- [4] S. Tiwari, M. Saxena, J. Appl. Polym. Sci., 2003, **87**, 110-120.
- [5] G. Xiao, M. Delamar, M. Shannahan, J. Appl. Polym. Sci., 1997, **65**, 449-458.

INFLUENCE OF BENTONITE FILLER ON THE THERMAL STABILITY OF GLYCIDYL METHACRYLATE BASED COMPOSITE

S. Marinović¹, Z. Vuković¹, A. Nastasović² and A. Milutinović-Nikolić¹

¹ *IChTM, University of Belgrade, Department of Catalysis and Chemical Engineering, Njegoševa 12, Belgrade, Serbia*

² *IChTM, University of Belgrade, Department of Chemistry, Njegoševa 12, Belgrade, Serbia*

Abstract

Macroporous crosslinked copolymer of glycidyl methacrylate, GMA, and ethylene glycol dimethacrylate, EGDMA, poly(glycidyl methacrylate-co-ethylene glycol dimethacrylate) and its composites were synthesized by suspension copolymerization. Composites were obtained by introducing 10 mass % of either raw bentonite (S₀) or acid modified bentonite (S_A) into reaction system. The composite synthesized with S_A as filler showed superior thermal stability comparing to starting copolymer and composite with S₀ embedded in copolymer matrix.

Introduction

Polymer/clay nanocomposites (PCN) were invented at Toyota Central R&D Labs, Inc. (Toyota) in 1985 [1, 2]. PCN have become increasingly important because they combine the structural, physical, and chemical properties of both clay and polymer [3]. PCN modify different properties of polymers i.e. thermal and mechanical endurance with minimal loss of ductility, flame, abrasion and chemical resistance, alter electrical, electronic and optical properties [4]. Several studies on nanocomposites demonstrated that introducing clay minerals into a polymer, if it results in intercalated or exfoliated structures, leads to thermal degradation shifted towards higher temperatures. Moreover, this improvement can arise at very low filler content (< 1 mass %) [5].

Experimental

Macroporous crosslinked copolymer of glycidyl methacrylate, GMA, and ethylene glycol dimethacrylate, EGDMA, poly(glycidyl methacrylate-co-ethylene glycol dimethacrylate), was synthesized by suspension copolymerization [6]. The monomer phase containing reaction mixture (20.8 g of GMA and 13.8 g EGDMA), AIBN as an initiator (0.35 g), 45.4 g of inert components (36.3 g cyclohexanol and 9.1 g of tetradecanol) was suspended in the aqueous phase which consisted of 240 g of water and 2.4 g of polyvinylpyrrolidone (Sigma-Aldrich). The copolymerization was carried out at 70 °C for 2h and at 80 °C for 6 h with stirring rate of 300 rpm. After reaction, the copolymer particles were washed with distilled water and vacuum dried at 40° C and denoted as CP. Composites were obtained in same

manner as CP, only 10 mass % of monomer mixture of either raw bentonite S₀ or acid modified S_A was introduced into reaction system [7, 8]. The obtained composites were denoted CP-S₀ and CP-S_A. Grafting of organic groups into bentonite structure of synthesized composites was confirmed by IR analysis [9]. The presence of inorganic constituents in composites was performed after the organic constituent was removed by heat treatment. The inorganic residues were 3.26 and 6.50 mass % for CP-S₀ and CP-S_A, respectively [9].

The thermogravimetric measurements were performed with heating rate 10 °C/min on SDT 2090 (TA Instruments) thermal analyzer under air atmosphere. The heating was performed from the ambient temperature up to 600 °C [9].

Results and Discussion

Results obtained by TGA for copolymer and composites are given in Fig. 1 and Table 1. CP is thermally stable in range of temperatures from 50 to 100 °C.

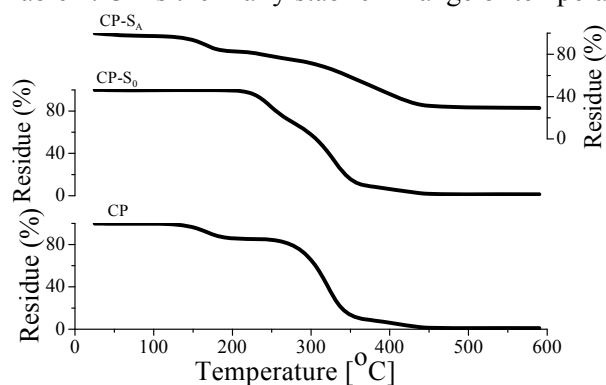


Fig.1. TGA for CP, CP-S₀ and CP-S_A.

Table 1. Thermal stability of samples.

Sample	$\Delta m_{350\text{ }^{\circ}\text{C}}$ [%]	$\Delta m_{600\text{ }^{\circ}\text{C}}$ [%]
CP	86.5	99.8
CP-S ₀	84.3	96.7
CP-S _A	41.4	70.7

Where: $\Delta m_{350\text{ }^{\circ}\text{C}}$ and $\Delta m_{600\text{ }^{\circ}\text{C}}$ are mass loss on denoted temperatures.

For CP it was observed 10 % mass loss in the first step of degradation (~200 °C). In the second step, (200-350°C) mass loss was significant ~86.5 %. In the temperature range 350-450 °C there was a continual mass loss.

For CP-S₀ was observed continual mass loss in the second step of degradation, while CP-S_A shows continual mass loss in range 130-450 °C. Mass residues at 600 °C were much different for CP-S₀ and CP-S_A. In CP-S_A amount of residue after decomposition is 29.3 mass %, which is almost five times more than amount of embedded inorganic component (6.5 mass %). The residue for CP-S₀ was equal to its inorganic constituent.

Conclusion

Composites of macroporous crosslinked poly(glycidyl methacrylate-*co*-ethylene glycol dimethacrylate) and bentonite-clays were synthesized by suspension copolymerization. Mass losses at 600 °C were much different for composite with raw clay (96.7%) from the composite having acid modified bentonite as filler (70.7%). In latter the amount of residue of 29.3 mass % was almost five times more than amount of embedded inorganic component (6.5 mass %). The assumption was that by embedding acid modified bentonite into copolymer matrix, polymer chain splitting was prevented. In this way, thermal decomposition of composite was lowered in temperature range 200-400 °C.

Acknowledgement

This work was supported by the Ministry of Science and Technological Development of the Republic of Serbia (Projects ON 166001 and ON 142039)

References

- [1] A. Okada, M. Kawasumi, T. Kurauchi, O. Kamigaito, *ACS Polym. Prepr.*, 1987, **28**, 447.
- [2] U. S. 4739007 (1988, priority date: Sep. 30, 1985), Toyota Chuo Kenkyusho, invs.: A. Okada, A. Fukushima, M. Kawasumi, S. Inagaki, A. Usuki, S. Sugiyama, T. Kurauchi, O. Kamigaito; *Chem. Abstr.*, 1987, **107**, 60084.
- [3] Q. T. Nguyen, D. G. Baird, *Advances in Polymer Technology*, 2006, **25**, 270
- [4] M. Celik, M. Onal, *J. Appl. Polym. Sci.*, 2004, **94**, 1532-1538.
- [5] P. Dubois "Overview of clay-based polymer nanocomposites (CPN) ", in: *Clay-based polymer nanocomposites (CPN)*, K. A. Carrado, F. Bergaya, The Clay Minerals Society, Chantilly (USA), 2007, 51.
- [6] S. M. Jovanović, A. Nastasović, N. N. Jovanović, K. Jeremić, Z. Savić, *Angew. Makromol. Chem.*, 1994, **219** 161-168.
- [7] Z. Vuković, A. Milutinović-Nikolić, J. Krstić, A. Abu-Rabi, T. Novaković, D. Jovanović, *Mater. Sci. Forum*, 2005, **494**, 339-344.
- [8] Z. Vuković, A. Milutinović-Nikolić, Lj. Rožić, A. Rosić, Z. Nedić, D. Jovanović, *Clays Clay Miner.*, 2006, **54**, 699-704.
- [9] Z. Vuković, Ph. D. Thesis, Faculty of Physical Chemistry, Belgrade, 2010.

THERMAL BEHAVIOUR OF SOME NONPOROUS METHACRYLATE POLYMERS

D. Maksin¹, A. Nastasović², R. Hercigonja³, V. Rakić⁴ and A. Onjia¹

¹*Vinča Institute of Nuclear Science, Belgrade, Serbia*

²*IChTM-Department of Chemistry, Njegoševa 12, Beograd, Serbia*

³*University of Belgrade, Faculty of Physical Chemistry, Belgrade, Serbia*

⁴*University of Belgrade, Faculty of Agriculture, Belgrade, Serbia*

Abstract

Three nonporous methacrylate polymer samples were synthesized by suspension polymerization, and subsequently investigated. The surface area and the surface morphology of the spherical beads were examined by the BET method from the low-temperature adsorption isotherms and by scanning electron microscopy (SEM), respectively. Thermal behaviour of the two homopolymer samples, poly(glycidyl methacrylate) (PGMA) and poly(ethylene glycol dimethacrylate) (PEGDMA), and the copolymer sample poly(glycidyl methacrylate-co-ethylene glycol dimethacrylate) (PGME) was investigated by thermogravimetric analysis (TGA) and differential scanning calorimetry (DSC). All samples exhibit complex thermal degradation behavior. The copolymer is intermediate in stability between PGMA and PEGDMA.

Introduction

Homopolymers and copolymers of glycidyl methacrylate (GMA) have received considerable attention in recent years owing to their versatile applications and low cost [1-3]. The reported glass transition temperature values for PGMA, T_g , are as low as 74°C, which may be a limiting factor in commercial uses [4]. It is well known that the addition of a crosslinking comonomer, such as ethylene glycol dimethacrylate, (EGDMA), can substantially increase thermal stability of polymers. Also, at high crosslinking densities, an absence of the glass transition is observed. It has also been reported that the homopolymer of EGDMA undergoes self-crosslinking during free radical polymerization, which makes it suitable for comparison with its copolymers with GMA [5]. The purpose of this paper was to investigate the possibility of thermal stabilization of PGMA by crosslinking with EGDMA, and compare thermal properties of the copolymer with two homopolymers.

Experimental

Three polymer samples, PGME, PGMA and PEGDMA were synthesized by suspension polymerization, in the form of spherical beads. The monomer phase consisting of 39.0 g GMA and 26.0 g EGDMA for the copolymer, and 65.0 g of GMA for one homopolymer and 65.0 g of EGDMA for the other homopolymer, and containing the same amount of AIBN initiator (0.65 g), was suspended in the

aqueous phase containing 200.0 g of distilled water and 2.0 g of poly(vinylpyrrolidone). The polymerization reactions were carried out at 70 °C for 2 h and at 80 °C for 6 h with the stirring rate of 300 rpm. The resulting particles were washed with distilled water, followed by a 24 h Soxhlett extraction with ethanol, and dried at 50°C. The absence of porosity was ascertained by means of scanning electron microscopy (JEOL JSM-646 OLV scanning microscope) and specific area measurements by the BET method from the low-temperature nitrogen adsorption isotherms (77 K) (Sorptomatic 1990 Thermo Finnigen). Thermal stability of PGME, PGMA, and PEGDMA was investigated using a TG/DSC111 equipment with He as a carrier gas (30 ml/min), and the heating rate of 10°Cmin⁻¹.

Results and Discussion

The measured specific surface area of all samples was less than 1 m²/g, which indicated absence of any porosity, as was confirmed with SEM images.

The thermograms for all the samples are shown in Fig. 1. The characteristic temperatures obtained for mass losses of 5, 10 and 50% ($T_{5\%}$, $T_{10\%}$, $T_{50\%}$) are shown in Table 1., including the initial temperature of degradation (T_i), along with the mass percent char content at 450°C (m_{cc}). Table 1. also shows temperatures corresponding to the maximum degradation rates below 350°C (T_{max}). It is evident from these results that the PGME copolymer is intermediate in stability between the two homopolymers. Thermal degradation of these polymers is complex, with considerable overlap of multiple processes, which is apparent from the DTG curves. It was previously reported that thermal degradation of PGMA proceeds mainly through depolymerization to monomer, which is a major reaction, and through ester decomposition [6]. In the case of PEGDMA, it was found that its degradation involved chain reactions [7]. Below 400°C, depolymerization results in monomers evolved in proportion higher than 95 %, and at higher temperatures, other products due to cracking reactions are present. The

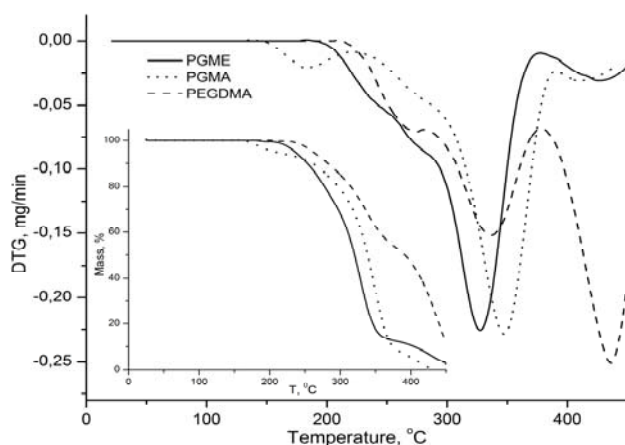


Fig.1. DTG and TGA thermograms of PGME, PGMA and PEGDMA.

DTG curve of PGME has similarities with the curves of both homopolymers, but even though the main degradation peak is at a lower temperature than for PGMA, the most important difference, from the practical point of view (threshold application temperature), is the shift of the 185°C peak to higher temperatures, or rather its absence.

Table 1. Characteristic temperatures of thermal degradation and char content of PGME, PGMA and PEGDMA

Sample	T _i , °C	T _{5%} , °C	T _{10%} , °C	T _{50%} , °C	m _{cc} , %	T _{max} , °C		
						240	284	327
PGME	180	235	253	320	2.3	240	284	327
PGMA	144	204	261	338	0.0	185	265	348
PEGDMA	204	261	281	390	8.1	-	270	336

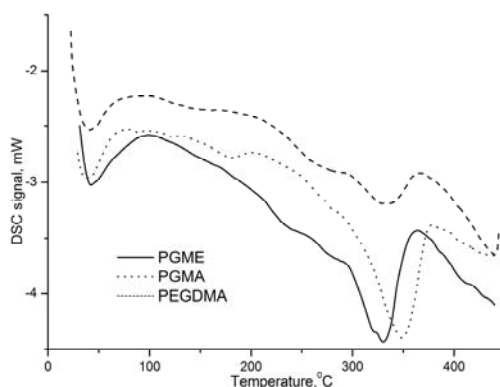


Fig.2. DSC curves for PGME, PGMA and PEGDMA.

Thermal degradation of all three polymers is dominantly endothermic. DSC curve for PGME does not show a discernible glass transition temperature, unlike PGMA curve, where we observe the glass transition at 86°C. The glass transition of PEGDMA is above 100°C, and it is spread out over a wide temperature interval, as is characteristic for crosslinked polymers. Even though the main degradation endotherm of PGMA is at a higher temperature than for PGME, the absence of thermal

transitions for PGME at temperatures lower than 200°C is of utmost importance.

Conclusion

In this study, it was shown that the thermal degradation profiles of the synthesized and investigated nonporous methacrylate polymers, PGME, PGMA and PEGDMA, are complex and composed of many overlapping processes. PGME copolymer is intermediate in stability between PGMA and PEGDMA homopolymers. It is evident that, in this case, crosslinking enhances thermal stability. There is no observable glass transition in the copolymer.

References

- [1] E. D. Felt, M. E. Wurtz, G. W. Kammlot, E. Vac, *J. Sci. Technol.*, 1978, **15**, 944-951.
- [2] Ch. Liu, R. Bai, L. Hong, *J. Colloid and Interf. Sci.*, 2006, **303**, 99-108.
- [3] D. Hórak, N. Chekina, *J. Appl. Polym. Sci.*, 2006, **102**, 4348-4357.
- [4] J. Bandrup, E. H. Immergut, in: 2nd Edition. *Polymer Handbook*, Wiley Interscience, New York, 1976.
- [5] O. Okay, C. Gurun, *J. Appl. Polym. Sci.*, 1992, **46**, 421-434.
- [6] S. Zulfiqar, M. Zulfiqar, M. Nawaz, *Polym. Degrad. Stab.*, 1990, **30**, 195.
- [7] C. N. Caşcaval, N. Hurduc, Ig. C. Poinescu, *J. Therm. Anal.*, 1988, **34**, 311-317.

ELECTROSPRAY IONIZATION MASS SPECTROMETRIC INVESTIGATION OF ALUMINIUM HYDROLYSIS IN CHLORIDE MEDIUM

M. Cvijović¹, P. Đurđević¹, M. J. Stankov², V. Kilibarda³, D. Stojšić³ and S. Đorđević³

¹Faculty of Science, 34000 Kragujevac, ²Faculty of Pharmacy, Belgrade, ³Military Medical Academy, Belgrade

Abstract

The hydrolysis of aluminium (III) ion with emphasis on polymeric species formation, was studied by ESI MS (Electrospray ionization mass spectrometry) in chloride solution ($\mu = 0.1$ mol/L NaCl) at 298 K. The total concentration of aluminium ion was 20–50 $\mu\text{mol/L}$ within the pH range 3.5 – 5.0. The following species were identified: $[\text{Al}_2\text{O}_2(\text{OH})(\text{H}_2\text{O})]^+$, $[\text{Al}_3\text{O}_4(\text{H}_2\text{O})]^+$, $[\text{Al}_3\text{O}_4]^+$, $[\text{Al}_7\text{O}_9(\text{OH})(\text{H}_2\text{O})]^{2+}$, $[\text{Al}_7\text{O}_9(\text{OH})(\text{H}_2\text{O})_3]^{2+}$, $[\text{Al}_5\text{O}_7]^+$, $[\text{Al}(\text{OH})_2(\text{H}_2\text{O})_n]^+$, $n = 1, 2, 3, 4$. The abundance of polymeric species was higher than 70%.

Introduction

ESI MS is a powerful technique for identifying species in hydrolyzed solutions of Al^{3+} ion [1-4]. It is more sensitive than potentiometry and can be thus used for identifying the species which could not be found by classical methods (potentiometry, spectrophotometry etc). In this work the ESI MS measurements were used for studying polymeric species formed in hydrolyzed aluminium ion solutions. It is known that kinetical effects play dominant role in aluminium hydrolysis giving rise to number of transient species which exist in supersaturated solution. Thus, esi ms may provide an answer by which reaction path the thermodynamically stable hydrolytic complexes of aluminium ion are formed.

Results and Discussion

ESI MS spectra have been taken on Waters LC/MSD instrument with Micromass ZQ Photodiode Array Detector operating under Mass Linux 4.0 software. The spectra were acquired in positive mode. The conditions in ESI source have been: cone voltage: 50.0 V, source temperature 125°C, desolvation temperature 430 °C, capillary voltage 3.5V. The spectra have been processed in MS mode. The pH of all solutions was adjusted by the addition of standard HCl or NaOH solutions. pH was measured using Mettler Toledo DL 50 titrator equipped with combined glass electrode. The calibration was performed with J. T. Baker pH 4.00 and 7.00 buffers. The total metal concentration was 2.0 - 5.0 $\times 10^{-5}$ mol/l.

The spectra obtained with varying cone voltage (in order to optimize conditions) are shown in Fig. 1.

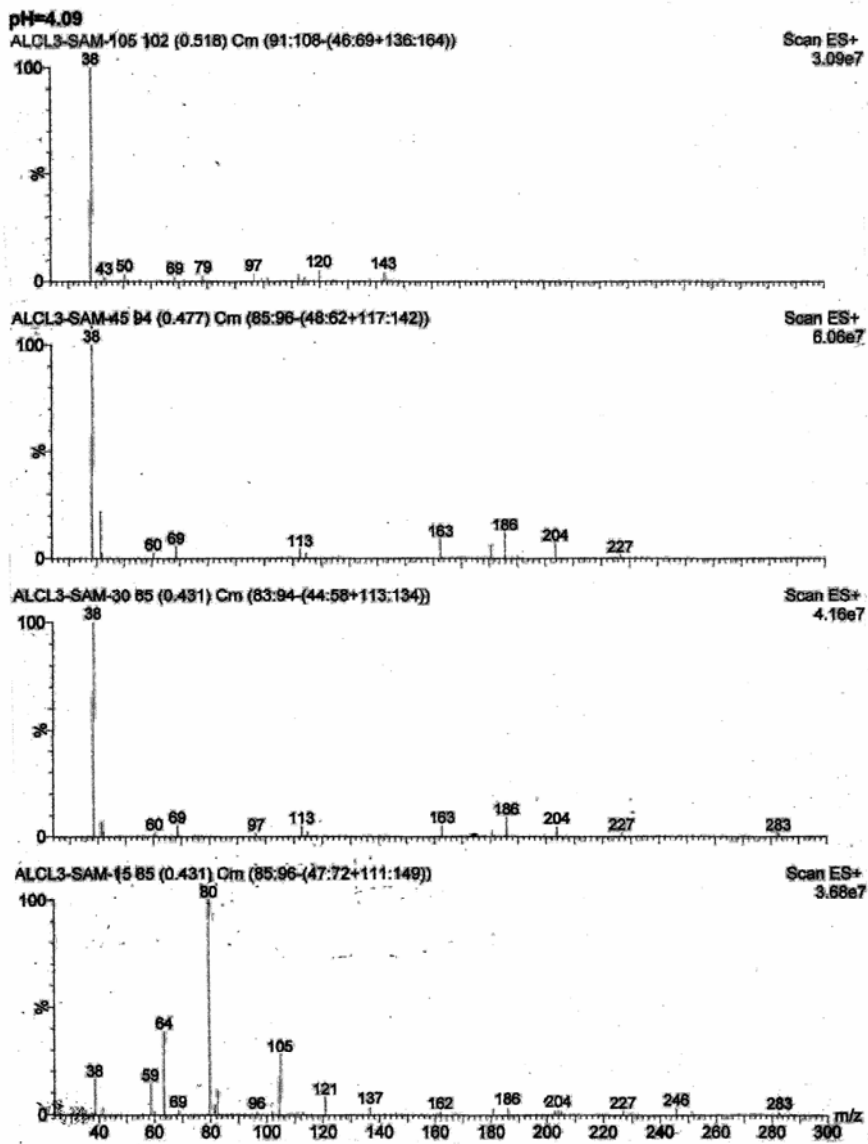


Fig.1. ESI MS of 20 $\mu\text{mol/L}$ AlCl_3 solution; pH = 4.1 with varying cone voltage.

The ESI MS spectra were evaluated with the aid of Mass linux 4.0 software. The identified signals are presented in Table 1. The experimental data are in well agreement with literature data [1-3].

Table 1. Identification of signals in ESI MS of hydrolyzed AlCl₃ solutions

m/z from spectra	Literature data	Identification of species	References
69	69	[Al(OH) ₂ (H ₂ O) _n] ⁺ 69+18n (n=1-4)	[1]
79	79	[Al(OH) ₂ (H ₂ O)] ⁺	[2]
97	97	[Al(OH) ₂ (H ₂ O) ₂] ⁺	[2]
121	121	[Al ₂ O ₂ (OH)(H ₂ O)] ⁺	[3]
143	(145 -diff)	[Al ₃ O ₄] ⁺	[3]
186	(184- diff)	[Al ₇ O ₉ (OH)(H ₂ O)] ²⁺	[3]
163	163	[Al ₃ O ₄ (H ₂ O)] ⁺	[3]
204	(202-diff)	[Al ₇ O ₉ (OH)(H ₂ O) ₃] ²⁺	[3]
246	(247-diff)	[Al ₅ O ₇] ⁺	[3]

Conclusion

In hydrolyzed aluminium ion solutions at pH values lower than 4.5 polymers of lower molecular mass prevail (up to Al₃). At higher pH values polymers with Al₅, Al₇ and Al₉ appear in significant concentrations. The tridecamer, Al₁₃ becomes dominant at pH values higher than 5. Tridecamer is characteristic for AlCl₃ solutions.

References

- [1] T. Urabe, T. Tsugoshi, M. Tanaka, J. Molecular Liquids, 2008, **143**, 70-74.
- [2] T. Urbae, M. Tanaka, J. Mass Spectrom., 2007, **42**, 591-597.
- [3] H. Zhao, H. Liu, J. Qu, J. Colloid and Interface Sci., 2009, **330**, 105-112.
- [4] A. Sarapola, V. Hietapelto, J. Jalonen, J. Jokela, R. Laitinen, J. Mass Spectrom., 2004, **39**, 423-430.

DETERMINATION OF GLYCOGEN FROM RUMEN PROTOZOA

D. Jakovljević¹, J. Kecić², J. Stefanović¹, M. Jovičin³ and M. Vrvic^{1,2}

¹*IchTM - Department of Chemistry, University of Belgrade, Njegoševa 12, P.O. Box 473, 11000 Belgrade, Serbia (djakovlj@chem.bg.ac.rs)*

²*Faculty of Chemistry, University of Belgrade, Studentski trg 12-16, P.O. Box 51, 11158 Belgrade, Serbia*

³*Scientific Veterinary Institute "Novi Sad" Rumenački put 6, 21000 Novi Sad, Serbia*

Abstract

Glycogen, a branched glucose polymer, is a common storage energy compound in both prokaryotic and eukaryotic cells. This work describes method for isolation and characterization of pure polymer from protozoa isolated from rumen of cattle and a rapid enzymatic assay for determination content of this polysaccharide from rumen protozoa.

Introduction

Rumen ciliate protozoa play diverse and important roles in ruminal metabolism of nutrients [1]. These microorganisms are represent up to 50 % of the total rumen microbial biomass. They are involved in many rumen functions, such as digestion of cellulose, starch, proteins and contribute in total fiber digestibility. They play an important role in biodegradation of plant toxins and mycotoxins and in the regulation of rumen condition. Because of the multifunctional properties of rumen protozoa is evident their importance for the health of the host. In this work glycogen as reserve material of protozoa was isolated, purified and characterized by common analytical procedures and spectral analyses and then determined content of this polysaccharide by enzymatic hydrolysis.

Experimental

Rumen contents were obtained from two cattle, each fitted with a permanent rumen cannula. Rumen liquor samples used for protozoal isolation were withdrawn 2 h after the feeding. Particulate material was removed by filtration and a mixed protozoal pellet recovered by sedimentation. Separated precipitate was washed two times by PBS and thus prepared samples were frozen in liquid nitrogen and kept until further use.

Isolation and purification of glycogen was performed by the successive extractions with DMSO. The GC of pure polysaccharide was shown only glucose after total hydrolysis. The polysaccharide was methylated and after hydrolysis, reduction and acetylation obtained partially methylated alditol acetate derivatives were analyzed by GLC/MS. On the basis of characteristic fragmentation patterns was determined presence of (1,6)- and (1,4)-glucosidic linkages as well as terminal glucose residues.

FTIR spectrum of glycogen displayed a broad absorption band at 3455 cm^{-1} due to the stretching frequency of the O-H groups. The bands at 1157 cm^{-1} and 2927 cm^{-1} are assigned to C-O stretching and C-H stretching, respectively. Two peaks at 1083 cm^{-1} and 1022 cm^{-1} are due to $\text{CH}_2\text{-O-CH}_2$ stretching vibrations [2].

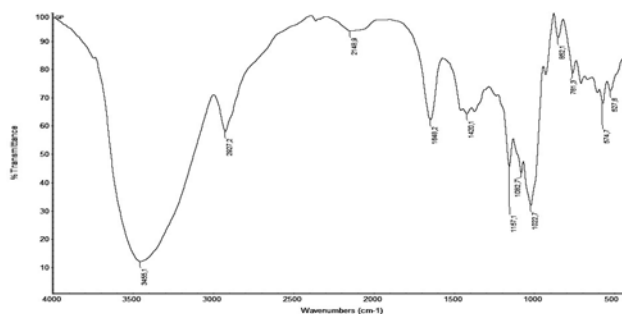


Fig.1. FTIR spectrum of isolated and purified glycogen.

The ^1H NMR spectrum (Fig.2) displayed characteristic signal (*inter alia*) at chemical shifts of 5.49 ppm and 4.99 ppm consistent with anomeric protons due to (1,4)- and (1,6)-linked D-glucopyranoses.

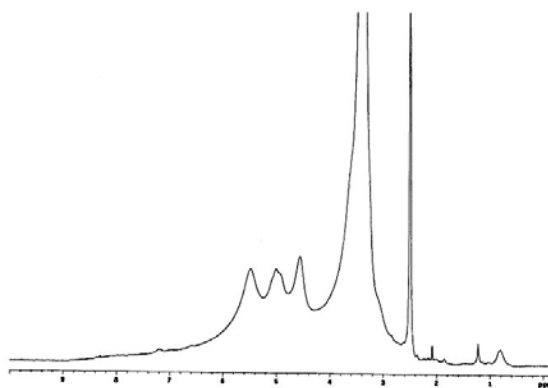


Fig.2. ^1H NMR spectrum of isolated glycogen from protozoa.

Procedure for determining the content of glycogen in the samples of protozoa was performed in successively treating $\sim 20\text{ mg}$ of sample with 80% ethanol, 2M KOH and enzymatic hydrolysis with amyloglucosidase in 1.2 M sodium acetate buffer (pH 4.5). Liberated glucose units were determined spectroscopically in the 96-well plate by glucose oxidase/peroxidase reagent [3] at 492 nm against the reagent blank in a reader KB 5060-006. All determinations were done in triplicate and glycogen content was calculated as a percentage (w/w) of the wet weight of mass protozoa.

In investigated samples was determined DNA content by the method of Burton [4]. These two parameters, glycogen content and concentration of DNA, can be used for evaluation of protozoa, and evaluation of animal health from which they were taken. Glycogen content and concentration of DNA in the samples of protozoa were combined and shown in Table 1.

Table 1.

Samples of infuzoria	Glycogen (%)	DNK $\mu\text{g/ml}$	Glycogen(%) / DNA(μg) $\times 10^{-3}$
Sample 1	0.58	70.96	8.22
Sample 2	0.50	73.30	6.78

Conclusion

In this work, the presence of glycogen in the rumen protozoa was examined, as well as the content of this polysaccharide by rapid enzymatic assay. In investigated samples was determined DNA content and these two parameters, glycogen content and concentration of DNA, can be used for evaluation of protozoa and indirectly for evaluation of host from which they were taken.

Acknowledgement

This work was supported by the Serbian Ministry of Science and Technology, Project ON 142018B

REFERENCES

- [1] A. G. Williams, G. S. Coleman, *The Rumen Protozoa*, Springer-Verlag, New York, 1992.
- [2] M. Mathlouthi, J. L. Koenig, Vibrational spectra of carbohydrates. *Adv. Carbohydr. Chem. Biochem.* 1986, **44**, 7–89.
- [3] D. Keppler, K. Decker in *Methods of Enzymatic Analysis* (3rd ed), VCH, Weinheim, 1984, **6**, 11–18.
- [4] K. Burton, Determination of DNA concentration with diphenyl-amine, in *Methods in Enzimology*, Academic Press, New York, 1968, **12B**, 163-166.

NOVEL CROSSLINKED POLYURETHANES BASED ON HYPERBRANCHED POLYESTER

M. V. Pergal¹, J. Džunuzović¹, M. Kićanović³, V. Vodnik² and S. Jovanović⁴

¹*ICTM-Center of Chemistry, Studentski trg 12-16, 11000 Belgrade, Serbia*

²*Institute of Nuclear Science "Vinča", P. O. Box 522, 11001 Belgrade, Serbia*

³*Holding Institute of General and Physical Chemistry, Studentski trg 12-16, Belgrade 11000, Serbia*

⁴*Faculty of Technology and Metallurgy, Karnegijeva 4, 11120 Belgrade, Serbia*

Abstract

The polyurethane (PU) elastomers based on hydroxy-terminated hyperbranched polyester (BH-20) and 4,4'-methylenediphenyl diisocyanate (MDI) as hard segments and hydroxyl-terminated ethylene oxide-poly(dimethylsiloxane)-ethylene oxide (PDMS-EO) as soft segment, were synthesized and examined in this work. The obtained results show that sol fraction decreases and thermal stability increases with increase of the hard segment content.

Introduction

Crosslinked polyurethanes (PUs) have numerous applications such as coatings, elastomers, sealants, foams and adhesives due to their unique properties and great efforts have been made in chemistry and physics of PUs. PU elastomers showed excellent mechanical and elastic properties, but lower thermal stability. Their thermal stability can be improved by introduction of PDMS segments in PU backbone. The properties of PU elastomers are depending on the molecular weight of the soft segment as well as on the chemical structure of all components. The use of hyperbranched (HB) polymers as crosslinker of PUs has attracted large scientific attention over the last years, because of their unique structure and properties and simple synthetic procedure [1-3].

In this work, the influence of the content of macrodiol on the structure, swelling and thermal properties of crosslinked PUs based on ethylene oxide-poly(dimethylsiloxane)-ethylene oxide, was investigated. Crosslinking agent was hydroxy-functional aliphatic HB polyester of the second pseudo generation (BH-20, Boltorn[®]).

Experimental

The PU networks were synthesized by catalyzed two-step polymerization in solution (NMP/THF) using PDMS-EO ($\bar{M}_n = 1200 \text{ g mol}^{-1}$), 4,4'-methylenediphenyl diisocyanate (MDI) as monomers and BH-20 ($M_n = 1340 \text{ g/mol}$, functionality $f_n = 12$) as crosslinking agent. The molar NCO/OH ratio was 1.05. The PU prepolymer was synthesized in an argon atmosphere by reacting PDMS-EO with excess MDI. Then the prepolymer was reacted with BH-20.

Reaction was carried out in reaction vessel at 40 °C for 1 h. The obtained mixture was then cast in Teflon® dish and heated in oven at 80 °C for 50 h and 1 h at 110 °C. The crosslinked samples were obtained as brown films.

IR spectra of the crosslinked PUs were recorded on ATR NICOLET 380 FTIR spectrometer. Swelling behavior of square samples was investigated in toluene at room temperature. The thermal stability of samples was determined by thermogravimetric (TG) analysis, using TGA Q500 V6.3 Build 189 instrument in nitrogen atmosphere, at heating rate of 10 °C/min.

Results and Discussion

Some important properties of the synthesized PU networks are listed in Table 1. The soft segments content, SSC, was varied in the range from 30 to 50 wt. %. The chemical structure of PUs was determined by IR spectroscopy. The characteristic stretching frequencies for PUs appear at 3310 cm^{-1} ($\nu_{\text{N-H}}$), 1533 cm^{-1} ($\nu_{\text{C-N}} + \delta_{\text{N-H}}$, amide III), 1259 cm^{-1} ($\nu_{\text{C-N}} + \delta_{\text{N-H}}$, amide II), 1733 cm^{-1} ($\nu_{\text{C=O}}$ ester), 1710 cm^{-1} ($\nu_{\text{C=O}}$ urethane), 1598 cm^{-1} ($\nu_{\text{C=C}}$ arom), 1015 and 1080 cm^{-1} ($\nu_{\text{C-O}} + \nu_{\text{Si-O-Si}}$). In the IR spectra of PU samples the isocyanate $-\text{N}=\text{C}=\text{O}$ band (2260 cm^{-1}) and hydroxyl group (3000 cm^{-1}) from BH-20, were not detected.

Table 1. The soft segments content, SSC, maximum swelling degree, q , and characteristic temperatures of thermal degradation of crosslinked PUs.

Sample	SSC, wt. %	q_{max}	Sol fraction, %	T_{10} , °C	T_{50} , °C	T_{max} , °C
PU1-30	30	0.3	4.5	287	356	302/415/563
PU1-40	40	0.5	8.3	278	341	299/336/406/560
PU1-50	50	0.4	10.3	283	335	292/324/423/554

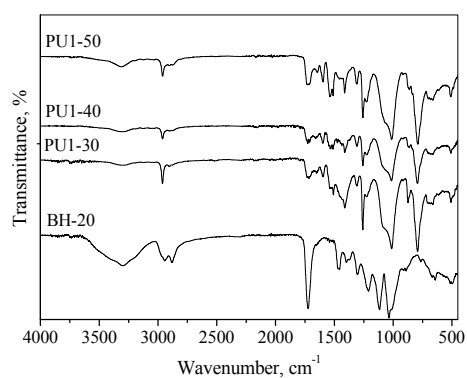


Fig.1. IR spectra of crosslinked PUs.

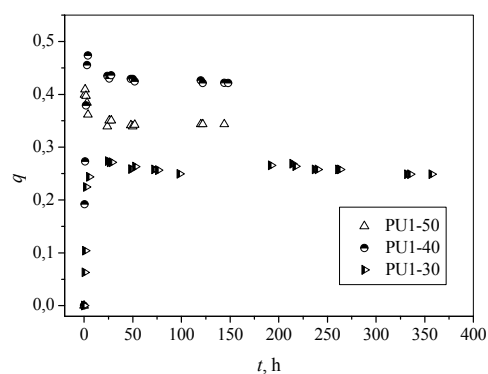


Fig.2. The change of the swelling degree, q , with time for crosslinked PUs.

The results obtained by investigation of swelling behavior of the synthesized crosslinked PUs in toluene at room temperature are presented in Table 1 and Fig. 2. Values of the swelling degree, q , were calculated using

conventional gravimetric method, equation $q = (m-m_0)/m_0$ and values of the sample weights before, m_0 , and after swelling, m . The sample weight was measured periodically, and the change with time was recorded. After reaching the maximum weight, the samples started losing weight because of the extraction of the sol fraction until constant values were obtained. The obtained sol fraction increases from 4.5 to 10.3 % with increasing soft segment content.

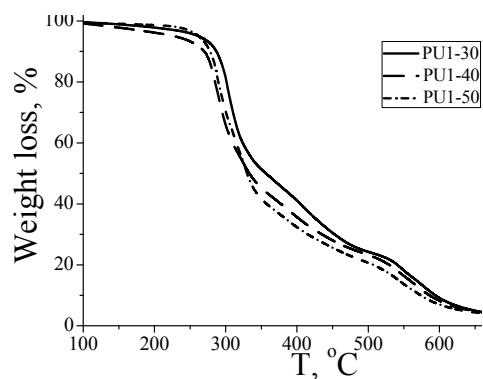


Fig.3. TG curves of investigated crosslinked PUs, determined in nitrogen atmosphere, at heating rate of 10°C/min.

From the results presented in Fig. 3 it can be observed that the thermal degradation of these crosslinked PUs is a three-step process in nitrogen. This is clearly demonstrated from the characteristic temperatures obtained from thermogram derivative curves (Table 1.). The thermal degradation of polyurethanes first goes via decomposition of urethane bonds, followed by breakage of the soft segment. Further decomposition in the region between 500 and 600 °C correlates with the aromatic content in polyurethanes [4]. The T_{10} value is considered to represent the beginning of degradation. The degradation of the PUs commences between 278 and 287 °C. Also, the temperature of 50 weight % loss (T_{50}) of the PUs increases with increasing content of hard segments.

Conclusions

The results presented in this work show that content of macrodiol have significant influence on the properties of PU networks. Thermal stability decreased with increase of macrodiol content. At the same time, as the content of PDMS-EO increase the determined sol fraction of these samples also increased.

References

- [1] A. S. Nasar, M. Jikei, M. Kakimoto, E. Polym. J., 2003, **39**, 1201-1208.
- [2] L. Okrasa, P. Czech, G. Boiteux, F. Mechin, J. Ulanski, Polymer, 2008, **49**, 2662-2668.
- [3] P. A. Gunatillake, G. F. Meijs, S. J. McCarthy, R. Adhikari. J. Appl. Polym. Sci., 2000, **76**, 2026-2040.
- [4] Z. S. Petrovic, Z. Zavargo, J. H. Flynn, W. J. Macknight, J. Appl. Polym. Sci., 1994, **51**, 1087-1095.

K
Environmental Protection,
Forensic Sciences,
Pharmaceutical Physical Chemistry

**The Session K is dedicated to the
80th Anniversary of the professor Dragan Veselinović birth**

ABOUT OUR PROFESSOR DRAGAN VESELINOVIĆ



Professor Dragan Veselinović

Eighty years of age (born in 1930) and fifty years of successful academic work in educational, science and various social activities is the anniversary worth remembering and respecting. It is also the opportunity for many students, collaborators, colleagues and friends of Professor Dragan Veselinović remind some achievements and details of his life and creative work that, among other things, are the reason why we love, appreciate and respect our Professor.

Forty years of active university career (1956 - 1996) of Professor Veselinović are associated with the Department - the Institute - Faculty of Physical Chemistry, Belgrade University, where he worked in all academic and administrative titles, from assistant to full professor and department manager.

At present the Faculty of Physical Chemistry, where he started and ended his active academic experience, he took part in the performance and creating classes for a number of subjects and courses. In the area of teaching and scientific work at the faculty's key contribution is the introduction of environmental protection in teaching and research facilities of the Faculty. The presence of Professor Veselinović in this area and today is clearly visible at the Faculty of Physical Chemistry, by written textbooks and programs that are still the basis for teaching, and by teaching staff who were mostly, students, graduates or PhD of professor Veselinović.

In addition to teaching at the Faculty of Physical Chemistry, Dragan Veselinović was involved in teaching in other faculties of Belgrade University: Faculty of Technology and Metallurgy, Faculty of defense and security and the Centre for Multidisciplinary Studies. He was also among the first teachers of novel

Universities of Priština and Kragujevac, where he performed several years teaching for which he formed cadres who will later take the classes.

Upon completion of active university career Professor Dragan Veselinovic not ceased to participate in academic activities. Together with his collaborators he publish scientific papers, participate in conferences, write books (until now more than 15 textbooks for high school and university classes, and another 4 books from the general scientific literature), participate in committees for the defense of master's and doctoral theses. He was leader in 12 and participated in the realization of much larger number of projects for the military, economic, scientific and other state organizations and institutions.

Initiator and president of multiple scientific and organizational boards more national and regional conferences in the field of environmental protection that have made a significant contribution to the development of this scientific field in the national framework.

He is an active member of the Society of Physical Chemists of Serbia. His special contribution was the work in the Scientific Committees of the Society of Physical Chemists of Serbia. Also, he is an active member of the Serbian Chemical Society, where he formed and was a longtime president of the Section for Environmental Protection. He has received numerous awards, medals, charters, plaques, and deserving of honorary degrees and other awards of universities, faculty, community and state institutions where he worked on a number of important activities and functions.

What is more lasting and profound, of all the quantitative indicators, it remains to those who have had the opportunity to meet, learn, collaborate and socialize with Professor Dragan Veselinović, these are his human qualities that is not possible to express in figures. Commitment in the needs of others, willingness to help, always giving more than the expectations that the provided with rewarded patience, moderation and consistency in the expression of all these features that unfortunately all rarely found in this hurried and insensitive world.

Let this be a reminder of our expression of great respect and gratitude that we feel for our teacher and friend Professor Dragan Veselinovic.

Professor Dragan Marković

NOVEL PLATINUM COMPOUND THAT OVERCOMES CISPLATIN RESISTANCE AND INDUCES APOPTOSIS

R. Paschke^a, A. Dietrich^d, T. Mueller^d, B. Kalinowski^a and G. N. Kaluderović^{a-c}

BioCenter, Martin-Luther-University Halle-Wittenberg, Weinbergweg 22, D-06120 Halle, Germany;^b*Department of Chemistry, Institute of Chemistry, Technology and Metallurgy, Studentski Trg 14, 11000 Belgrade, Serbia;*^c*Institut für Chemie, Martin-Luther-Universität Halle-Wittenberg, Kurt-Mothes-Straße 2, D-06120 Halle, Germany;*^d*Medical Faculty, Martin-Luther-University Halle-Wittenberg, Weinbergweg 22, D-06120 Halle, Germany,*

Abstract

New promising antitumor drug candidates were found to be able to overcome cisplatin resistance. Low water solubility of this compound could be a restriction for their use in *in vivo* tests. Liposomal formulation is an appropriate mean to achieve a better solubility.

Introduction

Despite cisplatin based chemotherapy is curative in testicular germ cell tumors (TGCT) and constitutes a component of standard treatment regimes for ovarian, cervical, bladder, head and neck, small cell and non-small-cell lung cancers, the development of platinum drugs with improved antitumoral activity continues to be a productive field of research. At this, the main focus concentrates on designing cytotoxic agents possessing either oral bioavailability, fewer side effects, or being able to circumvent intrinsic or acquired cisplatin resistance, which is a major clinical problem. It is obvious, that the chemical structure of those bioconjugates (Fig. 1) causes solubility problems. Liposomes are one interesting alternative to increase the water solubility up to a grade comparable to cisplatin.

Experimental

The compounds were prepared by procedures described in literature [1-2]. *In vitro* experiments were performed as described earlier [3].

Results and Discussion

Cisplatin fragments linked to bile acid tetrahydropyrane (THP) via aliphatic CH₂-spacers were tested in two TGCT cell lines. The most promising compound, 2-(4-(tetrahydro-2H-pyran-2-yloxy)-undecyl)-propane-1,3-diammine-dichloroplatinum(II) (THP-12), completely overcame cisplatin resistance in 1411HP cells, correlating with increased and accelerated cellular platinum uptake and much faster initiation of apoptotic cell kill. At equitoxic IC₉₀ concentrations, this compound

induced accelerated DNA fragmentation and caspase -3 and PARP cleavages. In contrast, DNA platination rate was much lower as compared to cisplatin and no upregulation of p53 as well as no initiation of cell cycle arrest were observed. To summarize, THP-12 overcomes cisplatin resistance and induces programmed cell death with molecular features different from cisplatin, suggesting that both drugs induce apoptosis through different initial pathways.

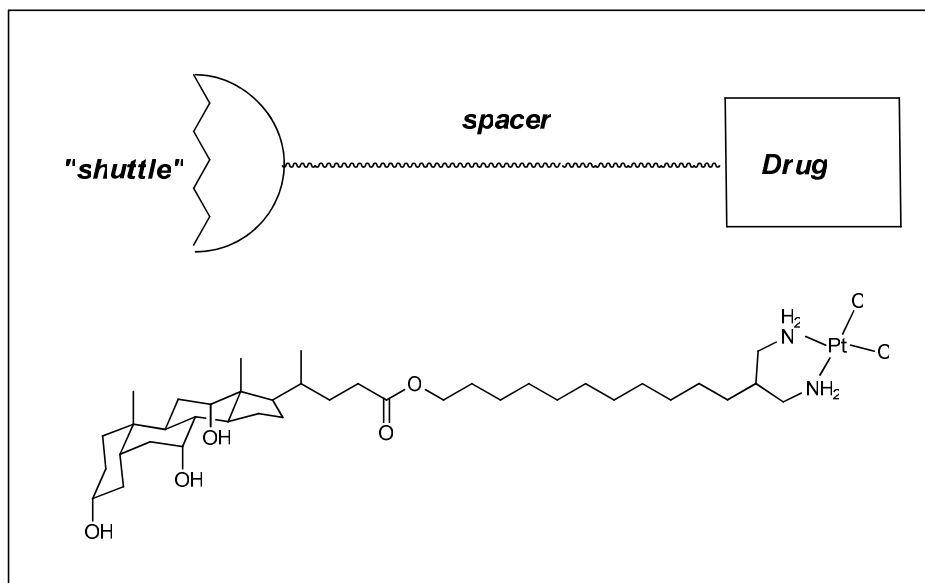


Fig.1. Cisplatin-conjugate with bile acid

The promising platinum(II) complex is only soluble in DMF and CHCl_3 . In order to test the compound in a nude mouse model, liposomal formulation has been carried out. The formed liposomes have a particle size of 120–140 nm and are stable under room temperature conditions. Liposomes containing THP-12 express similar *in vitro* activity as THP-12 alone in the cisplatin sensitive TGCT cell line H12.1 and in the cisplatin resistant TGCT cell line 1411HP. Moreover, liposomes alone are not toxic in investigated concentration range (Table 1).

Conclusions

In the present experimental study a compound which overcomes cisplatin resistance was investigated. This is obviously accounted by the organic fragment linked to cisplatin. This enables the compound to enter the cell and to accumulate much faster than cisplatin alone. The structure is also appropriate to be incorporated into liposomes and by the surmount the problem of poor solubility in water.

Table 1. IC₅₀ [μ M or %]^a for the 2, 6 and 96 h of action of investigated drug and liposome on H12.1 and 144HP TGCT cell lines determined by SRB assay.

Compound / Formulation	IC ₅₀ [μ M or %]		
	1411HP		
	2 h	6 h	96 h
THP-12	1.12 \pm 0.02	0.94 \pm 0.12	0.88 \pm 0.03
THP-12– Liposomes	3.86 \pm 0.40 (0.0046 \pm 0.0005)	2.50 \pm 0.07 (0.0030 \pm 0.0001)	2.36 \pm 0.05 (0.0028 \pm 0.0001)
Liposomes	> 0.120	> 0.120	0.0872 \pm 0.0044
cisplatin	26.0	-	2.8
	H12.1		
	2 h	6 h	96 h
	THP-12	1.39 \pm 0.10	1.10 \pm 0.07
THP-12– Liposomes	5.54 \pm 0.59 (0.0066 \pm 0.0007)	3.49 \pm 0.30 (0.0042 \pm 0.0004)	3.47 \pm 0.24 (0.0042 \pm 0.0003)
Liposomes	> 0.120	> 0.120	0.0440 \pm 0.0056
cisplatin	7.9	-	0.7

^agiven are values for liposomes in % and for THP-12 in μ M (50 μ M liposome-THP-12 \leftrightarrow 0.12% liposome)

References

- [1] R. Paschke, J. Kalbitz, C. Paetz, *Inorg. Chim. Acta*, 2000, **304**, 241.
- [2] R. Paschke, J. Kalbitz, C. Paetz, M. Luckner, T. Mueller, H. J. Schmoll, H. Mueller, E. Sorkau, E. Sinn, *J. Inorg. Biochem.*, 2003, **94**, 335.
- [3] A. Dietrich, T. Mueller, R. Paschke, B. Kalinowski, T. Behlendorf, F. Reipsch, A. Fruehauf, H. J. Schmoll, C. Kloft, W. Voigt, *J. Med. Chem.*, 2008, **51**, 5413.

AN APPLICATION OF ENVIRONMENTAL ISOTOPES TO TRACE THE ORIGIN OF CONTAMINANTS

Nives Ogrinc

*Department of Environmental Sciences, Jožef Stefan Institute, Jamova 39,
SI-1000 Ljubljana, Slovenia*

Abstract

The stable isotope measurements, particularly those of carbon, nitrogen, oxygen, hydrogen and sulfur, are well established tools in many field of investigation. In this presentation, some stable isotope approaches and methodologies used in our research in the field of environmental studies will be outlined.

Introduction

Natural biological, physical, and chemical processes operating over geological time have resulted in the establishment of recognizable patterns in the distribution of the stable isotopes of many of the light elements. Probably the greatest benefit to be gained from isotopic measurements is the ability to determine both the precursors and decomposition products of materials of interest and as a result, biogeochemical studies commonly include the distribution and isotopic composition of existing organic and inorganic compounds, which may be of significance in the biological assimilation and cycling of the elements.

The difference in mass between isotopes of the same elements results in measurable isotopic fractionation during physical and chemical processes. These fractionations are more pronounced for light elements because their isotopes (e.g. hydrogen, ^1H versus deuterium, ^2H) show proportionally larger differences in mass than isotopes of heavier elements (e.g. ^{12}C versus ^{13}C). The main mechanisms for fractionations include (1) equilibrium (or thermodynamic) exchange reactions and (2) kinetic effects associated with irreversible physical or chemical reactions. Natural variations occur in the isotopic composition of light elements due to fractionation effects, resulting in the creation of specific isotope ratio values that are characteristics of the origin, purity and manufacturing processes of the products and their constituents. Although generally only the lighter elements are affected by isotopic fractionation, the increased precision of modern instrumentation has enabled the natural variations as a result of isotopic fractionation to be observed in a number of heavier elements such as Hg [1].

The natural abundance of stable isotopes of light elements is exploited by isotope ratio mass spectrometry (IRMS). The procedure of IRMS consists of measuring the isotope ratio ($^2\text{H}/^1\text{H}$, $^{13}\text{C}/^{12}\text{C}$, $^{15}\text{N}/^{14}\text{N}$, $^{18}\text{O}/^{16}\text{O}$) of an analyte converted into a simple gas, isotopically representative of the original sample, before entering the ion source of an IRMS. The stable isotopic data are expressed in the delta (δ) notation as the per mil (‰) deviation of the isotope ratio of a

sample relative to that of a standard. V-PDB (Vienna – Peedee Belemnite Limestone) is used as international standard for carbon ($\delta^{13}\text{C}$), AIR for nitrogen ($\delta^{15}\text{N}$) and V-SMOW (Vienna – Standard Mean Ocean Water) for oxygen ($\delta^{18}\text{O}$) and deuterium (δD). Advances and the use of multicollector inductivity coupled plasma mass spectrometry (MC-ICP-MS) has improved the precision on isotope measurements of heavy elements such as Zn, Cu, Fe, Cr, Mo and Tl. The technique combines the strength of the ICP-technique with the high precision of thermal ions source mass spectrometry equipped with an array of Faraday collectors [2]. The recent growth of Hg isotope studies was facilitated by the development of a techniques using cold vapor multicollector inductivity coupled plasma mass spectrometry (CV-MC-ICP-MS) [3].

This presentation is focusing on three different cases indicating the application of stable isotopes to trace the origin of contaminants. First stable carbon and nitrogen isotopes are used to determine the mucilage formation in the Gulf of Trieste [4]. Some examples of recent application of compound specific isotope analysis (CSIA) in environmental sciences to allocate and distinguish sources of organic compounds are presented in the second part of the presentation. The use of stable isotopes of Hg in order to track the transport of Hg in the Gulf of Trieste is the subject of the last part of the presentation [5].

Natural processes

The ratio of two stable isotopes of C (^{12}C and ^{13}C) in natural materials varies as a result of isotopic fractionation during physical, chemical and biological processes. Organic matter produced from atmospheric CO_2 ($\delta^{13}\text{C} \approx -7 \text{‰}$) by land plants using the C3 pathway has an average $\delta^{13}\text{C}$ (PDB) value of approximately -27‰ and by those using the C4 pathway approximately -14‰ (O'Leary, 1988). Freshwater algae utilize dissolved CO_2 , which is usually in isotopic equilibrium with atmospheric CO_2 . Therefore the carbon isotopic ratios are useful to distinguish between marine and continental plant sources of sedimentary organic matter and to identify organic matter from different types of land plants. The carbon isotopic compositions of organic matter reflect principally the dynamics of carbon assimilation during photosynthesis and the isotopic compositions of the carbon source [6]. The source of inorganic carbon from marine algae is dissolved bicarbonate, which has a $\delta^{13}\text{C}$ value of approximately 0‰ . Marine organic matter consequently typically has $\delta^{13}\text{C}$ values between -20 and -22‰ [7]. The $\approx 7 \text{‰}$ difference between organic matter produced by C3 land plants and marine algae has successfully been used to trace the sources and distribution of organic matter in coastal ocean sediments [8].

Although not as widely used as carbon the nitrogen isotopic composition can also help to distinguish different processes influencing the nitrogen cycling in the environment. Application of $\delta^{15}\text{N}$ values to identify organic matter sources is founded on the difference between $^{15}\text{N}/^{14}\text{N}$ ratios of the inorganic nitrogen reservoir available to plants in water and those on land. In addition the ecology of coastal watersheds is an interlink between the human influence and natural

processes. Nitrogen-rich effluents from sewage treatment facilities are especially potential fertilizers in the downstream coastal zone. Nitrate isotopic composition can vary with land use [11] and the isotopic fingerprints of N derived from atmospheric, fertilizer, soil, and manure-derived sources often are sufficiently distinct to permit separation. For example $\delta^{15}\text{N}$ in synthetic fertilizers varies around $0 \pm 3\text{‰}$, while nitrate derived from animal manure has $\delta^{15}\text{N}$ values ranging from +10 to +25‰ [15].

Our research was performed in the Gulf of Trieste in northern Adriatic, which is exposed to direct anthropogenic pollution, and induced eutrophication can occur as a response to distributed natural equilibria in the ecosystem. Changes in the ecology and chemistry in the Gulf of Trieste have also occurred due to decreases in the quantity and quality of freshwater entering the gulf from the river Isonzo and pollution and stress to the ecosystem from nearby areas. Observed changes include an excess nutrient load and algal blooms leading occasionally to mucilage appearances [16] composed predominantly of heteropolysaccharides and lipids [18]. The $\delta^{13}\text{C}$ and $\delta^{15}\text{N}$ values of POM, studied in the Gulf of Trieste in a period of mucilage appearance (2004) and without mucilage formation (2003), underscore the importance of the biogeochemical properties of the water column in spring (April-June) since great differences between data measured in 2003 and 2004 were observed. Nanoflagellates dominated in 2003 and 2004 but diatoms were the predominant group in macroaggregates. Concentrations of N and P nutrients were generally higher in 2004 due to higher freshwater input. Concentrations of chlorophyll *a* were on average higher in 2004 compared to the same period in 2003. High $\text{NO}_3^-/\text{PO}_4^{3-}$ ratios occurred in late spring of 2004, due to N and especially P depleted condition. Concentrations of POC and PN were higher in late spring 2004, coinciding with the mucilage formation, compared to late spring 2003. The $\delta^{13}\text{C}$ and $\delta^{15}\text{N}$ values of POM were not directly linked to phytoplankton biomass. In 2004, the $\delta^{13}\text{C}_{\text{POC}}$ values followed $\delta^{15}\text{N}_{\text{PN}}$ and $\delta^{13}\text{C}_{\text{DIC}}$ variations, except during the macroaggregate appearance, the latter being probably more a result of increased summer photosynthetic usage of ^{12}C . The inverse relationship between $\delta^{15}\text{N}_{\text{PN}}$ values and nitrate concentrations in 2004 indicates intense nitrate depletion, of riverine origin, with a rather low fractionation factor ($\epsilon < 1$) probably due to species composition, i.e. the predominance of nanoflagellates. The »new primary production«, forming mucilage in late spring, is reflected in simultaneous positive $\delta^{13}\text{C}_{\text{POC}}$ variations, i.e. phytoplankton C uptake. Conversely, nitrate assimilation was not the major process controlling $\delta^{15}\text{N}_{\text{PN}}$ in 2003. The possible summer contribution of N_2 fixation and phytoplankton use of heterotrophically produced NH_4^+ was observed in summer. All $\delta^{15}\text{N}_{\text{PN}}$ and $\delta^{13}\text{C}_{\text{POC}}$ values, except of macroaggregates, fall in between typical marine and terrigenous end-members of OM in the Gulf of Trieste. Since the dynamics of nitrogen biogeochemical cycling are more complex than those of carbon, the $\delta^{13}\text{C}_{\text{POC}}$ values were tentatively used to calculate the terrestrial contribution to POM. In the spring, >60% of POM in the Gulf of Trieste can be of terrigenous origin in accordance with higher freshwater inflow. Also, higher terrigenous percentages were found in

2004 compared to 2003, most probably due to higher riverine input into the Gulf of Trieste [4].

The ability to interpret $\delta^{13}\text{C}$ data requires an increased understanding of the isotopic compositions of biological source materials at the molecular level. In addition, an understanding of the processes occurring during organic matter production and early diagenesis and how these processes influence the incorporation of biomarker signatures into the sedimentary record is also necessary [9]. Lipid biomarkers provide quantitative information about the structure of extant microbial communities without the need for culturing and isolation [22]. Lipids are also one of the most useful biochemical measures of in situ interactions between microbial species and their environments because lipid compositions can indicate temperature-, redox-, stress-, or nutritional conditions [23]. CSIA through the development of gas chromatography-combustion-isotope ratio mass spectrometry (GC-C-IRMS) allows the determination of the $\delta^{13}\text{C}$ composition of individual compounds. Consequently, $\delta^{13}\text{C}$ of specific biomarkers should be useful to improve the veracity of source identification, thereby allowing the origin of ubiquitous compounds with multiple potential sources to be determined [26]. Carbon isotopic ratios of n-alkanols from a saline sediment enabled to distinguish between the terrestrial long-chain n-alkanols (n-C₂₄, n-C₂₆: from -30 to -32 ‰) [27] and the marine short-chain n-alkanols (n-C₁₆ to n-C₂₂: 18 to -23 ‰). The isotopic compositions of long-chain fatty acids (C_{20:0}-C_{26:0}: from -31.0 to -30.7 ‰) reflect their sources from higher-land plants, whereas the C_{16:0} and C_{18:0} acids (-28.7 ‰ and -27.7 ‰) were from marine plankton, and C_{14:0} and C_{15:0} acids (-38.7 ‰ and -37.2 ‰) originated from bacteria [27]. Other classes of biomarkers, such as the hopanes, are also not always derived from a common precursor. Alternatively, the $\delta^{13}\text{C}$ obtained for biomarkers commonly associated with terrestrial sources (e.g., long-chain n-alkanes, n-alkanols and C₂₉Δ⁵ sterol) have elucidated sources other than higher plants. Other possible algal origin of long chain odd n-alkanes in immature sediments was revealed by distributions and carbon isotopic composition [27].

Environmental contaminants

The molecular isotopic signature of environmental contaminants can often be used to trace their sources on local to global scales. On a local scale it is often necessary to allocate a contamination to a specific source in order to allow appropriate means of risk reduction and/or to identify responsible parties in litigation. Traditional approaches in environmental forensics use chemical fingerprinting, biomarker analysis, and chemometrics. Chemical fingerprinting of the n-alkane fraction in crude oils and refined products in combination with isotopic characterization of carbon in the individual homologues has been successfully used to allocate sources of sediment contamination and bird feather oiling [28]. They suggest the preferred use of hydrogen isotopic composition of longer chain alkanes (n-C₁₉ to n-C₂₇) for source identification because the isotopic signature of hydrogen in crude oil components varies much more compared with carbon and is hardly changed during weathering and degradation of crude oil.

Source apportionment of polycyclic aromatic hydrocarbons (PAHs) both in the atmosphere and in sediment records has been studied intensely utilizing $\delta^{13}\text{C}$ analysis. With a combination of concentration measurements and $\delta^{13}\text{C}$ isotopic analysis of individual PAHs in sediments from Lake Erie it was possible to distinguish three areas of different contamination history. In a recent study, various sources of PAHs were distinguished in sediments along the St. Lawrence River. For example, very high $\delta^{13}\text{C}$ values were found for three ring PAHs originating from aluminum smelting in one area [29]. McRae et al. (2000) have shown that it is even possible to relate coal-derived PAHs released during different thermal conversion processes (combustion, pyrolysis, gasification) with the resulting $\delta^{13}\text{C}$ values and that these isotopic compositions are conserved in soil [30]. Isotopically extremely light PAHs ($\delta^{13}\text{C} = -31$ to -62 ‰) in lagoon sediments near Ravenna led to the conclusion that emissions were dominated by a former plant that used biogenic methane ($\delta^{13}\text{C} = -69$ to -73 ‰) as feedstock rather than by operating plants using petrogenic feedstocks of much higher ^{13}C content [28]. Wilcke et al. (2002) used $\delta^{13}\text{C}$ analysis of perylene to substantiate their earlier hypothesis that in tropical environments recent biological sources of PAHs related to termites are important, whereas pyrolytic sources dominate in temperate climate [31].

PAHs in atmospheric particles resulting from natural burning processes could be distinguished from those stemming from various anthropogenic combustion processes by using fingerprinting and $\delta^{13}\text{C}$ analysis of individual compounds [28]. In Chinese urban areas, PAH $\delta^{13}\text{C}$ analysis was successfully used to identify either vehicle exhaust or coal combustion as major PAH source [28]. Many of these studies show the necessity to combine chemical fingerprinting techniques and compound-specific isotope analysis. Often, neither compound-specific isotope analysis (CSIA) nor fingerprinting alone are conclusive for source apportionment but the information gain from isotopic analysis will certainly make CSIA indispensable in future source allocation investigations.

On a global scale, CSIA measurements can be used as a tool to characterize various sources and sinks of atmospheric gases and to estimate their relative importance. This approach has been used since the early 1980s but only recently GC/IRMS instead of dual-inlet IRMS was applied. The major advantage of GC/IRMS in this area is the much higher sample throughput that allows a higher sampling frequency [32]. Rice et al. (2001) presented a thorough method comparison for measuring $\delta^{13}\text{C}$ and $\delta^2\text{H}$ of methane with GC/IRMS and dual-inlet IRMS and found no systematic and only low random deviations between both methods. On a Pacific transect they found $\delta^{13}\text{C}$ values ranging from -47.0 ‰ to -47.3 ‰. An average global $\delta^{13}\text{C}$ for methane of -47.1 ‰ was found with average variations from northern to southern hemisphere of 0.6 ‰ and seasonal variations of 0.5 ‰ (consistent data only in the northern hemisphere). For chloromethane, Thompson et al. (2002) found a global $\delta^{13}\text{C}$ average of -36.2 ‰ [33]. Budgeting of atmospheric chloromethane based on isotopic composition of known sources suggests that additional emission sources with an average $\delta^{13}\text{C}$ value of -41.9 ± 7.8 ‰ exist. Harper et al. (2001) found very similar values in chloromethane emitted

by polypore fungi that was highly depleted in ^{13}C (-43.3 ‰) compared with the growth substrate, and an even higher depletion in two higher plant species [34]. Recently, the same group found that chloromethane produced by two tropical fern species is significantly depleted ($\delta^{13}\text{C}$ -69.3 ‰ and -72.7 ‰) compared to chloromethane resulting from biomass burning and industrial emissions [28].

Hg stable isotopes

Special attention was given to provide pre-industrial background levels of heavy metals for the Gulf of Trieste, particularly for Hg. Sedimentary records of this geochemical tracer were compared with the records of 500 years of ore extraction in order to reconstruct the Hg depositional history, determine the accumulation rate and calculate the cumulative metal inventory. The Hg historical trend is well correlated with extraction activity at the Idrija mine, thus allowing indicative sedimentation rate estimation and tentative assessment of the rate of Hg accumulation in bottom sediments (from 1.77 to 31.5 mg m⁻² y⁻¹ at the surface) that is from one to two orders of magnitude higher than the Po river's, the main freshwater supply of sediments in the Adriatic sea [35]. The results obtained from several research groups have so far unequivocally shown that Hg fractionation exists in nature and that analytical techniques have reached a level of precision and accuracy sufficiently sensitive to detect differences in Hg isotope ratios that may occur among environmental samples and during transformation reactions [36]. More importantly, these studies strongly suggest that Hg isotopes might be used in the future as tracers to distinguish between Hg sources according to their isotopic signatures and quantify chemical transformations in the environment. However, it is still debated, whether mercury from anthropogenic sources is isotopically different from geogenic mercury. To demonstrate the power of precise isotope ratio measurements of Hg in environmental samples and more particularly, to test the use of stable isotopes as distinct tracers of the contamination source, we investigated a well-documented system, the Hg mining region near Idrija, Slovenia. Sediments alongside the Idrijca River, the Soča/Isonzo River and in the Gulf of Trieste were analyzed to determine the variation in Hg isotopic composition versus distance from the source. No significant differences (mean $\delta^{202}\text{Hg} = -0.323 \pm 0.152\text{‰}$, $n = 17$) were observed among samples collected from the rivers Idrijca, Soča/Isonzo, around the river mouth in the Gulf of Trieste and Hg-ore originating from the Idrija Mine (red cinnabar, $\delta^{202}\text{Hg} = -0.258 \pm 0.117\text{‰}$), suggesting that sediments throughout the watershed of the Soča/Isonzo River to the Gulf of Trieste are dominated by Hg exported from the mining area. Only locations on the southern part of the gulf, outside the river plume, showed a lighter isotopic composition ($\delta^{202}\text{Hg}$ ranging from -1.189 to -2.529‰) comparable to the Hg isotopic signature of Adriatic Sea sediments (mean $\delta^{202}\text{Hg} = -2.000 \pm 0.463\text{‰}$, $n = 3$). Using a simple binary mixing-model, we could demonstrate that all samples investigated in this study were a result of variable combinations of Hg originating from the Idrija Mine (progressively decreasing from > 90% in the northern part to < 45% in the southern Gulf) and from the Adriatic Sea. These results are so far the

first evidence that tracking of mercury sources in natural systems using mercury stable isotope ratios is feasible [5].

References

- [1] F. Vanhaecke, K.G. Heumann, *Anal. Bioanal. Chem.*, 2004, **378**, 227-228.
- [2] J. Hoefs, *Stable Isotope Geochemistry*, Springer-Verlag, Berlin, Heidelberg, 2009.
- [3] D. S. Lauretta, B. Klaue, J. D. Blum, P. R. Buseck, *Geochim. Cosmochim. Acta*, 2001, **65**, 2807-2818.
- [4] J. Faganeli, N. Ogrinc, N. Kovač, K. Kukovec, I. Falnoga, P. Mozetič, O. Bajt, *Mar. Chem.*, 2009, **144**, 102-109.
- [5] D. Foucher, N. Ogrinc, H. Hintelmann, *Environ. Sci. Technol.*, 2009, **43**, 33-39.
- [6] J. M. Hayes, *Mar. Geol.*, 1993, **113**, 111-125.
- [7] P. A. Meyers, *Mar. Geol.*, 1994, **144**, 289-302.
- [8] I. Tolosa, J. F. Lopez, I. Bentaleb, M. Fontugne, J. O. Grimalt, *The Sci. Total Environ.*, 1999, **237/238**, 473-481.
- [9] H. T. S. Boschker, J.J. Middelburg, *FEMS Microbiol. Ecol.*, 2002, **40**, 85-95.
- [10] N. Ogrinc, G. Fontolan, J. Faganeli, S. Coveli, *Mar. Chem.*, 2005, **95**, 163-181.
- [11] R. R. Harrington, B. P. Kennedy, C. P., Chamberlain, J. D. Blum, C. L., *Flot. Chem. Geol.*, 1998, **147**, 281-294.
- [12] C. G., Hebert, L. I. Wassenaar, *Environ. Sci. Technol.*, 2001, **35**, 3482-3487
- [13] B. Mayer, E. W. Boyer, C. Goodale, N. A. Jaworski, N. van Breemen, R.W. Howarth, S. Seitzinger, G. Billen, K. Lajtha, K. Nadelhoffer, D. Van Dam, L. J. Hetling, M. Nosal, K. Paustian, *Biogeochem.*, 2002, **57/58**, 171-192.
- [14] M. Voss, B. Deutsch, R. Elmgren, C. Humborg, P. Kuuppo, M. Patuszak, C. Rolff, U. Schulte, *Biogeosci.*, 2006, **3**, 663-676.
- [15] C. Kendall, in: *Isotope Tracers in Catchment Hydrology*. Kendall, C., McDonnell, J. J., (Eds.). Elsevier, New York, NY, 1998, 519-576.
- [16] T.C. Malone, A. Malej, L.W. Harding, N. Smolaka, R. E. Turner, *Ecosystems at the land-sea margin: Drainage basin to coastal sea*. AGU, Washington, 1999, 381.
- [17] M. Giani, D. Degobbis, A. Rinaldi, *Sci. Total Environ.*, 2005, **353**, 1-379.
- [18] N. Kovač, J. Faganeli, O. Bajt, *Mucous macroaggregates in the Northern Adriatic*, in: Stefansson, O., (Ed.), *Geochemistry Research Advances*, Nova Science Publishers, New York, 2008, 119-141.
- [19] E. A. Canuel, K.H. Freeman, S. G. Wakeham, *Limnol. Oceanogr.*, 1997, **42** (7), 1570-1583.
- [20] C. L. Zhang, *Curr. Opin. Biotechnol.*, 2002, **13** (1), 25-30.
- [21] W. Meier-Augenstein, *GC and IRMS Technology for ¹³C and ¹⁵N Analysis on Organic Compounds and Related Gases*, *Handbook of Stable Isotope Analytical Techniques*, Elsevier Science BV, Amsterdam, 2004, Vol. I (Part 1, Chapter 8), 153-174.

- [22] D. C. White, *Advan. Limnol.*, 1988, **31**, 1–18.
- [23] P. H. Ray, D. C. White, T. D. Brock, *J. Bacteriol.*, 1971, **106**, 25–30.
- [24] D. C. Fork, N. Murata, N. Sato, *Plant Physiol.*, 1979, **63**, 524–530.
- [25] L. L. Jahnke, *FEMS Microbiol. Lett.*, 1992, **93**, 209–212.
- [26] I. Tolosa, S. de Mora, *Proceedings of an Advisory Group meeting held in Vienna, 20–23 September 1999*, 2001, 67-73.
- [27] B. R. T. Simoneit, R. E. Summons, L. L. Jahnke, *Origins of Life and Evolution of Biospheres*, 1998, **28**, 515-516.
- [28] T. C. Schmidt, L. Zwank, M. Elsner, M. Berg, R. U. Meckenstock, S. B. Haderlein, *Anal. Bioanal. Chem.*, 2004, **378**, 283-300.
- [29] A. Stark, T. Abrajano, J. Hellou, J. L. Metcalf-Smith, *Org. Geochem.*, 2003, **30**, 225-237.
- [30] C. McRae, C. G. Sun, C. F. McMillan, C. E. Snape, A. E. Fallick, *Plycycl. Aromat. Compd.*, 2000, **20**, 97-109.
- [31] W. Wilcke, M. Krauss, W. Amelung, *Environ. Sci. Technol.*, 2002, **36**, 3530-3535.
- [32] A. L. Rice, A. A. Gotoh, H. O. Ajie, S. C. Tyler, *Anal. Chem.*, 2001, **73**, 4104-4110.
- [33] A. E. Thompson, R. S. Anderson, J. Rudolph, L. Huang, *Biogeochem.*, 2002, **60**, 191-211.
- [34] D. B. Harper, R. M. Kalin, J. T. G. Hamilton, C. Lamb, *Environ. Sci. Technol.*, 2001, **35**, 3616-3619.
- [35] S. Covelli, G. Fontolan, J. Faganeli, N. Ogrinc, *Mar. Geol.*, 2006, **230**, 29-51.
- [36] B. A. Bergquist, J. D. Blum, *Elements*, 2009, **5**, 353-357.

APPLICATION OF PHYSICAL CHEMISTRY METHODS IN ENVIRONMENTAL MANAGEMENT: A STUDY OF MAIZE TASSEL SORPTION OF Pb(II) FROM AQUEOUS SOLUTION

C. M. Zvinowanda¹, M. Sekhula¹, J. O. Okonkwo¹ and N. M. Agyei²

¹*Department of Environmental, Water & Earth Sciences, Faculty of Science,
Tshwane University of Technology, Private Bag X680, Pretoria, 0001, South
Africa.*

²*Department of Chemistry, University of Limpopo, PO Box 235, Medunsa, 0204,
South Africa.*

Abstract

We report on adsorption capacity, breakthrough volumes, thermodynamic, equilibrium and kinetic studies on Pb(II) removal using maize tassel powder. Breakthrough volumes of 900 and 1400 mL and AER of 4.44 and 4.17 g L⁻¹ were obtained under gradient and high pressure conditions respectively for Pb(II). The K_c for Pb(II) ranged from 6.72-8.29 Jmol⁻¹. The values for ΔG, ΔH^o and ΔS^o were -2251.96 to -2774.23, -4091.74 and 31 Jmol⁻¹ respectively. The adsorption process could be well described by both the Langmuir and Freundlich isotherms with R² of 0.957 and 0.972, respectively. The kinetics of Pb(II) on tassel surface is well defined using linearity coefficients(R²) by pseudo-second-order(0.999), intra-particle diffusion (0.860) and pseudo-first-order(0.795) respectively.

Introduction

The ongoing discussions on global warming and its impact on water resources have increased the call for the treatment of wastewater from domestic and industrial sources. Typical industrial wastewater contains metals such as Pb, Cd and others that have health consequences [1]. Several techniques for metal removal from polluted water have been reported by many researchers [2-6]. Adsorption appears to be the most promising for treating large volumes of polluted water at reasonable cost. Synthetic adsorbents/resins have shown high removal, selectivity and recovery for heavy metals [7]. However, the high cost of these materials and availability have prevented their wide application in wastewater treatment.

The application of biomaterials of agricultural origin that are available for heavy metal uptake and recovery are now a major focus area for many researchers [8-10]. Some of the shortcomings of most biosorbents centre on poor adsorption capacities and decomposition when exposed to wet conditions for extended periods.

Maize tassel is the staminate (male) inflorescence part of the maize plant. Its major purpose is the production of pollen grains which fertilize the female part of the maize flower which then develops into a cob. It has no production value after fertilization. In recent years, the area dealing with the physical chemistry of

materials has become an emerging discipline in materials science that emphasizes the study of materials for pollution abatement applications. Focusing on this emerging discipline, the application of physical chemistry methods on adsorption potential of maize tassel for the removal of Pb(II) from aqueous solution are discussed.

Experimental

The maize tassel harvested from Tshwane University of Technology's Research Farm, Pretoria, South Africa, was milled into a powder after drying. Pb(II) stock solutions (1000 mg L^{-1}) were prepared from analytical reagent grade PbNO_3 (MERCK). A Varian Flame AAS 220 FS, Australia, Springvale, was used for the determination of Pb(II) ion concentrations in the effluent from the columns after adsorption.

Glass columns of internal diameter (I.D) of 15 mm was used for the breakthrough studies under gradient elution of 100 mg L^{-1} of Pb(II) solutions. The columns were packed with oven dried maize tassel material of particle size range of 150-300 μm . The experiments were run in triplicates with a tassel loading of 4.0 g at pH 4. Bed depth (B.D), flow rate (F.R), influent height (I.H) were determined which were used to evaluate the column performance.

A solution of Pb(II) with concentration of 100 mg L^{-1} and pH 4 was equilibrated at temperatures ranging from 298 °K to 337 °K. A set of triplicate samples for the metal ion at a particular temperature with adsorbent concentration of 10 g L^{-1} was allowed to react for 1 h. The mixture was then filtered and the filtrate analysed for none adsorbed metal ion from which the concentration of adsorbed species was calculated. The data obtained was then used to calculate thermodynamic parameters such as K_c , ΔG° , ΔH° and ΔS° . Freundlich and Langmuir models were used for the sorption equilibrium studies between the tassel and Pb(II) ions. The pseudo-first-order, pseudo-second-order and the intra-particle diffusion models were used for kinetic modeling studies.

Results and Discussion

The performance evaluation of adsorbents packed in columns depends on the adsorbent exhaustion rate (AER), which is determined by the equation:

$$AER = \frac{M}{V} \quad [1]$$

where M is the mass of adsorbent (g) used in the column and V is the volume (L) at breakthrough point. The breakthrough capacity ($Q_{0.5}$) (at 50% or $C_e/C_f = 0.5$) is another column parameter which can be used to determine its performance. The higher the $Q_{0.5}$ value of a column the better the performance and the more viable it is. The $Q_{0.5}$ value of a column is determined from the equation:

$$Q_{0.5} = \frac{\text{metal adsorbed on adsorbent bed (mg)}}{\text{mass of adsorbent in bed (g)}} \times \frac{\text{breakthrough time (at 50\%)} \times \text{flowrate} \times \text{feed concentration}}{\text{mass of adsorbent bed}} \quad [2]$$

The adsorption profile curves obtained under aforementioned conditions are illustrated in Figures 1 and 2. Adsorbent bed of 4.00 g was used in this study.

The profile of the curves mimicked those curves which were obtained by batch studies [6-8], [10-11]. The performance of tassel in gradient studies gave a high breakthrough volume of 900 mL and a lower adsorbent exhaustion rate of 4.44 g L⁻¹ with a Pb(II) solution of initial concentration of 100 mg L⁻¹ was used.

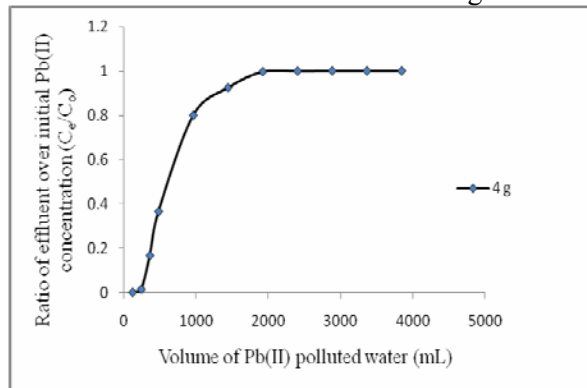


Fig.1. Adsorption profile of Pb(II) in effluent with volume of water treated under gravity

The results of column studies for Pb(II) under high pressure are shown in Figure 2. The curve was used to determine some of the important column parameters. In high pressure fixed bed column studies, pressure pumps were used to increase and maintain the influent flow rate through the adsorbent fixed bed.

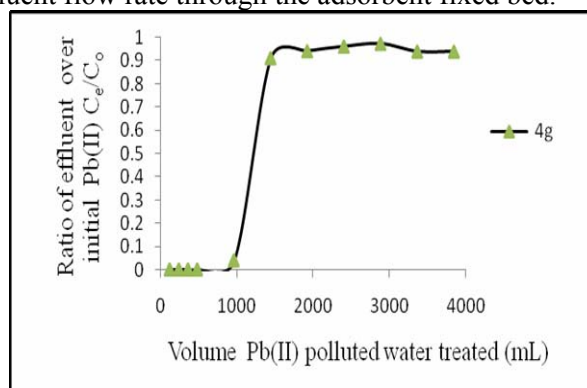


Fig.2. Adsorbent profile of gradient elution of Pb(II) on tassel under high pressure.

The lower the AER, the better the performance of the column since more water can be treated or be cleaned by the adsorbent before regeneration. In this study, the breakthrough volume of 1400 mL and AER of 4.17 g L⁻¹ were obtained. This means that at least, 1400 mL solution or wastewater influent containing 100 mg L⁻¹ Pb(II) could be treated by at least 4.17 g of tassel adsorbent depending on operation conditions. The best performing column had a feed concentration of 100 mg L⁻¹ Pb(II), flow-rate of 8.0 mL min⁻¹, breakthrough time of 150 min and mass of adsorbent bed of 4 g. From these parameters, a breakthrough capacity ($Q_{0.5}$) of 30.0 mg g⁻¹ on tassel bed was observed. Breakthrough capacities of natural adsorbents reported so far include neem oil, 30.0 mg g⁻¹ [12], granular activated carbon, 2.89 mg g⁻¹ depending on operating conditions [13]. The equilibrium constants, K_c , was calculated using equation 3. It was assumed that an equilibrium existed between the species in solution and those adsorbed on the surface of adsorbent. The homogenous system energetics were taken as a good approximate of events in a heterogenous systems.

$$K_c = \frac{C_{AE}}{C_E} \quad [3]$$

where C_{AE} and C_E are the equilibrium concentration (mg L⁻¹) on the adsorbent and in solution, respectively [12]. The values of K_c were calculated at temperatures of 25.6, 41.6, 57.0 and 64.0 °C. Equations 4 and 5 describe the relationship between the Gibbs free energy, the enthalpy of adsorption and the entropy of the system. The equilibrium constant K_c is related to the energy parameters as shown in equation 6, 7 and 8. Equation 8 was used to evaluate the parameters of standard enthalpy of adsorption (ΔH°) and the standard entropy change of the adsorbate ions on the adsorbent surface (ΔS°). The probability of a reaction to occur is defined thermodynamically from its change in the heat of reaction (ΔH) and entropy (ΔS). The enthalpy is the energy absorbed when an endothermic reaction occurs under constant pressure. When heat is given off. The combined effect of enthalpy and entropy gives the Gibbs free energy, G .

$$G = H - TS \quad [4]$$

The change in energy of a system at constant temperature is

$$\Delta G = \Delta H - T \Delta S \quad [5]$$

The Gibbs free energy is related to the equilibrium constant by the equations

$$K_c = e^{-\Delta G/RT} \quad [6]$$

$$\Delta G = -RT \ln K_c \quad [7]$$

$$\ln K_c = \frac{\Delta S^\circ}{R} - \frac{\Delta H^\circ}{RT} \quad [8]$$

where ΔG° is the change in free energy (Jmol^{-1}), ΔH° , the change in enthalpy (Jmol^{-1}), ΔS° the change in entropy ($\text{Jmol}^{-1}\text{K}^{-1}$), T the absolute temperature K, R the gas constant (8.314 K^{-1}). A plot of $\ln K_c$ versus $\frac{1}{T}$ gave a straight line with slope $\left(-\frac{\Delta H^\circ}{R}\right)$

which was used to determine the standard enthalpy change of adsorption of Pb(II). The intercept, $(\Delta S^\circ)/R$ was used to evaluate the entropy change of adsorption of the metal ion on the tassel surface (Figure 3) which are the Van't Hoff plots. From the Le-Chatelier's principle of chemical equilibria, the adsorption of Pb(II) decreases with increase in temperature as shown in Figure 3. This is further confirmed by the negative value of ΔH° obtained which indicates that the adsorption process is exothermic. Hence, the removal of Pb(II) should be effected at lower temperatures in order to maximise the recoveries of Pb(II) on the tassel adsorption sites. The negative values of ΔG obtained illustrate spontaneity of the adsorption process.

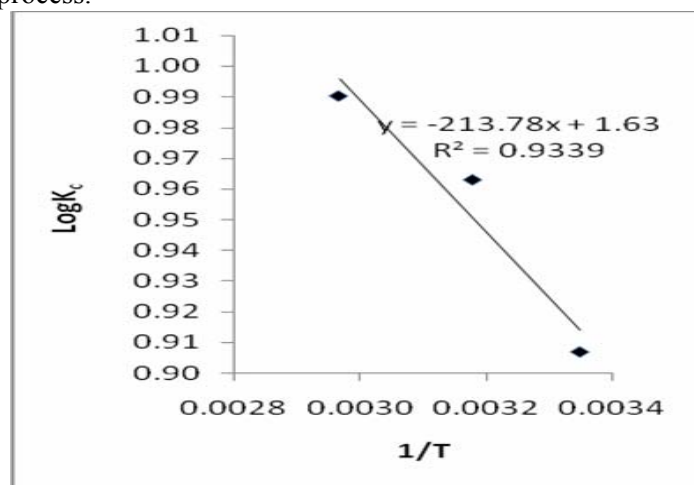


Fig.3. Plot of $\text{Log}K_c$ vs $1/T$ of Pb(II) on tassel

The summary of thermodynamics determined for the adsorption processes of Pb(II) on the tassel surface are shown in Table 3. Some of the materials whose thermodynamic properties have been reported include, Olive cake, ΔG , ΔH° , ΔS° values of $15.855 \text{ kJmol}^{-1}$, $44.530 \text{ kJmol}^{-1}$ and 0.199 kJmol^{-1} respectively for Pb(II) adsorption [12].

Table 3 Summary of thermodynamics for adsorption of Pb(II)

Temp °K	K _c	ΔG Jmol ⁻¹	ΔH ⁰ Jmol ⁻¹	ΔS ⁰ Jmol ⁻¹
298.6	7.46	-2251.96		
314.6	8.29	-2518.71	-4091.74	31.21
330.0	7.26	-2312.10		
337.0	6.72	-2774.23		

The model proposed by Langmuir suggests that the adsorption occurs on homogeneous surface by monolayer sorption with no interactions between sorbed species. The model assumes uniform energies of adsorption onto the surface and no transmigration of sorbate in the plane of the surface²⁶. The linear form of the Langmuir isotherm is defined by the following equation:

$$C_e/q_e = 1/(q_{\max} \cdot K_c) + (1/q_{\max}) \cdot C_e \quad [9]$$

where C_e is the equilibrium concentration of adsorbate (mg L^{-1}), q_e the amount adsorbed at equilibrium (mg g^{-1} adsorbate, and), and q_{\max} (mg g^{-1}) and K_c (L mg^{-1}) are the Langmuir constants related to the adsorption capacity and energy, respectively. A plot of C_e/q_e against C_e gives a straight line with slope $1/q_{\max}$ and intercept $1/(q_{\max} \cdot K_c)$ as shown in Figure 4. From the graph the values of q_{\max} (333.3 mg g^{-1}), K_c ($5.44 \times 10^{-3} \text{ L mg}^{-1}$) and R^2 (0.957) were obtained. The parameters maybe used for the comparison of and correlation of the sorptive properties of tassel.

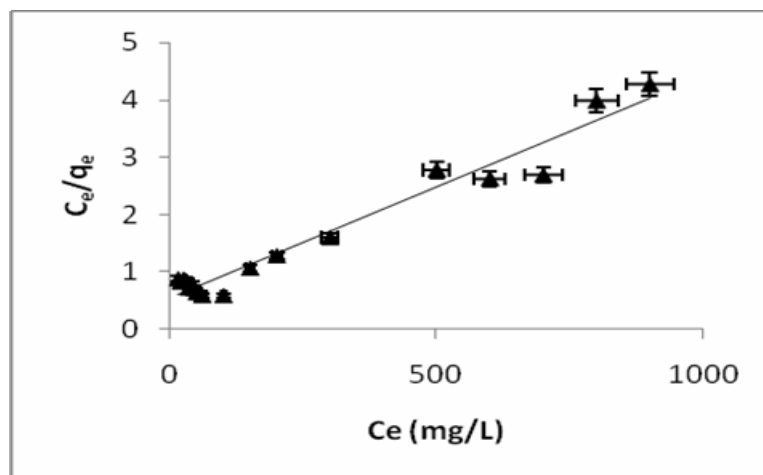


Fig.4. Langmuir plot for the adsorption of Pb(II) by tassel: (pH 4; 1g/100mL adsorbent; contact time, 1h; and temperature 25 °C).

The Freundlich isotherm model has been widely used for heterogeneous surface energies. The Freundlich equation has a general linear form [14].

$$\log q_e = \log K_f + (1/n) \log C_e \quad [10]$$

where q_e is the amount of adsorbate adsorbed per unit weight (mg/g adsorbent), C_e is the equilibrium concentration (mg L⁻¹) of adsorbate, and K_f and n are Freundlich constants. Both K_f and n are empirical constants being indicative of the extent of adsorption (sorption capacity) and the degree of nonlinearity between solution and concentration i.e. adsorption intensity respectively [15]. From the plot of $\log q_e$ versus $\log C_e$ (Fig.3.6), values of K_f (1.87 mg g⁻¹), n (1.49) and R^2 (0.972) were determined. From the linearity coefficients (R^2), it can be deduced that the Freundlich isothermal model described the adsorption of Pb(II) ions on tassel more successfully than the Langmuir. Consequently, the sorption of Pb(II) ions on tassel follows the Freundlich isotherm model where the adsorption occurs on heterogeneous surface and the adsorption energy varies as a function of surface coverage, q_e , strictly due to variations in heat of adsorption [14].

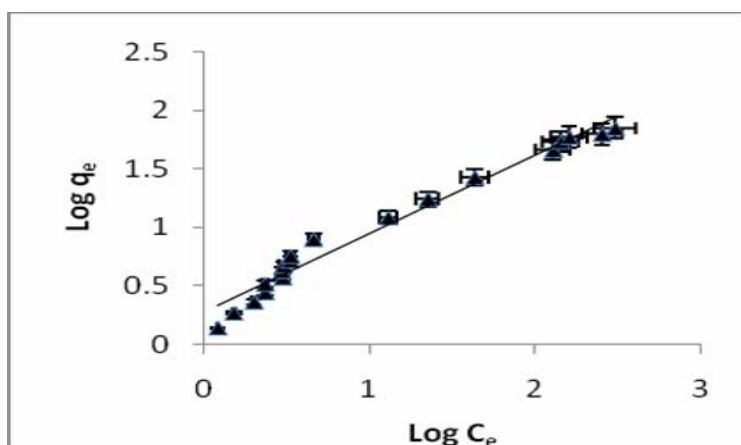


Fig.5. Freundlich plot for adsorption of Pb(II) by tassel: (pH 4; 1g/100 mL Adsorbent; contact time, 1h; temperature, 25 °C and 100 rpm shaker speed).

The kinetic parameters of Pb(II) ions sorption onto tassel powder were determined from the pseudo-first-order Lagergren equation, pseudo-second-order and the intra-particle diffusion models represented by the following linear equations respectively.

$$\log(q_e - q_t) = \log(q_e) - (k_1/2.303).t \quad [11]$$

$$t/q_t = 1/(k_2.q_e^2) + (1/q_e^2).t \quad [12]$$

$$\log R = \log K_s + b \log t \quad [13]$$

where q_e and q_t are the amounts of Pb(II) ions on the adsorbent at equilibrium and at time t respectively (mg g^{-1}), k_1 is the first-order biosorption rate constant (min^{-1}), k_2 is the second-order biosorption rate constant ($\text{g mg}^{-1} \text{min}^{-1}$), R is the percent Pb(II) adsorbed, t is the contact time (min), b is the gradient of linear plots and K_s is the intra-particle diffusion constant. The kinetic constants for pseudo-first-order, q_e (0.457), k_1 (1.38×10^{-3}) and R^2 (0.795) were determined from the graph (Figure 6). The kinetic constants K_s (1.283), b (0.520) and R^2 (0.860) were obtained from equation 13. The pseudo-second-order kinetic constants determined are q_e (1.66), k_2 (0.282) and R^2 (0.999) as shown in Figure 6. From the linearity coefficients (R^2) of the three models, pseudo-second-order best described the kinetic behaviour of Pb(II) ions on tassel surface since it gave the highest R^2 value.

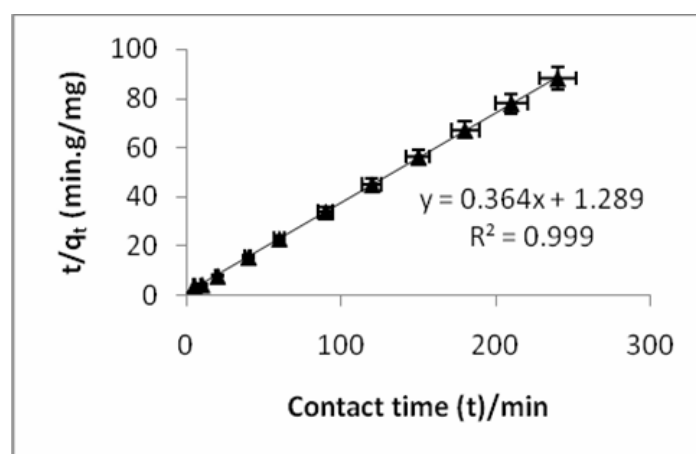


Fig. 6. Pseudo-second-order plot (t/q_t vs. t) ($C_0 = 30 \text{ mg/L Pb(II)}$ $1\text{g}/100\text{mL}$ adsorbent, agitation speed=100 rpm, contact time = 1h, temperature = 25°C , pH = 4).

Conclusion

The application of thermodynamic principles on heterogeneous systems was able to validate the results obtained experimentally for the energetic of Pb(II) adsorption. The Freundlich isothermal model was found as the best fit model to describe the adsorption behaviour of Pb(II) ions on tassel surface. Kinetic modelling studies demonstrated that the pseudo-second-order model gave the best fit for Pb(II) uptake with $R^2 \approx 1$.

References

- [1] V. B. H.Dang, H. D. Doan, T. Dang-Vu, A. Lohi, Bioresour. Technol., 2009, **100**, 211-219.
- [2] M.Schulte-Bokholt, M. Schuster, Sep. Purif. Technol., 2008, **63**, 172-178.
- [3] K. Vijayaraghavan, M.W.Lee, Biochem. Eng. J., 2008, **41**, 228-233.
- [4] S. R. Popuri, Y. Vijaya, V. M. Boddu, K.Abburi, Bioresour. Technol., 2009, **100**, 194-199.

- [5] G. McKay, M. El-Geundi, M. M. Nassar, *Adsorpt. Sci. Technol.*, 1997, **15**, 251-262.
- [6] J. Lakatos, S. D. Brown, C. E. Snape, *Fuel*, 2002, **81**, 691-698.
- [7] N. Sankararamakrishnan, P. Kumar, V. S. Chauhan, *Sep. Purif. Technol.*, 2008, **63**, 213-219.
- [8] C. M. Zvinowanda, J. O. Okonkwo, N. M. Agyei, P. Forbes, V. Mpangela, J. Phaleng, P. N. Shabalala, T. Dennis, K. I. Ozoemena, *Fresen. Environ. Bull.*, 2008, **17**, 814-818.
- [9] T. Vaughan, C. W. Seo, W. E. Marshall, *Bioresour. Technol.*, 2001, **78**, 133-139.
- [10] F. Gode, E. Moral, *Bioresour. Technol.*, 2008, **99**, 1981-1991.
- [11] J. Goel, K. A. Kadirvelu, C. Rajagopal, V. K Garg, *J. Hazard. Mater.*, 2005, **B125**, 211-220.
- [12] R. A. K. Rao, M. A. Khan, *Sep. Purif. Technol.*, 2007, **57**, 394-402.
- [13] A. Jusoh, L.S. Shiung, N. Ali, M.J.M.M. Noor, *Desalination*, 2007, **206**, 9-16.
- [14] A. W. Adamson in *Physical Chemistry of Surfaces*, 2nd ed., Interscience Publishers Inc., New York, 1967.
- [15] W. J. Weber, in *Physico-Chemical Processes for Water Quality Control*, John Wiley and Sons Inc., New York, NK, 1972.
- [16] S. T. Gregg, K. S. W. Sing in *Adsorption, Surface Area and porosity*. 2nd ed. London, 1992.

PELLETS FROM LONG-EARED OWLS (*Asio otus*) AS INDICATORS OF SOIL QUALITY

M. Demajo, J. Cvetičanin, M. Stoiljković, Đ. Trpkov, V. Andrić,
A. Onjia and O. Nešković

Vinča Institute of Nuclear Sciences, P.O. BOX 522, 11001 Belgrade, Serbia

Abstract

Pellets from Long-Eared Owls (*Asio otus*) were collected from four localities in the city and in the vicinity of Belgrade. The element content in the pellets was analyzed. The results indicate that owl pellets may be useful for monitoring environmental conditions, specifically soil quality.

Introduction

Certain species of birds, especially birds of prey, release through their beaks pellets containing undigested food remains, mostly bones and hair. Pellets from the Long-Eared Owl (*Asio otus*) were collected during January 2010, from under trees where the owls roost during winter. Rodents, voles (*Microtidae*) and field mice (*Muridae*) are the staple winter prey of these owls. Rodents have been previously analyzed as indicators of environmental quality [1] and [2]. The residues of rodenticides were studied in the Barn Owl (*Tyto alba*) pellets [3] under experimental conditions as well as organochlorine pollutants in eggs of the Little Owl (*Athene noctua*) [4]. Our report deals with the analysis of owl pellets containing remains of rodents with the aim of monitoring soil conditions in several localities.

Materials and Methods

Pellets were collected from four locations (geographical coordinates determined by Google Earth satellite images). The locations were: Cemetery "Lešće" (N. 44° 48' 28.44''; E. 20° 32' 46.63''), Cemetery "Bežanijska kosa" (N. 44° 48' 55.80'' ; E. 20° 22' 04.59''), Cemetery "Novo groblje" (N. 44° 48' 31.86'' ; E. 20° 29' 28.73'') and the "Vinča" Institute (N. 44° 45' 16.37'' ; E. 20° 36' 15.98''). The first groups of samples were designated as "bones". These samples were obtained by separating only the bones from the pellets collected. The other groups of the samples were the pellets themselves as they were collected. Samples were processed and prepared for chemical quantitative analysis performed by inductively coupled plasma optical emission spectroscopy (Spectroflame, Spectro Analytical Instrument (Germany), 2.5 kW, 27 MHz) and direct current argon arc plasma optical emission spectrometry. Mass spectrometry measurements were performed on MALDI TOF mass spectrometer Voyager de Pro (AB Applied Biosystem, UK). Alpha and beta radioactivity measurements were performed on a Protean MPC9400 low background gas proportional counter. The counter is calibrated with americium -241 for gross alpha determination and strontium-90 for gross beta determination. Low-background gamma-ray spectrometer with Canberra HPGe coaxial detector, multichannel analyzer and software was used.

Results and Discussion

All locations from which pellets were collected geologically originate from the Tortonian Miocene and consist mostly of sand, clay and marl [5]. The results of chemical quantitative analysis of bone samples and whole pellet samples are shown on Fig.1 and Fig.2, respectively. The results are presented by being normalized to sample mass.

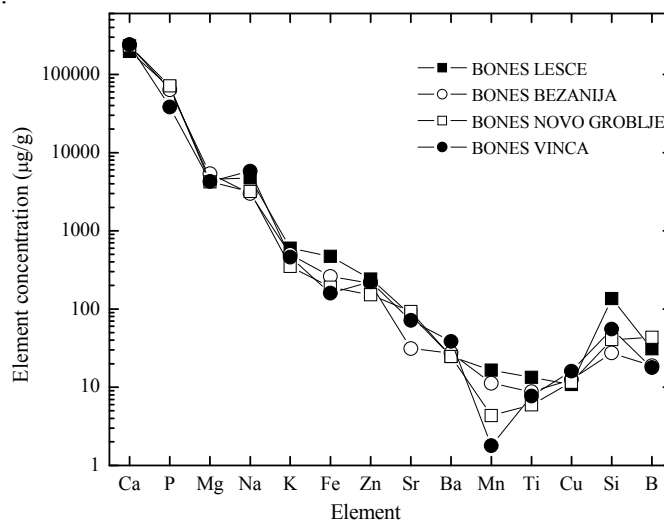


Fig.1. Element concentrations in bone samples

Radioactivity measurements showed only the presence of ^{40}K , while ^{137}Cs , ^{90}Sr , ^{238}Pu , ^{239}Pu , ^{240}Pu , ^{235}U and ^{241}Am were not detected. The same was confirmed by MALDI TOF.

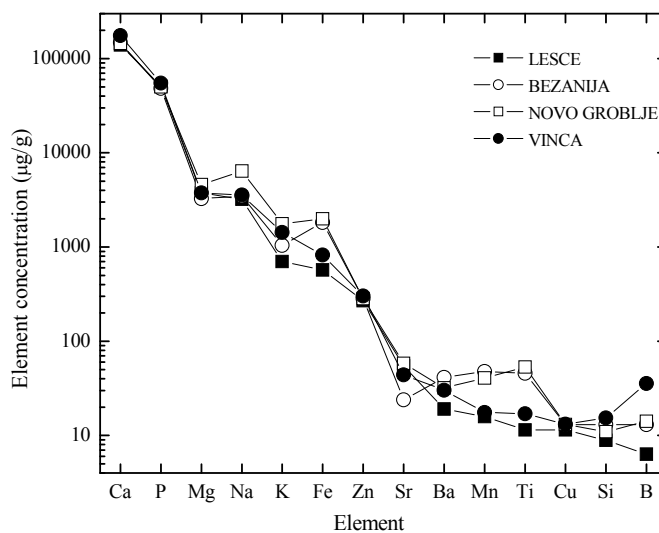


Fig.2. Element concentrations in whole pellet samples

Conclusion

Our results confirm that it is possible to measure a series of elements in owl pellets. Environmental radioactivity may also be monitored by this method, requiring the improvement of the pellet sample preparation for future radioactivity measurements, especially when low radioactivity doses are in question. Unusual for mammalian tissue, the high content of Zn in the samples may be an indicator of the use of the rodenticide Zn-phosphide in the field.

Acknowledgement

This work was financially supported by the Ministry of Science and Technological Development, Republic of Serbia, under Project No. 142001.

References

- [1] R. Miera *et al.* Health Physics, 1978, **34**, 603-609.
- [2]. T. Winsor and W. Whicker, Health Physics, 1980, **39**, 257-262.
- [3] C. Eadsforth *et al.* Pesticide Science, 1991, **32**, 105-119.
- [4] V. Jaspers *et al.* Environ.Pollution, 2005, **136**, 81-88.
- [5] K. Petković, Rědacteur, Gěologie de la Serbie, II-3, Beograd, 1977, 109.

ORGANO Gallium(III) COMPLEXES: A POTENTIAL ANTITUMOR AGENTS AGAINST THE HEAD AND NECK SQUAMOUS CELL CARCINOMA (HNSCC) CELL LINES

M. R. Kaluđerović^a, S. Gómez-Ruiz^b, R. Paschke^c,
T. W. Remmerbach^a and G. N. Kaluđerović^{c,e}

^aDepartment of Oral, Maxillofacial and Facial Plastic Surgery, University of Leipzig, Germany; ^bDepartamento de Química Inorgánica y Analítica, E.S.C.E.T., Universidad Rey Juan Carlos, Madrid, Spain; ^cBiozentrum^c, and Institut für Chemie^d, Martin-Luther-Universität Halle-Wittenberg, Germany; ^eDepartment of Chemistry, Institute of Chemistry, Technology and Metallurgy, University of Belgrade, Serbia.

Abstract

Ten organogallium(III) complexes (**1–10**) were tested against four different head and neck squamous cell carcinoma cell lines: HN (soft palate), Cal27, Cal33 (tongue) and FaDu (hypopharynx). Gallium(III) complexes demonstrated much higher cytotoxic activity than the reference compound Ga(NO₃)₃. In comparison with cisplatin, **1–10** expressed equal (e.g. IC₅₀ = 4.6 μM for **8** and cisplatin against Cal27 cell line) or lower *in vitro* antitumoral activity. The mode of cell death as well as caspase activation were further analysed for selected compounds.

Introduction

Head and neck cancer which comprises a diverse group of cancers affecting the oral cavity, sinuses, nasal cavity, pharynx, larynx, and other sites in this anatomical region with the majority being head and neck squamous cell carcinomas (HNSCC) [1]. Current treatment regimens for HNSCC often entail either a major surgical operation or a protocol using a platinum-based chemotherapeutic agent along with radiation therapy. The toxic effects of cisplatin are dose dependent and includes renal, otologic and bone marrow suppressive sequelae.

Bioorganometallic chemistry has become an interesting research area for the development of novel anticancer drugs. The early efforts in the assessment of platinum-based anticancer drugs have been shifted to non-platinum metal-based agents (Ti, Ga, Ge, Pd, Au, Co, Ru and Sn) [2].

Recently we reported the activity of various gallium(III) complexes against human tumor cell lines from five different histogenic origins: 8505C anaplastic thyroid cancer, A253 head and neck tumor, A549 lung carcinoma, A2780 ovarian cancer and DLD-1 colon carcinoma cell lines [3-5]. The compounds exerted dose-dependent antiproliferative effect toward all cancer, with IC₅₀ values higher than cisplatin but lower than gallium(III) nitrate. Selected gallium(III) compounds (Fig. 1) are further examined as potential agents against HNSCC cell lines and compared with the activity against A253 (submandibular duct) cell line from the same histological origin.

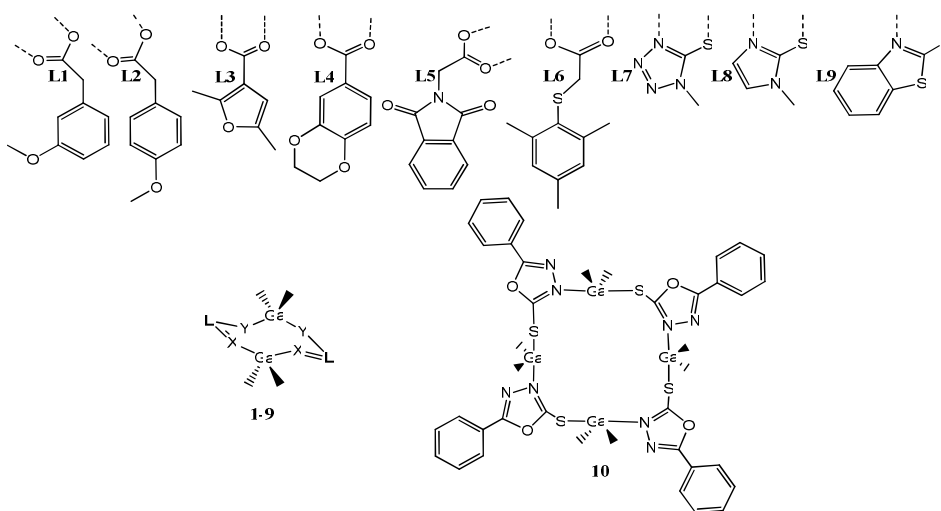


Fig.1. Investigated organogallium(III) complexes

Experimental

The compounds were prepared by procedures described in the literature [3-5]. SRB colorimetric assay, AO/EB staining and DNA laddering were performed as described earlier [3,6].

Results and discussion

Organogallium(III) complexes were tested for cytotoxic activity on human head and neck squamous cell carcinoma cell lines: HN (soft palate), Cal27, Cal33 (tongue) and FaDu (hypopharynx). Analyzed agents showed a dose-dependent antiproliferative effect toward all cell lines. Results are summarized in Table 1.

The lower activity from investigated organogallium(III) complexes was observed for compound **9** against all cell lines. On the other hand compound **8** showed the best activity from all compounds. Furthermore, gallium(III) nitrate exhibits lower activity when compared to any investigated compound. On the direct comparison of **1–10** with cisplatin the activity of gallium(III) complexes is lower with exception of compound **8** on Cal27 cell line where the activity is quite similar.

The mode of cell death was investigated for the most promising compounds **3**, **5** and **8** on the FaDu cell line using AO/EB staining as well as DNA laddering technique. It was shown that the compounds are inducing apoptosis. As concerns the exploration of parameters linked to apoptosis, there are two different well-identified pathways. First, the mitochondrial route, which involve activation of caspase 9 (initiator) followed by the activation of the effector caspase 3. Apart from the mitochondrial route, the cell death signal can be mediated through a receptor–ligand interaction which as a consequence involve activation of caspase 8 and then downstream effector caspases (caspases 3) leading to cell death. FaDu line was chosen for investigation of the activity of caspase 2, 3, 8 and 9. Compounds **3**, **5** and **8** were able to induce accumulation of caspases 8 and 3.

Table 1. IC₅₀ [μM]* for the 96 h of action of investigated compounds on HN, Cal27, Cal33, FaDu and A253 determined by SRB assay

Compound	IC ₅₀ ±SD				
	HN	Cal27	Cal33	FaDu	A253
1	15.3 ± 1.4	15.0 ± 1.6	18.5 ± 1.6	18.4 ± 0.6	7.4 ± 0.3
2	16.3 ± 1.4	15.2 ± 1.8	20.3 ± 3.6	15.9 ± 0.9	8.9 ± 0.3
3	15.3 ± 1.4	13.6 ± 1.2	19.4 ± 3.3	16.3 ± 0.2	7.9 ± 0.3
4	10.8 ± 1.9	10.6 ± 0.8	13.9 ± 1.5	14.3 ± 0.1	6.57 ± 0.2
5	12.4 ± 2.7	12.1 ± 1.2	16.3 ± 1.5	15.7 ± 0.1	5.7 ± 0.3
6	13.8 ± 2.2	11.6 ± 0.9	14.2 ± 1.4	15.4 ± 0.2	7.7 ± 0.3
7	10.9 ± 2.0	9.2 ± 0.1	11.4 ± 1.3	12.0 ± 0.1	13.7 ± 1.5
8	7.9 ± 0.2	4.6 ± 0.4	4.6 ± 0.4	4.3 ± 0.1	12.5 ± 1.3
9	22.0 ± 2.6	19.1 ± 2.9	29.9 ± 1.9	25.5 ± 3.2	20.0 ± 2.3
10	14.0 ± 2.5	12.8 ± 1.8	17.4 ± 1.4	19.4 ± 0.7	10.7 ± 0.9
Ga(NO₃)₃	> 100	> 100	> 100	> 100	33.9 ± 0.3
Cisplatin	1.5 ± 0.1	4.6 ± 0.1	2.5 ± 0.2	1.3 ± 0.4	0.8 ± 0.2

* Mean values ± SD (standard deviation) from three experiments.

Conclusions

The present experimental study brings together numerous biochemical arguments that organogallium(III) complexes may be suitable and promising compounds for the furthercoming *in vivo* experiments targeted to the head and neck squamous cell carcinomas.

References

- [1] E. Ito, K. W. Yip, D. Katz, S. B. Fonseca, D. W. Hedley, S. Chow, G. W. Xu, T. E. Wood, C. Bastianutto, A. D. Schimmer, S. O. Kelley, F.-F. Liu, *Mol. Pharmacol.* 2009, **76**, 969-982.
- [2] C. G. Hartinger, P. J. Dyson, *Chem. Soc. Rev.* 2009, **38**, 391.
- [3] S. Gómez-Ruiz, B. Gallego, M. R. Kaluderović, H. Kommera, E. Hey-Hawkins, R. Paschke, G. N. Kaluderović, *J. Organomet. Chem.*, 2009, **694**, 2191.
- [4] M. R. Kaluderović, S. Gómez-Ruiz, B. Gallego, E. Hey-Hawkins, R. Paschke, G. N. Kaluderović, *Europ. J. Med. Chem.*, 2010, **45**, 519.
- [5] B. Gallego, M. R. Kaluderović, H. Kommera, R. Paschke, E. Hey-Hawkins, T. W. Remerbach, G. N. Kaluderović, S. Gómez-Ruiz, *Invest. New Drugs*, 2010 doi: 10.1007/s10637-010-9449-8.
- [6] B. B. Krajčinović, G. N. Kaluderović, D. Steinborn, H. Schmidt, Ch. Wagner, Ž. Žižak, Z. D. Juranić, S. R. Trifunović, T. J. Sabo, *J. Inorg. Biochem.*, 2008, **102**, 892.

ASSESSMENT OF MOSS VITALITY DURING ACTIVE TRACE ELEMENTS BIOMONITORING

M. Aničić¹, A. Sabovljević² and M. Tomašević¹

¹*Institute of Physics, University of Belgrade, Belgrade, Serbia*

²*Institute of Botany, Faculty of Biology, University of Belgrade, Belgrade, Serbia*

Abstract

Biomonitoring of trace elements atmospheric deposition was conducted with moss *Sphagnum girgensohnii* Russow, exposed in bags, for periods of 1 to 5 months in urban area of Belgrade (July-November, 2008). A vitality of the moss in bags during the exposure periods was assessed determining the pigments contents and indexes (Chl *a/b*, D665/D665a) in moss tissue as well as applying color (TTC) test. Since different treatments, with and without irrigation, were applied to the moss bags during exposure, decreasing of the pigments ratio in the moss with time was more evident for dry than for wetted bags. Also, colorimetric TTC test showed higher vitality of wet moss bags.

Introduction

The use of native mosses as biomonitors is a convenient way of determining levels of trace elements atmospheric deposition [1, 2]. However, naturally growing epiphytic mosses have been difficult to find at some locations of interest (urban and industrial areas), so that transplanted moss has been employed as an option. The “moss bags” technique has been developed as one of the active biomonitoring methods [3, 4] where a suitable moss species has been sampled from an area under minor influence from air pollution and exposed at polluted locations for defined periods. Sampled moss should be properly cleaned from foreign materials, packed into nylon mesh bags and than exposed to atmospheric deposition. *Sphagnum* moss species are most suitable for the moss-bag method due to their very high element retention properties [5]. Bags filled with peat and cotton wool have retention capacities of only 43 and 35% respectively in the comparison to the capacity of a typical *Sphagnum* moss-bag [6].

Replacing the moss from their natural habitat for the purpose of active biomonitoring is a substantial stress for the moss due to changed macro- and microclimate and general meteorological conditions. The aim of this study was to assess not only element accumulation ability during extended exposure periods [7], but also a physiological activity of the moss (*Sphagnum girgensohnii*) under stress conditions, i.e. due to relocation of moss from the natural habitat and following exposure to atmospheric deposition in Belgrade urban area.

Experimental

Samples of the moss *Sphagnum girgensohnii* Russow were exposed in bags for periods of 1 to 5 months in urban area of Belgrade from July to November, 2008. Different treatments, with and without irrigation, were applied to the exposed moss bags. After the extended periods of moss exposure the ratios of the photosynthetic pigments, chlorophyll *a* and *b*, (*Chl a/b*) were determined in the moss tissue as well as the absorbance changes (D665/D665a) after acidifying (20 μ l of 1 N HCl) i.e. chlorophyll / phaeopigments (D665/D665a) ratio [8, 9, 10]. Also, triphenyltetrazolium chloride (TTC) color test was applied to the moss. TTC (2,3,5-triphenyltetrazolium chloride) is a redox indicator used to differentiate between metabolically active and inactive tissues. The white compound is enzymatically reduced to red TPF (1,3,5-triphenylformazan) in living tissues due to the activity of various dehydrogenases. Thus, vitality of plant tissue may visually be estimated observing red coloring under microscope.

Results and Discussion

As widely accepted in the literature, the ratios of the concentrations of the chlorophyll pigments (*Chl a/b*), and the absorbance changes (D665/D665a) after acidifying the extract of moss tissue, may indicate physiological disorders during senescence or stress [8, 9, 10]. However, different environmental factors may influence variations in the pigment contents, and such analysis is not specific for a certain kind of stress.

The pigment analysis were performed to assess physiological activity of the moss *S. girgensohnii* placed in dry (DMB) and wetted moss bags (WMB) during various time of exposure (1 to 5 months). This experiment was designed to follow a spatial-temporal investigation of atmospheric trace element deposition in dry and wet moss bags [7]. The pigment analyses in both types of MB were done after each period of exposure to atmospheric deposition (1, 2, 3, 4, and 5 months) starting from July to December of 2008. The results of this analysis are shown in Fig.1.

The results of the analyses showed a significant decrease of the *Chl a/b* as well as the A665/A665a ratios in the moss samples (DMB and WMB) after exposure to atmospheric deposition in relation to the unexposed moss. The ratios decrease the most after the first month of exposure, corresponding to the highest stress (strongly changed ecological factors) as the moss displaced from its natural habitat. A drop of the ratios further continues through the following months of the MB exposure, though less intensive after some time (3 months) when it even gets stable, and the *Chl a/b* ratio increased (Figure 1). This result indicated an adaptation of the moss to new conditions and some overcoming the previous stress.

Comparing the pigment ratios obtained for the two types of the used biomonitors, both (*Chl a/b* and D665/D665a) were significantly higher in WMB than in DMB, and it is obviously a consequence of water supply and keeping moss in better physiological condition.

As the moss was subjected to a color solution of the triphenyltetrazolium chloride (TTC) in water, a microscopic observation showed clear differences in coloration between the unexposed and exposed moss, as well as between WMB and DMB after the same exposure periods. Results from this study indicated decreasing color intensity of moss, more pronounced in DMB. On the other hand, the more intensive coloration of the WMB than DMB after the same exposure period implied also an extent of active moss (WMB) uptake of elements from atmospheric deposition.

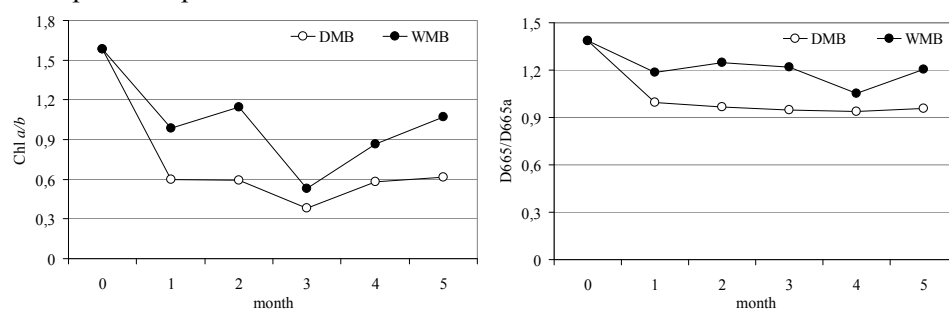


Fig.1. Concentration ratios of the pigments Chl *a/b* and D665/D665a in dry (DMB) and wetted moss bags (WMB) vs. exposure time.

Conclusion

Decreasing of the Chl *a/b* and D665/D665a ratios in the moss with time was evident for dry (more) and wetted (less) bags. Also, colorimetric TTC test showed higher vitality of wetted moss tissue. Generally, it may be suggested from this observation that in longer exposure periods of the moss in bags (especially dry) mostly acts as surface where particles are passively captured and passive ion exchange processes take place on the cell membranes.

References

- [1] Å. Rühling, G. Tyler, *J. Appl Ecol*, 1971, **8**, 497-507.
- [2] H. Harmens, A. D. Norris, R. G. Koerber, A. Buse, E. Steinnes, Å. Rühling, *Environ Pollut*, 2008, **151**, 368-376.
- [3] G. T. Goodman, T. M. Roberts, *Nature*, 1971, **231**, 287-292.
- [4] J. A. Fernández, J. R. Aboal, A. Carballeira, *Ecotoxicol. Environ. Saf.*, 2004, **59**, 76-83.
- [5] R. S. Clymo, *Annu. Bot.*, 1963, **27**, 309-324.
- [6] A. Mäkinen, *Suo Kirjalli*, 1977, **28**, 79-88.
- [7] M. Aničić, M. Tomašević, M. Tasić, S. Rajšić, A. Popović, M. V. Frontasyeva, S. Lierhagen, E. Steinnes, *J. Haz. Mat*, 2009, **171**, 182-188.
- [8] J. Martínez-Abaigar, E. Núñez-Oliveira, M. Sánchez-Díaz, *J. Bryol.*, 1994, **18**, 97-113.
- [9] J. López, R. Retuerto, A. Carballeira, *Ecol.*, 1997, **78**, 261-271.
- [10] J. R. Aboal, J. A. Couto, J. A. Fernández, A. Carballeira, *Environ. Pollut.*, 2008, **153**, 602-609.

DISPOSABLE ELECTROCHEMICAL SENSORS FOR HEAVY METALS DETECTION

F. Arduini¹, J. Quintana Calvo¹, A. Amine², G. Palleschi¹ and D. Moscone¹

¹*Dipartimento di Scienze e Tecnologie Chimiche, Università di Roma Tor Vergata, Via della Ricerca Scientifica, 00133 Rome, Italy (fabiana.arduini@uniroma2.it)*

²*Faculté des Sciences et Techniques, B.P.146, Mohammadia, Morocco*

Abstract

In this work, screen-printed electrodes (SPEs) were modified with nanostructured carbon material or bismuth film in order to obtain disposable sensor for mercury or lead, cadmium and zinc ions detection.

Introduction

Heavy metals are considered one of the main sources of pollution in the environment. For these reasons, heavy metals measurements are critically important in the areas of industrial, food and environmental safety as well as for clinical diagnosis and toxicology.

Analytical methods as flame atomic absorption spectrometry (FAAS), inductively coupled plasma mass spectrometry (ICP-MS), and inductively coupled plasma optical emission spectrometry (ICP OES) are the certified, standard techniques used for heavy metals determination [1], but they are characterized by high costs and complex instrumentation and are unsuitable for “applications in the field”. In addition, the analysis must be performed in a specialized laboratory by skilled personnel.

Electrochemical techniques have been widely recognized as a powerful technique for heavy metals detection, owing to its remarkable sensitivity that allows the detection of them at trace levels. It can also be readily coupled with inexpensive and easy-to-use instrumentation. For example, mercury electrode was largely applied for electrochemical stripping analysis, however the recent trend in chemistry (green chemistry) that aims to reduce and eliminate the use and generation of hazardous substances [2], has focused the attention on environmental friendly electrode materials.

Experimental

Amperometric measurements were carried out using a VA 641 amperometric detector (Metrohm, Herisau, Switzerland), connected to a *X-t* recorder (L250E, Linseis, Selb, Germany).

Cyclic voltammetry (CV) was performed using an Autolab electrochemical system (Eco Chemie, Utrecht, The Netherlands) equipped with PGSTAT-12 and GPES software (Eco Chemie, Utrecht, The Netherlands). The TEM images were recorded with a Philips CM120 Analytical instrument (LaB6). Micrographs of SPEs or CB-SPEs were obtained by scanning electron microscopy (SEM) using a

Hitachi model S-3200N microscope. Square-wave (SWV) voltammetry were carried out using a portable PalmSens Instrument (Palm Instruments, the Netherlands) in connection with a personal computer. All chemicals from commercial sources were of analytical grade and were obtained from Sigma (St. Louis, MO). Commercial CB N220 was obtained from Cabot Corporation (Ravenna, Italy). All the glass and plastic materials used for preparation and storage of samples and solutions were carefully cleaned by soaking in HNO₃ 3% (v/v) over 24 h, followed by thorough rinsing with copious amounts of ultrapure water.

Results and Discussion

For mercury detection, SPEs were modified with carbon black nanostructured material. Firstly, a stable dispersion of carbon black was prepared and characterized by the TEM technique (Fig.1A). The dispersion was then used to modify the screen printed electrodes (CB-SPEs) which were characterized by SEM technique (Fig.1B).

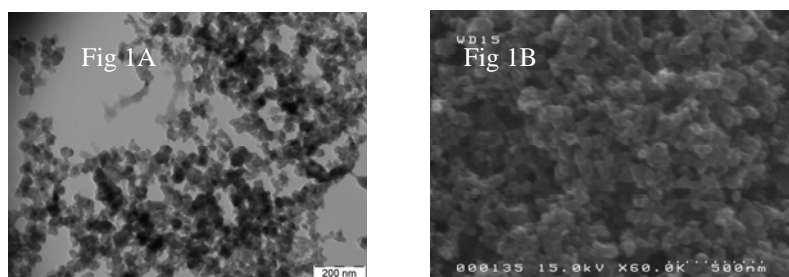


Fig.1 TEM images of the CB dispersion (Fig 1A), SEM imagine of CB-SPE (Fig 1B).

The CB-SPEs showed an enhanced oxidation current for several analytes such as NADH, cysteine, thiocholine and, in the case of epinephrine, norepinephrine and benzoquinone. The reduction of the peak-to-peak separation, compared with the bare SPE, was also evidenced. The CB-SPE was also challenged in an amperometric batch system with some analytes (for thiocholine a low detection limit=30 nM was obtained). The high sensitivity towards thiols allowed the development of a novel analytical method for mercury detection based on the effect of mercury ions on the thiocholine oxidation current. A decrease of thiocholine amperometric signal was in fact observed, due to the formation of a non-electroactive complex between thiocholine and Hg²⁺. This method allows the detection of mercury at concentration 5×10^{-9} M (1 ppb).

In the second part of this work, the SPE was modified with bismuth film in order to detect other heavy metals such as Zn²⁺, Pb²⁺ and Cd²⁺. In this case, the presence of bismuth coupled with the electrochemical anodic stripping technique allows the selective detection of these heavy metals in acetate buffer at ppb levels (Fig.2). The sensor was also challenged in media acid in order to apply this sensor

in milk acid treated. The treatment of milk optimised allows to detect milk contaminated with lead at concentration higher than 20 ppb (legal limit).

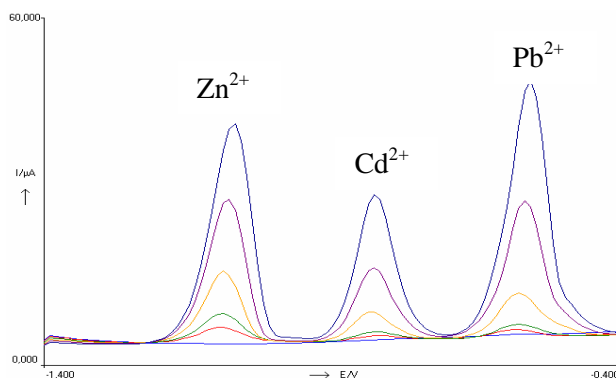


Fig.2 Anodic stripping voltammograms using SPE modified with Bi film without and with Zn²⁺, Cd²⁺ and Pb²⁺ at 5, 10, 25, 50 and 75 ppb in acetate buffer pH=4.6.

Conclusion

In this work we have demonstrated that the screen printed electrodes can be utilized as platform for heavy metals detection if properly modified with nanostructured material or bismuth film. These disposable sensors are characterized by the simplicity of the SPEs modification procedure, the low cost of carbon black or bismuth, the good analytical performances, the possibility for mass production of SPEs. In addition, the instrumentation and the devices used are miniaturisable and relatively inexpensive, and allow the heavy metals measurement “in situ” and “on-line” at very low concentrations.

References

- [1] M. A. Korn, J.B. de Nadrade, D. S. de Jesus, V. A. Leos, M. L. S. F. Bandeira, W. N. L. dos Santos, M. A. Bezerra, F. A. C. Amorin, A. S. Spuza, S. L. C. Ferreira, *Talanta*, 2006, **69**, 16-24.
- [2] S. Armenta, S. Garrigues, M. De la Guardia, *Trends. Anal. Chem.*, 2008, **27**, 497-511.

EFFECT OF ^{137}Cs AND ORGANIC COMPOUND DESORPTION FROM *C. islandica* LICHEN WITH ACID SOLUTIONS

A. Čučulović, J. Dimitrić-Marković¹, T. Brdarić¹,
D. Veselinović¹ and Š. S. Miljanić¹

*INEP-Institute for the Application of Nuclear Energy, Banatska 31b, Zemun,
anas@inep.co.yu, Serbia, ¹Faculty of Physical Chemistry, University of Belgrade,
P.O.Box 137, Belgrade, Serbia*

Abstract

Changes in absorbance and ^{137}Cs activity of solutions, obtained during successive extraction of *Cetararia islandica* lichen in acidic solutions (pH=4.61), were measured. Reduction of the ^{137}Cs content and absorbance was obtained. This can be presented with similar shaped curves indicating analogous processes and percentages of desorbed substances.

Introduction

Lichens are good bioaccumulators of pollutants (radionuclides, heavy metals, pesticides) in tissues or on the thallus surface [1,2]. Lichens pose remarkable ability for bioaccumulation of pollutants by their tissues or surfaces of thallus. *C. islandica* lichen was chosen as a model system for this investigation because of its increased use of radioactivity contaminations. Earlier research has shown that ^{137}Cs accumulated in lichen [3]. When exposed to surface waters or acid rain, lichens become secondary source of pollution by this radionuclide [4,5]. Besides ^{137}Cs and other inorganic substances, water or solutions are also used for the separate extraction of other organic substances from lichen tissue [6]. The purpose of this work was investigation of the simultaneous extraction of ^{137}Cs and organic substances using the same solutions simulating acid rain (pH =4.61).

Materials and Methods

200 cm³ of solutions with pH 4.61: (A) H₂SO₄, (B) HNO₃ and (C) H₂SO₄-HNO₃ mixture was poured over 10g of dry *C. islandica* lichen. Solutions (A) i.e. (B) were made by adding concentrated H₂SO₄ or HNO₃ to 200 cm³ of distilled water until the desired pH value of 4.61 was reached (pH meter Iskra MA 5730). The solution mixture (C) was obtained by mixing 100 cm³ of solution (A) and 100 cm³ of solution (B), with the same pH values. Samples were consecutively extracted with solutions in five steps and extraction series were repeated twice. Extractions were performed at room temperature during 24 hours. After each desorption, followed by filtration, lichen samples were dried at room temperature until constant mass was reached. Activity levels of ^{137}Cs were measured in samples before and after each extraction using ORTEC-AMETEK gamma spectrometer with 8192 channels,

efficiency 34% and resolution 1.65 keV (1.33 MeV ^{60}Co); measured time 1h; with a measurement error 5% (average value). Based on measurements the specific activities ^{137}Cs (Bq/kg) were calculated. Absorption spectra of solutions obtained by desorption were recorded using GPS spectrophotometer, Cintra 10e UV-Visible spectrometer, in wavelength range 200-500 nm, and recording speed of 1000 nm/min. Solutions (A); (B) or solution mixture (C) with pH 4.61, diluted in the ratio: 2.5 mL solution in 7.5 mL of distilled water were used as reference solutions.

Results and Discussion

The first extraction of *C. islandica* lichen using solutions (A), (B) or solution mixture (C) at pH 4.61 gave dark yellow solutions. During extraction sequence colour of solution changed from pale yellow to colorless. With the purpose of determining correlation between ^{137}Cs desorption and organic compounds spectrophotometric analysis of solutions obtained by lichen desorption was performed. The obtained absorption spectra of the solutions have similar band maximums that are in the range 270-285 nm. This is not spectra of complexes ^{137}Cs since this is alkaline metal and don't form complexes.

Table 1. ^{137}Cs content (%)* and solution absorbance values for the absorption band maximum (270-285 nm) in solutions obtained by extraction of *C. islandica* lichen using solutions (A), (B) and solution mixture (C) at pH 4.61.

pH 4.6 1	* ^{137}Cs content in solutions after each extraction (%)					Absorbance value (A) of the solution at the absorption band maximum after each extraction				
	I	II	III	IV	V	I	II	III	IV	V
(A)	27,9	12,4	11,1	1,3	1,2	0,77	0,26	0,10	0,08	0,09
(B)	24,0	11,8	9,3	1,9	5,1	1,22	0,21	0,12	0,10	0,09
(C)	27,4	10,6	3,2	3,3	1,9	0,95	0,26	0,11	0,08	0,11

* compared to initial ^{137}Cs activity in lichens

Table 1 gives the ^{137}Cs content (%) and absorbance values of solutions (A), (B) and solution mixture (C) at the absorption maximum, in solutions obtained after each solution extraction of lichen. Conclusion can be made that the highest ^{137}Cs content (%), and also absorbance were obtained for the first desorption solution. The ^{137}Cs content decreases with the number of desorptions and similar occurs for absorbance in the solution. There are still not enough data on the type of extracted organic compound to be able to define it with a good enough precision. This is theme for specific next investigation.

Figure 1 shows the change of absorbance (A) on the absorbance band maximum and the amount of extracted ^{137}Cs in the extraction solution with each consecutive extraction, n_x , of *C. islandica* lichen using solution (C). The curves showing the change in the amount of extracted ^{137}Cs with the extraction number and the curves showing absorption changes on the absorption band maximum, i.e. concentration

of the extracted organic substance with the extraction number are very similar. Figure 2 shows the absorption spectrum of solution mixture (C).

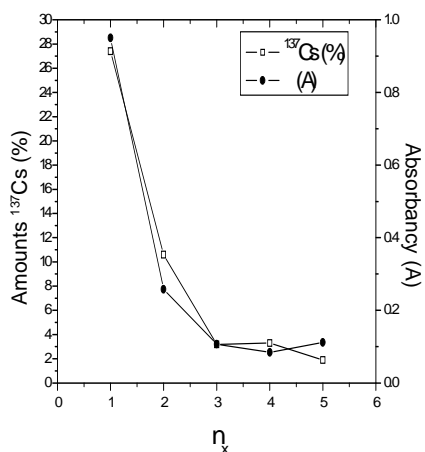


Fig.1

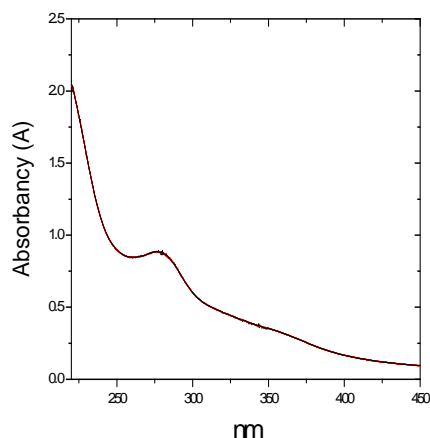


Fig.2

Conclusion

The obtained results lead to the conclusion that the extracted organic compound was most probably sorbed in a way similar to ^{137}Cs and is one of the lichen constitutive organic compounds.

References

- [1] M. E. Conti, G. Cecchetti, Environ. Pollut., 2001, **114**, 309-371.
- [2] A. Čučulović, D. Veselinović, Š. S. Miljanić, J. Serb. Chem. Soc., 2007, **72**, 673-678.
- [3] J. E. Sloof, B. T. Wolterbeek, J. Environ. Radioactivity, 1992, **16**, 229-242
- [4] A. Čučulović, M. S. Pavlović, D. Veselinović, Š. S. Miljanić, J. Serb. Chem. Soc., 2008, **73**, 405-413.
- [5] A. Čučulović, D. Veselinović, Š. S. Miljanić, J. Serb. Chem. Soc., 2009, **74**, 663-668.
- [6] S. Huneck, I. Yoshimura, Identification of lichen substances, Springer, Berlin, 1996.

METAL CONTENT IN DIFFERENT SIZES OF MUSSELS COLLECTED FROM THE SEAWALLS IN OSAKA BAY, JAPAN

V. Jovanović^{1*}, Y. Kozuki², R. Yamanaka² and M. Miyoshi¹

¹*Ecosystem Engineering, Graduate school of Engineering, University of Tokushima, Japan;*

²*Ecosystem Design, Institute of Technology and Science, University of Tokushima, Japan*

Abstract

Metal content in soft tissues and shells of mussels *Mytilus galloprovincialis* attached to the seawalls of Amagasaki port were analyzed using atomic absorption spectrometry. Regression analysis showed that metals were accumulated in the mussels at the same rate as biomass, *i.e.* that the food pathway from surrounding water prevail in uptake and storage of these metals by mussels.

Introduction

As a consequence of land reclamation in Japan, artificial structures occupy more than 30 % of whole coastline of Japan, and over 95% in Osaka Bay, where reclamation has taken place at such a rapid pace that the natural coastline is no longer discernible. Vertical coastal structures, breakwaters and quays, became habitat for sessile filter feeders confined to hard substrates. Introduced as alien species, Mediterranean mussel, *Mytilus galloprovincialis*, adapted excellently to a new landscape and now forms colonies on the seawalls of Osaka Bay. The growth of these bivalves is due to their great capacity to filter the water column, which also exposes them to dangerous contaminants, including heavy metals. This means that mussels can accumulate chemicals dissolved in sea water or those associated with material in suspension. Finally, due to decaying of dead mussels fallen from the seawalls metals and other toxicants are likely to escape into the receiving waters.

In this work we report a part of the results of our extensive study of the role of biological processes in the material dynamics near the coastal structures by determining the metal concentrations in the soft tissue and in the shells of mussels *Mytilus* collected in Amagasaki port in summer of 2007 and 2008. Amagasaki port was chosen as one of the areas with the worst environmental conditions in Osaka Bay. At the time of our experiments (late July 2007 and early August 2008) biomass is large and the activity of the mussels, due to increased concentration of phytoplankton, is the highest.

Experimental

At intervals of 0.5 m in depth, living biota was scraped off the quaywall from surface denoted with 30 x 30 cm sampling frame. Obtained mussel samples were packed into seal-tight prewashed polyethylene bags which are then stored on blue ice in a cooler box until return to the laboratory where all pretreatments and analytical procedures were performed. Pooled samples were used to obtain enough specimens for the analysis.

* Permanent address: IHTM, University of Belgrade, Belgrade, Serbia

Determination of metal content was carried out using Perkin Elmer atomic absorption spectrometer, model *AAnalyst 800* by employing both the flame (air-C₂H₂) and graphite furnace (TGHA™), depending on metal and metal concentration. Analytical quality assurance was performed by measurements of two certified referent materials for trace metals in mussel tissue (GBW 08571) and lobster hepatopancreas (TORT-2).

Results and discussion

Concentrations of analyzed metals in the soft tissues of *Mytilus galloprovincialis*, distributed through the size range of 5–40 mm, are presented in Table 1.

Table 1. Mean metal concentration and standard deviation ($\mu\text{g}\cdot\text{g}^{-1}$ dry wt) in mussel tissue for particular size classes (mm).

No. of samples*	Size classes	Fe	Mn	Zn	Cu	Cd	Cr	Pb
2 (616)	5-8	318±41	203±19	153±17	11.1±2.3	1.28±0.23	0.92±0.17	0.76±0.15
2 (435)	9-12	297±47	192±24	149±22	11.1±1.9	1.59±0.20	0.74±0.15	0.74±0.14
3 (310)	3-16	288±50	187±35	144±26	10.0±1.9	1.29±0.31	0.58±0.09	0.71±0.22
3 (199)	7-20	213±23	131±25	136±19	9.3±2.1	1.43±0.60	0.55±0.12	0.69±0.17
4 (203)	21-24	215±26	138±18	136±15	9.6±1.6	2.11±0.20	0.60±0.19	0.73±0.14
4 (182)	25-28	189±15	107±19	132±11	9.8±1.8	1.88±0.32	0.45±0.10	0.67±0.12
4 (121)	29-32	173±14	79.2±17.2	128±12	9.3±1.4	1.61±0.24	0.39±0.08	0.68±0.13
4 (87)	33-36	177±28	81.0±12.8	122±12	8.8±1.0	1.30±0.29	0.42±0.14	0.64±0.22
3 (25)	37-40	130±22	60.6±10.3	117±21	7.3±1.4	0.82±0.13	0.31±0.10	0.70±0.20
Range		115-333	49-219	87-160	6.8-11.5	0.72-2.32	0.25-0.96	0.58-0.78
Mean		225±64	133±53	136±16	9.6±1.9	1.50±0.42	0.56±0.19	0.70±0.15
Median		209	127	136	9.7	1.50	0.50	0.70

*Numbers of pooled samples and specimens are given in parentheses.

Ranges, mean values and medians were added in the bottom rows.

Metal concentrations were in the range as those found for mussels from the other urban areas and ports [1-2] and decrease in the order: Fe>Zn~Mn>>Cu>Cd>Pb>Cr as a consequence of their bioavailability at the studied site. The correlations between all metal burdens in tissues were found to be significant (at 0.01 level, Spearman's correlation matrix) except for Cd. Observed relationships can be attributed to similarity of physical and chemical variables affecting the metals at the same sample site [3], but also to the same food type. Uptake and storage of physiologically non-essential metal Cd took place according to different mechanism since it is not correlated with neither one of the analyzed metals.

Study of the relation between tissue metal content ($\mu\text{g}/\text{individual dry wt}$) and shell length (in mm) using power function [4-5] showed that variations of metal content with size are caused mainly by weight variation. It appears that the food pathway predominates in accumulating of these metals from surrounding water.

Table 2 contains the metal concentrations in the shells of different size classes of collected mussels.

Table 2. Mean metal concentration ($\mu\text{g}\cdot\text{g}^{-1}$ dry wt) and standard deviation in mussel shells for particular size classes (5-40 mm)

No. of Sampl*	Size clas.	Fe	Mn	Zn	Cu	Cd	Cr	Pb
3 (616)	5-8	34.6±5.3	92.3±14.1	6.97±1.31	0.79±0.12	0.08±0.02	0.31±0.10	n.d.
3 (435)	9-12	32.3±4.2	87.3±15.5	6.75±1.18	0.79±0.16	0.10±0.02	0.25±0.03	n.d.
3 (310)	13-16	31.3±5.5	84.9±16.0	6.53±0.89	0.71±0.13	0.08±0.02	0.19±0.03	n.d.
4 (199)	17-20	20.6±1.6	59.7±11.5	6.18±0.85	0.66±0.10	0.09±0.04	0.18±0.04	n.d.
4 (203)	21-24	23.3±2.8	62.8±8.1	6.17±1.12	0.69±0.12	0.13±0.03	0.20±0.06	n.d.
4 (182)	25-28	23.1±1.4	36.0±7.8	6.00±1.23	0.70±0.15	0.12±0.02	0.15±0.04	n.d.
4 (121)	29-32	18.8±1.6	48.7±8.6	5.81±1.55	0.63±0.13	0.10±0.02	0.13±0.03	n.d.
4 (87)	33-36	19.2±3.1	36.8±5.7	5.32±1.24	0.67±0.13	0.08±0.02	0.14±0.03	n.d.
3 (25)	37-40	14.1±1.4	27.5±3.8	5.33±1.40	0.52±0.14	0.05±0.01	0.10±0.03	n.d.
Range		13.9-39.3	24.6-105.7	4.86-8.06	0.62-0.89	0.05-0.15	0.12-0.30	
Mean		24.1±7.0	59.6±24.3	6.12±0.58	0.68±0.08	0.09±0.02	0.18±0.06	
PF		9.2±1.5	2.2±0.3	22.1±1.7	16.1±2.2	14.0±1.4	3.0±0.6	

*Numbers of pooled samples and specimens are given in parentheses; n.d.-not detected

Range, Mean values and Partitioning factor, PF (ratios of tissue metals and shell metals).

The shells of analyzed *Mytilus galloprovincialis*, similarly to the soft tissues, contain the highest levels of Mn, Fe and Zn, but the order of decreasing concentration is somewhat different: Mn>Fe>Zn>Cu>Cr>>Cd. Considering the all analyzed metals, Mn and Cr show the greatest propensity to be incorporated into the shell (PF = 2.2 and 3 respectively, Table 3-3).

Conclusion

Results showed that the mean metal concentration per dry gram of soft tissue and shells is higher in the smaller size classes of mussel. The relationship between metal content and body size, modeled by power function, indicated importance of the food pathway on accumulation of metals in mussels.

Incorporation of metals into the soft tissues is much easier than in the shells. Among analyzed metals, Mn and Cr show the greatest propensity to be incorporated into the shell (PF = 2.2 and 3 respectively).

References

- [1] D. J. H. Phillips, *Marin Biol.*, 1976, **38**, 59–69.
- [2] V. Besada, J. Fumega and A. Vaamonde, *Sci. Total. Envir.*, 2002, **288**, 239–253.
- [3] P. Szefer., K. Frelek K. Szefer, C. B. Lee, B. S. Kim, J. Warzocha, I. Zdrojewska and T. Ciesielski, *Environ. Pol.*, 2002, **120**, 423–444.
- [4] C. R. Boyden., *Nature* 1974, **251**, 311–314.
- [5] W.-X. Wang and N. S. Fisher, *Mar. Ecol. Pro. Ser.*, 1997. **161**, 103–115.

As LEVEL IN TREE-RINGS AND BARK OF LINDEN (*Tilia Platyphyllos* Scop.) DETERMINED BY U-SHAPED DC ARC

I. Milošević¹, D.M. Marković², D. Vilotić³ and Lj. Ignjatović⁴

¹*Institute of physics, P.O. Box 68, Pregrevica 118, Belgrade, Serbia.*

²*The Faculty of Applied Ecology, Singidunum University, Lazarevački drum 13, Belgrade, Serbia*

³*Faculty of Forestry, University of Belgrade, Kneza Višeslava 1, Belgrade, Serbia.*

⁴*Faculty of Physical Chemistry, University of Belgrade, Studentski trg 12-16, Belgrade, Serbia*

Abstract

As an indicator of environmental pollution we collected tree-rings and bark of *Tilia Platyphyllos* Scop. from four sampling locations in Serbia. Arsenic was determined with a spectrochemical method that has U-shaped DC arc as excitation source. The highest concentration of As in tree-rings was found at the location Debeli Lug and for the bark it was found at the location Zemun. A continuous activity of copper mine for the location Debeli Lug and a large number of local furnaces (homes that use coal as fuel) at the location Zemun can be a possible reason for these.

Introduction

Heavy metals are long-term contaminants with the ability to accumulate in soil and plants and have no natural way to be removed [1]. The use of vegetation monitors is well known and widely reported in literature. In recent years, however, use of tree-rings and tree barks as monitors is on the increase [2, 3, 4, 5, 6, 7]. Tree-rings represent a unique, widely available, cheap and simple source of long-term data for monitoring heavy metal levels.

A U-shaped low current argon DC arc with aerosol supply was applied as the

Table 1. Experimental operating conditions of our spectrochemical method

Excitation source	U-shaped DC arc
Spectrograph	PGS-2, Carl Zeiss, Jena
Gratings	Carl Zeiss, 2100 gr.mm ⁻¹ As
Photomultiplier	Hamamatsu, R-3788
Ad conversion card	ED-300
Arc current	7.5 A
Argon flow	3dm ³ min ⁻¹
Wavelength for As	234.98 nm

excitation source. The experimental operational conditions of our spectrochemical method are presented in Table 1. A series of reference solutions were prepared in the range from 1 to 1000 ng mL⁻¹, by appropriate dilution of the stock solutions (1 mg

mL⁻¹, Merck). Each solution contained 0.5% KCl as spectroscopic buffer.

Tree-ring samples were collected in March 2007 from four locations: Debeli Lug, Zemun, Obrenovac and Fruška Gora. Debeli Lug is forestry area in the municipality of Majdanpek. Zemun is a one of the municipalities which constitute the city of Belgrade, samples were taken from the Ugrinovacka Street. Obrenovac is situated 30km south-west of Belgrade near bends of the river Sava to the north

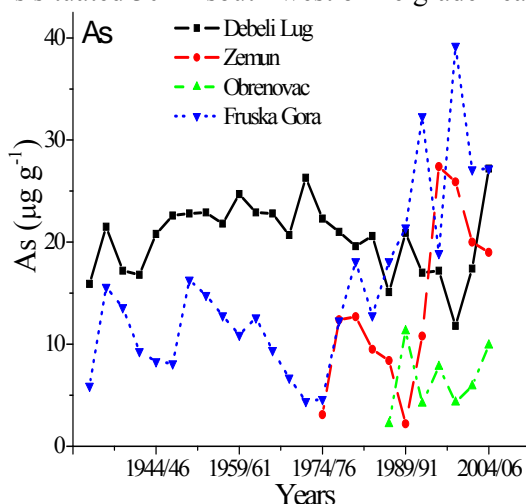


Fig.1. Trends in mean As concentrations ($\mu\text{g g}^{-1}$) for four sampling locations

Available, total concentrations (ISO 11460, ISO 11047) and pH (ISO 10 390) were measured in soil.

(samples were taken from the Vojvoda Mistic Street). Fruška Gora is a mountain in the north of Serbia.

Each linden core was divided into 3 year segments starting from 1932 for trees from Debeli Lug and Fruška Gora, from 1974 for trees from Zemun and from 1986 for those from Obrenovac. Bark was taken as a separate sample. Sample preparation for chemical analysis was as Orlandi et al. [8] proposed. Surface soil (0-10 cm depth) samples were collected from four sampling locations. Available, total concentrations (ISO 11460, ISO

Results and discussion

Arsenic was determined in tree-rings and bark of linden (*Tilia platyphillos Scop.*) collected on four locations with an AES spectrochemical method that has U-shaped DC arc as excitation source. Mean As concentrations in tree-rings for four sampling locations are shown in Fig. 1. From Fig. 1 it can be seen slow increase in As concentrations from 1974/76 on the Zemun and Fruška Gora locations. For the locations Obrenovac and Debeli Lug it can not be seen increase but the existence of maxima of As concentrations for the period 1989/91, 2004/06 on Obrenovac location and 1971/73, 2004/06 on the location Debeli Lug.

Average As concentrations in the tree-rings (wood) and tree bark of linden are shown in Fig. 2. According to the results shown in Fig. 2 we can observe elevated

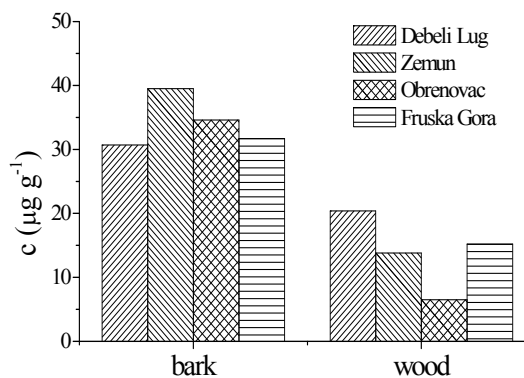


Fig.2. Average As concentrations ($\mu\text{g g}^{-1}$) in bark and tree-rings of linden for four sampling location

content of As in tree-rings at all four locations. Bark contains higher concentrations of As than tree-rings.

The highest concentration of As in tree-rings was found at the location Debeli

Table 2. As total and available concentration in soils ($\mu\text{g g}^{-1}$) and soil pH for four sampling locations.

As	Total concentration	Available concentration	pH	
			H ₂ O	KCl
Debeli Lug	52.4	7.0	5.8	4.1
Zemun	16.0	0.1	7.2	6.8
Obrenovac	25.4	1.9	6.7	6.5
Fruska Gora	17.3	0.1	7.0	6.4

Lug, than at the locations Fruška Gora, Zemun and Obrenovac.

In the case of the bark the highest As concentration was found at the location Zemun, than at the locations Obrenovac, Fruška Gora and Debeli Lug. Elevated content

of As in tree-rings at the Debeli Lug location can present an answer to the continuous activity of copper mine in the vicinity of Majdanpek for many years, while elevated content in bark on the Zemun location indicates on the influence of a large number of local furnaces (homes that use coal as fuel).

Total and available concentration of As in soils and soil pH are shown in Table 2. pH has a large influence on the availability of elements in soil. Thus, the availability of As increases with decreasing pH. As concentration in tree-rings is to some extent proportional to the concentration of these elements in the soil.

Conclusion

In this study As contents in linden tree-rings and bark together with soil on four locations were monitored. Bark contains higher concentrations of As than tree-rings in all cases. It can be a potential monitor of atmospheric pollution. pH has a large influence on the availability of elements in soil, and in tree-rings.

References

- [1] D. Butkus, E. Baltrėnaitė, *Ekologija*, 2007, **53**, 29-36.
- [2] K. L. Padilla, K. A. Anderson, *Chemosphere*, 2002, **49**, 575-585.
- [3] G. Liu, Y. Zhang, Y. Qi, L. Zheng, Y. Chen, Z. Peng, *Environ. Monit. Assess.*, 2007, **133**, 99-103.
- [4] L. Harju, K. E. Saarela, J., Rajantler, J.O. Lill, A. Lindroos, S.J. Heselius, *Nuclear Instrum. Methods B*, 2002, **189**, 163-167.
- [5] D. M. Marković, I. Novović, D. Vilotić, Lj. Ignjatović, *Environ. Monit. Assess.*, 2009, **151**, 377-382.
- [6] D. M. Marković, I. Novović, D. Vilotić, Lj. Ignjatović, *Russian J Phys.Chem.*, 2007, **81**, 1493-1496.
- [7] Z. Cheng, B. M. Buckley, B. Katz, W. Wright, R. Bailey, K. T. Smith, J. Li, A. Curtis, A. Geen, *Sci. Total. Environ.*, 2007, **376**, 324-334.
- [8] M. Orlandi, M. Pelfini, M. Pavan, M. Santilli, M. P. Colombini, *Microchem. J.*, 2002, **73**, 237-244.

DETERMINATION OF LEAD IN LINDEN BARK AND WOOD BY U-SHAPED DC ARC

D. M. Marković¹, I. Milošević², D. Vilotić³ and Lj. Ignjatović⁴

¹*The Faculty of Applied Ecology, Singidunum University, Lazarevački drum 13, Belgrade, Serbia*

²*Institute of physics, P.O. Box 68, Pregrevica 118, Belgrade, Serbia*

³*Faculty of Forestry, University of Belgrade, Kneza Višeslava 1, Belgrade, Serbia.*

⁴*Faculty of Physical Chemistry, University of Belgrade, Studentski trg 12-16, Belgrade, Serbia*

Abstract

The U-shaped DC arc with aerosol supply was applied for the determination of Pb in tree-rings and bark of *Tilia Platyphyllos* Scop. from four sampling locations in Serbia. Increased concentrations of Pb in tree-rings and barks of linden were found at the locations Fruška Gora and Zemun. Proximity to the road to Novi Sad at both locations can be a possible reason for these.

Introduction

The emission of heavy metals to the environment is one of the most serious environmental problems and the content of these elements tends to increase. Many reports have shown that environmental lead loadings are related to traffic volume and that lead levels in soils and vegetation rise as average daily traffic increases [1]. Trees can be used as sensitive biomonitors to record local and global environmental change over a considerable period of time [2, 3, 4, 5, 6]. Different parts of trees have been used to monitor heavy metal pollution in the environment e.g. leaves, bark and tree-rings.

A U-shaped low current argon DC arc with aerosol supply was applied as the excitation source. A laboratory modified spectrograph PGS-2 (Carl Zeiss, Jena) with holographic grating (Spectrogon, 2100 gr.mm⁻¹) was used as spectrometer. The intensity of the analyte spectral line was recorded by a photomultiplier (Hamamatsu, R-3788) and AD conversion card (ED-300) connected to a PC. The recorded signal intensities were accumulated during the integration time of 20s for Pb by application of the appropriate computer program. Spectral line intensities were measured for Pb I ($\lambda = 405.78$ nm) at 4 mm from the axis of the arc. A series of reference solutions were prepared in the range from 1 to 1000 ng mL⁻¹, by appropriate dilution of the stock solutions (1 mg mL⁻¹, Merck). Each solution contained 0.5% KCl as spectroscopic buffer.

Tree-ring samples were collected in March 2007 from four locations: Debeli Lug, Zemun, Obrenovac and Fruška Gora. Debeli Lug is forestry area in the municipality of Majdanpek. Zemun is a one of the municipalities which constitute the city of Belgrade, samples were taken from the Ugrinovacka Street. Obrenovac is situated 30km south-west of Belgrade near bends of the river Sava to the north

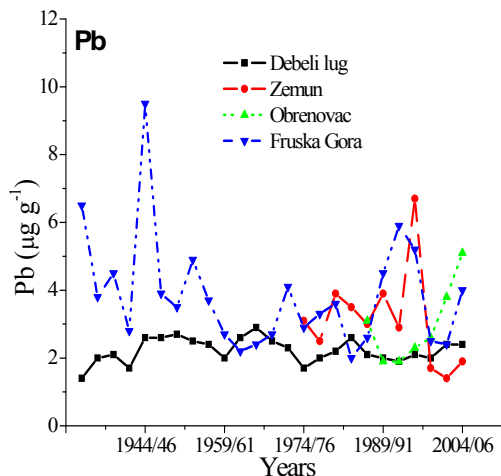


Fig.1. Trends in mean Pb concentrations ($\mu\text{g g}^{-1}$) for four sampling locations

Mean Pb concentration found in linden tree-rings for four sampling locations are shown in Fig. 1. From Fig. 1. it can be seen increased content of Pb in tree-rings of linden at the locations Zemun and Fruška Gora. At the location Fruška Gora Kadović et al., 2000 [8] also noticed increased Pb content in their investigations of the bark and leaves of the sessile oak. Slow increase of Pb concentration from 1998/2000 in tree-rings of linden can be seen at the location Obrenovac. At the Zemun and Fruška Gora locations we can observe the existence of maxima of Pb concentration. Most pronounced maxima at the Zemun location occurs in the periode 1995/97, and for the Fruška Gora in the periode 1944/46 and 1992/94.

Average Pb concentrations in the tree-rings (wood) and tree bark of linden are shown in Fig. 2. According to the results shown in

Fig. 2 we can observe that bark contains higher concentrations of Pb than tree-rings. The highest concentration of Pb in tree-rings was found at the location Fruška Gora, than at the locations Zemun, Obrenovac and Debeli Lug. In the case of the bark the highest Pb concentration was found at the location Zemun, than at the locations Fruška Gora, Obrenovac and Debeli Lug. Increased concentration of

(samples were taken from the Vojvoda Misic Street). Fruška Gora is a mountain in the north of Serbia.

Each linden core was divided into 3 year segments starting from 1932 for trees from Debeli Lug and Fruška Gora, from 1974 for trees from Zemun and from 1986 for those from Obrenovac. Bark was taken as a separate sample. Sample preparation for chemical analysis was as Orlandi et al. [7] proposed. Surface soil (0-10 cm depth) samples were collected from four sampling locations. Available, total concentrations (ISO 11460, ISO 11047) and pH (ISO 10390) were measured in soil.

Results and discussion

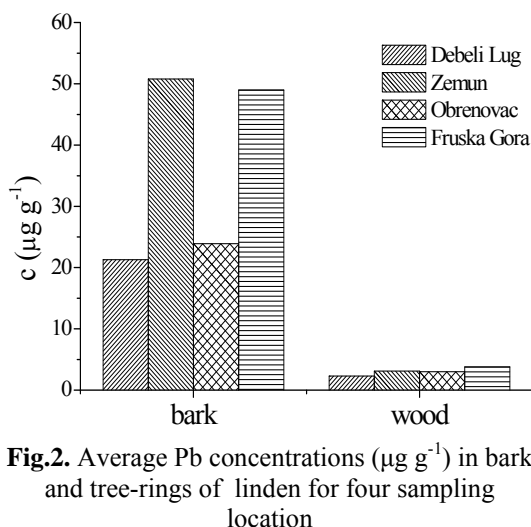


Fig.2. Average Pb concentrations ($\mu\text{g g}^{-1}$) in bark and tree-rings of linden for four sampling location

Pb in tree-rings and bark of linden at the locations Zemun and Fruška Gora can be a consequence of the increased road traffic (nearby is the road for Novi Sad).

Total and available concentration of Pb in soils and soil pH are shown in Table

Table 1. Pb total and available concentration in soils ($\mu\text{g g}^{-1}$) and soil pH for four sampling locations.

Pb	Total concentration	Available concentration	pH	
			H ₂ O	KCl
Debeli Lug	48.5	8.7	5.8	4.1
Zemun	101.3	21.3	7.2	6.8
Obrenovac	111.0	20.4	6.7	6.5
Fruska Gora	56.3	22.1	7.0	6.4

1. The highest total Pb is at the location Obrenovac, than at the locations Zemun and Fruška Gora while available Pb is at the location Fruška Gora than Zemun and Obrenovac. Pb concentration in tree-rings is to some extent

proportional to the concentration of these elements in the soil. Total and available values for Pb in soil at the locations Zemun, Obrenovac and Fruška Gora are similar which is reflected in the content of Pb in the growth rings for that site which is also similar.

Conclusion

In this study Pb contents in linden tree-rings and bark together with soil on four locations were monitored. Bark contains higher concentrations of Pb than tree-rings in all cases. Increased concentration of Pb in tree-rings and bark of linden at the locations Zemun and Fruška Gora can be a consequence of the increased road traffic. Total and available values for Pb in soil at the locations Zemun, Obrenovac and Fruška Gora are similar which is reflected in the content of Pb in the tree-rings for that site which is also similar.

References

- [1] O. O. Odokoya, T. A. Arowolo, O. Bamgose, *Environ. International*, 2000, **26**, 11-16.
- [2] T. El-Hasan, H. Al-Omari, A. Jiries, F. Al-Nasir, *Environ. International*, 2002, **28**, 513-519.
- [3] K. E. Saarela, L. Harju, J., Rajander, J. O. Lill, S. J. Heselius, A. Lindroos, K. Mattsson, *Sci. Total Environ.*, 2005, **343**, 231-241.
- [4] D. M. Marković, I. Novović, D. Vilotić, Lj. Ignjatović, *Environ. Monit. Assess.*, 2009, **151**, 377-382.
- [5] D. M. Marković, I. Novović, D. Vilotić, Lj. Ignjatović, *Russian J Phys.Chem.*, 2007, **81**, 1493-1496.
- [6] S. Rossini Oliva, M. D. Mingorance, *Chemosphere*, 2006, **65**, 177-182.
- [7] M. Orlandi, M. Pelfini, M. Pavan, M. Santilli, M. P. Colombini, *Microchem. J.*, 2002, **73**, 237-244.
- [8] R. Kadović, M. Knežević, M. Medarević, S. Belanović, *Šumarstvo*, 2000, **6**, 37-45.

SIZE DISTRIBUTED AEROSOL MASS CONCENTRATION AND CHEMICAL COMPOSITION IN BELGRADE DURING SUMMER-AUTUMN 2008

A. Gambaro,¹ D. Đorđević,² A. M. Stortini,¹ A. Mihajlidi-Zelić,³
Lj. Ignjatović,⁴ D. Relić,³ J. Huremović⁵ and T. Milovanović³

¹*Environmental Sciences Department, Ca' Foscari University of Venice, 30123
Venice, Italy*

²*IChTM – Centre of chemistry, University of Belgrade, Studentski trg 12–16, 11000
Belgrade, Serbia (dragadj@chem.bg.ac.rs)*

³*Faculty of Chemistry, University of Belgrade, Studentski trg 12–16, 11000
Belgrade, Serbia*

⁴*Faculty of Physical Chemistry, Studentski trg 12–16, 11000 Belgrade, Serbia,*

⁵*Analytical Chemistry Department, University of Sarajevo, 71000 Sarajevo,
Bosnia and Herzegovina*

Abstract

Physical and chemical characterizations of the atmospheric aerosol were carried out in urban area of Belgrade. This work focuses on the size-segregated aerosol chemical composition observed during the summer-autumn 2008th. Aerosol samples were submitted to gravimetric and chemical analyses. Mean random uncertainties associated with determination of Na⁺, NH₄⁺, K⁺, Mg²⁺, Ca²⁺, Cl⁻, NO₃⁻ and SO₄²⁻ were assessed.

Introduction

Due to the various atmospheric lifetimes because of various sizes of particles and complex chemical composition of atmospheric aerosols, their global distribution shows large regional differences and their properties are poorly known. Fine particles are produced by combustion processes, by coagulation of smaller particles, and by condensation of low-vapor-pressure products of gas-phase reactions. Mechanical action of the wind on the Earth's surface emits sea salt, soil dust, and vegetation debris into the atmosphere. These aerosols consist mainly of coarse particles ($1 < D_p < 10 \mu\text{m}$) but fine particles ($D_p < 1 \mu\text{m}$) are difficult to generate mechanically because they have large area-to-volume ratios and hence their surface tension per unit aerosol volume is high. Particles coarser than $10 \mu\text{m}$ are not easily lifted by the wind and have short atmospheric lifetimes because of their large sedimentation [1].

Sulphate, nitrate and ammonium ions are formed in the atmosphere in gas-particle conversion processes. Sulphates represent one of the main components of atmospheric aerosols. They are mainly obtained by the oxidation of SO₂, which was either directly emitted to the atmosphere (burning of fossil fuels, industrial processes, volcanoes, combustion of biomasses) or by the oxidation of lower

oxidation state sulphur compounds, mainly DMS, which is the dominant source of SO₂ in marine atmospheres. The main sources of NO_x are combustion of fossil fuels in high temperature processes (traffic, power plants, industry, and domestic fire-boxes), soil (microbiological activity), combustion of biomass, lightening [2] *etc.* The vapor pressure ensures that H₂SO₄ and HNO₃ are in the particulate phase in atmospheric conditions (with exception of HNO₃ in warm condition). Sulphate and nitrate aerosols can also be obtained by reaction of HNO₃ and H₂SO₄ in presence of salts or ammonia results in the neutralization of the acids and, together with NaCl from marine aerosol[2]. The sulphates in the atmosphere can also originate from other sources: *e.g.*, primary marine aerosol, gypsum CaSO₄ resuspended dust from the Sahara[3], *etc.*

The ammonia in precipitation is originating from the particulate phase. Seinfeld[4] reported that generally in the atmosphere ammonia occurs as (NH₄)₂(SO₄) but it is also possible to found in the form NH₄NO₃ [5]. The residence time of SO₂ and NO_x in the troposphere is 1 – 3 days[3], while the residence time of sulphates and nitrates is somewhat longer: for nitrates it is 3-9 days[3].

Very little is still known about the aerosol forcing related to the effect of particles on the size and number of cloud droplets [6].

This work focuses on the size-segregated aerosol chemical composition observed during the summer-autumn 2008th.

Experimental

During the June – December 2008th within the SIMCA project (INTERREG/CARDS-PHARE Adriatic New Neighborhood Programme) size-segregated aerosol was sampled using 6-stage High Volume Cascade Impactor. During the measured campaign were taken 32 samples every 6th day. Sampling duration for each sample was 48 hours. Particle size distribution in the size range 0.0 to 0.49 μm, 0.49 to 0.95 μm, 0.95 to 1.5 μm, 1.5 to 3.0 μm, 3.0 to 7.2 μm and > 7.2 μm in urban area of Belgrade were measured. Aerosol mass concentrations are determined by gravimetric measurements (m_{GM}). One-fifth of filter sample were extracted in 5 mL of ultra-pure water and analyzed by ion chromatography Metrohm for Na⁺, NH₄⁺, K⁺, Mg²⁺, Ca²⁺, Cl⁻, NO₃⁻ and SO₄²⁻.

Results and Discussion

The obtained results shown in Table 2 were done with the precisions 8% for Cl⁻, 2% for NO₃⁻, 2% for SO₄²⁻, 3.2% for Na⁺, 18% for NH₄⁺, 24% for Ca²⁺, 3% for Mg²⁺ and 8% for K⁺.

Table 1. Aerosol mass concentrations m_{GM} ($\mu\text{g m}^{-3}$), mean \pm standard deviation, of particles distributed through Dp intervals in urban area of Belgrade obtained in measured campaign.

Dp	0 to 0.49 μm	0.49 to 0.95 μm	0.95 to 1.5 μm	1.5 to 3.0 μm	3.0 to 7.2 μm	> 7.2 μm	Total
m_{GM}	2.4±1.5	4.4 ± 2.3	3.0±1.6	2.9±1.4	3.6±1.6	10.3±6.3	25.0±13.9

Table 2. Mass concentrations ($ng\ m^{-3}$), mean \pm standard deviation, of Cl^- , SO_4^{2-} , NO_3^- , NH_4^+ , Na^+ , K^+ , Mg^{2+} and Ca^{2+} distributed through Dp intervals in urban area of Belgrade obtained in measured campaign.

	0 to 0.49 μm	0.49 to 0.95 μm	0.95 to 1.5 μm	1.5 to 3.0 μm	3.0 to 7.2 μm	> 7.2 μm
Cl^-	21.1 \pm 20.1	11.5 \pm 12.0	9.7 \pm 8.8	8.0 \pm 7.0	12.3 \pm 11.1	6.5 \pm 5.9
SO_4^{2-}	226.8 \pm 227.2	86.7 \pm 96.2	38.9 \pm 48.9	17.9 \pm 20.4	22.1 \pm 20.3	8.5 \pm 7.8
NO_3^-	0.4 \pm 0.3					
NH_4^+	332.0 \pm 213.0	29.2 \pm 11.1	49.5 \pm 28.3	30.9 \pm 14.0	86.0 \pm 51.9	21.4 \pm 8.9
Na^+		16.3 \pm 19.5		7.0 \pm 5.6	5.0 \pm 5.5	
K^+	71.7 \pm 44.9	19.0 \pm 4.2	9.4 \pm 3.5	13.0 \pm 17.0		
Mg^{2+}	26.8 \pm 26.8					
Ca^{2+}	21.4 \pm 14.0	5.0 \pm 1.8	8.1 \pm 7.4	7.9 \pm 5.6	19.2 \pm 7.6	4.4 \pm 2.2

Conclusion

The largest contribution of SO_4^{2-} and NH_4^+ was in fine particles indicating main sources that are gas precursors SO_2 and NO_3 .

References

- [1] J. J. Daniel, Chapter 4: Atmospheric transport in: Introduction to Atmospheric chemistry, Princeton University Press, Chichester, 1999.
- [2] J. H. Seinfeld, S. N. Pandis, Atmospheric Chemistry and Physics From Air Pollution to Climate Change, John Wiley & Sons, Inc, New York, 1998, 363-381.
- [3] S. Glavas, N. Moschonas, Origin of observed acidic-alkaline rains in a wet-only precipitation study, in a Mediterranean coastal site, Patras, Greece. Atmospheric Environment, 2002, **36**, 3089-3099.
- [4] J. H. Seinfeld, Atmospheric Chemistry and Physics of Air Pollution, Wiley, New York, 1986.
- [5] V. Yoboue, C. Galy-Lacaux, J. P. Lacaux, S. Silue, Rainwater Chemistry and Wet Deposition over the Wet Savanna Ecosystem of Lamto (Côte d'Ivoire). Journal of Atmospheric Chemistry, 2005, **52**, 117-141.
- [6] J.-P. Putaud, R. Van Dingenen, A. Dell'Acqua, F. Raes, E. Matta, S. Decesari, M.C. Facchini, S. Fuzzi, Size-segregated aerosol mass closure and chemical composition in Monte Cimone (I) during MINATROC. Atmospheric Chemistry and Physics, 2004, **4**, 889-902.

THE INCORPORATION POTENTIAL OF LEAD AND ZINC FROM CONTAMINATED SEDIMENT IN A CLAY-BASED MATERIAL

M. Prica, J. Kiurski and S. Adamović

Faculty of Technical Sciences, Trg Dositeja Obradovića 6, Novi Sad, Serbia

Abstract

This study attempts to determine the immobilization potential of lead and zinc from contaminated sediment by their incorporation into clay-based material based on the leaching tests. It also focuses on the effects of some processing parameters such as pH and grain size. No leaching was observed to an extent that can have any hazardous impact on the environment. It was found that the efficiency of metal immobilization was dependent on the processing parameters. Incorporation of lead and zinc in a clay based matrix led to their immobilization.

Introduction

Pollution by heavy metals is a serious problem because of their toxicity and ability to accumulate in biota. One of the most crucial properties of these metals, which differentiates them from other toxic pollutants, is that they are not biodegradable in the environment. Heavy-metal concentrations in aquatic ecosystems have increased considerably as a result of inputs from human production and consumption activities. In the ecosystem, sediments are the main sink for these elements, but when environmental conditions change, sediments can act as a source of metals [1]. This study attempts to determine the possibility metal immobilization (Pb, Zn) from contaminated sediment by incorporation into clay-based materials. The effectiveness of sludge inactivation was assessed by US EPA TCLP leaching test [2]. It focuses on the effects of pH and grain size distribution on the fixing level of relevant metals (Zn, Pb) in thermally treated clay-based samples.

Materials and methods

Initial Pb (987 mg kg⁻¹) and Zn content (1250 mg kg⁻¹) in sediment showed a sewer sediment contamination (class 4 according to Dutch standards) [3]. According to Dutch regulations, class 4 sediments are of unacceptable quality and need highest urgency sanitation, dredging, disposal in special storage reservoirs and if possible, sediment clean-up measures.

The industrial clayey raw clay with 59 mass% of clay minerals (fireclay, muscovite, illite, smectite, chlorite) and 41 mass% of non clay minerals (quartz, oligoclase, calcite, dolomite, siderite, hematite) was used as basic solidification agent. Sediment possessing an average initial moisture content of 65% was dried at 105 °C to a value of 18%. The raw clay was mixed with the sediment in proportion of 80:20 mass % and the mixture was homogenized. After the homogenization, suitable shape of samples was produced (25 cm long and 10 cm width) by vacuum. The obtained samples were dried for 24 h in air, and then dried at 105 °C to constant mass. The

thermal treatment was carried out in a machinery electrical furnace at constant temperature. The samples were fired at 950 °C (SBT1) and 1100 °C (SBT2). Two leaching tests were performed after 28 days of curing: pH-modified static experiment (on sample SBT2) and TCLP leaching procedure (on samples SBT1, SBT2) [2, 3]. For pH-modified static experiments SBT2 brick samples were tested as cubes (2 cm edge length) and broken down to grain-size fractions: < 2 mm and > 2 mm. The samples were placed in a glass beaker. The pH was kept at a preset value (pH 4, 8, 11). The liquid/solid ratio was 10:1 (l kg⁻¹). After 4 h the solution was filtered (pore size: 0.45 µm), acidified and stored for subsequent analysis. The second leaching test - TCLP at present is used by the US EPA to evaluate whether a particular solidification/stabilization (S/S) process is effective in treating a given waste, in the sense of having toxicity characteristics [2]. About 1 g of sediment and clay sample was subjected to acid digestion to measure metals content (Pb and Zn) by atomic absorption spectrometry (AAS-Pye Unicam 190). Pb content (mg kg⁻¹) in sediment bricks was: 190±9.5 (SBT1) and 197±11 (SBT2), and zinc content (mg kg⁻¹) was 270±15 (SBT1) and 250±10 (SBT2). Data are obtained from triplicate measurements.

Results and discussion

Results for the pH modified static experiments are given in Table 1.

Table 1. Leaching in pH-static experiment at varying grain sizes and pH values.

	Grain size	pH 4	pH 8	pH 11
Pb (mg kg ⁻¹)	Cubes 20 mm	1.830	0.920	0.690
	> 2 mm	1.920	1.110	0.920
	< 2 mm	2.140	1.450	0.980
Zn (mg kg ⁻¹)	Cubes 20 mm	5.120	2.810	2.500
	> 2 mm	5.530	3.170	2.720
	< 2 mm	6.100	3.380	2.940

Lead and zinc similarly reacted. Leachability was highest at pH 4 and decreased with increasing pH values. Comparing the leaching from different grain sizes showed that samples with smaller grain sizes leached higher amounts of Pb and Zn than larger ones.

At present, TCLP is used by the USEPA to evaluate whether a particular solidification/stabilization process is effective in treating a given waste in terms of reduction of contaminant mobility and toxicity [2]. TCLP leachate analysis data is given in Table 2. The concentrations of the selected metals leached from samples were below USEPA regulatory thresholds limits for the samples obtained on both temperatures. Higher the temperatures, less metals are leached.

Table 2. TCLP concentrations (mg/l).

	Pb	Zn
SBT1	0.78±0.04*	1.29±0.10
SBT2	0.53±0.02	1.23±0.10

Data obtained from triplicate; * - standard deviation

Conclusion

The paper showed how bricks made with sediment have no environmental impact based on USEPA TCLP test. No leaching was observed to an extent that can have any hazardous impact on the environment. In further studies additional characterization of long period metals leaching behavior is needed.

Acknowledgment

The authors acknowledge the financial support of the Ministry of Science of the Republic of Serbia, in the frame of projects applied under No.21014.

References

- [1] D. J. Wilson and E. J. Chang , Tennessee Acad. Sci., 2000, **75**, 76–85.
- [2] USEPA Test Methods for Evaluating Solid Wastes, SW-846, 3rd Edition. Office of Solid Waste and Emergency Response, Washington, D. C., 1996.
- [3] Ministry of Housing, Spatial Planning and Environment Directorate-General for Environmental Protection. Circular on target values and intervention values for soil remediation, Netherlands Government Gazette, 2000, 39.
- [4] H. Kay, K. Volker, Waste Manage., 2002, **22**, 521–530.

ASSESSMENT OF VOCs CONCENTRATIONS IN BELGRADE SEMI-URBAN AREA

M. Perišić*, A. Stojić, S. Rajšić and Z. Mijić

Institute of Physics-University of Belgrade, Belgrade, Serbia

**Corresponding author, E-mail: mirjana@ipb.ac.rs*

Abstract

In order to assess the ambient levels and possible origin of VOCs, concentrations of thirty-one compound was measured on-line in a semi-urban site of Belgrade using Proton Transfer Reaction Mass Spectrometer (PTR-MS) – Ionicon Analytik, Innsbruck, Austria. Measurements were conducted during thirty days episode in February, 2010. The one-hour mean values from on-line measurements have been calculated and used for further statistical analyze. Meteorological parameters were monitored as well.

Introduction

Volatile organic compounds (VOCs) are very important local and regional atmospheric pollutants playing an important role in tropospheric chemistry by affecting OH radical concentrations and the production of photochemical oxidants. Chemical reactions of VOCs with nitrogen oxides under sunlight lead to the production of secondary air pollutants, resulting in tropospheric ozone and secondary organic aerosols [1]. Monitoring of VOCs in the urban area is important due to the adverse effects some of them have on human health [2]. Benzene, associated with traffic emissions and 1, 3-butadiene are considered to be the most toxic [3]. In semi-urban areas, VOC sources can be both anthropogenic and biogenic. Major anthropogenic sources include vehicle exhausts, gasoline evaporation, solvent use, natural gas emissions and industrial processes. Biogenic emissions, whose main sources are terrestrial plants, are globally the most important sources of the VOCs found in the atmosphere.

Proton-transfer-reaction mass spectrometry (PTR-MS) allows real-time measurements of VOCs in air with a high sensitivity and a fast time response [4]. A fraction of VOCs is ionized in proton-transfer reactions with hydronium ions (H_3O^+) – the soft ionization method that generally does not lead to fragmentation of the productions what simplifies the interpretation and the quantification of the mass spectra. The mass of the product ion equals the VOC mass plus one atomic mass unit. The measurements were performed at 4 m above ground, at the platform of the Institute of Physics, 10 km northwest of Belgrade centre (Serbia), in the semi-urban area and 100 m far from the right bank of the Danube River.

Meteorological parameters including temperature, relative humidity, rainfall, wind direction and speed were provided by the Meteorological Station at the same platform.

Results and Discussion

The most abundant compound measured was propanol (mean concentration 23.45 ppb), followed by methanol (22.12 ppb), propene (13.38 ppb) and acetaldehyde (11.39 ppb). Traffic related compounds benzene (3.29 ppb), toluene (2.45 ppb) and 1, 3 butadiene are at the upper regulatory limit [5].

In order to find correlation between measured compounds and with meteorological parameters, Pearson's correlation coefficients were calculated. The highest correlation coefficient was observed between methanol and acetaldehyde ($r = 0.96$) and benzene and acetonitrile ($r = 0.96$). Methanol also was highly correlated with formaldehyde ($r = 0.94$), acetone, 2,3-butadiene and cyclohexane.

The benzene to toluene ratio (B/T) was often used to identify VOCs sources. Toluene, m/p-xylene and benzene are emitted from vehicle exhaust and gasoline evaporation. Toluene and m/p-xylene also are released from the use of solvents (painting, printing, and dry cleaning, etc.). Most of the solvents do not contain benzene [6]. A B/T ratio of around 0.5 was characteristic of vehicular emissions [7]. In this study, B/T ratio was 1.5. It suggests vehicular emissions are the main source of VOCs in this sub-urban area during this winter episode.

Since one of the main difficulties in air pollution management is to determine the quantitative relationship between ambient air quality and pollutant sources, UNMIX receptor model has been used to analyze VOCs concentrations [8]. Model was run with 654 observations. Five factors were chosen as the optimum number for the model. The highest contribution has profile which has high loadings with compounds related to local production processes, followed by profiles related to using solvents (acrylic paints) and traffic emissions. Time series plot of observed and UNMIX predicted VOCs concentrations of benzene and toluene are shown at Fig. 1.

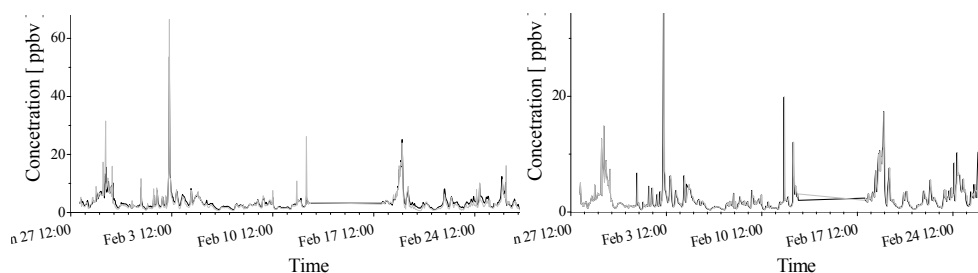


Fig.1. Time series plot of observed acetaldehyde and toluene concentrations and Unmix predicted

References

- [1] J. H. Seinfeld, S. N. Pandis, Atmospheric Chemistry and Physics, Wiley, New York, 1998.
- [2] Air Quality Guidelines for Europe, In: WHO Regional publications, European Series, second ed., No91, WHO, Copenhagen, 2000.

- [3] W. Laowagul, K. Yoshizumi, Behavior of benzene and 1,3-butadiene concentrations in the urban atmosphere of Tokyo, Japan, *Atmospheric Environment*, 2009, **43**, 2052-2059.
- [4] J. A. De Grouv, and C. Warneke, Measurement of volatile organic compounds in the Earth's atmosphere using proton-transfer-reaction mass spectrometry, *Mass Spectrometry Reviews*, 2007, **26**, 223-257.
- [5] EU Directive 2000/69/EC of the European Parliament and of the Council of 16 November 2000 relating to limit values for benzene and carbon monoxide in ambient air, *Official Journal of the European Communities* L313, 13th December, 2000.
- [6] K. Na, Y. P. Kim, K. C. Moon, Diurnal characteristic of volatile organic compounds in the Seoul atmosphere, *Atmospheric Environment*, 2003, **37**, 733-742.
- [7] J. Duan, J. Tan, L. Yang, S. Wu, J. Hao, Concentration, sources and ozone formation potential of volatile organic compounds (VOCs) during ozone episode in Beijing, *Atmospheric Research*, 2008, **88**, 25-35.
- [8] P. K. Hopke, Recent developments in receptor modeling, *Journal of Chemometrics*, 2003, **17**, 255-265.

CONCENTRATION LEVELS OF PAHs IN AMBIENT AIR AND SOIL OF NOVI SAD

J. Radonić, M. Turk Sekulić, M. Vojinović Miloradov, J. Kiurski and M. Đogo

Faculty of Technical Sciences, University of Novi Sad, Trg Dositeja Obradovića 6, 21000 Novi Sad

Abstract

The objective of the paper was to determine concentration levels of polycyclic aromatic hydrocarbons in ambient air and soil samples from selected urban, industrial, suburban and background localities in the city of Novi Sad, during the winter period. Limit value of total suspended particles in ambient air was exceeded at the urban measuring spot, while levels of PAHs in air samples were higher than limit value at urban, industrial and suburban localities. Concentration levels of PAHs in soil samples were in line with content of polycyclic aromatic hydrocarbons in particles suspended in ambient air.

Introduction

Polycyclic aromatic hydrocarbons (PAHs) form a large group of organic pollutants that consist of two or more condensed aromatic rings. Due to their well known carcinogenic, teratogenic and mutagenic properties, Agency for Toxic Substances and Disease Registry has included even 17 PAHs in the list of toxic pollutants. As polycyclic aromatic hydrocarbons are formed during the incomplete combustion of the organic matter, the main sources of PAHs in the atmosphere are motor vehicles, re-suspended soils, residential heaters and fireplaces, refineries and power plants [1, 2]. Primarily, PAHs are emitted into the atmosphere where they are mostly associated with particulate matter and easily come under dry and wet deposition processes to soil and water surfaces [3].

As the result of the sampling campaign conducted in January 2010, the concentration levels of sixteen PAHs were measured in ambient air and soil samples from different locations in order to determine the contamination of two environmental media by polycyclic aromatic hydrocarbons during the winter period and to estimate the air-soil partitioning of PAHs. Samples were collected simultaneously using four high volume samplers TCR Tecora at the four selected localities in Novi Sad - urban city centre (locality I1), Novi Sad heating plant in Šangaj (locality I2), suburban residential settlement Sremska Kamenica (locality I3) and mountain Fruška Gora as background site (locality I4). Gas chromatography coupled with MS detector was used for analysis of air and soil samples.

Results and Discussion

Concentration of total suspended particles in ambient air ranged from 43.26 $\mu\text{g}/\text{m}^3$ at locality I4 to 179.91 $\mu\text{g}/\text{m}^3$ at locality I1 (Fig. 1). Limit value of 120 $\mu\text{g}/\text{m}^3$ for

content of TSP in 24 hours air sample was exceeded only at the urban measuring spot.

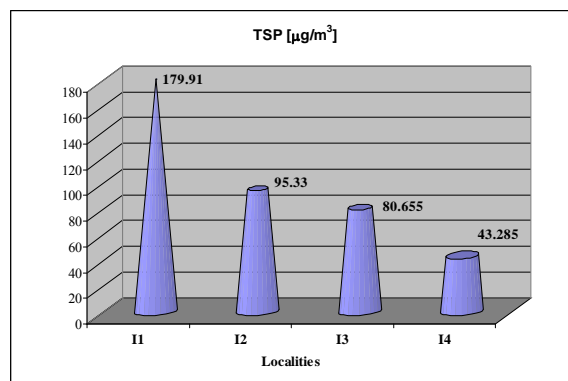


Fig.1. TSP concentrations in ambient air [µg/m³] at the sampling sites in Novi Sad.

Concentration levels of PAHs in ambient air varied between 5.56 ng/m³ at background site, Fruška Gora Mountain, to 93.85 ng/m³ at measuring site in the yard of heating plant (Fig. 2). The content of benzo(a)pyren in ambient air samples were higher than limit value of 1 ng/m³ at urban, industrial and suburban localities.

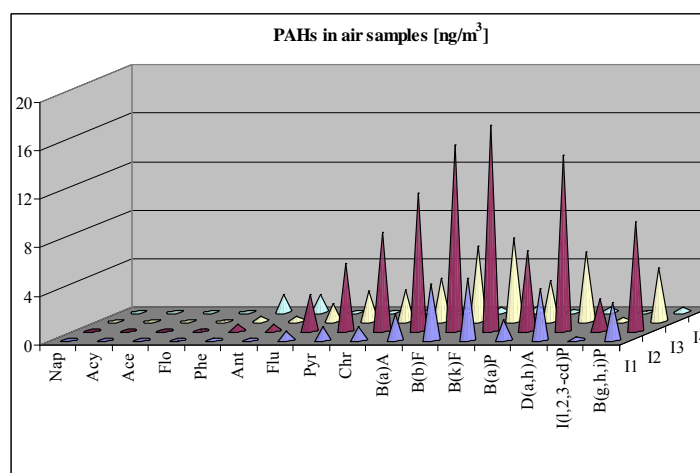


Fig.2. PAHs concentrations in ambient air [ng/m³] at the sampling sites in Novi Sad.

The levels of polycyclic aromatic hydrocarbons in soil lied in the interval <0.001 - 0.179 mg/kg of dry matter (Fig. 3). Like for the air samples, the highest concentrations were measured at locality Novi Sad heating plant (1.002 mg/kg), while the lowest content of total PAHs was detected at background sampling spot (0.038 mg/kg).

Also, concentration trend of individual PAHs in ambient air for every measuring site was in line with content of scattered pollutants in soil samples at the corresponding locations.

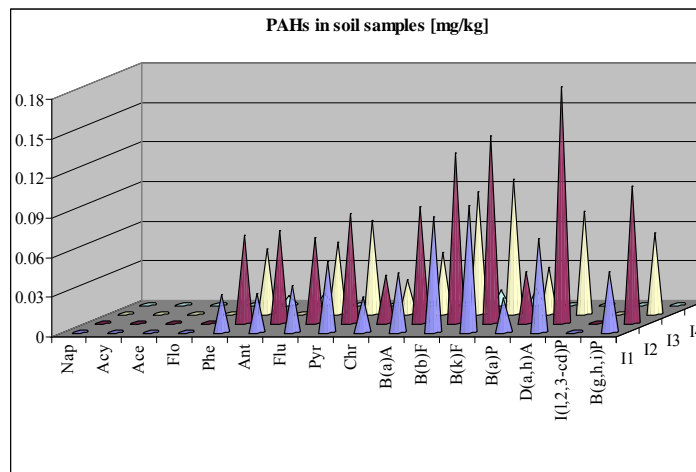


Fig.3. PAHs concentrations in soil [ng/m³] at the sampling sites in Novi Sad.

Conclusion

Results of conducted research confirmed correlation between the content of pollutants in the atmosphere and surface soil layers, as well as equivalent distribution of individual PAHs in the complex air-soil heterogeneous system.

Acknowledgments

The research was financially supported by Ministry of Science, Republic of Serbia, (Project number 21014).

References

- [1] E. Galarnau, T. F. Bidleman, P. Blanchard, Atmospheric Environment, 2006, **40**, 182-197.
- [2] K. Ravindra, R. Sokhi, R. Van Grieken, Atmospheric Environment, 2008, **42**, 2895-2921.
- [3] J. Radonic, M. Turk Sekulic, M. Vojinovic Miloradov, P. Čupr, J. Klánová, Environmental Science and Pollution Research, 2009, **16**, 65-72.

REDUCTION OF PCBs WITH POTASSIUM METAL

I. Bucur,^{a,b,c} I. Petrisor^d and G. Vasile^c

^a University "Vasile Alecsandri" of Bacau, Str. Marasesti no.157, , 600115, e-mail:
bucur_il@yahoo.com

^b University of Craiova, IMST Faculty, Drobeta Turnu Severin

^c Applied Systems SRL, Str. Pictor Ion Negulici, no.1, Craiova, Dolj

^d Regional Agency of Environmental Protection, Craiova, Dolj

Abstract

We study the ecological neutralization of polychlorobiphenyls (PCBs), used as additive to improve dielectric properties of oil in industrial transformers and capacitors.. Among other known methods, alkaline metals treatment is one of the most efficient PCBs neutralization methods, due to the reducing capacity of alkaline metals, thus removing chlorine atoms from polychlorobiphenyls molecules. In the present work, we study the utilization of metallic potassium, as reducing agents for PCBs ecological neutralization. Intensive mixing and fine division of alkaline metal particles make the reaction practically quantitative.

Introduction

Polychlorinated biphenyls (PCBs) with general chemical formula $C_{12}H_{10-x}Cl_x$ are a class of 209 different substances, highly toxic, used as additives to improve dielectric properties of cooling oil in electrical equipment, such as transformers and capacitors [1, 2].

The important quantities of PCBs produced and stocked are among the most dangerous ones by uncontrolled release in the environment, mainly by the capacity of bioaccumulation [2-6].

PCBs disposal methods are: pyrolysis, chemical methods (adsorption, catalytic hydrodechlorination, ozonation, ultrasonic, photolytic, wet air oxidation, reaction with a sodium salt in amine solvent, and etc.), supercritical water oxidation (SWO), and microbial degradation [7-10].

The utilization of metallic potassium for destruction of PCBs is proposed as a viable alternative.

Results and Discussion

Samples of PCBs containing transformer oil, obtained from Electrical Engines Factory Filiași, Romania are used for experiments.

A 250 ml thermostated glass laboratory balloon with mercury thermometer was used as reaction vessel. Magnetic stirrer was used to provide fine division of alkaline metal and efficient mixing. Reactions occur at 90°C under nitrogen inert gas.

Table 2. Reactions conditions

Nature of alkaline metal	K
Quantity of alkaline metal(g)	0,80
Quantity of oil(ml)	50
Reaction time(min)	10, 20, 30
Number of portions	2
Temperature(°C)	90

Amounts of reactants and rate of mixing were all kept constant during the run.

Samples for analysis were prepared by 100:1 dilution of initial oil with non-contaminated transformer oil.

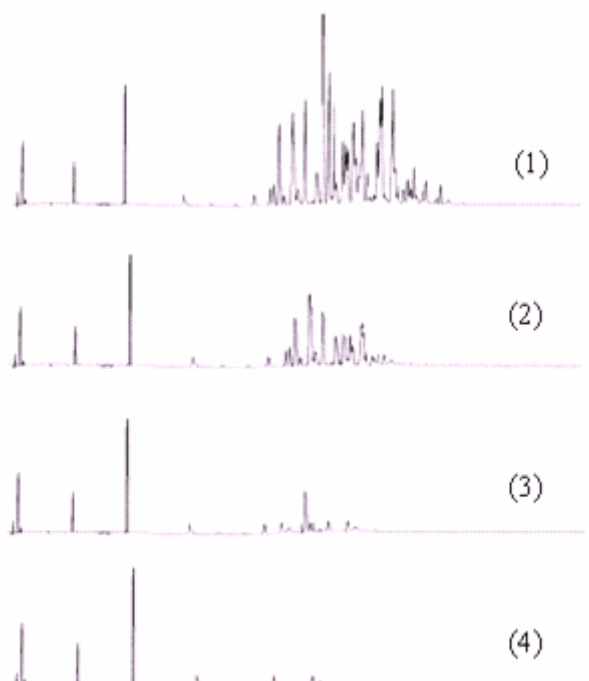


Fig. 1. Chromatograms of initial (1) and neutralized Oil for 90°C after 10 (2), 20 (3) and 30 (4) min reaction time

Pentachlorobenzene was used as retention time marker.

Samples were comparatively analyzed by gas chromatograph (GC 8000, Fisons Instruments, Milano, Italy) equipped with computer, interface Chromcard, electron capture detector and a 30 m × 0.25 mm, 0.25 μm, phase: RTX-5 fused silica capillary column was used for separation of quantification of PCBs.

The initial temperature of GC oven program is 180°C, and then increased at a rate of 5°C /min to 280°C. The injector and detector temperature is 160°C, respectively 300°C. The injection volume is 5 μl and is performed in a splitless mode.

The chromatograms of initial and the resulted neutralized oil are represented in Figure 1, with the ordinate 6 mV, identical for all four samples. The marker retention time is 12 min. In order to remain in the purpose of the work, we do not identify separately PCBs congeners.

Instead, we consider the global disappearance of PCBs chromatographic peaks group (retention time between 16 and 28 min) in the neutralized oil, as a measure of the efficacy of the neutralization method.

The resulted peaks: (1) initial, (2), (3) and (4), in Figure 3, show practical disparition of PCBs in products, after 30 min reaction time referring to the sensibility of used analysis method (more than 0.01 ppm).

Conclusion

We studied the chemical dechlorination process for the destruction of PCBs using metallic potassium. Experimentally results clearly demonstrated that proposed direct reduction with metallic potassium is quite effective for ecological elimination of PCBs at 90°C and 30 min reaction time.

References

- [1] K. Sang Ryoo et al., Bull. Korean Chem. Soc. 2007, **28**, 520-528.
- [2] A. Zhihui, Y. Peng, L. Xiaohua, Chemosphere, 2005, **60**, 824.
- [3] E. Betterton, N. Hollan, R. G. Arnold, S. Gogosha, L. Mckim K.Liu, Z. J. Environ. Sci. Technol., 2000, **34**, 1229.
- [4] B. Ruggeri, G. Sassi, Chem. Eng. Commun., 1996, **145**, 89.
- [5] B. Kuipers, W. R. Cullen, W. W. Mohn, Environ. Sci. Technol., 1999, **33**, 3579.
- [6] E. De Felip, F. Ferri, C. Lupi, N. M. Trieff, F. Volpi, A. DiDomenico, Chemosphere, 1996, **33**, 2263.
- [7] H. Yak, Q. Y. Lang, C. M. Wai, Environ. Sci. Technol., 2000, **34**, 2792.
- [8] W. Wu, J. Xu, H. Zhao, Q. Zhang, S. Liao, Chemosphere, 2005, **60**, 944.
- [9] M. A. Aramendia, M. A. Borau, I. M. Garcia, C. Jimenez, A. Marinas, J. M. Marinas, F. J. Urbano, Appl. Catal., 2003, **B43**, 71.
- [10] V. Simagina, V. Likhobov, G. Bergeret, M. T. Gimenez, A. Renouprez, Appl. Catal. B: Environ., 2003, **40**, 293.

SORPTION OF LEAD BY NATURAL AND ITS IRON (III) - MODIFIED ZEOLITE

M. Kragović,¹ A. Daković,¹ S. Milićević,¹ Ž. Sekulić,¹ M. Trgo,²
M. Ugrina² and N. Vukojević Medvidović²

¹*Institute for Technology of Nuclear and Other Mineral Raw Materials, Franchet
d'Esperey 86, P. O. Box 390, 11000 Belgrade; * e-mail: m.kragovic@itnms.ac.rs*

²*Faculty of Chemistry and Technology, University of Split, Teslina 10/V, 21000
Split, Croatia*

Abstract

In this paper, results of lead sorption by the natural and its iron (III)-modified zeolite are presented. It was determined that, for both zeolites lead sorption increased with increasing the initial concentration of lead in solution. Much higher sorption of lead was achieved with the iron (III)-modified zeolite. The results were fitted to the Langmuir and Freundlich sorption isotherm. The best fit of experimental data was achieved with the Freundlich sorption isotherm (correlation coefficient >0.93). From Langmuir isotherm, maximally sorbed amount of lead was 0.318 and 0.642 mmol/g for the natural and iron (III)-modified zeolite, respectively.

Introduction

The presence of lead in the environment is detrimental to a variety of living spaces. The major sources containing lead are the wastewaters from process industries engaged in lead (acid batteries, paint, electronic, automobile emissions, etc). Presence of lead in live organisms can cause anemia, chills, diarrhea, and dysfunction of kidneys, reproductive system, liver, brain and central nervous system, etc [1]. Conventional methods for lead removal include ion exchange, precipitation and co-precipitation, surface complexation, reduction, etc [2]. Among all the methods ion exchange/sorption on zeolites (tectoaluminosilicates) and smectites (phylosilicates) is highly effective and economical. Lead can be immobilized on zeolites by two mechanisms: ion exchange and chemisorption [3]. The ion exchange usually takes considerable part in the sorption process. To establish better sorption of lead, surface of zeolite is often modified with iron (III) oxyhydroxides. Such iron (III) modified zeolites can be several times better sorbents than natural zeolites. In the present work, sorption of lead on the natural and its iron (III)-modified zeolite is investigated.

Experimental

The starting material was the natural zeolitic tuff from the Zlatokop deposit, Vranjska Banja, Serbia. After crushing and grinding the zeolite was sieved to the particle size below 0.043 mm. The mineralogical composition of the starting sample was primarily clinoptilolite (~80%) with small amounts of feldspar, quartz and pyrite as determined by qualitative X-ray powder diffraction analysis (XRPD). Analysis was performed on diffractometer PHILIPS, Model PW-1710.

The iron (III)-zeolite was synthesized combining the method for pure goethite preparation [4] and method for preparation of iron-coated zeolite [5]. Thus, 50 g of zeolite was mixed with 25 ml of 10% $\text{FeCl}_3 \cdot 6\text{H}_2\text{O}$ solution and 700 ml of 0.1 M KOH (pH = 10) in 2 l container. The container was capped and the suspension was aged for 20 days at room temperature. After the reaction period the suspension was filtered and washed until Cl^- ions were no longer detected and dried. Chemical composition of the natural zeolitic tuff and its iron (III) –modified zeolite was done by the classical chemical analysis.

The examinations of lead sorption were carried out by shaking 1g of the natural and iron (III)-zeolite with 50 ml of aqueous solutions, containing various initial concentrations of PbNO_3 (1.7 – 34.8 mmol Pb^{2+}/L) at 25°C. The initial and non sorbed concentrations of lead in supernatants were determined by atomic absorption spectrophotometry using the Analytic Jena Spekol 1300.

Results and discussion

Chemical composition of the natural zeolitic tuff (NZ) and its iron (III)-modified zeolite (INZ) are listed in Table 1.

Table 1. Chemical composition of NZ and INZ.

	SiO_2	Al_2O_3	Fe_2O_3	CaO	MgO	K_2O	Na_2O	I.L.*
	Content, %							
NZ	66.57	13.13	2.30	3.85	0.56	1.17	1.27	11.05
INZ	63.44	12.71	3.97	3.85	1.06	4.36	0.80	9.43

*ignition loss

The isotherms for lead sorption on natural zeolitic tuff and iron (III)-modified zeolite are given at Figure 1a [6], while Figure 1b presents the percentage of sorbed lead by both zeolites. From Figure 1a, it is observed that much higher sorption of lead was achieved with the iron (III)-modified zeolite. The results of sorption of lead on natural and iron (III)-modified zeolite were fitted to the Langmuir and Freundlich sorption model and the best fits of the data were obtained using the Freundlich model ($R^2 > 0.93$). From Langmuir isotherm, the calculated maximum amount of lead sorbed by natural zeolite and iron (III)-modified zeolite are 0.318 mmol/g (64 meq/100g) and 0.642 mmol/g (128 meq/100g), respectively. The content of inorganic cations (Ca^{2+} , Mg^{2+} , Na^+ and K^+) released from the natural zeolite during lead sorption at the plateau of the isotherms was as follows: Ca^{2+} - 23 meq/100g, Na^+ - 21 meq/100g, Mg^{2+} - 6 meq/100g and K^+ - 2 meq/100g. The amounts of Ca^{2+} , Mg^{2+} , Na^+ and K^+ released from iron (III) modified zeolite were 35, 12, 2 and 44 meq/100g, respectively. Since in zeolites, for divalent cations the share of ion exchange is comparable to chemisorption [3], obtained results suggested that both processes are involved in lead sorption by both zeolites.

As can be seen from Figure 1b, for both sorbents, lead sorption indexes (calculated by dividing the sorbed amount of lead by the initial lead concentration)

decreases with increasing the initial concentrations of pollutant. For lower initial concentration of lead, sorption index for both sorbents are close to each other and they are almost 100%, while for the higher initial lead concentration, difference in percentage is much visible; for example: for the initial lead concentration of 35 mmol/L, its sorption was 18% for the natural zeolite and 35% for iron (III)-modified zeolite.

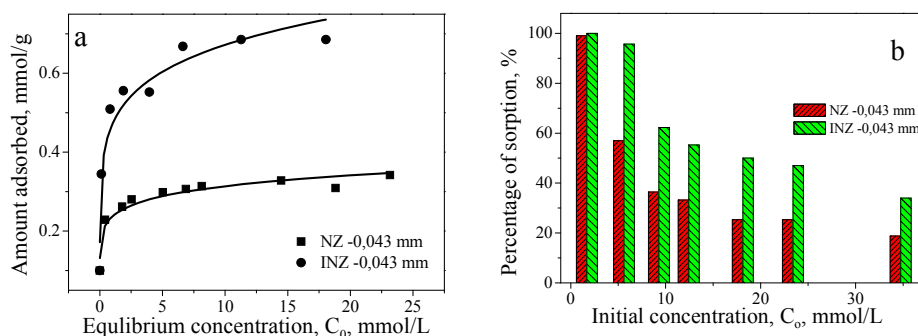


Figure 1. a Sorption of lead on natural (NZ) and iron (III)-modified zeolite (INZ); **b** Percentage of sorption of lead as a function of its initial concentration.

Conclusion

In this paper, results of sorption of lead by the natural zeolite and its iron (III)-modified zeolite showed that significantly higher lead sorption has been achieved on iron (III)-modified zeolite. The experimental results were fitted to the Langmuir and Freundlich sorption isotherms. The best fit of experimental data was achieved with the Freundlich sorption isotherm ($R^2 > 0.93$). The results suggest that ion exchange is not the only mechanism responsible for lead sorption by both zeolites. That means that especially for iron (III)-modified zeolite chemisorption of lead plays a role in its sorption. Results indicated that iron (III) present in modified zeolite has influence on sorption of lead.

Reference

- [1] C. Singh, J. Sahu, K. Mahalik, C. Mohanty, B. Mohan, B. Meikap, J. Hazard. Mater., 2008, **153**, 221-228.
- [2] S. Yhu, H. Hou, Y. Xue, Appl. Clay Sci., 2008, **40**, 171-178.
- [3] W. Mozgawa, M. Król, T. Bajda, J. Mol. Struct., 2009, **924-926**, 427-433.
- [4] G. Mustafa, B. Singh, R. Kookana, Chemosphere, 2004, **57**, 1325-1333.
- [5] C. Jeon, K. Baek, J. Park, Y. Oh, S. Lee, J. Hazard. Mater., 2009 **163**, 804-808.
- [6] M. Kragović, S. Milićević, A. Daković, J. Perić, M. Trgo, N. Vukojević Medvidović, M. Ugrina, Ž. Sekulić, I. Nuić, in O. E. Petrov, Y. K. Tzvetanova (Eds.), Proceedings of 8th Intern. Conf. on the Occurrence, Properties and Utilization of Natural Zeolites, Sofia, Bulgaria, 10-18 July 2010, 149-150.

ABSORPTION SPECTRA AS THE INDICATOR OF FOUNTAIN SOLUTION AGING

J. Kiurski¹, D. Ž. Obadović², M. Cvetinov², S. Adamović¹,
I. Radin Oros¹ and J. Krstić¹

¹*Faculty of Technical Sciences, Department of Graphic Engineering and Design,
Trg Dositeja Obradovica 6, Novi Sad, Serbia*

²*Faculty of Sciences, Department of Physics, Trg Dositeja Obradovica 4, Novi Sad,
Serbia*

Abstract

The objective of the paper was to determine absorption spectra in UV-VIS and IR region of fountain solutions (fresh and spent) from printing facility in Novi Sad. Based on experimental investigation we concluded that the spectral data could be the indications of fountain solution aging and could be the predict model for fountain solution regeneration.

Introduction

The printing industry uses various liquid resources, which after printing process can be classified as hazardous chemical waste. Fountain solution is an essential material in the offset printing process, which serves two purposes. It assists in the distribution of ink only to the image areas, and is important for keeping the printing plates and rubber blankets clean from possible contamination originating both from the ink and the paper [1].

Fountain solution is an aqueous mixture of the following components:

- Water;
- Wetting agents (isopropyl alcohol), which reduce surface tension;
- Desensitizing agents (gum arabic), which maintain the hydrophilic area of the printing plate;
- Corrosion inhibitors, which prevent oxidation and corrosion of the press;
- Biocides, which help control bacteria growth;
- Additives [2].

During printing process, printing ink, paper fibers, cleaning solution and other contaminants build up in fountain solution a negative impact to producing a quality-printed product. Spent fountain solutions have the potential to cause serious pollution if illegally discharged through a dry well or septic system to the ground, because their components can render drinking water supplies unfit for human consumption [3].

Experimental

Ultraviolet-visible (UV-VIS) absorption spectra were recorded using spectrophotometer UV-VIS SPECORD 205, Analytik Jena, while IR spectra were recorded using Thermo-Nicollet Nexus 670 FTIR spectrometer, at 25°C.

Results and discussion

Two samples of fountain solution (fresh and spent) from the same offset printing machine (Heidelberg SM 74 2-P-H) were analyzed. The fresh fountain solution was prepared by mixing 3% of a buffer concentrate, 10% isopropyl alcohol (IPA) concentrate and 87% tap water.

Ultraviolet-visible spectral absorption data of the fountain solutions indicates that the decrease in absorption values was due to the decomposition of the buffer (acedin DH2010) structure, which provided the direct evidence that chemical reaction took place during the fountain solution aging. However, the absorption peak at 634 nm diminished in time and finally disappeared during the use, which indicates that fountain solution has been aging (Figure 1).

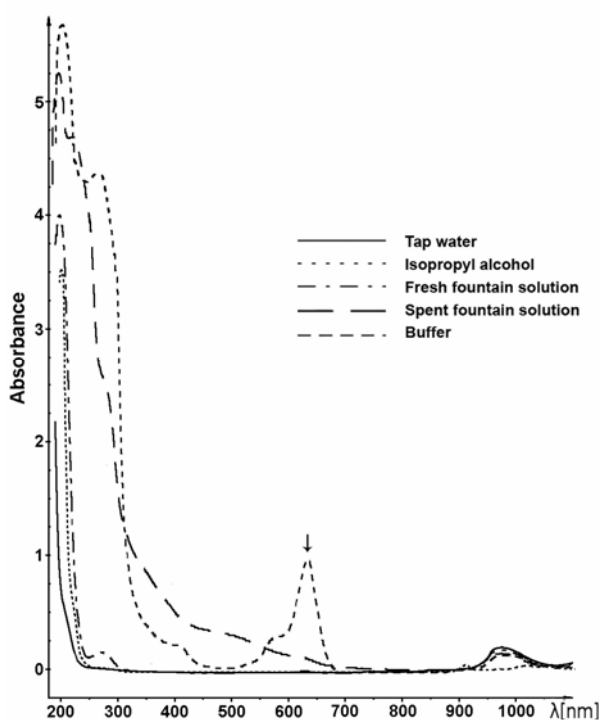


Fig.1. UV/VIS absorption spectra of fountain solutions.

No new absorption bands appear in either visible or UV regions. These are because the organic matters, OM (buffer – acedin) in the solution are attacked by hydroxyl radicals as soon as *OH is generated, as described in the equation [4]:



Complete removal of buffer was observed after three to six months usage with the fountain solution treatment system or one week to one month usage without mentioned system.

Spectral analysis in IR region of fountain solution (Fig.2) indicates to the presence of the intensive band at $\sim 3000\text{ cm}^{-1}$ characteristic for $\nu(\text{C-H})$ modes, and also band $\nu(\text{C-N})$ between 1060 and 1000 cm^{-1} indicating to the presence of impurities. On the basis of absorption spectral data in UV-VIS and IR region one can conclude that fountain solution has been aging. Spectra of fountain solutions were recorded on a Thermo-Nicollet Nexus 670 FTIR spectrometer, at 25°C .

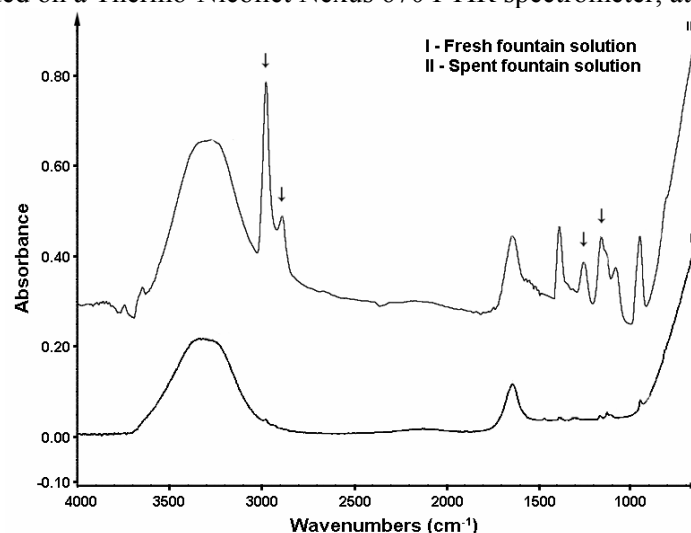


Fig.2. Infrared spectra of fountain solutions.

Conclusion

During the printing processes fountain solution has been losing its wetting quality because of aging processes, which can be identified by spectroscopic methods, such as UV-VIS and FTIR spectroscopy. Disappearance of some of the characteristic peaks in the absorption spectra in UV-VIS region and intensifying some of IR bands pointed out to degradation of the organic matters (buffer – acedin) in the fountain solution as a consequence of hydroxyl radicals formation.

Acknowledgment

This work has been supported by Grant No. 21014 and 141020 from the Ministry of Science and Technological Development of the Republic of Serbia.

References

- [1] J. C. Froberg, J. Voltaire, M. Sundin, F. Tiberg, TAPPI International Printing and Graphic Arts Conference, USA, 2006, 1-6.
- [2] Glatfelter, Technical Bulletin, Ohio, 2005, 1-8.
- [3] I. Radin Oros, J. Krstić, J. Kiurski, M. Vojinović Miloradov, D. Adamović, Ecological Truth, Proceedings, 2009, 112-116.
- [4] A. R. Khataee, V. Vatanpour, A. R. Amani Ghadini, Journal of Hazardous Materials, 2009, **161**, 1225-1233.

RADIOACTIVITY IN RAW MATERIALS USED IN CERAMICS INDUSTRY

M. Janković and D. Todorović

Institute Vinča, Radiation and Environmental Protection Department, P.O. Box 522, 11001 Belgrade, Serbia

Abstract

The natural radioactivity in zirconium samples used in the ceramics industry has been measured. One of the most important use of zircon is as opacifier for ceramic tiles. The measurements were made by gamma spectrometry with a high purity germanium detector (HPGe). The gamma index, I , the external hazard index, H_{ex} and the internal hazard index, H_{in} , were calculated. The investigated samples can be used as one component in the recipe for the production of ceramics only if 3% of the samples used.

Introduction

The investigation of zirconium ores as sources of TENORM (technologically enhanced natural radioactivity) began in the late 1970s and early 1980s [1,2]. These works highlighted the relatively high concentrations of natural radionuclides in zirconium ores. At present Australia, South Africa, Ukraine, India, China, Brazil and Sri Lanka are the largest exporters of zirconium minerals [2]. The aim of this study was to measure the radioactivity in zirconium used as raw material in ceramics industry for production of ceramic colors, glazes, tiles and sanitary and to estimate the radiological hazards. These materials are tested continuously in Laboratory for Radiation and Environmental Protection Department, Vinča Institute, Belgrade, as part of regular inspection of imported goods from the customs.

Experimental

The investigated material was zirconium glaze. Before measurements, the samples were crushed, sieved and placed in the plastic 500 cm³ Marinelli beakers. All samples were measured immediately after preparation because of the rapid assessment of whether the activity in a given sample is in accordance with applicable regulations or not. The spectra of samples were acquired using a high purity germanium detector (HPGe) with relative efficiency of 23 % and energy resolution of 1.8 keV for the 1332 keV ⁶⁰Co peak. The activity of ²²⁶Ra and ²³²Th was determined by measuring activity of their decay products: ²¹⁴Bi (609 keV, 1120 keV and also 1764 keV), ²¹⁴Pb (295 keV and 352 keV) and ²²⁸Ac (338 keV and 911 keV), respectively. The activities of ⁴⁰K and ¹³⁷Cs were determined from 1460 keV and 661 keV γ -lines, respectively. ²³⁵U was determined via its lines on 143 keV and 163 keV. ²³⁸U was determined by measuring activity of their decay products: ²³⁴Th (63 keV) or by ²³⁴Pa (1000 keV).

Results and discussion

The measured specific activities of ^{226}Ra , ^{232}Th , ^{235}U and ^{238}U are presented in Table 1. The ^{238}U concentration ranging from 672-6524 Bq kg⁻¹ was higher than concentration of ^{232}Th (187-885 Bq kg⁻¹), ^{235}U (42-279), ^{40}K (<MDC (16 Bq kg⁻¹)) and ^{137}Cs (<2 Bq kg⁻¹) in all samples. On the other hand activity ratio $^{238}\text{U}/^{226}\text{Ra}$ was approximately 1, and can be assumed that these two radionuclides are in the radioactive equilibrium. In order to estimate the radiological hazards the gamma index, the external hazard index and the internal hazard index must be calculated. Due to the high activity of ^{226}Ra and ^{232}Th in the samples, it must be determined what percentage of the sample can be used in the recipe for the production of ceramics. Gamma index can be calculated using the following relation [3]:

$$I = \frac{C_{Ra}}{200} + \frac{C_{Th}}{300} + \frac{C_K}{3000} \quad (1)$$

where C_{Ra} , C_{Th} and C_K are the activity concentrations of ^{226}Ra , ^{232}Th and ^{40}K in Bq kg⁻¹ in the building material, respectively. Gamma index must be less than 1 that the material could be used in high construction for interior, exterior and low construction. This applies to any building material. Gamma index for the investigated samples will be less than 1 only if 3% of the sample used. The obtained values for gamma index are presented in Table 1. For all investigated samples $I < 1$ (in the account, 3% of the activity of ^{226}Ra , ^{232}Th and ^{40}K was used).

Table 1. Activity concentrations of radionuclides in zirconium and appropriate gamma index

№	imported	Activity concentrations of radionuclides / Bq kg ⁻¹				I
		²²⁶ Ra	²³² Th	²³⁵ U	²³⁸ U	
1	Italy	2312 ± 347	367 ± 73	194 ± 58	2236 ± 894	0.38
2		2969 ± 297	816 ± 106	78 ± 33	3540 ± 1133	0.53
3		4147 ± 415	665 ± 80	266 ± 27	4522 ± 588	0.69
4		3967 ± 397	509 ± 61	230 ± 44	3855 ± 694	0.65
5		4350 ± 434	885 ± 88	178 ± 53	3853 ± 462	0.75
6		3201 ± 320	643 ± 64	191 ± 34	3948 ± 592	0.54
7		2732 ± 137	526 ± 68	164 ± 16	2425 ± 1336	0.46
8		3031 ± 303	630 ± 94	198 ± 20	3055 ± 611	0.52
9		3993 ± 399	555 ± 72	203 ± 32	3517 ± 914	0.66
10		3661 ± 366	658 ± 79	279 ± 28	3410 ± 682	0.62
11		2961 ± 296	570 ± 74	214 ± 21	2630 ± 736	0.50
12	Great Britain	2021 ± 202	396 ± 59	55 ± 26	1867 ± 672	0.35
13		3511 ± 351	454 ± 54	162 ± 41	2958 ± 740	0.57
14		3778 ± 378	584 ± 64	215 ± 54	4037 ± 1009	0.63
15	Slovenia	2603 ± 234	460 ± 60	42 ± 24	2266 ± 748	0.44
16		2106 ± 210	428 ± 51	54 ± 19	2687 ± 564	0.36
17		814 ± 163	187 ± 47	71 ± 14	672 ± 138	0.14
18	Sweden	2941 ± 294	565 ± 85	225 ± 56	2859 ± 715	0.50
19	Spain	3008 ± 301	596 ± 89	206 ± 21	3808 ± 762	0.51
20	Slovakia	4090 ± 1227	550 ± 165	193 ± 58	6524 ± 1174	0.67
21	Germany	4092 ± 409	624 ± 69	258 ± 52	3570 ± 714	0.68

The external hazard index, H_{ex} , is defined as [1]:

$$H_{ex} = C_{Ra} / 370 + C_{Th} / 259 + C_K / 4810 \quad (2)$$

where C_{Ra} , C_{Th} and C_K have the same meaning as in equation (1). The value of this index must be less than unity in order to keep the radiation hazard

insignificant. The obtained values of H_{ex} for the zirconium ranged from 0.09 to 0.46 as shown in Fig. 1, values which are indeed less than unity (results obtained with 3% of the activity of ^{226}Ra , ^{232}Th and ^{40}K). In addition to the external hazard, radon and its short-lived products are also hazardous to the respiratory organs. The internal exposure to radon and its decay products is quantified by the internal hazard index, H_{in} , which is given by the equation [4]:

$$H_{in} = C_{Ra} / 185 + C_{Th} / 259 + C_K / 4810 \quad (3)$$

For the safe use of a material in the ceramics industry, H_{in} should be less than unity. The calculated values of H_{in} ranged from 0.15 to 0.81 as shown in Fig. 1.

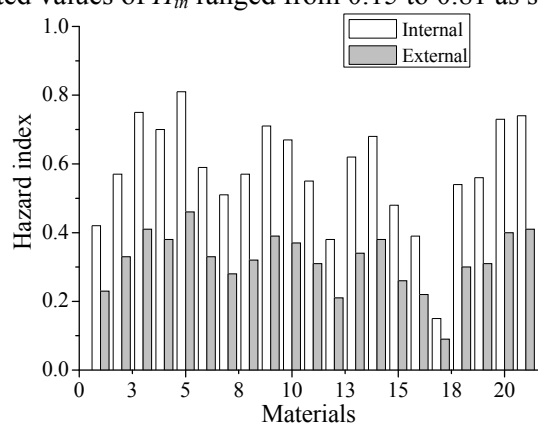


Fig.1. The measured values of both the external and the internal hazard indices.

Conclusion

Based on the results of measurement it can be concluded that the investigated materials are not radioactive in the context of the law [5]. Keeping in mind that the investigated samples used as one component in the recipe for the production of ceramics it can be concluded that there are no legal restrictions in terms of radioactivity in circulation and use of the investigated materials only if 3% of the samples used.

References

- [1] J. Beretka, P. J. Mathew, Natural radioactivity of Australian building materials, industrial wastes and by-products, *Health Phys.*, 1985, **48**, 87-95.
- [2] G. F. Bothe, D. Stewart Smith, D. Wagstaff, M. Dibblee, The radiological aspects of zircon sand use, *Health Phys.*, 1980, **38**, 393-398.
- [3] Official Journal of the Federal Republic of Yugoslavia, Regulations for the maximum limits of radioactive contamination of the human environment and decontamination procedures. Serbia, 1999, **9**, 4.
- [4] L. Xinwei, Radioactivity level in Chinese building ceramic tile, *Radiat. Prot. Dosim.*, 2004, **112**, 323-327.
- [5] Official Journal of the Federal Republic of Yugoslavia, Regulation on conditions for trade and use of radioactive materials, x-ray apparatus and other devices that produce radioactive radiation, 1998, **32**.

APPLICATION OF ASCORBIC ACID AS A RADIOLYTIC STABILIZER FOR [¹³¹I]mIBG

M. Lazarević, S.Vranješ, N. Nikolić, M. Mirković,
D. Janković and D.Stanković

*Laboratory for Radioisotopes, Vinča Institute, P.O.Box 522, 11000 Belgrade,
Serbia*

Abstract

In this paper the results of a stability of [¹³¹I]mIBG, stored under various conditions, are presented. The stability was followed during 14 days. The most important radiochemical impurity in [¹³¹I]mIBG is free [¹³¹I]iodide, formed by radiolysis. The results indicate that the rate of radiolytic decomposition of [¹³¹I]mIBG is much slower at higher concentration of ascorbic acid (20 mg/mCi) and at lower storage temperature (4°C).

Introduction

Meta-iodobenzylguanidine (mIBG) is an analogue of the adrenergic neuron blocking guanethidine. mIBG labeled with iodine-131 is intensively used radiopharmaceutical in diagnostic scintigraphy and radionuclide therapy of neural crest derived tumors such as neuroblastoma, malignant pheochromocytoma and paraganglioma [1]. [¹³¹I]mIBG undergoes radiolytic decomposition over time, resulting in the release of free [¹³¹I]iodide which after intravenous application accumulates mainly in the thyroid, causing unnecessary radiation damage. Moreover, only bound radioactivity in the form of [¹³¹I]mIBG will reach the targeted tumors [2]. As radiolabeled compound should stay unchanged for a period up to 2 weeks, the amount of free [¹³¹I]iodide in the pharmaceutical preparation of [¹³¹I]mIBG has to be reduced. In order to limit the formation of free [¹³¹I]iodide, some producers keep [¹³¹I]mIBG at -40°C or in lyophilized form that is inconvenient for transport and application in nuclear medicine departments. Therefore, addition of stabilizing agents such as ascorbic acid in the final kit preparation could solve the problems related to the relative instability of [¹³¹I]mIBG at room temperature.

Purpose of this experiment was to investigate the effects of temperature and amount of stabilizer on the radiopharmaceutical stability of [¹³¹I]mIBG.

Experimental

mIBG was synthesized according to a slightly modified version of Wieland et al [3] in the Laboratory for radioisotopes of the Vinča Institute.

The radiolabelling procedure of mIBG involved isotopic exchange reaction (160 °C, 45 min) catalyzed by Cu(I) generated *in situ* by addition of Na₂S₂O₅ to CuSO₄ [4]. Purification of radiolabelled mIBG from the excess of unbounded iodine-131 was performed by column chromatography (DEAE cellulose). To

ascertain the effect of temperature and the quantity of stabilizer on the stability of [¹³¹I]mIBG, three samples of purified radiopharmaceutical were formulated with 5mg, 10mg and 20 mg of ascorbic acid per 1mCi of [¹³¹I]mIBG. The stability was followed by investigation of the radiochemical purity of [¹³¹I]mIBG at 22°C, 15°C and 4°C during 14 days. Radiochemical purity of [¹³¹I]mIBG was determined by thin layer chromatography (TLC) on silica gel (Merck) using the mixture of ethyl acetate and ethanol as the mobile phase. The most important radiochemical impurity in the form of free [¹³¹I]iodide migrates with the solvent front (Rf=0.9-1.0), while [¹³¹I]mIBG remains at the origin. The radioactivity distribution was obtained by measuring 1cm long pieces of the strips and the percentage of both fractions were calculated against the total strip radioactivity.

Results and Discussion

It was found that the stability could be affected by both – the amount of stabilizer and temperature. According to Eur.Pharmacopoeia [5] the radiochemical purity of [¹³¹I]mIBG in use for nuclear medicine investigation in human, must be at least 95 %. Figure 1 shows the effect of temperature on the stability of [¹³¹I]mIBG in the kit formulation with 5 mg/mCi of ascorbic acid.

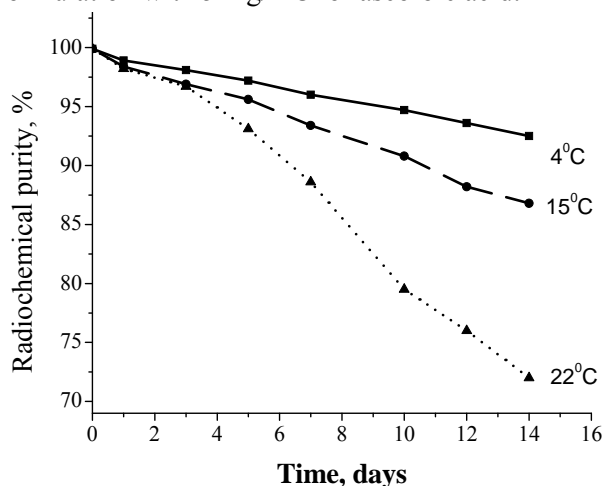


Fig. 1. The effect of temperature on the stability of [¹³¹I]mIBG

From this data, it is evident that at 4°C, level of [¹³¹I]iodide in [¹³¹I]mIBG increases from 0 % to 5 % in 10 days, while if it is stored at 15°C, the [¹³¹I]iodide level increased to 5% in 5 days. At room temperature (22°C) the radiochemical purity was decreased 2 % within 24 hours.

The stabilization effect of ascorbic acid on [¹³¹I]mIBG at room temperature (22°C) during two weeks (Fig. 2) was observed in the kit formulation with increasing concentration of ascorbic acid. It is evident that radio chemical stability of [¹³¹I]mIBG in the kit, at room temperature, increases with increasing concentration of the ascorbic acid.

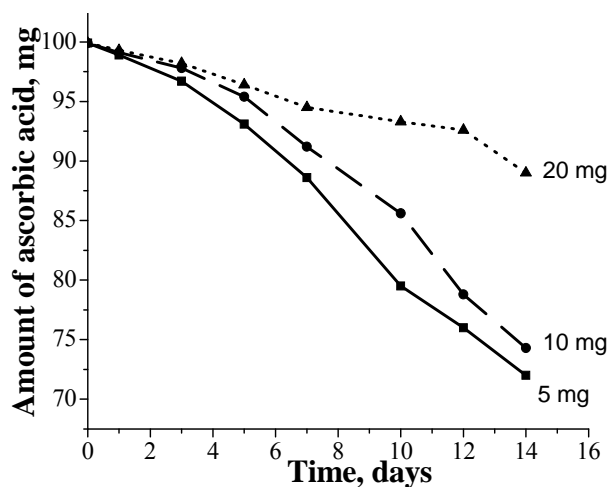


Fig.2. The effect of the concentration of ascorbic acid on the stability of [^{131}I]MIBG

Conclusion

In this study, we explored the factors influencing the stability of [^{131}I]mIBG and found that both temperature and the amount of ascorbic acid have significant impact on the stability of [^{131}I]mIBG. As results in Fig. 1 and Fig. 2 shows, the highest concentration of ascorbic acid (20 mg/mCi) as well as the lowest storage temperature (4 $^{\circ}\text{C}$) equally affected on the reduction of radiolytic decomposition of [^{131}I]mIBG. Further, [^{131}I]mIBG kit formulation with 20 mg of ascorbic acid per 1mCi, added after labeling, will be prepared since it is particularly simple for further handling in nuclear medicine departments and radiochemically stable for a longer period.

References

- [1] T. Yassine, M. A. Bakir, S. Shanan, M. Al-Asaad, *J. Radioanal. Nucl. Chem.*, 2003, **258**, 635-637.
- [2] A. R. Wafelman, C.A. Hoefnagel, R. A. A. Maes, J. H. Beijnen, *Appl. Radiat. Isot.*, 1994, **45**, 183-189.
- [3] D. M. Wieland, J. L. Wu, L.E. Brown, T. J. Mangner, D. P. Swanson, T. J. Mangwaltes, *J. Nucl. Med.*, 1980, **21**, 349.
- [4] N. S. Nikolić, M. D. Mirković, S. D. Vranješ-Đurić, D. D. Đokić, *Proceedings Phys. Chem*, 2006, 431-436.
- [5] *Eur. Pharmacopoeia* (Third Edition), Council of Europe, Strasbourg, 1997.

SYNTHESIS AND CHARACTERIZATION OF A NEW DIIMINEDIOXIME LIGAND AND ITS COPPER (II) COMPLEX AS POTENTIAL ⁶⁴Cu(II)-RADIOPHARMACEUTICALS

M. Mirković¹, D. Mijin², S. Vranješ-Đurić¹, M. Lazarević¹ and N. Nikolić¹

¹Laboratory for Radioisotopes, Vinča Institute of Nuclear Sciences, P. O. Box 522, 11001 Belgrade, Serbia, ²Department of Organic Chemistry, Faculty of Technology and Metallurgy, University of Belgrade, Karnegijeva 4, P. O. Box 3503, 11120 Belgrade, Serbia

Abstract

As a part of effort to an develop ⁶⁴Cu-based radiopharmaceuticals for PET (positron emission tomography) imaging of multidrug resistance in cancer, a new diiminedioxime ligand was prepared. Its Cu(II) complex was synthesized from Cu(OAc)₂ by heating in methanol. The structure of the ligand was established using elemental analysis, UV-Vis, IR, ¹H and ¹³C NMR technique. The isolated complex was characterized by means of elemental analysis, IR and UV-Vis, and its structure was proposed.

Introduction

Positron emission tomography (PET) is a valuable diagnostic tool, but its availability is limited because the half-lives of many PET radionuclides are too short to allow their delivery beyond the site where they are produced. There is, therefore, considerable interest in the development of PET radiopharmaceuticals based on positron-emitting radionuclides with longer half-lives (e.g., ¹²⁴I, t_{1/2} = 4.2 d; ^{94m}Tc, t_{1/2} = 52 min; ⁶⁴Cu, t_{1/2} = 12.7 h). Because of its convenient half-life and ease of production, ⁶⁴Cu is a strong candidate on which to build a family of PET radiopharmaceuticals for a variety of applications to complement ¹⁸F[FDG][1]. On another front, organic scaffolds capable of accommodating PET radionuclides that generate novel metallopharmaceuticals through short synthetic routes have been reported. Based upon rigorous prior contributions [2,3], a stable, monocationic radiolabeled complex of copper(II) was obtained as a potential ⁶⁴Cu PET radiopharmaceutical [4]. The desired diiminedioxime ligand was synthesized from 2,3-dimethyl-propane-1,2-diamine and heptane-2,3-dione-3-oxime. Diiminedioxime as tetradentate ligands can form complexes with transition metal ions, forming a hydrogen bond between the two oxime groups by removing one hydrogen ion [5].

Results and Discussion

Materials and methods: All reagents and solvents used in these studies were obtained from commercial sources without further purification. The ¹³C and ¹H NMR spectral measurements were performed on a Varian Gemini 2000

(200 MHz). The spectra were recorded at room temperature in deuterated dimethyl sulfoxide (DMSO- d_6). IR Spectra were recorded on a Bomem MB 100 FTIR spectrophotometer in the form of KBr pellets. Elemental (C, H, N) analysis of the samples was carried out by standard micromethods in the Center for Instrumental Analysis, Faculty of Chemistry, Belgrade. Spectrophotometric measurements were performed by using a Uvicon 810/820 spectrophotometer.

Preparation of the ligand: 4,9-Diaza-3,10-diethyl-3,9-undecadiene-2,11-dione bis-oxime (LH₂) was prepared using the method described in the literature [6], with a slight modification, which included heating of reaction mixture and crystallization of the product in petroleum-ether.

Preparation of the complex: Cu(II) acetate monohydrate in 10 ml of methanol was added to a hot methanol solution of ligand (1:1 molar ratio). The mixture was then refluxed for 3 h. An aqueous solution of sodium perchlorate was added to the reaction mixture and stirred well. The reaction mixture was allowed to stand at room temperature for 3 days, and brown crystals were formed. The crystals were collected and dried in a desiccator. Spectrophotometric investigation indicated complex formation in methanol (for UV-spectroscopy, min. 99.8 %) with absorption maximum at 240 nm and ratio M:L=1:1, depicted in Fig. 1.

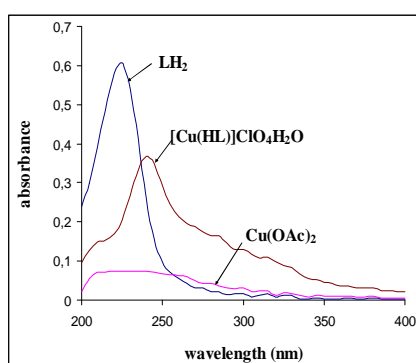


Fig. 1. UV absorption spectrum in methanol: LH₂, [Cu(LH)]ClO₄H₂O, Cu(OAc)₂, each 2×10^{-5} M.

Table 1. ¹H NMR and ¹³C NMR spectral data (δ ppm) for the ligand LH₂.

LH ₂ *	(a)	(b)	(c)	(d)	(e)	(f)	(g)	(h)
¹ H NMR	1.79(s)	3.48(s)	-	2.57(q)	0.96(t)	-	1.91(s)	11.41(s)
¹³ C NMR	28.99	50.29	155.52	19.67	11.69	167.9	9.27	-

s, singlet; t, triplet; q, quartet

* structure of LH₂ with all the protons and carbon atoms is presented in the Fig. 2.

All the protons and carbon atoms were found to be in their expected regions (Table 1). When the complex is formed from ligand, two C-N bonds are distinguishable. Two ν (C-N) are observed at lower frequencies than that in the free ligand, supporting the coordination at oxime and imine nitrogens (Table 2). According to presenting data proposed structures are shown in Fig. 2.

Table 2. Physical properties, elemental analysis and vibrational frequencies for the C-N bond of the ligand and complex.

Compound	m.p. (C°)	Yield (%)	Color	Calcd. (found)%			v (C-N)
				C	H	N	
LH ₂	143	65	white	59.55	9.28	19.84	1622 (s)
				(59.25)	(9.32)	(19.74)	
[Cu(HL)]ClO ₄ H ₂ O	>200	45	brown	36.37	5.89	12.12	1625 (w)
				(36.67)	(5.99)	(12.38)	1524 (m)

s, strong; m, medium; w, weak;

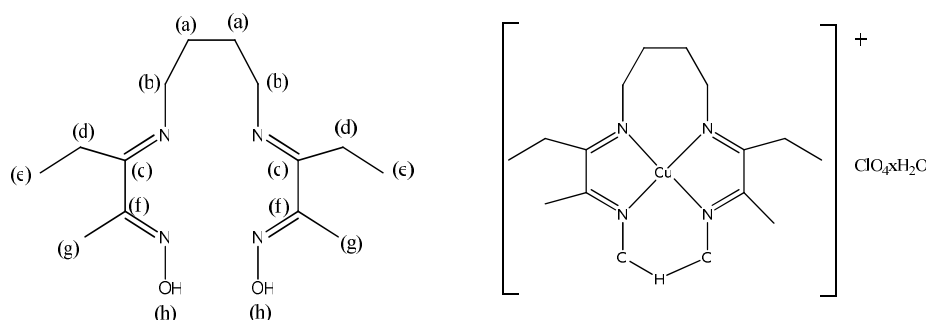


Fig. 2. Structures of LH₂ and Cu(LH)]ClO₄H₂O.

Conclusion

A new tetradentate diiminedioxime (LH₂) was successfully synthesized and characterized as well as its Cu(II) complex. On the basis of the obtained results and the literature data on similar compounds [1,5,7] we proposed structure of complex. Efforts are currently underway to prepare the corresponding ⁶⁴Cu complex.

References

- [1] S. Kiani, R. Staples, et al., *Polyhedron*, 2009, **28**, 775.
- [2] O. Anderson, A. Packard, *Inorg. Chem.*, 1980, **19**, 2941.
- [3] O. Anderson, A. Packard, *Inorg. Chem.*, 1979, **18**, 1940.
- [4] A. Packard, J. Kronauge, et al., *Nucl. Med. Biol.*, 2002, **29**, 289.
- [5] P. Kitiphaisalnont, S. Thohinung, et al., *Polyhedron*, 2006, **25**, 2710.
- [6] S. Banerjee, G. Samuel, et al., *Nucl. Med. Biol.*, 1999, **26**, 327.
- [7] Y. Sulfab, F. Al-Sogair, *Transition Metal Chemistry*, 2002, **27**, 299.

SYNTHESIS AND CHARACTERIZATION OF A NEW DIAMINODIOXIME, A POTENTIAL LIGAND FOR ^{99m}Tc RADIOPHARMACEUTICALS

M. Mirković¹, D. Mijin², D. Janković¹, S. Trifunović³ and N. Nikolić¹

¹Laboratory for Radioisotopes, Vinča Institute of Nuclear Sciences, P.O.Box 522, 11001 Belgrade, Serbia, ²Department of Organic Chemistry, Faculty of Technology and Metallurgy, University of Belgrade, Karnegijeva 4, P.O. Box 3503, 11120 Belgrade, Serbia, ³Faculty of Chemistry, University of Belgrade, Studentski trg 16, P.O. Box 158, 11000 Belgrade, Serbia

Abstract

This paper reports synthesis of a new diaminodioxime ligand, derivative of hexamethylpropyleneamine oxime (HM-PAO). The $^{99m}\text{Tc(V)-d,l-HM-PAO}$ complex is well-known radiopharmaceutical for regional blood flow imaging. The structure of the new ligand was investigated by elemental analysis, IR, ^1H and ^{13}C NMR. Complexation studies with ^{99m}Tc were carried out using stannous chloride as the reducing agent. The complex was characterized by paper chromatography and thin-layer chromatography. It was obtained in high yield when the reactions were carried out at pH=9. Also, it was found that the complex was stable up to 4 h.

Introduction

The radiopharmaceuticals currently being used for brain-perfusion studies are the ^{99m}Tc complexes of the tetradentate ligands hexamethylpropyleneamine oxime (HM-PAO) and ethylcysteinate dimer (ECD). Both the ligands form neutral and lipophilic complexes with ^{99m}Tc possessing an oxotechnetium core. While $^{99m}\text{Tc-HM-PAO}$ possesses two amine and two oxime donors, the $^{99m}\text{Tc-ECD}$ consist of two amine and two thiol donors [1]. The aim was to obtain the ligand which combines the best overall features of high brain uptake, fixed regional distribution within the brain and ease of radiopharmaceutical preparations [2]. The goal of this work was to examine the use of a new ligand as a potential candidate for the brain-perfusion imaging in single-photon emission computerized tomography (SPECT). The new ligand shows stereoisomerism, but we now report only preliminary research without the diastereo-enantio separation of isomeric mixtures of the meso- and d,l- diastereoisomers. This will be a part of further investigations.

Results and Discussion

Materials and methods: All reagents and solvents used in these studies were obtained from commercial sources without further purification. The $^{99m}\text{TcO}_4^-$ was

obtained from $^{99}\text{Mo}/^{99\text{m}}\text{Tc}$ generator prepared in our laboratory ("Vinča" Institute) and commercially available. IR Spectra were recorded on a Bomem MB 100 FTIR spectrophotometer in the form of KBr pellets. The ^1H and ^{13}C NMR spectral measurements were performed on a Varian Gemini 2000 (200 MHz). The spectra were recorded at room temperature in deuterated dimethyl sulfoxide (DMSO-d_6). Elemental (C, H, N) analysis of the samples was carried out by standard micromethods in the Center for Instrumental Analysis, Faculty of Chemistry, Belgrade. Radioactivity measurements of chromatography were performed in a NaI(Tl) well-type gamma counter.

Preparation of ligand: 4,9-Diaza-3,10-diethylundecadiene-2,11-dione bis-oxime (LH_2) was prepared using the method described in the literature [3], with a slight modification, which included crystallization of the imine in petroleum-ether.

Preparation of $^{99\text{m}}\text{Tc}$ complex: Complexation studies of the ligand with $^{99\text{m}}\text{Tc}$ were carried out using stannous chloride as the reducing agent. 1 mg of ligand LH_2 was dissolved in 2.5 ml of water adjusted to pH 1.5-2 with concentrated HCl. Then, 13.5 μl of stannous chloride (5 mg dissolved in 0.05 ml of concentrated HCl and 4.95 ml of distilled water) was added and pH was adjusted to 9. 1.5 ml of sodium pertechnetate ($^{99\text{m}}\text{TcO}_4^-$, 0.5 mCi/ml) was injected into the vial. The vial was shaken for 1 min. The total reaction volume in vial was maintained at 4 ml.

Paper chromatography and thin-layer chromatography: The labeling yield was determined using a combination of two chromatographic systems: paper chromatography on Whatman No.1 with acetonitrile:water (1:1) as the mobile phase and TLC on silica gel 60 strips with saline as the mobile phase.

All the protons and carbon atoms for LH_2 (Table 1) were found to be in their expected regions, in accordance to IR spectroscopic and elemental analysis data (Table 2).

Table 1. ^1H NMR and ^{13}C NMR spectral data (δ ppm) for the ligand LH_2 .

LH_2^*	(a)	(b)	(c)	(d)	(e)	(f)	(g)	(h)	(i)
^1H NMR	1.34 t	2.90 t	3.36 t	1.48 q	0.75 t	-	1.61 s	10.3 s	inv
^{13}C NMR	27.70	47.09	63.43	25.81	8.40	157.7	10.90	-	-

s, singlet; t, triplet; q, quintet, inv, invisible

* structure of LH_2 with all the protons and carbon atoms is presented in the **Fig. 1**.

Table 2. Physical properties, elemental analysis and some vibrational frequencies for the ligand LH_2 .

Comp.	m.p. ($^\circ\text{C}$)	Yield (%)	Color	Calcd. (found)%			ν (-OH)	ν (-OH, NH)
				C	H	N		
LH_2	167	55	white	58.71	10.56	19.56	3257	3190
				(58.39)	(10.56)	(19.35)		

According to the literature data for similar diaminodioxime ligands and their $^{99\text{m}}\text{Tc}$ -labelled complexes [4], proposed structures of LH_2 and $^{99\text{m}}\text{Tc-LH}_2$ are shown in Fig.1.

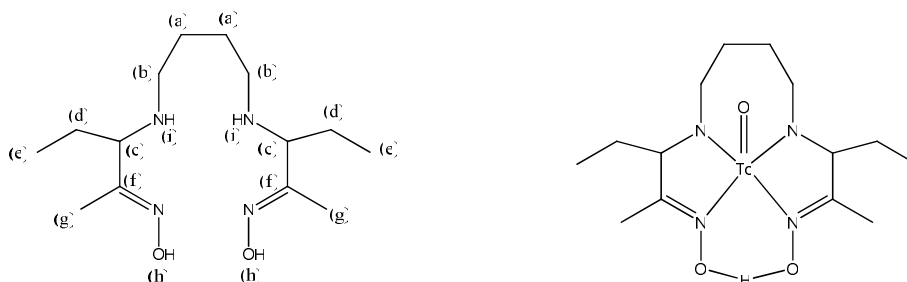


Fig. 1. Structure of LH_2 and proposed structure of ^{99m}Tc complex.

Radiochemical purity of the complex estimated at different time intervals are presented in Fig.2. Complexation reaction were done at pH=9.

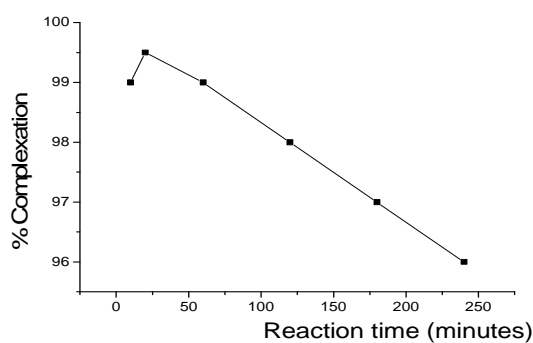


Fig. 2. Radiochemical purity of the complex.

Conclusion

A new tetradentate diaminedioxime ligand (LH_2) was successfully synthesized and characterized by elemental analysis, IR, 1H , and ^{13}C NMR. From the obtained results, it can be concluded that ^{99m}Tc complex could be made easy with a ligand such as LH_2 . This complex was obtained in good yield (> 95%) and was found to be stable in investigated conditions up to 4 h.

References

- [1] K. Kothari, S. Banerjee, et al., Applied Radiation and Isotopes, 2000, **52**, 69.
- [2] R. Neirinckx, L. Canning, et al., J. Nucl. Med., 1987, **28**, 191.
- [3] S. Banerjee, G. Samuel, et al., Nucl. Med. Biol., 1999, **26**, 327.
- [4] L. Canning, et al., United States Patent, 1988, Patent number, 4.789.736.

VALIDATION ASSAY FOR THE DIRECT SPECTROPHOTOMETRIC DETERMINATION OF HESPERIDIN IN THE PHARMACEUTICAL PREPARATION

S. Mićić, V. Kuntić and N. Pejić

Faculty of Pharmacy, University of Belgrade, Vojvode Stepe 450, P.O.Box 146, Belgrade, Serbia e-mail: svetlana.micic@pharmacy.bg.ac.rs

Abstract

A simple and rapid direct spectrophotometric method for the determination of hesperidin is proposed and validated. The influence of wavelength, solvent, the ionic strength, pH and temperature on hesperidin determination were investigated. Under the optimum conditions, $\lambda = 283$ nm, 60 % methanol as the solvent, ionic strength, $I = 2.5 \times 10^{-5}$ mol L⁻¹, pH = 6.4 and T = 37.0 °C, the Beer's law is obeyed in the concentration range 1.83 – 24.5 $\mu\text{g mL}^{-1}$. The molar absorptivity and Sandell's sensitivity were found to be 1.8×10^4 L mol⁻¹ cm⁻¹ and 0.03 $\mu\text{g cm}^{-2}$, respectively. The sensitivity of the proposed method was adequate (0.9 $\mu\text{g mL}^{-1}$ as limit of detection and 3.2 $\mu\text{g mL}^{-1}$ as limit of quantification). Applicability of the proposed method to the direct determination of total flavonoids as hesperidin equivalents in pharmaceutical formulation (Vitamin C with citrus bioflavonoids & Rose Hips) was demonstrated.

Introduction

Hesperidin belongs to the flavonoids of flavanone type, a ubiquitous group of polyphenolic substances which are present in most plants, concentrated in seeds, fruit skin or peel, bark, and flowers. Knowing that hesperidin easily reacts with metal ions forming chelates which are usually colored and as well as it absorb at a different wavelength than hesperidin, we optimise and utilize these chelating reactions for hesperidin determination by indirect spectrophotometric methods.

That direct UV spectrophotometry shows many advantages (simplicity, rapidity, adequate sensitivity, operational convenience, relatively low cost of equipment) over some other routine methods, we developed and validated a simple and inexpensive direct spectrophotometric method for hesperidin determination by simply selecting optimum parameters such as wavelength, solvent, pH, the ionic strength and temperature. In order to assess the analytical potential of the proposed method which would be suitable for the analysis of total flavonoids as hesperidin equivalent in pharmaceutical formulation, the effects of possible interfering

substances, predominantly ascorbic acid (AA) were also studied (Hesperidin is present in nutritional supplements such as *vitamin C with bioflavonoids*).

Experimental

For all absorbance measurements was used UV–VIS spectrophotometer Beckman DU-600 (Fullerton, Ca, USA) with 1 cm optical path length quartz cuvette. All of spectra were registered with a scan rate of 600 nm min^{-1} . Spectral scans were continuously collected from 260 to 400 nm during each run. For pH measurements, a pH-meter (pHM-82 Radiometer Copenhagen), accuracy of $\pm 0.001 \text{ pH}$, equipped with the combined electrode (No. CW. 733 Series No.35162, Russel) was used. The temperature was controlled within $\pm 0.2^\circ\text{C}$ by circulating water thermostat (Series U, MLW Freital, Germany). Ultrasonic bath (L.U.5.7 Fungilab, S.A, Spain) was used for dissolving the samples.

Results and discussion

Preliminary experiments were run to find out the best operative conditions to obtain the calibration curve, as well as for the measurements of real sample. The parameters optimized included wavelength, solvent, the ionic strength, pH and temperature.

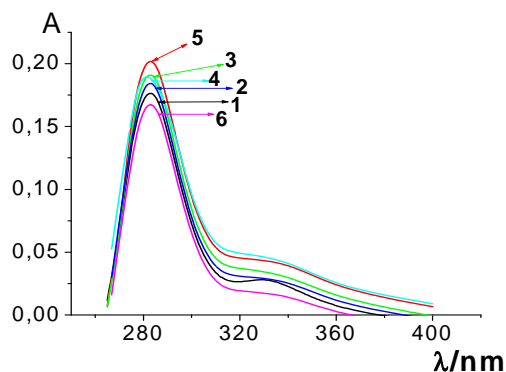


Fig.1. Absorption spectra of hesperidin in 60 % methanol at different pH values: 2.6 (curve 1), 3.7 (curve 2), 4.1 (curve 3), 4.9 (curve 4), 6.4 (curve 5) and 8.8 (curve 6); $[\text{Hesp}] = 6.1 \mu\text{g mL}^{-1}$.

Typically, two major absorption maxima (Figure 1) are observed in the UV-VIS spectrum of hesperidin: in the range around 280 nm (referred to as band II in flavonoids) and the one around 330 nm (band I). Absorbance measurements are carried out at 283 nm because this band is less sensitive to matrix influence, since absorption band II may be considered as to have originated from electron transitions in the A-ring benzoyl system of Hesperidin [1].

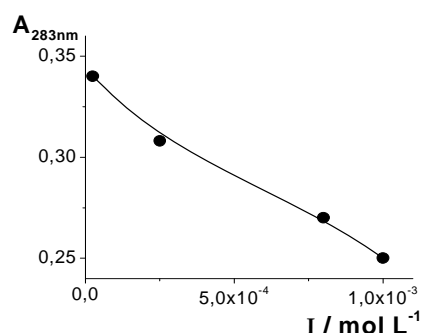


Fig.2. The influence of ionic strength on absorption maximum of the hesperidin solution; [Hesperidin] = 10.4 μ g mL⁻¹, pH = 6.4 and T = 37°C.

The optimum medium for direct hesperidin determination related to 60% methanol and pH = 6.4 (Figure 1, curve 5). Solvent with this percentage of methanol enables the best compromise among hesperidin solubility. The influence of the ionic strengths on absorption spectra of hesperidin, at the constant value of both, pH and temperature (pH = 6.4 and T = 37.0°C) were investigated and from the Figure 2, it is obvious that the best conditions (the higher absorbance) relate to the value of ionic strength $I = 2.5 \times 10^{-5} \text{ mol L}^{-1}$.

Conclusion

The developed spectrophotometric method is convenient and efficient for determination of hesperidin in bulk drug as well as in pharmaceutical preparation. It operates without any derivatization reaction and shows good analytical features. It is demonstrated that the proposed method is very suitable for routine analysis of pharmaceuticals with hesperidin as principal flavonoid, without any pretreatment of the samples, and apart from its dissolution.

Acknowledgments

We gratefully acknowledge the financial support from the Ministry of Science and Environment of the Republic of Serbia, grant No 143012 and No 142025.

References

- [1] N. Pejić, S. Blagojević, S. Anić, V. Vukojević and Lj. Kolar-Anić, *J. Anal. Bioanal. Chem.*, 2005, **381**, 775.
- [2] D. Malešev and V. Kuntic, *J. Serb. Chem.Soc.*, 2007, **72**, 921.
- [3] E. Middleton, C. Kandaswami and J. B. Harborne (Eds.), *The Flavonoids: Advances in Research Since 1986*, Chapman & Hall Ltd., London, 1994.

SYNTHESIS, CHARACTERIZATION AND *in vitro* ANTITUMORAL ACTIVITY OF PLATINUM(II) COMPLEXES WITH *O,O'*-DIALKYL ESTERS OF (*S,S*)-ETHYLENEDIAMINE-*N,N'*-DI-2-(4-METHYL)-PENTANOIC ACID DIHYDROCHLORIDE

J. M. Vujić,^{a,b} G. N. Kaluđerović,^{c,d} B. B. Zmejkovski,^c M. Milovanović,^e
V. Volarević,^e N. Arsenijević^e and S. R. Trifunović^a

^aDepartment of Chemistry, Faculty of Science, University of Kragujevac, R. Domanovića 12, 34000 Kragujevac, Serbia; ^bFaculty of Agronomy, University of Kragujevac, Cara Dušana 34, 32000, Čačak, Serbia; ^cDepartment of Chemistry, Institute of Chemistry, Technology and Metallurgy, University of Belgrade, Studentski Trg 14, 11000 Belgrade, Serbia; ^dInstitut für Chemie, Martin-Luther-Universität Helle-Wittenberg, Kurt-Mothes-Straße 2, 06120 Halle, Deutschland; ^eThe Medical Faculty, University of Kragujevac, Svetozara Markovića 69, 34000 Kragujevac, Serbia

Abstract

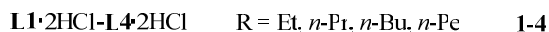
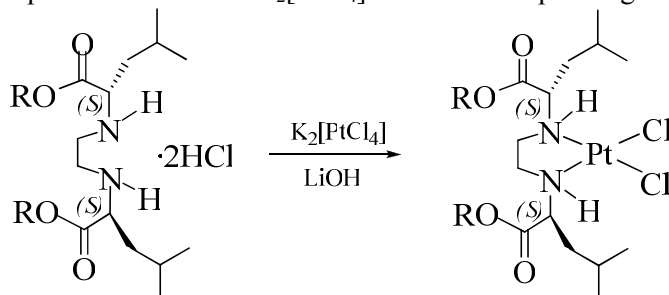
Four novel platinum(II) complexes **1–4** with bidentate *N,N'*-ligand precursors *O,O'*-dialkyl esters (alkyl = ethyl, *n*-propyl, *n*-butyl and *n*-pentyl), **L1**·2HCl–**L4**·2HCl, of (*S,S*)-ethylenediamine-*N,N'*-di-2-(4-methyl)-pentanoic acid dihydrochloride [(*S,S*)-H₄eddl]Cl₂ were synthesized and characterized by IR, ¹H NMR and ¹³C NMR spectroscopy and elemental analysis. *In vitro* cytotoxicity of compounds **1–4** was determined against chronic lymphocytic leukemia cells (CLL). The compounds were found to exhibit higher antitumoral activity than cisplatin on CLL cells.

Introduction

Platinum complexes have been widely used in *in vitro* antitumoral studies [1,2]. Recently, several platinum(II) and platinum(IV) complexes with H₂edda/R₂edda-derived ligands (H₂edda – ethylenediamine-*N,N'*-diacetic acid; R₂edda – corresponding esters) have been tested on L929 fibrosarcoma and U251 astrocytoma tumor cells [2]. Significantly, *in vitro* antitumoral activity of two platinum(IV) complexes with dibutyl and dipentyl esters of bidentate eddp, [PtCl₄(R₂eddp)] (R = *n*-Bu and *n*-Pe), respectively, was demonstrated on both cell lines. It was found that kinetics of the tumor cell death process induced by these complexes was considerably faster than that induced by cisplatin. Beside this *N,N'* ligands having normal chains in ester function, branched chain esters were also used for the synthesis and antitumoral testings [3]. As a part of our continuous study, here is described the synthesis, characterization and antiproliferative activity of four novel platinum(II) complexes.

Experimental

The esters **L1**·2HCl–**L4**·2HCl were prepared using the previously described procedure [4]. Platinum(II) complexes **1**–**4** were synthesized by combining aqueous solutions of $K_2[PtCl_4]$ and the corresponding esters (Scheme 1).



Scheme 1. Synthesis of the platinum(II) complexes **1**–**4**.

In vitro antitumoral investigations were performed as described for similar compounds [4].

1·OC(CH₃)₂: Yield 65.14 mg, 44.46%. Anal. calcd. for C₁₈H₃₆N₂O₄Cl₂Pt·OC(CH₃)₂: C, 37.73; H, 6.33; N, 4.19%. Found: C, 37.40; H, 5.84; N, 4.52%.

2: Yield 67.24 mg, 43.95%. Anal. calcd. for C₂₀H₄₀N₂O₄Cl₂Pt: C, 37.62; H, 6.31; N, 4.39%. Found: C, 37.87; H, 5.95; N, 4.29%. **3**: Yield 58.24 mg, 36.63%. Anal. calcd. for C₂₂H₄₄N₂O₄Cl₂Pt: C, 39.64; H, 6.65; N, 4.20%. Found: C, 39.37; H, 6.70; N, 4.16%. **4**·2H₂O: Yield 56.43 mg, 32.24%. Anal. calcd. for C₂₄H₄₈N₂O₄Cl₂Pt·2H₂O: C, 39.45; H, 7.17; N, 3.83%. Found: C, 39.34; H, 7.31; N, 4.18%.

Results and Discussion

Absorption bands for secondary amino groups were found for **1**–**4** at 3088, 3143, 3133, 3139 cm⁻¹, $\nu(C=O)$ at 1739, 1739, 1740, 1741 cm⁻¹, $\nu(C-O)$ at 1194, 1195, 1197, 1197 cm⁻¹ and $\nu(CH_3)$ at 2960, 2961, 2960, 2959 cm⁻¹, respectively.

In the ¹H NMR spectra of **1**–**4**, the broad signals of hydrogen atoms belonging to secondary amino groups occur between 5.8–6.6 ppm. The signals of CH₂ protons of the ethylenediamine bridge showed coordination induced shifts in spectra of **1**–**4** (up to 0.9 ppm) giving a clear indication of nitrogen coordination. Signals for all methyl protons were found within the range of 0.86 – 1.13 ppm for all compounds. In ¹³C NMR spectra ester carbon atom resonances were found as expected, at around 170 ppm for all compounds verifying that oxygen is not a ligating atom. For the complexes NMR spectroscopic measurements uphold their constitution.

The cytotoxic effects of the complexes **1**–**4** on CLL cells were determined using MTT colorimetric technique [4]. All complexes showed a dose dependent antiproliferative effect toward CLL cells (Figure 1).

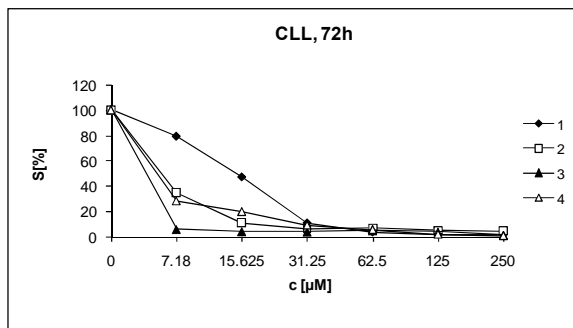


Fig.1. CLL cell survival after growth in the presence of platinum(II) complexes 1–4.

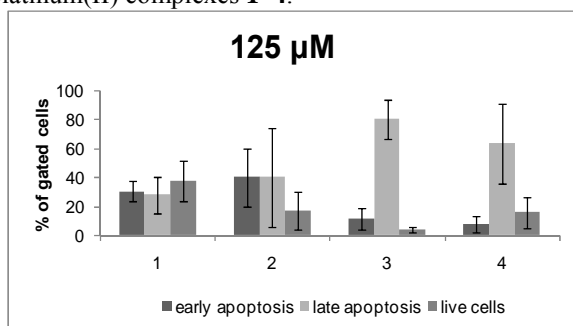


Fig.2. Percentages of apoptotic cells after 24 h of treatment with platinum(II) complexes 1–4.

Apoptotic effects of platinum(II) complexes were detected using the Annexin V–FITC Apo-ptosis Detection Kit after 24 hours of treatment with 125 µM platinum complexes.

Results showed that all platinum complexes induced apoptosis in CLL cells (Figure 2). Complexes 3 and 4 expressed significantly higher apoptotic effect in comparison to complexes 1 and 2 with mostly late apoptotic cells. The best effect showed complex 3; low concentration induced apoptosis in 60% (data not presented) of cells and most of them were in early stages of apoptosis.

Conclusion

Ligand precursors **L1**·2HCl–**L4**·2HCl and corresponding platinum(II) complexes 1–4 were synthesized and characterized. The cytotoxic activity of all the synthesized compounds was determined on chronic lymphocytic leukemia cells (CLL). The esters and their corresponding platinum(II) complexes exhibited moderate to low cytotoxic activity against selected CLL cell line.

References

- [1] L. Kelland, *Nature Reviews Cancer*, 2007, **7**, 573–584.
- [2] G. N. Kaluderović, H. Schmidt, D. Steinborn, T. J. Sabo, *Inorganic Biochemistry: Research Progress*, Nova Science Publishers, Inc. Hauppauge, NY, in press, 2008.
- [3] B. B. Krajčinović, G. N. Kaluderović, D. Steinborn, H. Schmidt, Ch. Wagner, Ž. Žižak, Z. D. Juranić, S. R. Trifunović, T. J. Sabo. *J. Inorg. Biochem.*, 2008, **102**, 892–900.
- [4] J. M. Vujić, M. Cvijović, G. N. Kaluderović, M. Milovanović, B. B. Zmejkovski, V. Volarević, N. Arsenijević, T. J. Sabo, S. R. Trifunović, *Eur. J. Med. Chem.*, 2010, doi:10.1016/j.ejmech.2010.05.005.

INVESTIGATION OF ANTIOXIDANT PROPERTIES OF COSMETICAL SKIN CREMES CONTAINING GRAPE EXTRACT

M. Legetic¹, D. Godevac², A. Ignjatović¹ and M. Mojović¹

¹*Faculty of Physical Chemistry, University of Belgrade, Studentski Trg 12–16, 11158, Belgrade, Serbia*

²*Institute of Chemistry, Technology and Metallurgy, Njegoševa 12, 11000 Belgrade, Serbia
milos@ffh.bg.ac.rs*

Abstract

Antioxidant activity of several grape extract containing cosmetic products; six commercially available and one homemade synthesized, was investigated. Several antioxidant effects were explored: effect of removing reactive oxygen species (hydroxyl and superoxide radicals) and capability of preventing lipid peroxidation. Electron paramagnetic resonance spin trap and spin-labeling spectroscopy was used. Obtained results, presented as antioxidant activity of each sample compared to controls, showed that concentrated homemade oily cream with grape extract have the highest efficiency removing even 90% of hydroxyl and 87 % of superoxide reactive oxygen species. Antioxidant additives in "Nature's" cream were the most efficient in prevention of lipid peroxidation.

Introduction

Reactive oxygen species (ROS) have an important role in various physiological processes such as receptor-mediated signaling pathways and the immune response. Both positive and negative biological functions are ascribed to superoxide ($\cdot\text{O}_2^-$), while the role of hydroxyl radical ($\cdot\text{OH}$) is concerned to be exclusively negative due to its high reactivity [1]. Reactive oxygen species can induce lipid peroxidation which can break down membrane integrity which affects properties and functions of the cell membrane including cell growth, signal transduction, membrane permeability, transport systems, receptor functions or enzyme activities [2]. Besides chemical and enzymatic production of free radicals, one specific process through which ROS can be generated is UV irradiation, which can provoke formation of $\cdot\text{OH}$ from water and $\cdot\text{O}_2^-$ from dissolved oxygen through photo-induced excitation [3], the processes which readily occur in skin. Therefore, there is a constant need for new, combined antioxidative mixtures which contain components which could decrease the amount of free radicals in skin and prevent declared counter effects. In this paper, the goal was to use specific EPR spectroscopy methods to evaluate the efficiency of different commercial promoted skin care products containing the grape as the key active component and one homemade synthesized skin cream composed of several commonly used components and, as

the main active component, grape extract. Our grape extract was analyzed by HPLC for content determination in order to point out which of the chemical species is responsible for its antioxidant activity (results not shown). The antioxidative activity and lipid peroxidation prevention of all cream samples were explored using EPR spin-trap DEPMPO and spin label 16-DS.

Experimental

Following creams were used in the experiments: Total fresh hydrating cream enriched with pure grape extract GARNIER, Micro-gold & grape whitening day cream PULLANA, Hydrating daily cream with vitamin C MURAD, Energizing hydrating emulsion based on pomegranate MURAD, Daily rumples cream with α -elastinol NATURE'S, Antioxidant daily cream with extract of seeds grape ORIFLAME and grape extract containing homemade skin cream. Synthesized oily cream with vitamin E and grape extract was made by commonly used components for one skin care cream: dissolving 10 mg or 50 mg of grape extract, mixed with vitamin E, boric acid, butyrum cacao, amandel oil, cholesterol, lanoline and vaseline. Grape extract was extracted with ethyl-acetate (90%) from dried grape seeds. 1 mg of this grape extract was dissolved in 1 ml of 18M Ω bidistilled and deionized water. Hydroxyl radical species were produced by Fenton reaction and superoxide radicals were generated by Hypoxantine/Xantine Oxidase system.

Results and Discussion

Results presented as antioxidant activity AA (in %) of all samples are presented in Fig.1 and Fig 2.

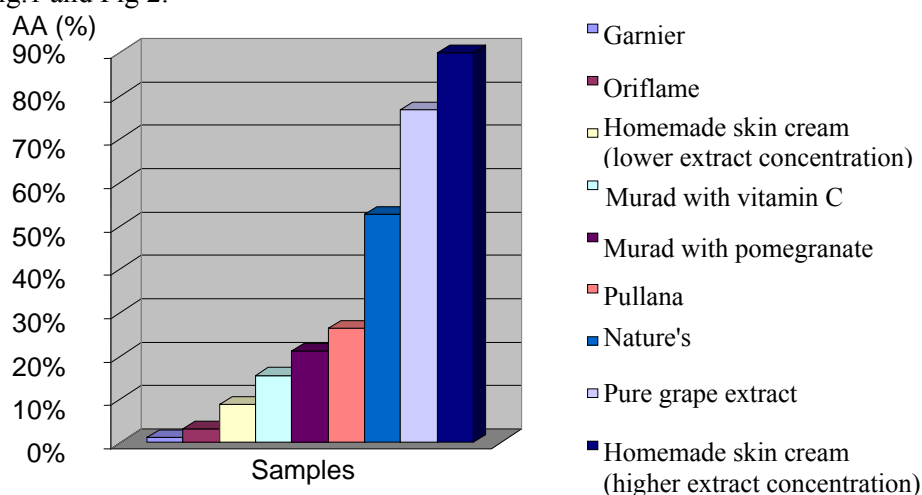


Fig.1. Antioxidative activity (in %) for different skin creams related to hydroxyl radical scavenging.

The best efficiency in reducing signal of hydroxyl and superoxide radicals (90% and 87%) was obtained by homemade skin cream with vitamin E and grape extract.

Vitamin E and butyrum cacao are probably responsible for the better activity of the cream comparing to the pure grape extract.

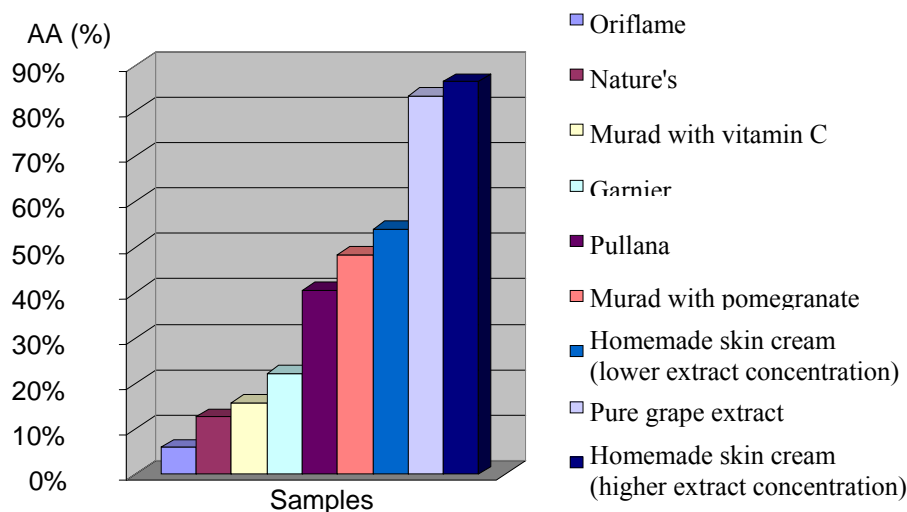


Fig.2. Antioxidative activity (in %) for different skin creams related to superoxide radical scavenging.

The best skin cream for Lipid peroxidation prevention induced by hydroxyl radical was Nature's cream followed by our by homemade skin cream (results not shown).

Conclusion

In this paper antioxidative activities of several different skin creams containing grape extract was investigated using EPR spectroscopy. From the presented results it could be concluded that different skin creams have diverse antioxidative qualities. Homemade skin cream with vitamin E and grape extract was shown to be the best choice for skin care probably owing to catechines, epicatechines and proanthocyanidin dimmers which were detected in pure grape extract using HPLC. Surprisingly to author expectations, some of the most commercial skin creams did not show any significant antioxidative value at all.

Acknowledgments

The authors acknowledge their gratitude to the Ministry of Science of Republic of Serbia for the financial support (Project #143016) and private pharmacy "Andjelkovic" for the help with homemade skin cream preparation.

References

- [1] B. Halliwell, J. M. Gutteridge., Free Radicals in Biology and Medicine, Oxford University Press, Oxford, 1999.
- [2] R. A. Cooper, N. Engl, J. Med., 1977, **297**, 371–377.
- [3] H. Nishikawa, Materials Lett., 2004, **58**, 14-16.

HYDROGELS IN CONTROLLED DRUG DELIVERY SYSTEMS

M. M. Babić¹, K. M. Antić¹, V. V. Pavelkić¹ and S. Lj. Tomić²

¹ Institute "Kirilo Savić", Vojvode Stepe 51, 11 000 Belgrade, Serbia

² Faculty of Technology and Metallurgy, Karnegijeva 4, 11000 Belgrade, Serbia

Abstract

In the present study hydrogels based on 2-hydroxyethyl acrylate P(HEA), 2-hydroxyethyl methacrylate P(HEMA), poly(alkylene glycol) (meth) acrylate (BIS) and itaconic acid (IA) are considered as systems for controlled release of active therapeutic agents. Antibiotic-cephalexin (CEX) and bronchodilators-theophylline (TPH) and fenethylline (FE) were used as a models of active agents for controlled release of drugs. The release profiles of the drugs, evaluated *in vitro* conditions (pH 7.40 at 37 °C, monitored by UV-VIS spectrophotometry), show that the hydrogels could be propound for the potential application as drug delivery systems for the controlled release of active therapeutic agents.

Introduction

Hydrogels, cross-linked polymer networks which do not dissolve in water but are able to absorb large amounts of water, have attracted great attention in the past thirty years due to their interesting properties. The absorption of water by a hydrogel is one of the most important factors which determine its properties and applications [1]. Due to their high water content, hydrogels also possess a degree of flexibility similar to natural tissues, which minimizes potential irritation to surrounding membranes and tissues. Thus, hydrogels have found widespread biomedical and pharmaceutical applications. They have been increasingly studied for uses such as matrices for tissue engineering, materials for immobilization of enzymes and cells, contact lenses, and drug delivery devices [2]. The aim of controlled release systems is to deliver the drug at a specified rate, keeping the drug concentration in the body at the therapeutically effective level, with convenient drug release profile [3].

Result and discussion

2-Hydroxyethyl methacrylate (HEMA), and poly(alkylene glycol) (meth)acrylates, Bisomers (BIS1, BIS2, BIS3, and BIS4), freshly distilled, and itaconic acid (IA) were used as components for hydrogel preparation. The hydrogels were prepared by gamma-irradiated radical copolymerization. Bulk cephalaxin (CEX), theophylline (TPH), and fenethylline (FE) were used as models of drugs. Release studies of the drugs have been carried out *in vitro* by placing the dried, loaded sample in a definite volume of the release medium (a buffer solutions of pH 7.40, at 37 °C), constantly stirred. The amount of drug released was measured spectrophotometrically, using a UV spectrophotometer (Shimadzu UV-Vis Spectrophotometer UV-1800).

The *in vitro* release of the drug was presented as fractional release profiles (M_t/M_e versus time), illustrated in Figure 1 (A, B, C, D).

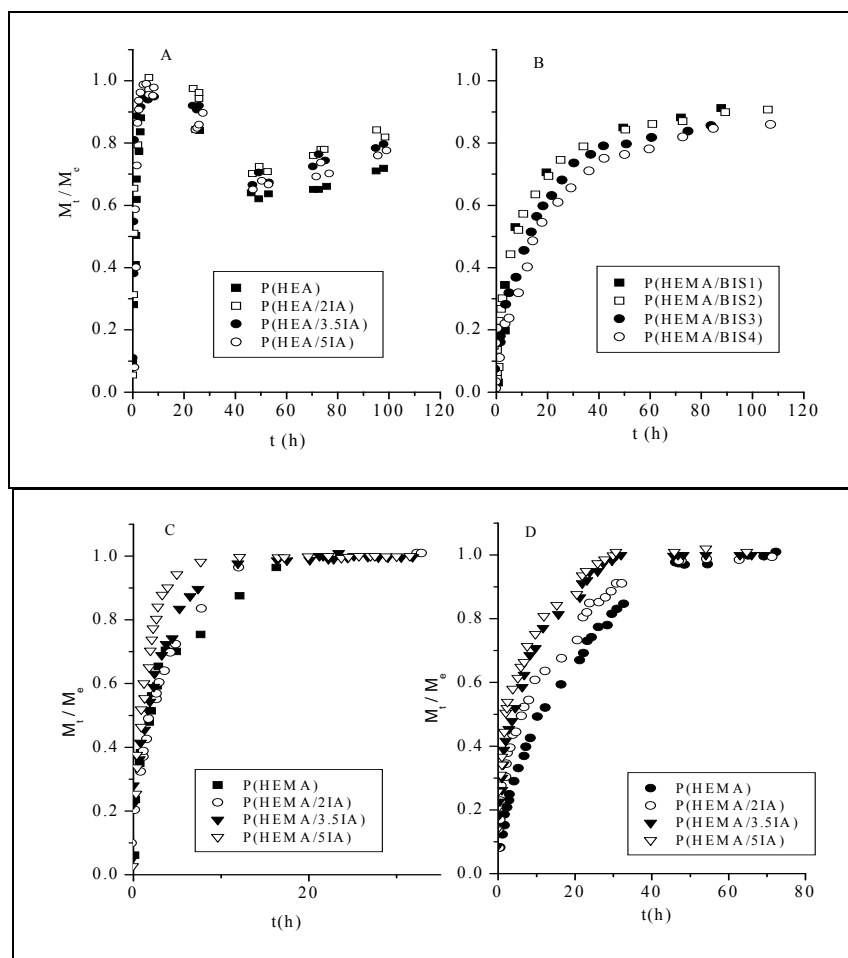


Fig.1. A. Drug release profiles of CEX from P(HEA/IA) hydrogels; B. Drug release profiles of CEX from P(HEMA/BIS) hydrogels; C. Drug release profiles of TPH from P(HEMA/IA) hydrogels; D. Drug release profiles of FE from P(HEMA/IA) hydrogels.

It can be seen for the release of the CEX from P(HEA/IA) hydrogels that there is a very pronounced "overshooting" effect, which results from the fact that these hydrogels have hydrophilic/hydrophobic transition during the drug release process (Fig. 1A). The release profiles of CEX from P(HEMA/BIS) samples (Fig. 1B) show slow and uniform release. The release of TPH from P(HEMA/IA) is faster, with the pronounced "burst" effect (Fig. 1C), while the of release of FE from P(HEMA/IA) (Fig. 1D) do not show a "burst" effect, especially for the samples with lower IA content. The slower release rate for FE than that for TPH from P(HEMA/IA) could be due to the larger size of FE molecule. Release process is

complex phenomenon. Therefore a variety of model equations concerning the mechanism of drug release can be found in the literature, but our systems could not be correlated with them. It established the following equations (obtained by correlation of ratio of $D_{d(\text{gel})}$ and $D_{d(\text{water})}$, and λ using program Origin pro 8.0) which could be relevant to characterize the release systems examined in our work:

$$\frac{D_{d(\text{gel})}}{D_{d(\text{voda})}} = 9.46 \times 10^{-3} + 8.02 \times 10^{-3} (1 - \lambda)^2$$

(for TPH release from P(HEMA/IA) hydrogels),

$$\frac{D_{d(\text{gel})}}{D_{d(\text{voda})}} = 6.34 \times 10^{-3} + 2.57 \times 10^{-3} (1 - \lambda)^2$$

(for FE release from P(HEMA/IA) hydrogels)

$$\frac{D_{d(\text{gel})}}{D_{d(\text{voda})}} = 0.41 - 0.11(1 - \lambda)^2 + 20(1 - \lambda)^4 - 2.15 \times 10^{-4} (1 - \lambda)^6$$

(for CEX release from P(HEMA/BIS) hydrogels)

$$\frac{D_{d(\text{gel})}}{D_{d(\text{voda})}} = 2.35 \times 10^{-4} \exp\left[\frac{(1 - \lambda)^2}{0.16}\right] + 7.2 \times 10^{-3}$$

(for CEX release from P(HEA/IA) hydrogels)

$D_{d(\text{gel})}$ is the diffusion coefficient of the drug during release process, $D_{d(\text{water})}$ is the diffusion coefficient of the drug in water and λ is the restriction coefficient (describes the ease of the drug release from the gels).

Conclusion

The aim of the present study was to develop controlled release drug delivery systems based on poly(meth)acrylate hydrogels. The release of drugs from these hydrogels showed controlled drug release profiles in therapeutic range of drug. It was found that the release profiles depend on the hydrogel composition (methacrylate or acrylate monomer residue, IA content and BIS type) and the type of drug. Different model equations is proposed for each drug-hydrogel system. It can be concluded that release process is complex and depends on the type of hydrogel and the drug. The hydrogels examined in this work may be used in drug delivery systems of active therapeutic agents.

Acknowledgement

This work was financially supported by the Ministry of Science and Technological Development, Republic of Serbia, under Project No. 142025.

References

- [1] S. Tomić, Pol. Bull., 2009, **63**, 837–851.
- [2] S. Tomić, Pol. Bull., 2006, **57**, 691–702.
- [3] A. Bajpai, S. Bhanu, S. Kankane, Prog. Polym. Sci., 2008, **33**, 1088–1118.

THE DIFFUSION OF METHYL SALICYLATE FROM MICROEMULSIONS AS A DRUG CARRIER

J. Veljković–Giga¹, J. Džopalić², N. Bošković–Vragolović²,
R. Garić–Grulović³ and R. Pjanović²

¹ *Galenika, a.d., Batajnički drum b.b., Zemun, Serbia*

² *Faculty of Technology and Metallurgy, Department of Chemical Engineering,
University of Belgrade, Karnegijeva 4., Belgrade, Serbia*

³ *Institute for Chemistry, Technology and Metallurgy, University of Belgrade,
Department of Catalysis and Chemical Engineering, Sector of Chemical
Engineering, Karnegijeva 4., Belgrade, Serbia*

Abstract

The formation of microemulsion phases was studied for systems containing: PEG-8 Caprylic/Capric Glycerides, Polyglyceryl-6 Dioleate, Isopropyl Myristate, and water/ethanol mixture. Results show that both, water-in-oil and oil-in-water microemulsion could be obtained with these surfactants. Diffusion of Methyl Salicylate from microemulsion and classic water-in-oil emulsion were investigated. Effective diffusion coefficients were determined from experimental data. Obtained results show that diffusion from microemulsion is significantly faster, which means that microemulsions successfully could be used for transdermal drug delivery.

Introduction

Microemulsions are thermodynamically stable, homogeneous, transparent dispersion of two immiscible liquids. The formation of microemulsions usually involves a combination of four components: oil, water, surfactant and cosurfactant. Microemulsions was described for the first time by Hoar and Schulman [1] in 1943., but interest in microemulsions for pharmaceutical purposes raised during the last two decades. As pharmaceutical drug delivery systems microemulsions have many advantages such as their clarity, high stability and easy preparation. Microemulsions are very suitable for transdermal drug delivery [2] because these systems make the skin more permeable and act as a drug vectors.

Methyl Salicylate is naturally occurring methyl ester of Salicylic Acid, which is widely used for topical muscle-pain relief products.

The objective of this work is preparation of microemulsion with 2 % w/w Methyl Salicylate and study of drug diffusion from the microemulsion and classic oil-in-water emulsion.

Diffusion is studied using static Franz diffusion cell with artificial cellulose acetate membrane. Effective diffusion coefficient (D_{eff}) for drug diffusion from semi-solids forms could be calculated from equation (1), which is simplified solution of second Fick's law [3]:

$$\frac{M}{M_R} = 2 \left(\frac{D_{eff} \cdot t}{\pi \cdot \delta_o^2} \right)^{\frac{1}{2}} \quad (1)$$

where is M amount of drug which crossed membrane, M_R is amount of drug which will be released at equilibrium point, t is time and δ_o is sample thickness.

Experimental

For microemulsions PEG-8 Caprylic/Capric Glycerides (Labrasol, Gattefosse) was used as surfactant, Polyglyceryl-6 Dioleate (Plurol Oleique, Gattefosse) was cosurfactant, while oil phase was Isopropyl Myristate. As a water phase ethanol/water (50 % w/w) was used.

Methyl Salicylate was used as active ingredient for both microemulsion and emulsion.

Emulsion was prepared using Glyceryl Stearate and mixture of ethoxylated fatty alcohols as emulsifier and Isopropyl Myristate as the oil phase. Emulsion is formulated to have the same viscosity as the microemulsion used in diffusion experiments.

Diffusion experiments from microemulsion and classic water in oil emulsion were carried in static Franz cell (20 ml) at 37°C with ethanol/water (1:1) mixture as the receptor fluid.

Results and discussion

Pseudo-ternary phase diagram was constructed by titrating surfactant/cosurfactant – oil mixture with ethanol/water mixture at room temperature. The regions of microemulsion existence were determined at the surfactant/cosurfactant weight ratio 1:1, and results are shown on Figure 1.

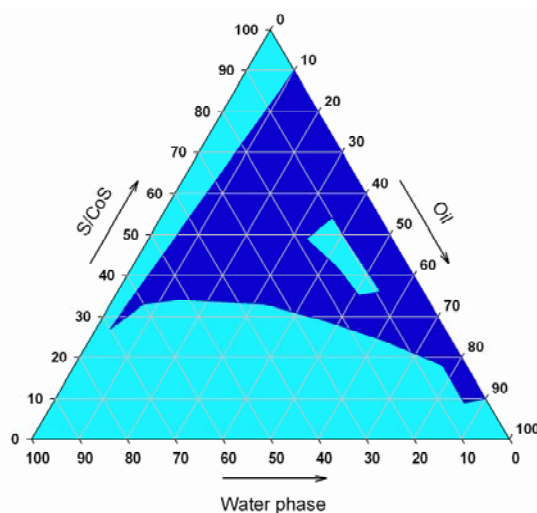


Fig.1. Phase diagram.

Comparison of phase diagram shown on Figure 1. with literature data [4] for the same surfactant/cosurfactant – oil systems, but with water instead of water/ethanol mixture shows wider range of microemulsion existence (dark area) when ethanol is used as a part of water phase.

Using phase diagram oil in water microemulsion containing 2 % w/w Methyl Salicylate was prepared.

Released curves of Methyl Salicylate are shown on Figure 2.

Using diffusion experiments data effective diffusion coefficients of Methyl Salicylate from microemulsion and emulsion were calculated using equation 1.

Effective diffusion coefficient from microemulsion is $1.28 \cdot 10^{-8} \text{ m}^2/\text{s}$ and from emulsion is $8.92 \cdot 10^{-9} \text{ m}^2/\text{s}$. These results shows that diffusion from microemulsion is significantly faster, which indicates that microemulsions could be used for successful transdermal delivery of Methyl Salicylate.

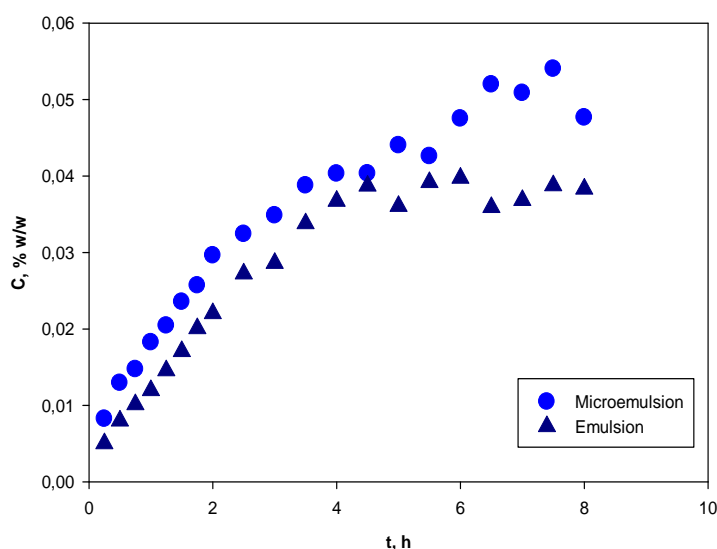


Fig.2. Release of Methyl Salicylate from microemulsion and emulsion.

Conclusions

Microemulsions prepared using PEG-8 Caprylic/Capric Glycerides as surfactant, and Polyglyceryl-6 Dioleate as cosurfactant show the widest existence range for surfactant/cosurfactant ratio 1:1. Adding of ethanol to water phase leads to even wider range of microemulsion existence comparing with pure water.

Release of Methyl Salicylate from microemulsion is faster than release from classic oil-in-water emulsion. Therefore, microemulsions are appropriate drug carriers for transdermal drug delivery, especially for unstable and hardly soluble drugs.

Literature

- [1] T. P. Hoar, J. Schulman, Nature, 1943, **152**, 102-103.
- [2] A. C. Sintov, L. Shapiro, J. Controll. Release, 2004, **95**, 173-183.
- [3] E. L. Cussler EL, Diffusion – Mass transfer in fluid systems, Cambridge University Press, Cambridge, 1984.
- [4] L. Djordjevic, M. Primorac, M. Stupar, D. Krajisnik, Int. J. Pharm., 2004, **271**, 11-9.

L Phase Boundaries

MICROEMULSIONS AND GRAND-CANONICAL MONTE CARLO SIMULATION

S. N. Blagojević and N. I. Potkonjak

Institute of General and Physical Chemistry, Studentski trg 12-16, 11000 Belgrade, Republic of Serbia

Abstract

The micellization properties and phase behavior of model ternary surfactant - oil - water systems were studied by grand-canonical Monte Carlo simulations.

Introduction

A microemulsion is defined as a system of water, oil and surfactant that forms a single, clear and thermodynamically stable solution [1, 2]. In contrast to an ordinary emulsion, where the droplets slowly coalesce and the phases eventually separate, the oil droplets in a microemulsion are in a highly dynamic state, but phase separation never occurs. Microemulsions usually form spontaneously and have particle size less than 0.1 μm . The small droplet size, compared to ordinary emulsions and the need for closely packed surfactants make the packing parameter of the surfactants critical as illustrated in the figure below. The close packing can be achieved by carefully matching two different surfactants to the right balance, sometime with extra help of a co-solvent.

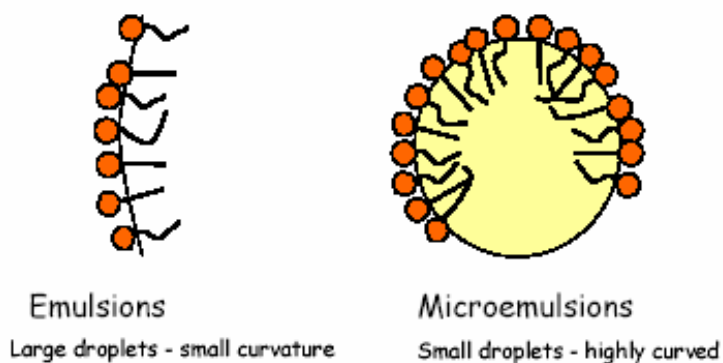


Fig.1. Difference between emulsion and microemulsion

Microemulsions are thermodynamically stable, optically transparent, isotropic dispersions of aqueous and hydrocarbon liquids stabilized by an interfacial film of surfactant molecules, and they are monodispersed spherical droplets (diameter < 100 nm) of water in oil or oil in water, depending on the nature of the surfactant.

Experimental

Formation of microemulsion can be represented as (Fig 2):

$$\Delta G_m = \Delta G_1 + \Delta G_2 + \Delta G_3 - T\Delta S$$

ΔG_m = free energy change for microemulsion formation

ΔG_1 = free energy change due to increase in total surface area

ΔG_2 = free energy change due to interaction between droplets

ΔG_3 = free energy change due to adsorption of surfactant at the oil/water interface
from bulk oil or water

ΔS = increase in entropy due to dispersion of oil as droplets

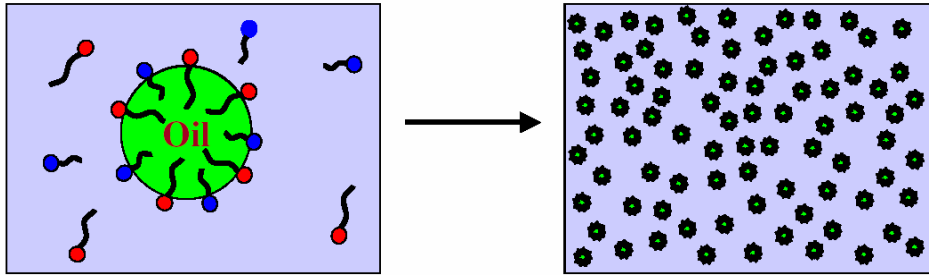


Fig 2. Formation of microemulsion

Results and discussion

We study micelle formation and phase behavior of ternary oil-water tenside systems using Monte Carlo simulations and mean-field theory. The grand-canonical Monte Carlo (GCMC) simulation methodology was used.[3]

A GCMC simulation is performed in a simulation cell of size $V = L \times L \times L = L^3$, under periodic boundary conditions. Temperature T and chemical potentials μ_1 and μ_2 are input parameters of the simulation while the numbers of molecules N_1 and N_2 and the configurational energy E fluctuate. Indices 1 and 2 denote oil and tenside, respectively. The probability distribution function for observing a configuration with N_1 , N_2 , and E in the parameter space $(\mu_1; \mu_2; \beta)$ is

$$f(N_1, N_2, E) = \{ \Omega(N_1, N_2, V, E) \exp [\beta (\mu_1 N_1 + \mu_2 N_2 - E)] \} / \Xi (\mu_1, \mu_2, V, \beta)$$

Where, $\beta = 1/k_B T$, $\Omega(N_1, N_2, V, E)$ is the density of states and $\Xi(\mu_1, \mu_2, V, \beta)$ is the grand partition function.

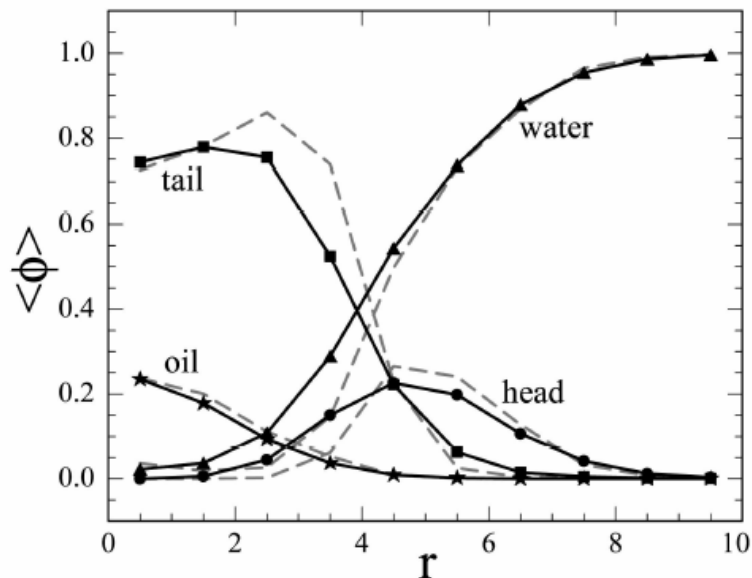


Fig 3 Volume fraction of water, head, tail, and oil, (Φ), versus radius, r , through a micellar aggregate consisting of 66 tenside (H4T4) chains and 6 oil (T4) chains. Results from single-chain mean-field theory are given by dashed lines and Monte Carlo results by solid lines with symbols: water sites (triangles), head sites (circles), tail sites (squares), and oil sites (stars).

Conclusion

Our Monte Carlo results indicate that the cmc (critical micellar concentration) decreases linearly as the volume fraction of oil is increased. The magnitude of this effect is greatest for longer chains at a fixed oil volume fraction.

Acknowledgement

The support of this research by the Ministry of Science of Republic of Serbia through projects No. TR 21020 is gratefully acknowledged.

References

- [1] L. M. Prince, *Microemulsions, Theory and Practice*, Academic Press, London, 1977.
- [2] M. Girardi, W. Figueiredo, *J.Chem. Phys.*, 2000, **112**, 4833-4835.
- [3] M. Zaldivar, R. G. Larson, *Langmuir*, 2003, **19**, 10434-10442.

KINETICS OF J-AGGREGATION OF TC-COATED AU COLLOIDAL NANOPARTICLES IN AQUEOUS SOLUTION

A. Vujačić^a, V. Vasić^a, M. Dramićanin^a, S. Sovilj^b, N. Bibić^a, S. Milonjić^a, J. Hranisavljević^c and G. Wiederrecht^c

^a*Vinča Institute of Nuclear Sciences, University of Belgrade, PO Box 522, Belgrade, Serbia, e-mail: evasic@vinca.rs*

^b*Faculty of Chemistry, University of Belgrade, P.O. Box 118, 11158 Belgrade, Serbia;*

^c*Center for Nanoscale Materials, Argonne National Laboratory, Argonne, Illinois 60439-4831*

Abstract

The kinetics of J-aggregation of thiocyanine dye (TC, 5,5'-disulfopropyl 3,3'-dichlorothiocyanine sodium salt) was studied in the presence of gold colloid. The synthesized Au colloidal dispersions were characterized by UV-Vis spectrophotometry. Kinetic measurements were carried out using a stopped-flow method to study the mechanism of J-aggregation, capturing both the slow and the fast phases of J-aggregate formation.

Introduction

The motivation for this work stems from a need to further understand the mechanism of the J-aggregate formation in aqueous solution consisting of thiocyanine dye (TC) and gold colloid. Hybrid nanoparticles consisting of noble metal cores functionalized with an organic dye shell are known for their unusual optical properties [1-3]. The modulation and enhancement of the dye's optical characteristics are due to the electronic coupling of the dye to the polarizations of the metallic nanoparticles [3]. Phenomena associated with these hybrid structures, such as dye-fluorescence quenching [4], interactions with enhanced optical fields [3], and non-linear behavior [5] render them potentially useful for future design of light energy conversion systems, molecular optoelectronic applications and sensory devices.

Since there is the lack of literature data considering kinetics of J-aggregate formation, the elucidation of the detailed reaction mechanism could provide the basis for obtaining further insights into this area of research. Therefore, the aim of this work was to investigate the kinetics of J-aggregation of the Au nanoparticles prepared using a NaBH₄ as a reducing agent and coated with TC dye.

Material and methods

Au colloidal nanoparticles were prepared by the reduction of 1 mM KAuCl₄ in aqueous solution with freshly prepared 0.1 M NaHB₄ solution under icy conditions (4° C) [6]. 30 mL milli-Q water was cooled with ice and then 330 μL freshly prepared NaHB₄ solution and 10 mL KAuCl₄ solution were added to it under

vigorous stirring, resulting in the vine – red Au colloidal solution. The colloid dispersions were stored at room temperature up to seven days. The concentration of stock dispersion of gold nanoparticles (7.4×10^{-8} M) was determined from the absorbance at 520 nm and molar absorptivity for the Au colloidal dispersion with average size of the particles 5-6 nm.

50 μ M aqueous TC stock solution containing 1mM KCl was prepared by dissolving the solid TC. The dye working solutions (concentrations 1.6 – 16.0 μ M) were prepared by appropriate dilution of 50 μ M TC stock solution, immediately before measurements. Water purified with a Millipore Milli-Q water system was used for preparing all solutions. The mixing ratio by volume of TC dye with Au colloid was 1:2. The rate of reaction was evaluated from the change of absorbance at 475 nm using a stopped flow accessory with thermostated quartz cuvette.

Results and discussion

The absorption spectrum of TC dye in aqueous solution shows a short-wavelength maximum at 409 nm assigned to the dye dimer and a long-wavelength maximum at 429 nm assigned to the dye monomer [1]. The absorption spectra of 7.4×10^{-8} M Au colloidal dispersion before and after adsorbing TC dye in the concentration range from 0.167×10^{-5} M – 1.67×10^{-5} M, were recorded in the presence of 0.1 M KCl and are shown in Fig. 1a. Inset in Fig. 1a shows the change of absorbance at 475 nm of 7.4×10^{-8} M dispersion of Au colloid, as the dependence on TC concentration. Upon addition of TC dye to the solution, a plasmon peak at ≈ 520 nm red-shifted to $\lambda \approx 550$ nm accompanied by the emergence of the sharp absorption dip at 475 nm, which coincides in the position with the J-band of the TC J-aggregate [1]. A clear isobestic points were observed at 464 nm and 524 nm indicating the reactivity involving two species, reactant (equilibrated mixture of monomers and dimers) and product (J-aggregate). Kinetic measurements were carried out using a stopped-flow method to allow capturing phases of J-aggregate formation by following the change of absorbance at 475 nm. Typical kinetic curve obtained from spectrophotometric measurements of reaction rate in the dispersion containing 1.4×10^{-5} M TC and 7.4×10^{-8} M Au colloid is presented in Fig. 1b (line 3). The values for the first order rate constants for faster and slower process, $k_{1\text{obs}} = (4.514 \pm 0.445) \text{ s}^{-1}$, $k_{2\text{obs}} = (1.81 \pm 0.45) \times 10^{-1} \text{ s}^{-1}$, as well as constants $A_1 = (2.4 \pm 0.2) \times 10^{-2}$, $A_2 = (5.6 \pm 0.2) \times 10^{-2}$ and $A_0 = (1.56 \pm 0.33) \times 10^{-3}$ were obtained by fitting the experimental data in Fig. 3 to Eq.: $A = A_0 + A_1 \exp(-x/t_1) + A_2 \exp(-x/t_2)$, which describes two parallel first-order reactions. As the results indicate, the kinetic curve can be divided into two separated curves, which present the fast (curve 1, Fig. 1b) and the slow reaction process (curve 2, Fig. 1b).

Conclusion

Based on the results presented here we propose a 2-step mechanism for J-aggregate interaction. The kinetic curve indicates two processes, a fast one ($t_1^{1/2} = 0.221 \pm 0.022$) and a slow one ($t_2^{1/2} = 5.524 \pm 0.136$). The kinetic curve was derived from the formation of absorption minimum at 475 nm, which is indicative of J-aggregate

formation on the surface of nanoparticles. A relatively fast drop in A^{475} suggests that J-aggregate formation is the fast process, with the dye possibly interacting with negatively charged Au nanoparticles via its sulfur from thiazole ring [7]. The slow process could be displacement of borate counterions from the surface of nanoparticles by the J-aggregate assemblies, but this assumption needs to be further investigated.

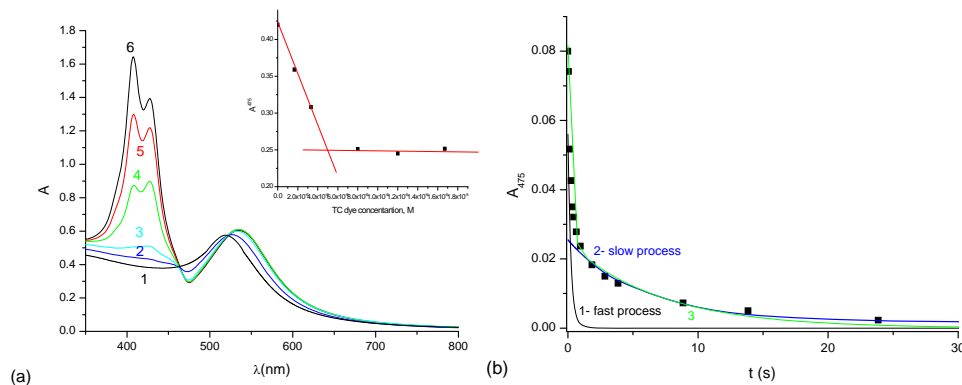


Fig. 1. (a) Absorption spectra of Au colloidal dispersion with TC dye. $C_{Au} : 7.4 \times 10^{-8}$ M, $C_{TC} :$ without TC (1), 0.167×10^{-5} M (2), 0.33×10^{-5} M (3), 0.83×10^{-5} M (4), 1.33×10^{-5} M (5), 1.67×10^{-5} M (6). Inset: dependence of absorbance at 475 nm (A^{475}) on TC concentration; (b) Plot of absorbance (A_{475}) vs time for the dispersion containing 1.4×10^{-5} M TC and 7.4×10^{-8} M Au colloid at 16° C. Squares - experimental points; curve (1) - fast process; curve (2) - slow process and curve (3) – fit of experimental results to Eq.: $A = A_0 + A_1 \exp(-x/t_1) + A_2 \exp(-x/t_2)$.

References

- [1] N. Kometani, M. Tsubonishi, T. Fujita, K. Asami, and Y. Yonezawa, *Langmuir*, 2001, **17**, 578-580.
- [2] S. Özçelik, I. Özçelik, and D. L. Akins, *Applied Physics Letters*, 1998, **73**, 1949-1951.
- [3] G. P. Wiederrecht, G. A. Wurtz, and J. Hranisavljevic, *Nano Letters*, 2004, **4**, 2121-2125.
- [4] E. Dulkeith, A. C. Morteani, T. Niedereichholz, T. A. Klar, J. Feldmann, S. A. Levi, F. C. van Veggel, D. N. Reinhoudt, M. Moller, D. I. Gittins, *Physical Review Letters*, 2002, **89**, 203002.
- [5] T. Kobayashi, Ed. *J-Aggregates*, World Scientific Publishing, Singapore, 1996.
- [6] J. A. Creighton, C. G. Blatchford, M. G. Albrecht, *Faraday Transactions 2*, 1979, **75**, 790-798.
- [7] L. Jeunieu, V. Alin, J. B. Nagy, *Langmuir*, 2000, **16**, 597-606.

ZETA POTENTIAL OF PYRITE UNDER FLOTATION CONDITIONS

D. R. Vučinić, D. Knežević and A.Đ. Tomašević

Faculty of Mining and Geology, Djušina 7, 11 000 Belgrade, Serbia

Abstract

Microelectrophoresis was used to determine the effect of Cu(II) and K-ethylxanthate (KEX) on the zeta potential of pyrite (SSA $1.32 \text{ m}^2 \text{ g}^{-1}$; 47.58 wt% Fe, 50.95 wt% S) within the pH range from 4.5 to 11.5. Zeta potential of the mineral is positive in an acidic medium and negative in alkaline pH range, with the isoelectric point at pH about 6.3. When KEX is present in the solution, the pyrite zeta potential indicates a weak chemisorption of surfactant ions, EX^- , in the tested pH range. The Cu(II) presence alone in the solution, however, gives a more positive pyrite surface, which indicates that the chemical adsorption of the copper species in the electrical double layer of mineral occurs in the pH range from 5.5 to 10. The zeta potential of Cu-treated mineral in the presence of EX^- confirms that copper has an activating effect on the pyrite KEX adsorption.

Introduction

Adsorption of dissolved mineral species, collectors (surfactants) and modifying reagents in the flotation of minerals is controlled by the electrical double layer at the mineral-water interface. Zeta potential can be used to delineate the interfacial phenomena in heterogeneous mineral suspensions [1]. For the pyrite (FeS_2)-xanthate (RCS_2M) flotation (xanthates are flotation collectors) it is generally accepted that dixanthogen (X_2), formed by the electrochemical mechanism in which xanthate ions, (X^- is RCS_2^-), are oxidized in the presence of dissolved atmospheric oxygen and pyrite as a catalyst, is the only surface xanthate product that makes pyrite floatable. However, some authors suggested that the Fe(III) xanthate compounds play important roles in controlling the flotation behavior of pyrite. Cu(II) may be present in the pulp during the selective flotation of sulphide minerals as a dissolved mineral constituent, added reagent or in the recycled flotation water, and may influence the pyrite surface properties. The present paper is an attempt to determine the influence of dissolved copper on the zeta potential of pyrite without and in the presence of ethylxanthate, $\text{C}_2\text{H}_5\text{SC}_2^-$, (EX^-).

Experimental

A natural pyrite sample (47.58 wt% Fe, 50.95 wt% S ; specific surface area, SSA $1.32 \text{ m}^2 \text{ g}^{-1}$, determined by the BET method) was used. The pH values were adjusted using HCl and NaOH. CuSO_4 was added in order to introduce copper ions into the mineral suspensions. NaNO_3 was used to adjust ionic strength in zeta potential measurements ($I=1 \times 10^{-2} \text{ mol dm}^{-3}$). All the reagents were of p.a. grade.

Commercial-grade potassium ethylxanthate was purified by repeated crystallization from acetone. Zeta potential measurements were taken on a Riddick Zeta-meter using microelectrophoretic technique. The mineral suspension was stirred for three minutes after each reagent addition, and then the electrophoretic mobility was detected. In all experiments, the solution of copper sulphate was always decanted before KEX addition to prevent formation of precipitate in the bulk of the solution.

Results and Discussion

The zeta potential of pyrite is positive in an acidic medium and negative in alkaline pH range, with the isoelectric point at pH about 6.3 (Fig.1. curve 1).

The acid/base properties of the mineral surface determine the activity of the surface in different sorption processes. The examined pyrite showed the deficiency of sulphur in the mineral. Thus, it may be concluded that the dominant surface sites formed on the examined pyrite in neutral and acidic medium are primary $-\text{Fe(II)}^{\delta+}$ and $-\text{Fe(II)}^{\delta+}(\text{H}_2\text{O})$, which contribute to the positive zeta potential values and to the hydrophilicity of the mineral [2]. Additionally, in the open circuit, the surface oxidation reaction of surface metal ion- $\text{Fe(II)}^{\delta+}$ to the $-\text{Fe(III)}^{(1+\delta)+}$ may be expected, coupled with reduction of dissolved atmospheric oxygen, giving more positive surface sites: $-\text{Fe(III)}^{(1+\delta)+}$, $-\text{Fe(III)}^{(1+\delta)+}(\text{H}_2\text{O})$ and $-\text{Fe(III)OH}^{\delta+}$.

However, in an alkaline pH medium, negative values of the pyrite zeta potential increase, confirming the chemisorption of hydroxyl ions in the electrical double layer of the mineral, and the formation of the surface sites like $-\text{Fe(II)OH}_n^{(n-\delta)-}$ or $-\text{Fe(III)OH}_n^{(n-1-\delta)-}$.

Our results corroborate weak chemisorption of the collector ions (surfactant ions), EX^- , on the positive surface sites of the mineral (curve 2). In respect of the thermodynamic stability of the Fe(III) xanthates in systems $\text{Fe-EX-H}_2\text{O}$, $\text{Fe-EX-CO}_3\text{-H}_2\text{O}$, $\text{Fe-EX-S-H}_2\text{O}$, some authors conclude that $\text{Fe(OH)}_2\text{EX}$ is formed on the pyrite surface, without making pyrite hydrophobic, but that it is a good contact site for the adsorption of ethyl dixanthogen, $(\text{EX})_2$, and EX^- ions [3]. The chemisorbed surfactants by head groups towards the solid and by hydrocarbon chain towards the water solution make the hydrophobic mineral surface. Flotation is limited in the

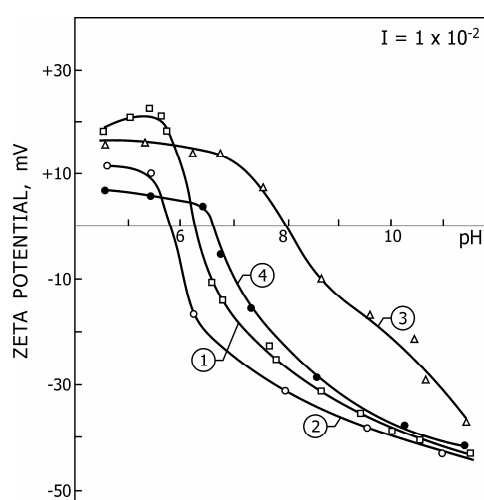


Fig.1. Pyrite zeta potential as function of pH: 1) without reagents; 2) $5 \times 10^{-4} \text{ mol dm}^{-3}$ KEX; 3) $5 \times 10^{-4} \text{ mol dm}^{-3}$ Cu(II); 4) Cu(II), KEX; (the ionic strength, $I=1 \times 10^{-2} \text{ mol dm}^{-3}$ NaNO_3).

case of low adsorption densities, when the surfactant ions are adsorbed individually as counter ions by electrostatic attraction, both in the diffuse layer and in the Stern layer [1]. When the adsorption density of the surfactant becomes sufficiently high, the interaction between the hydrocarbon chains of surfactant ions through van der Waals forces and their association into hemimicelles makes the mineral more hydrophobic (more floatable).

Cu(II) from the solution induces more positive zeta potential of pyrite notably above pH 5.5 (curve 3). The distribution diagram for copper shows that the dominant copper species present in the solution are Cu^{2+} , $\text{Cu}(\text{OH})^+$, $\text{Cu}_2(\text{OH})_2^{2+}$ from pH 6 to pH 8, and above pH 8 up to 10.0 is $\text{Cu}(\text{OH})_2$ [4]. The chemical adsorption of the copper-cation species in the Stern layer of the electrical double layer of mineral is evidenced by the electrokinetic behavior of pyrite in the pH range from 5.5 to 10. The surface negative sites on pyrite surface for adsorption of copper-cation species are: in acidic medium $-\text{S}^{\delta-}$ and $-\text{Fe}(\text{II})\text{OH}^{(1-\delta)-}$, and in alkaline medium $-\text{Fe}(\text{II})\text{OH}_n^{(n-\delta)-}$ or $-\text{Fe}(\text{III})\text{OH}_n^{(n-1-\delta)-}$. A ion exchange reaction between Fe(II) from the pyrite surface and Cu^{2+} from the acid solution may also be expected.

Adsorption of EX^- ions on the copper-modified mineral surface is corroborated by more negative zeta potential values throughout the tested pH range (curve 4). However, the kinds of the surface ethylxanthate species formed on Fe and Cu surface sites and their effect on the pyrite floatability will be detected by ATR-IR spectroscopy and floatability tests [2].

Conclusion

The obtained results showed that the examined pyrite, with the sulphur deficiency in the mineral lattice, has a positive zeta potential in an acidic medium and a negative one in the alkaline pH range, with the isoelectric point at pH about 6.3. The adsorption of the ethylxanthate surfactant ions is weak in the tested pH range from 4.5 to 11.5. Cu(II) alone gives the more positive zeta potential values of pyrite, confirming the chemical adsorption of the copper-cation species in the pH range from 5.5 to 10. Cu(II) also shows the effect on the EX^- adsorption on pyrite. Zeta potential of the Cu-treated mineral in the presence of EX^- is more negative than zeta potential of the Cu-treated mineral alone. This means that during the selective flotation of the Cu-sulphide minerals by xanthates from the ore containing pyrite an elevated content of iron in the copper-concentrate may be produced.

Acknowledgement

The authors are indebted to the Research Fund of the Republic of Serbia for the financial support.

References

- [1] D. W. Fuerstenau, Pradip, Adv. Colloid Interface Sci., 2005, **114–115**, 9-26.
- [2] D. R. Vučinić, to be published.
- [3] X. H. Wang, K. S. E. Forssberg, Int. J. Miner. Process, 1991, **33**, 275-290.
- [4] J. Ralston, T. W. Healy, Int. J. Miner. Process, 1980, **7**, 203-217.

M

Complex Compounds

MICROBIOLOGICAL CHARACTERIZATION OF THE RELATED Co(II)/Cu(II) COMPLEXES WITH OCTAAZAMACROCYCLE AND CARBOXYLATES

M. Antonijević-Nikolić¹, G. Vučković², S. B. Tanasković³, V. Živković-Radovanović² and G. Gojgić-Cvijović⁴

¹Higher Technological School of Professional Studies, 15000 Šabac, Serbia

²Faculty of Chemistry, University of Belgrade, P. O .Box 118, 11158, Serbia

³Faculty of Pharmacy, Vojvode Stepe 450, 11000 Belgrade, Serbia

⁴Center for Chemistry ICTM, Njegoševa 12, Belgrade, Serbia

Abstract

Cu(II) and Co(II) complexes with *N,N',N'',N'''*-tetrakis(2-pyridylmethyl)-1,4,8,11-tetraazacyclotetradecane (tpmc) and various carboxylates ligands were tested towards Gram (+) and Gram (-) bacteria and some strains of fungi. As control group, simple salts of Co(II)/Cu(II) used as starting material for the synthesis, ligands and solvents were also screened. The minimum inhibition concentrations suppressing the visible growth of bacteria showed moderate activity of the studied complexes against strains of bacteria, which was generally higher in the case of Co(II) complexes than the related Cu(II) ones. Under the same conditions and concentration the control groups were inactive. No one compound showed antifungal activity.

Introduction

A number of reports highlighting the use of transition metal complexes as both antibacterial and antifungal agents. The complexes of *N*-donor ligands (pyridine, 1,10-phenanthroline, 2,2'-bipyridine, Schiff bases and azamacrocycles), as well as with α,ω -dicarboxylates, aminocarboxylates and their derivatives exhibited broad-spectrum of antifungal and antibacterial activity *in vitro* [1]. A number of *in vivo* studies have indicated that biologically active compounds become more bacteriostatic and carcinostatic upon chelation [1b]. *In vitro* tests of the Cu(II)/Co(II) with *N,N',N'',N'''*-tetrakis(2-pyridylmethyl)-1,4,8,11-tetraaza-cyclotetradecane (tpmc) and some of the secondary ligands (aliphatic/aromatic or aminocarboxylates/their derivatives) were also active towards some microorganisms [2]. Previously we described preparation and characterization of the related Cu(II)/Co(II) tpmc complexes with α,ω -dicarboxylates/aromatic mono and dicarboxylates/ aliphatic aminocarboxylates [3]. Here we report microbiological study of Cu(II)/Co(II) of the mentioned complexes in order to compare their congeneric complexes.

Results and discussion

Eleven complexes presented in Table I were prepared in pure solid state [3]. The corresponding free ligands which could be present in small amount during complex dissociation, simple perchlorates of Cu(II)/Co(II) and solvents were screened simultaneously for better consideration of the results.

Preliminary experiment of all compounds was performed by well diffusion in agar [4] against the following strains of microorganisms: a) Gram (+) bacteria: *Micrococcus lysodeikticus* ATCC 4698, (**M. L.**), *Staphylococcus aureus* ATCC 25923, (**S. A.**), Gram(+) bacterium forming spores *Bacillus subtilis* ATCC 6633, (**B. S.**) and Gram (-) bacterium *Escherichia coli* ATCC 25922, (**E. C.**) b) fungi: *Candida albicans* ATCC 24433 (yeast) and *Aspergillus niger* (mould).

Table 1. Minimum inhibitory concentration (MIC) in µg/mL of the studied Cu(II)/Co(II) complexes in DMSO

Complex [*]		M.L. [#]	S.A. [#]	E.C. [#]	B.S. [#]
[Cu ₄ (succ)(tpmc) ₂](ClO ₄) ₆ ·2H ₂ O	1	400	>400	>400	>400
[Co ₂ (succ)tpmc](ClO ₄) ₂ ·H ₂ O	2	50	400	>400	200
[Cu ₄ (glut)(tpmc) ₂](ClO ₄) ₆ ·2H ₂ O	3	200	>400	>400	>400
[Co ₂ (glut)tpmc](ClO ₄) ₂ ·H ₂ O	4	100	>200	>100	>100
[Cu ₄ (adip)(tpmc) ₂](ClO ₄) ₆ ·7H ₂ O	5	200	>400	>400	>400
[Co ₂ (adip)tpmc](ClO ₄) ₂ ·1,5H ₂ O	6	100	>200	>100	>100
[Cu ₂ (S-pheala)tpmc](ClO ₄) ₃ ·7H ₂ O	7	>400	>400	>400	>400
[Co ₂ (S-pheala)tpmc](ClO ₄) ₃	8	50	100	200	>400
[Cu ₂ (C ₆ H ₅ COO)tpmc](ClO ₄) ₃ ·CH ₃ OH	9	200	>400	>400	>400
[Cu ₄ (tpht)(tpmc) ₂](ClO ₄) ₆ ·5H ₂ O	10	>400	>400	>400	>400
[Co ₂ (tpht)tpmc](ClO ₄) ₂ ·4H ₂ O	11	100	100	>400	>400

*succH₂=succinic acid; glutH₂= glutaric acid; adipH₂ = adipic acid; S-phealaH= S-phenylalanine; H₂tpht = terephthalic acid; [#]M.L.= *Micrococcus lysodeikticus* ATCC 4698, S.A.= *Staphylococcus aureus* ATCC 25923, E.C.= *Escherichia coli* ATCC 25922, B.S.= *Bacillus subtilis* ATCC 6633

100 µL of the compound solution in DMSO (c=1 mg/mL), was applied in the holes of agar plate. Mueller-Hinton agar for bacteria and Sabouraud dextrose agar for the fungi were used for cultivation. Temperature of incubation was 37°C for bacteria, and 28°C for fungi. No one of the investigated compounds showed antifungal activity. Therefore, the quantitative test was performed only against bacteria. Minimum inhibitory concentration (MIC) in µg/mL as the lowest concentration suppressing the growth of bacteria was detected by agar dilution method, after incubation of 24 h at 37°C [5]. Complex solutions were prepared in DMSO. Agar plates were prepared by mixing of the solutions of the studied compounds (0.5 mL) of the c= 8-0.125 mg/mL with melted and cooled 9.5 mL of Mueller-Hinton agar. On the surface of plates the bacteria were seeded. The same method is used for the controls. Experimental results are presented in Table I. Under the same conditions control groups were inactive, suggesting that the activities originated from the complexes alone.

The most of the studied Cu(II) complexes had MIC equal or higher than 400 µg/mL, excluding the complexes **3**, **5** and **9**. The related Co(II) complexes were generally more active. The values of MIC are in accordance of moderate selective antibacterial activity of the studied complexes.

Antimicrobial activity of the complex is influenced by the chelate effect, the electrical charge of the complex ion, the nature of the counter ion, number of central metal ions per molecule, the nature of *N*-donor atom, central metal ion, solubility, type and the bonds distance between metal and ligands, *etc.* The results of this *in vitro* test could be explained by the relative stability of the complexes toward hydrolysis and/or dissociation in the applied solvent. Due to the bonding of M(II) for the tpmc apart to the carboxylate, which hydrophobic macrocyclic cavity well protect metal center, it is less available for the microorganisms. For the differences in the activity of Cu(II) compared with Co(II) are responsible several factors: the nature of central atom, number of metal centers per molecule (Cu(II) complexes were generally tetranuclear and Co(II) always binuclear), different total charge of the complex ion, kinetical lability of Co(II) complexes against substitution of carboxylato ligand, mainly by OH⁻ ions.

Conclusion

Macrocyclic Cu(II) and Co(II) with octaazamacrocyclic and carboxylato ligands were screened *in vitro* towards some bacteria and fungi. It is found moderate activity of the complexes and some selectivity towards bacteria, which was enhanced compared with the control ligands, solvents and simple salts. Co(II) complexes were more active than the related Cu(II). No one compound had antigungal activity.

References

- [1] a) C. Dendrinou-Samara, G. Psomas, C. P. Raptopoulou, D. P. Kessissoglou, J. Inorg. Biochem., 2001, 83, 7-16; b) Z. H. Chohan, M. Arif, M. A. Akhtar, C. T. Supuran, Bioinorg. Chem. Appl., 2006, 2006, 1-13; c) M. Geraghty, J. F. Cronin, M. Devereux, M. McCann, BioMetals, 2000, 13, 1-8.
- [2] a) G. Vučković, S. B. Tanasković, M. Antonijević-Nikolić, V. Živković-Radovanović, G. Gojgić-Cvijović, J. Serb. Chem. Soc., 2009, 74, 629-640; b) G. Vučković, M. Antonijević-Nikolić, M. Korabik, J. Mroziński, D. D. Manojlović, G. Gojgić-Cvijović, N. Matsumoto, Polish J. Chem., 2005, 79, 679-687.
- [3] a) G. Vučković, M. Antonijević-Nikolić, T. Lis, J. Mroziński, M. Korabik, D. D. Radanović, J. Mol. Struct., 2008, 872, 135-144; b) M. Antonijević-Nikolić, S. B. Tanasković, G. Vučković, 7th International Conference on Fundamental and Applied Aspects of Physical Chemistry, Proceedings Vol II (in extenso), Belgrade, 2004, 799-801; c) G. Vučković, M. Antonijević, D. Poleti, J. Serb. Chem. Soc., 2002, 67, 677-684; d) G. Vučković private communication.
- [4] J. F. Acar, F. W. Goldstein, Disk Susceptibility Test in Antibiotics in Laboratory Medicine, Lorian V. Ed., 4th Edition, Williams & Wilkins, Baltimore, 1996, 1-51.
- [5] D. Amsterdam, Susceptibility Testing of Antimicrobial in Liquid Media, in Antibiotics in Laboratory Medicine, Lorian V. Ed., 4th Edition, Williams & Wilkins, Baltimore, 1996, 52-111.

EFFECT OF SILICA GEL POLY(ETHYLENE GLICOL)S IMPREGNATION ON BEHAVIOUR OF Co(III) COMPLEXES WITH EDTA-TYPE LYGANDS DURING SALTING-OUT THIN-LAYER CHROMATOGRAPHY

V. M. Živković-Radovanović¹, G. N. Vučković¹, M. I. Đuran²,
S. B. Tanasković³ and M. D. Antonijević-Nikolić⁴

¹*Faculty of Chemistry, University of Belgrade, P.O.Box 118, 11158 Belgrade;*

²*Faculty of Science, University of Kragujevac, P.O.Box 60, 34000
Kragujevac;*

³*Faculty of Pharmacy, Vojvode Stepe 450, 11000 Belgrade;*

⁴*Higher Technological School of Professional Studies, 15000 Šabac; Serbia
E-Mail: gordanav@chem.bg.rs*

Abstract

Eight Co(III) complexes with ligands of EDTA-type were separated by salting-out thin-layer chromatography (SOTLC) using ammonium-sulphate solutions on 5 modified sorbents obtained by impregnation of silica gel with polyethylene glycols (PEG-s) of different molecular mass. The increase of molecular mass of PEG used for impregnation causes increase of R_F ($R_F \times 100$) values of the investigated complexes. The combined separation mechanism of specific and non-specific interactions is proposed.

Introduction

Silica gel modified by impregnation with polyethylene glycols (PEG-s) of different molecular mass was successfully applied for SOTLC of some mixed aminocarboxylato Co(III) complexes with ammonium-sulphate solutions [1]. Such impregnated layers were more hydrophobic than non-modified silica gel. Their hydrophobicity increases with the degree of polymerization of PEG causing enhanced retention of the complexes, even those containing small hydrophobic parts in the molecule, which were not salted-out on non-modified sorbent. That was in accordance with the mechanism of non-specific hydrophobic interactions. In the present work we applied 5 modified silica gel layers (impregnated with PEG of molecular mass ranged from 400 to 5500) for the separation of 2 series of Co(III) complexes with ligands of EDTA-type using ammonium-sulphate solutions as in previous SOTLC separations of these complexes on non-modified silica gel [2].

Experimental

The investigated complexes (Table 1) were synthesized by the procedures cited in Ref.[2], excluding for the complex No.2 [3]. Silica gel H for TLC was impregnated with different PEG-s by immersion technique, giving a

series of modified sorbents having the same molar content (1.56×10^{-3} mol) of PEG /100 g

Table 1. hR_F ($R_F \times 100$) values obtained for investigated complexes using ammonium-sulphate solutions on silica gel impregnated with different PEG-s

a)

No.	Complexes as Na^+ salts*	PEG of average molecular mass							
		400				1000			
		$(\text{NH}_4)_2\text{SO}_4$ mol/dm ³				$(\text{NH}_4)_2\text{SO}_4$ mol/dm ³			
		1.0	2.0	3.0	4.0	1.0	2.0	3.0	4.0
1	$[\text{Co}(\text{edta})]^-$	81	69	65	58	83	78	68	63
2	$[\text{Co}(\text{ed3ap})]^-$	67	58	52	38	73	65	57	47
3	$[\text{Co}(\text{eddadp})]^-$	55	47	33	26	61	50	38	29
4	$[\text{Co}(\text{eda3p})]^-$	38	29	21	12	40	31	22	16
5	$[\text{Co}(\text{edtp})]^-$	26	18	13	7	28	19	13	9
6	$[\text{Co}(1,3\text{-pdta})]^-$	65	62	52	46	69	64	53	47
7	$[\text{Co}(1,3\text{-pd3ap})]^-$	45	39	33	27	48	43	37	28
8	$[\text{Co}(1,3\text{-pddadp})]^-$	30	21	19	14	34	27	21	16

b) Continued: Nos. of the complexes are the same as in Table 1 a)

No.	PEG of average molecular mass											
	1540				4000				5500			
	$(\text{NH}_4)_2\text{SO}_4$ mol/dm ³				$(\text{NH}_4)_2\text{SO}_4$ mol/dm ³				$(\text{NH}_4)_2\text{SO}_4$ mol/dm ³			
	1.0	2.0	3.0	4.0	1.0	2.0	3.0	4.0	1.0	2.0	3.0	4.0
1	86	80	72	65	89	83	75	67	92	84	76	67
2	78	67	60	50	84	77	67	55	87	80	69	57
3	64	58	49	33	78	64	56	39	83	71	59	42
4	47	38	30	21	66	49	31	26	72	63	47	31
5	35	22	15	12	48	39	23	17	61	50	36	23
6	74	69	57	49	79	73	63	55	80	73	63	58
7	60	50	39	31	64	55	44	37	72	63	52	45
8	40	35	25	16	50	42	28	19	63	53	35	29

*edta = ethylenediamine-*N,N,N',N'*-tetraacetate ion; ed3ap = ethylenediamine-*N,N,N'*-triacetate-*N'*-3-propionate ion; eddadp = ethylene-diamine-*N,N'*-diacetate-*N,N'*-di-3-propionate ion; eda3p = ethylenediamine-*N*-acetate-*N',N'*-tri-3-propionate ion; edtp = ethylenediamine-*N,N,N',N'*-tetra-3-propionate ion; 1,3-pdta = 1,3-propanediamine-*N,N,N',N'*-tetraacetate ion; 1,3-pd3ap = 1,3-propanediamine-*N,N,N'*-triacetate-*N*-3-propionate ion; 1,3-pddadp = 1,3-propanediamine-*N,N'*-diacetate-*N,N'*-di-3-propionate ion.

of silica gel as described in the Ref. [1]. Aqueous salt solutions of different concentration (1.0; 2.0; 3.0 and 4.0 mol/dm³) were prepared. The other details concerning chromatographic techniques (dimensions of the tank, saturation, development, detection, *etc.*) are also previously described [1,2].

Results and discussion

In the studied complexes within series 1-5 and 6-8 (Table I) N-O side chains were enlarged successively by introducing $-\text{CH}_2-$ group. Complexes 6-8, compared with the complexes 1-3, have enlarged ethylenediamine N-N chelate ring. The obtained hR_F -values ($R_F \times 100$) are given in Table I. On each of the modified sorbents with increase of the salt concentration enhance retention of the complexes, *i.e.* salting-out effect is observed and the reversed-phase order of complexes within series is found. Complexes 1-3 had higher hR_F -values than 6-8. All results were analogous to previously published one [2]. Nevertheless, the hR_F values on impregnated silica gel were higher than the corresponding obtained on non-modified one. Additionally, the increase of molecular mass of PEG used for impregnation causes higher hR_F values of investigated complexes, but the tailing of the spots decreased giving ideal form with PEG 5500. These results proved the assumption [4] that during SOTLC of Co(III) complexes with EDTA-type ligands on non-modified silica gel, a combined separation mechanism exists: specific interaction by H-bonding of silica $-\text{OH}$ group with carboxylato ligands' oxygen and non-specific interaction of the hydrocarbon complexes' parts with siloxane groups of the sorbent. The presence of PEG with higher polymerization degree causes better shielding of the polar silica $-\text{OH}$ groups and consequently weaker specific interactions.

Conclusion

Retention of Co(III) complexes with hexadentate ligands of EDTA-type during SOTLC with ammonium sulphate solutions on non-impregnated and impregnated silica gel with PEG-s of different molecular mass is caused by both: specific and non-specific hydrophobic interactions. It seems that specific interactions prevailed during separation on non-modified silica gel, while on impregnated layer they are weaker.

References

- [1] V. Živković-Radovanović, G.Vučković, *Chromatographia*, 2005, **62**, 91-97.
- [2] G.Vučković, D.Miljević, T.J.Janjić, M.I.Đuran, M.B.Ćelap, *Chromatographia*, 1995, **40**, 445-447.
- [3] D. J. Radanović, V. D. Miletić, T. Ama, H. Kawaguchi, *Bull. Chem. Soc. Japan*, 1998, **71**, 1605-1614.
- [4] G. Vučković, D. Miljević, T. J. Janjić, M. I. Đuran, M. B. Ćelap, *J. Serb. Chem. Soc.*, 1996, **61**, 615-618.

INTERACTION OF Pb(II) WITH HUMIC ACID AND HUMIC-MODEL LIGANDS STUDIED BY SCHUBERT METHOD

I. Kostić, T. Anđelković, M. Purenović, R. Nikolić and A. Bojić

*Faculty of Science and Mathematics, University of Niš,
Višegradska 33, Serbia, 18000 Niš,*

Abstract

The complexation of humic, benzoic and salicylic acid with Pb(II) was investigated at pH 4, under constant ionic strength of 0.01 and at 25°C. Stability constants of complexes formed between ligands and Pb(II) were determined by Schubert's ion-exchange equilibrium method using Dowex 50WX8, 100-200 mesh, Na⁺ form. Obtained log *K* values of Pb complexes show the following sequence of complex strength: humic acid > salicylic acid > benzoic acid, which is in accordance with ligand structure complexity.

Introduction

Humic acids (HA) are heterogeneous, polydisperse mixtures of natural organic polyelectrolytes, containing a large number of different functional groups.

HA play role in a range of environmental issues, due to their presence in water and soil. The most important processes are: soil and water acidification, nutrient control, weathering, soil formation, soil structure, mobility and distribution of heavy metals, radioactive waste disposal, pesticides, xenobiotics, ecosystem buffering, etc [1]. In almost all of those issues, cation binding is recognised to be an important factor.

Humic acid contains free and bound phenolic OH and COOH groups, quinone structures and nitrogen and oxygen, as bridge units. Due to the presence of hydroxyl, phenyl and carboxyl-reactive groups, coordination compounds of HA with metals are formed. This is extremely important in affecting the retention and mobility of metal contaminants in soil and water.

In an effort to understand and quantify humic-metal interactions some ligand models (such as citric, salicylic, benzoic and phthalic acids) have been used in the study of complexation properties of humics. In this paper, salicylic and benzoic acids are used as humic-model ligands.

Schubert's ion-exchange method for determining conditional stability constants involves measuring the distribution coefficients of a metal ion between a cation-exchange resin and solution phase, in both the presence and absence of the complexing agent [2].

Metal solutions were prepared by dissolving an appropriate quantity of Pb(NO₃)₂ in HNO₃. All the metal solutions were adjusted to pH 4 by 0.1M HCl and 0.1M NaOH. Ionic strength is set by NaCl to value 0.01.

The concentration of stock solutions of humic (HA), benzoic (BA) and salicylic (SA) acid are based on total acidity in miliequivalent/liter. The required amount of solid HA was dissolved in 0.1M NaOH. The concentration of stock solutions of all three acids were 5, 7.5 and 10 meq/l with ionic strength of 0.01.

The cation-exchange resin used was Dowex 50WX8 (100-200 mesh), Na-form, analytical grade from Fluka. Approximately 10 g of the resin was stirred with deionized water and fine particles were decanted. The resin was equilibrated with stock solution of 0.1M NaCl for several hours. The resin was washed several times with deionized water and after washing was air dried. The resin was stored in an airtight glass bottle.

Lead was determined by atomic absorption spectrophotometry with a Varian Analyst 300 with an air-acetylene flame.

Results and discussion

The stability constants of metal-humate complexes through ion-exchange method were determined as described by Schnitzer and Skinner [3].

The logarithm of the stability constant of the complex ($\log K$) was evaluated from the following relationship:

$$\log\left(\frac{D_0}{D} - 1\right) = \log K + n \log[L]$$

where D_0 is distribution constant of the Pb^{2+} in absence of ligand; D is distribution constant of Pb^{2+} in the presence of ligand; K is stability constant of Pb^{2+} complex; n is number of moles of ligand which combine with one mole of Pb^{2+} ; $[L]$ is concentration of ligand in mole per litre.

D_0 was determined from the expression:

$$D_0 = \frac{\alpha_0 \cdot V}{(100 - \alpha_0) \cdot m_{resin}}$$

where α_0 is percent of total metal bound to exchange resin (Dowex AG 50W-X8); $100 - \alpha_0$ is percent of total metal remaining in solution; V is volume of solution; m_{resin} is weight of exchange resin. D is measured in the same manner as D_0 in presence of different ligand concentrations. n is obtained from the slope of the plot of $\log [(D_0/D)-1]$ versus $\log [L]$, while the corresponding $\log K$ value is obtained from the intercept.

The linear range for lead was obtained from isotherm curve to estimate the D_0 in order to choose the appropriate concentrations for metal ion and ligand to avoid the effect of metal loading.

The obtained results are shown in Table 1.

Table 1. Stability constants of Pb²⁺- complexes at pH 4.0, under constant ionic strength of 0.01 and at 25°C.

	BA	SA	HA
log K	3.64	5.29	5.85

Conclusion

The obtained log *K* values show the following sequence: HA > SA > BA. The complex stability decreases with the decrease of donor atoms in ligands.

Thus, the most stable complex is formed between Pb²⁺ and HA, due to the largest number of carboxyl and phenol groups in HA structure, with probability that both carboxyl and phenol groups are involved in complexation of lead. Considering the size of the humic acid molecule and the number of binding sites per molecule, the binding of a lead ion to two groups of the same humic acid seems to be more probable.

References

- [1] E. Tipping, Cation binding by humic substances, Cambridge University Press, Cambridge, 2002.
- [2] H. Baker, F. Khalili, *Annals of Environmental Science*, 2007, **1**, 35-44.
- [3] M. Schnitzer and S. I. M. Skinner, *Soil Science*, 1966, **6**, 361-363.

CHARACTERIZATION OF Cu(II) COMPLEXES WITH REDUCED DEXTRAN DERIVATIVES BY THE COMPUTER SIMULATION OF EPR SPECTRA

G. M. Nikolić¹, Ž. Mitić¹, M. Cakić², R. Nikolić³, Lj. Ilić⁴,
R. Pavlović¹ and A. Veselinović¹

¹*Faculty of Medicine, Bulevar dr Zorana Djindjića 81, 18000 Niš, Serbia
e-mail: goranhem@yahoo.com,*

²*Faculty of Technology, Bulevar Oslobođenja 124, 16000 Leskovac, Serbia*

³*Faculty of Sciences and Mathematics, Višegradska 33, 18000 Niš, Serbia*

⁴*PCI "Zdravlje Actavis Co.", Vljakova 199, 16000 Leskovac, Serbia*

Abstract

Complexes of Cu(II) ion with reduced low-molar dextran (RLMD, M_w 5000 - 6000 g/mol) were synthesized in aqueous solutions, at the boiling temperature and at different pH values ranging from 7.5 to 12. The room temperature EPR spectra of complexes synthesized at high pH values were computer simulated and obtained parameters were used for the characterization of complexes. Prevailing ionic bonding, negligible exchange interaction, and significant distortion from axial symmetry of copper bonding site(s) were found to be the main features of these complexes.

Introduction

Biometal complexes of various polysaccharides (like dextran, pullulan, and inulin) are the subject of intensive research mainly because of its possible application in human and veterinary medicine [1]. Cu(II) complexes and their properties are of special importance since they could be used for the treatment of hypochromic microcitary anemia and hypocupremia. In this paper we present the results of characterization of Cu(II) complexes with reduced low-molar dextran derivatives by using the parameters obtained from computer simulated room temperature EPR spectra.

Experimental

Low-molar dextran (LMD, M_w = 5000 – 6000 g/mol) was obtained from "Zdravlje Actavis Co." pharmaceutical company (Leskovac, Serbia). All the other chemicals ($\text{CuCl}_2 \cdot 2\text{H}_2\text{O}$, HCl, NaOH) were of reagent grade and were used as received.

The reduction of dextran was performed with NaBH_4 (p.a. Merck, Darmstadt) with subsequent purification on ion-exchange columns filled with Amberlite IR-120 and Amberlite IRA-410 resins. The reduced group content in the final product was measured by the Somogyi method [2] and found to be below 0.05%.

The synthesis of the complexes was performed at the pH values ranging from 7.5 to 12.0 by boiling the reactant solution containing reduced low-molar dextran and CuCl₂. Green solution of the complex was filtrated and complex precipitated by the addition of 96% ethanol. Unbounded ions were removed by dialysis.

Cu(II) content of the complexes was measured by AAS on the Philips Pye Unicam SP9 spectrometer.

For the EPR measurements an X-band Bruker ESP 300 spectrometer was employed and spectra of powder samples in quartz tubes (3 mm i.d.) were recorded at room temperature. Measurement conditions used were: modulation amplitude – 10.2 G, modulation frequency – 100 kHz, microwave frequency – 9.64 GHz, and nominal microwave power – 200 mW (no power attenuation was used). Sodium nitroso-disulfonate (Fermly's salt) was used for frequency calibration ($g = 2.0055 \pm 0.0001$). For the computer simulation of experimental EPR spectra the program SimFonia version 1.25 (Bruker Analytische Messtechnik GmbH) was used.

Results and Discussion

Room temperature EPR spectra of Cu(II) complexes synthesized at high pH values had the same appearance in spite of the difference in metal content (8.20% and 6.97% for the complexes synthesized at pH 10 and 12, respectively) [3]. Also the appearance of these spectra strongly suggested axial symmetry for the copper coordination site and was very similar to the EPR spectra of some polysaccharide Cu(II) complexes obtained at high pH values which were reported in the literature [4]. EPR spectrum of the sample containing 6.97 % of copper synthesized at pH 12.0 is shown in Figure 1 together with its computer simulation. Good fit between the simulated and experimental EPR spectra of our samples was obtained with the following parameters:

$$A_{\parallel} = 183 \times 10^{-4} \text{ cm}^{-1}, g_{\parallel} = 2.235, \text{ and} \\ A_{\perp} = 28 \times 10^{-4} \text{ cm}^{-1}, g_{\perp} = 2.032$$

By using these values we were able to calculate in-plane sigma bonding parameter α^2 , geometric parameter G , and empirical factor f as an index of tetrahedral distortion which all are used for the characterization of Cu(II) bonding sites in complexes with various types of ligands [5,6]. Value of $\alpha^2 = 0.794$ for our samples indicates prevailing ionic bonding (α^2 value lies above 0.5 and below 1.0) with approximately 80% of spin population in the copper dx^2-y^2 orbital. However, this α^2 value is lower than the value for the Cu(II) incorporated in various types of starch (0.84 – 0.88) [6] thus indicating slightly higher covalency in our samples. Geometric factor G is a measure of the exchange interaction between copper centers ($G = (g_{\parallel} - g_e)/(g_{\perp} - g_e)$) and value of $G = 7.84$ for our samples indicate negligible exchange interaction since $G > 4$ [5]. The empirical factor f is an index of tetrahedral distortion ($f = g_{\parallel}/A_{\parallel}$) and its value vary from 105 to 135 for small to extreme distortion in square planar complexes [5]. Value of $f = 122$ for our samples indicate significant distortion from axial symmetry of copper bonding site. Slightly better fit between computer simulated and experimental EPR spectra for our

samples could possibly be obtained if we suppose the rhombic environment around the metal center as in some monosaccharide Cu(II) complexes [7] but the basic conclusions about the nature of copper bonding site would be the same.

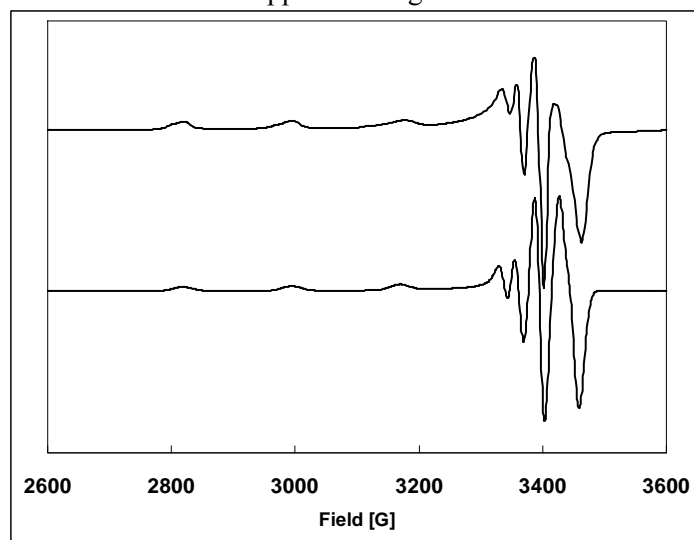


Fig.1. EPR spectrum of the sample containing 6.97 % of copper synthesized at pH 12.0 (upper trace) and its computer simulation (lower trace).

Conclusion

Computer simulation of experimental EPR spectra for Cu(II) complexes with reduced dextran derivatives synthesized at high pH values enabled the precise characterization of metal bonding site in these samples. Prevailing ionic bonding, negligible exchange interaction, and significant distortion from axial symmetry of copper bonding site are the main features of these complexes.

References

- [1] B. Gyurcsik, L. Nagy, *Coord. Chem. Rev.*, 2000, **203**, 81.
- [2] M. Somogyi, *J. Biol. Chem.*, 1945, **160**, 61.
- [3] M. Cakić, Ž. Mitić, G. S. Nikolić, Lj. Ilić, G. M. Nikolić, *Spectroscopy*, 2008, **22**, 177.
- [4] A. Bartkowiak, J. Jezierska, T. Szychaj, *Polym. Bull.*, 1998, **41**, 199.
- [5] E. Manoj, M.R. Prathapachandra Kurup, A. Punnoose, *Spectrochim. Acta A*, 2009, **72**, 474.
- [6] M. Łabanowska, E. Bidzińska, K. Dyrek, T. Fortuna, S. Petrzyk, J. Roźnowski, R. P. Socha, *Starch*, 2008, **60**, 134.
- [7] G. Cerchiaro, A. C. Sant'Ana, M. L. A. Temperini, A. M. de Costa Ferreira, *Carbohydr. Res.*, 2005, **340**, 2352.

N

General Physical Chemistry

ANALYSIS OF HAFNIUM IN ZIRCONIUM FLUORIDE BY ICP-OES

Lj. Marjanovic¹, R. I McCrindle² and W. Augustyn³

¹*University of Johannesburg, Department of Chemistry, Auckland Park, 2006
Johannesburg, RSA*

²*Tshwane University of Technology, Department of Chemistry, Pretoria, 0001,
RSA*

³*The South African Nuclear Energy Corporation (Ltd) Ltd. PO Box 582, Pretoria
0001, RSA*

Abstract

Analysis of hafnium in zirconium fluoride (ZrF_4) which is one of the intermediate products in the production of pure zirconium metal from zirconium ores, by inductively coupled plasma optical emission spectrometry (ICP-OES) is described in this paper. Typical small particle size of the material, high solubility of ZrF_4 (1.3 g/100 ml of water) as well as insolubility of hafnium fluoride (HfF_4), make the analysis an ideal application of slurry nebulisation ICP-OES. Results obtained for the analysis of commercially available 99.9% pure ZrF_4 showed that either aqueous standards or standards prepared from pure solid HfF_4 can be used for the calibration of the instrument. The concentration of hafnium in the pure ZrF_4 was found to be less than 30 ppm.

Introduction

Transparency of zirconium to thermal neutrons makes the zirconium metal one of the most often used materials for nuclear reactors. However, the purity of the metal is very important for such an application and especially the concentration of hafnium. Hafnium has a high absorption coefficient for neutrons and therefore its concentration in zirconium metal, should be very low.

Zirconium metal is produced from zirconium ores, which contain minerals such as alvite $HfThZrSiO_4 \cdot H_2O$ thortveitite $(ScY)_2Si_2O_7$ and zircon $ZrSiO_4$. However, the ores also contain 1-5% of hafnium which has to be removed. The separation of the two metals is however, quite problematic due to their chemical similarities and includes steps such as fluorination in which the metals are converted into their fluorides [1]. While the reported solubility of zirconium fluoride is 1.3 g/100ml the hafnium fluoride is practically insoluble.

High purity is also a very important prerequisite if zirconium fluoride is to be used as a component in optical fibres (used in telecommunications) since the impurities attenuate the optical signal [2]. This requires sensitive analytical methods, capable of handling high Zr matrices.

There are many analytical techniques described in the literature for the analysis of low concentration of Hf due to its hazardous nature [3]. However when the

hafnium is to be analysed in some zirconium based materials, extreme chemical treatments are required due to the refractive nature of zirconium materials [4]. A procedure exists for the direct analysis of impurities such as Fe, Co, Ni, Cr, Mn and Cu in high purity grade ZrF_4 and ZrO_2 by ETA-AAS [1], [5]. Hafnium, however, can not be analysed by this technique owing to strong tendency to form refractory hafnium carbide. Application of slurry nebulisation ICP-OES for the analysis of zirconium oxide is described in the literature [4]. The importance of adequate calibration standards as well as fine particle size of the sample is emphasised.

Experimental

A Spectro ARCOS ICP-OES equipped with a slurry nebulizer and cyclonic spray chamber was employed in order to provide efficient transport of the sample to the plasma. Samples were prepared by weighing 0.5000 g of ZrF_4 accurately, transferring it quantitatively to a 50.00 ml volumetric flask and making it up to the mark with deionized water. The flasks were then put in an ultrasonic bath for 5 min to ensure well-dispersed, homogeneous slurry prior their introduction into the plasma.

The instrument was calibrated either by using aqueous solutions of Hf prepared by dilution of a 1000 ± 3 mg/l of aqueous Hf stock solution, or by standards prepared from solid 99.99% HfF_4 . In the latter case exactly 0.14 g of solid HfF_4 was weighed accurately in a glove box under the nitrogen atmosphere, transferred to a 1000 ml volumetric flask and diluted to the mark with deionized water. A series of calibration standards (0.1, 0.2 and 0.3 mg/l) were prepared from this stock solution by dilution.

Results and Discussion

Optimization of the nebulizer gas flow (while keeping the plasma power and the observation height constant) showed that much higher emission intensities could be obtained at lower nebulizer gas flows (0.6-0.7 l/min) which were then used throughout the analysis. The need for longer exposure to the hot plasma was expected owing to the refractory nature of the analyte. Commercially available ZrF_4 , certified to 99.9 % purity, was analysed by using the above described method. Results obtained, for the three wavelengths investigated, are presented in Table 1. Results obtained for calibration with aqueous standards as well as calibration with standards prepared from solid HfF_4 are presented. Limits of detection were calculated from the calibration curves as 3 times standard deviation of the intercept divided by the slope of the calibration curve and were obtained in ppb range.

A clear solution was observed after the addition of 1 ml of 40% hydrofluoric acid, even before sonication of the slurry. The results obtained for the analysis of solution after the addition of HF acid are also shown in the Table 1 for both aqueous calibration as well as slurry (HfF_4) calibration.

Table 1. Analysis of Hf in 1% (m/v) slurry of 99.9% ZrF₄ using aqueous standards of Hf and standards prepared from HfF₄

Calibration of the instrument performed by:	Wavelength (nm)		
	Hf 264.141	Hf 232.247	Hf 282.022
	Hf concentration (mg/l) Before the addition of HF acid		
Standards prepared from aqueous 1000 mg/l Hf	0.277	0.261	0.273
Standards prepared from solid HfF ₄	0.266	0.242	0.261
	Hf concentration (mg/l) After the addition of HF acid		
Standards prepared from aqueous 1000 mg/l Hf	0.263	0.242	0.256
Standards prepared from solid HfF ₄	0.279	0.260	0.279

Conclusion

The slurry method can be used for the analysis of Hf in ZrF₄ while using aqueous standards calibration or standards prepared from solid HfF₄, with or without the addition of HF acid. The digestion can be achieved with small addition of HF (final concentration of HF is less than 1%) without the need for digestion of the sample.

Acknowledgements

We would like to thank the Department of Science and Technology's Advanced Metals Initiative programme and the South African Nuclear Energy Corporation for support.

Literature

- [1] S. Chen, L Wang, Z. Liao, T. Peng, B. Hu and Z. Jiang, *Analytical Sciences*, 2000, **16**, 877-879.
- [2] K. Kobayashi, T. Shigematsu, *Journal of Radioanalytical and Nuclear Chemistry*, 1987, **113**, 333-341.
- [3] A. Hulanicki, J Surgiewicz, I Jaron, *Talanta*, 1997, **44**, 1159-1162.
- [4] R. Lobinski, W. V. Borm, J. A. C. Broekaert, P. Tschopel, G Tolg, *Fresenius' Journal of Analytical Chemistry*, 1992, **342**, 569.
- [5] S. Chen, L Wang, Z. Liao, T. Peng, B. Hu and Z. Jiang, *Analytical Sciences*, 2000, **16**, 877-879; N. K. Bel'skii, L. I. Ochertyanova, *Journal of Analytical chemistry*, 1995, **50**, 1106-1107.

PHYSICOCHEMICAL CHARACTERISTICS OF COAL SLURRIES FOR INTRODUCTION INTO AN ICP-OES

R. I. McCrindle,¹ M. Mujuru¹ and L. Marjanovic-Bakovic²

¹*Tshwane University of Technology, Department of Chemistry, Arcadia Campus, P O Box 56208, Arcadia 0007, Pretoria, Republic of South Africa*

²*Department of Chemistry, University of Johannesburg, Bunting Rd, Auckland Park, 2006, Johannesburg, South Africa*

Abstract

A method for analyzing coal using dimethyl formamide (DMF) and Triton-X-100 was developed. In order to understand the reasons why the slurry method was successful, the characteristics of the mixture were investigated. Coal samples were ground by a micronizing mill. The particle size, zeta potential, viscosities, surface area, specific volume and mean pore width were determined. The particle size could be reduced to between 8-10 m. Different dispersants were studied. It was found that DMF partly dissolved the particles, reducing the size and stabilized the slurries.

Introduction

South Africa is both a supplier and user of coal. In excess of 90% of the power generation in the country is by means of fossil fuel. Determination of metals in coal is currently by means of X-ray fluorescence spectroscopy (XRF) which is expensive and unable to measure ultra-trace amounts. Slurry nebulization into an inductively coupled plasma-optical emission spectrometer, or mass spectrometer, has proved to be a viable alternative [1]. The nature of the slurry has not yet been explained or the reasons for its effectiveness [2].

Experimental

Coal samples were ground by a micronizing mill mounted with agate elements. Particle size, after grinding, was measured by a Malvern Mastersizer 2000 instrument. Zeta potentials of the prepared slurries were measured with a Zetasizer Nano ZS. The observations and pictures were taken with a JSM-6000F field emission scanning electron microscope. Viscosities were measured with a DV-II+ Pro Viscometer. In order to determine surface area, specific volume and mean pore width, the coal samples were first degassed and then subjected to N₂ adsorption. Dispersants, Triton X-100, glycerol and polyethylene imine (PEI) were investigated. Coal samples were from Witbank, South Africa and two reference material bituminous coals, SARM 18 and SARM 19 were supplied by SA Bureau of Standards, Pretoria, South Africa.

Results and Discussion

The particle sizes distribution, before and after grinding of the two different certified reference material coals, showed that the mineralogy of the coal affected the grinding efficacy of the coal. Comparison of particle size data with that of ash content, showed that for coals with higher ash content it was generally more difficult for the coal to be reduced to particle sizes in the 8-10 μm range.

The viscosities of the slurries slightly with the addition of DMF, however, viscosity of slurries with Triton X-100 increased by between 7% for 0.1% (m/v), to 18% for the 0.5% (m/v) Triton X-100, respectively. The viscosities increased by a maximum of 29 % for the 0.1 % glycerol slurry.

Dispersion of slurries was also studied by measuring of the zeta potential. An increase in zeta potential implies an increased repulsion between the coal particles. The zeta potential of the different slurries is given in Figure 1.

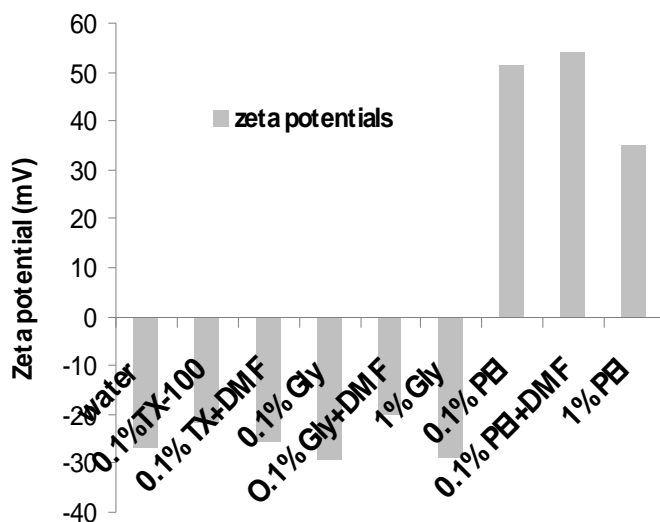


Fig.1. Zeta potentials of a coal CRM with different additives.

The adsorption characteristics, which relate to coal texture, were determined using the BET and BJH standard methods, as given by the Micromeritics instrument (Table 1).

Pore volumes of the two Witbank coals were increased by three to four times, as a result of the grinding process. According to the International Union of Pure and Applied Chemistry (IUPAC) [3], the pore size ranges obtained for the ground and unground coals put the pore sizes in the mesoporous range. The pore structure of mesoporous solids such as these Witbank coals, gave rise to a Type IV isotherm with a characteristic hysteresis loop [4].

The mesopores in the coal particles implies that once the surfactant molecules enter the pores and were adsorbed on the surfaces, they do not easily leave the particles and thus cause the coal particles to stay suspended for longer times. This then increases the possibility of effectively analyzing coal by slurry nebulization ICP OES.

Hysteresis loops at low temperature adsorption and desorption of nitrogen indicated that the process of capillary condensation occurred in the mesopores [4]. For the ground coals, the narrower hysteresis loops meant that desorption of adsorbed surfactant molecules occur at a relatively slower rate resulting in relatively longer suspension times of the ground coal particles and thus more stabilized slurries.

Table 1: Characteristics of some Witbank coals investigated

Coal sample	Surface area (m ² /g)		Pore volume (cm ³ /g)	Micropore volume (cm ³ /g)	Average pore size (Å)
	BET*	BJH**	BJH	t-Plot micropore vol.	BET BJH
Seam 5 (ground)	6.21	7.66	0.04	0.000	130 191
Seam 5(unground)	1.64	2.28	0.02	0.001	184 314
Seam 2 (ground)	18.9	23.9	0.05	0.000	73.3 78.6
Seam 2(unground)	2.06	3.28	0.03	0.002	182 321

*Brunauer, Emmett and Teller isotherms; **Barret-Joyner-Halenda (**BJH**) calculation scheme

Conclusion

The study demonstrated that the DMF both partially dissolved the coal, but also entered the capillaries at the surface. This ensured that the particles would be reduced in size and also would remain dispersed.

References

- [1] M. Mujuru, R. I. McCrindle, B. M. Botha and P. P. Ndibewu, Conference Proceedings, 24th Annual International Pittsburgh Coal Conference, 2007.
- [2] M. Mujuru, R. I. McCrindle, B. M. Botha and P. P. Ndibewu, Fuel, 2009, **88**, 719.
- [3] IUPAC Manual of Symbols and Terminology, Appendix 2, Pt. 1, Colloid and Surface Chemistry. Pure Appl. Chem., 1972, **31**, 578.
- [4] S. J. Gregg and K. S. W. Sing, Adsorption, Surface Area and Porosity, 2nd Edition, Academic Press, 1982.

MAJOR AND TRACE ELEMENT DISTRIBUTION IN LIGNITE COMBUSTION PROCESS AT THE POWER STATION TENT-A (SERBIA)

A. Dangić¹, B. R. Simonović² and S. Gajinov²

¹*University of Belgrade, Faculty of Mining & Geolog, Djušina 7, 11000 Beograd, Serbia*

²*Institute of General and Physical Chemistry, Stud. Trg 12-16, 11000 Beograd, Serbia*

Abstract

Power station (PS) TENT-A, one of biggest in Serbia, fires annually 10.5 Mt of lignite, producing 2 Mt solid wastes – electro filter ash (EA) and slag (SL). Major and trace elements have been analyzed in ash of coal feeding PS (CA), EA and SL sampled in two periods of the year. Composition of CA, EA and SL are near similar for each sampling set, but sets differ in some extent. According EA/SL ratio, 3 groups of elements are selected: (1) enriched in EA; (2) enriched in SL; (3) controversially enriched. Composition of EA and SL depend on quality of coal feeding PS, the combustion process in PS and geochemical features of elements.

Introduction

The power station (PS) “Nikola Tesla A” (TENT-A) at Obrenovac, with the install power of 1652 MW is the biggest lignite operating PS in Serbia. It annually fires 10.5 Mt of lignite from the Kolubara Basin producing 2 Mt of solid waste products. Lignite feeding PS varies in quality which impacts the process of coal firing in PS as well as composition of coal firing products [1; 2]. This study focuses on variations of major and trace elements in the process of coal firing in PS TENT-A and their distribution between solid firing waste products.

Materials and Methods

All three materials studied: coal feeding PS and electro filter ash (EA) and slag (SL) from PS, have been sampled two times: 13.06.2005 and 08.12.2005. Major and trace elements in these materials have been analyzed by atomic absorption and X-ray fluorescent spectrometry (coal referent standards used).

Results and Discussion

PS TENT-A uses lignite from the open pits in the Kolubara Basin, mostly the “Tamnava–W Field” (TWF) and the “Field D”. Lignite consists of organic (OM) and inorganic matter (IM). OM is represented by diverse coal micro-lithotypes and macerals, and IM by sands, aleurite, clay and pyrite [3]. For example, lignite quality in TWF varies as follows (based on 657 analyses): moisture 22.50-60.10 (average 47.86) %, ash 3.56-58.76 (18.63) %, combustable matter 15.69-85.89 (33.53) %, volatile matter 11.84-72.42 (20.53) %, sulfur-combustable 0.01-0.83

(0.19) %, sulfur-pyritic 0.04-0.59 (0,22) %, gross calorific value 2236-13212 (8140) kJ/kg, low calorific value 1168-11787 (6889) kJ/kg.

In PS, coal after pulverization enters boilers. In the boiler, OM particles are exposure to vaporization of moister remnants, firing, liberation and firing of volatile combustible compounds and combustion of coke remnants. IM particles may be more or less altered. Thus, EA in PS may consist of new formed minerals (NFM), relic (unaltered) minerals (RM), and unfired OM (UOM). In TENT-A, EA and SL are of similar mineral composition, consist of glass, mullite, hematite, anhydrite (NFM), quartz, feldspar (RM) and some UOM.

Major and trace element (ME and TE) contents in ash of coal entering PS (CA), EA and SL from PS are presented in Table 1. ME contents are (in %): 47-45 SiO₂; 23-26 Al₂O₃; 4-9 Fe₂O₃, CaO; 2-3 MgO, SO₃; 1-1.5 Na₂O, K₂O, and ≤0,1 P₂O₅. TE contents are (in mg/kg): 2500-3000 B; 650-1200 Ba, Mn; 150-750 Cr, Cu, Ni, Sr; 50-300 V, Zn; 19-50 As, Pb. Composition of CA, EA and SL are near similar for each sampling period, but sets of samples differ in some extent (Fig. 1).

Table 1. Major and trace element contents in ash of coal feeding PS (CA) and electro filter ash (EA) and slag (SL) produced by coal combustion in PS.¹

Material	Coal ash (CA)		EA		SL		EA/SL		
	I	II	I	II	I	II	I	II	
Sampled ²									
%	SiO ₂	54.70	49.6	54.34	47.34	54.57	51.43	1.00	0.92
	TiO ₂	0.80	0.75	0.76	0.79	0.73	0.75	1.04	1.05
	Al ₂ O ₃	22.77	26.46	25.28	27.75	25.7	25.98	0.98	1.07
	Fe ₂ O ₃	8.97	6.08	8.01	5.90	7.29	7.68	1.10	0.77
	MgO	2.04	2.61	1.79	3.03	1.8	2.28	0.99	1.33
	CaO	5.28	7.70	3.95	8.57	4.13	5.25	0.96	1.63
	Na ₂ O	0.91	1.01	0.71	0.77	0.9	0.91	0.79	0.85
	K ₂ O	1.23	1.20	1.48	1.33	1.29	1.23	1.15	1.08
	SO ₃	2.08	2.91	2.21	2.88	1.93	2.54	1.15	1.13
P ₂ O ₅	0.04	0.10	0.03	0.07	0.04	0.11	0.75	0.64	
mg/kg	As	50	37	40	38	28	32	1.43	1.19
	B	3775	3125	2800	2500	3050	3750	0.92	0.67
	Ba	783	800	700	950	735	650	0.95	1.46
	Cr	378	725	405	325	573	675	0.71	0.48
	Cu	250	300	263	400	200	300	1.31	1.33
	Mn	1195	675	1025	675	923	650	1.11	1.04
	Ni	188	375	175	200	150	375	1.17	0.53
	Pb	35	32	39	19	45	33	0.87	0.58
	Sr	300	325	270	400	270	250	1.00	1.60
	V	52	75	55	87	68	62	0.81	1.40
	Zn	105	325	65	300	68	250	0.96	1.20

¹- In all samples Cd <0.1 mg/kg. ²- I=13.06.2005, II=8.12.2005.

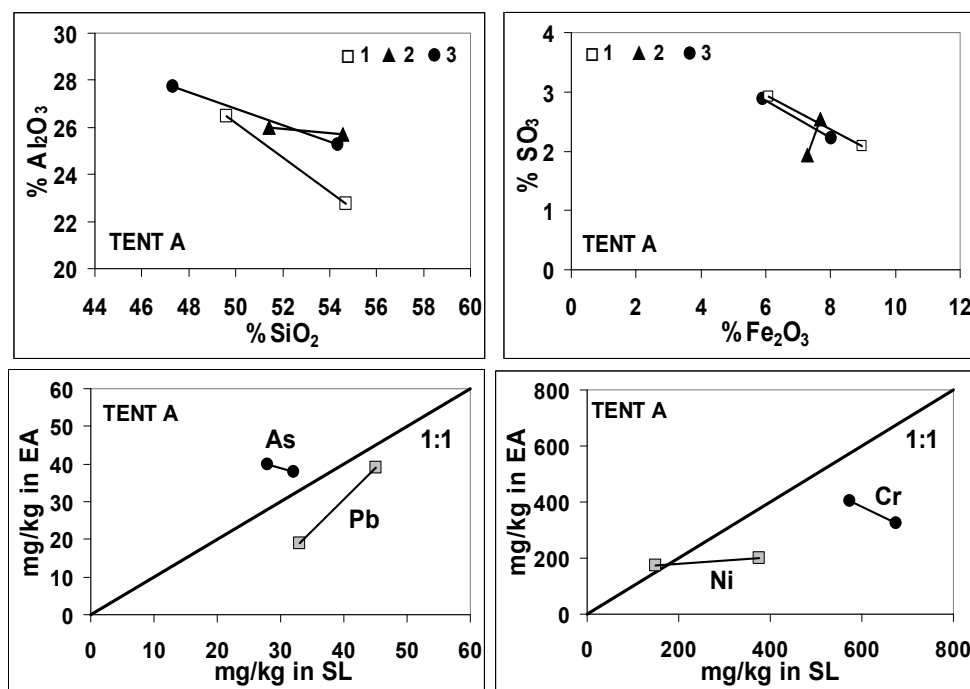


Fig.1. Distribution of major and trace elements between EA and SL from PS in two terms (based on data in Table 1). 1- coal ash; 2-EA; 3-SL.

In addition, EA and SL differ in contents of some elements. According ratio of concentrations in EA and SL, all elements may be divided in the following three groups: (1) enriched in EA (EA/SL >1)- S, Ti, K, As, Cu, Mn, Sr; (2) enriched in SL (EA/SL <1)- Si, Na, P, B, Cr, Pb; (3) controversially enriched (EA/SL >1 and <1)- Al, Fe, Mg, Ca, Ba, Ni, V, Zn (Fig. 2). The group 3 indicates that the processes of coal combustion in PS and IM alterations are complex.

Conclusion

The study indicates that coal feeding PS TENT-A varies in quality which causes variation in composition of solid waste products in PS (EA and SL). Due to that and some other variations in the combustion process in PS as well as their geochemical features, several major and trace elements are characterized by controversial patterns of enrichment between EA and SL.

References

- [1] S. M. Mardon, J. C. Hower, *Int. J. Coal Geology*, 2007, **59**, 153–169.
- [2] A. Dangić, B. Simonović, J. Cvetković, V. Nikolić, J. Milošević, 2nd Balkan Mining Congress, Proceedings, Belgrade, 2007, 415-420.
- [3] A. Dangić, B. Simonović, R. Dimitrijević, M. Babović, 2nd Balkan Mining Congress, Proceedings, Belgrade, 2007, 9-14.

MAJOR AND TRACE ELEMENT GEOCHEMISTRY OF LIGNITE IN THE TAMNAVA-W FIELD (KOLUBARA BASIN, SERBIA)

A. Dangić¹, B. R. Simonović² and S. Gajinov²

¹*University of Belgrade, Faculty of Mining & Geology, Djušina 7, 11000 Beograd, Serbia*

²*Institute of General and Physical Chemistry, Stud. Trg 12-16, 11000 Beograd, Serbia*

Abstract

In lignite of the Tamnava-W Field, one of biggest coal fields of the Kolubara Basin in Serbia, geochemistry of major and trace elements has been studied in a vertical profile of the coal seam (as thick as 28 m, 34 samples). Three geochemical associations, according to affinities to coal organic (OM) and inorganic (IM) matter are selected: (1) OM affinity-Ca, S, Sr, Mn, Pb, (2) IM affinity-Si, Al, Ti, Mg, K, Ba, V, and (3) No-affinity-Fe, P, Cl, Cu, Zr, As, Cr, Ni, Zn, Co, Hg. They indicate complex geochemical conditions of coal seam genesis and evolution.

Introduction

The Kolubara Basin, the most important and the largest lignite producing base in Serbia, consists of several coal fields (CFs) four of which are mining by open pits (total annual coal production of 30 Mt). The Tamnava-Western Field (TWF), one of biggest, located in the northern part of the basin, has an annual coal production of 9.6 Mt (2009). Almost all coal produced participates in feeding two large electric power stations (Nikola Tesla A and B) at Obrenovac. This study focuses on the geochemistry of major and trace elements (TEs) in coal of TWF.

Material and Methods

The TWF is characterized by one coal seam. We studied a vertical profile of the coal seam in the borehole Olm-OO/147.5 (as thick as 28 m), sampling all intervals with remarkable lithological changes (in total 34 samples). For all samples proximate, elemental, and major and trace element analyses have been made. Major and trace elements have been analyzed by atomic absorption and X-ray fluorescent spectrometry (coal referent standards used).

Results and Discussion

The lignite seams are built up by organic (coal) and inorganic (mineral) matter. In the Kolubara basin, ratio of organic matter/mineral matter significantly varies in coal fields, especially in vertical profiles of the coal seams, causing also significant variations of coal quality [1]. Organic matter is represented by diverse coal micro-lithotypes and macerals, and mineral matter by sands, aleurite, clay and pyrite. In

TWF, the proximate and elemental analyses of lignite indicate that lignite quality varies as follows (based on 657 analyses): moisture 22.50-60.10 (average 47.86) %, ash 3.56-58.76 (18.63) %, combustable matter 15.69-85.89 (33.53) %, volatile matter 11.84-72.42 (20.53) %, sulfur-combustable 0.01-0.83 (0.19) %, sulfur-pyritic 0.04-0.59 (0.22) %, gross calorific value 2236-13212 (8140) kJ/kg, low calorific value 1168-11787 (6889) kJ/kg.

In the studied vertical profile of the coal seam, results of proximate and elemental analyses are in the ranges presented above for TWF. Data on major and trace elements (minimal, maximal, average, st. deviation) are presented in Tables 1-2. Among major elements, most abundant are Si and Al and are followed by Fe, Ca and S. Their concentrations vary significantly in the coal seam profile (Fig. 1).

Table 1. Chemical composition of TMF coal, borehole profile (wt. %, dry basis).

n ¹ = 34	SiO ₂	TiO ₂	Al ₂ O ₃	Fe ₂ O ₃	MgO	CaO	K ₂ O	P ₂ O ₅	S
Minimal	3.06	0.01	0.98	0.94	0.07	0.34	0.08	0.01	0.006
Mmaximal	35.18	0.48	14.31	5.37	0.50	3.38	1.02	0.04	4.156
Average	15.94	0.19	5.58	1.87	0.22	1.72	0.42	0.02	1.040
St. deviation	11.63	0.13	4.26	0.86	0.14	0.89	0.26	0.01	0.930

¹-Number of analyses.

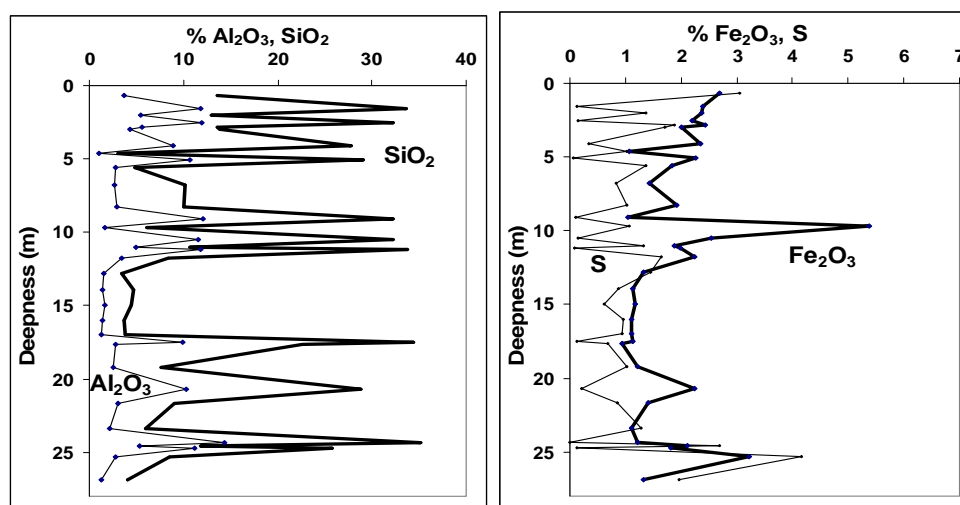


Fig.1. Distribution of major elements in the vertical profile of the main coal seam in the Tamnava-Western Field (borehole Olm-OO/147.5).

Among TEs analyzed, As, Ba, Cl, Co, Cr, Cu, Hg, Mn, Ni, Pb, Sr, V, Zn and Zr were detected and Be, Cd, Se, Th, U and W were below detection limits of the methods applied. According contents, TEs may be grouped as follows (in mg/kg): (1) up to >1000– Cr, Mn; (2) up to >100– Ba, Sr, Cl, Cu, V; (3) up to 50-100– As, Pb, Zn; (4) 1-50– Co, Ni, Zr; (5) <1– Hg. These ranges of amounts of the elements are typical for lignites. [2]

Table 2. Trace element contents in TMF coal, borehole profile (mg/kg, dry basis).¹

	As	Ba	Cl	Co	Cr	Cu	Hg	Mn	Ni	Pb	Sr	V	Zn
Min	27	15	100	5	35	55	0.18	35	15	44	20	20	15
Max	95	360	400	14	8140	115	0.31	2550	45	74	185	250	95
Aver	53	164	200	9	937	79	0.23	230	29	58	70	56	62
St.d.	18	102	100	2	1581	15	0.03	424	7	8	43	60	16

¹-Based on 34 samples. Zr (mg/kg): 4-9, aver. 7, st.d. 2. In all samples: Be, Se, U <0,1 mg/kg; Cd, Th, W <1 mg/kg.

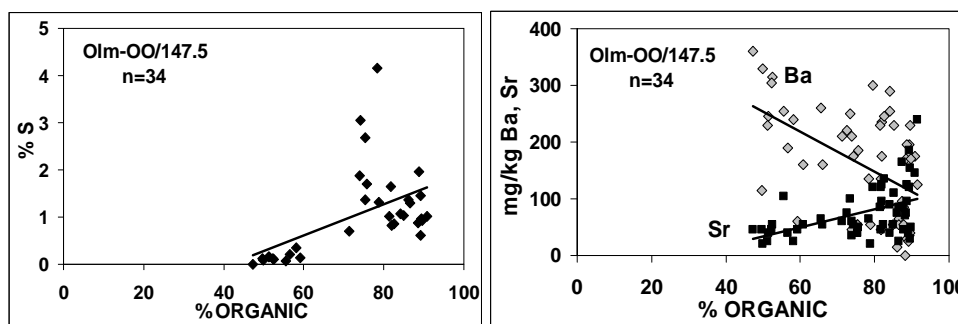


Fig.2. Correlation of S, Ba and Sr with content of organic matter in coal.

The major and trace elements may be grouped, based on coefficient of correlation (r) with coal organic matter (OM) or mineral matter (MM), into the following 3 geochemical associations: (1) OM-affinity—Ca ($r=0.91$), S, Sr (0.51-0.53), Mn (0.33), Pb (0.23), (2) MM-affinity— Si, Al, Ti, Mg, K, ($r=0.85-0.99$), Ba (0.53), V (0.36), and (3) No affinity – Fe, P, Cl, Cu, Zr ($r=\leq\pm 0.20$), As, Cr, Ni, Zn, Co, Hg ($r=\leq\pm 0.08$). Si and Al are strongly correlated with MM, as they constitute sand/aleurite and/or clay appearing in the coal seam. Accordingly, they appear to be major constituents of the coal ash. Sulfur is correlated with OM, but its distribution depends also on pyrite which is irregularly distributed across the coal.

Conclusions

Lignite of the Tamnava-W Field is characterized by significant variation in OM and IM matter, especially in vertical profiles of the coal seam. Among the major and trace elements in coal, the following three geochemical associations have been selected: (1) OM-affinity, (2) IM-affinity and (3) no-affinity. They indicate complex geochemical conditions during coal seam genesis and evolution.

References

- [1] A. Dangić, B. Simonović, R. Dimitrijević, M. Babović, 2nd Balkan Mining Congress, Proceedings, Belgrade, 2007, 9-14.
- [2] D. J. Swaine, Trace elements in coal, Butterworths, London, 1990, 278.

GEOCHEMISTRY OF THE HYDROTHERMAL DICKITE (NOWA RUDA, LOWER SILESIA, POLAND): CHROMIUM

N. S. Krstić¹, M. S. Pavlović², N. D. Nikolić¹, M. G. Đorđević¹ and P. I. Premović¹

¹Laboratory for Geochemistry, Cosmochemistry and Astrochemistry, Department
of Chemistry, University of Niš, P.O. Box 224, 18000 Niš, Serbia

²Institute of Nuclear Science Vinča, P.O. Box 522, 11001 Belgrade, Serbia
e-mail: nenad.krstic84@yahoo.com

Abstract

Geochemical analyses for trace Cr have been made on a representative sample of a typical hydrothermal dickite filling vein at Nowa Ruda. The mineralogy of the sample is comparatively simple, dickite being the principal component (ca. 91% of total sample). Geochemical fractionation and inductively coupled plasma-optical emission spectrometry (ICP-OES) indicate that most (>96 % of total metal) of Cr reside in the dickite. The combination of geochemical and spectroscopic tools applied on Cr³⁺ allow one to specify the Eh (>0.4 V, highly oxidizing) and pH (≤4.0, highly acidic) of the solution during the formation of dickite from the Nowa Ruda Basin. We suggest that hot hydrothermal waters leached the surrounding varieties of gabbroids enriched in Cr for the dickite-forming solution.

Introduction

Acid alteration in magmatic hydrothermal systems is often represented by kaolinite group minerals including kaolinite, dickite, nacrite and halloysite [1]. Hydrothermal dickite is mainly formed in situ through alteration of source minerals (mainly K-rich feldspars and other aluminosilicates) by hydrothermal acid waters. Geochemical studies indicate that Cr occurs in natural aquatic environments in two oxidation states: Cr(III) and Cr(VI). In low (suboxic/anoxic) Eh natural environments, the main aqueous Cr(III) species are Cr³⁺ and Cr(OH)²⁺. Under oxidizing conditions, aqueous Cr is present in a Cr(VI) anionic form, HCrO₄⁻ and/or Cr₄²⁻, depending on the pH. Cationic Cr(III) species are rapidly and strongly adsorbed by colloidal clay particles, but adsorption of anionic Cr(VI) species onto these particles is expected to be minimal [2, 3]. The hydrothermal dickites are not frequently studied and our knowledge of the physicochemical conditions necessary for their formation is still obscured. One way to get an objective evaluation of the nature of solutions during the formation (precipitation) of dickites is to examine components that undoubtedly were introduced into their lattice by these solutions. Such component is, for certain, Cr³⁺ ion.

Experimental

Sample location and description

The Nowa Ruda Basin is located in the Sudetes Mountains (southwestern Poland), near the city of Wrocław. Dickite is found throughout the abandoned coal mine Piast near the town of Nowa Ruda.

Analysis and fractionation

The fractionation procedure was similar to that used by Premović [4]. The flow chart in Fig. 1 outlines the major steps in preparing the four fractions.

Inductively coupled plasma–optical emission spectroscopy (ICP–OES) analysis.

The Cr contents of the various fractions of dickite sample were analyzed by a Spectroflame ICP–OES instrument using Ar as the plasma gas.

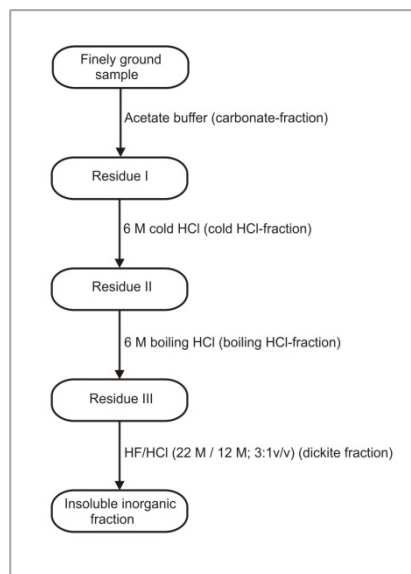


Fig.1. Flow chart of fractionation procedure.

Results and discussion

Table 1 shows the distributions of Cr among the fractions of dickite sample. These results show that most of Cr is containing in the dickite (>96 % of the total Cr (410 ppm)), indicating that the bulk of Cr resides primarily within the dickite structure.

Table 1. Geochemical distributions of Cr [ppm] from selective leaching experiments of dickite sample.

Fraction	Sediment (±5 wt%)	Cr
Acetate buffer	3	35
Cold-HCl	1	190
Boiling-HCl	3	340
Dickite	91	435
Insoluble residue	2	-
Total sample	100	410

Geochemical data suggest that the geological conditions under which dickite formed must have been relatively rich in Cr (i.e., Cr³⁺), and it was introduced into dickite during formation aided by an invasive hydrothermal water. The fact that >96 % of Cr (Table 1) resides within the dickite structure indicates that most Cr in dickite-forming solution was in a dissolved form.

We suggest that most of this metal was introduced into dickite by this solution already enriched in Cr.

The combination of geochemical and spectroscopic tools applied on Cr^{3+} allow one to specify the Eh (>0.4 V, highly oxidizing) and pH (≤ 4.0 , highly acidic) of the solution during the formation of dickite from the Nowa Ruda Basin (Fig. 2).

Conclusion

1. The geochemical analysis of the dickite sample shows that the most of Cr is containing in the dickite fraction.
2. From the geochemistry of Cr^{3+} , it is deduced that the oxidation potential, Eh, and pH of the dickite-forming solution were >0.4 V and ≤ 4 , respectively.

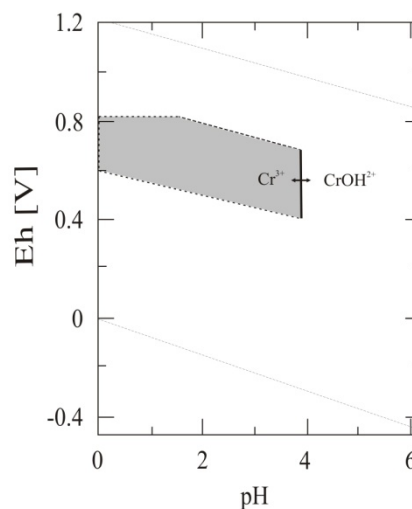


Fig.2. Eh-pH diagram for Cr^{3+} at 300 K and 1 atm for formation of dickite. The shaded area represents Eh/pH region of the hydrothermal waters defined by Kraynov and Ryzenko [5].

References

- [1] G. Izquierdo, V. M. Arellano, A. Aragón, E. Portugal, I. Martinez, Fluid acidity and hydrothermal alteration at the Los Humeros geothermal reservoir Pubela, Mexico. – Proceedings of World Geothermal Congress, Kyushu – Tohoku, Japan, 2000, 1301-1305.
- [2] D. Rai, J. M. Zachara, L. E. Eary, D. C. Girvin, D. A. Moore, C. T. Resch, B. M. Sass, R. L. Schmidt, Geochemical behavior of chromium species. Electric Power Research Institute, Palo Alto, California, Interim Report, EPRI, 1986, EA-4544.
- [3] D. Rai, B. M. Sass, D. A. Moore, Inor. Chem., 1987, **26**, 345-349.
- [4] P. I. Premović, Geochim. Cosmochim. Acta, 1984, **48**, 873-877.
- [5] S. R. Kraynov, B. N. Ryzenko, Geochem. Int., 1992, **29**, 1-8.

Ir ANOMALY IN THE CRETACEOUS-PALEOGENE BOUNDARY FISH CLAY AT HØJERUP (STEVNS KLINT, DENMARK): THE PROPORTION OF EXTRATERRESTRIAL COMPONENT

P. I. Premović*, B. S. Ilić and M. N. Stanković

*Laboratory for Geochemistry, Cosmochemistry and Astrochemistry, University of Niš, P.O. Box 224, 18000 Niš, Serbia, *pavle.premovic@yahoo.com*

Abstract

The carbonate-free fraction of the black marl of the Fish Clay at Højerup (Stevns Klint, Denmark) shows a considerable enrichment of Ir, compared with the terrestrial rocks. A simple calculation shows that this high Ir corresponds to 14% - 30% of the carbonaceous chondritic (CC) contribution. We conclude that this proportion is probably incorrect because the most of Ir in the Fish Clay was probably originated from CC material in the impact-derived ejecta fallout on the nearby soil at Stevns Klint.

Introduction

The lowermost Danian Fish Clay Member of the Rødvig Formation near the village of Højerup (hereafter referred as the Fish Clay) at Stevns Klint (Fig. 1) is a classic marine Cretaceous-Paleogene boundary section. Alvarez *et al.* [1] have first reported an anomalously high Ir (29 ppb) concentration in the Fish Clay; Kastner *et al.* [2] explained this enhanced Ir proposing an impact of extraterrestrial bolide (ca. 10 km in diameter) occurring at the Cretaceous-Paleogene boundary. It has been suggested that the impactor was a carbonaceous chondrite-type body [3].

Results and discussion

The mineralogy of the Fish Clay is comparatively simple, smectite and authigenic (mainly biogenic) calcite being the principal components. The lithology of the Fish Clay characterizes five distinctive layers: a bottom Maastrichtian bryozoan-rich limestone, black marl with a red goethite-rich underlain sublayer, brown-to-grey marl, the top light-grey marl. The light-grey marl is overlain by the Danian Cerithium limestone [4,5] Fig. 1. Geochemical studies show that the Ir profile (on a whole rock basis) across the Fish Clay column is characterized with a sharp maximum in the base of black marl with an upward gradual decrease (tailing-off) from its maximum [4]. The black marl and partly grey marls are here considered to

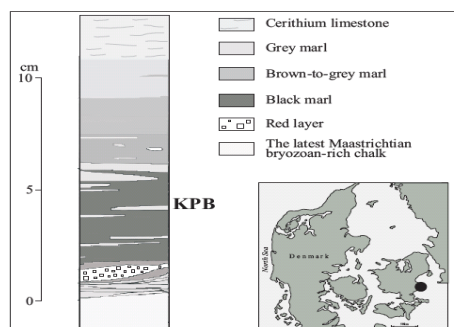


Fig.1. Expanded lithological log of the Fish Clay at Stevns Klint (Denmark)

constitute the main part of the boundary section at Højerup containing about 80 % of the total Ir in the Fish Clay [6].

Enrichment of Ir in the KPB clays is generally regarded as indicative of the presence of a meteoritic component [7]. Ir is a good geochemical marker of an impactor component because of the much greater concentration of Ir in carbonaceous chondrites compared to the potential terrestrial sources (Table 1).

Table 1. Concentrations [ppb] of Ir, for carbonaceous chondrites, continental crustal rocks, seawater and marine sediments.

	Ir [ppb]	Reference
Average	608.5	
Maximum	849.4	[11]
Minimum	406.0	
Crustal rocks	4×10^{-2}	[12]
Seawater	$< 5 \times 10^{-4}$	[13]
Marine sediments	<1	[14]

Schmitz [5] reported the instrumental neutron activation analysis data for Ir in the carbonate-free fraction across the Fish Clay as this metal is wholly located in this part. Using his data and assuming that all the Ir found in the Fish Clay originated from anhydrous CC component (min: 406.0 ppb, max: 849.4 ppb, Table 1), we estimated that the elevated abundance of Ir in the carbonate-free fraction of the black marl was derived from about 14 % - 30 % of the CC material (Fig. 2). Of note, that an impactor mass fraction globally dispersed after the Chicxulub impact ranges between 22 % [1] to 50 % [8].

CC material as a source of Ir obtained in this way is a lower limit because we have assumed Ir to be exclusively of CC origin. At the moment we are unable to make reasonable estimates about the contribution of Ir from terrestrial sources, although we believe this contribution is only a rather minor one. The estimated proportion of CC material which contributed to the Ir in the carbonate-free fraction of the black marl is, however, not supported with any geochemical or mineralogical evidence. Moreover, Trinquier *et al.* [3] have shown that Cr isotopic signature of the black marl represents a mixing of a carbonaceous chondrite of CM2 type with terrestrial material in a ratio 3.8-6.8 %, indicating that the extraterrestrial matter in this marl is probably mixed with a large amount of terrestrial material.

The CC material could be deposited in the Fish Clay by the direct airborne ejecta fallout settling through the seawater column or they were transported from the nearby soil into the Fish Clay bed by the surface water runoff. There is, however, a strong argument supporting the second possibility.

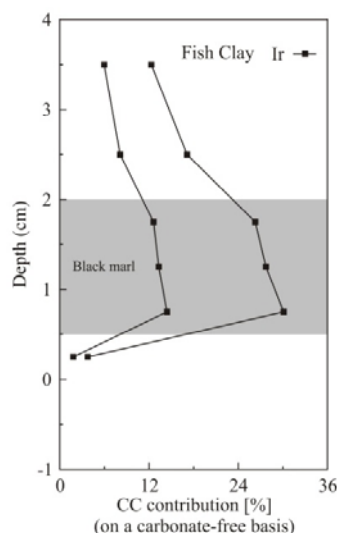


Fig.2. The CC contribution (on a carbonate-free basis) for the Fish Clay.

Indeed, anomalous amounts of Ir slowly decrease from the black marl upwards but this metal is still rather high in the brown-to-grey marl about 2 cm above the black marl (Fig. 2). It has been suggested that this extended “tailing effect” indicates that Ir were probably fluviially transported from the soil on adjacent land and redeposited in a shallow marine basin at Højerup [6,9,10]. It is rather likely that a predominant part of Ir in the black marl ultimately came from CC material associated with ejecta fallout covering nearby coastal soil, during, at least, 10 kyr. The only reasonable alternative would be to assume a CC impactor with an unusual low Ir content (say, about 100 ppb or even less).

In summary, the geochemistry of marine boundary clay is rather complex, and its Ir content may be influenced by various sedimentary and geochemical factors. The extent to which these factors operate highly depends of particular sedimentary site and its immediate environment. Consequently, Ir may have been concentrated or diluted in the boundary clay during its sedimentation and diagenesis. This makes ambiguous any attempt to assess the contribution of the impactor Ir to the Ir enrichment of the boundary clay.

Conclusion

A simple calculation based on the Ir concentrations shows that the non-carbonate fraction of the black marl in the Fish Clay appears to contain Ir derived from as much as 14 % to 30 % of CC material. It is suggested that this high proportion is probably erroneous because anomalous Ir in the Fish Clay was probably sourced from CC component of ejecta fallout covering nearby coastal soil. In general, the impactor Ir contribution to the Cretaceous-Paleogene boundary clay cannot be reliably estimated from the clay Ir content due to the fact that various sedimentary and geochemical factors may affect the boundary clay and Ir associated with.

References

- [1] L. W. Alvarez, W. Alvarez, F. Asaro, H. V. Michel, *Science*, 1980, **208**, 1095-1108.
- [2] M. Kastner, F. Asaro, H. V. Michel, W. Alvarez, L. W. Alvarez, *Science*, 1984, **226**, 137-143.
- [3] A. Trinquier, J. L. Birck, C. J. Alegret, *Earth Planet. Sci. Lett.*, 2006, **241**, 780-788.
- [4] B. Schmitz, *Geochim. Cosmochim. Acta*, 1985, **49**, 2361-2370.
- [5] B. Schmitz, *Geology*, 1988, **16**, 1068-1072.
- [6] P. I. Premović, *Geochem. International*, 2009, **47**, 513-521.
- [7] H. Palme, *Geol. Soc. Am. Spec. Pap.*, 1982, **198**, 223-233.
- [8] A. M. Vickery, H. J. Melosh, *Geol. Soc. Am. Spec. Pap.*, 1990, **247**, 289-300.
- [9] P. I. Premović, B. Ž. Todorović, M. S. Pavlović, *Bull. Soc. Géol. France*, 2007, **178**, 411-421.
- [10] P. I. Premović, B. Ž. Todorović, M. N. Stanković, *Geol. Acta*, 2008, **6**, 369-382.
- [11] R. J. Walker, *Chem. Erde-Geochem.*, 2009, **69**, 101-125.
- [12] R. L. Rudnick, S. Gao, Elsevier, 2004, 1-64.
- [13] C. P. Strong, R. R. Brooks, S. M. Wilson, R. D. Reeves, C. J. Orth, X. Mao, L. R. Quintana, E. Anders, *Geochim. Cosmochim. Acta*, 1987, **51**, 2769-2777.
- [14] A. D. Anbar, K. J. Zahnle, G. L. Arnold, S. J. Mojzsis, *J. Geophys. Res.*, 2001, **106**, 3219-3236.

SPECTROSCOPIC INVESTIGATION OF MILO MILUNOVIĆ'S CANVAS PAINTING "THE INSPIRATION OF THE POET"

Lj. Damjanović¹, J. Đurđević¹, V. Andrić², M. Gajić-Kvaščev², M. Stojanović³,
T. Lazić⁴ and S. Nikolić⁴

¹*Faculty of Physical Chemistry, Studentski trg 12-16, 11158 Belgrade 118, PAC:105305;* ²*Institute of Nuclear Sciences "Vinča", P.O. Box 522, 11000 Belgrade;* ³*National Museum Belgrade, Trg Republike 1a, 11000 Belgrade;* ⁴*Faculty of Applied Arts, Kralja Petra 4, 11000 Belgrade, Serbia*

Abstract

A canvas painting by Milo Milunović "The Inspiration of the poet" was investigated in this work by multianalytical approach in order to identify pigments used by the artist as well as his painting technique. Results obtained by optical microscopy, fluorescence photography under UV light, energy dispersive X-Ray fluorescence (EDXRF) and FTIR Spectroscopy revealed following pigments on the painting: lead white, zinc white, cobalt blue, red pigment vermilion, green pigment viridian, as well as several earth colours. Optical micrographs show regions with no separation between layers, indicating that these areas were painted wet paint over wet paint.

Introduction

Milo Milunović, distinguished painter and professor at the Faculty of Fine Arts in Belgrade, during his stay in Paris made a copy of the Nicolas Poussin's painting "The inspiration of the poet". Milunović was a great admirer of Poussin's work and by copying the great artist Milunović wanted to show that he also has mastered the art of painting. Milunović made his painting in Louvre in 1926/27. "The Inspiration of the poet" painted by Milunović is 2.18 x 1.80 cm large and it has been permanently exhibited in the hall of the Faculty of Fine Arts in Belgrade since 1990. This painting will undergo restoration at the Faculty of Applied Arts in Belgrade, which provided a unique opportunity for physico-chemical investigation of the painting.

Traditionally, characterization of art-works has mainly been carried out by art-historians and restores by naked eye and by microscopic analysis. Information obtained by these methods, combined with consistent evidence of the art materials obtained by physico-chemical methods can help conservators and restores to decide upon the most appropriate procedures to be followed for the purposes of restoration. The scientists always have to balance the possible risks of damage against the profits that are obtained from the investigation of the artefact. Hence, the risk-of-damage/information ratio should be considered and optimized carefully for each investigation [1,2].

In this work home-made portable energy dispersive X-Ray fluorescence (EDXRF) spectrometer was used for investigation of well preserved regions of the painting, while paint chips obtained from the edges of the damaged regions were investigated by optical microscopy and FTIR spectroscopy. The aim of this study is to obtain information about pigments, binders and ground layer in investigated painting and to identify if any over-paintings have been made by the artist.

Methodology

For the nondestructive and nonsampling analysis of the painting portable home-made EDXRF spectrometer was used which consists of a Oxford X ray tube (Rh anode, max voltage 50 kV, max current 1 mA) and complete X-ray spectrometer (X123, Amptek Inc.) equipped with Si-PIN detector (6 mm²/500 μm, Be window 0,5 mil/12,5 μm thickness and 1,5 inch detector extension). Measuring head was mounted on the housing which enables moving along all three axes allowing analysis of large scale paintings like the one analyzed in this work. Experimental setup for all measurements was the same: distance between sample and X-ray tube was 16 mm, distance between sample and detector was 21 mm and angle between detector and X-ray tube was 45°. The X-ray tube voltage was altered to give two excitation working modes 22 keV and 40keV which enable detection of all elements heavier than Si. For all measurements current setup was 300 μA and 40s acquisition time in order to avoid any damage of the painting by intensive X-rays. Total of 45 points were analyzed on this painting including several points for a particular colour and few sample points on the backside of the painting for the characterization of preparation layer. The FTIR spectra of 10 samples of paint flakes taken from the edges of preexisting damaged regions of the painting were recorded on a FTIR Nicolet 6700 spectrometer using KBr pellets technique, in the wave number range from 4000 cm⁻¹ to 400 cm⁻¹. Cross sections of these 10 samples were recorded by optical Olympus BX51M microscope equipped with UV lamp Olympus U-RFL-T and U-MWUS3 and U-MWBS3 filters.

Results and discussion

An optical image of the cross section of sample taken from the blue region of the sky on the Milo Milunović's "The Inspiration of the poet" painting is shown in Fig.1. Thin layer of red colour is clearly visible indicating that thicker layer of blue pigment was painted over red one.

In order to obtain information about ground layer, five EDXRF spectra of the painting's backside were recorded. Obtained spectra were identical, which leads to the conclusion that the ground layer was homogeneously applied on the canvas. Ground layer consists mainly of Pb with traces of Ca. In addition, EDXRF spectra of the unused canvas from the front side, which was folded under the frame, have also shown presence of only Pb with traces of Ca. From these results it can be concluded that lead white and calcium carbonate were used for ground layer. Optical micrographs of all investigated cross sections show compact, white monolayer below pigment layers (see Fig.1.). Based on the homogeneity of ground

layer and the fact that it spreads on the entire canvas it can be assumed that canvas was bought with already prepared ground layer.



Fig. 1. The cross section from the blue region (sky)

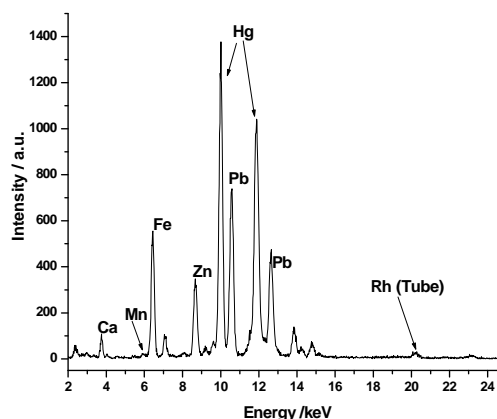


Fig. 2. EDXRF spectrum of the red region on the front side of the painting

The following pigments were identified: lead white [$2\text{PbCO}_2 \cdot \text{Pb}(\text{OH})_2$], zinc white [ZnO], cobalt blue [$\text{CoO} \cdot \text{Al}_2\text{O}_3$], red pigment vermilion [HgS], two different green pigments, one with Cr – viridian [$\text{Cr}_2\text{O}_3 \cdot 2\text{H}_2\text{O}$] and one without Cr – most probably green earth, as well as several other earth colours which were mixed with other used pigments, since amount of Fe differs on most of the investigated points, even within the same colour. Representative EDXRF spectrum of red colour from the front of the painting is shown in Fig. 2. Signals originating from Hg dominate the spectrum indicating use of HgS as red pigment. Signals originating from Pb and Ca are from the ground layer, while intensive signals of Fe and Zn indicate that red ochre and zinc white were used for hues in this particular region of the painting. In majority of EDXRF spectra Cr was detected in very small amounts. This result gives insight into painting technique of the artist - most probably Cr was present due to the mixing of earth colours with other pigments for achieving specific shades.

References

- [1] M. Ortega-Avilés, P. Vandenabeele, D. Tenorio, G. Murillo, M. Jiménez-Reyes, N. Gutiérrez, *Anal. Chim. Acta*, 2005, **550**, 164-172.
- [2] P. Dredge, R. Wuhler, M. R. Phillips, *Microsc. Microanal.*, 2003, **9**, 139-143.

MICRO-RAMAN AND INFRARED ANALYSIS OF MEDIÉVAL POTTERY FINDS FROM BRANIČEVO

I. Holclajtner-Antunović¹, D. Bajuk-Bogdanović¹, V. Bikić²,
M. Stojanović³ and J. Senćanski⁴

¹Faculty of Physical Chemistry, P.O. Box 47, 11158 Belgrade, Serbia

²Institute of Archaeology, Belgrade, ³National Museum Belgrade, Belgrade, Serbia

⁴Institute of General and Physical Chemistry, Belgrade, Serbia

Abstract

Medieval pottery shards from Braničevo (17 samples) were analyzed by infrared (IR) and micro-Raman spectroscopies. IR spectroscopy provided data for estimating the firing temperature and the basic mineralogical composition while micro-Raman spectroscopy was applied for the studying both the glaze and the body of shards. A total of 30 minerals were identified in the body of ceramics.

Introduction

Medieval town Braničevo has risen on the area of Roman town Viminacium, precisely on the hill by the left bank of Mlava River (near by present-day Požarevac). Because of its position – on the northern border of the Byzantine Empire, the area of Braničevo and its fortress had significant role during the Byzantine-Hungarian war affairs in the 12th century. Among archaeological finds, discovered in the medieval units, the most numerous are fragments of pottery. Except quantity, this pottery is very valuable because of its clear context and precise dating in the period between beginning of the 12th and the first half of the 13th century. The aim of this study is to investigate samples of table pottery made in different techniques and different decoration styles, imported from different Byzantine workshops.

Experimental

The chemical composition of the glaze and body of the selected samples was determined by SEM-EDS method (JOEL JSM 6460 LV, Oxford Inst. EDS). FTIR spectra were recorded on a Nicolet 6700 spectrophotometer, using KBr pellets technique in the wavenumber range from 4000 cm⁻¹ to 400 cm⁻¹. Micro-Raman spectra were recorded on DXR Raman Microscope (Thermo Scientific) using 532 nm laser with power on the sample 3-10 mW. Approximately fifty Raman spectra were acquired from different places on the surface of pellets prepared from 100 mg scratched powder of each ceramic shard. The Raman spectra of the glazes were recorded *in situ*.

Results and discussion

It is shown in literature that the position of the Si-O stretching vibration is temperature dependent and can be used for estimating of the firing temperature of

ceramics [1]. FTIR spectra of analyzed shards are characterized by prominent band due to the stretching Si-O mode in a range of 1085 and 1035 cm^{-1} . According to our simulation experiments by firing raw clay material, of chemical composition similar to our samples, with increasing firing temperature, obtained positions of stretching Si-O vibrations correspond to the temperatures between 700 and 900°C. Majority of samples were fired at temperature about 900°C. FTIR spectra have shown that few samples are produced from calcareous clays in accordance with results of chemical analysis.

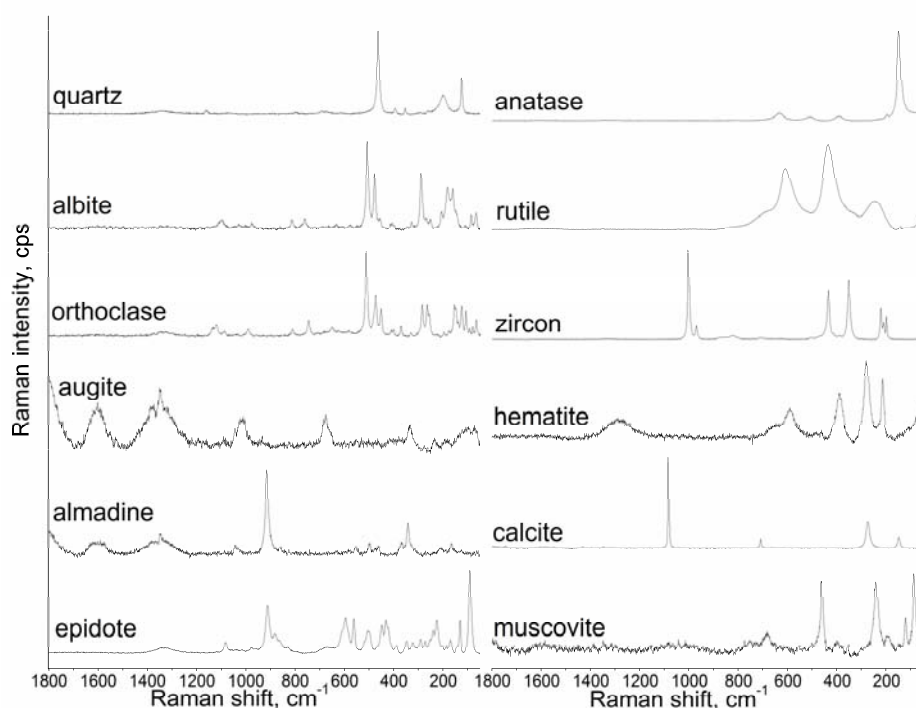


Fig.1. Raman spectra of minerals identified in the ceramics body.

Raman spectra of analyzed samples indicate very rich mineralogical composition. A total of 30 minerals were identified in ceramics body, spectra of some of them are presented in Fig. 1. The majority of spectra represent pure minerals which were identified by comparison with referent spectra from home made database. The most abundant mineral in the studied ceramics is quartz besides feldspars (albite, andesine, orthoclase and microcline), Fe oxides (hematite, magnetite and maghemite) and calcite in some samples. Anatase and rutile, polymorphs of TiO_2 , which have good Raman scatterer, are very abundant in spectra. Amorphous carbon, present in almost all samples in different quantities is produced from charring organic materials such as wood or bone. Apatite was identified by the characteristic peak of phosphate group (960 cm^{-1}) in some samples indicating charred bones as source of amorphous carbon. Carbon was

found in higher amount in samples which were possibly fired. Clay mineral of muscovite type mostly in dehydroxylated form was identified in almost all samples but with different abundance. Presence of Ca rich minerals such as augite, diopside, gehlenite and anorthite in analyzed samples are indication of their high temperature firing, not lower than 850°C. Titanite, CaTiSiO_5 , epidote, $\text{Ca}_2\text{Al}_2(\text{Fe}^{3+},\text{Al})(\text{SiO}_4)(\text{Si}_2\text{O}_7)\text{O}(\text{OH})$, forsterite, Mg_2SiO_4 , almandine, $(\text{Fe}^{2+})_3\text{Al}_2\text{Si}_3\text{O}_{12}$, andradite, $\text{Ca}(\text{Fe}^{3+})_2\text{Si}_3\text{O}_{12}$, actinolite, $\text{Ca}_2(\text{Mg},\text{Fe}^{2+})_5\text{Si}_8\text{O}_{22}(\text{OH},\text{F})_2$, enstatite, $\text{Mg}_2\text{Si}_2\text{O}_6$ and zircon, ZrSiO_4 were also identified in some of the samples but mostly in traces. Some of these minerals are not common minerals in clays and can be applied for provenance study.

For classification of analyzed glazed ceramics an approach proposed by Colomban [2], utilizing Raman spectroscopy of pottery and based on their composition, was used. The degree of polymerization, I_p , of SiO_4 units expressed by the area ratio of the bending and stretching envelopes (A_{500}/A_{1000}) was determined for all samples. Raman spectra of glazes are characterized by the higher intensity band of the stretching mode envelope between 1200 and 800 cm^{-1} . This behavior is observed in glassy networks containing a large amount of lead (lead-rich silicates) which breaks Si-O links, so the obtained structures are characterized by isolated and poorly connected tetrahedral, such as in the case of soft-paste porcelain and Islamic glazes. The calculated values of I_p between 0.17 and 0.40 indicate that the glazes are lead-rich and fired at temperatures about 700°C. The metals added in order to color glaze identified by SEM-EDX were: Cu, Mn, Fe, Ca, Zn and Ti.

Conclusion

According to the obtained variations in the mineralogical composition, the analyzed pottery shards were manufactured using raw material originating from different geological sites but with application of similar technological process.

References

- [1] S. Shoval, P. Beck, J. Therm. Anal. Calor., 2005, **82**, 609-616.
- [2] P. Colomban, A. Tournie, L. Bellot-Gurlet, J. Raman Spectrosc., 2006, **37**, 841-852.

VALIDATION OF OXIDATIVE STABILITY OF HIGH OLEIC SUNFLOWER OILS STUDIED BY PCA AND SWOT ANALYSIS

S. Ostojić, L. Pezo, S. Zlatanović, M. Kićanović, M. D. Pavlović, O.Kovačević and B. R. Simonović

*Institute of General and Physical Chemistry
Studentski trg 12/V, P.O. Box 551, 11000 Belgrade, Serbia*

Abstract

Cold pressed sunflower oils with enhanced oleic acid and tocopherol content, obtained from sunflower hybrides (NSH OL-1, NSH OL-2, NSH 2034, NSH 2073, NSH 2075, NSH 2076, Institute of Field and Vegetable Crops, Novi Sad), with genetically defined amount of saturated and unsaturated fatty acid and tocopherol, were analyzed by means of PCA and SWOT analysis of obtained oxidative parameters: peroxide value (PV), oxidation induction time (OIT), and oxidation onset temperature (OOT), prooxidative metal (Fe and Cu) concentration, unsaturated fatty acid composition, and tocopherol content. The PCA and SWOT analysis showed that oil from sunflower hybride NSH OL-2 has best characteristics according to oxidative stability, prooxidative metal concentration, tocopherol and fatty acid composition.

Introduction

The health benefits of oleic fatty acids and tocopherol are well documented [1]. That is why the protection of oil quality is an important objective of quality control in the oil industry [2]. Lipid oxidation is a major cause of deterioration of fats and oils leading to losses of quality and nutritional value [3]. Concerning vegetable oils, its trace metals composition is also an important factor for assesment oil quality. It is well known that metals affect their rate of oxidation and determinations of trace metals in vegetable oils is important. Trace metals like Fe and Cu directly increase oxidation rate of oil [4,5].

The aim of this work is to validate 6 sunflower oils from hybrids with genetically enhanced oleic acid and tocopherol content according to its obtained oxidative stability and prooxidative trace metal content, by using multivariate technique PCA (Principal Component Analysis) and the quantified SWOT (Strengths, Weaknesses, Opportunities and Threats) mathematical method, as the methods of solving multivariate problem [6,7].

Experimental

Cold pressed sunflower oils from sunflower hybrides (NSH OL-1, NSH OL-2, NSH 2034, NSH 2073, NSH 2075, and NSH 2076), with genetically defined amount of saturated and unsaturated fatty acids and tocopherol were obtained from Institute of Field and Vegetables Crops, Novi Sad.

Results of peroxide value (PV), oxidation induction time (OIT) and oxidation onset temperature (OOT) were obtained by differential scanning calorimetry (DSC) on Q

1000, TA instruments (Delaware, USA). The concentration of Fe and Cu were determined by GF AAS, atomic absorption spectrometer, model GBC Sens AA-GF (Dandenog, Australia) equipped with graphite furnace. Oil samples were digested in a microwave digestion unit (Milestone microwave laboratory system –START E-Shelton, USA) according to EPA method 3051A. Unsaturated fatty acid composition was determined by gas-chromatography after methylation and tocopherol content analysed by HPLC. PCA analysis involves a mathematical procedure that transforms a number of possibly correlated variables into a smaller number of uncorrelated variables called principal components. SWOT analysis represents the meaning of main factors represented in two-dimensional coordinate system.

Results and Discussion

Obtained oxidative parameters: peroxide value (PV), oxidation induction time (OIT) and oxidation onset temperature (OOT), prooxidative metal concentration Fe and Cu, unsaturated fatty acid composition, and tocopherol content of cold pressed sunflower oils with enhanced oleic acid, were analyzed by means of PCA and SWOT analysis.

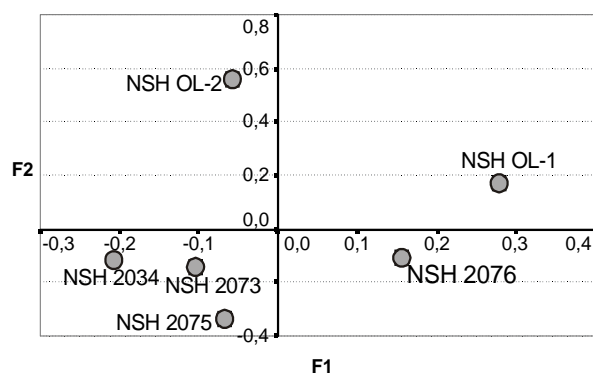


Fig.1. SWOT diagram of oils from sunflower hybrides

Abscissa on SWOT diagram (Fig. 1) is represented by scores of Cu, Fe, tocopherol and unsaturated fatty acids content (F1), while ordinate is represented by PV, OIT and OOT scores (F2).

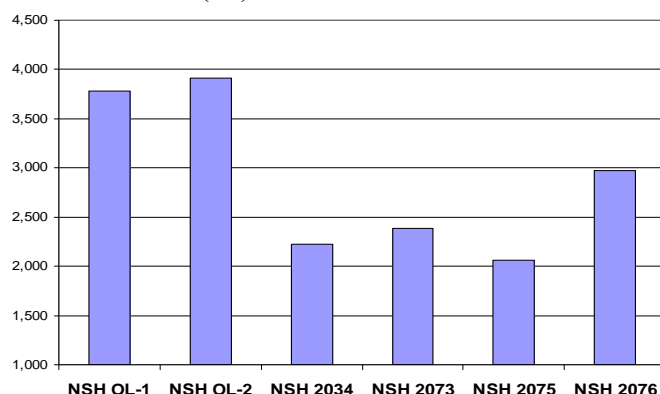


Fig. 2. Benchmark diagram, (intensity of SWOT vector) obtained by SWOT analysis of oils, showing the highestest value for oil from sunflower NSH OL-2.

From results shown on Fig. 1 and Fig. 2, it is possible to group NSH OL-1 and NSH OL-2, NSH 2075 and NSH 2076, NSH 2073 and NSH 2034 according to the position on SWOT diagram, and also according to their benchmark values. The oils of the first group are much better than others, for its benchmark values, and also because they occupy the first and the second quadrant. NSH 2076 showed good results.

Conclusion

The PCA and SWOT analysis showed that oil from sunflower hybrid NSH OL-2 has best characteristics according to oxidative stability, prooxidative metal concentration, tocopherol content and unsaturated fatty acids composition. It was shown that PCA and SWOT analysis are good tools for validation of oils concerning its crucial quality demands: oxidation stability, trace elements and antioxidant content, which directly impact on nutritional value of edible oils.

Acknowledgments

The present investigations are supported by Ministry of Science Technologies and development of Serbia; project No TR 20120.

References

- [1] D. Ni Eidhin, D O'Briene, *J. Food Sci. Technol.*, 2010, **45**, 444-452.
- [2] S. Arain, S. T. H. Sherazi, M. I. Bhangar, F. N. Talpur, S. A. Mahesar, *Thermochim. Acta*, 2009, **484**, 1-3.
- [3] J. Velasco, M. L. Andersen, L. H. Skibsted, *Food Chem.*, 2004, **85**, 623-632.
- [4] C. Benincasa, J. Lewis, E. Perri, G. Sindona, A. Tagarelli, *Anal. Chim. Acta*, 2007, **585**, 366-370.
- [5] R. Ansari, T. Gul Kazi, M. K. Jamali, M. B. Arain, M. Dowood Wagan, N. Jalbani, H. I. Afridi, A. Q. Shah, *Food Chem.*, 2009, **115**, 318-323.
- [6] A. Antonelli, M. Cocchi, G. Fava, G. C. Franchini, D. Manzini, A. Ulrici, *Anal. Chim. Acta*, 2004, **515**, 3-13.
- [7] J. Huang, H. Wium, K. B. Qvist, K. H. Esbensen, *Chemometr. Intell. Lab.*, 2003, **66**, 141-158.

PHYSICOCHEMICAL CHARACTERIZATION OF MINERAL MUD FROM SPA VRUJCI

I. Holclajtner-Antunović,¹ M. Pavlović,² B. Dojčinović,³ V. Tadić,⁴ M. Čutović,⁵
D. Bajuk-Bogdanović,¹ I. Arsić⁴ and D. Runjaić-Antić⁴

¹*Faculty of Physical Chemistry, P.O. Box 47, 11158 Belgrade,* ²*Institute of Nuclear Sciences Vinča,* ³*Center of Chemistry, Institute of Chemistry, Technology and Metallurgy,* ⁴*Institute for Medicinal Plant Research, Belgrade,* ⁵*School of Medicine, University of Belgrade, Serbia*

Abstract

Mineralogical and physicochemical analysis of healing mud from spa Vrujci was performed by ICP-OES analysis and FTIR and micro-Raman spectroscopy. The therapeutic effect of mud was improved by plant extracts implementation.

Introduction

Spa Vrujci is situated on the banks of the Toplica River. Thermal water (temperature 27°C) brings the finest mud (rich in minerals) from the depths. For therapeutic purposes peloid mud, combined with exposure to the sun, is used for different treatments (various rheumatic diseases, sciatica, varicous veins, and skin diseases). Medicinal mud consists of tiny, fine particles that enable close contact with the skin and strong therapeutic effect. These therapeutic effects are improved by plant extracts implementation.

For the explanation of the therapeutic effects it is indispensable to perform the complete analysis of mineral water and mud. In this study detailed mineralogical and physicochemical analysis of healing mud from spa Vrujci is performed.

Experimental

The healing mud from two sources in spa Vrujci was analyzed. The chemical composition was determined by inductively coupled plasma optical emission spectroscopy (ICP-OES), using a Thermo Scientific iCAP 6500 Duo ICP spectrometer. Prior to analysis by ICP-OES, the microwave-assisted acid digestion of samples was performed by means of ETHOS 1 Advanced Microwave Digestion System (Milestone, Italy) using HPR-1000/10S high pressure segmented rotor. The acid mixture consisting of 5 mL H₃PO₄ 85%, 3 mL HCl 37% and 0.5 mL HF 40% was used for the acid digestion. The sample dissolution procedures of microwave-assisted wet-acid decomposition and acid attack in open beaker were compared. The analytes were determined using multi-element matrix matched standard solutions. The accuracy of the method was checked by use of the standard reference material NCS DC73302, which has a chemical composition very close to the analyzed mud. Besides the main components, Si, Al, Fe, Ca, Mg, Ba, K, Na and Ti, essential and beneficial elements, Cu, Zn, Mn, Ni, Co and Se and heavy and toxic elements such as Pb, Cd, Hg, As, Sb, Tl, Bi and Te were determined.

The mineralogical composition of the mud was determined by FTIR and micro-Raman spectroscopy. FTIR spectra of the powdered samples, dispersed in potassium bromide and compressed into pellets, were recorded in the range of 4000–400 cm^{-1} , at 64 scans per spectrum, with 2 cm^{-1} resolution, using a Nicolet 6700 FTIR Spectrometer (Thermo Scientific). Micro-Raman spectra were recorded on a DXR Raman Microscope (Termo Scientific). The 532 nm line of a diode-pumped solid state high brightness laser was used as the exciting radiation and the power of illumination at the sample surface ranged between 3 and 10 mW.

Results and discussion

The water content of crude mud was 31,4 % and 32.6% for the source 1 and 2 respectively; pH of mud slurries was 7.8. The organic component was determined to be only about 5%. The microbiological analysis was performed as well.

The influence of matrix elements Al, Fe, Ca, Mg and K on determination of trace elements Cd, Co, Cr, Cu, Mn, Ni V and Zn was investigated. It is shown that matrix elements present in concentration corresponding to analysed mud have negligible effect between 1.5 and 6% on Cd, Zn and Ni.

The results of spectrochemical analysis determined for the main, minor and trace components are presented in Table 1.

Analysis of FTIR and micro-Raman spectra of crude mud from both source presented in Fig. 1, indicates that the most abundant mineral component is quartz. Broad band at 3440, and band in the region about 1630 cm^{-1} , assigned to water, is indication of some clay minerals which were identified as kaolinite and montmorinollite. Calcite identified by the broad band at 1433 cm^{-1} and sharp band at 877 cm^{-1} in FTIR spectra, is present in relatively low concentration in accordance with spectrochemical results (Table 1). On the basis of Raman spectra albite, hematite, rutile and anatase were also identified in healing mud.

Table 1. Chemical composition of main and trace components of healing mud

Source	Concentration, %									
	SiO ₂	Al ₂ O ₃	Fe ₂ O ₃	CaO	MgO	BaO	MnO	K ₂ O	Na ₂ O	TiO ₂
1	64.8	13.1	5.9	1.1	3.5	0.5	1.7	2.5	1.5	1.1
2	60.4	13.2	6.2	1.0	3.5	0.5	1.4	2.5	1.4	1.1
Source	Concentration, ppm									
	Cr	Cu	Zn	V	Co	Ni	Pb	Cd	Zr	Ce
1	235	52	116	92	13	122	52	32	69	91
2	238	50	120	100	13	122	58	31	74	92

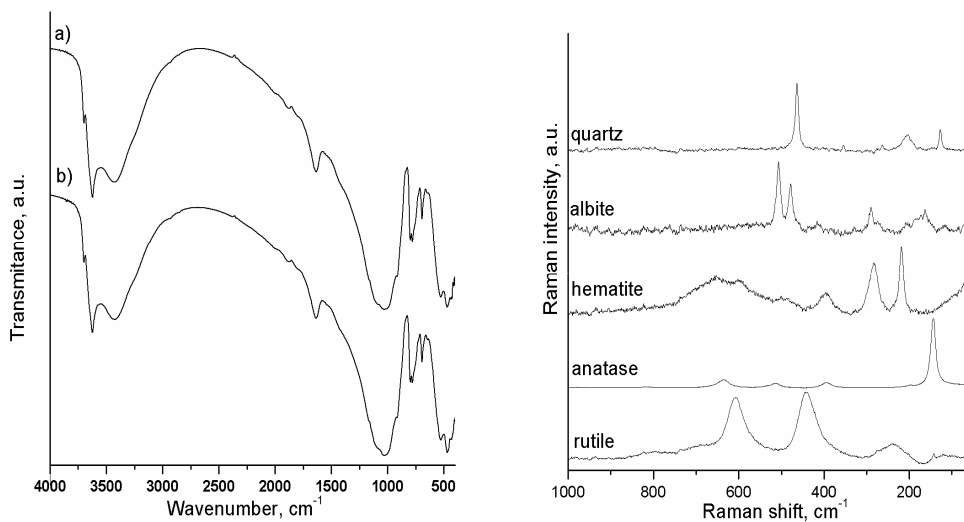


Fig.1. FTIR spectra of mud from: a) source 1 and b) source 2 (left) and micro-Raman spectra of minerals identified in mud (right).

On the basis of all presented results, it can be concluded that healing effects of mud from Vrujci is based on its very rich mineralogical composition and convenient morfological and textural characteristics. Therefore this mud after sterilization by γ radiation was used in combination with plant extracts for preparing of various healing phytopreparations. The pharmacological activity of the new preparations is determined by carefully selected plants extracts combination and their composition of bioactive substances.

PHYSICAL-CHEMICAL ANALYSIS OF ILLITE-KAOLINITE CLAYS

N. Marstijepovic,^{1*} D. Kovacevic² and Z. Potpara³

¹Ministry of Interior and Public Administration, Podgorica, Montenegro

²Ministry of Education and Science, Podgorica, Montenegro

³Fontis DOO, Podgorica, Montenegro

(e-mail: mpcltd@t-com.me)

Abstract

The aim of this paper was to determine of the influence the physical-chemistry content of illite-kaolinite clays on the microstructure of the sintered product. The sintering temperature of the samples was performed at the temperatures of 800°C, 900°C, 1000°C, 1100°C and 1200°C. The obtained results give contribute to the investigation for obtaining sintered product and defining physical-chemistry content of the samples of clays.

Introduction

During the sintering process the compact complex of the samples of small powder particles clays is transformed into solid body half crystal body. The new crystal phases, i.e. compounds formed by the solid state reactions during the sintering process, are given the physical-chemistry characteristic of the clay.

Experimental

Two types of illite-kaolinite clays (marked as "I") and kaolin (marked as "II")

Table 1. Chemical composition of clays of sample „I” and „II”

Oxides	Clay "I" Percentage by weight (%)	Clay "II" Percentage by weight (%)
SiO ₂	72,68	71
Fe ₂ O ₃	5,70	5,51
Al ₂ O ₃	10,98	10,55
CaO	0,48	1,42
MgO	0,70	0,62
Na ₂ O	0,31	0,45
K ₂ O	1,12	1,86
SO ₃	-	0,25
Ig. Loss	8,03	8,34

clays were used for sampling. The samples were shaped in a mould corresponding to a parallelepiped with the dimensions 7.7 cm x 3.9 cm x 1.6 cm and marked with the numbers 1, 2, 3, 4 and 5. The clays' analyses consisted of a determination of the mineral content with x-ray analysis, as well as chemical and granulometric analyses with a determination of the particle size distribution. The grain shape was determined microscopically.

Results and Discussion

The chemical analysis shows higher content of SiO₂, Fe₂O₃, Al₂O₃, MgO in

the of samples illite than in the of samples kaolin clay. It is also evident higher amount of CaO, Na₂O, K₂O and loss at higher annealing at the kaolin clay than in clay of samples illite (Table 1). The starting chemical content of clay dominantly influences the chemical content of the sintered product and its phase content. This influence is also important for total porosity and strength compressive of the sintering products (CO₂, SO₃ and firing loss), due to the emergence of new compounds in solid phase reaction. The sieve analysis the of samples (Table 2) determined the average particle size of the clays ($d_{mid.} = 9,62 \cdot 10^{-6}$ m, for kaolin „II” and $d_{mid.} = 10,47 \cdot 10^{-6}$ m for illite „I”), which brings to conclusion that “II” clays have smaller average particle size. This is certainly important for the influence on the microstructure of the sintered products, because this size significantly influences the grain size of the sintered products and their porosity. Results of the analysis indicate that kaolin clay has higher amount of carbonates and higher amount of SO₃ (1,42% and 0,25% related to 0,48% and 0% SO₃ in „I” clay).

The microstructure of the clay of samples illite and kaolin was shown in Figures 2–4. The analysis shows higher compactness in the samples illite within the temperature interval of 800°C - 1200°C, which is in accordance with the measured porosity (Figure 1). With the increase of the temperature of sintering sample „I” and sample „II” in interval of 800°C–1200°C it is visible the drop of porosity in both types of sintered products (samples), Figure 1.

Table 2. The results of particle size distribution of sample clay

The size of particles $1 \cdot 10^{-6}$ m	The share of particles, %, Sample „II	The share of particles, % Sample „I”
< 40	99.9	99.9
< 35	97.7	97.7
< 30	95.6	95.7
< 25	91.5	91.0
< 20	83.8	83.9
< 15	72.9	71.0
< 10	53.2	48.2
< 8	39.3	34.3

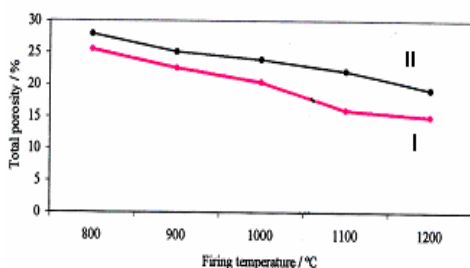


Fig.1. Total porosity of the firing temperature („I” and „II” clays)

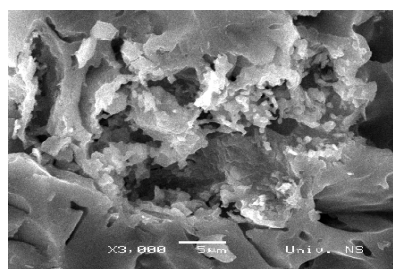


Fig.2. Microstructure of sintered product („II” clay, T= 1100°C)

Needle crystals of mullite (Figure 3) and crystals of anorthite (Figure 2) were also noticed. In that structure the crystals of mullite formed in glassy phase are noticed, and their dimension is $1 \cdot 10^{-6}$ m, or sometimes even smaller (Figure 4). It is important to mention that the mullite also influences the increase of the mechanical properties of the ceramic products. The presence of mullite is noticed

in every sample within the interval of 800°C to 1200°C in the samples illite over all the surface and volume of the samples, and they are less present in the observed interval of 800°C to 1200°C at the samples kaolin.

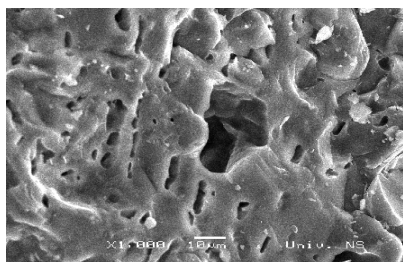


Fig. 3. Microstructure of sintered product („I” clay, T= 1200 °C)

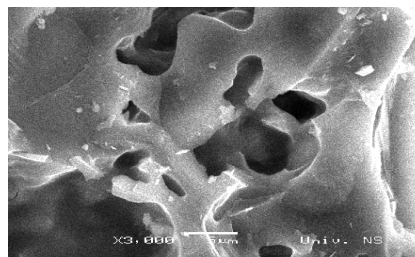


Fig.4. Microstructure of sintered product („I” clay, T= 1200 °C)

Conclusion

This paper gave contribute to the investigations on the sintering products and definition of physical-chemical properties sintered products. The variation of the temperature of sintering of sample „I” clay and „II” clay, within the interval of 800°C to 1200°C. The obtained results of the investigation provide the basis for the improvement of physical-chemical properties of the products on the basis of the raw material mixtures and confirm the importance of microstructure and raw material content.

The grain size distribution and the influence of the clays of sample „I” and „II”, on the microstructure, as well as the influence of the sintering, were determined. This is important because of the influence on the microstructure of the sintered samples, because this size has important influence on the grain size of the obtained products and their porosity. Other parameters also have influence on the microstructure, such as: chemical content, formation and isolation of gases, phase transformation and solid state reaction. We come to conclusion that the clays kaolin are used in the brick industry, and that the clays illite can be used for the production of fine ceramic (sanitary ceramic, ceramic dishes, porcelain and similar).

References:

- [1] M. Dondi, G. Guarini and M. Raimondo, Trends in the Formation of Crystalline and Amorphous Phases during Firing of Clay Bricks, Tile & Brick, 1999, 176-182.
- [2] M. Krgovic, N. Marstijepovic, S. Đurkovic, M. Ivanovic, R Zejak., M. Knezevic, Material in technology, 2007, **41**, 189-192.
- [3] N. Marstijepovic, Influence of the characteristics of clay from sites Bijelo Polje and Pljevlja on the properties sintered products, Master Thesis, University of Podgorica, Montenegro, 2008.

O
Education

SIR HENRY ROSCOE THE FIRST PHYSICAL CHEMIST IN ENGLAND

T. Halaši¹, S. Kalamković² and S. Cvjetičanin³

¹*Department of Chemistry, Faculty of Natural sciences and Mathematics, Novi Sad,
Trg Dositeja Obradovića 3, Novi Sad, Serbia, tibor.halasi@dh.uns.ac.rs*

²*Primary School "Prva vojvođanska brigada", Novi Sad*

³*Faculty of Pedagogy, Sombor*

Abstract

Sir Henry Enfield Roscoe is one of the foremost of English chemists; one of those who have played a distinguished part in the development of physical chemistry and chemical education. Roscoe's publications include: *Lectures on Spectrum Analysis* (1869) and *A New View of Dalton's Atomic Theory*. Roscoe has led an intensive correspondence, especially with German scientists: Robert Wilhelm Bunsen (1811-1899), Gustav Robert Kirchoff (1824-1887) and Sir Franz Arthur Friedrich Schuster (1851-1934). Roscoe's assistant, a native of Darmstadt, was Carl Ludwig Schorlemmer (1834-1892), with whom he has published scientific papers and books. Roscoe's most important works from the spectroscopic analysis are the determination of trace metals and microanalysis.

Introduction

Sir Henry Enfield Roscoe, was known as an English scientist on the field of General chemistry, Physical chemistry and Teaching chemistry. Roscoe's publications include, besides several books on basic chemistry which had a wide use and were translated into many foreign languages: *Lessons in Elementary Chemistry* (1866); *Lectures on Spectrum Analysis* (1869); *A Treatise on Chemistry* (the first edition which appeared in 1877-1892); *Chemistry* (1876); *A New View of Dalton's Atomic Theory*, with dr Arthur Harden (1896); and an *Autobiography, The Life and Experiences of Sir Henry Enfield Roscoe* (1906). Sir Arthur Harden (1865-1940) was an English biochemist. He shared the Nobel Prize in Chemistry in 1929 with Hans Karl August von Euler-Chelpin (1873-1956). The *Treatise on Chemistry* (3 vol., 1878-95), is written in collaboration with Carl Schorlemmer. Schorlemmer was professor of Organic chemistry in Manchester at Owens College and he became a member of the Royal Society in the UK in 1871 [1]. The mineral roscoelite was named after Sir Henry Enfield Roscoe, who first produced vanadium metal. **Roscoelite** is a green mineral from the mica group that contains vanadium. The chemical formula is: $K(V,Al,Mg)_2AlSi_3O_{10}(OH)_2$. Crystals of Roscoelite take on the monoclinic form, and are from the 2/m point group.

Research

Sir Henry Roscoe was known from his collaboration with Robert Wilhelm Bunsen in photochemistry and his study and analysis of Vanadium (V) compounds and the isolation of the metal, Caesium (Cs) and Thallium (Tl). His correspondence was widely spreaded in the world, and thanks to Ostwald, many are also archived. He corresponded with: Sir Benjamin Collins (1817-1880, known about determining the Atomic Weight of Graphite), Sir George Gabriel Stokes (1819-1903), Gustav Robert Kirchhoff, Hermann Kopp (1817-1892), Thomas Edward Thorpe (1845-1925), Hermann Ludwig Ferdinand von Helmholtz (1821-1894), James Prescott Joule (1818-1889), Thomas Henry Huxley (1825-1895), John Tyndall (1820-1893), Sir Charles Lyell (1797-1875) and Sir John Frederick William Herschel (1792-1871). With Herschel had excellent cooperation, as can be seen from the letter sent by Collingwood. Their letter refers to the metals Erbium and Didymium and the application of new photographic techniques in spectroscopy and astronomy.

In 1867, Roscoe corrected Berzelius's value for the atomic mass of Vanadium. Roscoe was awarded 1868. with the Bakerian Lecture for this work. The Bakerian Lecture (Henry Baker, 1698–1774, was an English naturalist) is a prize lecture of the Royal Society, a lecture on physical sciences.

Henry Roscoe also carried out researches on Niobium, Tungsten, Uranium, perchloric acid, and the solubility of ammonia. The critical insight that helped reduce the confusion came in 1857 as a result of a diversionary inquiry by Scottish professor William Swan (1818-1894). Hoping to reveal the mechanism by which light is other than that generated by the sun was produced, Swan observed the spectra of hydrocarbons placed in the colorless flame produced by means of a new laboratory burner devised by Bunsen and Roscoe. In the course of his investigation, Swan became intrigued by his observation that the outer portion of the lamp's flame flickered colorfully when anything, even the smallest dust specks passed through it. He wondered just how small an amount of a substance was required to create a colorful spectral display [2].

The short biography of Sir Henry Roscoe

Henry Roscoe was born in London in January 7, 1833. He died in December 18, 1915 in West Honey. In 1857, Roscoe was appointed to the chair of chemistry at Owens College, Manchester, where he remained until 1886 when the Victoria University had been established. From 1885 to 1895 he was MP (*Member of Parliament*) for Manchester South.

He served on several royal commissions appointed to consider educational questions, in which he was keenly interested, and from 1896 to 1902 was vice-chancellor of the University of London. He was knighted in 1884. Sir Henry Enfield Roscoe was awarded the Franklin Institute's Elliott Cresson (1796-1854) Medal in 1912.



Fig.1. Kirchhoff, Bunsen, and Roscoe (1862)

Acknowledgement

The authors wish to thank to Ministry of Sciences and technological advance of the Republic of Serbia for financial support this work with Programme 451-03-0295/2009-02 "Scientists and engineers who changed the awareness and understanding of mankind".

Literature

- [1] K. Heinig, Carl Schorlemmer, B. G. Teubner Verlagsgesellschaft, Leipzig, 1986, 17-34.
- [2] W. Ostwald, Sir Henry Roscoe, Ein Leben der Arbeit, Akademische Verlagsgesellschaft m. b. H., Leipzig, 1919, 18-145.

IVAN ALEKSEEVIC KABLUKOV

T. Halaši¹, S. Kalamković², B. Radulović³, M. Segedinac¹, R. Halaši⁴

¹*Department of Chemistry, Faculty of Natural sciences and Mathematics, Novi Sad, Trg Dositeja Obradovića 3, Novi Sad, Serbia, tibor.halasi@dh.uns.ac.rs*

²*Primary School "Prva vojvođanska brigada", Seljačkih buna 41a, Novi Sad,*

³*Department of Physics, Faculty of Natural sciences and Mathematics, Novi Sad*

⁴*DPNS, Novi Sad*

Abstract

Kablukov's creativity refers to the development of physical chemistry in Russia and the Soviet Union. His works are in the field of electrolytic dissociation in nonaqueous media. He also studied electric conductivity of ethers and hydrated ions in aqueous media. His experiments were referred to a saturated solution of hydrochloride acid and electrolytic dissociation. He had a rich correspondence with Arrhenius and other physical chemists, primarily with Wilhelm Ostwald and J. H. van't Hoff. His important works are from Thermochemistry, Electrochemistry and chemical equilibrium.

Introduction



Fig.1. I. A. Kablukov (1857-1942).

Creativity of I. A. Kablukov begins at Moscow University, where he defended his doctoral thesis "Contemporary Theory of solutions van't Hoff and Arrhenius in connection with learning of the chemical equilibrium" [1]. Many years later, 1936 Kablukov wrote a book about Van't Hoff. On the subject of his doctoral thesis collaborated with Kistjakovski (*Vladimir Alexandrovich Kistjakovski*, 1865-1952), known electrochemist [2].

Supporting correspondence and personal contacts Kablukov and other physical chemists got the impression that he must have excellent cooperation

between scientists and between eastern and western countries [2]. Although Kablukov in the world has not acquired such fame as Arrhenius, Willhem Ostwald (1853-1932) and Van't Hoff (Jacobus Henricus Van't Hoff, 1852-1911) [3] [4].

Capital work of I. A. Kablukov

Kablukov from 1904 to 1907 studied equilibrium in heterogeneous solutions systems of: $\text{Al}_2\text{Br}_6 \cdot \text{CuBr}_4$; $\text{Al}_2\text{Br}_6 \cdot \text{CuS}_4$; $\text{Al}_2\text{Br}_6 \cdot \text{SbBr}_3$; $\text{Al}_2\text{Br}_6 \cdot \text{SbJ}_3$ and the reaction of decomposition of the silver nitrate and potassium halides in the absence of solvents. With this problem except Kablukov were occupied Russian scientists Gavriil Gavrilovich Gustavson (1843-1908) and Alexey Lavrentjevich Potiljicin (*Алексей Лаврентьевич Потылицын*, 1845-1905). Gustavson and Kablukov were Butlerov's assistant. Later Kablukov worked at the Moscow Academy of Agriculture from 1892. to 1900, and his works are related to the catalytic reaction of aluminum halides. Kablukov and Sahonov studied binary alumina bromide organic compounds [5].

Notable opponents of the theory of electrolytic dissociation and the structure of organic compounds were: Dmitrij Ivanovich Mendeleev (1834-1907), *Nikolai Nikolaevich Beketov* (1827-1911), Dmitrij Petrovich Konovalov (*Дмитрий Петрович Коновалов*, 1856-1928), Flavian Mihailovich Flavickij (*Флавиан Михайлович Флавицкий*, 1848-1917), Henry Edward Armstrong (1848-1937), Pierre Eugène Marcelin Berthelot (1827-1907) and Isidor Traube (1860-1943). Isidor Traube was a great authority in physical chemistry who studied Capillary phenomena in chemistry and various properties of organic compounds. Isidor Traube was an excellent experimenter but had difficulty to prove the correctness of the theory of electrolytic dissociation.

Another large field with which deals Kablukov is Thermochemistry. He is the successor of the excellent Russian, later Swiss thermochemist, Vladimir Fedorovic Luginin (1911). Their common part of the determination of the enthalpy of chemical reaction was study of the reaction of bromine compounds and the hydrocarbons and their derivatives.

Short biography I. A. Kablukov

Ivan Alekseevic Kablukov (*Иван Алексеевич Каблуков*) was born in August 21, 1857, in Russian village Prusji (*Прусйы*). He graduated in 1876. at the Second Moscow classical school and enrolled at the Natural sciences department of physics and mathematics faculty of Moscow University. On the proposal of professor Vladimir Vasilevic Markovnikov (*Владимир Василевич Марковников*, 1838–1904), Kablukov was retained for two years at the Department of chemistry for the preparation of professorship. From 1881. to 1882. worked by Aleksandr Mihailovic Butlerov (1828 – 1886) at St. Peterburg University. Then continued to work at Moscow University and from 1889. he worked one year at the University of Leipzig, at Wilhelm Ostwald (1853–1932), under the direct supervision of Svante August Arrhenius (1859–1927). Since 1903 Kablukov was extraordinary professor at

Moscow University, where he worked until his death. From 1933 to early 1940's was the head of the Department of Inorganic and Analytical Chemistry [4].

In 1910. Kablukov received the title of Honored professor of Moscow State University, in 1928 he was elected to corresponding member of the Academy of Sciences of the USSR, and soon he was awarded the title of Honored worker of Science. Kablukov was died in May 05, 1942 in Taskend.

Conclusion

Kablukov emphasized the importance of the mathematical principles in Thermodynamics, Electrochemistry and in Physical chemistry, like in European Science revolution. He was the connection between the modern European Science and Russia.

Acknowledgement

The authors wish to thank to Ministry of Sciences and technological advance of the Republic of Serbia for financial support this work with Programme 451-03-0295/2009-02 "Scientists and engineers who changed the awareness and understanding of mankind".

References

- [1] M. Dzhua, Himiceskoje srodstvo v novesiji period, Istoria himii, Redactor V. M. Saharov, Izdatelstvo Mir, Moskva, 1965, 378-393.
- [2] T. Halaši, 2008, Svante August Arrhenius, in A. Antić-Jovanović (ed.), Physical Chemistry 2008, SPCS, Belgrade, 2008, **2**, 721-723.
- [3] T. Halaši, Contribution to the biography of the first Nobel prize winner and physical chemist, Jacobus Henricus Van't Hoff, in A. Antić-Jovanović (ed.), Physical Chemistry 2006, SPCS, Belgrade, 2006, **2**, 763-765.
- [4] E. Cohen, Van't Hoff's letter to Svante August Arrhenius, Amsterdam, 05.01.1890, Jacobus Henricus Van't Hoff und Wirken, Akademische Verlagsgesellschaft m. b. H., Leibzig, 1912, 277-278.
- [5] Yu. I. Solovjev, M. I. Kablukova, E. V. Kolesnikov, Ivan Alekseevic Kablukov, Izdatelstvo Akademiji Nauk SSSR, Moskva, 1957, 7-49.

DETERMINATION OF THERMODYNAMIC FUNCTIONS OF A COMMERCIAL ALKALINE MANGANESE DIOXIDE GALVANIC CELL

K. M. Krise and B. H. Milosavljevic*

*The Pennsylvania State University, Department of Chemistry
104 Chemistry Building, University Park, PA 16802, USA*

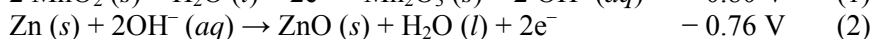
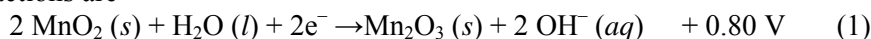
*corresponding author: bhm11@psu.edu

Abstract

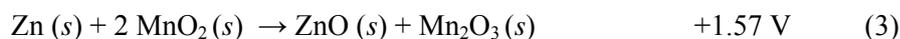
There is a need for a safe and cost effective experiment to address the thermodynamics of reactions occurring in electrochemical cells in the undergraduate chemistry curriculum. Such an exercise would serve to reinforce concepts traditionally taught in a chemical thermodynamic course. Here an experiment using a commercial alkaline-manganese dioxide galvanic cell to assess temperature dependence of emf is described. Thermodynamic parameters including free energy, enthalpy, entropy and equilibrium constant for the reaction in an alkaline-manganese dioxide galvanic cell can be determined with 1% error.

Theory

The alkaline-manganese dioxide galvanic cell has an anode composed of zinc powder (Zn) and a cathode composed of manganese dioxide (MnO₂), separated by a porous, highly absorbent and ion-permeable fabric, all of which is saturated with concentrated potassium hydroxide (KOH) providing high ionic mobility with a low freezing point [1, 2]. During discharge, manganese dioxide is reduced and the zinc becomes oxidized, while ions move through conductive alkaline electrolyte. The half-reactions are



with an overall electrochemical cell reaction



Spontaneous chemical reactions in the galvanic cell result in current and can be related to reaction thermodynamics as follows [3]. The relationship between the reaction Gibbs energy ($\Delta_r G$) and the electromotive force (emf), E , of the cell is given by

$$-vFE = \Delta_r G \quad (4)$$

where F is the Faraday constant ($9.6 \times 10^4 \text{ C mol}^{-1}$) and $v=2$ as a two electron transfer is required for the overall redox reaction. If the reaction reaches equilibrium, the equilibrium constant K can be determined.

$$\ln K = \frac{\nu FE^\circ}{RT} \quad (5)$$

The temperature coefficient of the standard cell emf dE°/dT , gives the standard entropy of the cell reaction. From the thermodynamic relationship $(\partial G/\partial T)_p = -S$ and equation 4:

$$\frac{dE^\circ}{dT} = \frac{\Delta_r S^\circ}{\nu F} \quad (6)$$

From the results of equations 4 and 6, the standard reaction enthalpy can be calculated

$$\Delta_r H^\circ = \Delta_r G^\circ + T\Delta_r S^\circ = -\nu F \left(E^\circ - T \frac{dE^\circ}{dT} \right) \quad (7)$$

Experimental

A commercial galvanic cell (Duracell® AA cell) was modified by soldering wires to both the positive and negative terminals. A Dewar with dry ice-chilled anhydrous ethanol (Sigma-Aldrich Chemical Company) was prepared for sub-zero temperature, an ice-deionized water bath was prepared for a zero-degree temperature reading, ice-chilled deionized water bath was prepared for below room temperature readings and a deionized water bath with a varistat (Cole Palmer Instrument Company) controlled heater was prepared for above room temperature readings. All baths were continuously stirred on a magnetic stirrer. Voltage was measured with a



measured with a Hewlett-Packard 34401A digital multimeter with ± 0.1 mV precision and temperature with a FLUKE 52-II digital thermometer with a precision of $\pm 0.1^\circ\text{C}$.

Fig.1. The experimental set-up for temperature and voltage measurements.

Performing the experiment

The commercial galvanic cell was attached to voltmeter leads and immersed in the appropriate bath. The cell was allowed to for 10 minutes prior to recording the voltage To maintain the appropriate temperature, ranging from -25°C to $+50^\circ\text{C}$, during equilibration, dry ice, ice or heat were added as needed. The presence of deionized water did not affect the measured cell voltage. Figure 2 shows typical student results, which gave a temperature coefficient (dE°/dT) (from the slope) for the galvanic cell equal to $(-1.24 \pm 0.01) \times 10^{-4} \text{ J C}^{-1} \text{ K}^{-1}$. Subsequently, from the relationships described by equations 4–7, the thermodynamic parameters for the

commercial alkaline-manganese dioxide galvanic cell were determined (Figure 1 insert).

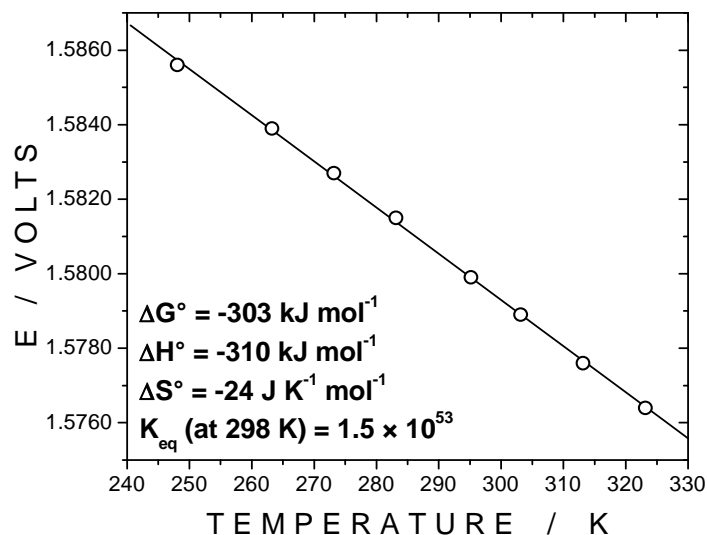


Fig.2. Cell potential dependence on temperature.

The design of the commercial alkaline-manganese galvanic cell used is not modified to an extent that alters the electrochemistry of the cell (private communication with Duracell® scientist), which is substantiated by the good agreement observed between the measured and predicted cell potential of the galvanic cell (1.57 V). The operative temperature range for the commercial alkaline-manganese dioxide galvanic cell used is -20°C to 54°C [2]. This experiment assesses the temperature dependence over the entire operational temperature range where previously published studies of zinc-silver oxide examined a more limited temperature interval [4]. The expanded temperature range results in a voltage difference of 10.0 mV, allowing undergraduate students to easily achieve an experimental error of 1%.

Literature

- [1] T. L. Brown, H. E. LeMay, B. E. Bursten and C. J. Murphy, Chemistry: The Central Science, 11th Ed., Pearson-Prentice Hall, 2009.
- [2] Duracell® Alkaline Manganese Technical Bulletin, 2005.
- [3] P. Atkins and J. De Paula, Physical Chemistry, 8th Ed., 2006, W.H. Freeman and Company.
- [4] M. J. Smith and C. A. Vincent. J. Chem. Educ., 1989, **66**, 529-531.

Author Index

AUTHOR INDEX

B. Abramović	143	T.P. Brdarić	69, 72, 343
A. Abu Rabi-Stanković	107, 283, 286	T. Brdarić	561
S. Adamović	576, 591	I. Bucur	585
B. Adnadjević	119, 167, 170	M. Budimir	292
M. Adzic	316, 337, 367	J. Budinski-Simendić	420, 482, 503, 506
J.I. Afanasjeva	40	J. Buha	453, 461
N. M. Agye	540	S. Cakić	482, 506
L. Aldous	6	M. Cakić	644
A. Amine	558	I. Cekić-Lasković	280
H. Amini Khoei	411	J. Charnay	464
M. Anachkov	164	M. Cindrić	60
T. Anđelković	81, 185, 641	M. Čip	221
V. Andrić	549, 667	G. Ćirić-Marjanović	146, 271, 432
S. Anić	215, 218, 224	G.A.P. Cirrone	376
M. Aničić	555	J. Colić	491
K. Antić	343	M. Čolović	325
V. V. Antić	476, 479	M.I. Čomor	143, 146
K. M. Antić	615	R.G. Compton.	6, 265
A. Antić-Jovanović	66	B. Cretin	464
M. Antonijević-Nikolić	635, 638	A. Čučulović	561
D. Arandžević	447	Ž. Čupić	200, 224, 236, 239
N.V. Arbuzova	155	M. Čutović	676
F. Arduini	9, 558	G. Cuttone	322, 376
N. Arsenijević	609	J. Cvetičanin	60, 549
I. Arsić	676	T. Cvetić-Antić,	379
W. Augustyn	649	M. Cvetinov	423, 591
M. Babić	343, 615	D. Cvetković	385
G. Bačić	364, 394	M. Cvijović	81, 515
D. Bajuk-Bogdanović	325, 432, 670, 676	N. Cvjetičanin	271, 295
M. R. Balaban	476	S. Cvjetičanin	685
P. Banković	107, 173, 286	A. Daković	588
Ya.E. Barbashin	155	Lj. Damjanović	667
L. Barloy	179	B. Damnjanović	87
Z. Baroš	113	A. Dangić	655, 658
Ch. Batchelor-McAuley	265	H. de Vries	179
N. Begović	215	N. Delić	358
M.V. Beljanski	331, 340, 343	M. Demajo	549
O. Bera	497, 500, 503	V. Despotović	143
H. Berta	482	A. Dietrich	529
N. Bibić	626	D. Đikanović	370
F.J. Bihelovic	152	J.M. Dimitrić Marković	69, 72, 87, 561
V. Bikić	670	A.S. Dimitrijević	152
S. Blagojević	218, 248, 623	D. Djikanović	319
C. Blanco	122, 125	D. Djokić	289
J. Bogdanović Pristov	370	J. Djonlagić	479
A. Bojić	185, 641	A. Djordjević	316, 337
V. Bojović	66	J. Djordjević	316, 337
N. A. Bošković-Vragolović	618	R. Đobrijević	289
N. Bošnjaković-Pavlović	325	M. Đogo	582
		B. Dojčinović	173, 676
		V. Dondur	444, 447

J. Donlagić	476	T. Halaši	685, 688
A. Doostmohammadi	411	R. Halaši	688
J. Đorđević	367	R. Hercigonja	444, 512
S. Đorđević	515	I. Holclajtner-Antunović	325, 670, 676
D. Đorđević	573	A. Horvat	334, 349, 373
M. G. Đorđević	661	B.D. Howes	3
A. Đordjević	367	J. Hranisavljević	626
S. Dragović	391	J. Huremović	573
D. Drakulić	334, 349, 373	A. Ignjatović	161, 361
M. Dramićanin	626	Lj. Ignjatović	567, 570, 573
E. Droghetti	3	A. Ignjatović	612
M. I. Đuran	638	D. Ilić	488
P. Đurđević	81	Lj. Ilić	644
P. Đurđević	515	B. S. Ilić	664
J. Đurđević	667	V. Iliev	164
J. Džopalić	618	E.D. Ivanchina	40
J. Džunuzović	473, 521	A.Z. Ivanović	233, 236, 283
N. Éber	423	M.B. Jadranin	72
I. Elaković	316	D. M. Jakovljević	485, 494, 518
A. Elias	164	Z. Jakšić	453, 461
A. Feis	3	R.M. Jankov	152
D. Filipović	382	I. Janković	143
A.R. Firooz	52	M. Janković	594
M. Franko	25	D. Janković	597, 603
E.V. Frantsina	40	Lj. Janković Mandić	391
M. Gabrovska	104, 128	V. Jašo	488, 506
M. Gajić-Kvašček	667	F. Javier del Campo	6
S. Gajinov	655, 658	S. Jelić	12
B. Gaković	417	M. Jelikić-Stankov	81
A. Gambaro	573	M. Jeremić	319
R. Garić-Grulović	618	D. Jovanović	104, 128, 131, 283
N. Gavrilov	277, 402	J. Jovanović	119, 167, 170
A. Gavrilović	43, 268	V.M. Jovanović	268, 292
W.J. Gehring	304	N. Jovanović	349
P. Glodić	289	Ž. Jovanović	358
D. Gođevac	612	V. Jovanović	420, 564
G. Đ.Gojgić	494	S. Jovanović	473, 521
G. Đ.Gojgić-Cvijović	485, 635	J. Jovanović	491
D. Golobočanin	251	M. Jović	441
S. Gómez-Ruiz	552	M. Jovičić	497, 500, 503
F. González	122, 125	M. Jovičin	518
K. Gopčević	343	N. Jović-Jovičić	107, 173, 286
S. Gorjanović	346	D. Jugović	441
S.N. Gorodsky	257, 260	I.O. Juranić	182
M. N. Govedarica	476, 479	Z. Kačarević-Popović	60, 110
S. R. Grujić	429	M. Kalagasidis Krusić	491
I. Gržetić	173	S. Kalamković	685, 688
I. Gutman	78	A. Kalauzi	319
J. Gvozdrenović	355	B. Kalinowski	529
S. Habibian Dehkordi	411	G. N. Kaluđerović	529, 552, 609
O. Hadač	209	M. R. Kaluđerović	552

L. Kashefi	52	M. Marinović-Cincović	420
J. Kecić	518	Lj. Marjanović	649
O. Keta	322, 376	L. Marjanović-Baković	652
M.A. Khakoo	66	Z.S. Marković	69, 72, 78
M. Kićanović	352, 521, 673	S. Marković	75, 78, 140
V. Kilibarda	515	V. Marković	200, 212, 239
J. Kiurski	576, 582, 591	R. Marković	280
D. Knežević	629	D. Marković	385
J.B. Knežević-Vukčević	331	G. Marković	420
M. Kohout	209	D. M. Marković	567, 570
Lj.Z. Kolar-Anić	49, 200, 212, 236	N. Marstijepović	679
S. Solarević	346	G. Matić	316
L. Korićanac	322, 376	S. Matijašević	426, 429
L.L. Korobitsyna	155	J. Matović	453, 461
I. Kostić 641		R. I. McCrindle	649, 652
D. Kovacević	679	S. Mentus	274, 295, 402
O. A. Kovačević	447, 673	K. Mészáros Szécsényi	482
B. T. Kovačević	447	M. Mičić	319
O. Kovačević 1	355	S. Mičić	606
V.V. Kozlov	155	A. Mihajlidi-Zelić	573
Y. Kozuki	564	Lj. Mihajlović	43
M. Kragović	426, 588	Z. Mijić	579
K. M. Krise	691	D. Mijin	600, 603
A. Krklješ	60, 110	J. Miladinović	37, 46
V. Krstić	125	Z. Miladinović	116, 346
J. Krstić	104, 110, 128, 591	M. Milenković	230, 233, 242
V. Krstić	122	M. M. Milić	467
D. Krstić	325	S. Milićević	426, 588
N. S. Krstić	661	Š. S. Miljanić	561
M. Kubíček	209	N. Miljević	251
J. Kuljanin-Jakovljević	399	N.B. Milojević	331
V. Kuntić	606	M. Milojević	432
A.V. Kurdiukov	260	S. Milonjić	626
M. Kuzmanović	66, 84	N. Milosavić	152
B. Kuzmanović	84	B. H. Milosavljević	691
R.R. Laher	66	M. Milošević	334, 349, 373
V. Lair	414	V. Milošević	426
M. Lazarević	597, 600	I. Milošević	567, 570
T. Lazarević-Pašti	328	T. Milovanović	573
T. Lazić	667	M. Milovanović	609
R. Leblanc	319	A. Milutinović-Nikolić	107, 173, 509
M. D. Lechner	473	D.M. Minić	43, 268, 280
M. Legetić	612	M. Mirković	597, 600, 603
G. Li Puma	164	M. Mitić	337, 316, 367
D. Lončarević	131, 224	Ž.J. Mitić	188
O. Lupan	414	N.S. Mitić	340
J.P. Maksimović	224, 230, 233	Ž. Mitić	644
D. Maksin	176	D. Mitić-Ćulafić	346
D. Maksin	444, 512	M. Mitrić	295
M. Marek	209	J. Mitrović	185
S. Marinović	509	M. Miyoshi	564

M. Mojović	161, 361, 612	I. Pašti	274, 277, 402
Z. Mojović	173, 283, 286	V.M. Pavelkić	69, 343
M. Momčilović	84, 391	V. V. Pavelkić	615
T. Momić	328	A. Pavicević	119
M.J. Montero	122	J. Pavličević	497, 500, 503
L. Morozova-Roche	301	M.D. Pavlović	346, 352, 355
D. Moscone	9, 558	R. Pavlović	644
T.M. Mudrinić	242	M. S. Pavlović	661
T. Mueller	529	M. D. Pavlović	673
M. Mujuru	652	M. Pavlović	676
B. Murić	438	G.M. Pavlović-Lažetić	340
D. Mutavdžić	313	N. Pejić	224, 230, 606
A. Nastasović	176, 509, 512	A. Perdigón	122
J.M. Nedeljković	17, 146, 435, 399	M. V. Pergal	476, 479, 521
Z. Nedić	137	M. Perišić	579
O. Nešković	60, 549	W. Perrie	417
V. Nevoral	209	C. Pesquera	122, 125
F.P. Nicoletti	3	M. Petković	87
Z. S. Nikolic	405, 408	B. Petković	292
G.M. Nikolić	188	I. Petrisor	585
R.S. Nikolić	188	I.Y. Petrov	134
B.J. Nikolić	331	B. Petrović	87
J. D. Nikolić	429	S. Petrović	137
Lj. Nikolić	488	V.P. Petrović	140
V. Nikolić	488	Z.D. Petrović	140
N. Nikolić	597, 600, 603	Dj. Petrović	289
R. Nikolić	641, 644	I. Petrović	322, 376
G. M. Nikolić	644	S. Petrović	334, 349, 373
N. D. Nikolić	661	N. Petrović	340
S. Nikolić	667	L. Pezo	352, 355
D. Nikolova	128, 131	L. Pezo	673
A. Nováková	227	M. Pfeffer	179
T. Novaković	137	R. Pjanović	618
M. Novaković	346	D. Popović	37, 46
M. Nyitrai	313	N. Popović	322
A.M. O'Mahony	6	R. Poreba	503
D. Ž. Obadović	423, 591	N.I. Potkonjak	248
N. Ogrinc	532	T.N. Potkonjak	248
J. O. Okonkwo	540	N. I. Potkonjak	623
A. Onjia	512, 549	Z. Potpara	679
B. Ortiz	122, 125	P. I. Premović	661, 664
B. Ostojić	63	S. Prendžov	500, 503
S. Ostojić	479, 673	M. Prica	576
N.M. Ostrovskii	93	M. Purenović	185, 641
S.B. Pajović	382	J. Quintana Calvo	558
G. Palleschi	558	G. Rackov	316
B. Panić	438	S. Radenković	78
N. Pannetier	179	Č. Radenović	358
D. Pantelić	438	R. Radičević	497, 500, 506
D.K. Papadopoulos	304	I. Radin Oros	591
R. Paschke	529, 552	M. Radoičić	143, 146

M. Radojčić	316, 337, 367	B. Šljukić	271
J. Radonić	582	G. Smulevich	3
V. Radonjić	119	D. Šojić	143
K. Radotić	313, 319, 370	J.B. Sortais	179
M. Radović	185	S.P. Sovilj	292, 626
B. Radulović	688	A.M. Spasić	254
L. Rafailović	43	I. Spasojević	161, 361
S. Rajšić	579	L. Spasov	104, 131
A. Rakić	432	M. Špírková	503
V. Rakić	512	D. Stanisavljev	230, 242, 331
S. Rakovsky	101, 164	V. Stankov	81
S. Randjelović	479	M. J. Stankov	515
D. Ranković	84	I.M. Stanković	49
D. Relić	573	M. Stanković	128
T. W. Remmerbach	552	D. Stanković	289, 597
R. Rigler	304	G. Stanković	358
A. Ringuedé	414	M. N. Stanković	664
Z. Ristanović	402	I. Stanojević	334, 349, 373
M. M. Ristić	408	S. Stanojlović	355
I. S. Ristić	482, 488, 506	J. Stašić	417
A. Ristić-Fira	322, 376	Pl. Stefanov	131
J. Rogan	268	J. R. Stefanović	485, 494, 518
E.I. Rogers.	6	J. Stevanic	370
Z. Rogić	361	S. Stevanović	268, 292
Lj. Rožić	137	D. Stoilković	497
D. Runjaić-Antić	676	M. Stoilković	549
A. Sabovljević	555	M. Stojanović	423, 667, 670
A. Sadegh Bigham	411	J. N. Stojanović	429
M. Saeri	411	Z. Stojanović	441
L. Salmén	370	A. Stojić	579
S. Samaržija-Jovanović	420	I. Stojković	271, 295
Z. Sandić	176	D. Stojšić	515
Z. Šaponjić	143, 146, 399	A. M. Stortini	573
A. Savić	313	G. Stupar	37
G. Schmitz	193, 236	Lj. Suručić	176
I. Schreiber	24, 209, 227, 245	D. Sužnjević	346
L. Schreiberová	221, 227, 245	Lj. Svilar	81
B. Šećerov	364	J.C. Tabet	81
M. Segedinac	688	V. Tadić	676
M. Sekhula	540	Lj. Tanasić	488
Ž. Sekulić	588	S. B. Tanasković	635, 638
A. Semnani	52	A.R. Tančić	57
J. Senčanski	670	M. Tanić	394
M. Shopska	128	O.N. Temkin	257, 260
V. Simendić	506	K. Tenchev	104
D. Simeonov	128, 131	L. Terenius	304
I. Simic	337, 316, 367	Ž. Lj. Tešić	447
J. Simonović	370	M. Todorović	37, 46
B. R. Simonović	655, 658, 673	D. M. Todorović	464, 594
C. Sirlin I	79	M. Tomašević	555
S. D. Škapin	441	A. Đ. Tomašević	629

S. Lj. Tomić	615	A.V. Vosmerikov	149, 155, 158
M. B. Tošić	429	L.N. Vosmerikova	158
M. Trgo	588	M. Vranješ	399
S. Trifunović	603, 609	S. Vranješ	597
D. Tripković	268	S. Vranješ-Đurić	600
A. Tripković	268	M. M. Vrvić	485, 494, 518
Đ. Trpkov	60	I. Vučinić	161
Đ. Trpkov	549	D. R. Vučinić	629
M. Trtica	84	G. Vučković	635, 638
M. Trtica	417	A. Vujačić	626
B.G. Tryasunov	134	J. M. Vujić	609
M. Turk Sekulić	582	M. Vujković	230, 233, 242
T. Tuvić	274	N. Vukelić	104
P. Tzvetkov	104	N. Vukić	488
M. Ugrina	588	I. Vukoje	435
E.V. Urzhumova	149	V. Vukojević	212, 304
D. Uskoković	75, 441	N. Vukojević Medvidović	588
A. Vajda	423	Z. Vuković	107, 137, 509
V. Vasić	325, 328, 626	F. Wakai	405
G. Vasile	585	K. G. Watkins	417
D. Vasiljević	438	G. Wiederrecht	626
T. Veber	245	J. Xu	319
L.M. Velichkina	149	R. Yamanaka	564
D.V. Veličković	152	V.I. Zaikovskii	155
N. Veličković	334, 349, 373	J. Zakrzewska	116, 379
J. Veljković-Giga	618	J. Žakula	322, 376
Lj. Veselinović	75, 441	S.P. Zhuravkov	155
A.M. Veselinović	188	V. D. Živanović	429
D. Veselinović	561	M. Živić	379
A. Veselinović	644	J.V. Živković	188
D. Vilotić	567	Lj. S. Živković	414
D. Vilotić	570	V. Živković-Radovanović	635, 638
V.D. Vitnik	182	M. Žižić	379
Ž.J. Vitnik	182	S. Zlatanović	355, 673
V. Vodnik	435, 473, 521	J. Zlatković	382
M. Vojinović Miloradov	582	B. B. Zmejkovski	609
E. Volanschi	280	M. Žunić	107, 173, 286
V. Volarević	609	C. M. Zvinowanda	540

Participating institutions

Analytical Chemistry Department, University of Sarajevo, 71000 Sarajevo,	573
Applied Systems SRL, Str. Pictor Ion Negulici, no.1, Craiova, Dolj	585
BioCenter, Martin-Luther-University Halle-Wittenberg, Weinbergweg 22, D-06120 Halle, Germany	529
Biomaterials Group, Department of Materials Engineering, Isfahan University of Technology, Isfahan, Iran	411
Biozentrum, and Institut für Chemie, Martin-Luther-Universität Halle-Wittenberg, Germany; ^c Department of Chemistry	552
Boreskov Institute of Catalysis SB RAS, Novosibirsk, Russia	155
CBRN Training Centre, Kruševac, Serbia	394
Center for Chemistry ICTM, Njegoševa 12, Belgrade, Serbia	280, 635
Center for Nanoscale Materials, Argonne National Laboratory, Argonne, Illinois 60439-4831	626
Center of Chemistry, Institute of Chemistry, Technology and Metallurgy Institute for Medicinal Plant Research, Belgrade	676
Center of Microelectronic Technologies and Single Crystals, Institute of Chemistry, Technology and Metallurgy, University of Belgrade, Belgrade, Serbia	453
Centro Nacional de Microelectrónica (CNM-IMB), CSIC, Campus Universidad Autónoma de Barcelona, 08193, Bellaterra, Barcelona, Spain.	6
CEST Centre of Electrochemical Surface Technology, Viktor-Kaplan-Strasse 2, A-2700 Wiener Neustadt, Austria	268
Chemistry department, National Research Tomsk Polytechnic University, Lenina avenue 30, Tomsk, Russia	40
CMT-Department of Chemistry, University of Belgrade, Njegoševa 12, Belgrade, Serbia	152
Departamento de Química Inorgánica y Analítica, E.S.C.E.T., Universidad Rey Juan Carlos, Madrid, Spain	552
Department of Basic Sciences, School of Veterinary Medicine, University of Shahrekord, Shahrekord, Iran	411
Department of Biochemical and Medical Sciences, State University of Novi Pazar, Vuka Karadžića bb, Novi Pazar 36300, Republic of Serbia	69, 72, 78
Department of Biochemistry, Institute for Biological Research "Siniša Stanković", University of Belgrade, 142 Despot Stefan Blvd., 11060 Belgrade, Serbia	316
Department of Biology, University of Novi Pazar, Vuka Karadžića bb, 36300 Novi Pazar, Serbia.	379
Department of Biophysics, Faculty of Medicine, University of Pécs, Pécs, Hungary	313
Department of Cell Biology, Biozentrum, University of Basel, Basel, Switzerland	304
Department of Chemistry, Faculty of Natural Sciences and Mathematics, University of Priština, 38220 Kosovska Mitrovica, Serbia	292
Department of Chemistry, Faculty of Science, University of Kragujevac, Kragujevac, Republic of Serbia	87, 609
Department of Chemistry, Faculty of Sciences, University of Novi Sad, Trg D. Obradovića 3, 21000 Novi Sad, Serbia	143

Department of Chemistry, Institute of Chemistry, Technology and Metallurgy, Studentski Trg 14, 11000 Belgrade, Serbia	529, 609
Department of Chemistry, Physical & Theoretical Chemistry Laboratory, University of Oxford, South Parks Road, Oxford, OX1 3QZ, UK	6, 265
Department of chemistry, University of Isfahan, Isfahan, IRAN	52
Department of Chemistry, University of Johannesburg, Bunting Rd, Auckland Park, 2006, Johannesburg, South Africa	652
Department of Chemistry, University of Limpopo, PO Box 235, Medunsa, 0204, South Africa	540
Department of Chemistry, University of Miami, Coral Gables, FL 33124, USA	319
Department of Chemistry, University of Shahrekord, P.O.Box 115, Shahrekord, IRAN	52
Department of Chemistry, Faculty of Natural sciences and Mathematics, Novi Sad, Trg Dositeja Obradovića 3, Novi Sad, Serbia	685, 688
Department of Clinical Neuroscience, Karolinska Institutet, CMM L8:01, 17176 Stockholm, Sweden	212, 304
Department of Clinical Sciences, School of Veterinary Medicine, University of Shahrekord, Shahrekord, Iran	411
Department of Environmental Sciences, Jožef Stefan Institute, Jamova 39, SI-1000 Ljubljana, Slovenia	532
Department of Environmental, Water & Earth Sciences, Faculty of Science, Tshwane University of Technology, Private Bag X680, Pretoria, 0001, South Africa	540
Department of Inorganic Chemistry and Catalysis, Debye Institute, Utrecht University, The Netherlands	402
Department of Materials Engineering, University of Shahrekord, Shahrekord, Iran	411
Department of Medical Biochemistry and Biophysics, Karolinska Institutet, Stockholm, Sweden	304
Department of Medical Biochemistry and Biophysics, Umeå University, Umeå, 90781 Sweden.	301
Department of Molecular Biology and Endocrinology, VINCA Institute of Nuclear Sciences, Belgrade, Serbia	316
Department of Oral, Maxillofacial and Facial Plastic Surgery, University of Leipzig, Germany	552
Department of Organic Chemistry Faculty of Technology and Metallurgy, University of Belgrade, Karnegijeva 4, P.O. Box 3503, 11120 Belgrade, Serbia	603, 600
Department of Physics, California State University, Fullerton CA 92834, U. S. A	66
Department of Physics, Faculty of Natural sciences and Mathematics, Novi Sad	423, 688
Department of Theoretical Physics and Physics of Condensed Matter 020/2, Vinča Institute of Nuclear Sciences, University of Belgrade, 11001 Belgrade, Serbia	212
Dipartimento di Chimica "Ugo Schiff", Università di Firenze, Via della Lastruccia 3, I-50019 Sesto Fiorentino (FI), Italy	3
Dipartimento di Scienze e Tecnologie Chimiche, Università di Roma Tor Vergata, Via della Ricerca Scientifica, 00133 Rome, Italy	9, 558

DPNS, Novi Sad	688
DSM research, Life sciences Geleen, The Netherlands	179
ECHEM Kompetenzzentrum für Angewandte Elektrochemie GmbH, Wiener Neustadt, Austria	43
Ecosystem Design, Institute of Technology and Science, University of Tokushima, Japan	564
Ecosystem Engineering, Graduate school of Engineering, University of Tokushima, Japan	564
Environmental Sciences Department, Ca' Foscari University of Venice, 30123 Venice, Italy	573
Faculté des Sciences Appliquées, Université Libre de Bruxelles, CP165/63, Av. Roosevelt 50, 1050 Bruxelles, Belgium	236
Faculté des Sciences et Techniques, B.P.146, Mohammadia, Morocco	558
Faculty of technology, Novi Sad	420
Faculty of Agriculture, Nemanjina 6, Belgrade – Zemun 11080, Serbia	479, 476
Faculty of Agronomy, University of Kragujevac, Cara Dušana 34, 32000, Čačak, Serbia	609
Faculty of Applied Arts, Kralja Petra 4, 11000 Belgrade, Serbia	667
Faculty of Applied Sciences, Université Libre de Bruxelles, CP165/63, Av. F. Roosevelt 50, 1050 Brussels, Belgium.	193
Faculty of Biology, Belgrade University, Belgrade, Serbia	331, 346
Faculty of Chemistry, University of Belgrade, P. O .Box 118, 11158, Serbia	51, 152, 182, 280, 292, 447, 494, 518, 573, 588, 603, 626, 635, 638,
Faculty of Chemistry, University of Bucharest, Romania	280
Faculty of Electronic Engineering, Department of Microelectronics University of Nish, Nish, Serbia	405, 408
Faculty of Forestry, University of Belgrade, Kneza Višeslava 1, Belgrade, Serbia	176, 567, 570
Faculty of Mathematics, Belgrade University, Belgrade, Serbia	340
Faculty of Medicine, Bulevar dr Zorana Djindjića 81, 18000 Niš, Serbia	188, 644
Faculty of Mining and Geology, Djušina 7, 11 000 Belgrade, Serbia	635
Faculty of Pedagogy, Sombor	685
Faculty of Pharmacy, University of Belgrade	81, 224, 218, 227, 230, 515, 638, 635, 606

Faculty of Physical Chemistry, Studentski trg 12–16, 11000 Belgrade, Serbia	43, 49, 66, 69, 72, 87, 104, 119, 137, 167, 146, 161, 170, 200, 212, 224, 227, 230, 233, 236, 239, 242, 268, 271, 274, 277, 280, 295, 325, 331, 358, 361, 364, 394, 402, 432, 444, 447, 491, 512, 561, 567, 570, 573, 612, 670, 667, 676
Faculty of Science and Mathematics, Mladena Stojanovića 2, 78000 Banja Luka, Bosnia and Herzegovina	476, 641, 644
Faculty of Science and Mathematics, Višegradska 33, 18000 Niš, Serbia	81, 185, 188
Faculty of Science Kragujevac	81, 78, 140
Faculty of science, Lole Ribara 29, Kosovska Mitrovica	420
Faculty of Science, Mladena Stojanovića 2, Banja Luka, Republic of Srpska (BIH)	176
Faculty of Science, Trg D. Obradovića 3, University of Novi Sad, Serbia	482, 591
Faculty of Science, University of Kragujevac, P.O.Box 60,34000 Kragujevac	638, 515
Faculty of Technical Sciences, Department of Graphic Engineering and Design, Trg Dositeja Obradovica 6, Novi Sad, Serbia	591
Faculty of Technical Sciences, Trg Dositeja Obradovića 6, Novi Sad, Serbia	576, 582
Faculty of Technology and Metallurgy, 4 Karmegijeva St.,11000 Belgrade, Serbia	46, 37, 268, 429, 473, 476, 479, 491, 521, 615, 618
Faculty of Technology and Metallurgy, Skopje, Macedonia	500, 503
Faculty of Technology, Bul. cara Lazara 1, University of Novi Sad, Serbia	352, 355, 482, 488, 503, 497, 500, 506
Faculty of Technology, Bulevar Oslobođenja 1, University of Nis, Serbia	482, 488, 506
Faculty of Technology, University of Nis, 16000, Leskovac, Serbia	385, 644
FEMTO-ST Institut, Université de Franche-Comté, CNRS, ENSMM, UTBM, 32 Avenue de l'Observatoire, F-25044, Besançon Cedex France	464
Fontis DOO, Podgorica, Montenegro	679
Galenika, a.d., Batajnički drum b.b., Zemun, Serbia	618
Group of Inorganic Chemistry, University of Cantabria E-39005 Santander, Spain.	122, 125
Higher Education School of Professional Studies - Belgrade Polytechnic, Brankova 17, 11000 Belgrade, Serbia	113
Higher Technological School of Professional Studies, 15000 ŠabaC, Serbia	638, 635
HIPOL a.d., Odžaci, Serbia	93
Holding Institute of General and Physical Chemistry, Studentski trg 12-16, Belgrade 11000, Serbia	479, 521
IChTM – Centre of chemistry, University of Belgrade, Studentski trg 12–16, 11000 Belgrade, Serbia	573, 485, 518, 494

IChTM – Department of Catalysis and Chemical Engineering, Belgrade, Njegoševa 12	218, 131, 137, 224, 107, 173, 233, 286, 509
IChTM-Department of Chemistry, Njegoševa 12, Beograd, Serbia	509, 512
ICTM Center for Chemistry, Njegoševa 12, Belgrade, Serbia	173, 182
ICTM- Center for Chemistry, Polymer Department, Studentski trg 12-16, Belgrade, Serbia	176
ICTM, Department of Electrochemistry, University of Belgrade, Njegoševa 12, Belgrade, Serbia	268, 292
ICTM-Center of Chemistry, Studentski trg 12-16, 11000 Belgrade, Serbi	476, 521, 479
IHTM – Institute of Microelectronic Technologies and Single Crystals Njegoševa 12, Belgrade University, Belgrade, Serbia	461
IHTM-Center of Chemistry, University of Belgrade, Studentski trg 12-16, 11000 Belgrade, Serbia	473
INEP-Institute for the Application of Nuclear Energy, Banatska 31b, Zemun, Serbia	561
INFN Laboratori Nazionali del Sud, via S. Sofia 62, Catania, Italy	322, 376
Innovation center of the Faculty of Chemistry, University of Belgrade, Studentski trg 12, Belgrade, Serbia	152
Innventia, Box 5604, SE-114 86 Stockholm, Sweden	370
Institut de chimie UMR7177CNRS/Université de Strasbourg, France	179
Institut für Chemie, Martin-Luther-Univerität Helle-Wittenberg, Kurt-Mothes-Straße 2, 06120 Halle, Deutschland	609, 529
Institut of General and Physical Chemistry, Beograd, Studentski trg 12/V, Serbia,	352, 355
Institute “Kirilo Savić“, Vojvode Stepe 51, 11 000 Belgrade, Serbia	343, 615
Institute for Chemistry, Technology and Metallurgy, University of Belgrade, Department of Catalysis and Chemical Engineering, Sector of Chemical Engineering, Karnegijeva 4., Belgrade, Serbia	618
Institute for Chemistry, University of Osnabrück, Barbarastraße 7, 49069 Osnabrück, Germany	473
Institute for Multidisciplinary Research, Kneza Višeslava 1, 11000 Belgrade, Serbia	35, 161, 313, 361, 379, 370
Institute for Multidisciplinary Research, University of Belgrade, Bul. Despota Stefana 142, 11000 Belgrade, Serbia	319
Institute for Multidisciplinary Research, University of Beograd, P.O.Box33, 11030 Belgrade, Serbia	464
Institute for Sensor and Actuator Systems – ISAS, Vienna University of Technology, Vienna, Austria	453
Institute for Technology of Nuclear and Other Mineral Raw Materials, P. O. Box 390, 11 000 Belgrade, Serbia	254, 426, 429, 588
Institute for the Application of Nuclear Energy – INEP, University of Belgrade, Banatska 31b, 11080 Belgrade, Serbia	391
Institute of Chemistry, Technology and Metallurgy, Njegoševa 12, 11000 Belgrade, Republic of Serbia	72
Institute of Archaeology, Belgrade	670
Institute of Botany, Faculty of Biology, University of Belgrade, Takovska 4, 11000 Belgrade, Serbia	379, 555

Institute of Catalysis, Bulgarian Academy of Sciences, Acad. G. Bonchev str., bl. 11, Sofia 1113, Bulgaria,	131, 101, 104, 128, 164
Institute of Chemical Technology Prague, Department of Chemical Engineering and Center for Nonlinear Dynamics of Chemical and Biological Systems, Technická 5, 166 28 Prague 6, Czech Republic	24, 245
Institute of Chemical Technology, Prague, Department of Chemical Engineering, Department of Mathematics and Center for Nonlinear Dynamics of Chemical and Biological Systems, Technická 5, 166 28 Prague 6, Czech Republic	209
Institute of Chemistry Technology and Metallurgy, University of Belgrade, Department of Catalysis and Chemical Engineering, Njegoševa 12, 11000 Belgrade, Serbia	239, 104, 128
Institute of Chemistry, Technology and Metallurgy, Njegoševa 12, 11000 Belgrade, Serbia	612, 552
Institute of Chemistry, Technology and Metallurgy, University of Belgrade, Studentski trg 14-16, 11 000 Belgrade, Serbia	63, 200, 215, 236, 283, 346
Institute of General and Inorganic Chemistry, Bulgarian Academy of Sciences, Sofia 1113, Bulgaria	104, 128, 131
Institute of General and Physical Chemistry, Belgrade, Serbia	215, 331, 346, 116, 248, 379, 340, 343, 447, 673, 655, 658, 623
Institute of Macromolecular Chemistry, Academy of Sciences, Czech Republic	503
Institute of Medicinal Chemistry, School of Medicine, University of Belgrade, Serbia	325
Institute of Nuclear Science "Vinča", P. O. Box 522, 11001 Belgrade, Serbia	364, 376, 367, 473, 521, 661, 667, 417
Institute of Petroleum Chemistry SB RAS, Tomsk, Russia	155, 158, 149
Institute of physics, P.O. Box 68, Pregrevica 118, Belgrade, Serbia	567, 570, 438, 555, 579
Institute of Sensors and Actuators, Faculty of Electrical Engineering & Information Technology, TU Vienna, Austria	461
Institute of Solid State Chemistry & Mechanochemistry, Kemerovo Division, SB RAS, 18 Sovetsky Ave, Kemerovo 650000, Russia	134
Institute of Technical Sciences of the Serbian Academy of Sciences and Arts, Knez Mihailova 35/IV, 11000 Belgrade, Serbia	75, 441
Institute Vinča, Radiation and Environmental Protection Department, P.O. Box 522, 11001 Belgrade, Serbia	594
Jaroslav Černi Institute for Development of Water Resources, Jaroslava Černog 80, 11226 Belgrade, Serbia	251
Jozef Štefan, Institute, Jamova 39, Ljubljana, Slovenia	441
Kirilo Savić Institute, Vojvode Stepe 51, 11000 Belgrade, Republic of Serbia	69, 72
Kuzbass State Technical University, 28 Vessennyaya St., Kemerovo 650026, Russia	134
Laboratory for Geochemistry, Cosmochemistry and Astrochemistry, Department of Chemistry, University of Niš, P.O. Box 224, 18000 Niš, Serbia	661, 664
Laboratory for Radioisotopes, Vinča Institute of Nuclear Sciences P.O.Box 522, 11001 Belgrade, Serbia	289

Laboratory for Radioisotopes, Vinča Institute of Nuclear Sciences, P. O. Box 522, 11001 Belgrade, Serbia	600, 603, 597
Laboratory of Biomedical Optics, Swiss Federal Institute of Technology, Lausanne, Switzerland	304
Laboratory of Molecular Biology and Endocrinology, Institute of Nuclear Sciences “VINČA”, University of Belgrade, P.O. Box 522, 11001 Belgrade, Serbia	334, 349, 373, 382
Laboratory of Physical Chemistry, Institute of Nuclear Sciences “Vinča”, University of Belgrade, Belgrade, Republic of Serbia	87
Laboratory of Theoretical Physics, INN Vinča, P.O.Box 522, 11001 Belgrade, Serbia	467
LECIME, UMR 7575 CNRS– ENSCP, Paris, France	414
Maize Research Institute, Zemun Polje, S. Bajića 1, Belgrade-Zemun, Serbia	358
Materials and Structures Laboratory, Tokyo Institute of Technology, Japan	405
Materials Science Division, Argonne National Laboratory, Argonne, IL 60439, USA	268
Medical Faculty, Martin-Luther-University Halle-Wittenberg, Weinbergweg 22, D-06120 Halle, Germany	529
Military Medical Academy, Cmotravska 17, 11000 Belgrade, Serbia	515, 391
Military Technical Institute, Belgrade, Serbia	43
Mining and Metalurgy Institute Bor, 19320 Bor, Serbia	122, 125
Ministry of Education and Science, Podgorica, Montenegro	679
Ministry of Interior and Public Administration, Podgorica, Montenegro	679
MP Biomedicals, LLC, 3 Hutton Center, Santa Ana, CA 92707, USA	319
National Museum Belgrade, Belgrade, Serbia	670, 667
PCI “Zdravlje Actavis Co.”, Vljakova 199, 16000 Leskovac, Serbia	644
Pliva, Zagreb, Croatia.	60
Primary School “Prva vojvođanska brigada”, Novi Sad	685, 688
Regional Agency of Environmental Protection, Craiova, Dol	585j
Research Institute for Solid State Physics and Optics of the Hungarian Academy of Sciences, H-1525 Budapest, P.O.Box 49, Hungary	423
Research Institute of High-Voltage Equipment, Tomsk Polytechnic University, Tomsk, Russia	155
SANU, Knez Mihajlova 35, Belgrade, Serbia	402
School of Medicine, University of Belgrade, Serbia	676
School of Medicine, University of Belgrade, Višegradska 26, Belgrade, Serbia	343
Scientific Veterinary Institute “Novi Sad” Rumenački put 6, Novi Sad, Serbia	518
Serbian Academy of Science and Arts, Knez Mihajlova 35, 11158 Belgrade, Serbia	274, 295, 408
Spitzer Science Center, California Institute of Technology, M/S 314-6, Pasadena, CA 91125, U. S. A.	66
Technical University of Moldova	414
The Faculty of Applied Ecology, Singidunum University, Lazarevački drum 13, Belgrade, Serbia	567, 570
The Institute of Chemical Technology Prague, Department of Chemical Engineering and Center for Nonlinear Dynamics of Chemical and Biological Systems, Technická 5, 166 28 Prague 6, Czech Republic	221

The Medical Faculty, University of Kragujevac, Svetozara Markovića 69, 34000 Kragujevac, Serbia	609
The South African Nuclear Energy Corporation (Ltd) Ltd. PO Box 582, Pretoria 0001, RSA	649
The University of Nottingham, University Park Nottingham NG7 2RD, United Kingdom	164
Tigar, Nikole Pašića 213, Pirot	420
Town Planning Institute of Belgrade, Palmotićeveva 30, 11000 Belgrade, Serbia	248
Tshwane University of Technology, Department of Chemistry, Arcadia Campus, P O Box 56208, Arcadia 0007, Pretoria, Republic of South Africa	652
Tshwane University of Technology, Department of Chemistry, Pretoria, 0001, RSA	649
University "Vasile Alecsandri" of Bacau, Str. Marasesti no.157, 600115	585
University of Belgrade - Faculty of Physical Chemistry, P.O. BOX 276, 11001 Belgrade, Serbia	84
University of Belgrade, Faculty of Mining & Geolog, Djušina 7, 11000 Beograd, Serbia	655, 658
University of Belgrade, Faculty of Agriculture, Belgrade, Serbia	512
University of Belgrade, Faculty of Chemistry, Studentski trg 12-16, Belgrade, Republic of Serbia	173
University of Craiova, IMST Faculty, Drobeta Turnu Severin	585
University of Johannesburg, Department of Chemistry, Auckland Park, 2006 Johannesburg, RSA	649
University of Liverpool, Department of Engineering, Liverpool, UK	417
University of Nova Gorica, Laboratory of Environmental Research, Vipavska 13, SI-5000 Nova Gorica, Slovenia	25
University Pier and Marie Curie (UPMC) Paris	81
VINCA Insitute of Nuclear Sciences, University of Belgrade, P.O. BOX 522, 11001 Belgrade, Serbia	17, 57, 60, 84, 110, 143, 146, 176, 251, 325, 322, 328, 337, 399, 414, 420, 435, 444, 512, 549, 626

NovoLab d.o.o

BRITISH-SERBIAN COMPANY

PRIMORSKA 22
11000 BEOGRAD
nola@EUnet.rs
www.novolab.com

Tel: (011) 7293 534
7293 758
6974 125
Fax: (011) 6974 128

Ovlašćeni zastupnik:

 **STANHOPE-SETA**

analiza ulja, goriva i maziva ...

JENWAY

*pH metri, konduktometri, plameni fotometri,
spektrofotometri ...*

CASELLA

*instrumenti za ispitivanje uslova radne i životne sredine i
meteorologije ...*

ADAM

Adam Equipment Co. Ltd

laboratorijske vage ...

CARBOLITE

laboratorijske žarne peći, inkubatori i sušnice ...

Spectrolab

atomska absorpcija, FT-IT spektrometri, hromatografi, plameni fotometri ...

Paragon Scientific Ltd

referentni standardi za naftne proizvode ...



Promochem

*referentni standardi za farmaceutsku
Industriju ...*

PHARMA
TEST

*oprema za ispitivanje u farmaceutskim
laboratorijama ...*

